Subsidence Detection by PSInSAR Based on High Resolution TerraSAR-X Images

Guoxiang Liu, **Hongguo Jia**, **Rui Zhang**, **Minyi Cen**, **and Tonggang Zhang**
Department of Surveying Engineering, Southwest Jiaotong University
Chengdu 610031, China

Abstract— Land subsidence is a major concern for land use planning and geological risk assessment. Here we describe a persistent scatterer interferometric synthetic aperture radar (PSInSAR) method for subsidence detection. The Jinghai County in Tianjin (China) is selected as the study area, which has been sinking due to the overuse of groundwater. The time series of high resolution SAR images collected by the X-band radar sensor onboard the satellite TerraSAR-X (TX) are utilized for the PS detection, PS networking and subsidence estimation. The test results show that the high resolution of TX SAR images can dramatically increase the PS density, especially in the built-up areas. Subsidence information can be extracted on the individual objects like buildings, street lamps and manhole covers, and on the linear engineering structures like the Jinghu high speed railway. The TX PSInSAR with short radar wavelength (3.1 cm) is quite sensitive to vertical motion, and the derived subsidence measurements are in good agreement with the *in situ* data taken by optical leveling.

1. INTRODUCTION

The spaceborne interferometric synthetic aperture radar (InSAR) has been developed as a unique technology for deformation mapping [1–4]. The recent imaging radar sensor advance resulted in a remarkable improvement of spatial resolution about one order of magnitude. This makes it possible to monitor the stability of individual buildings and linear engineering structures such as high speed railway (HSR). To extend applicability of InSAR, many research efforts have been made in recent years to analyze the temporal evolution of deformations using time series of SAR images [1–6]. As a further improvement, our previous paper [5] presented a PS-networking method in which all PS points within a given threshold of distance (e.g., 1 km) are connected to form a freely connected network (FCN). The advantage of the FCN approach used in our PS solution is that finer details of deformations can be derived.

With advent of high resolution SAR imagery, it is still necessary to explore the PSInSAR technique aiming at extending the range of applicability. In this paper, we present the FCN-based PSInSAR method applied to the time series of SAR images collected by TerraSAR-X (TX) over the Jinghai County in Tianjin (China), where subsidence has been occurring due to the overuse of groundwater. The experimental results show that the dense PSs can be identified with the high resolution TX images. The PSInSAR method can be employed to extract subsidence on both large and small scales.

2. STUDY AREA AND DATA SOURCE

As shown in the inset of Fig. 1, we select the Jinghai County (one of 18 counties/districts of Tianjin) as the study area. It is located at the southwestern part of Tianjin and has been reported as one of the severest subsiding areas in recent years. Being close to the Bohai Bay, the study area belongs to the alluvial plains of the Haihe River and has flat relief with elevation of 2–3 m. For PSInSAR analysis, we used 15 SAR images acquired by the X-band (wavelength of 3.1 cm) radar sensor onboard TX along descending orbits between 27 March and 30 September, 2009.

Table 1 lists the 15 images with acquisition dates. All the images were collected at an incidence angle of 41° in HH polarization. The original data were provided by Infoterra as single look complex (SLC) images with pixel spacing of 1.36 m in range and 1.90 m in azimuth. The 105 interferometric pairs were formed by full combinations and processed for the PS solution. There are 10%, 35%, 58% and 68% of pairs with spatial baseline shorter than 10, 60, 100, 120 m, respectively. The maximum spatial and temporal baselines are 318.9 m and 187 days, respectively, while the minimum ones are 3.6 m and 11 days.

Figure 1 shows the SAR amplitude image (4750×5500 pixels, equivalent to about $9.5 \times 11\,\mathrm{km}^2$) of the study area averaged from all images. The overhead bridge of Jinghu HSR being under construction is visible as a slender rectangle on the right side of the image. The leveling subsidence

Table 1: TerraSAR-X images used in this study.

No.	Acquisition dates	No.	Acquisition dates	No.	Acquisition dates
1	20090327	6	20090521	11	20090806
2	20090407	7	20090623	12	20090828
3	20090418	8	20090704	13	20090908
4	20090429	9	20090715	14	20090919
5	20090510	10	20090726	15	20090930

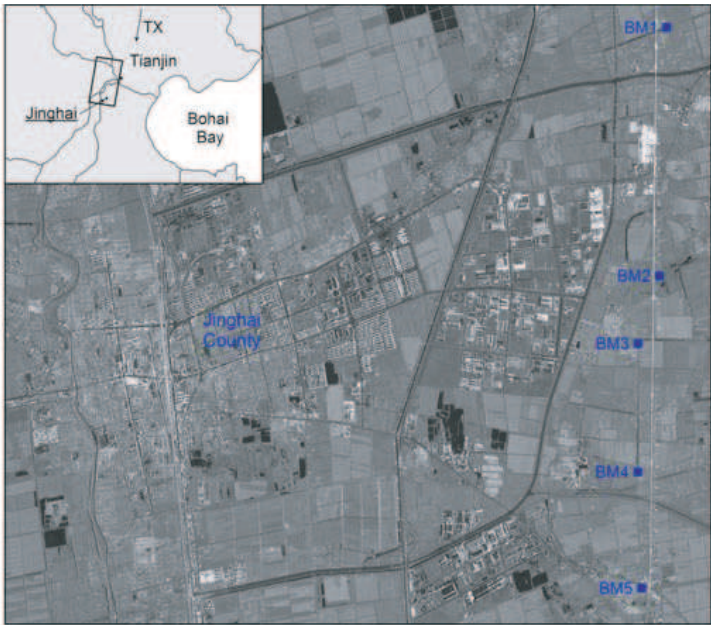

Figure 1: The TerraSAR-X amplitude image of the study area averaged from 15 images.

data provided by the Jinghu Company is used to evaluate the quality of PSInSAR results. As shown in Fig. 1, there are 5 leveling points (BM1-BM5) available for this study, which are deployed along the Jinghu HSR.

3. METHODOLOGY OF SUBSIDENCE ESTIMATION

Although the approach of the FCN-based PS-InSAR has been explained in [5], we brief here the key procedures for the extraction of linear subsidence. They include PS detection, FCN-based PS networking, differential phase extraction, data modeling and parameter estimation by function optimization, and adjustment of the PS network by a weighted least squares (LS) solution.

Before commencement of detecting the PS candidates, the TX image acquired on 23 June 2009 is selected as the reference image space, and the remaining 14 TX images are co-registered and resampled into the reference. Using the time series of 15 SAR amplitude samples at each pixel, we follow the strategy by Ferretti et al. [1] to identify the PS candidates on a pixel-by-pixel basis. Any pixel with amplitude dispersion index (ADI) less than 0.25 is determined as a PS candidate. After selection of all the PS candidates, the neighboring PSs are connected to form a strong network. Any two PSs are linked only if their distance is less than a give threshold (1 km used in this study), thus forming a FCN.

For each interferometric pair, the initial interferogram is derived by a pixel-wise conjugate multiplication between the master and slave SLC image. Both the precise orbital data and the external SRTM digital elevation model (DEM) are then used to remove flat-earth trend and topographic effects from each initial interferogram, thus resulting in 105 differential interferograms. The 105 differential interferometric phases (DIP) at each PS are extracted according to its pixel coordinates.

The data modeling for subsidence analysis is based on the idea of neighborhood differencing along each link of the FCN. Similar to the differential GPS, the differential modeling in the PS

network is important for largely canceling out the spatially correlated biases or errors due to the atmospheric phase delay and the uncertainty in orbital data. For each interferometric pair, the DIP increment between two PSs of each link can be modeled as a function of several parameters of the radar system and the interferometric pair, the subsidence-velocity increment and the elevation-error increment of each link. 105 observation equations are obtainable for each link with use of 105 interferometric pairs, which can be combined to form an objective function related to the entire model coherence (MC). Both the subsidence-velocity increment and the elevation-error increment of each link can be solved by searching a pre-defined solution space to maximize the MC value [1].

Prior to further analysis, the quality of PS network must be first assessed using as the measure the MC value of each link. If the MC value is less than 0.45, the relevant link is discarded for the subsequent LS solution, thus possibly resulting in some isolated PSs that are also removed from the list of PS candidates. The reduced PS network can be treated by a weighted LS adjustment in which the MC value of each link is used for weighting. The geometric inconsistency in the network can be eliminated to derive the most probable values of subsidence rates at all the valid PS points. In order to obtain a unique LS solution, at least a reference PS point with known subsidence rate should be employed. For this study area we selected the leveling point BM5 (Fig. 1) as the reference point of the PS network.

4. EXPERIMENTAL RESULTS

Figure 2 shows the distribution of 464680 true PSs that were determined for the study area. The number of valid PSs is about 4500 per square kilometer. Very dense PSs appear in the built-up areas due to the availability of many man-made and natural hard objects. However, very sparse PSs appear in the farming parcels due to their random surface changes with time, e.g., tilling, crop growth, and leaf fluttering caused by wind effects. The density of PSs in the built-up areas is largely associated with the spatial resolution of SAR imagery. The 2-m resolution of TX SAR imagery makes it easy to distinguish one by one the individual objects such as buildings, bridges, iron fences, and rocky or concrete slope of highway. Many PSs are available along the road networks. Interestingly, our field investigation indicates that most of the PSs correspond to the street lamps or the manhole covers. This demonstrates that the high resolution of TX SAR imagery can dramatically increase the PS density, particularly in the urban areas, which can not be achieved with the moderate resolution of SAR systems (e.g., ERS-1/2 case). It should be noted that few PSs can be picked out on the concrete or asphalt road surface. This is because the road surface is still smooth even with respect to the short radar wavelength (3.1 cm) of TX.

The high density of PSs in the study area is also attributed to the uniform height of the buildings and their roof materials. The uniform height may decrease the possibility of geometric distortion (i.e., shadow, layover and foreshortening) in SAR imagery, thus keeping satisfactory spatial correlation between two epochs of radar acquisitions. In tradition, most of the buildings in

Figure 2: The distribution of PSs identified in the study area.

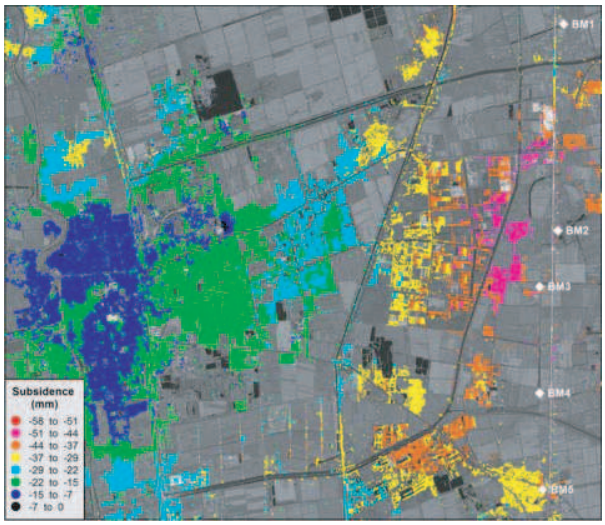

Figure 3: The classed map of subsidence at all PSs in the study area.

Jinghai are constructed with clay or metal tile roofs. Such kind of roofs may be considered as the perfect reflectors of the incident radar signals, thus guaranteeing temporal correlation even over months to years.

As a remark, the dense PSs can be identified along the northern portion of the overhead bridge of Jinghu HSR. This is because the primary engineering construction in this part was completed in early March, 2009, and the structural surface was not altered during the SAR acquisitions. The remaining parts were constructed with frequent surface changes during the SAR acquisitions, thus resulting in few PSs available. It is however expected that the high-resolution PS technique may be applied to monitor the linear structures like Jinghu HSR once they are in operation.

The FCN was first created by linking the adjacent PSs identified with a distance threshold of 1 km. The subsidence-rate and elevation-error increments of every link in the FCN were then estimated by maximizing the model coherence with use of multi-temporal differential phases extracted from 105 interferometric pairs. The subsidence rates at all the true PSs were finally estimated by the weighted LS solution in which the *in situ* subsidence measurement of the leveling point BM5 (Fig. 1) was used as a constraint.

We converted the PSInSAR subsidence rates into the absolute subsidence values using the time interval corresponding to the two epochs of leveling observations which were performed in March and September, 2009, respectively. Fig. 3 shows the distribution of PSInSAR subsidence values at all the valid PSs, which were estimated over the time period of six months. The subsidence can be obtained for each of the individual objects, including buildings, bridges, iron fences, street lamps, and manhole covers. The subsidence accumulated in half a year within the study area ranges between 0 and 58 mm, and the uneven sinking has been occurring. The large subsidence being up to 40 to 50 mm appears in the east part (suburb) of the study area, which is close to the Jinghu HSR and the manufacturing centers. The northern portion of Jinghu HSR declined about 22 to 32 mm in the six months. In the wide residential areas, the subsidence values range between 10 and 30 mm.

To assess the quality of the PS solution, we utilized four leveling points (i.e., BM1, BM2, BM3, and BM4) as the check points. The PSInSAR subsidence value at every check point was first interpolated from its adjacent PSs, and then compared with its leveling subsidence value. The maximum and minimum discrepancies are 7 and 4 mm, respectively. The root mean square of the discrepancies is ± 5 mm. This indicates that the FCN-based PS-InSAR method is accurate and reliable for subsidence estimation.

5. CONCLUSION

This paper describes a FCN-based PSInSAR method for subsidence detection on time series of high resolution TX SAR images. Selecting the Jinghai County in Tianjin (China) as the study area, the subsidence was detected using the 15 TX SAR images through several procedures, e.g., PS detection, PS networking and weighted LS adjustment. The experimental results show that the high resolution of TX SAR images can dramatically increase the PS density, particularly in the built-up areas. Subsidence information can be extracted on the individual objects such as buildings, street lamps and manhole covers, and on the linear engineering structures such as the Jinghu high speed railway. The TX PS-InSAR with short radar wavelength (3.1 cm) is quite sensitive to vertical motion, and the derived subsidence measurements are in good agreement (RMS = ± 5 mm) with the leveling data.

The detailed subsidence map derived from the high resolution TX SAR images is valuable not only for making the management policy of groundwater extraction, but also for optimizing the deployment of leveling points to monitor regional subsidence. Moreover, the subsidence information along the Jinghu HSR is useful for guiding engineering construction and designing compensation strategies.

ACKNOWLEDGMENT

This work was jointly supported by the National Natural Science Foundation of China under Grant 40774004, the Key Research Project of Ministry of Railways of China under Grant 2008G031-5, and the Program for New Century Excellent Talents in University under Grant NCET-08-0822. The authors would like to thank InfoTerra and USGS for providing TerraSAR-X SAR images and SRTM DEM, respectively.

REFERENCES

1. Ferretti, A., C. Prati, and F. Rocca, "Nonlinear subsidence rate estimation using permanent scatterers in differential SAR interferometry," *IEEE Trans. Geosci. Remote Sens.*, Vol. 38, No. 5, 2202–2212, 2000.
2. Berardino, P., G. Fornaro, R. Lanari, and E. Sansosti, "A new algorithm for surface deformation monitoring based on small baseline differential SAR interferograms," *IEEE Trans. Geosci. Remote Sens.*, Vol. 40, No. 11, 2375–2383, 2002.
3. Mora, O., J. J. Mallorqui, and A. Broquetas, "Linear and nonlinear terrain deformation maps from a reduced set of interferometric SAR images," *IEEE Trans. Geosci. Remote Sens.*, Vol. 41, No. 10, 2243–2253, 2003.
4. Colesanti, C., A. Ferretti, C. Prati, and F. Rocca, "Monitoring landslides and tectonic motions with the permanent scatterers technique," *Eng. Geology*, Vol. 68, No. 1, 3–14, 2003.
5. Liu, G. X., S. M. Buckley, X. L. Ding, Q. Chen, and X. J. Luo, "Estimating spatiotemporal ground deformation with improved persistent-scatterer radar interferometry," *IEEE Trans. Geosci. Remote Sens.*, Vol. 47, No. 9, 3209–3219, 2009.
6. Li, Z., E. J. Fielding, and P. Cross, "Integration of InSAR time-series analysis and water-vapor correction for mapping postseismic motion after the 2003 Bam (Iran) earthquake," *IEEE Trans. Geosci. Remote Sens.*, Vol. 47, No. 9, 3220–3230, 2009.

Multi-mode SAR Interferometry Processing Research and Implementation

Cunren Liang[1,2], **Qiming Zeng**[1,2], **Jianying Jia**[1,2], **Xiao Zhou**[1,2], **Jian Jiao**[1,2], **and Xi'ai Cui**[1,2]

[1]Institute of RS & GIS, Peking University, Beijing 100871, China
[2]Beijing Key Laboratory of Spatial Information Integration and 3S Application Beijing 100871, China

Abstract— Current operation mode of SAR can be roughly divided into two types: strip-map mode and burst mode. The most conventional mode is strip-map mode, in which the swath width is quite limited. The other type is burst mode, which is an active option to overcome this limitation by cyclically scanning several subswaths, known as ScanSAR. In addition, Envisat ASAR has another type of burst mode, that is, Alternating Polarization mode. ALOS PALSAR and Radarsat-1 also have their own ScanSAR operation modes, but each of them is distinctive from the others in implementation. Numerous theoretical results and applications of interferometry using strip-map data have been published before. Interferometry with burst mode data, however, is much rarer and different from the case of the traditional strip-map mode from raw data focusing to interferogram generation because of its burst nature of data acquisition pattern. In our study, we put our emphasis on each kind of burst mode interferometry and mixed mode interferometry. Until now, our successful research work includes Envisat ASAR WS-WS, IM-WS and ALOS PALSAR WB1-WB1 Interferometry. Other development activities including Envisat AP-AP and Radarsat-1 SNA-SNA interferometry are still on going. In the following paper, we will present our results and give an overview of multi-mode SAR interferometry for the present spaceborne SAR sensors.

1. INTRODUCTION

The most conventional operating mode of SAR is strip-map mode, in which echoes are collected continually by SAR. However, a continuous acquisition is not necessary to focus an image, that is, gaps can exist between sections of the acquired echoes [1]. This kind of operation of SAR is the so called "burst mode". The most important application of burst mode is ScanSAR, in which, SAR cyclically adjust its antenna look angle to cover several subswaths in order to achieve a much larger coverage than the strip-map mode, but with a coarser azimuth resolution. The gaps in each subswath are used to collect echoes of other subswaths. Envisat ASAR also applies burst mode to its AP (Alternating Polarization) mode.

The most remarkable advantage of ScanSAR over the traditional strip-map mode is its significant improvement in swath coverage. And that is beneficial to the interferometric applications, some of the examples can be found in [2–6]. Most of the recently launched spaceborne SAR sensors have the ability to work in ScanSAR mode, such as Radarsat-1/2, Envisat ASAR, ALOS PALSAR. The wide availability of ScanSAR data also promotes the development of ScanSAR interferometry. However, the problem of synchronization is the main bottleneck for most of the sensors. In addition to interferometry using the same mode data, a meaningful option is to combine burst mode and strip-map mode data to create an interferogram, which can highly improve the availability of SAR data in the aspect of interferometry, and several results can be found in [3, 5, 7, 8]. Considering that the strip-map mode interferometry is much mature, in this paper, we will report our achievements with an emphasis on ScanSAR interferomtry and mix-mode interferometry.

2. SCANSAR INTERFEROMETRY

The first problem for ScanSAR interferometry is to develop phase-preserving algorithms to focus raw burst mode data. So far, several algorithms have achieved this and we can get an overview from [1, 9]. In our research, we use the full-aperture algorithm developed by Richard Bamler to focus raw data in order to fully use the existing standard high precision SAR algorithms. To do this, gaps between continuous echoes is padded with zeros according to the time sequence and PRF. The resulting image has a geometry and radiometry consistent with the regular SAR mode images. However, the impulse response shows a periodic modulation and it can be eliminated using a low-pass filter [10].

An important parameter for ScanSAR interferometry is its synchronization between master and slave images, that is, the same point on the ground must be imaged from the same along-track positions both times [5]. Interferometry requires certain burst synchronization. The unsynchronized echoes will affect the coherence between master and slave and appear as noise in the interferogram. To improve the coherence, these echoes should be properly removed before the interferometry, which is referred as synchronization selection. However, this also needs some care, as the resolution affecting the coherence, too. In the case of good coherence, we advise not to perform synchronization selection, providing enough synchronized echoes.

After the interferogram generation, subswath interferograms have to be stitched together to make an entire one. All the subswaths of each current sensors share a unified range sampling frequency, the deference lies in the azimuth, that is, PRF varies among subwaths. Therefore, we only have to perform azimuth resampling when mosaicking these sub-interferograms together. A sinc kernel imposed with a Kaiser window is used to implement azimuth resampling. Because the geometric relation between subswaths is pre-determined, correlation calculation between adjacent subswaths using overlap samples in order to get this relation is not needed.

The most favourable option for ScanSAR interferometry is Envisat ASAR WS data as its better control on synchronization and baseline, while the ALOS PALSAR has an advantage of L-band wavelength meaning better coherence. It has been demonstrated that only SNA mode of Radarsat-1 is suitable for ScanSAR interferometry [2]. SNA mode only has two subswaths and therefore much more synchronization can be guaranteed, but the critical baseline is much shorter. Also to be considered is that there isn't any official phase-preserving focused product for the current space-borne sensors at first. Therefore, we start our processing with Level 0 raw data. Currently, only Radarsat-1, Envisat ASAR and ALOS PALSAR as mentioned above provide raw ScanSAR data. After 2005, ESA began to provide phase preserving Wide Swath product, namely, ASA_WSS_1P, which can also be used for interferometry.

To do differential interferometry, a less precise process is as follows: first the subswath interferograms are generated, then these interferograms are mosaicked together. After that, the normal strip-map interferometry process is applied without any change. We use Envisat ASAR WS mode data to test this process and the resulting displacement map is shown in Fig. 1 (Left). The acquisition dates of the interferometric pair are Jan. 16th, 2007 and Mar. 27th, 2007.

A more precise option is that, first each subswath is processed individually until the differential interferogram is created, then subswath interferograms are mosaicked. The afterwards filtering and phase unwrapping process are the same with the strip-map case. An ALOS PALSAR WB1 mode displacement map is generated using this method, which is shown in Fig. 1 (Right). The acquisition dates of the interferometric pair are Mar. 2nd, 2008 and Apr. 17th, 2008.

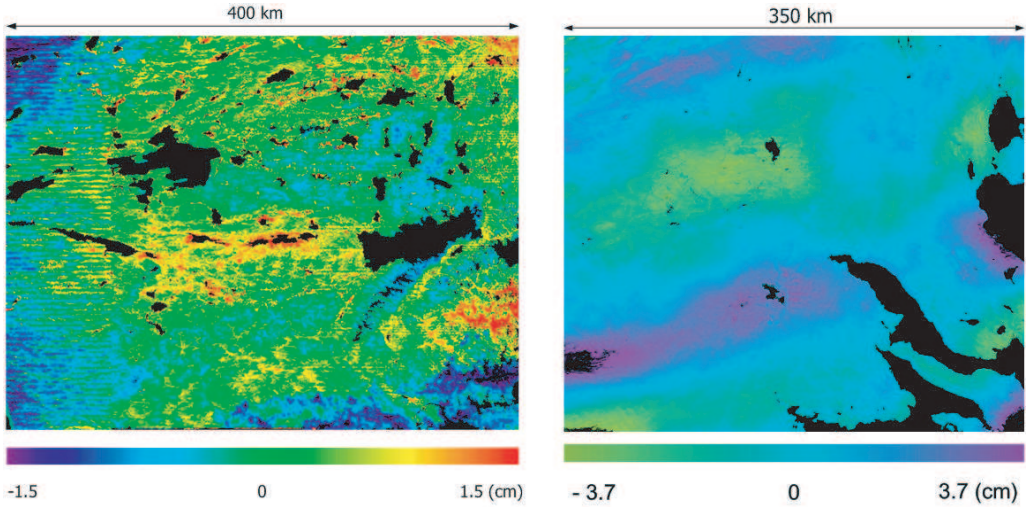

Figure 1: Displacement maps. Left: displacement map of Envisat ASAR WS mode; Right: displacement map of ALOS PALSAR WB1mode.

Boundary lines between adjacent subswaths in the mosaicked interferogram are thorny and current filters show inability to them. Considering this, we proposed the two-way filter to remove them. Experimental result (Fig. 2) proves that this is an effective method. Two-way filter fully

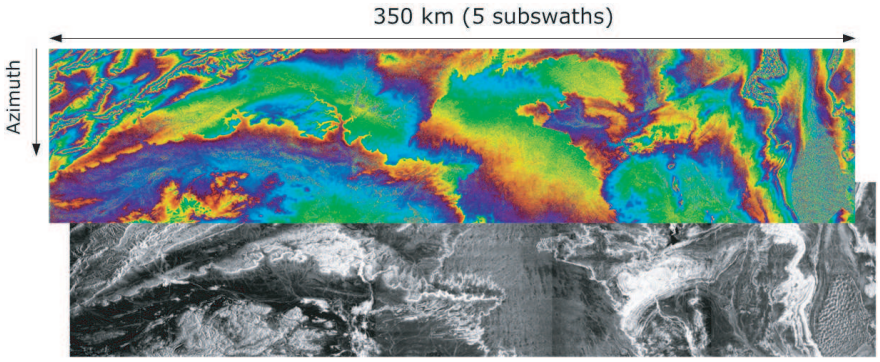

Figure 2: Mosaicked interferogram after two-way filtering, the lower figure is the corresponding magnitude image.

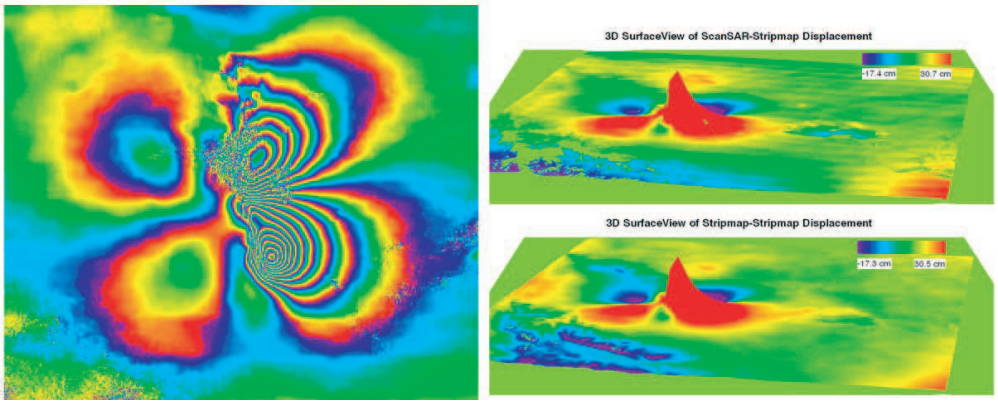

Figure 3: Left: interferogram formed by ScanSAR — strip map interferometry; Right: a comparison of the displacement maps of ScanSAR — strip-map and strip-map interferometry.

uses the overlap samples between subswaths and it can improve the precision of the overlap area. In two-way filter, the middle sample of the overlap area in each line is determined by both of the corresponding samples from the adjacent subswaths weighted with the same weight of 1/2. If the resultant sample is nearer to the left subswath, then sample of the left subswath is weighted with a bigger weight to determine it, and vice versa.

3. SCANSAR — STRIP-MAP INTERFEROMETRY

ScanSAR — strip-map interferometry has similar problem with ScanSAR interferometry in the aspect of synchronization. As we have mentioned before, strip-map mode maintain a continuous acquisition, whereas ScanSAR has gaps between burst trains. This also result to the un-synchronization de-coherence when they are used to do mixed-mode interferometry. To solve this problem, one approach is to filter the strip-map mode data with a low-pass filter. This can "cut" a slice out of the full spectral domain of IM data, and then both of the ScanSAR and the strip-map data share the common spectral domain [3]. In our research, however, we replace the lines corresponding to the zero-lines of ScanSAR data with zero-lines. To do this, azimuth offset between master and slave should be estimated. We first focus the raw data and use the normal correlation strategy to get the azimuth offset. Then the offset is used to coregister the raw slave to the master. Lines in the strip-map data corresponding to the gaps in ScanSAR data are replaced with zeros.

To do interferometry, data with the same track number should be used. We use Envisat ASAR data of Bam, Iran to implement ScanSAR — strip-map interferometry. Subswath 1 of ScanSAR mode corresponds to the strip-map mode, but with a slightly wider swath. To save computation and improve precision, we cut out the same area with strip-map mode in subswath 1 to do further processing. After the preconditioning of the data, ScanSAR — strip-map interferometry can be treated as strip-map interferometry. We use this method to get the interferogram as shown in Fig. 3 (Left). In order to prove the correctness of our result, we compare the displacement map of ScanSAR — strip-map interferometry with the one of traditional strip-map interferometry in

Fig. 3 (Right).

The success of ScanSAR — strip-map interferometry breaks the limit of same mode interferometry and highly improves the availability of current SAR datasets. It is meaningful for monitoring outburst disasters, especially in the case of lacking appropriate interferometric pairs using the traditional method.

4. FUTURE WORK

Other research and development work including Radarsar-1 SNA mode interferometry and Envisat AP mode interferometry is still on going. We will make ScanSAR interferometry and mixed mode interferometry as popular as possible. In addition, we will do more theory research about them.

5. CONCLUSION

In this paper, we have presented ScanSAR interferometry results of Envisat ASAR and ALOS PALSAR. In addition, we have achieved mixed mode interferometry using Envisat ASAR data. Points for attention are given in order to implement multi-mode SAR interferometry. We have also introduced our methods to implement multi-mode interferometry. Our development work is based on JPL's open source strip-map interferometry soft ware ROI_PAC.

ACKNOWLEDGMENT

This work is supported by the National High Technology Research and Development Program ("863" Program: 2006AA12Z150) of China. The authors would like to thank European Space Agency (ESA) for providing ALOS PALSAR data; JPL for its free open source software ROI_PAC; NASA for providing freely available SRTM.

REFERENCES

1. Cumming, I. G. and F. H. Wong, *Digital Processing of Synthetic Aperture Radar Data: Algorithms and Implementation*, Artech House, Norwood, 2005.
2. Holzner, J. and R. Bamler, "Burst mode and ScanSAR interferometry," *IEEE Trans. Geosci. Remote Sensing*, Vol. 40, No. 9, 1917–1934, 2002.
3. Guccione, P., "Interferometry with Envisat wide swath ScanSAR data," *IEEE Trans. Geosci. Remote Sensing Letters*, Vol. 3, No. 3, 377–381, 2006.
4. Shimada, M., "Palsar ScanSAR ScanSAR interferometry," *Proceedings of International Geoscience and Remote Sensing Symposium*, IV-93–IV-96, Boston, USA, July 2008.
5. Bamler, R., D. Geudtner, B. Schattler, P. W. Vachon, U. Steinbrecher, J. Holzner, J. Mittermayer, H. Breit, and A. Moreira, "Radarsat ScanSAR interferometry," *Proceedings of International Geoscience and Remote Sensing Symposium*, 1517–1521, Hamburg, Germany, June 1999.
6. Jia, J., Q. Zeng, J. Jiao, Y. Li, and X. Cui, "ScanSAR differential interferometry and wet delay correction: Case study in dangxiong, tibet," *Proceedings of International Geoscience and Remote Sensing Symposium*, IV-244–IV–247, Boston, USA, July 2008.
7. Ortiz, A. B. and H. Zebker, "ScanSAR-to-stripmap mode interferometry processing using Envisat/ASAR data," *IEEE Trans. Geosci. Remote Sensing*, Vol. 45, No. 11, 3468–3480, 2007.
8. Guarnieri, A. M., P. Guccione, P. Pasquali, and Y. L. Desnos, "Multi-mode Envisat ASAR interferometry: Techniques and preliminary results," *IEE Proceedings — Radar, Sonar and Navigation*, Vol. 150, No. 3, 193–200, 2003.
9. Cumming, I. and Y. Guo, "A comparison of phase-preserving algorithms for burst-mode SAR data processing," *Proceedings of International Geoscience and Remote Sensing Symposium*, 731–733, Singapore, 1997.
10. Bamler, R. and M. Eineder, "ScanSAR processing using standard high precision SAR algorithms," *IEEE Trans. Geosci. Remote Sensing*, Vol. 34, No. 1, 212–218, 1996.

Mitigation of Atmospheric Water-vapour Effects on Spaceborne Interferometric SAR Imaging through the MM5 Numerical Model

D. Perissin[1], **E. Pichelli**[2], **R. Ferretti**[2], **F. Rocca**[3], **and N. Pierdicca**[4]

[1]ISEIS, Chinese University of Hong Kong, Hong Kong, China
[2]CETEMPS, University of L'Aquila, Italy
[3]DEI, Politechnic of Milan, Italy
[4]DIE, Sapienza University of Rome, Italy

Abstract— Synthetic Aperture Radar (InSAR) imaging is a well established technique to derive useful products for several land applications. One of the major limitations of InSAR is due to atmospheric effects, and in particular to high water vapor variability.

In this work, we make an experimental analysis to research the capability of Numerical Weather Prediction (NWP) models as MM5 to produce high resolution (1 km–500 m) maps of Integrated Water Vapor (IWV) in the atmosphere to mitigate the well-known disturbances that affect the radar signal while traveling from the sensor to the ground and back. Experiments have been conducted over the area surrounding Rome using ERS data acquired during the three days phase in '94 and using Envisat data acquired in recent years. By means of the PS technique SAR data have been processed and the Atmospheric Phase Screen (APS) of Slave images with respect to a reference Master have been extracted. MM5 provides realistic water vapor distribution fields that can be converted into electromagnetic slant delays. PSInSAR APS's have then been compared to MM5 IWV maps revealing interesting results. MM5 IWV maps have a much lower resolution than PSInSAR APS's: the turbulent term of the atmospheric vapor field cannot be well resolved by MM5, at least with the low resolution ECMWF inputs. However, the vapor distribution term that depends on the local topography has been found quite in accordance. In this work, we will present experimental results as well as discussions over the adopted processing strategy.

1. INTRODUCTION

Water vapor is one of the most significant constituents of the atmosphere because its phase changes are responsible for clouds and precipitation, whose interaction with electromagnetic radiation is a crucial factor in atmospheric system regulation. Despite of its importance within atmospheric processes over a wide range of spatial and temporal scales, water vapor is one of the least understood and poorly described components of the atmosphere.

Current Numerical Weather Prediction (NWP) models can provide high spatial resolution able to reproduce realistic vapor distribution fields, but one of their most limiting factors is the poor resolution of the initial condition. On the other hand, from the point of view of SAR interferometric applications (e.g., earth motion monitoring), one of the biggest sources of noise for InSAR techniques is the delay caused by changes in the distribution of water vapor in the atmosphere [1]. By analyzing single interferograms, the water vapor delay contribution is practically indistinguishable from ground motion signal with amplitudes that can range from some millimeters up to several centimeters or even greater, leading to a real difficulty to detect ground deformations events. Several efforts have been spent to solve this problem [2], by developing methods to mitigate water vapor artifacts by reconstructing the most likely atmospheric scenario. Most known techniques tend to use observations, such as radiosondes, GPS receiver networks, ground or space based radiometers: the latter generally exhibit poor temporal or spatial resolution, and their accuracy may strongly depend on the surface (land/water) background over which the measurements are acquired [2]. Water vapor field, produced by NWP, can provide a good support to eliminate some of these problems. Meteorological model simulations, indeed, can be used to predict atmospheric delay to be subtracted from InSAR interferograms and to reduce noise on the geodetic signal.

In this paper, the preliminary results of high resolution water vapor field analysis are presented. The MM5 model version 3 [3] is used to produce high resolution water vapor fields to be compared with InSAR data, which have been processed with the Permanent Scatterers (PS) technique [4].

2. THE MM5 NWP MODEL

The fifth generation NCAR (National Center for Atmospheric Research) and Pennsylvania State University mesoscale model MM5 is used for this study; this is a non hydrostatic model at primitive equations with a terrain following vertical coordinates system and multiple nesting capabilities [3].

Four two-way nested domains are used to enhance the resolution over the urban area of Rome. The mother domain covers most of occidental Mediterranean area; it is centered at 41.5°N, 10.0°E and has a spatial resolution of 27 km. The nested domains run on Central Italy from a spatial resolution of 9 km for domain 2 to 1 km for the inner one; this last one covers the city area and its surroundings (Lazio region), greatly overlapping the ERS satellite swath.

Sensitivity tests and previous experiences [5] allowed us tailoring the optimal combination of physical parameterizations for the numerical experiments. All the numerical experiments last 24 hours, from 00:00UTC to the 24:00UTC of each chosen day of simulation. The European Centre for Medium-Range Weather Forecast (ECMWF) analysis at 0.25° for temperature, wind speed, relative humidity, and geopotential height are interpolated to the MM5 horizontal grid and to vertical levels to produce the model initial and boundary conditions.

3. COMPARISON METHODOLOGY

In order to compare SAR atmospheric phase screen (APS) and MM5 water vapor maps, some considerations have to be made.

- The two maps are required to be geocoded on the same grid in geographical coordinates. The MM5 grid has been taken as reference and the APS maps have been interpolated on it.
- The APS collects all spatially correlated noise in an interferogram. This means that also residual orbital errors can be included in APS maps. To get rid of such phase trends that can invalidate the comparison, a phase ramp has to be estimated in each interferogram and removed.
- To compare the two quantities, the electromagnetic delay has to be converted into height of integrated water vapor, by means of the well known formula [6]

$$ZWD \approx 6.4IWV \tag{1}$$

- By considering that the water vapor map integrates along the vertical direction while the radar is looking with an incidence angle of approximately 23°, the cosine of the angle has to be accounted for to map the water vapor in the satellite line of sight.
- InSAR data is a differential measure: each estimated APS is the difference of water vapor delays in two different dates. All available APS's have been referred to a common date (as it is implemented in the classical PS processing chain [4]). In this way, all APS's are affected by a common trend deriving by the reference image. Simply by averaging all available APS's together, the delay map of the reference image can be estimated and removed.
- The tropospheric delay can be modeled as a function of two main terms: a turbulent term and a quantity proportional to the terrain height [7]

$$\alpha_i = \varepsilon_i + k_i q \tag{2}$$

  where α_i is the tropospheric delay, ε_i the turbulent term, q the terrain height and k_i a proportionality constant.

  The proportionality constant changes depending on the local atmospheric parameters (humidity, pressure and temperature) [8], but in any case the tropospheric delay decreases with the height. Thus we can write

$$k_i = k_0 + \delta k_i \tag{3}$$

  where k_0 is a nominal value and δk_i takes into account the possible changes.

  Thus, the APS of a generic image i referred to a common master M can be written as

$$\alpha_{i,M} = \varepsilon_i + k_i q - (\varepsilon_M + k_M q) = \varepsilon_i - \varepsilon_M + \delta k_i q - \delta k_M q \tag{4}$$

  By averaging the stack of available APS's, it is possible to estimate just a differential component of the delay of the master acquisition,

$$\bar{\alpha}_M = \varepsilon_M + \delta k_M q \tag{5}$$

  Thus, in order to compare "absolute" IWV maps to "absolute" APS maps, also the "nominal" IWV trend with height (the one linked to k_0), common in all IWV maps, has to be estimated and removed.

4. EXPERIMENTAL DATA AND RESULTS

The comparison between MM5 and InSAR maps has been conducted over an area of about 100 km × 100 km over Rome, as shown in Figure 1. In Figure 2, the corresponding digital elevation model is reported, spanning about 1600 m. The data used in the experiment belong to 3 different datasets: the first one is composed by 27 ERS1 images, acquired between December 1993 and April 2004, during the so-called ERS1 3 days phase. Second and third data-sets have been acquired by Envisat over the same area in descending and ascending passes (35 and 41 images respectively) between 2002 and 2009. MM5 available data in correspondence of the SAR acquisitions are 7, 20 and 10 runs.

The main result of the first dataset can be summarized as in Table 1, where the standard deviations of the APS maps are reported before and after compensating for the IWV estimates. As visible from Table 1, in three cases out of seven, the water vapor estimated by the MM5 model is able to reduce the standard deviation of APS values. In other three cases the situation is strongly worsened. Just in one case (3rd February '94) the dispersion of water vapor is slightly increased. The reason can be further investigated by analyzing the trend of InSAR and MM5 maps with respect to the height: whenever the estimated trend is in accordance, MM5 is able to reduce the power of the atmospheric disturbances in InSAR data. On the contrary, when the turbulent term of the water vapor is predominant, MM5 is not able to predict the spatial features measured by InSAR.

Table 1: Standard deviation of the water vapor estimated by means of InSAR APS before and after compensating for the one estimated by MM5.

	19940131	19940203	19940212	19940215	19940227	19940305	19940308
APS	.78	.67	.7	.28	.79	1.1	.4
APS-IWV	.64	.71	.53	.98	1.45	.9	.52

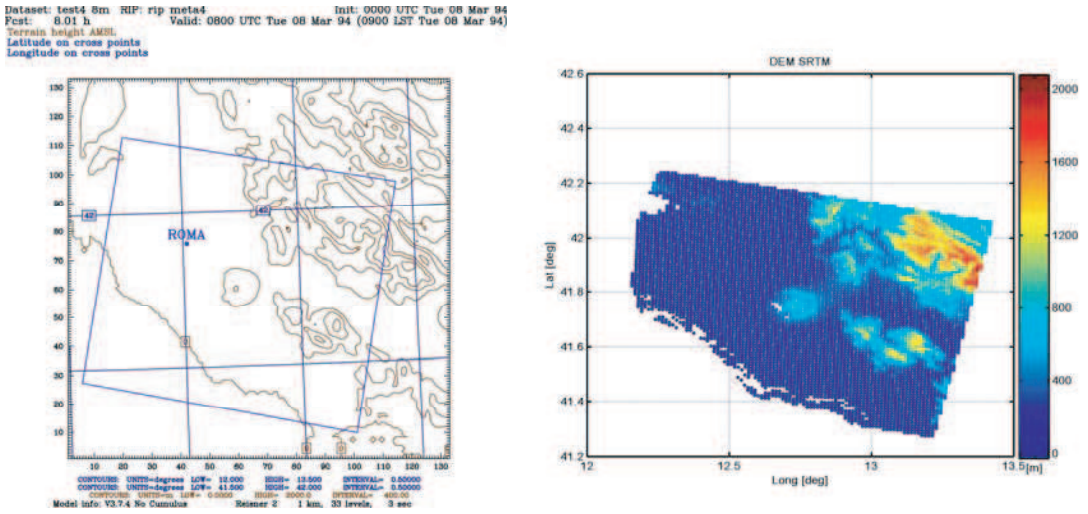

Figure 1: MM5 domain (left) and corresponding digital elevation model (right) over the analyzed area in Rome.

Figure 3 shows the scatter-plot of IWV retrieved by means of InSAR and MM5 for Envisat data acquired along one descending (on the left) and one ascending (on the right) orbits. In particular in the ascending pass where the number of acquisitions is higher, it is evident a higher correlation between MM5 and InSAR measures. The better performance with respect to '94 ERS data can be explained by the higher accuracy of ECMWF data. Figure 4 shows in a compact form the results analysis. There the scatter-plot between the IWV-height trend (δk_i in Eq. (4), in mm/m) estimated from MM5 and InSAR maps is shown. In the ascending orbit (image on the right) the two measures are quite well in accordance (dispersion of the scatter plot 0.7 mm/km for an InSAR δk_i dispersion

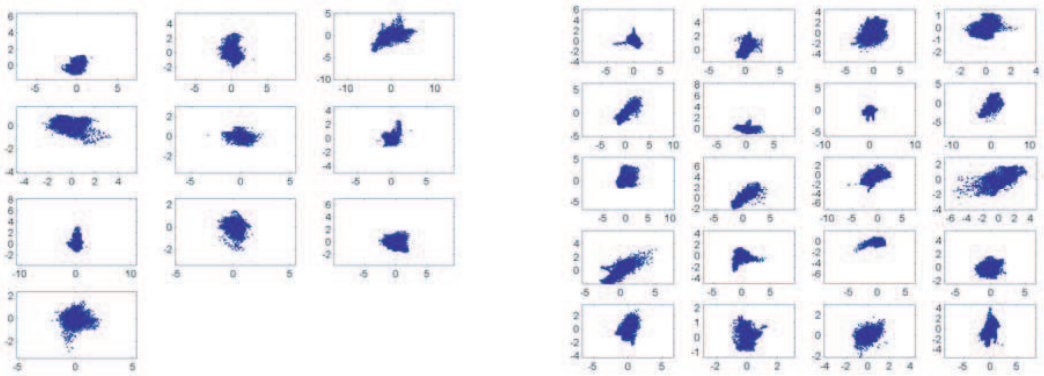

Figure 2: Scatter plot between InSAR (ordinate) and MM5 (abscissa) IWV in [mm]. Left descending, right ascending Envisat orbits over Rome.

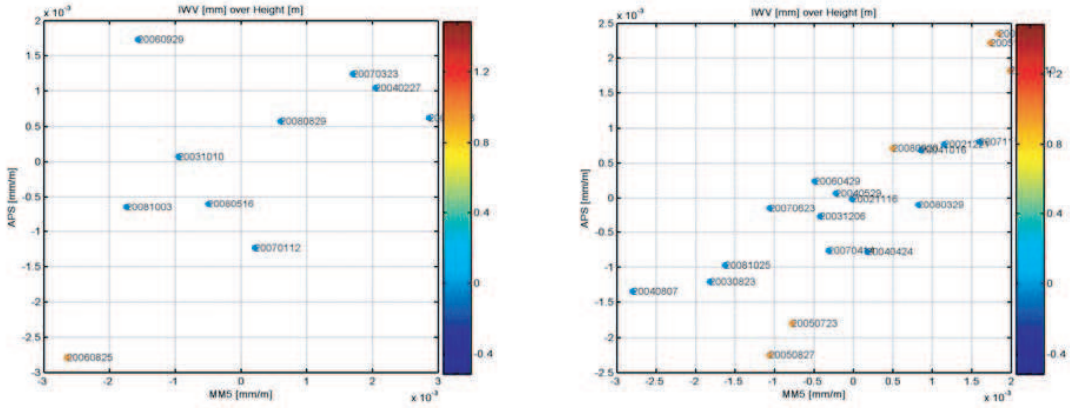

Figure 3: Scatter plot between InSAR (ordinate) and MM5 (abscissa) δk_i in [mm/m]. Left desce, right asce Envisat orbits over Rome.

of 1.3 mm/km). Moreover, the image shows in orange color those cases in which MM5 decreased the InSAR APS power, and in blue the other cases. Orange dots cluster in the upper and lower parts of the plot, i.e., MM5 succeeds in mitigating the atmospheric noise only when the IWV height dependent term is predominant (about 30% of cases in the ascending dataset). In the descending orbit (image on the left) the δk_i scatter plot is less accurate, and in only one case MM5 decreases the InSAR IWV power. It is interesting to observe at this point that ascending images are acquired around 9 pm, whereas the descending passes are at about 9.30 am, when the turbulent mixing of the atmosphere is higher.

5. CONCLUSION

In this work, an experimental analysis to compare the Atmospheric Phase Screen retrieved with InSAR data with MM5 IWV maps has been provided. About 40 data takes have been processed over Rome in three SAR datasets: during the 3-days phase of ERS1 in 1994, and in two different orbits of Envisat in the last 7 years. The results show a better matching in recent years, in particular for ascending passes taken at evening time. Nevertheless, whenever the turbulent part of the water vapor exceeds the stratification one, MM5 is not able to reduce the InSAR atmospheric disturbances. As an overall conclusion, in 30% of cases MM5 can be successfully used to mitigate the electromagnetic delay induced by the water vapor concentration.

ACKNOWLEDGMENT

The authors would like to thank ESA for providing ERS and Envisat images under the project METAWAVE, ITT AO/1-5424/07/NL/HE, as well as the whole staff of TRE for focusing and co-registering SAR data.

REFERENCES

1. Foster, J., B. Brooks, T. Cherubini, C. Shacat, S. Businger, and C. L. Werner, "Mitigating atmospheric noise for InSAR using a high resolution weather model," *Geophysical Research Letters*, Vol. 33, L16304, 2006.
2. Webley, P. W., R. M. Bingley, A. H. Dodson, G. Wadge, S. J. Waugh, and I. N. James, "Atmospheric water vapour correction to InSAR surface motion measurements on mountains: Results from a dense GPS network on Mount Etna," *Physics and Chemistry of the Earth*, Vol. 27, 363–370, 2002.
3. Dudhia, J., "A nonhydrostatic version of the Penn State-NCAR Mesoscale Model: Validation tests and simulation of an atlantic cyclone and cold front," *Mon. Wea. Rev.*, Vol. 129, 1493–1513, 1993.
4. Ferretti, A., C. Prati, and F. Rocca, "Permanent scatterers in SAR Interferometry," *IEEE TGARS*, Vol. 39, No. 1, 2001.
5. Ferretti, R., G. Mastrantonio, S. Argentini, L. Santoleri, and A. Viola, "A model-aided investigation of winter thermally driven circulation in the Italian Tyrrhenian coast for a case study," *J. Geophys. Res.*, 2003.
6. Emardson, T. R. and H. J. P. Derks, "On the relation between wet delayand the integrated precipitable water vapour in the European atmosphere," *Meteorological Applications*, Vol. 7, 61–68, 2000.
7. Onn, F., "Modeling water vapor using GPS with application to mitigating InSAR atmospheric distortions," Ph.D. Thesis, Stanford University, 2007.
8. Saastamoinen, J., "Contribution to the theory of atmospheric refraction," *Bulletin Géodésique*, Vol. 105, No. 1, 13–34, 1973.

Electromechanical Coupling Optimization Design of Large Reflector Antennas Include Feed (Sub Reflector) Support Structure

P. Li, **D. W. Yang**, **and F. Zheng**
Research Institute on Mechatronics, Xidian University, Xi'an, China

Abstract— The structure design of large reflector antennas is a typical electromechanical multidisciplinary optimization process, and both main reflector back frame and feed/sub reflector support structure should be include. From electromechanical coupling angle, a new coupling formula is presented by introducing the distortion of main reflector and position/angle error of feed/sub reflector into antenna's far field patterns formula. So the structure parameters (include back frame and feed support structure) is related to electrical parameter (include gain, side lobe, beam width and pointing accuracy). Based on the coupling formula, a coupling optimization model is proposed with design variable of feed/sub reflector support structure parameters besides back frame, and with constraint conditions of electrical parameter besides structure conditions. A numerical example has been done for an 8 m reflector antenna. Results of the example show that the coupling optimization model is more efficient than tradition structure optimization model.

1. INTRODUCTION

As typical electromechanical equipment, antennas' structure characteristic and electromagnetism characteristic are interinfluence and interrestrict. So in order to design high quality antenna which means high electrical performance and low structure cost, it is necessary to research from electromechanical coupling and discipline crossing angle [1]. There is much investigation on the relation between structure precision and electrical performance. The effect of main reflector's random error and system distortion on electrical performance has been further researched [2]. Correlative research result is applied to cylindrical reflector antenna and array-compensated spherical reflector antenna [3]. Analysis and optimization of reflector antennas have been dong with multiple load cases and environmental factors [4]. Wang do the optimization design in electromechanical integrated view based on Duan's work [5]. Most researches focus on structure precision of main reflector, but sub reflector also influence antennas' electrical profoemance. The effect of position error of sub reflector or feed on gain loss has been done [6]. Liu and Thompson [7] researched the effect of feed/sub reflector support structure on antennas' electrical performance and optimized support structure from the electromechanical coupling angle.

But these are two problems of the works above. One is the separate problem of antenna structural and electromagnetic analysis or design. Most antenna designers estimate gain loss by structure precision based on Ruze formula [8]. However only structure precision con not represent the full information of the distorted reflector, and con not represent some other main electrical parameters such as sidelobe, beamwidth, pointing accuracy [4]. The other is the separate problem of main reflector and sub reflector/feed. Main and sub reflectors have been addressed individually [1, 5], but the effect of sub reflector/feed and main reflector on electrical performance is intercoupling and combined working. As a whole antenna, they should be designed together.

For the deficiencies of previous works, form electromechanical coupling angle, the distortion of main reflector and sub reflector/feed are introduced to the formula of antenna far field pattern. And an coupling optimization model of reflector antennas with sub reflector/feed support structure is presented. Numerical example results of an 8 m antenna demonstrate the excellence of the coupling optimization model.

2. ELECTROMECHANICAL COUPLING FORMULA OF REFLECTOR ANTENNA

Various external loads (such as vibration shock, gravity, wind, ice and snow, sun illumination) will lead to distortion of main reflector, position error and pointing angle error of feed/sub reflector, these three factors effect far field parameter of antenna together, cause gain loss, pointing accuracy reduce, sidelobe degrade and so on.

The formula of far field pattern can be written as

$$E\left(\theta,\phi'\right)=\iint_s \frac{f(\xi+\delta_\xi,\phi+\delta_{\phi'})}{r'}e^{jkr'\cdot d}e^{j\delta}e^{j\varphi(\rho',\phi')}\rho' d\rho' d\phi' \tag{1}$$

where E is field value in some point of far field; $f(\xi,\phi)$ and $\varphi(\rho',\phi')$ are amplitude and phase distribution function of aperture field respectively, δ_ξ, $\delta_{\phi'}$ are the angles of pointing changes of feed in two directions; r' is the distance from focus to a point of main surface, d is the position error of feed; $e^{j\delta}$ is the error caused by main reflector distortion; $\delta = 4\pi/\lambda Z(\rho',\phi')\cos^2(\xi/2)$, $Z(\rho',\phi')$ is axial displacement of main reflector surface; $k = 2\pi\cdot freq/c$, c is velocity of light; *freq* is frequency. All of the variables are shown in Figure 1.

In formula (1), amplitude and phase distribution are functions of structure distortion (main reflector distortion, angles of pointing changes and position error of feed), structure distortion is a function of structure parameters (shape, size, topological structure and material of antenna back frame and feed/sub reflector support structure). So a relation of structure parameters and electrical performance is found via formula (1). Antenna designer could investigate antenna's main electrical performance directly on the base of structure parameters, and avoid the limitation of only structure precision couldn't represent electrical performance of antennas completely.

3. ELECTROMECHANICAL COUPLING OPTIMIZATION MODEL

For different use and working condition of antennas, different structure optimizations model is need. For ground based reflector antenna, optimization objective is surface precision, design variables are shape, size, topological structure and material of antenna back frame, constraint conditions are maximum weight, maximum stress and allowable range of design variables. For spaceborne antennas, because of special working environment in outer space, optimization objective is weight, constraint conditions is surface precision.

The antenna designers estimate gain loss according to the following formula [3]:

$$\Delta G = 685.81\left(\frac{2f}{R}\sqrt{\ln\left(1+\frac{1}{(2f/R)^2}\right)}\cdot\xi/\lambda\right)^2 \tag{2}$$

where, f, R, λ, ξ are focal length, radius, wavelength and surface rms error respectively.

In this paper, coupling formula (1) was used to analyse electrical performance instead of (2), so it was realized that considering gain, sidelobe, beam width, pointing accuracy in structure optimization design, and design variables include structure parameters of sub reflector/feed support structure. The electromechanical coupling optimization model is:

$$\mathbf{PI}: \quad \text{Find} \quad (\beta,\alpha) = (\beta_1,\beta_2,\ldots,\beta_R,\ \alpha_1,\alpha_2,\ldots,\alpha_r) \tag{3}$$

$$\text{Min} \quad W \quad \text{or} \quad G \tag{4}$$

$$\text{S.T.} \quad \Delta G(\beta,\alpha) \le \Delta G_{\max} \quad \text{or} \quad W(\beta,\alpha) \le W_{\max} \tag{5}$$

$$\sigma_K(\beta_1,\beta_2,\ldots,\beta_R) \le \overline{\sigma_K},\ \ (K=1,2,\ldots,m) \tag{6}$$

$$\sigma_k(\alpha_1,\alpha_2,\ldots,\alpha_r) \le \overline{\sigma_k},\ \ (k=1,2,\ldots,n) \tag{7}$$

$$\beta_{i\min} \le \beta_i \le \beta_{i\max},\ \ (i=1,2,\ldots,R) \tag{8}$$

$$\alpha_{i\min} \le \alpha_i \le \alpha_{i\max},\ \ (i=1,2,\ldots,r) \tag{9}$$

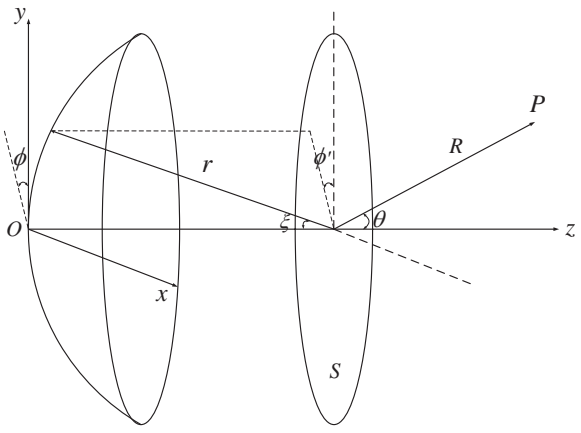

Figure 1: Variables in reflector antennas.

where β is structure design variables of antenna back frame, α is structure design variables of sub reflector/feed support structure, W is weight of antenna, G, ΔG is a electrical property parameter and its change, σ_i is stress of ith element, $\bar{\sigma}$ is allowable stress, m, n is total number of elements in back frame and support structure respectively, $\beta_{\min}$, $\beta_{\max}$ and $\alpha_{\min}$, $\alpha_{\max}$ are minimum and maximum allowable values of corresponding design variables.

According to different use and working condition, optimization objective and constraint conditions are different also. For high gain spacebron antenna, optimization objective is weight, constraint is gain loss. For low sidelobe antenna on ground, objective is gain, constraint are weight and sidelobe degradation. For high accuracy antenna, constraint should include pointing accuracy.

4. NUMERICAL EXAMPLE

A typical 8 m antenna is used for numerical example, the diameter of main reflector is 8 m, the focal length is 3 m, and the frequency is 12.5 GHz. In Figure 2, a quarter of back frame is examined because of its symmetry as shown. There are 32 nodes and 97 bar elements which are divided into 12 groups according to cross section areas as in Table 1. Material of element is steel, elastic modulu is 210 MPa, density is 7.85×10^{-3} kg/cm^3.

Tradition structure optimization and coupling optimization in this paper are used for comparing. The design variables include two parts. One part is back frame (A_i, R_j, Z_k), A is cross section areas of bar elements in antenna back frame, the number of A is 12, R and Z are the radius and Z coordinates of nodes 5, 6, 7 and 8, the number of R and Z is 4; the other part is feed support structure (B, N), B is cross section area of bar element in feed support structure, there is only one bar group of feed support structure, N is the juncture of feed support bar and back frame, note that N is a discrete variable, which is one of node 2, 3 and 4 as show in Figure 4. There are total 4 feed support bars in the whole antenna. Optimization object W is the weight of antenna. Constraint conditions $\Delta G(A, R, Z, B, N)$ is gain loss, is the maximum admissible gain loss, σ_i is stress of ith element, $\bar{\sigma}$ is admissible stress, $\Delta G_{\max}$ equal to 0.25 dB and $\bar{\sigma}$ equal to 2.1×10^7 MPa. $A_{i\min}$, $A_{i\max}$, $R_{j\min}$, $R_{j\max}$, $Z_{k\min}$, $Z_{k\max}$ and $B_{\min}$, $B_{\max}$ are upper and lower limit of corresponding design variables. The antenna is assumed with load of gravity and force with the same direction.

Tradition structure optimization: Design variables are back frame (A_i, R_j, Z_j) without feed support structure (B, N). Constraint conditions are surface precision less than 0.5 mm instead of gain loss besides admissible stress. The gain loss of 0.5 mm rms is 0.2463 dB, according to (2). Optimization objective is minimum structure weight. Other conditions are the same with coupling

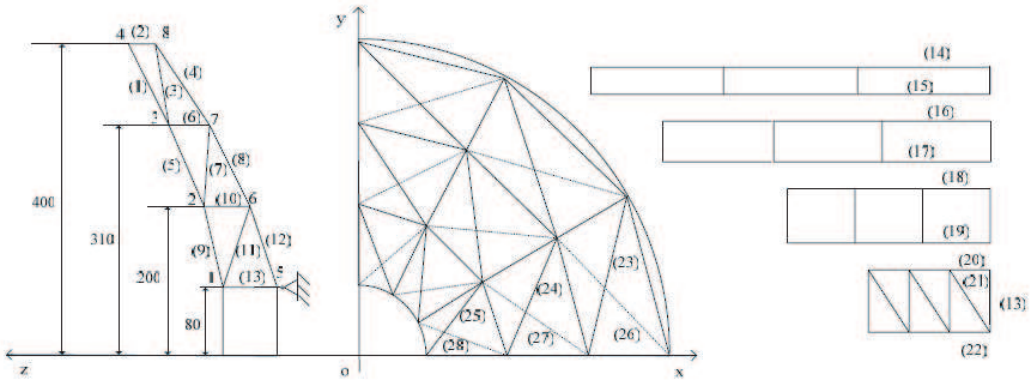

Figure 2: Back frame structural diagram of a 8 m reflector antenna (length unit: cm).

Table 1: Bar elements classify of back frame structural.

Group	Bar element	Group	Bar element	Group	Bar element
1	(9), (12)	5	(18), (19)	9	(6), (7)
2	(5), (8)	6	(16), (17)	10	(10), (11)
3	(1), (4)	7	(14), (15)	11	(13), (21)
4	(22), (20)	8	(2), (3)	12	(23), (24), (25), (26), (27), (28)

optimization model. The results of two optimizations can be seen in Table 2.

From Table 2, Structure weight of tradition structure optimization is 741.5 kg; Surface precision of main reflector is 0.499 mm, which leads to gain loss 0.2463 dB of main reflector according to (2). There is also position error of sub reflector/feed, which will lead to added gain loss. So the total gain loss is 0.5790 dB according to (1), and far field pattern can be obtained at the same time. Structure weight of coupling optimization is 573.58 kg, much lighter than 741.5 kg; gain loss is 0.2358 dB according to (1) considering distortion of main reflector and position error of feed/sub reflector. The electrical performance is better than the results of structure optimization as show Table 3. The gain loss reduce about 0.33 dB, side lobe hoist reduce about 0.70 dB of coupling optimization compared with structure optimization from Table 3.

The result of coupling optimization could be explanted by the best fit surface theory: when main reflector distort, if the feed is moved to the focus of the best fitting surface, there is no loss of antenna efficiency [6]. That means the distortion or displacement of sub reflector/feed could compensate the antenna electrical properties loss from main reflector distortion In fact, the effect of sub reflector/feed and main reflector on antenna electrical properties is intercoupling and combined working. So they should be studied together as a whole antenna during antenna structure design.

Table 2: Results comparison of structure optimization and coupling optimization (length unit: cm).

variable	A_1	A_2	A_3	A_4	A_5	A_6	A_7	A_8	A_9	A_{10}	A_{11}	A_{12}
Structure optimization	22.0	17.0	6.0	6.0	7.0	8.0	15.0	5.0	7.0	3.0	3.0	5.0
Coupling optimization	18.0	13.0	8.0	5.0	3.0	4.0	8.0	4.0	5.0	4.0	4.0	4.0
variable	Z_1	Z_2	Z_3	Z_4	R_1	R_2	R_3	R_4	B	N	S.T.	W
Structure optimization	2.0	53.0	121.0	162.0	150.0	200.0	281.0	342.0			rms	741.50
Coupling optimization	4.0	53.0	159.0	189.0	150.0	194.0	303.0	357.0	4.0	2	dG	573.58

Table 3: Main antenna parameters comparison of two optimization results and ideal condition.

	L-side lobe (dB)	Gain loss (dB)	R-side lobe (dB)
Ideal condition	−14.41	0	−14.41
Structure optimization	−12.67	0.5790	−13.25
Coupling optimization	−13.36	0.2351	−14.01

5. CONCLUSION

Position error of sub reflector/feed will influence antenna electrical properties, and this effect is interaction with main reflector. So in the structure optimization design of reflector antenna, main reflector back frame and sub reflector/feed support structure should be considered together. The application results of 8 m antenna show that the optimization model in this paper has obvious advantages; the optimization result can be referenced in engineering practice, and also has certain guidance functions for the same kind antenna. Even for spaceborne deployable reflector antenna, the optimization model could be applied.

REFERENCES

1. Wang, C. S., B. Y. Duan, and Y. Y. Qiu, "On distorted surface analysis and multidisciplinary structural optimization of large reflector antennas," *Int. J. Structural and Multidisciplinary Optimization*, Vol. 33, No. 6, 519–528, 2007.
2. Smith, W. T. and R. J. Bastian, "An approximation of the radiation integral for distorted reflector antennas using surface-error decomposition," *IEEE Transactions on Antennas and Propagation*, Vol. 45, No. 1, 5–10, 1997.

3. Bahadori, K. and Y. Rahmat-Samii, "Characterization of effects of periodic and aperiodic surface distortion on membrane reflector antenna," *IEEE Transactions on Antennas and Propagation*, Vol. 53, No. 9, 2782–2791, 2005.
4. Zhang, J. Y., H. L. Shi, Z. P. Chen, et al., "Time domain wind buffeting response of large-diameter antenna electric performances," *Chinese Journal of Applied Mechanics*, Vol. 25, No. 1, 84–88, 2008.
5. Duan, B. Y., Y. H. Qi, G. H. Xu, et al., "Study on optimization of mechanical and electronic synthesis for the antenna structural system," *Int. J. Mechatronics*, Vol. 4, No. 6, 553–564, 1994.
6. Zhang, J. Y., H. L. Shi, H. B. Zhang, et al., "Error analysis and compensation for sub-reflector and feed of 40 m radio telescope antenna," *Astronomical Research & Technology*, Vol. 4, No. 1, 42–47, 2007.
7. Liu, J. S. and G. Thompson, "The multi-factor design evaluation of antenna structures by parameter profile analysis," *Proc. Inst. Mech. Eng., B, J. Eng. Manuf.*, 449–456, 1996.
8. Ruze, J., "Antenna tolerance theory — A review," *Proc. IEEE*, Vol. 54, 633–640, 1966.

Updating Methods for Antenna Servomechanism Structures

Hong Bao, **Congsi Wang**, **and Jun Cheng**
Key Laboratory of Electronic Equipment Structures Design of Ministry of Education
Xidian University, Xi'an, China

Abstract— A new updating method is presented based on the model condensation technique and frequency response function (FRF) for antenna servomechanism dynamic structures As a result of the introduction of the ratio of damping to stiffness, this method reduce the numbers of parameters than the traditional FRF updating methods. The finite element model (FEM) condensation technique is used to overcome the disadvantage of the traditional FRF updating methods that the testing mode dimension is too large, it decrease the request of the testing model dimension. Finally the numerical result shows the validity and feasibility of the method.

1. INTRODUCTION

Antenna servomechanism is a key part of the antenna, its capability determines the level of antenna's performance, the rationality of modeling the antenna servomechanism is very useful for the design of the follow-up control system. However, there are a large number of uncertainties factors such as damping, friction and gap and so on in practice works. Thus, the error exists between the mathematical model and the physical model. It would need to update the mathematical model when these errors beyond expectation, it means the dynamic structure updating [1, 2]. In the past 30 years, dynamic model updating methods have great development, especially the model updating using vibration data, which contains mode and FRF. Mode method is the algorithm that adjusting the forecast parameters by the eigenvalue and eigenvector. At present, the mode method developed updating process based on a few front degree of freedom (DOF) of the measured modal frequencies and mode shapes [3], however, relying solely on a few modes to update FEM is not entirely reasonable, for the mode set is incomplete, the updating model can only be used on subspace of mode space, so the results just can be used in a very small range, the other shortcoming of the mode method is that it can not be used to update damping.

The updating method of using FRF data is developed in recent years, Xu Zhang Ming [4] studied the frequency response function that get from testing and finite element model analysis, and deduced an updating method, which based on the sensitivity analysis of FRF. Hemez [5] analyzed the problem of using FRF to update the dynamic model, then improved this method and applied it to the actual mode. Ting [6] presented an improved calculation method of the sensitivity of FRF to study the technology of updating the FRF model. This approach overcome the need of corresponding mode shape and it's frequency range for updating calculation is very wide, but there are no updating to the structure damping. RM Lin [7] improved the FRF method with combining the structural damping characteristics, and achieved the identification updating of damping. However, the DOF of finite element model are generally much larger than the testing's. Because of neglecting the problem of model reduction, Lin's method have many limitations in practical applications. For studying the model reduction, Xu Zhang Ming provided another improved method of reducing the FEM using FRF [8], this method presented an independent model reduction of the structure model unit, but in the end it needed to reduce the stiffness or mass of the unit, so it would increase the step of reduction, and this method updated mass, stiffness and damp separately, it also increased the number of updating parameters, it would need more frequency points, and would increase the workload.

An improved method for damping updating using the FRF has been presented in this paper, for FRF can not reduce the model and have low efficiency of calculating. This method combines the unit model reduction technology, and introduces the concept of damping ratio of stiffness based on the important of the structure damping in the project, it reduces the numbers of updating parameters and the work of calculation. The finally numerical simulation results prove the feasibility and reliability of the method.

2. PRINCIPLE AND PROBLEM

Usually the structural dynamics equations can be expressed as:

$$M\ddot{\theta} + C_1\dot{\theta} + iC_2\theta + K\theta = F \tag{1}$$

where M and K are mass and stiffness matrices, respectively, C_1 and C_2 are viscous and structural damping, respectively From text [9], generally the damping force and experimental frequency (speed) is almost irrelevant, against that, it shows that the energy consumption of damping in a cycle is proportional to the square of the amplitude, that is $W_e = aX^2$, This equation change into an equivalent viscous damping can be expressed as $C_1 = \frac{k\gamma}{\omega}$, substituting it into Eq. (1), the frequency response function of the model can be written as:

$$H(\omega) = \frac{1}{-\omega^2 M + iD + K} \tag{2}$$

where $D = \omega C_1 + C_2$, from reference [6], the dynamic stiffness matrix of the structure can be showed as:

$$Z = K + iD - \omega^2 M \tag{3}$$

When the product of the frequency response function H_X that be tested and the dynamic stiffness matrix Z_A that be analysis in the theoretical is identity matrix, that $Z_A H_X = I$ means that the theoretical model and the actual physical model is fully consistent, when difference presence between them, their product would not be a identity matrix, so Lin [7] update modal with this advantage, the basic ideal present as follow:

$$\{H_X\}_j - \{H_A\}_j = -[H_A]\Delta Z\{H_X\}_j \tag{4}$$

Here ΔZ is the minus between the actual dynamic stiffness matrix of the structure and the theoretical dynamic stiffness matrix, $\{H_A\}_j$ and $\{H_X\}_j$ are the jth column of frequency response function via FEM analysis and test, respectively. The total differential equations of the formula (3) can be expressed as:

$$\Delta Z = \sum_{k=1}^{N} \frac{\partial Z]}{\partial p_k} \Delta p_k \tag{5}$$

The p_k is the parameter of the various cells, put (5) into (4) and multiply $-[Z_A]$ in the two side of the equation at the same time, then the equation can be gained via the nature of the FRF that $[Z][H] = [I]$ as:

$$[I]_j - Z_A\{H_X\}_j = \sum_{k=1}^{N} \frac{\partial Z_A}{\partial p} \Delta p\{H_X\}_j \tag{6}$$

The updating numerical value of various cells can be got by solving Δp from the front equation. The problem is that this method requested the same dimension of the actual test and the FEM in the application, it is difficult in practice to meet this require, it destroy the connection of the frame of element matrix, and make the element matrix which has been updated lose it's physical meaning when solving formula (6) with multiplication and division.

3. MODEL REDUCTION AND UPDATING

As the measurement dimension smaller than the dimension of the finite element model, it needs indent the finite element model dimension to the measurement dimension, so the dynamic stiffness matrix and the frequency response function matrix can be divided into mesurable DOF **n** and inmesurable DOF **s**, there can get the equation via realigning the dynamic stiffness matrix and the frequency response function matrix:

$$\begin{bmatrix} Z_{nn} & Z_{ns} \\ Z_{sn} & Z_{ss} \end{bmatrix} \begin{bmatrix} H_{nn} & H_{ns} \\ H_{sn} & H_{ss} \end{bmatrix} = \begin{bmatrix} I_{nn} & \\ & I_{ss} \end{bmatrix} \tag{7}$$

The equation can be got from (7)

$$H_{nn}^{-1} = Z_{nn} - Z_{ns} Z_{ss}^{-1} Z_{sn} \tag{8}$$

Let's put the reduction matrix $Z^{red} = Z_{nn}$ and $Z_{nn} H_{nn} = I_{nn}$ into (8), there can be,

$$Z^{red} = H_{nn}^{-1} = Z_{nn} - Z_{ns} Z_{ss}^{-1} Z_{sn} \tag{9}$$

Formula (9) is the reduction matrix of modal dynamic stiffness matrix Z, the $(n+s)$-dimensional matrix can be reduced into a n-dimensional matrix which has the same DOF with the actual testing matrix, then use the $[Z^{red}]$ matrix that has been reduced instead of Z_A in (6),

$$S\Delta p = \Delta I \tag{10}$$

$$\Delta I = \begin{Bmatrix} [I]_j - Z^{red}\{H_x(\omega_1)\}_j \\ [I]_j - Z^{red}\{H_x(\omega_2)\}_j \\ \cdots \\ [I]_j - Z^{red}\{H_x(\omega_n)\}_j \end{Bmatrix},\ S = \begin{bmatrix} \dfrac{\partial Z^{red}}{\partial_{p1}}\{H_x(\omega_1)\}_j & \dfrac{\partial Z^{red}}{\partial_{p2}}\{H_x(\omega_1)\}_j & \cdots & \dfrac{\partial Z^{red}}{\partial_{pN}}\{H_x(\omega_1)\}_j \\ \dfrac{\partial Z^{red}}{\partial_{p1}}\{H_x(\omega_2)\}_j & \dfrac{\partial Z^{red}}{\partial_{p2}}\{H_x(\omega_2)\}_j & \cdots & \dfrac{\partial Z^{red}}{\partial_{pN}}\{H_x(\omega_2)\}_j \\ \cdots & \cdots & \cdots & \cdots \\ \dfrac{\partial Z^{red}}{\partial_{p1}}\{H_x(\omega_n)\}_j & \dfrac{\partial Z^{red}}{\partial_{p2}}\{H_x(\omega_n)\}_j & \cdots & \dfrac{\partial Z^{red}}{\partial_{pN}}\{H_x(\omega_n)\}_j \end{bmatrix}$$

$\{H_x(\omega_i)\}_j$ is the frequency response function measured when frequency is ω_i, the equation can be got from (9),

$$\frac{\partial Z^{red}}{\partial p_i} = \frac{\partial Z_{nn}}{\partial p_i} - \frac{\partial Z_{ns}}{\partial p_i} Z_{ss}^{-1} Z_{sn} - Z_{ns}\frac{\partial Z_{ss}^{-1}}{\partial p_i} Z_{sn} - Z_{ns} Z_{ss}^{-1}\frac{\partial Z_{sn}}{\partial p_i} \tag{11}$$

Put the theory unit parameters as the initial value into (10) and (11), Δp can be got in (10), but S, ΔI are complex number can be known from (2) and (3), so the number of mass sell and stiffness sell matrix in Δp also may be complex number, this is inconsistent with the physical concept, so divide the real and imaginary part can get,

$$\begin{bmatrix} \mathrm{Re}(S) & -\mathrm{Im}(S) \\ \mathrm{Im}(S) & \mathrm{Re}(S) \end{bmatrix} \begin{Bmatrix} \mathrm{Re}(\Delta p) \\ \mathrm{Im}(\Delta p) \end{Bmatrix} = \begin{Bmatrix} \mathrm{Re}(\Delta I) \\ \mathrm{Im}(\Delta I) \end{Bmatrix} \tag{12}$$

In order to facilitate the solution of equation, introduction the error rate of variable X_i and Y_i of mass and stiffness unit. So consider there is the connection between the initial value and the actual value of finite element model,

$$M = \sum_{i=1}^{N} (1 + X_i) M_i^e \tag{13}$$

$$K = \sum_{i=1}^{N} (1 + Y_i) K_i^e \tag{14}$$

There, N is the sum of the frame cell, M_i^e and K_i^e means the ith unit's mass and stiffness matrix. In the finite element model because the cell structure's damping matrix and stiffness matrix has the same form, so use the stiffness damping coefficient γ, so the ith unit's damp matrix can be expressed as,

$$D_i^e = \gamma_i K_i^e \tag{15}$$

According formula (13)–(15) the error of frame dynamic stiffness matrix can be expressed as,

$$\Delta Z = \Delta K + i\Delta D - \omega^2 \Delta M = \sum_{i=1}^{N} (X_i + i\gamma_i)[K^e]_i - \omega^2 \sum_{i=1}^{N} Y_i M_i^e \tag{16}$$

Via using the above variable, it can change the parameter problem about unit stiffness matrix, mass matrix and damping matrix into the problem about solving the error rate variable and stiffness damping ratio coefficient, put (13) and (14) into (11), it can gain that,

$$\frac{\partial Z^{red}}{\partial X_i} = -\omega^2 M_i^e + \omega^2 M_i^e Z_{ss}^{-1} Z_{sn} - \omega^2 Z_{ns} Z_{ss}^{-1} M_i^e Z_{ss}^{-1} Z_{sn} + \omega^2 Z_{ns} Z_{ss}^{-1} M_i^e \tag{17}$$

$$\frac{\partial Z^{red}}{\partial Y_i} = K_i^e - K_i^e Z_{ss}^{-1} Z_{sn} + Z_{ns} Z_{ss}^{-1} K_i^e Z_{ss}^{-1} Z_{sn} - Z_{ns} Z_{ss}^{-1} K_i^e \tag{18}$$

$$\frac{\partial Z^{red}}{\partial \gamma_i} = i\frac{\partial Z^{red}}{\partial Y_i} \tag{19}$$

Combine (16) and (12), can get that,

$$\mathrm{Re}(\{\Delta p\}) = \left\{ \begin{array}{c} \{X_i\} \\ \{Y_i\} \end{array} \right\} \tag{20}$$

$$\mathrm{Im}(\{\Delta p\}) = \left\{ \begin{array}{c} \{\gamma_i\} \\ \{0\} \end{array} \right\} \tag{21}$$

Put (20), (21) into (12), and eliminate $\{0\}$ vector, the finally result can be that:

$$\left[\begin{array}{cc} \mathrm{Re}([S]) & (-\mathrm{Im}([S]))^K \\ \mathrm{Im}([S]) & (\mathrm{Re}([S]))^K \end{array} \right] \left\{ \begin{array}{c} \{X\} \\ \{Y\} \\ \{\gamma\} \end{array} \right\} = \left\{ \begin{array}{c} \mathrm{Re}(\{\Delta I\}) \\ \mathrm{Im}(\{\Delta I\}) \end{array} \right\} \tag{22}$$

There $(([S]))^K$ means the part of updating parameter that connect with siffness matrix. Put the $\{X\}$, $\{Y\}$ and $\{\gamma\}$ solved from (22) into formula (13)–(15), can gain the $[K]$, $[M]$ and $[D]$ updated. According to the description above, the model updating method steps summarized as follows:

1. According the definition of frequency response function obtaine $[Z]$ using the numerical parameters finite element model as the initial value. Then according (8) and the measurable node, gain the $[Z^{red}]^0$ that updated the modal;
2. Via (17), (18) and (19) and unite the first step $[Z^{red}]^0$ obtaine the sensitivity matrix S that after the reduction of dynamic stiffness matrix, and finally express the equation as (12);
3. Translate (12) into (22), and gain the unknown $\{X\}$, $\{Y\}$ and $\{\gamma\}$, then obtaine updated matrix $[K]$, $[M]$ and $[D]$;
4. Repeat the above steps until $\|Z^{red}H_X - I\|_\infty \leq \varepsilon$ (ε is the given iteration stop condition).

4. SIMULATION RESULTS

In order to verify the accuracy of methods, in this paper, the multi-axis gear transmission system (Figure 1) gave in the paper of Wu [8] using the above analysis of the theory of model updating.

From the reference literature can get the model's finite element dynamic equation and its various units' mass and stiffness matrix:

Table 1: The mass matrix of the unit.

M_1		M_2		M_3		M_4		M_5		M_6	
(1, 1)	9721.9	(2, 2)	198.925	(3, 3)	0.0501	(4, 4)	0.0257	(2, 2)	104.7260	(6, 6)	26.8135
(2, 1)	1.0	(3, 2)	−1.1775	(4, 3)	0.0250	(5, 4)	0.0129	(6, 2)	−2.1950	(7, 6)	−0.0805
(1, 2)	1.0	(2, 3)	−1.1775	(3, 4)	0.0250	(4, 5)	0.0129	(2, 6)	−2.1950	(6, 7)	−0.0805
(2, 2)	988.3	(3, 3)	403.0158	(4, 4)	234.05	(5, 5)	234.0257	(6, 6)	300.911	(7, 7)	81.6191

Table 2: The stiffness matrix of the unit: 1.0e+006*.

K_1		K_2		K_3		K_4		K_5		K_6	
(1, 1)	5.4600	(2, 2)	9.3508	(3, 3)	35.2800	(4, 4)	68.7000	(2, 2)	45.0372	(6, 6)	152.0510
(2, 1)	−5.4600	(3, 2)	4.0337	(4, 3)	−35.2800	(5, 4)	−68.7000	(6, 2)	9.3473	(7, 6)	18.0806
(1, 2)	−5.4600	(2, 3)	4.0337	(3, 4)	−35.2800	(4, 5)	−68.7000	(2, 6)	9.3473	(6, 7)	18.0806
(2, 2)	5.4600	(3, 3)	1.7400	(4, 4)	35.2800	(5, 5)	68.7000	(6, 6)	1.9400	(7, 7)	2.1500

Note: The (x, y) in table means the (x, y) position in matrix, there be 0 where had no data.

Assume the unit damping stiffness rate γ expressed in Table 3.

Assume the test frequency ω = [10 20 50 100], so there can get the full FRF combining the above data. In this paper, they use node 2 as the actuator, choosing the FRF on node 1, 2, 3, 4 go along the iteration. At the same time, in order to verify the effectiveness of the algorithm, assuming the unit model error rates that assigned the finite element initial number shown in Tables 4 and 5.

And assume the damping stiffness ratio of the every finite element unit no updating are all 0.

Table 6 is the damping element stiffness of each unit after the 5th iteration.

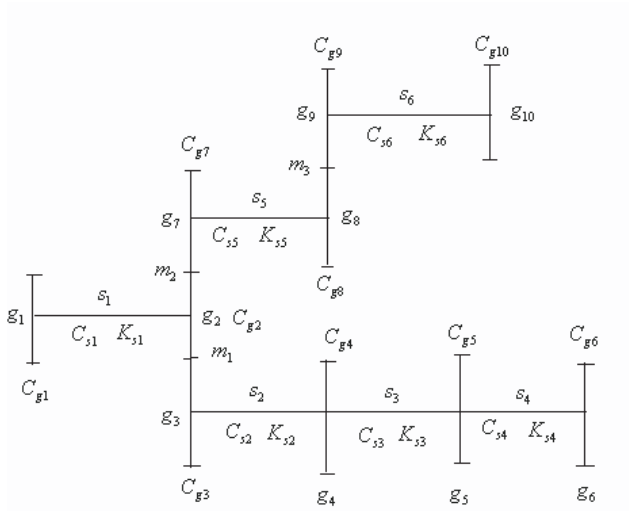

Figure 1: The picture of multi-axis gear transmission system.

The stiffness matrix and mass matrix after 5th iteration,

$$M = \begin{bmatrix} 9722.1 & 1.000 & 0 & 0 & 0 & 0 & 0 \\ 1.000 & 1291.9 & -1.1775 & 0 & 0 & -2.194 & 0 \\ 0 & -1.1775 & 403.07 & 0.025 & 0 & 0 & 0 \\ 0 & 0 & 0.025 & 234.08 & 0.0129 & 0 & 0 \\ 0 & 0 & 0 & 0.0129 & 234.03 & 0 & 0 \\ 0 & -2.194 & 0 & 0 & 0 & 327.64 & -0.0805 \\ 0 & 0 & 0 & 0 & 0 & -0.0805 & 81.620 \end{bmatrix}$$

$$K = 1.0e+006 \times \begin{bmatrix} 5.46 & -5.46 & 0 & 0 & 0 & 0 & 0 \\ -5.46 & 59.85 & 4.034 & 0 & 0 & 9.348 & 0 \\ 0 & 4.034 & 37.02 & -35.28 & 0 & 0 & 0 \\ 0 & 0 & -35.28 & 103.98 & -68.70 & 0 & 0 \\ 0 & 0 & 0 & -68.70 & 68.70 & 0 & 0 \\ 0 & 9.348 & 0 & 0 & 0 & 153.51 & 18.02 \\ 0 & 0 & 0 & 0 & 0 & 18.02 & 2.143 \end{bmatrix}$$

After comparative the stiffness matrix, mass matrix given in literature [8] and a given initial value in this article, as well as updating the various units of the stiffness, mass, it can show that the relative error of cell parameters that adding the man-made unit stiffness (the biggest difference between the 70 times) and damping matrix (the biggest difference between the 30 times) before updating at the maximum of 0.031% (occurred in the stiffness matrix in the first 6 units) others are all less than 0.03% after 5 iterations with the using of the method of this paper It should be noted that ignores the existence of damping before updating, while after updating (compare Table 6 and Table 3), they are very close.Analysed the FRF using the system equation before and after updating, the frequency response function curves after updating and the frequency response function curves using the analysis method in paper [8] can be showed.

Therefore, combining the above data, the thing can be believed that this method in this paper

Table 3: Unit damping stiffness rate.

Unit number	1	2	3	4	5	6
Unit damping stiffness rate γ	0	0.4	0.6	0	0	0

Table 4: Stiffness error rate Y.

Unit number	1	2	3	4	5	6
Error rate/%	0	−70	−50	0	−10	15

Table 5: Mass error rate X.

Unit number	1	2	3	4	5	6
Error rate/%	−20	0	20	0	30	0

Table 6: Damping and stiffness ratio of each unit after updating.

Unit number	1	2	3	4	5	6
Damping and stiffness ratio γ	$7.82e-018$	0.4000	0.6000	$4.11e-013$	$4.03e-015$	$3.58e-013$

not only can reduce the stiffness of each element of error significantly, but also can identify all of the damping unit correctly that it has be assumed at the beginning.

5. CONCLUSION

In this paper, a new updating method be showed based on the traditional FRF model updating method, its characteristic showed as follow:

1. It can update the damping model, and overcome the shortage of modal updating method.
2. It reduce the test number using the model reduction, and introduce into the unit damping stiffness ratio, compare to the traditional FRF method it reduce the unknown value of updating, improve computational efficiency, and the results of updating are more accurate.
3. Consider the effect of the nonlinear factors, it is the focus of future research.

ACKNOWLEDGMENT

This work was supported by National Natural Science Foundation of China (50775170, 50805111) and Natural Science Basic Research Plan of Shaanxi Provincial (SJ08E203) and Basic Research Foundation of Universities, Ministry of Education of China.

REFERENCES

1. Zhu, H., B. Xu, and Y. Huang, "Comparison and evaluation of analytical approaches to structural dynamic model correction," *Advances in Mechanics*, Vol. 32, No. 4, 513–525, 2002.
2. Li, H. and H. Ding, "Progress in model updating for structural dynamics," *Advances in Mechanics*, Vol. 35, No. 2, 170–180, 2005.
3. Bao, H., D.-Z. Zhao, and Y.-Q. Qiao, "Methods updating for the dynamic model with orthogonal vector basis," *Journal of Xidian University*, Vol. 36, No. 1, 151–155, 2009.
4. Xu, Z.-M., R.-Y. Shen, and H.-X. Hua, "Updating finite element midel by the sensitivity analysis of FRF correlation function," *Journal of Mechanical Strength*, Vol. 25, No. 1, 5–8, 2003.
5. Hemez, F. M. and G. W. Brown, "Improving structural dynamics models by correlating simulated to measuredfrequency response functions," *39th AIAA/ASME/ASCE/AHS/ASCS Structures, Structural Dynamics and Materials Conference, AIAA-98-1789*, 772–782, Apr. 1998.
6. Ting, T., "Design sensitivity analysis of structural frequency response," *4th AIAA/USAF/NASA/OAI Symposium on Multidisciplinary Analysis and Optimization, AIAA-92-4799-CP*, 878–881, Sep. 1992.
7. Lin, R. M. and J. Zhu, "Model updating of damped structures using FRF data," *Mechanical Systems and Signal Processing*, Vol. 20, 2200–2218, 2006.
8. Xu, Z.-M., T.-M. Gao, and R.-Y. Shen, "Improved finite element model updating method based on frequency response functions," *Journal of Vibration and Shock*, Vol. 21, No. 3, 43–46, 2002.
9. Fu, Z.-F., *Vibration Modal Analysis and Parameter Identification*, Machine Press, Beijing, China, 1990.
10. Wu, J. S. and C.-H. Chen, "Trisonal vibration analysis of gear-branched systems by finite element method," Institute of Naval Architecture and Marine Engineering, 2000.

Improved Coupling Matrix Extracting Method for Chebyshev Coaxial-cavity Filter

Hongbo Ma, **Daiwen Yang**, **and Jinzhu Zhou**
Key Laboratory of Electronic Equipment Structure Design (Xidian University), Ministry of Education
Xi'an 710071, China

Abstract— Coupling matrix is an important means for design and analysis to Chebyshev filters, which is also an effective method for improving the efficiency and precision of the microwave filters tuning. In this thesis, an improved coupling matrix extraction method was developed based on the combination of Jacobi Method and the optimization method. The method gets the initial matrix from the solutions of the Jacobian Method. Then the matrix is utilized as the initial value of the iterative optimization to obtain the accurate coupling matrix. This method has the advantages of both methods. To obtain the initial coupling matrix, experiments on coupling matrix extracting for coaxial-cavity tunable filter is designed. S parameters are measured in the experiments. Then zeros and poles are measured. Proved by engineering experiments and analysis, the method is feasible and rational.

1. INTRODUCTION

Chebyshev filter is a high performance filter, and it has the optimization characteristic. Currently, tuned filter mainly rely on manual adjustment of experience, which spend a lot of time and cost. While extracting the coupling matrix from the test data of filter is the key of improving efficiency and accuracy of the filter.

The equivalent circuit model of modern general Chebyshev filter is proposed by A. E. Atia [1, 2] in 1972, who raised the concept of coupling matrix and gived an improved coupling matrix extraction method by integrated approach. According this, R. J. Cameron [3–5], S. Tamiazzo [6], G. Macchiarella [7] and H. C. Bell [8] improved the method of extracting coupling matrix of general Chebyshev filter and separately gave the elimination method of folded, Cul-de-Sac, CT/CQ and wheel structure. In the domestic, research on the coupling matrix got some achievements. Qiang Rui [9] got the coupling matrix by optimization. Zuo Tao [10] made Jacobi matrix inverse eigenvalue method of getting coupling coefficient matrix.

In this paper, proposing a new method of extracting the coupling matrix, which combined the Jacobi Inverse Eigenvalue Method and optimization. This method is of higher accuracy.

2. EQUIVALENT CIRCUIT ANALYSIS OF COAXIAL CAVITY FILTERS

As shown in Figure 1, the circuit model of the filter is formed by equivalent capacitances and inductances. Adjacent resonators generate coupling through mutual inductance.

In Ref. [1], circuit matrix equation is:

$$(M_n - \lambda I - jR)i = Zi = -je \tag{1}$$

where, λ is the normalized low-pass frequency, R is the matrix in which most elements are zero besides $R_1 = r_1$, $R_2 = r_n$. M_n is the Coupling coefficient matrix. $e = [1, 0, 0, 0 \ldots, 0]^T$ is voltage vector, i is Ring-current vector. And Z is the impedance matrix.

From Eq. (1), the admittance matrix Y can be obtained as

$$Y = Z^{-1} = (M_n - \lambda I - jR)^{-1} \tag{2}$$

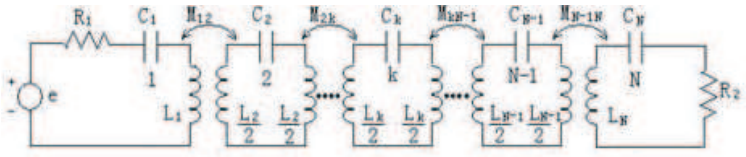

Figure 1: Filter network equivalent schematic.

Then the input admittance y_{11} can be expressed as

$$y_{11}(\lambda) = (-\lambda I + M_n)^{-1}_{11} = \begin{bmatrix} -\lambda I + m_{11} & m_{1,2} & 0 & 0 & 0 & 0 & 0 \\ m_{2,1} & -\lambda I + m_{11} & m_{2,3} & 0 & 0 & 0 & 0 \\ 0 & m_{2,3} & -\lambda I + m_{11} & \ddots & 0 & 0 & 0 \\ 0 & 0 & \ddots & \ddots & \ddots & 0 & 0 \\ 0 & 0 & 0 & \ddots & \ddots & \ddots & 0 \\ 0 & 0 & 0 & 0 & \ddots & -\lambda I + m_{11} & m_{n-1,n} \\ 0 & 0 & 0 & 0 & 0 & m_{n,n-1} & -\lambda I + m_{11} \end{bmatrix}^{-1}_{11}$$

where, λ is the normalized low-pass frequency. $m_{i,i+1}$ is normalized coupling coefficient between the resonator and $(i+1)$th resonator. $m_{i,i}$ is normalized resonant frequency, which is off-center frequency of the ith resonator.

The y_{11} can be calculated as matrix inversion

$$y_{11}(\lambda) = (-\lambda I + M_n)^{-1}_{11} = \frac{|-\lambda I + M_{n-1}|}{|-\lambda I + M_n|} \tag{3}$$

From Eq. (3), it is known that n poles and $n-1$ zeros are separately equal to eigenvalue of M_n and M_{n-1}. M_{n-1} is the remaining $n-1$ order sequence master matrix.

3. COUPLING MATRIX EXTRACTION BY COMBINED METHOD

Combined Method is developed based on the combination of the inverse eigenvalue method for Jacobian matrices and the optimization method. Firstly, the coupling matrix can be calculated by the solutions of the inverse eigenvalue of Jacobian matrices. Secondly, using the matrix as the initial value of optimization method, the accurate values of coupling coefficients can be obtained. Compared with both approaches, the method has higher searching speed and precision.

3.1. Coupling Matrix Extraction by the Solutions of the Inverse Eigenvalue of Jacobian Matrices

Figure 1 shows that when $R_n = 0$, the reflection coefficient of input port is [1]:

$$S_{11} = |S_{11}| e^{j\theta} = \frac{y_{11} - r_1^{-1}}{y_{11} + r_1^{-1}} \tag{4}$$

From (4), it can been seen $S_{11} = \mp 1$ at the zeros and poles of y_{11}. When the Phase of S_{11} is at $\theta = \pm 180^\circ$ and $\theta = 0^\circ$. So the frequency corresponding to the phase at $\theta = \pm 180^\circ$ and $\theta = 0^\circ$ can be obtained from Vector Network Analyzer, which is zeros and poles of y_{11} and the eigenvalue of M_n and M_{n-1}.

$$Aq_1 = a_1 q_1 + b_1 q_2 \quad Aq_i = a_i q_i + b_{i-2} q_{i-1}, \quad i = 2, 3 \ldots n \tag{5}$$

According to Eq. (5)

$$a_n = q_n^T A q_n, \quad b_{n-1} = \left[\left(Aq_{n-1} - a_{n-1} q_{n-1} - b_{n-2} q_{n-2} \right) \left(Aq_{n-1} - a_{n-1} q_{n-1} - b_{n-2} q_{n-2} \right) \right]^{\frac{1}{2}} \tag{6}$$

According to the iterative formula, the coupling matrix T_n can be obtained

$$T_n \begin{bmatrix} a_1 & b_1 & & 0 \\ b_1 & \ddots & \ddots & \\ & \ddots & \ddots & b_{n-1} \\ 0 & & b_{n-1} & a_n \end{bmatrix}, \quad A = \begin{pmatrix} m_1 & & 0 \\ & \ddots & \\ 0 & & m_n \end{pmatrix} \tag{7}$$

In order to improve the accuracy of extracting the coupling matrix, the coupling coefficients can be utilized as the initial value of the iterative optimization and then optimize.

3.2. Extraction of Coupling Coefficient by Optimization

In this thesis, the optimization method is utilized to calculate the accurate value of coupling coefficients matrix, which was only decided by the zeros, poles and In-band return loss:

$$\begin{aligned} K \;=\; & \sum_{i=1}^{N} |S_{11}(\omega_{zi})|^2 + \sum_{i=1}^{P} |S_{21}(\omega_{pi})|^2 + \left(|S_{11}(\omega=-1)| - \frac{\varepsilon}{\sqrt{1+\varepsilon^2}} \right)^2 \\ & + \left(|S_{11}(\omega=1)| - \frac{\varepsilon}{\sqrt{1+\varepsilon^2}} \right)^2 (P \le N) \end{aligned} \tag{8}$$

where, ω_{zi} and ω_{pi} are respectively zeros and poles of $C_N(\omega)$, the last two expressions are used to decide In-band return loss. Optimization would be terminated when $K = 0$, where ε and ω_{pi} are designated variables. ω_{zi} can be regarded as the function of ω_{pi}. From Ref. [11], it shows that

$$C_N(\omega) \;=\; \frac{1}{2} \frac{G_N(\omega) + G'_N(\omega)}{\prod_{i=1}^{N} (1 - \omega/\omega_{pi})} \tag{9}$$

$$G_N(\omega) \;=\; \prod_{i=1}^{N} \left[\left(\omega - \frac{1}{\omega_{pi}} \right) + \left(\omega^2 - 1 \right)^{1/2} \left(1 - \frac{1}{\omega_{pi}^2} \right)^{1/2} \right] \tag{10}$$

$$G'_N(\omega) \;=\; \prod_{i=1}^{N} \left[\left(\omega - \frac{1}{\omega_{pi}} \right) - \left(\omega^2 - 1 \right)^{1/2} \left(1 - \frac{1}{\omega_{pi}^2} \right)^{1/2} \right] \tag{11}$$

According to the Ref. [11], after derivation, it has N zero $-\omega_{zi}$ and then take zeros, poles and ε which is related to Return Loss to Eq. (8). It can determine the parameters of the objective function.

Finally, the relationship between Circuit parameters M and the objective function is established.

On the analysis above, the optimal model of extracting the coupling matrix can be established as model **PI:**

$$\begin{aligned} \text{Min}: \quad & K = \sum_{i=1}^{N} |S_{11}(\omega_{zi})|^2 + \sum_{i=1}^{P} |S_{21}(\omega_{pi})|^2 + \left(|S_{11}(\omega=-1)| - \frac{\varepsilon}{\sqrt{1+\varepsilon^2}} \right)^2 \\ & + \left(|S_{11}(\omega=1)| - \frac{\varepsilon}{\sqrt{1+\varepsilon^2}} \right)^2, (P \le N) \\ s.\,t.: \quad & C_N(\omega) = \frac{1}{2} \frac{G_N(\omega) + G'_N(\omega)}{\prod_{i=1}^{N} (1 - \omega/\omega_{pi})} \\ & G_N(\omega) = \prod_{i=1}^{N} \left[\left(\omega - \frac{1}{\omega_{pi}} \right) + \left(\omega^2 - 1 \right)^{1/2} \left(1 - \frac{1}{\omega_{pi}^2} \right)^{1/2} \right] \\ & G'_N(\omega) = \prod_{i=1}^{N} \left[\left(\omega - \frac{1}{\omega_{pi}} \right) - \left(\omega^2 - 1 \right)^{1/2} \left(1 - \frac{1}{\omega_{pi}^2} \right)^{1/2} \right] \end{aligned}$$

PI

4. EXPERIMENT AND ANALYSIS

4.1. Experiment and Results

A Chebyshev coupled coaxial cavity tunable filter is taken to certify the methods. Its structure consists of tuning Structure and coupled structure. Tuning unit consists of four capacitors and $\lambda/4$ coaxial cavity. Taking into account the thickness effect, it reduces loss through the cavity surface of silver-plated. Tuning is achieved by the tuning screw which can make inner conductor elongate or shorten. Coupled structure is formed by the coupling ring and the coupling hole. The input and output stage coupling reactance of the filter achieved by the coupling ring. Inter-stage coupling reactance achieved by the coupling hole.

In the experiment, the Center Frequency and S parameter are measured in different frequency. Then coupling matrix can be extracted by Combined Method. Finally the experiment compared the extracted Coupling matrix and analysised which method is more accurate to extract the coupling matrix.

(1) Measuring S parameter in different frequency and the phase of S_{11} when terminal is shorted through Vector Network Analyzer. The results are shown in Table 1.

Table 1: S_{11} after terminal is shorted.

Pole (790 MHz)	775.4612	782.9054	796.3457	803.3478
Zero (790 MHz)	776.5713	789.7815	800.7714	
Pole (810 MHz)	795.3089	803.5078	816.7825	823.8236
Zero (810 MHz)	796.4614	809.9546	820.9478	
Pole (830 MHz)	815.0625	823.4296	837.0223	844.0613
Zero (830 MHz)	816.2852	829.9869	841.2266	
Pole (870 MHz)	854.7989	863.5047	876.8458	884.7071
Zero (870 MHz)	855.9455	871.8836	881.5679	

(2) Taking zeros and poles in different frequency.

Table 2: The inverse eigenvalue method for Jacobian matrices.

JACOBI	M12	M23	M34	M11	M22	M33	M44
790	0.9583	0.7398	0.9096	0.1263	0.0167	−0.2332	−0.0936
810	0.9352	0.7317	0.9814	0.1968	0.0188	−0.2370	−0.0438
830	0.9055	0.6763	0.9181	0.1899	0.0064	−0.2301	−0.0189
870	0.8755	0.6330	0.8662	0.2251	0.0144	−0.2211	0.0191

(3) Taking the extracted coupling matrix as initial matrix to optimization.

Table 3: Extraction of the coupling matrix by combined method.

Combined	M12	M23	M34	M11	M22	M33	M44
790	0.6875	0.5666	0.9207	0.0901	0.0703	−0.0291	0.1047
810	0.6625	0.5678	0.8582	0.0802	0.0881	−0.0480	0.0183
830	0.6519	0.5627	0.9427	0.1236	0.0456	−0.0782	−0.0650
870	0.6268	0.5528	0.9155	0.1058	0.0707	−0.0937	−0.0848

4.2. Experimental Analysis

It get the coupling matrix corresponding to S-parameter diagram through the MATLAB program. Figure 2 shows different bands S parameter results of measurements, Jacobi and combined method.

Figure 2 shows that: (1) Insertion loss of the curve responding to the two ways is basically the same, the error does not exceed 0.3 dB. But bandwidth of the Jacobi corresponding curve (red dotted line) is wider than the measured curve (green dotted line) and have greater errors, while the bandwidth of the combined method of the corresponding curve (blue dashed line) are close to measured values. (2) Similarly, the bandwidth of Jacobi corresponding curve (red solid line) is wider than measured (green curve), which have greater error, while the bandwidth of the combined method corresponding curve (blue solid line) are close to measured value. The error of the Return loss obtained by Jacobi is greater, which is about 2.5 dB, while the combined method has the error without exceeding 0.5 dB.

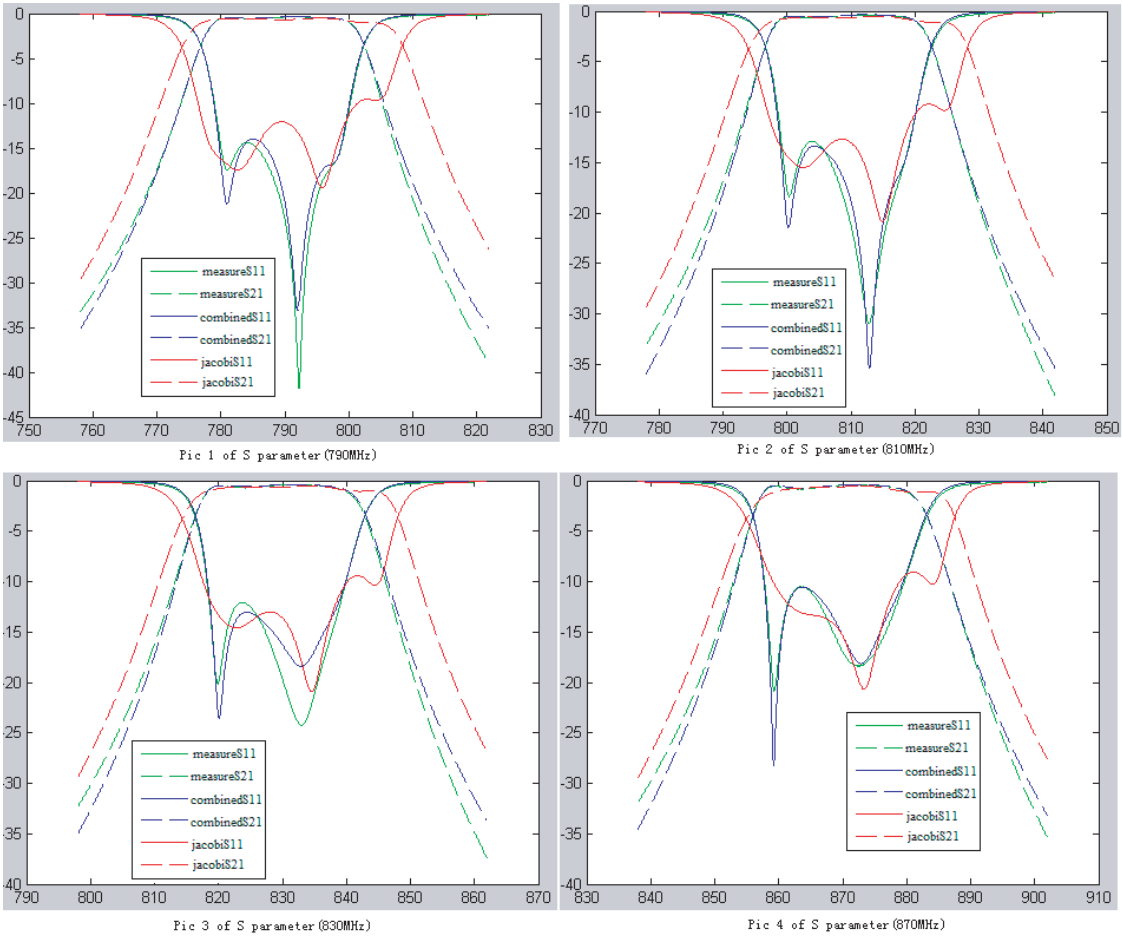

Figure 2: S parameter comparison charts of different frequency bands.

5. CONCLUSION

This thesis presents an improved method of extracting coupling matrix. It can quickly and accurately extract the coupling matrix by combination of Jacobian Matrices and optimization. And it is suitable for Chebyshev cascade filter. The method is proved to be correct by an engineering example.

REFERENCES

1. Atia, E. and A. E. Williams, "Narrow-bandpass waveguide filters," *IEEE Trans. Microwave Theory Tech.*, Vol. 20, 258–265, Apr. 1972.
2. Atia, E. and A. E. Williams, "Narrow-band multiple-coupled cavity synthesis," *IEEE Trans. Circuits Syst.*, Vol. 21, 649–655, Sep. 1974.

3. Cameron, R. J., "General coupling matrix synthesis methods for chebyshev filtering functions," *IEEE Trans. Microwave Theory Tech.*, Vol. 47, No. 4, 433–442, 1999.
4. Cameron, R. J., "Advanced coupling matrix synthesis techniques for microwave filters," *IEEE Trans. Microwave Theory Tech.*, Vol. 51, No. 1, 1–10, 2003.
5. Cameron, R. J., M. Yu, and Y. Wang, "Direct-coupled microwave filters with single and dual stopbands," *IEEE Trans. Microwave Theory Tech.*, Vol. 53, No. 11, 3288–3297, 2005.
6. Tamiazzo, S. and G. Macchiarella, "An analytical technique for the synthesis of cascaded N-tuplets cross-coupled resonators microwave filters using matrix rotations," *IEEE Trans. Microwave Theory Tech.*, Vol. 53, No. 5, 1693–1698, 2005.
7. Macchiarella, G., "Accurate synthesis of inline prototype filters using cascaded triplet and quadruplet sections," *IEEE Trans. Microwave Theory Tech.*, Vol. 50, No. 7, 1779–1783, 2002.
8. Bell, H. C., "Canonical asymmetric coupled-resonator filters," *IEEE Trans. Microwave Theory Tech.*, Vol. 30, No. 9, 1335–1340, 1982.
9. Qiang, R. and Y. Wang, "Quasi-elliptic function filter prototype circuit parameters of the optimized extraction," *Microwave Journal*, Vol. 18, No. 3, 18–22, 2002.
10. Zuo, T., "Coupling matrix extraction based on solutions of the inverse eigen problem for Jacobi matrices," *J. T. Singhua Univ. (Sci. & Tech.)*, Vol. 48, No. 10, 1028–1031, Dec. 2003.
11. Amari, S., "Synthesis of cross-coupled resonator filters using an analytical gradient-based optimization technique," *IEEE Trans. Microwave Theory Tech.*, Vol. 48, No. 9, 1559–1564, 2000.

Subreflector Real-time Compensation for Main Reflector Deformation of Shaped Cassegrain Antenna

W. Wang, G. J. Leng, and H. P. Li
School of Electromechanical Engineering, Xidian University, Xi'an, Shaanxi 710071, China

Abstract— On the degradation of electrical performance of large shaped Cassegrain antennas by the main reflector deformation, a method for compensation by moving subreflector is presented. A group of best-fit paraboloids are found by least-square fitting the theoretical discrete data. The group of paraboloids are used to fit the deformed main reflector, with the constraint of all these focuses being in line. The best-fit parameters are optimized and the adjustments of subreflector are derived with the ratio of main reflector and subreflector. The adjustments at various attitudes are saved in a look-up table to real-time compensate for main reflector deformation. From the experimental verification on a 64 m reflector antenna, satisfactory results are obtained and will be used in practice.

1. INTRODUCTION

Cassegrain antennas are widely used in many fields, such as radar tracing, satellite communication and deep space exploration, due to their advantages of higher illumination efficiency and lower side loss. The main and sub-reflector are both shaped for the uniform distribution of phase in aperture, which will improve the efficiency of the antenna system. The precision of reflector surface has an important effect on the electrical performance. There are many loads, such as gravity, wind, rain and so on, which drive the antenna structure deform from their design shape [1]. The surface accuracy gets down which will result in gain loss and beam distortion [2]. However, the influence of these coefficients changes with the variation of elevation angles.

S. Von Hoerner had given a very important theory as "homologous design" which will reduce the effect of those deformation [3], but never elimination totally. Panels aligned on the main reflector can be adjusted fine and reduce the deviation of the surface shape [4], but only in some degrees. To change the relative position of dual reflectors via subreflector motion may eliminate some phase error in aperture. In 100 m GBT antenna [5], the method is adopted, however the main reflector is a piece of surface cut from a big standard paraboloid which is different from the shaped surface we discuss here.

The dominant course of gain loss and beam distortion is identified to be the deformation of the main reflector surface with elevation. This paper describe a method to compensate the effect caused by the main reflector deformation with subreflector adjustment.

2. SEGMENTED BEST FIT OF DEFORMED SURFACE

Assumed that there are M samples in the shaped design surface generatrix and they are divided into N segments in which the former $N-1$ segments are with the same samples. To guarantee the continuity, neighbor segments should have a public sample. Consequently, there are $[M-M\%(N-1)]N+M\%(N-1)$ samples in the Nth segment as well.

If the nth parabolic segment can be described as

$$r_n^2 = 4f_n\left(z_n + \Delta H_n\right) \quad (n = 1, 2, \ldots, N) \tag{1}$$

the coefficient f_n and ΔH_n of the stepwise function in (1) can be optimized by

$$\begin{cases} \text{Find} \ \ (N, f_1, f_2, \ldots, f_N, \Delta H_1, \Delta H_2, \ldots, \Delta H_N) \\ \min \ \ \sigma = \sqrt{\dfrac{\sum\limits_{n=1}^{N}\sum\limits_{i=1}^{D_n}\left(\frac{r_{ni}^2}{4f_n} - z'_{ni} - \Delta H_n\right)^2}{M}} \\ s.t. \quad N \le M-1, \\ \qquad f_n > 0, \quad (n = 1, 2, \ldots, N) \end{cases} \tag{2}$$

where, N is the amount of segments; $f_1, f_2, \ldots, f_N$ are individual focal length; $\Delta H_1, \Delta H_2, \ldots, \Delta H_N$ are individual axial coordinates of parabolic vertexes; D_n is sample amount of the nth parabolic segment; M is the amount of all samples. The program can be solved using the least square method.

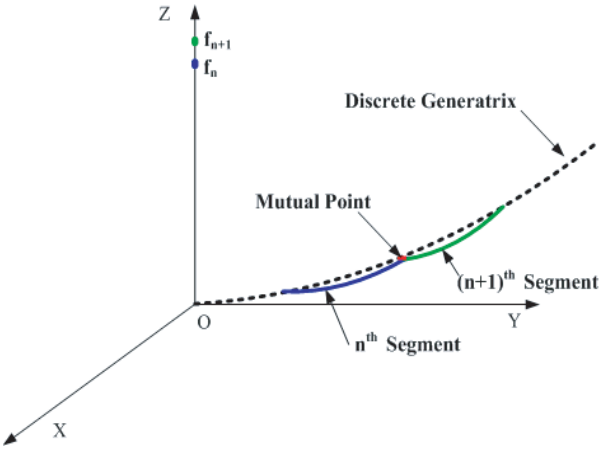

Figure 1: Parabolic curve fitting of discrete generatrix samples.

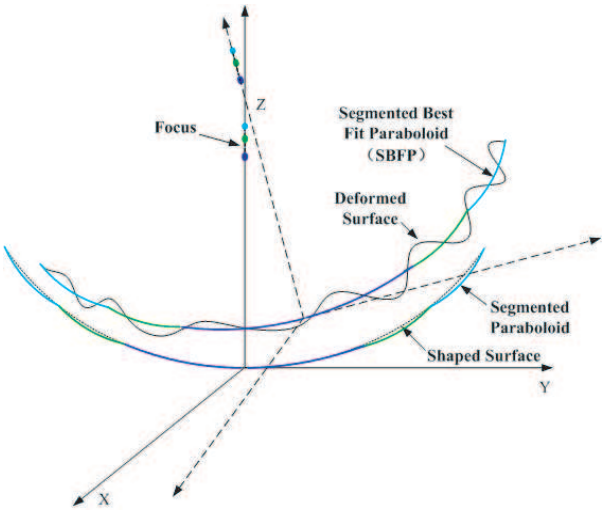

Figure 2: Segmented best fitting of deformed surface.

Firstly, making the partial differential of the function equal to zero results in the normalized equations as

$$\begin{cases} \frac{\partial \sigma}{\partial N} = 0 \\ \frac{\partial \sigma}{\partial fi} = 0 \\ \frac{\partial \sigma}{\partial \Delta Hi} = 0 \end{cases} \qquad (i = 1, 2, \ldots, N) \tag{3}$$

Solve the equations and some segmented parabolic curves will be obtained. Segmented parabolic curves turning around on the focus axis result in a group of paraboloids, with focuses in line. And the range of focal length variance, called as focal line, can be calculated by

$$\Delta F_0 = \max\left(f_n - \Delta H_n\right) - \min\left(f_n - \Delta H_n\right) \qquad (n = 1, 2, \ldots, N) \tag{4}$$

In order to make the group of standard paraboloids best fit the deformed surface, we should rotate them, translate them and change their focal length, shown in Figure 2. According the requirement of match, all the group of paraboloids should rotate with the same angle. Then each the group of paraboloids may translate along the public axis and change focal length individually to approach the proper region of the deformed surface.

Then, minimizing the root mean square of z deviation from the deformed surface to the best fit paraboloids, we can construct the optimization model as

$$\begin{cases} \text{Find } H = (\Delta x, \Delta y, \Delta z, \varphi_x, \varphi_y, \Delta f_1, \Delta f_2, \ldots, \Delta f_K, t_1, t_2, \ldots, t_K) \\ \min\ rms = \sqrt{\dfrac{\sum\limits_{j=1}^{K}\sum\limits_{i=1}^{D_j}\left[\frac{(x_{ji}-\Delta x-mt_j)^2+(y_{ji}-\Delta y-nt_j)^2}{4(f_j+\Delta f_j)}+\Delta z+pt_j+y_{ji}\varphi_x-x_{ji}\varphi_y+\Delta H_j-z'_{ji}\right]^2}{M}} \\ s.t.\ \ \overline{OF_j}' = \overline{OF}_j \cdot T_j\ , \\ \qquad T_j = \begin{bmatrix} \cos\varphi_y & 0 & -\sin\varphi_y & 0 \\ \sin\varphi_x \sin\varphi_y & \cos\varphi_x & \sin\varphi_x \cos\varphi_y & 0 \\ \cos\varphi_x \sin\varphi_y & -\sin\varphi_x & \cos\varphi_x \cos\varphi_y & 0 \\ \Delta x + mt_j & \Delta y + nt_j & \Delta z + pt_j & 1 \end{bmatrix}, \\ \qquad \max\left(\overline{OF_j}' - \overline{OF}_j\right) - \min\left(\overline{OF_j}' - \overline{OF}_j\right) \le \Delta f_0\ , \quad (j = 1, 2, \ldots, K) \end{cases} \tag{5}$$

where, Δx, Δy, Δz, φ_x, φ_y are quantities of the whole translation and rotation of every paraboloid; $\Delta f_1, \Delta f_2, \ldots, \Delta f_K$ are variations of every focal length; $t_1, t_2, \ldots, t_K$ are displacements of every paraboloid along the public axis; K is the amount of standard paraboloids; D_j is the amount of nodes in the jth paraboloid; M is the amount of nodes.

3. DISTORTION COMPENSATION

The position of the actual subreflector can be determined by the virtual focal line, shown as Figure 3. Using the variations of focal length and the original coordinates of focal points, the real coordinates

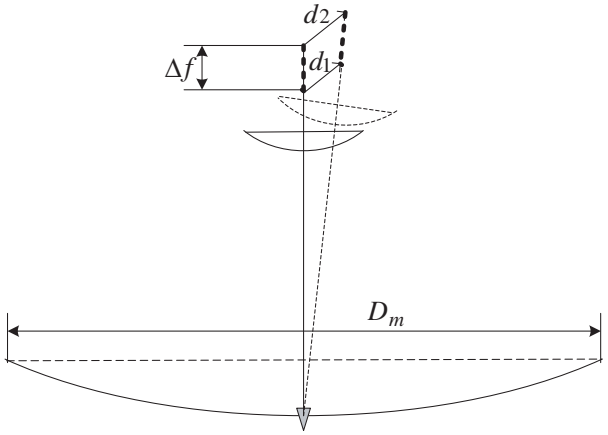

Figure 3: Subreflector motion by virtue focal line.

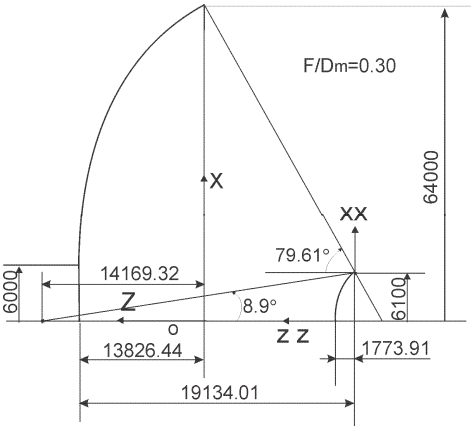

Figure 4: The diagram of 64 m antenna.

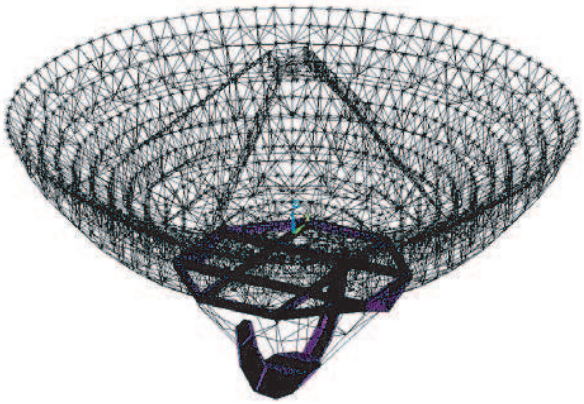

Figure 5: The FEM model of 64m antenna back-up structure.

$(x_i^{FR},\ y_i^{FR},\ z_i^{FR})$ of focal points can be calculated by

$$\left.\begin{aligned} x_i^{FR} &= x_i^{FO} + \Delta x + (f_i + \Delta f_i)\sin(\varphi_y) \\ y_i^{FR} &= y_i^{FO} + \Delta y - (f_i + \Delta f_i)\sin(\varphi_x) \\ z_i^{FR} &\cong z_i^{FO} + \Delta z + \Delta f_i + \Delta t_i \end{aligned}\right\} \tag{6}$$

The focal line for matching dual reflectors is composed with focal points in line. During the determining the subreflector motion, the relative position may change within the constraint range ΔF_0. Using the coordinates of both ends of focal line, the near point displacement $\mathbf{d}_1 = (\ \Delta X_1^F \quad \Delta Y_1^F \quad \Delta Z_1^F\ )$ and the far point displacement $\mathbf{d}_2 = (\ \Delta X_2^F \quad \Delta Y_2^F \quad \Delta Z_2^F\ )$ can be calculated as the subreflector motion.

Large radio telescopes usually trace the cosmic object within a region of elevation angle. The gravity deformation of antenna main reflector can be described as the function of elevation angle, as well as the matching position of subreflector. In order to meet the requirement of surface precision and electrical performance in the whole working range, it is necessary to consider the situation in a whole. The tracing speed of telescope is not too high, so the subreflector motion may have enough time to proceed. Dividing the working range into lots of elevation angles, the main reflector deformation and subrefelctor motion at each angle can be calculated and saved into a look up table. When the antenna is working, the proper parameter of subrefelctor motion can be queried from the database and used to drive the subreflector into the optimal position, then the gravity deformation of main reflector will be compensated real time.

4. NUMERICAL SIMULATION

The simulation is carried on a 64 m shaped Cassegrain dual reflector antenna, which is used for deep space exploration. The diagram is shown in Figure 4, with main reflector diameter 64000 mm, subreflector diameter 6000 mm, center body diameter 6100 mm, and F/D ratio 0.30. The FEM model of the antenna back up structure is built using Ansys software, shown as Figure 5.

Using the method in Section 2, the discrete samples of design generatrix can be fit by segmented parabolic curves. It is 29000 mm in radial and there 5801 samples with 5 mm between two neighbor samples. The fitting precision is assigned by 0.01 mm to improve the degree of approximation. Using the least square method to solve Equation (2), the vertex coordinates and radial zone of every fitting parabolic curve are obtained and the focal length is 2243.568 mm. Static structural analysis is made at every 15 degrees from face-side (0 degree) to face-up (90 degrees), then the group of standard paraboloids are used to bet fit the upnodes at every attitude.

The main reflector deformation has an effect on the electrical performance of the antenna. Y. Rahmat-Samii gave an equation which demonstrates the gain loss by the rms of reflector deviation [6], as shown

$$\Delta G = 10 \log e^{-(4\pi\kappa\varepsilon_{rms}/\lambda)^2} \tag{7}$$

where, $\kappa \cong (4F/D)\sqrt{\ln[1 + 1/(4F/D)^2]}$; F/D is the ratio of focal length to diameter, with the value of 0.3 in this case. In order to verify the contribution of subreflector compensation to electrical performance, the gain loss of the antenna is calculated and compared with the original one. The results are in Table 1, from which it is found that the gravity deformation increase with the elevation angle and the increment of the error relative to the BFP is less than to the design surface. As the antenna works at 3 GHz, the rms of 1 mm will induce the gain loss of about 0.2 dB. There is an obvious decrease after the subreflector motion compensattion. Otherwise, the effect of compensation gets more and more obvious with the incremental elevation angle. If the main reflector surface is pre-adjusted at 35 degree, the gain loss decreases a little at lower elevation angles, sometimes even increase. With the increment of elevation angle, pre-adjustment improves limitedly performance. However, using subreflector motion to compensate, the gain loss may decrease enormously near pre-adjustment angle.

Note: in Table 1, RMS_o is root mean square of gravity deformation; RMS_p is root mean square of gravity deformation with main reflector pre-adjustment at 35 degrees; RMS_f is the best fit error; ΔG_{bc} is the gain loss before subreflector compensation; ΔG_{bc} is the gain loss after subreflector compensation.

Table 1: Comparision of gain loss between before and after subreflector compensation (working at 3 GHz).

Elevation angle (degree)	Without main reflector pre-adjustment				Main reflector pre-adjustment at 35 degrees			
	RMS_o (mm)	RMS_f (mm)	ΔG_{bc} (dB)	ΔG_{ac} (dB)	RMS_p (mm)	RMS_f (mm)	ΔG_{bc} (dB)	ΔG_{ac} (dB)
0	1.1833	1.0552	– 0.2211	– 0.1758	3.3116	1.3063	– 1.7318	– 0.2695
15	1.8805	1.1747	– 0.5584	– 0.2179	1.8217	0.7258	– 0.5241	– 0.0832
30	3.0595	1.4512	– 1.4782	– 0.3326	0.4275	0.1730	– 0.0289	– 0.0047
45	4.1608	1.7599	– 2.7338	– 0.4891	0.7805	0.3232	– 0.0962	– 0.0165
60	5.0261	2.0219	– 3.9892	– 0.6456	1.7263	0.7398	– 0.4706	– 0.0864
75	5.5747	2.1938	– 4.9075	– 0.7600	2.3549	1.0632	– 0.8757	– 0.1785
90	5.7621	2.2533	– 5.2430	– 0.8018	2.6399	1.2919	– 1.1005	– 0.2636

5. CONCLUSIONS

By using segmented parabolic curves to fit the discrete samples of design generatrix, a group of best-fit paraboloids are found to best fit the deformed main reflector, with the constraint of all focal points in line. The best fit parameters are calculated at various attitudes and saved into a

look-up table. The subreflector motion are derived with the ratio of main reflector and subreflector and will real-time compensate for gravity deformation of the main reflector. From the experimental verification on a 64 m reflector antenna, satisfactory results are obtained and will be used in practice.

Although segmented best fit paraboloids may describe the gravity deformation of shaped main reflector, however the electrical performance of the antenna is very sensitive to the deformation of subreflector. It is efficient and accurate to compensate gravity distortion of the main reflector by changing the shape of subreflector properly, which is our future work.

REFERENCES

1. Subrahmanyan, R., "Photogrammetric measurement of the gravity deformation in a Cassegrain antenna," *IEEE Trans. Anten. Propag.*, Vol. 53, No. 8, 2590–2596, 2005.
2. Ruze, J., "Antenna tolerance theory — A review," *Proc. IEEE*, Vol. 54, 633–640, 1966.
3. Von Hoerner, S., "Homologous deformations of tilteable telescopes," *J. Structural Division Proc. ASCE,* Vol. 93, 461–486, 1967.
4. Wang, W., B. Y. Duan, and B. Y. Ma, "A method of panel adjustment of large reflector antenna surface and its application," *Acta Electronica Sinica*, Vol. 36, No. 6, 1114–1118, 2008 (in Chinese).
5. Nikolic, B., R. M. Prestage, et al., "Out-of-focus holography at the green bank telescope," *A & A*, Vol. 465, 685–693, 2007.
6. Rahmat-Samii, Y., "An efficient computational for characterizing the effects of random surface errors on the average power pattern of reflectors," *IEEE Trans. Anten. Propag.*, Vol. 31, No. 1, 92–98, 1983.

Performance of Planar Slotted Waveguide Arrays with Surface Distortion

Li-Wei Song
Research Institute on Mechatronics, Xidian University, Xi'an, Shaanxi 710071, China

Abstract— The performance of planar slotted waveguide arrays with distortion was investigated in this paper. Errors in array element (radiating slot) positions as a result of structural deformation are considered as predictable. Practically discrete points on the plane containing the radiating slots were measured with the help of API measurement system. But these points are too few to determine the radiation slot positions by the methods of interpolation or fitting accurately. So the finite element method was used to settle out the radiation slot positions with ANSYS according to the given points. The slot voltages were obtained from finite element solution or antenna measurement system in an anechoic chamber and assumed to be unchangeable for the distortional antenna used in the calculation of far-field pattern. The pattern for distortion and undistortion antenna was obtained by an analytical formula. Finally, measurements were found to be in a good agreement with the calculation results.

1. INTRODUCTION

Since the slotted waveguide arrays antenna have the advantage of compact configuration, stable mechanical characteristics, low loss and perfect efficiency, it is widely used in communication and radar systems. Evaluation of antenna performance under the influence of distortion is an important part of the engineering work in the course of design and development of a new antenna system, because structural deformation can seriously affect the electromagnetic performance due to undesirable phase shift of the microwave energy. In the past, the prime interest has been in the determination of the boresight gain loss, and for this, Ruze's [1] simple formula has been used very effectively. However, recent advances in using very large antennas, antennas with low sidelobe levels have demanded that accurate and detailed information be available for the degradation of sidelobes as a function of surface errors. Later on, H. S. Wang [2] summarize the result of antenna performance under the influence of two kinds of structural distortions including the bent-slab and bowl distortion in a predictable manner. But, in his paper, the distortion is different from the structural deformation forced by loads, such as the temperature, the vibration or self weight, and the element excitation (amplitude and phase) is the value of design. Peter Tamas [3] present a coupled calculation technique of tilted rectangular waveguide slot antenna. In his paper, the basic idea of the analysis of the tilted slot antenna is the space segmentation of the device into internal and external regions, different calculation techniques are used in the different regions, while finite element method is applied to solve the internal (waveguide) problem, analytical calculations are performed in the external (free space) region. Namely, the slot voltages (element excitation) are obtained by the finite element method, the radiation pattern is calculated by an analytical formula. However, the focus of his paper is to characterize the pattern of the titled waveguide arrays, the structural deformation of antenna can be not considered too.

So, in this paper, we present an analytical methodology of the performance of planar slotted waveguide arrays with structural deformation. Firstly, the mathematic model relating the performance of antenna and structural deformation is given. Then, to calculate the model the distortion is obtained by finite element method with ANSYS, and slot voltage can be given by two kinds of methods. For the first kind of methods, the finite element solution of the region formed by waveguide results in the electric field distribution of each slot of the antenna. The peak values are used as the slot voltages for each radiating slot element. For the second kind of methods, it utilizes near-field measurement data to determine slot voltage over a fictitious planar that encompasses the antenna [4]. Simultaneity the slot voltages assumed to be unchangeable for the distortional antenna used in the calculation of far-field pattern. Finally, the two practical slot antennas with the frequency bands of ku and X were used for this study.

2. THE MATHEMATICAL MODEL

The geometry of a slotted waveguide arrays is depicted in Fig. 1 with reference to the particular case of a traveling wave planar array. At a glance, we distinguish two regions: the internal one,

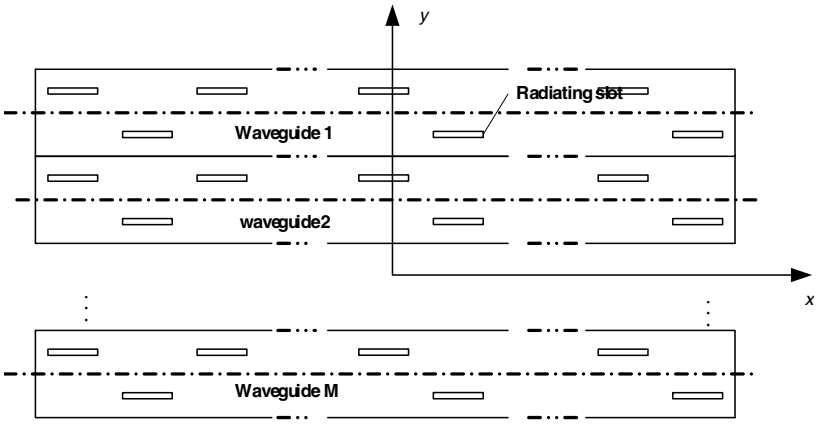

Figure 1: Geometry of the slotted waveguide arrays.

formed by the waveguide rows, placed side by side, and the external one, consisting of the front plate containing the radiating slot. The EM and structural performance of the slot antenna vary according to the loads on its structure: temperature distribution, vibration, and so on. So we present the mathematical model which formula the EM performance with structural deformation.

During the solution of the internal problem the effect of the deformation of the waveguide is neglected. Although the deformation causes internal reflections in the waveguide, the insensitivity of the radiation pattern of the slots to this reflection allows neglection of this effect in practical configurations. The net radiation pattern is calculated with a simple (vectorial) superposition of the radiation pattern of the radiating slot, taking into consideration the location of each slot. The surface containing the radiating slot is not the ideal plane after deformation, the displacement of each slot can be determined by structural finite element analysis software with ANSYS. So the effect of displacement of slot from the ideal planar position is to introduce additional phase factors in the pattern function,

$$E_{total}(\theta,\phi) = \sum_p V_p f_p(\theta,\phi) e^{jk\sin\theta[(x_p+\Delta x_p)\cos\phi+(y_p+\Delta y_p)\sin\phi]} e^{jk\Delta z_p\cos\theta} \tag{1}$$

where $V_p, f_p(\theta,\phi)$ is the slot voltage and pattern of the pth radiating element, θ,ϕ are the standard spherical coordinate variables, $\Delta x_p, \Delta y_p, \Delta z_p$ are the displacements of the pth element from the planar position $z = 0$.

Once the slot voltages and the displacements are known, the radiation pattern of the array may be calculated. For this purpose, a piecewise sinusoidal approximation for the slot electric fields is used, which simplifies the expression for the radiated fields pattern to

$$E_{total}(\theta,\phi) = \sum_p \frac{V_p}{j\pi} F(kL_p/2,\theta) \frac{\sin[k\sin\theta\cos\phi w_p/2]}{k\sin\theta\cos\phi w_p/2} \cdot e^{jk\sin\theta[(x_p+\Delta x_p)\cos\phi+(y_p+\Delta y_p)\sin\phi]} e^{jk\Delta z_p\cos\theta} \tag{2}$$

where

$$F(c,\theta) = \frac{\cos[c\cos\theta] - \cos c}{\sin\theta} \tag{3}$$

and L_p, w_p are the length and width of the pth radiating slot.

3. ANTENNA STRUCTURAL DEFORMATION AND SLOT VOLTAGES

In analyzing slotted waveguide arrays antenna structural performance it is necessary to accurately characterize the surface containing the radiating slots. Any deviation from its ideal geometry causes the antenna performance to degrade. The most important aspect of the antenna structural static analysis is the evaluation of the antenna's accuracy. It involves structural finite element analysis and the calculation for the displacement of the radiating slots according to the coordinate of the discrete point obtained by structural analysis.

Although slotted waveguide antenna is made of the material of alloy with aluminum, the distortion will be appearing due to loads on the structure. So the device must be made to force the

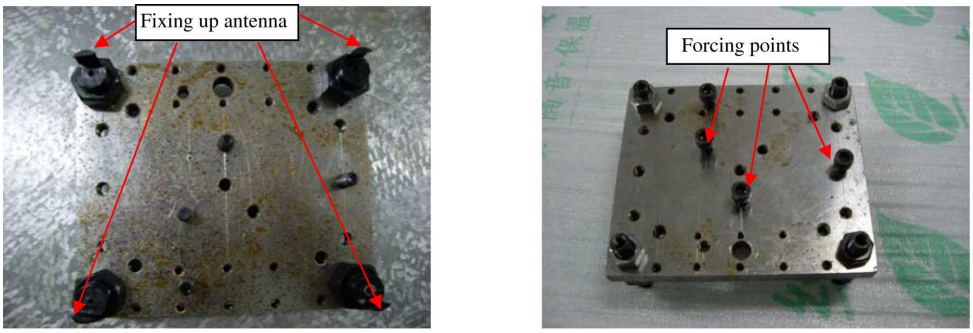

Figure 2: The device of forcing the antenna to deformation.

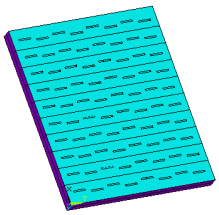

Figure 3: The finite element model of antenna with shell elements.

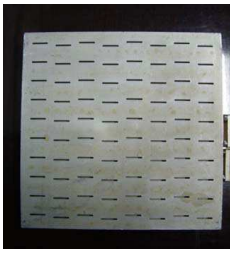

Figure 4: The slot antenna formed by 80 radiating slot with resonant rectangular waveguide.

antenna deformation. This device can provide the arbitrary shape of distortion which is shown in Fig. 2. The four vertex of the device are used to fix up the slot antenna, and those nuts to force the back of antenna to anticipant distortion. The surface containing the radiating slot is measured with API to acquire its displacement of discrete points on the surface. Due to the measured discrete points are too few to determine the position of radiate slot, so finite element analysis with ANSYS is used to work out the displacement of the surface precisely with the help of the measured points. The finite element model of slotted waveguide is shown in Fig. 3 with shell element. The positions of the measured discrete points and the displacement of those nuts are the structural displacement forced to the finite element model. Then the displacement of the radiating slot can be obtained with the help of the method of interpolation according to results of structural analysis.

Then, Slot voltage can be given by two kinds of methods. For the first kind of methods, the finite element solution of the region formed by waveguide results in the electric field distribution of each slot of the antenna. The peak values are used as the slot voltages for each radiating slot element [3]. For the second kind of methods, it utilizes near-field measurement data to determine slot voltage over a fictitious planar that encompasses the antenna [4]. These methods are used to slotted waveguide antenna with frequency bands of Ku and X separately.

4. NUMERICAL RESULTS

We have applied the mathematical model to the analysis of several slotted antennas, formed by the 80 and 1172 of element, resonant in rectangular waveguide. We have obtained results very close to the measurements.

Case 1:

For the simpleness of analysis, firstly we have applied the model in a resonant waveguide formed by the 80 radiating slot operating in Ka bands, shown in Fig. 4. The slot voltages have be obtained by the finite element method of electromagnetism with undistorted antenna. for the purpose of antenna distortion, we have used the above the device forcing the antenna in a straight way. Then the above mathematical model can be analyzed. Fig. 5 shows a comparison between measured and computed radiation patterns of the arrays under the ideal slot antenna. In Fig. 5, one may see that the calculated results and measured pattern in azimuth and elevation plane are in a good agreement under the ideal antenna. So the slot voltages from the finite element solution are considered for a correct prediction. Then the slot voltages are used to calculate the mathematical model presented in this paper, Fig. 6 shows pattern of the same antenna under distorted antenna by the forcing

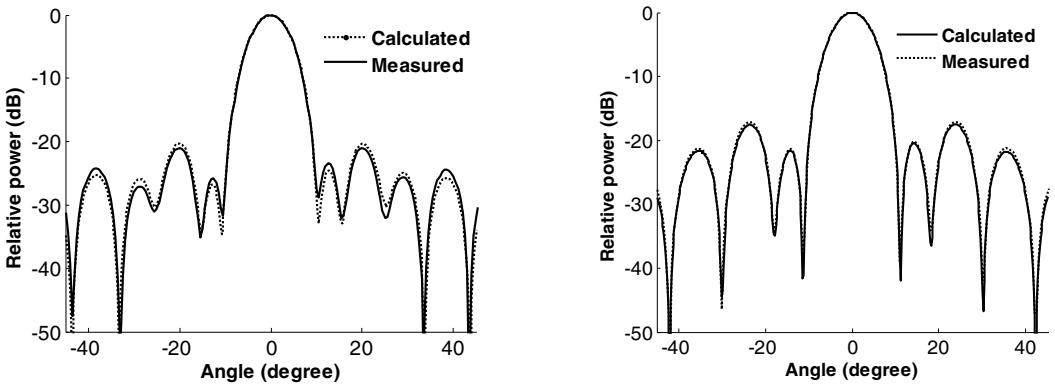

(a) Azimuth plane (b) Elevation plane

Figure 5: The radiation pattern of a slotted array of 80 slots under the ideal antenna.

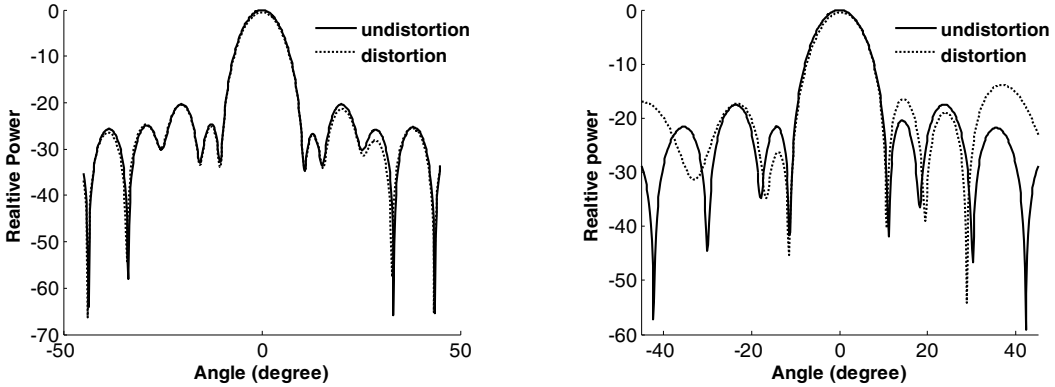

(a) Azimuth plane (b) Elevation plane

Figure 6: The radiation pattern of a slotted array of 80 slots under the deformation.

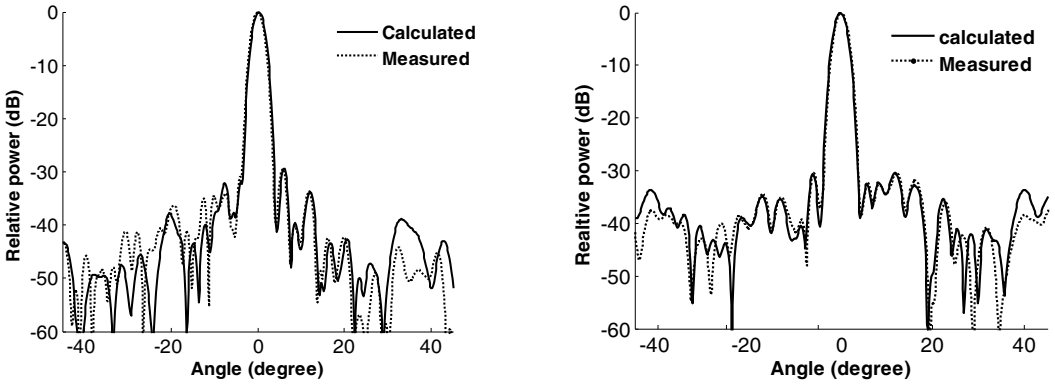

(a) Azimuth plane (b) Elevation plane

Figure 7: The radiation pattern of a slotted array of 1172 slots under the ideal antenna.

device. By comparing with the undistorted case, it is seen that the distortion has caused a reduction in the gain in the two planes and in the azimuth plane, a rise in near sidelobl level in the elev-ation plane under the maximum of one tenth of wavelength.

Case 2:

Then we have applied the model to a large slotted waveguide arrays formed by 1172 of radiating elements. Due to the antenna is the very large electronic dimension, the slot voltages are too hard to be obtained by the method of finite element. So we have measured the near field data to calculate the slot voltages by the method in [4]. And the structural analysis is carried out by the structural model of shell and beam element. Fig. 7 shows a comparison between measured and computed radiation patterns of the arrays under the ideal slot antenna. Fig. 8 shows pattern of the same

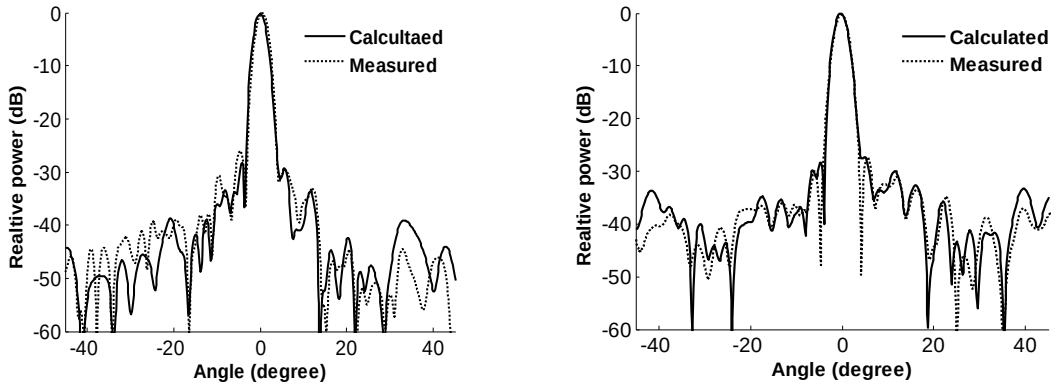

(a) Azimuth plane (b) Elevation plane

Figure 8: The radiation pattern of a slotted array of 1172 slots under the ideal antenna.

antenna under distorted antenna.

Figure 7 has a good agreement between calculated and measured under ideal antenna, which prove that slot voltages calculated from the data of near field measurements is correct. When the antenna is deformed, the prediction of the mathematical model has also a very good agreement, except for very few positions in the pattern. These deviations are due to the hypothesis of changeless slot voltage and the pattern of each radiating slot element.

5. CONCLUSIONS

From the results of our study reported here, we see that mechanical errors in a slotted waveguide array generally produce a phase error in the signals of each radiating slot element due to changes of its position in an ideal plane. Antenna structural distortion as a result of loads is predictable by the structural analysis with ANSYS. The effect of the errors can be estimated by the direct calculations. It is demonstrated that the impact of the distortion if manifested primarily in the gain loss and the sidelobel level rise. For a maximum element displacement of 0.1λ out of the plane containing 80 radiating slots, the loss of peak response is on the order of 0.5 dB for the loads from the nuts.

ACKNOWLEDGMENT

The authors wish to thank Research Institute on Mechatronics, Xidian University, who supplied the fund for the device and the measured performance of the slotted waveguide array.

REFERENCES

1. Ruze, J., "Pattern degration of space fed phased arrays," Project Report SBR-1, M.I.T. Lincoln Laboratory, Lexington, MA, Dec. 1979.
2. Wang, H. S. C., "Performance of phased-array antennas with mechanical errors," *IEEE Transactions on Aerospace and Electronic Systems*, Vol. 28, No. 2, 535–545, Apr. 1992.
3. Peter, P. and K. S. Tapan, "Planar near-field to far-field transformation using an equivalent magnetic current approach," *IEEE Transaction on Antennas and Propagation*, Vol. 40, No. 11, 1348–1356, Nov. 1992.

Performance Enhancement of FDTD-PIC Beam-wave Simulations Using Multi-core Platforms

Andrew J. Woods, Lars D. Ludeking, and David L. Rhoades
Alliant Techsystems (ATK), 8560 Cinderbed Road, Suite 700, Newington, VA 22122, USA

Abstract— The MAGIC electromagnetic (EM) finite difference time domain particle-in-cell (FDTD-PIC) code has been tested for performance speed on typical large-scale electro-energetic calculations. Computer systems employed were the ATK and University of Miami (UMIA) Linux clusters and several single platforms including Windows and Linux dual quad core Intel and AMD machines. A gain of a factor of $10x$ over 2006 state-of-the-art personal computers (PCs) was also achieved on the ATK cluster, and $27x$ on the larger UMIA system. The AMD server achieved up to a $6x$ speedup for parallel processing compared to only $1.6x$ for Intel-based platforms resulting in a $2x$ best rate for AMD compared to Intel. Computer science analysis of the low-latency AMD platform compared to the less expensive Intel architecture explains the enhanced AMD performance for EM FDTD-PIC.

1. INTRODUCTION

In response to frequent inquiries from our large customer base regarding optimal computer systems for EM FDTD-PIC, we have tested the MAGIC code [1] for performance speed on Linux clusters and several single platforms including dual quad core machines. Both Windows and Linux operating systems (OS) were evaluated on the single platforms. Performance statistics for large electro-energetic calculations containing both EM fields and macro-particles in large numbers requiring intensive CPU usage were obtained.

2. LINUX CLUSTERS

The ATK Linux OSCAR 5.0 cluster [2] has a master node and 10 slave nodes all with 3.0 GHz, 2.1 GB RAM dual CPU processors. The 32-bit Intel (R) Xeon (TM) nodes are interconnected with Gigabit Ethernet. The operating system is Red Hat Enterprise 4.0 and the compiler was Intel FORTRAN 10.026. MAGIC 1.0.5 32-bit (September 2007) was executed in double precision. Parallel processing is administered through MPICH2 [3].

The University of Miami (UMIA) [3] cluster has fifty four 64-bit quad core Intel Xeon 5350 nodes also interconnected with Gigabit Ethernet. The operating system is Linux Centos 4.3 64-bit (a clone of RedHat Enterprise 4.3 — see www.rocksclusters.org). MAGIC calculations compiled for 32-bit PCs were executed in double precision on the 64-bit machines. A native Linux 64-bit version of MAGIC was not operational at the time of this study, but now is (version 2.1.9 December 2009).

3. TIMING TEST CONFIGURATION

The test problem is called "Serpentine" for the geometric oscillations in the simulated slow wave structure (SWS) geometry (Fig. 1). One-half of the conducting block is shown in the cutaway with the beam tunnel half exposed. Electrons of energy 10.9 keV guided by an axial magnetic field of 0.67 tesla pass through the tunnel causing excitations of the numerous connected cavities. The red rectangular volume represents an attenuating region of conductance 0.19 mho/m.

This example terahertz-regime problem is representative of the many high-power microwave (HPM) sources to which the MAGIC analysis tool has been applied, such as: magnetrons, klystrons, and multi-beam klystrons (MBKs).

The 101-period test configuration used on the clusters contains 3.25 M cells (1500 in the long dimension). The code follows an average of 70 k particles for 178 ps (30 k time steps). The required memory of the single process case is less than the RAM of the individual computers of the cluster. Multiple process cases solved individual segments of the SWS divided along its major axis.

4. LINUX CLUSTER RESULTS

Results obtained from the timing of the calculations for different numbers of CPUs are shown in Fig. 2. The units are "Serpentines per hour" showing that the single processor double precision case required ~ 7.1 hours (obtained by inverting the plotted computing rate of 0.14 Serp/hr.), and the 22 processor case only 0.85 hours to compute the serpentine test problem. This best ATK rate

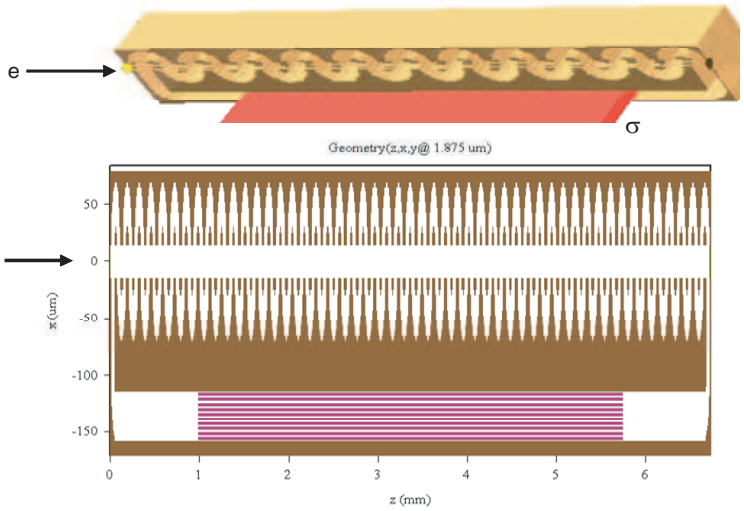

Figure 1: Slow wave structure test problem illustrated with 11 periods. The largest MAGIC3D test calculations had 101 periods.

at 22 CPUs demonstrated a significant $10x$ potential gain for MAGIC customers running circa 2006 state-of-the-art PCs.

The "Ideal" curve corresponds to the perfect infinite bandwidth, zero-latency (zero data transfer time — see computer science analysis below) case normalized to the double precision value for a single processor. The actual curve bends away from the ideal as more processes are added due to increased relative wait times for data transfer among the nodes, as expected. The ATK cluster curves are almost linear to 11 CPUs, and show only modest benefit from dual processors reaching $10x$ its single process speed (going from 11 to 22 processes). The UMIA curve increases well beyond 22 processes due to only 1 process per CPU until it reaches a maximum of $27x$ its single process (well of the ordinate of the graph, as indicated).

5. SINGLE PLATFORM RESULTS

The serpentine test problem was also run on a variety of single platforms including multi-core machine systems. The number of periods was reduced to 21 for quicker execution times (at the expense of some efficacy of parallelism). The problem had 703 k cells (330 in the long dimension), 22 k average particle number, and 178 ps maximum simulation time (30 k time steps). The required memory of the (worst case) single process case is less than the RAM of each system.

Computer and operating system parameters and results are detailed in Table 1. The CPU times listed are the execution times logged after problem setup and before post-processing. Multiple process cases required up to an additional minute to sew the results back together in this smaller test problem. Different versions of the MAGIC code from 2.1.0 (September 2008) to 2.1.9 (June 2009) were tested demonstrating only modest ($< 10\%$) variations in total CPU requirements on the same OS. Each platform/OS combination was run with multiple processes up to at least the number which provided the fastest execution time.

The MPICH2 shared memory model ("shm") was found to improve the best Windows times by up to almost $2x$ during this exercise. These fastest Windows cases are the ones included in Table 1. The "shm" model brings the total CPU time for AMD/Windows to within 2% of AMD/Linux. A modest 30% benefit accrues from the "shm" model on quad-core multi-CPUs with Intel/Windows, however, resulting in a best achievable computing rate of only half as fast as AMD.

The sought-after quad-core machine results are summarized in Fig. 3. Only the best memory model CPU times are plotted there for the Windows cases. A major benefit from AMD over Intel is shown by the curves. The fastest time with AMD is half that available from Intel (comparing the curves "AMD..." and "Intel..."). On the same AMD machine, a factor of up to $1.6x$ is seen between Linux and Windows, but no significant difference in fastest possible time which occurs at 8 processes (one process per core). Only a few percent differences occurred between Windows Vista and Server 2008, or on Intel machines with 4 and 8 GB RAM (Table 1.).

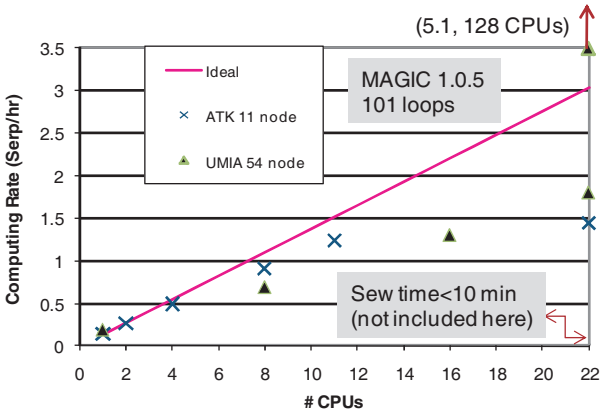

Figure 2: MAGIC3D Linux cluster computing rate vs. number of processes for EM FDTD-PIC 101 period test.

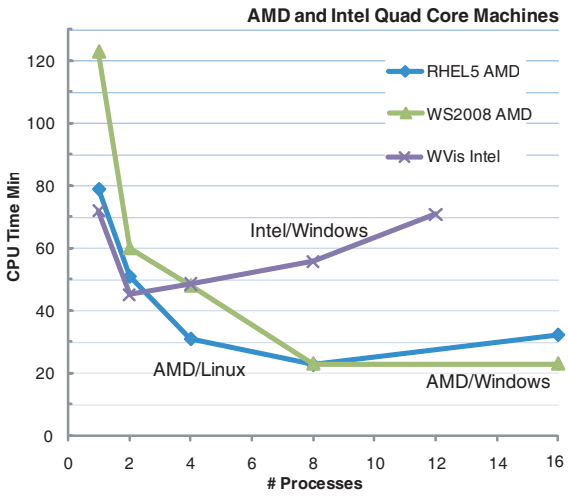

Figure 3: MAGIC3D CPU time vs. number of processes for EM FDTD-PIC 21 period test on AMD and Intel platforms.

Table 1: Fastest CPU times for MAGIC3D calculations on EM FDTD-PIC 21 period test on AMD and Intel platforms.

Platform	Cores	CPUs per Core	Architecture bits	System ID	OS	CPU GHz	RAM GB	Bus Speed MHz	Best Wall Time (min)	Best Number of Procs
AMD	2	4	64	S-maglin64	RHEL5	2	8	1000	**22.7**	8
AMD	2	4	64	S-magser64	WS2008	2	8	1000	**23**	8
AMD	2	4	64	S-magvis64	WS2008	2	8	1000	**24.2**	8
AMD	2	2?	64	90D00022	WVis	2.2	8	1000	**60.2**	2
Intel	1	2	32	90S-linux01	RHEL4	3	2	800	**14.4**	22
Intel	2	4	64	90W5000	WVis	2	8	1333	**45.2**	2
Intel	2	4	64	W-magvis64	WVis	2	4	1333	**48.5**	4
Intel	1	2	32	90L00005	WXp	2	2	997	**67**	2
Intel	1	1	64	90D00018	WXp	3.4	4	800	**68**	1
AMD	1	2	64	90S-OPTER	RHEL4	1.4	3	800	**166**	1

6. COMPUTER SCIENCE ANALYSIS

Virtually all PIC applications, due to the nature of PIC where particles are highly connected to each other through the fields, put a strain on the inter-processor interconnect and/or switching technology (technically there is a difference, because the switch and the NIC are really separate technologies, but obviously have to be compatible). There are two characteristics of any interconnect that affect computation efficiency. One is bandwidth and the other is latency. Bandwidth is the theoretical maximum transfer rate. Latency is the time required to initiate a transfer. The ideal interconnect would have infinite bandwidth and zero latency. The reality is something less than ideal on both counts. In reality large bandwidth is relatively inexpensive to buy but low latency is VERY expensive.

Every time a process talks to another process the wait time, or latency, is time the application is idle, along with the transfer.

There are a number of mostly proprietary low-latency solutions available. A list is available at http://en.wikipedia.org/wiki/Myrinet. The most notable one is Infiniband, which has largely replaced the earlier Myrinet.

The Dell AMD PowerEdge server employed here uses one that is not on the Wikipedia list to interconnect their processors. It evolved from HyperBus (or HyperChannel) which was bought from Alpha Networks a number of years ago, and is now called HypterTransport. It is the underlayment

of what they call their Direct Connect Architecture (see http://en.wikipedia.org/wiki/HyperTransport).

AMD's performance is due to the very high bandwidth (51 GB/s — and yes that's BYTE) and very low latency.The balance of processor and interconnect is the key to ANY high-performance computer, from Crays to GPUs to PCs.

The typical latency figures for the three technologies give a clue to performance results here. Ethernet is approximately 40–60 usec, Myrinet is around 1.4 usec, Infiniband is about the same, but more expandable to higher bandwidth and less expensive. Hypertransport is as low as 0.5 usec, with real-world results at 1.5 usec.

More information on Hypertransport is available at http://www.hypertransport.org/.

7. CONCLUSION

Linux on the 32-bit cluster in double precision or native on the 64-bit AMD provides the fastest computation rate for MAGIC 64-bit-accurate computing. One process per physical machine was found to be the optimal performance solution on the ATK cluster. A significant $10x$ increase in computation speed ($8.5x$ wall time with sewing) for the ATK Linux cluster over the single process case (and 2006 state-of-the-art PCs) was shown in this work for a typical large-scale EM FDTD-PIC calculation. The speed increased to $27x$ over the single process case for the UMIA cluster.

A significant boost to the fastest Linux cluster parallel result shown here would be expected from Myrinet (or equivalent) versus Gigabit Ethernet. This finding is based on other coupled EM FDTD-PIC particle plasma calculations with the LSP code [5] performed on the ATK and Voss Scientific (www.vosssci.com) clusters (not reported here).

For single machines, the quad-core multi-CPU AMD server was twice as fast as the best Intel time. Overall speedup due to parallel computing on 64-bit machines was shown to be greater than $5x$ for all OS's on the AMD machine, but only $1.6x$ on Intel compared to the respective single process cases. Computer science discussion of low latency interconnect and switching technology explains the clear advantage of the AMD server over Intel processors for parallel EM FDTD-PIC calculations.

A possible explanation for the surprisingly small improvement with multiple Intel processors on the same machine is that benefits have already been obtained through efficient use in the "single CPU" cases (notice in Fig. 3. the single process case is fastest for Intel). Shared components on Intel are more likely the bottleneck on that less expensive architecture. The latest MPICH2 (version 1.1) should be tested to see if the recommended "nemesis" channel model could speed the Windows results (no benefit has been obtained on Intel-based processors with Windows to-date).

REFERENCES

1. Goplen, B., et al., "User-configurable MAGIC for electromagnetic PIC calculations," *Computer Physics Communications*, Vol. 87, 1995, http://www.mrcwdc.com.
2. Open Source Cluster Application Resources, http://www.oscar.openclustergroup.org.
3. Monti, M. and M. Huerta, "New serpentine tests on university of miami physics cluster," *Private Comm.*, March 21, 2008, http://www.physics.miami.edu/cluster/ydra_cluster_description.html.
4. "MPICH2 is a high-performance and widely portable implementation of the message passing interface (MPI) standard," *Argonne National Laboratory*, 2008, http://www.anl.gov/techtransfer/Software_Shop/index.html.
5. LSP is an EM PIC Plasma Code Product of Alliant Techsystems, 2005, http://www.mrcwdc.com/LSP/description.htm.

X-ray Microbeams for Radiobiological Studies: Current Status and Future Challenges

G. Schettino[1], **M. Folkard**[2], **B. Vojnovic**[2], **A. Michette**[3], **and K. M. Prise**[1]

[1]CCRCB, Queen's University Belfast, 97 Lisburn Road, Belfast BT9 7BL, UK
[2]Gray Institute for Radiation Oncology and Biology, Old Rd. Campus, Oxford OX3 7DQ, UK
[3]King's College London, Strand, London WC2R 2LS, UK

Abstract— Recent technological advances and new radiobiology challenges are behind the great interest in the use of microirradiation techniques for radiobiological studies. Radiobiological microbeams are facilities able to deliver precise doses of radiation to preselected individual cells (or part of them) *in vitro* and assess their biological consequences on a single cell base. They are therefore uniquely powerful tools to address specific problems where very precise targeting accuracy and dose delivery are required. The majority of radiobiological microbeams are centred on particle accelerators in order to irradiated biological samples with an exact number of ions. Currently there are only three microbeam facilities in routine use which employ focused X-rays: two are based on laboratory bench X-ray sources (Queen's University Belfast and Nagasaki University) and one developed using synchrotron X-ray beams (Photon Factory in Tsukuba, Japan). While low dose rates limit laboratory bench sources to a few keV, micronsize X-ray probes of a few tens of keV are achievable using synchrotron sources. Each facility has however their own benefits and draw back points. Techniques for focusing X-rays are well established and continuously improving with focal spots down to 50 nm achievable for ultrasoft X-rays using circular diffraction gratings known as "zone plates". Reflection X-ray optics such as Kirkpatrick-Baez mirrors and polycapillary systems are also used to produce micron size X-ray spots. Combined with nano-positioning accuracy of the new generation of stages, improved optics and image analysis algorithms, X-ray microbeams are able to address radiobiological issues in an unprecedented way.

Microbeams have contributed significantly to the discovery and characterization of important new findings regarding the mechanisms of interaction of ionizing radiation with cells and tissues. In particular, they have played a fundamental role in the investigation of non-targeted effects where radiation response is induced in samples whose DNA has not been directly exposed. The exquisite resolution offered by focused X-ray probes has allowed important questions regarding the locations and mechanisms of subcellular targets to be precisely addressed. Evidences of the critical role played by the cytoplasm have been collected and radio-sensitivity across the cell nucleus itself is attracting considerable interest. Moreover using the microbeam single cell approach, it has been possible to study the mechanisms underpinning the bystander effect where radiation damage is expressed in cells which have not been directly irradiated but were in contact or shared medium with directly exposed samples. As a result, microbeam facilities are regarded as a main tool for the formulation of a new radiobiological paradigm where direct damage to cellular DNA is not a requirement. Additionally, the implications of the non-targeted effects in *in vivo* systems and ultimately humans have still to be fully understood. The new generation of X-ray microbeams equipped with 3D image stations and higher X-ray energies offers the perfect approach to extend targeted studies to complex biological models. Finally, the single-cell approach and the high spatial resolution offered by the microbeam provide the perfect tool to study and quantify the dynamic processes associated with the production and repair of DNA damage. Using green fluorescent protein (GFP), it is now possible to follow the spatio-temporal development of the DNA damage sites which is currently of great interest in order to monitor the remodelling of chromatin structure that the cell undergoes to deal with DNA damage.

1. INTRODUCTION

Ionizing radiation is playing an increasingly important role in modern society with human population continuously subjected to a range of environmental, occupational and medical exposures. Although a lot is known about the physical interaction of ionizing radiation with biological samples (which has led to the development of sophisticated diagnostic equipment widely used in medicine), our understanding of the biological effects caused by ionizing radiation is still limited, especially in the low dose region. Despite being widely used in cancer radiotherapy applications, ionizing radiation is itself a proved carcinogenesis agent. Current estimation of radiation risks for cancer inductions are derived from the survival of the Japanese atomic bomb that were exposed to

high dose and high dose-rates. This approach suffers from limited statistical power and inability to resolve uncertainties from confounding factors forcing the adoption of the conservative linear non-threshold model (LNT) which assumes a gradual linear decreasing of the risk with the dose absorbed. However, there is now considerable evidence of non-linearity in the dose response curves. While phenomena such as genomic instability [1], hypersensitivity [2] and bystander effect [3] may increase radiation risk at low doses, adaptive response [4] may act as a protective mechanism. Microbeam facilities were therefore developed to investigate the effect of very low doses of radiation with great precision in order to estimate radiation risks for the general population. Although the advantages of a deterministic irradiation have been recognized since the beginning of radiobiological studies [5], technology for developing sophisticated microirradiation facilities have only become available in the late 1990s. Following the achievements of the first microbeams, recent technological advances and new radiobiology challenges has now inspired a second generation of microbeams. Modern radiobiological microbeams are facilities able to deliver precise doses of radiation to preselected individual cells (or part of them) *in vitro* and assess their biological consequences on a single cell base.

Microbeams have significantly contributed to the advances in radiobiology of last decades by providing critical investigations to determine the shape of the dose-response curve in the very low dose region. Oncogenic transformation [6], micronuclei formation [7] and genetic instability [8] resulting from a single particle traversal have been characterized together with the relevance of new phenomena such as hypersensitivity [9] and bystander effect [10, 11]. Although the majority of modern microbeams use particle accelerators, X-ray microbeams have also been developed offering a unique approach to the investigation of biological effects caused by ionizing radiation. Apart the use of a different type of radiation (X-rays induce qualitatively different damage than charged particles), X-ray microbeam can reach resolutions up to an order of magnitude smaller than what is possible to irradiated biological samples with charged particles. Techniques for focusing X-rays are well established and continuously improving with focal spots currently down to 50 nm using circular diffraction gratings known as "zone plates". Combined with nano-positioning accuracy of the new generation of stages, improved optics and image analysis algorithms, X-ray microbeams are able to address radiobiological issues in an unprecedented way.

2. X-RAY MICROBEAMS

X-ray microbeams have started to be developed towards the end of the 1990s [12] in order to provide quantitative and mechanistic radiobiological information that complement the charged particle studies. Damage caused by X-rays is qualitatively different than lesions produced by charged particles due to minor clustering of the ionization pattern. It is now commonly accepted [13], that radiation effects strongly depends on the clustering of ionizations requiring the introduction of the LET parameter (i.e., linear energy transfer) to take into account the distribution of energy deposition inside biological samples. Electrons produced by the absorption of soft X-rays will produce ionization patterns that closely resemble that of a low-LET irradiations (i.e., gamma and high energy X-rays) as routinely adopted in diagnostic and therapeutic treatments. Moreover, unlike charged particles, soft and ultrasoft X-rays (i.e., $\sim 100\,\mathrm{s\,eV}$–$10\,\mathrm{s\,keV}$) interact almost exclusively by photoelectric effects and therefore don't suffer from scattering issues making it possible to achieve radiation spots in samples of an order of magnitude or more smaller than those so far achieved with ion beams. Finally, such high spatial resolution is maintained as the X-ray beam penetrates through samples making it possible to irradiate with micron and sub-micron precision, targets that are several tenths or hundreds of micron deep. Currently there are only three microbeam facilities routinely used for biological experiments which employ X-rays: two are based on laboratory bench X-ray sources (Queen's University Belfast and Nagasaki University) and one has been developed around a synchrotron X-ray beams (Photon Factory in Tsukuba, Japan).

2.1. X-ray Sources

Microbeam facilities [14] have mainly used electron bombardment X-ray sources where electrons generated by heated tungsten filaments (or more recently using single crystal filaments with brightness above $1 \times 10^6\,\mathrm{Amp/cm^2}$ steradiant) are accelerated up to 20–30 kV and focused (either by permanent magnets or by electrostatic lenses) onto a solid target producing a "point-like" X-ray source. Due to the limited distance between the X-ray source and the X-ray optic device, the dimensions of the focused X-ray spot are dominated by the size of the X-ray source requiring considerably efforts to produce a "point-like" X-ray source. Despite electron bombardment X-ray

sources are widely used, focusing a high electron current into a small spot is not easily achievable and still represents a major limitation for X-ray microbeams. Currently the Queen's University X-ray microbeam is able to focus up to 1 mA of 15 keV electrons into $< 20\,\mu$m diameter spot. The radiation spectrum generated by electron bombardment sources is contaminated by Bremsstrahlung which are removed either by filtration and/or by reflection to achieve a near monocharomatic beam required both for optimum working conditions of the X-ray focusing devices and for a correct interpretation of the biological effects induced. The major limit of the electron bombardment X-ray sources is represented by their limited brightness and size. The spot size is ultimately limited by the electron beam current as space charge effects will produce a repulsive force which will compromise the focusing action of the electromagnetic lenses. Moreover, X-ray production by electron bombardment is not a very efficient process with most of the energy dissipated in heat. When using fixed thick targets, it is therefore necessary to compromise between high electron currents and size of the electron focus as the maximum power that it is possible to dissipate on a thick target depends on the power density of the impinging beam. Cooled or rotating targets have also been investigated as potential microbeam sources in order to increase the electron current and therefore the final X-ray production rate. Cooling the target, however, is not a suitable option as the requirement of a small electron focus and the limited electron penetration imply that it is extremely hard to efficiently cool the area of the target where the electrons impinge. Rotating targets offer more promising benefits and have indeed been used to produce X-ray sources for microbeam applications [15]. However, rotation of the target inevitably introduces vibration into the system which ultimately affects the resolution and accuracy of the final X-ray focused beam. To date, the smallest X-ray spot size achieved using a rotating target X-ray source is 7 µm [personal communication, Rigaku Americas Corporation]. Synchrotron radiation, on the other hand, provides an ideal source of X-rays for microbeams applications. Despite horizontal beam imposes some constriction of the sample conditions, the high brightness, wide range of energies available and nearly parallel beam offer great potentials for fine probe development as well as for radiobiological applications. In particular, the parallel and monochromatic beam assures that the best focusing resolution can be achieved by the employed X-ray optical devices while the tunable X-ray energy is an incredibly powerful tool to address critical radiobiological phenomena. So far the only microbeam facility taking advantage of synchrotron light is based at the Photon Factory in Japan [16] where biological sample are irradiated with a 5 µm X-ray beam of 4–20 keV. Finally, laser plasma or electrostatic pinch plasma sources [17] are also being considered as possible X-ray sources for microbeams. Such sources are characterized by small size and high brightness and may provide valuable input in microbeam development.

2.2. X-ray Optics

The great interest in the development of X-ray microbeam is definitely due to the high spatial resolution achievable. Microbeam facilities rely on sophisticated X-ray optics developed for lithography and astrophysics applications. X-ray beams can be focused using two different principles: reflection or diffraction. Focusing methods based on reflection use highly polished curved single- or multi-layer surfaces to bend X-rays in a single spot (Kirkpatrick-Baez mirrors). They benefit from high efficiencies, large acceptance and can be used for a wide range of X-ray energies. However, the complex procedures for the mirror alignments and the long focal distance required have so far limited their use for microbeam applications. More recently, new X-ray optics based on the principle of total reflection that occurs at shallow incident angles have been considered. Glass capillaries using total internal reflection offer the possibility to concentrate divergent radiation onto small spots by "guiding" the X-ray beam. In the focal spot a considerable increase of relative intensity up to a few orders of magnitude can be obtained although spot size smaller than 10 µm are hard to achieve. On the other hand, microoptical X-ray imaging system (MOXI) [18] uses microfabricated reflecting channels mechanically deformed to provide the curvature necessary for focusing (i.e., working in Kirkpatrick-Baez mode). Suitable fluxes are expected to be focused into a microspot size. Glass capillaries and MOXI systems also benefit from wavelength independent focal length which makes them very appealing for variable energy microbeams.

Diffraction techniques have so far been favoured for microbeam applications mainly due to their straightforward application. Using Fresnel zone plate lenses (circular diffraction gratings with increasing line density), X-ray probes down to 50 nm in diameter have been achieved for microscopy purposes. Zone plates, however, are generally very small devices (typically $\sim 100\,$s microns in diameter) due to diffraction principle constraints and suffer from low focusing efficiencies. Both

these features significantly affect the final X-ray dose rate and for radiobiological applications the spatial resolution is generally bartered in favour of dose rate. Despite these limitations, zone plates have been successfully exploited for radiobiological microbeams developing sub-micrometer irradiation facilities with dose rates up to 0.2 Gy/sec [14, 19].

3. CURRENT RADIOBIOLOGICAL CHALLENGES FOR MICROBEAMS

A recently growing area of interest for the use of microbeams is in probing the spatial and temporal evolution of radiation damage. There are currently two main aspects of great interest of the spatio-temporal evolution of DNA double strand breaks (DSB): the first is related to breaks mobility within the cell nucleus while the second concerns the dynamic interaction and alternation of DNA repair proteins. Extensive DSB migration and large scale interactions are the centre of open debates [20, 21] for current conflicting models attempting to explain the formation of complex chromosome aberrations. Using microbeams, DSBs can be induced at precise locations within the cell nucleus (recent biological developments allow staining of chromosome domains in live cells [22]) at precise times and investigate their spatio-temporal evolution by following DNA repair proteins using conventional immunofluorescence techniques and 3D microscopy. On the other hand, a better understanding of the subsequential steps followed by the DNA repair proteins in time is needed to further understand this fundamental cell mechanism. The dynamic interaction and exchanges of DNA repair proteins at the site of damage is critical as it provides clues of the necessary steps, functionality and requirements of the different enzymatic activities involved in the repair process. Being able to *a priori* determine the irradiation details (i.e., dose, irradiation site and time) for each sample combined to the use of green fluorescent proteins (GFP) for live imaging, represent a powerful tool for the analysis of the spatio-temporal evolution of the DSBs.

REFERENCES

1. Kadhim, M. A., S. A. Lorimore, K. M. Townsend, D. T. Goodhead, V. J. Buckle, and E. G. Wright, "Radiation-induced genomic instability: Delayed cytogenetic aberrations and apoptosis in primary human bone marrow cells," *International Journal of Radiation Biology*, Vol. 67, No. 3, 287–293, 1995.
2. Lambin, P., B. Marples, B. Fertil, E. P. Malaise, and M. C. Joiner, "Hypersensitivity of a human tumour cell line to very low radiation doses," *International Journal of Radiation Biology*, Vol. 63, No. 5, 639–650, 1993.
3. Prise, K. M., G. Schettino, M. Folkard, and K. D. Held, "New insights on cell death from radiation exposure," *Lancet Oncology*, Vol. 6, 520–528, 2005.
4. Boreham, D. R., J.-A. Dolling, J. Broome, S. R. Maves, B. P. Smith, and R. E. J. Mitchel, "Cellular adaptive response to single tracks of low-LET radiation and the effect on nonirradiated neighboring cells," *Radiation Research*, Vol. 153, 230–231, 2000.
5. Zirkle, R. E. and W. Bloom, "Irradiation of parts of individual cells," *Science*, Vol. 117, 487–493, 1953.
6. Miller, R. C., G. Randers-Pehrson, C. R. Geard, E. J. Hall, and D. J. Brenner, "The oncogenic transforming potential of the passage of single alpha-particles through mammalian cell nuclei," *Proc. Natl. Acad. Sci.*, Vol. 96, 19–22, USA, 1999.
7. Prise, K. M., M. Folkard, A. M. Malcomson, C. H. L. Pullar, G. Schettino, A. G. Bowey, and B. D. Michael, "Single ion actions: The induction of micronuclei in V79 cells exposed to individual protons," *Advances in Space Research*, Vol. 25, No. 10, 2095–2101, 2000.
8. Kadhim, M. A., S. J. Marsden, A. M. Malcomson, D. T. Goodhead, K. M. Prise, and B. D. Michael, "Long-term genomic instability in human lymphocytes induced by single-particle irradiation," *Radiation Research*, Vol. 155, 122–126, 2001.
9. Schettino, G., M. Folkard, K. M. Prise, B. Vojnovic, A. G. Bowey, and B. D. Michael, "Low-dose hypersensitivity in Chinese hamster V79 cells targeted with counted protons using a charged-particle microbeam," *Radiation Research*, Vol. 156, 526–534, 2001.
10. Prise, K. M., O. V. Belyakov, M. Folkard, and B. D. Michael, "Studies of bystander effects in human fibroblasts using a charged particle microbeam," *International Journal of Radiation Biology*, Vol. 74, No. 6, 793–798, 1998.
11. Schettino, G., M. Folkard, B. D. Michael, and K. M. Prise, "Low-dose binary behaviour of bystander cell killing after microbeam irradiation of a single cell with focused Ck X-rays," *Radiation Research*, Vol. 163, 332–336, 2005.

12. Folkard, M., B. Vojnovic, G. Schettino, M. Forsberg, G. Bowey, K. M. Prise, B. D. Michael, A. G. Michette, and S. J. Pfauntsch, "Two approaches for irradiating cells individually: A charged-particle microbeam and a soft X-ray microprobe," *Nuclear Instruments and Methods in Physics Research B*, Vol. 130, 270–274, 1997.
13. Goodhead, D. T., "The initial physical damage produced by ionising radiations," *International Journal of Radiation Biology*, Vol. 56, No. 5, 623–634, 1989.
14. Folkard, M., G. Schettino, B. Vojnovic, S. Gilchrist, A. G. Michette, S. J. Pfauntsch, K. M. Prise, and B. D. Michael, "A focused ultrasoft X-ray microbeam for targeting cells individually with submicrometer accurancy," *Radiation Research*, Vol. 156, 796–804, 2001.
15. Lekki, J., J. Bielecki, S. Bozek, Z. Stachura, and W. M. Kwiatek, "Design of the Krakow X-ray microprobe facility for targeted X-ray irradiations of biological objects," *Journal of Radiation Research*, 50 (Supplement), A98, 2009.
16. Kobayashi, Y., T. Funayama, N. Hamada, T. Sakashita, T. Konishi, H. Imaseki, K. Yasuda, M. Hatashita, K. Takagi, S. Hatori, K. Suzuki, M. Yamauchi, S. Yamashita, M. Tomita, M. Maeda, K. Kobayashi, N. Usami, and L. Wu, "Microbeam irradiation facilities for radiobiology in Japan and China," *Journal of Radiation Research*, 50 Suppl. A, A29–47, Tokyo, 2009.
17. Blackborow, P. A., D. S. Gustafson, D. K. Smith, M. M. Besen, S. F. Horne, R. J. D'Agostino, Y. Minami, and G. Denbeaux, "Application of the Energetiq EQ-10 electrodeless Z-Pinch EUV light source in outgassing and exposure of EUV photoresist," *Emerging Lithographic Technologies XI, Proceedings of the SPIE*, 2007.
18. Al-Aioubi, M., P. D. Prewett, S. E. Huq, V. Djakov, and A. G. Michette, "Micro-opto-elctromechanical system for X-ray focusing," *Microelectronic Engineering*, Vol. 84, 1252–1255, 2007.
19. Thompson, A. C., E. A. Blakely, K. A. Bjorstad, P. Y. Chang, C. J. Rosen, D. Sudar, and R. I. Schearz, "Microbeam studies of low-dose X-ray bystander effect on epithelial cells in fibroblasts using synchrostron radiation," *Radiation Research*, Vol. 161, 101–102, 2004.
20. Anderson, R. M., D. L. Stevens, and D. T. Goodhead, "M-FISH analysis shows that complex chromosome aberrations induced by alpha -particle tracks are cumulative products of localized rearrangements," *Proc. Natl. Acad. Sci.*, Vol. 99, No. 19, 12167–12172, USA, 2002.
21. Nelms, B. E., R. S. Maser, J. F. MacKay, M. G. Lagally, and J. H. J. Petrini, "In situ visualisation of DNA double-strand break repair in human fibroblasts," *Science*, Vol. 280, 590–592, 1998.
22. Essers, J., W. A. Van Cappellen, A. F. Theil, E. Van Drunen, N. G. Jaspers, J. H. Hoeijmakers, C. Wyman, W. Vermeulen, and R. Kanaar, "Dynamics of relative chromosome position during the cell cycle," *Molecular Biology of the Cell*, Vol. 16, No. 2, 769–775, 2005.

Design of Narrowband Multilayer for Cr K_α X-rays

H. Jiang, **A. G. Michette**, **S. J. Pfauntsch**, **D. Hart**, **and M. Shand**
Department of Physics, King's College London, Strand, London WC2R 2LS, UK

Abstract— Narrowband multilayer monochromator mirrors have been designed for a soft x-ray microfocus source, selecting a narrow band around the chromium K_α line. The reflected beam from the mirror can be focused by a zone plate in a microprobe to study radiation effects in cell and tissue samples. The design, taking into account fabrication limitations, was based on theoretical analysis and a local optimal algorithm. The results show that Cr/B_4C and Ni/B_4C multilayer mirrors working in first or second order can provide high reflectivity and energy resolution to satisfy the requirement of the zone plate. Potential problems in fabrication are also discussed briefly.

1. INTRODUCTION

Systems using X-ray focusing techniques being developed in King's College London for micro-irradiation of tissue, cells and sub-cellular targets are potentially significant for the biological and medical sciences.

These studies require the development of a variable-energy soft X-ray microprobe capable of delivering focused C K_α (0.28 keV), Al K_α (1.48 keV), Ti K_α (4.5 keV) and, notably, Cr K_α (5.4 keV) X-rays. The higher energies are capable of penetrating well beyond the first cellular layer and are therefore better suited to studies involving tissues and multi-cellular layers. However, the X-rays produced by electrons bombarding a chromium target include bremsstrahlung so that the focal spot produced by a zone plate is degraded, since focal length is proportional to energy. Hence the radiation must be monochromated, but at these energies crystals are not suitable. A feasible and effective method to overcome this problem is to design a monochromator using one or more grazing multilayer mirrors [1] to select a narrowband around the Cr K_α line while rejecting other energies.

In this paper, the design of narrowband multilayers based on theoretical analysis and computer optimization is discussed, along with potential fabrication problems which influence the optical performance.

2. DESIGN

The multilayer design goals are to obtain a reflected beam with high energy resolution and high intensity. Thus a suitable merit function, F, to be maximized is the product of the energy resolution, $E/\Delta E$, and the reflectivity, R, both determined at the wavelength of the Cr K_α line

$$F = RE/\Delta E \tag{1}$$

in which ΔE is the full width at half maximum of the reflectivity curve.

For this merit function, in kinetic theory, the resolution depends on the number of bilayers penetrated by the X-rays (effective layers) and the order of Bragg reflectivity peak. For $1/e$ attenuation, the effective number of bilayers N_{eff} is

$$N_{eff} = \frac{\sin^2\theta}{2\pi m\overline{\beta}}, \tag{2}$$

where θ is the grazing incidence angle, m is the reflectivity order, $\overline{\beta} = \Gamma\beta_a + (1-\Gamma)\beta_s$ is the average of the imaginary parts of the refractive indices (the absorption indices) of the two materials (absorber β_a, spacer β_s), and Γ is the ratio of the absorber, d_a, and period, $d = d_a + d_s$, thicknesses.

According to Eq. (2), in order to obtain energy resolutions of several hundreds, the two materials should have small absorption indices. They must also have a large difference in the real parts of their refractive indices ($n = 1 - \delta$) to obtain high reflectivity. As can be seen in Fig. 1, and considering the interface quality, Cr and Ni are potential absorber materials, and B_4C and C are ideal spacer materials.

At 5.4 keV, material absorption is small, and the reflectivity of an N-pair multilayer may be determined by the kinematical approximation:

$$R = \frac{\sin^2(N\xi/2)}{\sin^2(\xi/2)} \left[\int_0^{d_a} f_a \exp(iqx)\, dx + \int_{d_a}^{d_a+d_s} f_s \exp(iqx)\, dx \right], \tag{3}$$

where $\xi = (4\pi d \sin\theta)/\lambda$, f_a and f_s are the scattering factors of materials and $q = 2\pi S/\lambda$, S being the magnitude of the scattering vector. At a small grazing incidence angle, θ, the ratio of the $\sin^2$ terms in Eq. (3) tends to N^2. Combined with the Bragg diffraction equation, Eq. (3) may be written in the form

$$R = \frac{N^2 d}{\pi^2 m} \sin^2(m\pi\Gamma) \left(f_{a,\theta} - f_{s,\theta}\right)^2 \exp\left[-\left(\frac{4\pi \sin\theta\sigma}{\lambda} \right)^2 \right], \tag{4}$$

where the exponential term, the Debye-Waller factor, characterizes interfacial roughness. In Eq. (4), N can be substituted by Eq. (2). Hence the merit function can be expressed as

$$F = AB(\theta)\, C(\Gamma), \tag{5}$$

where

$$\begin{aligned} A &= \frac{\lambda}{16 m^2 \pi^5} \left(f_a - f\right)_s^2 \\ B(\theta) &= \sin^5\theta \exp\left(-\frac{2k\sin\theta}{\lambda} \right) \exp\left[-\left(\frac{4\pi\sin\theta\sigma}{\lambda} \right)^2 \right] \\ C(\Gamma) &= \frac{\sin^2(m\pi\Gamma)}{\left[\Gamma(\beta_a - \beta_s) + \beta_s\right]^3}. \end{aligned} \tag{6}$$

To find the best thickness ratio to optimize the merit function, the differential of $C(\Gamma)$ with respect to Γ must equal zero, resulting in Γ maxima satisfying

$$\tan(m\pi\Gamma) = \frac{2}{3} m\pi \left(\Gamma + \frac{\beta_s}{\beta_a + \beta_s} \right) \tag{7}$$

and $\Gamma - 1$ minima satisfying $\Gamma = i/m$ with $i = 1, 2, 3 \ldots$.

For a large difference in absorption coefficients, as for Cr and B_4C, the best thickness ratio Γ is very small, leading to ultra-thin metal layers which are limited by deposition technology. Although a larger value of results from using the second-order reflection, generally it is better to use the first order. Hence the key to realizing this design is to obtain ultra-thin metal films in the multilayer.

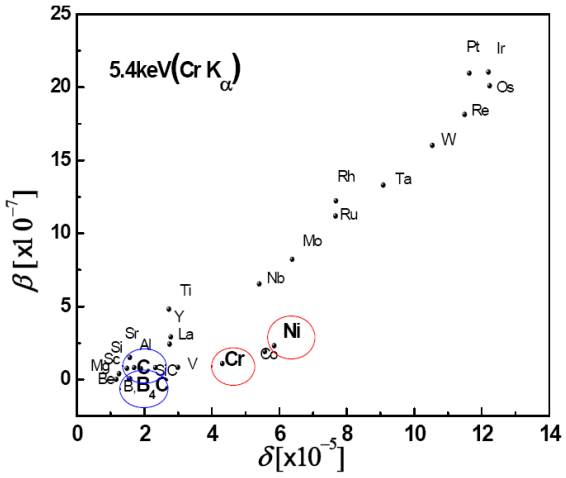

Figure 1: Optical constants at 5.4 keV.

According to Eq. (6), $B(\theta)$ increases with θ for small grazing angles, but then decreases for angles larger than 5°. As the grazing incidence angle increases, the reflectivity decreases and the resolution increases. It is also necessary to consider the efficiency and resolution requirements of the zone plate and size of the source tube, leading to an optimum working angle of about 2–3°.

For ultra-thin multilayers, the interfacial roughness should be paid especial attention. In the design, the roughnesses of the interfaces is set by what has been achieved previously [2–5]; the roughness of the metal-on-spacer interface is fixed at 0.3 nm and that of the spacer-on-metal interface is fixed at 0.5 nm.

3. RESULTS AND DISCUSSION

The Cr/B_4C and Cr/C multialyers have similar optical features with high reflectivity and the best resolution. The absorption of Ni is slightly larger than Cr, and so the reflectivity and resolution of Ni/B_4C are not good, but the number of periods is lower, meaning easier fabrication. In the following the design performances of Cr/B_4C and Ni/B_4C multilayers are compared.

Based on the theoretical analysis describe in Section 2, a group of narrowband multilayers near 3° grazing incidence using Cr/B_4C pairs was designed. To be realistic design the thickness of the Cr layers was fixed at 1 nm, which the thinnest continuous layer that can be deposited by magnetron sputtering.

The results are shown in Table 1. As the Bragg order increases the reflectivity decreases slightly, while the resolution improves significantly, directly proportional to the Bragg order number. Although the saturated number of periods (beyond which no improvement is achieved) is smaller for higher orders, the overall multilayer thickness increases, detrimental to deposition stability, increasing the overall stress and possibly causing fracture.

In practical applications, limited by current fabrication technology and instrument alignment difficulties, multilayer structures have to be improved to satisfy the following requirements:

(i) In order to overcome thickness fluctuations in the deposition process, the number of periods should be decreased to be less than 200, which means that Ni/B_4C multilayers may have better optical features than Cr/B_4C .

(ii) To reduce the overall multilayer stress requires $\Gamma > 1/3$, so that high-order reflection is not suitable.

Table 1: Designs of Cr/B_4C multilayers at $\approx 3°$ grazing incidence.

Order	Saturated periods	Working angle [°]	B_4C thickness [nm]	Reflectivity	Resolution $E/\Delta E$
1	~ 843	3.11	1.14	79.5%	313.2
2	~ 786	3.10	3.28	78.0%	619.4
3	~ 733	3.09	5.44	76.8%	919.2
4	~ 690	3.06	7.66	76.0%	1178.0

Table 2: Improved designs for practical applications.

Materials	Order	Periods	Grazing angle [°]	Metal layer [nm]	B_4C layer [nm]	Energy resolution	Cr K_α reflectivity	Angular width [°]
Cr/B_4C	1st	200	2.00	1.20	2.14	89	87%	~ 0.022
Cr/B_4C	1st	150	2.00	1.20	2.14	82	83%	~ 0.024
Cr/B_4C	2nd	200	2.01	2.20	4.45	186	76%	~ 0.011
Ni/B_4C	1st	200	2.06	1.20	2.06	67	84%	~ 0.031
Ni/B_4C	2nd	130*	2.05	2.30	4.25	133	67%	~ 0.016
W/B_4C	2nd	22*	1.88	2.30	4.95	36	37%	~ 0.054
Cr/B_4C	1st	200	3.02	1.20	1.00	174	50%	~ 0.017
Cr/B_4C	2nd	200	3.02	1.20	3.19	347	48%	~ 0.009
Ni/B_4C	1st	200	3.14	1.20	0.92	152	56%	~ 0.020
Ni/B_4C	2nd	200	2.99	1.50	2.94	303	52%	~ 0.010
W/B_4C	2nd	45*	2.94	1.50	3.04	89	18%	~ 0.031

* indicated that the number of periods is saturated

(iii) High energy resolution leads to a small angular width, leading to possible alignment difficulties.
(iv) For a small source, the layer thicknesses should be laterally graded to accommodate a range of grazing angles.

Requirements (i)–(iii) all decrease the energy resolution. In practice the energy resolution should match that of the following focusing component such as a zone plate, $\sim r^2/\lambda f$, where f is the focal distance and r is the zone plate radius. This typically means that the multilayer energy resolution should be ~ 100–< 1000.

Table 2 and Fig. 2 show the results for three different multilayers, Cr/B_4C, Ni/B_4C and W/B_4C at grazing angles of 2° and 3°. At 2°, the reflectivity for Cr K_α radiation is relatively high with unsaturated period numbers, due to the shallow penetration depth. The disadvantage is that the energy resolution is too low, unlike at 3°. The best second-order multilayer, Ni/B_4C, has a resolution of 133 and a reflectivity of 66% with only 130, saturated, periods. For a grazing angle of 3°, the theoretical resolution increases while, obviously, the reflectivity decreases. However, high resolution results in a small angular range leading to difficult alignment.

In the calculations the thickness of each is modeled by

$$d_j^* = d_j^0 + \delta_j^{\text{random}} + \delta_j^{\text{system}} \tag{8}$$

where the left hand side is the real thickness of the jth absorber/spacer layer, the first term on the RHS is the design thickness, the second is the random thickness error and the third is the cumulative system error; the ratio of the random error to the design thickness is normally distributed and that of the system error to the design thickness is uniformly distributed.

The second-order Ni/B_4C multilayer was used to study the stability of reflectivity and resolution with thickness variation. Two cases were considered: (i) only including random thickness error, with standard deviation of 5% and 10%, and (ii) 10% random thickness error and maximum 3% cumulated thickness variation, the layer thickness increasing from the substrate. To obtain the distribution of Cr K_α peak reflectivity and energy resolution, 5000 Monte Carlo simulations were used, with the working angle always determined to be optimal. The results are shown in Fig. 3.

Random thickness errors of 10% can lead to a 10% decrease in reflectivity which can be acceptable. But cumulative system variations should be controlled to avoid serious decrease of reflectivity. As can be seen in Fig. 3, it is more difficult to avoid loss of resolution with random thickness errors. There is a high probability that the energy resolution is smaller than 100 if the random thickness error is 10%.

Irrespective of whether a first or second order multilayer is used, in practical applications total and higher-order reflection in the required angular range should be prevented by using a slit between the source and the multilayer. For a second order reflection multilayer, if necessary the first order reflection at half the energy should be removed by using filter. In addition, X-rays diverge from the slit so that the working angle varies along the multilayer in the transvere direction. In order to utilize the whole multilayer fully and effectively to obtain high reflected flux, the thickness of each layer in the multilayer should be deposited with a linear lateral gradient. If the reflected beam is

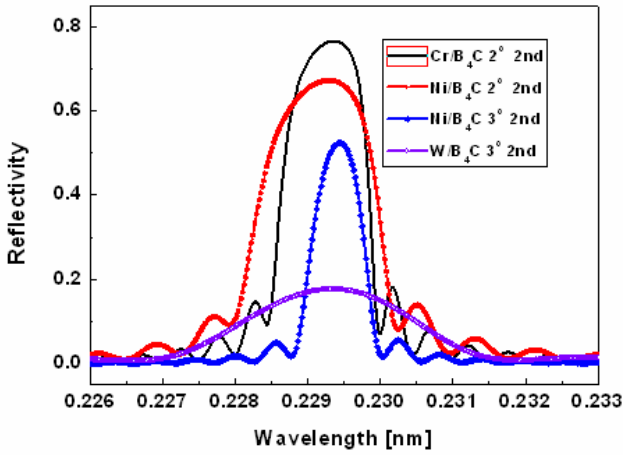

Figure 2: The reflectivity profiles of designed multilayers.

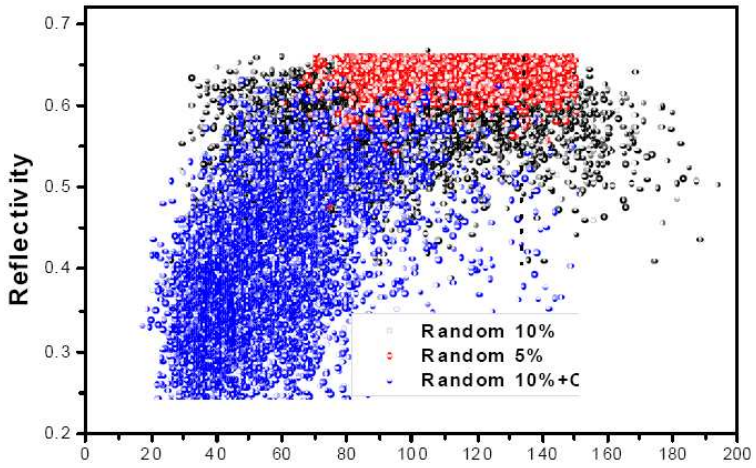

Figure 3: Monte Carlo method is used to simulate the fluctuations of resolution and reflectivity with different random thickness errors and systemic cumulative variation.

to be used with a zone plate, two multilayers can be used to give a higher resolution. The details of the alignment will be discussed in a subsequent paper.

Designs of narrowband multilayers providing high reflectivity and satisfactory energy resolution for Cr K_α radiation have been presented. First or second order reflection Cr/B_4C and Ni/B_4C pairs were chosen to deposit the multilayers working at small grazing incidence angles. The multilayer can be aligned in front of focusing components to monochromatize and reflect x-ray beams. The results show that it is easy to obtain high reflectivity, over 50%, and resolution larger than 100 taking fabrication considerations into account. The potential difficulties caused by thickness errors and stress were discussed.

REFERENCES

1. Morawe, C., et al., "High resolution multilayer x-ray optics," *Proc. SPIE*, Vol. 4145, 61–71, 2001.
2. Puik, E. J., et al., "Two methods to improve the optical quality of Ni-C multilayer coatings ion bombardment and optimization of the substrate temperature," *Proc. SPIE*, Vol. 1547, 221–227, 1992.
3. Jergel, M., et al., "Ultrashort period CuSi and NiC multilayers for X-ray mirrors," *Z. Kristallogr. Suppl.*, Vol. 23, 305–310, 2006.
4. Majkova, E., et al., "Interfaces in Ni/C and Ni/B4C multilayers," *8th International Conference on the Physics of X-ray Multilayer Structures*, Grenoble, 2006.
5. Zhu, J., et al., "Fabrication of multilayer reflective mirrors for Ni-like Ta soft X-ray laser," *Optical Instruments*, Vol. 28, 146–149, 2006 (in Chinese).

Energies in Electromagnetic Field and Gravitational Field

Zi-Hua Weng
School of Physics and Mechanical & Electrical Engineering, Xiamen University, Xiamen 361005, China

Abstract— The paper studies the conventional and new energies in the case for coexistence of electromagnetic field and gravitational field. Rephrasing with the algebra of quaternions, there are the kinetic energy, potential energy, work, proper energy, and the interacting energy between magnetic strength with magnetic moment etc. Those conventional energies are the same as that in classical gravitational theory and electromagnetic theory with the vector terminology. Besides the above energies, the study claims that there are a few new kinds of energies, which can be considered as the candidate for the dark energy.

1. INTRODUCTION

In current electromagnetic and gravitational theories, there are some kinds of energies, including the kinetic energy [1], potential energy [2], work, field energy [3], and proper energy, etc. Rephrasing the electromagnetic theory and gravitational theory with the octonions, the paper claims that there are a few new kinds of energies, besides the existing sorts of energies we found before. The new energy may be considered as one candidate for the dark energy [4].

The quaternion was first used by J. C. Maxwell [5] to describe the properties of electromagnetic field in 1861. Two quaternions can be combined together to become an octonion [6]. The latter can be used to rephrase the gravitational field and electromagnetic field simultaneously, although these two fields are quite different from each other. In the octonion space, we can study the features of field potential, field strength, field source, angular momentum, and energy, etc.

To incorporate various kinds of energies within a single definition, the angular momentum and energy both will be extended to apply within electromagnetic field and gravitational field. In the octonion space, the angular momentum can be defined from the linear momentum, the radius vector, and one new physical quantity. The last is similar to Hertz vector in the electrodynamics theory, and its derivation will yield the electromagnetic potential and gravitational potential [7].

Defining from the angular momentum, the energy involves the existing sorts of energies, and some new kinds of energies. The latter is total different from the former, and is related with above new physical quantity. In general, this new physical quantity is much less than the radius vector, and then we neglect the new energy. The results state that when the radius vector is almost equal to zero, the influence of new energies will become powerful obviously.

2. ENERGIES IN GRAVITATIONAL FIELDS

The energies can be defined from the angular momentum in the gravitational field. And the energies include the kinetic energy, potential energy, work, field energy, and proper energy, etc.

2.1. Gravitational Field

The energy in the gravitational field can be described by quaternions. In the quaternion space, the coordinates are r_0, r_1, r_2, and r_3, with the basis vector $\mathbb{E}_g = (\mathbf{i}_0, \mathbf{i}_1, \mathbf{i}_2, \mathbf{i}_3)$. Here, $r_0 = v_0 t$, t is the time, v_0 is the speed of light. The radius vector is $\mathbb{R}_g = \Sigma(r_i \mathbf{i}_i)$, and the velocity is $\mathbb{V}_g = \Sigma(v_i \mathbf{i}_i)$, with $\mathbf{i}_0 = 1$. $j = 1, 2, 3$, and $i = 0, 1, 2, 3$.

The gravitational potential is $\mathbb{A}_g = \Sigma(a_i \mathbf{i}_i)$, and the gravitational strength is $\mathbb{B}_g = \Diamond \circ \mathbb{A}_g$, with $\circ$ being the quaternion multiplication. Here $\Diamond = \Sigma(\mathbf{i}_i \partial_i)$, $\partial_i = \partial / \partial r_i$, $\nabla = \Sigma(\mathbf{i}_j \partial_j)$. The gravitational strength $\mathbb{B}_g = \Sigma(b_i \mathbf{i}_i)$ includes two parts, $\mathbf{g}/v_0 = \partial_0 \mathbf{a} + \nabla a_0$ and $\mathbf{b} = \nabla \times \mathbf{a}$.

$$\mathbf{g}/v_0 = \mathbf{i}_1 (\partial_0 a_1 + \partial_1 a_0) + \mathbf{i}_2 (\partial_0 a_2 + \partial_2 a_0) + \mathbf{i}_3 (\partial_0 a_3 + \partial_3 a_0), \tag{1}$$

$$\mathbf{b} = \mathbf{i}_1 (\partial_2 a_3 - \partial_3 a_2) + \mathbf{i}_2 (\partial_3 a_1 - \partial_1 a_3) + \mathbf{i}_3 (\partial_1 a_2 - \partial_2 a_1), \tag{2}$$

where $\mathbf{a} = \Sigma(a_j \mathbf{i}_j)$. The gauge is selected as $b_0 = \partial_0 a_0 + \nabla \cdot \mathbf{a} = 0$. The $\mathbf{b}$ is too weak to be detected presently, and that there are $\mathbf{a} = 0$ and $\mathbf{b} = 0$ in Newtonian theory.

The field source $\mathbb{S}$ of gravitational field includes the linear momentum density $\mathbb{S}_g = m \mathbb{V}_g$ and an extra part $v_0 \triangle m$.

$$\mu \mathbb{S} = -(\mathbb{B}_g / v_0 + \Diamond)^* \circ \mathbb{B}_g = \mu_g \mathbb{S}_g - \mathbb{B}_g^* \circ \mathbb{B}_g / v_0, \tag{3}$$

Table 1: The quaternion multiplication table.

	1	$\mathbf{i}_1$	$\mathbf{i}_2$	$\mathbf{i}_3$
1	1	$\mathbf{i}_1$	$\mathbf{i}_2$	$\mathbf{i}_3$
$\mathbf{i}_1$	$\mathbf{i}_1$	-1	$\mathbf{i}_3$	$-\mathbf{i}_2$
$\mathbf{i}_2$	$\mathbf{i}_2$	$-\mathbf{i}_3$	-1	$\mathbf{i}_1$
$\mathbf{i}_3$	$\mathbf{i}_3$	$\mathbf{i}_2$	$-\mathbf{i}_1$	-1

where m is the mass density, $*$ denotes the quaternion conjugate, μ is a coefficient, and μ_g is the gravitational constant. $\mathbb{B}_g^* \circ \mathbb{B}_g/(2\mu_g)$ is the field energy density, $\triangle m = -\mathbb{B}_g^* \circ \mathbb{B}_g/(\mu_g v_0^2)$.

The linear momentum density $\mathbb{P}_g = \mu\mathbb{S}/\mu_g$ is defined from the field source density $\mathbb{S}$. We introduce the definition so as to recover various linear momentum density associated with a gravitational field including conventional linear momentum density $\mathbb{S}_g$ and an extra part $v_0\triangle m$.

2.2. Angular Momentum

To incorporate various kinds of energies within a single definition, the angular momentum and the energy both will be extended to apply within gravitational fields.

The angular momentum density $\mathbb{L}_g = \Sigma(l_i\mathbf{i}_i)$ is defined from the linear momentum density $\mathbb{P}_g$ and the radius vector $\mathbb{R}_g$ as follows,

$$\mathbb{L}_g = (\mathbb{R}_g + k_{rx}\mathbb{X}_g) \circ \mathbb{P}_g, \tag{4}$$

where $l_0 = (r_0 + k_{rx}x_0)p_0 + (\mathbf{r} + k_{rx}\mathbf{x}) \cdot \mathbf{p}$, $\mathbf{l} = (r_0 + k_{rx}x_0)\mathbf{p} + p_0(\mathbf{r} + k_{rx}\mathbf{x}) + (\mathbf{r} + k_{rx}\mathbf{x}) \times \mathbf{p}$, $k_{rx} = 1$. $\mathbf{x} = \Sigma(x_j\mathbf{i}_j)$. $\mathbf{p} = \Sigma(mv_j\mathbf{i}_j)$, $p_0 = \widehat{m}v_0$, with $\widehat{m} = m + \triangle m$.

In the above, the angular momentum density $\mathbb{L}_g$ includes the orbital angular momentum density $\mathbf{r} \times \mathbf{p}$, scalar part l_0, and some other omissible terms etc.

The quaternion $\mathbb{X}_g = \Sigma(x_i\mathbf{i}_i)$ is similar to Hertz vector in the electrodynamics theory. And the derivation of $\mathbb{X}_g$ yields the gravitational potential, with $k_{rx}\mathbb{X}_g \ll \mathbb{R}_g$. In case $\mathbb{X}_g$ is neglected in the above, the energy definition will exclude mistakenly the potential energy etc.

2.3. Energy and Torque

We choose the following definition of energy to include various energies in the gravitational field. In quaternion space, the quaternion energy density $\mathbb{W}_g = \Sigma(w_i\mathbf{i}_i)$ is defined from the angular momentum density $\mathbb{L}_g$,

$$\mathbb{W}_g = v_0(\mathbb{B}_g/v_0 + \lozenge) \circ \mathbb{L}_g, \tag{5}$$

where the $-w_0/2$ is the energy density, including the kinetic energy density, potential energy density, and field energy density etc. While the $\mathbf{w}/2 = \Sigma(w_j\mathbf{i}_j)/2$ is the torque density.

Expressing the energy density as follows

$$w_0 = v_0\partial_0 l_0 + v_0\nabla \cdot \mathbf{l} + (\mathbf{g}/v_0 + \mathbf{b}) \cdot \mathbf{l}. \tag{6}$$

In case of $r_0 = 0$, $x_0 = 0$, $\mathbf{a} = 0$, $\mathbf{b} = 0$, $\mathbf{r} \parallel \mathbf{p}$, and $\mathbf{x} \parallel \mathbf{p}$, the above can be reduced to

$$-w_0/2 \approx mv_0^2 + \triangle mv_0^2 - v_0\mathbf{r} \cdot \partial_0\mathbf{p}/2 - a_0p_0/2 - v_0(\partial_0\mathbf{r}) \cdot \mathbf{p}/2 - (\mathbf{g}/v_0) \cdot (p_0\mathbf{r})/2, \tag{7}$$

Table 2: The operator and multiplication of the physical quantity in the quaternion space.

definition	meaning
$\nabla \cdot \mathbf{a}$	$-(\partial_1 a_1 + \partial_2 a_2 + \partial_3 a_3)$
$\nabla \times \mathbf{a}$	$\mathbf{i}_1(\partial_2 a_3 - \partial_3 a_2) + \mathbf{i}_2(\partial_3 a_1 - \partial_1 a_3) + \mathbf{i}_3(\partial_1 a_2 - \partial_2 a_1)$
∇a_0	$\mathbf{i}_1\partial_1 a_0 + \mathbf{i}_2\partial_2 a_0 + \mathbf{i}_3\partial_3 a_0$
$\partial_0\mathbf{a}$	$\mathbf{i}_1\partial_0 a_1 + \mathbf{i}_2\partial_0 a_2 + \mathbf{i}_3\partial_0 a_3$

where the last three terms in the above are equal to the sum of kinetic energy density and potential energy density in classical field theory. $a_0 = v_0(\partial_0 x_0 + \nabla \cdot \mathbf{x})$ is the scalar potential of gravitational field, and $\mathbf{a} = v_0(\partial_0 \mathbf{x} + \nabla x_0 + \nabla \times \mathbf{x})$ is the vectorial potential of gravitational field.

When $x_0 \neq 0$ and $\mathbf{x} \neq 0$, besides the conventional energy parts in Eq. (7), there is a new energy density, $-w_0'/2$, in the gravitational field from Eq. (6),

$$\begin{aligned} w_0' \approx\ & v_0 \{x_0 \partial_0 p_0 + \mathbf{x} \cdot \partial_0 \mathbf{p} + \mathbf{x} \cdot \nabla p_0 + x_0 \nabla \cdot \mathbf{p} + \mathbf{x} \cdot (\nabla \times \mathbf{p})\} \\ & + (\mathbf{g}/v_0 + \mathbf{b}) \cdot (x_0 \mathbf{p} + p_0 \mathbf{x} + \mathbf{x} \times \mathbf{p}). \end{aligned} \tag{8}$$

The new energy in the above is different to conventional energy in classical gravitational theory, and then can be considered as the candidate for the dark energy.

3. ENERGIES IN GRAVITATIONAL AND ELECTROMAGNETIC FIELDS

More energy terms can be defined from the angular momentum in the electromagnetic field and gravitational field. The energy includes the gravitational potential energy, electromagnetic potential energy, proper energy, kinetic energy, work, and interacting energy between the magnetic strength with magnetic moment, etc.

3.1. Gravitational and Electromagnetic Fields

The gravitational field and electromagnetic field both can be illustrated by quaternions. And their quaternion spaces can be combined together to become the octonion space. In other words, the features of gravitational and electromagnetic fields can be described with the octonion space.

In the quaternion space for electromagnetic field, the basis vector is $\mathbb{E}_e = (\mathbf{I}_0, \mathbf{I}_1, \mathbf{I}_2, \mathbf{I}_3)$, the radius vector is $\mathbb{R}_e = (R_0, R_1, R_2, R_3)$, and the velocity is $\mathbb{V}_e = (V_0, V_1, V_2, V_3)$. The $\mathbb{E}_e$ is independent of the $\mathbb{E}_g$, with $\mathbb{E}_e = \mathbb{E}_g \circ \mathbf{I}_0$. The symbol $\circ$ denotes the octonion multiplication.

The basis vectors $\mathbb{E}_g$ and $\mathbb{E}_e$ comprise the basis vector of octonion space. In the octonion space, the basis vector is $\mathbb{E} = (1, \mathbf{i}_1, \mathbf{i}_2, \mathbf{i}_3, \mathbf{I}_0, \mathbf{I}_1, \mathbf{I}_2, \mathbf{I}_3)$, the radius vector is $\mathbb{R} = \Sigma(\mathbf{i}_i r_i + \mathbf{I}_i R_i)$, and the velocity is $\mathbb{R} = \Sigma(\mathbf{i}_i v_i + \mathbf{I}_i V_i)$. Here $R_0 = V_0 T$, T is the time-like, V_0 is the speed of light-like. When the electric charge is combined with the mass to become the electron or proton etc., we have the inference, $R_i \mathbf{I}_i = r_i \mathbf{i}_i \circ \mathbf{I}_0$ and $V_i \mathbf{I}_i = v_i \mathbf{i}_i \circ \mathbf{I}_0$.

The electromagnetic potential is $\mathbb{A}_e = \Sigma(\mathbf{I}_i A_i)$, which can be combined together with the gravitational potential $\mathbb{A}_g$ to become the field potential $\mathbb{A} = \mathbb{A}_g + k_{eg}\mathbb{A}_e$, with k_{eg} being a coefficient. The strength, $\mathbb{B} = \Diamond \circ \mathbb{A} = \mathbb{B}_g + k_{eg}\mathbb{B}_e$, consists of gravitational strength $\mathbb{B}_g$ and electromagnetic strength $\mathbb{B}_e$. And the gauge equations are $b_0 = 0$ and $B_0 = 0$.

The electromagnetic strength $\mathbb{B}_e$ covers two parts, $\mathbf{E} = (B_{01}, B_{02}, B_{03})$ and $\mathbf{B} = (B_{23}, B_{31}, B_{12})$,

$$\mathbf{E}/v_0 = \mathbf{I}_1(\partial_0 A_1 + \partial_1 A_0) + \mathbf{I}_2(\partial_0 A_2 + \partial_2 A_0) + \mathbf{I}_3(\partial_0 A_3 + \partial_3 A_0), \tag{9}$$

$$\mathbf{B} = \mathbf{I}_1(\partial_3 A_2 - \partial_2 A_3) + \mathbf{I}_2(\partial_1 A_3 - \partial_3 A_1) + \mathbf{I}_3(\partial_2 A_1 - \partial_1 A_2). \tag{10}$$

The electric current density $\mathbb{S}_e = q\mathbb{V}_g \circ \mathbf{I}_0$ is the source for electromagnetic field, and the linear momentum density $\mathbb{S}_g = m\mathbb{V}_g$ is for gravitational field. And the field source $\mathbb{S}$ satisfies,

$$\mu\mathbb{S} = -(\mathbb{B}/v_0 + \Diamond)^* \circ \mathbb{B} = \mu_g \mathbb{S}_g + k_{eg}\mu_e \mathbb{S}_e - \mathbb{B}^* \circ \mathbb{B}/v_0, \tag{11}$$

Table 3: The octonion multiplication table.

	1	$\mathbf{i}_1$	$\mathbf{i}_2$	$\mathbf{i}_3$	$\mathbf{I}_0$	$\mathbf{I}_1$	$\mathbf{I}_2$	$\mathbf{I}_3$
1	1	$\mathbf{i}_1$	$\mathbf{i}_2$	$\mathbf{i}_3$	$\mathbf{I}_0$	$\mathbf{I}_1$	$\mathbf{I}_2$	$\mathbf{I}_3$
$\mathbf{i}_1$	$\mathbf{i}_1$	-1	$\mathbf{i}_3$	$-\mathbf{i}_2$	$\mathbf{I}_1$	$-\mathbf{I}_0$	$-\mathbf{I}_3$	$\mathbf{I}_2$
$\mathbf{i}_2$	$\mathbf{i}_2$	$-\mathbf{i}_3$	-1	$\mathbf{i}_1$	$\mathbf{I}_2$	$\mathbf{I}_3$	$-\mathbf{I}_0$	$-\mathbf{I}_1$
$\mathbf{i}_3$	$\mathbf{i}_3$	$\mathbf{i}_2$	$-\mathbf{i}_1$	-1	$\mathbf{I}_3$	$-\mathbf{I}_2$	$\mathbf{I}_1$	$-\mathbf{I}_0$
$\mathbf{I}_0$	$\mathbf{I}_0$	$-\mathbf{I}_1$	$-\mathbf{I}_2$	$-\mathbf{I}_3$	-1	$\mathbf{i}_1$	$\mathbf{i}_2$	$\mathbf{i}_3$
$\mathbf{I}_1$	$\mathbf{I}_1$	$\mathbf{I}_0$	$-\mathbf{I}_3$	$\mathbf{I}_2$	$-\mathbf{i}_1$	-1	$-\mathbf{i}_3$	$\mathbf{i}_2$
$\mathbf{I}_2$	$\mathbf{I}_2$	$\mathbf{I}_3$	$\mathbf{I}_0$	$-\mathbf{I}_1$	$-\mathbf{i}_2$	$\mathbf{i}_3$	-1	$-\mathbf{i}_1$
$\mathbf{I}_3$	$\mathbf{I}_3$	$-\mathbf{I}_2$	$\mathbf{I}_1$	$\mathbf{I}_0$	$-\mathbf{i}_3$	$-\mathbf{i}_2$	$\mathbf{i}_1$	-1

Table 4: The operator and multiplication of the physical quantity in the octonion space.

definition	meaning
$\nabla \cdot \mathbf{S}$	$-(\partial_1 S_1 + \partial_2 S_2 + \partial_3 S_3)\mathbf{I}_0$
$\nabla \times \mathbf{S}$	$-\mathbf{I}_1(\partial_2 S_3 - \partial_3 S_2) - \mathbf{I}_2(\partial_3 S_1 - \partial_1 S_3) - \mathbf{I}_3(\partial_1 S_2 - \partial_2 S_1)$
$\nabla \mathbf{S}_0$	$\mathbf{I}_1\partial_1 S_0 + \mathbf{I}_2\partial_2 S_0 + \mathbf{I}_3\partial_3 S_0$
$\partial_0 \mathbf{S}$	$\mathbf{I}_1\partial_0 S_1 + \mathbf{I}_2\partial_0 S_2 + \mathbf{I}_3\partial_0 S_3$

where $k_{eg}^2 = \mu_g/\mu_e$, q is the electric charge density, μ_e is the constant, $*$ denotes the conjugate of octonion. In the octonion space, $\triangle m = -\mathbb{B}^* \circ \mathbb{B}/(v_0^2\mu_g)$. The field energy density is,

$$\mathbb{B}^* \circ \mathbb{B}/\mu_g = \mathbb{B}_g^* \circ \mathbb{B}_g/\mu_g + \mathbb{B}_e^* \circ \mathbb{B}_e/\mu_e. \tag{12}$$

The linear momentum density $\mathbb{P} = \mu\mathbb{S}/\mu_g$ can be defined from the field source density $\mathbb{S}$. And the linear momentum density includes the conventional linear momentum density $(\mathbb{S}_g + k_{eg}\mu_e\mathbb{S}_e/\mu_g)$ and an extra part $v_0\triangle m$ in the electromagnetic field and gravitational field.

3.2. Angular Momentum

In the case for coexistence of electromagnetic field and gravitational field, the octonion angular momentum density $\mathbb{L} = \Sigma(l_i\mathbf{i}_i) + \Sigma(L_i\mathbf{I}_i)$ is defined from the octonion linear momentum density $\mathbb{P} = \Sigma(p_i\mathbf{i}_i) + \Sigma(P_i\mathbf{I}_i)$ and octonion radius vector $\mathbb{R}$.

$$\mathbb{L} = (\mathbb{R} + k_{rx}\mathbb{X}) \circ \mathbb{P}, \tag{13}$$

with

$$\begin{aligned}
l_0 &= (r_0 + k_{rx}x_0)p_0 + (\mathbf{R}_0 + k_{rx}\mathbf{X}_0) \circ \mathbf{P}_0 + (\mathbf{r} + k_{rx}\mathbf{x}) \cdot \mathbf{p} + (\mathbf{R} + k_{rx}\mathbf{X}) \cdot \mathbf{P}, && (14)\\
\mathbf{l} &= (r_0 + k_{rx}x_0)\mathbf{p} + (\mathbf{R} + k_{rx}\mathbf{X}) \circ \mathbf{P}_0 + (\mathbf{r} + k_{rx}\mathbf{x}) \times \mathbf{p} + (\mathbf{R}_0 + k_{rx}\mathbf{X}_0) \circ \mathbf{P}\\
&\quad + p_0(\mathbf{r} + k_{rx}\mathbf{x}) + (\mathbf{R} + k_{rx}\mathbf{X}) \times \mathbf{P}, && (15)\\
\mathbf{L}_0 &= p_0(\mathbf{R}_0 + k_{rx}\mathbf{X}_0) + (\mathbf{R} + k_{rx}\mathbf{X}) \cdot \mathbf{p} + (r_0 + k_{rx}x_0)\mathbf{P}_0 + (\mathbf{r} + k_{rx}\mathbf{x}) \cdot \mathbf{P}, && (16)\\
\mathbf{L} &= (r_0 + k_{rx}x_0)\mathbf{P} + (\mathbf{r} + k_{rx}\mathbf{x}) \circ \mathbf{P}_0 + (\mathbf{R}_0 + k_{rx}\mathbf{X}_0) \circ \mathbf{p} + (\mathbf{R} + k_{rx}\mathbf{X}) \times \mathbf{p}\\
&\quad + (\mathbf{r} + k_{rx}\mathbf{x}) \times \mathbf{P} + p_0(\mathbf{R} + k_{rx}\mathbf{X}), && (17)
\end{aligned}$$

where $\mathbb{X} = \Sigma(x_i\mathbf{i}_i) + \Sigma(X_i\mathbf{I}_i)$. $\mathbf{X}_0 = X_0\mathbf{I}_0$, $\mathbf{X} = \Sigma(X_j\mathbf{I}_j)$. $\mathbf{L}_0 = L_0\mathbf{I}_0$, $\mathbf{L} = \Sigma(L_j\mathbf{I}_j)$. $\mathbf{P}_0 = P_0\mathbf{I}_0$, $\mathbf{P} = \Sigma(P_j\mathbf{I}_j)$. $\mathbf{R}_0 = R_0\mathbf{I}_0$, $\mathbf{R} = \Sigma(R_j\mathbf{I}_j)$. $P_i = MV_i$, with $M = k_{eg}q\mu_e/\mu_g$. Similarly, the derivation of octonion $\mathbb{X}$ will yield the potentials of gravitational field and electromagnetic field.

3.3. Energy and Torque

In the case for coexistence of electromagnetic field and gravitational field, the octonion energy density $\mathbb{W} = \Sigma(w_i\mathbf{i}_i) + \Sigma(W_i\mathbf{I}_i)$ is defined from the octonion field strength $\mathbb{B}$ and octonion angular momentum density $\mathbb{L}$.

$$\mathbb{W} = v_0(\mathbb{B}/v_0 + \Diamond) \circ \mathbb{L}, \tag{18}$$

where the $-w_0/2$ is the energy density, which includes the kinetic energy, potential energy, and field energy etc. While the $\mathbf{w}/2 = \Sigma(w_j\mathbf{i}_j)/2$ is the torque density.

Expressing the energy density as follows

$$w_0 = v_0\partial_0 l_0 + v_0\nabla \cdot \mathbf{l} + (\mathbf{g}/v_0 + \mathbf{b}) \cdot \mathbf{l} + k_{eg}(\mathbf{E}/v_0 + \mathbf{B}) \cdot \mathbf{L}. \tag{19}$$

In case of $r_0 = 0$, $x_0 = 0$, $\mathbf{x} = 0$, $\mathbf{X}_0 = 0$, $\mathbf{X} = 0$, $\mathbf{a} = 0$, $\mathbf{b} = 0$, $\mathbf{r} \parallel \mathbf{p}$, and $\mathbf{x} \parallel \mathbf{p}$, the above can be reduced to

$$\begin{aligned}
-w_0/2 &\approx mv_0^2 + \triangle m v_0^2 - a_0 p_0/2 - v_0\partial_0(\mathbf{r} \cdot \mathbf{p})/2 - (\mathbf{g}/v_0) \cdot (p_0\mathbf{r})/2 - \mathbf{A}_0 \circ \mathbf{P}_0/2\\
&\quad -\mathbf{A} \cdot \mathbf{P}/2 - (\mathbf{E}/v_0) \cdot (\mathbf{r} \circ \mathbf{P}_0)/2 - \mathbf{B} \cdot (\mathbf{r} \circ \mathbf{P})/2, && (20)
\end{aligned}$$

where $\mathbf{A}_0 + \mathbf{A} = k_{eg}\mathbb{A}_e$. $\mathbf{A}_0 = v_0(\partial_0\mathbf{X}_0 + \nabla \cdot \mathbf{X})$ and $\mathbf{A} = v_0(\partial_0\mathbf{X} + \nabla \circ \mathbf{X}_0 + \nabla \times \mathbf{X})$ are related to the scalar potential and vectorial potential of electromagnetic field respectively. The last four

terms are the electric potential energy density, magnetic potential energy density, and interacting energy density between dipole moment with electromagnetic strength in classical field theory.

When $x_0 \neq 0$, $\mathbf{x} \neq 0$, $\mathbf{X}_0 \neq 0$, and $\mathbf{X} \neq 0$, besides the energy parts in Eq. (20), there is a new energy density, $-w_0'/2$, in the electromagnetic field and gravitational field from Eq. (19),

$$\begin{aligned} w_0' \approx\ & v_0 \{x_0 \partial_0 p_0 + \mathbf{X}_0 \circ \partial_0 \mathbf{P}_0 + \mathbf{x} \cdot \partial_0 \mathbf{p} + \mathbf{X} \cdot \partial_0 \mathbf{P} + \mathbf{x} \cdot \nabla p_0 + \mathbf{X} \cdot (\nabla \circ \mathbf{P}_0)\} \\ & + v_0 \{x_0 \nabla \cdot \mathbf{p} + \mathbf{X}_0 \cdot (\nabla \circ \mathbf{P}) + \mathbf{X} \circ (\nabla \times \mathbf{P}) + \mathbf{x} \cdot (\nabla \times \mathbf{p})\} \\ & + (\mathbf{g}/v_0 + \mathbf{b}) \cdot (x_0 \mathbf{p} + p_0 \mathbf{x} + \mathbf{x} \times \mathbf{p} + \mathbf{X}_0 \circ \mathbf{P} + \mathbf{X} \circ \mathbf{P}_0 + \mathbf{X} \times \mathbf{P}) \\ & + k_{eg} (\mathbf{E}/v_0 + \mathbf{B}) \cdot (x_0 \mathbf{P} + \mathbf{x} \circ \mathbf{P}_0 + \mathbf{X}_0 \circ \mathbf{p} + \mathbf{X} \times \mathbf{p} + \mathbf{x} \times \mathbf{P} + p_0 \mathbf{X}). \end{aligned} \tag{21}$$

The energy in the above is different to conventional energy in classical gravitational field and electromagnetic field, and then can be considered as the candidate for the dark energy.

4. CONCLUSION

In the gravitational theory or electromagnetic theory, the conventional energy can be rephrased with the algebra of quaternions, such as the kinetic energy, potential energy, proper energy, and work etc. In contrast to classical field theory with vector terminology, we find that there are some new kinds of energies, besides the conventional energies we found before. Meanwhile those new kinds of energies can be considered as the candidate for the dark energy.

Rephrasing with the algebra of octonions, the new energies in the gravitational field and electromagnetic field can be described simultaneously. The related inferences about the new energy can be extended through to the case for coexistence of electromagnetic field and gravitational field. In case of the radius vector is almost equal to zero, the influence of new energies will become powerful obviously around the electrons. When the radius vector is immense enough, the impact of the new energies on the stars may be able to observe directly.

It should be noted that the study for various energies in the electromagnetic and gravitational fields examined only some simple cases in quaternion spaces. Despite its preliminary characteristics, this study can clearly indicate that the conventional energy in either electromagnetic field or gravitational field can be deduced with the algebra of quaternions. In the octonion space, some new kinds of energies in these two fields can be drawn out simultaneously. For the future studies, the research will concentrate on only some predictions about the new energy.

ACKNOWLEDGMENT

This project was supported partially by the National Natural Science Foundation of China under grant number 60677039.

REFERENCES

1. Feoli, A. and D. Mele, "Improved tests on the relationship between the kinetic energy of galaxies and the mass of their central black holes," *International Journal of Modern Physics D*, Vol. 16, No. 8, 1261–1272, 2007.
2. Diakonov, D., "Potential energy of Yang-Mills vortices in three and four dimensions," *Modern Physics Letters A*, Vol. 14, No. 25, 1725-1732, 1999.
3. Vasile, R., R. Messina, and R. Passante, "Time-dependent Maxwell field operators and field energy density for an atom near a conducting wall," *Physical Review A*, Vol. 79, No. 6, 062106, 2009.
4. Miao, H.-X. and Y. Zhang, "Analytic spectrum of relic gravitational waves modified by neutrino free streaming and dark energy," *Physical Review D*, Vol. 75, No. 10, 104009, 2007.
5. Maxwell, J. C., *A Treatise on Electricity and Magnetism*, Dover Publications Inc., New York, 1954.
6. Leo, S. D. and K. Abdel-Khalek, "Towards an octonionic world," *International Journal of Theoretical Physics*, Vol. 37, No. 7, 1945–1985, 1998.
7. Weng, Z.-H., "Adjoint charge in electromagnetic field," *PIERS Proceedings*, 904–907, Moscow, Russia, August 18-21, 2009.

Electromagnetic Sources and Observers in Motion I — Evidence Supporting the EM Propagation Medium for the Transmission of Light

S. E. Wright
Moor Lane Laboratory, ECASS Technologies Ltd., Kirkburton, Huddersfield, HD8 0QS, UK

Abstract— A propagation medium (ether) has long been thought essential to facilitate the transmission of light. Conflicting scientific evidence both substantiated and contradicted the medium's existence. Einstein's ether-less universe was reluctantly accepted by the establishment, although the controversy was never resolved. This study concludes that there is extensive data supporting the medium, challenging Einstein's special relativity (SR). Measurements on and above the Earth, through satellite and space communications show that away from gravitational matter, the medium is basically at rest in space. Close to a gravitational body the medium appears to be attracted to and moves with the body. Einstein was not aware of this detail in developing his SR, which now appears to be in error. It is confirmed that Lorentz's time and space contraction is in fact a direct result of motion with respect to the medium, as Lorentz predicted. And that clear distinction is found between source and observer motion relative to the medium, which SR cannot distinguish between. These medium distinctions appear to restore rationality and remove paradox present in Einstein's relativity. Experimental methods, an order of magnitude more sensitive than that of Michelson and Morley, are available that can finally investigate in detail claims that the medium exists.

1. INTRODUCTION

It appears that there is irrefutable data supporting the propagating medium, which was not often referred to by Einstein, in which he would have had difficulty disputing. Sagnac [5], with his rotating optical mirrors, established that the medium exists and moves with the surface of the Earth. He showed that light moving in the medium stationary on the Earth's surface, around a rotating system of mirrors, produced a propagation delay according to the mirror speed relative to the medium. Michelson and Gale (M&G) [6], with their fixed optical loop on Earth, showed that the medium rotates with the surface relative to a 'stationary' medium surrounding and orbiting with the Earth. This was demonstrated through a phase difference across the optical loop, caused by the Earth surface and it's medium increasing in velocity towards the equator, relative to the surrounding 'stationary' medium. This data was well documented in Einstein's time. With modern technology, Hafele and Keating (H&K) [8], in a high flying aircraft, using atomic clocks to measure time slowing, confirmed the medium orbits with the Earth. The medium model has been confirmed further through asymmetric propagation time differences of 300 ns ($300 \times 10^{-9} \times 0.3 \times 10^{9} \approx 100$ m), corresponding to the direction and against the direction of the Earth's motion, in satellite communications across the Pacific, Saburi et al. [9]. Also confirmation is by signal displacements through satellite Global Positioning Systems (GPS) [11], considered in detail later. The 'stationary' propagation medium orbiting with the Earth, in turn, is shown to move relative to a 'stationary' medium surrounding the Sun and Solar System, moving through space, measured in the Viking-Mars Lander project by Reasenburg et al. [10]. Whereas, the cosmic microwave background (CMB), discovered by Penzias and Wilson (P&W) [7], is shown to be an electromagnetic radiation, radiating uniformly in all directions throughout the universe relative to the medium at rest in space. In depth details of the above medium based confirmation experiments are given in [13]. If the medium did not exist, there would be no rational explanation on how these effects could occur. It appears that Einstein's concept of relativity, based on no propagation medium, has not been verified theoretically or confirmed experimentally. *Researchers claiming to have verified Einstein's special relativity have usually verified the kinematic aspects of SR (Lorentz's time and space contraction, leading to $E=mc^2$ etc), not relativity or the absence of the propagation medium.* Removing the medium, as Einstein attempted to do, besides making light propagation impossible, appears to create fundamental analytical difficulties. Without the medium's presence, Einstein could not solve the electromagnetic (EM) motional wave equation. Without its solution, there can be no predictability of an observed sequence of events, no formal definition of time, no causality. This takes relativity into a metaphysical, philosophical realm, whereas, in fact light propagation is a very real and predictable phenomenon.

SR, without a medium, can predict only relative motion between projectiles. Without satisfying the solution of the motional wave equation, SR apparently, cannot describe observations of motion of any kind, whether relative or absolute. The description of observed motion, complete with emission, reception and retarded time appears to be absent. To predict observations one should acknowledge the existence of the medium and use the full solution of the motional wave equation reflected through Lorentz's medium based transform (LT). *The LT is a complete observable theory, it does not depend on SR. Whereas, SR is based on LT, but without its medium, SR appears incomplete, it is unobservable and cannot be supported by LT.* The solution to the electromagnetic motional wave equation, for sources and observers in motion relative to the propagation medium is available, Wright [13]. This new medium based theory supports Fresnel's light convection, transverse Doppler (1842), changes in time, space, mass, momentum and Einstein's energy equation. Relativistic quantum mechanics, which is Lorentz invariant, quantum electrodynamics and the Standard Model in particle physics, all appear to be in agreement with this medium based theory. The new theory is also in accord with general relativity; here the medium inclusion leads to Schwarzschild (1916) metric and event horizon. Assuming the medium to be homogeneous and isotropic, the Robertson (1936)-Walker (1937) metric in cosmology is obtained. There appears to be nothing in any of the above theories to doubt the existence of the medium and the exact application of the LT with respect to this medium. Therefore, this new approach is not rewriting history, but offers a more robust, physical understanding of electromagnetic sources and observers in motion relative to their propagation medium.

2. MEDIUM PROPERTIES

Classically, and through modern physics, there is no difficulty in identifying the propagation medium. To describe light propagation in the form of electromagnetic (EM) waves, Maxwell's equations [1] are used. In this case, an EM source of electric charge q, energizes the propagation medium with an electric field E. Changes in q, either strength or positioning, produce electric field wave disturbances ΔE, accompanied by magnetic field variations ΔH. The q variations could be lightning, electrons jumping orbit or moving at high speed leaving an accelerator into a more dense medium. The light energy transmission is given approximately by $(\Delta E)^2/z$, where the medium impedance $z = \mu c$. Here μ, the permeability, is a measure of the medium electrical density, $c = dE/d\mu = (1/\mu ę)^{1/2}$ is the speed of light, and ę is the permittivity, equivalent to an electrical rigidity term. *According to Maxwell, light propagation depends precisely on its electrical properties μ and ę not on its material structure. No other mechanism is required, there is no mechanical ether.* In an unstressed medium, (free space), measurements show $\mu = 1.25 \times 10^{-6}\,\mathrm{N/A^2}$ and ę$= 8.85 \times 10^{-12}\,\mathrm{F/m}$, giving $c = (\mu ę)^{-1/2} = 3 \times 10^8\,\mathrm{m/s}$. For optical media, μ tends to be similar, it's ę that varies. A diamond's electrical rigidity has the highest value and varies widely with frequency, causing its spectacular sparkle. For gases including a vacuum, ę is small (electri-

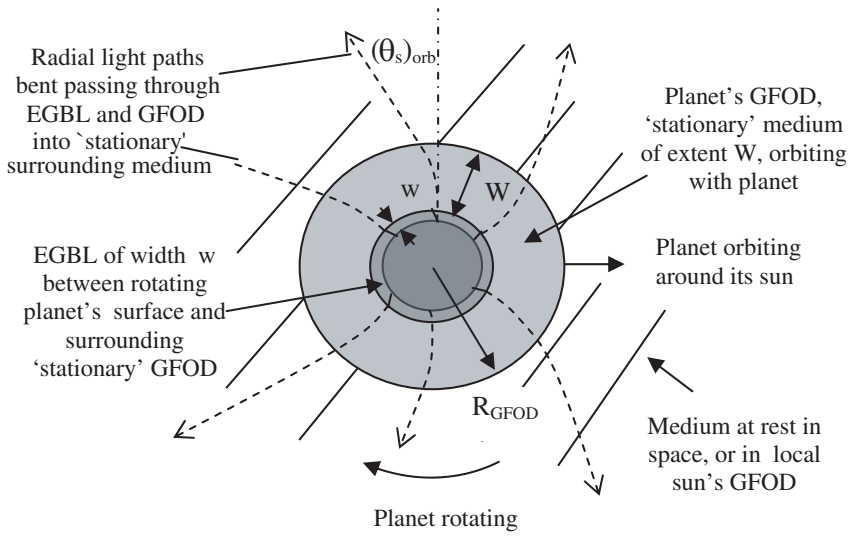

Figure 1: Medium profile around orbiting planet, according to Sagnac, M&G, H&K and P&W (forward motion effect is exaggerated).

cally soft), up to 100 times softer than that of liquids and solids. *The universal medium, pervading over all space, being a compressible fluid, supporting transverse waves and having no rigid structure, appears to be attracted to and forms medium velocity gradients around moving gravitational bodies.* Maxwell's equations (ME's) are 'static' equations, describing propagation in the stationary medium. *According to Lorentz, it is the equal shrinking of time and space with motion relative to the medium, that makes the speed of light and ME's invariant in the moving frame.* The existence of the medium, with its well defined properties, μ and ę is difficult to dismiss. Maxwell and Lorentz were obviously believers in the medium and supported it fervently to their deaths. Therefore there is a choice; we can put our faith in Einstein's metaphysical ether-less universe, or trust in Maxwell's defined and measurable ether.

3. MEDIUM AROUND A PLANET

Based on the established data discussed in the introduction, the medium details around a typical orbiting planet can be constructed, as illustrated in Figure 1. Sagnac (medium moving with surface), M&G (surface medium rotating relative to 'stationary' medium surrounding planet), H&K (medium surrounding planet 'stationary' and orbiting with planet) and P&W (medium at rest in space). *This situation can be interpreted as a medium in the form of a gravitational sphere (gravisphere) surrounding the planet. It appears to be controlled by the planet's gravitational field of dominance (GFOD) over existing fields in the vicinity*, effectively extending to a radius R_{GFOD}. Imaginary radial light rays are shown bending through a source orbital angle $(\theta_s)_{orb}$, as they pass from the moving source (planet), through the planets GFOD moving with the planet, to the 'stationary' medium within the sun's GFOD. The Earth's orbital velocity is 30 km/s (Mach number $M = v/c \approx 10^{-4}$) giving a source orbital deflection angle behind the normal to the planet's orbital motion of $(\theta_s)_{orb} \approx \tan^{-1}(M) = 5.7 \times 10^{-3}$ degrees. If there was no propagation medium there could be no motional deflection angle. This angle is difficult to measure directly. However, the displacement angle below, although smaller, is precisely measureable.

4. SIGNAL DISPLACEMENT

According to Sagnac, and M&G, the propagation medium is at rest (rotating) with the Earth's surface. In that case the propagation times on Earth will be symmetrical in any direction, giving no propagation variation between a stationary Earth and one moving through the universe, as demonstrated in the Michelson and Morley experiment (MMX). If *the medium rotates with the planet's surface, but is stationary within its GFOD, an electro gravitational boundary layer (EGBL) will exist between these two media. Communication paths between the Earth and its artificial satellites must then pass through the EGBL, causing a signal displacement*, exaggerated in Figure 2. For simplicity, an overhead geostationary satellite above the equator is assumed rotating with the Earth.

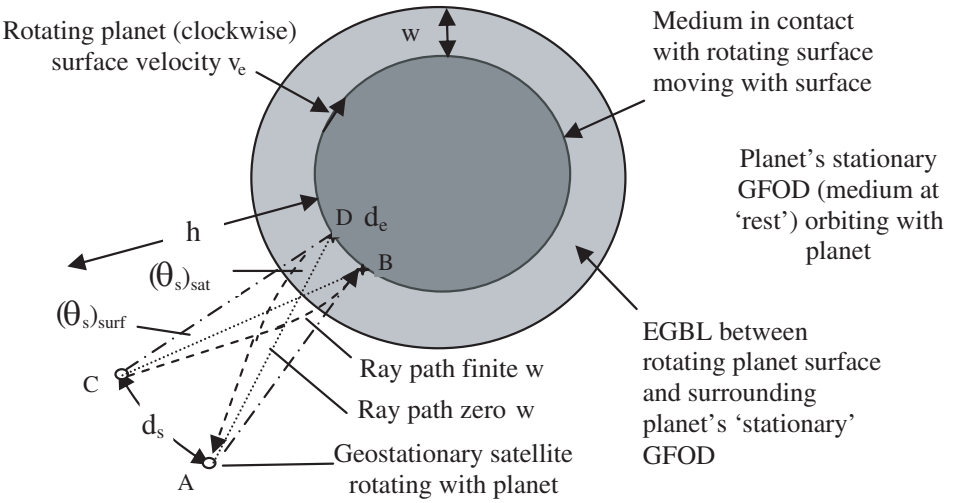

Figure 2: Global Positioning System showing propagation through the Earth's EGBL. Earth's rotation relative to the surrounding 'stationary' medium causes motional displacement angles and spatial displacement not predicted by SR (not to scale).

For rotation against a 'stationary' medium and zero boundary layer width w, propagating paths between satellite and ground station should be straight lines. *The satellite signal will go from C-B making a source surface motional displacement angle $(\theta_s)_{surf}$ to the rear of the normal to the direction of the Earth's motion.* For a finite boundary layer thickness, the propagation paths will be slightly curved. For transmission from ground to satellite, the signal will go from D–A, making a satellite angle $(\theta_s)_{sat}$. Either way, rotational displacements d_e and d_s on the Earth and at the satellite, respectively, are formed. For small Mach numbers M_e, the Earth displacement d_e (positional error) is given by the Earth's surface velocity v_e times the propagation time h/c, the resulting source surface angle $(\theta_s)_{surf}$ then follows:

$$d_e \approx v_e h/c \approx hM_e \quad \text{and} \quad (\theta_s)_{surf} \approx \tan^{-1}(d_e/h), \quad d_e/h \approx v_e/c \approx M_e \tag{1}$$

h is the satellite height above the planet's surface. The kinematic (Lorentzian) contraction (space and time), at moderate speeds, as well as the gravitational compression for moderate planet sizes, is small compared to the rotational displacement effect, Ashby [12].

5. DISPLACEMENT CONFIRMATION

At low speeds and vast distances from the planet, the effect of the local GFOD and the EGBL will be very small, but none the less close to the planet's surface both effects are important and measureable. For an Earth radius of $r_e \approx 6 \times 10^6$ m, rotation $\omega_e \approx 7.3 \times 10^{-5}$ radians/s, satellite radius $r_s \approx 26 \times 10^6$ m, height $h = r_s - r_e \approx 20 \times 10^6$ m propagation time $t = h/c = 20 \times 10^6/3 \times 10^8 = 66$ ms and surface velocity at the equator $v_e = \omega_e r_e = 7.3 \times 10^{-5} \times 6 \times 10^6 = 440$ m/s, the Earth's rotational Mach number becomes $M_e = v_e/c = 440/300 \times 10^6 \approx 1.5 \times 10^{-6}$. The source surface angle and displacement are then, respectively, $(\theta_s)_{surf} \approx \tan^{-1}(M) = \tan^{-1}(1.5 \times 10^{-6}) \approx 10^{-4}$ degrees and $d_e \approx hM_e \approx 20 \times 10^6 \times 1.5 \times 10^{-6} \approx 30$ m. The displacement correction is automatically taken into account in the Global Positioning System (GPS) [11], in calculating position. It is verified countless times daily, again confirming the presence of the propagation medium. According to Einstein's Inertial Frame (EIF) (no medium, no propagation time difference between a stationary and moving frame), the propagation time for an overhead satellite path A-B should be simply $t = h/c$. Here, the source motional angles and resulting displacement should not exist ($(\theta_s)_{sat} = (\theta_s)_{surf} = 0$, $d_s = d_e = 0$). i.e., *It appears Einstein cannot account for these finite displacement angles and distances in transmissions between satellites and ground stations. To account for the displacement, it should be acknowledged that the medium exists, and that the Earth and satellite rotate relative to the 'stationary' medium surrounding them.*

6. MEASURING MEDIUM VELOCITY PROFILES

The MMX type measurement was not a very sensitive method of measuring motion with respect to the medium. Even at Earth orbital speeds of 30 km/s, $M = 10^{-4}$, and assuming motion relative to the medium at rest in space, only a small fraction of an interference fringe would have been measured. To measure motion with respect to the medium at Earth rotational speeds i.e., 480 m/s, $M \approx 1.5 \times 10^{-6}$, or practical speeds on Earth, a more sensitive system is required. The MMX is insensitive because it is based on a second order effect M^2, relying on the difference in the propagation times in each direction in a round trip measurement, where the differences tend to cancel. *The sensitivity can be increased by an order of magnitude compared with the MMX, by measuring the propagation time in one direction or normal to the direction of motion.* Two possible arrangements are illustrated in Figure 3. Figure (a) measures the propagation over a large separation distance (many km). Here two, one way linear systems are facing in opposite directions, forming a dual system, which measures signal propagating distance change in and against the direction of motion. The phase is locked at one end and the phase difference measured at the other end. In this way the total phase change is recovered, not the difference. Figure 3(b) is a portable system, where the propagation delay is not measured in the direction of motion, but folded back on itself, measuring the delay normal to the direction of motion. Here the propagation path length is independent of motion. To increase sensitivity there can be multiple folded path lengths. This system should be able to measure the motion of an aircraft, fast train or even a well sprung slow truck, if sufficient multiple folded path lengths are used.

The propagation time t, at right angles or in the direction of motion, between two fixed points of path length d, is $t = d/c$. If the system moves at velocity v, then the incremental distance travelled

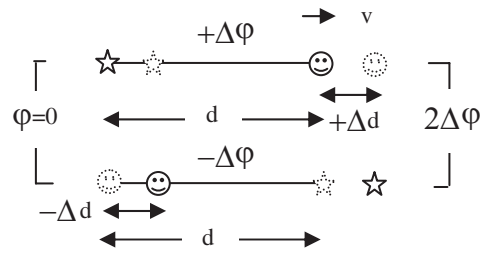

(a) Two, one way systems facing in opposite directions, propagation in the direction of motion

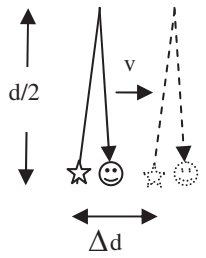

(b) Portable folded back system, propagation path normal to direction of motion

Figure 3: First order, propagation time delay cosmic speed ohmmeters. These are considerably more sensitive than the round trip second order MMX method.

by the system in time t is $\Delta d = vt = vd/c$, and the incremental propagation time is:

$$\Delta t = \Delta d/c = vd/c^2 = Mt, \quad \text{and} \quad \Delta\varphi = 2\pi f \Delta t, \quad \text{where} \quad M = v/c \quad \text{and} \quad t = d/c \tag{2}$$

If N is the number of interference fringes, f is the frequency and λ the wavelength of the source (laser), then:

$$N = \Delta\varphi/2\pi = f\Delta t = fvd/c^2 = fMd/c = Md/\lambda \tag{3}$$

If $v = 300\,\mathrm{m/s}$, $M = 10^{-6}$, $\lambda = 6 \times 10^{-7}\,\mathrm{m}$ and $d = 3\,\mathrm{m}$, then $N = 10^{-6} \times 3 \times 6^{-1} \times 10^7 = 5$ fringes. Whereas for the Michelson and Morley experiment (MMX), $N = fM^2d/c = M^2d/\lambda = 10^{-12} \times 3 \times 6^{-1} \times 10^7 = 5 \times 10^{-6}$ fringes, i.e., one million times smaller. The first objective of using the one way system should be to reassure oneself that the system works. Here the presence of the propagation medium on Earth could be measured using the compact portable system in a moving ground transport system. The second task would be to confirm the medium velocity profile above the Earth surface using an aircraft or tethered balloons. The third task would then be to map the medium velocity profiles around planets, the Sun and moons in the Solar System and elsewhere, using orbital satellites and space craft.

7. CONCLUSION

Extensive data is provided in support of the propagation medium. It appears that the medium exists, is generally at rest in free space, moves with gravitational bodies and rotates if the body rotates. Within the body's gravitational field of dominance (GFOD), the propagation medium is attracted to and moves with the body. On the surface of a rotating body, the propagation medium appears to rotate with the surface, producing an electro-gravitational boundary layer (EGBL) between the rotating surface and its GFOD. The EGBL has been confirmed through Sagnac [5], M&G [6], and H&K [8]. The GFOD has been established through asymmetric signal propagation delays in satellite communication relay systems (Saburi et al. [9]), signal displacement in Global Positioning Systems (GPS) [11] and in interplanetary communications, Reasenberg et al. [10]. This new medium based model appears to explain all known observations without ambiguity or paradox. Further details of the EGBL and GFOD should be investigated on and around the Earth. Their extent, gradients and their asymmetry, if any, with motion, should be compared with other planet sizes within the Solar System and elsewhere.

REFERENCES

1. Maxwell, J. C., "A dynamical theory of the electromagnetic field," *Philosophical Transactions of the Royal Society of London*, Vol. 155, 459–512, 1865.
2. Michelson, A. A. and E. W. Morley, "On the relative motion of the Earth and the luminiferous ether," *American Journal of Science*, Vol. 34, No. 203, 333–345, 1887.
3. Lorentz, H. A., "Simplified theory of electrical and optical phenomena in moving systems," *Proc. Acad. Science Amsterdam*, Vol. 1, 427–442, 1899.
4. Einstein, A., "On the electrodynamics of moving bodies," *Annalen der Physik*, Vol. 17, 891–921, 1905.
5. Sagnac, G., "L'éther lumineux démontré par l'effet du vent relatif d'éther dans un interféromètre en rotation uniforme," *Comptes Rendus*, Vol. 157, S. 708–710, 1913.

6. Michelson, A. A. and H. G. Gale, (M&G), "The effect of the Earth's rotation on the velocity of light," *The Astrophysical Journal*, Vol. 61, S. 140–145, 1925.
7. Penzias, A. A. and R. W. Wilson, (P&W), "A measurement of the flux density of CAS A at 4080 Mc/s," *Astrophysical Journal Letters*, Vol. 142, 1149–1154, 1965.
8. Hafele, J. and R. Keating, (H&K), "Around the world atomic clocks. Predicted relativistic time gains," *Science*, Vol. 177, No. 4044, 166–168, 1972.
9. Saburi, Y., M. Yamamoto, and K. Harada, "High precision time comparison via satellite and observed discrepancy of synchronization," *IEEE Transactions*, Vol. 25, 473–477, 1976.
10. Reasenberg, R. D., I. I. Shapiro, P. E. MacNeil, R. B. Goldstein, J. C. Breidenthal, J. P. Brenkle, D. L. Cain, T. M. Kaufman, T. A. Komarek, and A. I. Zygielbaum, "Viking relativity experiment. Verification of signal retardation by solar gravity," *Astrophysical Journal*, Vol. 234, L219–L221, 1979.
11. Logsdon, T., *The NAVSTAR Global Positioning System*, Van Nostrand Reinhold, 1992.
12. Ashby, N., "Relativity in global positioning systems," *Living Reviews in Relativity 2003–2001*, Max Planck Institute for Gravitational Physics, 2003.
13. Wright, S. E., *Problems with Einstein's Relativity*, Trafford Publishing, 2010.

Electromagnetic Sources and Observers in Motion II — Einstein's Ether-less Relativity Versus Lorentz's Medium Based Theory

S. E. Wright
Moor Lane Laboratory, ECASS Technologies Ltd., Kirkburton, Huddersfield, HD8 0QS, UK

Abstract— Considerable data is shown to exist in support of an electromagnetic (EM) propagation medium (ether). However, Einstein decided, in his special relativity (SR), that there was no propagation medium. Having no medium appears to disqualify SR from being a solution of the motional wave equation, and therefore gives a non causal sequence of events (prediction of time). This was in spite of Lorentz, who had established causality and Sagnac, who had actually measured motion relative to the medium. Many in the scientific community including Maxwell, Poincaré and Lorentz fervently resisted the medium's abandonment. Even so, Einstein's SR was used unsuccessfully to account for the Michelson and Morley experiment and its implied missing medium. The medium's removal was attempted through using Einstein's inertial frame, where without a medium he assumed that stationary and constantly moving frames are indistinguishable. Mathematically this was equivalent to simulating the removal through an oblique time and space axes transform. It appears that Einstein's non-causal, ether-less, oblique axes transform is not supported by Lorentz's causal, medium based, rectangular axes transform. Based on Maxwell's wave equation, a new transform extends Lorentz's theory, for both source and observer motion relative to the medium. It explains observations in the universe quite naturally, removing optical simultaneity and reciprocity, predicted by SR, which appear not to have been observed.

1. INTRODUCTION

The data in support of the existence of the propagation medium for the transmission of light is considered in a companion paper [1]. The medium is found to be complex, it appears to be attracted to and moves with gravitational bodies. Aware that light propagation was not straight forward, but having no suspicion of the complexity of the medium velocity profiles produced by the body's motion, Einstein [2], decided to simplify (unify) the situation by removing the propagation medium altogether. In an attempt to simulate the medium's removal, Einstein's special relativity (SR) effectively used hypothetical oblique transform axes, instead of rectangular regular ones used by the medium based Lorentz transform [3]. *It appears that these oblique axes have not been verified theoretically or confirmed experimentally.* Researchers claiming to have verified Einstein's relativity have usually verified the kinematic aspects of SR. These are basically Lorentz's time and space contraction, not relativity or the absence of the propagation medium. Having no medium, besides the obvious effect of making light impossible, also appears to restrict SR to describing a positional sequence of events, creating fundamental observational difficulties. Without accepting the medium's presence, Einstein could not solve the motional wave equation. Without its solution, there appears to be no predictability of an observed sequence of events, no formal definition of time, no causality. This appears to take Einstein's unobservable relativity into a metaphysical, realm, whereas, light propagation is an observable and predictable phenomenon. As a consequence, SR cannot describe observations of motion of any kind, whether relative or absolute. The description of observed motion, complete with emission, reception and retarded time appears to be absent. *To predict observations one should acknowledge the existence of the medium and use Maxwell's wave equation, with motion being included through the Lorentz's transform (LT).* The medium based LT is a complete observational theory, it is independent of SR. Whereas, it appears that SR is incomplete, without a propagation medium SR cannot be observed and cannot be supported by the LT.

2. EINSTEIN'S ETHER-LESS THEORY

For regular media movement, such as air and water, it is expected that the upstream and downstream propagation times will be different and change with medium speed (simultaneity not upheld), similar to water waves on a rapidly moving river. If the water speed, for example, equals the wave speed the waves would appear stationary upstream relative to the river bank, giving half the downstream and an infinite upstream propagation time. This information, through the propagation medium, is predicted by solving the classical wave equation. This equation predicts the whole

process of generation transmission and reception for all kinds of rational (causal) wave motions. In the case of the electromagnetic wave equation, it predicts the source events (light) as seen by an observer. However, Einstein believed the asymmetric propagation time is not supposed to happen for EM waves. Without any definitive proof, and against basic physics, there was thought to be an unidentified light propagation mechanism, not requiring a medium. As a result of the apparently missing medium, and supposedly equal propagation times up stream and down, Einstein proposed his concept of special relativity (SR), based on his Inertial Frame (EIF). In an attempt to explain Einstein's SR and simulate the absence of the medium, an oblique time and space axes transform was effectively constructed, as described by Born [4], based on earlier work in 1924. The concept of optical reciprocity (observations are the same interchanging the source and observer) and simultaneity (propagation times are the same in and against the direction of motion), resulting from SR, are simulated in the space-time diagram in Figure 1. The 45° angled dotted lines BA' and BC' in the figure are the propagation light paths into and out of B in an upward direction. The 45° angle is obtained using time in years and distance in light years (LY). The relation between the oblique time and space axes ct', x', are shown symmetrically positioned each side of the light paths. The ct', x' axes have gradients $1/M$ and M, respectively where $M = v/c$ is the Mach number i.e., ratio of system speed over light speed. In the figure $M = 0.6$ giving a Lorentz contraction of $\alpha = (1 - M^2)^{1/2} = 0.8$. The figure is an equi-sided rhombus, symmetrically placed about the 45° light paths, forming four smaller rhombuses between axes. The top two rhombuses represent a stationary source at B, and moving observers approaching on the left hand side (LHS) along $A''A'$ and receding on the right hand side (RHS) along $C''C'$. The bottom two rhombuses are for a stationary observer at B, and moving sources approaching on the LHS along $A'''A''$ and receding on the RHS along $C'''C''$. Thus all times and spaces are now equal i.e., $BA'' = BC'' = A'''A'' = A''A' = C''C'$ etc., making approaching & receding, and source & observer motion times appear equal.

Thus an approaching source-stationary observer time scale ($A'''A''$) is identical to an approaching observer-stationary source time scale ($A''A'$), as measured on the oblique ct' axis, upholding the optical reciprocity of motion, i.e., $(A'''A'') = (A''A')$. This implies that there is no difference between source and observer motion, they can be inter-changed and observations of each other's system time and space scales are symmetrical. Also, that the approaching ($A''A'$) and receding ($C''C'$) observer time scales, for a stationary source at B, are equal satisfying simultaneity, i.e., $(A''A') = (C''C')$. *Thus, through a subtle rotation of the space-time axes, optical reciprocity and simultaneity appear to be simulated, giving the concept of relativity some credibility. However, there appears to be fundamental difficulties created with this simulation.* For zero velocity, $M = 0$, $\alpha = 1$, the rhombus becomes a square with sides centred on A_p, C_p and D_p. All sides (times and distances) then increase with speed (square flattens and widens). It can be shown [5], that the expansion ratio between the distance BC'' in the moving frame compared with the distance BC_p, in the stationary frame becomes:

$$\alpha^* = BC''/BC_p = \left[\left(1 + M^2\right) / \left(1 - M^2\right)\right]^{1/2} = (1 + M^2)^{-1/2}/\alpha \tag{1}$$

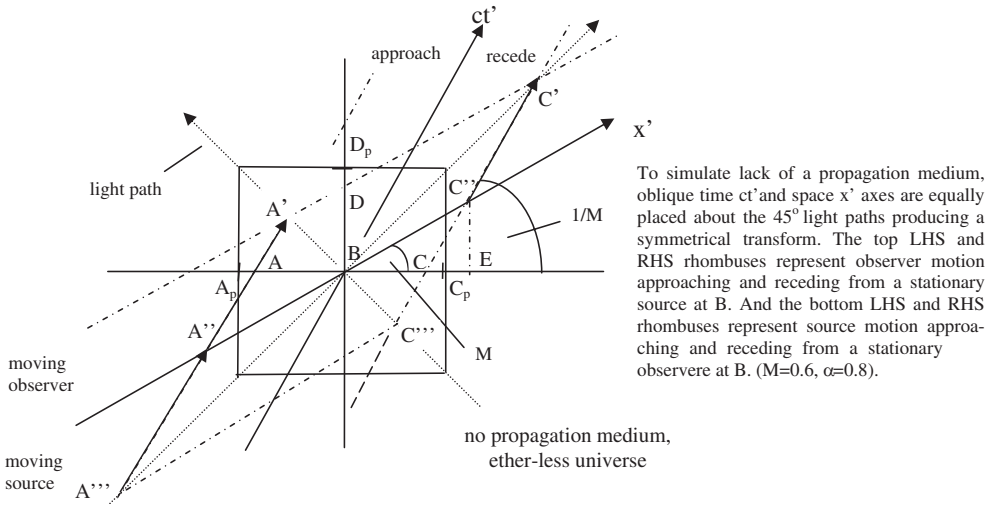

Figure 1: Einstein's special relativity with no medium and oblique time and space axes, simulating optical reciprocity and simultaneity.

This α^* expansion of $(1+M^2)^{-1/2}/\alpha$ in the ether-less transform, is obviously not in agreement with the well established Lorentz transform (LT) contraction of $\alpha = (1 - M^2)^{1/2}$. This oblique axes SR transform does not appear to represent reality. It attempts to simulate the effect of no medium with a medium construction, which appears to be a contradiction. It attempts to simulate simultaneity and reciprocity, whose existences have actually never been established. This transform, portrayed in Figure 1, is a departure from the rectangular axes LT and is therefore not representative of it. *There appears to be no justification for the oblique model, apart from trying to remove the medium to satisfy the Michelson and Morley experiment (MMX)* [6], *which can be justified quite naturally using a medium* [1]. According to Einstein's Inertial Frame (EIF), supported by Einstein's two postulates (physics and the speed of light are invariant in the moving frame), propagation changes cannot occur for constant motion at any speed. With Einstein's medium removal, there can be no way of judging optically the motion of EIF, creating non causality, simultaneity and reciprocity, artificially.

3. LORENTZ'S MEDIUM BASED THEORY

According to Maxwell [7], the properties of the propagation medium are well defined. The electrical impedance z of the medium to the transmission of light is given by $z = \mu c$, where μ, the permeability, is a measure of the medium's electrical 'density', $c = (\mu ę)^{-1/2}$ is the propagating speed of light, and ę is the permittivity, equivalent to an electrical 'rigidity' term. For light to propagate, the EM medium requires an equivalent electrical mass and compressibility, a 'springiness' provided by μ and ę. For optical medium μ is fairly constant, it is ę that varies. *A diamond has the largest ę whereas gases, including a vacuum, have a small but a finite μ and ę and no physical structure. Thus they appear to behave as a fluid medium, being attracted to and forming velocity gradients around moving bodies, including the Earth.* For a homogeneous propagation medium at rest in space or moving with a gravitational body, the symmetrical space time diagram illustrated in Figure 1 is modified to the asymmetrical one shown in Figure 2. Here the oblique ct' and x' axes rotate back to their Galilean rectangular positions, coinciding with the vertical and horizontal axes. These rectangular axes become the absolute time t_p in years and space x_p in light years respectively, in the real world (stationary propagating medium), providing a legitimate reference to measure the light propagation and corresponding flight paths. The square in the figure again represents the stationary source and observer case, where light from B reaches A_p and C_p simultaneously at time D_p. For dynamic motion, the square becomes a rhombus. To accommodate the kinematic effects,

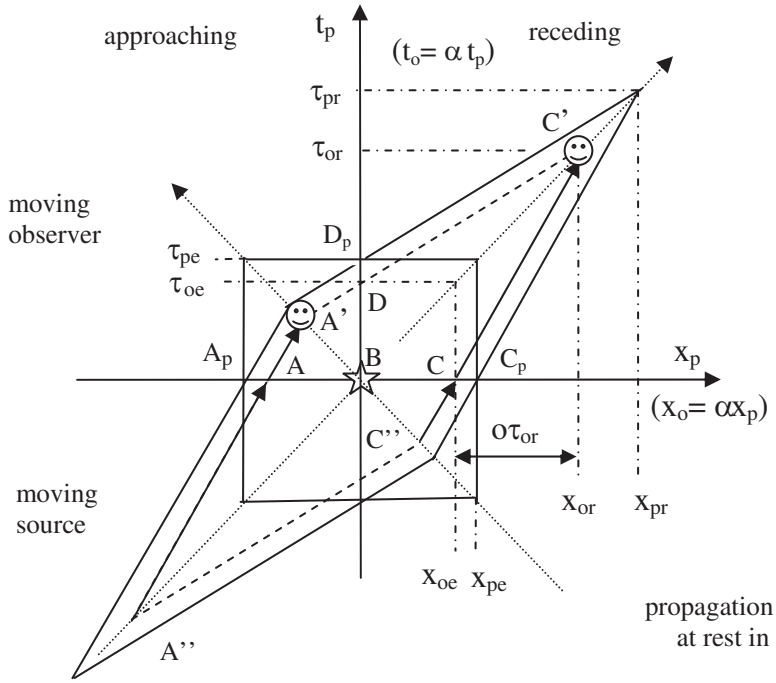

The oblique axes are returned to their rectangular position, giving an asymmetrical Lorentzian contracted Galilean Transform. AA' and CC' are the approaching and receding observer flight paths with a stationary source at B. The static square becomes a dynamic rhombus, which shrinks by α, through kinematic motion.

Figure 2: Lorentz's medium based, rectangular axes, motional transform, showing asymmetric propagation paths removing simultaneity and optical reciprocity.

the Galilean time and space axes shrink by α, according to Lorentz, thus:

$$BC/BC_p = x_o/x_p = BD/BD_p = t_o/t_p = \alpha, \quad \text{where} \quad \alpha = (1 - M^2)^{1/2} \tag{2}$$

The outer rhombus represents dynamic (Galilean) motion, and the inner rhombus represents dynamic modified by kinematic (Lorentzian) motion. Extensions to the LT, for source and observer motion in general, relative to the medium, are portrayed in the four quadrants of Figure 2. Here a stationary source with an approaching and receding observer are represented in the top left and right hand quadrants. A stationary observer and approaching and receding source are illustrated in the lower quadrants. Where BA', BC', $A''B$, and $C''B$ are the light propagation paths in the medium. Also AA', CC' are the approaching and receding observer flight paths and $A''A$, $C''C$ are the approaching and receding source flight paths. *Through restoring the propagating medium, it can be seen that the symmetry in Figure 1 is broken, making a clear distinction between source and observer motion.* Also the restoration invalidates the optical reciprocity of motion i.e., the viewing of each other's time and space scales between two systems in relative motion, are no longer identical, equivalent or interchangeable. Further, that the propagation in and against the direction of motion is no longer equal-simultaneity is no longer upheld. Figure 2 is an exact graphical application of the LT, portrayed in the top right-hand quadrant. It can be seen that it physically corresponds to a receding observer and stationary source configuration. The subscripts o and p indicate a moving and stationary observer in the propagation medium respectively. From the 45° gradients (constant velocity of light c) for the light propagation in both the stationary and moving fames, and from the LT, where time and space contract across frames by α, one has:

$$x_p/\tau_p = x_o/\tau_o = c, \quad \tau_o/\tau_p = x_o/x_p = \alpha \tag{3}$$

where segments of time t are represented by τ. Distinction now has to be made between 'e' emission time and 'r' reception times. Using Equation (3) and Figure 2, top LHS for propagation against, and RHS in the direction of motion, the observer flight paths, during the corresponding light propagation, are given by:

$$x_{oe} = x_{or} \pm o\tau_{or}, \quad x_{oe} = \alpha_o x_{pe} = c\tau_{or} \pm o\tau_{or}, \quad c\alpha_o\tau_{pe} = \tau_{or}(1 \pm M_o)c \tag{4}$$

where the minus sign is for receding. Or rearranging in terms of the observed event time and space:

$$\tau_{or} = \tau_{pe}\alpha_o/(1 \pm M_o), \quad x_{or} = x_{pe}\alpha_o/(1 \pm M_o) \tag{5}$$

These results can be obtained from the wave equation directly [5]. Rearranging in the form of the Lorentz transforms, one has:

$$\tau_{oe} = \alpha_o\tau_{pe} = \tau_{or}(1 \pm M_o) = \tau_{or} \pm M_o x_{or}/c = \tau_{or} \pm o x_{or}/c^2 \tag{6}$$

This theory is based on light propagating in a medium between source and observer motion relative to the medium. The resulting observed events determine the speed and direction of time in a causal manner (observed event cannot occur before the source event, for positive direction of time). Non observable relativity, not being based on a propagation medium, and not being a solution of the wave equation, cannot satisfy causality. Causally, time can run backwards for a receding observer and $M > 1$. If $M = 1$ can be avoided, one can look back in time to past events, but one cannot interfere or participate in them, i.e., material time travel to the past is impossible. Looking ahead of the present source event emission time also appears impossible, i.e., one cannot travel into the future, by definition it has not yet happened. Equation (5) gives the moving observer reception time τ_{or} in terms of stationary source emission time τ_{pe}. It depends on the Doppler shift $(1 \pm M_o)^{-1}$ and the Lorentz contraction α_o. Also the reception propagation distance x_{or}, with motion, is changed in terms of the initial stationary emission distance x_{pe}, in the medium, by $\alpha_o/(1 \pm M_o)$. *This propagation time/distance variance with observer motion, is in direct conflict with Einstein Inertial Frame (EIF), which is based on no medium and no propagation time variance with frame motion.* Equation (6) can be recognized now as the classical Lorentz transform.

As an example, consider the famous lightning strike at the centre of a railway carriage. It would be seen obviously simultaneous at each end of the stationary carriage, and on each side of the stationary rail track, for the same distance apart, as illustrated in Figure 3(a). For a moving carriage, the light would, of course, still be seen simultaneously on each side of the track by a stationary observer. But now according to causality and the medium based LT, the light would not be seen simultaneously at each end of the carriage, for a moving observer and carriage relative to the Earth and its medium, as shown in Figure 3(b). This asymmetrical propagation time delay, in a frame moving with respect to the propagation medium, is predicted by the Lorentz

transform, Equation (5), and has been verified by Sagnac [8]. Einstein's Inertial Frame (EIF) used in his SR, is illustrated in Figure 3(c). According to EIF, nothing changes without a medium, for constant motion at any speed, creating non causality and producing non observable simultaneity and reciprocity. *The existence of the propagation medium with its measured asymmetric propagation retarded time delay upstream and down, and the non-compliance of the ether-less SR theory with Lorentz's medium based theory, implies that EIF is not a complete description of the propagation process.* Thus Einstein's SR, simultaneity and reciprocity created by SR, appear to be erroneous.

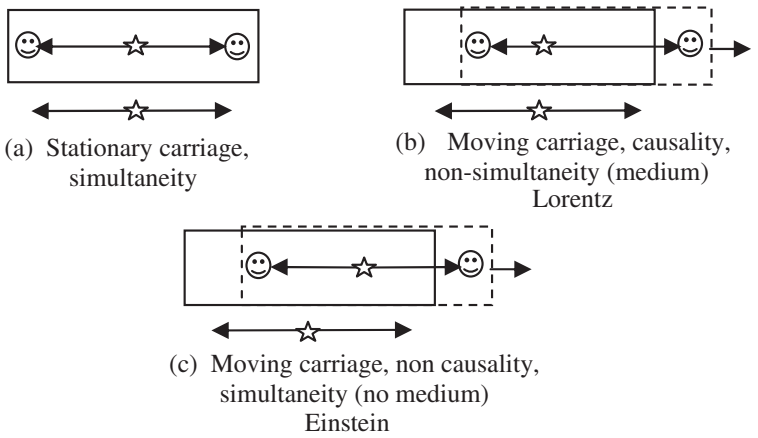

Figure 3: Lightning flash at centre of stationary and moving carriage with and without a propagation medium.

4. CONCLUSION

It appears SR is adequate only for describing relative motion between objects, it is inadequate for describing observations of motion of objects. Without a medium, Einstein's inertial frame cannot be judged optically to be in motion. This appears to result in no absolute motion (time and space), equal propagation time upstream and down (simultaneity upheld), optical reciprocity between moving frames (time and space scales appear to be identical) and no distinction between source and observer motion. These concepts, which have not been established (observed) in practice, effectively arise through artificially removing the propagation medium, using an oblique time and space axes transform. This model, is not supported by the medium base rectangular axes Lorentz transform. To restore reality (causality), allowing propagation with respect to the propagation medium, the oblique axes of the ether-less relativity theory are rotated back to their original medium based Galilean rectangular positions. This removes the simulated concepts of simultaneity and reciprocity, restores the variant propagation time in the moving frame and establishes the difference between source and observer motion. There appears to be no basis for Einstein's ether-less theory, apart from satisfying the MMX, which is accounted for quite naturally through accepting the presence of the propagation medium.

REFERENCES

1. Wright, S. E., "Electromagnetic sources and observers in motion I — Evidence supporting the EM propagation medium for the transmission of light," *Progress In Electromagnetics Research Symposium*, Xi'an, China, March 22–26, 2010.
2. Einstein, A., "On the electrodynamics of moving bodies," *Annalen der Physik*, Vol. 17, 891–921, 1905.
3. Lorentz, H. A., "Simplified theory of electrical and optical phenomena in moving systems," *Proc. Acad. Science Amsterdam*, Vol. 1, 427–442, 1899.
4. Born, M., *Einstein's Theory of Relativity*, First published in 1924, Dover, New York, 1962.
5. Wright, S. E,. *Problems with Einstein's Relativity*, Trafford Publishing, 2010.
6. Michelson, A. A. and W. Morley, "On the relative motion of the earth and the luminiferous ether," *American Journal of Science*, Vol. 34, No. 203, 333–345, 1887.
7. Maxwell, J. C., "A dynamical theory of the electromagnetic field," *Philosophical Transactions of the Royal Society of London*, Vol. 155, 459–512, 1865.
8. Sagnac, G., "L'éther lumineux démontré par l'effet du vent relatif d'éther dans un interféromètre en rotation uniforme," *Comptes Rendus*, Vol. 157, 708–710, 1913.

On the A, B, C Numbers and Their Application in the Theory of Circular Waveguide with Azimuthally Magnetized Ferrite

Mariana Nikolova Georgieva-Grosse[1] and Georgi Nikolov Georgiev[2]

[1]Meterstrasse 4, D-70839 Gerlingen, Germany
[2]Faculty of Mathematics and Informatics
University of Veliko Tirnovo "St. St. Cyril and Methodius", BG-5000 Veliko Tirnovo, Bulgaria

Abstract— An iterative method is worked out and applied to calculate the A, B, C numbers — positive real numbers, connected with the normalized differential phase shift, produced by the circular waveguide, containing azimuthally magnetized ferrite which sustains normal TE_{01} mode. It is based on the recently formulated definition of the quantities in question and uses the positive purely imaginary zeros of a certain complex Kummer confluent hypergeometric function, determined for a varying imaginary part of its first complex parameter. The results of investigation are presented graphically. The influence of the normalized guide radius and of the magnitude of off-diagonal ferrite permeability tensor element on the numbers is analyzed. A numerical example is presented, demonstrating the way of figuring out the phase shift with their help.

1. INTRODUCTION

The A, B, C numbers have been advanced in the theory of azimuthally magnetized circular ferrite waveguides, propagating normal TE_{0n} modes, built through the medium of the complex confluent hypergeometric functions, as a means for computation of the differential phase shift provided by these structures [1, 2]. Finding the quantity mentioned is important in view of the possible application of geometries in the development of nonreciprocal digital phase shifters for microwave frequencies [1–9]. This requires knowledge of the numbers, the information for which still is scarce [1, 2].

The discussion is confined here to the circular waveguide, entirely filled with ferrite that supports normal TE_{01} mode. An iterative technique is elaborated that might yield A, B and C in the whole area of phase shifter operation of configuration [3, 8]. For the purpose, the definiens: $A = A_- - A_+$, $B = B_- - B_+$ and $C = C_- - C_+$ of the numbers, introduced newly [2], are harnessed in which $A_\pm$, $B_\pm$ and $C_\pm$ are set through the roots of a specially constructed biquadratic equation, involving the positive purely imaginary zeros of wave function for propagation — the complex Kummer function [10]. The effect of the magnitude of the off-diagonal ferrite permeability tensor element $|\alpha|$ and of the normalized guide radius $\bar{r}_0$ on the quantities studied, is examined. The benefit of the latter in the exact reckoning of the differential phase shift, called into being by the set-up, is shown.

2. ITERATIVE METHOD FOR COMPUTATION OF THE A, B, C NUMBERS

The pair $\{|\alpha|, \bar{r}_0\}$ of positive real numbers $|\alpha| < 1$ and $\bar{r}_0 > \nu_{1,n}$, where $\nu_{1,n}$ is the nth zero of Bessel function $J_1(z/2)$, $n = 1, 2, 3, \ldots$, $z > 0$ is chosen, subject to the requirement [3]:

$$\nu_{1,n} < \bar{r}_0\sqrt{1-\alpha^2} < L(c,n)/|\alpha| \tag{1}$$

in that the symbols $L(c, n)$ and c in it designate certain real positive and integer numbers, resp., e.g., $L(3, 1) = 6.59365\,41068$ [3]. Next, the nth positive purely imaginary roots $\zeta_{k,n}^{(c)}$ in x_0 (in z_0) of the equation [1–4, 8]:

$$\Phi(a, c; x_0) = 0, \tag{2}$$

written in terms of the complex Kummer function [10] with $a = c/2 - jk$, $c = 3$, $x_0 = jz_0$, k, z_0 — real, $-\infty < k < +\infty$, $z_0 > 0$, are found for an arbitrarily selected numerical equivalent of the parameter $k_\pm$, satisfying the condition [2]:

$$1 - \bar{\beta}_{2\pm}^2 \geq 4\bar{\beta}_{2\pm}|k_\pm| \tag{3}$$

in which [2–4]

$$\bar{\beta}_{2\pm} = \zeta_{k_\pm,n}^{(c)}/\left(2\bar{r}_0\right). \tag{4}$$

Afterwards the roots

$$\sigma^2_{1\pm,2\pm} = 0.5\left[\left(1-\bar{\beta}^2_{2\pm}\right) \pm \sqrt{\left(1-\bar{\beta}^2_{2\pm}\right)^2 - 4\times 4\bar{\beta}^2_{2\pm}k^2_{\pm}}\right] \tag{5}$$

of the equation

$$\sigma^4_{\pm} - \left(1-\bar{\beta}^2_{2\pm}\right)\sigma^2_{\pm} + 4\bar{\beta}^2_{2\pm}k^2_{\pm} = 0 \tag{6}$$

are specified [2]. The parameter $k_{\pm}$ is varied, until $\sigma_{1\pm}$ (or $\sigma_{2\pm}$) coincides with the singled out $|\alpha|$ within the framework of the prescribed accuracy. Then, the values of $\sigma_{1\pm}$ and $\sigma_{2\pm}$ obtained, are substituted in the expressions [2]:

$$A_{\pm} = \sigma_{1\pm}/\sigma_{2\pm} \quad \text{or} \quad A_{\pm} = \sigma_{2\pm}/\sigma_{1\pm}, \tag{7}$$

$$B_{\pm} = \sigma_{1\pm}\bar{r}_0 \quad \text{or} \quad B_{\pm} = \sigma_{2\pm}\bar{r}_0, \tag{8}$$

$$C_{\pm} = (\sigma_{1\pm}/\sigma_{2\pm})\,\bar{r}_0 \quad \text{or} \quad C_{\pm} = (\sigma_{2\pm}/\sigma_{1\pm})\,\bar{r}_0, \tag{9}$$

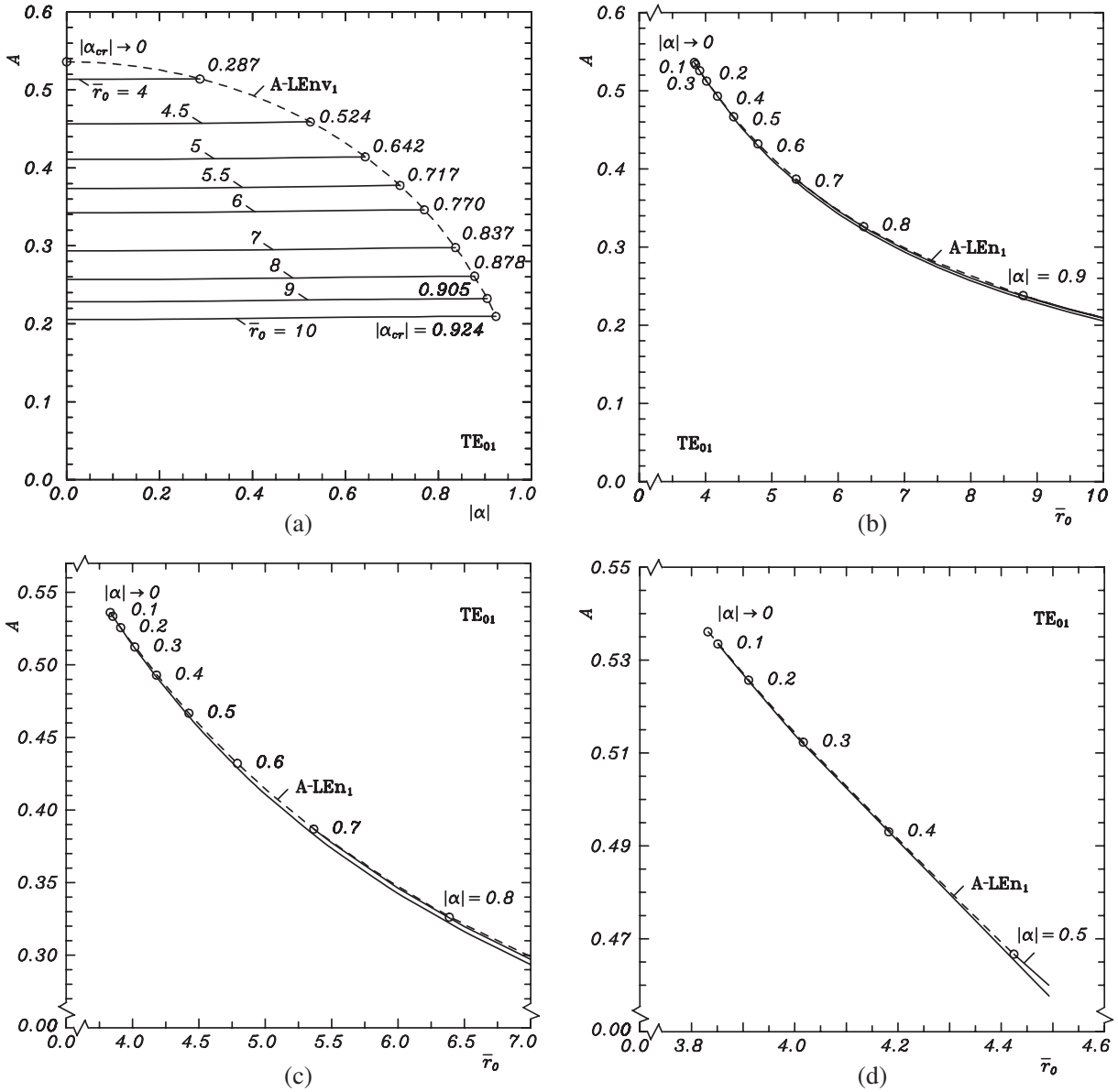

Figure 1: A numbers for normal TE_{01} mode vs.: (a) $|\alpha|$ in the interval $\langle 0 \div 1.0\rangle$ with $\bar{r}_0$ as parameter; (b) $\bar{r}_0$ in the interval $\langle 3.5 \div 10\rangle$ with $|\alpha|$ as parameter; (c) $\bar{r}_0$ in the interval $\langle 3.5 \div 7\rangle$ with $|\alpha|$ as parameter; (d) $\bar{r}_0$ in the interval $\langle 3.8 \div 4.6\rangle$ with $|\alpha|$ as parameter.

resulting in the $A_{\pm}$, $B_{\pm}$ and $C_{\pm}$ numbers. If $\sigma_{1\pm} \equiv |\alpha|$ ($\sigma_{2\pm} \equiv |\alpha|$), the second (first) group of formulae is used. Finally, the quantities of interest are counted from [2]:

$$A = A_- - A_+, \tag{10}$$

$$B = B_- - B_+, \tag{11}$$

$$C = C_- - C_+. \tag{12}$$

(The subscripts "+" and "−" answer to positive and negative sign of k, resp.)

3. BASIC CHARACTERISTICS OF THE A, B, C NUMBERS

Figures 1–3 illustrate the dependence of A, B and C on $|\alpha|$ and $\bar{r}_0$ with solid lines, assuming $n = 1$. In Figs. 1(a), 2(a) and 3(a), (b), $|\alpha|$ is considered as a variable and $\bar{r}_0$ — as a parameter, whereas in all the rest — the opposite holds. The ends (origins) of the curves in the first (second) set of Figures are denoted by circles with abscissas, determined through the formula: $|\alpha_{cr}| = \sqrt{1-(v_{1,n}/\bar{r}_0)^2}$ ($\bar{r}_{0cr} = v_{1,n}/\sqrt{1-|\alpha|^2}$) [3]. $LEnv_1-$ (LEn_1-) dashed envelope lines link them. (The letter, preceding the notation given, indicates the number with which the curves in question are associated.) In each of the sets the values of the components of the pairs $\{|\alpha_{cr}|, \bar{r}_0\}$ or $\{|\alpha|, \bar{r}_{0cr}\}$, describing the relevant circles, are the same for the three numbers. The parameter $\bar{r}_0$ ($|\alpha|$) relates to the whole line, depicting certain number in a Figure from the first (second) group, including its end (starting) point, while the answering to it $|\alpha_{cr}|$ ($\bar{r}_{0cr}$) — to the latter only (cf. Fig. 1(a), resp. Figs. 2(b) and 3(d)). To avoid overcrowding in Figs. 2(a) and 3(a), (b) the numerical equivalents of $\bar{r}_0$ solely, are written at the termination of the curves with which they are connected. For the same reason in Figs. 1(b), (c), (d) and 3(c), the value of relevant parameter $|\alpha|$ is shown at the beginning of lines only, whereas in Figs. 2(b) and 3(d), that of $\bar{r}_{0cr}$ is also presented. All characteristics in Figs. 2(a) and 3(a), (b), have a common initial point at $|\alpha| \to 0$, labeled by $\bar{r}_{0in} = 3.832$. The value of the abscissa $\bar{r}_{0cr} = 3.832$ for $|\alpha| \to 0$ of the origin of the LEn_1 — lines in the second series of Figures (cf. Figs. 2(b) and 3(d)) coincides with the one of $\bar{r}_{0in}$. Obviously, $|\alpha_{cr}|$ ($\bar{r}_{0cr}$) is the largest (smallest) value of the parameter $|\alpha|$ ($\bar{r}_0$) at which the A, B and C numbers exist for certain $\bar{r}_0$ ($|\alpha|$); $\bar{r}_{0in}$ is the smallest value that $\bar{r}_{0cr}$ might attain when $|\alpha| \to 0$. The graphs reveal that the A numbers almost do not alter with $|\alpha|$ and follow approximately the function $1/\bar{r}_0$, the B ones increase practically linearly with $|\alpha|$ and are not affected by the change of $\bar{r}_0$ and the impact of both parameters on the C numbers, is slight.

4. APPLICATION

Equation (2) governs the propagation and Eq. (4) yields the eigenvalue spectrum of the normal TE_{0n} modes with phase constant $\beta_{\pm}$ and radial wavenumber $\beta_{2\pm} = \sqrt{\omega^2\varepsilon_0\mu_0\varepsilon_r\left(1-\alpha_{\pm}^2\right)-\beta_{\pm}^2}$ in

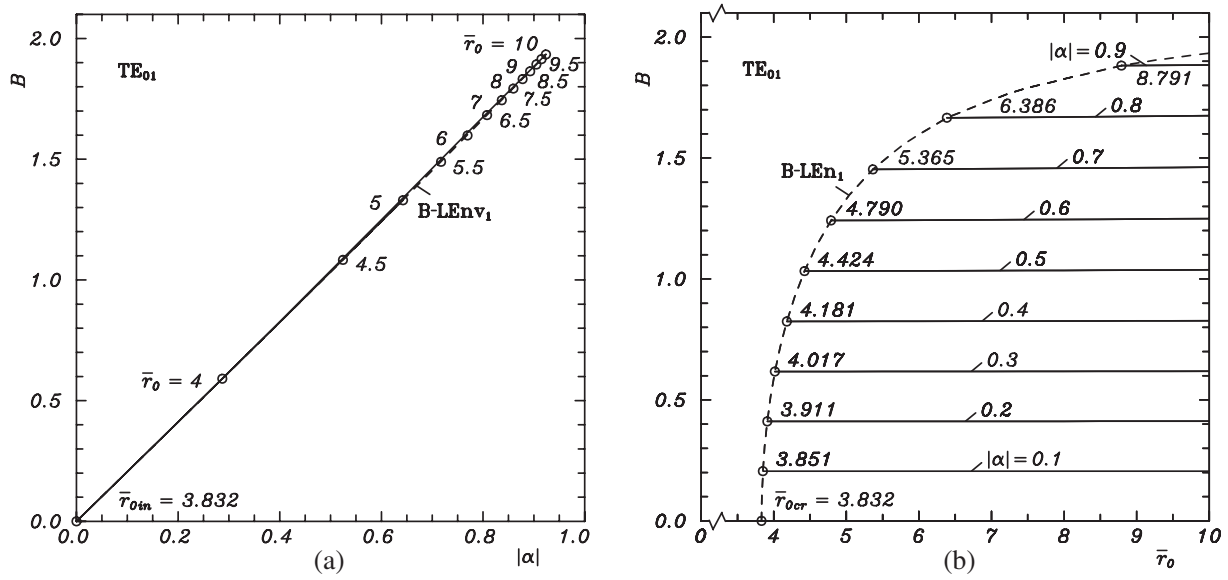

Figure 2: B numbers for normal TE_{01} mode vs.: (a) $|\alpha|$ in the interval $\langle 0 \div 1.0\rangle$ with $\bar{r}_0$ as parameter; (b) $\bar{r}_0$ in the interval $\langle 3.5 \div 10\rangle$ with $|\alpha|$ as parameter.

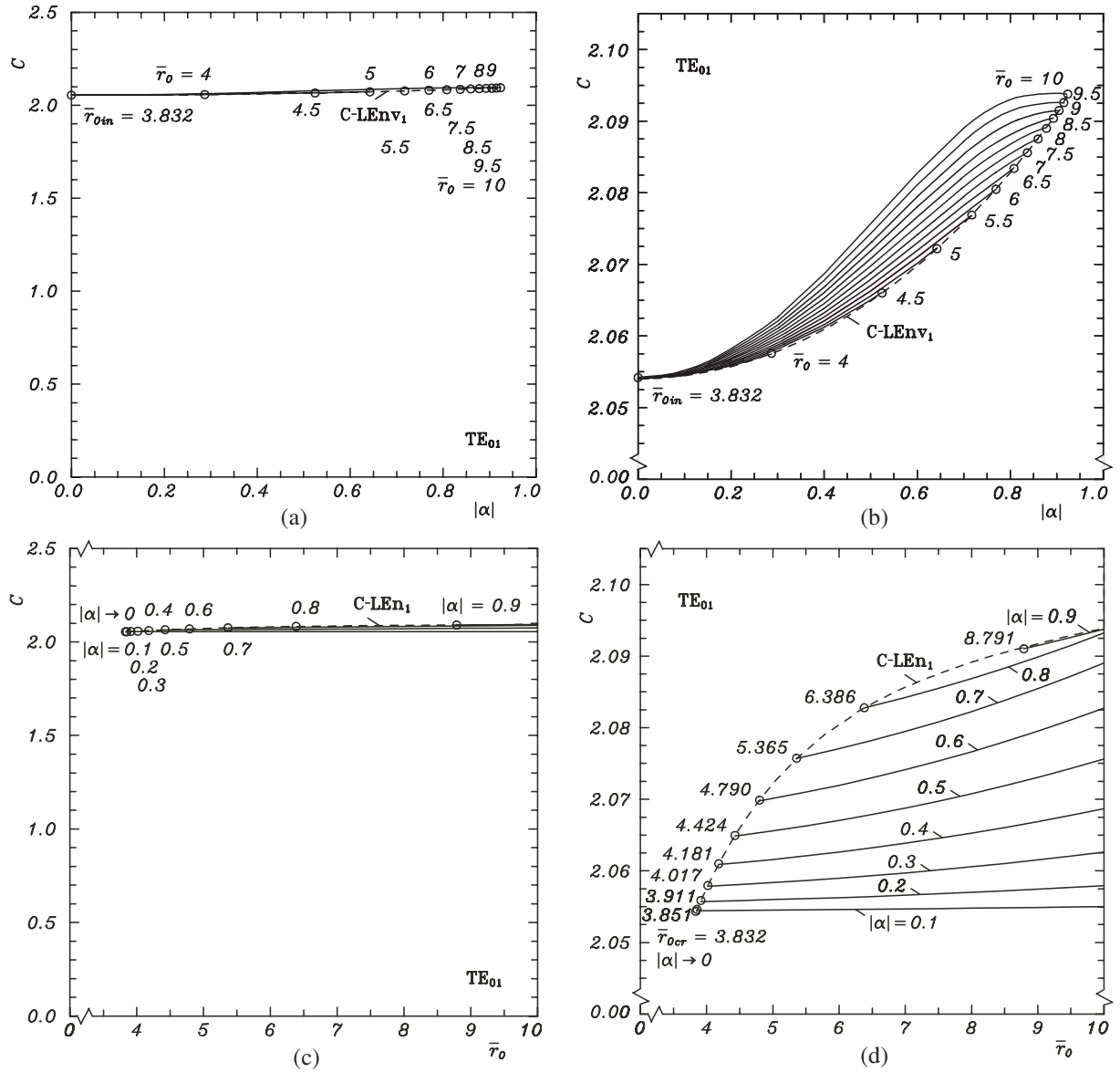

Figure 3: C numbers for normal TE_{01} mode: (a) in the interval $\langle 0 \div 2.5\rangle$ vs. $|\alpha|$ in the interval $\langle 0 \div 1.0\rangle$ with $\bar{r}_0$ as parameter; (b) in the interval $\langle 2.05 \div 2.10\rangle$ vs. $|\alpha|$ in the interval $\langle 0 \div 1.0\rangle$ with $\bar{r}_0$ as parameter; (c) in the interval $\langle 0 \div 2.5\rangle$ vs. $\bar{r}_0$ in the interval $\langle 3.5 \div 10\rangle$ with $|\alpha|$ as parameter; (d) in the interval $\langle 2.05 \div 2.10\rangle$ vs. $\bar{r}_0$ in the interval $\langle 3.5 \div 10\rangle$ with $|\alpha|$ as parameter.

the circular waveguide of radius r_0, entirely filled with azimuthally magnetized ferrite, described by a Polder permeability tensor of off-diagonal element $\alpha = \gamma M_r/\omega$, ($\gamma$ — gyromagnetic ratio, M_r — ferrite remanent magnetization, ω — angular frequency of the wave) and a scalar permittivity $\varepsilon = \varepsilon_0\varepsilon_r$, if it is fulfilled $k_\pm = \alpha_\pm\bar{\beta}_\pm/\left(2\bar{\beta}_{2\pm}\right)$ and $z_0 = 2\bar{\beta}_2\bar{r}_0$ ($\bar{\beta} = \beta/\left(\beta_0\sqrt{\varepsilon_r}\right)$, $\bar{\beta}_2 = \beta_2/\left(\beta_0\sqrt{\varepsilon_r}\right)$, $\bar{r}_0 = \beta_0 r_0\sqrt{\varepsilon_r}$, and $\beta_0 = \omega\sqrt{\varepsilon_0\mu_0}$). Moreover, $\bar{r}_{0cr}$ ($|\alpha_{cr}|$) is the critical value of the normalized (barred) guide radius (of the off-diagonal element) at which the transmission ceases both for positive ($\alpha_+ > 0$, $k_+ > 0$) and negative ($\alpha_- < 0$, $k_- < 0$) magnetization [3]; $\bar{r}_{0in}$ stands for $\bar{r}_{0cr}$ when the load is dielectric ($|\alpha| = 0$) of permittivity ε_r. Thus, the circles (the envelopes), designating the ends (origins) of the A —, B —, C — curves, are relevant to the cutoff state of configuration. They mark the limit of the domain of existence of the numbers from the side of lower frequencies. The sequence of inequalities (1) represents the condition for phase shifter operation of this structure, i.e., it specifies the set of values of parameters $\{|\alpha|, \bar{r}_0\}$ for which it might provide differential phase shift $\Delta\bar{\beta} = \bar{\beta}_- - \bar{\beta}_+$. The latter could be calculated in normalized form by means of the formula [2]:

$$\Delta\bar{\beta} = AB/C. \tag{13}$$

Numerical example: The case $\bar{r}_0 = 4$ and $|\alpha| = 0.1$ is considered. Employing for it the method, worked out in Section 2, yields: $A = 0.513\,613$, $B = 0.205\,445$ and $C = 2.054\,453$. Accordingly, it is obtained: $\Delta\bar{\beta} = 0.051\,361$. Since finding the quantities A, B and C for each set of parameters by the reiterative scheme is difficult, it is suggested to use for this purpose the Figures presented. This allows to get $\Delta\bar{\beta}$ from Eq. (13) for all $\bar{r}_0 \in \langle 3.832 \div 10\rangle$ and $|\alpha| \in \langle 0 \div 1.0\rangle$ in which graphical outcomes for the numbers studied are available. (All results relate to normal TE_{01} mode ($n = 1$).)

5. CONCLUSION

Based on the definitions of the positive real numbers A, B and C in terms of the roots of a certain biquadratic equation, an iterative technique is developed and harnessed to specify their values. The equation mentioned is equivalent to the ones, binding the normalized in a suitable way phase constant $\bar{\beta}$ of the normal TE_{0n} modes in the azimuthally magnetized ferrite-loaded circular waveguide, resp. the magnitude of the off-diagonal ferrite permeability tensor element $|\alpha|$ with the normalized radial wavenumber $\bar{\beta}_2$ (with the eigenvalue spectrum of waves), expressed through the zeros of a definite complex Kummer function and the normalized guide radius $\bar{r}_0$. The analysis of the graphically shown upshots indicates that the A (B) numbers are almost independent of $|\alpha|$ ($\bar{r}_0$) and that the C ones slightly vary when both parameters change. The application of quantities examined in the counting up the differential phase shift, provided by the structure pointed out, is manifested.

ACKNOWLEDGMENT

We express our gratitude to our mother Trifonka Romanova Popnikolova for her self-denial, patience and for the tremendous efforts she exerts to support all our undertakings.

REFERENCES

1. Georgiev, G. N. and M. N. Georgieva-Grosse, "Formulae for differential phase shift computation in an azimuthally magnetized circular ferrite waveguide," *Proc. Millenn. Conf. Antennas Propagat., AP-2000*, 517, in Abstracts, Vol. I-Antennas, 1002, in CDROM, Davos, Switzerland, April 9–14, 2000.
2. Georgieva-Grosse, M. N. and G. N. Georgiev, "The A, B, C numbers and their application in the theory of waveguides," *PIERS Proc.*, 1043–1047, Moscow, Russia, August 18–21, 2009.
3. Georgiev, G. N. and M. N. Georgieva-Grosse, "A new property of the complex Kummer function and its application to waveguide propagation," *IEEE Antennas Wireless Propagat. Lett.*, Vol. 2, 306–309, December 2003.
4. Georgiev, G. N. and M. N. Georgieva-Grosse, "A theorem for the properties of some classes of numbers, connected with the zeros of complex Kummer function and its application in the theory of circular ferrite waveguides with azimuthal magnetization," *Proc. XXIX URSI General Assembly*, D05.4(182), in CDROM, Chicago, IL, USA, August 7–16, 2008.
5. Georgiev, G. N. and M. N. Georgieva-Grosse, "An application of the complex Tricomi function," *Proc. Eleventh Int. Conf. Electromagn. Adv. Applicat., ICEAA'09*, 819–822, in CDROM, Turin, Italy, September 14–18, 2009.
6. Georgiev, G. N. and M. N. Georgieva-Grosse, "Effect of the dielectric filling on the phase behaviour of the circular waveguide with azimuthally magnetized ferrite toroid and dielectric cylinder," *Proc. Asia-Pacific Microwave Conf., APMC-2009*, WE4B-4(1680), in CDROM, Singapore, December 7–10, 2009.
7. Georgieva-Grosse, M. N. and G. N. Georgiev, "Differential phase shift characteristics of normal TE_{0n} modes in an azimuthally magnetized coaxial ferrite waveguide," *Proc. 4th Europ. Conf. Antennas Propagat., EuCAP 2010*, Barcelona, Spain, April 12–16, 2010 (in print).
8. Georgieva-Grosse, M. N. and G. N. Georgiev, "Advanced studies of the differential phase shift in the azimuthally magnetized circular ferrite waveguide," *PIERS Proc.*, Cambridge, MA, USA, July 5–8, 2010 (in print).
9. Georgiev, G. N. and M. N. Georgieva-Grosse, "Analysis of the differential phase shift in the circular ferrite-dielectric waveguide with azimuthal magnetization," *Proc. 2010 IEEE Int. Symp. Antennas Propagat. & CNC-USNC/URSI Radio Science Meeting, AP-S 2010*, Toronto, ON, Canada, July 11–17, 2010 (in print).
10. Tricomi, F. G., *Funzioni Ipergeometriche Confluenti*, Edizioni Cremonese, Rome, Italy, 1954.

Cosmic Deceleration Parameter $q(Z)$ Dependence upon Gravitons? Implications for DM Models, DE, and the Search for Gravitons as Measured via E and M Interactions in Detectors

Andrew Walcott Beckwith
American Institute of Beamed Energy Propulsion, USA

Abstract— In this paper, the author asks if DM and gravitons could also impact the cosmic acceleration of the universe, leading to an increase of acceleration one billion years ago, in a manner usually attributed to DE. Following Alves, et al. (2009) the author will high light what KK style gravitons, with a slightly different mass profile could mean in terms of DM. The consequences are from assuming that axions are CDM, and KK gravitons are for WDM, then up to a point, $\rho_{Warm\text{-}Dark\text{-}Matter}$ would dominate not only structure formation in early universe formation. Further efforts in obtaining data for such suppositions would lie in electro magnetic-graviton interactions contributing toward $h_0^2\Omega_{gw}(f)$ being appropriately measured.

1. INTRODUCTION

When at the 12 Marcell Grossman meeting, July 2009 17th, the author talked with Roszkowski, at the Paris Observatory as to what would happen to DM if hot and cold DM models were mixed together, Dr. Roszkowsk stated there would be no structural changes which would occur in galaxy formation, if two cold DM candidates would be partially mixed. For the sake of investigating Roszkowski's research views, the author decided to investigate the probability of DM as a KK graviton. Next, the author looked to find a different setting for joint DM and DE models. Having settled upon looking at the KK graviton as a dark matter candidate, which could influence different forms of galaxy formation, at or before red shift $Z \sim 1.0$ to 1.5, the author decided to find a higher dimensional setting to re duplicate what Marcio E. S. Alves et al., (2009) accomplished in having a non zero graviton act in promoting a re acceleration of the universe, the author is considering what happens if there is a tiny mass, $m_{graviton} \propto 10^{-65}$ grams, as the first KK mode, in contrast to the zero mass predicted as to the zeroth mode of the KK graviton. I.e., a slight modification of the usual KK graviton mass equation $m_n(Graviton) = \frac{n}{L} + 10^{-65}$ grams, it so happens that this red shift pre dates the $Z \sim 55$ point of inflection with the zeroth mode of the KK graviton, if with a tiny mass, influencing DE type cosmological expansions.

2. HOW DM WOULD BE INFLUENCED BY GRAVITONS, IN 4 DIMENSIONS

This can be conflated with Marcio E. S. Alves, Oswaldo D. Miranda, Jose C. N. de Araujo's results arguing that non zero graviton mass may lead to acceleration of our present universe, in a manner usually conflated with DE, i.e., their graviton mass

$$q = -\frac{\ddot{a}a}{\dot{a}^2} \tag{1}$$

This leads to Eq. (1) having increasingly positive acceleration values as would be definitely be given for masses of $m_{graviton}(4 - Dim\, GR) \sim 10^{-48} \times 10^{-5}\,\text{eV} \sim 10^{65}$ grams for red shift values $z \sim 0.3$ for Eq. (1) just becoming > 0 to maximum values of (1) today, with $z = 0$, all at mass of the order of 10^{-65} grams. This increase of (1) then leads us to consider how to configure the Friedman equations if using and for RS brane world values. As can be related to, if we wish to look at string theory versions of the FRW equation, in FRW metrics, we can do the following decomposition,

$$\left(\frac{\dot{a}}{a}\right)^2 = \frac{\rho_{Total}}{3M_{Planck}^2} - \frac{k}{a^2} + \frac{\Lambda}{3} \tag{2}$$

As well as

$$\left(\frac{\ddot{a}}{a}\right) = -\frac{(\rho_{Total} + 3p_{Total})}{6M_{Planck}^2} + \frac{\Lambda}{3} \tag{3}$$

Not only this, if looking at the brane theory Friedman equations as presented by/for Randall Sundrum theory, it would be prudent working with

$$\dot{a}^2 = \left[\left(\frac{\rho}{3M_4^2} + \frac{\Lambda_4}{3} + \frac{\rho^2}{36M_{Planck}^2}\right)a^2 - \kappa + \frac{C}{a^2}\right] \tag{4}$$

For the purpose of Randall Sundrum brane worlds, Eq. (21) is differentiated with respect to $d/d\tau$, and then terms from Eq. (20) will be used, and put into a derivable equation version of $q = -\frac{\ddot{a}a}{\dot{a}^2}$. Note that Roy Maartens has written as of 2004 that $m_n(Graviton) = \frac{n}{L}$, with $m_0(Graviton) = 0$, and L as the stated 'dimensional value' of higher dimensions. The value $m_0(Graviton) \sim$ '$10^{-65} - 10^{-60}$ gram in value picked is very small, ALMOST zero.

3. CREATING AN ANALYSIS OF HOW GRAVITON MASS, ASSUMING BRANES, CAN INFLUENCE EXPANSION OF THE UNIVERSE

Following presenting of Eq. (1) above with $\hbar = c = 1$, so then when writing

$$q = A1 + A2 + A3 \tag{5}$$

Then, assume that the density has a small graviton mass component added in, as follows:

$$\rho \equiv \rho_0 \cdot \left(\frac{a_0}{a}\right)^3 - \left[\frac{m_g c^6}{8\pi G\hbar^2}\right] \cdot \left(\frac{a^4}{14} + \frac{2a^2}{5} - \frac{1}{2}\right) \tag{6}$$

So, then one can look at $d\rho/d\tau$ obtaining

$$d\rho/d\tau = -\left(\frac{\dot{a}}{a}\right) \cdot \left[3 \cdot \rho_0 \cdot \left(\frac{a_9}{a}\right)^3 + 4 \cdot \left(\frac{a^4}{14} + \frac{a^2}{5}\right) \cdot \left(\frac{m_g c^6}{8\pi G\hbar^2}\right)\right] \tag{7}$$

Here, use, $\left(\frac{\dot{a}}{a}\right) = \sqrt{\frac{C}{a^4} - \frac{\kappa}{a^2} + \left(\frac{\rho}{3M_4^2} + \frac{\Lambda_4}{3} + \frac{1}{36} \cdot \frac{\rho^2}{M_P^6}\right)}$, and assume Eq. (28) covers ρ. Now, if $\hbar \equiv c \equiv 1$ and $d\Lambda_4/d\tau \sim 0$, and, also, we neglect Λ_4 as of being not a major contributor.

With such assumptions put in,

$$\rho \equiv \rho_0 \cdot \left(\frac{a_0}{a}\right)^3 - \left[\frac{m_g}{8\pi G}\right] \cdot \left(\frac{a^4}{14} + \frac{2a^2}{5} - \frac{1}{2}\right), \tag{8}$$

afterward, the following function should be used as a way of collecting terms

$$\Phi(\rho, a, C) = \frac{C}{a^4} + \left(\frac{\rho}{3M_4^2} + \frac{1}{36} \cdot \frac{\rho^2}{M_P^6}\right) \tag{9}$$

For what it is worth, use $1 + z = a_0/a$. Assume also that C is the dark radiation term which in the brane version of the Friedman equation scales as a^{-4} and has no relationship to the speed of light. a_0 is the value of the scale factor in the present era, when red shift $z = 0$, and $a \equiv a(\tau)$ in the past era, the following representation of the density function, in terms of red shift should be acceptable. Furthermore, $q(z)$ has the following forms of de composition

$$\rho(z) \equiv \rho_0 \cdot (1+z)^3 - \left[\frac{m_g}{8\pi G}\right] \cdot \left(\frac{a_0^4}{14 \cdot (1+z)^4} + \frac{2a_0^2}{5 \cdot (1+z)^2} - \frac{1}{2}\right) \tag{10}$$

$$A1(z) \cong \frac{C \cdot (1+z)^3}{a_0^3} \cdot \left[1 \Big/ \sqrt{\Phi(\rho(z), a_0/(1+z), C)}\right] \tag{11}$$

$$A2(z) \cong -\left(\frac{\rho(z)}{3M_4^2} + \frac{1}{36} \cdot \frac{\rho(z)^2}{M_P^6}\right) \Big/ \left[\Phi(\rho(z), a_0/(1+z), C)\right] \tag{12}$$

$$A3(z) \cong \frac{1}{2}\left(\cdot\left[\frac{1}{3M_4^2} + \frac{1}{18} \cdot \frac{\rho(z)\cdot}{M_P^6}\right] \Big/ \left[\Phi(\rho(z), a_0/(1+z), C)\right]^{1/2}\right) \cdot \left[3 \cdot \rho_0 \cdot (1+z)^3 + 4 \cdot \left(\frac{a_0^4 \Big/ (1+z)^4}{14} + \frac{a_0^2 \Big/ (1+z)^2}{5}\right) \cdot \left(\frac{m_g}{8\pi G}\right)\right] \tag{13}$$

$$\Phi\left(\rho(z), a_0/(1+z)\right), C) = \frac{C\cdot(1+z)^4}{a_0^4} + \left(\frac{\rho(z)}{3M_4^2} + \frac{1}{36}\cdot\frac{\rho(z)^2}{M_P^6}\right) \tag{14}$$

So, for $4 < z \leq 0$, i.e., not for the range, say $z \sim 1100$ 380 thousand years after the big bang, it would be possible to model, here

$$q(z) = A1(z) + A2(z) + A3(z) \tag{15}$$

And here are the results! Assume X is red shift, $Z \cdot q(X)$ is De-Celeration. Here we have a graph of De celeration parameter due to small $m_{graviton} \propto 10^{-65}$ grams, with one additional dimension added.

4. UNANSWERED QUESTIONS, AND SUGGESTIONS FOR FUTURE RESEARCH ENDEAVORS

First of all, what can researchers expect if KK gravitons exist, and exist in inter stellar space with axions? Cembranos; Feng; and Strigari (2007) give a partial answer. It is not just the gamma ray spectrum which may be altered. I.e., Boyarsky, Lesgourgues, Ruchayskiy and Viel (2009) have strict Baysian statistical limits as to what sort of warm to cold dark matter mixes are allowed. One of their basic result, which is put here, $\rho_{Baryons}$, $\rho_{Cold\text{-}Dark\text{-}Matter}$, $\rho_{Warm\text{-}Dark\text{-}Matter}$ refer to density profiles, of the respective baryons, CDM, and WDM candidates, whereas, the density fluctuations $\delta_{Baryons}$, $\delta_{Cold\text{-}Dark\text{-}Matter}$, $\delta_{Warm\text{-}Dark\text{-}Matter}$ are with regards to the fluctuations of these density values. So

$$\left(\frac{\delta\rho}{\rho}\right) \equiv \frac{\rho_{Baryons}\delta_{Baryons} + \rho_{Cold\text{-}Dark\text{-}Matter}\delta_{Cold\text{-}Dark\text{-}Matter} + \rho_{Warm\text{-}Dark\text{-}Matter}\delta_{Warm\text{-}Dark\text{-}Matter}}{\rho_{Baryons} + \rho_{Cold\text{-}Dark\text{-}Matter} + \rho_{Warm\text{-}Dark\text{-}Matter}} \tag{16}$$

If axions are CDM, and KK gravitons are for WDM, then up to a point, $\rho_{Warm\text{-}Dark\text{-}Matter}$ would dominate Eq. (40) in earlier times, i.e., up to $Z \sim 1000$. However, Boyarsky, et al. (2009) also stress that as of the recent era, i.e., probably for $Z \sim 0.55$ to $Z \sim 0$ today, they would expect to see the following limiting behavior

$$\begin{aligned} &\delta_{Baryons} \equiv \delta_{CDM}, \\ &\delta_{WDM} \ll \delta_{CDM} \end{aligned} \tag{17}$$

In earlier times, what is put in, with regards to Eq. (17) would be probably far different. However, up in the present era, the denominator of Eq. (16) would be dominated by KK DM, whereas there would be rough equality in the contributions $\rho_{Cold\text{-}Dark\text{-}Matter}\delta_{Cold\text{-}Dark\text{-}Matter}$, $\rho_{Warm\text{-}Dark\text{-}Matter}\delta_{Warm\text{-}Dark\text{-}Matter}$, with the baryon contribution to the numerator being ignorable, due to how small baryon values would be for $Z \sim 0.55$ to $Z \sim 0$ today. Somehow, contributions as to Eq. (40) should be compared with.

$$\left(\frac{\delta\rho}{\rho}\right)_{Horizon} \cong \frac{k^{3/2}\left|\delta_k\right|}{\sqrt{2}\pi} \propto \frac{k^{(3/2)+3\alpha-3/2}}{\sqrt{2}\pi} \approx \left(1/\sqrt{2}\pi\right)\cdot k^{3\alpha} \tag{18}$$

where $-0.1 < \alpha < 0.2$, and $\alpha \equiv 0 \Leftrightarrow n_s \equiv 1$ and to first order, $k \cong Ha$. The values, typically of $n_s \neq 1$. If working with $H^2 = \left(\frac{\dot{a}}{a}\right)^2 = \left[\left(\frac{\rho}{3M_4^2} + \frac{\rho^2}{36M_{Planck}^2}\right) + \frac{C}{a^4}\right]$, and with a density value $\rho \equiv \rho_0 \cdot \left(\frac{a_0}{a}\right)^3 - \left[\frac{m_g c^6}{8\pi G\hbar^2}\right]\cdot\left(\frac{a^4}{14} + \frac{2a^2}{5} - \frac{1}{2}\right)$ where $m_g \approx 10^{-65}$ grams, and $\alpha < 0.2$ is usually picked to avoid over production of black holes, a complex picture emerges. Furthermore, $\alpha < 0.2$ and $\alpha \neq 0$. The following limits as of Eq. (18) in early and later times should be reconciled with.

$$\left(\frac{\delta\rho}{\rho}\right)_{Horizon} \cong \left(1/\sqrt{2}\pi\right)\cdot k^{3\alpha} \sim \frac{H^2}{\dot{\phi}} \propto 10^{-4} - 10^{-5} \tag{19}$$

The above equation gives inter relationships between the time evolution of a pop up inflaton field ϕ, and a Hubble expansion parameter H, and a wave length parameter $\lambda = (2\pi/k)\cdot a\,(t)$ for a mode given as δ_k. What should be considered is the inter relation ship of Eq. (19) and $\lambda \leq H^{-1}$ in order to explain deviations of galaxy formation from the standard 'tree model' of $Z \sim 2$ to today in increasing complexity of structure.

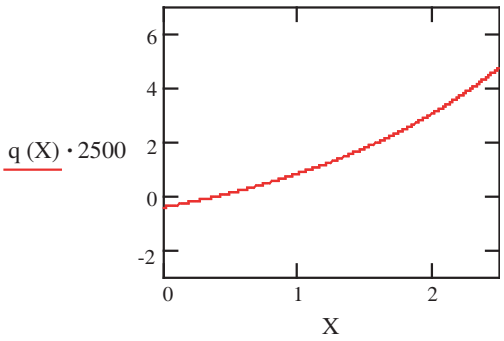

Figure 1: Re duplication of basic results of Alves, et al. (2009), using their parameter values, with an additional term of C for 'Dark flow' added, corresponding to one KK additional dimensions. Figure 1 suggest that additional dimensions are permissible. It does not mean that the initial states of GW/ initial vaccum states have to form due to either quantum or semi classical processes.

5. CONCLUSION

It is useful to note that normalized energy density of gravitational waves, as given by Michele Maggiore (2008)

$$\Omega_{gw} \equiv \frac{\rho_{gw}}{\rho_c} \equiv \int_{f=0}^{f=\infty} d(\log f) \cdot \Omega_{gw}(f) \Rightarrow h_0^2 \Omega_{gw}(f) \cong 3.6 \cdot \left[\frac{n_f}{10^{37}}\right] \cdot \left(\frac{f}{1\,\mathrm{kHz}}\right)^4 \tag{20}$$

where n_f is a frequency based count of gravitons per unit cell of phase space. In terms of early universe nucleation, the choice of n_f may or may not depend upon semi classical representations of the graviton. What is to be brought up in consideration would be if there is a slight mass to the graviton, as given by $m_{graviton} \sim 10^{-65}$ grams, $m_{photon} \sim 10^{-51}$ grams, leading to a new numerical count per phase space to consider

$$n_f \propto n_f\,[graviton] + n_f\,[photon] \tag{21}$$

And also a weighted average of photon-graviton coupled frequency $\langle f \rangle$, so that

$$h_0^2 \Omega_{gw}(f) \cong \frac{3.6}{2} \cdot \left[\frac{n_f\,[graviton] + n_f\,[photon]}{10^{37}}\right] \cdot \left(\frac{\langle f \rangle}{1\,\mathrm{kHz}}\right)^4 \tag{22}$$

The author believes that finding proper values of n_f in experiment will go a long way toward proving Eqs. (21) and (22) above. The slight difference from zero for spin two gravitons, if due to semi classical processes may not only give proof of Eqs. (20) and (22) above, but may give foundational clues as to how gravitons formed in the first place, and the relative stability of their states as they move toward the conditions reflected in Figure 2 above. In future work, the author intends to present an inatanton-anti instanton model for gravitons, and their relative stability which the author believes will be important not only in confirming predictions given in Figure 2, and Eq. (22) but which will be important to the question of if a graviton can actually carry information. The instanton — anti instanton coupling for gravitons would have to fit in with appropriate space time metrics, as outlined by Belunski, and Verdaguer (2001), and may confirm t'Hoofts (2006) treatment of quantum mechanics as being part of a larger theoretical construction.

REFERENCES

1. Allen, B., E. E. Flanagan, and M. A. Papa, "Is the squeezing of relic gravitational waves produced by inflation detectable?," *Phys. Rev. D*, Vol. 6102, No. 2, 2000. http://arxiv.org/PS_cache/gr-qc/pdf/9906/9906054v2.pdf.
2. Alves, M. E. S., O. D. Miranda, and J. C. N. de Araujo, "Can massive gravitons be an alternative to dark energy?," arXiv:0907.5190, July 2009.
3. Belunski, V. and E. Verdaguer, *Gravitational Solitons*, in series: Cambridge Monographs on Mathematical physics, Cambridge, UK, 2001.

4. Bischoff-Kim, M., H. Montgomery, and D. E. Winget, "Strong limits on the DFSZ axion mass with G117-B15A," *The Astrophysical Journal*, Vol. 675, No. 2, 2008.
5. Jedamzik, K., M. Lemoine, and G. Moultaka, "Gravitino, axino, and Kaluza-Klein graviton warm and mixed dark matter and reionization," *Journal of Cosmology and Astroparticle Physics*, No. 07, 010, 2006. http://arxiv.org/abs/astro-ph/0508141.
6. Kahniashvili, T., "Relic gravitational waves as a test of the early universe," arXiv:0705.1733 [astro-ph], 2007.
7. Lehners, J.-L. and P. J. Steinhardt, "Non-gaussian density fluctuations from entropically generated curvature perturbations in Ekpyrotic models," *Phys. Rev. D*, Vol. 79, No. 12, 2009. http://arxiv.org/abs/0712.3779.
8. Maggiore, M., *Gravitational Waves, Volume 1: Theory and Experiment*, Oxford University Press, Oxford, UK, 2008.
9. Maartens, R., "Brane-world gravity," 2004. http://www.livingreviews.org/lrr-2004-7.
10. Roszkowski, L., "Discussions with A. Beckwith at 12 Marcel Grossman meeting," in Paris Observatory, during the Dark Matter Section of the Conference, in Parallel Section Run by Dr. Chardin, July 17, 2009.
11. t'Hooft, G., "The mathematical basis for Deterministic Quantum Mechanics," 2006. http://arxiv.org/PS_cache/quant-ph/pdf/0604/0604008v2.pdf.

Underground Diseases Identification of Airport Runway Using GPR

Xuejing Song, **Renbiao Wu**, **and Jiaxue Liu**
Tianjin Key Laboratory of Advanced Signal Processing, Civil Aviation University of China, China

Abstract— The identification method of airport runway diseases using GPR presented in this paper has two steps. First, Hough transform is introduced to classify the two kinds of GPR B-scan images. In this method, the crack images are focused on one point after being transformed to parametric space. The hyperbolic equation with a time-delay factor is introduced in void images, in order to locate the position of the hyperbolic vertex accurately. Then a curve fitting method is used to identify the void type. The simulation results demonstrate that the method has advantages of small calculation quantity, fast-speed and high-accuracy. It is good at real-time predicting tracking.

1. INTRODUCTION

Cracks and voids are the most common diseases in airport runway. By far the widely used target detection methods relying on manual intervention are divided into two kinds: One is on-site detection, that is, the operator taking the data directly at the scene to make judgments based on experience; the other is off-line detection, that is based on the results of imaging to determine whether there is objective. Clearly, both of these methods have a fatal disadvantage — the dependence on human subjective experience, which has led to the instability of the detection result and low efficiency, especially when dealing with massive amount of data. Therefore, the domestic and foreign scholars have done a lot of research in the GPR [1, 2] automatic target detection and put forward a variety of methodssignal energy-based detection method [3] for its small amount of calculation is used to on-site rough target detection; detection methods based on image pattern [4], such as, ANN, fuzzy clustering and other pattern recognition methods, which require a lot of samples to be training before they can attain better detection quality; the automatic detection method depended on imaging results, which is not only limited by the image quality, but also has very large amount of calculation.

The identification method of airport runway diseases using GPR presented in this paper has two steps. First, Hough transform is introduced to classify the two kinds of GPR B-scan images. Then a curve fitting method is used to identify the void type. The simulation results demonstrate that the method has advantages of small calculation quantity, fast-speed and high-accuracy. It is good at real-time predicting tracking.

2. CHARACTERISTICS OF THE DISEASE ECHO

In the airport runway, the dielectric constants are different supposed to surface layer, base layer, air void, water void and crack. As the electromagnetic wave would generate reflected wave in different media interface, so the A-scan data and B-scan data recorded by GPR are directly used for diseases identification.

2.1. A-Scan Characteristic

It requires a certain degree of permeability between the base layer and the sub-base under concrete slab. When the base layer has bad quality of permeability, the water will be accumulated between concrete slab and base layer, where gradually developed to water void. Sometimes, the quality of permeability is good, but the grain size ratio is inappropriate, so the fine particles will be taken away by infiltrative rain water, forming air void. Where there is a void, the reflection coefficient at the interface is as follows:

$$R_{db} = (\sqrt{\varepsilon_d} - \sqrt{\varepsilon_b})/(\sqrt{\varepsilon_d} + \sqrt{\varepsilon_b}) \tag{1}$$

in which ε_d presents the dielectric constant of rigid surface layer, and ε_b presents the dielectric constant of void. The dielectric constant of ordinary cement concrete is 6 to 12, and the dielectric constants of pure water and air are 80 and 1. According to Equation (1), we can learn that the reflection coefficient is negative when water void occurs, otherwise when air void exists, the reflection coefficient is positive.

2.2. B-Scan Characteristic

When a point scatterer appears under the ground, due to the impact of transmitting and receiving antenna beam width, its reflected waveform in the B-scan pattern shows hyperbolic structure.

Assuming the wave velocity in uniform medium is v, and the distance between the transmitting antenna and receiving antenna is small enough to be approximated as single-base case. As is shown in Fig. 1(a), a point scatterer is located in (x_0, z_0), and the coordinate of the antenna is $(x, 0)$, so the distance between the antenna and target is $\sqrt{(x-x_0)^2+z_0^2}$. From the data $A(x,t)$ recorded in Fig. 1(b) we could read the reflection time of the point scatterer in each A-scan is $t = 2\sqrt{x^2+z_0^2}/v$. In B-scan image, the relationship between the delay time of target echo and the horizontal position of the antenna is as follows:

$$t^2/t_0^2 - 4(x-x_0)^2/(vt_0)^2 = 1 \tag{2}$$

in which $t_0 = 2z_0/v$.

After discretization, $t_j = jdt$, $x_i = idx$, $x_0 = i_0dx$, $t_0 = j_0dt$, $t_j = jdt$, $x_i = idx$, $x_0 = i_0dx$, $t_0 = j_0dt$.

Equation (2) turns to:

$$j^2/j_0^2 - 4(i-i_0)^2(dx)^2/(j_0vdt)^2 = 1 \tag{3}$$

in which (i_0, j_0) presents the coordinate of the hyperbola apex. We could calculate the accurate position of the target with the help of hyperbola apex coordinate and the echo velocity.

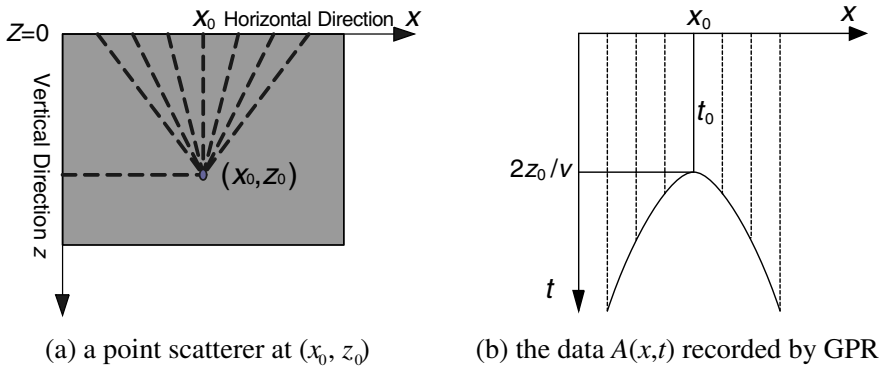

Figure 1: Scattering model of point target.

3. DISEASES IDENTIFICATION ALGORITHM

3.1. Pre-Processing

In the beginning of disease identification, the clutter should be suppressed in original B-scan images. As the airport runway is layered structure which contain the surface layer and base layer, so the surface echo and layer interface are main clutter echo components. Either surface echo or layer interface echo in B-scan images is distributed at some lines nearby, so the mean method is used to suppress background clutter.

Most background clutter could be removed after mean filtering. But there are still some clutter and noise, and the connectivity of disease part has also been influenced. Hence, morphological filtering is used to eliminate noise and clutter, and the target connectivity in original image is restored.

3.2. Diseases Classification

The reflected wave group in B-scan will leap (presenting as linear) when there are cracks in the runway. From the characteristics of GPR two-dimensional echo, the clear hyperbolic structure is existed in B-scan images due to the differ of dielectric constant between the void and surrounding. Based on the characteristics of two diseases in B-scan images, Hough transform is used to classify diseases. Flow chart is shown in Fig. 2.

Hough transform is an effective way of detection, location and analytical curve. It is not sensitive to random noise and some covering, and has strong anti-interference capability. The basic principle of Hough transform is mapping a given curve in original image space into a parameter space point

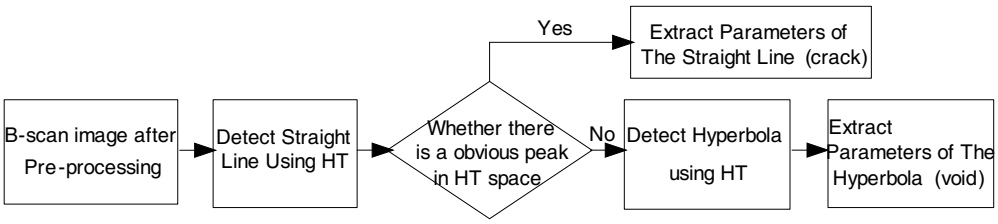

Figure 2: The diseases classification flow chart.

by using duality property between the point and line. This puts given curve identification problem in original image into peak detection problem in parameter space. Algorithm is shown as follows:

(1) Initialize an array of transform domain space;
(2) Searching all non-zero pixel point in images Sequentially. For each non-zero pixel point, the corresponding point in the transform domain plus 1;
(3) Finding the maximum point in the transform domain and recording it. The location coordinate of maximum point is the curve parameters in original image.

Building model for cracks in B-scan images, the equation of straight line is as follows:

$$Ax + By + C = 0, \quad (A^2 + B^2 \neq 0) \tag{4}$$

Polar equation of straight line as follows:

$$\rho = x\cos\theta + y\sin\theta \tag{5}$$

The line detection process of Hough Transform is to transform the image from (x, y) space to space (ρ, θ). A straight line in rectangular coordinate system corresponds to a point in polar coordinate system.

Modeling for hyperbola in void image with the equation given by Equation (2), which is used to extract hyperbola in most identification methods [5]. But the antenna is not close to the ground in actual detection process, so a starting time variable is introduced in this equation. The relationship between the time-delay and antenna horizontal position as follows:

$$(t - t')^2/t_0^2 - 4(x - x_0)^2/(vt_0)^2 = 1 \tag{6}$$

The equation after discretization is:

$$(j - d)^2/j_0^2 - 4(i - i_0)^2(dx)^2/(j_0 vdt)^2 = 1 \tag{7}$$

Here the image space (i, j) is known, and the parameter space is three-dimensional space (i_0, j_0, d), in which (i_0, j_0) is the hyperbolic apex coordinate. Hough transform obtains the hyperbolic parameters by detecting the peak through mapping space (i, j) to space (i_0, j_0, d), then obtains the void position.

3.3. Void Identification

Hough transform can accurately confirm the void apex in B-scan image, but it couldn't recognize the void type. In order to identify the void type, a section of A-scan signal is intercepted by extracting typical Road echo data in void B-scan image. The signals are shown in Fig. 3.

As known from the one-dimensional GPR echo signal analysis in Section 2.1, the reflection coefficient is negative in water void, while reflection coefficient is positive in air void is positive. As shown in Fig. 3, water void signal and air void signal have opposite phases. The former has a negative peak, while the later is positive.

In this paper, the maximum peak of absolute value in intercepted signal is searched. With this peak point as the center, the data in neighborhood area is selected and is fitted by least square method. Then the void type is determined by the sign of fitted quadratic coefficient. As the wave peak is relatively sharp, so the absolute value of quadratic coefficient is considered to be authentic when it exceeds a certain threshold.

4. SIMULATION RESULT

4.1. Classification Result of the Diseases

After pre-processing, the Hough transform for line detection is introduced in B-scan images. The images after Hough transform are as in Fig. 4.

From the Hough transformed images we can draw a conclusion: the crack image is focused on one point after being transformed to parametric space, while there is no obvious peak in the transformed image of void.

According to the focused crack image, we can obtain the coordinates of the peak point, so as to extract the crack, as shown in Fig. 5(b). Since the void image can't focused in the parametric space of straight line, then it is transformed to the hyperbolic parametric space defined by Equation (7). If there is a hyperbola in initial B-scan image, there is an obvious peak point in the hyperbolic parameter space. From the coordinates of the peak point (i_0, j_0, d), we could get the hyperbola apex (i_0, j_0). The dot in Fig. 5(d) shows the hyperbola apex detected using Generalized Hough transformation.

4.2. Void Type Recognition

In simulation, the dielectric constants of concrete, base layer, water void and air void are 10, 15, 22 and 1.2. Ricker pulse is transmitted by GPR with the center frequency of 900 MHz. Those data in Table 1 are all intercepted at echoes of interface where voids exist.

Analyze the curve shape in Fig. 3, the echo reflected at the interface between concrete and water void could be fitted to a quadratic curve with positive quadratic coefficient. In contrary, the echo

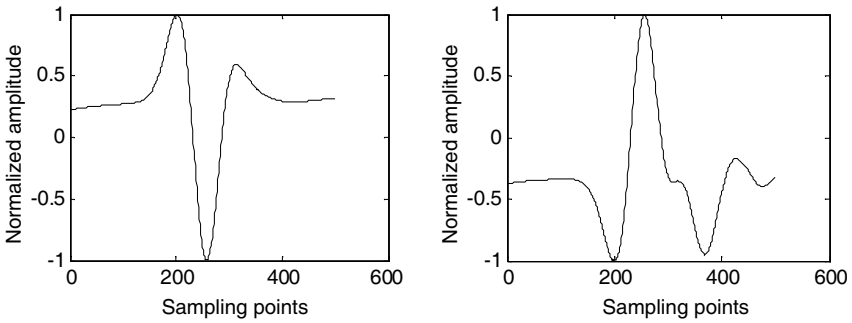

Figure 3: (a) A section of A-scan signal with water void. (b) A section of A-scan signal with air void.

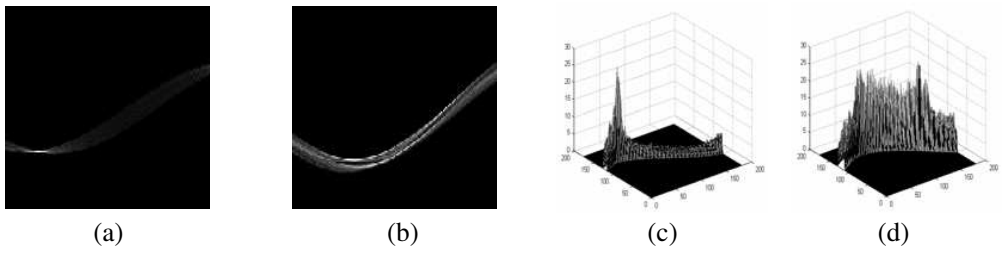

Figure 4: (a) Crack image after HT (2-D view). (b) Void image after HT (2-D view). (c) Crack image after HT (3-D view). (d) Void image after HT (3-D view).

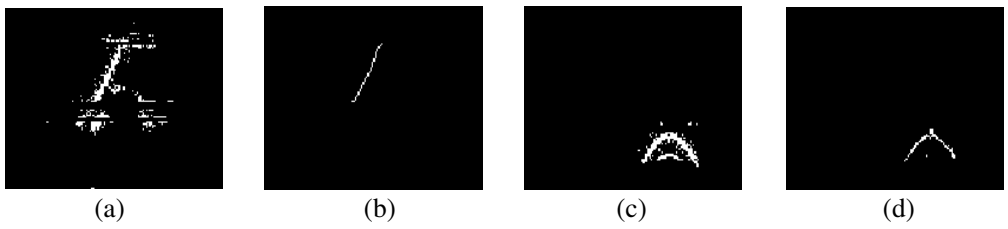

Figure 5: (a) Binary image with crack after pre-processing. (b) Crack extracted by HT. (c) Binary image with void after pre-processing. (d) Apex locating using generalized Generalized Hough transform.

Table 1: Void type recognition.

Group of A-scan	Quadratic Coefficient Fitting Results	Recognition Results	Real Type
1	21.5502	Water void	Water void
2	19.3954	Water void	Water void
3	−22.9984	Air void	Air void
4	23.4832	Water void	Water void
5	−18.7237	Air void	Air void
6	−19.3351	Air void	Air void
7	20.5202	Water void	Water void
8	23.3275	Water void	Water void
9	−21.5502	Air void	Air void
10	−21.0425	Air void	Air void

reflected at the interface between concrete and air void could be fitted to a quadratic curve with negative quadratic coefficient The experimental results showed in Table 1 are basically consistent with the theoretical analysis. Analysis of statistical results, the absolute values of those fitting quadratic coefficients are in the range of 15 to 40. The fitting quadratic coefficient intercepted from the echo of good runway section is 9.5955. In this paper we set 15 as the threshold. When the absolute value of fitted quadratic coefficient goes up to the threshold, there could be void, the type of which depending on positive or negative of the coefficient. The simulation results demonstrate that the method has advantages of small calculation quantity and reliable recognition results.

5. CONCLUSIONS

This paper analyzes the characteristics of GPR echo in airport runway, and based on this, puts forward a disease identification algorithm aiming to classify the most common diseases crack and void in the airport runway. The simulation results demonstrate that this algorithm can classify the two kinds of disease accurately.

REFERENCES

1. Zhao, J., "Introduction of non-destructive testing technology and its development prospects in road works," *Shanghai Road*, No. 1, 57–60, 2004.
2. Han, X., S. Chen, L. Zhong, and Q. Wang, "Review for void detective methods of the concrete pavement," *Journal of Chongqing Jiaotong University*, Vol. 25, No. 4, 73–76, 2006.
3. Xu, X. and E.. L. Miller, "Statistical method to detect subsurface objects using array ground penetrating radar data," *IEEE Trans. on Geosciences and Remote Sensing*, Vol. 40, No. 4, 963–975, 2002.
4. Gamba, P. and S. Lossani, "Neural detection of pipe signatures in ground penetrating radar data," *IEEE Trans. on Geoscience and Remote Sensing*, Vol. 38, No. 2, 790–797, 2000.
5. Chen, D., C. Huang, and Y. Su, "An integrated method of statisticai method and hough transform for GPR targets detection and location," *Acta Electronica Sinca*, Vol. 32, No. 9, 1468–1471, 2004.
6. Riando, L., "Using GPR to monitor cracks in a historical building," *Proceeding of the 4th International Workshop on Advanced Ground Penetrating Radar*, 45–48, Jun. 27–29, 2007.
7. Wang, Z. W. and G. Slabaugh, "Partial differential equation-based GPR signature discrimination for automatic detection of bridge deck delamination," *IEEE International Conference on Automation Science and Engineering*, 431–435, Aug. 23–26, 2008.
8. Zhou, W., G. Wang, and X. Chen, "Classification of ground penetrating radar echo signals using wavelet packet and RBF," *IEEE Conference on Radar*, 432–436, Apr. 24–27, 2006.

Satellite Thermal Monitoring of Arctic Ice Front in Relation to Dynamics of a Polar Orbital Ocean Circulation

Shigehisa Nakamura
Kyoto University, Japan

Abstract— This work concerns an ice front evolution in the Arctic Sea referring to the satellite thermal monitoring. The satellite thermal pattern of the sea surface in a global scale have been introduced by this time. The author introduces his note to a hydrodynamic understanding of the ice front evolution in the interested sea area. The ice front evolution for the time period between 1980 and 2008 is too short to find what process of the ice front is an effect of global climate change. A theoretical analysis of equations of motion for the sea water around the ice front is introduced in order to realize what dynamical process may support the ice front evolution.

1. INTRODUCTION

There have been introduced many global chart of the sea surface thermal patterns after processing the existing satellite thermal data by this time. The author introduces a dynamical model for a model case of the ice front evolution. A special reference is taken for the ice front in the Arctic Sea. In order to evaluate a satellite monitoring of the ice front in the Arctic Sea, a ocean water intrusion from the Bering Sea to the Arctic Sea through the Bering Strait is studied on the basis of fluid dynamics. Then, it is noticed that a solution suggests that a meridional orbital ocean circulation as a geophysical fluid dynamics supports the trend of the ice front evolution in the Arctic Sea. For the author's convenience, the September ice front evolution in the period of 1980 to 2008 is noted for a special reference in this work. In order to realize the process of the September ice front evolution, it should be in need to have a data set of the satellite thermal monitoring for a long time, for example, more than several hundred years in the interested sea area.

2. ICE FRONT EVOLUTION

First, an illustration of the ice front evolution in the Arctic Sea is introduced referring to the satellite data. For example, Perovich and Richter-Menge [1] introduced the ice front evolution during 1997 to 2008 for the season of September.

The Arctic Sea is covered by a sea ice sheet in the cold season, for example, in December, January and February. So that, the author considers it better to concentrate his interest in a September ice front evolution in the Arctic Sea. The September ice front evolution in the Arctic Sea can be found by a mapping of the ice front location in a several years interval monitoring (for example, in 1980, in 2005 and in 2007 [1]) as shown in Figure 1. This makes us easy to see what process is found in the September ice evolution.

Nevertheless, this time interval of 17 years is too short to see the global trend of the September ice front in the Arctic Sea. The author has to notice here the global processes on the earth should be considered in a time scale of more than several thousand years for a problem on climate change of the earth.

Looking at Figure 1, it is easily seen that the specific patterns in the September ice front evolution is the sea water intrusion from the Bering Sea into the Arctic Sea through the Bering Strait. This is clearly found in the polar zone where the satellites have had monitored on the earth surface.

3. FORMULATION OF INERTIA MOTION

The equation of motion for the ocean water on the rotating earth is described in a form as shown in a following form, i.e.,

$$(\partial v_r/\partial t) - f' v_\lambda - \left(v_\lambda^2 + v_\phi^2\right)/r = -g - (1/\rho)(\partial p/\partial r), \tag{1}$$

$$(\partial v_\lambda/\partial t) - f' v_\phi - f' v_r + (v_\lambda v_r) - [(v_\lambda v_\phi)/r]\tan\phi = -(1/\rho)(1/r\cos\phi)(\partial p/\partial\lambda), \tag{2}$$

$$(\partial v_\phi/\partial t) + f v_\lambda + (v_\phi v_r)/r + (v_\lambda^2)\tan\phi = -(1/\rho)(1/r)(\partial p/\partial\phi) \tag{3}$$

where, the origin of the co-ordinate is at the center of the earth, the notations (r, λ, ϕ) are for the radial axis, the longitudinal axis and latitudinal axis, and the notations of v and p are for

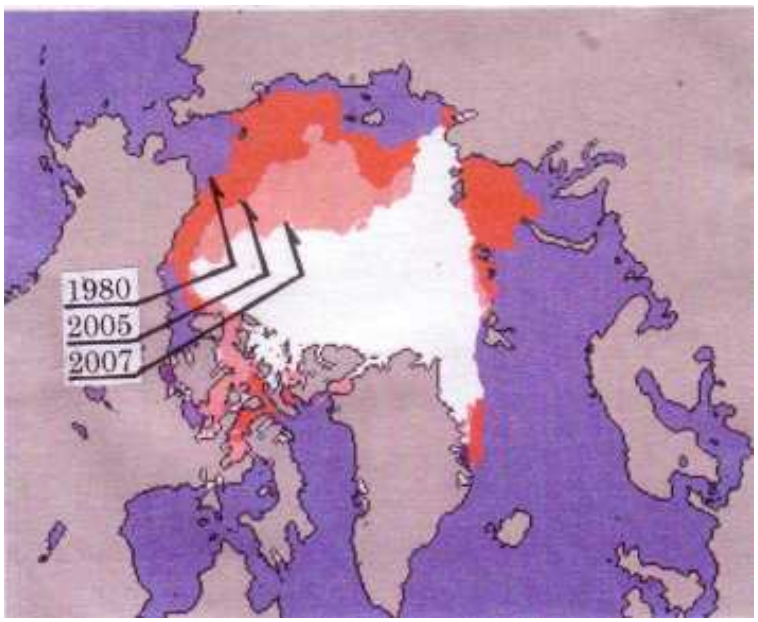

Figure 1: Arctic September ice front for 1980, 2005 and 2007 (cf. Perovich and Richter-Menge, 2009).

velocity and pressure respectively. Each of the subscriptions (r, λ, ϕ) denotes the axis component respectively. The notation r in this case is the radius r of the earth. The density of the sea water is denoted by ρ. The effects of the earth's rotation are expressed by $f = 2\omega \sin\phi$ and $f' = 2\omega \cos\phi$ with the notation ω for the earth's angular velocity of rotation.

When a case of no pressure gradient on the sea surface is seen, the term of $(\partial p/\partial\lambda)$ in (2) and the term $(\partial p/\partial\phi)$ in (3) are vanish and to be zero value respectively, and the formulation can be described more simple form [2, 3].

With consideration of no pressure gradient in the equation of motion, the following form can be reduced to describe as

$$v_r(\partial v_r/\partial t) + v_\lambda(\partial v_\lambda/\partial t) + v_\phi(\partial v_\phi/\partial t) = -\left[g + (1/\rho)(\partial p/\partial r)\right] v_r \tag{4}$$

In a case of horizontal water motion ($v_r = 0$), the above equation can be expressed in an integrated form, i.e.,

$$(1/2)\left[v_\lambda^2 + v_\phi^2\right] = \text{constant} = (1/2)v_i^2 \tag{5}$$

This tells us that the kinetic energy is conservative. In this case, absolute angular momentum is also conservative, so that,

$$r\cos\phi\,(v_\lambda + r\omega\cos\phi) = M. \tag{6}$$

The path of the sea water motion can be obtained from (5) and (6).

When an angle θ_t between the orbit and the x axis (a zonal axis in a cartesian co-ordinate on the sea surface) is defined, then, we have

$$v_\lambda = v_i\cos\theta_t. \tag{7}$$

Substituting the above (7) into (6), then, it can be reduced the following formulation for the earth's radius a, i.e.,

$$av_i\cos\phi\cos\theta_t + a^2\omega\cos^2\phi = M. \tag{8}$$

This expression shows the relation between ϕ and θ_t, and the orbital pattern of the water motion can be obtained. In 1950, Yoshikazu Sasaki had solved for several orbital motions as solutions in his work "On the trajectory of the inertia motion of a parcel of air" [3].

4. MERIDIONAL ORBITAL INERTIA MOTION

One of the solutions obtained by Sasaki (1950) can be the meridional orbital inertia motion which show that a air or water particle takes a meridional path to trace from the Pacific to the Atlantic through Bering Sea and Arctic Sea.

Introducing several parameters, an approximated solution can be obtained to demonstrate several patterns can be possible motion of the interested sea waters under some specific condition. Some bold illustration gives us that one of the several solutions may be actively supporting what process found around the Arctic September ice front evolution (cf. Figure 1). This process may be a scale of longer time than the global climate changing process, because the sea water inertia motion can not be easily changed or affected to induce a variation like an atmospheric inertia motion.

The path as one of the solutions supports the satellite thermal monitoring of the Arctic September ice front evolution in pattern.

A more detailed study should be promoted for clarifying what this polar orbital water motion though it is clearly expected that there is a meridional or polar orbital inertial motion link to the global ocean circulation.

This inertia motion could be accelerated or degenerated by the dynamical effects of the winds on the sea surface of the interested oceans.

5. CONCLUSIONS

In this work, an Arctic September ice front is introduced first as a result of the satellite thermal monitoring of the ice front evolution. Then, a simplified linearized model is introduced for the purpose of seeing what factor is essential as a driving trigger of the ice front evolution. The author takes it possible that a solution of the model is supporting a meridional or polar orbital inertia motion of the sea water could be a part of the actual sea water motion in the Arctic Sea as the interested sea area. This motion suggests that the sea waters of the Pacific and the Atlantic are linked through the Bering Sea and the Arctic Sea.

It is expected a more advanced research for this inertia motion in relation to the global climate changes as the following step in the new age.

REFERENCES

1. Perovich, D. K. and J. A. Richter-Menge, "Loss of sea ice in the Arctic," *Annual Review of Marine Science*, Vol. 1, No. 1, 417–441, 2009.
2. Shono, S., *Introduction to Meteorological Dynamics*, Iwanami, Tokyo, 1954.
3. Sasaki, Y., "On the trajectory of the inertia motion of an parcel of air," *Geophysical Notes*, Vol. 3, No. 32, 1–16, University of Tokyo, 1950.

Satellite Thermal Monitoring of Ocean Water Front Formation after an Intruding Bering Sea Water into the Arctic Sea

Shigehisa Nakamura
Kyoto University, Japan

Abstract— A model is introduced to see the intruding Bering Sea water to form an ocean thermal front in the Arctic Sea. First, a brief note is given about the phenomenological processes around the Bering Strait and the Arctic Sea. A dynamical illustration is introduced to see what part is caused by the natural process and to distinguish the man-made effect out of the information in the satellite thermal monitoring.

1. INTRODUCTION

The author introduces a model for a dynamical understanding of the intruding Bering Sea water to form an ocean thermal front in the Arctic Sea For a convenience, recent reported contents are introduced to see what processes are found in these ten years. Then, a recent work on the global ocean circulation is introduce in order to help at considering on the Bering Sea water intrusion into the Arctic Sea on the bases of the satellite thermal monitoring for not only seeing the natural process but distinguishing the man-made disturbances in the global process of the ocean circulation. A model might help us to have a dynamical understanding of the intrusion in the interested sea area.

2. NOTE TO THE ARCTIC SEA

The author has had several reports on satellite thermal monitoring of ocean front evolution in a mid latitude zone. It was the site of the Northwest Pacific so that satellite thermal mentoring had been undertaken after directly receiving the satellite signal and processing the signal for obtaining a series of the ocean front evolution by utilizing a desk top personal computer. What is the point must be that the ocean thermal front can be found as a maximum of thermal gradient on the sea surface in the obtained pattern after processing the satellite data.

In this work, an example of ocean front in the Arctic Sea formed by an intrusion of the Bering Sea water. This intrusion might have been appeared many times in some other scientific publications. For example, Shimada et al. [1] in 2006 noticed on the Pacific Ocean inflow as an effective factor for influence on catastrophic reduction of sea ice cover. Stroeve et al. [2] in 2007 have noted on the Arctic Sea ice decrease, that was greater than forecast. Stroeve et al. [3] in 2008 noted about Arctic sea ice content plummets in the year of 2007. Gasaard et al. [4] in 2008 noted the Arctic trans-polar drift during dramatic sea ice retreat. These notes on phenomenological process seem to suggest the author to promote a research on the specific process in the Antarctic Sea in a scope of hydrodynamics.

3. GLOBAL OCEAN CIRCULATION

The author found in this time a review on the driving processes of the Atlantic meridional overturn circulation [5] by Kuhlbrot et al.. This should be evaluated after finding the contributions by Marotzke and Willebrand [6] and Marotzke [7]. These works are descriptive works that notices simply on the phenomenological process in fact.

Nevertheless, what they have written were invaluable at understanding what processes are found in fact in the area covering not only the Atlantic but the ocean area of a world-wide scale.

Now, the author is tending to consider the ocean front formed by the intruding Bering Sea in the Antarctic in a global scale.

4. LINK OF PACIFIC-ANTARCTIC-ATLANTIC

Referring to the reports introduced as above and the information about satellite thermal monitoring of the ocean surface in a global scale, the author produced a modified map of the deep ocean water circulation as found in Figure 1. In Figure 1, arrows indicate deep ocean water circulation with a starting point just off the Newfoundland (blue colored arrows), and the red mark corresponds to the ocean front formed by the Bering Sea water intrusion into the Arctic Sea.

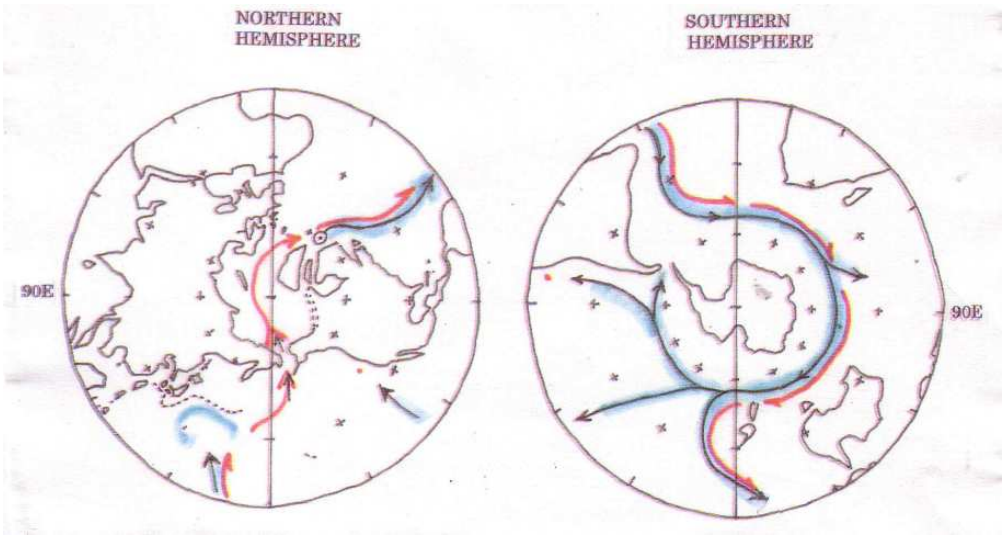

Figure 1: The North Atlantic meridional overturn in relation to a polar orbital ocean inertia circulation. 1 – The warm water of the Bering Sea intruding into the Arctic Sea found after the satellite thermal monitoring. 2 – Link is formed by the Pacific, Bering Sea, Arctic Sea, Atlantic, and the Antarctic circum-polar circulation.

It is already found a recent trend of the September sea ice extent in the Arctic Sea [8]. In the cold season in every year, the Arctic sea surface area is covered by the frozen sea ice. Sea ice of one year might melt away in every summer season but old sea ice group maintain to cover the sea surface of the Arctic Sea. At the bottom of the old sea ice, salt trapped in the ice is squeezed with time elapse. When the cold wind blows on the sea surface opened in the worm season, the sea surface is easily cooled down to be a higher density of sea water. In addition, the sea ice contains salts as named it in term of "**brine**". This sea ice tends to squeeze out the salts of the ice content. Then, the salinity of the sea water just under the old sea ice tends to be dense, and the sea ice tends to be an ice of more purified frozen water with less salt contents. These processes in the Arctic Sea might be one of the important factors to determine the salinity and temperature of the waters in the surface layer in the Arctic Sea.

5. OCEAN CIRCULATION MODELS

As for the upper layer of the ocean, the wind-induced current system is understood to be actual pattern in fact, for example, in the ages of Ekman [9] and also in the ages of Henry Stommel [10] and Munk [11]. Their theoretical works were a key to find a f-plane model for the westward intensification of wind-driven ocean currents.

As for thermohaline circulation, a mathematical model was hard to construct for a long time, though some of the scientists have had challenged to have a mathematical solution as an approximated solution.

On the other hand, Shono [12] introduced a brief note on inertia motion of air particle. Inertia motion in the tropical zone was analyzed by Whipple [13]. Sasaki analyzed a more general form of the aimed solution for inertia motion in a global scale which was reduced under the conditions of conservation of kinetic energy and conservation of absolute angular momentum for a case of no atmospheric pressure gradient [14].

An application of the Sasaki's solution may support a meridional or polar orbital inertia motion in the ocean. Now, the author may take it possible to consider an inertia motion with a meridional or polar orbit of the water mass under some assumptions. The author here introduces only one example of a polar orbital motion as a circulation as shown in Figure 2.

A simple hydrodynamic model is introduced to show that horizontal inertia motion of the sea water is on a polar orbital path. This polar orbital motion is boldly supporting a link of the deep water flow from the Atlantic to Arctic through the Pacific and Bering.

Then, the global ocean circulation may be formed by coupling of the wind-induced ocean current in the upper layer and the down flow at an cold area in the North Atlantic. The Atlantic down flow get to the mid of the Pacific after flowing around the Antarctic circum-flow deep south of the Indian Ocean and off the Australia.

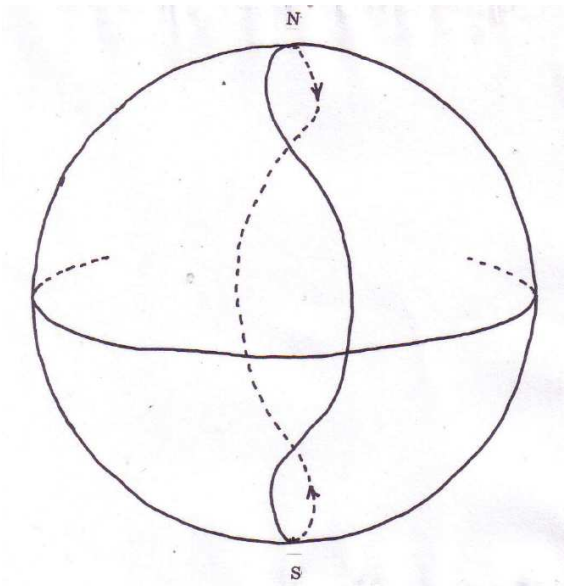

Figure 2: Meridional orbital path of an inertia motion as a solution of dyamical theory. 1– Refer to Sasaki model solved in 1950. 2 – Shono (1957) introduced a brief note on Sasaki model of 1950.

A recent September thermal front evolution in the Arctic Sea suggests a link of the Pacific to the Atlantic through the Bering Sea and Antarctic Sea referring to the satellite thermal monitoring of the ocean surface.

6. DISCUSSIONS AND CONCLUSIONS

First, a brief review note of the ocean circulation in the early age. After that, a model of a meridional or polar orbital ocean inertia motion is introduced to suggest a supporting data is found in the satellite data. That is for the satellite thermal monitoring of the intruding Bering Sea water as a key to formation of an ocean front in the Arctic Sea.

The open sea area of the Arctic Sea in summer is easily affected by the cooling effect caused by the atmospheric winds. In addition, the young sea ice melts in every year to make an open sea and the old ice grows to cover the sea surface of the Arctic Sea. This ice cover is effective as a thermal isolator for the sea water under the old ice pack. The old sea ice shows to affect the ice of quality to be more purified as squeezing the trapped salt in the ice. The squeezed salt go down to diffuse into the sea water. These effects control the density and temperature of the sea water under the ice cover in the Arctic Sea.

A simple hydrodynamic model is introduced to suggest that the horizontal inertia motion of the sea water is on a polar orbital path. This polar orbital motion is boldly similar to the deep sea water flow in the ocean.

With the above notices, the author tends to consider it to be expected an existence of a link between the Pacific, the Bering Sea, the Arctic Sea and the Atlantic.

REFERENCES

1. Shimada, K., T. Kamoshima, M. Itoh, S. Nishino, E. Carmack, F. McLaughlin, S. Zimmermann, and A. Prognutinsky, "Pacific ocean inflow: Influence on catastrophe reduction of sea ice cover in the Arctic Ocean," *Geophysical Research Letters*, Vol. 33, L08605, doi: 10.1029/2005GL025624, 2006.
2. Stroeve, S., M. Sereze, S. Drobot, S. Gearheard, M. Holland, J. Maslanik, W. Mehler, and T. Scambos, "Arctic Sea ice content plummets in 2007," *EOS, Transaction of American Geophysical Union*, Vol. 89, No. 2, 13–14, 2008.
3. Stroeve, J., M. Holland, W. Meiner, T. Scarbros, and M. Serreze, "Arctic Sea ice decrease: Greater than forecast," *Geophysical Research Letters*, Vol. 34, L09591, 2007.
4. Gasaard, J. C., et al., "Exploring Arctic trans-polar drift during dramatic sea ice retreat," *EOS, Transaction of American Geophysical Union*, Vol. 89, No. 3, 21–22, 2008.

5. Kuhlbrot, T., A. Greisel, M. Montoya, A. Levermann, M. Hoffmann, and S. Rahmstorf, "On the driving processes of the Atlantic meridonal overturn ciculation," *Reviews of Geophysics*, Vol. 45, RG2001, 1–32, doi:10.1029/2004RG000166, 2007.
6. Marzke, J. and J. Willebrand, "Multiple equibria of global thermohaline circulation," *Journal of Physical Oceanography*, Vol. 21, 1372–1385, 1991.
7. Marzke, J., "Boundary mixing and the dynamics of the three-dimensional thermo-haline circulation," *Journal of Physical Oceanography*, Vol. 21, 1372–1385, 1997.
8. Perovich, D. K. and J. A. Richter-Menge, "Loss of sea ice in the Arctic," *Annual Review of Marine Sciences 2009*, Vol. 1, 417–441, 2009.
9. Ekman, V. W., "On the influence of the earth's rotation on ocean-currents," *Arkiv fur Mathematik, Astronomy och Fysik*, Vol. 2, No. 11, Stockholm, 1905.
10. Stommel, H., "The westward intensification of wind-driven ocean currents," *Transaction of American Geophysical Union*, Vol. 29, 202–206, 1948.
11. Munk, W. H., "On the wind-riven ocan circulation," *Journal of Meteorology*, Vol. 7, 79–93, 1950.
12. Shono, S., *Introduction to Meteorological Dynamics*, Iwanami, Tokyo, 1954.
13. Whipple, F. J. W., "The motion of a particle on the surface of a smooth rotating globe," *Philosophical Magazine*, Vol. 33, 457–471, 1917.
14. Sasaki, Y., "On the trajectory of the inertia motion of an parcel of air," *Geophysical Notes*, Vol. 3, No. 32, 1–16, University of Tokyo, 1950.

Satellite Thermal Monitoring of Ocean Front Evolution in Relation to Ocean Climate in the North Atlantic, Pacific and Arctic Sea

Shgehisa Nakamura
Kyoto University, Japan

Abstract— This work is an extensive work of satellite thermal monitoring of ocean front evolution. The author has found a meridional ocean circulation consistent to the satellite thermal monitoring of sea surface in Arctic Sea. The North Atlantic water down flow is a trigger for a global deep ocean circulation. Considering the wind-induced upper layer ocean circulation, a theoretical model for meridional inertia ocean circulation in the two layered ocean circulation combining the Pacific Ocean, Arctic Sea and the Atlantic Ocean may be supported by the data of satellite thermal monitoring of the sea surface between the Pacific and Arctic Sea. This inertia circulation could be an ocean climate index in relation to the down flows in the North Atlantic.

1. INTRODUCTION

A possible model of ocean front evolution in a global scale is studied in relation to ocean climate in the North Atlantic.

This model could be a helpful for realizing a ocean front evolution process directly monitored in the northwestern Pacific. The recent contributions on the three dimensional structure of the global ocean circulation tells us that the ocean water in the surface layer is taken to be mainly governed by the winds the sea surface, especially by the wind stress. Nevertheless, the scientists have found the thermohaline ocean circulation should be a more reasonable at considering on what was the actual ocean circulation system in the global scale. A recent oceanographic contribution has been obtained by the advanced instrumentations for a more detail of the ocean structures. The launched satellites have given the data of the ocean surface supporting a theoretical model of a meridional ocean inertia circulation.

2. SATELLITE MONITORING

For this, the satellite monitoring and the oceanographic observations are taken as the references.

The deutsche oceanographic expedition (for example, in 1932) must be the first and works by the sails for many years. A glance of the vertical pattern of the oceanographic factors had been seen after the expedition. Since then, they have undertaken various kinds of surveys by use of the ships or boats for finding the ocean structure (for example, Sverdrup et al., 1942 and, Dietrich, 1957).

In these years, the satellites have been launched to monitor the earth surface. Nevertheless, the electromagnetic waves can only informs the sea surface state but what are undersea. What is found by analyses of the data has given an understanding not only on the sea surface pattern but the deep sea area. Then, we had a three dimensional structure of the ocean circulation in a global scale boldly.

3. DOUBLE DIFFUSION AND OCEAN FRONT

In order to see an ocean front evolution, it is necessary to remind what physical process is on the interested ocean front which is on the ocean surface though a subsurface interface between the coastal and ocean water is formed.

The ocean front and the ocean subsurface interface is formed by a different two waters as noted above. The two waters are interacting each other in their motions.

In this case, equation of motion for the waters around the ocean front should be described as that is done for a densimeric water motion. That is to say, equation of motion for each of the waters can be described as follows:

$$\partial u/\partial t + u\nabla u = -(g/\rho)\nabla h + \nabla[\mu\nabla u], \tag{1}$$

where, water velocity u under the water surface h in the frame of time t and an arbitrary space governed by the earth's gravity g for the water of density ρ of viscosity μ. The notation ∇ denotes special gradient. The numerals of ρ and μ for the coastal water and for the ocean water should be

specified, for example, as those expressed in a given suffices. As for the coastal water, notation is $\rho = \rho_c$ and $\mu = \mu_c$, and as for the ocean water, $\rho = \rho_o$ and $\mu = \mu_o$ respectively.

Then, the water motion in the sea should be determined as a function of temperature T (Kelvin) and salinity (unit per mille) S "in situ" in practice.

The bathymetric condition in the ocean is also an important factor at considering the deep water motion in a stratified layer. In this case, the density is determined by an additional depth factor because the compressibility of the ocean water is effective to see the vertical structure of the ocean, $\rho = \rho\ (S,\ T,\ D)$, for water depth D (in meter).

The two factors T and S of the sea water, both of the coastal water and the ocean water, are diffusive property respectively. Then, a diffusion equation should be introduced at the analyses of the ocean water motion, especially around the ocean front. Now, it can be expressed the diffusion equation for the ocean water as follows:

$$[\partial T/\partial t, \partial S/\partial t] + u[\nabla T, \nabla S] = -[\nabla \kappa_T(\nabla T), \nabla \kappa_S(\nabla S)]. \tag{2}$$

where, the notation κ is diffusion parameter with suffices for T and S respectively.

Exactly, the sea water is a solution of many solvents essentially though the symbolic index S may be useful at extending the formulation of the diffusion process as well as the other physical, chemical or biological process. In these years, a more convenient index is introduced for biological processes in the ocean after defining index for concentration of Chlorophill-a as a representative of the other minor factors. Satellite monitoring for the visible band and optical remote sensing have been cast for these years in order to find a biological process in relation to a dynamics of ocean flow.

4. DOWN FLOW OF OCEAN WATER

As is well understood, the meridional ocean circulation system is effective to see the global ocean circulation as a three dimensional process, even though it is yet primitive. This process could be possible to consider the two layers of the ocean, i.e., the surface layer and the deep layer with the down flows surface to the deep in Labrador Sea and Nordic Sea.

In the ocean water circulation updated, the deep water flow is formed by the ocean water of the down flow in the North Atlantic with several minor down flows just around the Antarctic coastal zones, for example, Kuhlbrot et al. in 2007. A remark is that Marotzke has already noted on "the Atlantic Meridional Overturning Circulation" in 1991 and 1997. The down flow in the North Atlantic forms a deep water flow along the western part of the Atlantic to get to the circum polar deep flow which direct to east to form a upwelling in the Indian Ocean, and direct to more east to intrude into the South Pacific.

In the South Pacific, an upwelling off Peru contributes the surface flow to the west. This flow in the tropical zone strongly affects to the ocean climate in the northwestern Pacific.

A branch of the circum polar deep flow passing off the south of Australia and New Zealand, crosses the equator to get to the Philippines Basin to be stored as an exhausted water. This water might be the most aged ocean water in the world. Amount of this storage must be increase to raise the sea level in the Basin.

It must be possible to see what age is the oldest deep ocean water in the Basin if the sampling could be successful or a remote sensing of the radio-isotopic monitoring for a specific element. The decay of specific atomic radio-isotope, for example "Kalium" is a good index for the sea wate aging in natural condition in the deep sea water.

5. AGED DEEP WATER EFFECT TO OCEAN FRONT EVOLUTION

As noted above, the down flow in the North Atlantic suggesting to get to the Philippine Basin of the northwestern Pacific through the Southern Circum Polar Current. Some of the recent reports tell us that the oldest water has been found in the deep sea of the Philippine Basin after aging of the dissolved oxygen. The water from the North Atlantic might have got to the Basin after dissipating the original dissolved oxygen. This oldest ocean water might increase and be stored there to raise the sea level of the Basin in a long year period. The author here considers that this water in the tropical zone forms a stable deep layer to swell up the sea surface and to raise the sea level in the tropical zone. This could affect the ocean front evolution in the northwestern Pacific which had been monitored well by the recent satellites. This effect of the oldest deep sea water to the ocean front evolution might be found in a spacial undulation and in a timely variation.

With our knowledge on the potential of the water motion on the earth, increase of the old water in the northwestern Pacific can be effective to spread the surface ocean water to intensify degree of convergence on the ocean front to result an ocean front evolution activated around the spreading water mass. This might be a cause of no intermediate eddies in the offshore side of the ocean front in the northwestern Pacific. Nevertheless, the details to this process must be clarified by utilizing a more advanced instrumentation and a more advanced numerical model in near future.

As it has been well understood, the ocean front evolution process in the northwestern Pacific is not so simple in spacial undulation of its pattern and in timely variations of its form as seen on the sea surface.

Considering some other factors possibly related to the ocean front evolution, one of the factors controlling the ocean front evolution process in a long time scale than the age of the oldest water could be the deep water mass transported from the Atlantic.

Then, the author tends to introduce a conceptual model on the basis of what stated as above. This model is now a hypothetical one but realistic when the data of the sea level and ocean surface flow obtained for these one hundred years and the satellite monitoring of the ocean front evolution.

The author here feels it necessary to notice that any numerical model can not give us any answer to the interested process of the ocean front evolution because numerical computation is an approximated technique for a related dynamical theory but a solution of a theory which is constructed on the bases of the dynamical background. Numerical processing for an interested process is simply a replaced approximation in a manipulation technique as that the numerical model gives a realistic solution equivalent to the actual ocean processes.

An expression of differential equation is formed in a dynamical background with an assumption and under some specifying conditions. Generally, this equation is in a form of nonlinear. A linear equation has been used for an approximated form in convenience. It is only for some restrict case that the exact solution can be obtained for the nonlinear case of the equation. Mathematical techniques does not necessarily promise an exact solution for the interested differential equation constructed on the bases of dynamics.

At present, the author feels that it forces an introduction of numerical model in convenience for his display of the possible ocean front evolution as a result of the effect of the old water swelling in the Philippines Basin.

In near future, an advanced mathematical technique might be an effective for the purpose of the problem introduced in this work.

On the other hand, the other advanced remote sensing techniques might be developed well for realizing what process is fact even when a model is solved mathematically.

Recently, in the early stage of the year of 2008, the 21st century, the EU project of the JASON-2 mission is started for the expected earth surface monitoring.

What is important here is to see what process is actually effective at considering the mechanism of the ocean front evolution in relation to the ocean climate in the North Atlantic.

6. EFFECTS OF OCEAN TIDES

Considering the global ocean circulation, some of the scientists are anxious to evaluate water mass transport across the equatorial zone to the other hemisphere. This problem might be rather minor problem in the global ocean circulation. As we have had learned already by this time, it is clear that the ocean tides might be little contributive factors only for energy exchange of the ocean water masses in the northern and southern hemisphere. Several straits around the islands of Indonesia and Papua New Guinea are in the equatorial zone of the western Pacific. These straits are connecting several basins with sea area of about 4000 meters, so that it is hard to consider any significant water mass exchange and mixing in the sea area in the equatorial zone. Nevertheless, the author feels it unfortunate that there is no up-dated data but a poor data of ocean observation in the interested equatorial zone even at present.

There has been introduced a concept of "tidal residual current" for a problem on coastal processes but "tidal residual sea level" in the last quarter of the twenty century. This concept is not consistent to the phenomena of periodic tides found not only in the ocean but in the atmosphere and on the earth.

The author has understanding of that the tidal residual current is simply defined as that for convenience of a issue to a citizen notice to describe the water mass displacement in a coastal zone in 24 hours. Hence, this "residual" does not have any dynamical meaning.

Essentially, the ocean tides are consists many constituents of solar and lunar tides. The ocean tides are a resultant process of these constituents so that the ocean tide process is a resultant process of the corresponding periodical processes essentially.

7. BERING SEA AND ARCTIC SEA

Adding to the above, the author has to notice about a thermohaline leakage of the Bering Sea to the Arctic Sea through the Bering Straight. This must be the most contributive process for the September sea ice extent change in the Arctic Sea as a natural process.

What the author noticed above could be understood looking at a satellite thermal pattern of the sea surface around the Bering Strait, even though the pattern must be a resolution of around a 5 km or 10 km scale in a period of September ice extent in the Arctic Sea. The pattern on the sea surface shows a thermal tongue which is suggesting that the sea water in the Bering Sea is intruding into the Arctic Sea through the Bering Sea. The pattern is composed by a data set of a satellite thermal monitoring of the sea surface after a data which was processed for making a global satellite thermal pattern on the sea surface in a resolution of a 5 km or 10 km scale. This satellite thermal pattern tells us that a leakage of the Bering Sea water into the Arctic Sea at least in September every year.

The above global satellite thermal pattern forces to aware of us that the satellite thermal monitoring informing an intrusion of the Bering Sea linked to the Pacific into the Arctic Sea through the Bering Strait. When the open sea is found in the Arctic Sea, the surface water is easily controlled by an atmospheric effect in a form of wind dynamical action or by a thermal effect in a form of cooling on the sea surface just around a local area of the Arctic Sea where the Bering Sea.

Then, the sea surface of the Arctic Sea could easily get to the North Atlantic. When the ice sheet is covering the surface water of the Arctic Sea, the ice sheet acts as a isolator of any atmospheric cooling during the cold season. This might make it possible to aintain a water leakage of the Bering Sea into the Arctic Sea.

This means that the global satellite monitoring has given a linkage of the sea waters of the down flow of cold sea water to form a deep current in the North Atlantic flowing as a Antarctic circum current in the deep layer, and a part of this Antarctic circum current might turn to get to a terminal in a deeper layer of the northwestern Pacific. A compiling water of this deeper layer could be a trigger to raise the sea level of the interested area in the Pacific, to affect for the ocean front evolution, and to affect for the water motion in the Bering Sea. This linkage must be not so strong at comparing to that of the circum-polar current induced by the atmospheric effects in the surface layer around the Antarctic Sea. This can be named as a meridional link of Pacific-Arctic-Atlantic (in short, as "PAA-Link").

Then, it can be understood that two kinds of ocean current circulation is existing in a global scope. This fact has been found by the satellite monitoring of the sea surface thermal pattern since the first satellite mission of the earth surface.

Next step of the satellite thermal monitoring of the sea surface might be to see its evolution for a long tome period in a global scale.

Since 1990s, it has been raised that a consistent trend of the man-made activity may be the decrease the September sea ice extent in the Arctic Sea as noted in the period between 1900 to 2100, for example, by Stroeve et al. in 2007 (in Geophysical Research Letters, 2007). This is introduced in the publication by Carlson and Giorannoni.

Nevertheless, the author has to notice here that the global processes have the history of about 4500,000,000 years though the significant man-made processes have been raised their attentions for these several ten years. We have to be careful at considering the future of the global processes with consideration in a proper time scale.

8. CONCLUSIONS

The author introduced a problem of ocean front evolution in relation to the ocean climate in the North Atlantic where the down flow of the ocean water of the surface layer moving to the deep layer to form a vertical circulation in the global ocean.

Referring to see what is found in a satellite thermal monitoring of global ocean circulation after the author's work for updating the global ocean surface thermal pattern, it can be accepted an existence of a meridional link of Pacific-Arctic-Atlantic.

The EU project of the JASON-2 mission and the other operating satellites are surely effective for advanced works in the following hundreds years in relation to processes introduced by the author

as noted as above.

The author wishes to have an advanced mathematical technique for solving the equation in order to realize much more about the ocean front evolution in a scope of dynamics.

An advance in the remote sensing techniques is also expected in near future for promoting the interested problem to realize what should be the actual process in the global ocean circulation.

Possible Abnormal Phenomenon of the Atmospheric Water Vapor before Hengchun Earthquake

Yuntao Ma[1, 3], **Yiyang Zhao**[1], **Shanjun Liu**[1], **and Lixin Wu**[1, 2]

[1]Institute for Geoinformatics & Digital Mine Research, Northeastern University
Shenyang 110004, China
[2]Academe of Disaster Reduction and Emergency Management, Beijing Normal University
Beijing 100875, China
[3]School of Civil Engineering, Shenyang Jianzhu University, Shenyang 110168, China

Abstract— Earthquake is the major natural disaster that human beings are facing. The complexity of the earthquake pregnancy remains the earthquake prediction an unresolved problem. Low density of observation stations and small coverage of observation do not provide the necessary information for earthquake predictions. But satellite space monitoring techniques, which have such advantages as wide coverage, rich information, dynamic and high resolution, can provide more comprehensive seismic precursor information. There have been many studies and achievements on satellite thermal infrared, cloud, geoelectricity, gravity and magnetism abnormities before earthquakes, yet there has been little concern about the atmospheric water vapor abnormity during earthquakes.

In this paper we analyzed the atmospheric water vapor anomaly during Hengchun earthquake by use of the MODIS satellite data. The study results indicated that there was possible water vapor anomaly to appear during Hengchun earthquake, but further studies are still needed to conduct.

1. INTRODUCTION

With the use of satellite remote sensing technology in earthquake prediction, there have been a lot of explorations and researches carried on by many scholars on satellite thermal infrared anomalies before and after earthquakes and a variety of thermal anomaly extraction methods put forward [1–10]. For example, in the case of Hengchun earthquake on December 26, 2006 in Taiwan, Shanjun Liu analyzed thermal infrared satellite data from FY-2C and found there were thermal anomalies over the oceans around epicenter before and after the earthquake [12]. C. Filizzola proposed a robust approach for estimator of thermal infrared radiance anomalies [13]. However, there have been relatively few studies in the atmospheric water vapor anomalies before and after earthquakes. S. Dey analyzed the water vapor of the Gujarat earthquake, found that water vapor over the epicentral region increased just before the earthquake whereas over the ocean, water vapor increased after the earthquake [14]. Lihua Cui analyzed atmospheric water vapor of the Wenchuan earthquake and found that water vapor along the faults increased 11 days before the earthquake [15].

In this paper, We carried out analysis of the atmospheric water vapor, and found that the possible negative anomalies of atmospheric water vapor appeared surrounding the epicenter before and after Hengchun earthquake.

2. DATA AND PROCESSING

China Taiwan Region is located in rendezvous site of Philippine Sea Plate, The South China Sea plate and the Eurasian Plate. Special and complex tectonic stress environment leads Taiwan to be the Multi-earthquake region in China. There have been some moderately strong even violent earthquakes annually. The Hengchun earthquake of magnitude 7.2 occurred at 20:26 (12:26 UTC) on December 26, 2006 was the main shock. The epicenter was located at 120.6°E and 21.9°N. After the main shock, there were continuous aftershocks occurred four times in 14 hours (respectively, Ms 6.7 at 20:34 (12:34 UTC), Ms 5.0 at 23:41 (15:41 UTC), Ms 5.0 at 01:35 (17:35 UTC) and Ms 5.3 at 10:30 (2:30 UTC) in the next day).

2.1. MODIS Data Range

The data of the earthquake were the TERRA/MODIS image data downloaded from GODDARD SPACE FLIGHT CENTER (http://ladsweb.nascom.nasa.gov/). The data which we used were surface reflectance of 19th band, atmospheric window of 2nd band and the thermal radiation intensity of 31st band. The data set was in resolution of 1 km × 1 km. Data range: {Date Range: [2003-11-10, 2004-1-10], [2004-11-10, 2005-1-10], [2005-11-10, 2006-1-10], [2006-11-10, 2007-1-10]; time range: [01:00,04:25]; latitude and longitude range: 12°N∼30°N, 112°E∼130°E.}

2.2. Retrieval of Atmospheric Water Vapor Content and Brightness Temperature

Atmospheric water vapor content is the quality of all water vapor on per unit area, the height on per unit area can be understood as an extension of up to infinite, unit is $g \cdot cm^{-2}$. The atmospheric water vapor was produced by two channels of MODIS, 2nd and 19th bands. The retrieval of brightness temperature played two main roles, one was to generate the ocean surface brightness temperature map to view the thermal distribution and the other was to judge the distribution of clouds over the ocean. In the retrieval of water vapor, we also made a judgment if the pixels were interfered by clouds; the retrieval results assigned zero value directly. Brightness temperature was calculated by 31st band of MODIS data.

2.3. Processing

The atmospheric water vapor content in a region is closely related with the speed of evaporation and the speed of evaporation under the stable conditions of water supply is mainly due to the temperature. Then the temperature in a large region is affected by the topography, the feature type, solar radiation, weather, seasonal changes and many non-shock factors while the temperature of a small area may also be subject to some external influence, such as human activities, construction activities and etc. So is the atmospheric water vapor content.

We used statistical method of a large area as background datum to determine whether there was a water vapor anomaly in a small area during the earthquake (small area lies in large area). Statistical method of a large area as background datum referred to the paper "Pre-earthquake Thermal Infrared Anomaly Recognition Method and Quantitative Analysis Model" written by Dr. Jinping Li [11]. We conducted a change to the method of that paper in which the anomaly recognition and quantitative extraction method as a unit based on the pixel has become the anomaly recognition method as a unit based on the region. The procedures are as following:

1) Suppose the mean water vapor content in a small area can be expressed as the following formula:

$$W = W_r + \Delta W \tag{1}$$

where W and W_r represent the mean water vapor content in a small area and a large area respectively, ΔW is the value of changes in water vapor affected by the external force in a small area.

2) The mean ($\overline{\Delta W}$) and the standard deviation ($\sigma(\Delta W)$) of the variation of water vapor in a small region (the same period of the previous three years) are calculated so as to get the background trend of a small area.

$$\overline{\Delta W} = \frac{\sum_{i=1}^{n} \Delta W_i}{n} \tag{2}$$

$$\sigma(\Delta W) = \sqrt{\frac{\sum_{i=1}^{n} \left(\Delta W_i - \overline{\Delta W}\right)^2}{n-1}} \tag{3}$$

3) The daily anomaly index of a small area can be calculated as:

$$WI_i = \frac{\Delta W_i - \overline{\Delta W}}{\sigma(\Delta W)} \tag{4}$$

4) If $WI_i > 1.5$, the small area is considered to be an anomaly area.

3. RESULTS AND DISCUSSION

We extracted the atmospheric water vapor content and the brightness temperature from MODIS data set that we choose. The atmospheric water vapor data and the brightness temperature data were converted into the color maps by the density slice. Some atmospheric water vapor data were excluded because of the influence of the cloud. By visual interpretation of the color maps, we found that the water vapor content was at about $2.0\,g \cdot cm^{-2}$ surrounding epicenter at the same period of the previous three years before the earthquake, the distribution of the water vapor had no obvious anomaly along the fault zone. However, Fig. 1 shows the phenomenon of water vapor low-value appeared in the South China Sea region on December 15, 2006, 11 days before the earthquake,

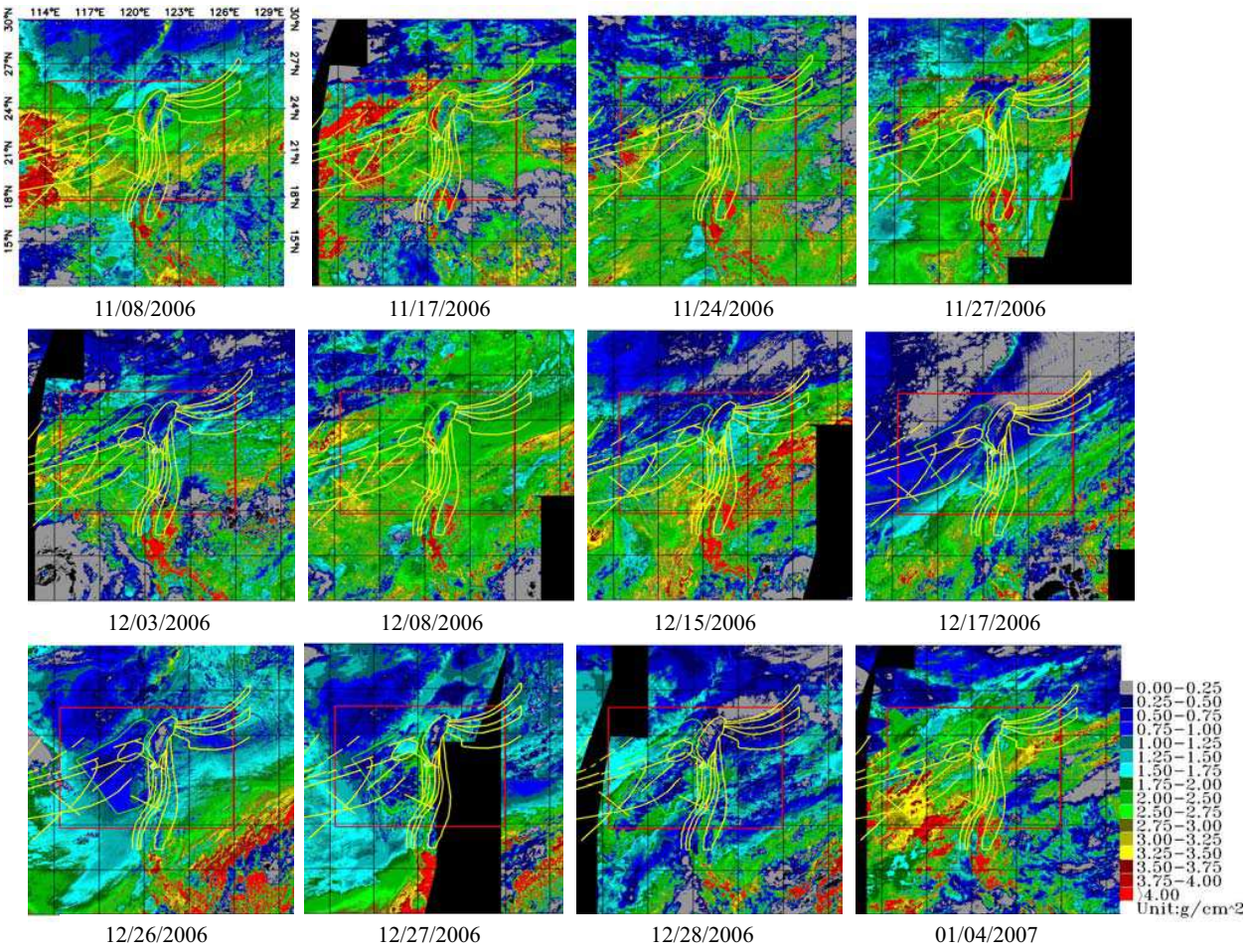

Figure 1: The maps of atmospheric water vapor in the South China Sea. White point indicates the position of the epicenter; Yellow lines show the faults; Cyan polygon represents the small region we chosen; Red polygon represents the large region as the reference background.

Table 1: The anomaly index of small area in seismogenic year.

$\overline{\Delta W} = 0.137\,\mathrm{g\cdot cm^{-2}}$, $\sigma(\Delta W) = 0.204\,\mathrm{g\cdot cm^{-2}}$, Unit: $\mathrm{g\cdot cm^{-2}}$

Date	W	W_r	WI_i	Date	W	W_r	WI_i
2006-11-08	2.490	2.299	0.265	2006-12-15	1.683	1.937	−1.914
2006-11-09	2.797	2.701	-0.200	2006-12-17	0.801	1.053	−1.906
2006-11-10	1.954	1.624	0.949	2006-12-18	0.903	0.983	−1.063
2006-11-15	2.005	2.178	-1.519	2006-12-19	1.472	1.324	0.058
2006-11-16	2.621	2.449	0.176	2006-12-20	1.583	1.694	−1.214
2006-11-17	2.757	2.360	1.274	2006-12-22	1.069	1.079	−0.716
2006-11-18	2.610	2.532	-0.287	2006-12-25	1.514	1.408	−0.151
2006-11-24	1.863	2.008	-1.381	2006-12-26	0.891	1.160	−1.990
2006-11-27	2.333	2.151	0.224	2006-12-28	1.268	1.101	0.151
2006-11-29	1.666	1.646	-0.571	2006-12-29	1.343	1.255	−0.238
2006-12-03	1.798	1.671	-0.046	2007-01-02	1.814	1.801	−0.606
2006-12-04	2.105	1.842	0.620	2007-01-04	2.441	2.245	0.291
2006-12-06	2.279	1.890	1.237	2007-01-05	1.925	1.838	−0.243
2006-12-07	2.730	2.222	1.819	2007-01-06	1.689	1.537	0.076
2006-12-08	2.448	2.331	-0.096	2007-01-07	1.566	1.483	−0.264
2006-12-14	2.474	2.127	1.029				

which was consistent until the end of year. The minimum appeared on December 17, 2006, and the water vapor value was only $0.801\,\mathrm{g}\cdot\mathrm{cm}^{-2}$, less than half the mean value. The second smallest value was only $0.891\,\mathrm{g}\cdot\mathrm{cm}^{-2}$, also did not meet the half mean value on the day of earthquake. The water vapor values returned to the level of about $2.0\,\mathrm{g}\cdot\mathrm{cm}^{-2}$ after January 2, 2007.

Then we calculated that $\overline{\Delta W}$ of the small area minus the large area (chosen by us in Fig. 1) was equal to $0.137\,\mathrm{g}\cdot\mathrm{cm}^{-2}$ and $\sigma(\Delta W)$, standard deviation, was equal to $0.204\,\mathrm{g}\cdot\mathrm{cm}^{-2}$. After calculating the anomaly index of small area in seismogenic year (Table 1), we found that from December 15th to 26th, the anomaly index was negative apart from December 19th that was equal to 0.058. On December 15th and December 17th, the anomaly index reached -1.914 and -1.906 respectively. It reached -1.990 on the December 26th when the earthquake happened.

According to the brightness temperature map retrieved from MODIS, We found that there were thermal phenomena in the earthquake. Prof. Shanjun Liu also has such report on Hengchun earthquake thermal anomalies. However the water vapor negative anomalies emerged not because of thermal anomalies during the earthquake.

4. CONCLUSION

The analysis of atmospheric water vapor has shown anomalous behavior during the earthquake. The result shows that:

1) In Hengchun earthquake in Taiwan, there was no phenomena of the increase in water vapor before and after the earthquake, but the phenomena of the reduction in water vapor and the negative anomalies.

2) There are some shortcomings to the anomaly analysis method of regional background reference such as it can not detect abnormal range, the choice of reference region and non-reference region is impacted from Human factors as well.

The reason for water vapor negative anomalies in the South China Sea nearby the epicenter is not very clear. Detailed investigations of atmospheric water vapor content and its temporal variations prior and after earthquakes which occur especially near the ocean are required to continue to study in other earthquakes.

ACKNOWLEDGMENT

This work is supported by the National Natural Science Foundations of China (No. 50774017) and the Liaoning Province Technology Project (2008231001)

REFERENCES

1. Gorny, V. I., "The earth outgoing IR radiation as an indicator of seismic activity," *Proc. Acad. Sci. USSR*, Vol. 30, No. 1, 67–69, 1988.
2. Tronin, A. A., "Satellite thermal survey-a new tool for the study of seismoactive regions," *INT. J. Remote Sensing*, Vol. 17, No. 8, 1439–1455, 1996.
3. Tronin, A. A., "Remote sensing and earthquakes: A review," *Physics and Chemistry of the Earth*, Vol. 31, 138–142, 2006.
4. Qiang, Z. J., X. D. Xu, and C. G. Dian, "Thermal infrared anomaly precursor of impemding earthquake," *Chinese Science Bulletin*, Vol. 36, No. 4, 319–323, 1991.
5. Qiang, Z. J and C. G. Dian, "Satellite thermal infrared impending temperature increase precursor of Gonghe earthquake of magnitude 7.0, Qinghai Province," *Geoscience*, Vol. 6, No. 3, 297–300, 1992.
6. Ouzounov, D. and F. Freund, "Mid-infrared emission prior to strong earthquakes analyzed by remote sensing data," *Advances in Space Research*, Vol. 33, 268–273, 2004.
7. Tramutoli, V., V. Cuomob, C. Filizzola, et al., "Assessing the potential of thermal infrared satellite surveys for monitoring seismically active areas: The case of Kocaeli earthquake. August 17, 1999," *Remote Sensing of Environment*, Vol. 96, 409–426, 2005.
8. Freund, F. T., "Rocks that crackle and sparkle and glow: Strange pre-earthquake phenonmena," *Journal of Scientific Exploration*, Vol. 17, 37–71, 2003.
9. Pulinets, S. A., V. D. Ouzouno, A. V. Kareline, et al., "The physical nature of thermal anomalies observed before strong earthquakes," *Physics and Chemistry of the Earth*, Vol. 31, 143–153, 2006.
10. Wu, L. X., S. J. Liu, Y. H. Wu, et al., "Precursors for fracturing and failure-Part 1: IRR image abnormalities," *Int. J. Rock Mech. & Min. Sci.*, Vol. 43, No. 3, 473–482, 2006.

11. Li, J. P., L. X. Wu, S. J. Liu, et al., "Pre-earthquake thermal infrared anomaly recognition method and quantitiative analysis model," *Journal of China University of Mining & Technology*, Vol. 37, No. 6, 1–6, 2008.
12. Liu, S. J., L. X. Wu, J. P. Li, et al., "Features and mechanisms of the satellite thermal infrared anomaly before Hengchun earthquake in Taiwan region," *Science & Technology Review*, Vol. 25, No. 6, 2007.
13. Filizzola, C., N. Pergola, C. Pietrapertosa, et al., "Robust satellite techniques for seismically active areas monitoring: A sensitivity analysis on September 7th 1999 Athens's earthquake," *Physics and Chemistry of the Earth*, Vol. 29, 517–527, 2004.
14. Dey, S., S. Sarkar, and R. P. Singh, "Anomalous changes in columu water vapor after Gujarat earthquake," *Advances in Space Research*, Vol. 33, 274–278, 2004.
15. Cui, L. H., "Study on Anomaly of Remote Sensing Information and Mechanism before the Wenchuan Earthquake," Hebei Polytechnic University, 1–63, 2008.

The Time-space Relationship between Strain, Temperature and Acoustic Emission of Loaded Rock

Yingwei Shi[1], **Qun He**[1], **Shanjun Liu**[1], **and Lixin Wu**[1, 2]

[1]Institute for Geo-informatics & Digital Mine Research, Northeastern University, Shenyang 110004, China
[2]Academe of Disaster Reduction and Emergency Management, Beijing Normal University
Beijing 100875, China

Abstract— The tectonic activity and rock fracture will cause many physical phenomena, including strain, temperature change and acoustic emission (AE). In theory these physical variables exist determinate relationships because they are the results of stress activity of curst. How to obtain the relationship between them is the key to monitor the tectonic activity and rock cataclysm (including geological disasters, earthquake and mine disasters and so on) by use of remote sensing technology. In this paper the tortuously non-connected fault and the hole-rock samples were loaded to simulate the tectonic activity and rock engineering failure in the real world. In the process of loading, an infrared thermal imager was used to detect the temperature field change of the loaded models, and a digital CCD camera and the digital speckle correlation method (DSCM) were used to collect and analyze images to obtain the evolution processes of displacement and strain fields. Meanwhile, the AE field changes were also simulated with RFPA software. Some experimental results were found: There are two kinds of thermal effects control the temperature field change pattern in the loading process, thermoelastic effect and frictional-heat effect. They have different features at the different loading stages; High strain, high temperature and strong AE signals appear simultaneously in the same area. The three physical fields existed nice relationship between them. The research was beneficial to early warning of tectonic activity and the monitoring of rock fracturing.

1. INTRODUCTION

Some solid Earth disasters such as earthquake are the results of tectonic activity, and there are some physical phenomena (strain, temperature variation and so on) during the activity. How to set up early warning of earth disasters system by use of different technique is the problem that people try to find out. From the late of last century, Geng [1–3], Wu [4, 5] took several experiments of loading different kinds of rock, and found out some phenomena between temperature-change and stress-change. Zhang [6] took use of Epoxy Resins material to research the relationship between image of thermal infrared radiation (TIR) temperature and image of photoelastic during the process of distortion, and found out the area of compressing stress and tensive-stress correspond the high and low temperature. Ma [7, 8] and Liu [9, 10] made loading of en echelon faults to reveal the relationship between temperature field and distortion field, and discussed the mechanism of temperature at the different stages. Liu [11, 12] considered that there were two kinds of thermal effects control the TIR variation in the loading process-Thermoelastic effect and frictional effect, they played a role at the different stages.

This paper analyzes the time-space relationship of strain field, temperature field and AE field by the loading experiment for tortuously non-connected fault and the hole-rock samples by use of different monitor instruments.

2. EXPERIMENTAL DESIGN

In the experiment, the type of servo-control loader was WAW-2000, and it was used to uniaxially load the samples. The loading type was displacement-controlling at 0.2 mm/min. The infrared thermographic camera was VarioSCAN 3021ST, and its temperature precision was 0.03°. The spatial resolution was 360 × 240 pixel. The visible light CCD camera was 1624×1236 pixel. The DSCM was used to obtain the evolution processes of displacement and strain fields. RFPA software was used to simulate the AE field.

The tortuously non-connected fault samples were made of granite with the size of 150 mm × 150 mm × 50 mm, and its four corners were cut. Two 3 mm-width cracks were made, which were cut along the direction of diagonal with included angle 15°. The cracks were filled with gesso, and the distance between two cracks was 30 mm. The hole-rock samples with the size of 85 mm × 170 mm × 25 mm were made, and each of them also had a 25 mm-diameter hole in the center. The samples were used to simulate the rock engineering such as laneway and tunnel.

3. EXPERIMENTAL RESULTS

3.1. Tortuously Non-connected Fault Samples

Figure 1 is the Comparison of different physical fields of tortuously non-connected fault sample Z1-2 in the loading process. The figure shows that at the beginning stage of loading, the strain field, temperature field and AE field have no obvious change. As the loading time is up to 212 s, the end of lower fault form a strain-concentrated area with the round shape. Meanwhile in the TIR image, a high temperature point formed in the same area. Besides, a high temperature appears in the local area of the lower fault due to high strength sliding friction. When the loading time is 220s, the strain-concentrated area at the end of lower fault become smaller, at the same time, the end of upper fault's strain become larger, and the end of lower fault's temperature become lower and the high temperature appear at the end of upper fault in the TIR image. When the loading time is 249 s, the strains at the end of lower fault focus again, where form a strain-concentrated area again, and the high temperature point appear again in the corresponding area. As the progress of load, the degree of strain-concentrated strengthens both at the end of lower and upper faults gradually. Finally, two end of faults with focusing high-strain happen to link along the jog, and then the focusing strains have chance to release, the sample loses stability and breaks down. When the sample breaks down, accompanying with the phenomena of friction in the linking area, the obvious high temperature appear in the TIR image.

The AE field simulated with RFPA software presents the change of AE: the quantity of AE signals become larger as loading, and they appear at the end of lower fault firstly then the end of upper fault, the energy of signals become larger gradually, the phenomena of AE's activity

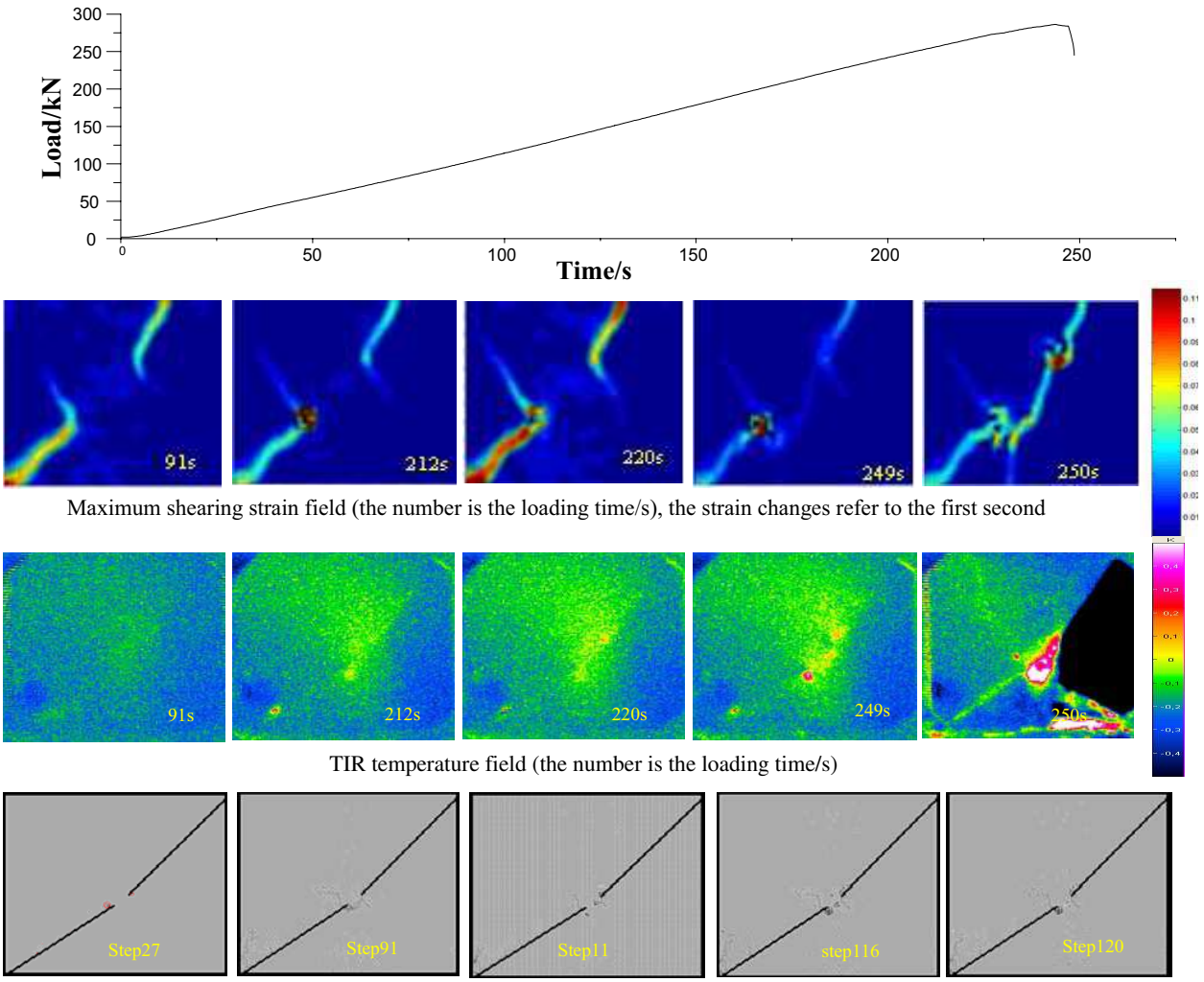

Figure 1: Comparison of different physical fields of sample Z1-2 in the loading process.

correspond with the strain and temperature. The following conclusion can be obtained:

1) Large strain points and high temperature points appear at the same time, with AE signals increase obviously. The three physical fields have nice time-relationship.

2) The change of strain-concentrated has the trend that it happens from the end of two faults to linking the faults along the jog, with the change of TIR temperature in the same area, and the area has the similar shape with large strain area. AE signals appear in the approximate area too. The three physical fields have nice space-relationship.

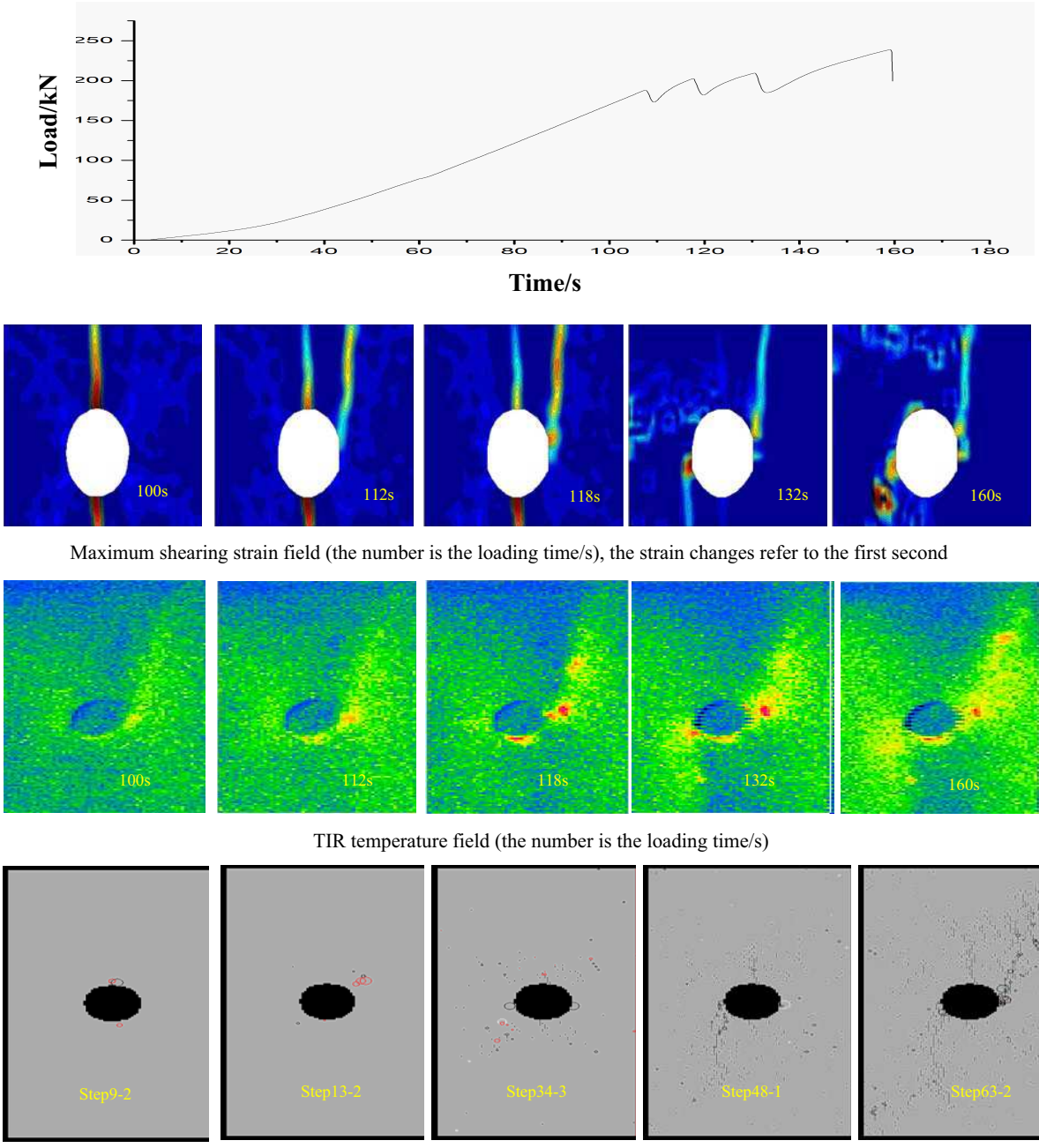

Figure 2: Comparison of different physical fields of sample K1-2 in the loading process.

3.2. Hole-rock Samples

Figure 2 is the Comparison of different physical fields of hole-rock sample K1-2 in the loading process. The figure shows that at the beginning stage of load, the strain field, temperature field and AE have no obvious change. With the loading development, strains focus around the hole gradually, over and under of the hole appear tensile strain along the direction of loading and grow gradually.

According to thermoelastic effect, tensile strain induces to decrease temperature, the phenomena of low temperature show up in the same area in the TIR image. At 100 s strain-concentrated area with X-shape show up near the hole, the temperature is higher comparatively. When the loading time is 112 s, at the right of hole, it grows a linearity strain-concentrated area along the up direction of tangent, with the higher temperature in the TIR image. At 118 s strain-concentrated become obvious, and there is a high strain-concentrated point near the hole, the high temperature point show up at the same time. At 132 s, at the left of hole, it grows a linearity strain-concentrated area along the down direction of tangent, and there is a high strain-concentrated point near the left of hole, high temperature point show up in the same area. At 160 s, the sample breaks down along the two linearity strain-concentrated areas.

In the AE image, AE signals appear along up and down of the hole firstly, and signals with larger energy appear along left and right of the hole later, and they grow up and down along the direction of tangent, which correspond the change of strain and temperature. The following conclusion can be obtained:

1) The left and right of hole are the compressing strain-concentrated areas, the over and under of the hole is the concentrated area of tensile strain, which correspond the high or low temperature. AE signals change obviously in the approximate area. The three physical fields have nice space-relationship.

2) The appearing and transferring of the large strain-concentrated points correspond the appearing and transferring of high temperature points, and the AE signals have corresponding activity when the strain and temperature change. The three physical fields have nice time-relationship.

4. CONCLUSIONS AND DISCUSSION

The experimental results show that the strain field, temperature field and AE field all exist time-space change. The strain-concentrated area correspond the area of changing temperature, compressing strain and tensile strain area correspond the high or low temperature area, where the AE signals increase accordingly. The appearing and transferring of large strain-concentrated points correspond with the change of high temperature points and large energy AE signals. The three fields had nice relationship between them.

At the aspect of plane strain in mechanics, shear strain is the common effect of compressing strain and tensile strain. It can contain the changes of compressing and tensile strain by using the shear strain image to express the strain field. There are two kinds of thermal effects control the temperature field change pattern in the loading process, thermoelastic effect and frictional-heat effect. 1) At the early stage of load, the temperature field mainly controlled by thermoelastic effect, the change of temperature is linearly related to the sum change of principal stresses, tensile stress or compressing stress induce to drop or rise temperature. There is a little deformation due to lower stress at this stage, and the change of temperature is not well obvious. High strength Sliding friction may appear in the local area at this stage, so some local areas will appear high temperature due to frictional-heat effect. 2) At the plastic stage, the samples appear irreversible plastic-distortion, the change of strain become larger, and the temperature field controlled by the frictional-heat effect, it exists obvious high temperature. Meanwhile, AE signals with large energy increase obviously. Some basis can be applied for early warning of tectonic activity and the monitoring of rock fracturing base on the relationship between the three fields.

REFERENCES

1. Geng, N. G., C. Y. Cui, and M. D. Deng, "Remote sensing detection of rock fracturing experiment and the beginning of remote rock mechanics," *Acta Geoscientia Sinica*, Vol. 14, 645–652, 2002.
2. Geng, N. G. and M. D. Deng, "The simulated experimental studies on cause of thermal infrared precursor of earthquakes," *Acta Geoscientia Sinica*, Vol. 18, 83–88, 1998.
3. Cui, C. Y., M. D. Deng, and N. G. Geng, "Study on the features of spectrum radiation of rocks under different loading," *Chinese Science Bulletin*, Vol. 38, No. 6, 538–541, 1993.
4. Wu, L. X., S. J. Liu, Y. H. Wu, et al., "Remote sensing-rock mechanics (I)-Laws of thermal infrared radiation from fracturing of discontinuous jointed faults and its meanings for tectonic earthquake omens," *Chinese Journal of Rock mechanics and Engineering*, Vol. 23, No. 1, 24–30, 2004.
5. Wu, L. X. and S. J. Liu, "Changes in IR with rock deformation," *Rock Mech. & Min. Sci.*, Vol. 39, No. 6, 825–831, 2002.

6. Zhang, D. S. and L. Q. An, "Stress distribution and variation on infrared thermograph and photoelastic technique," *Journal of Jiaozuo Institute of Technology*, Vol. 20, No. 3, 225–228, 2001.
7. Ma, J., S. P. Ma, P. X. Liu, et al., "Thermal field indicators for identifying active fault and its instability from laboratory experiments," *Seismology and Geology*, Vol. 30, No. 2, 364–381, 2008.
8. Ma, J., L. Q. Liu, P. X. Liu, et al., "Thermal precursory pattern of fault unstable sliding — An experimental study of EN echelon faults," *Chinese Journal of Geophysics*, Vol. 50, No. 4, 1141–1149, 2007.
9. Liu, P. X., J. Ma, L. Q. Liu, et al., "An experimental study on variation of thermal fields during the deformation of a compressive en echelon fault set," *Progress in Natural Science*, Vol. 17, No. 3, 298–304, 2007.
10. Liu, P. X., L. Q. Liu, S. Y. Chen, et al., "An experiment on the infrared radiation of sruficial rocks during deformation," *Seismology and Geology*, Vol. 26, No. 3, 502–511, 2004.
11. Liu, S. J., L. X. Wu, Y. H. Wu, et al., "Analysis of affecting factors and mechanics of infrared radiation coming from loaded rocks," *Mine Surveying*, No. 3, 67–68, 2003.
12. Liu, S. J., L. X. Wu, Y. H. Wu, et al., "Remote sensing-rock mechanics (V)-analysis on the factors affecting thermal infrared radiation in process of rock viscosity sliding," *Chinese Journal of Rock mechanics and Engineering*, Vol. 23, No. 5, 730–735, 2004.

Modelling the Effect of a Defect on Crosstalk Signals under the Weak Coupling Assumption

M. Franchet, **M. Olivas**, **N. Ravot**, **and L. Sommervogel**
Embedded Systems Reliability Laboratory, CEA, LIST
Point Courrier 94, Gif-sur-Yvette, F-91191, France

Abstract— This paper proposes a model for better understanding and quantifying the effects on crosstalk signals of the presence of a fault on a wire. This model provides a symbolic solution helping to identify the factors that influence time domain induced signals. This can be useful when assessing the deterioration, due to this defect, of the performances of neighbouring wires.

1. INTRODUCTION

Nowadays automotive electronic systems rely on intricate wire networks. The reliability of the system depends on the health and the quality of the cables used for communication or power supply. It is all the more important to monitor and predict the network's state as a simple defect, such as short or open circuit on a wire can have heavy consequences such as failure breakdown.

Most of the time it is implicitly assumed that only the wire, where the fault is located, is sensitive to it. One method commonly used to locate this defect is called Time Domain Reflectometry (TDR) and can be extended to on line diagnosis ([1]). It is based on the injection of probe signal(s) into the wire network and the analysis of the reflected signals at the injection point. However the presence of such a fault on a wire can also have an impact on the neighbouring wires and can significantly change crosstalk signals. As a consequence it can disrupt the performances of the other wires. In order to quantify the level of this deterioration, the impact of a defect on induced signals needs to be well understood and modelled.

This paper proposes an analytical model for near-end voltages in the case of a three-conductor line of total length l, shown in Fig. 1, under the weak coupling assumption. The ground symbolizes the reference conductor. The conductor referred to as the Generator circuit is driven by a source $V_s(t)$ and is terminated by a resistive load R_{lG}. The other conductor is referred to as the Receptor circuit and is terminated at the near end in a resistive load, R_{NE}, and at the far end in a resistive load, R_{FE}. We will focus on the near-end voltage, V_{NE}, of this circuit. A soft fault (e.g., a portion of dielectric removed) is localized on the Generator circuit, between the abscissa d_1 and d_2. It introduces a change in the per-unit-length parameters of the Generator circuit.

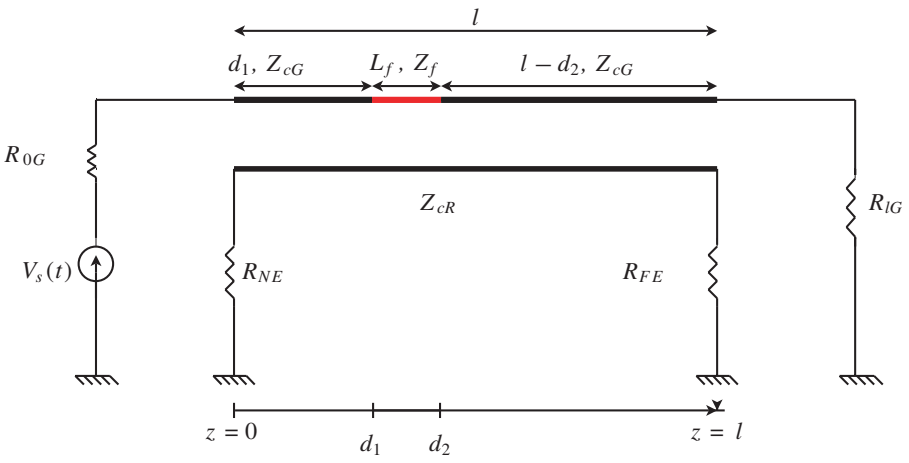

Figure 1: The crosstalk circuit to be investigated.

2. MODELLING THE IMPACT OF A SOFT FAULT ON NEAR END VOLTAGES UNDER THE WEAK COUPLING ASSUMPTION

In the following, $v_G(z,t)$, $v_R(z,t)$ are the voltages (with respect to the reference conductor) of the Generator and the Receptor circuits. The quantities L_R, C_R are the per-unit-length inductance

and capacitance of the Receptor circuit. Its characteristic impedance is Z_{cR} and the velocity of propagation is v_{cR} on this wire. In order to define the per-unit-length parameters of the Generator circuit, we have to distinguish 3 cases:

- **First case:** $z \leq d_1$. The per-unit-length inductance and capacitance of the Generator circuit are L_G and C_G. Its characteristic impedance is $Z_{cG} = Z_1$ and the velocity of propagation is $v_{cG} = v_1$. $L_m = L_{m1}$ and $C_m = C_{m1}$ are the per-unit-length mutual inductance and capacitance between the two circuits.
- **Second case:** $d_1 \leq z \leq d_2$. The per-unit-length inductance and capacitance of the Generator circuit are L_f and C_f. Its characteristic impedance is $Z_f = Z_2$ and the velocity of propagation is $v_f = v_2$. $L_{mf} = L_{m2}$ and $C_{mf} = C_{m2}$ are the per-unit-length mutual inductance and capacitance between the two circuits.
- **Third case:** $d_2 \leq z$. The per-unit-length parameters, the characteristic impedance and the velocity of propagation are the same as the one of the first case.

We will assume that the line is lossless and uniform on each of the three portions defined above. Moreover we will consider the special case of a symetric line, where $L_G = L_R$, $C_G = C_R$, $v_{cG} = v_{cR} = v$ and $Z_{cG} = Z_{cR}$. Furthermore we will consider the weak coupling assumption. It means that we neglect the feedback of Receptor circuit on the Generator one. This assumption is valid as long as

$$L_m \ll L_G \tag{1}$$

On each portion i, $i = 1 \ldots 3$, the voltage and current of the Generator circuit in the Laplace Domain are

$$V_{Gi}(z,p) = \frac{Z_G}{R_{0G} + Z_G}.V_s(p)\left[A_i \mathrm{e}^{-\frac{z}{v_i}p} + B_i \mathrm{e}^{+\frac{z}{v_i}p}\right] \tag{2a}$$

$$I_{Gi}(z,p) = \frac{Z_G}{Z_i(R_{0G} + Z_G)}V_s(p)\left[A_i \mathrm{e}^{-\frac{z}{v_i}p} - B_i \mathrm{e}^{+\frac{z}{v_i}p}\right] \tag{2b}$$

where,

$$\begin{aligned}
A_1 &= 1 \\
B_1 &= \rho_f \mathrm{e}^{-2\frac{d_1}{v}p} + \rho_{lG}(1-\rho_f^2)^2 \mathrm{e}^{-2(L_f\cdot\delta+\frac{l}{v})p} - \rho_f(1-\rho_f^2)\mathrm{e}^{-2(\frac{L_f}{v_f}+\frac{d_1}{v})p} + \rho_f\rho_{lG}^2(1-\rho_f^2)^2\mathrm{e}^{-(\frac{4l-2d_2}{v}+2L_f\cdot\delta)p} \\
A_2 &= (1+\rho_f)\mathrm{e}^{d_1\cdot\delta\cdot p} \\
B_2 &= \rho_{lG}(1+\rho_f)(1-\rho_f^2)\mathrm{e}^{-((L_f+d_2)\delta+2\frac{l}{v})p} - \rho_f(1+\rho_f)\mathrm{e}^{-(\frac{d_1}{v}+\frac{L_f+d_2}{v_f})p} \\
&\quad +(1+\rho_f^2)(1+\rho_f)\rho_f\rho_{lG}^2\mathrm{e}^{-(\frac{4l-2d_2}{v}+(L_f+d_2)\delta)p} \\
A_3 &= (1-\rho_f^2)(\mathrm{e}^{-L_f\cdot\delta\cdot p} + \rho_f\cdot\rho_{lG}\mathrm{e}^{-(2\frac{l-d_2}{v}+L_f\cdot\delta)p}) \\
B_3 &= \rho_{lG}(1-\rho_f^2)(\mathrm{e}^{-(\frac{2l}{v}+L_f\cdot\delta)p} + \rho_f\cdot\rho_{lG}\mathrm{e}^{-(\frac{4l-2d_2}{v}+L_f\cdot\delta)p}) \\
\rho_{lG} &= \frac{R_{lG}-Z_G}{R_{lG}+Z_G} \qquad \rho_f = \frac{Z_f-Z_G}{Z_f+Z_G} \qquad \delta = \frac{1}{v_f}-\frac{1}{v} \qquad \kappa = \frac{1}{v_f}+\frac{1}{v}
\end{aligned}$$

For simplicity's sake, we don't consider all reflections at the interfaces $z = 0$, $z = d_1$, $z = d_2$ and $z = l$.

In order to compute the near-end voltage, we will consider the following model of the Receptor circuit, introduced by S. Bazzoli in [2]:

The voltage and current sources of each portion i ($i = 1 \ldots 3$), $dE_i(z,t)$ and $dI_i(z,t)$, characterize the impact of the Generator circuit on the Receptor one:

$$dE_i(z,t) = L_{mi}\frac{\partial I_i}{\partial t}(z,t)dz \qquad dI_i(z,t) = C_{mi}\frac{\partial V_i}{\partial t}(z,t)dz \tag{3}$$

The voltage $dV_{+_i}(z,t)$ propagates toward $z = 0$ and the voltage $dV_{-_i}(z,t)$ propagates toward $z = l$:

$$dV_{+_i}(z,t) = \frac{dE_i(z)}{2} + Z_R\frac{dI_i(z)}{2} \qquad dV_{-_i}(z,t) = -\frac{dE_i(z)}{2} + Z_R\frac{dI_i(z)}{2} \tag{4}$$

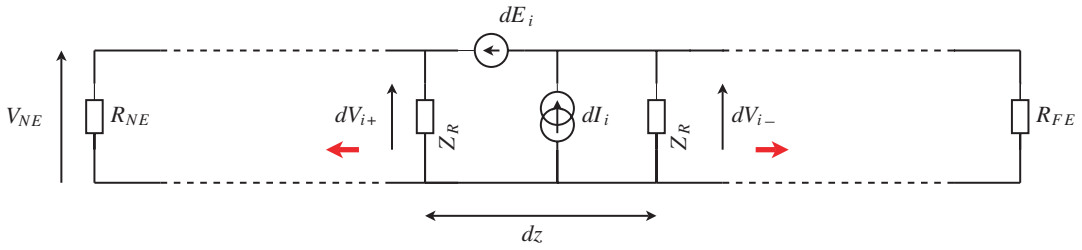

Figure 2: The Receptor Circuit.

3. ANALYTICAL RESULTS IN THE TIME-DOMAIN

Each portion i contributes to the near-end voltage. This contribution is called $NEAR_i$. Then we can compute the near-end-voltage in the Laplace domain:

$$V_{NE}(p) = \frac{2 \cdot R_{NE}}{R_{NE} + Z_R} \sum_{i=1}^{3} NEAR_i \tag{5}$$

where the voltages $NEAR_i$ are computed in the following manner (in the Laplace Domain):

- **For i = 1.** We define $V_{+tot_1}(p)$ and $V_{-tot_1}(p)$:

$$V_{+tot_1}(p) = \int_0^{d_1} \mathrm{e}^{-\frac{z}{v}p} dV_{+_1}(p) \qquad V_{-tot_1}(p) = \int_0^{d_1} \mathrm{e}^{-\frac{d_1 - z}{v}p} dV_{-_1}(p)$$

  Then, $Near_1(p) = V_{+tot_1}(p) + \rho_{NE} \cdot \rho_{FE} V_{+tot_1}(p) \mathrm{e}^{-2\frac{l}{v}p} + \rho_{FE} V_{-tot_1}(p) \mathrm{e}^{-\frac{2l-d_1}{v}p}$.

  With $\rho_{NE} = \frac{R_{NE} - Z_R}{R_{NE} + Z_R}$ and $\rho_{FE} = \frac{R_{FE} - Z_R}{R_{FE} + Z_R}$

- **For i = 2.** We have

$$V_{+tot_2}(p) = \int_{d_1}^{d_2} \mathrm{e}^{-\frac{z-d_1}{v}p} dV_{+_2}(p) \qquad V_{-tot_2}(p) = \int_{d_1}^{d_2} \mathrm{e}^{-\frac{d_2 - z}{v}p} dV_{-_2}(p)$$

  Then, $Near_2(p) = V_{+tot_2}(p) \mathrm{e}^{-\frac{d_1}{v}p} + \rho_{NE} \cdot \rho_{FE} \cdot V_{+tot_2}(p) \mathrm{e}^{-\frac{2l+d_1}{v}p} + \rho_{FE} \cdot V_{-tot_2}(p) \mathrm{e}^{-\frac{2l-d_2}{v}p}$

- **For i = 3.** We have

$$V_{+tot_3}(p) = \int_{d_2}^{l} \mathrm{e}^{-\frac{z-d_2}{v}p} dV_{+_3}(p) \qquad V_{-tot_3}(p) = \int_{d_2}^{l} \mathrm{e}^{-\frac{l-z}{v}p} dV_{-_3}(p)$$

  Then, $Near_3(p) = V_{+tot_3}(p) \mathrm{e}^{-\frac{d_2}{v}p} + \rho_{NE} \cdot \rho_{FE} V_{+tot_3}(p) \mathrm{e}^{-\frac{2l+d_2}{v}p} + \rho_{FE} V_{-tot_3}(p) \mathrm{e}^{-\frac{l}{v}p}$

For the near-end voltage too we didn't consider all of the multiple reflections on the interface $z = 0$ and $z = l$.

We can then write the near-end voltage in the Laplace Domain as the sum of several delayed signals:

$$V_{NE}(p) = \frac{2 \cdot R_{NE}}{R_{NE} + Z_R} \cdot \frac{Z_G}{R_{0G} + Z_G} \cdot V_s(p) \cdot \sum_{k=0}^{N} \left[(T_{ak} + p \cdot T_{bk}) \mathrm{e}^{-\tau_k \cdot p} \right] \tag{6}$$

with the first ten time-delays (if we are interested in $t \leq \frac{2 \cdot 1}{v}$, we can consider only the first ten delays):

$$\begin{aligned}
\tau_0 &= 0; \qquad \tau_1 = 2\frac{d_1}{v}; \qquad \tau_2 = 2\frac{d_1}{v} + 2\frac{L_f}{v_f}; \qquad \tau_3 = \frac{d_1+d_2}{v} + \frac{L_f}{v_f} \\
\tau_4 &= 2\frac{l}{v} + 2L_f \cdot \delta; \qquad \tau_5 = 2\frac{l}{v} + L_f \cdot \delta \qquad \tau_6 = 2\frac{l}{v} \\
\tau_7 &= \frac{4l-2d_2}{v} + 2L_f \cdot \delta; \qquad \tau_8 = \frac{6l-4d_2}{v} + L_f \cdot \delta; \\
\tau_9 &= \frac{4l-2d_2}{v} + L_f \cdot \delta; \qquad \tau_{10} = \frac{4l+d_1-3d_2}{v} + L_f \cdot \delta \\
C_1 &= \frac{L_m}{Z_{cG}} + C_m Z_{cR}; \qquad C_2 = C_m Z_{cR} - \frac{L_m}{Z_{cG}}; \qquad C_3 = \frac{L_{m_f}}{Z_f} + C_{m_f} Z_{cR}; \qquad C_4 = C_{m_f} Z_{cR} - \frac{L_{m_f}}{Z_f} \\
T_{0a} &= \frac{v \cdot C_1}{4} \qquad T_{0b} = 0 \\
T_{1a} &= -\frac{v \cdot C_1}{4} + \frac{C_3}{2\kappa}(1+\rho_f) \qquad T_{1b} = \frac{d_1 \cdot C_2}{2}\rho_f \\
T_{2a} &= \frac{C_4}{2\delta}\rho_f(1+\rho_f) \qquad T_{2b} = -\frac{d_1 \cdot C_2}{2}\rho_f(1-\rho_f^2) \\
T_{3a} &= \frac{v \cdot C_1}{4}(1-\rho_f^2) - \frac{C_3}{2\kappa}(1+\rho_f) - \frac{C_4}{2\delta}\rho_f(1+\rho_f) \qquad T_{3b} = 0 \\
T_{4a} &= -\frac{C_4}{2\delta}\rho_{lG}(1+\rho_f)(1-\rho_f^2) \qquad T_{4b} = \frac{d_1 \cdot C_2}{2}\rho_{lG}(1-\rho_f^2)^2 \\
T_{5a} &= \frac{C_4}{2\delta}(1+\rho_f)(\rho_{lG}(1-\rho_f^2)-\rho_{FE}) - \frac{C_3}{2\kappa}\rho_{FE} \cdot \rho_f(1+\rho_f) + \frac{v \cdot C_1}{4}(1-\rho_f^2)\rho_{lG}(\rho_{FE}+\rho_f) - \frac{v \cdot C_1}{4}(1-\rho_f^2) \\
T_{5b} &= \frac{(l-d_2)C_2}{2}(\rho_{FE}+\rho_{lG})(1-\rho_f^2) \\
T_{6a} &= \frac{v \cdot C_1}{4}\rho_{FE}(\rho_{NE}+\rho_f) + \frac{C_4}{2\delta}\rho_{FE}(1+\rho_f) \qquad T_{6b} = \frac{d_1 \cdot C_2}{2}\rho_{FE} \\
T_{7a} &= -\frac{C_4}{2\delta}\rho_{lG}^2 \cdot \rho_f(1-\rho_f^2)(1+\rho_f) \qquad T_{7b} = \frac{d_1 \cdot C_2}{2}\rho_f \cdot \rho_{lG}^2(1-\rho_f^2)^2 \\
T_{8a} &= \frac{C_3}{2\kappa}(1+\rho_f)\rho_{FE} \cdot \rho_f \cdot \rho_{lG}^2(1-\rho_f^2) \qquad T_{8b} = 0 \\
T_{9a} &= \frac{C_3}{2\kappa}\rho_{lG} \cdot \rho_{FE}(1+\rho_f)(1-\rho_f^2) \qquad T_{9b} = 0 \\
T_{10a} &= \frac{C_4}{2\delta}\rho_{lG}^2 \cdot \rho_f(1+\rho_f)(1-\rho_f^2) \qquad T_{10b} = 0
\end{aligned}$$

We can now transpose the result given in (7) in the Time Domain:

$$V_{NE}(t) = \frac{2 \cdot R_{NE}}{R_{NE}+Z_R} \cdot \frac{Z_G}{R_{0G}+Z_G} \cdot \sum_{k=0}^{N}\left[T_{ak} \cdot V_s(t-\tau_k) + T_{bk}\frac{dV_s}{dt}(t-\tau_k)\right] \tag{7}$$

Under the weak coupling assumption, the near-end voltage can be written as a sum of the injected delayed signal and its derivative, whereas we could have expected it to be only a sum of the injected delayed signal as presented in [4]. In the case of a three-conductor line without defect, we could have shown that the near-end voltage is also the superposition of a signal and its derivative. This was done by Paul in [3].

4. SIMULATIONS

In order to illustrate the accuracy of this model, we will compare computed crosstalk results with those obtained with CST MWs. We will consider the case where $l = 1.95m$, $d_1 = 70\,\text{cm}$, $L_f = 5\,\text{cm}$, $R_{0G} = R_{lG} = R_{NE} = R_{FE} = Z_{cG}$ and $V_s(t)$ is a gaussian pulse. The metal is a perfect electric conductor and the relative permittivity of the dielectric is $\epsilon_r = 2.6$. The per-unit-parameters

computed with a Laplace code are:

$$C_G = C_R = 18.39\,\mathrm{pF}\cdot\mathrm{m}^{-1},\ C_m = 0.51\,\mathrm{pF}\cdot\mathrm{m}^{-1},\ L_G = L_R = 644.4\,\mathrm{nH}\cdot\mathrm{m}^{-1},\ L_m = 15.99\,\mathrm{nH}\cdot\mathrm{m}^{-1}$$
$$C_f = 11.81\,\mathrm{pF}\cdot\mathrm{m}^{-1},\ C_{mf} = 0.4674\,\mathrm{pF}\cdot\mathrm{m}^{-1},\ L_f = L_G \text{ and } L_{mf} = L_G.$$

Then $\frac{L_m}{L_G} = 0.0248$ so the weak coupling assumption is checked.

Figure 3 presents a good agreement between the weak coupling model and CST results, both for amplitudes and positions. Indeed the correlation coefficient of this two results is equal to 0.9986. We can notice that the velocity is slightly different between the two results. Besides The characteristic impedance considered by CST is weaker than the one computed with the Laplace code which can explain the differences with the proposed model.

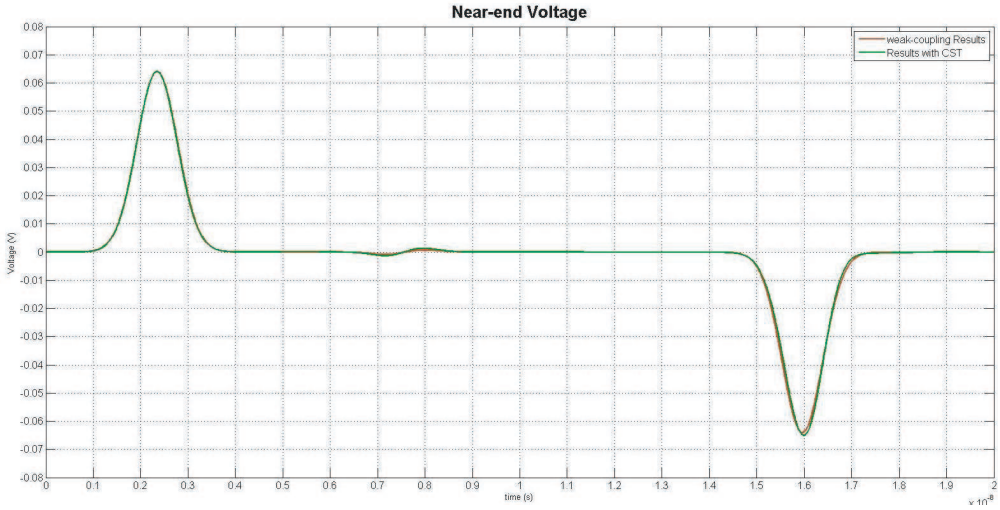

Figure 3: Comparison of the near-end voltage between the weak-coupling model and CST.

5. CONCLUSIONS

We have presented a theoretical model that enables to simulate crosstalk voltages in time domain for a three-conductor line under the weak coupling assumption. We could have extended these results to $(n+1)$-conductor lines where $n > 2$.

This model helps to understand time domain reflectometry results, by explaining the impact of a fault on near-end voltages. Besides it shows a good agreement with the results provided by CST Mws.

This model is based on two strong assumptions which are the weak coupling assumption and the fact that the generator and receptor circuits are supposed to be identical (excepted for the faulty portion) and lossless. As a consequence it can't be used if the conductors are too close from each others, which is often the case in bundles for example. Another model needs to be considered for this kind of structures.

REFERENCES

1. Lelong, A., M. Olivas Carrion, V. Degardin, and M. Lienard, "On line wiring diagnosis by modified spread spectrum time domain reflectometry", *PIERS Proceedings*, 182–186, Cambridge, USA, July 2–6, 2008.
2. Bazzoli, S., "Caractrisation et Simulation de la susceptibilit des circuits intgrs face aux risques d'induction engendrs par des micro-ondes de forte puissance," Ph.D. Thesis, Universitdes Sciences et Technologie de Lille, France, 2005.
3. Paul, C. R., "Solution of the transmission-line equations under the weak-coupling assumption," *IEEE Trans. EMC*, Vol. 44, No. 3, 413–423, 2002.
4. Paul, C. R., *Analysis of Multiconductor Transmission Lines*, John Wiley & Sons, 1994.

A Theoretical Study of Transition Probabilities for Rare Gas Atoms in an Alternating Electric Field

E. V. Koryukina
Tomsk State University, Lenin avenue 36, Tomsk 634050, Russia

Abstract— In this work, the influence of an external electric field on the behavior of transition probabilities between energy levels was investigated, and dependences of these characteristics on frequency and strength of the electric field were obtained. It was found that the transition probabilities and lifetimes of the energy levels in the electric field have a polynomial dependence on the electric field strength, and the higher the electric field frequency is, the bigger the polynomial degree is. The dependences of the transition probabilities and lifetimes on the electric field strength and frequency were investigated for the He, Ne, Ar and Kr atoms.

1. INTRODUCTION

In this paper, the influence of an external electric field on the behavior of transition probabilities between energy levels was investigated, and dependences of these characteristics on frequency and strength of the electric field were obtained. Rare gas atoms under the effect of the circular polarized electric field (electric fields of such polarization are generated in a high-frequency discharge in electrodeless lamps [1] and under laser excitation [2]) were chosen as subjects for study. Rare gases are widely used in plasma physics, therefore, this problem is topical both from a theoretical point of view and for practical applications of the calculation results. In particular, the calculated probabilities are necessary at a solution of the population density balance equations and at calculation of the spectral line intensities and lifetimes of the energy levels in the electric field [3].

In the circular polarized electric field, the non-stationary Schrödinger equation, the energies and wave functions of atoms in the electric field are determined from, can be reduced to the stationary one. In traditional works, the stationary Schrödinger equation is solved in the framework of perturbation theory [4]. However, it is much more convenient to solve this equation by the method of the energy matrix diagonalization [5]. This method, free from limitations inherent in perturbation theory, is suitable for a wide range of frequency and strength of the electric field. The wave functions and energies of atoms in the electric field obtained from the energy matrix diagonalization are used for calculating the transition probabilities between the Stark levels. And then the lifetimes of the Stark levels are calculated using the obtained transition probabilities. This theoretical method was realized in a special software package written in FORTRAN.

By virtue of calculation complexity, a systematic study of dependences of the Stark effect, transition probabilities and lifetimes on frequency and strength of the electric field was not performed to the present day. This work makes up this deficiency.

2. CALCULATION METHOD

In a circular polarized electric field, the non-stationary Schrödinger equation is written as

$$i\frac{\partial\psi_n(\vec{r},t)}{\partial t} = \left(\widehat{H}_0(\vec{r}) - eF(x\cos\omega t \pm y\sin\omega t)\right)\psi_n(\vec{r},t), \tag{1}$$

where ψ_n is the wave function of the n-th state of the system, $\widehat{H}_0(\vec{r})$ is the unperturbed Hamiltonian, and the operator $-eF(x\cos\omega t \pm y\sin\omega t)$ describes perturbation induced by the interaction of an atom with a circular polarized field of frequency ω and strength F. To go to the stationary Schrödinger equation, it is necessary to use the rotating-wave approximation [6].

In order to go to a rotating coordinate system rotating around the Z-axis with the frequency ω, let us introduce a wave function in this coordinate system

$$\varphi(\vec{r},t) = \exp\left(i\omega t\widehat{J}_z\right)\psi(\vec{r},t), \tag{2}$$

where $\widehat{J}_z$ is the z-component of the total angular momentum operator. On substituting Eq. (2) in Eq. (1), we get

$$i\frac{\partial\varphi(\vec{r},t)}{\partial t} = \widehat{Q}\varphi(\vec{r},t), \quad \widehat{Q} = \left(\widehat{H}_0 - \omega\widehat{J}_z \pm F\widehat{D}_x\right). \tag{3}$$

As seen from Eq. (3), the operator $\widehat{Q}$ is time-independent. Hence, in the rotating-wave approximation, it is possible to go from the non-stationary Schrödinger Eq. (1) to the stationary one, and we get

$$\widehat{Q}\varphi(\vec{r}) = \varepsilon\varphi(\vec{r}), \quad \varphi(\vec{r},t) = \exp(-i\varepsilon t)\varphi(\vec{r}) \tag{4}$$

where $\widehat{Q}$ is the operator of energy of an atom in the electric field, and ε and $\varphi(\vec{r},t)$ are the energy and wave function of the atom in the electric field in the rotating coordinate system. Instead of a solution of the Schrödinger equation within perturbation theory, it is much more convenient to solve this equation by the method of the energy matrix diagonalization [5]. It was shown in [5] that the wave functions and energies of the atom, being solutions to the Schrödinger Eq. (4), are determined from diagonalization of the energy matrix with elements

$$Q_{mn} = E_n^{(0)}\delta_{mn} - \omega\langle\varphi_m^{(0)}(\vec{r})\left|\widehat{J}_z\right|\varphi_n^{(0)}(\vec{r})\rangle \pm F\langle\varphi_m^{(0)}\left|D_x\right|\varphi_n^{(0)}\rangle, \tag{5}$$

where $\varphi_n^{(0)}$ and $E_n^{(0)}$ are the wave function and energy of the n-th state of an atom in the absence of external electric field, and D_x is the x-component of the dipole transition operator. Diagonalization of the energy matrix with elements (5) gives a set of wave functions and an energy spectrum for the n-states of the atom in the electric field. Upon diagonalization of the $\widehat{Q}$ matrix, we get the energies ε_n and wave functions as

$$\varphi_n(\vec{r},t) = e^{-i\varepsilon_n t}\sum_k C_{nk}\varphi_k^{(0)}(r) \tag{6}$$

for the n states of the atom in the external electric field in the rotating coordinate system. The coefficients C_{nk} in the wave functions (6) depend on the frequency and strength of the external electric field. To find the average energies of the atom in the initial coordinate system, it is necessary to perform averaging over the oscillation period. Upon averaging, the average energy of the system in the electric field in the initial coordinate system is written in the following form

$$\bar{E}_n = \langle\psi_n(\vec{r},t)\left|H(\vec{r},t)\right|\psi_n(\vec{r},t)\rangle = \varepsilon_n + \omega\langle\varphi_n(\vec{r})\left|\widehat{J}_z\right|\varphi_n(\vec{r})\rangle. \tag{7}$$

It follows from Eq. (7) that $\bar{E}_n$ is time-independent. The matrix elements of the D_x operator are calculated as follows

$$\begin{aligned}\langle\varphi_m^{(0)}\left|D_x\right|\varphi_n^{(0)}\rangle &= \langle\gamma JM\left|D_x\right|\gamma' J'M'\rangle \\ &= \frac{(-1)^{J-M}}{\sqrt{2}}\left[\begin{pmatrix} J & 1 & J' \\ -M & -1 & M'\end{pmatrix} - \begin{pmatrix} J & 1 & J' \\ -M & 1 & M'\end{pmatrix}\right]\langle\gamma J\left\|D\right\|\gamma' J'\rangle\end{aligned} \tag{8}$$

where the reduced matrix elements $\langle\gamma J\left\|D\right\|\gamma' J'\rangle$ are calculated depending on a coupling scheme [5].

The wave functions and energies derived from diagonalization of the $\hat{Q}$ matrix are used for the calculation of the probabilities of spontaneous transitions in the electric field. In the dipole approximation, the total transition probability of a radiation polarized with respect to the $\mathbf{e}_q$ direction and averaged over all possible orientations in the vector $\mathbf{D}$ space is calculated using the formula

$$A_{nm} = \frac{4\omega_{nm}^3}{3\hbar c^3}\sum_q |\langle\Psi_n|D_q|\Psi_m\rangle|^2, \tag{9}$$

where D_q are the cyclic components of the dipole moment operator of an atom. The wave functions Ψ_n and Ψ_m are determined from diagonalization of the $\widehat{Q}$ matrix with the matrix elements (5). On substituting the wave functions Ψ_n and Ψ_m to Eq. (9) and using the Wigner-Eckart theorem, the expression for the probability of the $JM \to J'M'$ transition between the Stark energy levels takes on the form

$$A(JM \to J'M') = \frac{4\omega_{JM,J'M'}^3}{3\hbar c^3}\left|D_{JM,J'M'}\right|^2,$$

$$|D_{JM,J'M'}|^2 = \sum_q\left|\sum_{ij} C_i^{(JM)^*}C_j^{(J'M')}(-1)^{J_i-M_i}\begin{pmatrix} J_i & 1 & J_j \\ -M_i & q & M_j\end{pmatrix}\cdot\langle\gamma_i J_i||D||\gamma_j J_j\rangle\right|^2, \tag{10}$$

where $C_i^{(JM)}$ and $C_j^{(J'M')}$ are the expansion coefficients from Eq. (6) and $\omega_{JM,J'M'}$ is the frequency of the $JM \to J'M'$ transition. The probabilities of the $J \to J'$ transitions between energy levels and the J-state lifetime τ_J of an atom in the electric field are calculated using the formulas

$$A(J \to J') = \frac{1}{2J+1} \sum_{MM'} A(JM \to J'M'), \quad \tau_J = \frac{1}{\sum\limits_{J'} A(J \to J')}. \tag{11}$$

As seen from the above formulas, our theoretical method is free from limitations inherent in perturbation theory and allows us to simulate emission spectra and calculate the transition probabilities of any atoms in a wide range of electric field strengths and frequencies.

This theoretical method was realized in special software package written in FORTRAN. Input data for software package are the unperturbed energy level positions, the frequency ω and strength F of the electric field. Output data obtained at sequential passing of the software blocks are following: wave functions of an atom, spectral-line shifts and splitting (the Stark effect), transition probabilities, and Stark-level lifetimes in the electric field.

3. RESULTS AND DISCUSSION

In the present work, the electric fields of strength up to 10 kV/cm were considered. The calculations were carried out for different frequencies of the electric fields generated by real excitation sources, namely, $\omega = 100$ MHz (a high-frequency discharge HFD) [1], $\omega = 151.91 \cdot 10^3$ MHz (NH_3-laser), $\omega = 243.52 \cdot 10^4$ MHz (HCN-laser), $\omega = 241.813 \cdot 10^5$ MHz (CO_2-laser) and $\omega = 283.005 \cdot 10^6$ MHz (Nd-laser) [2]. The calculations were performed with the LS coupling scheme for the He atom, and the JL coupling scheme for the rest rare gas atoms.

Our calculations have shown that the extent of the energy level interactions has significant effect on the behavior of the transition probabilities in the electric field. As follows from Eq. (10), this influence is specified by the transition frequency $\omega_{JM,J'M'}$ in an explicit form and the matrix elements $D_{JM,J'M'}$ in an implicit form. It was found that for the transitions with J, $J' \leq 1$ the behavior of spectral lines and transition probabilities essentially depends on the core type (for the Ne, Ar, and Kr atoms). The probabilities of the $n_1 l_1'[K_1]J_1M_1 \to n_2 l_2'[K_2]J_2M_2$ and $n_1 l_1[K_1]J_1M_1 \to n_2 l_2[K_2]J_2M_2$ transitions demonstrate completely different behavior at the changes in both strength and frequency of the external electric field. The reason for such dissimilarity is a difference in the degree of mixture of energy levels in the electric field. The probabilities of the $n_1 l_1'[K_1]J_1M_1 \to n_2 l_2'[K_2]J_2M_2$ transitions (where the mixture of the energy levels is weak) are practically independent of the changes in the electric field frequency and strength, and they are equiprobable for the $M \to \pm M'$ transitions. The probabilities of the $n_1 l_1[K_1]J_1M_1 \to n_2 l_2[K_2]J_2M_2$ transitions (strong energy level interactions) can both decrease and increase with the electric field strength and frequency. A strong interaction of the energy levels leads to unequiprobable probabilities of the $n_1 l_1[K_1]J_1M_1 \to n_2 l_2[K_2]J_2M_2$ transitions. For the transitions with J, $J' \leq 1$, a polynomial dependence of $A(J \to J')$ on the electric field strength was revealed (Fig. 1), and it was found that a degree of the polynomial increases with the electric field frequency (Fig. 2). If the mixture of the energy levels is strong, the polynomial dependence is broken (Fig. 3).

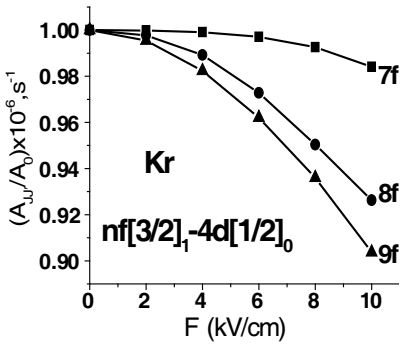

Figure 1: Transitions probabilities for the Kr atom ($\omega = 100$ MHz).

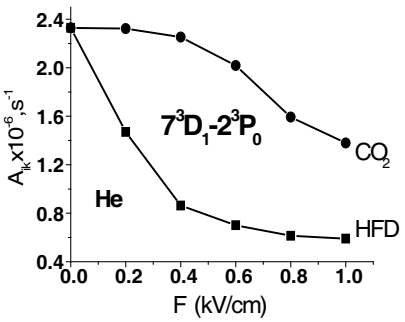

Figure 2: Transitions probabilities for the He atom with different ω.

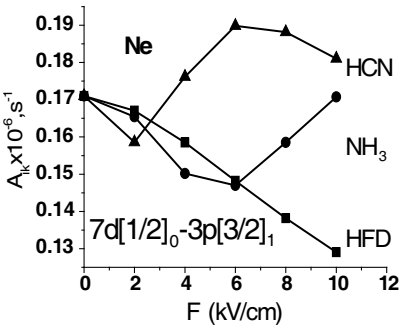

Figure 3: Transitions probabilities for the Ne atom with different ω.

As for the transitions with J, $J' > 1$, the interaction of the energy levels increases in comparison with the above considered case. This increase leads to the vanishing of the difference in the behavior

of probabilities for the transitions with a different core. And now the probabilities of the transitions from the M-state to different M'-states are unequiprobable in any case (Fig. 4).

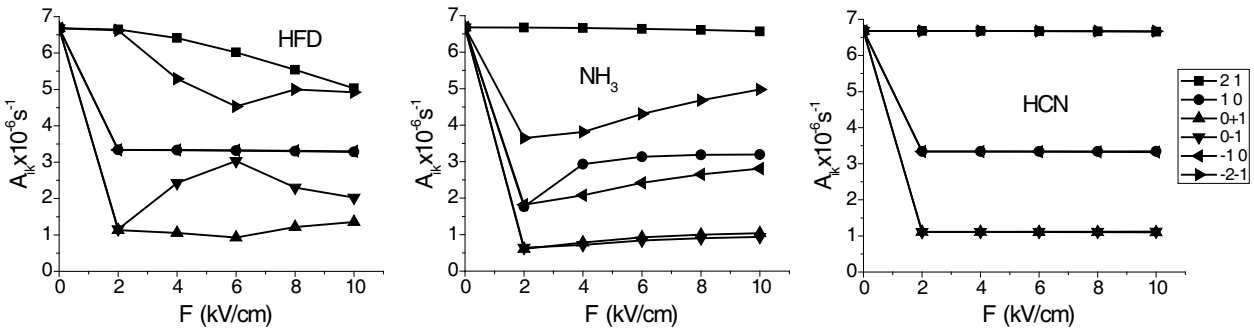

Figure 4: The dependence of the transition probabilities on the frequency and strength of the electric field for the $4d[5/2]_2 - 3p[3/2]_1$ spectral line of the Ne atom.

It follows from Eq. (11) that the dependence of the lifetimes of the atomic energy levels τ_J on strength and frequency of the electric field is entirely specified by the behavior of the transition probabilities $A(J \to J')$.

4. CONCLUSIONS

Based on the calculation results, it was shown that the interaction of atomic energy levels in the electric field plays a key role in the behavior of transition probabilities. This interaction leads to anomalies in the emission spectra and unequiprobable filling of atomic levels. Moreover, it was found that the transition probabilities have a polynomial dependence on the electric field strength, and the higher the electric field frequency is, the bigger the polynomial degree is. The polynomial dependence also is broken, if the energy levels have a strong interaction in the electric field.

The obtained theoretical results allow us to explain the processes taking place in plasma, clarify the mechanism of filling of the excited levels and reasons for changes in spectral line intensities. The transition probabilities can be used as input data for calculations of lifetimes, spectral line intensities, and for solution of the population density balance equations. In addition, the calculation results are very useful for plasma diagnostics. And, finally, the revealed regularities can be used for construction of new devices.

ACKNOWLEDGMENT

This work is continuation of the investigations initiated by grant INTAS No. 01-0200.

REFERENCES

1. Revalde, G. and A. Skudra, "Optimization of mercury vapour pressure for high-frequency electrodeless light sources," *J. Phys. D: Appl. Phys.*, Vol. 31, 3343–3348, 1998.
2. Prohorov, A. M., *A Handbook of Lasers*, v. 1, Soviet Radio, Moscow, 1978.
3. Denisova, N., G. Revalde, A. Skudra, et al., "High-frequency electrodeless lamps in argon-mercury mixtures," *J. Phys. D: Appl. Phys.*, Vol. 38, No. 17, 3275–3784, 2005.
4. Delone, N. B. and V. P. Krainov, *Atoms in Strong Light Fields*, Atompress, Moscow, 1984.
5. Koryukina, E. V., "Modelling of the dynamic Stark effect and calculation of the transition probabilities for an Ar atom," *J. Phys. D: Appl. Phys.*, Vol. 38, No. 17, 3296–3303, 2005.
6. Bunkin, F. V. and A. M. Prohorov, "Excitation and ionization of atoms in a strong radiation field," *Zh. Eksp. Teor. Fiz.*, Vol. 46, No. 3, 1091–1097, 1964 (in Russian).

Influence of Carbon Coatings on the Breakdown Threshold for an S-band Pillbox Output Window

Fang Zhu, **Zhaochuan Zhang**, **and Jirun Luo**
R & D Center for High Power Microwave Device, Institute of Electronics
Chinese Academy of Sciences, Beijing 100190, China

Abstract— On the basis of the results of X-ray photoelectron spectrum (XPS) detection, theoretical analyses and numerical simulations, the failure mechanism of an S-band pillbox output window applied in high average power klystron was discussed. The influences of high order cylindrical guide modes on the electric breakdown in the window were investigated, which shows that the TM_{11} mode existing on the surface of the window ceramic disk may decrease the electric breakdown threshold and power capacity of the output window.

1. INTRODUCTION

Output window is a key component located at the output port of a klystron. It is generally used to separate the high vacuum of the device from atmosphere environment and to transmit microwave power to the load. However, in the developing process of the klystron, the output window may be cracked with the increase of the output power and results in the failure of the vacuum seal, which makes that the further development of the higher power level and higher efficiency for vacuum microwave devices confronts puzzledom.

The electric field distribution inside the alumina ceramic disk has great effect on the failure mechanism of the output window, especially for its breakdown. A number of the experimental and theoretical works on this issue has been done in recent years [1–4]. In this paper, the failure mechanism of the s-band pillbox output window applied in a high average power klystron was studied. The electric fields distribution pattern was calculated to analyze the effect on the window breakdown. On the basis of the results of XPS detection, the organic matter pollution on the vacuum-side surface of the window ceramic disk because of the surface evaporation of the cathode and collector of the klystron was discussed, which may result in the inhomogeneity of the electromagnet energy on the disk. These problems may decrease the electric breakdown threshold of the output window, cause its local over-heating, and thus add the risk of its breakdown.

2. CHARACTERISTICS AND SURFACE ANALYSES OF THE CRACKED WINDOW DISKS

The crackles of all the cracked window disks discussed here were always along the diameter of the disk on the H-plane, and there were two fawn elliptic stains located symmetrically on the vacuum-side surface. The direction of the crackles was in good agreement with that of the maximum E-field of the TE_{11} cylindrical guide mode, and there was no obvious pollution on the air-side surface of it. A typical photograph of the cracked window disks is shown in Figure 1.

The polluted area on the vacuum-side surface and that on the air-side surface of the cracked disks were sampled and detected with XPS technique, and the typical XPS results are shown in Figures 2(a) and 2(b). The x-axis denotes the binding energy of the different kinds of the elements

Figure 1: Photograph of a cracked window disk on the vacuum side.

on the surface, and the y-axis denotes the number of photoelectrons indicating the element content. It has been found that there are the same elements, C, O and Si on both sides of the sample, but there is obvious difference on the content: the content of the oxygen on the atmosphere side is higher than that of on the vacuum side, and the peak value of the carbon element in Figure 2(b) was over two times of that in Figure 2(a), which shows that there is more carbon on the vacuum-side surface than that on the air-side surface. The silicon is an additive in the alumina ceramic sintering. The XPS results show that the elliptic stains come from organic matter pollution, and the ingredient of the organic matter is mainly carbon, whose thickness is in the range of nanometers.

Based on the XPS detection results of five cracked window disks on the vacuum-side surface, the content of carbon element of the five samples was compared. As seen in Figure 3, the higher the content of carbon, the lower the output average power cracking the window. When a klystron enduring over 50kW average power was damaged because of the other component malfunction, no stain was found on its window disk surface. The above-mentioned results show that the thin film of the carbon deposited on the vacuum-side surface of the disk has an obviously negative influence on the breakdown threshold of a pillbox output window.

3. ELECTROMAGNETIC SIMULATION AND ANALYSES

Figure 4 is the schematic of an S-band pillbox window discussed here. The cold testing shows that the voltage standing wave ratio (VSWR) of the pillbox window discussed here is under 1.1. It has well been known that the VSWR of the pillbox window obtained with conventional cold testing can just show the effect of the reflection of the transverse electric field component on electromagnetic wave propagation and is irrelevant to that of the longitudinal electric field component which may exist on the ceramic disk surface. In fact, high-order modes containing longitudinal component may be excited in the vicinity of the window disk by the input TE_{10} rectangular guide mode because of the sharp change of the boundary condition [5, 6].

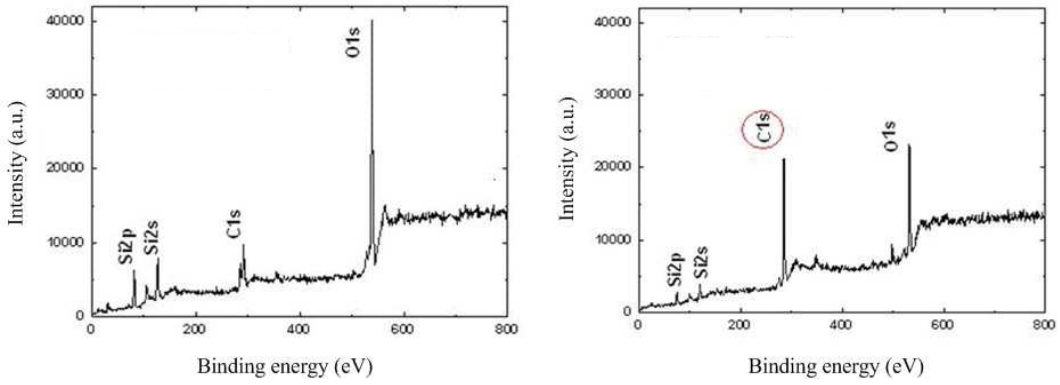

(a) Atmosphere Side (White Surface) (b) Vacuum Side (Yellow Surface)

Figure 2: Typical XPS results of the surfaces of cracked window disk sample.

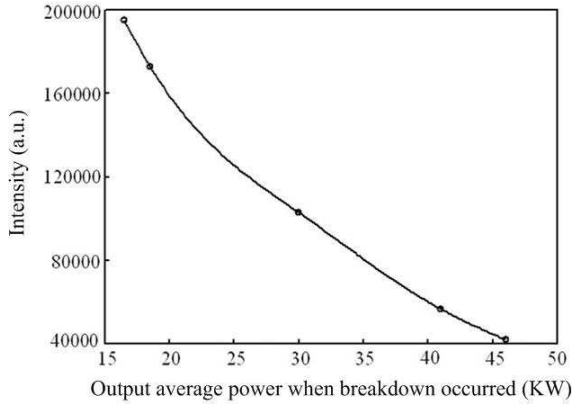

Figure 3: Correspondence between carbon content and output power when breakdown occurred.

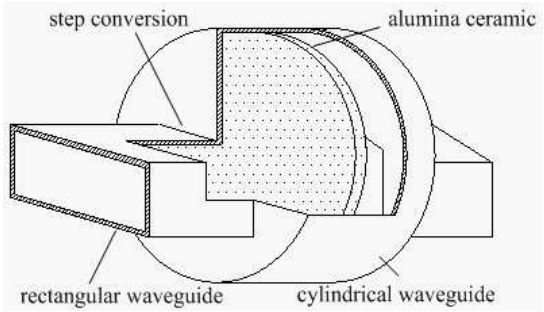

Figure 4: The schematic diagram of an S-band pillbox RF window.

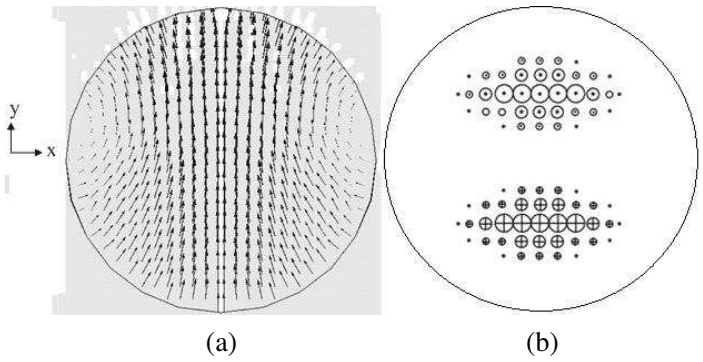

Figure 5: Electric field along surface: (a) transverse-component TE_{11} (b) longitudinal-component TM_{11}.

On the basis of the model of the pillbox output window (Figure 4), the electric field distribution pattern in the model has been calculated to analyze its effect on the electric breakdown in the output window by a three-dimensional numerical electromagnetic calculation software, MAFIA [14]. The simulations show that the phase difference between the transverse and the longitudinal component of the electric field on the window disk surface is $\pi/2$ when their amplitudes are all maximum. The electric field distributions are shown in Figures 5(a) and 5(b) when the transverse and longitudinal component of it on the window disk surface is maximum. As seen in Figure 5(a), the electric field is symmetrical about the y-axis, and its direction is parallel to the disk surface. The electric field amplitude reduces from the center to the fringe of the disk, with the maximum field intensity of 466 V/m at the point of $x = 0$, $y = 0$. The appearance of the field is similar to that of the TE_{11} cylindrical guide mode. As seen in Figure 5(b), the electric field is anti-symmetrical about the x-axis, and its direction is perpendicular to the surface. The longitudinal electric field is concentrated on two separate regions, $6.5\,\text{mm} \leq |y| \leq 29.5\,\text{mm}$, with the maximum field amplitude of 368 V/m at the points of $x = 0$, y=$\pm$22.5 mm. The appearance of the field is similar to that of the TM_{11} cylindrical guide mode.

It can be seen from the above results that the electric field existing on the disk surface are mainly determined by the TE_{11} mode and the TM_{11} mode. Usually, a proper size of the rectangular guide is chosen to avoid high order modes. However, the TM_{11} mode is likely to be excited or oscillated in the cylindrical guide. The numerical calculation and the sweep-frequency testing all show that there is no resonant modes in the window, but the TM_{11} mode and the TE_{11} mode always exist in the window in the operational frequency range of $f_0 \pm 35\,\text{MHz}$. So it can be speculated from the simulations that the TE_{11} and the TM_{11} are the two main modes in the window. The former is the operating mode, the amplitude of the latter on the disk surface is maximum and reduces with the distance away from the disk. The maximum electric field amplitude of the TM_{11} mode is 20% lower than that of the TE_{11} mode.

By comparing the photo of the cracked window disk in Figure 1 with the simulation results, it has been seen that the maximum value of the longitudinal electric field component of the TM_{11} mode is distributed on the almost same zones as the two fawn elliptic stains observed on the disk surface, and the crackle appearing on the disk is in good agreement with that of the direction of the maximum electric field of TE_{11} mode. That is the window breakdown is closely relative to the maximum field intensity and organic matter pollution. The reason leading to this phenomenon may be the ionization and deposition of the organic matter molecules on the vacuum-side surface of the ceramic disk. Under the condition of the high-power operation of the window, the organic matter molecules dissociating on the vacuum-side surface were ionized due to strong transverse electric field action, and in the 1/4 RF period the electrons and ions generated by the ionization might move toward the vacuum-side surface and were deposited on it because the transverse electric field decreased and the longitudinal electric field increased gradually. When the transverse field became strong again in the next 1/4 RF period, more electrons and ions were produced and deposited on the surface. This process was repeated, and a large amount of organic matter would be accumulated on the vacuum-side surface. The source of the organic matter might be the surface evaporation of the surface coating materials of the cathode and the collector in the klystron. These materials, such as TaC, were absorbed on the vacuum-side surface of the window disk, and eventually form the organic matter pollution. The maximum zones of the longitudinal electric field are also the

zones where the ionization is the most intensive and the deposition of the organic matter is the maximum, so the pollution were almost concentrated on the two specified zones on the ceramic disk.

The thin film of organic matter pollution will significantly influence the surface performance of the ceramic disk, for example, increasing the RF losses of ceramic dielectric and reducing its voltage withstanding capability [16–20], and the more the organic matter deposition, the worse the effect of the pollution on the surface performance of the disk. As the RF power passing through the window increase, the temperature gradient between the center and the fringe of the ceramic will enlarge because of the additional RF loss from the surface polluted by the organic matter, while the decrease of the voltage withstanding capacity will also add the risk of the electric breakdown. The thicker the thickness of the pollution film, the larger the dielectric losses, and the lower the voltage breakdown threshold. That means the more serious the organic matter pollution on the disk surface, the more easily the window disk is cracked.

4. CONCLUSION

From the XPS detection of the cracked window disk samples, it has been found that window breakdown may be relevant to the organic matter pollution deposited on the vacuum-side surface of the window disks. Theoretical analysis and numerical simulation show that there are very intensive electric fields of the TE_{11} mode and the TM_{11} mode on the disk surface, the former causes the ionization of the organic molecules, the latter deposits the organic matter on the ceramic disk surface. The organic matter pollution on the disk surface decreases the voltage breakdown threshold and power capacity of the window, and eventually results in the window breakdown for high average output power operation of the klystron. The theory is in good agreement with the experiments.

REFERENCES

1. Saito, Y., "Surface breakdown phenomena in alumina RF windows," *IEEE Trans. Dielectr. Electr. Insul.*, Vol. 2, No. 2, 243–250, Apr. 1995.
2. Yamaguchi, S., Y. Saito, S. Anami, and S. Michizono, "Trajectory simulation of multipactoring electrons in an S-band pillbox RF window," *IEEE Trans. Nucl. Sci.*, Vol. 39, No. 2, 278–282, Apr. 1992.
3. Kishek, R. A. and Y. Y. Lau, "Multipactor discharge on a dielectric," *Phys. Rev. Lett.*, Vol. 80, No. 1, 193–196, Jan. 1998.
4. Kishek, R. A., Y. Y. Lau, L. K. Ang, A. Valfells, and R. M. Gilgenbach, "Multipactor discharge on metals and dielectrics: Historical review and recent theories," *Phys. Plasmas*, Vol. 5, No. 5, 2120–2126, May 1998.
5. Zhang, Z. C., Y. G. Ding, J. J. Fan, Y. F. Guo, Y. W. Zhang, B. Shen, C. J. Fu, and X. D. Fan, "Development of an S-band 50 kW average power klystron," *IEEE Trans. Electron Devices,* Vol. 56, No. 5, 891–895, May 2009.
6. Torregrosa, G., A. Coves, C. P. Vicente, A. M. Pérez, B. Gimeno, and V. E. Boria, "Time evolution of an electron discharge in a parallel-plate dielectric-loaded waveguide," *IEEE Electron. Devices Lett.*, Vol. 27, No. 7, 629–631, Jul. 2006.

Resistance to Earth of Grounding Grids in Tow-layer Soil Structure Using FEM and GA

P. Hajebi, **A. A. Heidari**, **and A. Mirzaei**
Electrical and Computer Engineering Department, Yazd University, Yazd, Iran

Abstract— Numerical methods such as finite element method (FEM) are the most accurate methods for computing of grounding grid resistance. Generally, these methods are complicate and time consuming for designing a grounding system, therefore, in many cases empirical relations are employed. In this paper, many grounding grids in two-layer soil with different dimensions and soil parameters are simulated using FEM. The FEM results are used to optimize the expressions for estimating the grounding resistance. The expressions are optimized by introducing an objective function and using genetic algorithm (GA). Simulations show that the proposed expressions give accurate results that match well with those obtained by complete FEM modeling of the grounding grids.

1. INTRODUCTION

Design and implementation of a grounding grid is one of the important problems in the power station and electrical and communication installations. Many different numerical and practical methods have been proposed for computing the grounding grid resistance. Numerical methods such as FEM are complicated and time consuming especially in the designing of a grounding grid. Therefore, empirical expressions are employed in many cases. The exact numerical methods can be used for modifying the empirical formulas or suggesting new expressions for calculation of the grounding resistance. Several expressions for vertical electrode grids and horizontal grounding grids buried in uniform soil have been proposed [1–4]. In [5, 6], grounding resistance in multi-layer soils has been investigated. The introduced expressions in [6] for two layer soil have more accurate results than the uniform soil expressions. However, these expressions can be optimized for better matching with the accurate FEM results. In this paper, the relations for computing the grounding grid resistance in two-layer soils are optimized using FEM results by introducing an objective function and using GA.

2. HORIZONTAL GROUNDING GRIDS

Horizontal grounding grids are usually in square or rectangular shapes as shown in Figure 1. Internal meshes are applied in these grids for decreasing the grounding resistance. In this section, a number of reported expressions for computing grounding resistance of these grids in uniform and two layer soils are expressed.

2.1. Grounding Resistance in Uniform Soils

Various expressions are used in the designing process to determine the resistance to earth of earthing grids. The well-known relation was suggested by Laurent [1] has the following form:

$$R = \frac{\rho}{2D} + \frac{\rho}{L} \tag{1}$$

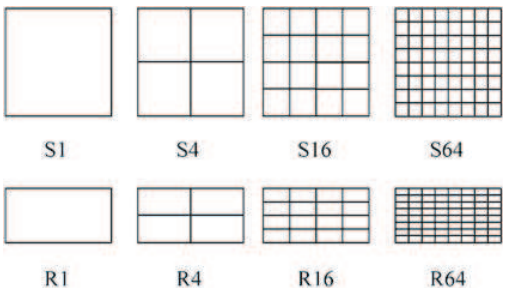

Figure 1: Various shapes of horizontal grounding grids.

where ρ is the soil resistivity and L is the total length of grid conductors. D is the diameter of a round plate covering the same area A as the grid.

$$D = \left(\frac{4}{\pi}\right)^{\frac{1}{2}} A^{\frac{1}{2}} \tag{2}$$

Another empiric expression was proposed in [5], matching well with the results obtained by exact computer modeling for a wide set of square and rectangular grids:

$$R_{Grid} = 0.13\frac{\rho}{\sqrt{A}} \log_{10}\left[\frac{2400}{N}\sqrt{\frac{A}{A_0}}\right] \tag{3}$$

where N is the number of grid meshes and $A_0 = 1\,\mathrm{m}^2$. This expression was obtained by correcting the expression for a round plate covering area A to be adequate for sparse grids, such as single contour or four-mesh grids.

2.2. Grounding Resistance in Two-layer Soils

Uniform soil structure isn't an appropriate model of the soil structure in many practical implementations. The effects of the bottom layer of a two-layer soil can be taken into account using the following general expression [5]:

$$R(\rho_1, \rho_2) = C_{2/1} R(\rho_1) \tag{4}$$

where ρ_1 and ρ_2 are respectively the top and bottom soil layer resistivity. $R(\rho_1)$ designates the resistance to earth of the grid buried in uniform soil with earth resistivity equal to the resistivity of the top soil layer and $C_{2/1}$ is the correction factor where incorporates the effect of the actual two-layer soil structure. Under assumption that the earthing grid is in the top soil layer, the following empirical expression was suggested for $C_{2/1}$ [5]:

$$C_{2/1} = \left(\frac{\rho_2}{\rho_1}\right)^x \tag{5}$$

where:

$$\begin{aligned} x &= 0.14 \log_{10}\left[44N\left(\frac{A}{A_0}\right)^{\frac{1}{2}}\left(\frac{h_0}{h}\right)^2\right] \quad \text{for } \rho_2/\rho_1 < 1 \\ x &= 0.12 \log_{10}\left[3160N\left(\frac{A}{A_0}\right)^{\frac{1}{2}}\right] - 0.2\log_{10}\left(\frac{h}{h_0}\right)\log_{10}\left[1000\left(\frac{A_0}{A}\right)^{\frac{1}{2}}\right] \quad \text{for } \rho_2/\rho_1 > 1 \end{aligned} \tag{6}$$

where h is the thickness of the top soil layer, $A_0 = 1\,\mathrm{m}^2$ and $h_0 = 1\,\mathrm{m}$.

3. OPTIMIZATION OF THE EXPRESIONS USING GA

The above expressions give relatively accurate results, but as mentioned in [6], for some situations these results don't match well with those obtained by complete modeling of the grounding grids. In order to obtain more accurate results, we can optimize the coefficients in these expressions. Equation (6) can be written in the following general form with variable parameters:

$$\begin{aligned} x &= a_1 \log_{10}\left[a_2 N\left(\frac{A}{A_0}\right)^{\frac{1}{2}}\left(\frac{h_0}{h}\right)^2\right] \quad \text{for } \rho_2/\rho_1 < 1 \\ x &= b_1 \log_{10}\left[b_2 N\left(\frac{A}{A_0}\right)^{\frac{1}{2}}\right] - b_3\log_{10}\left(\frac{h}{h_0}\right)\log_{10}\left[b_4\left(\frac{A_0}{A}\right)^{\frac{1}{2}}\right] \quad \text{for } \rho_2/\rho_1 > 1 \end{aligned} \tag{7}$$

These parameters (a_1, a_2, b_1, b_2, b_3, b_4) are in Equation (6) as:

$$a_1 = 0.14,\ a_2 = 44,\ b_1 = 0.12,\ b_2 = 3160,\ b_3 = 0.2,\ b_4 = 1000 \tag{P.1}$$

Our work is to optimize these parameters for increasing the accuracy of the estimated grounding resistance using Equation (7) together with Equations (4) and (5). At first, many horizontal

Table 1: Objective function values for the parameters (P.1) and (P.2).

F_g (Objective Function)	(P.1)	(P.2)
$\rho_2 > \rho_1$	3.3645	1.3876
$\rho_2 < \rho_1$	0.9405	0.7425

Table 2: Comparison of correction factor $C_{2/1}$ computed using (P.1) and optimized parameters (P.2) for the case $\rho_2 < \rho_1$.

Grid	A (m^2)	h (m)	ρ_2/ρ_1	$R_{\rm FEM}(\Omega)$	$C_{\rm FEM}$	$C_{2/1}(P.1)/C_{\rm FEM}$ (%)	$C_{2/1}(P.2)/C_{\rm FEM}$ (%)
S_1	10×10	5	1/3	4.02	0.850	97	113
R_1	10×20	5	1/3	2.7	0.701	115	132
R_4	10×20	5	1/5	1.94	0.701	91	100
S_{16}	25×25	25	1/3	1.59	0.920	87	99
S_{16}	25×25	12.5	1/3	1.37	0.797	91	97
S_{16}	25×25	6.25	1/3	1.09	0.658	101	99
S_{16}	25×25	3.125	1/3	0.83	0.548	110	101
S_{64}	50×50	25	1/3	0.66	0.800	87	89
S_{64}	50×50	12.5	1/3	0.52	0.655	96	91
S_{64}	50×50	6.25	1/3	0.39	0.491	118	103

grounding grids with various parameters in two-layer soil structure are considered and their accurate resistances are obtained using the FEM software. FEM is a numerical method that has more accurate results than the others in the grounding grid computations [6–8]. These FEM results are used in an optimization process using GA and the following objective function:

$$F_g = \sum_{i=1}^{N} \frac{|C_{\rm FEM} - C_C|}{C_{\rm FEM}} \tag{8}$$

where N is the number of grounding grids simulated using FEM , $C_{\rm FEM}$ is the accurate correction factor which is computed based on FEM results and C_C is the calculated correction factor using Equation (7) with substituting in Equation (5). By decreasing F_g, Equation (7) convergences to exact resistance values. Equation (7) has two part for $\rho_1 < \rho_2$ and $\rho_1 > \rho_2$, then optimization is performed in each part separately. To minimize F_g, we use genetic algorithm, in which initial population is 40, probability of crossover is 0.6 and probability of mutation is 0.05.

4. SIMULATION RESULTES

Many horizontal grounding grids with various types (dimensions and number of meshes as shown in Figure 1) are considered and after optimization, the following results are obtained:

$$a_1 = 0.25148,\ a_2 = 3.335,\ b_1 = 0.12369,\ b_2 = 9975.5,\ b_3 = 0.32395,\ b_4 = 1937.2 \tag{P.2}$$

The objective function value for the both initial parameters (P.1) and optimized parameters (P.2) are compared in Table 1. This table shows that the objective function is reduced for optimized parameters significantly. Tables 2 and 3 show detailed results for simulated grids for both cases $\rho_2 < \rho_1$ and $\rho_2 > \rho_1$, respectively. For all cases, the grids buried in depth 0.7 m and $\rho_1 = 100\,\Omega$m. In these tables, $R_{\rm FEM}$ is the accurate grid resistance obtained using FEM and $C_{\rm FEM}$ is the exact correction factor ($C_{2/1}$ in Equation (4)) which is computed from FEM results. Furthermore, the correction factors are computed using Equation (7) with the parameters (P.1) and (P.2) and are shown in Tables 2 and 3 as the percentage of $C_{\rm FEM}$. As it can be observed, the correction factors $C_{2/1}$ computed using optimized parameters (P.2) are more accurate than the ones computed using (P.1), especially for the case $\rho_2 > \rho_1$ and $h > 10$ m.

Table 3: Comparison of correction factor $C_{2/1}$ computed using (P.1) and optimized parameters (P.2) for the case $\rho_2 > \rho_1$.

Grid	$A\,(\mathrm{m}^3)$	$h\,(\mathrm{m})$		$R_{\mathrm{FEM}}\,(\Omega)$	C_{FEM}	$C_{2/1}(P.1)/C_{\mathrm{FEM}}$ (%)	$C_{2/1}(P.2)/C_{\mathrm{FEM}}$ (%)
S_1	10×10	5	5	8.44	1.601	94.9	73
R_1	10×20	5	5	6.64	1.722	94	74
R_4	10×20	5	5	6.29	1.722	106	84
S_{16}	25×25	25	6	2.69	1.075	155	87
S_{16}	25×25	12.5	6	3.37	1.297	152	100
S_{16}	25×25	6.25	6	4.4	1.781	132	101
S_{16}	25×25	3.125	6	5.65	2.510	111	100
S_{64}	50×50	25	6	1.67	1.290	182	112
S_{64}	50×50	12.5	6	2.19	1.490	181	128
S_{64}	50×50	6.25	6	2.82	2.950	105	85

5. CONCLUSIONS

In this paper, the grounding resistance expressions for two-layer soil structure were optimized. Different types of grounding grids in two-layer soil were considered and their resistances were computed using finite element method. Using the FEM results and the introduced objective function, the expressions were optimized using genetic algorithm. The simulation results show that the optimized relations are more accurate than the primary relations.

REFERENCES

1. Vijayaraghavan, G., M. Brown, and M. Barnes, *Practical Grounding Bonding, Shielding and Surge Protection*, ELSEVIER, 2004.
2. Laurent, P. G., "Guide sur le calcul l' éxécution et la mesure des prises de terre," *Rev. Gen. Electr.*, Vol. 53, 455–467, 563–572, 1972.
3. *IEEE Guide for Safety in AC Substation Grounding*, 2000.
4. *IEEE Guide for Measuring Earth Resistivity, Ground Impedance, and Earth Surface Potentials of Ground System*, Institute of Electrical and Electronics Engineers, 1983.
5. Nahman, J. and V. Djordjevic, "Resistance to earth of substation earth electrodes in uniform and two layer-soils," *Electrical Engineering*, Vol. 80, No. 5, 337–342, Springer, 1997.
6. Nahmanm, J. and I. Paunovic, "Resistance to earth of earthing grids buried in multi-layer soil," *Electrical Engineering*, Vol. 88, No. 4, 281–287, Springer, 2006.
7. Qi, L., X. Cui, Z. Zhao, and H. Li, "Grounding performance analysis of the substation grounding grids by finite element method systems by vector finite-element analysis multilayer soil," *IEEE Trans. Magn.*, Vol. 43, No. 4, 262–262, 2007.
8. Silva, V. C., J. R. Cardoso, S. I. Nabeta, M. F. Palin, and F. H. Pereira, "Determination of frequency-dependent characteristics of substation grounding systems by vector finite-element analysis," *IEEE Trans. Magn.*, Vol. 43, No. 4, 1825–1828, 2007.

Analysis for the Stability of Hughes-type Coupled Cavity in an Extended-interaction Klystron

Jian Cui, **Ji Run Luo**, **Min Zhu**, **and Wei Guo**
Institute of Electronics, Chinese Academy of Sciences, Beijing 100190, China

Abstract— The analytical expressions for the beam-wave coupling coefficients and the beam-loaded conductance of Hughes-type coupled cavity with n gaps are derived. The analytical theories show that the beam-wave coupling coefficients and the beam-loaded conductance of the operating mode (2π mode) may be very sensitive to the beam voltage with the increase of the gap numbers. In addition, the stability of the circuit was discussed through calculating the quality factor of three-gap coupled cavity. And the $\pi/3$ mode may self-oscillate due to negative beam-loaded conductance.

1. INTRODUCTION

Extended-interaction klystron (EIK) is invented to achieve a large power, wide frequency bandwidth and high gain in the millimeter/sub-millimeter wave length range. Hughes-type coupled cavity in it is a key technique for enhancing the gain-bandwidth product and power capability. The higher impedance of Hughes-type coupled cavity can compensate for the lower beam conductance, and keep the efficiency high in millimeter-scale circuits. The low electric field intensity on each gap and the enlarged inner surface area of Hughes-type cavities also improve the power-handling capacity [1–5].

However, with the increase of the gap number, the maximum absolute value of the negative beam-loaded conductance becomes greater, which means that the oscillation may appear more easily and is difficult to suppress [6].

2. THRETICAL MODEL

Figure 1 shows a model of Hughes-type coupled cavity. It consists essentially of several re-entrant resonant cavities one by one, coupled to each other by a single slot on the common wall in z direction and by the electron beam which passes through the cavity gaps. The adjacent slot is staggered from side to side across the beam hole.

Expressions for the space-charge wave theory will be derived from three general equations: the wave equation for Maxwell's equations, the continuity of charge and the force equation. By calculating the RF current and the complex power extracted from the beam at gaps, the expressions for the beam-wave coupling coefficients M_n and the beam-loaded conductance G_b of Hughes-type coupled cavity with n gaps can be given by

$$M_N(x) = M_g(x)\left(\frac{\sum V_n e^{jz_n x}}{\sum |V_n|}\right) = M_g(x)M_p(x) \tag{1}$$

$$G_b = \frac{1}{4Z_0}\left(M_N^2(\beta_e - \beta_q) - M_N^2(\beta_e + \beta_q)\right) \tag{2}$$

where M_g is the single gap coupling coefficient, n is the number of gaps, V_n is the voltage amplitude, z_n is the position of the gap relative to the center of the structure. β_e and β_q denote the electronic wave number and the reduced plasma wave number respectively. Z_0 is the beam characteristic impedance.

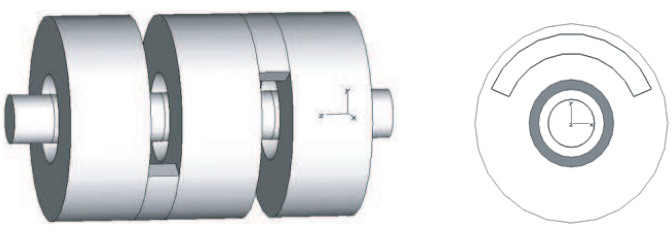

Figure 1: The structure of Hughes-type coupled cavity.

Because of its periodic structure, Hughes-type coupled cavity can be considered as a shorted slow wave circuit at both ends. The field is the superposition of two components, one forward wave and one backward wave. They form a standing wave corresponding to an integer multiple of a half guide wavelength along the structure. A Hughes-type coupled cavity with N gaps gives N resonant cavity mode and $N-1$ resonant slot mode. The amplitudes of electromagnetic fields excited by the beam at the interaction gaps with certain energy stored in the cavities are different for each mode. The beam loaded conductance only represents the capability of the exchange of energy between the beam and electromagnetic fields at the interaction gaps. Nevertheless, the results of the $1/Q_b$ calculation are used to show the modes self-excitation capability and analyze the stability of the structure:

$$1/Q_b = \frac{T}{2\pi}\frac{P}{W} = \frac{V^2 G_b}{\omega W} = G_b(R/Q) \tag{3}$$

Q_b is the beam loaded quality factor, T and ω denote the cycle of the mode and the angular frequency of the wave respectively, P is the beam-absorbed real power. W is the energy stored in the cavity. V is the equivalent voltage on the gaps. R/Q is the characteristic impedance.

Therefore, a $1/Q_b$ with a negative value may lead to the monotron oscillation. The more negative the $1/Q_b$ is, the more easily the mode self-excites. The $1/Q_b$ is important for determining the stability of the interaction cavities, however, no oscillation appears if the total quality factor Q_t is positive, when it is calculated as a parallel combination of Q_b, Q_0 and Q_e:

$$\frac{1}{Q_t} = \frac{1}{Q_0} + \frac{1}{Q_e} + \frac{1}{Q_b} = \frac{1}{Q_c} + \frac{1}{Q_b} \tag{4}$$

Q_0 and Q_e denote the inherent quality factor and the external loaded quality factor respectively. Q_c is the quality factor of the resonator without the beam.

If the power released by the beam is larger than that dissipated in the cavities and the external load, the surplus energy makes the system unstable and gives rise to an oscillation. We shall define a stability parameter S by:

$$S = \frac{1/Q_t - 1/Q_c}{1/Q_c} = \frac{1/Q_b}{1/Q_c} \tag{5}$$

If $S > 0$, the beam obtains energy, for this situation, the system will not oscillate even if there is no external circuit load. If $-1 < S < 0$, the power released by the beam is less than that dissipated in the cavities and the eternal load, the system will remain stable. Otherwise, values of S in the range of $S < -1$ indicate that the system is unstable.

3. CALCULATION RESULTS AND ANALYSES

Figure 2 shows the square of the beam-wave coupling coefficients and the normalized beam-loaded conductance of the 2π mode which are calculated as a function of the beam voltage for values of N from 1 to 7. The square of the coupling coefficient M_g for a typical single-gap cavity moderately rises monotonically with the beam voltage. The larger the value of N, the more rapidly the square of the coupling coefficient M_N varies with beam voltage, which tends to be the same maximum value at certain voltage. Unlike the single-gap, the coupling coefficient of Hughes-type coupled cavity lies with the function M_p which depends on the difference between the longitudinal velocity of the beam and the forward wave phase velocity in the circuit. The difference will directly affect the variation of the beam-wave coupling coefficient. The variation will become more acute with the increase of the gap numbers. As the gap number N tends to be infinite, the coupling coefficient M_N will have an infinite number of discrete spatial Fourier components:

$$\lim_{N\to\infty} M_N(\beta_e) = M_g(\beta_e)\delta(p\beta_e - 2m\pi) = \begin{cases} M_g(\beta_e), & \beta_e = \frac{2m\pi}{p},\ m = 1, 2\ldots \\ 0, & \text{else} \end{cases} \tag{6}$$

Here, p is the spacing between the adjacent gaps. Therefore, with the increase of the gap number the maximum coupling coefficient M_N tends to be M_g at synchronous voltage $V = 20.065\,\text{kV}$. The exhibited asymmetries, particularly at the lowest values of N, mainly result from the interaction with the backward wave.

With the beam voltage from 10 kV to 30 kV, the normalized beam-loaded conductance for a single-gap cavity is nearly unchanged. As expected, the normalized beam-loaded conductance

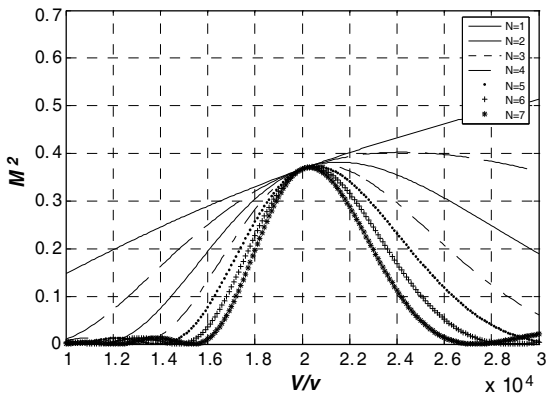

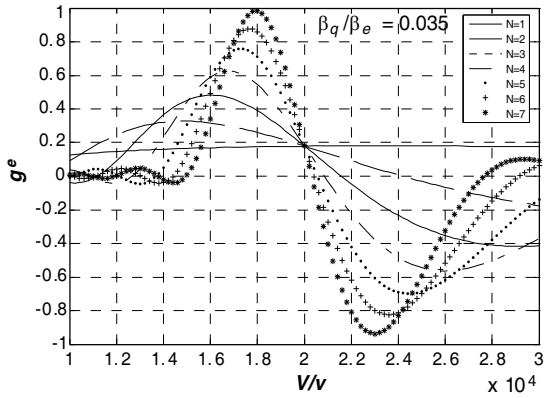

Figure 2: Square of the coupling coefficient M and normalized beam-loaded conductance g_e vs. beam voltage for values of n from 1 to 7.

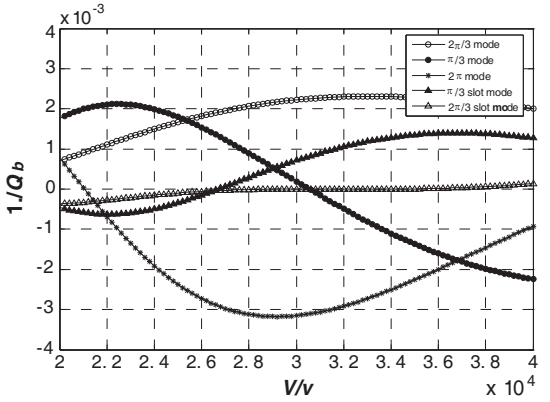

Figure 3: $1/Q_b$ of the mode in three-gap Hughes-type coupled cavity vs. beam voltage.

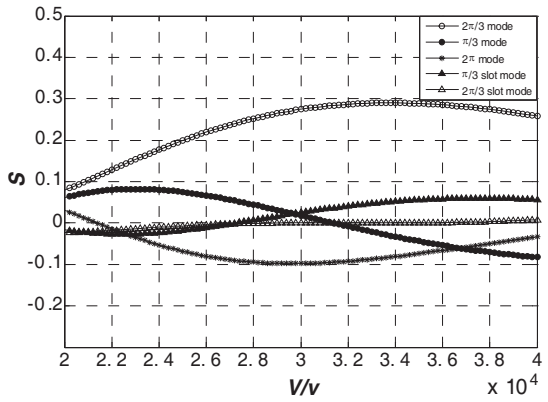

Figure 4: S of the mode in three-gap output circuit vs. beam voltage.

changes greatly and generate a maximum positive value and a negative value on both sides of synchronous voltage for larger values of N. With the increase of the gap number N, both maximum absolute values become greater and the voltages corresponding to them are closer to the synchronous voltage. When the gap number N tends to be infinite, the normalized beam-loaded conductance g_e as well as the coupling coefficient M_N will have an infinite number of discrete spatial Fourier components:

$$\lim_{N\to\infty} g_e = \lim_{N\to\infty} \frac{G_b}{G_0} = \begin{cases} \frac{1}{8}\frac{\beta_e}{\beta_q} M_g^2(\beta_e - \beta_q), & \beta_e - \beta_q = \frac{2m\pi}{p},\ m = 1, 2\ldots \\ -\frac{1}{8}\frac{\beta_e}{\beta_q} M_g^2(\beta_e + \beta_q), & \beta_e + \beta_q = \frac{2m\pi}{p},\ m = 1, 2\ldots \\ 0 & \text{else} \end{cases} \tag{7}$$

Below the synchronous voltage, the longitudinal velocity of the beam is slower than the forward wave phase velocity in the circuit. Under the circumstances, the beam obtains energy from the circuit, which leads to the positive beam loaded conductance. When the beam voltage is greater than the synchronous voltage, the beam loaded conductance is negative.

On the basis of the model of three-gap Hughes-type coupled cavity which is taken as the output circuit, the resonant frequencies and characteristic impedance in the model have been calculated by three-dimensional numerical electromagnetic calculation software, MAFIA. It can be seen from the above analysis that three-gap Hughes-type coupled cavity has three cavity modes and two slot modes: $2\pi/3$ mode, $\pi/3$ mode, 2π mode, $\pi/3$ slot mode and $2\pi/3$ slot mode. Fig. 3 shows the reciprocal of the beam loaded quality factor of the mode versus the beam voltage. With the beam voltage from 21 kV to 40 kV, the $1/Q_b$ of the 2π mode has been negative and much lower than that of other modes around $V = 29$ kV, while the $1/Q_b$ of these modes are all positive. Generally, for the 2π mode there is a matching external load to absorb the energy released by the beam to suppress oscillation. Hence, the 2π mode is chosen as the operating mode. Because the $1/Q_b$ of the $2\pi/3$ mode has been positive and large, the $2\pi/3$ mode is the most stable mode in them. The $1/Q_b$ of the $\pi/3$ mode changes greatest and reach the same negative value as that of the 2π mode

at $V = 37\,\text{kV}$, so the mode is sensitive to beam voltage and easily self-excites. The $1/Q_b$ of the $\pi/3$ slot mode varies moderately and remains positive from 26 kV to 40 kV. And the $1/Q_b$ of the $2\pi/3$ slot mode is always near the horizon. Therefore, these two slot modes are unlikely to self-excite.

Taking account of the external load and inherent ohmic loss, Fig. 4 shows the stability parameter S of the modes calculated as a function of the beam voltage. Because of the small signal condition, the energy released by the beam can be completely by external load, all the modes are stable according to definition (5). Nevertheless, the $\pi/3$ mode is still most likely to self-excite.

4. CALCULATION RESULTS AND ANALYSES

The analytical expressions for the beam-wave coupling coefficients and the beam-loaded conductance of Hughes-type coupled cavity with n gaps in the EIK are derived based on the space-charge wave theory. Theoretical analysis and calculation show that the interaction of the beam with wave depends on the difference between the longitudinal velocity of the beam and the wave phase velocity in the circuit. The difference will directly affect the variation of the beam-wave coupling coefficients and the beam-loaded conductance. The variation will become more acute with the increase of the gap numbers. In addition, the 2π mode is suited as the operating mode, and the $\pi/3$ mode is most likely to self-excite in the three-gap Hughes-type coupled cavity output circuit.

REFERENCES

1. Chodorow, M. and T. Wessel-Berg, "A high-efficiency klystron with distributed interaction," *IRE Trans. on Electron Devices*, Vol. 8, 44–55, January 1961.
2. Golde, H., "A stagger-tuned five cavity klystron with distributed interaction," *IRE Trans. on Electron Devices*, Vol. 8, 192–193, May 1962.
3. Preist, D. H. and W. J. Leidigh, "A two-cavity extended interaction klystron yielding 65 per cent efficiency," *IEEE Trans. on Electron Devices*, 369–373, 1964.
4. Chodorow, M. and B. Kulke, "An extended-interaction klystron: Efficiency and bandwidth," *IEEE Trans. on Electron Devices*, Vol. 13, No. 4, 439–447, April 1966.
5. Preist, D. H. and W. J. Leidigh, "Experiments with high-power CW klystron using extended interaction catchers," *IEEE Trans. on Electron Devices*, Vol. 10, No. 3, 201–211, 1963.
6. Randall, J. P., D. Perring, and V. R. Nuth, "Broadband klystrons," *Proceedings of the Conference on Vacuum Devices*, Vol. 30, No. 11/12, March 25–27, 1980.

Experimental Study on the Microwave Monitoring of Rock Stress and Fracture

Zhongyin Xu[1], **Shanjun Liu**[1], **Lixin Wu**[1, 2], **and Zhe Feng**[1]

[1]Institute for Geo-informatics & Digital Mine Research, Northeastern University, Shenyang, China
[2]Academe of Disaster Reduction and Emergency Management, Beijing Normal University
Beijing, China

Abstract— Recent years many authors reported thermal anomaly change around epicenter before earthquake. Some researchers tried to predict the earthquake based on the analysis on the temperature anomaly feature by using satellite thermal infrared data. However the infrared radiation can not pass through the thick-layer cloud, so as to hardly achieve the earthquake monitoring. Microwave is also a kind of thermal radiation and some scholars have found microwave radiation anomaly appearing before earthquake. To explore the feature of microwave emission anomaly before earthquake, a group of physical simulation experiments were carried out. In the experiment, a hydraulic loader (YGA-3000), whose maximum vertical load is 3000 kN, was applied as loading machine for the granite samples. A microwave radiometer was used for microwave emission detection in the loading process of rock. Its detection wavelength is 8 mm, temperature sensibility 0.01°C. The experimental results showed that microwave emission energy changed along with the change of stress. The microwave emission energy varied little in the beginning loading stage, increased in the elastic loading stage, decreased in the plastic loading stage and increased again in the fracturing stage. The AIRT has the close relationship with the load, but the brightness temperature of microwave emission has the close relationship with the AE energy. The microwave emission precursor for rock failure is more obvious than the AIRT precursor. These experiment results indicated that it was possible to use the microwave remote sensing for monitoring the stress variation and fracturing of rock masses, including earthquakes.

1. INTRODUCTION

Remote sensing is becoming an effective method to monitor the anomalous changes associated with earthquake. Gorny et al. [1] first used the remote sensing data (NOAA/AVHRR) to indicate seismic activity of middle Asia region, moreover preliminarily explored the idea and the method to predict earthquake. Afterwards, many authors reported thermal anomaly change around epicenter before earthquake [2–6]. Some researchers tried to predict the earthquake based on the analysis on the temperature anomaly feature by using satellite thermal infrared data [7]. However, infrared radiation can not pass through the thick-layer cloud, so as to hardly achieve the earthquake monitoring in the cloud days. Microwave is also a kind of thermal radiation, but its can pass though the cloud, fog and rain. Some scholars have found microwave radiation anomaly appearing before earthquake [8], and some experimental results have verified that microwave signal changes with the loading of rock samples [9, 10].

To explore further the feature of microwave emission anomaly before earthquake, a group of physical simulation experiments were carried out in this paper. And the relationship between load and microwave emission was studied.

2. MICROWAVE EMISSION DETECTION EXPERIMENTAL FOR LOADING ROCK

2.1. Experimental Design

The typical crustal rock, granite was processed as standard cylindrical samples of diameter 50 mm and length 100 mm. A hydraulic loader (YGA-3000), whose maximum vertical load is 3000 kN, was applied as loading machine for the granite samples, meanwhile the vertical and horizontal strains were measured. A microwave radiometer was used for microwave emission detection in the loading process of rock. Its detection wavelength is 8 mm, temperature sensibility 0.01°C. A modern TIR imaging system, VarioSCAN 3021ST with temperature precision 0.03°C and image resolution 360×240 pixel was applied for the TIR radiation detection and image recording. The TIR imaging system was aligned in level with the rock sample and approximately 1 m away from it. Besides, an acoustic emission (AE) monitoring instrument was applied to detect the AE signal in the loading process of rock samples. The loading was displacement controlled at the rate 0.3 mm/min. In order to minimize environmental effects on the detection of TIR radiation from the rock surface,

a aluminum box was used for enclosing both the rock sample and the load platform. The photo 1 shows the experimental scene.

2.2. Experimental Results

2.2.1. The Variation Feature of Load and Strain

Figures 1(a), (b), (c) and (d) are respectively the load-time curve, vertical strain-time curve, horizontal strain-time curve and AE count-time curve of the rock sample in the loading process. These curves show that the variation process of load and strains can be divided into four stages:

(1) Initial loading stage (0–50 s). In the stage, load increased slowly but the vertical strain increased quickly. The original holes and cracks within the rock were compressed, so the rock sample shrunk.

(2) Elastic loading stage (50–128 s). In the stage, the load and strains increased proportionately, and there was not new crack to be produced. Therefore, there was not AE signal appearing in this

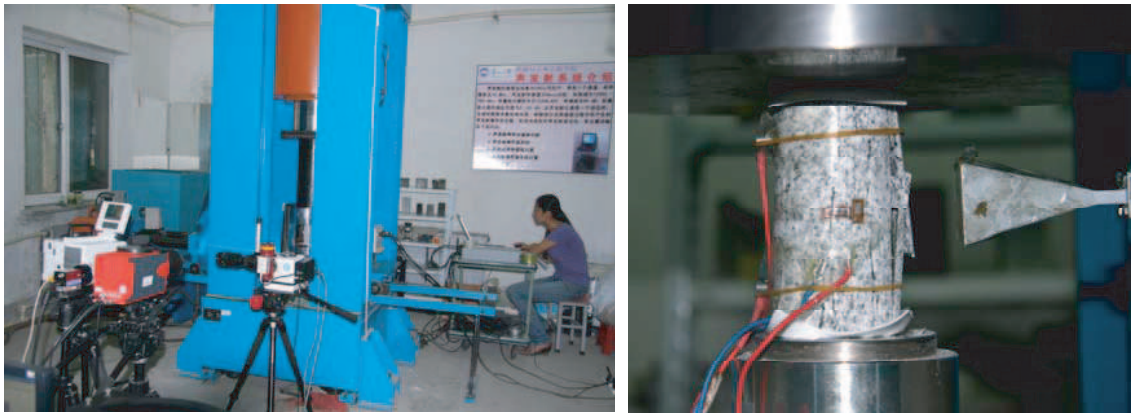

Photo 1 Experimental scene (left) and the sample (right)

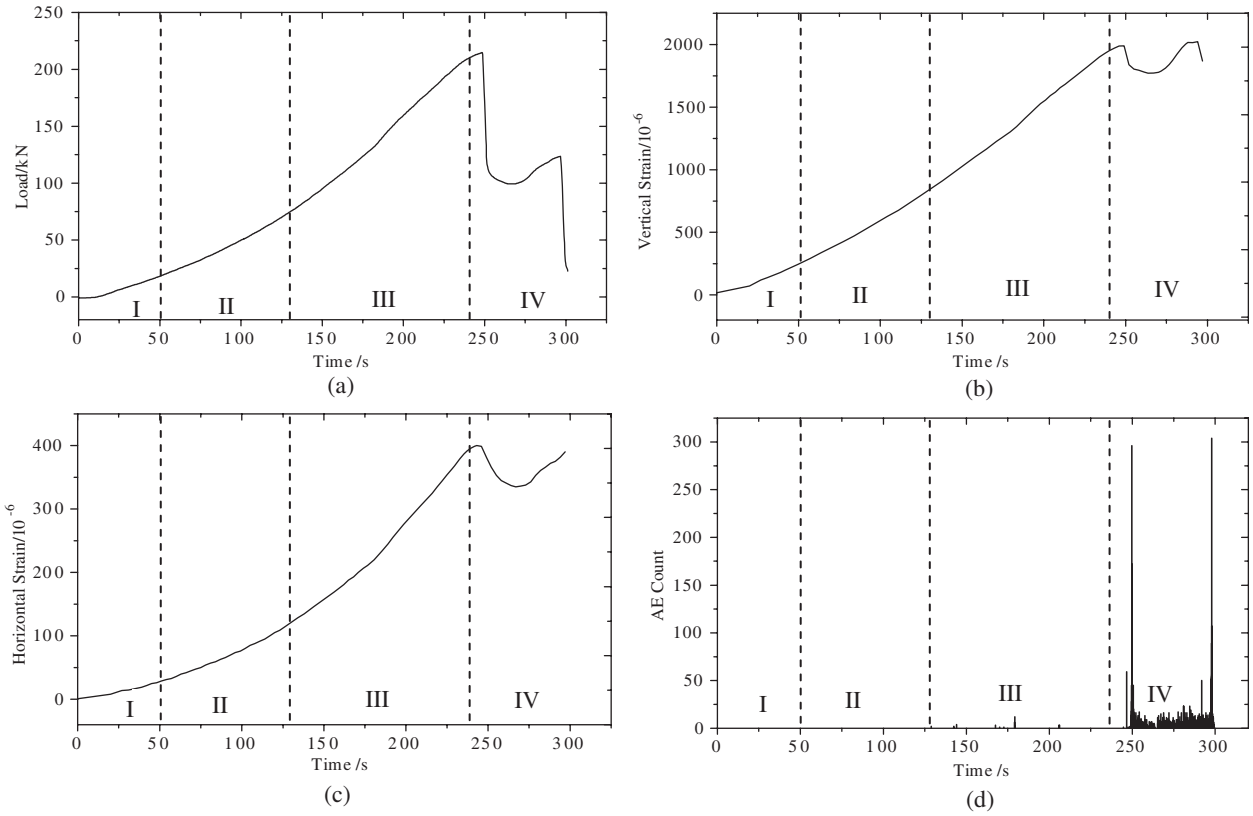

Figure 1: Detection result of several instruments in the loading process of the rock sample. (a) Load-time curve, (b) vertical strain-time curve, (c) horizontal strain-time curve, (d) AE count-time curve.

stage.

(3) Crack appearing stage (129–238 s). In the stage, the horizontal strain increases quickly due to some new cracks producing inside the rock. Therefore, there were AE signals appearing in this stage.

(4) Fracturing stage (238 s–). In the stage, large numbers of cracks appeared and the increase of load became slowly. When the load increased up to peak the sample fractured suddenly. Immediately the load decrease distinctly. After that, the load increased and decreased again, and finally the sample failed.

2.2.2. The Microwave Detection Result

Figure 2 is the brightness temperature-time curve of microwave emission. The figure shows following feature:

(1) In the loading stage I the brightness temperature varied little with the increase of the load.

(2) In the loading stage II the brightness temperature increased steadily with the increase of the load.

(3) In the loading stage III the brightness temperature of microwave emission firstly stopped to increase and kept stability, then decreased.

(4) In the loading stage IV the brightness temperature turn to increase again from decrease and until the failure of rock sample.

If relating the Fig. 1 with Fig. 2 it can be found that in the loading stage II, the brightness temperature of microwave emission increased with the increase of load and strain, the rock is in the elastic state. When the rock developed into loading stage III from loading stage II, some new cracks began to appear and the horizontal strain increased quickly, which lead to the volume of the rock become larger and the density begin to decrease. Thus the microwave emission stopped increases and turn to decrease. The turning point A (to see Fig. 2) was the important early-precursor of rock failure. When the rock was close to facture the load increase became slow down due to large quantity of cracks appearing. When the loading enter into stage IV from loading stage III the microwave emission stopped decrease and increase again until the failure of rock sample. The turning point B was the important later-precursor for rock failure.

2.3. The TIR Detection Result

Past research showed that the AIRT (average infrared radiation temperature) was the valid quantitative index to represent the energy of infrared radiation in the loading process of rock [11]. Fig. 3 shows the detection result of infrared imager 3021ST. It can be found that from the loading stage I to loading stage III the AIRT increased with the increase of the load. They kept the similar variation step during this time. The point C was the turn point of AIRT variation. Before the point C the increase of AIRT was slower but quicker after that. The point C was the early-precursor of rock failure in TIR detection. When the loading entered into the stage IV, AIRT stopped increase and turn to decrease. The point D was the turn point of AIRT variation. When the load increased to its peak the rock sample fractured and AIRT dropped. After that AIRT waved with the load. In this stage the point D is the later-precursor of rock failure in TIR radiation.

Comparing the Fig. 2 and Fig. 3 with Fig. 1 it can be found that AIRT variation is different from the variation of the microwave emission. AIRT has the close relationship with the load, but the brightness temperature of microwave emission has the close relationship with the AE energy. The microwave emission precursor is more obvious than the AIRT precursor for the prediction of rock failure.

3. DISCUSSION ON THE MECHANISM OF MICROWAVE EMISSION OF LOADED ROCK

Any substance whose physical temperature is above 273.15 K will radiate microwave. According to the Rayleigh-Jeans Law the microwave emission energy is in direct proportion with emissivity and physical temperature of the object. So the brightness temperature can be expressed by following formula,

$$T_B = eT \tag{1}$$

where T_B is the brightness temperature of the object, e is the emissivity which represents the emission ability of the object, and T is the physical temperature of the object.

Therefore the higher the emissivity and the physical temperature, the larger is the brightness temperature of object. The parameter e is mainly decided by the dielectric constant ε. For rock

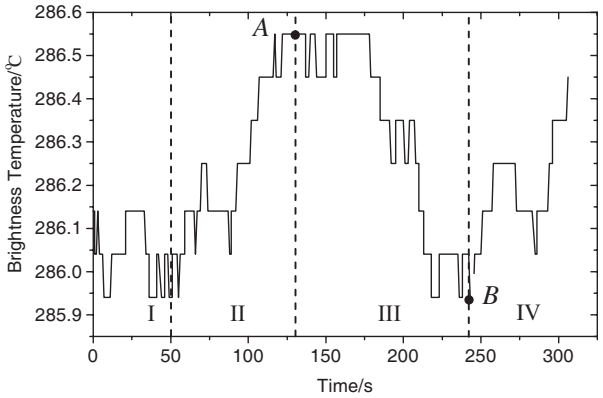

Figure 2: Brightness temperature-time curve of microwave emission.

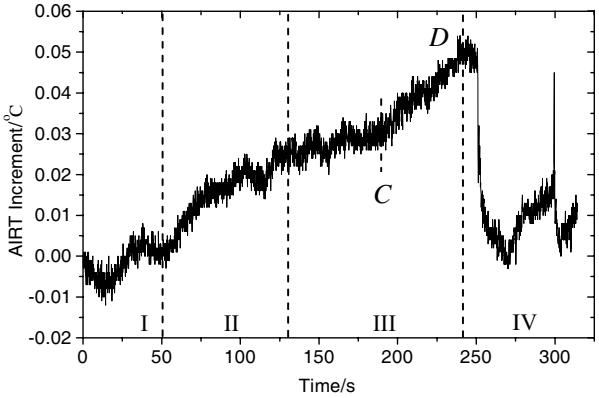

Figure 3: AIRT increment-time curve of TIR radiation.

material the parameter ε is related to many factors, such as mineral ingredient, water contents, rock structure and temperature etc [12].

From Fig. 1, we can see that the loading process of the rock sample can be divided into four stages. In the initial loading stage I and elastic loading stage II, the increase of the load will produce the heat and cause the physical temperature increase due to the thermoelastic effect, which result in the increase of AIRT and brightness temperature of microwave emission. So the variation steps of AIRT and brightness temperature of microwave emission are coincident in the two stages. The decreases of them in initial loading stage I are mainly due to the endothermal effect induced by the pore-gas effluent of rock.

When the load enters into the stage III some new cracks will appear, and the horizontal strain and the volume of the rock sample increases quickly, which will result in the density decrease. That causes the dielectric constant increase due to the increase of vacuum volume. Past experiment showed that dielectric constant was in inverse proportion with brightness temperature, i.e., the lager the ε, the lower is the brightness temperature T_B. Therefore brightness temperature of microwave emission will decreases in the loading stage III.

When the load enters into the stage IV large quantity of cracks appear inside the rock. The friction-heat effect happened between cracks will produce plentiful heat and cause the physical temperature increase, which results in the increase of the brightness temperature of microwave emission also.

4. CONCLUSIONS

The loading of rock will cause the microwave emission change. This change can be divided into several stages due to the staged variation of the load. In initial loading stage I and elastic loading stage II the microwave emission basically is incremental with the load increase. But when the load enter into the stage III microwave emission will stop to increase and turn to decrease due to large quantity of cracks produced. The turn point is the important early-precursor of rock failure. When the load enter into the stage IV the microwave emission stop decrease and turn to increase again due to the large quantity of cracks produced. The turn point is the important later-precursor of rock failure. The experiemtal results show that AIRT has the close relationship with the load, but the brightness temperature of microwave emission has the close relationship with the AE energy. The microwave emission precursor for rock failure is more obvious than the AIRT precursor.

ACKNOWLEDGMENT

This work is supported by the National Natural Science Foundations of China (No. 50774017) and the Liaoning Province Technology Project (2008231001).

REFERENCES

1. Gornyi, V. I., A. G. Salman, A. A. Tronin, and B. B. Shilin, "The Earth's outgoing IR radiation as an indicator of seismic activity," *Proc. Acad. Sci. USSR*, Vol. 301, 67–69, 1988.
2. Tronin, A. A., "Satellite thermal survey: A new tool for the study of seismoactive regions," *Int. J. Remote Sensing*, Vol. 17, 1439–1455, 1996.

3. Qiang, Z., L. Kong, and Y. Wang, "Earth gas releasing, thermal infrared anomaly and seismic activity," *Chinese Scinece Bulletin*, Vol. 37, 2259–2262, 1992.
4. Arun, K. S. and C. Swapnamita, "Thermal remote sensing technique in the study of pre-earthquake thermal anomalies" *J. Ind. Geophys. Union*, Vol. 9, No. 3, 197–207, 2005.
5. Ouzounov, D. and F. Freund, "Mid-infrared emission prior to strong earthquakes analyzed by remote sensing data," *Advances in Space Research*, Vol. 33, No. 3, 268–273, 2004.
6. Tramutoli, V., V. Cuomob, C. Filizzola, N. Pergolab, and C. Pietrapertosa, "Assessing the potential of thermal infrared satellite surveys for monitoring seismically active areas: The case of Kocaeli (Izmit) earthquake," *Remote Sensing of Environment*, Vol. 96, 409–426, 2005.
7. Qiang, Z.-J. and L.-T. Du, "Earthdegassing, forestfire and seismic activities," *Earth Science Frontiers*, Vol. 8, No. 1, 235–245, 2001.
8. Maeda, T., "Detection of microwave signals associated with rock failures in an earthquake from satellite-borne microwave radiometer data," *IEEE International Geoscience and Remote Sensing Symposium*, South Africa, 2009.
9. Deng, M., Z. Fan, C. Cui, et al., "The experimental study for earthquake prediction by passive microwave remote sensing," *J. Infrared Millim. Wave*, Vol. 14, No. 6, 401–406, 1995.
10. Maki, K., T. Takano, E. Soma, S. Yoshida, and M. Nakatani, "An experimental study of microwave emissions from compression failure of rocks," *Journal of the Seismological Society of Japan*, Vol. 58, No. 4, 375–384, 2006.
11. Wu, L., S. Liu, Y. Wu, and C. Wang, "Precursors for rock fracturing and failure — Part II: IRR T-curve abnormalities," *Int. J. Rock Mech. & Min. Sci.*, Vol. 43, No. 3, 483–493, 2006.
12. Xiao, J., "Study on the dielectric property of mineral and rock and its remote sensing significance," *Remote Sensing of Environment China*, Vol. 3, No. 2, 135–146, 1988.

Analysis of Saturation Effects on the Operation of Magnetic-controlled Switcher Type FCL

Faramarz Faghihi and Homa Arab
Young Researchers Club, Islamic Azad University South Tehran Branch, Iran

Abstract— With the extensive application of electrical power system, suppression of fault current limiter is an important subject that guarantees system security. The superconducting fault current limiters (SFCL) have been expected as a possible type of power apparatus to reduce the fault current in the power system. The results shown that under normal state, the FCL has no obvious effect on the power system; under fault state, the current limiting inductance connected in the bias current will be inserted into the fault circuit to limit the fault current. By regulating the bias current, the FCL voltage loss under normal state and the fault current can be adjusted to prescribed level. This kind of SFCL used the nonlinear permeability of the magnetic core for create a sufficient impedance and The transient performance considering the magnetic saturation is analyzed by Preisach model.

Preisach model that intrinsically satisfies nonlinear properties is used as the numerical method for analysis of saturation effects. It is able to identification isotropic and no isotropic behaviour. The main idea is to compute the magnetization vector in two steps independently, amplitude and phase. The described model yield results in qualitative agreement with the experimental results.

1. INTRODUCTION

There has been an increase in the number of studies on superconducting fault current limiters (FCLs) to improve the reliability of electrical power systems [1–3]. The development of effective FCLs is becoming more and more important in relation to rising fault current levels as more generators and dynamic loads are added to transmission grids [4]. Among the various type SFCL's, the saturated iron core high temperature superconducting FCL (SICSFCL) has many advantages and is more compact in design [5]: It is a rare exception that does not need the quench of superconductivity to create a sufficient impedance for fault current limiting, but by the nonlinear behavior of the magnetic core, which does not have the problem of recovery time [6]. The high temperature superconducting coils are supplied by a *dc* source and do not have *ac* power loss. It is thought to be one of the promising candidates for the practical one. However, as mentioned above, the SICSFCL limit the fault current by the nonlinear permeability of the magnetic core, so the *ac* windings must have a certain number of turns to ensure the sufficiently large impedance under fault conditions which will result in comparatively large impedance and undesirable voltage loss under normal operation state.

In order to solve this problem, a novel magnetic controlled switcher type fault current limiter topology for high voltage electric network based on the structure of the SICSFCL is proposed. A current limiting inductance is been connected into the bias circuit, and it will be inserted into the *ac* circuit automatically to limit the fault current when a short circuit fault occurs. In this paper, the current limiting mechanism of the proposed FCL is discussed, and the relationship between magnetic flux density B and magnetic field intensity H discussed by Preisach model. Nonlinear permeability of the magnetic core has very important rule in operation of this fault current limiter. Preisach model gives the exact result for FCL output waves that have the most agreement with the previous presented numerical approaches.

2. THEORETICAL CHARACTERISTICS OF MAGNETIC-CONTROLLED SWITCHER TYPE FAULT CURRENT LIMITER

The topology of the magnetic-controlled switcher type FCL is illustrated in Fig. 1. The FCL composed of a magnetic core with three columns which has the effect of magnetic controlled switcher, current limiting inductance and *dc* bias source. The section area of the yokes and middle column are larger than that of the side columns; the *ac* windings 1 and 2 are connected in series to a power line, *dc* bias winding 3 and current limiting inductance is connected into the *dc* circuit. three-phase full-bridge controlled rectifier provides *dc* bias current for the FCL. Under normal operation state, the *dc* bias current is adjusted to make the side columns core in deep saturated state, while the

yokes and the middle column core are in unsaturated state due to the larger section area than the side columns.

Under normal state, the magnetic-controlled switcher is turned off, the current limiting inductance has no obvious effect on the *ac* circuit, the impedance of the FCL is very low and the voltage drops on the *ac* windings are low. When a fault occurs, the amplitude of the fault current is increased and generates an *ac* magnetic motive force (mmf) large enough to counteract the *dc* bias mmf and desaturated the side columns core. In the negative half cycle of the *ac* current, the right side column will be desaturated, the FCL works like a single phase transformer, the right side winding as the primary winding and the bias winding as the secondary winding, the magnetic-controlled switcher is turned on, the current limiting inductance L will be converted into the *ac* circuit to limit the fault current automatically. At the same time, the *ac* mmf in the left side column is in the same direction with the *dc* bias mmf, the left side column will be in deeper saturate state and has no effect on the fault current.

Two side columns are used here for the fault current limitation in positive and negative half cycle of the *ac* current alternatively. The section area of the yokes and middle column are larger than that of the side columns, this kind of design has two advantages: One is that the side columns can be easily be driven into saturation by the bias current while the middle column and the yokes are in unsaturated state; the other is that when the side columns are been desaturated after the fault, it will be work as a single phase transformer with the middle column immediately, the magnetic controlled Switcher switches on and the current limiting inductance L will be connected into the *ac* circuit to limit the fault current.

3. BIAS CURRENT INFLUENCE ON THE FCL VOLTAGE LOSS UNDER NORMAL STATE

The bias current plays a very important role in the magnetic-controlled switcher type FCL operation. Under normal operation state, the bias current must provide a *dc* mmf large enough to saturated the side columns core; under fault state, the magnitude of bias current determines the period of time when the current limiting inductance be converted into the fault circuit, thus determines the magnitude and form of the limited current. The bias current influence on the characteristic of the FCL will be analyzed in the following paragraphs. Template Suppose the bias current is i_{dc}, then the bias mmf can be written as

$$F_{dc} = i_{dc} N_{dc} \tag{1}$$

where, N_{dc} is the turn of bias winding. The bias magnetic field intensity is

$$H_0 = F_{dc}/l \tag{2}$$

where, l is the mean length of magnetic circuit. Then the bias magnetic flux density can be written as

$$B_0 = f(H_0) \tag{3}$$

where in Equation (3), f is the function expressing the relationship between magnetic flux density B and magnetic field intensity H. Preisach model is used for identification this function.

4. USING OF PREISACH MODEL FOR STUDYING OF SATURATION EFFECT IN MAGNETIC-CONTROLLED SWITCHER TYPE

Several methods are described for modeling of B-H curve of magnetic material [9–12]. In this section, the category of vector Preisach coupled-hysteron models is presented for modeling of B-H curve of the transformer core. From several Preisach-type models, this model satisfies both saturation and loss properties basically.

The magnetization is computed in two dimensions, amplitude and angle between vector magnetization and vector applied field which can expressed by means of the following function:

$$P_\alpha\left(U_\alpha, V_\alpha\right) = \left(1 - G(\alpha)\right) P_x\left(U_x, V_x\right) + G(\alpha) P_y\left(U_y, V_y\right) \tag{4}$$

where two Preisach independent functions computed in the easy P_x (U_x, V_x) and hard P_y (U_y, V_y), and weight function $G(a)$ has magnitude between 0 and 1, the magnetization is computed solving the double Everett integral [6].

$$M(H(\alpha, t)) = \iint\limits_{D+} P\alpha(U_\alpha, V_\alpha) dU_\alpha dV_\alpha - \iint\limits_{D-} P_a(U_\alpha, V_\alpha) dU_\alpha dV_\alpha \tag{5}$$

the $P_\alpha(U_\alpha, V_\alpha)$, computation as follows :

$$P_\alpha(U_\alpha, V_\alpha) = F\left(P_x(U_x, V_x), P_y(U_y, V_y), \alpha\right) \tag{6}$$

where F satisfies the following properties:

$$\begin{cases} P_x(U_x, V_x) = F\left(P_x(U_x, V_x),\ P_y(U_y, V_y),\ 0\right) \\ P_y(U_y, V_y) = F(P_x(U_x, V_x),\ P_y(U_y, V_y),\ \pi/2) \end{cases} \tag{7}$$

The analysis is given in detail in [12] the results may be summarized as follows:

$$M_\alpha = (1 - G(\alpha))M_x + G(\alpha)M_y. \tag{8}$$

where with P_x and P_y as Preisach function, obtaining two valves of magnetization (M_x, M_y). The strict definition of M is

$$B = \mu(M + H) \tag{9}$$

$\bar{\mu}$ can be achieved from Equation (2) up to (9).

5. TRANSIENT ANALYSIS OF TRANSFORMER TYPE SFCL

The schematic diagram used for transient analysis shown in Fig. 2.

By using this schematic diagram, the equations of voltage are given as follows.

$$V_1(t) = L_{11}\frac{di_1(t)}{dt} + R_1 i_1(t) + L_{12}\frac{di_2(t)}{dt} + L_{13}\frac{di_3(t)}{dt} \tag{10}$$

$$V_2(t) = L_{21}\frac{di_1(t)}{dt} + L_{22}\frac{di_2(t)}{dt} + R_2 i_2(t) + L_{23}\frac{di_3(t)}{dt} \tag{11}$$

$$V_3(t) = L_{31}\frac{di_1(t)}{dt} + L_{32}\frac{di_2(t)}{dt} + R_3 i_3(t) + L_{33}\frac{di_3(t)}{dt} \tag{12}$$

$$V_3(t) = L_{SC}\frac{di_3(t)}{dt} + R_{SC}(t) i_3(t) \tag{13}$$

L_{sc} is residual inductance of the super conducting current limiting device, which is equal to 28 mH. It is measured experimentally under a variety of fault condition.

In normal condition, resistive type SFCL is zero. If path current through the SFCL is more than its circuit current, R_{SC} can be represented by the following expression.

$$R_{sc} = R\left[1 - \exp\left(-\frac{t - t_q}{\tau}\right)\right] \tag{14}$$

where R is the maximum value of the current limiting device resistance, and τ is the time constant of the resistance increase. Moreover, $t = 0$ is the time when the transmission line fault occurs, and $t = t_q\,(> 0)$ is the time when the S-N transition starts.

The magnetizing current $i_3(t)$ is expressed by considering the magnomotive force and By combining Equations (9) and (15) we can obtain that

$$\varphi = \left(\frac{NA}{l\bar{\mu}}\right) i_3(t) \tag{15}$$

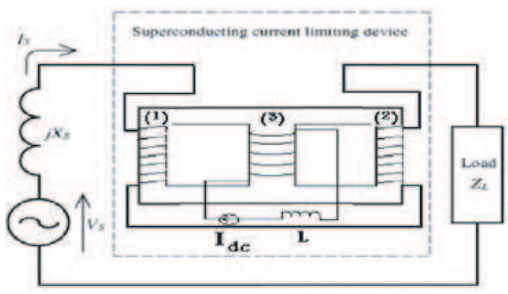

Figure 1: Topology of the magnetic controlled switcher type fault current limiter.

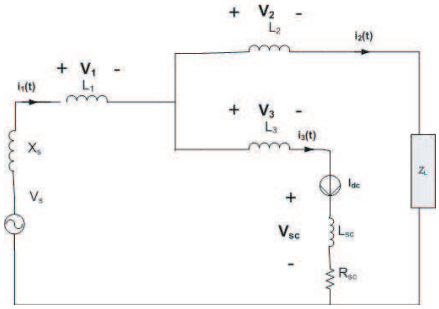

Figure 2: Equivalent circuit used for transient analysis.

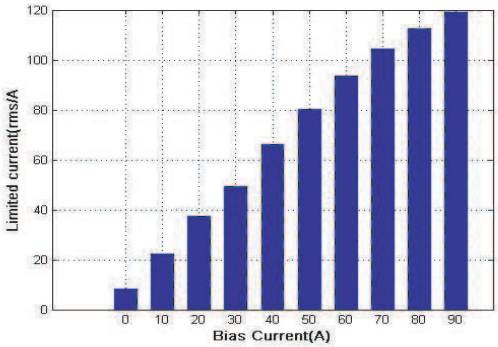

Figure 3: Relation between limited currnt and bias current.

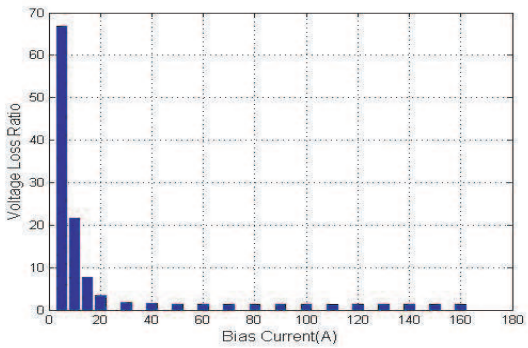

Figure 4: Relation between bias current and voltage loss ratio.

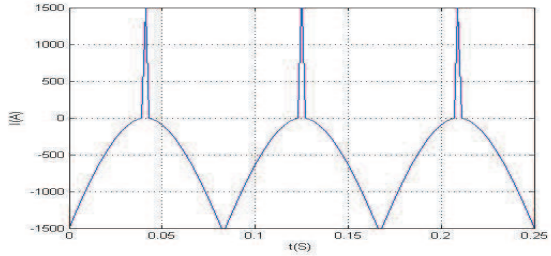

Figure 5: Short circuit fault current without FCL.

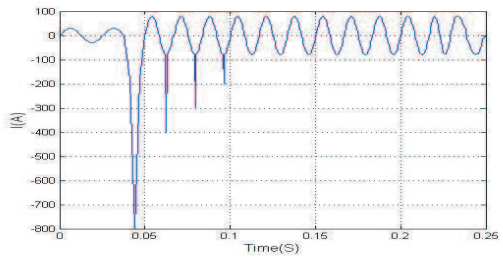

Figure 6: Short circuit fault current with FCL.

By using (10)–(14) and (15), the transient waveforms of the transformer type SFCL can be calculated.

6. RESULT AND DISCUSSIONS

As shown in Figs. 3, 4, when the bias current is small, the SFCL voltage is very high for the side columns core has not been saturated by the bias current, the FCL impedance is large and the voltage lost can not be neglected. With the increase of the bias current, the bias mmf drives the side columns core in saturation and the FCL impedance becomes low, so does the FCL voltage.

Figures 5, 6 demonstrate the fault current limiting effect and examine the relationship between the bias current and the limited fault current, hence as to determine the bias current by the requirement of preset fault respectively.

The fault current wave form with FCL is shown in Fig. 6 when the bias current is 50 A and without FCL is shown in Fig. 5. Comparing the fault current with and without the FCL, the amplitude of the Fault current was reduced by about 50% in this model.

The calculated Waveform based on suggested model is very close to those obtained from Froehlich Formula [10].

7. CONCLUSION

Effects of *B-H* curve on the operation of transformer type SFCL is very crucial. In this paper, a novel optimized procedure for modeling of magnetic saturation effects was proposed. Preisach model gives the exact result for FCL output waves that have the most agreement with the previous presented numerical approaches such as Froehlich formula. The results of this analysis are very useful fo quantitative estimation and have to be considered in the design of magnetic controlled switcher type fault current limiter.

REFERENCES

1. Muta, I., T. Doshita, T. Nakamura, T. Egi, and T. Hoshino, "Influences of superconducting fault current limiter (SFCL) on superconducting generator in one-machine double-line system," *IEEE Trans. Appl. Supercond.*, Vol. 13, No. 2, Dept. of Electr. Eng., Kyoto Univ., Japan, Jun. 2003.

2. Muta, I., T. Doshita, T. Nakamura, T. Egi, and T. Hoshino, "Influences of superconducting fault current limiter (SFCL) on superconducting generator in one-machine double-line system," *IEEE Trans. Appl. Supercond.*, Vol. 13, No. 2, Jun. 2003.
3. Yamaguchi, H. and T. Kataoka, "Comparative study of transformer-type superconducting fault current limiters considering magnetic saturation of iron core," *IEEE Trans. Appl. Supercond.*, Vol. 42, No. 10, Oct. 2006.
4. Lim, S.-H., H.-S. Choi, D.-C. Chung, and Y.-H. Han, "Fault current limiting characteristics of resistive type SFCL using a transformer," *IEEE Trans. Appl. Supercond.*, Vol. 15, No. 2, Jun. 2005.
5. Reimers, A., M. Gyimesi, E. Della Torre, and D. Ostergaard, "Implementation of the preisach DOK magnetic hysteresis model in acommercial finite element package," *IEEE Trans. Magnetics*, Vol. 37, No. 5, Sep. 2001.
6. Torre, E. D., *Magnetic Hystesis Piscataway*, IEEE Press, NJ, 2000.
7. Endo, H., S. Hayano, and Y. Saito, "An imagebased approach for preisach function calculation," *IEEE Trans. Magnetics*, Vol. 38, No. 5, Sep. 2002.
8. Mayergoyz, I. D., *Mathematical Models of Hysteresis*, Springer-Verllag, New York, 1991.
9. Azzerboni, B., et al., "*Ä* comparative study of Preisach scalar hysteresis models," *Physica B*, Vol. 343, 1–9, 2004.
10. Yamaguchi, H. and T. Kataoka, "Effect of magnetic saturation on the current limiting charactrictics of transformer-type superconducting fault current limiters," *IEEE Trans. Appl. Supercond.*, Vol. 16, No. 2, Jun. 2006.

Radiation Force of a Focused Stochastic Electromagnetic Beam

Chengliang Zhao and Yangjian Cai
School of Physical Science and Technology, Soochow University, Suzhou 215006, China

Abstract— Radiation force of a focused stochastic electromagnetic beam on a Rayleigh dielectric sphere is investigated. It is found that the degree of polarization, correlation factors and twist phase of the initial beam affect the radiation force. The trapping stability is also analyzed.

1. INTRODUCTION

Gaussian Schell-model (GSM) beam is a typical stochastic beam (i.e., partially coherent beam), whose spectral degree of coherence and the intensity distribution are Gaussian functions [1–4]. Beams of this class can be generated by scattering a coherent laser beam with a rotating grounded glass and then by transforming the intensity distribution of the scattered light into profile with Gaussian amplitude [3, 4]. A more general GSM beam can possess a twist phase [5].

In the past decades the two important properties of light waves: coherence and polarization were studied separately. After the unified theory of coherence and polarization was formulated [6], it became evident that these properties are interrelated. Scalar Gaussian Schell-model (GSM) beams were then extended to electromagnetic domain (called EGSM beams) and studied in details [7–11]. More recently, twisted EGSM beam was proposed [12].

The first optical trapping experiment dates back to early 1970s when Ashkin used radiation pressure of a laser beam for trapping micro-sized particles [13]. Since then, numerous theoretical and experimental papers have been published on manipulation of particles, and the radiation force has been extensively studied for various laser beams [14–18]. It has been found that coherence and spatial profile of the laser beam all affect the radiation force. This paper is aimed to investigate the radiation force produced by a focused twisted electromagnetic GSM beam on a Rayleigh particle.

2. FOCUSING PROPERTIES OF A TWISTED EGSM BEAM

The second-order statistical properties of a twisted EGSM beam can be characterized by the 2×2 cross-spectral density matrix $\vec{W}(\mathbf{r}_1, \mathbf{r}_2; 0)$ specified at any two points with position vectors $\mathbf{r}_1$ and $\mathbf{r}_2$ in the source plane with elements [6–12]

$$\begin{aligned} W_{\alpha\beta}(\mathbf{r}_1, \mathbf{r}_2; 0) &= W_{\alpha\beta}(\tilde{\mathbf{r}}; 0) = \langle E^*_\alpha(\mathbf{r}_1; 0) E_\beta(\mathbf{r}_2; 0) \rangle \\ &= A_\alpha A_\beta B_{\alpha\beta} \exp\left[-\frac{ik}{2} \tilde{\mathbf{r}}^T \mathbf{M}^{-1}_{0\alpha\beta} \tilde{\mathbf{r}} \right], \quad (\alpha = x, y;\ \beta = x, y) \end{aligned} \tag{1}$$

where A_α is the square root of the spectral density of electric field component E_α, $B_{\alpha\beta} = |B_{\alpha\beta}| \exp(i\phi)$ is the correlation coefficient between the E_x and E_y field components, satisfying the relation $B_{\alpha\beta} = B^*_{\beta\alpha}$, $\mathbf{M}^{-1}_{0\alpha\beta}$ is a 4×4 matrix of the form [12]

$$\mathbf{M}^{-1}_{0\alpha\beta} = \begin{pmatrix} \frac{1}{ik}\left(\frac{1}{2\sigma^2_{\alpha\beta}} + \frac{1}{\delta^2_{\alpha\beta}}\right)\mathbf{I} & \frac{i}{k\delta^2_{\alpha\beta}}\mathbf{I} + \mu_{\alpha\beta}\mathbf{J} \\ \frac{i}{k\delta^2_{\alpha\beta}}\mathbf{I} + \mu_{\alpha\beta}\mathbf{J}^T & \frac{1}{ik}\left(\frac{1}{2\sigma^2_{\alpha\beta}} + \frac{1}{\delta^2_{\alpha\beta}}\right)\mathbf{I} \end{pmatrix}, \tag{2}$$

where $\sigma_{\alpha\beta}$ and $\delta_{\alpha\beta}$ denote the widths of the spectral density and correlation coefficient, respectively. $\mu_{\alpha\beta}$ represents the twist factor and is limited by $\mu^2_{\alpha\beta} \le 1/\left(k^2\delta^4_{\alpha\beta}\right)$ if $\alpha = \beta$ due to the non-negativity requirement of the cross-spectral density (Eq. (1)) [12]. A_α, $B_{\alpha\beta}$, $\sigma_{\alpha\beta}$, $\delta_{\alpha\beta}$ and $\mu_{\alpha\beta}$ are independent of position but, in general, depend on the frequency.

Assuming that $A_y = \eta A_x$ and that the total transmitted power of the twisted EGSM beam is Q, we find that

$$Q = \frac{A_x \pi (1 + \eta)\left(\sigma^2_{xx} + \sigma^2_{yy}\right)}{2}. \tag{3}$$

The degree of polarization of an electromagnetic beam at point $\mathbf{r}$ is defined by the expression [6]

$$P_0(\mathbf{r};0) = \sqrt{1 - \frac{4\mathrm{Det}\overleftrightarrow{W}(\mathbf{r},\mathbf{r};0)}{[\mathrm{Tr}\overleftrightarrow{W}(\mathbf{r},\mathbf{r};0)]^2}}, \tag{4}$$

where Tr denotes the trace of the matrix.

For the conciseness of the analysis, in this paper we will only consider the twisted EGSM beams that are generated by sources whose cross-spectral density matrices are diagonal, i.e., of the form

$$\overleftrightarrow{W}(\mathbf{r}_1,\mathbf{r}_2;0) = \begin{pmatrix} W_{xx}^{(0)}(\mathbf{r}_1,\mathbf{r}_2;0) & 0 \\ 0 & W_{yy}^{(0)}(\mathbf{r}_1,\mathbf{r}_2;0) \end{pmatrix}. \tag{5}$$

Furthermore, we will assume that $\sigma_{xx} = \sigma_{yy}$, exploring the effect of difference between correlations δ_x and δ_y alone. For such restricted type of beams the degree of polarization across the source is given by the formula

$$P_0(\mathbf{r};0) = \frac{|1-\eta|}{1+\eta}. \tag{6}$$

By applying the tensor ABCD law for partially coherent beams [19], after paraxial propagation through a general astigmatic ABCD optical system, we can express the elements of the cross-spectral density matrix of a twisted EGSM beam as follows

$$W_{\alpha\beta}(\mathbf{u}_1,\mathbf{u}_2;z) = W_{\alpha\beta}(\tilde{\mathbf{u}};z) = A_\alpha A_\beta B_{\alpha\beta}\left[\mathrm{Det}\left(\bar{\mathbf{A}} + \bar{\mathbf{B}}\mathbf{M}_{0\alpha\beta}^{-1}\right)\right]^{-1/2} \exp\left[-\frac{ik}{2}\tilde{\mathbf{u}}^T\mathbf{M}_{1\alpha\beta}^{-1}\tilde{\mathbf{u}}\right], \tag{7}$$

where $\mathbf{M}_{1\alpha\beta}^{-1}$ and $\mathbf{M}_{0\alpha\beta}^{-1}$ are related by the following tensor ABCD law [19]

$$\mathbf{M}_{1\alpha\beta}^{-1} = \left(\tilde{\mathbf{C}} + \tilde{\mathbf{D}}\mathbf{M}_{0\alpha\beta}^{-1}\right)\left(\tilde{\mathbf{A}} + \tilde{\mathbf{B}}\mathbf{M}_{0\alpha\beta}^{-1}\right)^{-1}. \tag{8}$$

The spectral density of a twisted EGSM beam at the output plane is given by $I(\mathbf{u};z) = \mathrm{Tr}\overleftrightarrow{W}(\mathbf{u},\mathbf{u};z)$. The power Q of all considered beams in this paper at the input plane is set to be 1 W and the wavelength is set to be $\lambda = 632.8\,\mathrm{nm}$.

Figure 1 shows the intensity distribution of a twisted EGSM beam at the real focal plane for different values of the initial degree of polarization P_0 with $\sigma_{xx} = \sigma_{yy} = 10\,\mathrm{mm}$, $\delta_{xx} = 1\,\mathrm{mm}$, $\delta_{yy} = 2\,\mathrm{mm}$. In calculation of Fig. 1, we have chosen the twist factors to be $\mu_{xx}/\gamma_{xx} = 0.04$, $\mu_{yy}/\gamma_{yy} = 0.1$ with $\gamma_{xx} = [k^2\delta_{xx}^4]^{-1/2} = 0.1\,\mathrm{m}^{-1}$ and $\gamma_{yy} = [k^2\delta_{yy}^4]^{-1/2} = 0.025\,\mathrm{m}^{-1}$. From Fig. 1, it is clear that the focused intensity is also determined by the initial degree of polarization of the twisted EGSM beam. A partially polarized twisted EGSM beam can be focused more tightly than a completely polarized one.

3. RADIATION FORCE INDUCED BYA FOCUSED TWISTED EGSM BEAMS ON A RAYLEIGH PARTICLE

In this section we determine the magnitudes of radiation forces induced by a focused twisted EGSM beam on a Rayleigh dielectric sphere with radius a, ($a \ll \lambda$) and refractive index n_p. The reader can refer to Fig. 1 where the schematic diagram for trapping a Rayleigh dielectric sphere placed near the focus of the beam is given.

The radiation force is a combination of the scattering force and the gradient force. The former force component, which is caused by scattering of light by the sphere, is proportional to the beam intensity and acts along its direction of propagation. It can be expressed as [16]

$$\vec{F}_{\mathrm{Scat}}(\mathbf{r};z) = \vec{e}_z n_m \alpha I(\mathbf{r};z)/c, \tag{9}$$

where $I(\mathbf{r};z)$ is the intensity of the focused beam at the output plane, $\vec{e}_z$ is a unity vector along the direction of propagation, $\alpha = (8/3)\pi(ka)^4a^2[(\chi^2-1)/(\chi^2+2)]^2$, $\chi = n_p/n_m$ with n_m being the refractive index of the ambient. In the following text, we choose $a = 50\,\mathrm{nm}$, $n_p = 1.59$ (glass) and

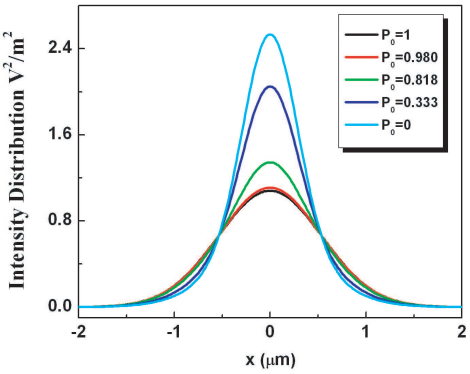

Figure 1: Intensity distribution of a twisted EGSM beam at the real focal plane for different values of the initial degree of polarization.

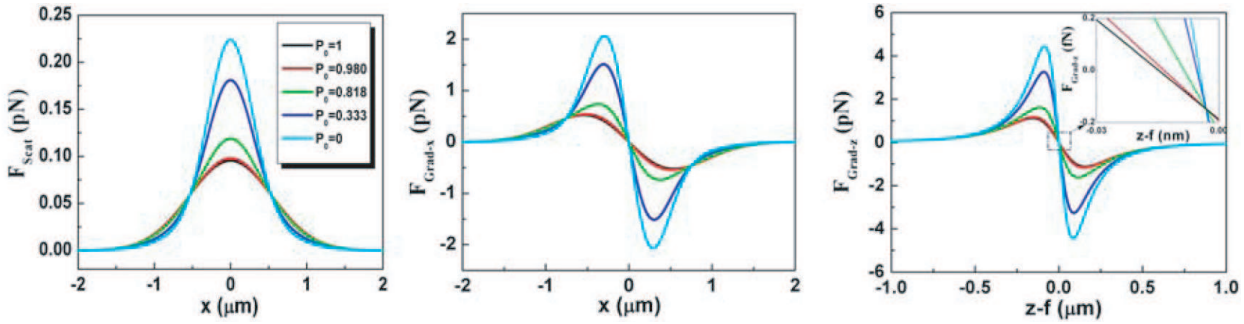

(a) (b) (c)

Figure 2: (a) Scattering force (cross-section $y = 0$) at the real focal plane, (b) transverse gradient force (cross-section $y = 0$) at the real focal plane, and (c) longitudinal gradient force at $\mathbf{r} = 0$ of a twisted EGSM beam for different values of the initial degree of polarization. In Fig. 2(c) the inset shows the zoomed region where the crossing of the radiation forces with zero occurs.

$n_m = 1.33$ (water). The gradient force, produced by a non-uniform field, acts along the gradient of light intensity, and can be expressed as [16]

$$\vec{F}_{\mathrm{Grad}}(\mathbf{r}; z) = 2\pi n_m \beta \nabla I(\mathbf{r}; z)/c, \tag{10}$$

where $\beta = a^3(\chi^2 - 1)/(\chi^2 + 2)$.

We calculate in Fig. 2(a) the scattering force (cross-section $y = 0$) at real focal plane, in Fig. 2(b) the transverse gradient force (cross-section $y = 0$) at real focal plane, and in Fig. 2(c) the longitudinal gradient force at $\mathbf{r} = 0$ of a twisted EGSM beam for different values of the initial degree of polarization with $\sigma_{xx} = \sigma_{yy} = 5\,\mathrm{mm}$, $\delta_{xx} = 1\,\mathrm{mm}$ and $\delta_{yy} = 2\,\mathrm{mm}$. In calculation of Fig. 2, we have chosen the twist factors to be $\mu_{xx}/\gamma_{xx} = 0.04$, $\mu_{yy}/\gamma_{yy} = 0.1$ with $\gamma_{xx} = [k^2\delta_{xx}^4]^{-1/2} = 0.1\,\mathrm{m}^{-1}$ and $\gamma_{yy} = [k^2\delta_{yy}^4]^{-1/2} = 0.025\,\mathrm{m}^{-1}$. From Fig. 2, one finds that the radiation force induced by a twisted EGSM beam is also closely determined by its initial degree of coherence and correlation coefficients. As the values of the initial degree of polarization or correlation coefficients decrease, the radiation force decreases (i.e., the trapping stability becomes worse), while the positions of peak values of the gradient forces deviate away from the focus (i.e., trapping ranges become larger). From above discussions, we come to the conclusion that we can control the trapping stability and the trapping ranges by choosing suitable values of degree of polarization of the partially coherent beam at the input plane.

4. ANALYSIS OF THE TRAPPING STABILITY

Now we analyze the trapping stability in greater detail by taking into consideration the Brownian motion of the trapped particle. The magnitude of the Brownian force is expressed as $|F_B| =$

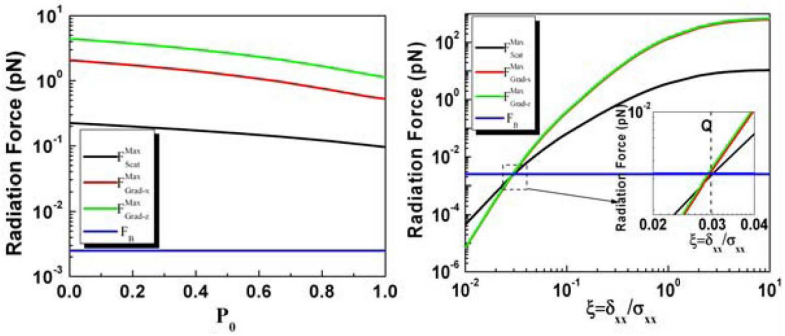

Figure 3: (a) Dependence of the radiation forces $F_{\text{Scat}}^{\text{Max}}$, $F_{\text{Grad-}x}^{\text{Max}}$ and $F_{\text{Grad-}z}^{\text{Max}}$ induced by a twisted EGSM beam on the initial degree of polarization at $z_1 = 0$, (b) dependencies of the radiation forces $F_{\text{Scat}}^{\text{Max}}$, $F_{\text{Grad-}x}^{\text{Max}}$ and $F_{\text{Grad-}z}^{\text{Max}}$ on the initial correlation coefficients with $\xi = \delta_{xx}/\sigma_{xx}$ and $\delta_{yy} = 2.5\delta_{xx}$. In Fig. 3(b), the inset shows the zoomed region where the crossing of the three radiation forces with the Brownian force occurs.

$(12\pi\kappa a k_B T)^{1/2}$ according to the fluctuation-dissipation theorem of Einstein [18], here κ is the viscosity of the ambient (in our case, for water [20], $\kappa = 7.977 \times 10^{-4}\,\text{Pas}$ at $T = 300\,\text{K}$), a is the radius of the particle and k_{B} is the Boltzmann constant. Thus, the magnitude of the Brownian force becomes $F_{\text{B}} = 2.5 \times 10^{-3}\,\text{pN}$.

We illustrate in Fig. 3(a) the dependence of the radiation forces $F_{\text{Scat}}^{\text{Max}}$, $F_{\text{Grad-}x}^{\text{Max}}$ and $F_{\text{Grad-}z}^{\text{Max}}$ induced by a twisted EGSM beam on the initial degree of polarization at the real focal plane with $\sigma_{xx} = \sigma_{yy} = 5\,\text{mm}$, $\delta_{xx} = 1\,\text{mm}$, $\delta_{yy} = 2.5\,\text{mm}$, and in Fig. 3(b) the dependence of the radiation forces $F_{\text{Scat}}^{\text{Max}}$, $F_{\text{Grad-}x}^{\text{Max}}$ and $F_{\text{Grad-}z}^{\text{Max}}$ on the initial correlation coefficients with $\eta = \delta_{xx}/\sigma_{xx}$, $\delta_{yy} = 2.5\delta_{xx}$, $\sigma_{xx} = \sigma_{yy} = 5\,\text{mm}$. In calculation of Figs. 3(a) and (b), we have chosen the twist factors to be $\mu_{xx}/\gamma_{xx} = 0.04$, $\mu_{yy}/\gamma_{yy} = 0.1$ with $\gamma_{xx} = [k^2\delta_{xx}^4]^{-1/2} = 0.1\,\text{m}^{-1}$ and $\gamma_{yy} = [k^2\delta_{yy}^4]^{-1/2} = 0.025\,\text{m}^{-1}$. One finds from Fig. 3(a) that although the radiation force decreases as the degree of polarization increases, it remains larger than the Brownian force. Hence, by tuning the degree of polarization of the input partially coherent beam it is possible to control particle trapping. From Fig. 3(b), we see that the radiation force decreases as the values of the correlation coefficients decrease. If the correlation coefficients are smaller than certain values, the radiation force becomes smaller than the Brownian force, and the particle cannot be trapped. The line Q in Fig. 3(b) also represents critical line. From above discussion, we conclude that it is necessary to choose suitable values of the twist phase, degree of polarization and correlation coefficients of a partially coherent beam for particle trapping.

5. CONCLUSION

In conclusion, we have studied the focusing properties of twisted EGSM beams, and the radiation force induced by such beams on a Rayleigh dielectric sphere. Our results have shown that the induced radiation force is closely related to the degree of polarization, correlation coefficients and twist phase of the beam. In particular we found that the transverse and longitudinal trapping ranges can be increased at the real focus by increasing the values of the degree of polarization or by decreasing the values of correlation coefficients. We have also found that the trapping stability decreases as the trapping ranges increases. Thus it is necessary to choose suitable degree of polarization and correlation coefficients of the initial partially coherent beam in order to trap a particle stably.

ACKNOWLEDGMENT

Y. Cai acknowledges the support by the Foundation for the Author of National Excellent Doctoral Dissertation of PR China under Grant No. 200928, the Natural Science of Jiangsu Province under Grant No. BK2009114 and the National Natural Science Foundation of China under Grant No. 10904102.

REFERENCES

1. Mandel, L. and E. Wolf, *Optical Coherence and Quantum Optics*, Cambridge U. Press, 1995.

2. Wolf, E. and E. Collett, "Partially coherent sources which produce same far-field intensity distribution as a laser," *Opt. Commun.*, Vol. 25, 293–296, 1978.
3. Gori, F., "Collet-Wolf sources and multimode lasers," *Opt. Commun.*, Vol. 34, 301–305, 1978.
4. Wang, F. and Y. Cai, "Experimental observation of fractional Fourier transform for a partially coherent optical beam with Gaussian statistics," *J. Opt. Soc. Am. A*, Vol. 24, 1937–1944, 2007.
5. Simon, R. and N. Mukunda, "Twist phase in Gaussian-beam optics," *J. Opt. Soc. Am. A*, Vol. 15, 2373–2382, 1998.
6. Wolf, E., "Unified theory of coherence and polarization of random electromagnetic beams," *Phys. Lett. A*, Vol. 312, 263–267, 2003.
7. James, D. F. V., "Changes of polarization of light beams on propagation in free space," *J. Opt. Soc. Am. A*, Vol. 11, 1641–1643, 1994.
8. Gori, F., M. Santarsiero, G. Piquero, R. Borghi, A. Mondello, and R. Simon, "Partially polarized Gaussian schell-model beams," *J. Opt. A: Pure Appl. Opt.*, Vol. 3, 1–9, 2001.
9. Korotkova, O., M. Salem, and E. Wolf, "Beam conditions for radiation generated by an electromagnetic Gaussian Schell-model source," *Opt. Lett.*, Vol. 29, 1173–1175, 2004.
10. Cai, Y., O. Korotkova, H. T. Eyyuboğlu, and Y. Baykal, "Active laser radar systems with stochastic electromagnetic beams in turbulent atmosphere," *Opt. Express*, Vol. 16, 15835–15846, 2008.
11. Yao, M., Y. Cai, H. T. Eyyuboğlu, Y. Baykal, and O. Korotkova, "The evolution of the degree of polarization of an electromagnetic Gaussian Schell-model beam in a Gaussian cavity," *Opt. Lett.*, Vol. 33, 2266–2268, 2008.
12. Cai, Y. and O. Korotkova, "Twist phase-induced polarization changes in electromagnetic Gaussian Schell-model beams," *Appl. Phys. B*, Vol. 96, 499–507, 2009.
13. Ashkin, A., "Acceleration and trapping of particles by radiation forces," *Phys. Rev. Lett.*, Vol. 24, 156–159, 1970.
14. Ashkin, A., "Trapping of atoms by resonance radiation pressure," *Phys. Rev. Lett.*, Vol. 40, 729–732, 1978.
15. Ashkin, A., J. M. Dziezic, J. E. Bjorkholm, and S. Chu, "Observation of a single-beam gradient force optical trap for dielectric particles," *Opt. Lett.*, Vol. 11, 288–290, 1986.
16. Harada, Y. and T. Asakura, "Radiation forces on a dielectric sphere in the Rayleigh scattering regime," *Opt. Commun.*, Vol. 124, 529–541, 1996.
17. Zhao, C., Y. Cai, X. Lu, and H. T. Eyyuboğlu, "Radiation force of coherent and partially coherent flat-topped beams on a Rayleigh particle," *Opt. Express*, Vol. 17, 1753–1765, 2009.
18. Okamoto, K. and S. Kawata, "Radiation force exerted on subwavelength particles near a nanoaperture," *Phys. Rev. Lett.*, Vol. 83, 4534–4537, 1999.
19. Lin, Q. and Y. Cai, "Tensor ABCD law for partially coherent twisted anisotropic Gaussian-Schell model beams," *Opt. Lett.*, Vol. 27, 216–218, 2002.
20. Kestin, J., M. Sokolov, and W. A. Wakeham, "Viscosity of Liquid Water in the Range — 8°C to 150°C," *J. Phys. Chem. Ref. Data*, Vol. 7, 941–948, 1978.

Broaden the Bandwidth of Patch Antenna by Using Inhomogeneous Metamaterial Substrate

Lei Xing, **Qian Xu**, **Jing Li**, **Zhixia Wei**, **Jun Ding**, **and Chenjiang Guo**
School of Electronic and Information, Northwestern Polytechnical University, Xi'an 710129, China

Abstract— Inhomogeneous substrate has proven to be an efficient approach to broaden the bandwidth of the patch antenna. Because of its inhomogeneity, it is very difficult to manufacture it by using ordinary materials. In this paper, we first optimize the inhomogeneity of the substrate with physical insight and then use nonresonant metamaterial elements to realize it. By tuning the geometrical parameter of the metamaterial element, the effective constitutive parameters can be controlled; the permittivity and permeability are well designed to optimize the bandwidth of the antenna. As the working frequency is far from the resonant region of the element, it is expected to exhibit stable effective constitutive parameters in a large frequency range. Our results have shown that the metamaterial substrate broadened the bandwidth of the antenna from 10.5% to 20.6% (−10 dB).

1. INTRODUCTION

Metamaterials have been widely explored in recent years [1]. By tuning the geometrical structure of the metamaterial element, we can control the material properties and form a powerful form of electromagnetic design. Combined with transformation optics [2], there have been numerous applications such as invisible cloak [3, 4], invisible umbrella [5], perfect lens [6, 7], polarizers [8], wave retarder [9], high gain antennas [10], etc. There has also been a great deal of interest in the use of metamaterials for the enhancement of patch antenna performance [11–13]. The bandwidth of the antenna has been pursued for a long time, bandwidth-broadening techniques among them are: the use of thick substrate with low dielectric constant [14], parasitic patches [15], capacitive loading [16], patch shape optimization [17], and so forth.

One part of the antenna that can be optimized is the substrate, although a substrate of high dielectric constant can be used to reduce the physical height of the patch, special care is needed to avoid excessive impedance mismatches and surface-wave loss [18]. Inhomogeneous substrate has been validated to have the ability to broaden the bandwidth of the patch antenna [19], it is sometimes not easy to create with conventional materials but much easier to build with artificially structured metamaterials, in which spatial variations of the material parameters can be achieved by modifying the geometry and the placement of the constituent element. In this paper, we seek to improve the bandwidth performance of the square patch antenna by incorporating a substrate that is made by nonresonant metamaterial elements. As the substrate makes use of nonresonant elements, it is expected to exhibit stable effective parameters in a large frequency range. Finally, the result shows that the bandwidth of 11.3% (−15 dB) can be achieved.

2. PATCH BANDWITDTH USING INHOMOGENEOUS SUBSTRATES

The main idea of optimizing the substrate under the patch for bandwidth broadening is to grade the dielectric according to the field amplitude under the patch. As the most radiation occurs from the peak field region, we adopt low dielectric constant in those regions to lower the capacitance and better enable the radiation. When the modification is done, the field intensity also spreads, thus leading to improved bandwidths. This is the physical insight of band-broadening. We first optimize the substrate without considering the practical implementation and assume that the inhomogeneous dielectric exists in theory.

The structure of the patch antenna is given in Fig. 1(a). The thickness of the substrate is 4 mm. After optimization, the inhomogeneous configuration of the substrate is shown in Fig. 1(b). Except the blocks below the patch, the permittivity of the rest of the substrate is $\varepsilon_r = 6$. In Fig. 2, the H-field distributions are given at central frequency (7.36 GHz). The permittivity of the homogeneous case is $\varepsilon_r = 6$. As expected, the lower effective dielectric constant around the patch region causes the field intensity to decrease and spread out which will result in bandwidth broadening.

Next, the inhomogeneous substrate will be realized by metamaterial elements.

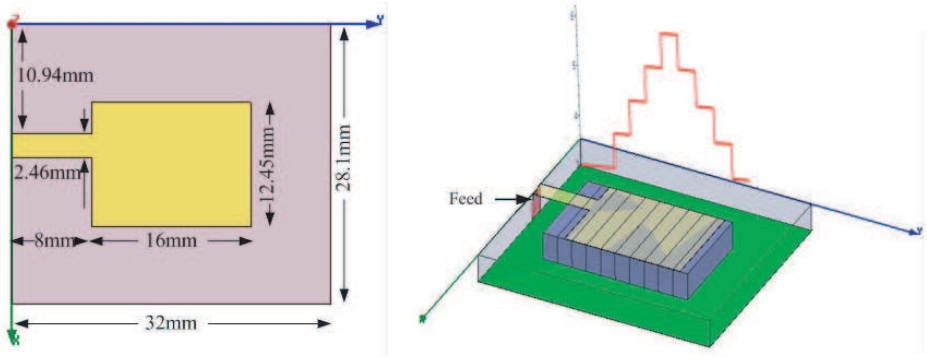

Figure 1: (a) The structure of the patch antenna. (b) The optimized relative permittivity of the substrate, which are 3, 3, 3.7, 4.4, 5.1, 5.8, 5.1, 4.4, 3.7 and 3 in staircase.

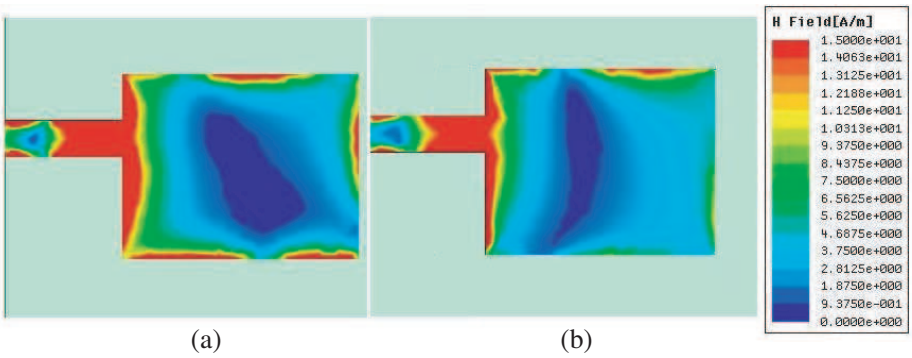

Figure 2: Comparison of the H-field distribution between (a) homogeneous substrate with $\varepsilon_r = 6$ and (b) optimized inhomogeneous substrate.

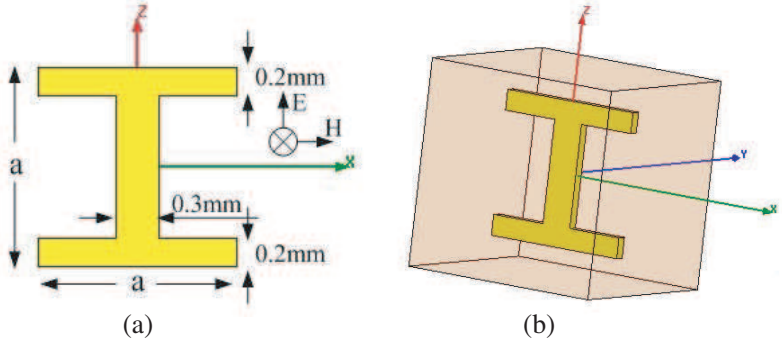

Figure 3: The nonresonant I-shape element used in the substrate. (a) The geometrical structure of the element with characteristic parameter a, the thickness is 0.1 mm. The polarization of the electric field is along z-axis. (b) Each element is embedded in the center of a cube with size of 2 mm × 2 mm × 2 mm, and the background material is $\varepsilon_r = 3$.

3. SUBSTITUTE THE INHOMOGENEOUS SUBSTRATE WITH NONRESONANT METAMATERIAL

To ensure the stability of effective parameters in a broadband, we use an ultra-broad band metamaterial consisted by non-resonant structure [4]. Because it works far from the resonant region, the dispersion is very small. By tuning the size of the geometrical parameter, we are able to accurately control its influence on the effective constitutive parameters.

Figure 3 illustrates the "I-shape" structure used in this paper. The S parameters for it are computed using HFSS (Ansoft), then the numerical S-parameter retrieval procedure [20] is applied to retrieve the effective constitutive parameters from transmission and reflection coefficient, as shown in Fig. 4. Note that the resonant frequency occurs at about 16 GHz and our interesting band is far from the resonant region. After a parametric sweep, Fig. 5 gives the effective parameters

varying with characteristic parameter in 7.36 GHz, the element do not couple with magnetic field, so it has little effect on permeability. Because the working frequency is far from 16 GHz, the stability of the effective parameters enables us to assume that the permittivity and permeability remains unchanged with frequency.

To implement the substrate defined in Fig. 1(b), the entire substrate is divided into 2 mm × 2 mm × 2 mm cubes, which will be replaced by 356 metamaterial elements, as shown in Fig. 6. Because the effective medium theory is an approximate theory, there might be some errors when comes to substitution, we tune the parameter a around the patch to 1.66 mm to achieve a better performance. the H-field distribution of the patch is also given, it looks very similar to Fig. 2(b).

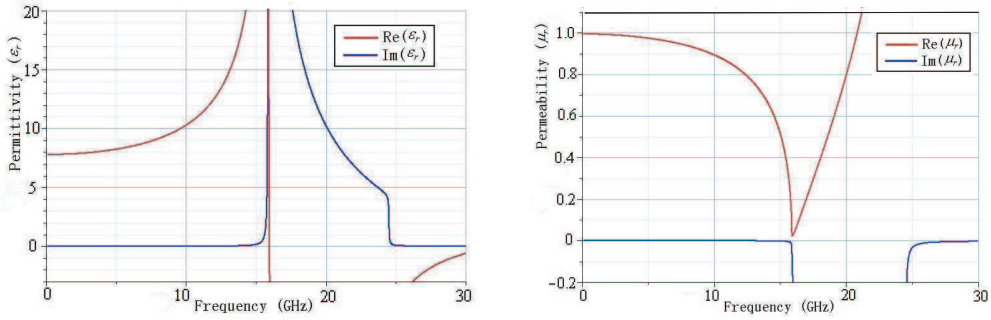

(a) (b)

Figure 4: Retrieved (a) permittivity and (b) permeability of the unit in Fig. 3 in 7.36 GHz, the values beyond the frame are not shown.

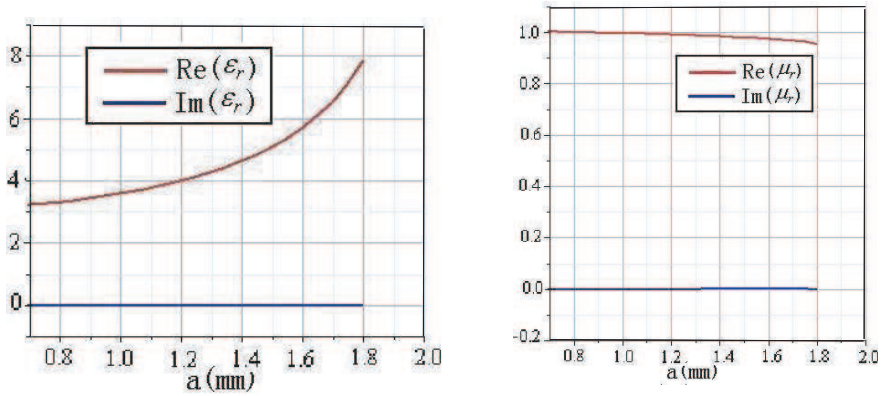

(a) (b)

Figure 5: The relation between the effective permittivity, permeability and the characteristic dimension.

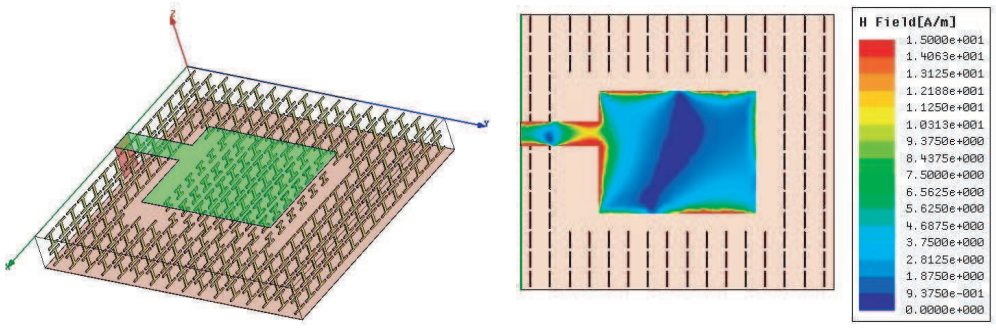

(a) (b)

Figure 6: (a) Substitute the inhomogeneous with metamaterial elements. (b) Gives the H-field distribution with metamaterials loaded.

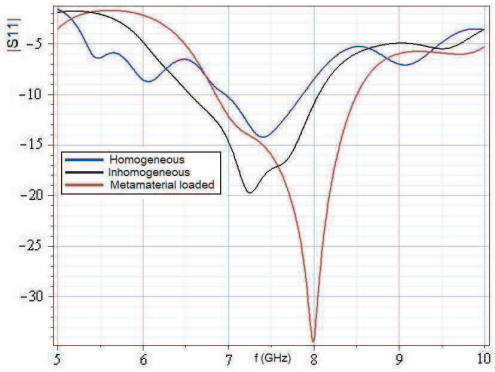

Substrate	Resonant Frequency (GHz)	Fractional Bandwidth (%)	
		$\lvert S_{11}\rvert < -10$ dB	$\lvert S_{11}\rvert < -15$ dB
Homogeneous	7.36	10.5	0
Inhomogeneous	7.25	20.7	10.1
Metamaterial	7.99	20.6	11.3

Figure 7: Comparison among homogeneous, inhomogeneous and metamaterial loaded cases.

Finally, the simulated S values and the radiation pattern of the metamaterial loaded structure are given in Fig. 7 compared with previous homogeneous and inhomogeneous cases. As we can see from the figure, there is no -15 dB band in the homogeneous case, 10.1% in the inhomogeneous case and 11.3% in the metamaterial loaded case.

4. CONCLUSION

In this paper, a metamaterial loaded inhomogeneous substrate is proposed to broaden the bandwidth of the square-patch antenna. By controlling the effective constitutive parameters of the nonresonant metamaterial element, the inhomogeneous substrate is realized by metamaterial elements. The simulated results show that the bandwidth of the patch antenna is improved from 0.5% to 20.6% (-10 dB). We note that the proposed inhomogeneity of the substrate may not be the best and is only used to demonstrate the bandwidth-broadening ability; by combining with other techniques mentioned before the bandwidth can be further improved.

ACKNOWLEDGMENT

This work is supported by graduate starting seed fund of Northwestern Polytechnical University.

REFERENCES

1. Engheta, N. and R. W. Ziolkowski, "A positive future for double-negative metamaterials," *IEEE Trans. Microwave Theory Tech.*, Vol. 53, No. 4, 1535–1556, 2005.
2. Pendry, J. B., D. Schurig, and D. R. Smith, "Controlling electromagnetic fields," *Science*, Vol. 312, 1780–1782, 2006.
3. Schurig, D., et al., "Metamaterial electromagnetic cloak at microwave frequencies," *Science*, Vol. 314, 977–980, 2006.
4. Liu, R., et al., "Broadband gound-plane cloak," *Science*, Vol. 323, 366–369, 2009.
5. Yun, L., et al., "A complementary media invisibility cloak that can cloak objects at a distance outside the cloaking shell," arXiv:0811.0458v1.
6. Pendry, J. B., "Negative refraction makes a perfect lens," *Phys. Rev. Lett.*, Vol. 85, No. 18, 3966–3969, 2000.
7. Fang, N., H. Lee, C. Sun, and X. Zhang, "Sub-diffraction-limited optical imaging with silver superlens," *Science*, Vol. 308, 534–537, 2005.
8. Chin, J. Y., M. Lu, and T. J. Cui, "A transmission polarizer by anisotropic metamaterials," *International Symposium on Antennas and Propagation*, San Diego, 2008.
9. Chin, J. Y., et al., "An efficient broadband metamaterial wave retarder," *Opt. Express.*, Vol. 17, No. 9, 2009.
10. Jiang, W. X., et al., "Layered high-gain lens antennas via discrete optical transformation," *Appl. Phys. Lett.*, Vol. 93, 221906, 2008.
11. Rajab, K. Z., R. Mittra, and M. T. Lanagan, "Size reduction of microstrip antennas using metamaterials," *International Symposium on Antennas and Propagation*, Washington, D.C., 2005.
12. Zhu, F. and H. Jun, "Improved patch antenna performance by using a metamaterial cover," *Journal of Zhejiang Univ. Sci. A*, Vol. 8, 192–196, 2007.

13. Li, L. W., Y. Li, and J. R. Mosig, "Design of a novel rectangular patch antenna with planar metamaterial patterned substrate," *Proceedings of IWAT*, Chiba, Japan, 2008.
14. Chen, W. and K. F. Lee, "Input impedance of coaxially fed rectangular microstrip antenna on electrically thick substrate," *Microw. Opt. Technol. Lett.*, Vol. 6, 387–390, 1993.
15. Lee, R. Q., K. F. Lee, and J. Bobinchak, "Characteristics of a two-layer electromagnetically coupled rectangular microstrip antenna," *Electron. Lett.*, Vol. 23, No. 20, 1070–1072, 1987.
16. Hall, P. S., "Probe compensation in thick microstrip patches," *Electron. Lett.*, Vol. 23, No. 11, 606–607, 1987.
17. Choo, H., A. Hutani, L. C. Trintinalia, and H. Ling, "Shape optimization of broadband microstrip antennas using genetic algorithm," *Electron. Lett.*, Vol. 36, No. 25, 2057–2058, 2000.
18. Bhattacharyya, A. K. and R. Garg, "Effect of substrate on the efficiency of an arbitrary shaped microstrip patch antenna," *IEEE Trans. Antennas Propagat.*, Vol. 34, 1181–1188, 1986.
19. Chen, C. C. and J. L. Volakis, "Bandwidth broadening of patch antennas using nonuniform substrates," *Microw. Opt. Technol. Lett.*, Vol. 47, No. 5, 421–423, 2005.
20. Smith, D. R., et al., "Electromagnetic parameter retrieval from inhomogeneous metamaterials," *Phys. Rev. E*, Vol. 71, 036617, 2005.

Application of Periodic Structure on the Isolation and Suppression for Notebook Multi-antennas Coupling

Han-Nien Lin, **Ching-Hsien Lin**, **Chun-Chi Tang**, **and Ming-Cheng Chang**
Department of Communications Engineering, Feng-Chia University
100 Wen-Hua Rd., Taichung 40724, Taiwan, R.O.C.

Abstract— Due to the increasing add-on functions demand for consumer electronics, currently multi-radios, such as WLAN, WWAN, GPS, Bluetooth, and even DVB-H modules, have all been crowdedly embedded and highly integrated in a tiny space of wireless communications platform. Nowadays notebook computers or PDA phones usually have been equipped with more than one antennas, the purpose is to fit for different communication system such as Cellular mobile communications, wireless local area networking, and personal area networking. Under this situation, the performance of various kinds of wireless communications is usually degraded by the mutual coupling and interference of closely arranged antennas inside the mobile device. Since the RF modules co-existence has become a critical design problem for wireless communications, the isolation technique has gained increasing attention recently. We will investigate the coupling effect between 2.4 GHz antennas not only because Bluetooth and 802.11b/g WiFi share the same frequency band, but they also have been widely adopted for ubiquitous wireless networking, wireless headphone, wireless mouse, and wireless keyboard. Since the isolation requirement is relatively stringent for both WiFi and Bluetooth concurrent operation, therefore we will in this paper investigate the coupling of Bluetooth and 802.11b/g WiFi antennas placed inside the prototype mold of notebook computer. Then, we will utilize the distance, orientations between antenna, and application of periodic structure to provide the isolation between antennas and resolve the problem of mutual interference.

1. INTRODUCTION

Due to the increasing add-on functions demand for consumer electronics, currently multi-radios, such as WLAN, WWAN, GPS, Bluetooth, and even DVB-H modules, have all been crowdedly embedded and highly integrated in a tiny space of wireless communications platform. With the highly integration of powerful computing and multi-radio communications devices in a single product nowadays, multiple antennas are usually implemented to achieve the seamless and convenient communication services. However, the closely placed antennas have resulted in intra-system coupling interference and therefore severely degraded the performance of various kinds of wireless communications. The isolation technique for antenna systems must be implemented to reduce the mutual coupling between coexistent various RF systems [1], especially for the systems with embedded Bluetooth and 802.11b/g WiFi applications sharing the same frequency band. Recently some researches about built-in antennas' isolation technique inside a PDA phone has been proposed [2, 3] by increasing their separation to reduce coupling from each other. In this paper, we will investigate the coupling effect between 2.4 GHz antennas for Bluetooth and 802.11b/g WiFi inside a prototype mold of notebook computer. Finally, we will show the optimal isolation achieved from antennas separation, orientation, and utilization of periodic structure to reduce the mutual coupling interference.

2. ANALYSIS OF MUTUAL COUPLING BETWEEN COEXISTENT BLUETOOTH AND 802.11B/G WIFI ANTENNAS

The conventional isolation requirement for popular wireless communications is frequently asked for 20 dB as reference standard. However, the minimum isolation requirement for coexistent Bluetooth and 802.11b/g WiFi systems is 40 dB, because both system operating in same frequency band (2.4 GHz–2.483 GHz). To avoid the severe in-band mutual interference between each other, we will develop isolation technique by implementing periodic structure to provide better isolation in this paper. The isolation requirement between coexistent RF systems is shown in Table 1. The placement of two chip antennas under investigation for Bluetooth and 802.11b/g WiFi systems inside the mold notebook computer is shown in Figure 1. The chip antennas are fabricated on FR4 with dimension of 1.6 mm thickness and 35 mm × 30 mm area, and it is fed by microstrip to achieve 50 Ω impedance-matching. The configurations for different spacing and orientation between coexistent antennas are shown in Figure 2 to analyze the mutual coupling effect.

We first placed both antennas in vertical direction with 0 mm, 10 mm, and 20 mm separation for each case, the reflection coefficients (S_{11} and S_{22} are reflection coefficients for Bluetooth and 802.11b/g respectively) and isolation (S_{21}) between each other were then measured and shown in Figure 3. The results clearly show that the isolation between antennas is much worse when they are both placed in vertical polarization with main lobes coupling. We then oriented the antennas in orthogonal direction to each other and separated antennas by moving 0 mm, 10 mm, and 20 mm respectively. The measured results of reflection coefficient covering 2.4 GHz–2.483 GHz in Figure 4 show that the isolation is much better due to orthogonal polarization to each other when they are oriented in orthogonal direction. Finally, we placed both antennas in horizontal direction and

Transmitter	Minimum Isolation Recommendations			
	Receiver			
	Bluetooth	802.11b/g	802.11a	GSM
Bluetooth	n/a	40dB	20dB	20dB
802.11b/g	40dB	n/a	n/a	20dB
802.11a	20dB	n/a	n/a	20dB
GSM	20dB	20dB	20dB	n/a

Table 1: Isolation requirement between coexistent systems.

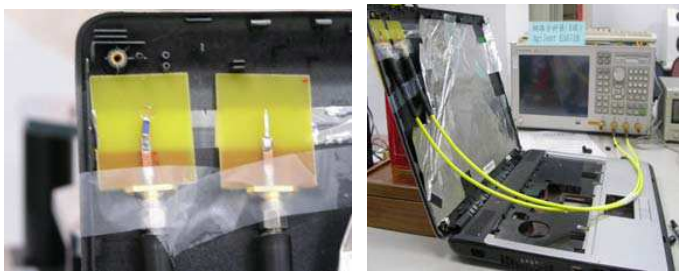

Figure 1: Placement of two chip antennas inside mold.

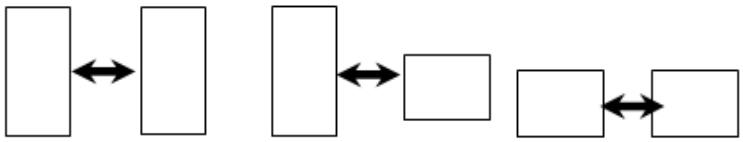

(a) Vertical (b) Orthogonal (c) Horizontal

Figure 2: Three orientation for antennas placement.

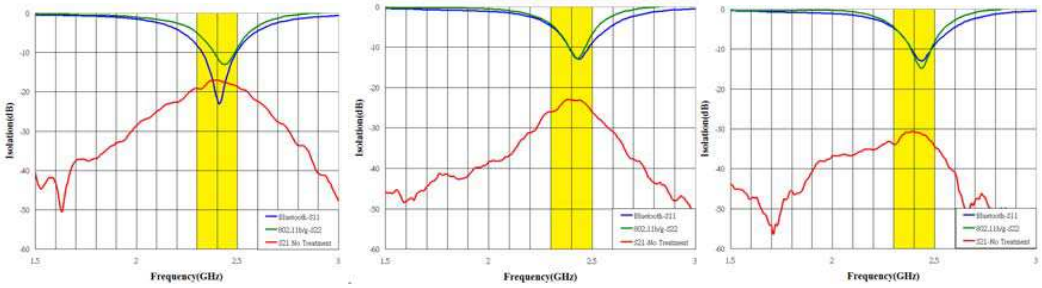

(a) 0 mm (b) 10 mm (c) 20 mm

Figure 3: Measured results for various antenna spacing with both antennas oriented in vertical direction.

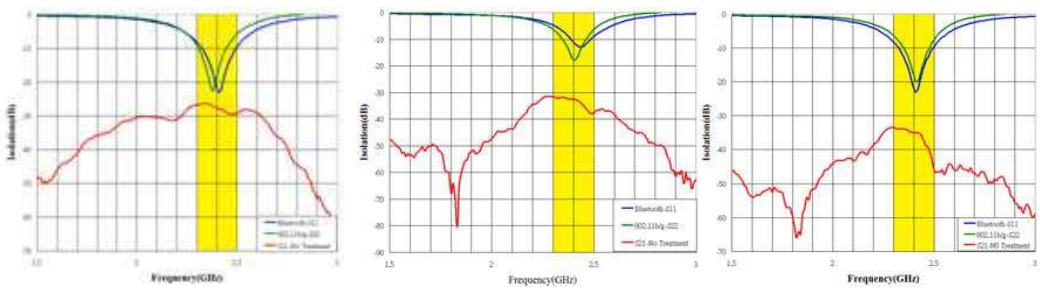

(a) 0 mm (b) 10 mm (c) 20 mm

Figure 4: Measured results for various antenna spacing with both antennas oriented in orthogonal direction.

adjusted the separation between them, the results in Figure 5 also show better isolation than vertical placement due to main lobes decoupling. Table 2 compares the isolation performance between various orientation and separation for both antennas, and it shows that the orthogonal and horizontal orientations gain almost 6–9 dB improvement in isolation except 4 dB difference for 0 mm separation.

3. SUPPRESSION OF MUTUAL COUPLING INTERFERENCE BETWEEN COEXISTENT ANTENNAS

The applications of EBG structure in antenna not only could improve gain and radiation efficiency, it could also help suppress side lobes and reduce coupling effect. Since isolation requirement could not be met by orientation and separation arrangement between antennas from the above measurement, we therefore chose the best placement configuration with orthogonal orientation and 20 mm separation for further investigation utilizing EBG structure. We placed the EBG structure beneath

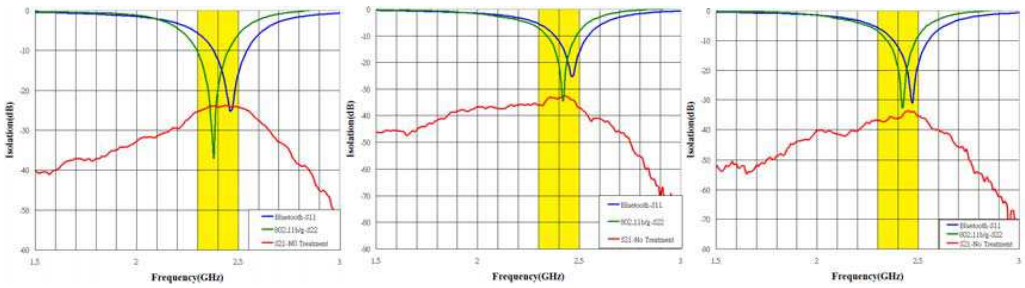

(a) 0 mm (b) 10 mm (c) 20 mm

Figure 5: Measured results for various antenna spacing with both antennas oriented in horizontal direction.

Table 2: Measured results for various antennas placement configuration.

Orientation / Separation	Vertical 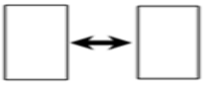	Orthogonal 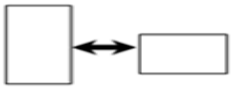	Horizontal 
	Isolation		
0 mm	16.9 dB	28 dB	24.1 dB
10 mm	23.1 dB	32.6 dB	33.1 dB
20 mm	30.8 dB	36.2 dB	36 dB

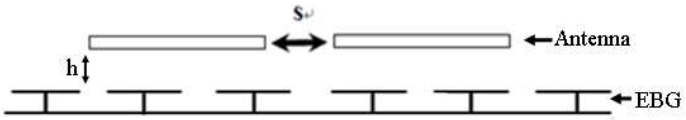

Figure 6: Configuration of antennas and EBG structure placement.

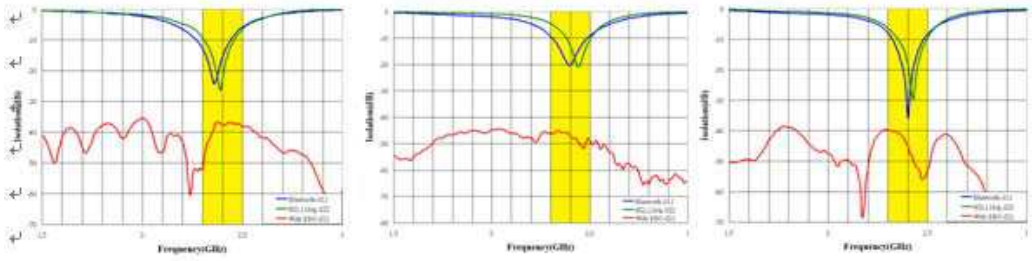

(a) Vertical (b) Orthogonal (c) Horizontal

Figure 7: (a) Isolation and S_{11} of antennas for various orientation with antennas separation 20 mm and EBG-antennas spacing 7.5 mm.

the antennas with 7.5 mm (less that $\lambda/4$) and 15 mm (about $\lambda/4$) distances as shown in Figure 6 and investigated the mutual coupling characteristics. Figure 7 shows the results with 7.5 mm separation between antennas and EBG structure for various antenna orientations. Because of high impedance surface from EBG structure, the 40 dB isolation requirement between antennas could be achieved and parallel-plate guided wave coupling could also be suppressed. Figure 8 shows the results with 15 mm separation between antennas and EBG structure for various antenna orientations. Because of constructively interfering reflection from $\lambda/4$ separation between antennas and EBG structure, not only isolation between antennas is improved, better radiation efficiency is also achieved. Table 3 compares the isolation performance with and without EBG structure for various antenna orientations, and it shows that 37.7 $\sim$ 48 dB and 35.7 $\sim$ 40.9 dB isolation between antennas can be achieved with EBG structure placed beneath antennas 7.5 mm and 15 mm respectively. When EBG structure moves closer to antennas, we can obtain better isolation between antennas.

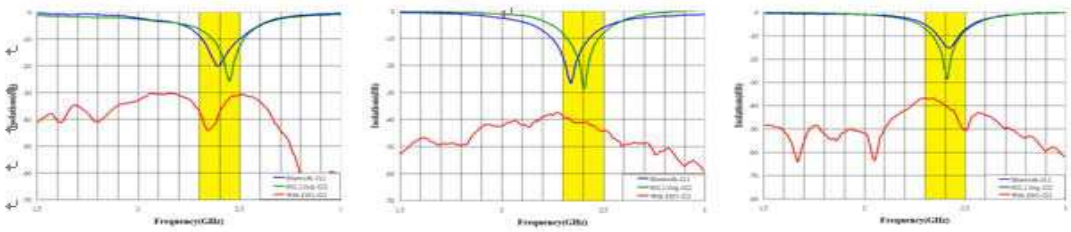

(a) Vertical (b) Orthogonal (c) Horizontal

Figure 8: Isolation and S_{11} of antennas for various orientation with antennas separation 20 mm and EBG-antennas spacing 15 mm.

Table 3: Comparison of isolation improvement from EBG structure with antennas separation 20 mm.

Orientation / **Separation between Antennas and EBG**	Vertical 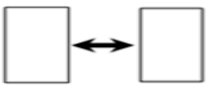	Orthogonal 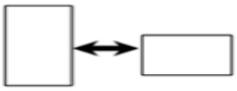	Horizontal 
	Isolation		
Without EBG	30.8 dB	36.2 dB	36 dB
7.5 mm	37.7 dB	48 dB	47.4 dB
15 mm	35.7 dB	40.9 dB	40.5 dB

4. CONCLUSION

In this paper, we investigated the isolation techniques for coexistent antennas of multi-radios system by analyzing their mutual coupling effect. We first compared the isolation measured results from different antenna orientation and found that orthogonal orientation has 6–9 dB better performance that vertical case. We then compared the effect from antennas separation and found that 20 mm separation achieved the optimal isolation performance. However, the 40 dB isolation requirement still can not be met with only separation and orientation adjustment. We therefore implemented the EBG structure on antenna configuration to further suppress antenna coupling. The results show that 37.7 $\sim$ 48 dB and 35.7 $\sim$ 40.9 dB isolation between antennas can be achieved with EBG structure placed beneath antennas 7.5 mm and 15 mm respectively, and it proves that the application of EBG structure can efficiently improve the isolation of coexistent antennas integral to multi-radios system and also the wireless communications performance.

REFERENCES

1. Rogers, S., J. Marsh, W. McKinzie, and G. Mendolia, "AMC edge treatments enable high isolation between 802.11b and Bluetooth^{TM}, antennas on laptop computers," *IEEE Antennas and Propagation Society International Symposium*, Vol. 2, 38–41, Jun. 22–27, 2003.

2. Wong, K.-L. and C.-I. Lin, "Internal GSM/DCS antenna backed by a step-shaped ground plane for a PDA phone," *IEEE Transactions on Antennas and Propagation*, Vol. 54, No. 8, 2408–2410, Aug. 2006.
3. Suh, S.-Y., V. K. Nair, D. Souza, and S. Gupta, "High isolation antenna for multi-radio antenna system using a complementary antenna pair," *IEEE Antennas and Propagation International Symposium*, 1229–1232, Jun. 9–15, 2007.

Tunable Metamaterial Ferrite Stepped Impedance Resonator (SIR)

S. Karimian[1], **M. Abdalla**[2], **and Z. Hu**[1]

[1]MACS Group, School of EEE, University of Manchester, UK
[2]EEE Department, University of Cairo, Cairo, Egypt

Abstract— A novel tunable microstrip metamaterial ferrite $\lambda_g/4$-type stepped impedance resonator (SIR) is introduced for the first time. The presented resonator has been designed over ferrite substrate in left-handed configuration. The tunability theoretical concepts of its operation are discussed. Also, its performance has been validated using the numerical electromagnetic fullwave simulations. The results show that the operating resonant frequency can be tuned from 5.1 GHz to 5.65 GHz by changing the applied DC magnetic bias.

1. INTRODUCTION

Left-handed (LH) metamaterials are artificially constructed materials with electromagnetic properties that do not exist in nature. These properties include simultaneous negative permittivity ε and permeability μ. LH metamaterials (MTMs) have been realised in planar version using transmission line periodically loaded with series capacitors and shunt inductors [1, 2]. Many novel planar microwave components have been introduced making use of the unique properties of the LH structures [3, 4].

Stepped impedance resonator (SIR) has been utilised in many different microwave applications thanks to its high unloaded quality factor-Q [5]. Considering the fact that electrical parameters of the LH TL MTM can be controlled through its loading and parasitic elements, the authors have demonstrated in their earlier papers that, such features can introduce size reduction in the LH SIR compared to its conventional one [6, 7].

Moreover, due to the dispersive properties of ferrite medium [8], and utilising a ferrite substrate, a tunable and nonreciprocal LH TL has been demonstrated in [9, 10]. Consequently, new ferrite LH microwave components have been realised as applications of those novel TLs. Examples of these components are couplers, zeroth order resonators, and transformers [11–13].

In this paper, we introduce a tunable left-handed MTM SIR to be presented for the first time. The left-handed configuration is formed using only one unit cell for each cascaded LH TL, with both TL sections being printed on microstrip ferrite substrate. All LH unit cell configurations are designed using series interdigital capacitors and shunt stub inductors. The proposed resonator is studied analytically and its performance has been verified using numerical simulations.

2. THEORY

The conventional SIR can be designed by cascading two transmission lines of different characteristic impedances (Z_{oi}) and electrical lengths (θ_i) terminated by either short or open circuit load. The short circuited SIR has very high input impedance at its resonant frequency whereas it is almost zero for the open circuited one. In our work, we investigate the case of short circuited $\lambda_g/4$-type SIR.

The characteristic impedances and electrical lengths of cascaded sections are calculated to satisfy the resonance condition at a particular frequency. For the proposed case, i.e., the case of short circuited $\lambda_g/4$-type SIR, the resonance condition can be expressed as [5]

$$\tan(\theta_1)\tan(\theta_2) = \frac{Z_{o2}}{Z_{o1}} \tag{1}$$

In case of LH MTM SIR, both cascaded transmission lines are designed and realised using LH TL. The practical LH TL is a combination of both left handedness due to the effect of the loading elements and right handedness due to parasitic elements of the hosting TL medium. Thus, the equivalent circuit of each LH TL unit cell can be expressed as shown in Figure 1 [3]. As a result, the electrical lengths and characteristic impedances of both lines can be expressed in terms of the loading and parasitic elements of the hosting transmission lines as [3]

$$\theta_i = \omega\sqrt{\left(L_{\mathrm{Ri}} - \frac{1}{\omega^2 C_{\mathrm{Li}}}\right)\left(C_{\mathrm{Ri}} - \frac{1}{\omega^2 L_{\mathrm{Li}}}\right)} \tag{2}$$

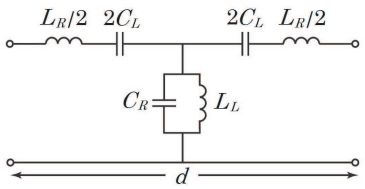

Figure 1: Equivalent circuit model of a practical LH transmission line.

where ω is the angular frequency, L_{Ri} and C_{Ri} are the parasitic hosting transmission line whereas L_{Li} and C_{Li} are the loading shunt inductance and series capacitance for each cascaded LH TL, respectively. The subscript i is corresponding to the two cascaded LH TLs. On the other hand, the characteristic impedance, Z_{oi}, is given as [3]

$$Z_{\mathrm{oi}} = Z_{\mathrm{Li}}\sqrt{\frac{(\omega/\omega_{\mathrm{sei}})^2 - 1}{(\omega/\omega_{\mathrm{shi}})^2 - 1}} \tag{3}$$

$$\omega_{\mathrm{sei}} = \frac{1}{\sqrt{L_{\mathrm{Ri}}C_{\mathrm{Li}}}} \tag{4}$$

$$\omega_{\mathrm{shi}} = \frac{1}{\sqrt{L_{\mathrm{Li}}C_{\mathrm{Ri}}}} \tag{5}$$

where Z_{Li}, the characteristic impedance of each ideal LH TL is given as

$$Z_{\mathrm{Li}} = \sqrt{\frac{L_{\mathrm{Li}}}{C_{\mathrm{Li}}}} \tag{6}$$

From (3), it can be shown that at low frequencies, Z_{oi} is reduced to the LH impedance (Z_{Li}).

When a ferrite medium is used as a substrate, it has a dispersive permeability (μ_f) that changes with the applied DC magnetic bias and the ferrite material properties [8–10]. Therefore, the phase shift and characteristic impedance of a ferrite microstrip LH TL will change according to the applied DC magnetic bias. Thus, a tunable LH ferrite SIR can be achieved by varying the applied DC magnetic bias.

3. STRUCTURE AD RESULTS

The LH ferrite SIR structure is shown in Figure 2, where its layout consists of two different LH TLs. Each LH TL is formed using only one unit cell of series interdigital capacitor and shunt stub inductor. Different configurations of the two cascaded LH TLs were chosen to satisfy the desired electrical parameters, including characteristic impedance and electrical lengths, of each TL.

The employed ferrite substrate is the commercial Trans Tech G113* with thickness of 1 mm. This ferrite material has dielectric constant $\varepsilon_f = 15$, dielectric loss tangent < 0.0002, saturation

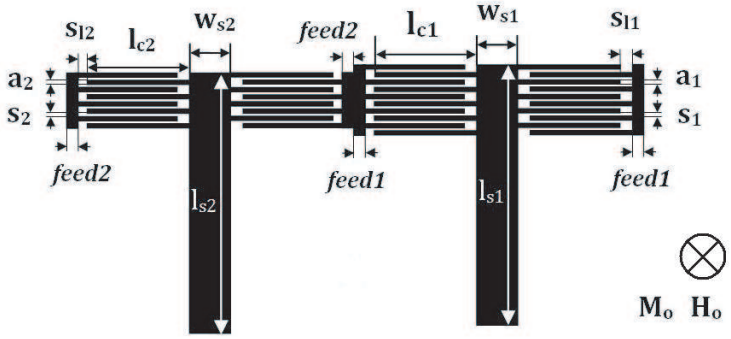

Figure 2: Microstrip layout of the ferrite $\lambda_g/4$-type CRLH SIR: $w_{s2} = 1.9\,\mathrm{mm}$, $a_2 = 0.17\,\mathrm{mm}$, $s_2 = 0.05\,\mathrm{mm}$, $l_{c2} = 3.85\,\mathrm{mm}$, $l_{s2} = 15.2\,\mathrm{mm}$, $s_{l2} = 0.19\,\mathrm{mm}$, $feed2 = 0.1\,\mathrm{mm}$; and $w_{s1} = 1.9\,\mathrm{mm}$, $a_1 = 0.17\,\mathrm{mm}$, $s_1 = 0.05\,\mathrm{mm}$, $l_{c1} = 3\,\mathrm{mm}$, $l_{s1} = 15.2\,\mathrm{mm}$, $s_{l1} = 0.11\,\mathrm{mm}$, $feed1 = 0.1\,\mathrm{mm}$.

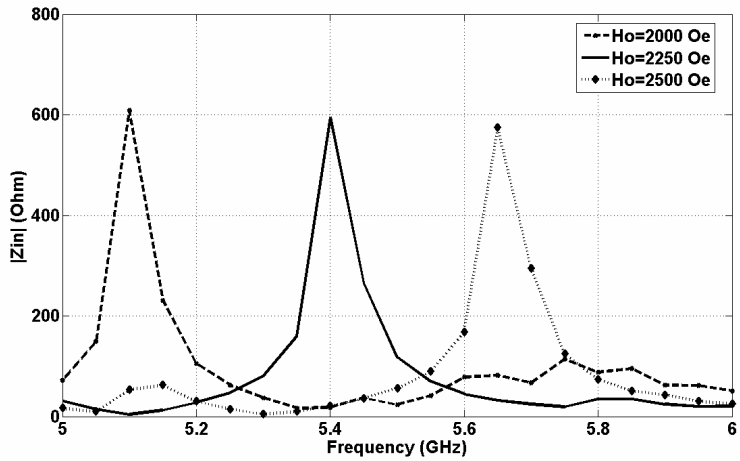

Figure 3: HFSS simulation responses of the ferrite LH $\lambda_g/4$-type SIR for different H_0 values.

magnetisation $4\pi M_S = 1780$ Gauss, and magnetic linewidth $\Delta H_0 \leq 25$ Oe. An internal DC magnetic field (H_0) is applied to the ferrite substrate, resulting in the saturation magnetisation in the direction shown in Figure 2.

To verify the analytical study, the proposed ferrite LH SIR has been analysed using full-wave simulation, for which the commercial software Ansoft HFSS was employed. For simplicity, the applied DC magnetic field was assumed to be uniform in all studied cases.

The tuning capability of the ferrite LH SIR can be illustrated by simulating the above structure for different DC magnetic bias cases from $H_0 = 2000$ Oe, to 2500 Oe. However, in practical measurements, these DC magnetic bias values have to be increased to compensate the demagnetisation field [14]. The magnitude of input impedances in these cases are shown in Figure 3.

It is clear that the operating frequency of the resonator can be tuned from 5.1 GHz to 5.4 GHz, and 5.65 GHz for $H_0 = 2000$, 2250, and 2500 Oe, respectively.

4. CONCLUSION

A novel tunable microstrip ferrite LH $\lambda_g/4$-type SIR was introduced for the first time. Only one LH unit cell, formed of series interdigital capacitor and shunt stub inductor, was employed for the design of each section of the cascaded TL. The proposed resonator has been studied analytically and numerically. The numerical results confirm that the resonant frequency can be tuned from 4.6 GHz to 5.65 GHz by changing the applied DC magnetic bias.

REFERENCES

1. Elefteriades, G. V., A. K. Iyer, and P. C. Kremer, "Planar negative refractive index media using planar LC loaded transmission line," *IEEE Trans. Microwave Theory & Tech.*, Vol. 50, No. 12, 2702–2712, 2002.
2. Caloz, C. and T. Itoh, "Transmission line approach of left-handed (LH) materials and microstrip implementation of an artificial LH transmission line," *IEEE Trans. Antennas and Propagation*, Vol. 52, No. 5, 1159–1166, 2004.
3. Caloz, C. and T. Itoh, *Electromagnetic Metamaterials Transmission Line Theory and Microwave Applications*, 1st Edition, John Wiley & Sons, New Jersey, 2006.
4. Eleftheriades, G. V. and K. G. Balmain, *Negative Refractive Metamaterials*, 1st Edition, John Wiley & Sons, New Jersey, 2005.
5. Makimoto, M. and S. Yamashita, *Microwave Resonators and Filters for Wireless Communication — Theory, Design and Application*, 11–19, Springer, 2001.
6. Karimian, S. and Z. Hu, "Miniaturised left-handed stepped impedance resonator for WLAN applications," *3rd IEEE International Symposium on Microwave, Antenna, Propagation (MAPE) and EMC Technologies for Wireless Communications*, 27–29, October 2009.
7. Karimian, S., M. Abdalla, and Z. Hu, "Left-handed stepped impedance resonator for WLAN applications," *3rd International Congress on Advanced Electromagnetic Materials in Microwaves and Optics*, Queen Mary University of London, August 30–September 4, 2009.
8. Lax, B. and K. J. Button, *Microwave Ferrites and Ferrimagnetics*, McGraw Hill, 1962.

9. Tsutsumi, M. and T. Ueda, "Nonreciprocal left-handed microstrip lines using ferrite substrate," *Proceedings of IEEE MTTS Int. Microwave Symposium*, 249–252, USA, June 2004.
10. Abdalla, M. and Z. Hu, "On the study of CWP dual band left-handed propagation with reciprocal and nonreciprocal characteristics over ferrite substrates," *Proceedings of IEEE APS Int. Symp.*, 2578–2581, USA, June 2007.
11. Tsutsumi, M. and K. Okubo, "On the left handed ferrite coupled line," *EMTS International URSI Commission B Electromagnetic Theory Symposium Digest*, 13, Ottwa, Canda, 2007.
12. Abdalla, M. and Z. Hu, "Design and analysis of tunable left handed zeroth order resonator on ferrite substrate," *IEEE Trans. Magnetics*, Vol. 44, 3095–3098, November 2008.
13. Abdalla, M. A. and Z. Hu, "On the study of left handed CPW transformer on ferrite substrate," *Proceedings IEEE APS Int. Symp.*, 14, San Diego, California, USA, 2008.
14. Aharni, A., "Demagnetizing factor for rectangular ferromagnetic prisms," *Journal of Applied Physics*, Vol. 83, 3432–3434, March 1998.

a-*b* Plane Dielectric Discussion on Layered Multiferroic Oxides

Yalin Lu and R. J. Knize
Laser Optics Research Center, United Air Force Academy, CO 80840, USA

Abstract— With a goal to investigate possible anisotropic dielectric properties in layered multiferroic oxides, infrared reflection measurement was used to measure dielectric constants inside the *a*-*b* lane of highly *c*-oriented double layered Bi_2FeCrO_6 thin film, and the results were compared to that from highly *c*-oriented $BiFeO_3$ thin film. The dielectric spectra were identified according to optical phonons, and the areas with negative permittivity were analyzed. The preliminary effort will actually lead to a very interesting area of finding new photonic materials for efficiently controlling EM waves.

1. INTRODUCTION

While ferroelectricity (FE) in perovskite oxides has long been the subject of intensive experimental and theoretical study, interest has recently grown in exploring FE and ferromagnetic (FM) in other structural oxides. This is motivated by expanded opportunities for tuning polarization-related properties, and by the searching for new multiferroics with stronger magnetic ordering and magnetoelectric (ME) coupling above room temperatures (RT). Of particular interest are layered structures consisting of two-dimensional (2D) perovskite layers separated by intergrowth layers of other metal oxides: a series of oxides such as the Dion-Jacobson $A[A'_{n-1}B_nO_{3n+1}]$, Ruddlesden-Popper $A_2[A'_{n-1}B_nO_{3n+1}]$, and Aurivillius $[Bi_2O_2][A'_{n-1}B_nO_{3n+1}]$ (where A is alkali metal, A′ alkaline earth, and B transition metal) compounds. In these layered structures, magnetic cations could be introduced into intergrowth layers, leading to both magnetic ordering and multiferroic behavior. By doing so, magnetic and ME properties are then governed by coupling between those magnetic cations, and as such, it becomes interesting to modulate the layer number, the interlayer distance and to insert other magnetic ions in order to promote intra and interlayer magnetic interactions. For example, when half Fe^{3+} sites in a four-layer Aurivillius phase, $Bi_5FeTi_3O_{15}$ being substituted by Co^{3+} ions, over 3 times enhancement on magnetic moment and a remarkable coexistence of FE and FM above RT can be observed in the resulting new composition $Bi_5Fe_{0.5}Co_{0.5}Ti_3O_{15}$. This remarkable effect was attributed to a coupling among Fe^{3+} and Co^{3+} ions [1]. Room temperature occurrence of FE and FM plus an ordered long-range lattice modulation are prerequisites for realizing both permittivity and permeability anomalies [2, 3]. Therefore, it will be interesting to analyze such anomalies along different crystalline directions inside the layered multiferroic single crystals, when further to explore their potential applications in controlling electromagnetic (EM) waves.

Unfortunately, research in this area had encountered many challenges arising not only from the complicated nature of such layered oxides, but also from their rare availability, especially in the form of single crystal, due to difficulties in material synthesis [1]. As a preliminary effort toward this direction, in this research we will only discuss high frequency negative dielectric anomalies inside the *a*-*b* plane of a double multiferroic perovskite oxide, Bi_2FeCrO_6 (BFCO), and compare the results to that from $BiFeO_3$ (BFO), both in the form of highly *c*-oriented crystalline thin films. It should be mentioned here that dielectric property along the *c*-axis will be much more useful in order to understand its relationship with the layered structure. Unfortunately, the used infrared (IR) measurement technique limits the responses only inside the *a*-*b* plane.

2. EXPERIMENTS

Because that we are interesting in phonon-associated dielectric responses of layered multiferroic materials, methods for dielectric measurement are required able to cover a frequency range as broad as possible, and to be able to polarization-selective and accurate. Unfortunately, low frequency dielectric measurement on BFCO and BFO films is not accurate, due to their high *dc* conductivity. Such conductivity will be not very appreciated in THz time-domain spectroscopy (TDS) measurement too. Apparently high frequency dielectric measurement will be then advantageous. An additional benefit from the use of the high frequency infrared measurement is an easy extension into the far infrared (FIR) ($< 200\,\mathrm{cm}^{-1}$), which is otherwise hardly achievable. In the IR measurement, one can select either transmission or reflection modes, which have different requirements on substrate selection. For the transmission mode, the substrate should be transparent to a broad range of IR

spectrum, and then the ultimate measurement will be limited by the substrate's transparency For the reflection mode, the substrates are required to have responses to IR as simple as possible. Because of this reason, (100)-oriented $LaAlO_3$ (LAO) is preferred than (100)-oriented $SrTiO_3$ (STO) in the thin film growth of both BFCO and BFO.

BFCO was predicted with ferromagnetic and ferroelectric properties allegedly much larger than majority of those known multiferroic materials [4]. The predicted ground state structure is very similar to that of the rhombohedral $R3c$ structure of BFO, but with Fe^{3+} cations substituted with Cr^{3+} cations in every second (111) layer, reducing the symmetry to the space group of $R3$. In our experiments, about 500 nm thick BFCO and BFO thin films were grown on (100)-oriented $LaAlO_3$ substrates via the pulsed laser deposition (PLD). X-ray diffraction analysis (XRD) shows the $00l$ peaks of BFCO are typically near the $h00$ reflections of the LAO. The calculated out-of-plane lattice parameters are typically $\sim$3.96Å. Polarized IR reflectance spectra were recorded using a Nicolet 6700 FTIR at the room temperature, which are similar to those published results (using unpolarized light) in Ref. [5]. Changing the incident polarization didn't cause much difference for both BFCO and BFO thin film materials, and therefore it should be reasonable to assume nearly isotropic inside the a-b plane. Because of this reason and because that we don't have the temperature adjustment inside the IR measurement system, unpolarized results from Ref. [5] for BFCO thin films, which are a very complete set of data, will be used to support below analyses.

3. RESULT AND DISCUSSION

Figure 1 shows the complex dielectric spectra of BFO and BFCO thin films obtained from the measured IR reflectance spectra at room temperature. Since that we are interesting in the real dielectric constant discussion, the tangent loss spectra are not shown. In order to extract the complex dielectric spectra, a same procedure of measuring IR reflectance on substrate-only (LAO) and on 'film + substrate' two-layer, as suggested in Ref. [5]. Reflectivity from the rare substrate LAO will be fit using the formula

$$R(\omega) = \left| \frac{\sqrt{\varepsilon^*(\omega) - 1} - 1}{\sqrt{\varepsilon^*(\omega) - 1} + 1} \right|^2, \tag{1}$$

here $\varepsilon^*(\omega) = \varepsilon'(\omega) - i\varepsilon''(\omega)$, and for LAO, this complex dielectric constant can have the factorized form as suggested in Ref. [6]. Subsequently, the IR reflection spectra from the two-layer structure can be fit using above Eq. (1) and the classical Lorentz model of the damped harmonic oscillators (see Ref. [5]). In this fitting, the oscillator parameters from the LAO substrate are already known (from the previous fitting). Subsequently, relationship between real/imaginary dielectric constants and wavelength can be obtained.

For BFO and BFCO, five and six polar modes can be roughly identified at room temperature, respectively. They are from lattice vibrations (optical phonons), if comparing to the prediction of factor group analysis. For BFO, Factor group analysis of lattice vibrations in the $R3c$ structure with two formula units per unit cell gives out the following 13 optical phonons (neglecting the silent modes):

$$\Gamma_{R3c} = 4A_1(z, x^2 + y^2, z^2) + 9E(x, y, xy, xz, yz, x^2 - y^2) \tag{2}$$

For BFCO with an assumed rhombohedral space group of $R3 - C_3^4$, it corresponds to 18 optical phonons

$$\Gamma_{R3c} = 9A_1(z, x^2 + y^2, z^2) + 9E(x, y, xy, xz, yz, x^2 - y^2) \tag{3}$$

Here two issues may complicate the above analysis: 1) in the IR measurement, only a-b plane interactions are considered. This may reduce the polar mode number; and 3) because of the lattice mismatching between thin film and substrate, the film may be stressed either compressively or expansively. This could simplify the analysis too, due to that the substrate is pseudo-cubic. Less mode number observed in the Fig. 1 is because of mode softening and mode damping due to the increased temperature.

As the arrows indicated inside the Fig. 1, there are a few areas showing negative permittivity in a small frequency range after the phonon resonance frequencies. For BFCO, both amplitude and the valley-frequency of those negative permittivity areas are dependent on temperature, as can be seen from Ref. [5]. Fig. 2 here shows the data extracted from Ref. [5], focusing on the mode at the wavelength around $100\,\mathrm{cm}^{-1}$, which indicates a shifting of the phonon modes to lower

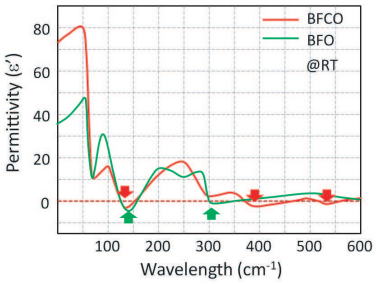

Figure 1: Real dielectric spectra of BFO and BFCO thin films at room temperature.

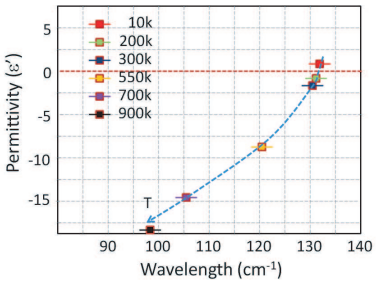

Figure 2: Relationship among valley permittivity, valley position, and the temperature.

frequencies when increasing temperature (phonon softening). It is interesting to note that the negative permittivity amplitude at valley actually increases as the temperature increases. Reasons for this are unclear. It may relate to the intensified vibrations under high temperatures. However, the result indicates a new way of adjustment when trying to optimize this negative permittivity effect.

According to Fig. 1, the observed negative permittivity behavior for both BFO and BFCO shows a certain level of similarity. This may be explained by the *a*-*b* plane's structural similarity among both thin films. This does make sense if only considering their lattice mismatching with the substrate. Apparently, contribution from the double layered structure of BFCO cannot be distinguished, when compared to the single unit cell structure (BFO). In this research the IR reflectance measurement was actually performed on *c*-oriented thin films, the layered structure is aligned along the *c*-axis direction.

There are a few ways possibly able to break the above method's limitation, for examples, 1) to simply use layered multiferroic single crystals, if available; 2) to use THz wave generation via nonlinear optical rectification effect. This method will be useful for highly oriented thin films. It is understandable that this method for thin films will be challenged by low sensitivity; 3) to perform nonlinear optical frequency conversion measurement. This method will depends on finding a suitable fundamental laser wavelength inside the infrared wavelength range. However, it could be very sensitive.

4. CONCLUSIONS

This research tries to reveal some interesting anisotropic dielectric behaviors inside the layered multiferroic materials. Because of the limitation from the used IR reflectance measurements, only *a*-*b* plane dielectric behaviors are analyzed and compared to that from the single unit cell material BFO. The research performed so far is preliminary. However, it leads to a very interesting area of finding new photonic materials for efficiently controlling EM waves.

ACKNOWLEDGMENT

The authors appreciate the support from the United States Air Force Office of Scientific Research (AFOSR) and from the United States Air Force Research Laboratories (AFRL).

REFERENCES

1. Mao, X. Y., W. Wang, X. B. Chen, and Y. Lu, "Multiferroic properties of layer-structured $Bi_5Fe_{0.5}Co_{0.5}Ti_3O_{15}$ ceramics," *Appl. Phys. Lett.*, Vol. 95, 082901, 2009.
2. Lu, Y., G. J. Brown, and K. Reinhardt, "Negative refraction oxide superlattices," *Integrated Ferroelectrics*, 2009, to be published.
3. Duan, C. G., S. S. Jaswal, and E. Y. Tsymbal, "Predicted magnetoelectric effect in Fe/$BaTiO_3$ multilayers: Ferroelectric control of magnetism," *Phys. Rev. Lett.*, Vol. 97, No. 4, 047201, 2006.
4. Baettig, P. and N. A. Spaldin, "Ab initio prediction of a multiferroic with large polarization and magnetization," *Appl. Phys. Lett.*, Vol. 86, 012505, 2005.
5. Kamba, S. and A. Pignolet, "Infrared and magnetic characterization of multiferroic Bi_2FeCrO_6 thin films over a broad temperature range," *Phys. Rev. B*, Vol. 77, 104111, 2008.
6. Gervis, F., *Infrared and Millimeter Waves*, edited by Button K. J., Academic, New York, 1983, Vol. 8, Chap. 7, 279, 1983.

Realization of Negative Refraction via Overlapping Ferroelectric and Ferromagnetic Oxides

Yalin Lu and R. J. Knize
Laser Optics Research Center, United Air Force Academy, CO 80840, USA

Abstract— Two possible mechanisms in periodically overlapped ferroelectric and ferromagnetic oxides toward realizing negative refraction are discussed. When using the superlattice structure, phonon spectral coupling among an incident electromagnetic waves, dielectric dipoles and magnetic moments will generate special polaritons showing both $-\mu$ and $-\varepsilon$ in a short frequency range after the resonance. When using a multilayer, new resonance frequency-tuning approaches will be used to fine-tune both dielectric and magnetic resonances to concurrence at the same frequency. Similarly, negative refraction could be expected after the concurred resonance frequency.

1. INTRODUCTION

Artificial metamaterials that exhibit unique properties consistent with simultaneous negative permittivity ($-\varepsilon$) and negative permeability ($-\mu$) have recently attracted extensive attentions. New properties in such 'metamaterials', including negative refraction in so-called negative index materials (NIMs), have been demonstrated mainly for microwave wavelengths [1] with a potential of an exciting array of applications from new designs in radar to high resolution nuclear magnetic resonance imaging for medical analyses. Majority of the previously demonstrated NIMs uses metallic split-ring resonance, surface plasmon resonance, or a combination of magnetic and metallic materials having naturally occurred negative ($-\varepsilon$) and ($-\mu$). When further extending the operation to optical frequencies, negative refraction will portend the 'super-lenses' effect that can image with resolution far below the diffraction-limit. Optical NIM offers many exciting opportunities to develop high-performance photonic devices.

Complex ferroelectric (FE), piezoelectric (PE), and piezomagnetic (PM) oxide materials are well-known for their extraordinary responses to optical and THz frequencies. Their complicate phase and domain structures offer many unique opportunities as potential frequency-tunable materials through efficient compositional and structural engineering. The use of such complex PE and PM oxide materials for potential NIMs has the potential to significantly reduce optical losses, when comparing to those metallic- and semiconductor-involved open split-ring metamaterials. Complex PE and PM oxide can be also fair-easily made into thin films via many film deposition methods including sputtering, pulsed laser deposition (PLD), solution deposition, etc. This will be cost-effective in fabrication of photonic devices, comparing to advanced nanofabrication needed in current metamaterials. This paper introduces a theoretical description of possibly realizing negative refraction using both 'superlattice' and 'multilayer' structures, which are a combination of complex PE and PM oxides.

2. THE SUPERLATTICE CONCEPT

Coupling among electronic dipoles has been observed in many ferroelectric (FE), dielectric, or PE superlattice or multilayer structures. In a dielectric/piezoelectric superlattice, for example, this coupling produces a new type of dielectric polariton, in which $-\varepsilon$ can be obtained near the high frequency side of the resonance [2]. Similarly, negative permeability (μ) could be obtained near the spin polariton resonance in a piezomagnetic superlattice [3]. The superlattice NIM mechanism is to combine the above two effects together using a rigid and ordered lattice structure composing of piezoelectric (PE) and piezomagnetic (PM) effects. In such PE/PM superlattice, both PE and PM coefficients will be periodically modulated (in this case, both dipole and spin are Δ-modulated, see Fig. 1), the lattice vibration will couple the propagating electromagnetic wave with both dielectric and magnetic polaritons, and this will result in special polaritons showing resonances coincident to the phonon spectrum. Then simultaneous $-\mu$ or $-\varepsilon$ could be produced in a frequency range immediately after the (phonon) resonance frequency [4, 5].

Figure 2 shows the simulated result when using an elastic coefficient $C_{11}^S = 300$ GPa, static permittivity $\varepsilon_0 = 30$, static permeability $\mu_0 = 50$, the mass density $\rho = 6.5 \times 10^3\,\mathrm{kg/m^3}$, and the layer thickness $d_1 = d_2 = 40\,\mathrm{nm}$. Both piezoelectric and piezomagnetic coefficients are Δ-modulated

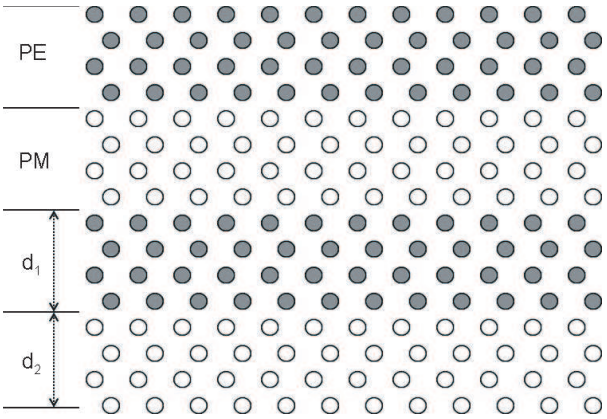

Figure 1: Schematic of the oxide superlattice potentially showing negative refraction.

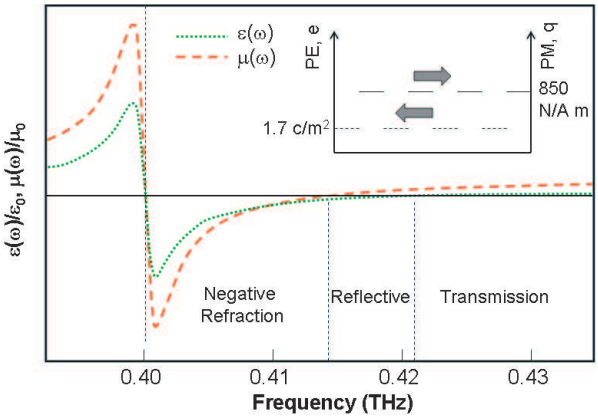

Figure 2: Typical $-\varepsilon$ and $-\mu$ after the resonance. Inset shows the delta-modulated PE and PM effects.

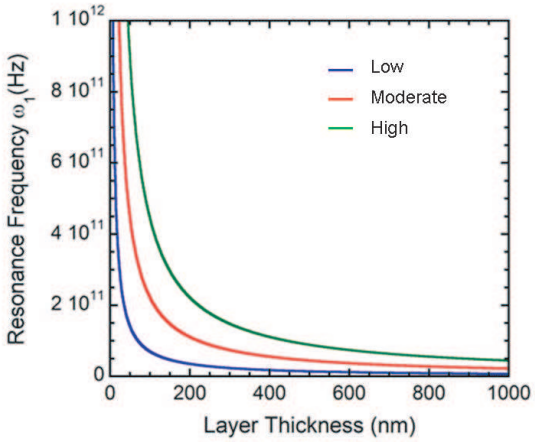

Figure 3: Simulated relationship between the resonance frequency and the superlattice period for the three cases of low, moderate, and high dielectric constant and piezoelectric coefficient.

(the inset in Fig. 2). The result indicates a resonance frequency and a negative refraction in the THz range.

In order to fabricate such superlattice NIMs, many strict requirements have to be met: 1) both PE and PM oxides have to be physically and chemically similar. This includes the growth temperature, phase, stability, lattice structure, etc. Lattice similarity, for example, is highly required for realizing an epitaxial superlattice growth. Normally, lattice mismatch between the selected two oxides for a high quality superlattice growth is limited to ∼5%. 2) Availability of a nearly lattice-matched substrate for the superlattice growth. The substrate should be a good optical material too. 3) Practicability in fabrication of such superlattice NIMs. For example, for a predetermined operation frequency the designed superlattice's periodicity should be not too small or not too big either. In most complex oxide superlattices, a small periodicity usually causes the loss of structural distinction, ferroelectricity and magnetism in each corresponding layer and a large periodicity causes the loss of the stacking order.

Since that generally the material pool for PE material selection are much larger than that for PM material selection, in this preliminary effort we assume the PM material is fixed and then classify those possible PE materials into three categories: low, moderate, and high, roughly according to their dielectric constants and piezoelectric coefficients (listed in Table 1). Fig. 3 shows the simulated results obtained using the similar structure in Fig. 2. The result indicates that increasing both dielectric constant and piezoelectric coefficient actually increases the anticipated superlattice's period at a fixed operation frequency, which makes the expected NIM more practical in fabrication.

3. THE MULTILAYER CONCEPT

A split-ring resonance [6] in a metamaterial that produces $-\varepsilon$ and $-\mu$ will be similar to a multilayer composed by alternating $-\varepsilon$ and $-\mu$ layers — the later is much easier to fabricate in general. It is also well known that some natural materials have inherent $-\varepsilon$ or $-\mu$, which will be useful for the proposed multilayer NIM fabrication. For example, certain ferrites have $-\mu$ in microwave frequencies, and many conducting materials have $-\varepsilon$ below the plasma frequency. Studies toward this direction have been performed, mostly by simulation, in stacked ferrite-dielectrics, ferrite-metal, ferromagnetic-superconductor, and ferrite-semiconductor multilayers [7]. However, the use of conductive materials may excite surface waves at their interfaces, which in turn change their electromagnetic characters. More seriously, it may result in a concern for high optical losses. Apparently, a possible multilayer NIM composing of non-conductive optical materials such as oxides will be promising An alternative mechanism to build the oxide multilayer NIM is to use resonance-tuned multilayer (RTM) composing of alternative dielectric and magnetic oxide layers having naturally occurring $-\varepsilon$ or $-\mu$, and having their resonance frequencies finely tuned to concurrence via both structural and compositional engineering to the used two materials.

The RTM mechanism considers the non-lattice-matched multilayer case and the two alternative oxide layers as the multilayer have $-\mu$ or $-\varepsilon$, respectively. For example, the oxide multilayer can be represented as $(A/B)_m$, and 'A' has an intrinsic dielectric resonance and 'B' represents a material with an intrinsic magnetic resonance. The RTM approach will be used to fine-tune the two resonance frequencies concurrence together, and realize the negative refraction immediately after the merged resonance frequency. Fine-tuning to each oxide material can be realized by changing composition, structure, temperature, magnetic field, etc. Schematic of the RTM NIM is shown in Fig. 4. In Fig. 4, only two adjacent laminas having thickness of d_1 and d_2 are shown. The insets on the right side schematically show the frequency spectra of both permittivity and permeability around their resonance frequencies. Arrows indicate the directions of frequency tuning to make two resonance frequencies concurrence. Fig. 5 shows the multilayer schematic and the concurrence frequency spectra showing the frequency region with both $-\mu$ and $-\varepsilon$.

In order to achieve a concurrence of both dielectric and magnetic resonances in dielectric and magnetic oxide materials, different origins of dielectric and magnetic responses have to be considered for different frequencies ranging from the UV/visible, far-infrared, to microwave. For the UV to visible spectrum, the dielectric response is primarily from the electronic polarization modes and the magnetic response from the magnetic dipoles. In the far-IR range, ionic polarization modes and antiferromagnetic resonances (AFMR) are mainly responsible for dielectric and magnetic responses, respectively. Similarly, for those microwave frequencies, electronic dipole reorientation (domain wall moving) and ferromagnetic resonances (FMR) are the main causes.

Other than the resonance frequency of the concerning materials, both degree of damping and amplitude of dielectric and magnetic responses will also play the key rule. For example, in optical frequencies, direct magnetic dipole response is orders of magnitude weaker than electronic dipole response. The above-discussed SCS mechanism actually provides an indirect coupling of the magnetic dipole response to a strong electronic dipole resonance via the phonon resonance, yielding both negative permeability and permittivity after the phonon resonance frequency.

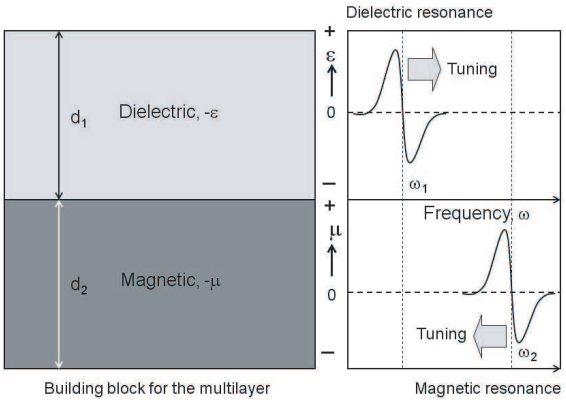

Figure 4: Schematic of the RTM mechanism.

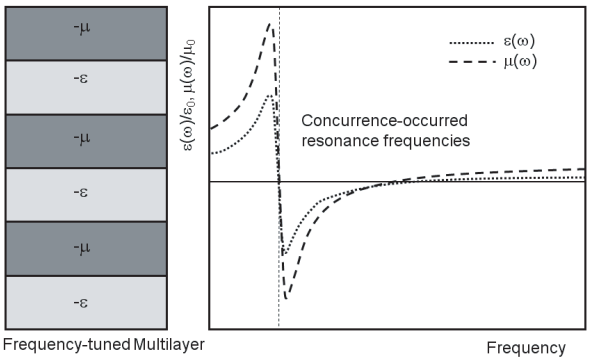

Figure 5: Concurrence of the frequencies after fine-tuning.

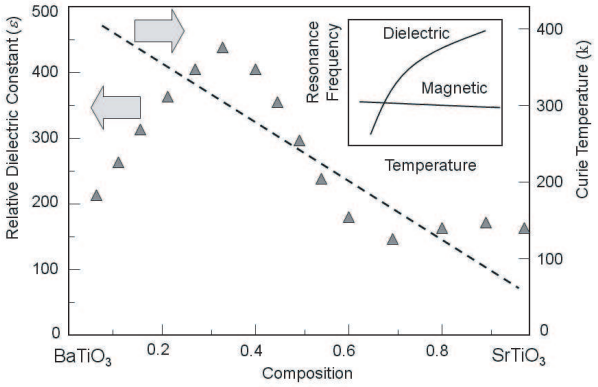

Figure 6: Dielectric property vs composition in BST.

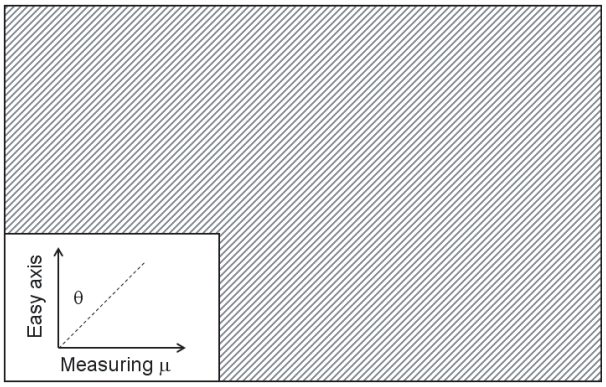

Figure 7: Schematic for structural magnetic tuning.

Actual frequency tuning of both dielectric and magnetic resonances may follow a few different ways. In certain ferroelectric materials, optical mode of the lattice (phonon) is dependent on both temperature (T) and the material's Curie temperature (T_c), roughly following an empirical relation: $\omega^2 \propto (T - T_c)$ as an example. As an example, Fig. 6 shows the dependence of relative dielectric constant on the composition. The dielectric maximum occurs at $x_{Ba} \sim 0.7$ [at where the ferroelectric-paraelectric boundary (FPB) occurs], and it Curie temperature changes from 415 K ($x_{Ba} \sim 1$) to about 40 K ($x_{Ba} \sim 0$) almost linearly [8]. Similarly, tuning by changing both temperature and material composition is also applicable to some magnetic oxide materials. Inset in Fig. 6 show a general frequency tuning schematic via changing the temperature, in order to reach a concurrence at the same frequency for both dielectric and magnetic resonances. Apparently, tuning their compositions to reach a room temperature operation of the NIMs will be the most attractive, simply because of the practicability for applications.

An alternative way of possibly tuning the magnetic resonance frequency is by changing the magnetic layer's alignment inside the multilayer structure. Fig. 7 shows the schematic of such a structure in which the FMR frequency will be tuned by changing either the orientation angle θ or the layer thickness, following the rewritten Kittel's formula involving both uniaxial anisotropy field (H_u) and the additional shape anisotropy field ($H_{k,eff}$) into the total effective anisotropy field ($H_{A,eff}$)

$$H_{A,eff} = H_u + H_{k,eff} \cos\theta, \tag{1}$$

and

$$2\pi\omega_{AFMR}/\gamma = \sqrt{4\pi M_s H_{A,eff}}, \tag{2}$$

In Fig. 7, the main picture shows the parallel strait structure to be made in the magnetic layer inside the superlattice, via selective etching the as-fabricated magnetic layer or mask-shielding growth, etc. The inset shows that when one measures the permeability horizontally, the result will be actually tunable by changing the strait's size (both period and width) or by changing the angle respective to the easy axis of the magnetic material. The multilayer structure itself to be discussed in this theory actually provides the great easiness to reach such frequency tuning for the magnetic part inside the multilayer. Structural parameters that can be varied when designing include the layer thickness, periodic duty cycle, and magnetic orientation, etc. An efficient way to optimize material compositions and structural parameters may follow the combinatorial strategy [9].

4. CONCLUSIONS

A possible mechanism toward realizing negative refraction in a fully oxide-based superlattice was discussed. Preliminary material selection consideration was discussed, which will lead the research in this area in a right direction, when focusing on future optical frequency operation of such superlattice NIMs.

REFERENCES

1. Smith, D. R., J. P. Willie, D. C. Vier, S. C. Nemat-Nasser, and S. Schultz, *Phys. Rev. Lett.*, Vol. 84, 4184, 2000.
2. Liu, H., S. N. Zhu, Z. G. Dong, Y. Y. Zhu, Y. F. Chen, N. B. Ming, and X. Zhang, *Phys. Rev. B*, Vol. 71, 125106, 2005.

3. Zhao, J., T. Fan, R. C. Yin, M. H. Lu, C. L. Du, Y. F. Chen, Y. Y. Zhu, S. N. Zhu, and N. B. Ming, *Physics Letts.*, Vol. 372, 486, 2008.
4. Liu, H., S. N. Zhu, Y. Y. Zhu, Y. F. Chen, N. B. Ming, and Z. Zhang, *Appl. Phys. Lett.*, Vol. 86, 102904, 2005.
5. Tarkhanyan, R. H. and D. G. Niarchos, *Optics Express*, Vol. 14, 5433, 2006.
6. Zheng, H., J. Wang, S. E. Lofland, Z. Ma, L. Mohaddes-Ardabili, T. Zhao, L. Salamanca-Riba, S. R. Shinde, S. B. Ogale, F. Bai, D. Viehland, Y. Jia, D. G. Schlom, M. Wuttig, A. Roytburd, and R. Ramesh, *Science*, Vol. 303, 661, 2004.
7. Lu, Y., *Appl. Phys. Lett.*, Vol. 85, 979, 2004.
8. Li, J. W., F. Duewer, C. Gao, H. Y. Chang, X. D. Xiang, and Y. Lu, *Appl. Phys. Lett.*, Vol. 76, 769, 2000.
9. Lu, Y., *Active and Passive Electronic Components*, Vol. 2007, Article ID 17692, 2007.

Electromagnetic Tunneling in Nonconjugated Epsilon-negative and Mu-negative Metamaterial Pair

Yaqiong Ding[1, 2], **Yunhui Li**[1, 2], **Haitao Jiang**[1, 2], **and Hong Chen**[1, 2]

[1]Pohl Institute of Solid State Physics, Tongji University, Shanghai 200092, China
[2]Shanghai Key Laboratory of Special Artificial Microstructure Materials and Technology, China

Abstract— In this paper, the tunneling phenomenon occurring at the interface with great impedance contrast is investigated by numerical calculation. It is found even in this case, perfect transmission can still be achieved theoretically when nonconjugated sub-wavelength epsilon-negative (ENG) and mu-negative (MNG) metamaterial pair is introduced. Moreover, the calculated electromagnetic field distributions show that, only one component of the tunneling mode (either the electric or the magnetic field) is amplified, suppressing another one at the same time. Therefore, the nonconjugated ENG-MNG pair is promising to be applied in modern optic and microwave communication systems for less reflection, compact device volume and flexible control of EM field distribution.

1. INTRODUCTION

As is known, reflection is a common and inevitable optical phenomenon for interfaces with notable impedance contrast. To enhance the transmission, many methods are introduced. For instance, in optics, quarter-wavelength antireflective coatings are widely used to reduce the reflection of optical devices [1–3]. In order to achieving perfect transmission efficiency, multiple antireflective layers should be involved. Therefore, the length of these layers will be very long, which greatly restricts the possibility to design compact optical communication devices with high transmission efficiency. Metamaterials [4–16], which have attracted wide interests recently, may be a solid candidate to solve this problem. Metamaterials include double negative (DNG) materials (both the permittivity and the permeability are negative) and single negative (SNG) materials (only one of the permittivity or the permeability is negative). In SNG materials, the EM waves are evanescent since their wave vectors are complex. In particular, a tunneling scenario will emerge when a pair of lossless ENG and MNG slabs is conjugated matched between two similar half spaces.

In this paper, we investigate the tunneling phenomenon occurring at the interface between two different materials with great impedance contrast by numerical calculation. It is shown that, when a nonconjugated sub-wavelength epsilon-negative (ENG) and mu-negative (MNG) metamaterial pair is introduced between two different materials with great impedance contrast, perfect transmission can still be achieved theoretically. The tunneling condition of the nonconjugated ENG-MNG pair in above case is also figured out. Moreover, the calculated electromagnetic field distributions show clearly that, by choosing proper parameters we can even amplify only one component of the tunneling mode (either the electric or the magnetic field), suppressing another one at the same time. Therefore, the nonconjugated ENG-MNG pair is promising to be applied in modern optic and microwave communication systems for less reflection, compact device volume and flexible control of EM field distribution.

2. SECTION 1

First, we investigate the tunneling phenomenon in a ENG-MNG pair sandwiched between two different semi-infinite regions by means of the transfer-matrix method [17]. Let EM waves be normally incident from the left region to the ENG-MNG pair, as shown in Fig. 1.

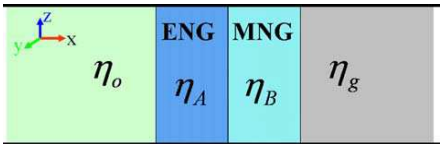

Figure 1: Schematic of an ENG-MNG pair sandwiched between two different semi-infinite regions.

Admittance of the left region, ENG, MNG and the right region are η_o, η_A, η_B and η_g respectively. (Here, η_o, η_A, η_B and η_g are real numbers. in other words, in the calculation, the admittance of

ENG and MNG are $-i\eta_A$, $i\eta_B$, $i^2 = 1$) when EM waves normally incident from the left region with η_o, through the ENG-MNG pair, and finally into the right region with η_g, Given all materials discussed here is lossless, zero reflection phenomena will occur under the conditions as follows:

$$T = \eta_g |t|^2/\eta_0 = 1 \tag{1}$$

$$|R| = 0 \tag{2}$$

where T is the transmittance, R is the reflectance and t is the transmission coefficient. Assuming $\delta_A = \delta_B$, (δ_A and δ_B are the phase shift of ENG and MNG respectively) the following expression can be concluded from Equations (1) and (2):

$$(\eta_A^2 - \eta_B^2)(\eta_0^2\eta_g^2 - \eta_A^2\eta_B^2) = 0 \tag{3}$$

(1) Because $\eta_A > 0$, $\eta_B > 0$, $\eta_g = \eta_0$ and $\eta_A = \eta_B$ is an obvious solution satisfying Equation (3). It should be noticed that this is exactly the matching condition used generally to describe the tunneling phenomenon occurring in the *conjugated* ENG-MNG pair surrounded by *same* environment materials.

(2) When a *nonconjugated* ENG-MNG pair is placed between two *different* environment materials ($\eta_A \neq \eta_B$, $\eta_g \neq \eta_0$), another matching condition can be deduced from Equation (3), which is $\eta_0\eta_g = \eta_A\eta_B$ (4). This condition implies that, with properly designed nonconjugated ENG-MNG pair the reflection at the interface between two different materials can even be reduced to zero, no matter how great the impedances of these materials contrast. It must be mentioned that, the zero reflection frequency is obviously independent of the scaling of the introduced ENG-MNG pair. Therefore, this matching condition provides us a new approach to reduce the reflection at interfaces, keeping the device volume much compact at the same time.

To verify the matching condition mentioned above, we use Drude mode to describe the isotropic single-negative materials, given as:

$$\varepsilon_A = \varepsilon_a - \frac{\alpha}{\omega^2}, \quad \mu_A = \mu_a$$

in ENG materials and

$$\varepsilon_B = \varepsilon_b, \quad \mu_B = \mu_b - \frac{\beta}{\omega^2}$$

in MNG materials. These kinds of dispersion for ε_A and μ_B can be realized in some well designed metamaterials [18]. The angular frequency $\omega/2\pi$ is in units of GHz. In the following calculation, we choose two sets of parameters. The first group are $\varepsilon_a = 1$, $\mu_a = 1$, $\varepsilon_b = 25$, $\mu_b = 1$, $\alpha = 680$, $\beta = 40$, $\eta_0 = 25$ and $\eta_g = 1$. The thicknesses of the ENG slab (d_A) and the MNG slab (d_B) are both 10 mm; the second group are $\varepsilon_a = 1$, $\mu_a = 1$, $\varepsilon_b = 25$, $\alpha = 70.9$, $\beta = 36.9$, $\eta_0 = 1$ and $\eta_g = 25$, d_A and d_B are the same as the first group. We consider the transverse electric wave case, with electric field $\overrightarrow{E}$ along the y direction. The treatment for the transverse magnetic wave is similar.

Observing the calculated results of the structure shown in Fig. 1, it is clear that, in the first group, at frequency $f_0 = 0.581$ GHz the transmittance can be increased to 1, as shown in Fig. 2(a). Using the second group, we can get perfect transmittance at frequency $f_0 = 0.948$ GHz, as shown in Fig. 2(b). The electromagnetic field distribution in the ENG-MNG pairs is also studied. By means of the transfer-matrix method, we can figure out the electromagnetic fields of the tunneling modes at 0.581 GHz and 0.948 respectively, as shown in Fig. 3.

It is clear that, similar to the case in which the ENG-MNG slabs is surrounded by same materials, the electric and the magnetic field of tunneling mode are also localized at the interface of MNG-ENG slabs. However, as shown in Fig. 3(a), when the surrounding materials are different, only magnetic field is amplified, with electric field suppressed simultaneously. The electric field can be much higher than the magnetic field depending on the impedance contrast of surrounding materials. In Fig. 3(a), the admittance of the right environment is 25 times greater than the left environment, leading to the amplification of magnetic field. While in Fig. 3(b), the admittances of surrounding materials are exchanged compared with the case in Fig. 3(a), it is find only the electric field can be amplified. In a word, in nonconjugated ENG-MNG slabs surrounded by different materials, only one component of the tunneling mode (either the electric or the magnetic field) can be amplified, suppressing another one at the same time.

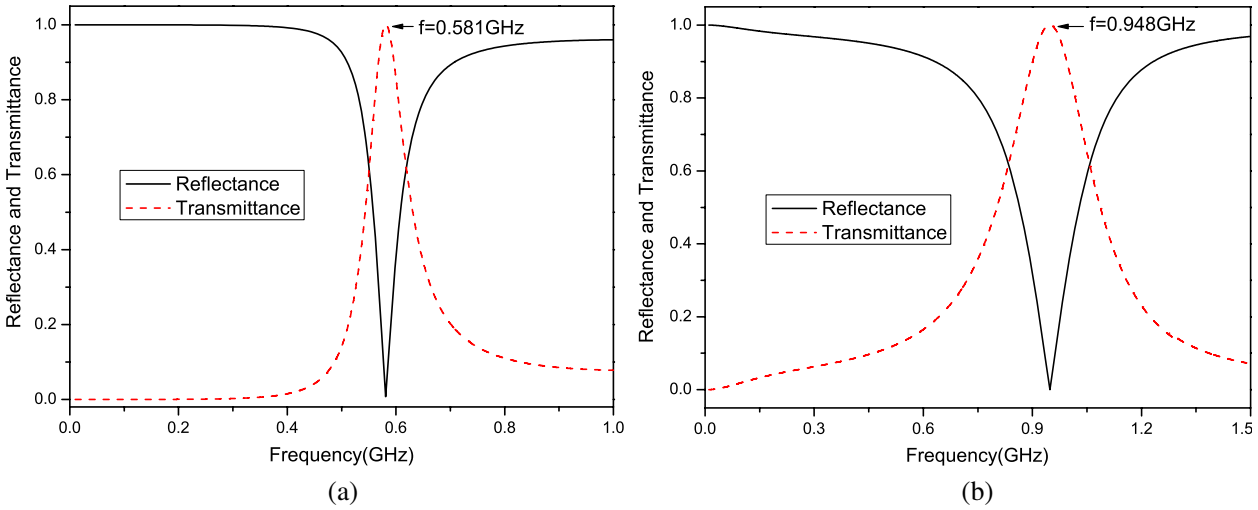

Figure 2: Transmittance (red dashed line) and (black solid line) of the ENG-MNG pair sandwiched between two different semi-infinite regions. (a) the transmittance and reflectance of the first group (b) the transmittance and reflectance of the first group.

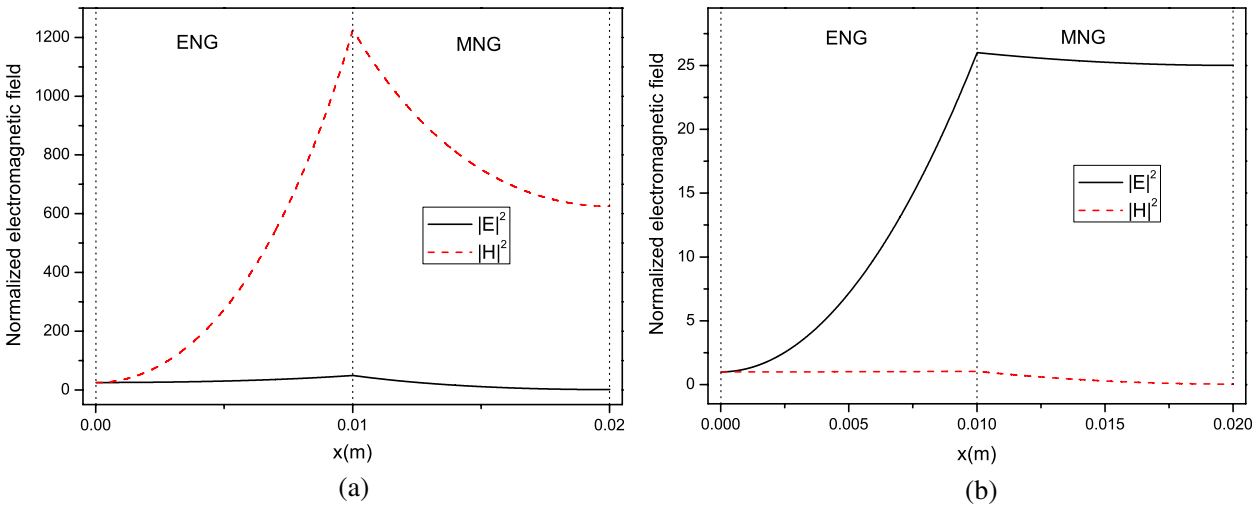

Figure 3: The distribution of the electric field (red dashed line) and the magnetic field (black solid line) at the tunneling frequency. (a) The distribution of the electric field and the magnetic field at 0.581 GHz, (b) The distribution of the electric field and the magnetic field at 0.948 GHz, the electric field can be amplied.

3. CONCLUSIONS

The tunneling phenomenon at interfaces with single negative metamaterial insertions is investigated by numerical simulation. It is found that although the impedance contrasts greatly at the interface, tunneling phenomenon will still emerge when insertions consisting of nonconjugated epsilon-negative/mu-negative metamaterial pair are introduced. The electromagnetic field distribution of the tunneling modes shows that only one component of the tunneling mode (either the electric or the magnetic field) can be amplified, suppressing another one at the same time. Therefore, these properties make the nonconjugated epsilon-negative/mu-negative metamaterial pair promising to be applied in the modern optic and microwave communication systems for less reflection and more compact device volume flexible control of EM field distribution.

ACKNOWLEDGMENT

This work was supported by the National Basic Research Program of China (Grant 2006CB921701), the National Natural Science Foundation of China (Grant No. 10634050, 10704055), the Program for Key Basic Research of the Shanghai Science and Technology Committee (Grant No. 08dj1400301), the Shanghai Committee of Science and Technology (Grant No. 07DZ22302), the Ph.D. Programs

Foundation of Ministry of Education of China (Grant No. 200802471091), the Program for Young Excellent Talents in Tongji University.

REFERENCES

1. Prakash, S. S., C. J. Brinker, A. J. Hurd, and S. M. Rao, "Silica aerogel films prepared at ambient pressure by using surface derivatization to induce reversible drying shrinkage," *Nature*, Vol. 374, 439–443, 1995.
2. Kim, H. J. and J. S. Im, "New excimer-laser-crystallization method for producing large-grained and grain boundary-location-controlled Si films for thin film transistors," *Appl. Phys. Lett.*, Vol. 68, 1513–1515, 1996.
3. Krogman, K. C., T. Druffel, and M. K. Sunkara, "Anti-reflective optical coatings incorporating nanoparticles," *Nanotechnology*, Vol. 16, S338–S343, 2005.
4. Pendry, J. B., "Negative refraction makes a perfect lens," *Phys. Rev. Lett.*, Vol. 85, 3966–3969, 2000.
5. Grbic, A. and G. V. Eleftheriades, "Overcoming the diffraction limit with a planar left-handed transmission-line lens," *Phys. Rev. Lett.*, Vol. 92, 117403-1–117403-4, 2004.
6. Fang, N., H. Lee, C. Sun, and X. Zhang,"Sub-diffraction-limited optical imaging with a silver superlens," *Science*, Vol. 308, 534–537, 2005.
7. Liu, H. K. and W. K. J. Shivanand, " Subwavelength imaging with nonmagnetic anisotropic bilayers," *Opt. Lett.*, Vol. 34, 2243–2245, 2009.
8. Fang, A., T. Koschny, and C. M. Soukoulis, "Optical anisotropic metamaterials: Negative refraction and focusing," *Phys. Rev. B*, Vol. 79, 245127-1–245127-7, 2009.
9. Schurig, D., J. J. Mock, B. J. Justice, S. A. Cummer, and J. B. Pendry, "Metamaterial electromagnetic cloak at microwave frequencies," *Science*, Vol. 314, 977–980, 2006.
10. Chen, H. S., B. I. Wu, B. Zhang, and J. A. Kong, "Electromagnetic wave interactions with a metamaterial cloak," *Phys. Rev. Lett.*, Vol. 99, 063903-1–063903-4, 2007.
11. Pendry, J. B., D. Schurig, and D. R. Smith, "Controlling electromagnetic fields," *Science*, Vol. 312, 1780–1782, 2006.
12. Cai, W., U. K. Chettiar, A. V. Kildishev, and V. M. Shalaev, "Optical cloaking with metamaterials," *Nature Photonics*, Vol. 1, 224–227, 2007.
13. Alù, A. and N. Engheta, "Pairing an epsilon-negative slabwith a mu-negative slab: Resonance, tunneling and transparency," *IEEE Trans. Antennas Propagat.*, Vol. 51, 2558–2571, 2003.
14. Zhou, L., W. J. Wen, C. T. Chan, and P. Sheng, " Electromagnetic-wave tunneling through negative-permittivity media with high magnetic fields," *Phys. Rev. Lett.*, Vol. 94, 243905-1–243905-4, 2005.
15. Feng, T. H., Y. H. Li, H.T. Jiang, Y. Sun, L. He, H. Q. Li, Y. W. Zhang, Y. L. Shi, and H. Chen, "Electromagnetic tunneling in a sandwich structure containing single negative media," *Phys. Rev. E*, Vol. 79, 026601-1–026601-4, 2009.
16. Xiao, S. M., U. K. Chettiar, A. V. Kildishev, V. Drachev, I. C. Khoo, and V. M. Shalaev, "Tunable magnetic response of metamaterials," *Appl. Phys. Lett.*, Vol. 95, 033115-1–033115-3, 2009.
17. Yeh, P. (Ed.), *Optical Waves in Layered Media*, Wiley, 1988.
18. Eleftheriades, G. V., A. K. Iyer, and P. C. Kremer, "Planar negative refractive index media using periodically *L-C* loaded transmission lines," *IEEE Trans. Microwave Theory Tech.*, Vol. 50, 2702–2712, 2002.

FDTD Study of a Novel Terahertz Emitter with Electrical Field Enhancement Using Surface Plasmon Resonance

Shuncong Zhong, Yao-Chun Shen, Hao Shen, and Yi Huang
Department of Electrical Engineering and Electronics, University of Liverpool
Liverpool L69 3GJ, UK

Abstract— In this work, the finite-difference time-domain (FDTD) technique is used to study novel terahertz (THz) emitter structures. The proposed THz antenna requires less pump power of the femtosecond laser pulse whilst provides higher THz output power. This is achieved by the enhancement of the localized electric field in the THz emitter This electric field enhancement is found to have two origins: One is owing to the enhancement of the static electric field of the bias voltage, and the other is the enhancement of the electric field of the incoming femtolaser pulse. The latter enhancement is caused by the interaction of the pump laser and the surface plasmon resonance at the conical gold structure of the photoconductive emitter. This new terahertz emitter could lead to new applications where high-power and broadband terahertz sources are needed.

1. INTRODUCTION

Much of the recent interest in terahertz (THz) radiation stems from its ability to penetrate deep into many organic materials without causing damages since it is not ionizing radiation like X-rays. THz radiation can also help scientists understand the complex dynamics involved in condensed-matter physics and processes such as molecular recognition and protein folding. Recently terahertz pulsed imaging (TPI) has been adopted by the pharmaceutical industry for non-destructive and quantitative characterization of pharmaceutical tablet coatings [1]. The most common device for generating broadband THz radiations is a biased photoconductive antenna, pumped with high-power laser pulses from a femtosecond laser [2, 3]. Photoconductive antenna is one of the most commonly used emitters and detectors for THz radiation. The typical structure of a THz emitter is illustrated in Fig. 1. The gold antenna is fabricated on a low-temperature grown GaAs substrate. The antenna has a gap at the centre, which is biased with a DC voltage and is illuminated with femtosecond laser pulses. After excitation at the photoconductive gap, photo-excited carriers are accelerated under the bias field and create an ultra-short current pulse, which decays with a time constant determined by the carrier lifetime in the photoconductive substrate. The transient current generates ultrashort electromagnetic pulsed radiation (THz radiation) which is collected and collimated by Si lens. However, this photoconductive emitter, though widely used for THz spectroscopy and imaging systems, has a limited THz power. This prohibits some important applications of the THz technology.

Here we demonstrate a novel THz antenna that requires less pump power of the femtosecond laser pulse whilst provides higher output power of the generated THz pulse. This is achieved by exploiting the local field enhancement induced by resonant plasmons within a gold cone-cylinder structure. Field enhancement is attributed to the collective motion of free electrons confined in narrowly localized regions [4], similar to that observed in colloidal nanoparticles exposed to an external electromagnetic field [5]. Using appropriate fabrication techniques, it is consequently possible to optimize the shape of the nanostructure to be tailored to a particular application [6, 7]. We employ this approach to study a novel THz emitter structure with two different sizes (in nano and micron scales) using the finite-difference time-domain (FDTD) technique. Furthermore, the FDTD is used to study a second novel THz emitter with different antennas fabricated on a GaAs substrate. The enhancement of the static electric field of the bias voltage on the new antennas is demonstrated.

2. FDTD ANALYSIS OF NOVEL TERAHERTZ EMITTERS

The FDTD is one of the most popular numerical methods for solving electromagnetic problems with arbitrary geometries and inhomogeneous materials. One of the major advantages of the FDTD is that broadband results can be obtained with the FDTD algorithm run only once, taking a pulse as the excitation source. This is will dramatically save calculation time compared with a series of steady-state calculations [8]. Gold is a dispersive material whose constitutive parameters can

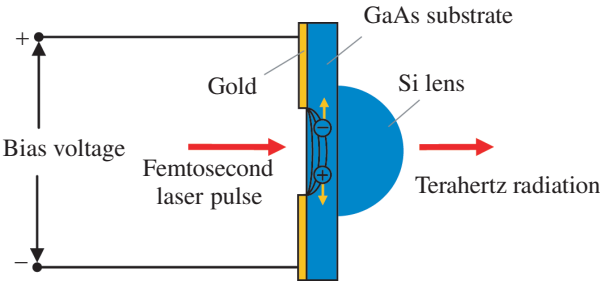

Figure 1: A typical biased THz emitter consists of a Gold photoconductive antenna fabricated on low-temperature grown GaAs substrate pumped with femtosecond laser pulse. THz radiation is collected and collimated by Si lens.

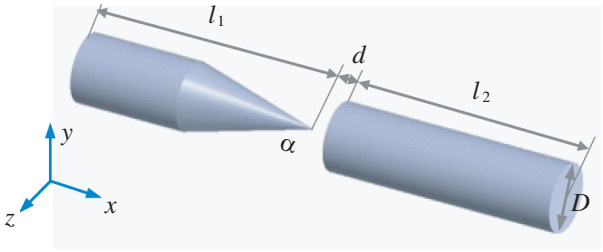

Figure 2: Gold cone-cylinder structure of a novel terahertz emitter: d is the gap between cone and cylinder structures; α is the angle of tip; l_1 and l_2 are the length of cone and cylinder; D is the diameter of the cone and cylinder structures.

be usually described its frequency-dependent behavior by modified Debye model (MDM) [8]. The frequency-dependent permittivity of MDM is

$$\hat{\varepsilon}(\omega) = \varepsilon_\infty + \frac{\varepsilon_s - \varepsilon_\infty}{1 + i\omega\tau} + \frac{\sigma}{i\omega\varepsilon_0} = \varepsilon' - i\varepsilon'' \tag{1}$$

where $\hat{\varepsilon}$ is the complex relative permittivity, ω is the angular frequency, ε_∞ is the infinite-frequency relative permittivity, ε_s is the static relative permittivity, i is the imaginary unit, τ is the relaxation time, σ is the conductivity, ε_0 is the permittivity of free space, and ε' and ε'' are the real and imaginary parts of the complex relative permittivity. A nonlinear optimization method can be used to obtain these parameters [8]. The optimized gold parameters used in the simulation by XFDTD are: $\varepsilon_\infty = 11.575$, $\varepsilon_s = -15789$, $\tau = 8.71 \times 10^{-15}$, and $\sigma = 1.6062 \times 10^7$.

The pulse intensity builds up when the femtosecond pulse passes through a nanostructure. The degree of field enhancement is significantly affected by the geometrical shape of the nanostructure [4]. Here, we propose a novel gold THz emitter whose structure is shown in Fig. 2. The tip of cone is headed at the centre of the cylinder with a small gap between them. When exposed to the femtosecond pulse, free electrons are confined within the tip of cone element and the opposing face of cylinder is filled with positive charges, which makes the pulse capable of producing a strong field enhancement between them. In the FDTD simulation, the polarization direction of the incident femtosecond pulse is positioned parallel to the axis of the structures (x direction) so $E_x = 1\,\mathrm{V/m}$, $E_y = E_z = 0\,\mathrm{V/m}$. The incident pulse is assumed to have a bandwidth of 100 nm with a carrier wavelength of 800 nm The structures with two different size scales are investigated: One is in nano scale; the other is in micron scale which is easily fabricated in real applications.

The localized electric field can be also enhanced by the static electric field of the bias voltage applied. Generally, the traditional photoconductive antenna is fabricated on the same surface of GaAs substrate, as shown in Fig. 1. Here, we investigate a second novel THz emitter whose electric filed is enhanced by the bias voltage. Fig. 3 shows the structure of traditional and novel emitters with metal antenna fabricated on GaAs substrate. For the novel emitter, metal film is fabricated on both the opposing surfaces of GaAs substrate. The antennas of these two emitters are biased with a DC voltage of 50 V. In the FDTD simulation, material dispersion at optical frequencies has been included in the model. The frequency-dependent dispersion relation of the dielectric constant is best represented by the Lorentz equation

$$\varepsilon_R(\omega) = \varepsilon_\infty + \frac{(\varepsilon_s - \varepsilon_\infty)\omega_0^2}{\omega_0^2 + 2i\omega\delta - (i\omega)^2} \tag{2}$$

where ω_0 is the material resonance frequency and δ is the damping factor [9]. Here the parameters of GaAs used are: $\omega_0 = 8.76\,\mathrm{THz}$, $\delta = 7.2 \times 10^{10}$.

3. RESULTS

Figure 4 shows the electrical field enhancement around the tips of gold cone-cylinder nano-structure and micron-structure. The enhancement factors for these two structures are 164 and 27 respectively. The static electric fields for the traditional and the second novel THz emitter with metal antenna

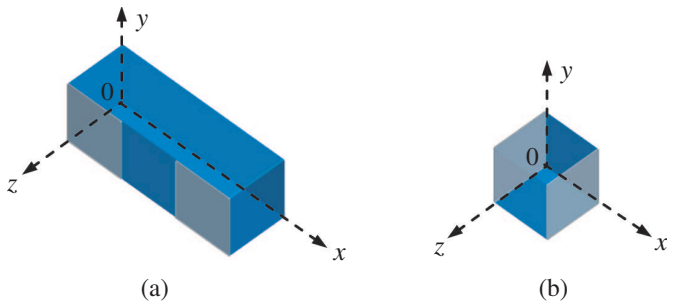

Figure 3: (a) Traditional and (b) novel emitters with metal antenna fabricated on GaAs substrate. The dimensions of GaAs substrate are, respectively, $1.5 \times 0.5 \times 0.53$ mm and $0.5 \times 0.5 \times 0.53$ mm. The thickness of coated metal film is 10 μm.

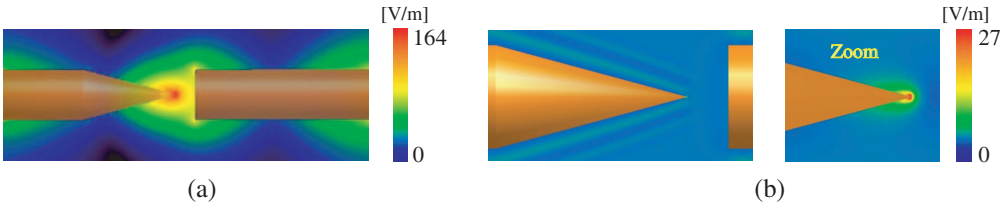

Figure 4: Electrical field enhancing properties of gold cone-cylinder (a) nano-structure and (b) micron-structure. The right part of (b) is the zoom of electrical field enhancement around the tip of the novel terahertz emitter. The intensity ($|E|$) enhancement in X-Y plane at the tip of the nano-structure is $|E|/|E_0| = 164$ whilst the intensity enhancement for the micron-structure $|E|/|E_0| = 27$, where $|E_0|$ is the incident intensity. The dimensions for the nano-structure are: $d = 20$ nm, $\alpha = 30°$, $l_1 = l_2 = 175$ nm, and $D = 50$ nm; the ones for the micro-structure are: $d = 2$ μm, $\alpha = 30°$, $l_1 = 11$ μm, $l_2 = 1.5$ μm, and $D = 10$ μm.

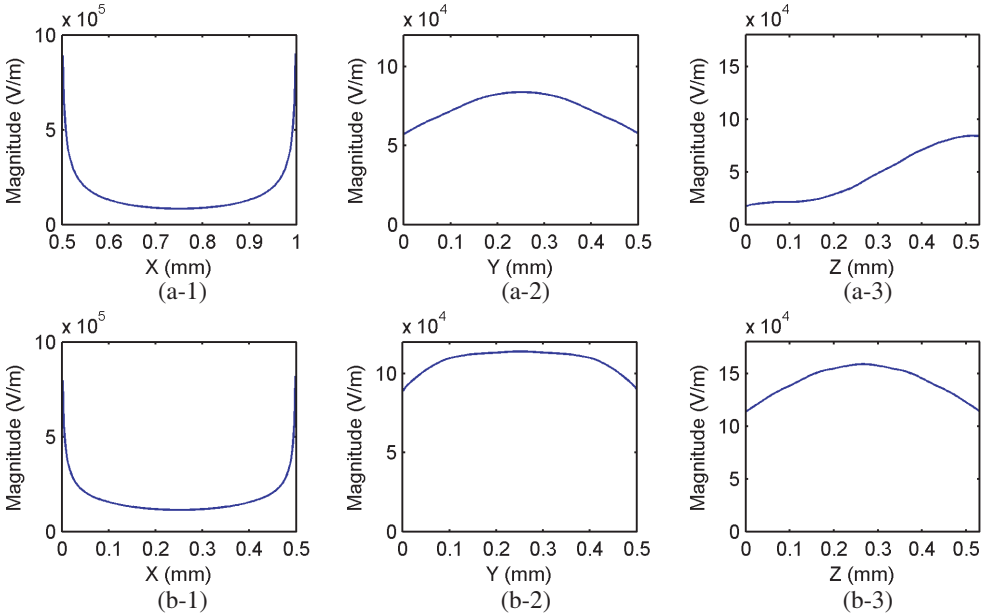

Figure 5: Comparisons of static electric fields taken along x-direction line ($y = 0.25$ mm, $z = 0.53$ mm), y-direction line ($x = 0.75$ mm, $z = 0.53$ mm), and z-direction line ($x = 0.75$ mm, $y = 0.25$ mm) for the (a) traditional and (b) novel THz emitters with metal antenna fabricated on GaAs substrate.

fabricated on GaAs substrate are demonstrated in Fig. 5. Except that the static electric fields taken x-direction line are similar, the other ones (taken from along from y- and z-direction lines) for the novel emitter are greater than the traditional emitter. The static electric field energy within $0.5 \times 0.5 \times 0.53$ mm region for these two emitters were used to evaluate the enhancement, and it is

calculated by the formula as

$$W = \iiint \frac{1}{2}\varepsilon_0\varepsilon_r E^2 dV \tag{3}$$

The enhancement factor of the static electric field energy for the novel THz emitter is about 8. Therefore, the electrical field enhancements by surface plasmon resonance and the static electric field of the bias voltage, are demonstrated.

4. CONCLUSION

Novel terahertz emitter structures have been investigated by using FDTD technique. We found that our proposed terahertz antenna requires less pump power of the femtosecond laser pulse whilst provides higher output power of the generated terahertz pulse. This was achieved by the enhancement of the localized electric field in the terahertz emitter. This electric field enhancement was found to have two origins: One is owing to the enhancement of the static electric field of the bias voltage, and the other is the enhancement of the electric field of the incoming femtolaser pulse. The latter enhancement is caused by the interaction of the pump laser and the surface plasmon resonance at the conical gold structure of the photoconductive emitter. We believe that this new terahertz emitter could lead to new applications where high-power and broadband terahertz sources are needed.

ACKNOWLEDGMENT

The authors would like to acknowledge the financial support from UK Technology Strategy Board (AB293H).

REFERENCES

1. Shen, Y. C. and P. F. Taday, "Development and application of terahertz pulsed imaging for non-destructive inspection of pharmaceutical tablet," *J. Selected Topics in Quantum Electronics*, Vol. 14, No. 2, 407–415, 2008.
2. Tani, M., M. Herrmann, and K. Sakai, "Generation and detection of terahertz pulsed radiation with photoconductive antennas and its application to imaging," *Meas. Sci. Technol.*, Vol. 13, 1739–1745, 2002.
3. Shen, Y. C., P. C. Upadhya, H. E. Beere, E. H. Linfield, A. G. Davies, I. S. Gregory, C. Baker, W. R. Tribe, and M. J. Evans, "Generation and detection of ultrabroadband terahertz radiation with photoconductive emitter and receiver antennas," *Appl. Phys. Lett.*, Vol. 85, No. 2, 164–166, 2004.
4. Kim, S., J. Jin, Y. J. Kim, I. Y. Park, Y. Kim, and S. W. Kim, "High-harmonic generation by resonant plasmon field enhancement," *Nature*, Vol. 453, No. 5, 757–760, 2008.
5. Roth, R. M., N. C. Panoiu, M. M. Adams, and R. M. Osgood, Jr., "Resonant-plasmon field enhancement from asymmetrically illuminated conical metallic-probe tips," *Opt. Exp.*, Vol. 14, No. 7, 2921–2931, 2006.
6. Sundaramurthy, A., K. B. Crozier, and G. S. Kino, "Field enhancement and gap-dependent resonance in a system of two opposing tip-to-tip Au nanotriganles," *Phy. Rev. B*, Vol. 72, 165409, 2005.
7. Yang, J., J. Zhang, X. Wu, and Q. Gong, "Electric field enhancing properties of the V-shaped optical resonant antennas," *Opt. Exp.*, Vol. 15, No. 25, 16852–16859, 2007.
8. Gai, H., J. Wang, and Q. Tian, "Modified Debye model parameters of metals applicable for broadband calculations," *Appl. Opt.*, Vol. 46, No. 12, 2229–2233, 2007.
9. Alsunaidi, M. A., F. S. Alhajiri, and H. M. Masoudi, "A FDTD algorithm for the analysis of short optical pulse second harmonic generation in dispersive media," *Microwave Opt. Technol. Lett.*, Vol. 51, No. 4, 1097–1100, 2009.

PML-FDTD Method in Prolate Spheroidal Coordinates

Maoyu Zhang and Jianguo Wang
Northwest Institute of Nuclear Technology
P. O. Box 69-12, Xi'an, Shaanxi 710024, China

Abstract— This paper presents a three-dimensional (3-D) finite-difference time-domain (FDTD) formulation of Maxwell's equation and perfectly matched layers (PML) in 3-D prolate spheroidal coordinates. The perfectly matched layer formulation relies on the complex stretching coordinates approach. Numerical simulation result of the perfectly matched layer finite-difference time-domain (PML-FDTD) method shows very good agreement with reference solution computed on an extremely large space.

1. INTRODUCTION

Nuclear burst of low or middle altitude may produce Compton current that are produced by the nearly spherical distribution of gamma rays interacting with the atmosphere. The density of Compton current is strongly attenuated with the distance to the burst point. Consequently, the simulations of electromagnetic pulse (EMP) due to the Compton current need very fine mesh in the near region of the burst point. In order to take into account simultaneously the large simulation region and the fine mesh, the prolate spheroidal coordinates which are suitable for the ground/air boundary problem better than the common orthogonal coordinates are chosen [1].

To simulate wave propagation in an unbounded medium, the absorbing boundary conditions (ABC's) must be used to terminate the simulation region [2]. Many researchers have contributed to ABC's [3–5]. In this work, the unsplit-field PML ABC's of three-dimensional prolate spheroidal coordinates which is based on the complex stretched coordinates approach for the FDTD schemes are derived [6].

We first introduce in Section 2 the prolate spheroidal coordinates. The FDTD schemes and PML ABC's in these coordinates are developed in Section 3 and Section 4. Finally, we validate the algorithm with analytical solutions in Section 5.

2. PROLATE SPHEROIDAL COORDINATES

By referring to Figure 1, the prolate spheroidal coordinates are defined as

$$\xi = \frac{1}{2a}\left(r' - r\right) \qquad \zeta = \frac{1}{2a}\left(r' + r\right) \qquad \varphi = \tan^{-1}\frac{y}{x} \tag{1}$$

where r' and r are distances from P to two identified points that are separated by $2a$ and φ is the usual azimuthal angle. The surfaces defined by constant values of ξ are hyperboloids of revolution and surfaces of constant ζ are orthogonal prolate spheroids. The transformation equations from prolate spheroidal coordinates to Cartesian coordinates are

$$x = a\sqrt{(\zeta^2 - 1)(1 - \xi^2)}\sin\varphi \tag{2}$$

$$y = a\sqrt{(\zeta^2 - 1)(1 - \xi^2)}\cos\varphi \tag{3}$$

$$z = a\zeta\xi \tag{4}$$

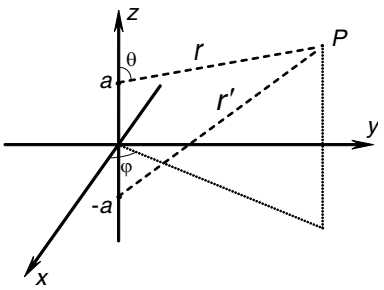

Figure 1: Geometry for the prolate spheroidal coordinates.

In a similar manner, the transformation equations from a spherical polar coordinate system centered at the upper foci to prolate spheroidal coordinates can be derived as

$$\xi = \frac{r}{2a}\left[\sqrt{1+(4a/r)(a/r+\cos\theta)}-1\right] \tag{5}$$

$$\zeta = \frac{r}{2a}\left[\sqrt{1+(4a/r)(a/r+\cos\theta)}+1\right] \tag{6}$$

$$\varphi = \phi \tag{7}$$

From these, the scale factors of the prolate spheroidal coordinates can be derived as

$$h_\xi = a\sqrt{\frac{\zeta^2-\xi^2}{1-\xi^2}} \tag{8}$$

$$h_\zeta = a\sqrt{\frac{\zeta^2-\xi^2}{\zeta^2-1}} \tag{9}$$

$$h_\phi = a\sqrt{(\zeta^2-1)(1-\xi^2)} \tag{10}$$

3. FDTD SCHEMES

Faraday's and Ampere's law of The Maxwell's equations in prolate spheroidal coordinates can be written as

$$\frac{\partial E_\xi}{\partial t} = \frac{1}{\varepsilon h_\zeta h_\phi}\left(\frac{\partial h_\phi H_\phi}{\partial \zeta} - \frac{\partial h_\zeta H_\zeta}{\partial \phi}\right) \tag{11}$$

$$\frac{\partial E_\zeta}{\partial t} = \frac{1}{\varepsilon h_\xi h_\phi}\left(\frac{\partial h_\xi H_\xi}{\partial \phi} - \frac{\partial h_\phi H_\phi}{\partial \xi}\right) \tag{12}$$

$$\frac{\partial E_\phi}{\partial t} = \frac{1}{\varepsilon h_\xi h_\zeta}\left(\frac{\partial h_\zeta H_\zeta}{\partial \xi} - \frac{\partial h_\xi H_\xi}{\partial \zeta}\right) \tag{13}$$

$$\frac{\partial H_\xi}{\partial t} = \frac{1}{\mu h_\zeta h_\phi}\left(\frac{\partial h_\zeta E_\zeta}{\partial \phi} - \frac{\partial h_\phi E_\phi}{\partial \zeta}\right) \tag{14}$$

$$\frac{\partial H_\zeta}{\partial t} = \frac{1}{\mu h_\xi h_\phi}\left(\frac{\partial h_\phi E_\phi}{\partial \xi} - \frac{\partial h_\xi E_\xi}{\partial \phi}\right) \tag{15}$$

$$\frac{\partial H_\phi}{\partial t} = \frac{1}{\mu h_\xi h_\zeta}\left(\frac{\partial h_\xi E_\xi}{\partial \zeta} - \frac{\partial h_\zeta E_\zeta}{\partial \xi}\right) \tag{16}$$

The discretization of Maxwell's equations in prolate spheroidal coordinates is the same as in Cartesian coordinates. For example, the discretized form of (11) and (14) can be derived as follows

$$\begin{aligned} E_\xi^{n+1}\left(i+\frac{1}{2},j,k\right) &= E_\xi^{n}\left(i+\frac{1}{2},j,k\right) \\ &+\frac{\Delta t}{\varepsilon a}\cdot\left(\begin{array}{l} \dfrac{H_\phi^{n+1/2}\left(i+\frac{1}{2},j+\frac{1}{2},k\right)-H_\phi^{n+1/2}\left(i+\frac{1}{2},j-\frac{1}{2},k\right)}{\Delta\zeta_j} \\ -\dfrac{1}{\zeta^2(j)-1}\dfrac{H_\zeta^{n+1/2}\left(i+\frac{1}{2},j,k+\frac{1}{2}\right)-H_\zeta^{n+1/2}\left(i+\frac{1}{2},j,k-\frac{1}{2}\right)}{\Delta\phi_k} \end{array}\right) \end{aligned} \tag{17}$$

$$H_\xi^{n+\frac{1}{2}}\left(i,j+\frac{1}{2},k+\frac{1}{2}\right)=H_\xi^{n-\frac{1}{2}}\left(i,j+\frac{1}{2},k+\frac{1}{2}\right)$$
$$-\frac{\Delta t}{\mu a}\left(\begin{array}{l}\dfrac{E_\phi^n\left(i,j+1,k+\frac{1}{2}\right)-E_\phi^n\left(i,j,k+\frac{1}{2}\right)}{\Delta\zeta_j}\\ -\dfrac{1}{\zeta^2\left(j+\frac{1}{2}\right)-1}\dfrac{E_\zeta^n\left(i,j+\frac{1}{2},k+1\right)-E_\zeta^n\left(i,j+\frac{1}{2},k\right)}{\Delta\phi_k}\end{array}\right) \tag{18}$$

For convenience, the fields in discretized equations have been transformed as follows

$$\left\{\begin{array}{l}E_\xi\\H_\xi\end{array}\right\}=\sqrt{(1-\xi^2)(\zeta^2-\xi^2)}\left\{\begin{array}{l}E'_\xi\\H'_\xi\end{array}\right\} \tag{19}$$

$$\left\{\begin{array}{l}E_\zeta\\H_\zeta\end{array}\right\}=\sqrt{(\zeta^2-1)(\zeta^2-\xi^2)}\left\{\begin{array}{l}E'_\zeta\\H'_\zeta\end{array}\right\} \tag{20}$$

$$\left\{\begin{array}{l}E_\phi\\H_\phi\end{array}\right\}=\sqrt{(\zeta^2-1)(1-\xi^2)}\left\{\begin{array}{l}E'_\phi\\H'_\phi\end{array}\right\} \tag{21}$$

4. UNSPLIT-FIELD PML

In this work, we derive the unsplit-field PML ABC's of the prolate spheroidal coordinates in ζ direction which is based on the complex stretched coordinates. The complex stretched coordinates are defined with the following change of variables:

$$\tilde{\zeta}=\zeta_0+\int_{\zeta_0}^{\zeta}s_\zeta(\zeta')d\zeta' \tag{22}$$

where $s_\zeta(\zeta')$ are the complex stretching variables. From which the modified Faraday's law reads:

$$i\omega S_\zeta H_\xi=-\frac{1}{\mu h_\zeta h_\phi}\left(\frac{\partial h_\phi E_\phi}{\partial\zeta}-\frac{\partial h_\zeta E_\zeta}{\partial\phi}\right) \tag{23}$$

$$i\omega\frac{1}{S_\zeta}\frac{\tilde{\zeta}^2-1}{\zeta^2-1}H_\zeta=-\frac{1}{\mu h_\xi h_\phi}\left(\frac{\partial h_\xi E_\xi}{\partial\phi}-\frac{\partial h_\phi E_\phi}{\partial\xi}\right) \tag{24}$$

$$i\omega S_\zeta\frac{(\zeta^2-1)(\tilde{\zeta}^2-\xi^2)}{(\zeta^2-\xi^2)(\tilde{\zeta}^2-1)}\frac{\partial H_\phi}{\partial t}=-\frac{1}{\mu h_\xi h_\zeta}\left(\frac{\partial h_\zeta E_\zeta}{\partial\xi}-\frac{\partial h_\xi E_\xi}{\partial\zeta}\right) \tag{25}$$

The modified Ampere's law follows by duality. The discretization schemes of the PML ABC's are same as those of the FDTD.

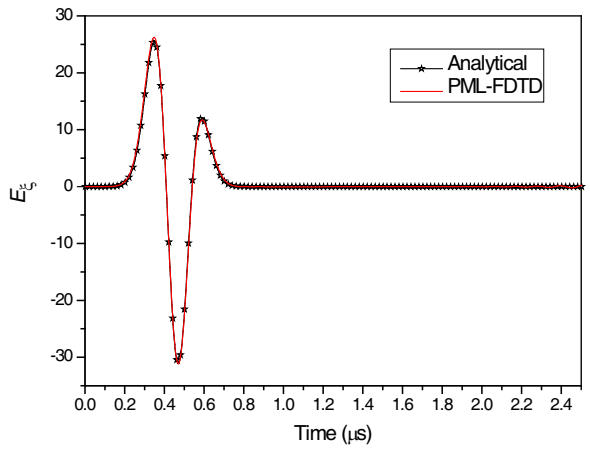

Figure 2: Analytic solutions for a electric dipole on free-space versus 3-D PML-FDTD solution in prolate spheroidal coordinates

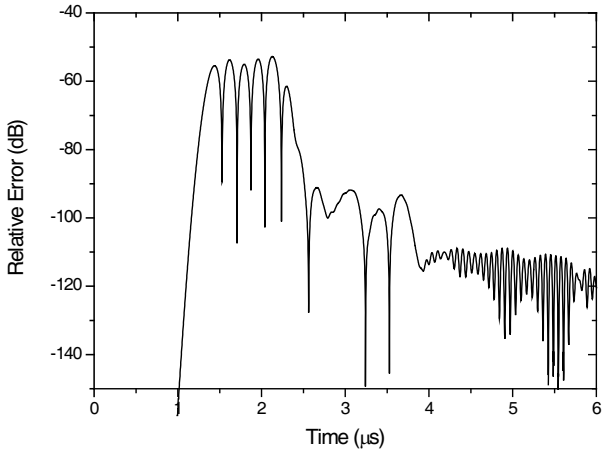

Figure 3: Relative error due to PML termination compared with a reference computation.

5. NUMERICAL RESULTS

The formulation is validated with analytic solutions obtained by solving the radiation field of electric dipole excited by a Gauss pulse

$$p(t) = 10^{-10} \exp\left[-\left(\frac{t-3T}{T}\right)^2\right]$$

where $T = 2\,\text{ns}$. Figure 2 shows the field computed by using the analytic formulation and the 3-D PML-FDTD schemes of the prolate spheroidal coordinates. The curves are in excellent agreement and the relative error due to PML termination compared with a reference computation where the terminating grid boundary is far enough from the source is showed in Figure 3.

6. CONCLUSION

PML-FDTD schemes for prolate spheroidal coordinates are derived, which is based on the complex stretching coordinate approach. The accuracy of the formulation is validated by computing the radiating field from a Gauss pulse exciting electric dipole against the known analytic results.

REFERENCES

1. Knight, R. L., E. R. Parkinson, and V. W. Pine, "Electromagnetic pulse environment studies, science applications," Report SAI-74-502-AQ, May 1974.
2. Berenger, J., "A perfectly matched layer for the absorption of electromagnetic waves," *J. Comput. Phys.*, Vol. 114, 185–200, 1994.
3. Liao, Z. P., H. L. Wong, B. P. Yang, and Y. F. Yuan, "A transmitting boundary for transient wave analysis," *Sci. Sinica A*, Vol. 27, 1063–1076, 1984.
4. Lindman, E. L., "Free space boundary conditions for the time dependent wave equation," *J. Comput. Phys.*, Vol. 18, 66–78, 1975.
5. Engquist, B. and A. Majda, "Absorbing boundary conditions for the numerical simulation of waves," *Math. Comput.*, Vol. 31, 629–51, 1977.
6. Chew, W. C. and W. Weedon, "A 3D perfectly matched medium from modified Maxwell's equations with stretched coordinates," *Microwave Opt. Tech. Lett.*, Vol. 7, No. 13, 599–604, 1994.

Investigation of UPML in the FDTD Analysis of Planar Microstrip Structures

Junjun Wu, **Huiling Zhao**, **and Nakun Jing**
Northwestern Polytechnical University, Xi'an, Shaanxi 710072, China

Abstract— Planar microstrip structures are analyzed with a three dimensional finite difference time domain method (FDTD). Uniaxial anisotropic perfectly matched layer (UPML) absorbing boundary condition is utilized to truncate the FDTD lattices. In order to validate the numerical model, scattering parameters of a line-fed rectangular patch antenna and a low-pass filter are investigated. Simulation results are compared with measurements given by published works. Moreover, efficiency and convergence of FDTD-UPML are also compared with Mur's absorbing boundary condition. Simulation results demonstrated that FDTD-UPML needs less total mesh and convergences faster than Mur's ABC. The method presented in this paper is valid for arbitrary microstrip geometries, such as microstrip circuits and microstrip antennas.

1. INTRODUCTION

The time field finite difference has been mostly used in the calculation electromagnetism fields, since it was founded by K. S. Yee from 1966 [1]. In 1990, D. M. Sheen employed FDTD to analyze the structure of the planar microstrip circuits [2], and demonstrated that the method was effective for calculating the complex planar microstrip circuits. The transient wave source was used to get a broad band impedance and the scattering parameter, and it is also requested that the feed source must be far from the discontinuity spot of microstrip. This results in the gridding space so broad that it will takes more time to calculate. In reference [3], the time spent on convergence is greatly reduced through adjusting the feed source model. But it is not suit for some cases, for example, some circuits such as two-end or multi-end Microstrip circuits.

PML absorbing boundary condition was first proposed by J. P. Berenger [4]. Compare to the conventional twice steps Mur absorbing boundary condition, PML can improve the precision about 40 dB. Uniaxial PML (UPML), presented by Sacks [5] and Gedney [6], avoids dividing the electromagnetism field and so it reduces the demand for the computer memory. Moreover, it is easily to be understood or implemented.

In this paper, planar microstrip structures have been analyzed using three dimensional FDTD, adopting UPML absorbing boundary condition instead of two step Mur absorbing boundary condition. The advantage of choosing UPML is that there is no strict requirement of source position as in Reference [2] if properly set the conductance and reluctance of the UPML. So, the grid space and computation time can be reduced greatly.

2. UPML FINITE-DIFFERENCE EQUATIONS

UPML absorbing boundary is a hypothetical anisotropic medium which can generate electric loss and magnetic loss. FDTD truncation boundary is set by this special kind of medium layer, which match exactly with the wave impedance of the adjacent medium layers. Therefore, incident wave will decay rapidly in the UPML layer. Even if the UPML layer has a finite thickness, and the outermost boundary is set to be PEC, there will be no reflect on the interface of UPML layer.

The frequency domain Maxwell's curl equations [7] in the UPML regions can be written as

$$\begin{cases} \nabla \times \vec{H} = j\omega\varepsilon_0\varepsilon_r(\omega)\hat{\varepsilon}_p(\omega) \cdot \vec{E} \\ -\nabla \times \vec{E} = j\omega\mu_0\mu_r(\omega)\hat{\mu}_p(\omega) \cdot \vec{H} \end{cases} \tag{1}$$

where $\varepsilon_r(\omega)$ and $\mu_r(\omega)$ are, respectively, the relative permittivity and permeability of the FDTD computational domains. $\hat{\mu}_p(\omega)$ and $\hat{\varepsilon}_p(w)$ are defined as

$$\hat{\mu}_p(\omega) = \hat{\varepsilon}_p(\omega) = S_x \cdot S_y \cdot S_z = \begin{bmatrix} s_y s_z/s_x & 0 & 0 \\ 0 & s_x s_z/s_y & 0 \\ 0 & 0 & s_x s_y/s_z \end{bmatrix} \tag{2}$$

where S_{axis} (axis $= x, y, z$) are defined as $S_{\text{axis}} = 1 + \sigma_{\text{axis}}/j\omega\varepsilon_0$, σ_{axis} is the conductivity along the axis direction in the UPML regions.

To avoid convolution terms, we choose D-H FDTD algorithm. So, we obtain Eq. (3)

$$j\omega\left(1+\frac{\sigma_x(x)}{j\omega\varepsilon_0}\right)\left(1+\frac{\sigma_y(y)}{j\omega\varepsilon_0}\right)D_Z = \frac{1}{\varepsilon_0}\left(1+\frac{\sigma_x(x)}{j\omega\varepsilon_0}\right)\left(\frac{\partial H_y}{\partial x}-\frac{\partial H_x}{\partial y}\right) \tag{3}$$

Using Eq. (3), according to the procedure and formulas given in the chapter 4 of Reference [8], the finite difference equation of D_z can be obtained. Other directions of D can be obtained similarly.

In the cross-interface, tangent electric field in the boundary is expressed by the mean of both boundary medium to improve precision.

3. NUMERICAL RESULTS

To verify the behavior of UPML absorbing boundary condition, numerical results have been carried out for microstrip antenna or microstrip low pass filter, respectively. The structure of line feed microstrip antenna and microstrip low pass filter (LPF) are illustrated in Fig. 1. All the parameters used in this two microstrip structures are set identical with Reference [2] for comparison. In calculation, Gauss pulse source is chosen as the feed source.The UPML layers.will be set the six layers.

Figure 2 shows the convergence of electric field in z direction with time steps. Figs. 2(a) and 2(b) are sampled from input port of microstrip antenna and LPF, respectively. Fig. 2(c) is sampled

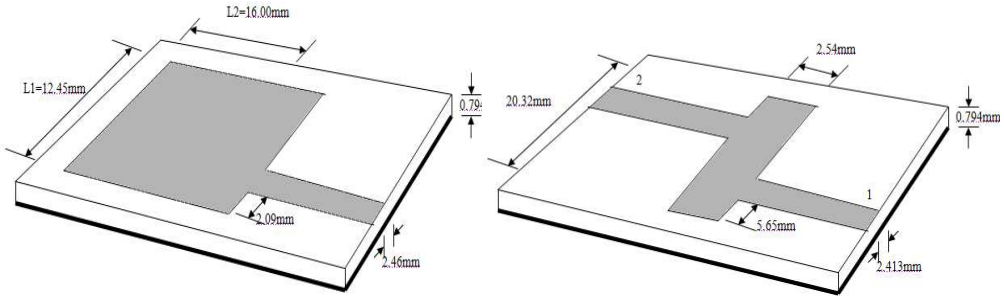

Figure 1: Mircostrip structure (a) line feed microstrip antenna; (b) microstrip low pass filter.

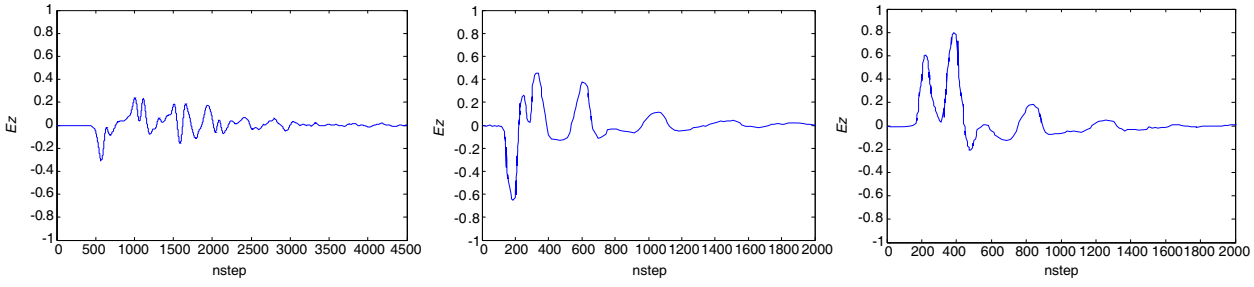

Figure 2: Convergence of Ez with time step (a) electric field in input port of microstrip antenna; (b) electric field in input port of LPF; (c) electric field in output port of LPF.

Table 1: Comparison of UPML and Mur absorbing boundary conditions.

	Microstrip Antenna		LPF	
	UPML	Mur	UPML	Mur
Gridding Space	$54 \times 72 \times 14$	$60 \times 100 \times 16$	$72 \times 43 \times 14$	$80 \times 100 \times 16$
Convergence Time	$4000\Delta t$	$8000\Delta t$	$2000\Delta t$	$4000\Delta t$

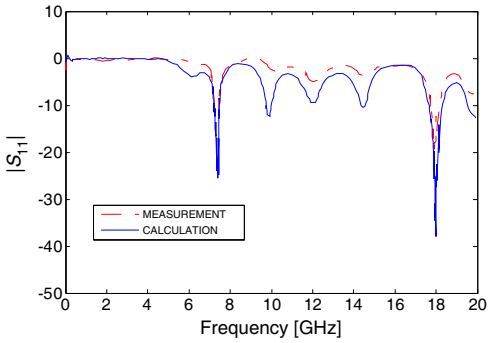

Figure 3: Return loss of microstrip antenna.

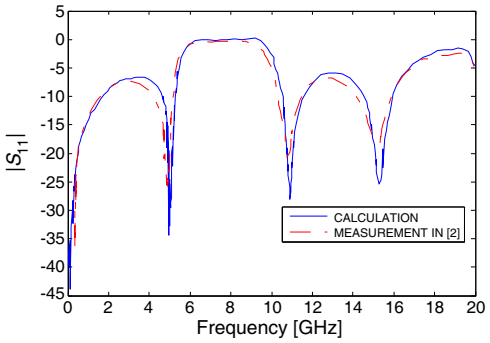

Figure 4: Return loss of LPF.

from output port of LPF. This figure demonstrateS that electric field convergence very well using UPML. Table 1 shows the comparison of parameters in FDTD implementation with Reference [2].

It can be seen from Table 1 that UPML needs less total mesh and convergence faster than Mur absorbing boundary condition. The reason for less mesh in UPML is that UPML has no strict requirement of source position. Here, only 10y used in UPML, while there are 50y needed in Mur.

Figure 3 is the simulated results of return loss of the line feed microstrip antenna, Fig. 4 is for LPF. Measured data is given by Reference [2]. It can be seen that FDTD-UPML simulated results and measured data match very well. This demonstrates the validity of FDTD-UPML in analyzing planar microstrip circuits. Small difference between the simulated and measure results can be moved by increase the grid number or the number of UPML layers.

4. CONCLUSIONS

In this paper, scattering parameters of a line-fed rectangular patch antenna and a low-pass filter are investigated using FDTD with UPML absorbing boundary condition. Simulation results demonstrated that FDTD-UPML needs less total mesh and convergences faster than Mur's absorbing boundary condition. The method presented in this paper can be used to analyze arbitrarily complex structures of the microstrip circuit.

REFERENCES

1. Yee, K. S., "Numerical solution of initial boundary value problems involving Maxwell's equations in isotropic media," *IEEE Trans. Antennas Propagat.*, Vol. 14, 302–307, May 1966.
2. Sheen, D. M., S. M. Ali, M. D. Abouzahra, and J. A. Kong, "Application of the three-dimensional finite-difference time-domain method to the analysis of planar microstrip circuits," *IEEE Trans. Microwave Theory Tech.*, Vol. 38, 849–857, 1990.
3. Luebbers, R. J. and H. S. Langdont, "A simple feed model that reduces time steps needed for FDTD antenna and microstdp calculations," *IEEE Trans. Antennas Propagat.*, Vol. 44, No. 7, 1000–1005, 1996.
4. Berenger, J., "A perfectly matched layer for the absorption of electromagneticwaves," *J. Computational Phys.*, Vol. 114, 185–200, 1994.
5. Sacks, Z. S., D. M. Kingsland, D. M. Lee, and J. F. Lee, "A perfectly matched anisotropic absorber for use as an absorbing boundary condiction," *IEEE Trans. Antennas Propagat.*, Vol. 43, No. 12, 1460–1463, Dec. 1995.
6. Gedney, S. D., "An anisotropic perfectly matched layer absorbing media for the truncation of FDTD lattices," *IEEE Trans. Antennas Propagat.*, Vol. 44, No. 12, 1630–1639, Dec. 1996.
7. Li, J. and C. Miao, "A new implementation of the uniaxial perfectly matched layer," *Microwave and Millimeter Wave Technology*, Vol. 2, 770–773, Apr. 21–24, 2008.
8. Sullivan, D. M., R. D. Pollard, and R. Booton, *Electromagnetic Simulation Using the FDTD Method*, Series on RF and Microwave Technology, IEEE Press, 2000.

Application of Moving Coordinate FDTD Method on Electromagnetic Pulses Propagation

Yong Li and Jianguo Wang
Northwest Institute of Nuclear Technology, P. O. Box 69-12, Xi'an, Shaanxi 710024, China

Abstract— The moving coordinate frame finite-difference time-domain (FDTD) method is developed to simulate the propagation of electromagnetic pulses over long distances. In this paper, this method is extended to three dimensional cases. The discretized form of moving coordinate frame FDTD in three dimensions is given, and is applied to calculate propagation of different pulses in rectangular waveguides. The widths of pulses in propagation direction increase when pluses propagate in waveguide. Dispersion phenomena appear, and slow parts of the pulses move to the tail of pulses. By comparing the results of both FDTD method and moving coordinate frame FDTD method, this method is numerically validated. Relative difference between two methods is less than 0.1%, the simulation results are shown to be accurate.

1. INTRODUCTION

With the increasing applications on communication and detection, there is an ever-increasing interest in the propagation of pulses over long distance. The finite-difference time-domain (FDTD) method [1] is widely used in electromagnetic simulation. Because the FDTD method is a full-wave method, when simulating propagation of electromagnetic pulses over very long distance, the computational burden quickly becomes too large to afford.This is the major difficulty why FDTD method can not be applied to simulate long distance propagation of pulses directly. In order to overcome this difficulty, moving coordinate is combined with FDTD method. Models of one dimension as electromagnetic pulse propagation over large distance in medium [2] and acoustic wave propagation in waveguide has been studied [3] approach this method. Coordinate of the direction in which pulse's propagation is transformed into moving coordinate, which is 'frozen' with pulses, and the pulses are in small calculation zones when simulating (as shown in Fig. 1). Moving grid whose size is limited to the order of the pulse length is created, and moves along the approach of the center-of-mass of the wavepacket. This method takes advantage of the fact that when an electromagnetic pulse propagates over long distance, the significant pulse energy exists only over a small part of the propagation path at any time. The FDTD meshes (in the direction of the propagation path) need only to be large enough to contain the pulses while using this method to simulate the propagation of pulses. This method is useful in particular for tracking well-collimated short pulse beam, referred to as pulsed beams or localized waves.

In this paper, the models are extended to simulate electromagnetic pulses propagating in waveguide over large distance and results are compared with the results using FDTD approach in order to testify the validity and feasibility of the moving coordinate FDTD method.

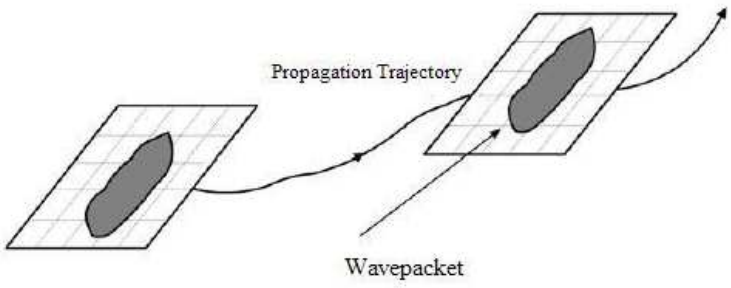

Figure 1: A moving coordinate frame along pulse propagation trajectory.

2. MOVING COORDINATE FDTD METHOD

Moving coordinate concepts have been used extensively in various analytical and numerical methods in the past. Moving coordinate FDTD method is general, robust and fully vectorial, with no

limitations on the medium inhomogeneity. In order to deal with inhomogeneous medium, z axis in propagation direction is modified into a speed-normalized coordinate defined as

$$\zeta(z) = \int_0^z \frac{c_0}{c(z')} dz', \tag{1}$$

where c_0 is the velocity of light in free space, $c(z)$ is the wave speed in media, and z is the position of the media. Developed transform is defined as

$$\zeta' = \zeta(z) - c_0 t. \tag{2}$$

Coordinate frame moves with a velocity of c_0 as (2) shows, with no limitations on the medium inhomogeneity, and pulses are 'frozen' with the coordinate in arbitrary medium. One discretized form of the field components is

$$\begin{aligned} H^{n+1}_{\zeta'(i,j,k)} &= H^{n-1}_{\zeta'(i,j,k)} + c_0 \Delta t' \frac{H^n_{\zeta'(i,j,k+1)} - H^n_{\zeta'(i,j,k-1)}}{\Delta \zeta'} \\ &\quad - \frac{\Delta t'}{\mu} \left(\frac{E^n_{y(i+1,j,k)} - E^n_{y(i-1,j,k)}}{\Delta x} - \frac{E^n_{x(i,j+1,k)} - E^n_{x(i,j-1,k)}}{\Delta y} \right) \end{aligned} \tag{3}$$

FDTD formulation of other electromagnetic field components can be obtained by discretized the Maxwell's equations.

In FDTD method, Courant-Friedrichs-Lewy (CFL) condition is the limitation of stability, time and space steps must obey the CFL condition in order to avoid instability problems. In moving coordinate, CFL condition is changed into

$$\Delta t \leq \frac{0.5}{c_0 \sqrt{\frac{1}{(\Delta x)^2} + \frac{1}{(\Delta y)^2} + \frac{1}{(\Delta \zeta')^2}}}. \tag{4}$$

As a result of dispersion analysis [5], there is an limitation of wave numbers vertical and parallel to the propagation direction

$$k_{\zeta'} \gg k_T, \tag{5}$$

where $k_{\zeta'}$ is parallel to the propagation direction, and k_T is vertical to the propagation direction.

3. SIMULATION RESULT

In this paper, we simulate propagation of pulse in an rectangular waveguide. The waveguide is discretized into a $60 \times 28 \times 1000$ FDTD grid, and the space step is set as $\Delta x = \Delta y = 0.001\,\mathrm{m}$, $\Delta z = \Delta \zeta' = 0.0001\,\mathrm{m}$. Time step is set as

$$\Delta t = \frac{0.495}{c_0 \sqrt{\frac{1}{(\Delta x)^2} + \frac{1}{(\Delta y)^2} + \frac{1}{(\Delta z)^2}}}. \tag{6}$$

Mur absorbing boundary conditions [3, 4] are set in the back and front boundaries of the waveguide. The pulse in this example is a TE_{10} mode wave with a Gaussian modulation in the z-axis direction, as specified by the initial conditions

$$E_y = E_0 \exp\left(- \left(\frac{z - z_0}{z_2} \right)^2 \right) \cos(\beta_z z) \sin\left(\frac{\pi x}{a} \right), \tag{7}$$

where E_0 is the amplitude, z_0 and z_2 are parameters of Gaussian modulation, β_z is the wave number in z axis, a is the length of waveguide in x axis. Relative difference is defined as

$$\eta = 20 \lg \frac{|X_{MCFDTD} - X_{FDTD}|}{|X_{FRTD}|}, \tag{8}$$

where X_{MCFDTD} is the electromagnetic field calculated by using the moving coordinate FDTD method, and X_{FDTD} is the result of FDTD method.

The simulation results of both moving coordinate FDTD method and FDTD method are nearly the same, as shown in Figs. 2 and 3, relative difference between two methods are less then 0.1% as shown in Fig. 4.

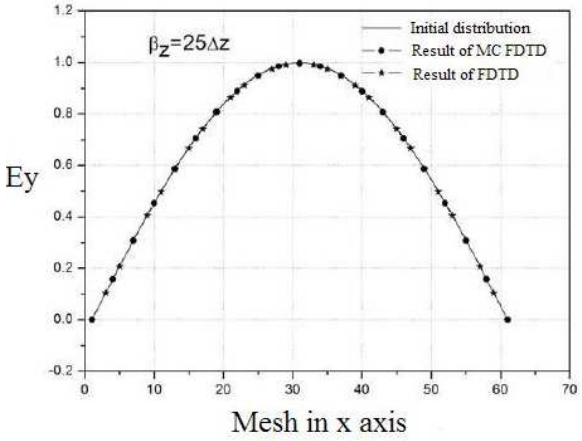

Figure 2: Field distribution of pulse in x axis of waveguide.

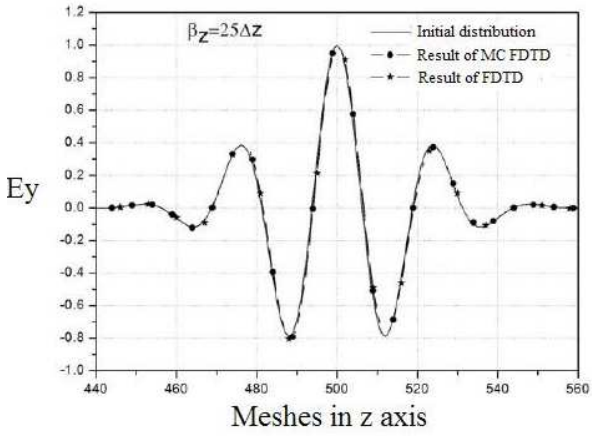

Figure 3: Field distribution of pulse in y axis of waveguide.

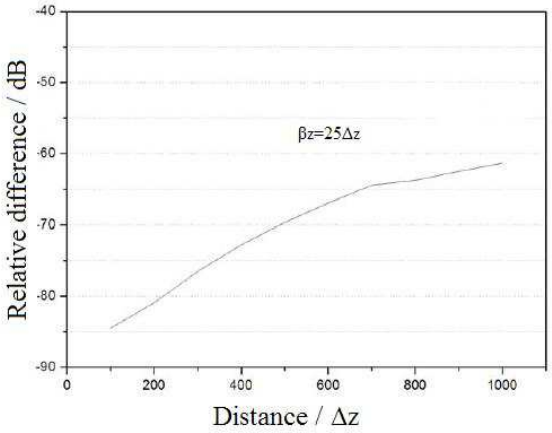

Figure 4: Relative difference between moving coordinate FDTD and FDTD method.

4. CONCLUSION

In this paper, several numerical applications of moving coordinate FDTD method in the propagation of pulses in rectangular waveguide is introduced, and it has been shown that result of moving coordinate FDTD method is feasible. The sum of time-steps increases when the distance over which the pulse propagated increases, and each time-step costs more time because the FDTD method, being a full-wave method, needs to be discretized the whole propagation trajectory of pulses and update field values of all meshes in one time-step. Total time of the simulation increases as a square function of the length of propagation trajectory. While using moving coordinate FDTD method, the size of meshes needs only to contain the pulse, not all the trajectory, thus each time-step costs nearly constant cpu time. In the moving coordinate approach, total time of simulation increase linearly with the length of propagation trajectory since it only needs to increase the sum of time-steps. It can efficiently reduce the cost of calculation time. There are various applications of this method in remote sensing and communication.

REFERENCES

1. Yee, K. S., "Numerical solution of initial boundary value problems involving Maxwell's equations in isotropic media," *IEEE Trans. Antennas Propagat.*, Vol. 14, No. 3, 302–311, 1966.
2. Fidel, B., E. Heyman, R. Kastner, and R. W. Ziolkowski, "Hybrid ray-FDTD moving window approach to pulse propagation," *Proc. of the 1994 International IEEE/AP-S Symposium*, 1414–1417, Seattle, WA, 1994.
3. Pemper, Y., V. Lomakin, et al., "Moving coordinate frame FDTD analysis of long range

tracking of pulsed fields in graded index waveguide," *Progress In Electromagnetics Research*, PIER 26, 133–164, 2000.

4. Mur, G., "Absorbing boundary conditions for the finite-difference approximation of the time-domain electromagnetic field equations," *IEEE Trans. Electromagn. Comput.*, Vol. 23, No. 4, 377–382, 1981.

An Efficacious Computational Procedure to Solve Electromagnetic Transients on Transmission Lines Represented by State Equations

E. C. M. Costa[1], **S. Kurokawa**[2], **A. J. Prado**[2], **and J. Pissolato**[1]

[1]School of Electric Engineering and Computation, State University of Campinas, Brazil
[2]School of Engineering of Ilha Solteira, São Paulo State University, Brazil

Abstract— This work presents an analytic solution to evaluate electromagnetic transients on transmission lines. Several papers apply a line modeling by lumped parameters and state space representation due the relative facility implementation and accuracy over considerable frequency rage. Although the efficacy and precision of transients simulations is intrinsically attached to the methodology applied for resolution of state equations which represent these phenomena. Therefore the current work describes a procedure to solve the state equations based on matrix diagonalization and Eigensystem-Based Solution for state equations. This procedure is compared to results obtained by well known numerical solution of Trapezoidal Rule and to results obtained by EMTP. The transients are evaluated considering a variable integration step Δt and from this procedure, the proposed solution proves to be greatly robust, numerically stable and more efficient than the widely applied Trapezoidal Rule. The transmission line modeling applied in the proposed analyses takes into account the variation of longitudinal parameters in function of frequency and then it is inserted in a cascade of π circuits through the synthesis of a rational function $F(\omega)$, this method is entitled as *Vector Fitting* and also described by this paper.

1. INTRODUCTION

When a lumped parameters line model is adopted, it is very common to use state space techniques to evaluate the currents and voltages along the line. In this way, it is possible for the model to carry out simulations directly in time domain without the explicit use of inverse transforms and it can be easily implemented. These characteristics of the lumped parameters model are the same as those used to simulate electromagnetic transients on lines with non-linear components, such as corona effects and fault arcs [1–2], or when a detailed voltage and current profile is needed.

The line distributed parameters behavior is approximated by a rational function $F(\omega)$ and, from this function, it is possible to synthesize an equivalent electric circuit by lumped resistances and inductances that describes the line longitudinal impedance $Z(\omega)$.

The use of the state space techniques presents several advantages as the possibility of the methodology to be extended to time-variable and non-linear systems. Another advantage is that if state space techniques are used, the transmission line is represented by a system of first order differential equations obtained from this approach and this system can be easily evaluated by numerical integration methods [3].

The integration method known as Trapezoidal Rule for lumped parameters is widely used in computational algorithms for transients simulation and commercial softwares based on *Electromagnetic Transients Program* (EMTP).

The simulation precision is intrinsically dependent of the procedure applied to solve the state equations and emphasizing that Trapezoidal Rule as well as other numerical methods are iterative procedures and largely dependent of integration step Δt, thus the simulation results are also directly dependent of Δt.

However, numerical solutions have an ideal performance when Δt is significantly small otherwise the simulation presents numerical oscillations hence several inaccuracies. Another limitation is associated to the great number of lumped elements used to represent adequately long transmission lines, thus this fact associated to a very small Δt results in a great computational processing and sometimes it results in numerical errors and computational faults. Based on this assertion, this paper proposes an analytical procedure to solve the state equations, less dependent of Δt and then less computational cost.

The results are obtained by numerical solution based on trapezoidal integration method, by analytical solution and from MICROTRAN (EMTP) and then all results are compared and analyzed in function of integration step Δt.

2. FITTING LINE LONGITUDINAL PARAMETERS

To include the frequency dependence of the longitudinal parameters in the state matrices, initially it is necessary to approximate it by a rational function which can be associated with an equivalent electric circuit representation.

The per unit length (*p.u.l.*) longitudinal impedance $Z(\omega)$ of a transmission line, tabulated taking into account soil and skin effects, is an improper function. In this way, for fitting $Z(\omega)$ it is necessary initially to obtain a modified function $F(\omega)$ [4].

Many fitting procedures are available to obtain an approximated rational function for $F(\omega)$, starting from tabulated values from $Z(\omega)$ and in this paper the Vector Fitting algorithm will be used [4]. In a general way, the Vector Fitting algorithm is accurate, robust and can be applied to both smooth and resonant responses with high orders and wide frequency bands.

Once the functions $Z(\omega)_{fit}$ has been fitted, it is possible to associate it with the equivalent circuit shown in Figure 1.

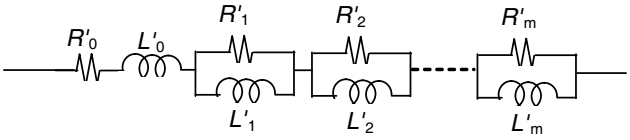

Figure 1: Equivalent circuit used for fitting the *p.u.l.* parameters of a transmission line.

3. FREQUENCY DEPENDENCE OF LONGITUDINAL PARAMETERS IN LUMPED MODEL

It is known that if the frequency effect in the longitudinal parameters is disregarded, a single phase line can be approximated by a cascade of $n\pi$ circuits [1–5]. If soil and skin effects are taken into account, each π circuit of the cascade will be the aspect of the network shown in Figure 2.

In Figure 2, $R_0, R_1, R_2, \ldots, R_m$ are resistors and $L_0, L_1, L_2, \ldots, L_m$ are inductors. These elements are used to represent the frequency dependence of the longitudinal parameters of the line. The terms G and C are, respectively, the shunt conductance and shunt capacitance.

The cascade shown in Figure 2 describes a non-homogeneous system with $n(m+2)$ state equations that represents the currents and voltages along the line.

The parameters of the circuit shown in Figure 2 are calculated as:

$$R_k = R'_k \frac{d}{n} \tag{1}$$

$$L_k = L'_k \frac{d}{n} \tag{2}$$

$$C_k = C'_k \frac{d}{n} \tag{3}$$

$$L_k = L'_k \frac{d}{n} \tag{4}$$

In (1)–(4) d is the length of the line and n is the quantity of π circuits used to represent the line. The terms R'_k and L'_k are resistances and inductances used for fitting *p.u.l.* longitudinal parameters of the line whereas C'_k and G'_k are, respectively, *p.u.l.* shunt parameters of the line.

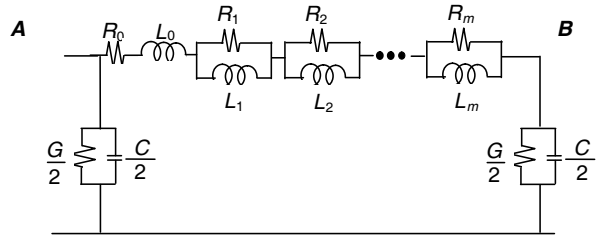

Figure 2: A generic π circuit that represents a frequency dependent single phase line.

Considering the circuit described in Figure 1, presented in Figure 2, where the terms $I_{k0}, I_{k1}, I_{k2}, \ldots, I_{km}$ are currents in the inductors $L_0, L_1, L_2, \ldots, L_m$, respectively.

Considering that currents in inductances L_0 to L_m and voltage between terminals A and B are written in time domain, it is possible to write the differential equations of the line:

$$\frac{dI_{k0}}{dt} = \frac{I_{k0}}{L_0}\left(-\sum_{j=1}^{m} R_j\right) + \frac{1}{L_0}\left(-\sum_{j=1}^{m} R_j I_{kj}\right) + \frac{1}{L_0}V_{k-1} - \frac{1}{L_0}V_k \tag{5}$$

$$\frac{dI_{k1}}{dt} = \frac{R_1}{L_1}I_{k0} - \frac{R_1}{L_1}I_{k1} \tag{6}$$

$$\frac{dI_{km}}{dt} = \frac{R_m}{L_m}I_{k0} - \frac{R_m}{L_m}I_{km} \tag{7}$$

$$\frac{dV_k}{dt} = \frac{1}{C}I_{k0} - \frac{1}{C}I_{(k+1)0} - \frac{G}{C}V_k \tag{8}$$

The equations presented in (5)–(8) are applied in each π circuit of the cascade shown in Figure 2, thus it describes a non-homogeneous system with $n(m+2)$ state equations that represents the currents and voltages along the line. These equations are written in state space as:

$$[\dot{\mathbf{X}}] = [\mathbf{A}][\mathbf{X}] + [\mathbf{B}]u(t) \tag{9}$$

The vector $[X_n]$ has dimension $(m+2)$ and $u(t)$ is a voltage source. A generic vector $[X_k]$ is written as being:

$$[X_k]^T = [\ I_{k0} \quad I_{k1} \quad I_{k2} \quad \cdots \quad I_{km} \quad V_k\ ] \tag{10}$$

where $[X_k]^T$ is the transposed vector of $[X_k]$. Vector $[\mathbf{X}]$ has dimension $n(m+2)$.

Matrix $[\mathbf{A}]$, written in (9), is a square matrix with dimension $n(m+2)$ and it is a tridiagonal matrix that elements are also square submatrices with dimension $(m+2)$.

A generic submatrix $[A_{kk}]$ in main diagonal of matrix $[\mathbf{A}]$, is written as:

$$[A_{kk}] = \begin{bmatrix} -\dfrac{\sum_{j=0}^{j=m} R_j}{L_0} & \dfrac{R_1}{L_0} & \dfrac{R_2}{L_0} & \cdots & \dfrac{R_m}{L_0} & -\dfrac{1}{L_0} \\ \dfrac{R_1}{L_1} & -\dfrac{R_1}{L_1} & 0 & \cdots & 0 & 0 \\ \dfrac{R_2}{L_2} & 0 & -\dfrac{R_2}{L_2} & \cdots & 0 & 0 \\ \vdots & \vdots & \vdots & \ddots & \vdots & \vdots \\ \dfrac{R_m}{L_m} & 0 & 0 & \cdots & -\dfrac{R_m}{L_m} & 0 \\ \dfrac{1}{C} & 0 & 0 & \cdots & 0 & -\dfrac{G}{C} \end{bmatrix} \tag{11}$$

It is observed in (11) that a generic submatrix $[A_{kk}]$ has only non-null elements in main diagonal, in first row and in first column.

The elements of the first diagonal above, in matrix $[\mathbf{A}]$, are matrices with only one non-null element. This non-null element is the first element of the last row and it is expressed as $-1/C$. In the matrices situated in the first diagonal below, the non null element is the last element of the first row and it is written as $1/L_0$.

The vector $[\mathbf{B}]$ in (9) has $n(m+2)$ elements and it is written as:

$$[\mathbf{B}] = \begin{bmatrix} \dfrac{1}{L_0} & 0 & \ldots & 0 \end{bmatrix}^T \tag{12}$$

Taking into account (11), it is observed that matrix $[\mathbf{A}]$ is highly sparse. Therefore, to save space in computer memory and to reduce processing time, sparsety techniques can be used to store only non-null elements.

4. ANALITICAL SOLUTION FOR STATE EQUATIONS

There are several analytic methods that can be used to solve differential equations as *Eigensystem-based solution*, *Vandermond Matrix and Lagrange Interpolation Formula* [3]. In this paper the analytic solution of the state equations was obtained by a procedure based on Eigensystem-based solution and matrices diagonalization.

The state equations describe a non-homogeneous or coupled system, because **[A]** is not a diagonal matrix. Although matrix **[A]** can be converted in a diagonal matrix by a similarity transformation. Therefore this coupled system is decoupled hence it is possible to obtain $n(m+2)$ decoupled equations.

Considering a full square matrix **[T]** with dimension $n(m+2)$ whose the columns are eigenvectors of matrix **[A]**, thus it is possible to define a vector **[Y]** written in function of **[X]**.

$$[\mathbf{X}] = [\mathbf{T}][\mathbf{Y}] \tag{13}$$

In state space form:

$$[\dot{\mathbf{Y}}] = [\mathbf{T}]^{-1} + [\mathbf{A}][\mathbf{T}][\mathbf{Y}] + [\mathbf{T}]^{-1}[\mathbf{B}]u(t) \tag{14}$$

From similarity transformation described in [3]:

$$[\dot{\mathbf{Y}}] = [\lambda][\mathbf{Y}] + [\mathbf{G}] \tag{15}$$

where

$$[\mathbf{G}] = [\mathbf{T}]^{-\mathbf{1}}[\mathbf{B}]u(t) \tag{16}$$

$$[\lambda] = [\mathbf{T}]^{-\mathbf{1}}[\mathbf{A}][\mathbf{T}] \tag{17}$$

Matrix $[\lambda]$ is a diagonal matrix whose non-null elements are the eigenvalues of matrix **[A].** This way, the column T_k of matrix **[T]** is an eigenvector associated with eigenvalue λ_k.

It is important to observe that any eigenvalue of matrix **[A]** is repeated and they are real eigenvalues or pairs of complex conjugate eigenvalues. Therefore an element λ_k is written as:

$$\lambda_k = \alpha_k + j\beta_k \tag{18}$$

Considering that $[\lambda]$ is a diagonal matrix, the system shown in (16) is an uncoupled system. Taken into account that the initial conditions are considered null, the integration of (16) results in a vector **[Y]** described as:

$$[\mathbf{Y}]^T = [y_1 \quad y_2 \quad y_3 \quad \cdots \quad y_{n(m+2)}] \tag{19}$$

where $[\mathbf{Y}]^T$ is the transposed of **[Y]**.

The k-th element of vector **[Y]** is written as:

$$y_k = c_k e^{\lambda_k t} - \frac{g_k}{\lambda_k}u(t) \tag{20}$$

In (20) g_k is the k-th element of the vector **[G]** and c_k is the integration constant.

Then, it is possible to obtain the vector **[X]**:

$$[\mathbf{X}] = [\mathbf{T}]\,[y_1 \quad y_2 \quad y_3 \quad \cdots \quad y_{n(m+2)}]^T \tag{21}$$

If the initial conditions of the line are null, a generic element x_k of vector **[X]** in (21) will be written as:

$$x_k(t) = \sum_{i=1}^{\varphi} e^{\alpha_i t}(a_{ki} - b_{ki})\sin\beta_i t + \sum_{i=1}^{\varphi} e^{\alpha_i t}(a_{ki} + b_{ki})\cos\beta_i t \tag{22}$$

where

$$\varphi = (m+2)n \tag{23}$$

$$a_{ki} = \mathrm{Re}\left(T_{ki}\frac{g_i}{\lambda_i}\right) \quad \text{and} \quad b_{ki} = \mathrm{Im}\left(T_{ki}\frac{g_i}{\lambda_i}\right) \tag{24}$$

In (26) a_{ki} and b_{ki} are, respectively, the real and imaginary parts of the term $T_{ki}\frac{g_i}{\lambda_i}$. The term T_{ki} is the element $T(k,i)$ of matrix **[T]**, g_i is i-th element of vector **[G]** and λ_i is i-th eigenvalue of the matrix **[A]**.

By using (22) it is possible to obtain the state variables $x_k(t)$ that are the currents and voltages along the line.

5. ANALISYS OF METHODOLOGIES

To analyze the efficacy of analytical methodology for state equations solution and numerical solution based on the classical trapezoidal integration, it describes a single-phase transmission line with length 100 km, illustrated by Figure 3.

In Figure 3, the commuter S and the voltage source $u(t)$ simulate the transients occasioned from line energization.

For simulations of electromagnetic transients from transmission line energization, a transformer can be represented by a capacitance connected between line terminal and ground [5]. Thus, the transformer illustrated in Figure 4 is modeled by a shunt capacitance C_T equal $6\eta F$ [5]. To represent this line is applied a cascade with 110π circuits.

From Figure 4, it verifies the voltage transients calculated by trapezoidal integration and by analytical procedure, considering Δt equal 0.05 µs.

It is possible to verify that the results obtained from both solution methods, when a small integration step Δt is determined, and from Microtran (EMTP) are similar. Then, from this procedure, it possible to assert that analytical solution method is according to the simulation evaluated by EMTP.

To demonstrate the influence of Δt over the iterative solution method using trapezoidal rule, it

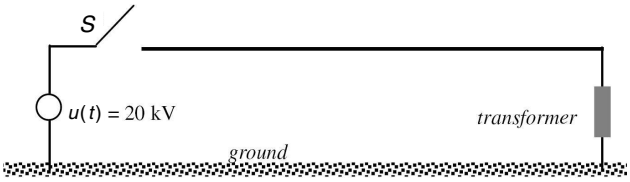

Figure 3: Single-phase transmission line.

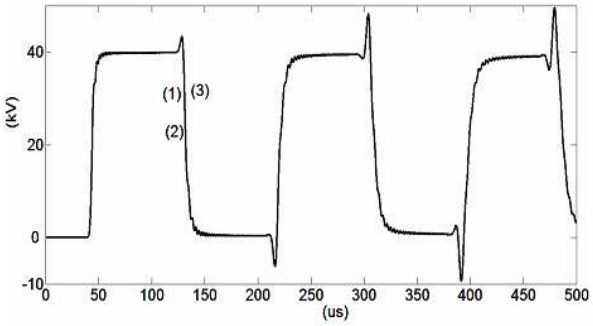

Figure 4: Transient voltage with $\Delta t = 0.05\,\mu s$: analytical solution (1); trapezoidal integration solution (2) and EMTP (3).

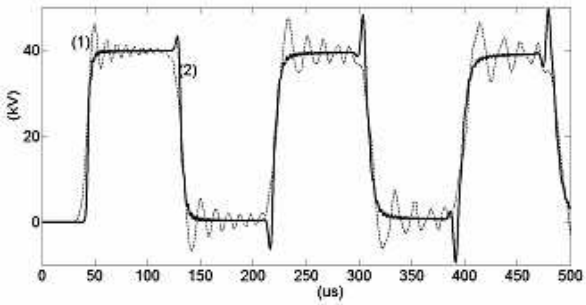

Figure 5: Transient voltage calculated using trapezoidal integration: $\Delta t = 2\,\mu s$ (1) and $\Delta t = 0.05\,\mu s$ (2).

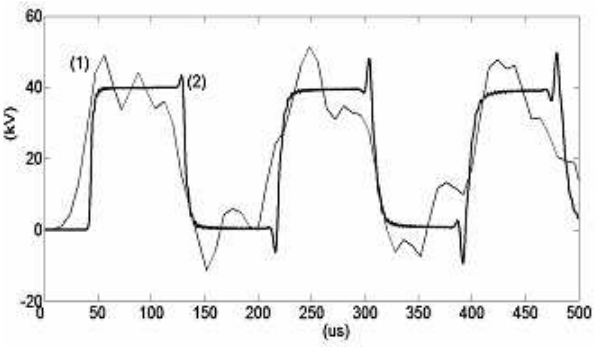

Figure 6: Transient voltage calculated using trapezoidal integration: $\Delta t = 8\,\mu s$ (1) and $\Delta t = 0.05\,\mu s$ (2).

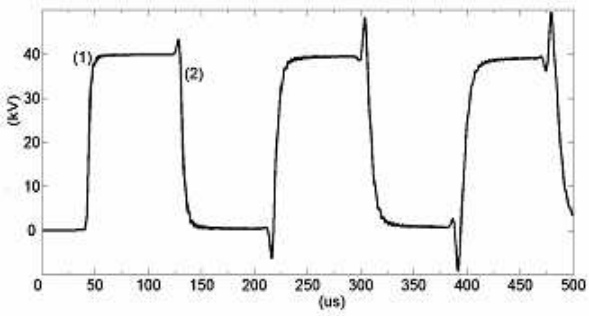

Figure 7: Transient voltage calculated using analytical solution: $\Delta t = 8\,\mu s$ (1) and $\Delta t = 0.05\,\mu s$ (2).

is evaluated the transients voltages on transformer terminal, considering Δt 0.05 and 8 µs.

From Figures 5 and 6, it is possible to observe the sensibility of trapezoidal rule solution in function of Δt. Observing that increasing Δt, numerical oscillations increases as well, as verified in Figures 5 and 6.

From Figures 5 and 6, it is possible to conclude that trapezoidal rule is greatly dependent of variation of Δt, describing numerical instabilities in function of Δt increment.

The same procedure applied to analyze the trapezoidal rule in function of Δt is used for analytical solution as well. Thus, Figure 7 shows the analytical solution considering Δt equal 0.05 and 8 µs.

It verifies, from Figure 7, that the analytical solution is practically invariable with variation of Δt and without numerical oscillations. Thus, considering the time interval adopted between 0.05 and 8 µs, it is possible to assert that the presented analytical methodology is robust in function of integration step Δt.

6. CONCLUSION

It verifies, from Figure 7, that the analytical solution is practically invariable with variation of Δt and without numerical oscillations. Thus, considering the time interval adopted between 0.05 and 8 µs, it is possible to assert that the presented analytical methodology is robust in function of integration step Δt.

Firstly, considering the results described in Figure 4, it concludes that both solution methodologies applied for lumped parameters modeling are according with the results obtained from EMTP. Thus, it is possible to conclude that when a small integration step Δt is adopted, both methodologies presents adequate results.

Afterward, the behavior of trapezoidal rule solution was analyzed in function of a variable Δt. Concluding that with increment of Δt, trapezoidal integration solution presents numerical oscillations, decreasing the quality of the results, as described in Figures 5 and 6.

After that, a similar procedure was done to analytical method and from this procedure the analytical solution shown to be invariable in function of Δt, as described in Figure 7. Thus, it is possible to assert that the analytical solution is robust, at lest, in analyzed interval for Δt.

Therefore, from this work, it is possible to conclude that the analytical solution is less dependent of Δt and, from this assertion, this methodology shows to be an efficient computational tool to evaluate electromagnetic transients on transmission lines, once that using a large integration step the computational processing is considerably reduced.

ACKNOWLEDGMENT

This research was supported by *Coordenação de Aperfeiçoamento de Pessoal de Nível Superior* (CAPES) and National Counsel of Technological and Scientific Development (CNPq).

REFERENCES

1. Mamis, M. S., "Computation of electromagnetic transients on transmission lines with nonlinear components," *IEE Proc. Gener. Trans. Distr.*, Vol. 150, No. 2, 200–203, 2005.
2. Mamis, M. S. and M. E. Meral, "State-space modeling and analysis of fault arcs," *Electric Power Systems Research*, Vol. 76, No. 1, 46–51, 2005.
3. Macías, J. A. R., A. G. Expósito, and A. Soler, "A comparison of techniques for state-space transient analysis of transmission lines," *IEEE Trans. on Power Delivery*, Vol. 20, No. 1, 894–903, 2005.
4. Marti, J. R., "Accurate modeling of frequency-dependent transmission lines in electromagnetic transient simulation," *IEEE Trans. on Power Apparatus and Systems*, Vol. 101, No. 1, 147–155, 1982.
5. Nelms, R. M., G. B. Sheble, S. R. Newton, and L. L. Grigsby, "Using a personal computer to teach power system transients," *IEEE Trans. on Power Systems*, Vol. 4, No. 3, 1293–1297, 1989.

Processing of MR Slices of Human Liver for Volumetry

J. Mikulka[1], **E. Gescheidtova**[1], **and K. Bartusek**[2]

[1]Department of Theoretical and Experimental Electrical Engineering, Brno University of Technology
Kolejni 2906/4, Brno 612 00, Czech Republic
[2]Institute of Scientific Instruments, Academy of Sciences of the Czech Republic
Kralovopolska 147, Brno 612 64, Czech Republic

Abstract— This article deals with a segmentation of MR images of human liver. The aim of the segmentation is bounding of tumors in MR images of the human liver in each slice. It is possible to reconstruct the original shape of the tumor from these bounded areas and if we know the thickness of each slice the volume can be solved. This method is suitable for monitoring the development of tumor volume during the treatment. The volume reducing means successful treatment. There was chosen an active contour method based on level set partial differential equation for the MR image segmentation [1]. There was found the boundary of the liver tumor in the noised image of low contrast with suitable parameters and initial curve without any kind of preprocessing. The article shows our results of the segmentation of some MR slices with visible liver tumors. These results are poised to following postprocessing which will be the 3D model creation and the volumetry of the tumor.

1. INTRODUCTION

The aim of this work is 3D model creation of tumors in the human liver (Fig. 1). It is useful for diagnosis and decision about the treatment success. In traditional way it consists of many steps of MR image processing — preprocessing the images (noise suppression, contrast and edge enhancement), edge analysis and segmentation, segmented images processing. The goal of the proposed processing method is elimination of needful steps of processing and its simplification. The modern segmentation method was found and tested. The MR slices with visible tumors in human livers were segmented by region-based level set segmentation method. This level set approach gives very good results in segmentation of noised MR images with predictable number of homogenous subareas with low contrast and smooth edges so that it is not necessary to preprocess the image before the segmentation of image. The second step will be calculation of the tumor volume. The number of pixels in each bounded tumor will be numbered and multiplied by the slice thickness. We get the resultant volume of tumor by normalizing the number of all tumor subarea pixels with the one pixel dimensions.

The mentioned level set methods known as active contours are based on partial differential equation solution. There is defined the deformable model of active contour with initial shape and location in the image and by iterative solution of equation(s) the contour can change own shape, topology and location. In the steady state the active contour bounds the found objects with different mean value of the intensity. The basic method can find 2^n areas with the n partial differential equations. In the given MR images of human liver we can find the bright areas of the

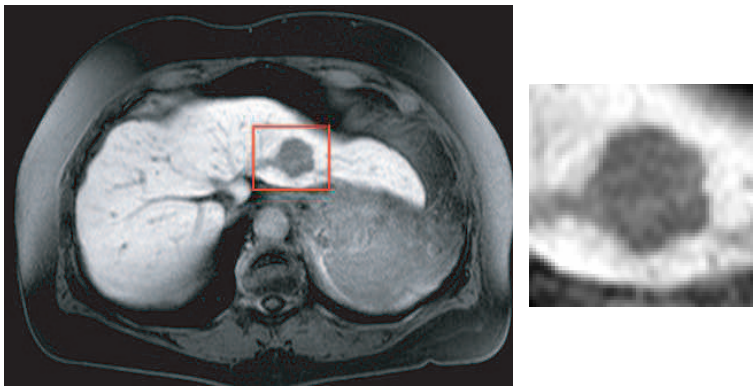

Figure 1: Example of one slice of the human liver (left), detail of the liver tumor (right).

liver and the dark areas with the tumor, so it is possible to use only one equation. The disadvantage of this approach is that the background of the liver has the similar intensity as the tumor. The solution of this problem will be the aim of the future work.

2. DEFORMABLE MODELS

The region-based segmentation is described by this energy functional [1]:

$$F(c_1, c_2, \phi) = \int_{\Omega} (u_0(x,y) - c_1)^2 H(\phi)\, dx\mathrm{d}y + \int_{\Omega} (u_0(x,y) - c_2)^2 (1 - H(\phi))\, \mathrm{d}x\mathrm{d}y + \nu \int_{\Omega} |\nabla H(\phi)|, \quad (1)$$

where the first two terms divide the area Ω of the original image u_0 to two subareas with the mean values of intensity c_1 and c_2. The third term minimizes the length of the resultant contour. It can be used for suppression of noise in the image and the final contour is smoother. This term is weighted by the coefficient ν. H is the Heaviside function. This function recognizes where the level set function ϕ is positive, respectively negative.

$$\frac{\partial \Phi}{\partial t} = \delta_{\varepsilon}(\Phi) \left[\nu \,\mathrm{div}\left(\frac{\nabla \Phi}{|\nabla \Phi|} \right) - (u_0 - c_1)^2 + (u_0 - c_2)^2 \right]. \quad (2)$$

This gradient flow is the evolution equation of the level set function Φ. The first term in the brackets (2) corresponds to the length functional.

3. IMPLEMENTATION

The algorithm was implemented in Matlab 7.0. The Equation (2) was approximated by central and forward difference schemes and solved by iterative process. The Dirac function was approximated by:

$$\delta_{\varepsilon}(x) = \begin{cases} 0, & |x| > \varepsilon \\ \dfrac{1}{2\varepsilon} \left[1 + \cos\left(\dfrac{\pi x}{\varepsilon} \right) \right], & |x| \le \varepsilon \end{cases} \quad (3)$$

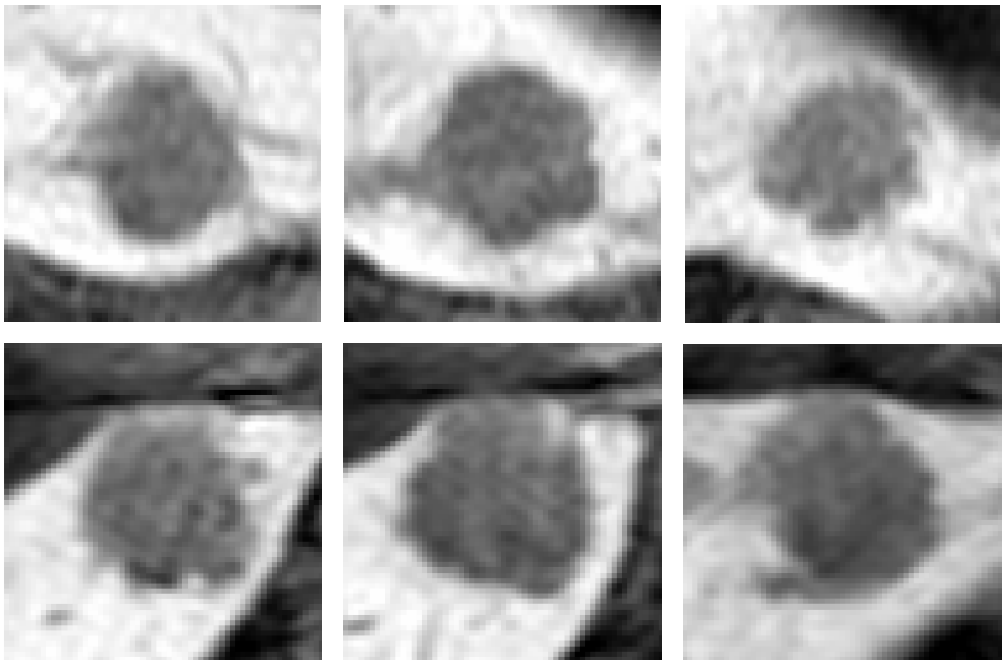

Figure 2: Six chosen original cropped slices with liver in the human liver.

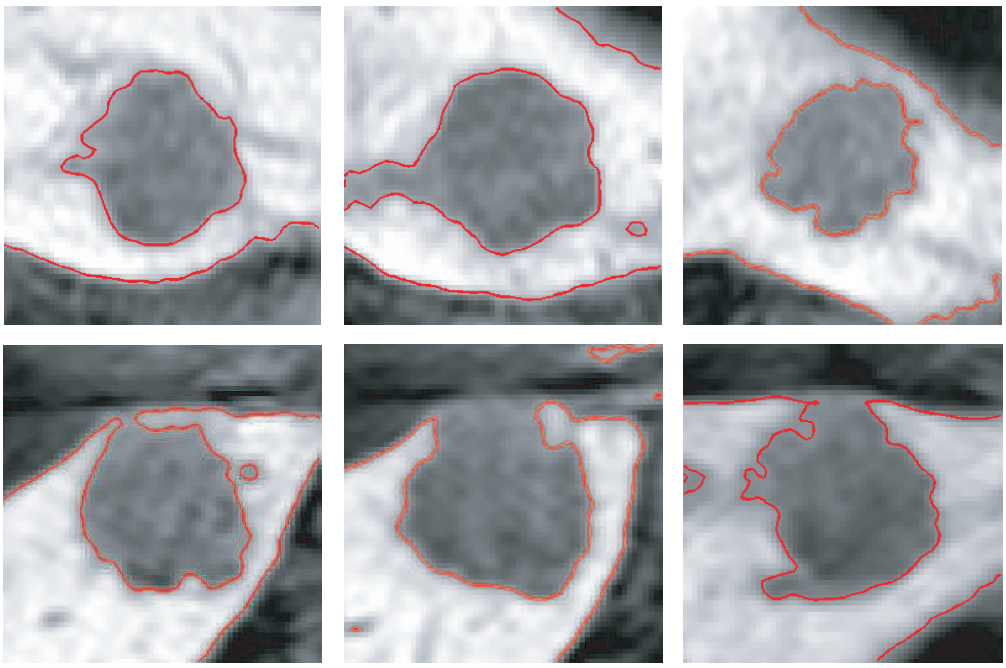

Figure 3: Segmentation results of the region-based level set method — the red contours bound the liver tumor.

4. SEGMENTATION RESULTS

The results of direct segmentation of images (Fig. 2) without any kind of the preprocessing are shown in the Fig. 3. The slices of the liver were segmented by the region-based level set method with circular initial contour in the middle of the ROI. The segmentation process was done in about 5 seconds (AMD 1600XP, 768MB RAM).

5. CONCLUSION

The paper presents segmentation of 6 MR slices of human liver in three projections. There were overall 14 MR slices with visible disc and all the images were automatically successfully segmented. The future work will be design of an algorithm for the statistical evaluation of the intensities in a region of interest. The aim of this algorithm will be recognizing of the dark background and the liver tumor which has a similar mean intensity. When the tumor will be bounded without the background tissues, the area and the volume of the tumor can be calculated. The shape of the volume can be reconstructed too.

ACKNOWLEDGMENT

This work was supported within the framework of the research plan MSM 0021630516 and project of the Grant Agency of the Czech Republic GA102/07/0389.

REFERENCES

1. Vese, L. and F. Chan, "A multiphase level set framework for image segmentation using the Mumford and Shah model," *International Journal of Computer Vision*, Vol. 50, No. 3, 271–293, 2002.
2. Aubert, G. and P. Kornprobst, *Mathematical Problems in Image Processing: Partial Differential Equations and the Calculus of Variations*, 2nd Edition, 377s, Springer Science + Business Media, LLC, New York, 2006, ISBN 0-387-32200-0.

Detection of Magnetization of 6 Hz, 10 μT Magnetic Field Applied Water Using PT-MI Sensor

K. Mohri[1, 2], M. Fukushima[3], Y. Mohri[4], and Yu. Mohri[5]

[1]Nagoya Industrial Science Research Institute (NISRI), Nagoya 464-0819, Japan
[2]Aichi Micro Intelligent Co., Tokai 476-8666, Japan
[3]TRI, Foundation for Biomedical Research and Innovation, Kobe 650-0047, Japan
[4]Graduate School of Eng., Meijo Univ., Nagoya 468-8502, Japan
[5]Graduate School of Arts, Meijo Univ., Nagoya 468-8502, Japan

Abstract— We constructed an extremely sensitive magnetic sensor having one pico-Tesla resolution using single amorphous wire core CMOS IC magneto-impedance sensor with *dc* selective negative feedback circuitry ("pT-MI sensor") for detection of the water magnetization. The water magnetization M is measured using a pendulum oscillation sample magnetic measurement method, in which a water sample bottle of 100 ml oscillates as a pendulum with 1.5 Hz in front of the pT-MI sensor head at 50 mm apart position showing 3 Hz magnetic field sinusoidal wave. Sample water (purified water and tap water) with 6 Hz, 10 μT magnetic field application through more than 1 hour showed a clear 3 Hz sinusoidal wave output of around 1 nT amplitude ($M = 2.3$ pT) during at least 30 min. and not for samples without *ac* magnetic field application and also magnet *dc* field application. Mechanism of water magnetization has been proposed with an assumption of the cyclotron resonance of the water cluster ($H_3O^+(H_2O)_n$) which activates the proton transport in water under the geo-magnetic field ("magneto-protonics").

1. INTRODUCTION

Possibility of magnetization of water has been discussed for a long time, which may change the water structure and reinforce the water function on physical and bio-chemical operations. A comprehensive investigation paper on the *dc* magnetization of water has recently been reported by X. F. Pang and Bo Deng [1] gathering the spectra of infrared, Raman, visible, ultraviolet lights and X-ray, in which the intensity of light absorption is higher in the *dc* magnetized water.

We represent measured results for the magnetization of water after application of a ultra-low frequency (6 Hz) small magnetic field superimposed with the geo-magnetic field using a newly constituted pico-Tesla resolution magneto-impedance sensor ("pT-MI sensor"). A double frequency sinusoidal magnetic field of around 1 nano-Tesla amplitude is detected when a 200 ml bottle with 100 ml magnetized water (purified water and public tap water) is pendulum type oscillated in a vertical plane at 5 cm apart from the pT-MI sensor head. The magnetization of the *ac* magnetized water under the geo-magnetic field is estimated as around 2.3 pT. No magnetization was detected for water samples without application of *ac* magnetic field or after application of *dc* magnetic field using NdFeB magnets. The magnetization mechanism resulting the long-range proton transport ("proton activation") in *ac* magnetized water is explained using a model of cyclotron resonance of water clusters $H_3O^+(H_2O)_n$, $n = 0, 1, 2, \ldots$ under the geo-magnetic field ("magneto-protonics").

2. PT-MI SENSOR

An extremely sensitive magnetic field sensor is needed to detect the magnetization of magnetized water. We newly constructed a pico-Tesla resolution *ac* magnetic sensor as illustrated in Figure 1 on the basis of the amorphous wire & CMOS IC magneto-impedance sensor (MI sensor) [2–5] by suppressing both the magnetic noises in the sensor head using an amorphous wire and the electronic circuit noises introducing the notch filters and a *dc* negative feedback circuitry. A tension annealed zero-magnetostrictive FeCoSiB amorphous wire of 30 μm diameter and 10 mm length (made by UNITIKA LTD.) with coil windings of 600 and 200 turns is used as the sensor head. The frequency response of the pT-MI sensor is set as $0.5 \sim 15$ Hz.

3. MEASUREMENT OF MAGNETIZATION

Figure 2 represents measured results of magnetization of magnetized water at the room temperature using the pT-MI sensor without any magnetic shielding box. A 100 ml water is set in a plastic bottle of 60 mm diameter and 100 mm height hanged with a pair of 20 mm long strings and is oscillated as a pendulum with around 1.5 Hz in a vertical plane of 50 mm apart from the sensor head.

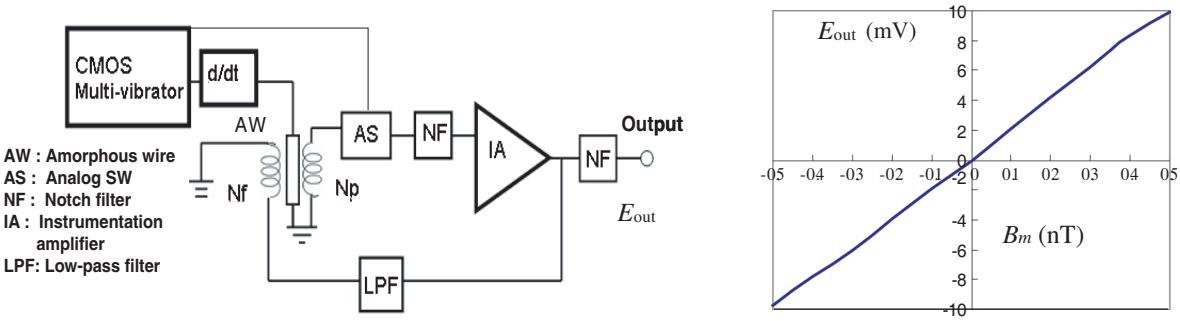

Figure 1: pT-MI sensor circuitry and magnetic field detection characteristics.

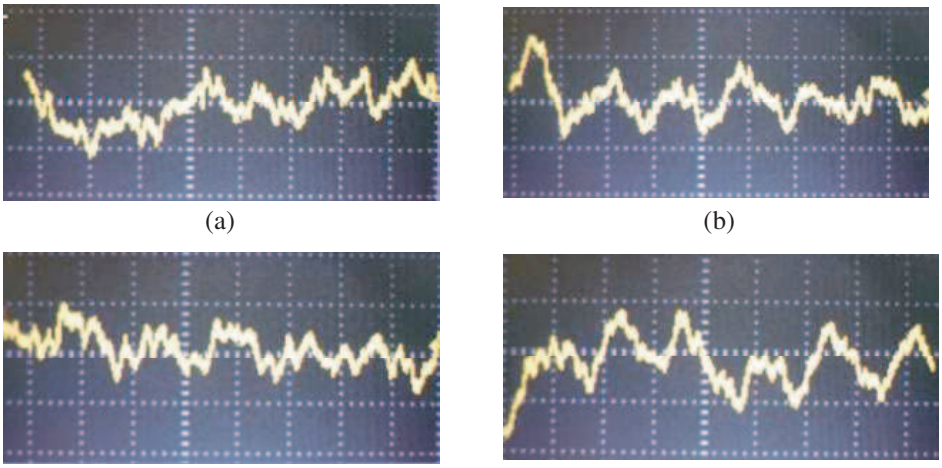

Figure 2: Oscillatory magnetic field waveforms of pendulum oscillated water samples 50 mm apart from the pT-MI sensor head. (a) Public distributing water (140 Ω-m, 100 ml) 2 nT/div, 0.25 s/div. (b) 6 Hz, 10 μT pulse magnetic field, 3 hour applied public distributing water (140 Ω-m, 100 ml) 2 nT/div, 0.25 s/div. (c) Purified water (8 kΩ-m, 100 ml) 2 nT/div, 0.25 s/div. (d) 6 Hz, 10 μT pulse magnetic field, 3 hours applied purified water (8 kΩ-m, 100 ml) 2 nT/div, 0.25 s/div.

Only *ac* magnetized water samples ((b) and (d)) showed clear oscillatory double frequency (around 3 Hz) waveform for sample pendulum oscillation (around 1.5 Hz). That is, water (purified water and tap water or public distributing water) is magnetized along the geomagnetic field after application of 6 Hz, 10 μT pulse magnetic field with few hours in the room temperature.

Water is also magnetized by application of pulse magnetic field with frequencies of $1 \sim 60$ Hz, $1 \sim 100$ μT through 10 min. to 20 hours. No magnetization is detected for water of as-prepared and *dc* magnetic field applied using magnets such as NdFeB through few hours. The magnetic moment m of the magnetized water center in the geomagnetic field is estimated using expressions as follows,

$$\begin{aligned} H(r) &= m \sin\theta / 4\pi\mu_0 r^3 \\ r &= \left(r_0^2 + 2\ell^2(1-\cos\varphi)\right)^{1/2} \\ \partial H &= H(r_0) - H(r) \end{aligned} \tag{1}$$

where $H(r)$ is a magnetic field along the vertically set sensor head, m the magnetic moment, θ the angle of the geomagnetic field against vertical direction, μ_0 the vacuum permeability ($4\pi \times 10^{-7}$ H/m), r the distance between the center of water sample and the sensor head, ℓ the pendulum length, φ the angle of pendulum string against the vertical direction, r_0 the minimum distance for r at $\varphi = 0$, and ∂H the amplitude of detected H for pendulum oscillation. Therefore, $m = 2.3$ pT-m^3 for $\mu_0 \partial H = 1$ nT, $r_0 = \ell = 8$ cm, and $\theta = \varphi = \pi/4$, resulting the magnetization M of the magnetized water is around 2.3 pT.

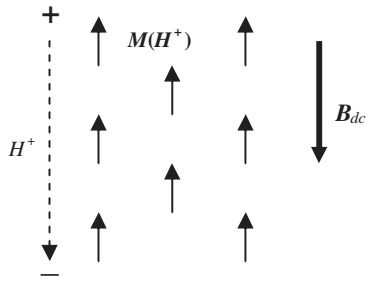

Figure 3: Model for proton magnetic moment $M(H^+)$ alignment in cyclotron rotated clusters against the geomagnetic field B_{dc} accompanied with the long range proton transport (dotted line).

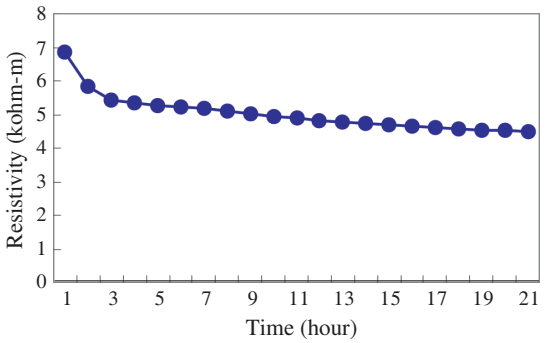

Figure 4: Decreasing of the electric resistivity of purified water during application of 6 Hz, 10 μT pulse magnetic field through 20 hours at 24°C.

4. MAGNETO-PROTONICS

We have proposed a model for mechanism of the magnetization of water assuming cyclotron resonance of the water cluster $H_3O^+(H_2O)_n$, $n = 0, 1, 2, \ldots$ under the geo-magnetic field B_{dc} with the cyclotron frequency $f_n = qB_{dc}/2\pi m_n$, $n = 0, 1, 2, \ldots$ (q: proton charge, m_n: mass of the water cluster) [6]. When an *ac* magnetic field with frequency f_p ($n = p$) is applied to water, same sized water clusters with the mass of m_p are gradually gathered each other due to the magnetic moment of the proton in each cluster which is inversely aligned to B_{dc} direction during the cyclotron resonance with the proton rotation current. Forming of a domain of some water cluster strings is assumed during the cyclotron resonance as illustrated in Figure 3 in which each proton can transport to adjacent clusters ("long range ordered proton transport") and decreases the electric resistivity of the magnetized water. Figure 4 represents measured results of the electric resistivity (inverse of the proton concentration; Proton Concentration Meter, EC/pH Meter WM-22EP, TOA DKK Co.) versus time characteristics in purified water at 24°C during application of 6 Hz, 10 μT pulse magnetic field. An exponential decreasing curve of the characteristics was resulted in which the resistivity decreased around 20 % at 2 hours, 28 % at 10 hours and 34 % at 20 hours. Therefore, around 60 % of the resistivity change occurs by application of 6 Hz magnetic field through 2 hours.

5. CONCLUSION

(1) Magnetization of magnetized water is measured using a pT-MI sensor.
(2) Water is magnetized by application of a ultra low frequency magnetic field through few hours in the geo-magnetic field.
(3) Magnetization of water is accompanied with the long range proton transport (proton activation) which is generated through the cyclotron resonance of water clusters in the geo-magnetic field (Magneto-Protonics model).

The proton activation reinforces the ATP production for mitochondria molecular motor operation in the bio cell (bio activation) and is useful for blood flow promotion in the human body, marine culture, plant culture, and industrial applications such as fuel cell activation.

ACKNOWLEDGMENT

The authors express their gratitude to Mr. Hideo Arakawa of Aichi Micro Intelligent Co. and Dr. Chang Mei Cai of Aichi Steel Co. for their construction of the pT-MI sensor, and to Dr. Kenichi Bushida of UNITIKA LTD. for his presentation of the high permeability amorphous wires with micro coils.

REFERENCES

1. Pang, X. F. and B. Deng, "Investigation of changes in properties of water under the action of a magnetic field," *Sci. China Ser. G — Phys. Mech. Astron.*, Vol. 51, No. 11, 1621–1632, 2008.
2. Panina, L. V. and K. Mohri, "Magneto-impedance effect in amorphous wires," *Appl. Phys. Lett.*, Vol. 65, No. 9, 1189–1191, 1994.

3. Kanno, T., K. Mohri, K. Yagi, T. Uchiyama, and L. P. Shen, "Amorphous wire MI micro sensor using CMOS IC multivibrator," *IEEE Trans. Magn.*, Vol. 33, No. 5, 3358–3360, 1997.
4. Mohri, K., T. Uchiyama, L. P. Shen, C. M. Cai, L. V. Panina, Y. Honkura, and M. Yamamoto, "Amorphous wire and CMOS IC based sensitive micromagnetic sensors utilizing magnetoimpedance (MI) and stress-impedance (SI) effects," *IEEE Trans. Magn.*, Vol. 38, No. 5, 3063–3068, 2002.
5. Mohri, K. and Y. Honkura, "Amorphous wire and CMOS IC based magneto-impedance sensors — Orign, topics, and future," *Sensor Letters*, Vol. 5, 267–270, 2007.
6. Mohri, K. and M. Fukushima, "Milligauss magnetic field triggering reliable self organization of water with long range ordered proton transport through cyclotron resonance," *IEEE Trans. Magn.*, Vol. 39, No. 5, 3328–3330, 2003.

An Optimized Universal Adaptive ARC Filter Block

Martin Friedl, **Lubomír Fröhlich**, **and Jiří Sedláček**
Brno, FEEC BUT, UTEE, Kolejní 2906/4, Brno 612 00, Czech Republic

Abstract— Active RC filters designed using cascade synthesis method are in practice used very often. Each selective building biquads can be designated using many different circuits. There are divided most often according number of active elements (Operational Amplifiers OAs) to different groups. These circuits with three or four active elements exhibit some advantages. Their outputs enable concurrently to obtain all required kinds of filter types (Low pass LP, high pass HP, band pass BP, band reject BR, all pass AP). The flexibility of above mentioned biquads also allows it to be used in some special applications — as tuning requirements or switchable — filter options.

This paper deals with optimized universal biquad blocks with modern active elements, which are usable for many special filter applications. Here are presented some results and achieved parameters of realized tuneable and switchable blocks with modern operational amplifier too. Briefly here are also discussed and presented possible tuning circuits realized using microprocessor technique.

1. INTRODUCTION

In the filter literature have been prescribed many connections of universal active RC circuits which enable to realize transfer function [1] in form of biquads:

$$H(s) = K \cdot \frac{N(s)}{D(s)} = K \cdot \frac{b_2 s^2 + b_1 s + b_0}{a_2 s^2 + a_1 s + a_0} = K \cdot \frac{s^2 + s \cdot \omega_z / Q_z + \omega_z^2}{s^2 + s \cdot \omega_0 / Q_0 + \omega_0^2}. \tag{1}$$

Some from these circuit exhibit very low sensitivities to variations in the passive and active components and possibility of trimming all of required basic parameters independently each by one element which may be electronically tuned and used for specific applications as universal adaptive filter blocks. Their filter transfer can be electronically switched to required mode (LP, BP, HP, BR, AP) including trimming of their basic parameters (f_0, Q).

2. UNIVERSAL FILTER BLOCKS

Most often are in practice used circuits known as K-H-N (Kerwin-Huelsman-Newcomb — see Fig. 2) [6] and A-M (Akerberg-Mossberg — see Fig. 1) [4], or some their optimized variations [5], which enable concurrently to obtain many kinds of transfer functions of filters (LP, HP, BP, BR, AP).

Denominator $D_K(s)$ (see Eq. (1)) of mentioned K-H-N circuit from Fig. 2 can be expressed [2] as:

$$D_K(s) = s^2 + s \cdot \frac{R_{Q1}\left(R_3 R_4 + R_3 \cdot R_{ko} + R_4 \cdot R_{ko}\right)}{R_1 R_3 R_{ko} \cdot \left(R_{Q1} + R_{Q2}\right) \cdot C_1} + \frac{R_4}{R_1 R_2 C_1 C_2 R_3}, \tag{2}$$

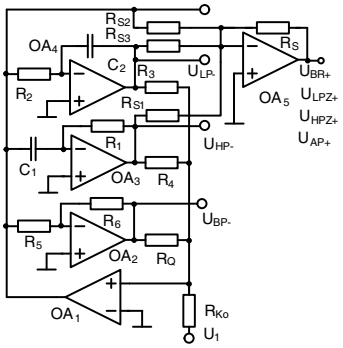

Figure 1: A-M biquad building block.

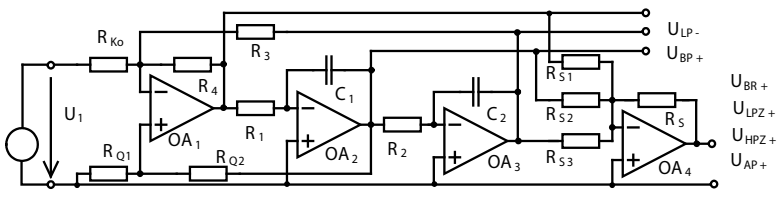

Figure 2: K-H-N biquad building.

while denominator $D_A(s)$ of A-M circuit from Fig. 1 can be written [2] as:

$$D_A(s) = s^2 + s \cdot \frac{R_4 R_6}{R_1 R_5 R_Q C_1} + \frac{R_4}{R_1 R_2 C_1 C_2 R_3}. \tag{3}$$

In the case of optimized K-H-N circuits are circuit elements chosen according equations:

$$C_1 = C_2 = C, \quad R_1 = R_2 = R, \quad R_3 = R_4 = R_A \tag{4}$$

and similarly for optimized A-M circuit:

$$C_1 = C_2 = C, \quad R_1 = R_2 = R, \quad R_3 = R_4 = R_5 = R_6 = R_A. \tag{5}$$

In this case can be derived from Eq. (2) for K-H-N circuit Q_K factor as:

$$Q_K = \frac{R_{Q1} + R_{Q2}}{R_A + 2R_{k0}} \tag{6}$$

and for A-M circuit Q_A factor is given as:

$$Q_A = \frac{R_{Q1}}{R_A}. \tag{7}$$

Other parameters of K-H-N circuit as well as A-M circuits then can be given by the same Eqs. (8)–(13), constant K in Eq. (1) is determined using ratio of resistors ($K = R_A/\mathrm{R}_{K0}$). Thus the resonant frequency f_0 can be expressed as:

$$f_0 = \frac{1}{2\pi} \cdot \frac{1}{RC}. \tag{8}$$

The nominators $N(s)$ from Eq. (1) are given for different types of filter transfers by next expressions:

$$N_{LP}(s) = \omega_0^2, \tag{9}$$

$$N_{HP}(s) = -s^2, \tag{10}$$

$$N_{BP}(s) = s\omega_0, \tag{11}$$

$$N_{BR}(s) = R_S \cdot \left(s^2 \frac{R_S}{R_{S1}} + \frac{R_S \omega_z^2}{R_{S3}} \right), \tag{12}$$

$$N_{AP}(s) = R_S. \left(s^2 \frac{1}{R_{S1}} - s\frac{\omega_0}{R_{S2}} + \frac{\omega_0^2}{R_{S3}} \right). \tag{13}$$

From comparison between Eqs. (6) and (7) determining of Q-factors of above mentioned circuits is clear, that A-M circuit exhibits advantage in trimming of Q factor. By using of A-M block can be Q-factor very easy and linear controlled. The second advantage of above presented modification of A-M circuit is in wider usable frequency range. The prescribed modification of A-M circuit [3] enable better to compensate real parameters of used active elements (real operational amplifiers OA) and then to reach approximately constant Q-factor in wider frequency range then in case of K-H-N circuit. The resulting transfer functions of both circuits by different circuit outputs have been verified using PC analysis. All simulated frequency responses have been found very closely to assumed theoretical results. Regard to conclusions in comparison of both circuit block parameters further optimizations and design of required universal adaptive filter biquad block have been realized on the base of modified A-M circuit.

3. ELECTRONIC TUNNING OF UNIVERSAL BLOCK

These above discussed universal building biquad blocks enable to fulfil many special requirements on tuning of filter parameters or adaptive switchable filter options. The principle of electronic universal block function adjustment and control of all required filter parameters is sketched in Fig. 3. Full control of filter transfer ratio, filter type and adjustment of frequency and Q-factor is realized electronically. Using MOSFET switches can be also commutated band pass output of block, similarly can be trimmed values of transfer ratio constant b_0, b_1, b_2 using blocks of programmable operational amplifiers A, B and C.

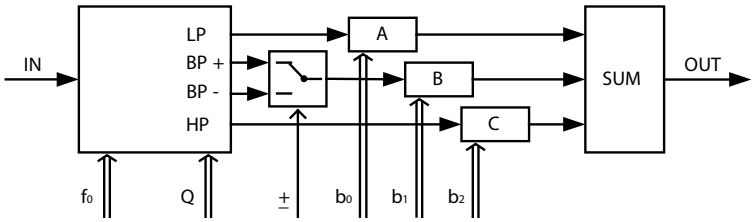

Figure 3: Block diagram of electronic control of adaptive biquad.

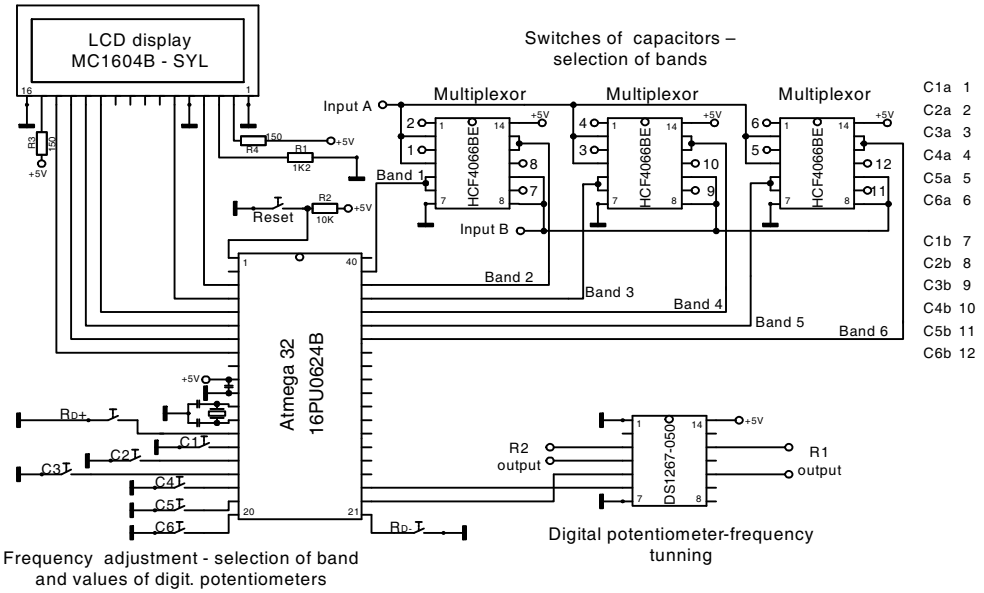

Figure 4: Main part of microprocessor control of universal adaptive filter.

To fulfil requirement of filter tuning in wide range of frequencies the adjustment of filter frequency have been divided to two steps. A main part of control circuit is drawn in Fig. 4. The filter frequency is adjusted roughly using multiplexers which by overswitched capacitors C define six frequency bands; fine frequency tuning is realized using electronically controlled digital potentiometers.

Multiplexers, digital potentiometers and next electronic control circuits are controlled by microprocessor Atmega 32. Using developed software the all required parameters of filter (filter type, frequency, Q-factor) is given using minikeybord, all included filter parameters are concurrently displayed on LCD display.

4. ARC FILTER REALIZATION

Resulting universal adaptive filter block have been realized and all required functions have been measured. Some from resulting transfer responses are presented in next figures. How we can see from transfer responses the functions of designed filter are very good and without problems in range from 10 Hz to 10 kHz. Above frequency approximately 50 kHz there are in transfer responses some imperfections due to real parameters of active elements. As main influence have been determined real parameters of OAs, which shifted frequency curves and changed resulting Q-factor in comparison to calculated values and imperfections in limited transfer function of digital potentiometers, how we can see from presented figures. As have been investigated, these imperfections can be eliminated and compensated using proper software with cooperation in microprocessor control. Then maximum usable range of frequency for required successful filter function have been reached up frequency about 100 kHz, then main limited factor have been found as limited transfer ratio of real parameters of digital potentiometers. Due this fact there are some imperfections mainly in biquad block function as HP. In BP filter function there is some limitation due a parasitic pole in transfer ratio in upper part of usable frequency range.

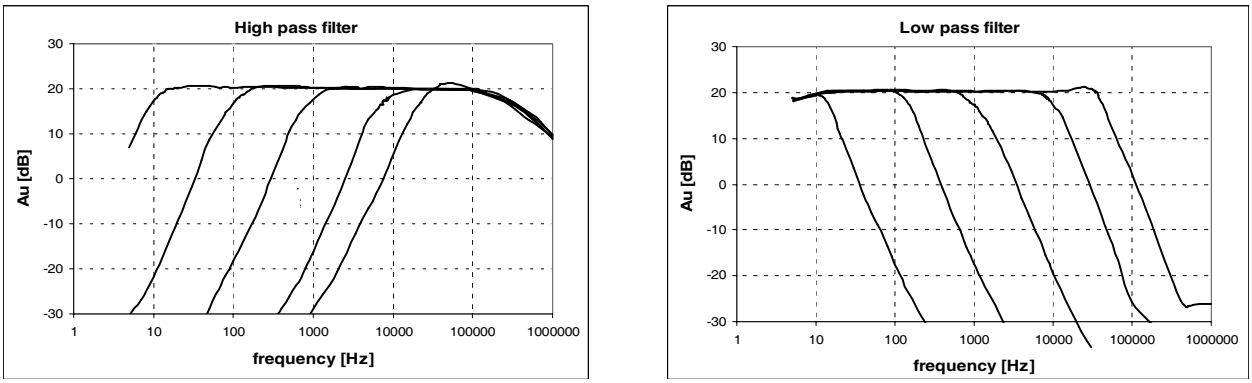

Figure 5: The transfer responses of adaptive biquad block by filter function as HP and LP.

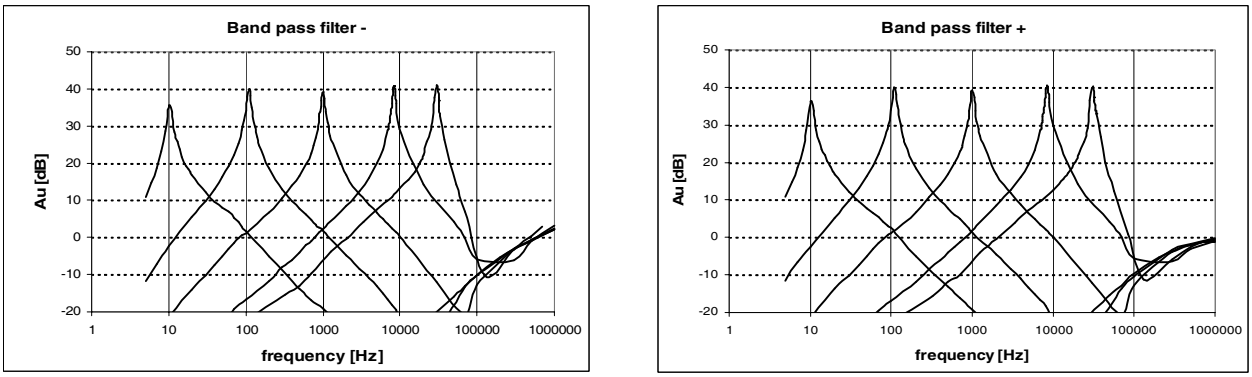

Figure 6: The transfer responses of adaptive biquad block by filter function as BP.

5. CONCLUSIONS

In the contribution here were shortly presented some possibilities and problems by universal adaptive biquad circuit design and optimization. Resulting designed universal adaptive biquad block and reached circuit parameters here have been briefly commented. An example of main parameters and frequency characteristics of optimized universal tuneable building biquad including designed microprocessor control circuit for all kinds of outputs (LP, HP, BP, AP) in wide frequency range here were also briefly prescribed. This presented universal adaptive block designed on base of modified A-M biquad circuit enable to fulfil many requirements. The wide flexibility of above mentioned adaptive biquad block allows it to be used in some special applications as electronically tuneable or adjustable filter options.

ACKNOWLEDGMENT

This work has been supported by the Research Project: MSM 0021630513 of the Czech Republic.

REFERENCES

1. Daryanani, G., *Principles of Active Network Systems and Design*, Bell Lab. Inc., USA, 1976.
2. Hájek, K. and J. Sedláček, *Kmitočové Filtry*, Vydavatelství BEN Praha, 2002.
3. Hajek, K. and J. Sedlacek, "New type of universal tnable ARC biquad filter for high frequency band," *Radioelektronika 2000*, II 22–25, Bratislava, září, 2000.
4. Akerberg, D. and K. Mossberg, "Low-sensitivity easily trimmed standard building block for active RC filters," *Electronic Letters*, Vol. 5, No. 21, 628–629, October 1969.
5. Akerberg, D. and K. Mossberg, "A versatile active RC building block with inherent compensation for the finite bandwith of the amplifier," *IEEE Trans. Circ. Systems*, CAS 21, 75–78, January 1974.
6. Kerwin, W. J., L. P. Huelsman, and R. W. Newcomb, "State-variable synthesis for insensitive integrated-circuit transfer functions," *IEEE J. of Solid-State Circuits*, Vol.2, 87–92, January 1967.

Processing of MR Slices of Temporomandibular Disc for 3D Visualization

J. Mikulka[1], **E. Gescheidtova**[1], **K. Bartusek**[2], **and Z. Smekal**[3]

[1]Deptartment of Theoretical and Experimental Electrical Engineering, Brno University of Technology
Kolejni 2906/4, Brno 612 00, Czech Republic
[2]Institute of Scientific Instruments, Academy of Sciences of the Czech Republic
Kralovopolska 147, Brno 612 64, Czech Republic
[3]Department of Telecommunications, Brno University of Technology
Purkynova 118, Brno 612 00, Czech Republic

Abstract— This article deals with a segmentation of MR images in temporomandibular joint (TMJ) area. The TMJ belongs to small but the most overloaded joint of the human body. It consists of the head of the mandible and articular fossa [1]. Between them is the mandibular disc. The mandibular disc is a cartilage for a force transmission. The physiological placement of the disc is on the top of the mandibular head. One of the frequent diseases is the disc dislocation from the physiological placement therefore there is a blocking of the mandibular head movement. In the worse case it can come to the total disc deformation [2]. The aim of this work is to obtain the most exact image or model of the mandibular disc for the right assessment of a treatment in order to minimize the invasive surgery. There was chosen an active contour method based on level set partial differential equation for the MR image segmentation [3, 4]. There was found the boundary of the mandibular disc in the noised image of low contrast with suitable parameters and initial curve without of any kind of preprocessing. The article shows our results of the segmentation of some MR slices with visible mandibular disc. These results are poised to following postprocessing which will be the 3D model of the mandibular disc creation. There are described some methods for this kind of preprocessing.

1. INTRODUCTION

The aim of this work is 3D model creation of tissues in the temporomandibular disc area (Fig. 1). It is useful for diagnosis and decision about an invasive or non-invasive medical procedure because the mandibular disc is the most frequent causation of disease of the joint. In traditional way it consists of many steps of MR image processing — preprocessing the images (noise suppression, contrast and edge enhancement), edge analysis and segmentation, segmented images processing. The goal of the proposed processing method is elimination of needful steps of processing and its simplification. The modern segmentation method was found and tested. The MR slices with visible mandibular discs were segmented by edge-based level set segmentation method. This level set approach gives very good results in segmentation of noised MR images with low contrast and smooth edges so that it is not necessary to preprocess the image before the segmentation of image. The second step will be registration of the MR images where soft tissues are visible with CT images where the hard tissues are visible. It is necessary to creation of precise 3D model.

The mentioned level set methods known as active contours are based on partial differential equation solution. There is defined the deformable model of active contour with initial shape and location in the image and by iterative solution of equation(s) the contour can change own shape, topology and location. In the steady state the active contour bounds the found objects.

2. DEFORMABLE MODELS

The edge-based segmentation is described by this energy functional [3]:

$$F(\phi) = \lambda \int_{\Omega} g\delta(\phi) |\nabla\phi| \, dxdy + \nu \int_{\Omega} gH(-\phi) \, dxdy, \tag{1}$$

where the first term means the length of the zero level curve of Φ (level set distance function) and the second term is called weighted area of Ω_{Φ}^{-}. λ, ν are the weighted coefficients of the mentioned terms, $\delta(\phi)$ is the Dirac function and H is the Heaviside function. The g function is the edge indicator defined by

$$g = \frac{1}{1 + |\nabla G_{\sigma} * I|^2}, \tag{2}$$

Figure 1: Example of one slice of the human head with focus to temporomandibular disc.

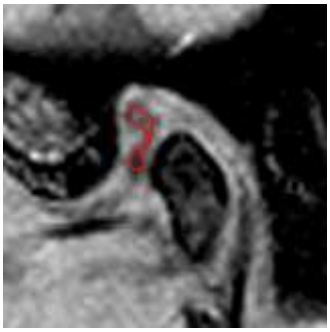

Figure 2: The example of initial shape of contour inside the mandibular disc.

where I is the original image and G_σ is the Gaussian kernel with standard deviation σ.

By calculus of variation, the first variation of the functional in (2) can be written as

$$\frac{d\phi}{dt} = \mu\left[\Delta\phi - \operatorname{div}\left(\frac{\nabla\phi}{|\nabla\phi|}\right)\right] + \lambda\delta\left(\phi\right)\operatorname{div}\left(g\frac{\nabla\phi}{|\nabla\phi|}\right) + \upsilon g\delta\left(\phi\right). \tag{3}$$

This gradient flow is the evolution equation of the level set function Φ. The second and third term in the Equation (3) correspond to the length and area energy functional. The first term penalizes the deviation of the level set function from a signed distance function during its evolution.

3. IMPLEMENTATION

The algorithm was implemented in Matlab 7.0. The Equation (3) was approximated by central and forward difference schemes and solved by iterative process. The Dirac function was approximated by:

$$\delta_\varepsilon\left(x\right) = \begin{cases} 0, & |x| > \varepsilon \\ \dfrac{1}{2\varepsilon}\left[1 + \cos\left(\dfrac{\pi x}{\varepsilon}\right)\right], & |x| \le \varepsilon \end{cases} \tag{4}$$

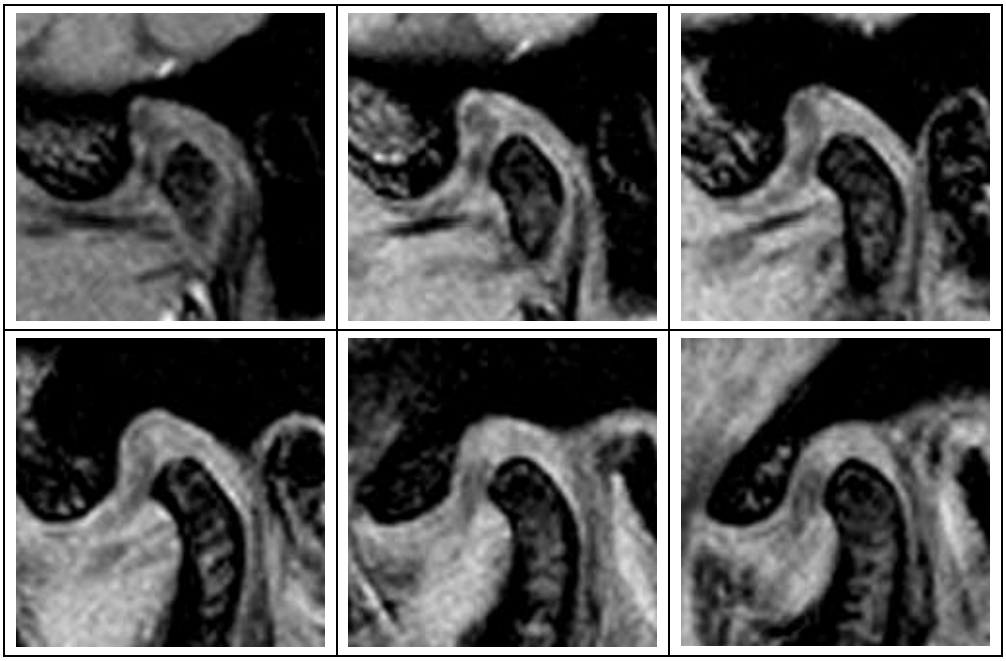

Figure 3: Six chosen original cropped slices with visible mandibular disc.

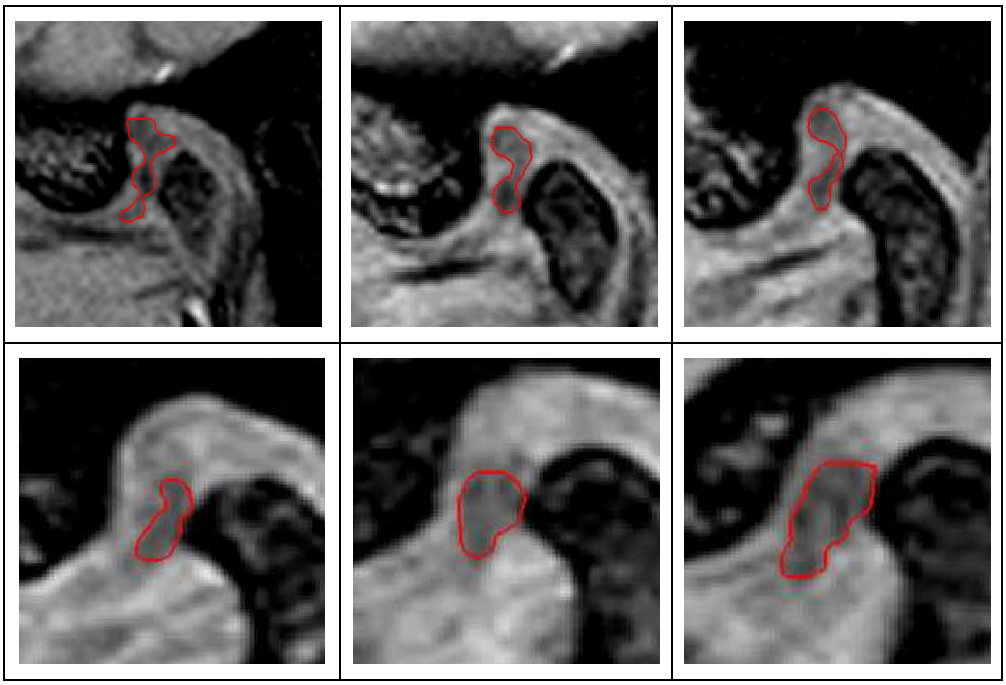

Figure 4: Segmentation results of the edge-based level set method — the red contours bound the mandibular disc.

4. SEGMENTATION RESULTS

The results of direct segmentation of images (Fig. 3) without any kind of the preprocessing are shown in the Fig. 4. The slices of the mandibular disc were segmented by the edge-based level set method with initial piecewise smooth contour inside the disc as it is shown in the Fig. 2. The segmentation process was done in about 30 seconds.

5. CONCLUSIONS

The paper presents segmentation of 3 MR slices of temporomandibular disc in one projection. There were overall 7 MR slices with visible disc and all the images were automatically successfully segmented. The future work will be creation of the 3D model of the mandibular disc and its visualization.

ACKNOWLEDGMENT

This work was supported within the framework of the research plan MSM 0021630513 and project of the Grant Agency of the Czech Republic 102/07/1086 and GA102/07/0389.

REFERENCES

1. Cihak, R., *Anatomie 1*, Grada Publishing, 2001.
2. Machon, V., *Onemocnění Čelistního Kloubu* [online], Superservis.cz, c2006 [cit. 2009-04-15], Available on WWW: ⟨http://www.webclient.cz/klouby/index.php?action=obsah&id=28⟩.
3. Li, C., C. Xu, C. Gui, and M. D. Fox, "Level set evolution without re-initialization: A new variational formulation," *Proceedings of the 2005 IEEE Computer Society Conference on Computer Vision and Pattern Recognition CVPR'05*, Vol. 1, 430–436, San Diego, USA, 2005.
4. Aubert, G. and P. Kornprobst, *Mathematical Problems in Image Processing: Partial Differential Equations and the Calculus of Variations*, 2nd Edition, 377, Springer Science Business Media, LLC, New York, 2006.

Modeling of Saturation Characteristic of an Aspiration Condenser

Z. Roubal, **M. Steinbauer**, **and Z. Szabó**
Faculty of Electrical Engineering and Communication, Brno University of Technology
Kolejní 2906/4, Brno 612 00, Czech Republic

Abstract— It was confirmed that light air ions have positive influence on human health. For its appraisal it is necessary to know the concentration of air ions and air ion mobility spectrum. This spectrum is usually found out using the saturation characteristic measurement with a gerdien tube; another design option consists in the aspiration condenser with a segmented inner electrode. The second method is faster, but the resolution of air ion mobility spectrum shows worse characteristics.. This paper deals with the mathematical analysis and numerical modeling of saturation characteristic evaluation for this aspiration condenser with a segmented inner electrode. Using a combination of both methods may increase the resolution of air ion mobility spectrum, and the progress of measurement is still better than with the gerdien tube solution.

1. INTRODUCTION

The presumption that ions contained it the air have significant influence on living organisms has been discussed in a large number of scientific papers with a focus on the problem of concrete effects of ions on bacteria, animals, and humans [1–3]. Light and negative ions feature positive effects on the human organism, whereas their heavy and positive counterparts bring about negative impact. It was shown by N. I. Goldshtein [3] that the complete absence of negative air ions in the inhaled air is fatal to animals. Any evaluation of air ions and their impact on the human organism is only made possible after and on the basis of air ions concentration measurement and air ions spectrum mobility. One of its methods is based on measurement using the aspiration capacitor. In a simple aspiration condenser — gerdien tube the internal electrode is not divided into several segments. This method will be modeled saturation characteristics for the natural spectrum of negative air ions measured in [4]. Here, the disadvantage consists in considerable time consumption inherent with the measurement of air ions spectrum. However, if an aspiration condenser with a segmented inner electrode is applied, the pace of measurement can be substantially accelerated. We will obtain an estimation of the air ions spectrum in the given interval, whose accuracy can be further advanced by measurement at several voltages. For the purpose, saturation characteristics will be modeled again of individual segments of the aspiration condenser inner electrode.

2. THE ASPIRATION METHOD PRINCIPLE

The basic principle of the aspiration method is shown in Fig. 1 on an elementary aspiration condenser — gerdien tube; the principle (model) was taken over from [1] and [5]. Here, it holds that d_1 — inner electrode diameter, d_2 — outer electrode diameter, L — length of gerdien tube, v_x — air flow velocity, "+" — positive air particle (ion), "−" — negative air particle (ion). The gerdien tube consists of two electrodes. There is an electric field between the inner electrode (the collector) and the outer electrode. The field is imposed by voltage source U. The air mass with ions is actuated by a fan through the gerdien tube. Negative ions in the electric field impact the collector, and the current produced is measured by an electrometer. The measured current is proportional to air ion concentration [2]. By means of the change of polarity it is also possible to measure positive air ions.

An important parameter of the aspiration condenser is the air flow volume rate M defined as

$$M = \left(r_2^2 - r_1^2\right) \cdot \pi \cdot v_x. \tag{1}$$

In [7], the equation of motion was derived for a ion entered to gerdien tube with a segmented inner electrode for initial point $A[0, y_0]$.

$$y^2 = -2 \cdot x \cdot k \cdot \frac{U}{v_x \cdot \ln\left(\frac{r_2}{r_1}\right)} + y_0^2. \tag{2}$$

It is possible to establish by the help of this equation whether a given ion will impinge upon the internal collecting electrode and whether, thus, it will share in the current passing through

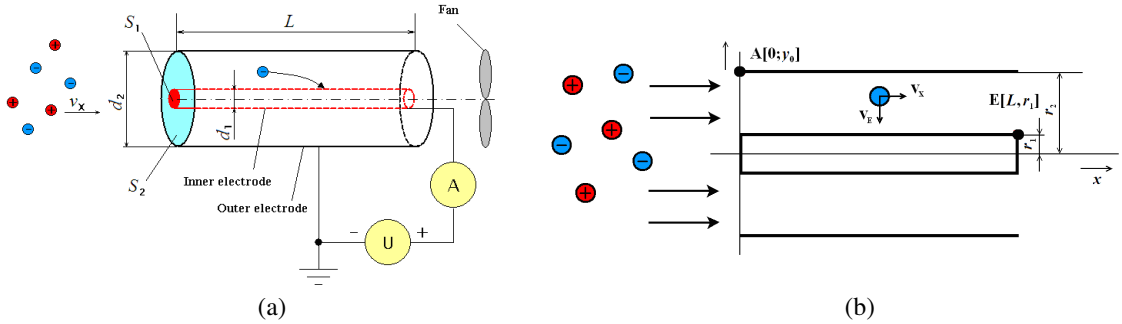

(a) (b)

Figure 1: (a) An elementary aspiration condenser. (b) The coordinates for boundary mobility determination.

the aspiration condenser. If we need to determine the current induced by ions entering the gerdien tube, it is advantageous for us to define k_m. From coordinates $A[0; y_0]$ and $E[L; r_1]$ it can be derived that

$$k_m = \frac{\varepsilon_0 \cdot \varepsilon_r \cdot M}{C \cdot U}. \tag{3}$$

All ions with a mobility higher than k_m will impinge upon the inner electrode. From the group of ions with $k < k_m$ only a proportionate part will impinge upon the inner electrode. Applying the cylindrical condensers volume ratios, we can establish

$$I_{k<k_m} = \frac{k}{k_m} n \cdot q \cdot M, \tag{4}$$

$$I_{k\geq k_m} = n \cdot q \cdot M. \tag{5}$$

Let us assume a continuous spectrum. The current, then, will be determined by the sum of ions with a given mobility; for ions with $k < k_m$ there will hold Equation (4), for ions with $k \geq k_m$ will hold (5). It is good to start with the charge concentration density [8]. Then there holds

$$I = M \cdot \frac{1}{k_m} \int_0^{k_m} k \cdot \rho\,(k) \cdot dk \; + M \cdot \int_{k_m}^{\infty} \rho\,(k) \cdot dk. \tag{6}$$

And after substituting for the boundary mobility

$$I = \frac{C \cdot U}{\varepsilon_0} \int_0^{k_m} k \cdot \rho\,(k) \cdot dk \; + M \cdot \int_{k_m}^{\infty} \rho\,(k) \cdot dk\;. \tag{7}$$

It is advantageous [2] to express the characteristics of the aspiration condenser by the help of function G. Equation (7) can be modified to the form

$$I = \int_0^{\infty} G(k) \cdot \rho\,(k) \cdot dk, \tag{8}$$

for the gerdien tube, function G is given

$$G = \begin{cases} \dfrac{C \cdot U \cdot k}{\varepsilon_0} & k < k_m \\ M & k \geq k_m \end{cases} \tag{9}$$

3. MODELING OF THE GERDIEN TUBE SATURATION CHARACTERISTICS

For the new gerdien tube type (Fig. 10) designed at the Department of Theoretical and Experimental Electrical Engineering, Brno University of Technology, the ratio was described in Fig. 2 of function G to air flow volume rate M directly from the motion Equation (2) for the polarization

voltage of 25 V. Fig. 3, then, shows the Matlab-modeled saturation characteristics with a natural concentration of negative ions in the laboratory.

For the spectrum determination, the saturation characteristics must be measured in the point-to-point mode; after that, it is possible to determine the spectrum of air ions from the constructed tangent lines. The first derivation, however, highlights the fluctuations and noises. A detailed description of the method can be found in [1, 2, 5, 7].

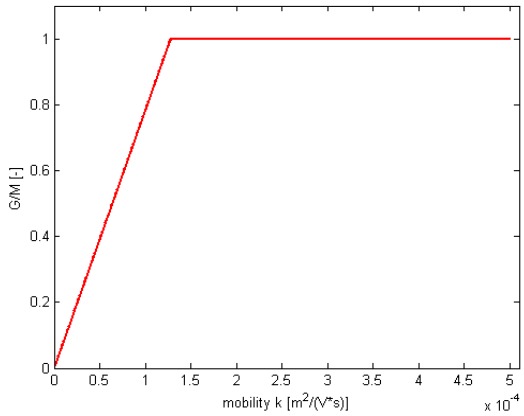

Figure 2: The ratio of function G to air flow volume rate M.

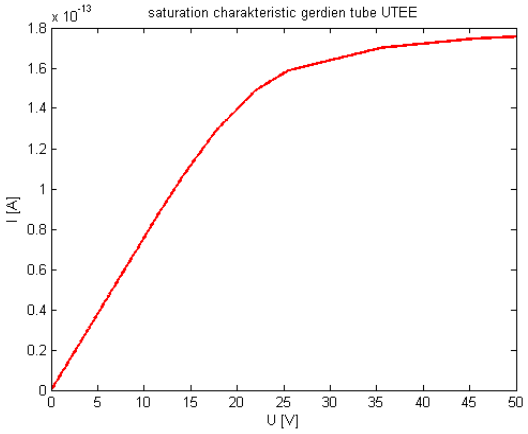

Figure 3: The saturation characteristics with a natural concentration of negative ions in the laboratory.

4. SATURATION CHARACTERISTICS MODELING FOR AN ASPIRATION CONDENSER WITH A SEGMENTED INNER ELECTRODE

For the motion equation pertaining to the aspiration condenser with a segmented inner electrode there holds Equation (2). With that said, it should also be noted that it is necessary to establish a new initiatory distance y_0 for each segment. The measuring connection of electrometers and polarization voltage for an aspiration condenser with four segments of the inner electrode (currently under development at the DTEE) is described in Fig. 4.

The G_i functions for the individual segments are modeled (for the voltages of 12 V and 25 V) in Figs. 5 and 6. Function G_1 of the first segment is highlighted in red, while for the second segment it is depicted in green, for the third in blue, and for the fourth in black.

As is obvious from images 5 and 6, direct establishment of the spectrum from G_i functions is inconvenient because all G_i functions interlap markedly and are permeable for heavy ions too. The solution to the problem consists in measuring the currents that pass through the individual segmented electrodes at two voltages and deducting these currents suitably from one another. In [7] there are introduced relations necessary for the spectrum estimation. Fig. 7 describes the acquired function G for a small voltage ratio $a = U_2/U_1$; Fig. 8 represents function G for a large ratio a. Even though the spectrum determination from Fig. 7 appears to be more favorable thanks to a lesser degree of interlapping of G functions, the measurement shows a considerable error owing to

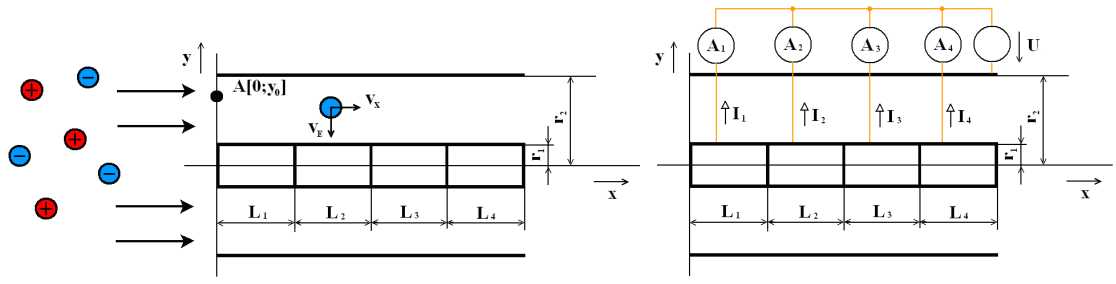

Figure 4: The trajectory of air ions in the gerdien tube is shown on the left, whereas the measurement of individual segment currents of the inner electrode and the applied polarization voltage are shown on the right.

small differences in currents I_1 and I_2. In Fig. 8, the estimation of air ions mobility spectrum is encumbered with the error of interlapping of functions G that have passed from the trapezoidal to the triangular shape.

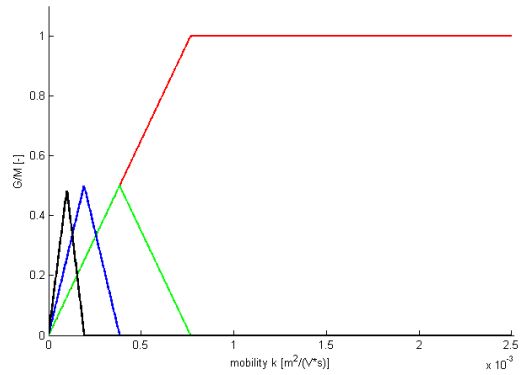

Figure 5: Function G_i for individual segments of the inner electrode and polarization voltage of 25 V.

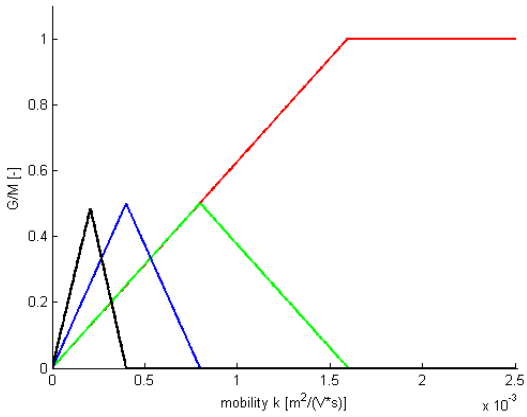

Figure 6: Function G_i for individual segments of the inner electrode and polarization voltage of 12 V.

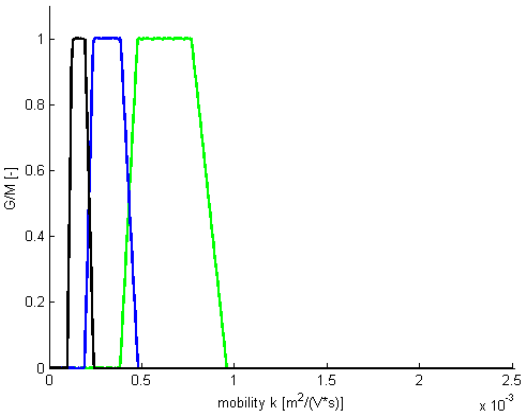

Figure 7: The deduction of functions G_i for $U_1 = 20$ V and $U_2 = 25$ V.

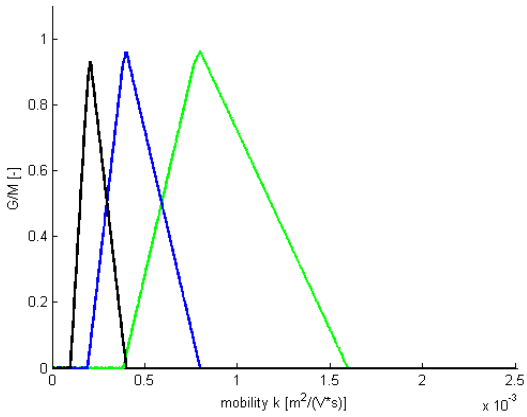

Figure 8: The deduction of functions G_i for pro $U_1 = 12$ V and $U_2 = 25$ V.

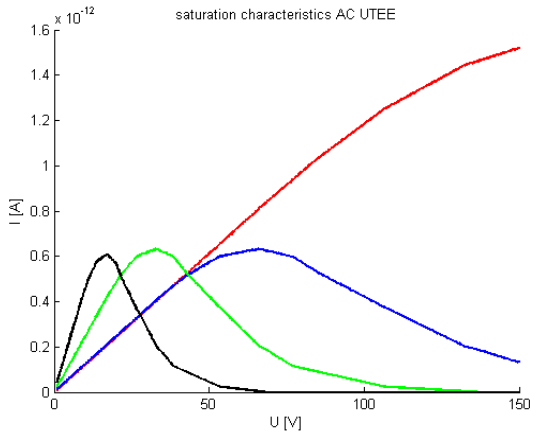

Figure 9: Saturation characteristics of the aspiration condenser with a segmented inner electrode.

Figure 10: The new gerdien tube designed at the Department of Theoretical and Experimental Electrical Engineering, Brno University of Technology.

Here, however, the error caused by the deduction of currents is lower.

For the optimal ratio of voltage it is appropriate to start from the saturation characteristics modeling for all segments of the inner electrode. In Fig. 9, the saturation characteristics were described for the natural concentration of ions in the laboratory as measured in [5].

5. CONCLUSION

The problem of suitable selection of the voltage ratio as well as of the absolute magnitude pertaining to U_1 and U_2 is dependent on the type of ions assumed in the measured environment. For this reason it is advantageous to establish, by means of modeling the saturation characteristics of the related aspiration condenser with a segmented inner electrode, the optimum working area in such a way that the measured currents are not too small and their variance for the given voltages is sufficient. Through repeated measurement for other pairs of voltage, the estimation of the air ion mobility spectrum can be gradually made more accurate.

ACKNOWLEDGMENT

The research described in the paper was financially supported research plans MSM 0021630513 and MSM 0021630516 of the Ministry of Education, Youth and Sports of the Czech Republic.

REFERENCES

1. Charry, J. M. and R. Kavet, *Air Ions: Physical and Biological Aspects*, CRC Press, Inc., Boca Raton, Florida, 1987.
2. Steinbauer, M., P. Fiala, K. Bartušek, and Z. Szabó, "Experiments with accuracy of air ion field measurement," *PIERS Proceedings*, 1062–1066, Hangzhou, China, March 24–28, 2008.
3. Goldstein, N. I. and T. V. Arshavskaya, "Is atmospheric superoxide vitally necessary?," *Z. Naturforsch*, Vol. 52, No. 5–6, 396–404, May–June 1997.
4. Bartušek, K., "Měření spektrálních charakteristik iontových polí," 2001, http://www.elektrorevue.cz/clanky/01038/index.html.
5. Vojtek, T., T. Skoupil, P. Fiala, and K. Bartušek, "Accuracy of air ion field measurement," *PIERS Online*, Vol. 2, No. 4, 412–415, 2006.
6. Roubal, Z., M. Steinbauer, Z. Szabó, and R. Kubásek, "Real-time measurement of air ion spectrum using gerdien tube with segmented inner electrode," *PIERS Proceedings*, 1744–1748, Moscow, Russia, August 18–21, 2009.
7. Tammet, H. F., *The Aspiration Method for Determination of Atmospheric-ion Spectra*, IPST, Jerusalem, 1970.

Integrated Programming and Application of Genetic Algorithm and Conjugate Gradient Method

Wei Xie and Jian-Xin Liu
School of Info-physics and Geomatics Engineering, Central South University
Changsha 410083, China

Abstract— The power of dealing with matrix operations in MATLAB write this paper, the procedure of hybrid genetic algorithm has great advantages. Because of the characteristics: partly depending the primary estimation and having the global convergence, it can be used to solve different complex applications, such as the optimal design of projects, artificial intelligence,strategic system, geo-physical inversion and so on. Although the genetic algorithm is an efficient global-optimization method, from the simulation results the defaults of time-consuming and vain local-researching ability can be detected. But the conjugate gradient algorithm belongs to a non-heuristic global-optimization search method, with the characteristics of swift convergence, easily dumping into local extreme value and severely depending on the primary estimation. This essay adopts a hybrid genetic algorithm of geo-physical inversion, according to the properties of the genetic algorithm and the conjugate gradient algorithm. The method has the attributes of the global-convergence of the genetic algorithm and the swift convergence of the conjugate gradient. Finally in accordance with procedures to test simulation algorithm and analysis with examples to prove that the procedure has good practicability.

1. THE BASIC THEORY

The 20th century, the early 90s, in order to allow the computer to automatically carry out programming, J. R. Koza basic idea of using genetic algorithms is proposed genetic programming (genetic programming) concept [2].

MATLAB is a Mathwork company's products, is a powerful mathematical software, numerical calculation of its excellent ability to make it in the industrial sector and the academic usage is very high. The use of MATLAB matrix operations dealing with the power to write this paper, hybrid genetic algorithm program has a huge advantage. Genetic algorithm and other optimization algorithms compared to a lot of features. Generic coding of genetic algorithm technology and a simple and effective genetic manipulation of its wide range of applications and laid the foundation for success.

2. HYBRID GENETIC ALGORITHM DESIGN

Hybrid genetic algorithm designed by the idea as follows: for each generation, groups, repeated the following: (1) for the genetic operations (selection, crossover and mutation) to generate intermediate group; (2), according to a certain group in the middle of the probability of selecting individuals to conduct some conjugate gradient method search, the newly generated individual is not selected for genetic manipulation and search of individuals to form a new population. These two operations repeatedly until the stop criterion to meet up.

3. PROGRAM DESIGN

3.1. Encoding and Initial Population is Generated

```
function [pop] = initialize(num, bounds, evalFN)

    estr=['[ pop(i,:) pop(i,xZomeLength)]=' evalFN '(pop(i,:));'];
    numVars= size(bounds,1);
    rng= (bounds(:,2)-bounds(:,1))';
    xZomeLength = numVars+1;
    pop= zeros(num,xZomeLength);
    pop(:,1:numVars)=(ones(num,1)*rng).*(rand(num,numVars))+(ones(num,1)*
    bounds(:,1)');
    for i=1:num
    [pop(i,:) pop(i,xZomeLength)]=feval(evalFN,(pop(i,:))
```

```
end
Parameter Description:
```

p1: first a parent on behalf of the individual
p2: The second parent individual

3.2. Mutation Operation

```
function parent=mutation(parent,bounds,gen)

    df = bounds(:,2) - bounds(:,1);
    numVar = size(parent,2)-1;
    mPoint = round(rand * (numVar-1)) + 1;
    md = round(rand);
    if md
      newValue=parent(mPoint)+delta(cg,mg,bounds(mPoint,2)-parent(mPoint),b);
    else
      newValue=parent(mPoint)-delta(cg,mg,parent(mPoint)-bounds(mPoint,1),b);
    end
    parent(mPoint) = newValue;
```

3.3. Conjugate Gradient Operation

```
c(1:numVar)=fminsearch(FN,endPop(a,(1:numVar)));

    for i=1:numVar
      if c(i)<bounds(i,1)
        c(i)=bounds(i,1);
      elseif c(i)>bounds(i,2)
          c(i)=bounds(i,2);
        end
    end
    [c c(xZomeLength)] = feval(evalFN,c3);
    endPop(a,:)=c;
```

4. ALGORITHM TESTING AND TEST SIMULATION

In order to verify the validity of the algorithm proposed in this paper, special choice of a representative of the more complex test functions for testing.

F2: Shubert [4] $(-10 < x_1, x_2 < 10)$

$$\begin{aligned}
\min F(x) &= -\sum_{j=1}^{5} j[\sin((j+1)x_1 + j) + \sin((j+1)x_2 + j)] \\
F_{\min} &= -24.062499, \text{ 400local minima, 9 gloal minima} \\
x_{\min} &= \left\{ \begin{bmatrix} a \\ a \end{bmatrix}, \begin{bmatrix} a \\ b \end{bmatrix}, \begin{bmatrix} a \\ c \end{bmatrix}, \begin{bmatrix} b \\ a \end{bmatrix}, \begin{bmatrix} b \\ b \end{bmatrix}, \begin{bmatrix} b \\ c \end{bmatrix}, \begin{bmatrix} c \\ a \end{bmatrix}, \begin{bmatrix} c \\ b \end{bmatrix}, \begin{bmatrix} c \\ c \end{bmatrix} \right\} \\
a &= -6.774576,\ b = -0.491391,\ c = 5.791794
\end{aligned}$$

Function graph is as follows.

Using the proposed hybrid genetic algorithm to calculate the test function, taking $m = 100, 0.2$, $0.01, = 0.05$, $T = 100$, the calculation results in Table: The optimal value of the function extreme point iterations

Numerical experiments show that the proposed hybrid genetic algorithm can effectively function, the global optimal solution obtained, the algorithm is a feasible method of global optimization.

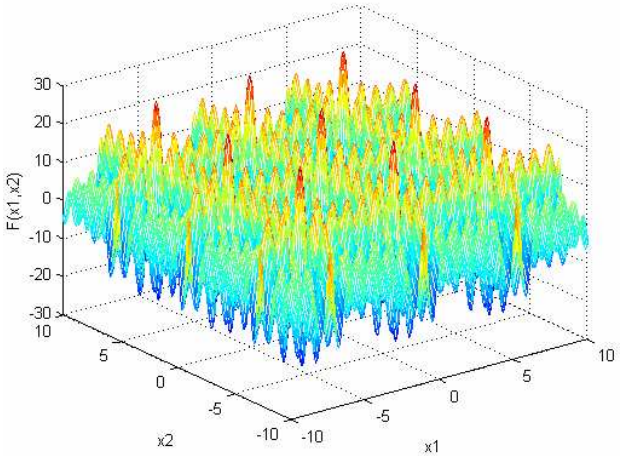

function	Extreme point	optimum	number of iterations
F2	(5.79180,5.79180)	24.06248	13
	(5.79180, −0.49139)		
	(5.79180, −6.77457)		
	(-0.491395.79180)		
	(−0.49139, −0.49139)		
	(−0.49139, −6.77457)		
	(−6.77457, 5.79180)		
	(−6.77457, −0.49139)		
	(−6.77457, −6.77457)		

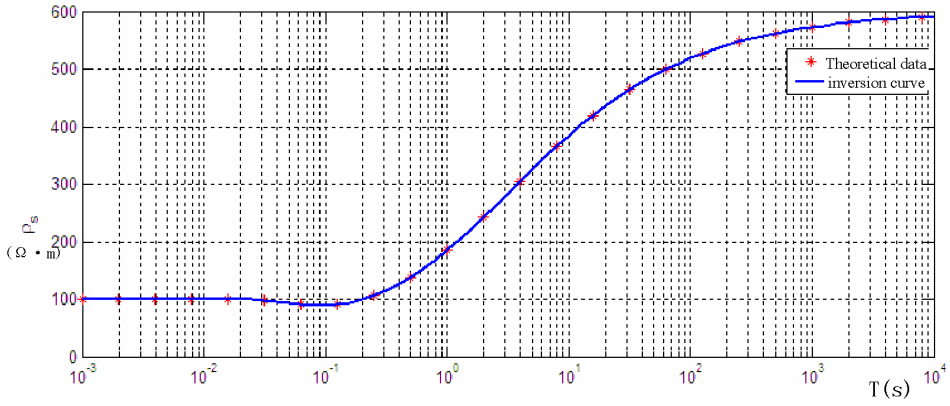

Figure 1. MT measured data and inversion results.

5. APPLICATION EXAMPLES

In March 2006, the author carried out a certain place in Hubei magnetotelluric sounding studies, using the instruments for the V5-2000. As our predecessors have done logging in this work, that the formation is divided into five levels: from top to bottom order of: $h_1 = 100\,\text{m}$, $h_2 = 1400\,\text{m}$, $h_3 = 3580\,\text{m}$, $h_4 = 3591.5\,\text{m}$. In this paper, hybrid genetic algorithm to obtain the inversion of MT data, and the results shown in Figure 1:

Icons can be seen from the above, hybrid genetic algorithm and logging data fit better, just a kilometer after the relatively large error in 1:00, which is totally acceptable, and shows this hybrid genetic algorithm is a line of of effective algorithms.

6. CONCLUSION

The general application of non-linear geophysical inversion inversion algorithm, is a continuous optimization process. In this process, to make theoretical model and inverse model fit as much as possible. Nonlinear inverse algorithms, including heuristic inversion method and non-heuristic inversion method.

This idea is to combine these two advantages and disadvantages of anti-algorithm, genetic algorithms and conjugate gradient method to carry out a comprehensive program of one-dimensional inversion of geophysical and achieved good results. Finally, according to a pilot simulation algorithm program in conjunction with case analysis, certification procedures and has good practicability.

REFERENCES

1. Aarts, E. H. L. and P. J. M. Van Laarhoven, *Simulated Annealing: Theory and Application*, D Reidel Publisheng Company, Dordrecht, 1987.
2. Lundy, M. and A. Mess, "Convergence of an annealing algorithm," *Math Programming*, Vol. 34, 111–124, 1986.
3. Schwefel, H. P., *Numerical Optimization of Computer Models*, John Wiley, Chichester, UK, 1981.
4. Goldberg, D. E., *Genetic Algorithms in Search, Optimization and Machine Learning*, Addison Wesley, Reading, MA, 1989.
5. Holland, J. H., *Adaptation in Natural and Artificial Systems*, The University of Michigan Press, MIT Pressm, 1975.

Student Projects of Extended Study in Introductory Electromagnetics

Y. Du, X. M. Zhang, S. L. Zheng, X. F. Ye, and K. S. Chen
The Department of Information Science and Electronic Engineering
Zhejiang University, Hangzhou 310027, China

Abstract— It is well recognized that Electromagnetics is one of the most important disciplines yet is also a difficult subject for undergraduate students to grasp. In the literature it has been advocated to incorporate real-world examples of applications to help improve student learning. In this work, we propose an approach that is complementary to the real-world examples one. In our approach, we encourage the students to extend the material from what has been covered in the class through participation in individual project. Positive results are obtained in terms of comprehension of the material, improvement of mathematical skills, as well as buildup of confidence in the participants.

Electromagnetics is one of the most important bases of our modern life, upon which lay the life style enhancing technologies such as communication, RFID, wireless sensor network, antenna, and other electronic systems. Understanding the principles of Electromagnetics is thus required for undergraduate students majoring in Electrical Engineering to prepare them for a smooth and successful career. However, since electromagnetics is a strongly mathematical subject, it is often the case for a student to find it very difficult to apply advanced mathematical techniques while maintaining a physical comprehension [1–5]. In the literature it is observed that incorporating real-world examples of applications serves to improve student learning and to bring a colorful course material presentation. This is undoubtedly an effective way of teaching electromagnetics. However, there might also be some limitations of this approach: The chosen real-world examples may have to be simple and the applicable principles from electromagnetics may be restricted considering the limited knowledge span and mathematical skills of the average student. For instance, the real world examples taken from one study were almost associated with electrostatics or magnetostatics. The very nature of electromagnetics, that is, time varying aspect, is unwantedly de-focused in this approach. In this work, we propose an approach that is complementary to the real-world examples one. In our approach, we encourage the students to extend the material from what has been covered in the class. For instance, after learning the reflection and transmission of a plane wave at the interface of two homogeneous media in the conventional setting, the students may proceed to work out with the help of the instructors the reflection and transmission phenomena when one of the media is anistropic. In this way, the comprehension of the material, the employment or even improvement of mathematical skills can be greatly boosted, which will in turn help build up the confidence and further curiosity of the students.

The proposed extended study is not introduced as a mandatory part of the fundamental EM course; rather, it is based on voluntary participation. To maximize the participation among the students who are taking the EM class, we decide to provide the students with incentives to participate. Specifically, based on historical grades distribution of the EM class, the incentive for participation is set to some additional points within the range of one to six on a 100 scale. To minimize the confusion among the participants, they are instructed that either of three types is legitimate project: theoretical analysis, application oriented, and visualization generation. Yet for the first two categories, the content of the project can not be readily available from either the textbook or some other reference books. Rather, participants who choose these two categories need to work out something of their own: to fill in the details that are omitted in either the analytical material or the connection between EM theory and the specific application at hand. With that in mind, the participants are provided by a limited number of project topics which they can choose, yet the majority of topics is to be identified by the participants. For the current study, each project is treated as an individual one, while interaction with each other and solicitation of assistance from the instructor are still highly encouraged. The project delivery package includes an oral presentation which lasts about 10 minutes plus some question and answer session, a written report, and source code (optional for those whose projects have involved some kind of numerical simulations or computer visualization). The performance is evaluated based on a number of factors including originality, thoroughness of comprehension, scope, and presentation (both oral and written).

Out of 210 undergraduate students who take the EM course (split among four small class sessions), 37 students participate, resulting in a participation ratio of around 15%. The topics covers all three types of permissible projects, with a surprisingly wide range of interests considering

Table 1: Exemplary project topics.

Wireless transmission of electricity
Introduction to FDTD and its simulation of TE101
Electromagnetic wave propagation in plasma
Dispersion of Polarization Mode
RFID technology
RF identification
Study of Electromagnetic cloking
Electromagnetic black holes
Antenna technology in UWB wireless communications
Smart antennas
Reflection and refraction at the interface of left- and right- handed materials
Negative refraction index material
Detection of surface stress using polarization interference
Determination of the dispersion of rectangular dielectric waveguide via EDC method
One dimensional optical crystal transmission line based on characteristic matrix method
Principle of wireless detection of direction of arrival
Analysis of the directional coupler
Synthesis filter design of cascaded couplers
Animation of electromagnetic fields in a rectangular resonator
Static and dynamic analysis of TE modes in a rectangular waveguide
3D visualization of surface currents of circular waveguide
Numerical analysis of scattering from a cylinder with arbitrary cross section
Skin depth effect of metals
Application of genetic algorithm to design of antenna array
Discussion of ways of hole opening in an elevator for unblocked cellular communication

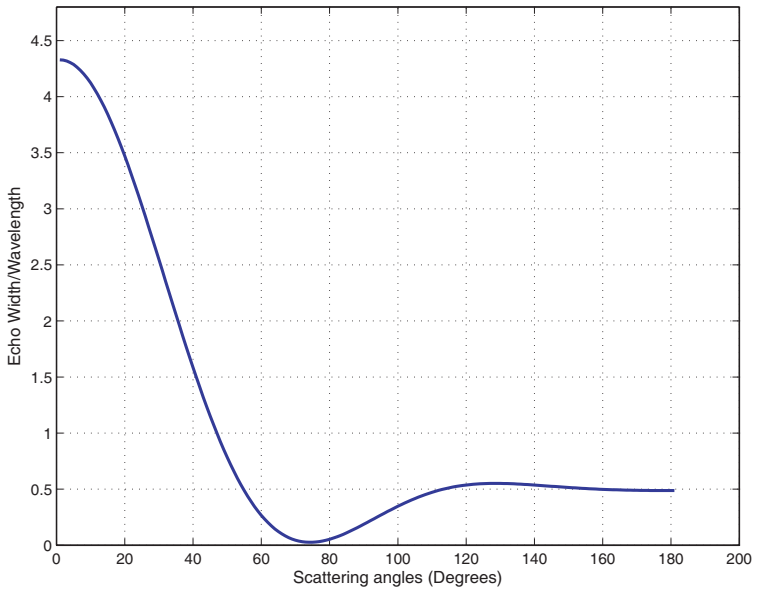

Figure 1: Scattering pattern of a circular dielectric cylindrical shell with plane-wave incident.

their limited *a priori* knowledge of EM theory. The topics are exemplified in Table 1.

Next we highlight some of the projects. The first one concerns numerical analysis of scattering from a cylinder with arbitrary cross section. The participant is expected to learn the concepts such as integral equation, method of moment, boundary conditions, scattering cross section or scattering width. The learning material is taken from one technical paper in IEEE Transactions on Antennas and Propagation [6]. Fig. 1 illustrates scattering pattern of a circular dielectric cylindrical shell with plane-wave incident with parameters chosen identical to that of Fig. 4 in [6]. Very good agreement is obtained, which speaks of good comprehension of the material and implementation of the method of moment. The second project is an analysis of the microstrip directional coupler, where all the details have been dutifully worked out. Numerical illustrations are also provided (See Fig. 2 as one example). The third one is to provide a visualization package of fields distribution of the rectangular waveguide, in accordance with the increasing recognition of the significance of visualization in scientific and engineering learning [7]. Fig. 3 illustrates a 3D visualization of the z

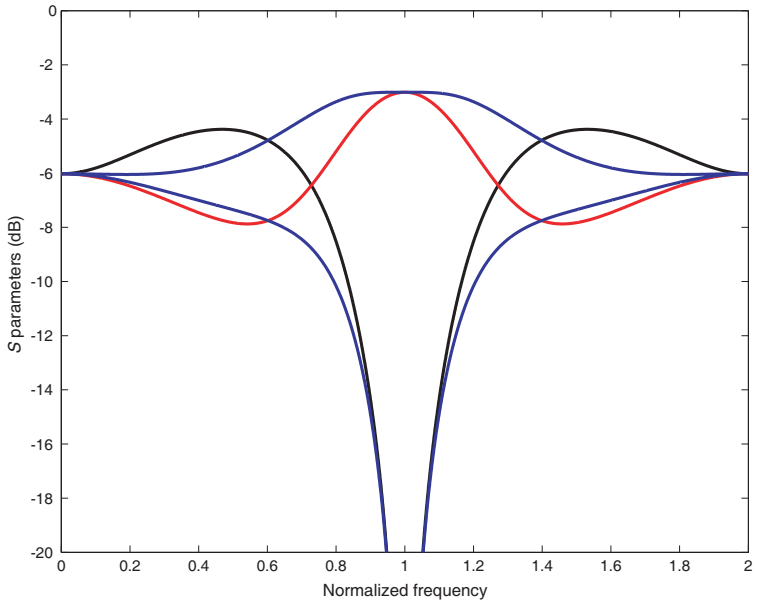

Figure 2: Frequency response of the 3 dB directional coupler.

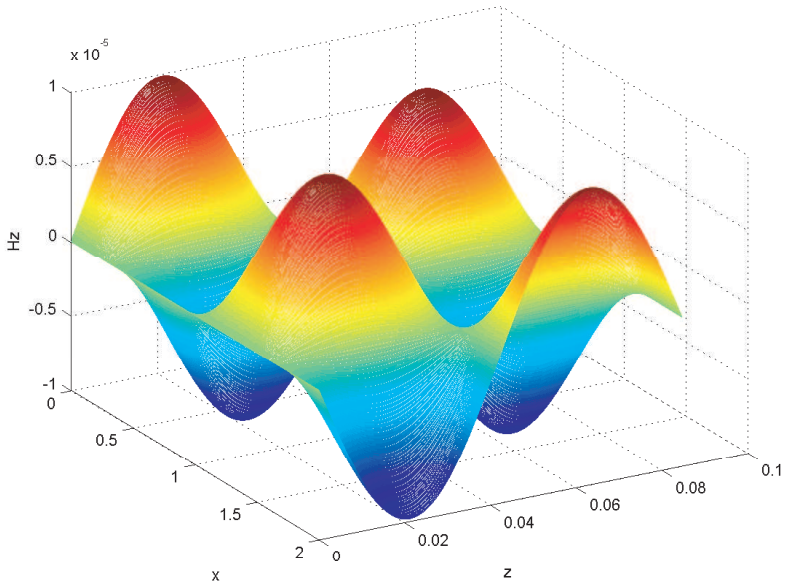

Figure 3: 3D visualization of the z component of the magnetic field in a rectangular waveguide.

component of the magnetic field in a rectangular waveguide.

In summary, in the current study to facilitate the teaching of electromagnetic theory to undergraduate students in their sophomore or junior years, we proposed a student project based approach. In this approach students are given the opportunity to do projects closely related to electromagnetic theory. Their participation is voluntary yet they are told up front that there is reward for those who choose to participate and who has done it well. The form of reward is tentatively set to be some additional points to their final grades (within the range of one to six on a 100 scale). Yet we observe that although most participants are attracted by the additional credits at the beginning, their curiosity and satisfaction with the enhanced understanding of the electromagnetic theory and with the realization of the wide spectrum of fields to which the theory can be readily applied gradually substitute as the true motivations for going along with the project. The wide range of project topics as exemplified in Table 1 also testifies to the breadth and depth of the students, with a encouraging mix of purely theoretical analysis to real-world applications. This very fact also strongly implies the unnecessity of the instructor to attempt to limit the scope of the projects within a preset limited range.

REFERENCES

1. Cheng, K. W. E., X. D. Xue, K. F. Kwok, and T. K. Cheung, "Improvement of classroom teaching of electromagnetics by means of an electronic book," *IEEE Trans. Magn.*, Vol. 39, 1570–1573, 2003.
2. Lowther, D. A. and E. M. Freeman, "A new approach to using simlation software in the electromagnetics curriculum," *IEEE Trans. Education*, Vol. 36, No. 2, 219–222, 1993.
3. Sadiku, M. N. O., "Problems faced by undergraduates studying electromagnetics," *IEEE Trans. Educaton*, Vol. 29, No. 1, 31–32, 1986.
4. Beker, B., D. W. Bailey, and G. J. Cokkimdes, "An application-enhanced approach to introductory electromagnetics," *IEEE Trans. Education*, Vol. 41, No. 4, 31–36, 1998.
5. Iskander, M., "Technology-based electromagnetic education," *IEEE Trans. Microwave Theory Tech.*, Vol. 50, No. 3, 1015–1020, 2002.
6. Richmond, J. H., "Scattering by a dielectric cylinder of arbitrary cross section shape," *IEEE Trans. Antennas. Propag.*, Vol. 13, 334–341, 1965.
7. De Magistris, M., "A MATLAB-based virtual laboratory for teaching introductory quasi-stationary electromagnetics," *IEEE Trans. Educaton*, Vol. 48, No. 1, 81–88, 2005.

Discussion on Teaching Electromagnetic Field and Wave Course

Xianfeng Ye, **Xianmin Zhang**, **Shilie Zheng**, **and Yang Du**
Department of Information and Electronics Engineering
Zhejiang University, Hangzhou 310027, China

Abstract— We have already launched certain teaching reform that we combined the course Theory of Electromagnetic Field (including the antenna) and the course Microwave and Optical Guided Wave Technology into a single course, Electromagnetic Fields and Electromagnetic Wave. Although the depth and coverage of the course has increased, the course hours have been compressed. This requires teachers to make greater efforts and take more effective measures. So we have focused on three aspects of EM teaching. We have seized the keys of vector field theory to clear students' obstacles about mathematics, made students to understand the rigorous logic system of electromagnetic theory which deeply enhances the students' sense of innovation, and combined the theories with practical applications to improve their capabilities of applying knowledge and solving engineering problems.

1. INTRODUCTION

The course Theory of Electromagnetic Field and Wave is one of the most important technical foundation courses in electronic engineering. With the recent great advances in electronics and information technology, particularly in the internet technology as the representative of the network and communication technologies, the course teaching methodology should keep pace with them. We have already launched certain teaching reform that we combined the course Theory of Electromagnetic Field (including the antenna) and the course Microwave and Optical Guided Wave Technology into a single course, Electromagnetic Fields and Electromagnetic Wave. Although the depth and coverage of the course has increased, the course hours have been compressed. This requires teachers to make greater efforts and take more effective measures. First, we strengthen the foundations of mathematics and seize the heart of vector and field theory. Second, we have analyzed electromagnetic theory systematically and rigorously to cultivate innovative thinking ability of students. Finally, we introduce electromagnetic theory by combining it with practice applications.

2. STRENGTHENING FOUNDATIONS OF MATHEMATICS

This course is abstract and difficult for students to understand, mainly because students can not combine mathematical tools with the physical concepts. It is necessary to clear mathematical obstacles. The main mathematical tool of the course is the vector and field theory. For a vector field, divergence and curl are core concepts. The vector dot product and cross product have a wonderful correspondence with them.

Hamilton operator ∇ has a double feature with a vector and operator. It is an operator and also a vector, but it is different with the vector.

For example, from the perspective of vectors: Dot product can be exchanged.

$$\mathbf{A} \cdot \mathbf{B} = \mathbf{B} \cdot \mathbf{A}$$

However, as an operator, operator and field dot product can not be exchanged, that is,

$$\mathbf{A} \cdot \nabla \neq \nabla \cdot \mathbf{A}$$

Similarly, the cross product of two vectors can be counter-exchanged, that is,

$$\mathbf{A} \times \mathbf{B} = -\mathbf{B} \times \mathbf{A}$$

However, as an operator, the cross product with field can not be counter-exchanged, that is,

$$\mathbf{A} \times \nabla \neq -\nabla \times \mathbf{A}$$

When the ∇ as an operator acts on the field, it is just like as differential operator.

Only combining the field, the ∇ displays its physica meaning or it is just one operation symbol. From the micro perspective, divergence $\nabla \cdot \mathbf{D} = \rho$, $\nabla \cdot \mathbf{B} = 0$ can be indicated that electric field is active but magnetic field is passive. The Curl $\nabla\times$ displays contribution from the flow, $\nabla \times \mathbf{H} = \mathbf{J} + \frac{\partial \mathbf{D}}{\partial t}$, $\nabla \times \mathbf{E} = -\frac{\partial \mathbf{B}}{\partial t}$.

By clarifying these relationships, We reduce the difficulty of students on mathematics.

3. ANALYZING ELECTROMAGNETIC THEORY SYSTEMATICALLY

Maxwell extracted from the essential characteristic of electromagnetic phenomena the concept of electric and magnetic fields from the Faraday line force, and using these two concepts he rewrote Coulomb's law, Ampere's law and Faraday's law. By conjecturing the displacement current, Ampere's Law was rewritten into the Ampere's full current law, and finally the construction of electromagnetic theory system was completed.

The introduction of displacement current has an important significance to the establishment of entire electromagnetic theory. The introduction of displacement current, make two curl equations of Maxwell $\nabla \times \mathbf{E} = -\frac{\partial \mathbf{B}}{\partial t}$, $\nabla \times \mathbf{H} = \mathbf{J} + \frac{\partial \mathbf{D}}{\partial t}$. The logic diagram of the introduction of displacement current is shown as Fig. 1.

The curl equations show presence of coupling beween $\mathbf{E}$ and $\mathbf{H}$, and two-way conversions between time and space, that is, $\mathbf{E}$ converted into $\mathbf{H}$, then $\mathbf{H}$ into $\mathbf{E}$; the time change $\frac{\partial}{\partial t}$ converted into the space change $\nabla\times$, then the space change $\nabla\times$ converted to the time change $\frac{\partial}{\partial t}$. It is just this two-way change that reveals the existence of electromagnetic waves.

Maxwell's electromagnetic theory predicted the existence of electromagnetic waves. Electromagnetic wave is not a result through perception but a logical reasoning one. It is a sure existence which was confirmed by the German physicist Hertz in the experiment. The establishing process of electromagnetic theory could make students to recognize the logic of the relationship in the electromagnetic theory, and appreciate the power of logical reasoning and Maxwell's creative spirit. So, we have analyzed electromagnetic theory systematically and rigorously to cultivate innovative thinking ability of students.

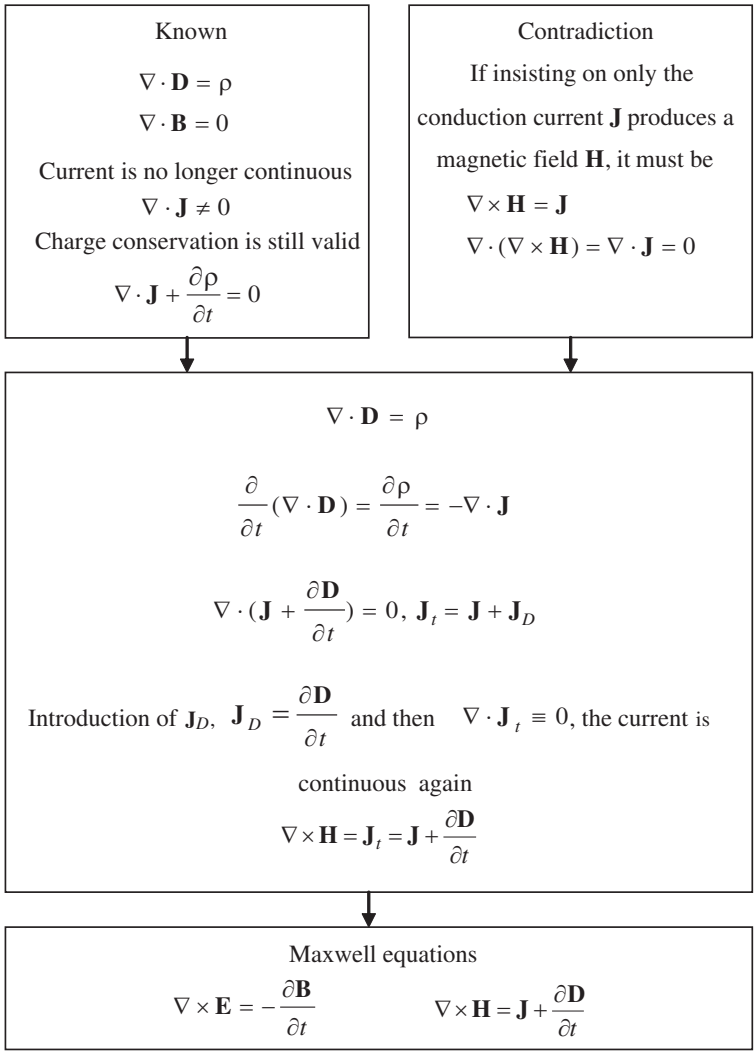

Figure 1: The logic diagram of the introduction of displacement current.

4. COMBINING ELECTROMAGNETIC THEORY WITH APPLICATIONS

Electromagnetic theory is abstract, but the application is extensive. During the course we select the content and problems about new technologies, such as communication, networking, radar, navigation, remote sensing and so on.

An antenna is an essential component in a radio communication system that is needed in both the transmitting and receiving terminals. Several types of antennas have been developed for various applications. For example, we introduce the principles and applications of patch antenna (also called microstrip antennas) in the class.

Figure 2 [1] shows a typical probefed rectangular patch antenna. The patch antenna consists of four major parts: The conductive patch, the dielectric substrate, the ground plane, and the feed line. Some of the advantages of patch antennas are:

- Low fabrication cost and complexity.
- Can be easily conformed to a curved surface of a vehicle or product.
- Resistant to shock and vibration.

Because of these, Patch antennas are used in several wireless applications like global positioning system (GPS) receivers, wireless LANs and radar sensors systems [1].

GPS patch antennas are widely used in GPS receivers. Also, a patch antenna can be easily mounted on the roof of a vehicle because of its planar structure.

Wireless LANs are deployed in office or other buildings. The physical link between the machine and the wireless access point dictates that the machine would have some kind of hemispherical radiation shape to cover all points above the machine almost equally, which makes patch antennas a good candidate.

Arrays of patch antennas could be used as near-range radar sensors. The array could be placed at the front of the car, so that the safety of driving has increased.

In addition to wireless communications and radar applications, electromagnetic waves can also be used in the wireless energy transfer.

Wireless energy transfer is currently the academic frontier. In the same way as the requirement of wireless communications, people are looking forward to a future when the energy supply could slipped the leash of the electrical wire. There are three types of methods having been researched. The first one is transferring energy over very high frequency (VHF, frequency $>$ 300 MHz) in the form of electromagnetic. When proper controls are put on the transfer antenna and receiver antenna, the energy transfer can be highly directional in such a high frequency field. The second one is transferring energy by loosely coupled transformer device of which primary side is separated from secondary side. The third one is transferring energy by the "strongly-coupled" resonances coupling of the mutual inducted magnetic field [2–4].

MIT in American did some research on principle simulation and experimental verification about technology of third type [3]. The basic principle of this technology is that two separate coils with same resonance frequency are possible to form a resonant system based on high frequency magnetic coupling and exchange energy in a high efficiency, while the coupling effect is weak between those objects with different resonance frequency. The medium of energy transfer is an alternating

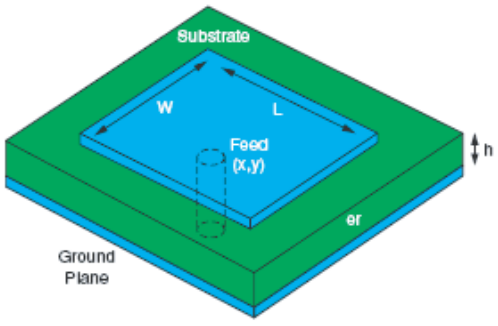

Figure 2: Structure of microstrip antenna.

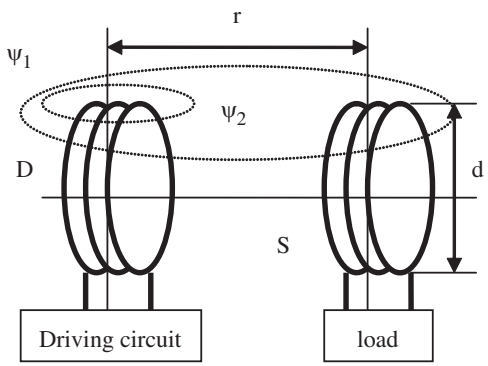

Figure 3: Structure of the wireless power transfer system.

magnetic field. In the Fig. 3 [4], resonator is composed of two coils and lumped parameters capacitance. Connected to the driving circuit, the driver coil D is used to generate magnetic field which is supposed to be either zero-order or one-order field. A part of flux (ψ_2) of these two close and coupled coils (D) intersects with each other besides the self-coupled flux (ψ_1).

By studying these these application examples, students' interest is stimulated. On the one hand students learn more knowledge about academic frontier of the electromagnetic theory and applications, on the other hand they have also more deeply understanded the theories of resonator, antenna and so on, and appreciated the importance of electromagnetic theory.

In short, we have focused on three aspects of EM teaching. We have seized the keys of vector field theory to clear students' obstacles about mathematics, made students to understand the rigorous logic system of electromagnetic theory which deeply enhances the students' sense of innovation, and combined the theories with practical applications to improve their capabilities of applying knowledge and solving engineering problems.

ACKNOWLEDGMENT

This work was supported by the Ministry of Education of China for National Characteristic Specialty Program of Higher Education.

REFERENCES

1. Sharawi, M. S., "Use of low-cost patch antennas in modern wireless technology," *IEEE Potentials Magazine*, Vol. 25, No. 4, 35–47, July/August 2006.
2. Fotopoulou, K. and B. W. Flynn, "Wireless powering of implanted sensors using RF inductive coupling," *IEEE Sensors 2006 EXCO*, Daegu, Korea, October 22–25, 2006.
3. Kurs, A., A. Karalis, R. Moffatt, J. D. Joannopoulos, P. Fisher, and M. Soljacic, "Wireless power transfer via strongly coupled magnetic resonances," *Science*, Vol. 317, 83–86, July 6, 2007.
4. Zhu, C., C. Yu, K. Liu, and R. Ma, "Research on the topology of wireless energy transfer device," *IEEE Vehicle Power and Propulsion Conference (VPPC)*, Harbin, China, September 3–5, 2008.

Perspective of Electromagnetics Education

X. M. Zhang, S. L. Zheng, Y. Du, X. F. Ye, and K. S. Chen
Department of Information Science & Electronic Engineering
Zhejiang University, Hangzhou 310027, China

Abstract— Electromagnetic Field and Wave is the backbone of electricity professional foundation courses. The course involves a large number of field theory and vector analysis relying on mathematical knowledge. The application examples of electromagnetic theory in engineering practice, scientific research and daily life help students understand course contents. Integrated with scientific research and achievements, the teaching conducts undergraduates to research and training programs. The capabilities of problem-solving are strengthened, and initiative and creativity are motivated. Thereby the teaching effect of the course is enhanced.

1. INTRODUCTION

Electromagnetic theory was fully founded by James Clerk Maxwell in 1864. The Maxwell equations govern all electromagnetic phenomena and their engineering applications in modern electronic technology. Many modern technologies, such as telecommunications, broadcasting, television, navigation, radar, remote sensing, monitoring and control, electronic warfare, electronic instrumentation and measurement systems, household appliances, industrial automation, geological exploration, power facilities, transportation, health and so on, are directly or indirectly related to the electromagnetic theory. It is also pregnant with a number of emerging disciplines. Electromagnetic Field and Wave is the backbone of electricity professional foundation courses for undergraduate students. The course involves a large number of field theory and vector analysis relying on mathematical knowledge. Relative to the application-oriented courses, it covers wider contents and requires more theoretical analysis. The subject is very abstract, and is difficult to learn for most students.

Electromagnetic problems arise in diverse areas, such as radar systems, antennas, communication systems, EMC, RFIC, RFID, and other electronic systems. The electromagnetic applications in everyday lives can be used as a vehicle to explain fundamental theoretical concepts. With the extensive use of simulation tools, rigorous analytical methods and their engineering approximations for these application examples can be omitted, and the role of basic electromagnetic theory in engineering practice can be clearly presented. The abstract theories are shown in realistic existence so that students can deepen their understanding of the course contents.

How to make students not only feel the latest developments and applications in the field of electromagnetics, but also with great interest to learn the basic theory is the key to success of teaching, which requires teaching contents to be constantly updated. The integration with the modern science and technology ensures the advanced nature of teaching contents. The introduction to the hot electromagnetic issues in recent years can greatly enhance the student's enthusiasm, and arouse their curiosity to explore the unknown world, which also lays the foundation to learn the basic theory.

Students tend to become best motivated to learn something when they can see its relevance. Integrated with scientific research and achievements, the teaching conducts undergraduates to research and training programs. Many students will relate topics into their own research projects, and present the corresponding small research reports in the end of course. This process helps students understand the abstract theories deeply.

2. VISUALIZATION TEACHING

Electromagnetic field and wave is characterized by vector three-dimensional dynamic distribution. A number of important models, such as field distribution in a variety of transmission lines, the wall current distribution, the antenna radiation patterns, as well as the propagation of three-dimensional electromagnetic waves, etc., should be shown as vivid images to students. This will strengthen the profound understanding of these models built from many concepts. In the course teaching, the use of modern information technology and computer-assisted teaching is essential [1–6]. The aim is to make three-dimensional animation software, combined with the electromagnetic simulation tools. The three-dimensional electromagnetic field distribution under different conditions, the

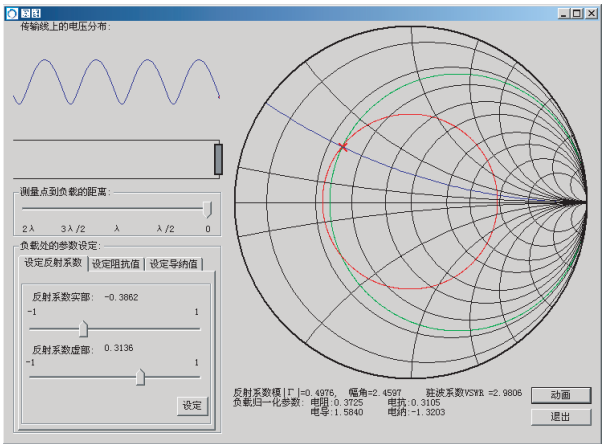

Figure 1: Smith chart courseware.

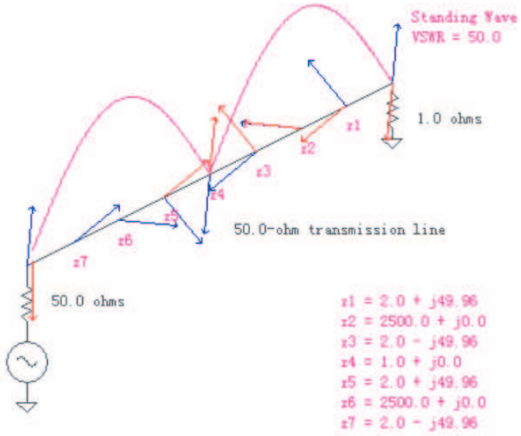

Figure 2: Standing wave in transmission line.

waveform distribution in microwave transmission lines, wall-current distribution, are shown into three-dimensional space to create animated graphics, so that students can observe the full three-dimensional field dynamic distribution patterns. The physical models became vivid images. The models can be demonstrated in the computer, and it also can be made through the Internet web remote teaching. This stimulates student enthusiasm for learning, and improves teaching quality and effectiveness.

The motivation is the key to the success of electromagnetics learning. If we can clearly let students know that the knowledge about electromagnetic waves is the future job needs, it will inspire student interest and motivation to learn this course. The applications of electromagnetic theory in engineering practice, scientific research and everyday life are broad and in-depth. In the teaching process, it will not only help students understand the basic principles and approaches of electromagnetic theory, but also to enable students to appreciate the great vitality of electromagnetic theory, and to understand the important role and significance of electromagnetic theory in many fields.

For example, in the teaching the concept of wave reflection and Brewster angle, the principle of polarized sunglasses can be introduced. Normally, a light source produces waves which go in all directions. Light reflected from surfaces such as a flat road or smooth water is generally horizontally polarized. This means that, instead of light being scattered in all directions in more usual ways, reflected light generally travels in a more horizontally oriented direction. This creates an annoying and sometimes dangerous intensity of light that we experience as glare. A vertical polarizing lens can reduce the brightness of these light waves while still allowing optical information through. Because of their vertical polarizing orientation, polarized sunglasses are ideal for dealing with reflective glare conditions, depending on the angle.

In the teaching the concept of electric dipole, the principles of microwave heating can be introduced in order to enable students to better understand the electric dipole in everyday life. The majority of foods contain water, fiber, fat and other polar molecules. Positive and negative charge center of these molecules do not coincide, which is equivalent to an electric dipole. Under external electric field, electric moment turns to the direction of the external electric field. If the direction of external electric field changes, the orientation of the electric moment corresponds to change. The collision with the surrounding molecules during rotation will convert electrical potential energy into thermal energy of the surrounding molecules.

3. RESEARCH-BASED LEARNING

Electromagnetic technology has now broken through the traditional areas of technology, and becomes one of main factors for the development of new technologies in modern electronics, wireless communications, bio-engineering and nano-technology, etc. Electromagnetic problems and signal integrity has become the main obstacles for development of high-performance integrated circuits, nano-scale electronics, RFIC, and electronic packaging technology. Three-dimensional integrated system packaging, high-performance chip and the electromagnetic propagation in complex biological environment (e.g., Body area network) has become a new and very important discipline.

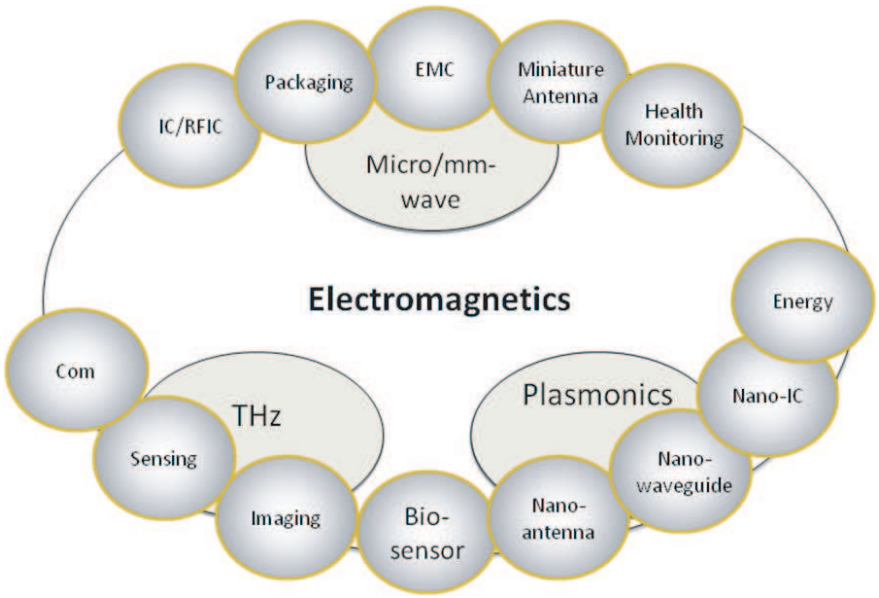

Figure 3: New horizon of electromagnetics.

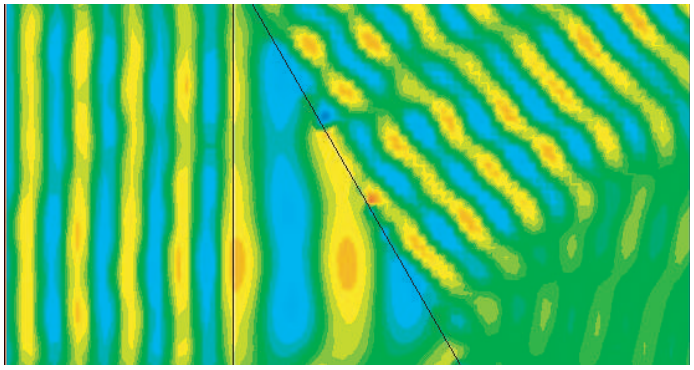

Figure 4: Electromagnetic wave propagation in left-handed meidum.

The integration with the modern science and technology ensures the advanced nature of teaching contents.

From the establishment of Maxwell equations to today, with the development of electromagnetic theory and technology, electromagnetic applications are more and more widely. There are many hot electromagnetic problems in recent years, such as left-handed materials, electromagnetic black hole, electromagnetic invisibility cloak, plasmonics, wireless power transmission, three-dimensional integrated circuit, bio-electromagnetics, etc. By combining the hot electromagnetic problems with the course teaching, it can greatly enhance the student enthusiasm for learning electromagnetics, arouse their curiosity to explore the unknown world.

Many students will choose an interesting topic as their research projects. In the end of the course, they will offer the corresponding research reports. Figure 4 shows the electromagnetic wave propagation in left-handed medium, which is simulated by a student. This research-based learning process helps students understand the abstract theories deeply. Students have also gained self confidence and have improved interest in electromagnetics. Some students will set it to be one of their directions for future efforts.

ACKNOWLEDGMENT

This work was supported by the Ministry of Education of China for National Characteristic Specialty Program of Higher Education.

REFERENCES

1. Sevgi, L., "A new electromagnetic engineering problem and teaching via virtual tools," *Progress In Electromagnetics Research B*, Vol. 6, 205–224, 2008.
2. Magistris, M., "A MATLAB-based virtual laboratory for Teaching introductory quasi-stationary electromagnetic," *IEEE Trans. Education*, Vol. 48, No. 1, 81–88, 2005.
3. Mukhopadhyay, S. C., "Teaching electromagnetic at the undergraduate level: A comprehensive approach," *Eur. J. Phys.*, Vol. 27, 727–742, 2006.
4. Cheng, K. W. E., X. D. Xue, K. F. Kwok, and T. K. Cheung, "Improvement of classroom teaching of electromagnetics by means of an electronic book," *IEEE Trans. Magnetics*, Vol. 39, No. 3, 1570–1573, 2003.
5. Okayama, E., V. Cingoski, S. Noguchi, K. Kaneda, and H. Yamashita, "Interactive visualization system for education and design in electromagnetics," *IEEE Trans. Magnetics*, Vol. 36, No. 4, 995–998, 2000.
6. Beker, B., D. W. Bailey, and G. J. Cokkinides, "An application-enhanced approach to introductory electromagnetics," *IEEE Trans. Education*, Vol. 41, No. 1, 31–36, 1998.

Study on the Duality of Frequency Selective Surfaces with Rectangular Complementary Elements

Xin Ma, **Guobin Wan**, **and Ning Ren**
School of Electronic and Information, Northwestern Polytechnical University, Xi'an 710129, China

Abstract— New dual structures which are aperture-type Frequency Selective Surfaces (FSS) residing on a dual magnetic dielectric slab and patch-type FSS on an electric dielectric slab are proposed. The relative permittivity of electric dielectric is equal to the relative permeability of magnetic dielectric. The duality of aperture-type and patch-type FSS without any dielectric with an electric dielectric and with a dual magnetic dielectric are analyzed. The spectral Green's functions of arrays on different slabs are derived through spectral domain immittance approach. The affection of substrate on the reflection and transmission characteristics of rectangular FSS compared with the FSS in a free space is considered, and the effects are discussed through changing thickness and parameter of dielectric. It shows that the proposed structures are complementary around resonant frequency, but resonant frequency offset emerges, and the magnitude of resonant frequency offset has relations with the dielectric type, thickness and parameter.

1. INTRODUCTION

In a free space we can obtain scattering field of aperture in a perfectly conducting screen through known problem of the same shape conducting plate according to Babinet's principle which is applied to free-standing FSS. Whereas in the application of FSS to practical ends, such as being exploited to make more efficient use of reflector antennas, and applied in dielectric radome design to reduce reflection, FSS are etched or resided on a substrate to provide mechanical support, and therefore the research of the dielectric effect on the duality of FSS is useful The complementary problem of scattering by a conducting screen perforated periodically with apertures was treated by Kieburtz and Ishimaru [1] through variational approach, but the accuracy depends on choosing an appropriate trial function. Chen solved the aperture problem [2] as well as the complementary problem [3] by mode functions, which preclude the analysis of arbitrary shaped apertures or plates. In [4], the dual magnetic dielectric was not taken into account. Therefore, creating an accurate and comprehensive solution is necessary.

This paper describes a precise method to compute the dual FSS structure. The technique is based on a spectral domain method of moment, similar to that proposed in [7], but spectral Green's functions of arrays on various slabs are different through spectral domain immittance approach [5]. The current on the conductor is represented by smooth subsectional elements, therefore any shape elements can be accommodated, although only the rectangular element as an example is discussed.

2. FORMULATION AND CALCULATION METHOD

An infinite periodic array of perfectly conducting patches or apertures with periodicities of T_x and T_y resides on a slab in Fig. 1. Region 0 and 2 are air and region 1 is a dielectric layer, which may be air for free-standing FSS, an electric dielectric slab or a dual magnetic dielectric slab for patch or aperture arrays.

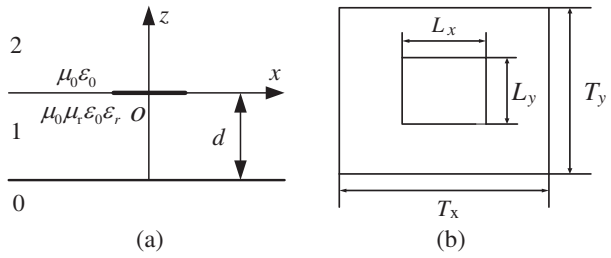

Figure 1: Geometry of FSS. (a) Side view, (b) the structure of a cell.

Spectral dyadic Green's function for a layered dielectric medium can be conveniently obtained via the spectral domain immittance approach [5], in connection with printed circuit transmission

line. Making $\mu_r = 1.0$, the spectral domain Green's function of FSS on an electric dielectric slab which can be easily found, similar to that in [7].

$$\begin{aligned}
\tilde{G}_{xx}(k_x,k_y) &= \frac{Z_0}{k_0\beta^2}\left(\frac{jk_{z1}k_{z2}k_x^2}{\varepsilon_r k_{z2}\Gamma_1 - jk_{z1}} + \frac{k_0^2k_y^2}{jk_{z1}\Gamma_2 - k_{z2}}\right)\\
\tilde{G}_{yy}(k_x,k_y) &= \frac{Z_0}{k_0\beta^2}\left(\frac{jk_{z1}k_{z2}k_y^2}{\varepsilon_r k_{z2}\Gamma_1 - jk_{z1}} + \frac{k_0^2k_x^2}{jk_{z1}\Gamma_2 - k_{z2}}\right)\\
\tilde{G}_{yx}(k_x,k_y) &= \tilde{G}_{xy}(k_x,k_y) = \frac{Z_0}{k_0\beta^2}\left(\frac{jk_{z1}k_{z2}k_xk_y}{\varepsilon_r k_{z2}\Gamma_1 - jk_{z1}} - \frac{k_0^2k_xk_y}{jk_{z1}\Gamma_2 - k_{z2}}\right)
\end{aligned} \tag{1}$$

In the above $\beta^2 = k_x^2 + k_y^2$ and Z_0 is the free-space intrinsic impedance. Γ_1 and Γ_2 are:

$$\Gamma_1 = \frac{\varepsilon_r k_{z2}\sin k_{z1}d - jk_{z1}\cos k_{z1}d}{\varepsilon_r k_{z2}\cos k_{z1}d + jk_{z1}\sin k_{z1}d} \qquad \Gamma_2 = \frac{k_{z2}\cos k_{z1}d + jk_{z1}sink_{z1}d}{k_{z2}\sin k_{z1}d - jk_{z1}\cos k_{z1}d}$$

In the same way, making $\varepsilon_r = 1$, the spectral domain Green's function of FSS on magnetic dielectric slab are:

$$\begin{aligned}
\tilde{G}_{xx}(k_x,k_y) &= \frac{Z_0}{k_0\beta^2}\left(\frac{jk_{z1}k_{z2}k_x^2}{k_{z2}\Gamma_1 - jk_{z1}} + \frac{\mu_r k_0^2k_y^2}{jk_{z1}\Gamma_2 - \mu_r k_{z2}}\right)\\
\tilde{G}_{yy}(k_x,k_y) &= \frac{Z_0}{k_0\beta^2}\left(\frac{jk_{z1}k_{z2}k_y^2}{k_{z2}\Gamma_1 - jk_{z1}} + \frac{\mu_r k_0^2k_x^2}{jk_{z1}\Gamma_2 - \mu_r k_{z2}}\right)\\
\tilde{G}_{yx}(k_x,k_y) &= \tilde{G}_{xy}(k_x,k_y) = \frac{Z_0}{k_0\beta^2}\left(\frac{jk_{z1}k_{z2}k_xk_y}{k_{z2}\Gamma_1 - jk_{z1}} - \frac{\mu_r k_0^2k_xk_y}{jk_{z1}\Gamma_2 - \mu_r k_{z2}}\right)
\end{aligned} \tag{2}$$

where Γ_1 and Γ_2 are:

$$\Gamma_1 = \frac{k_{z2}\sin k_{z1}d - jk_{z1}\cos k_{z1}d}{k_{z2}\cos k_{z1}d + jk_{z1}\sin k_{z1}d} \qquad \Gamma_2 = \frac{\mu_r k_{z2}\cos k_{z1}d + jk_{z1}sink_{z1}d}{\mu_r k_{z2}\sin k_{z1}d - jk_{z1}\cos k_{z1}d}$$

For scanning at the angle (θ, ϕ), the current on the p', q' elements must be phased as $e^{jk_0(p'T_Xa+q'T_yb)}$ ($a = \sin\theta\cos\phi$, $b = \sin\theta\sin\phi$). Using the Poission sum [6], the Green's function of an infinite array can be found. The scattering field is the product surface integral of Green's function and the current in one period. The application of the boundary condition at $z = d$ yields:

$$\bar{E}_t^S(x,y,d) = -\bar{E}_t^i(x,y,d) - \bar{E}_t^r(x,y,d) \tag{3}$$

where $\bar{E}_t^i(x,y,d)$ and $\bar{E}_t^r(x,y,d)$ denote the transverse component of the incident field and the reflected field by the slab in the absence of conductor, respectively. The excitation field is a plane wave of either transverse electric (TE) or transverse magnetic (TM) polarization. Especially, for a dual structure, the excitation should be dual with the same incident angle. The current is expanded with roof-top subdomain basis function, and the Equation (3) can be solved to obtain unknown coefficient of current, according to Galerkin's technique.

3. NUMERICAL CALCULATION AND DISCUSSION

In order to investigate the effect of dielectric slab on the duality of FSS, the case of the patch-type FSS is illuminated by TE incidence and for the case of the aperture-type FSS by TM incidence with the same incident angle $\theta = 0°$, $\phi = 0°$ in the results of following part. Fig. 2(a) shows the specular reflection coefficients and forward coefficients of free-standing ($d = 0\,\text{mm}$) aperture-type and patch-type FSS which dimensions are $T_x = 20\,\text{mm}$, $T_y = 20\,\text{mm}$, $L_x = 10\,\text{mm}$, $L_y = 10\,\text{mm}$. With the same size in Fig. 2(b), the reflection coefficients of patch arrays and transmission coefficients of aperture arrays on an electric dielectric slab, and the transmission coefficients of aperture arrays on a dual magnetic dielectric slab are plotted. The dielectric parameters of electric dielectric are $\varepsilon_r = 3.5$, $\mu_r = 1.0$, and dielectric parameters of dual magnetic dielectric are $\varepsilon_r = 1$, $\mu_r = 3.5$, the thickness is $d = 0.5\,\text{mm}$. As we can see from the figure, the free-standing aperture-type and patch-type FSS turn out to be completely complementary to each other in accordance with Babinet's

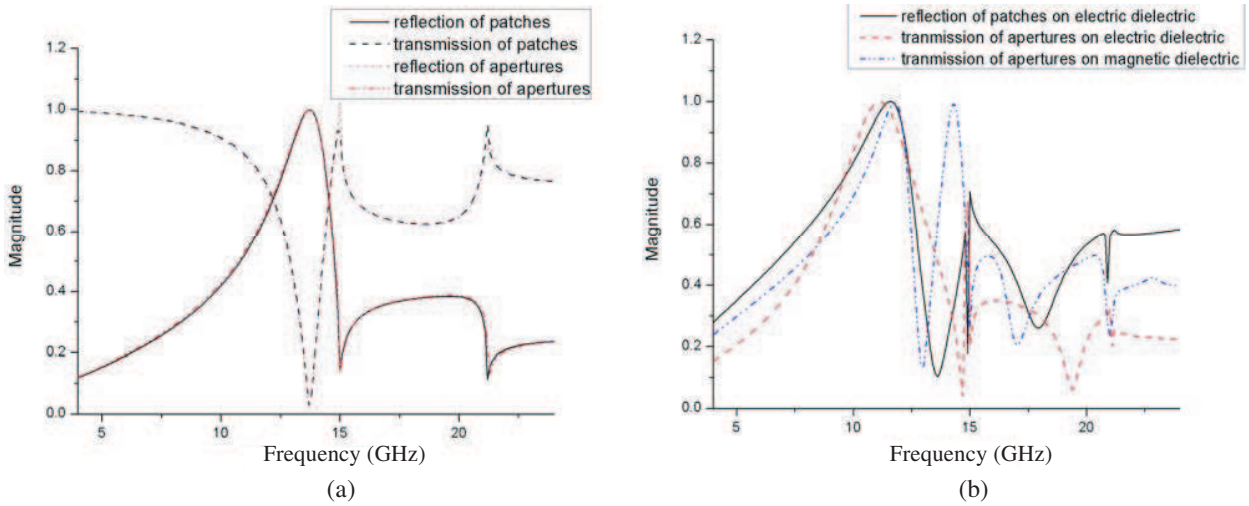

Figure 2: Effect of dielectric type. (a) Free-standing FSS, (b) FSS on electric dielectric slab and dual magnetic dielectric slab.

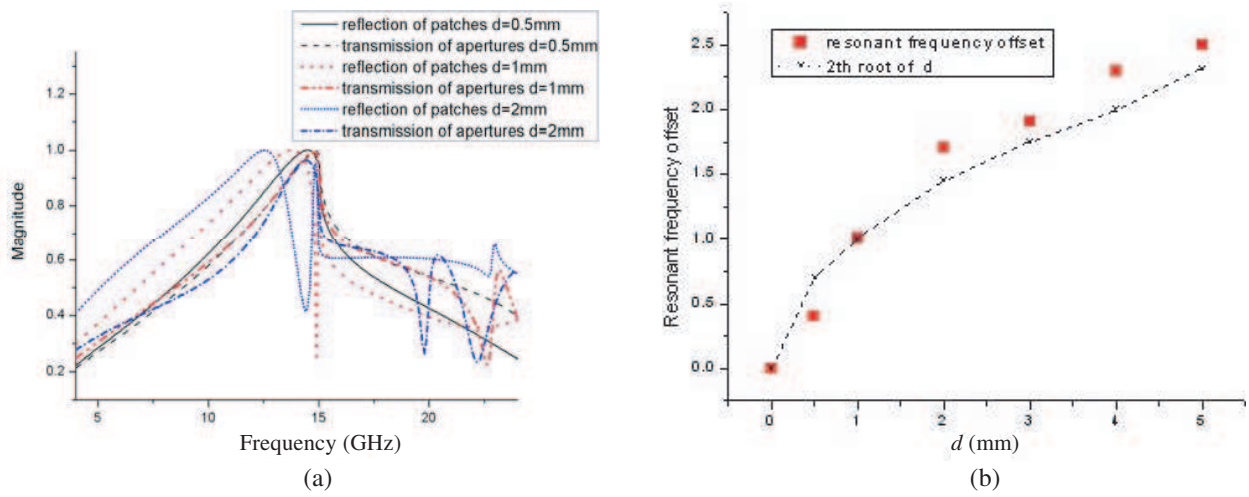

Figure 3: Effect of dielectric thickness. (a) Reflection and transmission coefficients against frequency, (b) resonant frequency offset against thickness.

principle, but when the FSS resides on the dielectric the scattering properties change. Fig. 2(b) indicates the properties are complementary around the resonant frequency but over the wide range of frequency are not strictly complementary. The resonance frequency of aperture arrays on an electric dielectric slab shifts to lower frequency comparing with that of patch arrays on a same slab, whereas a dual magnetic dielectric slab makes the resonance frequency of aperture arrays shift to a little higher frequency.

To analyze the influence of dielectric thickness and parameter, the rectangular element with the dimension of $T_x = 10\,\text{mm}$, $T_y = 20\,\text{mm}$, $L_x = 5\,\text{mm}$, $L_y = 10\,\text{mm}$ is tested in a following part. In Fig. 3(a), reflection coefficients of patch arrays on an electric dielectric slab which relative permittivity is $\varepsilon_r = 3.5$ are compared with transmission coefficients of aperture arrays on a dual magnetic dielectric slab by changing the thickness of dielectric. It seems that there are dual trend around resonant frequency, but resonant frequency offset occurs, and the magnitude of it becomes larger with respect to the increase of thickness. We can also see from Fig. 3(b) that the trend of resonant frequency offset seems to be proportional to $\sqrt{d}$.

For certain dielectric thickness $d = 2\,\text{mm}$, Fig. 4 illustrates the effect of dielectric parameter by altering the relative permeability of magnetic dielectric along with the relative permittivity of electric dielectric from 2.0 to 4.0. Note that resonant frequency offset occurs, and it seems to be proportional to $\sqrt{\varepsilon_r - 1}$ or $\sqrt{\mu_r - 1}$, similar to the effect of thickness. Clearly, the effect of dielectric

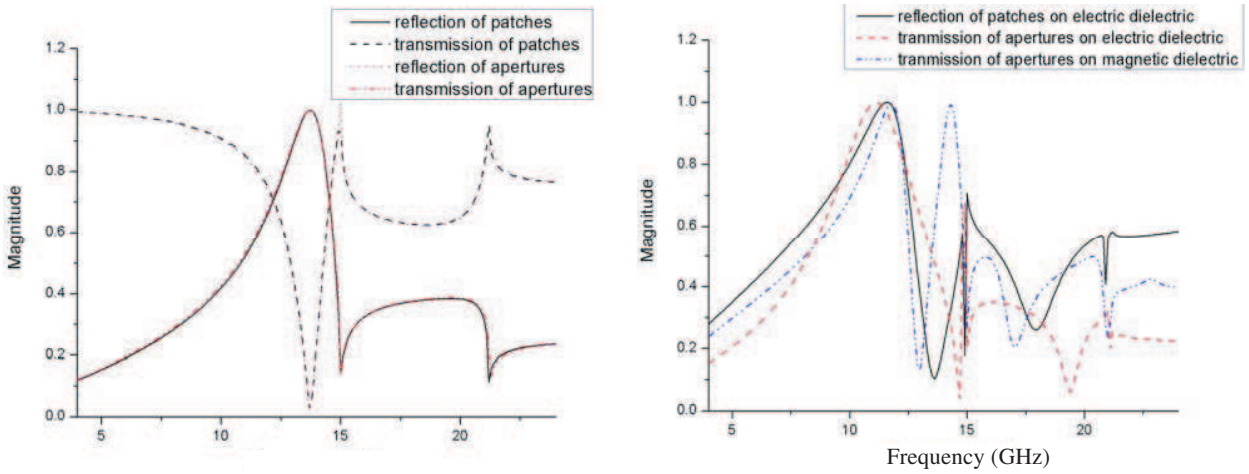

(a) (b)

Figure 4: Effect of dielectric parameter. (a) Reflection and transmission coefficients against frequency, (b) resonant frequency offset against dielectric parameter.

thickness and parameter on the electric dimension of FSS residing on an electric dielectric differs from that on the electric dimension of FSS residing on a dual magnetic dielectric.

4. CONCLUSION

In this paper, we have studied the duality of rectangular FSS with complementary elements. Spectral Green's functions of arrays on various slabs are given through spectral domain immittance approach. The method employing a rooftop current representation and spectral method of moment is used Affection of the dielectric type thickness and parameter on the duality of FSS has been discussed. It is found that all variables mentioned above may affect the duality of complementary screens in different ways. For the arrays in free space, the properties of the patch-type and aperture-type FSS are complementary to each other. However, for the dual structure on dielectric slab, they are not strictly complementary over the wide range of frequency, and resonant frequency offset occurs, because the effects of dielectric thickness and parameter on the electric dimension of arrays with an electric dielectric is different from that on the electric dimension of arrays with a dual magnetic dielectric.

REFERENCES

1. Kieburtz, R. B. and A. Ishimaru, "Scattering by a periodically apertured conducting screen," *IEEE Trans. Antennas and Propagat.*, Vol. 9, No. 11, 506–514, 1961.
2. Chen, C. C., "Transmission through a conducting screen perforated periodically with apertures," *IEEE Trans. on Microwave Theory Tech.*, Vol. 18, No. 9, 627–632, 1970.
3. Chen, C. C., "Scattering by a two-dimensional periodic array of conducting plates," *IEEE Trans. Antennas and Propagat.*, Vol. 18, No. 9, 660–665, 1970.
4. Wakabayashi, H., M. Kominami, H. Kusaka, and H. Nakashima, "Numerical simulations for frequency-selective screens with complementary elements," *IEE Proc. — Microw. Antennas Propagat.*, Vol. 141, No. 6, 477–482, 1994.
5. Itoh, T., "Spectral domain immitance approach for dispersion characteristics of generalized printed transmission lines," *IEEE Trans. Antennas and Propagat.*, Vol. 28, No. 7, 1–4, 1980.
6. Pozar, D. M. and D. H. Schaubert, "Scan blindness in infinite phased arrays of printed dipoles," *IEEE Trans. Antennas and Propagat.*, Vol. 32, No. 6, 602–610, 1984.
7. Jin, J.-M. and J. L. Volakis, "Electromagnetic scattering by a perfectly conducting patch array on a dielectric slab," *IEEE Trans. Antennas and Propagat.*, Vol. 38, No. 4, 556–563, 1990.

Observation of Geometric Resonance in a Corrugated Waveguide

X. Y. Cheng, **R. Chakraborty**, **S. Mishra**, **V. A. Pogrebnyak**, **and J. J. Whalen**
Department of Electrical Engineering, Faculty of Engineering
State University of New York at Buffalo, 332 Bonner Hall, NY 14260-1920, USA

Abstract— Geometric resonance phenomenon in a corrugated waveguide is investigated both theoretically and experimentally. By solving wave equation under the periodic boundary condition in a corrugated waveguide, geometric resonance conditions are derived. This resonance is associated with the waveguide thickness and the phase shift between the corrugated walls of the waveguide. A corrugated waveguide is fabricated and measured by an HP 8510c Vector Network Analyzer, measurement results agree with the theoretical prediction. This work is meaningful for microwave communications, quantum physics, photonic crystals, integrated optical and electronic devices. The theory is also of significance to the research on periodic quantum well.

1. INTRODUCTION

Wave propagation in periodic structure is a classical problem. It is now still of great interest due to its applications in microwave communications, quantum physics, photonic crystals, integrated optical and electronic devices [1–7]. Although this topic has been investigated for decades, there are still some issues, such as electromagnetic wave propagation in a corrugated waveguide, need further study.

Wave propagation in periodic structure can be characterized by Bragg's Law. Under certain conditions, Bragg reflection, which will lead to a forbidden gap in transmission spectrum, can be observed. In this paper, resonance due to geometry configurations is presented. For a carefully chosen waveguide thickness and phase shift between corrugated walls, geometric resonance will occur, in this case, a band gap will open around one of the higher mode cutoff frequencies; meanwhile, the corrugation of the waveguide walls will lead to a shift for lower mode cutoff frequency.

2. WAVE EQUATION AND BOUNDARY CONDITIONS

We assume electromagnetic (EM) wave travels along x-direction in Cartesian coordinates. Waveguide with periodically corrugated walls is considered. The corrugated walls have the profiles of $y_d = \frac{d}{2} + \xi\cos(\frac{2\pi}{a}x)$, $y_{-d} = -\frac{d}{2} + \rho\cos(\frac{2\pi}{a}x + \theta)$ for upper and lower walls respectively, where d is the waveguide thickness, a is the period of corrugation, ξ, ρ and θ are amplitudes and phase shift of the corrugated walls. The configuration is shown in Figure 1.

If we denote $\varphi(x, y, z)$ as the $\boldsymbol{z}$-component of the E field of the TE wave in the waveguide, wave propagation in this corrugated waveguide can be characterized using the two-dimensional wave equation:

$$\nabla^2\varphi + \frac{\omega^2}{c^2}\varphi = 0 \tag{1}$$

subject to the following boundary conditions:

$$\varphi(x, y_{-d}) = \varphi(x, y_d) = 0 \tag{2}$$

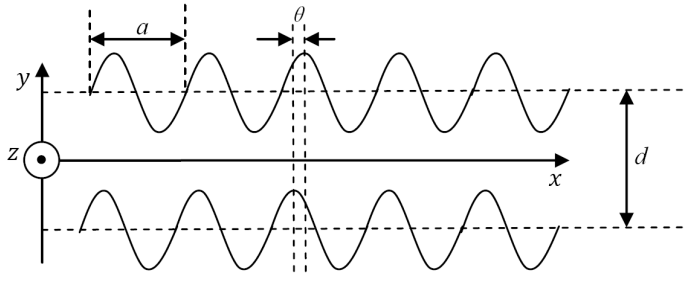

Figure 1: Corrugated wall configurations.

where ω is the frequency of the EM wave in rad/s, c is the propagating velocity of the wave in m/s. Due to the periodicity of the waveguide boundary, Eq. (2) can be expanded into the following Fourier series:

$$\varphi(x,y) = \Sigma_n \left[a_n \cos(k_{yn} y) + b_n \sin(k_{yn} y)\right] \times e^{[j(k_x + n\frac{2\pi}{a})x]} \tag{3}$$

where a_n and b_n are Fourier series coefficients, k_{yn} and k_x are components of wave vector along y-and x-directions.

For small corrugation, i.e., $\frac{\rho}{d} \ll 1$, and $\frac{\xi}{d} \ll 1$, it is sufficient to consider the first three harmonics [7]. Based on Eq. (2) and Eq. (3), the following characterization equation is used to find out allowable k_{yn}.

$$\tan(k_0 d) = \frac{1}{2} \times (\xi^2 + \rho^2) \times \frac{k_0 k_1}{\tan(k_1 d)} - \frac{\rho\xi k_0 k_1 \cos\theta}{\cos(k_0 d)\sin(k_1 d)} \tag{4}$$

where $k_1^2 = k_{-1}^2 = k_0^2 + q^2 = k_0^2 + (\frac{2\pi}{a})^2$ is the wave number of the first harmonic. In Eq. (4) and the following sections, we will drop the footnote y in wave vector, so k_{yn} will be simply denoted as k_n.

3. CUTOFF FREQUENCY SHIFT AND GEOMETRIC RESONANCE

The solution to Eq. (4) can be obtained by the method of successive approximation. For smooth waveguide, $\rho = \xi = 0$, the cutoff frequency of TE_{0p} mode is:

$$f_{0p} = \frac{c}{\sqrt{\varepsilon}} \times \frac{p\pi}{d}, \quad p = 1, 2, 3 \ldots \text{ is the order of TE wave} \tag{5}$$

For corrugated waveguide, $\rho \neq 0$ and $\xi \neq 0$, we have the cutoff frequency:

$$f'_{0p} = f_{0p}\left[1 + \frac{1}{2} \times (\xi^2 + \rho^2) \times \frac{k_1}{\tan(k_1 d)} + (-1)^{p+1} \frac{\rho\xi k_1 \cos\theta}{2d \times \sin(k_1 d)}\right] \tag{6}$$

Comparing with a smooth waveguide with the same average thickness, the cutoff frequency shift is:

$$\delta f'_{0p} = \frac{1}{2} \times (\xi^2 + \rho^2) \times \frac{k_1}{\tan(k_1 d)} + (-1)^{p+1} \frac{\rho\xi k_1 \cos\theta}{2d \times \sin(k_1 d)} \tag{7}$$

From Eq. (4) and Eq. (6) the resonance condition is:

$$k_{0p}^2 = k_{1m}^2 + \left(\frac{2\pi}{d}\right)^2 \tag{8}$$

where $k_{1m} = k_1 = \frac{m\pi}{d}$, $m = 1, 2, 3 \ldots$ is the order of resonance.

When geometric resonance occurs, one can observe the opening of a forbidden gap in the transmission spectrum as well as cutoff frequency shift.

1) Asymmetric waveguide: In this case, there is no phase difference between corrugated walls, $\theta = 0$. If the TE wave mode p and harmonic order m are both even or both odd, the resonance frequency is

$$f_{pm}^{\pm} = f_{0p}\left(1 \pm \frac{1}{\sqrt{2}} \times \frac{m}{p} \times \frac{|\rho - \xi|}{d}\right) \tag{9}$$

where f_{pm}^{+} and f_{pm}^{1} corresponds to upper and lower cutoff frequencies of the band gap; the gap width could be determined by:

$$\delta f_{pm} = \sqrt{2} \times \frac{m}{p} \times \frac{|\rho - \xi|}{d} f_{0p} \tag{10}$$

If the p is odd and m is even or on contrary,

$$f_{pm}^{\pm} = f_{0p}\left(1 \pm \frac{1}{\sqrt{2}} \times \frac{m}{p} \times \frac{|\rho + \xi|}{d}\right) \tag{11}$$

$$\delta f_{pm} = \sqrt{2} \times \frac{m}{p} \times \frac{|\rho + \xi|}{d} f_{0p} \tag{12}$$

2) Symmetric waveguide: In this case, phase difference between corrugated walls $\theta = \pi$. If the TE wave mode p and harmonic order m are both even or both odd, the resonance frequency is determined by Eq. (11), bad gap width is calculated by Eq. (12); If the p is odd and m is even or on contrary, resonance frequency can be found by Eq. (9), band gap is determined by Eq. (10).

4. EXPERIMENTAL OBSERVATION OF GEOMETRIC RESONANCE

A waveguide with corrugated lower and upper walls is fabricated. The lower wall is fixed, while the upper one is free to move, which makes the waveguide thickness and phase shifts between corrugated walls can be adjusted as desired. Measurements are done on a HP 8510C Vector Network Analyzer, proper antenna pairs are used. Both corrugated walls have periodic of 3.15 cm, amplitudes for upper and lower corrugation are the same, $\rho = \xi = 0.415$ cm. Since $\frac{\rho}{d} = \frac{\xi}{d} = 0.15 \ll 1$, Eq. (4) holds. According to Eq. (8), the average thickness of the waveguide is chosen to be $d = 2.73$ cm, we have $p = 2$ and $m = 1$, geometric resonance occurs.

We will begin our measurement with observing the cutoff frequency shift of TE_{01} mode. It can be seen from Figure 2(a) that the smooth waveguide has a cutoff frequency of 5.53 GHz which is very close to the theoretical value of 5.5 GHz. According to Eq. (6) and Eq. (7), the cutoff frequency of TE_{01} mode should shift to 6.02 GHz. The measured result in Figure 2(b) shows the cutoff frequency shifted to 5.87 GHz, which generally agrees with our prediction. The difference might be caused of unevenness of the corrugation.

It is supposed that we should have a band gap around the cutoff frequency of TE_{20} mode for the corrugated waveguide. According to Eq. (8), we have $p = 2$, $m = 1$. For symmetric waveguide, $\theta = \pi$, since p is even, m is odd, substitute data to Eq. (9), it is supposed that the gap is minimized in this case; for asymmetric waveguide, $\theta = 0$, using Eq. (11) and Eq. (12), there should have a gap between 9.82 GHz to 12.18 GHz.

It is seen from Figure 3 that a band gap opens from 9.875 GHz to 12.08 GHz, this measurement result agrees with our theoretical prediction. When the phase shift between corrugated walls is

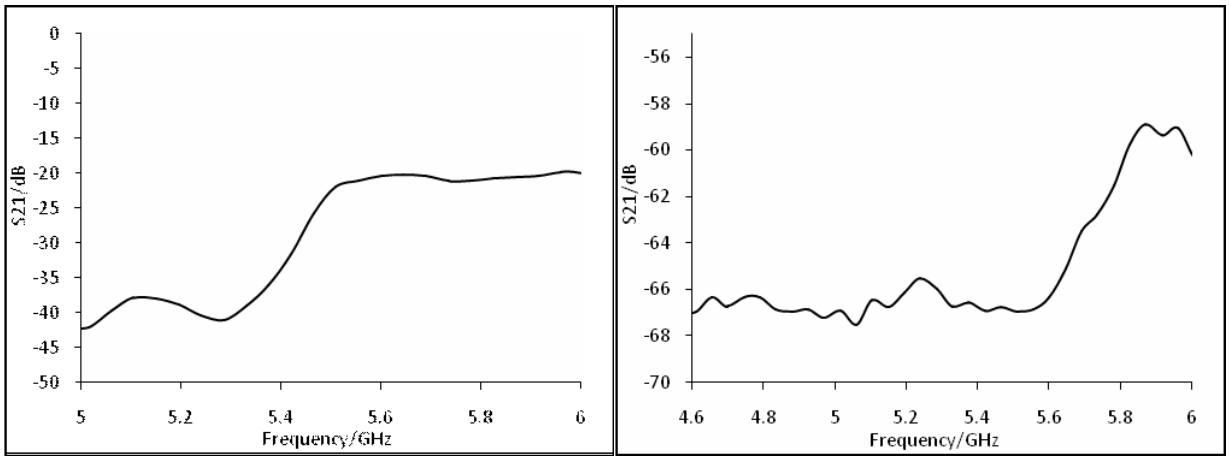

(a) (b)

Figure 2: TE_{01} mode cutoff frequency shift. (a) TE_{01} mode cutoff frequency of smooth waveguide. (b) TE_{01} mode cutoff frequency of corrugated waveguide.

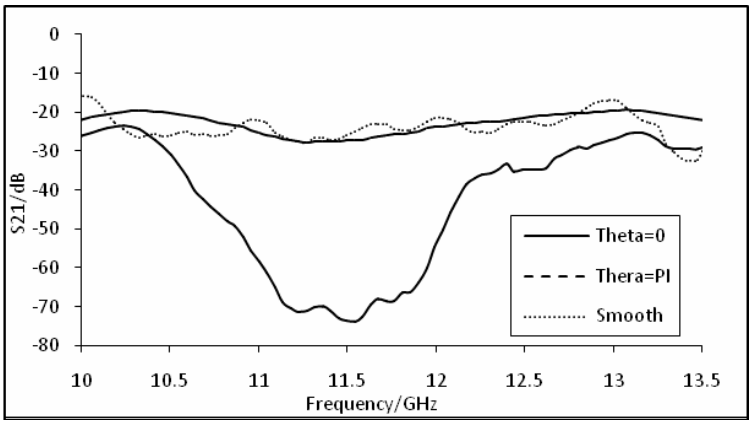

Figure 3: Band gap due to geometric resonance.

$\theta = \pi$, the forbidden gap is minimized, and it is very close to the performance of a smooth waveguide which has the same average thickness.

5. CONCLUSIONS

Resonance caused by specific geometric configurations is investigated both theoretically and experimentally. The geometric resonance will alter transmission spectrum of a corrugated waveguide. By solving wave equation under periodic boundary conditions, geometric resonance conditions are derived; cutoff frequency shift and opening of a bag gap are predicted. Waveguide with periodically corrugated walls is fabricated, under carefully chosen configurations, geometric resonance occurs in the waveguide, band gap in the transmission spectrum as well as cutoff frequency shift are observed. Measurement results show good agreement with theoretical calculations. Unevenness of the periodicity of the corrugations may lead to differences between theoretical prediction and measurement results.

REFERENCES

1. Pogrebnyak, V. A. "Controllable band structure in a periodic quantum well," *Phys. Rev. B*, Vol. 69, 245307, 2004.
2. Brillouin, L., *Wave Propagation in Periodic Structures*, 2nd Edition, Dover Publications, New York, 1953.
3. Pogrebnyak, V. A. and J. J. Whalen, "Controllable microwave transmission in rectangular periodically corrugated waveguide," *Electron. Lett.*, Vol. 43, No. 4, 226–228, 2007.
4. Joannopoulos, J. D., *Photonic Crystals: Molding the Flow of Light*, Princeton University Press, Princeton, 2008.
5. Lewin, L., *Theory of Waveguides*, John Wiley & Sons, New York, 1975.
6. Kim, C. S., J. S. Park, and D. Ahn, "A novel 1-D periodic defected ground structure for planar circuits," *IEEE Microwave and Guided Wave Letters*, Vol. 34, No. 10, 1064–1076, 1986.
7. Pogrebnyak, V. A., "Geometric resonance in a periodic waveguide," *J. Appl. Phys.*, Vol. 94, No. 10, 6979–6981, 2003.

Compact Coplanar-waveguide Band-rejection DGS Resonators

De-Liang Sun[1], **Chien-Jen Wang**[1], **Chia-Hsien Lin**[1], **and Yi-Che Tsai**[2]

[1]Depart. of Electrical Engineering, National University of Tainan, Tainan, Taiwan
[2]Depart. of Electrical Engineering, National Chiao-Tung University, Hsin-Chu, Taiwan

Abstract— In this paper, compact coplanar-waveguide (CPW) defected-ground-structure (DGS) resonators are demonstrated, by placing floating patches. Two T-shaped slots as a bandstop resonator are etched in two ground planes of a CPW 50 Ω transmission line. Two rectangular patches are symmetrically placed on the bottom layer of the substrate. The patches modeled as an additional capacitance increase the effective capacitance of the resonator. By tuning the geometrical dimension of the patches, the resonance frequency is lowered.

1. INTRODUCTION

A microstrip slotted-ground-plane bandstop resonator with a compact size and spurious suppression has attracted a growing amount of interest in the field of radio frequency /microwave (RF/MW) circuits design. Such resonators are widely used in designs for low-pass filters [1], power dividers [2], power amplifiers [3], frequency multipliers [4], and so on. The resonator, which has a patterned slot in the backside metallic ground plane, can exhibit stopband characteristics due to the resonance property, making a slow-wave structure. This slot disturbs the shield current distribution in the metallic ground plane, and this disturbance changes the frequency characteristics of the transmission line, modeled as inductance and capacitance. By employing circuit analysis theory, an equivalent resonance circuit of the slotted-ground-plane resonator is derived and lumped-element parameters are extracted. The lumped elements construct an LC tank, and then a stopband effect is obtained. In this paper, the structures of the DGS resonators with elliptical and patch-cut patches beside the transmission line are utilized to achieve a smaller size and narrower bandwidth. A comparative study is carried out to show the resonant frequency versus geometrical dimensions of the patches, targeting construction of a miniaturized resonator. Variations of the transfer characteristics on dimensional parameters of the patches are also studied.

2. DESIGNS OF THE COMPACT DGS RESONATOR

The circuits in this paper are designed and fabricated on a high frequency printed circuit board FR4 with a relative dielectric constant of 4.4 and a thickness of 0.8 mm. The dimensions of the H-shaped slot in the ground plane are determined so that the operating frequency of the conventional resonator (without the patches) is resonated at 3 GHz.

The schematic configuration of the H-slot resonator with the two identical elliptical patches is shown in Fig. 1. The two identical elliptical patches are symmetrically placed beside the transmission line. The horizontal and vertical axes of the elliptical patches are h and v. The mutual coupling effect between the patches and the ground plane can be treated as a parallel-plate capacitor, resulting in generation of the parasitic capacitance and an increase in the total capacitance. In our experiment, the outer parts of the elliptical patches are also cut so that the effective capacitance of the resonator increases and the resonant frequency reduces. A top-side layout of the patch-cut resonator is shown in Fig. 2.

3. RESULTS

Figure 3 shows the simulated results of the transfer characteristics of the conventional DGS resonator, and those for the elliptical patches when the occupying area and the horizontal-axis length (h) of the elliptical patch are fixed. The S-parameters and the surface current distribution in this paper are predicted by Ansoft HFSS. The resonant frequency of the conventional resonator (without the patches) is 3.03 GHz, and its 10-dB bandwidth at the stopband is 1.54 GHz. The resonant frequencies of the patched resonator are shifted down to 2.97 and 2.63 GHz when the length (v) of the vertical axis is tuned by 4 mm and 8 mm. Because the edges of the elliptical patches are close to the transmission line, the length v is limited by 8 mm.

Figure 4 shows dependence of the resonant frequency on the length (h) of the horizontal axis with $v = 8$ mm. As h increases, the rejection bandwidth and resonant frequency both decrease.

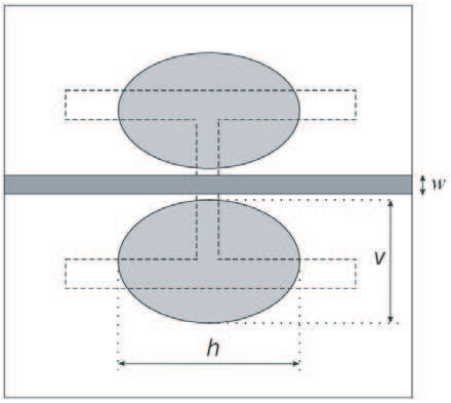

Figure 1: Schematic view of the DGS resonator with two identical elliptical patches.

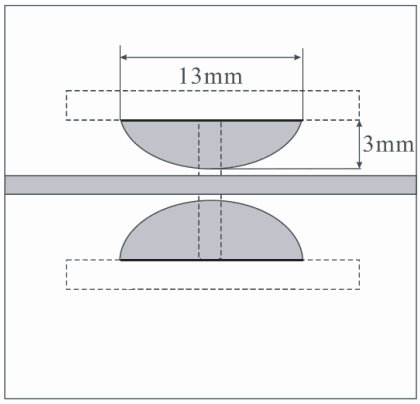

Figure 2: Layout of the patch-cut resonator.

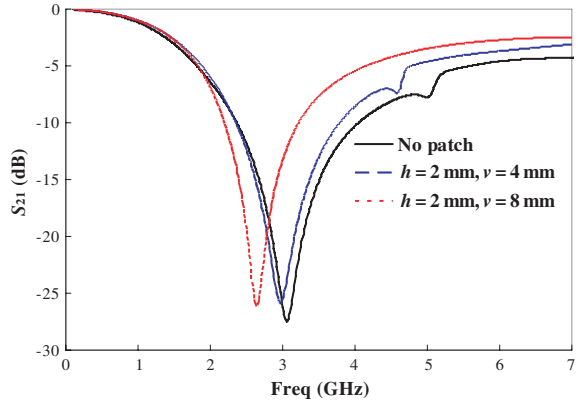

Figure 3: Simulated results of S_{21} of the conventional and patched resonators when the length v is tuned by 4 mm and 8 mm.

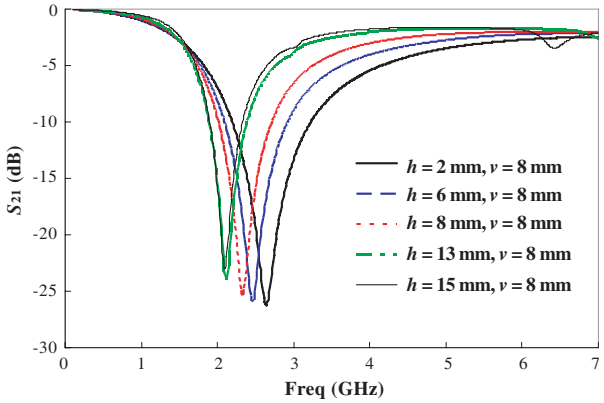

Figure 4: Dependence of the frequency response on the length h with $v = 8$ mm.

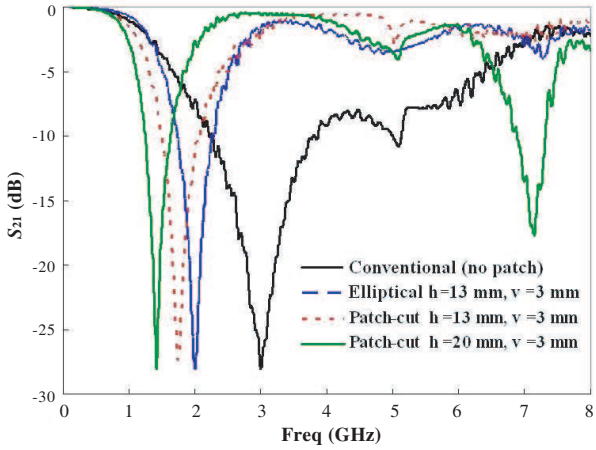

Figure 5: Comparison of measured S_{21} for the three configurations.

For the resonator with $h = 15$ mm, a harmonic stopband resonating at 6.46 GHz seems large, so (h, v) are chosen by (13, 8). As the physical area of the elliptical patches increases, the parasitic capacitance and the total capacitance of the patched resonators also increase.

Figure 5 is the comparison of the measured results of S_{21} for the conventional and patch-cut resonators. The resonant frequency of this patch-cut resonator with $h = 20$ mm and $v = 3$ mm is reduced to 1.44 GHz (the 10-dB bandwidths of 0.4 GHz), while the conventional resonator provides the corresponding resonant frequency of 3.00 GHz (the 10-dB bandwidth of 1.67 GHz).

The measured Q of the patch-cut resonator is 21.712 larger than that (7.628) of the conventional resonator.

4. CONCLUSION

The compact designs of the bandstop DGS resonator have been presented and demonstrated in this paper. By introducing two identical and parasitically coupled patches, the proposed resonators offer a significant reduction of the resonant frequency and the bandstop bandwidth. The advantages of the proposed resonators, including size miniaturization, wideband suppression of harmonics, and good frequency selectivity, all make the DGS resonator attractive for wireless communication applications.

REFERENCES

1. Zhang, R. and R. R. Mansour, "Novel digital and analogue tunable lowpass filters," *IET Microw. Antennas Propag.*, Vol. 1, No. 3, 549–555, Jun. 2007.
2. Yang, J. P., C. F. Gu, and W. Wu, "Design of novel compact coupled microstrip power divider with harmonic suppression," *IEEE Microw. Wireless Comp. Lett.*, Vol. 18, No. 9, 572–574, Sep. 2008.
3. Jeong, Y. C., S. G. Jeong, J. S. Lim, and S. W. Nam, "A new method to suppress harmonics using $\lambda/4$ bias line combined by defected ground structure in power amplifiers," *IEEE Microw. Wireless Comp. Lett.*, Vol. 13, No. 12, 538–540, Dec. 2003.
4. Jeong, Y. C. and J. S. Lim, "A novel frequency doubler using feedforward technique and defected ground structure," *IEEE Microw. Wireless Comp. Lett.*, Vol. 14, No. 12, 557–559, Dec. 2004.

Spatial Beam Splitter Design Using Fishnet-type Periodic Structure

N. C. Hsu, C. Y. Chin, and R. B. Hwang
Department of Electrical Engineering, National Chiao-Tung University
University Road 1001, Hsinchu, Taiwan 300, R.O.C.

Abstract— In this paper, we present a metamaterial-based beam splitter. Such a power splitter was made up of a metamaterial sandwiched by two metallic plates. The metamaterial consists of three-dimensional (3D) fishnet arranged in a two-dimensional square lattice. As is well known from Snell's law, the refracted wave tends to be normal to the interface when the wave is incident from a medium having effective refractive index much smaller than unity into the air region. We properly synthesize the metamaterial having effective refractive index smaller than unity. Furthermore, a line source made by a monopole was embedded in the metamaterial to excite four beams propagating toward four directions. In addition to the calculation of wave-propagating characteristics in the metamaterial, we also implemented a beam-splitting structure invoking the unique characteristic of the metamaterial. The electric-field radiating pattern was measured to prove its spatially beam-splitting characteristics.

Metamaterial is an artificially engineered structure which obtains its properties from its structure rather than directly from its composition. Generally, a metamaterial is synthesized by embedding specific inclusions, for example, periodic structures, in a host medium. The applications of metamaterial in waveguides and antennas designed were intensively developed [1, 2]. A metamaterial with zero-index was demonstrated to have the capability to narrow the far-field pattern associated with an antenna located within it. Besides, a matched zero-index slab could be used to transform curved wave fronts into planar ones [3]. The metamaterial made up of wire medium has been studied intensively, particularly on its effective refractive index, permittivity and permeability. Specifically, the structure composed of metallic mesh wires, which has very small electrical length in the period and wire thickness, can be characterized as a homogeneous medium with a low plasma frequency [4].

1. INTRODUCTION

This paper demonstrates a metamaterial-based beam splitter exciting four directional beams toward four sectors. Specifically, the multi-beam characteristic was due to the extraordinary properties of wave propagating in a metamaterial inserted in a radiating structure to be presented in this paper. Metamaterial possesses its property rather than its substance composition but structure. So far, a rich variety of metamaterials were invented, and their basic physical mechanism was studied thoroughly using experimental or theoretical way. To mention a few, the characteristics of electromagnetic wave propagating in anisotropic left-handed materials were investigated. The extraordinary phenomenon of negative group velocity in a metamaterial was investigated and its correlation to slanted stop-band was verified theoretically. Additionally, some researchers used the effective medium method to consider the metamaterial slab as a uniform medium. The single-mode approximation was employed to extract the effective parameters using the scattering parameters of the metamaterial slab.

2. STRUCTURE CONFIGURATION

In this research, we studied beam-splitting characteristics of a commonly used parallel-plate structure consisting of a metamaterial in microwave region. As shown in Fig. 1(a), this spatial beam splitter comprises a metamaterial sandwiched by two metallic parallel plates. The metamaterial is made up of fishnet arranged in a three-dimensional (3D) pattern like a jungle gym shown in Fig. 1(b), where the unit cell is depicted in Fig. 1(c). The number of unit cells along the x- and y-direction are both 5. Moreover, the periods (or lattice constant) along the x- and y-direction are denoted as d_x (14.2 mm) and d_y (14.2 mm), respectively. Each row or column of the 3D fishnet structure was constructed by the building block depicted in Fig. 1(d). The mesh wire was printed on the dielectric substrate RO4003 with relative dielectric constant 3.55 and thickness 0.508 mm using photo lithography and chemical etching process. The dimensions of the metal strip were attached in the figure. Notice that the same pattern was printed on both sides of the dielectric substrate. The metallic parallel plates are made by aluminum with thickness 1.6 mm. The distance between the parallel plates is denoted as h (12.8 mm). To excite propagating waves, a line source made from a coaxial probe was placed in the center of the metamaterial.

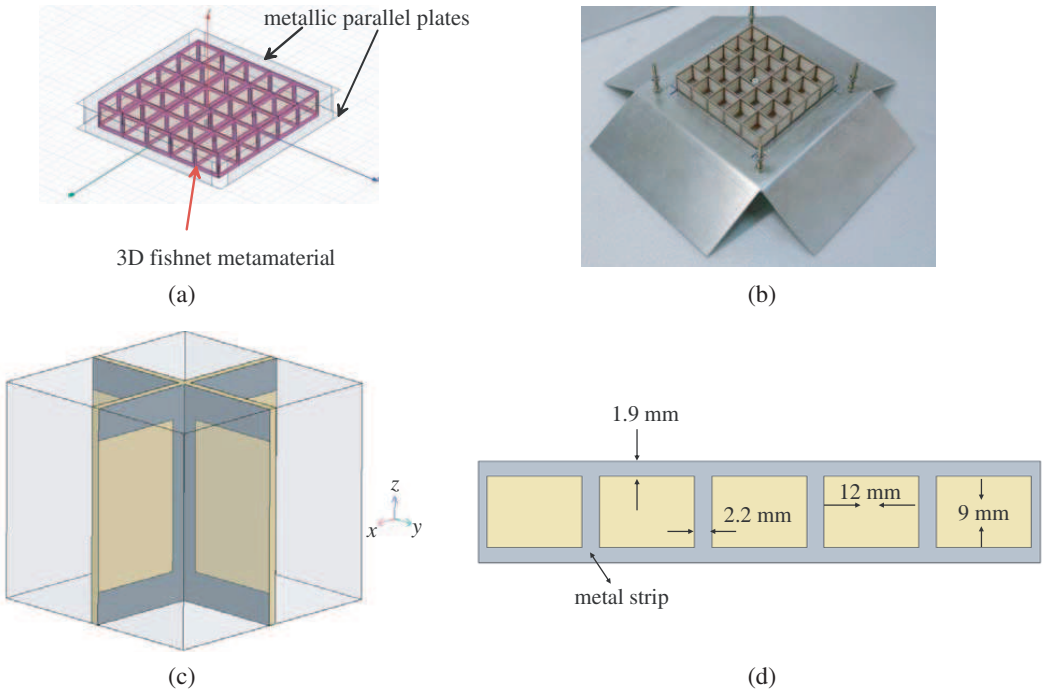

Figure 1: Structure conguration: (a) Metamaterial inside metallic parallel plates, (b) photo of the 3D fishnet metamaterial, (c) unit cell of the metamaterial, and (d) front view of the fishnet structure.

3. DISPERSION AND PHASE RELATIONS

As far as a periodic medium is concerned, the dispersion (or phase) relation of the eigen-wave supported in the medium is an important issue to be studied in detail. Returning to the unit cell of the metamaterial shown in Fig. 1(c), the top- and bottom-surface of the unit cell are perfect electric conductors. Since the metamaterial can be regarded as a 2D periodic structure, from the Floquet-Bloch theory the phase differences along the x and y directions are $k_x d_x$ and $k_y d_y$, respectively. After specifying all the boundary conditions on the unit cell, we are able to solve the eigen-value problem of the closed structure using finite-element method. Notice that the eigen-value (frequencies) obtained represents propagating modes for given phase constants k_x and k_y. After iterating the phase constants k_x and k_y, we determine the phase relation (the relationship among frequency, k_x and k_y) in the format of constant contour map.

In Fig. 2(a), we demonstrate the dispersion relation of the metamaterial medium. It is obvious to see the cutoff frequency is at 7 GHz, where wave starts to propagate after 7 GHz. Although numerous propagating modes exist and will appear at higher frequency range, we consider only the eigen-waves corresponding to the dominant mode supported in the medium.

In Fig. 2(b), the horizontal and vertical axes respectively represent the normalized phase constant (k_x and k_y) along the x- and y-axis. Because of the symmetry in the unit cell along the x- and y-axis, the phase relation also possesses the symmetry. The circles in colored lines with smaller radius are the normalized phase relations of wave in the metamaterial calculated from 7.2 GHz to 8.0 GHz with 0.2 GHz step, while the circle with larger radius corresponds to the parallel-plate region filled with the air for reference. Apparently the n_{eff} of the wave in the metamaterial is much smaller than that in the region without metamaterial. Notice that below 7 GHz no real frequency was found, it is due to the cutoff phenomenon (plasma-like property) of this structure.

4. POWER SPITTING CHARACTERISTIC

After understanding the phase relation of eigen-waves supported in the metamaterial, we are now in a good position to observe the physical picture of wave process in the beam splitting structure consisting of the metamaterial. We numerically simulated the overall beam-splitting structure, particularly for observing its electric-field and Poynting power distribution. By properly tuning the length of the monopole (line source) in the metamaterial, the wave propagating in the medium with effective refractive index smaller than unity was excited. As was explained previously, the refractive waves shall be normal to the metamaterial surface. To prove this conjecture, we calculated the

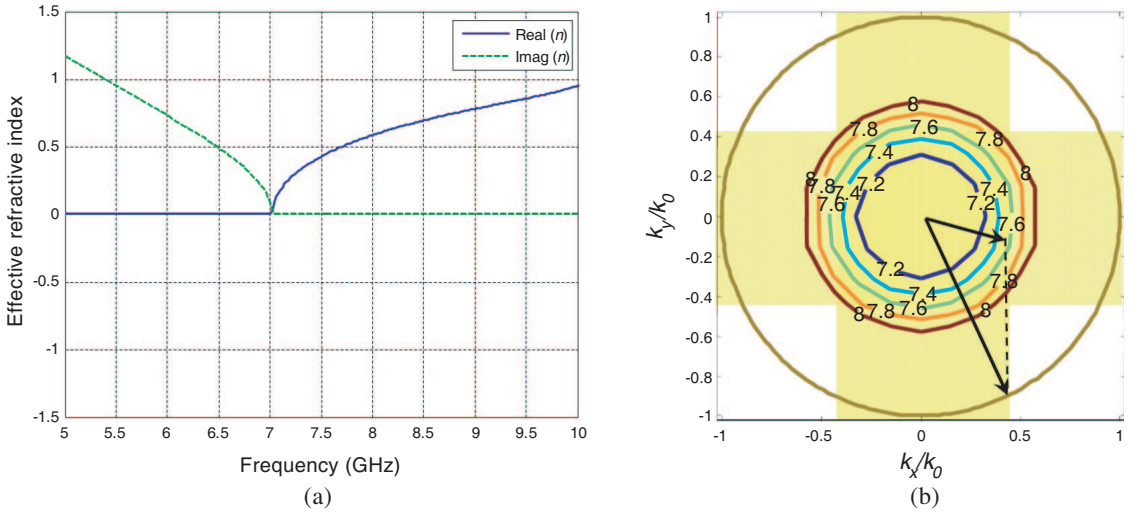

Figure 2: (a) Dispersion and (b) phase relations of waves propagating in the metamaterial.

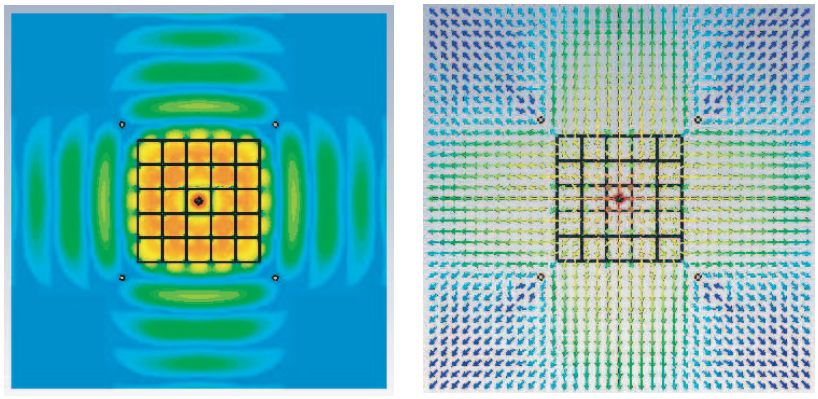

Figure 3: Electric-field strength in (a) the structure with metamaterial, and (b) Poynting vector distribution; all the results were evaluated at 7.5 GHz.

electric-field distribution and vectorized Poynting power in the parallel-plate region. As shown in Figs. 3(a) and 3(b), the refracted wave leaving the metamaterial tends to be perpendicular to the metamaterial surface in particular for those around the central part, while the others propagate at a small angle deviated from the normal direction.

5. CONCLUSION

In conclusion, we employed a metamaterial in a spatial beam splitter design. Through the rigorous calculation for the phase relation of waves propagating in metamaterials, we can synthesize a medium having an effective refractive index smaller than unity. Thus, the Poynting vectors leaving the metamaterial boundaries tend to be perpendicular to the interface between uniform medium and metamaterial. Accordingly, the input power can be equally distributed to four ways. In this research, the electric-field and Poynting power distribution were numerically investigated. Although such a metamaterial exhibiting its unusual properties was demonstrated in microwave region, it shall be able to be implemented in the THz frequency band where the metal strip retains the property of perfect electric conductor rather than plasma.

REFERENCES

1. Engheta, N. and R. W. Ziolkowski, "Introduction, history and fundamental theories of double-negative (DNG) metamaterials," *Metamaterials: Physics and Engineering Explorations*, Ch. 1, 5–41, IEEE Press, John Wiley & Sons, Inc., Jun. 2006.

2. Ziolkowski, R. W., "Propagation in and scattering from a matched metamaterial having a zero index of refraction," *Phys. Rev. E*, Vol. 70, No. 4, 046608, 2004.
3. Pendry, J. B., A. J. Holden, D. J. Robbins, and W. J. Stewart, "Low frequency plasmons in thin-wire structures," *J. Phys. Condens. Matter*, Vol. 10, No. 22, 4785–4809, 1998.
4. Garcia, N., E. V. Ponizovskaya, and J. Q. Xiao, "Zero permittivity materials: Band gaps at the visible," *Appl. Phys. Lett.*, Vol. 80, No. 7, 1120–1122, 2002.

Thermal Infrared Spectrum Property of Loaded Rock

Zhe Feng[1], **Shanjun Liu**[1], **Lixin Wu**[1, 2], **and Zhongyin Xu**[1]

[1]Institute for Geo-informatics and Digital Mine Research
Northeastern University, Shenyang 110004, China
[2]Academe of Disaster Reduction and Emergency Management
Beijing Normal University, Beijing 100875, China

Abstract— The phenomenon of satellite thermal Infrared anomaly before earthquake has been reported since the late 1980s. The reported abnormal rise of surface temperatures reaches 2–4°C, and occasionally higher than that. Usually, the anomaly appears from one month to several days before the earthquake. To study the mechanisms of Infrared anomaly, some infrared radiation detection experiments for rock fracture were carried out. The experimental results showed that the TIR anomaly precursors appeared before the fracture of rock samples. However which bands are suitable for detecting the stress and fracture of rock by the thermal infrared equipment is an open question by now. In this paper, we subjected several blocks of granite to uniaxial deviatory stress up to failure. We measured the IR spectrum variation from the rock samples over the 3–15 μm range by the TurboFT infrared spectroradiometer. The experimental result showed that the radiation strength variations were different in various bands, the radiation strength variations in band 3.6–3.7 μm and 8.5–10 μm were distinct along with the change of rock stress, but in other bands the radiation strength variations was not obvious or the relation between the infrared radiation and stress is not clear. It was possible to conclude that the bands 3.6–3.7 μm and 8.5–10 μm were the suitable bands for the detection of stress and fracture of rock.

1. INTRODUCTION

The former USSR seismologists V. I. Gorny [1] found a number of infrared anomalies appearing on the pre-earthquake satellite images in many medium-intensity earthquakes during studying Central Asia earthquakes. Subsequently, Qiang, Lin [2], etc. also found thermal infrared anomalies before some earthquakes based on the analysis on China's meteorological satellite thermal infrared data.

For finding out the internal mechanism of infrared anomaly before earthquake, Deng [4], Cui [5] and Geng [6] carried out the rock loaded experiment in the 1990s. It was found that the infrared radiation temperature, infrared spectral radiance and thermal images of rock changed with pressure significantly. The increment of infrared radiation temperature and spectral radiation of wet rock was greater than the dry rock when rock was compressed.

However, which bands are suitable for detecting the stress and fracture of rock by the thermal infrared equipment is an open question by now. So we select the granite as the rock samples to measure the rock infrared spectrum variation over the 3–15 μm range in rock compressed loading. The notable wave bands in which infrared radiation of rock changes with stress were analyzed, and the best possible band for the infrared detection of a rock fracture was also identified.

2. EXPERIMENT OF INFRARED SPECTRAL RADIANCE OBSERVATION IN ROCK LOADING PROCESS

2.1. Experimental Design

The granite blocks were processed into cuboids, the size of which was 7 cm × 7 cm × 14 cm or 15 cm× 15 cm ×5 cm, and the rock amount of two sizes is 7 and 2 respectively. A servocontrol loader, YAG-3000, was used to uniaxially load the samples. An infrared spectroradiometer, TurboFT, with spectral range of 2.55–16 μm and spectral resolution of 4 cm^{-1} is used. The infrared spectroradiometer was aligned in level with the rock sample and approximately 1.5m away from it. The loading was displacement controlled at 0.3 mm/min. In order to minimize environmental effects on the detection of infrared radiation from the rock surface, an alumin μm box with a rectangular detecting hole was used for enclosing both the rock sample and the load platform, and the infrared spectroradiometer detected the sample through the hole.

2.2. Spectral Data Processing and Analysis

In order to rapidly analyze and process the spectrum curves, the range of 2.55–16 μm is divided into many bands with an interval of 0.1 μm, and then the energy of every spectral curves in the

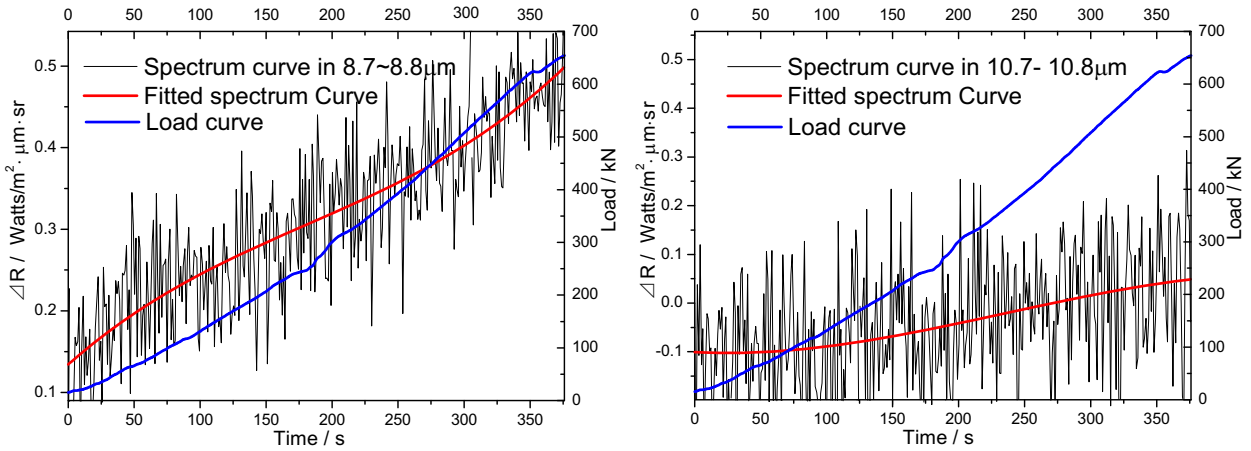

Figure 1: Variation of spectral radiation intensity of rock sample hg-4 with the load.

Table 1: Statistics results on correlation coefficient in band 8–14 μm.

Band range	Correlation coefficient			Band range	Correlation coefficient			Band range	Correlation coefficient		
(μm)	z45-1	hg-1	hg-4	(μm)	z45-1	hg-1	hg-4	(μm)	z45-1	hg-1	hg-4
8.0–8.1	0.15	0.15	0.42	10.0–10.1	0.76	0.65	0.65	12.0–12.1	0.17	0.38	0.27
8.1–8.2	0.31	0.18	0.46	10.1–10.2	0.75	0.71	0.71	12.1–12.2	0.18	0.38	0.26
8.2–8.3	0.51	0.27	0.50	10.2–10.3	0.65	0.63	0.61	12.2–12.3	0.15	0.37	0.24
8.3–8.4	0.64	0.34	0.53	10.3–10.4	0.63	0.63	0.52	12.3–12.4	0.19	0.39	0.21
8.4–8.5	0.73	0.42	0.58	10.4–10.5	0.59	0.60	0.48	12.4–12.5	0.25	0.38	0.17
8.5–8.6	0.82	0.54	0.64	10.5–10.6	0.55	0.58	0.46	12.5–12.6	0.23	0.43	0.16
8.6–8.7	0.92	0.72	0.74	10.6–10.7	0.54	0.56	0.42	12.6–12.7	0.20	0.45	0.27
8.7-8.8	0.97	0.88	0.85	10.7–10.8	0.48	0.54	0.39	12.7–12.8	0.20	0.40	0.36
8.8–8.9	0.93	0.85	0.83	10.8–10.9	0.43	0.51	0.41	12.8–12.9	0.14	0.39	0.38
8.9–9.0	0.91	0.83	0.84	10.9–11.0	0.39	0.50	0.34	12.9–13.0	0.14	0.36	0.28
9.0–9.1	0.94	0.88	0.84	11.0–11.1	0.32	0.47	0.35	13.0–13.1	0.17	0.36	0.23
9.1–9.2	0.89	0.79	0.75	11.1–11.2	0.29	0.44	0.33	13.1-13.2	0.16	0.33	0.20
9.2–9.3	0.88	0.73	0.80	11.2–11.3	0.27	0.44	0.32	13.2–13.3	0.19	0.34	0.19
9.3–9.4	0.86	0.79	0.81	11.3–11.4	0.25	0.45	0.39	13.3–13.4	0.14	0.34	0.13
9.4–9.5	0.93	0.84	0.83	11.4–11.5	0.26	0.43	0.28	13.4–13.5	0.15	0.34	0.15
9.5–9.6	0.94	0.86	0.85	11.5–11.6	0.24	0.43	0.28	13.5–13.6	0.15	0.35	0.15
9.6–9.7	0.90	0.83	0.82	11.6–11.7	0.24	0.39	0.28	13.6–13.7	0.09	0.28	0.11
9.7–9.8	0.85	0.65	0.67	11.7–11.8	0.20	0.42	0.29	13.7–13.8	0.12	0.31	0.13
9.8–9.9	0.74	0.51	0.50	11.8–11.9	0.18	0.40	0.30	13.8–13.9	0.12	0.32	0.09
9.9–10.0	0.87	0.67	0.70	11.9–12.0	0.17	0.40	0.28	13.9–14.0	0.12	0.27	0.09

interval band is summed as the radiation energy of the respective band. Thus the two atmospheric windows 3–5 μm and 8–14 μm are divided into 20 and 60 bands respectively.

In the spectral data processing, we express the spectral radiation intensity at beginning moment of loading as the benchmark $R(t_0)$, and the radiation intensity at the loading time t_i is expressed as $R(t_i)$, then radiation intensity variations $\Delta R(t)$ from t_0 to t_i can be obtained according to the Equation (1),

$$\Delta R(t) = R(t_i) - R(t_0) \tag{1}$$

Figure 1 is the data processing result of sample hg-4 in the band 8.7–8.8 μm and 10.7–10.8 μm according to the Equation (1). It can be found that the radiation strength variation is different in different band with the increase of load, and the variation trendy is also different. So we choose two indices, "correlation coefficient" and "signal — noise ratio" as the evaluating standard to determine the suitable bands for detecting of stress and fracture of rock.

1) Correlation coefficient. We make the correlation analysis between the spectral curve and

the load curve, and calculate the correlation coefficient between the two curves. The larger the correlation coefficient, the better the correlation degree of the two curves. Only the band in which the correlation coefficient is larger is the suitable for thermal Infrared detection of rock stress.

2) "Signal — noise ratio". From the Fig. 1, it can be found that spectrum curve is undulant due to the influence of environment and equipment conditions. In order to reflect the fluctuation degree of spectral radiation intensity in the loading process, spectrum curve is firstly fitted by using cubic polynomial fitting method, and then the standard deviation σ is obtained from the result of fitted curve, which represents the fluctuation degree of spectral radiation intensity. Then we choose the maximum variation of the fitted curve as $\Delta R_{\max}$, which represent the maximum variation of spectral radiation intensity induced by the loading of rock. Thus the index s/n (signal — noise ratio) can be obtained by the formula (2), which represents the signal strength of the infrared spectroradiometer induced by the loading of rock. Only the band in which the s/n is larger is the suitable for thermal Infrared detection of rock stress.

$$s/n = \Delta R_{\max}/\sigma \tag{2}$$

2.2.1. Calculation of Correlation Coefficient

Table 1 shows the statistics results on correlation coefficient of there samples in the band 8–14 μm. From the table we can find the correlation coefficients of three rock samples between spectral curve

Table 2: Statistics results on σ, $\Delta R_{\max}$ and s/n of three samples in band 8–11 μm.

Band range	z45-1			hg-1			hg-4		
(μm)	σ	$\Delta R_{\max}$	s/n	σ	$\Delta R_{\max}$	s/n	σ	$\Delta R_{\max}$	s/n
8.0–8.1	0.35	–0.10	–0.17	0.35	0.47	1.36	0.34	0.82	2.39
8.1–8.2	0.23	0.15	0.65	0.22	0.23	1.02	0.24	0.52	2.20
8.2–8.3	0.22	0.33	1.50	0.21	0.28	1.35	0.22	0.58	2.68
8.3–8.4	0.18	0.42	2.39	0.17	0.36	2.15	0.17	0.57	3.46
8.4–8.5	0.18	0.49	2.72	0.17	0.28	1.65	0.17	0.55	3.31
8.5–8.6	**0.12**	**0.50**	**4.17**	**0.11**	**0.32**	**2.91**	**0.12**	**0.46**	**3.83**
8.6–8.7	**0.07**	**0.56**	**8.00**	**0.08**	**0.29**	**3.87**	**0.09**	**0.49**	**5.44**
8.7–8.8	**0.05**	**0.60**	**12.00**	**0.05**	**0.30**	**5.88**	**0.06**	**0.50**	**8.47**
8.8–8.9	**0.06**	**0.51**	**8.50**	**0.05**	**0.28**	**5.19**	**0.06**	**0.35**	**6.25**
8.9–9.0	**0.08**	**0.64**	**8.00**	**0.07**	**0.30**	**4.41**	**0.06**	**0.41**	**6.41**
9.0–9.1	**0.06**	**0.46**	**8.36**	**0.05**	**0.31**	**6.89**	**0.05**	**0.24**	**4.80**
9.1–9.2	**0.08**	**0.61**	**7.82**	**0.06**	**0.34**	**5.67**	**0.06**	**0.26**	**4.13**
9.2–9.3	**0.08**	**0.55**	**6.63**	**0.07**	**0.36**	**5.14**	**0.06**	**0.32**	**5.61**
9.3–9.4	**0.07**	**0.46**	**6.87**	**0.06**	**0.37**	**6.17**	**0.06**	**0.37**	**6.38**
9.4–9.5	**0.06**	**0.4**	**7.02**	**0.05**	**0.29**	**5.69**	**0.06**	**0.34**	**6.18**
9.5–9.6	**0.06**	**0.42**	**7.50**	**0.05**	**0.27**	**5.87**	**0.05**	**0.30**	**5.77**
9.6–9.7	**0.06**	**0.53**	**8.41**	**0.04**	**0.21**	**5.00**	**0.05**	**0.26**	**5.53**
9.7–9.8	**0.09**	**0.41**	**4.56**	**0.08**	**0.28**	**3.50**	**0.07**	**0.26**	**3.71**
9.8–9.9	**0.11**	**0.26**	**2.36**	**0.10**	**0.28**	**2.80**	**0.09**	**0.21**	**2.33**
9.9–10	**0.07**	**0.38**	**5.43**	**0.06**	**0.27**	**4.50**	**0.07**	**0.27**	**3.86**
10.0–10.1	0.09	0.35	3.96	0.07	0.20	2.92	0.08	0.29	3.60
10.1–10.2	0.10	0.41	4.02	0.06	0.19	3.01	0.06	0.19	3.11
10.2–10.3	0.12	0.50	4.13	0.08	0.19	2.30	0.08	0.22	2.91
10.3–10.4	0.12	0.31	2.63	0.09	0.18	1.95	0.09	0.17	1.91
10.4–10.5	0.11	0.30	2.68	0.10	0.24	2.39	0.10	0.06	0.61
10.5–10.6	0.12	0.25	2.17	0.10	0.29	2.75	0.11	0.13	1.23
10.6–10.7	0.10	0.26	2.61	0.09	0.15	1.72	0.09	0.04	0.46
10.7–10.8	0.13	0.30	2.37	0.12	0.18	1.53	0.12	0.04	0.31
10.8–10.9	0.12	0.27	2.21	0.10	0.16	1.55	0.10	0.07	0.66
10.9–11.0	0.12	0.26	2.12	0.11	0.19	1.74	0.11	0.01	0.15

and the load curve are high in 8.5–10 μm range. The correlation coefficients are basically above 0.5. In the partial bands, the correlation coefficients are even higher than 0.8.

In the atmosphere windows of band 3–5 μm, four rock samples exist prominent correlation between spectral curve and the load curve in the range 3.6–3.7 μm, and the correlation coefficient is above 0.8. The coefficient correlation in other wave bands is relatively lower, mostly under 0.4.

2.2.2. Calculation of Signal-noise Ratio

We obtain the standard deviation σ and the maximum $\Delta R_{\max}$ of the fitted spectrum curve for calculation of s/n. Table 2 is the statistics results of three samples in band 8–11 μm. The statistics results show that the s/n is higher in band 8.5–10 μm range, but in other bands the s/n is lower. The statistics results in band 11–14 μm show the s/n are lower also. This indicates that in the band 8.5–10 μm the signal is strong and the noise is lower. Thus the band 8.5–10 μm is suitable for thermal infrared detection of rock stress.

In the atmosphere windows of band 3–5 μm, the statistics results show that the values of s/n are high in band 3.6–3.7 μm, but in other bands the s/n is lower.

3. CONCLUSIONS

1) In 3–5 μm range, the band that the spectral radiation intensity varies with the stress significantly is mainly in 3.6–3.7 μm. In this band, the correlation coefficients between spectral radiation intensity curve and load curve are more than 0.8. The correlation degree of the two curves is much higher. Simultaneously in the same band 3.6–3.7 μm the s/n is also high. Therefore the band 3.6–3.7 μm is the suitable band for thermal infrared detection of rock stress.

2) In 8–14 μm range, the correlation coefficients between spectral radiation intensity curve and load curve are above 0.5 in band 8.5–10 μm, especially in 8.7–9.1 μm and 9.4–9.7 μm the correlation coefficients are more than 0.8. On the other hand the values of s/n in 8.5–10 μm are also high. Therefore the band 8.5–10 μm is the suitable band for thermal infrared detection of rock stress.

Therefore, we can consider the band 3.6–3.7 μm and 8.5–10 μm as the detecting bands for the rock failure process in the atmosphere windows.

ACKNOWLEDGMENT

This work is supported by the National Natural Science Foundations of China (No. 50774017) and the Liaoning Province Technology Project (2008231001).

REFERENCES

1. Gorny, V. I., et al., "The earth outgoing IR radiation as an indicator of seismic activity," *Proc. Acad. Sci. USSR*, Vol. 30, No. 1, 67–69, 1988.
2. Qiang, Z. J., X. D. Xu, and C. G. Lin, "Satellite thermal infrared anomaly — The sign before earthquake," *Chinese Science Bulletin*, Vol. 35, No. 17, 1324–1327, 1990.
3. Qiang, Z. J., L. C. Kong, and Y. P. Wang, et al., "Earth's degasification, thermal Infrared anomaly and seismicity," *Chinese Science Bulletin*, Vol. 37, No. 24, 2259–2262, 1992.
4. Geng, N. G., C. G. Cui, and M. D. Deng, "Remote sensing detection of rock fracturing experiment and the beginning of remote rock mechanics," *Acta Seismologica Sinica*, Vol. 14, 645–652, 1992.
5. Cui, C. Y., M. D. Deng, and N. G. Geng, "Study on the features of spectrum radiation of rocks under different loading," *Chinese Science Bulletin*, Vol. 38, No. 6, 538–541, 1993.
6. Geng, N. G., C. X. Cui, and M. D. Deng, et al., "Remote sensing rock mechanics and its application prospects," *Progress in Geophysics*, Vol. 8, No. 4, 1–7, 1993.
7. Deng, M. D., C. X. Cui, and N. G. Geng, "Application of principle of remote sensing to earthquake prediction and the experimental results," *Earthquake Research in China*, Vol. 9, No. 2, 163–169, 1993.
8. Deng, M. D., C. X. Cui, and N. G. Geng, et al., "Study on the infrared waveband radiation characteristics of rocks," *Journal of Infrared and Millimeter Waves*, Vol. 13, No. 6, 425–430, 1994.

Generalized Maximum Efficiency Theory on Multi-stage Inductive Coupling

S. Bai[1, 2], D. C. Ng[2], E. Skafidas[2], and I. M. Y. Mareels[1]

[1]Department of Electrical & Electronic Engineering, The University of Melbourne, Australia
[2]Victoria Research Laboratory, National Information & Communication Technology Australia
The University of Melbourne, Victoria 3010, Australia

Abstract— Inductive coupled coils have been implemented to transmit power wirelessly for many applications such as micro-systems, RFID, and many biomedical implants. All these applications benefit from the distinct advantage to power these devices without any physical connections comparing to conventional energy transmission method using wires and connectors. Despite their different modes, geometries, coupling distances and power consumption requirements, they share the same rules which govern the design of the coils in order to achieve better efficiency of power transfer. The efficiency is even more critical in biomedical implants since any power loss due to the inefficient power link will finally be transformed into heat accumulated in the body which leads to safety problem. A novel feature on maximizing the efficiency is derived in this paper and it is further generalized to multi-stages inductive links which may be of special interest to be used in a high-density 1024-electrode epi-retinal prosthesis. Although multi-stage coupling include more coils with power loss internally, it is still possible to attain higher overall efficiency by improving each coupling stage individually whenever wireless connection is required. This is especially in the case of weakly-coupled coils where the air gap between transmitter and receiver is too large. Such multi-stages coupling configuration is also suitable for surgery in epi-retinal prosthesis.

1. INTRODUCTION

Wirelessly power transferring was proposed in early 20th century firstly by Nikola Tesla [1]. As the trend of integration continues in personal electronic devices (PED) recently, it also begins to demand a way of transmitting energy wirelessly in short distance, with high efficiency and high integration. Specifically, biomedical implants [2–4] have benefited largely from the advantages of powering the internal device(s) without any physical connections throughout the skin which may cause trauma and infections. Such wirelessly power supply technology also eliminates the need to use batteries for longer lifespan.

All these wireless power supply share the common feature by using inductive coupled coils to transmit power from a transmitter coil to another receiver coil. Despite their different coupling modes, geometries, coupling distances and power consumption requirements, they all follow the same law and follow the same rules during the design of coils. A lot of previous works has been done to study the inductive power links theoretically and experimentally [5, 6]. Here, we derive the links in a different way in which forward and backward transformation is utilized to analyze the sole role that the pair of inductive coupled coils play as the main part of the circuit. Then the condition for optimizing the efficiency for any inductive power link is derived and represented in a simple form (which is consistent with previous results). This result is further developed into a general form and applied into a multi-stage inductive coupling system which may be of interest in the implementation of wireless power supply in a high-density 1024-electrode epi-retinal prosthesis device.

2. QUALITY FACTOR OF INDUCTOR

Quality Factor is used frequently in many literatures in describing the quality of resonant system [7, 8]. It is one of the most important concepts to describe how lossy in terms of energy the system is, which is also directly related to efficiency of inductive coupling system. Although we are free to choose the way to describe the quality of the system at maintaining (or storing) energy during the operation over cycles, normally, one way is to measure the ratio of maximum stored energy in the system to the loss of energy per duration of certain time which is as below:

$$Q = \frac{W_{\text{max stored}}}{W_{\text{loss in one radian}}} = \frac{W_{\text{max stored}}}{\frac{P_{\text{avg}} \times T}{2\pi}} = \omega \frac{W_{\text{max stored}}}{P_{\text{avg}}} \tag{1}$$

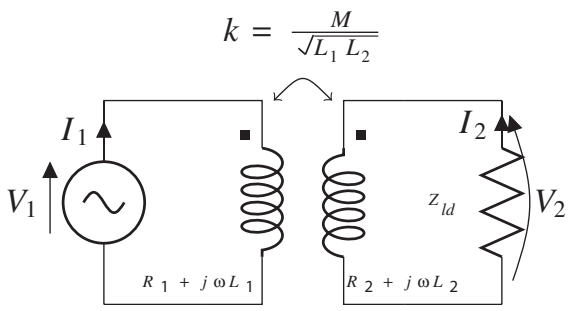

Figure 1: Connected pair of inductors with source and loader.

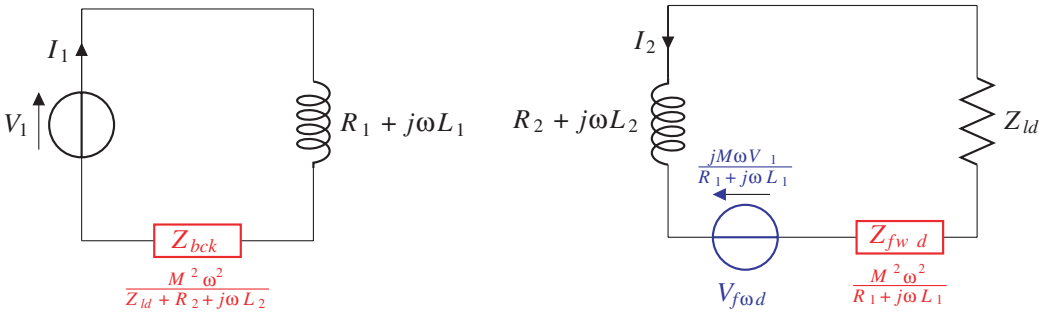

(a) Backward Transformationa

(b) Forward Transformation

Figure 2: Backward and forward transformation.

where the duration of time normally is taken as one radian[1] of an oscillation, and P_{avg} is the average power loss over a whole cycle. Another way is by specifying the decay rate Γ as in [6] which specify how quickly the stored energy will be gone. They result in the same Q value.

To accurately measure quality factor, both analytical and experimental methods can be used [7, 9, 10]. For an inductor carrying alternating current as a mean to store energy, by following the definition of quality factor according to Equation (1), quality factor of inductor is defined to be $Q = \omega \frac{W_{\text{max stored}}}{P_{\text{avg}}} = \frac{\omega L}{R}$. This definition for quality factor of inductor will be used throughout this paper.

3. FORWARD AND BACKWARD TRANSFORMATION

Another important aspect of an inductive coupled system is coupling coefficient k between two inductors as in Figure 1. It is defined as the ratio of mutual inductance between the two inductors to the geometric mean of their self inductances. Hence, it measures how closely these two inductors are coupled together and is a key figure in determining the efficiency of the power transmission. The square dots notation is used as a convention to denote the orientation of two inductors which affects the sign of mutual inductance. Two square dots residing at the same side of the inductors where currents enter means that, based on the directions of currents, the magnetic flux induced by current in each inductor are mutual constructive and the mutual inductance is therefore positive.

By applying Kirchhoff's circuit laws, V_1 can be solved and represented using I_1, arriving at

$$V_1 = R_1 I_1 + L_1 s I_1 + \frac{-M^2 s^2 I_1}{Z_{ld} + R_2 + L_2 s} = I_1 \left(R_1 + j\omega L_1 + \frac{M^2 \omega^2}{Z_{ld} + R_2 + j\omega L_2} \right) \tag{2}$$

By inspection at the equation, at left side of the pair of coils, the whole circuit looks as if there is another additional impedance connected (Z_{bck}) in series with the inductor, as in Figure 2(a). The additional impedance introduced into the primary side when there is a load connected with the secondary coil is

$$Z_{bck} = \frac{M^2 \omega^2}{Z_{\text{secondary}}} \tag{3}$$

[1]Such that value of Q is the number of cycles after which the system energy decays to $e^{-2\pi} \approx \frac{1}{535.5}$ of the initial value while there is no input of energy.

Here $Z_{\text{secondary}}$ should include the whole impedance in the secondary circuit introduced by the connected loader as well as the secondary inductor itself ($R_2 + j\omega L_2$).

Alternatively, if V_2 is solved and represented by I_2, another forward transformation can be obtained as:

$$\frac{-jM\omega V_1}{R_1 + j\omega L_1} = \left(Z_{ld} + R_2 + j\omega L_2 + \frac{M^2\omega^2}{R_1 + j\omega L_1} \right) I_2 \tag{4}$$

At left side of the equation, there is an equivalent source term coming from the primary side's source via inductive coupling. Additionally, like the backward transformation of impedance, there's forward transformed impedance relating with the impedance in the primary side as well, in the same form of backward transforming due to certain symmetry. The transformed source can be viewed as $jM\omega$ times unloaded current in the primary side. The direction of the source is shown in Figure 2(b). Together with the impedance introduced into the secondary side, V_{fwd} and Z_{fwd} are given as below:

$$Z_{fwd} = \frac{M^2\omega^2}{Z_{\text{primary}}} \tag{5}$$

$$V_{fwd} = jM\omega I_{1(\text{unloaded})} = \frac{jM\omega V_1}{R_1 + j\omega L_1} \tag{6}$$

4. MAXIMUM EFFICIENCY IN SINGLE STAGE INDUCTIVE COUPLING

In Figure 1 above, the circuit is simplified with a pair of inductive coupled coils only. However, in order to transfer more power into the secondary with a limited source, it's better to include a capacitor to resonate together with each coil at a certain frequency. The selection of resonant frequency can be dependent on the best lossless frequency band available for the usage of power transferring system, but theoretically any frequency will suffice as long as the condition for resonance is met.

Considering the single pair of inductive coupled coils with resonating capacitors as in Figure 3, for simplicity, series connection of capacitor is used. But parallel scheme can also be used and it can be easily converted to series connection under a given frequency and it will not affect the analysis on efficiency of the coupling. So the load impedance can be assumed to be a real number represented by R_{ld} where the imaginary part can be lumped into the resonant capacitor. All the other equivalent series resistance is lumped to R_1 or R_2 depending on which side they originate from.

In the whole circuit, there are basically three components which will dissipate energy, R_1, R_2 and R_{ld}. The efficiency of the inductive coupling η is simply defined as the ratio of power of the load P_{ld} to the input power at the primary coil. It can be further divided into two parts: η_1, being the ratio of power in the whole secondary side to the input power and η_2, being the ratio of power delivered into the load solely to the power in the whole secondary side. In the secondary side, the efficiency is easily calculated since the currents in R_2 and R_{ld} are the same. It is given by

$$\eta_2 = \frac{R_{ld}}{R_2 + R_{ld}} \tag{7}$$

To calculate η_1, by using backward transformation, the total power delivered to the secondary is equivalent to Z_{bck} as in Figure 2(a). If the capacitor C_{2s} is chosen such that it cancels the imaginary

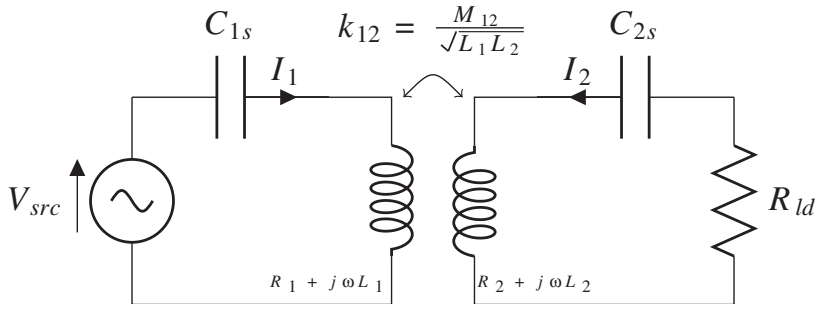

Figure 3: Single pair of power transferring inductive coils.

part $j\omega L_2$, i.e., at resonance, then Z_{bck} becomes a real number and maximized. And η_1 can be calculated similarly as

$$\eta_1 = \frac{\frac{M_{12}^2\omega^2}{R_2+R_{ld}}}{R_1 + \frac{M_{12}^2\omega^2}{R_2+R_{ld}}} \tag{8}$$

By substituting R_1, R_2 with the corresponding quality factors of two inductors, and M_{12} with the coupling coefficient, the final combined efficiency η is given and represented as

$$\eta = \eta_1\eta_2 = \frac{\alpha\beta}{(1+\beta)^2 + \alpha(1+\beta)} \tag{9}$$

where $\alpha = k^2Q_1Q_2$ is a **overall quality figure** describing the quality of inductors and the quality of coupling, it is the same figure κ/Γ as described in [6], and $\beta = \frac{R_{ld}}{R_2}$ is the load ratio with respect to secondary coil's loss. From the Equation (9) above, it can be easily found that the **overall quality figure** α only depends on the parameters of the pair of inductors, so it can be used as a figure of merit in describing the overall quality of the pair of inductor at transmitting power. It is easily found via inspection at the equation that the larger α is, the better efficiency.

By taking differential of η with respect to β, it can be found that η reaches its **maximum efficiency** value

$$\eta_{\max} = \left(\sqrt{1+\frac{1}{\alpha}} - \sqrt{\frac{1}{\alpha}}\right)^2 = \frac{\beta_{opt}-1}{\beta_{opt}+1} \quad \text{when} \quad \beta_{opt}^2 = 1+\alpha \tag{10}$$

Therefore, in order to obtain maximum power transmission efficiency, given a fixed pair of inductive coupling, the load should be designed such that the load ratio β with respect to the secondary coil's resistance is matched with the overall quality figure of the inductive coupling.

5. MAXIMUM EFFICIENCY IN MULTI-STAGES INDUCTIVE COUPLING

In order to generalize the calculations to a multi-stages inductive coupling, it would be easier to use the power ratio representation instead of using the resistance ratio. In the single-pair or single stage case, if the currents in both primary side and secondary side are calculated by backward and forward transformation, the power dissipated in R_1, R_2 and R_{ld} under maximum efficiency condition can be proved as:

$$\frac{P_{all}}{P_1} = \frac{P_{ld}}{P_2} = \beta_{opt} \tag{11}$$

where β_{opt} is defined by $\beta_{opt}^2 = 1+\alpha$ as before, and P_1, P_2 and P_{ld} correspond to the power of R_1, R_2 and R_{ld} respectively, while P_{all} is the sum of them.

Now, we consider multiple stages power transferring using inductive coupled coils as in Figure 4. There are n stages of inductive couples. Each pair is composed of two inductors which are numbered sequentially from left to right. There are $n+1$ capacitors which should be designed to resonate with the connected inductors in each sub-circuit at the same frequency as in the single stage case,

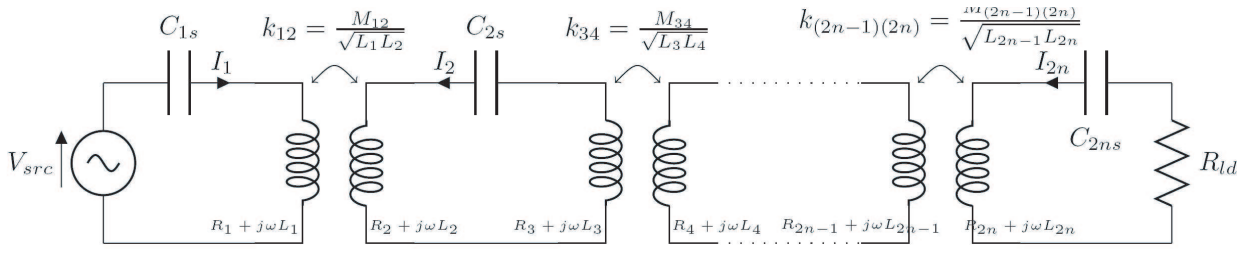

Figure 4: n stages of power transferring using inductive coils

given by

$$\begin{aligned} C_{1s} &= \frac{1}{\omega^2 L_1} \\ C_{2is} &= \frac{1}{\omega^2 (L_{2i} + L_{2i+1})}, \text{ for } i = 1, 2...n-1 \\ C_{2ns} &= \frac{1}{\omega^2 L_{2n}} \end{aligned} \tag{12}$$

If $Z_{bck_{2i}}$ is defined as the equivalent load seen by coil $2i$, and β_i is defined as the ratio of equivalent load seen by coil $2i$ to coil $2i$'s resistance, then the backward transformed impedances are

$$\begin{aligned} Z_{bck_{2n}} &= R_{ld} \\ Z_{bck_{2i}} &= R_{2i+1} + \frac{M^2_{(2i+1)(2i+2)}\omega^2}{Z_{bck_{2i+2}} + R_{2i+2}}, \text{ for } i = 0, 1, \ldots, n-1 \end{aligned} \tag{13}$$

and loader ratio for each stage is

$$\begin{aligned} \beta_n &= \frac{R_{ld}}{R_{2n}} \\ \beta_i &= \frac{Z_{bck_{2i}}}{R_{2i}}, \text{ for } i = 1, 2...n-1 \end{aligned} \tag{14}$$

When each stage achieves its maximum efficiency,

$$\beta^2_{opt_i} = 1 + \frac{M^2_{(2i-1)(2i)}\omega^2}{R_{2i-1}R_{2i}}, \quad \text{for } i = 1, 2, \ldots, n \tag{15}$$

Then we can have

$$\frac{P_{2i-1}}{P_{all_{n-i+1}}} = \frac{P_{2i}}{P_{all_{n-i}}} = \frac{1}{\beta_{opt_i}}, \text{ for } i = 1, 2...n \tag{16}$$

$$P_{all_{n-i+1}} = P_{all_{n-i}} + P_{2i} + P_{2i-1} \tag{17}$$

$$\frac{P_{all_{n-i}}}{P_{all_{n-i+1}}} = \frac{\beta_{opt_i} - 1}{\beta_{opt_i} + 1}, \quad \text{for } i = 1, 2, \ldots, n \tag{18}$$

where P_i is the power dissipated in coil i, P_{all_i} is the power delivered to the last i stages. So the combined maximum efficiency is

$$\eta = \frac{P_{all_0}}{P_{all_n}} = \prod_{i=1}^{i=n} \frac{P_{all_{i-1}}}{P_{all_i}} = \prod_{i=1}^{i=n} \frac{\beta_{opt_{n+1-i}} - 1}{\beta_{opt_{n+1-i}} + 1} = \prod_{i=n}^{i=1} \frac{\beta_{opt_i} - 1}{\beta_{opt_i} + 1} \tag{19}$$

which is exactly the product of maximum efficiency for each individual stages.

As an illustration, we consider the case when $n = 2$. Assuming that an inductive coupling system with two stages, and the overall quality α for each coupling is the same whose value is α_2. Comparing this with a system with one stage with overall quality α_1, in order to have a higher efficiency using two stages, the requirement for the overall quality figure for two stages case can be derived as:

$$\begin{aligned} &\sqrt{\eta_2\eta_2} \geqslant \sqrt{\eta_1} \\ \Longrightarrow &\left(\sqrt{1 + \frac{1}{\alpha_2}} - \sqrt{\frac{1}{\alpha_2}}\right)^2 \geqslant \left(\sqrt{1 + \frac{1}{\alpha_1}} - \sqrt{\frac{1}{\alpha_1}}\right) \\ &\Longrightarrow \alpha_2 \geqslant 2\alpha_1 \left(1 + \sqrt{1 + \frac{1}{\alpha_1}}\right) \approx 4\alpha_1 \text{ if } \alpha_1 \gg 1 \end{aligned} \tag{20}$$

Therefore, a two stages coupling system will be more efficient than a single stage, provided that the overall quality figure α for each stage is at least as four times as good as the overall quality for single stage.

Multi-staged inductive coupling is more difficult to design since more tuning capacitors are required for each sub-circuit reaching its resonant state. However, it does provide a promising means to bridge the large distant inefficient gaps between two coils with wired connections while wireless coupling is used whenever wires are not tolerable. Such hybrid concept of inductive coupled power transmission will be further tested in the retinal prothesis implant device.

REFERENCES

1. Tesla, N., U.S. Patent 1,119,732, 1914.
2. McDermott, H., "An advanced multiple channel cochlear implant," *IEEE Trans. Biomedical Engineering*, Vol. 36, No. 7, 789–797, 1989.
3. Kendir, G. A., W. Liu, R. Bashirullah, G. Wang, M. Humayun, and J. Weiland, "An efficient inductive power link design for retinal prosthesis," *2004 IEEE Int. Symp. Circuits and Systems*, 2004.
4. Kelly, S. K. and J. Wyatt, "A power-efficient voltage-based neural tissue stimulator with energy recovery," *2004 IEEE Int. Solid-state Circuits Conf.*, 228–524, 2004.
5. Ko, W. H., S. P. Liang, and C. D. F. Fung, "Design of radio-frequency powered coils for implant instruments," *Med. Biol. Eng. Comput.*, Vol. 15, 634–640, 1977.
6. Kurs, A., A. Karalis, R. Moffatt, J. D. Joannopoulos, P. Fisher, and M. Soljacic, "Wireless power transfer via strongly coupled magnetic resonances," *Science*, Vol. 317, No. 5834, 83, 2007.
7. Petersan, P. J. and S. M. Anlage, "Measurement of resonant frequency and quality factor of microwave resonators: Comparison of methods," *J. Appl. Phys.*, Vol. 84, No. 6, 3392–3402, 1998.
8. Lin, S. Y., E. Chow, S. G. Johnson, and J. D. Joannopoulos, "Direct measurement of the quality factor in a two-dimensional photonic-crystal microcavity," *Optics Letters*, Vol. 26, No. 23, 1903–1905, 2001.
9. Pereda, J. A., L. A. Vielva, A. Vegas, and A. Prieto, "Computation of resonant frequencies and quality factors of opendielectric resonators by a combination of the finite-differencetime-domain (FDTD) and Prony's methods," *IEEE Microwave and Guided Wave Letters*, Vol. 2, No. 11, 431–433, 1992.
10. Drozd, J. M. and W. T. Joines, "Determining Q using S parameter data," *IEEE Transactions on Microwave Theory and Techniques*, Vol. 44, No. 11, 1996.

The Computation of Coupling onto the Wires Enclosed in Cavity with the Apertures

Jianshu Luo, **Jiyuan Shi**, **and Xufeng Zhang**
Science College, National University of Defense Technology, Changsha 410073, China

Abstract— The paper proposes a new hybrid method based on MoM-GF (method of moments-Green's Function) and FWTLT (Full Wave Transmission line theory) to compute the coupling onto the wires enclosed in cavity with apertures when illuminated by a plane wave. The MoM-GF can accurately calculate the equivalent magnetic flux which will be used to get the electromagnetic field in cavity. Then, use the FWTLT to deal with the three- dimensional wire like structures enclosed in cavity. It is a fast and accurate method to analyze wire bunds by employing the cavity Green's function. Last, numerical results of the wire coupling current are provided.

Electromagnetic coupling and penetrations through an aperture on an infinite conduction plane have been widely researched. The coupling of the outer electromagnetic field onto the wires enclosed in cavity with an aperture is an important part of the EMI and EMC analyses. The mature methods for these problems include the EMT simulation algorithm based on the electromagnetic topology [1], calculations of the aperture coupling parameters using transmission line matrix [2], the ML-FMM to simulate aperture coupling in a rectangular cavity [3], the transfer function method in which the transmission lines in cavity be treated as antennas. When dealing with apertures on a complex enclosure, the traditional methods, such as the FDTD and ML-FMM, are quite slow with meaningless accuracy. The MOM-GF can guarantee calculation speed and enough accuracy. Reference [5] shows the accuracy of the MOM-GF by simulation of the electromagnetic coupling onto wires in cavity, and deals with the situation of multi-conductor transmission lines with simulations and analyses.

1. MODEL ESTABLISHMENT

Consider a rectangular cavity with an aperture illuminated by harmonic plane wave, the electromagnetic wave will penetrate through the aperture and act on the wires in the cavity. The incident wave is

$$\begin{aligned} \bar{H}^i &= \left(H_{ox}\hat{x} + H_{oy}\hat{y} + H_{oz}\hat{z}\right) e^{-j\bar{k}^i\bar{r}} \\ \bar{E}^i &= Z_0\bar{H}^i \times \hat{k}^i \end{aligned} \tag{1}$$

In which

$$\begin{aligned} \bar{k}^i &= -k_0\left[\left(\widehat{x}\cos\phi + \widehat{y}\sin\phi\right)\sin\theta + \widehat{z}\cos\theta\right] \\ H_{ox} &= Y_0(\sin\alpha\cos\theta\cos\phi + \cos\alpha\sin\phi) \\ H_{oy} &= Y_0(\sin\alpha\cos\theta\sin\phi - \cos\alpha\cos\phi) \\ H_{oz} &= -Y_0\sin\alpha\sin\theta \end{aligned} \tag{2}$$

k_0 is the wave number of the free space, $Z_0 = 1/Y_0$ is the impedance of the free space [5–7].

As shown in Figure 1, the wires are placed on the plane $z = -t$ $(0 < t < c)$ in the shape of a rectangular. The length of the rectangular is L, and the width d. Radius of the wires is r_a. The coordinates of the left and right endpoints of L_1 are $(x_1,\, y_1,\, -t)$ and $(x_1,\, y_1 + L,\, -t)$, while $(x_1 + d,\, y_1,\, -t)$ and $(x_1 + d,\, y_1 + L,\, -t)$ of L_2.

2. DISTRIBUTION OF THE INTERNAL FIELD

From the MoM-GF the distribution of the field inside the cavity is given by

$$\bar{H}^b\left(\bar{r}, \bar{r}'\right) = -j\omega\varepsilon \int_s \bar{\bar{G}}_{HM} \cdot \bar{M} ds \tag{3}$$

$$\bar{E}^b\left(\bar{r}, \bar{r}'\right) = -\int_s \nabla \times \bar{\bar{G}}_{HM} \cdot \bar{M} dvs \tag{4}$$

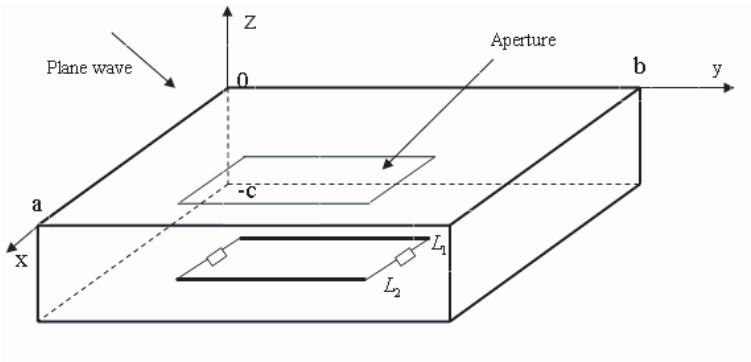

Figure 1: Coupling onto the wires enclosed in cavity with an aperture.

$\bar{M}$ is the equivalent magnetic current on the aperture. $\bar{\bar{G}}_{HM}$ is the first dyad Green's function of the rectangular cavity with the following representation

$$\bar{M} = \bar{E} \times \hat{n} = \bar{E} \times \hat{z} = \hat{x}E_x - \hat{y}E_y$$

$$\bar{\bar{G}}_{HM} = -\frac{1}{k_0^2}\hat{z}\hat{z}\delta\left(\bar{r} - \bar{r}'\right) + \sum_{m,n} \frac{2(2-\delta_{mn})}{abk_c^2 k_z \sin(k_z c)} \left[\bar{M}_{oe}(z+c)\bar{M}'_{oe}(0) + \bar{N}_{eo}(z+c)\bar{N}'_{oe}(0)\right]$$

in which

$$\begin{aligned}
\bar{M}_{oe}(z) &= (k_y \sin(k_x x)\cos(k_y y)\cos(k_z z)\hat{x} - k_x \cos(k_x x)\sin(k_y y)\cos(k_z z)\hat{y}) \\
\bar{N}_{eo}(z) &= \frac{1}{k_0}\begin{pmatrix} -k_z k_x \sin(k_x x)\cos(k_y y)\cos(k_z z)\hat{x} - k_z k_y \cos(k_x x)\sin(k_y y)\cos(k_z z)\hat{y} \\ +k_c^2 \cos(k_x x)\cos(k_y y)\sin(k_z z)\hat{z} \end{pmatrix} \\
k_x &= \frac{m\pi}{a}, \quad k_y = \frac{n\pi}{b}, \quad k_c^2 = k_x^2 + k_y^2 \\
k_z &= \begin{cases} \sqrt{k_0^2 - k_c^2}, & k_0^2 > k_c^2 \\ -j\sqrt{k_0^2 - k_c^2}, & k_0^2 < k_c^2 \end{cases}, \quad \delta_{mn} = \begin{cases} 1, & m = 0 \text{ or } n = 0 \\ 0, & \text{else} \end{cases}
\end{aligned} \tag{5}$$

The exterior scattered field can be expressed as the radiation caused by the equivalent magnetic current

$$\bar{H}^a\left(\bar{r}, \bar{r}'\right) = j\omega\varepsilon \int_s \bar{\bar{G}}_0 \cdot 2\bar{M} ds \tag{6}$$

where $\bar{\bar{G}}_0$ is the free space dyadic Green's function, and the factor 2 due to the image.

$$\bar{\bar{G}}_0\left(\bar{r}, \bar{r}'\right) = \left(\bar{\bar{I}} + \frac{1}{k_0^2}\nabla\nabla\right)\frac{e^{-jk_0|\bar{r}-\bar{r}'|}}{4\pi|\bar{r}-\bar{r}'|} \tag{7}$$

To solve the unknown current $\bar{M}$, we match the boundary condition that the tangential magnetic field across the aperture is continuous.

$$\hat{z} \times \left[\bar{H}^a\left(\bar{r}, \bar{r}'\right) + \bar{H}^i\right] = \hat{z} \times \bar{H}^b\left(\bar{r}, \bar{r}'\right), \; z = 0 \tag{8}$$

By using the Method of Moment (MoM), $\bar{M}$ could be calculated.

According to the dyad computation rules

$$\vec{\vec{A}} \cdot \vec{c} = \vec{a}\vec{b} \cdot \vec{c} = \left(\vec{b} \cdot \vec{c}\right)\vec{a}$$

$$\nabla \times \vec{\vec{A}} = \nabla \times \vec{a}\vec{b} = \left(\nabla \times \vec{a}\right)\vec{b} - \vec{a} \times \nabla\vec{b}.$$

Then substitute (5) into (3) and (4), the fields in the cavity should be:

$$\begin{aligned} H_x^b &= \sum_{m,n}\left[-\frac{jk_bY_bk_y}{k_z}A_{mn}-\frac{jk_zY_bk_x}{k_b}B_{mn}\right]\sin(k_xx)\cos(k_yy)\cos(k_z(z+c)) \\ H_y^b &= \sum_{m,n}\left[\frac{jk_bY_bk_x}{k_z}A_{mn}-\frac{jk_zY_bk_y}{k_b}B_{mn}\right]\cos(k_xx)\sin(k_yy)\cos(k_z(z+c)) \\ H_z^b &= \sum_{m,n}\frac{jk_c^2Y_b}{k_b}B_{mn}\cos(k_xx)\cos(k_yy)\sin(k_z(z+c)) \end{aligned} \tag{9}$$

$$\begin{aligned} E_x^b &= \sum_{m,n}\left[k_xA_{mn}-k_yB_{mn}\right]\cos(k_xx)\sin(k_yy)\sin(k_z(z+c)) \\ E_y^b &= \sum_{m,n}\left[k_xA_{mn}+k_yB_{mn}\right]\cdot\sin(k_xx)\cos(k_yy)\sin(k_z(z+c)) \\ E_z^b &= \sum_{m,n}-\frac{k_c^2}{k_z}A_{mn}\cdot\sin(k_xx)\sin(k_yy)\cos(k_z(z+c)) \end{aligned} \tag{10}$$

in which

$$\begin{aligned} A_{mn} &= \frac{2\left(\varepsilon_nk_yI_x^{mn}-\varepsilon_mk_xI_y^{mn}\right)}{abk_c^2\sin(k_zc)} \\ B_{mn} &= \frac{2\left(\varepsilon_nk_xI_x^{mn}+\varepsilon_mk_yI_y^{mn}\right)}{abk_c^2\sin(k_zc)} \\ I_x^{mn} &= \int_S M_x\left(x',y'\right)\sin\left(k_xx'\right)\cos\left(k_yy'\right)ds' \\ I_y^{mn} &= \int_S M_y\left(x',y'\right)\cos\left(k_xx'\right)\sin\left(k_yy'\right)ds' \end{aligned}$$

3. COUPLING ONTO WIRES INSIDE THE CAVITY

According to Taylor's research, the telegraph equation of a transmission line with finite length L and terminal loads Z_1 and Z_2 is [10–12]

$$\frac{d}{dy}\begin{bmatrix} V(y) \\ I(y) \end{bmatrix}+\begin{bmatrix} 0 & Z' \\ Y' & 0 \end{bmatrix}\begin{bmatrix} V(y) \\ I(y) \end{bmatrix}=\begin{bmatrix} V'_{s1}(y) \\ I'_{s1}(y) \end{bmatrix} \tag{11}$$

After analyses of the model as shown in Figure 2, we can get the source voltage distribution

$$\begin{aligned} V'_{S_1}(y) &= -j\omega\mu_0\int_{x_1}^{x_1+d}H_z^b(x,y,-t)\,dx \\ &= -j\omega\mu_0\int_{x_1}^{x_1+d}\sum_{m,n}\frac{jk_c^2Y_b}{k_b}B_{mn}\cos(k_xx)\cos(k_yy)\sin(k_z(-t+c))dx \\ &= \sum_{m,n}\frac{\omega\mu_0k_c^2Y_b}{k_b}B_{mn}\left[\sin(k_x(x_1+d))-\sin(k_xx_1)\right]\sin(k_z(-t+c))\cos(k_yy) \end{aligned} \tag{12}$$

and source current distribution

$$\begin{aligned} I'_{S_1}(y) &= -j\omega C'\int_{x_1}^{x_1+d}E_x^b(x,y,-t)\,dx \\ &= -j\omega C'\int_{x_1}^{x_1+d}\sum_{m,n}\left[k_xA_{mn}-k_yB_{mn}\right]\cos(k_xx)\sin(k_yy)\sin(k_z(-t+c))dx \\ &= -\sum_{m,n}j\omega C'\left[k_xA_{mn}-k_yB_{mn}\right]\left[\sin(k_y(x_1+d))-\sin(k_yx_1)\right]\sin(k_z(-t+c))\sin(k_yy) \end{aligned} \tag{13}$$

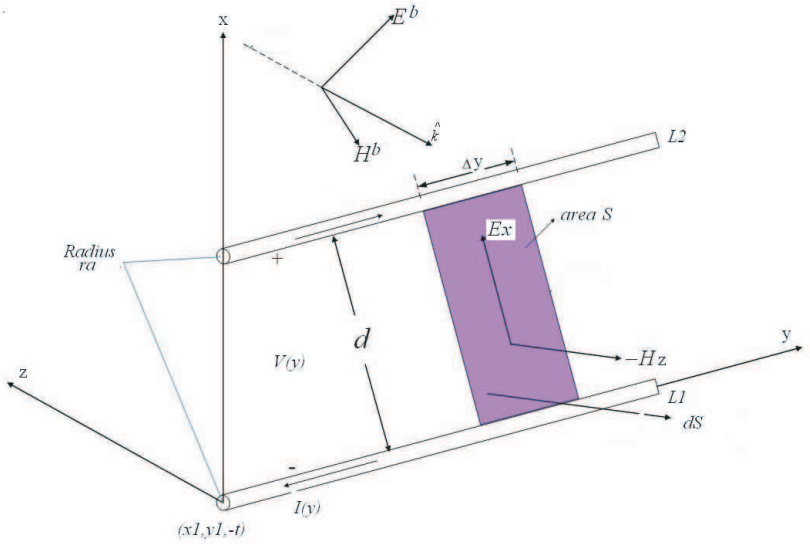

Figure 2: The wires enclosed in cavity with an aperture.

The BLT equation of the terminal current and voltage on the double wires is

$$\begin{bmatrix} I(0) \\ I(L) \end{bmatrix} = \frac{1}{Z_c} \begin{bmatrix} 1-\rho_1 & 0 \\ 0 & 1-\rho_2 \end{bmatrix} \begin{bmatrix} -\rho_1 & e^{jk_0L} \\ e^{jk_0L} & -\rho_2 \end{bmatrix}^{-1} \begin{bmatrix} S_1 \\ S_2 \end{bmatrix} \tag{14}$$

$$\begin{bmatrix} V(0) \\ V(L) \end{bmatrix} = \begin{bmatrix} 1+\rho_1 & 0 \\ 0 & 1+\rho_2 \end{bmatrix} \begin{bmatrix} -\rho_1 & e^{jk_0L} \\ e^{jk_0L} & -\rho_2 \end{bmatrix}^{-1} \begin{bmatrix} S_1 \\ S_2 \end{bmatrix}. \tag{15}$$

And the sources are

$$\begin{bmatrix} S_1 \\ S_2 \end{bmatrix} = \begin{bmatrix} \frac{1}{2}\int_{y_1}^{y_1+L} e^{jk_0y}\left[V'_{S_1}(y) + Z_cI'_{S_1}(y)\right]dy \\ -\frac{1}{2}\int_{y_1}^{y_1+L} e^{jk_0(L-y)}\left[V'_{S_1}(y) - Z_cI'_{S_1}(y)\right]dy \end{bmatrix} \tag{16}$$

which are equations of the induced current and induced voltage on wire terminals responding to the plane wave.

4. SIMULATIONS

Consider a rectangular cavity whose size is $0.3\,\mathrm{m} \times 0.3\,\mathrm{m} \times 0.12\,\mathrm{m}$. It's a common example in HFSS and FEKO to calculate the cavity's electromagnetic shielding effectiveness. In order to verify the program's reliability, the model will be simulated at first. When the aperture is a rectangle of the size $0.1\,\mathrm{m} \times 0.03\,\mathrm{m}$, the following figure can be got with the software Mathematica.

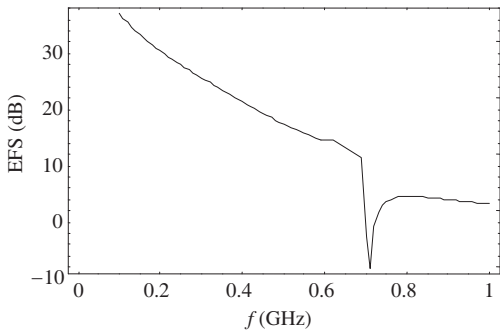

Figure 3: The EFS for a cavity with an aperture.

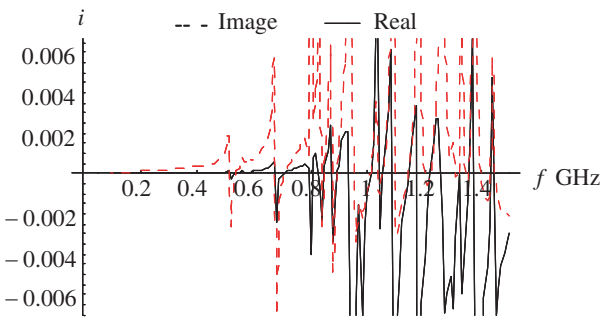

Figure 4: The induced current on one end of two-wire lines.

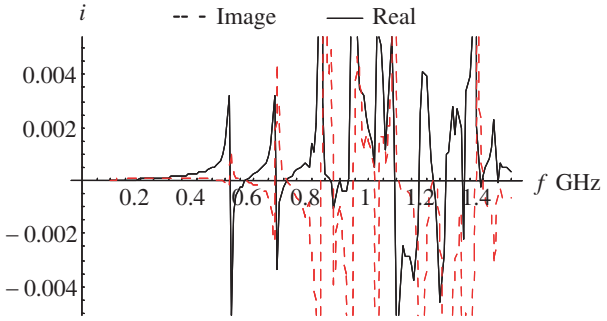

Figure 5: The induced current on the other end of two-wire lines.

The figure shows that 0.7 GHz is the resonant frequency, which corresponds with results from MLFMM and HFSS.

Then consider a cavity with double wires inside. The position of one terminal is (0.1, 0.1, −0.1) and the length of the wires is 0.15 m, the radius 0.0003 m. The distance between the two wires is 0.02 m. The simulation results of responses of the terminal loads are shown as follows:

5. CONCLUSION

Detailed calculations and analyses of coupling onto double wires enclosed in a cavity illuminated by plane wave have been got based on the MoM-GF and the BLT equation. MoM-GF can calculate the coupling onto the wire enclosed in a cavity. The BLT equation is applied when considering the double wires situation, which gives the coupling on any point along the wires. The simulations in this paper of the proposed model will provide theory support and data basis for future research.

ACKNOWLEDGMENT

The paper is supported by the National Science Foundation (approved number: 10871231) and the Chinese Postdoctoral Science Foundation (approved number: 20080431399).

REFERENCES

1. Kirawanich, P., S. J. Yakura, C. Christodoulou, et al., "Electromagnetic wave penetrating through apertures: comparison of electromagnetic topology technique with FDTD method," *IEEE Antennas and Wireless Propagation Letters*, Vol. 4, 151–154, 2005.
2. Kirawanich, P., D. Gleason, A. Cornell, et al., "Analysis of field through apertures by applying transmission line matrix method to electromagnetic topology simulations," AFRL-SR-AR-TR-05, 2005.
3. Konefal, T., J. F. Dawson, and A. C. Marvin, "A fast multiple mode intermediate level circuit model for the prediction of shielding effectiveness of a rectangular box containing a rectangular aperture," *IEEE Trans. on Electromagnetic Compatibility*, Vol. 47, No. 4, 678–691, 2005.
4. Tzeremes, G., P. Kirawanich, and N. E. Islam, "Transmission lines as radiating antenna in sources aperture interactions in electromagnetic topology simulations," *IEEE Antennas and Wireless Propagation Letters*, Vol. 3, 283–286, 2004.
5. Yang, T. and J. L. Volakis, "Coupling onto wires enclosed in cavities with apertures," *Electromagnetics Journal*, Vol. 25, No. 7–8, 655–678, 2005.
6. Mautz, J. R. and R. F. Harrington, "Electromagnetic transmission through a rectangular aperture in a perfectly conducting plane," Scientific Report, No. 10, prepared under contract F9268-73-C-0047 with the A. F. Cambridge Labs, Hanscom AFB, Feb. 1976.
7. Barkeshli, K. and J. L. Volakis, "Electromagnetic scattering from an aperture formed by a rectangular cavity recessed in a ground plane," *Journal of Electromagnetic Waves and Applications*, Vol. 5, No. 7, 715–734, 1991.
8. Tai, C. T., "Dyadic Green's functions in electromagnetic theory," *IEEE Press*, NJ, 1994.
9. Li, C. and F. Zhao, *Tutorial of Electrodynamics*, National University of Defense Technology Press, Changsha, 2005.
10. Tesche, F. M. and C. M. Butler, "On the addition of EM field propagation and coupling effects in the BLT equation," *Interaction Note 588*, Vol. 13, 1–43, 2003.

11. Baum, C. E., "Generalization of the BLT equation," *Proceedings of the 13th Zurich EMC Symposium*, 131–136, 1999.
12. Taylor, C. D., R. S. Scatterwhite, and C. W. Harrison, "The response of a terminated two-wire transmission line excited by a nonuniform electromagnetic field," *IEEE Trans. Antennas Propag.*, Vol. 13, No. 6, 987–989, 1987.

3D GL EMFH Modeling and Inversion for Leakless Auto EMS in Steel Metal Casting and Biomedical EM Instruments Design

Jianhua Li, **Ganquan Xie**, **Lee Xie**, **and Feng Xie**
GL Geophysical Laboratory, USA

Abstract— In this paper, we propose a new 3D GL ElectroMagnetic, Fluid, and Heat coupled GL EMFH modeling and AGILD inversion for steel and metal casting auto leakless EM stirring (EMS) and biomedical EM instruments design. We propose a novel GL cylindrical layer leakless cloak metamaterials to reduce the leakage of magnetic field and electric current lose. The 3D GL EM, fluid, heating, and crystal stress four processing models are consistently coupled in our 3D GL EM string method for the steel and metal casting. The method contains the macro and micro, periodic and non periodic steel and metal material structure and content analysis and simulation. It has wide application in steel and metal casting and biomedical EM instruments design. Based on our GL EMFH method and our GL cylindrical layer leakless cloak metamaterials, we develop a full automatical controlling and visualization electromagnetic stirring operation system for steel and metal casting.

1. INTRODUCTION

New AGILD EMS Electromagnetic Field Modeling was proposed in PIERS 2005 in Hongzhou and published in PIERS online in 2005 [1]. The "3D and 2.5D AGLID EMS Stirring Modeling in the Cylindrical Coordinate System has been presented in PIERS 2006 in MIT Cambridge and published in PIERS online in 2006 [2]. The 3D GL EM-flow-heat-stress coupled modeling," has been proposed in PIERS 2007 in Beijing and published in PIERS online in 2007 [3]. A GLEMFHS EMS Imaging System and Management of the Operation and Environment in the EM Stirring have presented in PIERS 2008 in Hangzhou. The A GLEMFCS Coupled Modeling and Inversion and GL EM Modeling for Electromagnetic Wave Propagation in Helix Pipe Crystals and Structures for Icing and Stirring were presented in PIERS 2008 in Cambridge. The Cylindrical Cloaking Material for MRI and XRAY and 3D GL Transform EM Modeling Simulation was presented in PIERS 2009 in Beijing. In this paper, we propose a GL EM, Fluid, and heat EMS modeling and AGILD EMS inversion for EMS design. and EMS automatic operation system for Steel, Aluminum and metal casting and biomedical EM instruments design. We propose and develop a new GL cylindrical layer EM metamaterials to reduce the leakage magnetic and electric current lose in the stirring.

The EM field in the stirring generates the Lorenz force. The volume distributed Lorenz force drives the steel and metal liquid rotationally to move under high temperature. Then the strain and stress occur in the solidification process. Therefore, it is necessary to consider EM, fluid, heat, stress coupled effective action in the EM stirring caster. In this paper, we propose a 3D Global and Local GL EM, flow, heat and stress coupled GL EMFH modeling [3] and AGILD EMFH inversion. The GL EMFH coupled modeling can consistent couple EM, fluid, temperature, and stress field in the EM stirring processes. The modeling can exactly calculate EM, fluid, temperature, and displacement coupled field in the stirring in the caster. The GL EMFHS coupled modeling and inversion have wide application in the EM stirring in the caster design and the automatic EMFH operation system, cloak,atmosphere, environment, geophysics, earth sciences and space sciences and engineering. in Steel and Aluminum and metal casting industrical engineering and Steel productive factor.

In common EMS simulation, Meir et al. [4] described Finite Element Method (FEM) for flow velocity in molten metals during electromagnetic stirring. The artificial boundary condition for the magnetic field is difficult. Some researcher used current, in stead of magnetic field, to avoid artificial boundary condition for the magnetic field. The complete EM, flow, heat, and stress coupled modeling is lack in the previous study. Our GL EMFH coupled modeling has advantages than the previous method in [4]. The inhomogeneous EM, flow, heat, and mechanical parameter domain are divided into several small sub domains. The parameters in the sub domain are isotropic or anisotropic piecewise constant. The initial Global EM, flow, temperature, and displacement field are updated successively by the local scattering field in each sub domain. When all sub domains are scanned, the GL coupled EM, flow, heat, and stress field are obtained. In the GL EMFH method, there is no artificial boundary and error boundary reflection. There is no big matrix needs to be

solved. The coordinate singularity in the $\rho = 0$ is removed. The GL EMFHS coupled modeling is accurate, fast, consistent, and stable. The GL EMFHS coupled modeling has advantages over FEM and Finite Difference method (FD).

The plan of this paper is as follows. The introduction is described in Section 1. The GL EMFH modeling and agild inversion is described in Section 2. In Section 3, we propose the GL cylindrical layer leakless cloak metmaterial to reduce leakage of the magnetic field. The simulations of the GL EM fluid heat GLEMFH automatic controlling leakless EM stirring system is presented in Section 4. In Section 5, we propose the theory of the EM wave field through the GL cylindrical layer leakless cloak. In Section 6, we describe the history and advantages. Finally, we conclude this paper in Section 7.

2. GL EMFH MODELING AND AGILD INVERSION

The novel Global and Local field modeling and inversion is proposed in [5, 6], the GL EMFHS modeling has been proposed in [3, 5], it is briefly described here.

2.1. 3D GL Iteration for Solving the EM, Fluid, and Heat Coupled Nonlinear Equations

We use GL EM, fluid, and heat coupled modeling [3] to solve the following EM, Navier Stocks fluid, heat equations.

$$\begin{aligned} &\nabla \times \frac{1}{(\sigma + i\omega\varepsilon)} \nabla \times H^{(n)} + \left(\nabla \times \mu V^{(n-1)} \times H^{(n)} \right) = Q_M, \\ &- \eta \Delta V^{(n)} + \rho \left(V^{(n-1)} \cdot \nabla \right) V^{(n)} + \nabla p = J^{(n)} \times \mu H^{(n)} - \beta \rho T^{(n-1)} g, \\ &\Delta T^{(n)} - q \left(V^{(n)} \cdot \nabla \right) T^{(n)} = h \left(E^{(n)}, H^{(n)}, V^{(n)} \right) \end{aligned} \tag{1}$$

2.2. AGILD EMFH Coupled Nonlinear Inversions

The AGILD [2, 7] and GL Metre Carlo EM, fluid and heat coupled nolinear inversions [6] are used to EM Stirring materials and construction design and automatic controling EM stirring operation and visualizing displaying monitoring.

3. THE GL CYLINDRICAL LAYER LEAKLESS CLOAK META MATERIALS

For overcoming the weakness of the leakage of the magnetic and electric current lose, we proposed the GL layer cloak metamaterial to coat the EMS surface.

3.1. GLC Cylindrical layer leakless Cloak Anisotropic Material for EM Stirring and Biomedical Instrument

On the cylindrical layer domain, $\Omega_{\text{GLC}} = \rho_1 \leq \rho \leq \rho_2$, by the GL EM modeling and inversion [5, 6], we propose an anisotropic metamaterial as follows:

$$\begin{aligned} [D]_{\text{GLC}} &= \text{diag}\left[\bar{\varepsilon}_{\text{glc}}, \bar{\mu}_{\text{glc}}\right], \\ \bar{\varepsilon}_{\text{glc}} &= \text{diag}\left[\varepsilon_{\rho,\text{glc}}, \varepsilon_{\phi,\text{glc}}, \varepsilon_{z,\text{glc}}\right] \varepsilon_b, \\ \bar{\mu}_{\text{glc}} &= \text{diag}\left[\mu_{\rho,\text{glc}}, \mu_{\phi,\text{glc}}, \mu_{z,\text{glc}}\right] \mu_b, \\ \varepsilon_{\rho,\text{glc}} &= \mu_{\rho,\text{glc}} = \frac{\rho_2^2 - \rho^2}{\rho_2^2}, \\ \varepsilon_{\phi,\text{glc}} &= \mu_{\phi,\text{glc}} = \frac{\rho_2^2}{\rho_2^2 - \rho^2}, \\ \varepsilon_{z,\text{glc}} &= \mu_{z,\text{glc}} = \frac{\rho_2^2 - \rho_1^2}{\left(\rho_2^2 - \rho^2\right)^2} \rho_2^2 \end{aligned} \tag{2}$$

The Ω_{GLC} is called as GL cylindrical layer cloak, the materials, $[D]_{\text{GLC}} = \text{diag}[\bar{\varepsilon}_{\text{glc}}, \bar{\mu}_{\text{glc}}]$ in (2), are the anisotropic GL cylindrical layer cloak metamaterials. Where the subscript GLC means the GL cylindrical layer, the symbol diag denotes the diagonal matrix, $[D]_{\text{GLC}}$ is 6×6 diagonal matrix, $\bar{\varepsilon}_{\text{glc}}$ is 3×3 dielectric diagonal matrix in the cylindrical layer, the subscript c denotes the cylindrical layer, $\bar{\mu}_{\text{glc}}$ is 3×3 magnetic permeability diagonal matrix in the cylindrical layer, $\varepsilon_{\rho,\text{glc}}$ is the relative dielectric cloak metamaterial which is formulated by the fourth sub equation in (2), the subscript index ρ, glc denotes the dielectric is in ρ direction and in the cylindrical

layer, $\varepsilon_{\phi,\mathrm{glc}}$ is the relative dielectric cloak metamaterial in ϕ direction and in the cylindrical layer which is formulated by the fifth sub equation in (2), The $\mu_{\rho,\mathrm{glc}}$ is the relative permeability cloak metamaterial which is formulated by the fourth sub equation in (2), ε_b is the basic dielectric in free space, $\varepsilon_b = 0.88541878176\ldots\times 10^{-11}\,\mathrm{F/m}$, μ_b is the basic magnetic permeability in free space, $\mu_b = 1.25663706\times 10^{-6}\,\mathrm{m\ kg\ s^{-2}A^{-2}}$, other symbols in (2) have similar explanation.

The EM wavefield of sources located inside EM stirring or Biomedical instruments is completely absorbed by the cylindrical layer and never reaches the outside boundary, ρ_2 of the cylindrical layer, also, the EM wavefield excited in stirring and Bioedical instruments is not disrupted by the cylindrical layer cloak. The cylindrica layer metamaterial, in Equation (2), cloaks and protects the Biomedical instrument and stirring and annihilate the exterior wavefiled, which can also be useful for making a complete absorption boundary condition to truncate infinite domain in numerical simulation.

4. THE SIMULATIONS OF THE GL EM FLUID HEAT AUTOMATIC CONTROLLING LEAKLESS EM STIRRING SYSTEM

Our GL EMFHS coupled modeling has been used to calculate the EM field, flow velocity, pressure, temperature, displacement, strain, and stress field for some EM stirring. The outer radius of the stirring is 500 mm, the internal radius is 350 mm, and it is divided into 6 sectors. The electric current has inverse direction for any adjoining two sectors. The thick of the copper tube is 3.5 mm. The conductivity, ssteel, of the carbon steel is 749617 S/M, the conductivity, scopper, of the copper tube is 3.16628779×10^7, the conductivity, sstirring, of the stirring is 369417 S/M. The steel liquid is in inside of the copper tube. The stirring surrounds the copper tube and is outside of the tube. The length of the stirring is 250 mm. The density of the steel, ρ_{steel}, is $2.38\times 10^3\,\mathrm{kg\ m^{-3}}$. The viscosity, η, of the steel fluid is $1.8\times 10^{-3}\,\mathrm{kg\ m^{-1}s^{-1}}$. The thermal conductivity of the steel, ksteel, is 28 Btu/(hr·Ft·F). The Young's modulus of the steel is $200\times 10^9\,\mathrm{N/M^2}$. The frequency is 4 Hz. The input electric current density intensity is $1\,\mathrm{A/mm^2}$. The GL EMFHS coupled modeling calculates EM, flow velocity, temperature, displacement, strain, and stress field. Due to the page limitation, we present the electric current density and the magnetic flux density distribution on the horizontal section at $Z = 0.25$ M in the Figures 4–6. Before installation of the stirring without steel flow, the factor did measure the magnetic flux intensity. By using digit magnetic GAUSS meter, the measurement value of the magnetic flux intensity at center of the stirring is 1300 Gauss. By using our GL EMFHS coupled modeling simulation, the evaluated magnetic flux intensity is 1308 Gauss at the center of the stirring. The simulation results of the stirring in steel caster and in uninstallation show that the GL EMFHS modeling is accurate, fast, consistent, and stable. To compare the EM field in Figures 4–6 with the EM field in the corresponding figures in paper [2], The GL EMFHS modeling accurately calculates the coupled effect in the EM field in Figures 4–6. The EM wavefield propagation in the cylindrical stirring or Biomedical Instruments are presented in Figures 1–3. In the Figure 1, at time step $50dt$, the vertical magnetic flux using GL EMFHS modeling. In the Figure 2, at time step $100dt$, the vertical magnetic flux using GL EMFHS modeling. In the Figure 3, at time step $150dt$, the vertical magnetic flux using GL EMFHS modeling. These simulation figures obviously show that the GLC cylindrical layer leakless cloak materials reduce the leakage of the magnetic field. The GLC cylindrical layer leakless cloak materials are proposed by AGILD and GL metre Carlo inversion.

5. THEORY OF THE CYLINDRICAL LAYER CLOAK

5.1. Theory of the EM Wave Field through the GL Cylindrical Layer Leakless Cloak

We propose the theory of the GL cylindrical layer cloaks for leakless EMS, metal casting and biomedical instrument in this section.

Statement 1: Let domain Ω_{GLC} and the metamaterial D_{GLC} in (2) be GL cylindrical layer cloak, and ε=ε_{b}, $\mu = \mu_b$ be basic permittivity and permeability, respectively, inside of the stirring $|\vec{r'}| < R_1$ and outside of the GLC cloak $|\vec{r'}| > R_2$, we have the following statements: (1) provide the local source is located inside of the stirring, $|\vec{r}_s| < R_1$, the excited EM wave field inside of the stirring never be disturbed by the GLC cloak; (2) provide the local source is located inside of the stirring and cylindrical layer, Ω_{GLC}, $|\vec{r}_s| < R_2$, the EM wave field is vanished outside of the cylindrical layer GLC cloak and is always propagating and going to the boundary $r = R_2$ and before $r = R_2$.

5.2. There Exists No Maxwell EM Wavefield Can Be Excited by Sources in Free Space Which Is Outside of the Cylindrica Layer Cloak

Statement 3: Suppose that a 3D anisotropic inhomogeneous GLC cylindrical layer cloak domain separates the whole 3D space into three sub domains, one is the GLC cylindrical layer cloak domain Ω_{GLC} with the cloak material (2); the second one is the EMS stirring; other one is the free space outside of the GLC cloak. If the Maxwell EM wavefield excited by a point source or local sources inside of the stirring is vanished outside of the GL cylindrical layer Ω_{GLC}, then there exists no Maxwell EM wave field can be excited by the sources in Free space outside the Ω_{GLC}.

The statement 2 is proved by the GL method in author's paper [12].

6. HISTORY AND DISCUSSIONS

6.1. History

A double layer cloth phenomenon to prevent the GILD inversion [7, 8] detection has been observed in paper [9] in 2001 which is published in SEG online *http://segdl.org/journals/doc/SEGLIB-home/dci/searchDCI.jsp*. The double layer cloth to cloak fly from the exterior wave GILD detection is obvious around the fly which is shown in Figure 10 in [13]; the double cloth around the bar is shown in Figure 11 in [13]. We developed a novel and effective Global and Local field (GL) modeling and inversion [5, 6] to study the meta materials, periodic photonic crystals and condense physics etc. wide physical sciences. 3D GL EM modeling and inversion [5, 6] and computational mirage have been presented in PIERS 2005 and published in proceeding of PIERS 2005 in Hangzhou, which can be downloaded from *http://piers.mit.edu/piersproceedings/piers2k5Proc.php*, please see the references of [12, 13]. We developed 3D FEM for the elastic mechanics first in China in 1972 [10] and discovered the superconvergence of the 3D cubic curve isoparameter element first in the world [11]. The 3D isoparameter element can be used for making arbitrary curve cloak [10]. We deeply to know the merits and drawbacks of FEM. The GL method overcomes the drawbacks of FEM and FD methods. The history of development of FEM and GILD and GL method has been described in [11] and reference of [12, 13]. The 3D and 2D GL parallel software is made and patented by GLGEO. The GL modeling and its inversion [3, 5] and GL EM quantum field modeling are suitable to solve quantization scattering problem of the electromagnetic field in the dispersive and loss metamaterials, cloaks and more wide anisotropic materials. We have been doing research work on the EM stirring and metal casting and biomedical instruments simulation and design since 2005. We find that the GL cylindrical layer cloak has relationship with EM stirring, metal casting and biomedical instrument design.

6.2. Advantages of the GL Method

These simulation Figures 1–9 obviously show that the GLC cylindrical layer leakless cloak materials reduce the leakage of the magnetic field. The GLC cylindrical layer leakless cloak materials are proposed by AGILD and GL metre Carlo inversion. The GL EM modeling is fully different from

Figure 1: (color online) At time step $50dt$, the vertical magnetic flux using GL EMFHS modeling. The GL cloak layer coating materials by AGILD and GL metre Carlo inversion reduce the leakage of the magnetic field.

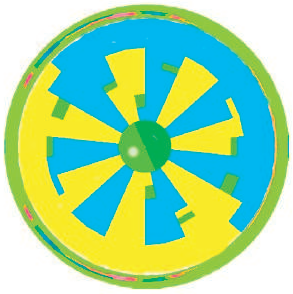

Figure 2: (color online) At time step $100dt$, the vertical magnetic flux using GL EMFHS modeling. The GL cloak layer coating materials by AGILD and GL metre Carlo inversion reduce the leakage of the magnetic field.

Figure 3: (color online) At time step $150dt$, the vertical magnetic flux using GL EMFHS modeling. The GL cloak layer coating materials by AGILD and GL metre Carlo inversion reduce the leakage of the magnetic field.

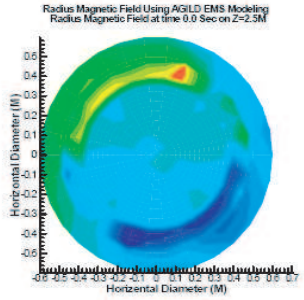

Figure 4: (color online) At time step $50dt$, the radius magnetic flux using GL EMFHS modeling.

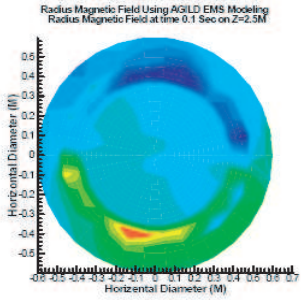

Figure 5: (color online) At time step $100dt$, the radius magnetic flux using GL EMFHS modeling.

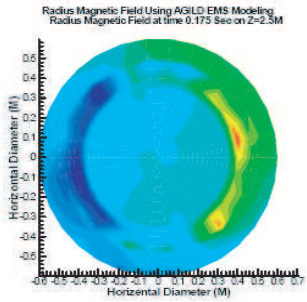

Figure 6: (color online) At time step $150dt$, the radius magnetic flux using GL EMFHS modeling.

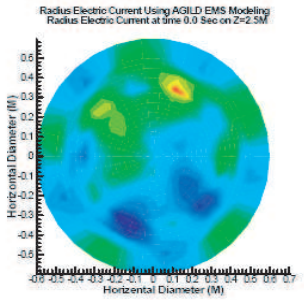

Figure 7: (color online) At time step $50dt$, radius electric current. using GL EMFHS modeling.

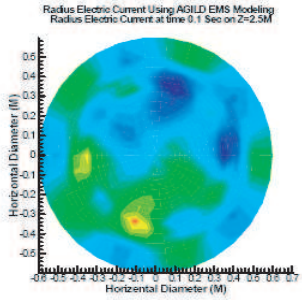

Figure 8: (color online) At time step $100dt$, radius electric current. using GL EMFHS modeling.

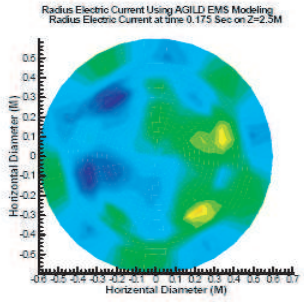

Figure 9: (color online) At time step $150dt$, radius electric current. using GL EMFHS modeling.

FEM and FD and Born approximation methods and overcome their difficulties. There is no big matrix equation to solve in GL method. Moreover, it does not need artificial boundary and absorption condition to truncate the infinite domain. Born Approximation is a conventional method in the quantum mechanics and solid physics. However, it is one iteration only in whole domain which is not accurate for high frequency and for high contrast materials. The GL method divides the domain as a set of small sub domains or sub lattices. The Global field is updated by the local field from the interaction between the global field and local subdomain materials successively. Once all subdomain materials are scattered, the GL field solution is obtained which is much more accurate than the Born approximation. GL method is suitable for all frequency and high contrast materials. When the size of the sub domain is going to zero, the GL method is convergent and has $O(h^2)$ if the trapezoidal integral formula is used, moreover, is has super convergence $O(h^4)$ if the Gaussian integral formula is used [10]. The GL method has double capabilities of the theoretical analysis and numerical simulations that has been shown in this paper.

7. CONCLUSION

The simulations of the EM wave propagation through the GL cylindrical layer leakless stirring and biomedical instruments obviously show that the GL cylindrical layer cloak can reduce the leakage of the EM field. The simulations also show that the EM wavefield speed is slower that the light speed in the GL cylindrical layer cloak and Stirring and medical instrument. Therefore the leakless function will be avaliable in wide frequency band that is benefit for their optimal design. The GL cylindrical layer cloak has merits to protect the inner stirring and biomedical instrument. In the internal stirring and instrument of the GL cylindrical cloak, the electromagnetic environment is normal. Howver, the PS cloak damaged the EM enviroment and shut down the stirring and instrument working, such that there exists no EM wavefield can be excited in the strring and instrument inside of the PS cloak.

The GLC cylindrical layer leakless cloak materials and the 3D and 2D GL parallel algorithms and software are made by authors in GL Geophysical Laboratory and are patented by GLGEO and

ACKNOWLEDGMENT

We wish to acknowledge the support of the GL Geophysical Laboratory and thank the GLGEO Laboratory to approve the paper publication. Authors thank to Professor P. D. Lax for his concern and encouragements Authors thank to Dr. M. Oristaglio, Professor Q. Lin, Professor Y. Li, Senior EM engineering J. Li, Professor X. Zhou, Professor T. T. Lu, Professor J. Cui, Profesoor H. S. Chen, and Professor Q. Jiang for their encouragements.

REFERENCES

1. Xie, G., J. Li, and J. H. Li, "New AGILD EMS electromagnetic field modeling," *PIERS Online*, Vol. 1, No. 2, 168–172, 2005.
2. Li, J. H, G. Xie, and J. Li, "3D and 2.5D AGLID EMS stirring modeling in the cylindrical coordinate system," *PIERS Online*, Vol. 2, No. 5, 505–509, 2006.
3. Xie, G., J. H. Li, L. Xie, F. Xie, and J. Li, "The 3D GL EM-flow-heat-stress coupled modeling," *PIERS Online*, Vol. 3, No. 4, 411–417, 2007.
4. Meir, A. J. and P. G. Schmidt, "Analysis and finite element simulation of MHD flows, with an application to liquid metal processing," 561–569, *Fluid Flow Phenomena in Metals Processing, Proceedings of the 1999 TMS Annual Meeting*, Pennsylvania, 1999.
5. Xie, G., F. Xie, L. Xie, and J. Li, "New GL method and its advantages for resolving historical diffculties," *Progress In Electromagnetics Research*, PIER 63, 141–152, 2006.
6. Xie, G., J. Li, L. Xie, and F. Xie, "GL metro carlo EM inversion," *Journal of Electromagnetic Waves and Applications*, Vol. 20, No. 14, 1991–2000, 2006.
7. Xie, G. and J. Li, "New parallel SGILD modeling and inversion," *Physics D*, Vol. 133, 477–487, 1999.
8. Xie, G., "A new iterative method for solving the coefficient inverse problem of wave equation," *Comm. on Pure and Applied Math.*, Vol. 39, 307–322, 1986.
9. Li, J. H., G. Xie, C. Lin, and J. Liu, "2.5 dimensional GILD electromagnetic modeling and application," *SEG, Expanded Abstracts,* Vol. 21, No. 1, 692–695, 2002, http://www.segdl.org/journals/doc/SEGLIBhome/dci/searchDCI.jsp.
10. Xie, G., "The 3-D finite element method in the elastic structure," *Mathematical Practice and Knowledge,* Vol. 1, 28–41, 1975 (Chinese).
11. Brandts, J. and M. Krizek, "History and futures of superconvergence in three dimensional finite element method," *Mathematical Sciences and Applications*, Vol. 15, 24–35, 2001.
12. Li, J. H., G. Xie, F. Xie, and L. Xie, "No maxwell electromagnetic wavefield excited inside cloaked concealment and broadband GL cloaks," *PIERS Proceedings*, 66–72, Moscow, Russia, August 18–21, 2009.
13. Xie, G., J. Li, F. Xie, and L. Xie, "Global and local field EM modeling and novel GL double layered electromagnetic cloaks," *PIERS Proceedings*, 335–343, Moscow, Russia, August 18–21, 2009.

Iterative Method for Differential Phase Shift Computation in the Azimuthally Magnetized Circular Ferrite Waveguide

Georgi Nikolov Georgiev[1] **and Mariana Nikolova Georgieva-Grosse**[2]

[1]Faculty of Mathematics and Informatics, University of Veliko Tirnovo "St. St. Cyril and Methodius"
Veliko Tirnovo BG-5000, Bulgaria
[2]Meterstrasse 4, Gerlingen D-70839, Germany

Abstract— A reiterative technique is developed for finding in normalized form the differential phase shift provided by the circular waveguide, completely filled with azimuthally magnetized ferrite which propagates normal TE_{01} mode. It consists in a repeated numerical solution of the structure's characteristic equation, derived in terms of a definite complex Kummer confluent hypergeometric function, followed by a computation of the normalized guide radius and phase constant at a fixed value of the off-diagonal ferrite permeability tensor element. The idea of the method is to vary arbitrarily or according to a certain scheme the imaginary part of the first complex parameter of wave function until the counted numerical equivalent of the guide radius coincides with a chosen one of the same with a prescribed accuracy. The relevant value of the phase constant is accepted as the one, looked for. Calculations are performed for both signs of the imaginary part (of the ferrite magnetization), yielding the phase shift sought. The numerically presented results are discussed.

1. INTRODUCTION

The characteristics of the circular waveguides, containing a disc- or ring-shaped azimuthally magnetized coaxial ferrite area have been an object of a comprehensive study in view of their possible application in the design of various microwave control components [1–7]. Such are e.g., the nonreciprocal digital phase shifters, operating in the normal TE_{01} mode [2–7]. The development of the devices mentioned requires calculation of the differential phase shift which the configurations in question might produce. This however is an arduous task [5, 7].

Here an iterative method is elaborated and applied to reckon the differential phase shift provided by the circular waveguide, entirely filled with ferrite, magnetized in azimuthal direction by an infinitely thin central switching wire that supports normal TE_{0n} modes. The approach uses the characteristic equation of the structure [2]:

$$\Phi\left(a, c; x_0\right) = 0, \tag{1}$$

written by the complex Kummer confluent hypergeometric function [8] in that $a = c/2 - jk$ — complex, $c = 3$, $x_0 = jz_0$, $k = \alpha\bar{\beta}/\left(2\bar{\beta}_2\right)$, $\bar{\beta}_2 = \sqrt{1-\alpha^2-\bar{\beta}^2}$, $z_0 = 2\bar{\beta}_2\bar{r}_0$, k, z_0 — real, $-\infty < k < +\infty$, $z_0 > 0$, $\operatorname{sgn} k = \operatorname{sgn}\alpha$ ($\alpha = \gamma M_r/\omega$ — off-diagonal ferrite permeability tensor element, $-1 < \alpha < 1$, γ — gyromagnetic ratio, M_r — ferrite remanent magnetization, ω — angular frequency of the wave, $\bar{\beta} = \beta/\left(\beta_0\sqrt{\varepsilon_r}\right)$, $\bar{\beta}_2 = \beta_2/\left(\beta_0\sqrt{\varepsilon_r}\right)$, $\bar{r}_0 = \beta_0 r_0\sqrt{\varepsilon_r}$, β — phase constant, β_2 — radial wavenumber, r_0 — guide radius, $\beta_0 = \omega\sqrt{\varepsilon_0\mu_0}$ — free space phase constant, ε_r — ferrite relative permittivity).

2. ITERATIVE METHOD FOR DIFFERENTIAL PHASE SHIFT COMPUTATION

2.1. Description of the Method

A network of $\{|\alpha|, \bar{r}_0\}$ pairs, satisfying the condition for phase shifter operation of the geometry [2], is constructed. Anyone of them $\left\{\left|\alpha^{ch}\right|, \bar{r}_0^{ch}\right\}$ is chosen. For an arbitrarily picked out value k^{ch} of the parameter k the positive purely imaginary roots $\zeta_{k,n}^{(c)}$ of Eq. (1) (the eigenvalue spectrum of geometry $\bar{\beta}_2 = \zeta_{k,n}^{(c)}/(2\bar{r}_0)$) are (is) found ($n = 1, 2, 3, ...$). The numerical equivalents of quantities α^{ch}, k^{ch} and $\zeta_{k^{ch},n}^{(c)comp}$ are put in the expressions [2]:

$$\bar{r}_0 = \left(k\zeta_{k,n}^{(c)}/\alpha\right)\left\{\left[1 + \left(\alpha/\left(2k\right)\right)^2\right]/\left(1-\alpha^2\right)\right\}^{1/2}, \tag{2}$$

$$\bar{\beta} = \left\{\left(1-\alpha^2\right)/\left[1 + \left(\alpha/\left(2k\right)\right)^2\right]\right\}^{1/2}. \tag{3}$$

The computed value of the normalized phase constant $\bar{\beta}^{comp}$ is accepted as the one looked for, if the determined in the same way value of the normalized guide radius $\bar{r}_0^{comp}$ coincides with $\bar{r}_0^{ch}$ within the boundaries of the set in advance accuracy. Otherwise, the parameter k is changed and the procedure is done over again. The calculations are performed twice for $k_+ > 0$ and $k_- < 0$, yielding the numerical equivalents of phase constants $\bar{\beta}_+$ and $\bar{\beta}_-$, resp. the normalized differential phase shift $\Delta\bar{\beta} = \bar{\beta}_- - \bar{\beta}_+$. For simplicity the discussion is restricted to the normal TE_{01} mode ($n = 1$) only. (Note that $\bar{\beta}$ is independent of n. In addition, the subscripts "+" and "−" answer to positive ($\alpha_+ > 0$, $k_+ > 0$) and negative ($\alpha_- < 0$, $k_- < 0$) magnetization, resp. The superscripts "*ch*" and "*comp*" are attached to the symbols, standing for the parameters chosen, resp. the quantities computed which are used in the numerical analysis. In the final outcomes they are dropped.)

2.2. Numerical Example

Let $|\alpha^{ch}| = 0.1$ and $\bar{r}_0^{ch} = 4$. Taking $k_+^{ch} = \mathbf{0.}1$ gives $\zeta_{k_+^{ch},1}^{(c)comp} = 8.08179\,43987$, $\bar{r}_{0+}^{comp} = 9.08124\,11201$ and $\bar{\beta}_+^{comp} = \mathbf{0.}88994\,38185$. As might be expected, $\bar{r}_{0+}^{comp}$ is different from $\bar{r}_0^{ch}$. (In the case considered $\bar{r}_{0+}^{comp} > \bar{r}_0^{ch}$.) Next, let a second arbitrary value of k_+, e.g., $k_+^{ch} = \mathbf{0.}2$ be singled out and the technique depicted be repeated, resulting in: $\zeta_{k_+^{ch},1}^{(c)comp} = 8.51421\,01832$, $\bar{r}_{0+}^{comp} = 17.64092\,01739$, $\bar{\beta}_+^{comp} = \mathbf{0.}96527\,95998$. The numerical equivalent of quantity $\bar{r}_{0+}^{comp}$, reckoned now, is even larger than the previous one. Thus, the value of k_+ searched for is less than the ones adopted in both examples. Choosing $k_+^{ch} = \mathbf{0.0}5$ yields: $\zeta_{k_+^{ch},1}^{(c)comp} = \mathbf{7.}87074\,25109$, $\bar{r}_{0+}^{comp} = 5.59349\,31386$, $\bar{\beta}_+^{comp} = \mathbf{0.}70356\,23640$. Again $\bar{r}_{0+}^{comp}$ is larger than $\bar{r}_0^{ch}$, but the deviation from it is already smaller and correspondingly, the numerical equivalent of k_+, used in the calculations, should additionally be diminished. So, for $k_+^{ch} = \mathbf{0.01}$, it is obtained: $\zeta_{k_+^{ch},1}^{(c)comp} = \mathbf{7.7}0457\,05431$, $\bar{r}_{0+}^{comp} = 3.94836\,69922$, $\bar{\beta}_+^{comp} = \mathbf{0.}19513\,30907$. Thus, $\bar{r}_{0+}^{comp}$ is less than $\bar{r}_0^{ch}$. Obviously, a larger k_+ is needed, e.g., $k_+^{ch} = \mathbf{0.0}2$, giving: $\zeta_{k_+^{ch},1}^{(c)comp} = \mathbf{7.7}4588\,45001$, $\bar{r}_{0+}^{comp} = \mathbf{4.}19230\,06316$, $\bar{\beta}_+^{comp} = \mathbf{0.}36952\,90572$. Varying k_+, gradually better and better approximations of $\bar{r}_0^{ch}$ (of $\bar{\beta}_+$) might be attained, if its values are appropriately chosen: $k_+^{ch} = \mathbf{0.01}1$, $\zeta_{k_+^{ch},1}^{(c)comp} = \mathbf{7.7}0869\,49739$, $\bar{r}_{0+}^{comp} = 3.96640\ 24213$, $\bar{\beta}_+^{comp} = \mathbf{0.2}1378\,47745$; $k_+^{ch} = \mathbf{0.012}$, $\zeta_{k_+^{ch},1}^{(c)comp} = \mathbf{7.71}282\,09567$, $\bar{r}_{0+}^{comp} = 3.98589\ 98097$, $\bar{\beta}_+^{comp} = \mathbf{0.2}3220\,31559$; $k_+^{ch} = \mathbf{0.013}$, $\zeta_{k_+^{ch},1}^{(c)comp} = \mathbf{7.71}694\,84899$, $\bar{r}_{0+}^{comp} = \mathbf{4.00}684\,26785$, $\bar{\beta}_+^{comp} = \mathbf{0.2}5037\,25213$; $k_+^{ch} = \mathbf{0.012}5$, $\zeta_{k_+^{ch},1}^{(c)comp} = \mathbf{7.71}488\,45296$, $\bar{r}_{0+}^{comp} = 3.99619\ 16375$, $\bar{\beta}_+^{comp} = \mathbf{0.24}131\,99000$; $k_+^{ch} = \mathbf{0.012}7$, $\zeta_{k_+^{ch},1}^{(c)comp} = \mathbf{7.715}71\,00672$, $\bar{r}_{0+}^{comp} = \mathbf{4.000}40\,90727$, $\bar{\beta}_+^{comp} = \mathbf{0.244}94\,87442$, etc.

2.3. Comments

To find the numerical equivalent of k for which $\bar{r}_0^{comp} \equiv \bar{r}_0^{ch}$, determining the subsequent approximations k^{ch} to it just arbitrarily, without employing any sort of system, is difficult. It is advisable to specify first an interval, involving it (an interval for $\bar{r}_0$, including $\bar{r}_0^{ch}$). Dividing the same into

Table 1: Numerical values of the quantities k_+^{ch}, $\zeta_{k_+^{ch},n}^{(c)comp}$ and $\bar{\beta}_+^{comp}$ for normal TE_{01} mode ($n = 1$, $c = 3$) in case $|\alpha^{ch}| = 0.1$, $\bar{r}_0^{ch} = 4$ and $m^{ch} = 10$ as a function of the number of iteration N.

N	k_+^{ch}	$\zeta_{k_+^{ch},n}^{(c)comp}$	$\bar{r}_{0+}^{comp}$	$\bar{\beta}_+^{comp}$	N	k_+^{ch}	$\zeta_{k_+^{ch},n}^{(c)comp}$	$\bar{r}_{0+}^{comp}$	$\bar{\beta}_+^{comp}$
1	**0.01**	**7.7**0457 05431	3.94836 69922	**0.**19513 30907	6	**0.01268 07**	**7.71563 04**002	3.99999 95886	**0.24459 9**0112
	0.02	**7.7**4588 45001	**4.**19230 06316	**0.**36952 90572		**0.01268 0**8	**7.71563 0**8129	**4.00000** 17089	**0.244**60 08235
2	**0.012**	**7.71**282 09567	3.98589 98097	**0.2**3220 31559	7	**0.01268 071**	**7.71563 04**414	3.99999 98006	**0.24459 9**1924
	0.013	**7.71**694 84899	**4.00**684 26785	**0.2**5037 25213		**0.01268 07**2	**7.71563 048**27	**4.00000 00**126	**0.24459 93**737
3	**0.012**6	**7.715**29 72907	3.99829 31796	**0.24**313 56119	8	**0.01268 0719**	**7.71563 04**786	3.99999 99914	**0.24459 93**555
	0.0127	**7.715**71 00672	**4.000**40 90727	**0.244**94 87442		**0.01268 07**20	**7.71563 048**27	**4.00000 00**126	**0.24459 93**737
4	**0.01268**	**7.7156**2 75107	3.99998 47469	**0.244**58 63248	9	**0.01268 07194**	**7.71563 04802**	3.99999 99999	**0.24459 9362**8
	0.01269	**7.7156**6 87889	**4.000**19 68381	**0.244**76 75474		**0.01268 07195**	**7.71563 04807**	**4.00000 000**20	**0.24459 936**46
5	**0.01268 0**	**7.7156**2 75107	3.99998 47469	**0.2445**8 63248	10	**0.01268 07194**	**7.71563 04802**	3.99999 99999	**0.24459 9362**8
	0.01268 1	**7.71563** 16385	**4.00000** 59495	**0.244**60 44482		**0.01268 07194**	**7.71563 0480**3	**4.00000 0000**1	**0.24459 936**30

parts and taking that of them which incorporates the value of k looked for (resp. $\bar{r}_0^{ch}$), would accelerate the process to a large extent. The initial and all subsequent intervals could be split up e.g., in two, ten, one hundred, etc. parts, localizing in this way better and better the numerical equivalent of k of interest (approaching from both sides $\bar{r}_0^{ch}$). The procedure winds up as before when the prescribed accuracy for $\bar{r}_0^{comp}$ is achieved. Accordingly, the arbitrary choice is restricted to the initial stage of the method only, until the interval in question is tracked down.

3. IMPROVED ITERATIVE METHOD FOR DIFFERENTIAL PHASE SHIFT COMPUTATION

3.1. Description of the Method

A network of $\{|\alpha|, \bar{r}_0\}$ pairs, meeting the criterion for phase shifter operation of configuration [2], is composed and one of them $\left\{\left|\alpha^{ch}\right|, \bar{r}_0^{ch}\right\}$ is selected. Then, Eq. (1) is solved with respect to $x_0\,(z_0)$, changing k in an arbitrary interval $\Delta k^{(0)ch} = \left[k_{left}^{(0)ch}, k_{right}^{(0)ch}\right]$ with an arbitrary step $\delta k^{(0)ch}$. Introducing its roots $\zeta_{k^{ch},1}^{(c)comp}$ and the parameters α^{ch}, k^{ch} in expressions (2), (3), the relevant values $\bar{r}_0^{(0)comp}$ and $\bar{\beta}^{(0)comp}$ are counted. The limits of $\Delta k^{(0)ch}$ are varied, until it is obtained: $\bar{r}_0^{ch} \in \Delta\bar{r}_0^{(0)comp}$, $\Delta\bar{r}_0^{(0)comp} = \left[\bar{r}_{0left}^{(0)comp}, \bar{r}_{0right}^{(0)comp}\right]$. (The endpoints of $\Delta\bar{r}_0^{(0)comp}$ correlate to the ones of $\Delta k^{(0)ch}$). The quantities mentioned are considered as a zeroth approximation to the ones sought. The closest larger and smaller calculated values of normalized guide radius are accepted as first approximations $\bar{r}_{0left}^{(1)comp}$, $\bar{r}_{0right}^{(1)comp}$ to the $\bar{r}_0^{ch}$ selected ($\bar{r}_0^{ch} \in \Delta\bar{r}_0^{(1)comp} \in \Delta\bar{r}_0^{(0)comp}$, $\Delta\bar{r}_0^{(1)comp} = \left[\bar{r}_{0left}^{(1)comp}, \bar{r}_{0right}^{(1)comp}\right]$) and the respective parameters k are taken as left and right ends of the new interval $\Delta k^{(1)ch} = \left[k_{left}^{(1)ch}, k_{right}^{(1)ch}\right]$. Next, it is fixed $\delta k^{(1)ch} = \delta k^{(0)ch}/m^{ch}$, ($m^{ch}$ is any positive integer, larger than 1). This is repeated, till for the nth approximation it holds $\bar{r}_{0right}^{(n)comp} - \bar{r}_{0left}^{(n)comp} <$

Table 2: Numerical values of the quantities $k_{\pm}^{comp}$, $\zeta_{k_{\pm}^{comp},n}^{(c)comp}$ and $\bar{\beta}_{\pm}^{comp}$ for normal TE_{01} mode ($n = 1$, $c = 3$) as a function of the parameters $\bar{r}_0$ and $|\alpha|$.

$\bar{r}_0$	$k_{\pm}^{comp}$	$\zeta_{k_{\pm}^{comp},n}^{(c)comp}$	$\bar{\beta}_{\pm}^{comp}$	$k_{\pm}^{comp}$	$\zeta_{k_{\pm}^{comp},n}^{(c)comp}$	$\bar{\beta}_{\pm}^{comp}$	$k_{\pm}^{comp}$	$\zeta_{k_{\pm}^{comp},n}^{(c)comp}$	$\bar{\beta}_{\pm}^{comp}$
	$\lvert\alpha\rvert = 0.1$			$\lvert\alpha\rvert = 0.2$			$\lvert\alpha\rvert = 0.3$		
4.0	−0.01557768	7.59960959	0.29596068	−0.02793929	7.54925430	0.26365103			
	0.01268072	7.71563048	0.24459936	0.01664397	7.73200218	0.16086400			
5.0	−0.04379040	7.48504529	0.65554631	−0.08945920	7.30236931	0.65326413	−0.13331420	7.13028201	0.63371191
	0.03925796	7.82587855	0.61445606	0.07171903	7.96197439	0.57102508	0.09494858	8.06030916	0.51020992
6.0	−0.06321588	7.40691829	0.78039147	−0.13083297	7.13992926	0.77844847	−0.19963002	6.87650094	0.76264222
	0.05667866	7.89872257	0.74614836	0.10512425	8.10362599	0.70990632	0.14360689	8.26873398	0.65969289
7.0	−0.08069088	7.33717184	0.84577555	−0.16872540	6.99378653	0.84287818	−0.26137774	6.64742211	0.82737530
	0.07177603	7.96221473	0.81642306	0.13346639	8.22503165	0.78411804	0.18382581	8.44339148	0.73910157
8.0	−0.09738928	7.27100637	0.88514756	−0.20572026	6.85359306	0.88120182	−0.32321246	6.42521571	0.86529575
	0.08571968	8.02114911	0.85946288	0.15925758	8.33645078	0.82977686	0.21987145	8.60165609	0.78802441
9.0	−0.11375565	7.20661909	0.91088182	−0.24283915	6.71545308	0.90598608	−0.38717603	6.20310564	0.88951624
	0.09894922	8.07732216	0.88804972	0.18343249	8.44167339	0.86026509	0.25328256	8.74973765	0.82079849
10.0	−0.13000962	7.14313290	0.92867601	−0.28064371	6.57740806	0.92295409	−0.45466737	5.97741497	0.90591185
	0.11167857	8.13160371	0.90812585	0.20644817	8.54253346	0.88179522	0.28480609	8.89061217	0.84403349
11.0	−0.14627789	7.08005418	0.94150490	−0.31951917	6.43828242	0.93507029	−0.52696409	5.74560407	0.91749303
	0.12402791	8.18447917	0.92282165	0.22856491	8.64006114	0.89764308	0.31486813	9.02595084	0.86120736
12.0	−0.16264208	7.01707634	0.95105993	−0.35977855	6.29726871	0.94400926	−0.60546298	5.50555007	0.92594632
	0.13607156	8.23624596	0.93393233	0.24994670	8.73489492	0.90969089	0.34373882	9.15679484	0.87431829
13.0	−0.17915965	6.95399427	0.95836551	−0.40171081	6.15374604	0.95077935	−0.69186661	5.25519327	0.93228020
	0.14785878	8.28709898	0.94255412	0.27070480	8.82746005	0.91909071	0.37160288	9.28384346	0.88459051

ε^{ch} (ε^{ch} — positive real number, less than unity, specifying the prescribed accuracy. Note that $\bar{r}_{0right}^{(n)comp} > \bar{r}_{0left}^{(n)comp}$). (Each of the inequalities: $\bar{r}_{0right}^{(n)comp} - \bar{r}_0^{ch} < \varepsilon^{ch}$ or $\bar{r}_0^{ch} - \bar{r}_{0left}^{(n)comp} < \varepsilon^{ch}$ where $\bar{r}_{0left}^{(n)comp} < \bar{r}_0^{ch} < \bar{r}_{0left}^{(n)comp}$ could serve also as a condition for terminating the iterative scheme.) Any of the computed values $\bar{\beta}^{(n)comp}$, belonging to the interval $\left[\bar{\beta}_{left}^{(n)comp}, \bar{\beta}_{right}^{(n)comp}\right]$ which corresponds to the one $\Delta\bar{r}_0^{(n)comp} = \left[\bar{r}_{0left}^{(n)comp}, \bar{r}_{0right}^{(n)comp}\right]$, might be accepted as the numerical equivalent of $\bar{\beta}$ searched for. The procedure is reiterated two times for both signs of k, yielding $\bar{\beta}_-$ and $\bar{\beta}_+$, resp. $\Delta\bar{\beta} = \bar{\beta}_- - \bar{\beta}_+$ for the set $\left\{\left|\alpha^{ch}\right|, \bar{r}_0^{ch}\right\}$ singled out. Then, the latter is changed and the computations begin anew.

3.2. Numerical Example

Let again $\left|\alpha^{ch}\right| = 0.1$ and $\bar{r}_0^{ch} = 4$. Table 1 illustrates the results for the subsequent iterations executed, following the above method. It is assumed that $m^{ch} = 10$. Data for the zeroth approximation are not included in the Table. Throughout the paper the digits in a given result, being identical with these in the final one, are distinguished by bold face type. The values of parameters $k_\pm^{comp}$, of the relevant roots of characteristic equation $\zeta_{k_\pm^{comp},n}^{(c)comp}$ and of the phase constants $\bar{\beta}_\pm^{comp}$ for both directions of magnetization, pertinent to the normal TE_{01} mode ($n = 1$), determined, applying the improved approach, are listed in Table 2, on condition that $\bar{r}_0 = 4(1)13$ and $|\alpha| = 0.1$, 0.2 and 0.3. The first (second) of each couple of rows for specific $\bar{r}_0$ is relevant to k_-^{comp} (k_+^{comp}).

3.3. Comment

The improved method is to be preferred, since it provides a better convergence of the iterative process and allows to specify the results faster than in case the parameter k is changed arbitrarily.

Table 3: Numerical values of the normalized differential phase shift $\Delta\bar{\beta}$ for normal TE_{01} mode as a function of the parameters $\bar{r}_0$ and $|\alpha|$.

$\bar{r}_0$ \ $\lvert\alpha\rvert$	0.1	0.2	0.3	0.4	0.5	0.6	0.7	0.8	0.9
4.0	0.05136131	0.10278704							
4.5	0.04565513	0.09137120	0.13720660	0.18321436	0.22943897				
5.0	0.04109025	0.08223905	0.12350199	0.16492848	0.20655804	0.24841570			
5.5	0.03735542	0.07476777	0.11229067	0.14997074	0.18784339	0.22592763	0.26421974		
6.0	0.03424311	0.06854215	0.10294933	0.13750913	0.17225349	0.20719608	0.24232517		
6.5	0.03160967	0.06327471	0.09504643	0.12696761	0.15906726	0.19135420	0.22380923	0.25637562	
7.0	0.02935248	0.05876014	0.08827374	0.11793476	0.14776965	0.17778282	0.20794799	0.23819788	
7.5	0.02739630	0.05484787	0.08240522	0.11010885	0.13798298	0.16602790	0.19421058	0.22245351	
8.0	0.02568468	0.05142496	0.07727134	0.10326358	0.12942396	0.15574890	0.18219885	0.20868632	
8.5	0.02417447	0.04840505	0.07274246	0.09722593	0.12187597	0.14668540	0.17160834	0.19654747	
9.0	0.02283210	0.04572099	0.06871775	0.09186128	0.11517054	0.13863487	0.16220224	0.18576563	0.20914867
9.5	0.02163106	0.04331974	0.06511761	0.08706340	0.10917466	0.13143742	0.15379361	0.17612661	0.19824641
10.0	0.02055016	0.04115888	0.06187835	0.08274728	0.10378192	0.12496514	0.14623290	0.16745906	0.18844004
10.5	0.01957224	0.03920406	0.05894843	0.07884409	0.09890619	0.11911447	0.13939905	0.15962426	0.17957306
11.0	0.01868325	0.03742720	0.05628567	0.07529756	0.09447698	0.11380070	0.13319299	0.15250872	0.17151739
11.5	0.01787159	0.03580509	0.05385521	0.07206116	0.09043609	0.10895385	0.12753292	0.14601870	0.16416725
12.0	0.01712760	0.03431837	0.05162803	0.06909614	0.08673500	0.10451559	0.12235065	0.14007606	0.15743449
12.5	0.01644316	0.03295080	0.04957973	0.06636994	0.08333295	0.10043695	0.11758891	0.13461520	0.15124505
13.0	0.01581139	0.03168864	0.04768969	0.06385503	0.08019547	0.09667647	0.11319923	0.12958058	0.14553628

4. DIFFERENTIAL PHASE SHIFT

Table 3 presents $\Delta\bar{\beta}$, depending on the quantities $\bar{r}_0 = 4(0.5)13$ and $|\alpha| = 0.1(0.1)0.9$. It is seen that for fixed $|\alpha|$ ($\bar{r}_0$) the normalized differential phase shift decreases monotonously with $\bar{r}_0$, following on the whole the function $1/\bar{r}_0$ (increases almost linearly with $|\alpha|$). The relevant factor of proportionality gets smaller (larger) when the numerical equivalent of the first (second) parameter grows. It is interesting to note that, if $\bar{r}_0 = 5$, the ratios between the values of $\Delta\bar{\beta}$ for $|\alpha| = 0.2(0.1)0.6$ and the one for $|\alpha| = 0.1$ are 2.00142 48218, 3.00562 72962, 4.01381 02586, 5.02693 49901, 6.04561 10808, (equal approximately 2, 3, 4, 5, 6), resp. Further, in case $|\alpha| = 0.1$ the products of the numerical equivalents of $\Delta\bar{\beta}$ by the ones of $\bar{r}_0 = 4(0.5)6$ are almost identical: 0.20544 52511, 0.20544 80787, 0.20545 12710, 0.20545 47988, 0.20545 86566, resp. Dividing the last sequence of numbers by 0.1, it is easy to establish that the same holds also for the quantities $\Delta\bar{\beta}\bar{r}_0/|\alpha|$. Similar results could be obtained for any $\bar{r}_0$ and $|\alpha|$ which submit to the rule for functioning of the set-up as a phase shifter [2]. Provided this is not fulfilled, $\Delta\bar{\beta}$ is not produced ($k_\pm$, $\zeta^{(c)}_{k_\pm,n}$ and $\bar{\beta}_\pm$ do not exist) and for this reason the relevant positions in Tables 2 and 3 are empty.

5. CONCLUSION

An iterative method is worked out for calculation of the differential phase shift due to the azimuthally magnetized ferrite-loaded circular waveguide, operating in the normal TE_{01} mode. The characteristic equation of the geometry, written through the complex Kummer confluent hypergeometric function $\Phi(a, c; x)$ with $a = c/2 - jk$ — complex, $c = 3$, $x = jz$, k, z — real, $z > 0$, is employed. The roots $\zeta^{(c)}_{k,n}$ of this equation in x (in z) are used to compute the guide radius $\bar{r}_0$, normalized with respect to frequency and relative permittivity of the medium, for a fixed value of the off-diagonal permeability tensor element of the latter. The parameter k is varied arbitrarily or in a specific way, until the computed value of $\bar{r}_0$ becomes identical with the preliminary singled out one of the same within the boundaries of the prescribed accuracy. The difference between the corresponding calculated numerical equivalent of the phase constants for both signs of k (of the ferrite magnetization), gives the phase shift looked for.

ACKNOWLEDGMENT

We express our gratitude to our mother Trifonka Romanova Popnikolova for her self-denial, patience and for the tremendous efforts she exerts to support all our undertakings.

REFERENCES

1. Che, W., E. K. Yung, and J. Wen, "Cutoff characteristics of modes in a circular waveguide filled with microwave ferrite," *J. Electromagn. Waves Applicat.*, Vol. 16, No. 8, 1103–1118, August 2002.
2. Georgiev, G. N. and M. N. Georgieva-Grosse, "A new property of the complex Kummer function and its application to waveguide propagation," *IEEE Antennas Wireless Propagat. Lett.*, Vol. 2, 306–309, December 2003.
3. Georgiev, G. N. and M. N. Georgieva-Grosse, "A property of the $L(c, \rho, n)$ numbers and its application to waveguide propagation," *Proc. XXIX URSI General Assembly*, in CDROM, BK.6(120), Chicago, IL, USA, August 7–16, 2008.
4. Georgiev, G. N. and M. N. Georgieva-Grosse, "Phase behaviour of a two-layered circular ferrite-dielectric waveguide with azimuthal magnetization," *PIERS Proc.*, 1473–1477, Moscow, Russia, August 18–21, 2009.
5. Georgiev, G. N. and M. N. Georgieva-Grosse, "An application of the complex Tricomi function," *Proc. Eleventh Int. Conf. Electromagn. Adv. Applicat., ICEAA'09*, 819–822, in CDROM, Turin, Italy, September 14–18, 2009.
6. Georgiev, G. N. and M. N. Georgieva-Grosse, "Effect of the dielectric filling on the phase behaviour of the circular waveguide with azimuthally magnetized ferrite toroid and dielectric cylinder," *Proc. Asia-Pacific Microwave Conf., APMC-2009*, in CDROM, WE4B-4(1680), Singapore, December 7–10, 2009.
7. Georgieva-Grosse, M. N. and G. N. Georgiev, "Differential phase shift characteristics of normal TE_{0n} modes in an azimuthally magnetized coaxial ferrite waveguide," *Proc. 4rd Europ. Conf. Antennas Propagat., EuCAP 2010*, Barcelona, Spain, April 12–16, 2010 (in print).
8. Tricomi, F. G., *Funzioni Ipergeometriche Confluenti*, Edizioni Cremonese, Rome, Italy, 1954.

A Franklin Array Antenna for Wireless Charging Applications

Shih-Hsiung Chang, **Wen-Jiao Liao**, **Kuo-Wei Peng**, **and Chih-Yao Hsieh**
Department of Electrical Engineering, National Taiwan University of Science and Technology
43, Sec. 4, Keelung Rd., Taipei 106, Taiwan

Abstract— A Franklin array antenna is proposed in this work to be used for wireless charging applications. It is a fascinating idea to use radio waves as the power source for portable devices. However, due to the relative long wavelength, the power density of microwave radiation dilutes as it propagates. According to power budget analysis, at a distance of one meter, if transmitting and receiving antennas of moderate gains are used, only a few mW is available with a one watt transmitter. In order to enhance the available power level and increase the remote operation distance, larger antennas, which intercept more radiated power, can be employed. In this work, a rectenna made of a high gain Franklin array and RF-to-DC rectifier was developed. RF-to-DC power conversion efficiency was evaluated.

1. INTRODUCTION

As wireless communication technology evolves, more and more mobile devices are entering our everyday life. How, most "portable" gadgets still require charging via cables and adaptors from time to time. One can't help but imagine how convenient it would be if those devices can be charged wirelessly to avoid tangled wires. In this work, we probe the wireless charging and powering issues using radio frequency.

The most well known and developed application for wireless power transmission is radio frequency identification (RFID) [1, 2], which usually employs a passive IC embedded antenna to receive the RF power emitted from the reader. RFID tags then scatter back modulated signals using the incoming RF energy. Wireless power transmission methods can be divided into three categories according to the operating range. They are near field, moderate range of magnetic resonance, and farfield. In this work, we focus on the scenario of powering up a device with a moderate power rating at a distance of a few meters, which falls into the farfield category. For example, a small LCD panel requires tens of μW. A well engineered wireless mouse operates with tens of mW.

The wireless charging and powering scheme is illustrated in Fig. 1. RF power is emitted from the transmitter via a directive antenna to provide a coverage area. Devices that require charging or powering may intercept the RF power via a receiving antenna when placed within the coverage area. RF signal is next rectified to DC power via RF diodes. Note the coverage area size and remote charging distance constitutes a trade-off. A proper transmitting antenna should be chosen according to the required operation range.

The RF power available to portable devices can be estimated via Friis transmission equation in (1)

$$\frac{P_r}{P_t} = G_t G_r \left(\frac{\lambda}{4\pi R}\right)^2 \tag{1}$$

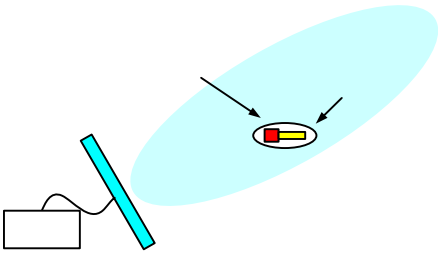

Figure 1: Operation scenario for wireless charging and powering applications.

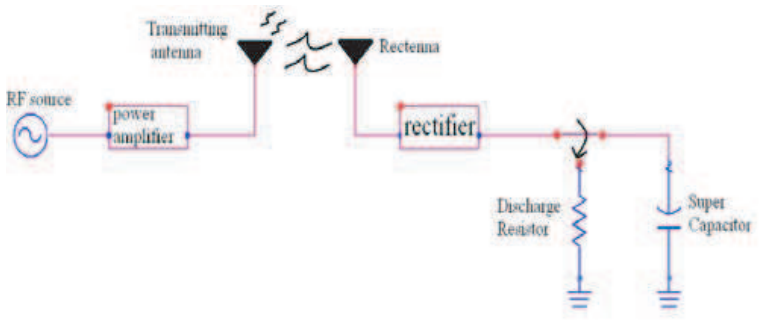

Figure 2: Rectenna configuration.

Assuming the RF frequency is 2.4 GHz, then the wavelength is 0.125 m. If the transmitting and receiving antenna gains are 12 and 6 dBi, respectively, and the device is placed 1 m in front of the transmitter, the received power is only 6.23 mW when 1 W is emitted from the transmitter. Since the RF-to-DC rectification circuit is in general of poor efficiency with a low input RF power level, the converted DC power may be too small to operate the device.

According to the Friis transmission equation, there are a couple of measures to power up devices at a longer distance. For example, one can increase the transmitted power or improve the rectification efficiency. Directive antennas can also be used. In this work, we attempt to develop a high gain receiving antenna based on the Franklin array antenna configuration [3, 4]. This antenna increases the received power using its enlarged antenna aperture.

Development and performance verification of the high gain Franklin array antenna is presented in Section 2. In Section 3, the receiver assembly is tested with resistive and capacitive loads to examine its power conversion efficiency. A brief summary of this work is given at the end.

2. DEVELOPMENT OF A RECTENNA USING HIGH GAIN FRANKLIN ARRAY

In order to extend the operation distance of the rectenna module, which is a combination of rectification circuitry and antenna, the Franklin array configuration is used to increase the antenna aperture. The System diagram is shown in Fig. 2, which includes a RF transmitter and the rectenna module connected to either a discharge resistor or a super capacitor.

Figure 3 shows the geometry of the proposed stacked Franklin array antenna design, which contains 8 Franklin array elements and a total of 32 patch elements. Those elements are grouped into two set of perpendicular orientations. Each set rest on a 0.6 mm thick FR4 slab. The two slabs are glued together and placed on a metal ground plane with a spacing of 2.1 mm. The total height

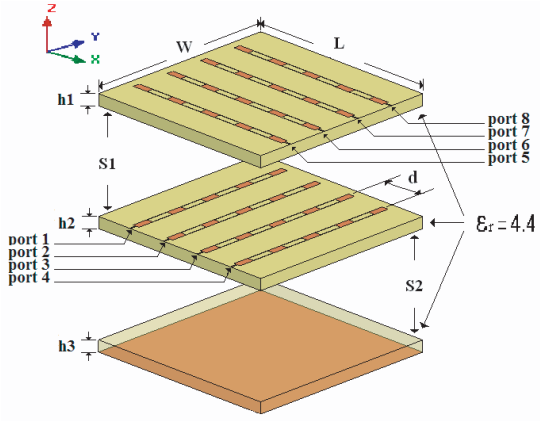

Figure 3: Stacked Franklin array antenna design.

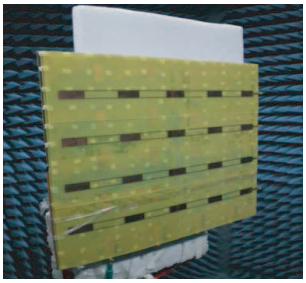

Figure 4: Prototype Franklin array antenna.

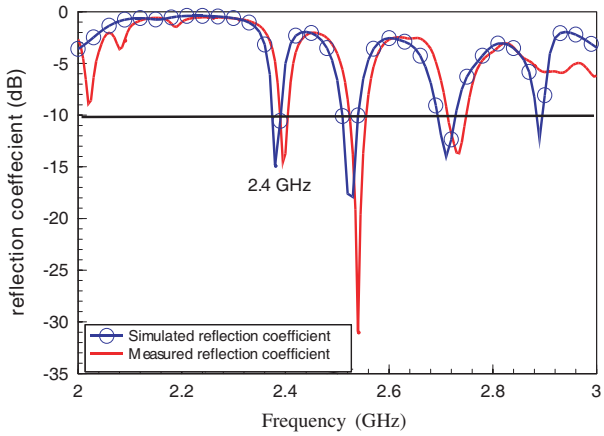

Figure 5: Simulated and measured reflection coefficient spectra.

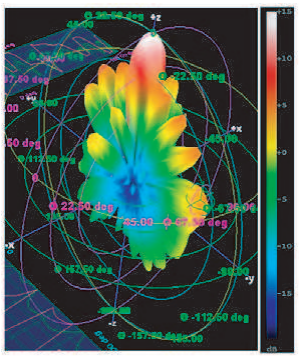

Figure 6: Measured radiation pattern.

Table 1: Detail antenna design parameters (Unit: mm).

W	L	h_1	h_2	h_3	S_1	S_2	W_1	L_1	d
520	520	0.6	0.6	0.8	1.5	3	19.2	62.5	108
Line1	160 Ω, Length = 15 mm, W_2 = 3.6 mm								
Line2	228.5 Ω, Length = 19.2 mm, W_2 = 1.14 mm								

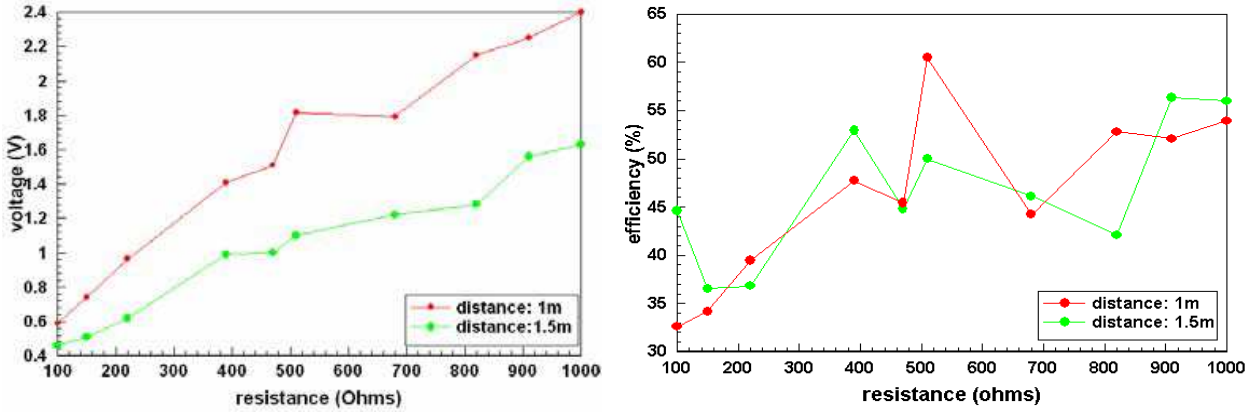

(a) Voltage (b) Power conversion efficiency

Figure 7: Measured voltage and calculated power conversion efficiency of the rectenna with different resistive loads.

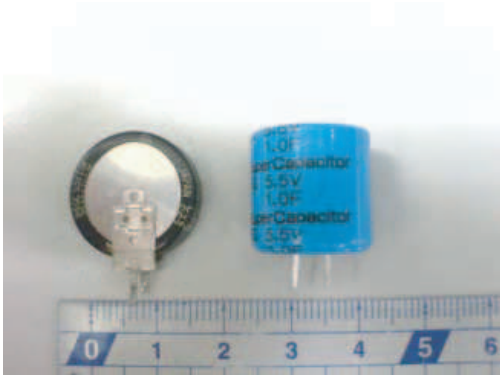

Figure 8: 1 F super capacitors used for rectenna efficiency evaluation.

of the antenna is 4.4 mm. Principle design parameters of the array are listed in Table 1.

The fabricated prototype Franklin array antenna is shown in Fig. 6. Simulated and measured reflection coefficient spectra are provided in Fig. 7. Multiple resonances are observed. However, the principle radiation mode occurs near 2.4 GHz and the bandwidth is approximately 20 MHz. The antenna's radiation pattern was measured in a 3D nearfield anechoic chamber. Fig. 8 shows the concentrated beam, which is formed by 16 patch elements. The antenna gain is approximately 12 dBi.

3. POWER CONVERSION EFFICIENCY EVALUATION

The power delivered to the rectenna can be estimated from the aforementioned Friis transmission equation. In the following experiments, a transmitter of 30.6 dBm (1.148 W) is hooked up with a patch array antenna of 11 dBi to provide RF power. The rectenna is placed in front of the transmitter by either 1 or 1.5 m. The rectenna is connected to either a resistor or a capacitor to evaluate the power conversion efficiencies when used in powering and charging applications.

We first examine the power conversion efficiency of the rectenna by connecting to resistors of different values. Fig. 7(a) shows the measured DC voltage with resistors ranging from 100 to 1000 Ω. As expected, the converted DC voltage is proportional to the load resistance and is inversely proportional to the remote powering distance. The power conversion efficiency is defined in (2).

The RF power available to the rectenna, P_r, can be estimated by the Friis transmission equation in (1).

$$\eta(\%) = \frac{P_{DC}}{P_r} \times 100\% = \frac{V_{DC}^2}{R_L \cdot P_r} \times 100\% \tag{2}$$

According to the calculated curves shown in Fig. 7(b), the power conversion efficiency is a function of the load resistance. Take the results of 1 m for example; optimal power conversion performance is achieved with a 510 Ω load. The power conversion efficiency in general ranges between 35% to 60%.

Next the load is changed to capacitors to evaluate the rectenna's charging efficiency. Two super capacitors of 1 F are used. As shown in Fig. 8, one looks a disk while the other shapes like a cylinder. The efficiency is estimated by tracing the output DC voltage as time progresses. In (3), the denominator is difference in energy stored in the capacitor. The nominator is the RF work accumulated at the antenna.

$$\eta(\%) = \frac{0.5 \times \left[CV\left(t_2\right)^2 - CV\left(t_1\right)^2\right]}{P_r \times \left(t_2 - t_1\right)} \times 100\% \tag{3}$$

Figure 9(a) records the DC voltage every ten seconds for the rectenna connected to the cylinder-like capacitor. The efficiency is calculated for each time slot. Therefore, the curves in Fig. 9(b) are somewhat volatile. In general, the efficiency varies from 35% to 65% when placed 1 m away from the transmitter. When the disk-like capacitor is connected, although the labeled capacitance

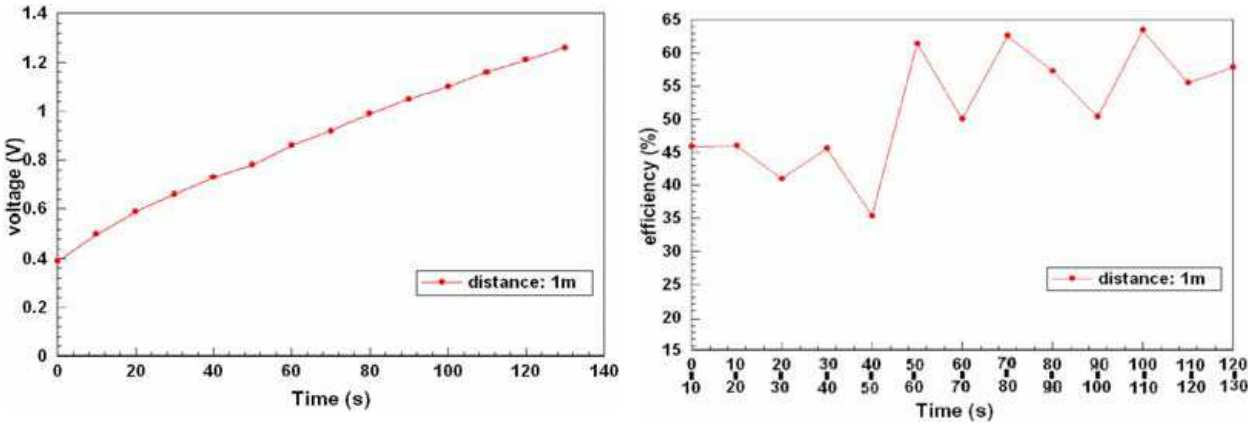

(a) Voltage (b) Power conversion efficiency

Figure 9: Measured voltage and calculated power conversion efficiency with a cylinder-like 1 F capacitor

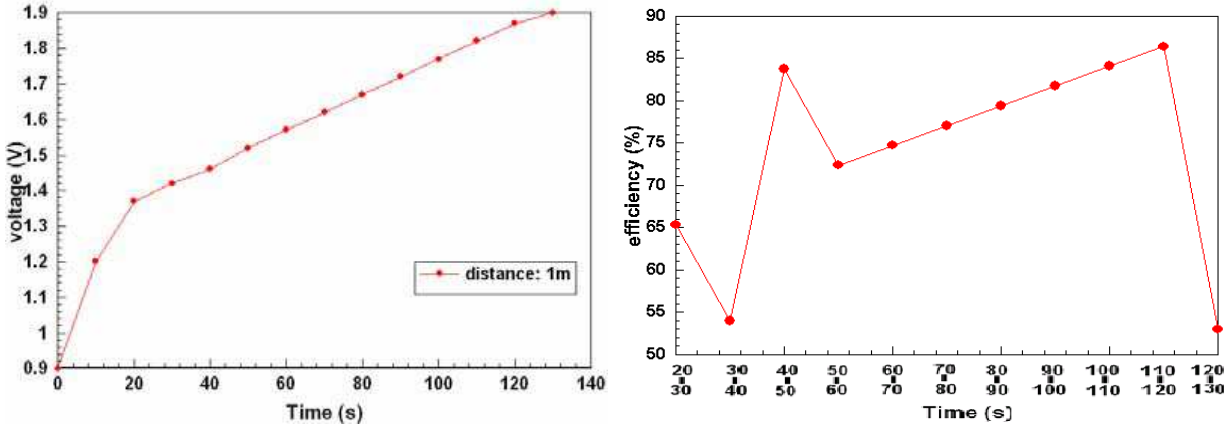

(a) Voltage (b) Power conversion efficiency

Figure 10: Measured voltage and calculated power conversion efficiency with a disk-like 1 F capacitor.

is the same as the previous one, a better efficiency performance is achieved. As Fig. 10 shows, the voltage increases very quickly for the first 20 seconds. Afterward, the voltage rises with a steady pace. The calculated efficiency values range from 50% to 85%.

4. CONCLUSION

In this work, the wireless charging and powering issues are explored via the radio frequency technique. A high gain antenna is connected to the rectification circuit made of RF diodes to extend the wireless charging and powering distance. The main advantage of using a high gain antenna is that the enlarged antenna aperture not only increases the available power but also helps to improve the rectification efficiency. Measurement result shows the conversion efficiency can be as high as 65% at 1 m away from a 1 W transmitter. For capacitive loads, the charging efficiency can reach 85% at 1 meter, which is promising for wireless charging application.

REFERENCES

1. Landt, J., "The history of RFID," *IEEE Potentials*, Vol. 24, No. 4, 8–11, 2005.
2. Shameli, A., A. Safarian, A. Rofougaran, M. Rofougaran, and F. De Flaviis, "Power harvester design for passive UHF RFID tag using a voltage boosting technique," *IEEE Transactions on Microwave Theory and Techinques*, Vol. 55, No. 6, 1089–1097, Jun. 2007.
3. Solbach, K., "Microstrip-Franklin antenna," *IEEE Transactions on Antennas and Propagation*, Vol. 30, No. 4, 773–775, Jul. 1982.
4. Metzler, T., "Microstrip series antennas," *Proceedings of Workshop on Printed Circuit Antennas*, 20.1–20.16, New Mexico State University, Las Cruces, NM, Oct. 1979.

A Miniatured WLAN/Wi-MAX Chip Antenna for Mobile Phone Applications

Long-Kun Li, **Wen-Jiao Liao**, **and Shao-En Hsu**
Department of Electrical Engineering, National Taiwan University of Technology, Taiwan, R.O.C.

Abstract— A compact WLAN/Wi-MAX chip antenna for mobile phone applications is presented in this paper. Two chip antenna designs are proposed. One is for WLAN (2.4 ∼ 2.48, 5.15 ∼ 5.35, 5.725 ∼ 5.85 GHz) and Wi-MAX (3.4 ∼ 3.7 GHz). Its dimensions are 3 mm × 9 mm × 1.6 mm. The other is for WLAN (2.4 ∼ 2.48, 5.15 ∼ 5.35, 5.725 ∼ 5.85 GHz)/Wi-MAX (2.5 ∼ 2.7 GHz). The dimensions are 3 mm × 11 mm × 1.6 mm. The antenna configuration of the two designs comprises two resonant branches. Not only the fundamental mode but also the second order resonance are utilized. Furthermore, the meander line structure is used to create two adjacent resonant frequencies to achieve a tri-band operation. Measurements of the return loss and antenna patterns were performed. The measured result shows good agreement with simulated ones. The main advantage of the proposed chip antenna is that it doesn't require a guard region from other circuit components and is therefore attractive to mobile devices.

1. INTRODUCTION

The wireless communication market is growing up quickly. So does consumers' demand for multifunctional handsets. Nowadays, mobile phones not only provide voice calls but also need to offer connectivity to the Internet. Among various protocols, wireless local area network (WLAN) and worldwide interoperability for micro-wave access (Wi-MAX) are current and potential future candidates for this application. At the same time, compact mobile devices are popular in the market and therefore produce demands for miniaturized antennas. By using meandered metal strip structure, it can offer WLAN connectivity in a compact foot print. In [2], the radiator of the monopole is loaded with a cylindrical ceramic dielectric piece to achieve a dual-band operation. In [3], the miniaturized surface-mount chip antenna contains two radiating structures with a feeding pin and a shorting pin. The antenna yields a superior performance in size reduction and is cost effective. For Wi-MAX, the most common licensed bands are 2.5 ∼ 2.7 GHz and 3.4 ∼ 3.7 GHz. This paper proposes two chip antenna designs One can cover WLAN and Wi-MAX at 3.4 ∼ 3.7 GHz, while the other can operate at WLAN and Wi-MAX at 2.5 ∼ 2.7 GHz. The proposed antenna does not require additional matching circuit and guard region so that the sizes on PCB are 9 × 3 mm^2 and 11 × 3 mm^2, respectively. A low cost FR4 substrate of 45 mm by 100 mm is served as the platform to mount the chip antenna. Both simulations and measurement results are provided to validate the antenna performance.

2. ANTENNA CONFIGURATION

The proposed miniaturized WLAN (2.4 ∼ 2.48, 5.15 ∼ 5.35, 5.725 ∼ 5.85 GHz)/Wi-MAX (3.4 ∼ 3.7 GHz) chip antenna is illustrated in Figs. 1(a) and (b) The substrate is FR4 with a dielectric constant of $\varepsilon_r = 4.4$ and its thickness is 0.8 mm The dimensions are 3 mm × 9 mm × 1.6 mm. The detailed antenna configuration and antenna dimensions are show in Fig 2. The other chip antenna design is tuned to WLAN (2.4 ∼ 2.48, 5.15 ∼ 5.35, 5.725 ∼ 5.85 GHz)/Wi-MAX (2.5 ∼ 2.7 GHz) operation. As shown in Figs. 3(a) and (b), its dimensions are 3 mm × 11 mm × 1.6 mm. Fig. 4 provides detailed geometric parameters of this antenna design.

3. ANALYSIS OF SIMULATION AND MEASUREMENT RESULTS

Figure 5(a) shows simulated and measured reflection coefficient spectra of the first chip antenna design. The two curves agree well and the resonant bands are located within WLAN (2.4 ∼ 2.48, 5.15 ∼ 5.35, 5.725 ∼ 5.85 GHz) and Wi-MAX (3.4 ∼ 3.7 GHz) bands. The input impedance is shown in Fig. 6. As the simulated results in Figs. 7 and 8 indicate the resonance is largely invariant to the changes in neither test board length nor width. The chip antenna comprises two resonant branches and takes advantage of its second order resonance to achieve a tri-band response. According to the current distributions in Fig. 9, the second order resonance and the coupled meander line section result in a wide resonant band around 5.7 GHz The branch at circumference offers WLAN operation and the meander line in the middle works for Wi-MAX at the 3.4 to 3.7 GHz band

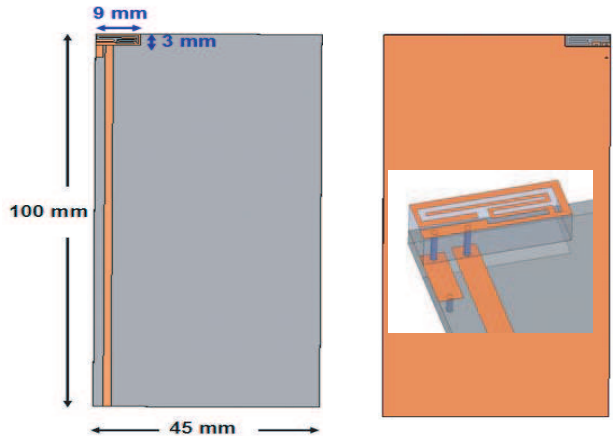

Figure 1: Proposed WLAN/Wi-MAX (3.4 ∼ 3.7 GHz) chip antenna. (a) Top layer. (b) Bottom layer.

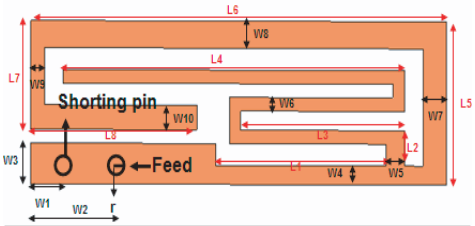

W1	0.75mm	W2	2.75mm
W3	0.75mm	W4	0.35mm
W5	0.4mm	W6	0.25mm
W7	0.5mm	W8	0.5mm
W9	0.3mm	W10	0.45mm
L1	3.7mm	L2	0.65mm
L3	3.55mm	L4	7.4mm
L5	3mm	L6	15mm
L7	2mm	L8	3.6mm
r	0.2mm		

Figure 2: Detailed dimensions of the proposed WLAN/Wi-MAX (3.4∼3.7 GHz) chip antenna.

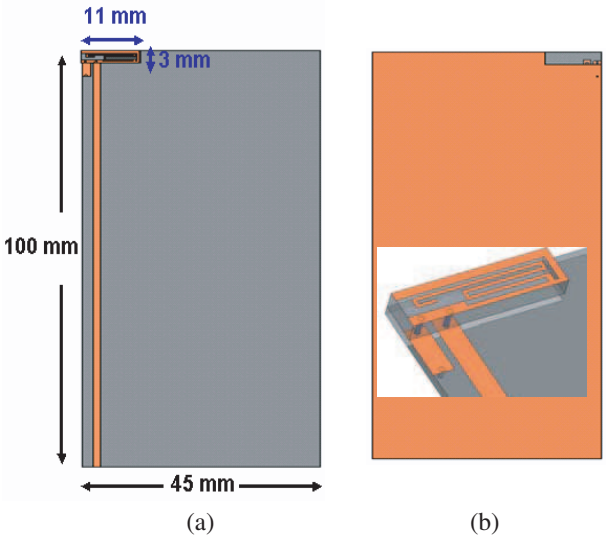

Figure 3: Proposed WLAN/Wi-MAX (2.5 ∼ 2.7 GHz) chip antenna. (a) Top layer. (b) Bottom layer.

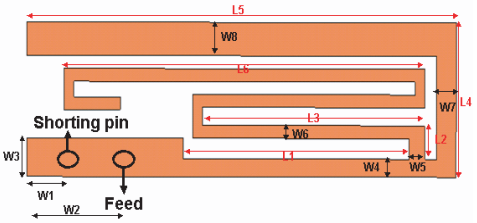

W1	0.75mm	W2	2.75mm
W3	0.75mm	W4	0.35mm
W5	0.4mm	W6	0.25mm
W7	0.5mm	W8	0.65mm
r	0.2mm	L1	5.8mm
L2	0.65mm	L3	5.7mm
L4	3mm	L5	11mm
L6	9.25mm		

Figure 4: Detailed dimensions of the proposed WLAN/Wi-MAX (2.5 ∼ 2.7 GHz) chip antenna.

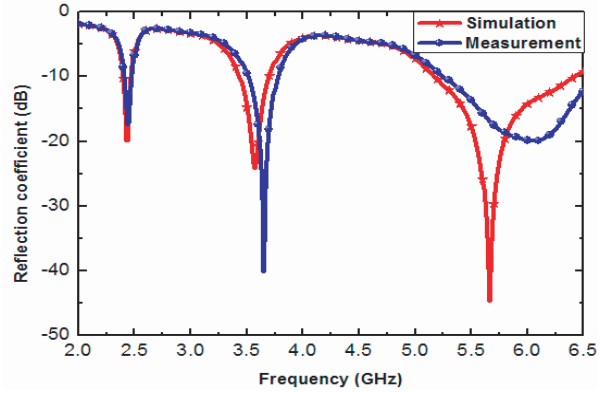

Figure 5: Reflection coefficient spectra of WLAN/Wi-MAX (3.4 ∼ 3.7 GHz) chip antenna.

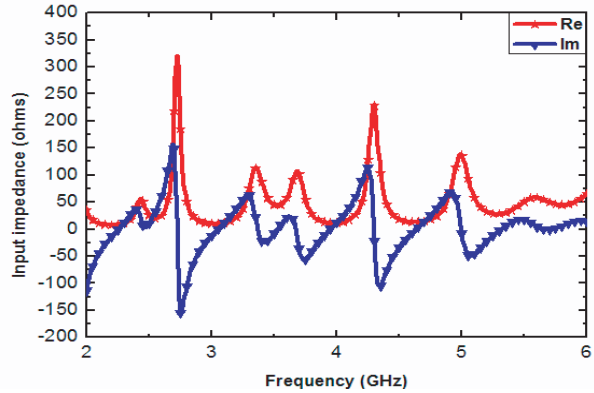

Figure 6: Input impedance spectra of WLAN/Wi-MAX (3.4 ∼ 3.7 GHz) chip antenna.

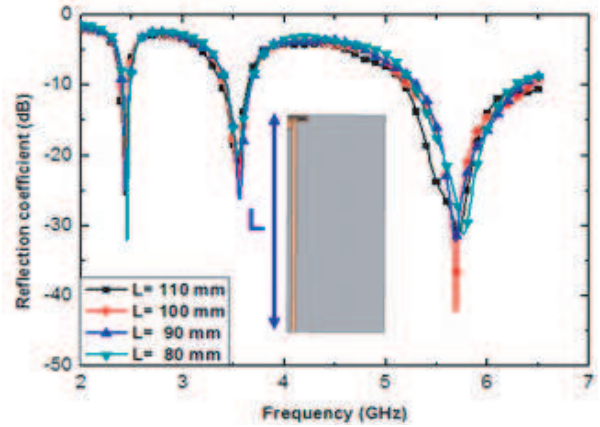

Figure 7: Simulated reflection coefficient spectra of various test board lengths (L).

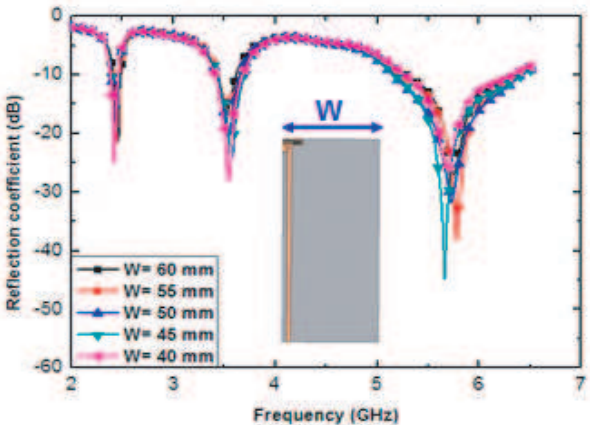

Figure 8: Simulated reflection coefficient spectra of various test board widths (W).

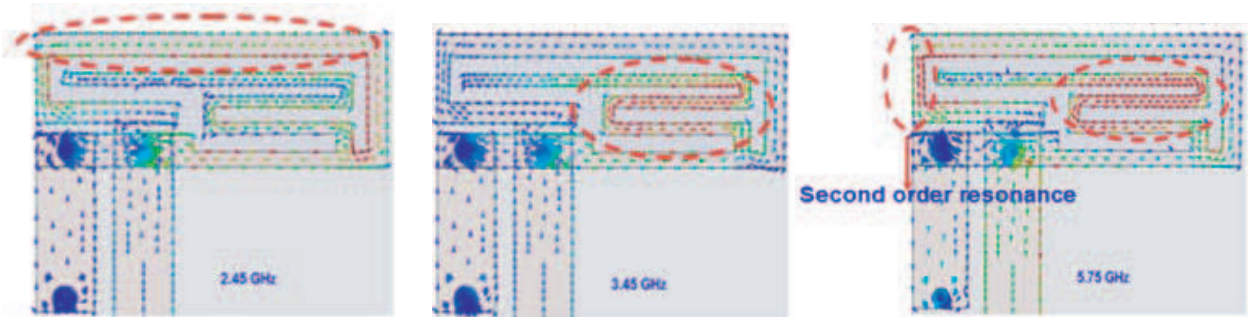

Figure 9: Current distributions of WLAN/Wi-MAX ($3.4 \sim 3.7$ GHz) chip antenna at 2.45, 3.45, and 5.75 GHz.

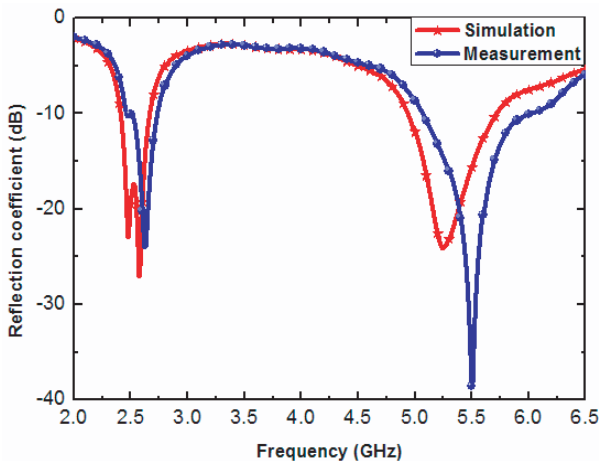

Figure 10: Reflection coefficient spectra of WLAN/Wi-MAX (2.5∼2.7 GHz) chip antenna.

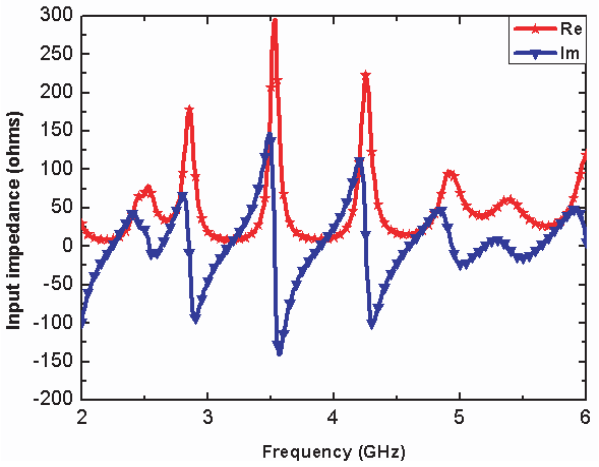

Figure 11: Input impedance spectra of WLAN/Wi-MAX (2.5∼2.7 GHz) chip antenna.

Figure 10(a) shows simulated and measured reflection coefficient spectra of the second chip antenna design. The two curves largely agree with desired resonant bands, which are WLAN and Wi-MAX at $2.5 \sim 2.7$ GHz band. Fig. 11 shows the input impedance. The resonance is also invariant to the changes in test board length and width as shown in Figs. 12 and 13. The current distributions shown in Fig. 14 indicate a broad resonant band is available from 2.4 to 2.7 GHz. The coupled meander line sections excite a second order resonance at 5.2 GHz.

In order to evaluate the radiation patterns, the chip antennas were put in a spherical near-field anechoic chamber as shown in Fig. 15. The fabricated prototype antenna is shown in Fig. 16,

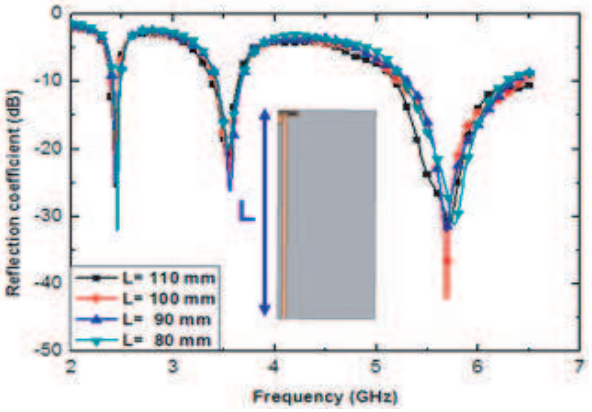

Figure 12: Simulated reflection coefficient spectra of various test board lengths (L).

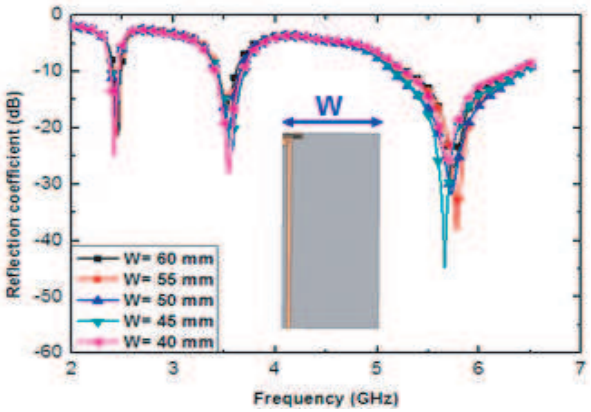

Figure 13: Simulated reflection coefficient spectra of various test board widths (W).

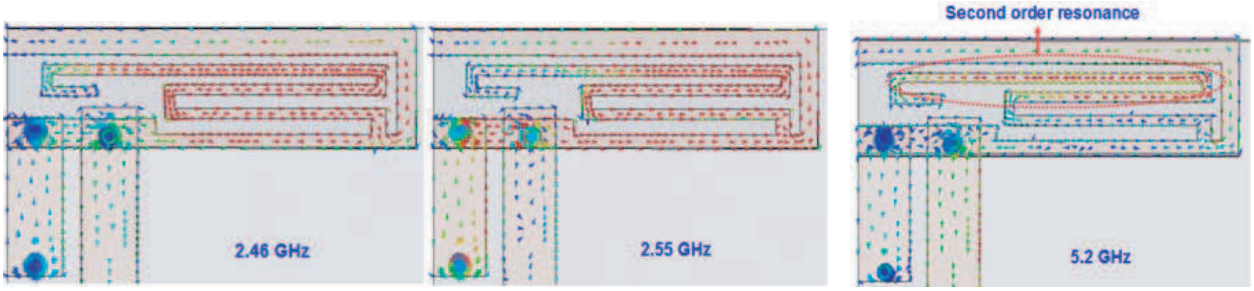

Figure 14: Current distributions of WLAN/Wi-MAX (2.5 $\sim$ 2.7 GHz) chip antenna at 2.45, 2.55, and 5.2 GHz.

Figure 15: Spherical near-field chamber used for radiation pattern measurement.

Figure 16: Fabricated prototype WLAN/Wi-MAX antenna.

Table 1: Performance summary of miniaturized chip antennas.

Dimension(mm^3)	9(L)x3(W)x1.6(H)		
Application	WLAN/Wi-MAX		
Center frequency (GHz)	2.46	3.5	5.75
Peak Gain (dBi)	0.8	1.2	2.8
Efficiency (%)	42	47	59
VSWR	2		
Return loss (dB)	-10		
Polarization	Linear		
Pattern	Omni-directional		
Impedance (Ω)	50		

Dimension(mm^3)	11(L)x3(W)x1.6(H)		
Application	WLAN/Wi-MAX		
Center frequency (GHz)	2.48	2.6	5.3
Peak Gain (dBi)	0.2	2.3	3.1
Efficiency (%)	43	62	59
VSWR	2.5		
Return loss (dB)	-7.5		
Polarization	Linear		
Pattern	Omni-directional		
Impedance (Ω)	50		

Figs. 17 and 18 provide the xz-plane radiation patterns at various bands, which are in general omnidirectional. Table 1 summarizes the antenna performance features.

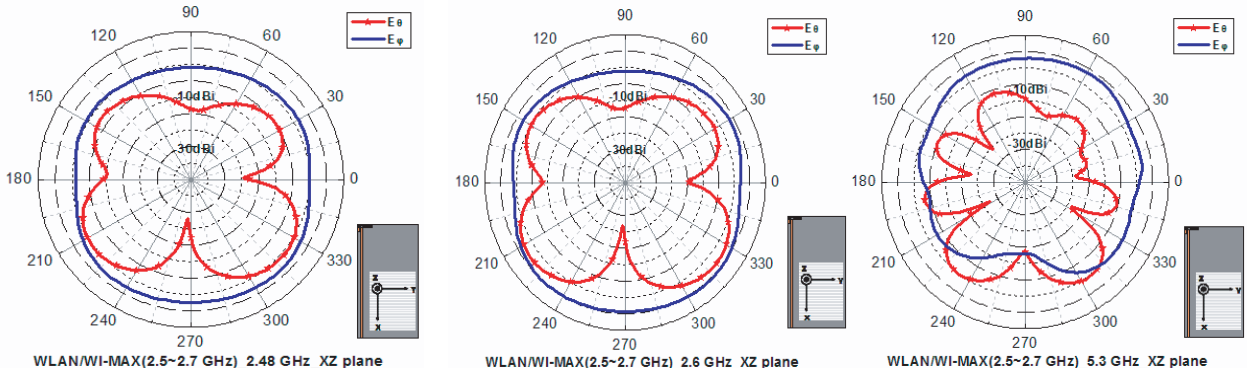

Figure 17: Measured radiation patterns of the WLAN/Wi-MAX ($2.5 \sim 2.7$ GHz) chip antenna.

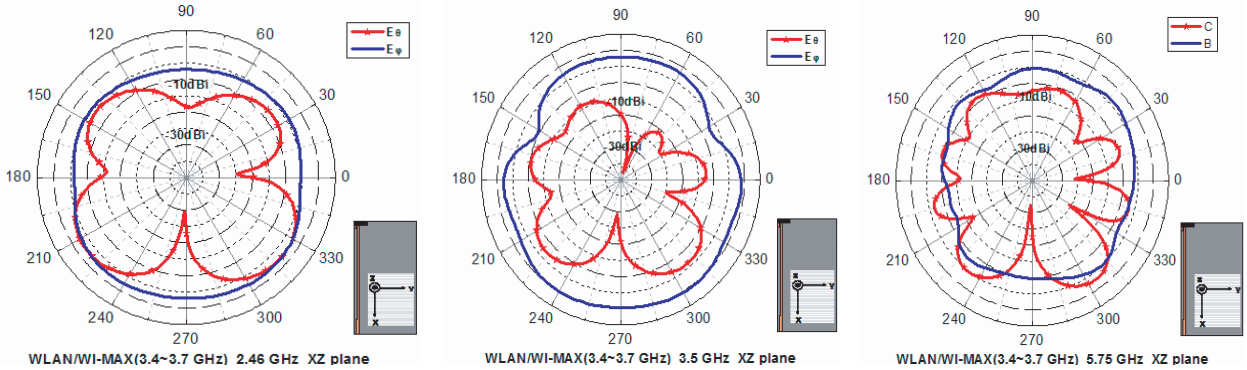

Figure 18: Measured radiation patterns of the WLAN/Wi-MAX ($34 \sim 3.7$ GHz) chip antenna.

4. CONCLUSIONS

The chip antennas proposed in this work come with low profile, light weight, small form factor features. Their omni-directional radiation patterns are quite suitable for mobile communications. Furthermore, their impedance matching performance is invariant to variations in test board sizes. There is no need for a guard region on the circuit board and therefore is particularly attractive for portable devices.

REFERENCES

1. Fang, C.-Y., L.-S. Cheng, J.-H. Li, C.-F. Yang, J.-H. Lin, C.-L. Liao, C.-H. Chen, S.-T. Lin, K.-C. Cheng, S.-F. Wang, M.-C. Pan, C.-L. Hu, and Y.-C. Chien, "A planar chip antenna for 2.4/5.2 GHz ISM band applications," *IEEE Antennas and Propagation Society International Symposium*, Vol. 1B, 455–458, July 3–8, 2005.
2. Lin, Y. F., C. H. Lin, H. M. Chen, J. Y. Jan, and W. S. Chen, "Design of ceramic chip antenna for 2.4/5 GHz WLAN applications," *IEEE Antennas and Propagation Society International Symposium*, 985–988, 914, July 2006.
3. Shin, Y. S. and S. O. Park, "A novel PIFA for 2.4 and 5 GHz WLAN application," *IEEE Antennas and Propagation Society International Symposium*, 645–648, 915, July 2006.

A Beam Switching Planar Yagi-patch Array for Automotive Applications

Shao-En Hsu, **Wen-Jiao Liao**, **Wei-Han Lee**, **and Shih-Hsiung Chang**
Department of Electrical Engineering, National Taiwan University of Science and Technology, Taiwan

Abstract— In this work, a planar beam switching antenna is proposed for wireless communication used in automotive environment. By integrating a Yagi patch antenna array with a one-to-four RF switch, RF power can be delivered to four different driven patch elements and generate directive beams toward different directions. The prototype antenna is designed to operate at the GSM 1800/1900 MHz band for cellular phone uses. The size and height of the fabricated antenna are 293 mm by 293 mm by 3 mm, respectively. Measurement results indicate the antenna's gain is approximately 9.478 dBi with a 3 dB beamwidth of 68°.

1. INTRODUCTION

Due to the rapid growth of wireless communication applications, interference and multi-path fading phenomena become critical and need to be resolved to ensure communication quality. In this paper, a planar beam switching antenna, which is a combination of logic control circuits, a one-to-four RF switch, and Yagi patch antennas [1–5] are proposed to provide spatial diversity. The antenna configuration is shown in Fig. 1. The Yagi patch comprises four driven patch elements, which are connected via a one-to-four RF switch and five parasitically coupled director patch elements. By selecting a specific through path of the RF switch, RF power is fed to one of the driven patch elements. Because directive radiating elements are used, the antenna can be reconfigured to four different beam directions and therefore reduces potential blind angles. Since the antenna comes with a planar structure, it can be employed in the automotive environment. For instance, the planar antenna can be mounted on top of a vehicle. The switching directive beam enables the moving vehicle to track a specific base station and extends the communication distance. Such a planar beam switching antenna can also be used for mobile devices to ensure connection quality.

The design procedure and geometric parameters of the planar one-to-four beam switching antenna are presented in Section 2. The measured antenna performance, including the operational frequency, gain, 3 dB beamwidth, and the squint angle, are provided in Section 3. Analysis based on the comparison of simulated and measured results is also given. A brief summary is drawn at the end.

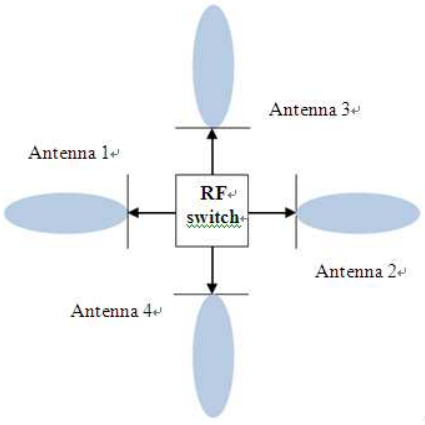

Figure 1: The one-to-four beam switching antenna system.

2. ANTENNA CONFIGURATION AND ANALYSIS

Figure 2 shows the geometric configuration of a Yagi patch antenna. This design is aimed to operation around the GSM 1800/1900 band. It consists of a driven patch element and four parasitically coupled director patch elements. All elements are square patches and are elevated above

the grounded by a dielectric slab of 4 mm thick. The sizes of the five patches are 52 mm × 52 mm. The substrate used is Teflon. Its dielectric constant ε_r is 2.2, while the loss tangent tanδ is 0.001.

According to the microstrip antenna design formula (1) [3], the dimensions of the microstrip antenna can be reduced approximately 1.45 times by using Teflon substrate instead of air spacing. The length L_1 determines the resonant frequency and the position of the feed point (L_2) decides the input impedance. The input impedance increases when the feed point approaches toward the edge. Since the characteristic impedance of the cable line is 50 Ω, the goal of antenna matching is 50 Ω also. The width W_2 affects the antenna efficiency. When the width W_2 increases, so does the efficiency performance. The analysis of the antenna is carried out using HFSS, which is a full wavelength numerical EM tool based on the FEM technique.

Figure 3 shows simulated reflection coefficients of the basic Yagi patch antenna. The antenna resonates at 1.85 GHz. The 10 dB bandwidth is 5.4% and covers the frequency band from 1.80 to 1.90 GHz.

$$W = \frac{1}{2\,f_r\,\sqrt{\mu_0\,\varepsilon_0}}\sqrt{\frac{2}{\varepsilon_r - 1}} \quad \text{When} \quad \frac{w}{h} > 1 \tag{1}$$

In order to provide four radiation beams toward different directions, two Yagi patch antennas are arranged as a cross as shown in Fig. 4. It consists of four driven patch elements located at the ends, five parasitically coupled director patches placed in the middle. Each driven element contains one RF feed to produce a directive beam.

Figure 5 shows simulated reflection coefficients of the four-port Yagi patch antenna. Multiple nulls are observed around 1.8 GHz band due to the cross-shaped geometry. Although the bandwidth is nominally increased, the directive radiating pattern is also altered due to additional resonant modes as shown in Fig. 6. This is because the horizontal and the vertical Yagi patch antennas are mutually coupled, the side lobe is even bigger than the main lobe. Fig. 7 clearly reveals the strong side lobes at directions perpendicular to the main lobe. Similar results are also observed for the other three Yagi patch antennas.

In order to improve the isolation performance of the cross Yagi antenna design, we refer to the crossing element design with fillisters proposed in [7] to reduce coupling. Fig. 8 shows the revised cross Yagi patch antennas. The fillister dimensions are 10 mm × 3 mm. According to simulation results, the isolation performance is dramatically improved. Note the shape of patch element is

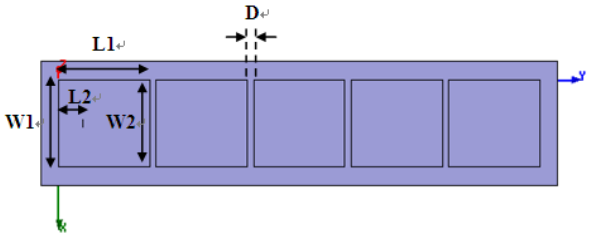

Figure 2: Geometric parameters of the basic Yagi patch antenna. [W_1 = 72 mm, W_2 = 52 mm, L_1 = 52 mm, L_2 = 14 mm, D = 3.5 mm].

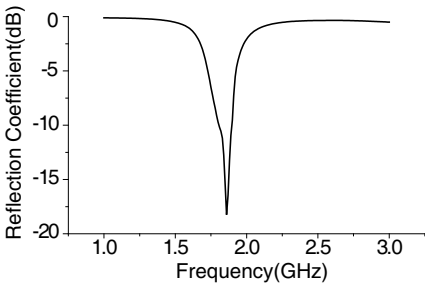

Figure 3: Simulated reflection coefficients of the basic Yagi patch antenna.

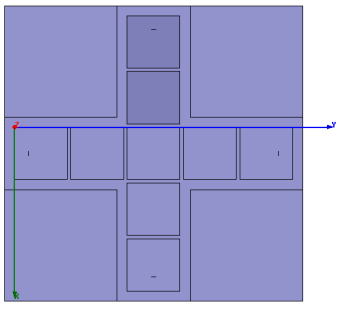

Figure 4: Geometric configuration of the cross Yagi patch antenna.

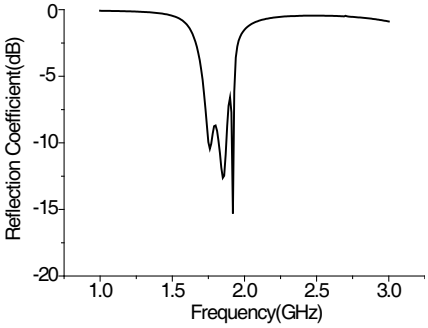

Figure 5: Simulated reflection coefficients of the cross Yagi patch antenna.

changed to a rectangle. Since the length and width are not equal, resonant frequencies of two orthogonal directions are separated and therefore improve the isolation performance.

Because the cross Yagi patch antennas has a symmetric structure, only results of one feed are presented. Fig. 9 shows simulated reflection coefficient of the revised cross Yagi patch antenna. The antenna resonates at 1.84 GHz. The 10 dB bandwidth is 7.6% and covers the frequency band from 1.77 to 1.91 GHz. S_{31} and S_{41}, which are equivalent to isolation performance, are below −25 dB. Fig. 10 shows simulated radiation patterns of the planar beam switching antenna at 1.85 GHz. Table 1 shows the gain performance and main lobe properties at different frequencies. Note the gain of main beam at 1.90 GHz is smaller than other frequencies. This is because S_{21} at 1.90 GHz is larger as indicated in Fig. 9, part of the energy is fed to the opposite port. The difference between main beam and side lobe levels are 8.405, 8.369, and 6.568 dB at 1.80, 1.85, and 1.90 GHz, respectively.

When the operation frequency increases, the squint angle also increases. This is due to the reduced wavelengths at higher frequencies. The constructive interference approaches to the hor-

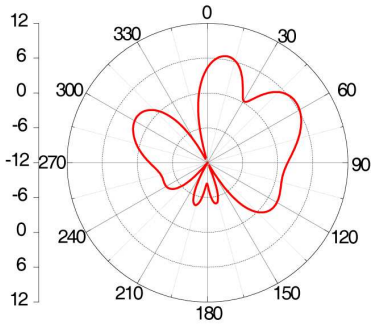

Figure 6: Simulated 2-D pattern of the cross Yagi patch antenna. (E-plane/1.85 GHz).

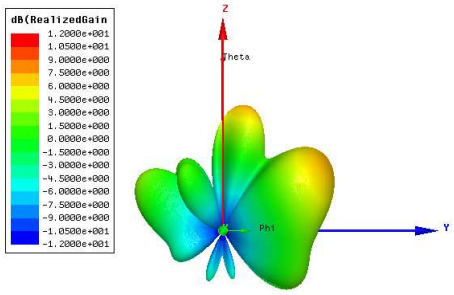

Figure 7: Simulated 3-D pattern of the cross Yagi patch antenna. (1.85 GHz).

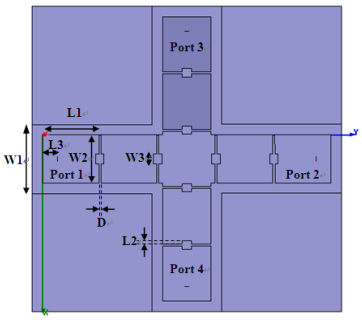

Figure 8: Geometric parameters of the four ports cross Yagi patch antennas: $W_1 = 66$ mm, $W_2 = 46$ mm, $W_3 = 10$ mm, $L_1 = 53$ mm, $L_2 = 3$ mm, $L_3 = 14$ mm, $D = 2$ mm.

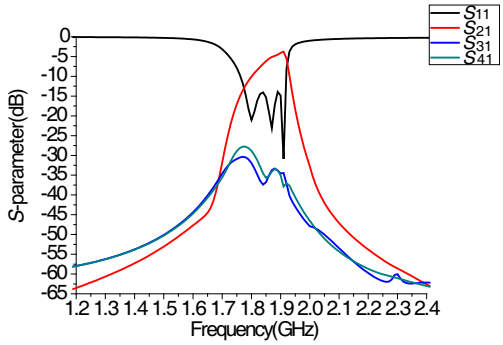

Figure 9: Simulated S-parameter spectra of the revised cross, Yagi patch antennas.

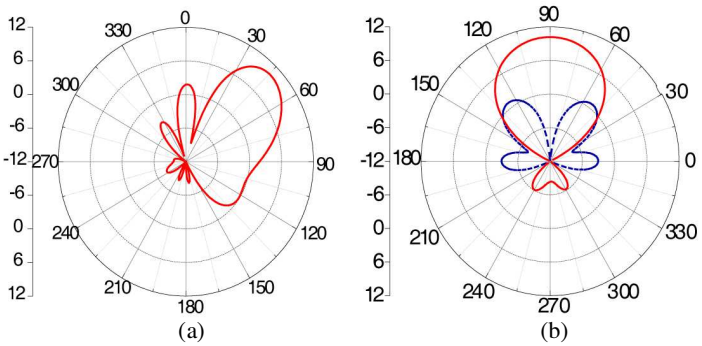

Figure 10: Simulated 2-D patterns of the revised cross Yagi patch antenna at 1.85 GHz (a) E-plane (b) H-Plane at 47°.

Table 1: Comparison of simulated performance.

Frequency (GHz)	Main beam (dB)	Side lobe level (dB)	Squint angle (degree)	3 dB beamwidth (degree)
1.80	10.885	2.480	37	68
1.85	10.169	1.800	47	58
1.90	8.093	1.525	57	46

Figure 11: Fabricated cross Yagi patch antenna.

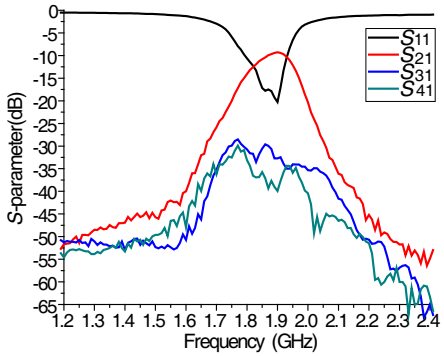

Figure 12: Measured S-parameter spectra of cross Yagi patch antennas.

Table 2: Comparison of measured performance.

Frequency (GHz)	Main beam (dB)	Side lobe level (dB)	Squint angle (degree)	3 dB beamwidth (degree)
1.80	8.455	3.653	36	70
1.85	9.478	3.562	40	68
1.90	8.857	4.038	45	63

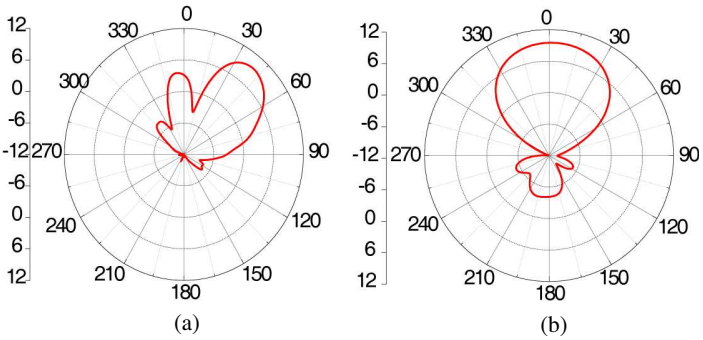

Figure 13: Measured 2-D patterns of the cross Yagi patch antenna at 1.85 GHz (a) E-plane (b) H-Plane at 40°.

izontal plane when the horizontal separation distance among patch elements is fixed. On the contrary, the 3 dB beamwidth increases when the frequency reduces. The directivity performance also deteriorates accordingly.

3. MEASURED RESULTS AND ANALYSIS

As to the prototype antenna fabrication, instead of using Teflon, an acrylic slab is used due to availability. The dielectric constant ε_r of acrylic is 2.2. Fig. 11 shows the fabricated prototype antenna. Measured reflection coefficient of the fabricated cross Yagi patch antenna is provided in Fig. 12. The antenna resonates at 1.865 GHz. The 10-dB bandwidth is 7% and covers the frequency band from 1.80 to 1.93 GHz. The isolation performance, which is represented by S_{31} and S_{41} spectra are below −30 dB. Comparing the simulated and measured S_{21}, the measured S_{21} is

smaller than −10 dB at 1.9 GHz and therefore ensure its gain performance. Fig. 13 shows measured radiation patterns at 1.85 GHz. Table 2 lists measured gains, side lobe levels, squint angle and 3 dB beamwidth. Note the measured gains are smaller than simulated ones by $1 \sim 2$ dB due to the larger loss tangent of acrylic. The difference between the main lobe and side lobe levels are 4.802, 5.916, and 4.819 dB at 1.80, 1.85, and 1.90 GHz, respectively. Similar to the simulation results, the main beam squint angle increases while the 3 dB beamwidth diminishes as the operation frequency goes up.

4. CONCLUSION

A Planar one-to-four beam switching antenna with low profile, low cost, and directive beams has been proposed by utilizing rectangular patches with fillisters. At the designated frequency band, which extends from 1.80 to 1.90 GHz, the antenna's main beam is tilted upward with a 45° squint angle. The isolation is below −30 dB, and the directive gain is approximately 9 dBi.

The antenna gain performance can be further improved by substituting the lossy acrylic slab with less lossy substrates. As to the future work, the feeding path switches can be cascaded to extend the number of Yagi patch antennas accessible from an RF reader, which therefore extends its coverage area and achieves a better spatial diversity performance.

REFERENCES

1. Huang, J. and A. C. Densmore, "Microstrip Yagi array antenna for mobile satellite vehicle application," *IEEE Trans. Antennas Propagation,* Vol. 39, 1024–1030, 1991.
2. Huang, J., "Planar microstrip Yagi array antenna," *IEEE Antennas Propagat. Soc./Ursi Symposium Dig.*, 894–897, June 1989.
3. Lee, K. F., et al., "Microstrip antenna array with parasitic elements," *IEEE AP-S Symposium Digest*, 794–797, June 1987.
4. Yang, X.-S., B.-Z. Wang, W. Wu, and S. Xiao, "Yagi patch antenna with dual-band and pattern reconfigurable characteristics," *IEEE Trans. Antennas and Wireless Propagation*, Vol. 6, 168–171, 2007.
5. Padhi, S. K. and M. E. Bialkowski, "Parametric study of a microstrip Yagi antenna," *Proc. 2000 Asia-Pacific Microw. Conf.*, 715–718, Sydney, Australia, December 2000.
6. Balanis, C. A., *Antenna Theory: Analysis and Design*, 3rd Edition, John Wiley & Sons Inc., 2005.
7. Lin, Y.-S., "A study on RFID microstrip array antennas and associated circuits," Master's Thesis, The Department of Electrical Engineering, National Taiwan University of Science and Technology, 2009.

Dual-band Dual-polarized Hybrid Antenna Array

L. N. Zhang[1], **S. S. Zhong**[1], **and X. L. Liang**[2]

[1]School of Communication and Information Engineering, Shanghai University, China
[2]Department of Electronic Engineering, Shanghai Jiao Tong University, China

Abstract— A novel hybrid antenna array with combination of microstrip antenna and dielectric resonator antenna (DRA) elements is proposed for dual-band dual-polarized SAR applications. Owing to its high efficiency, the DRA is adopted as the higher frequency radiation element operated in X-band. In order to obtain the dual polarization with a low cross-polariztion, the horizontal polarization is excited in the center of the DR while the vertical polarization is fed by two slot feeds with 180° out of phase. Two orthogonal microstrip dipoles are used as the S-band element to provide the horizontal and vertical polarization. As a test model, The array of 2×1 elements for S band and 2×6 elements for X-band is designed and analyzed. Simulation results show that the impedance bandwidth of return loss less than −10 dB, are 6.6% (3.08–3.29 GHz) and 11.5% (8.92–10.01 GHz) for S-band and X-band, respectively. The cross-polarization levels of the antenna array are −36 dB for X-band and −27 dB for S-band in both planes.

1. INTRODUCTION

Recently dual-band and dual polarized antenna arrays have been widely studied for satellite and wireless communication applications, particularly for synthetic aperture radar (SAR) applications [1–4]. Most of the antennas adopt microstrip structures to realize the dual band and dual polarization function. Microstrip antenna has good performances in lower frequency, however in higher frequency, the radiation efficiency deteriorates apparently, i.e., the radiation efficiency decreases by 15% as the frequency rises from C-band to X-band. Compared to the microstrip antenna, the radiation efficiency of the dielectric resonator antenna is as high as 95% even for frequencies up to 10 GHz, due to the absence of inherent conductor losses [5].

This paper proposes a new design of dual-band dual-polarized antenna array. For the X-band, the hybrid feeding structure in the dielectric resonator antenna element design adopts an H-shaped slot coupling for the horizontal polarization and two U-shaped slot coupling feeds with 180° out of phase for the vertical polarization. For S-band, the two stacked dipoles with different polarization are located orthogonally in different layers. The microstrip dipoles are fed by the microstrip line with tuning stubs. The proposed antenna array has been designed and simulated with Ansoft HFSS based on the finite-element method (FEM). References [6, 7] have been certified the correctness of the software Ansoft HFSS. The simulated results imply that the antenna array has good performance.

2. X-BAND DIELECTRIC RESONATOR ANTENNA ELEMENT DESIGN

The configuration of the X-band dual-polarized dielectric resonator antenna element is shown in Fig. 1. The rectangular dielectric resonator (DR) has length 6.6 mm, width 6.6 mm and height $H = 6.35$ mm with dielectric constant $\varepsilon_{rDR} = 9.8$. The ground plane is fabricated on the substrate with dielectric constant $\varepsilon_{rS} = 10.2$ and thickness $d_S = 0.762$ mm.The vertical polarization is excited at the center of the dielectric resonator by a 50 Ω microstrip line via an H-shaped slot in the ground plane. The H-shaped slot is defined by parameters l_1, w_1, l_2, w_2. The horizontal polarization is excited through two U-shaped slots in the ground plane with a 180° out of phase microstrip feeding network, which is located at two sides of the dielectric resonator.

The optimized parameters are $l_1 = 2.4$ mm, $l_2 = 1.4$ mm, $l_3 = 1.5$ mm, $l_4 = 3$ mm, $l_5 = 1.15$ mm, $l_6 = 2.9$ mm, $l_7 = 7.5$ mm, $w_0 = 0.7$ mm, $w_1 = 0.4$ mm, $w_2 = 0.3$ mm, $w_3 = 0.5$ mm, $w_4 = 0.7$ mm, $w_5 = 0.3$ mm, $w_6 = 0.1$ mm, $w_f = 0.1$ mm. The simulated return loss and port isolation for the dielectric resonator antenna element are shown in Fig. 2. It is observed that, for RL ≤ -10 dB, the antenna covering frequency ranges are 8.92–10.01 GHz, or BW $\approx$ 11.5% for Port 1 and 8.86–9.95 GHz, or BW≈11.6% for Port 2, respectively. Over the bandwidth 9–10 GHz, the port isolation is below −43 dB. For briefly, the E- and H-plane far-field radiation patterns around the frequency 9.6 GHz, for both polarizations are not shown. But from the simulated results, it is observe that the levels of the cross-polarization in both planes are improved obviously, about 10 dB.

3. S-BAND MICROSTRIP DIPOLES ELEMENT DESIGN

The S-band element adopts traditional microstrip dipoles [6]. Two separated orthogonal stacked dipoles are used to provide the horizontal and vertical polarizations. The top and side views of a stacked dual polarized S-band dipole element are shown in Fig. 3. Each of two stacked dipoles is fed by a microstrip line with a tuning stub. The lengths of the driven dipoles are $a = 31\,\text{mm}$, $b = 32\,\text{mm}$ and the lengths of the parasitic dipoles are $pa = 35\,\text{mm}$, $pb = 33.6\,\text{mm}$. A width of 4 mm for vertical driven and parasitic dipoles and a width of 2.4 mm for the horizontal ones are chosen. The parameters of the tunning stub are $w_{s1} = 1.2\,\text{mm}$, $w_{s2} = 2\,\text{mm}$, $w_{l1} = 23\,\text{mm}$, $w_{l2} = 20\,\text{mm}$.

The simulated return loss and port isolation for the dipole element are shown in Fig. 4. It

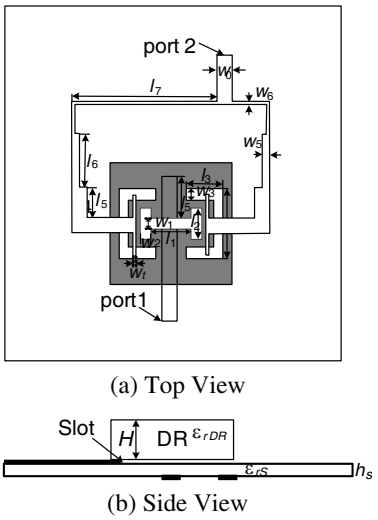

Figure 1: Configuration of X band element.

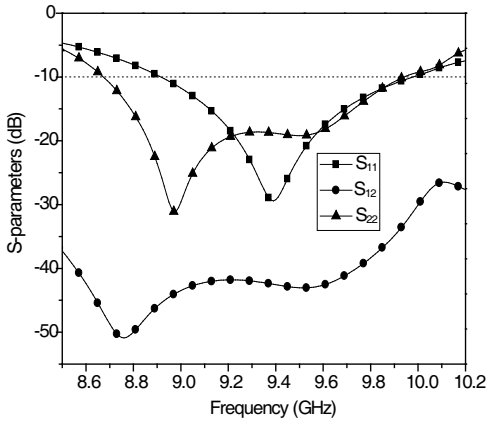

Figure 2: Simulated S parameters of X-band.

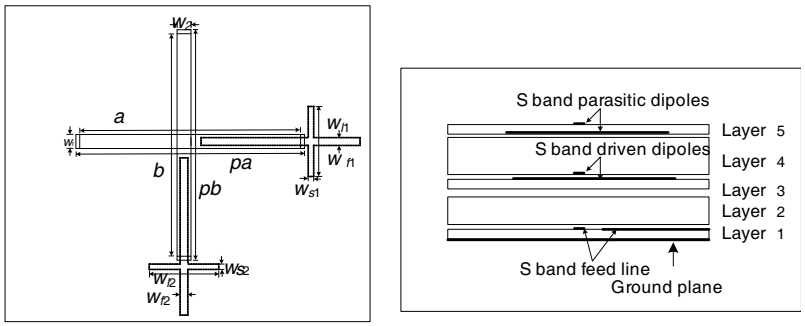

Figure 3: Configuration of S-band element.

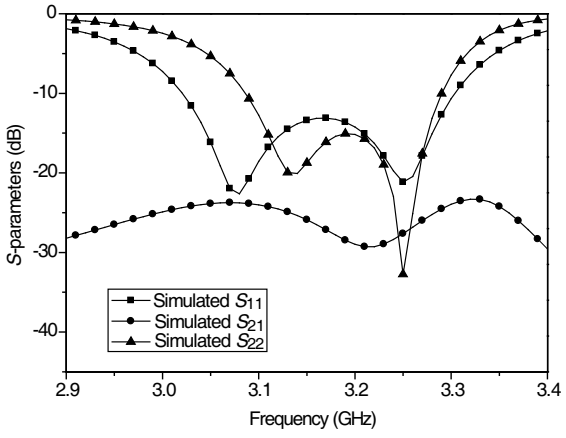

Figure 4: Simulated S parameters of S-band.

is observed that, for RL ≤ -10 dB, the antenna covers frequency ranges of 3.02–3.30 GHz, or BW $\approx$ 8.9% for Port 1 and 3.08–3.29 GHz, or BW $\approx$ 6.6% for Port 2. Over the bandwidth, the port isolation is below -24 dB.

4. S AND X BAND DUAL POLARIZED ARRAY DESIGN

The geometry of the proposed dual-band dual-polarized hybrid antenna array is shown in Fig. 5. The layer parameters of the multi-layered substrate configuration for the antenna array are listed in Table 1. To meet the requirement of the scan range ($\pm 30^\circ$), the X-band element spacing is selected to be 22 mm, about $0.7\lambda_1$, and the S-band element spacing is triple that of the X band, 66 mm, about $0.7\lambda_2$. (λ_1 and λ_2 are the wavelength in free space at the center frequencies of S- and X-bands, respectively). The cross-polarization suppression technique is both used in S- and X-bands for array design [8]. The simulated radiation patterns of S-band at the center frequency 3.2 GHz are plotted in Fig. 6. The cross-polarization levels are ≤ -30 dB in both planes. For $-$X

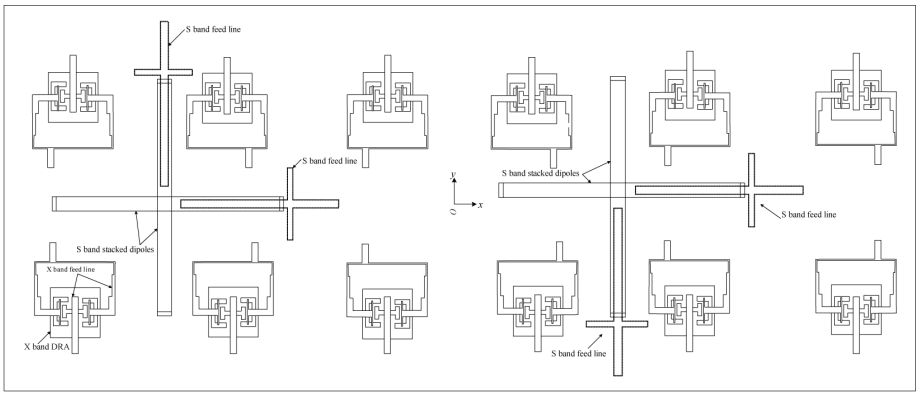

(a) Top View

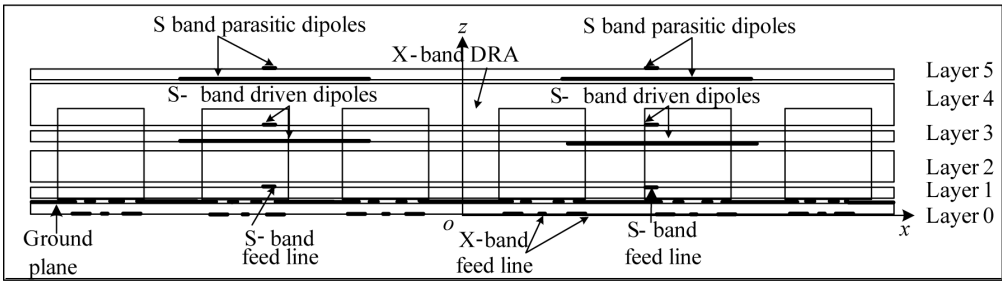

(b) Side View

Figure 5: Configuration of the S/X band array.

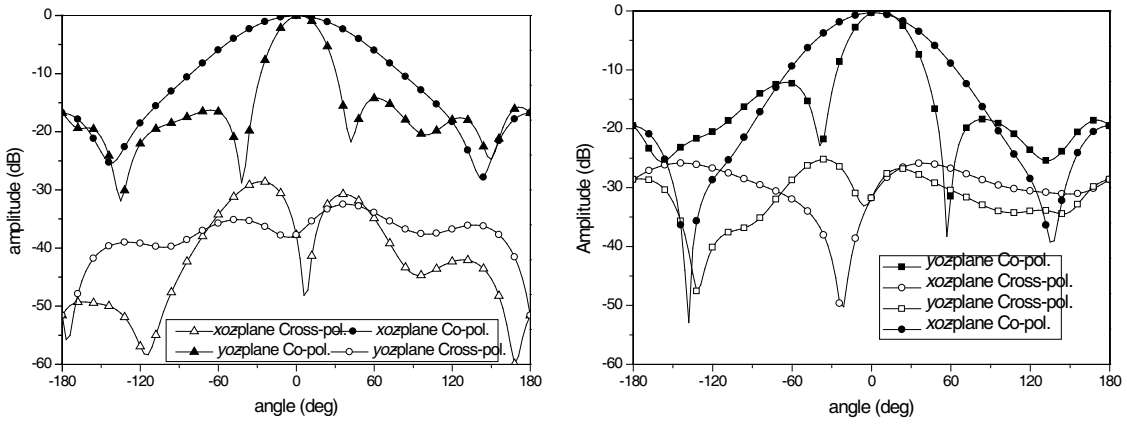

(a) Horizontal polarization (b) Vertical polarization

Figure 6: Simulated radiation patterns of S-band 2×1 array.

band, the simulated radiation patterns at the center frequency 9.6 GHz are plotted in Fig. 7. It is observed that the cross-polarization levels are ≤ -37 dB in both planes.

Table 1: Layer parameters.

Layer	Material	ε_r	Thickness, mm
Layer 0	Rogers RT3010	10.2	0.762
Layer 1	Rogers RT6002	2.94	0.762
Layer 2	Rohacell 51HF	1.07	1.5
Layer 3	Rogers RT6002	2.94	0.762
Layer 4	Rohacell 51HF	1.07	4
Layer 5	Rogers RT6002	2.94	0.762

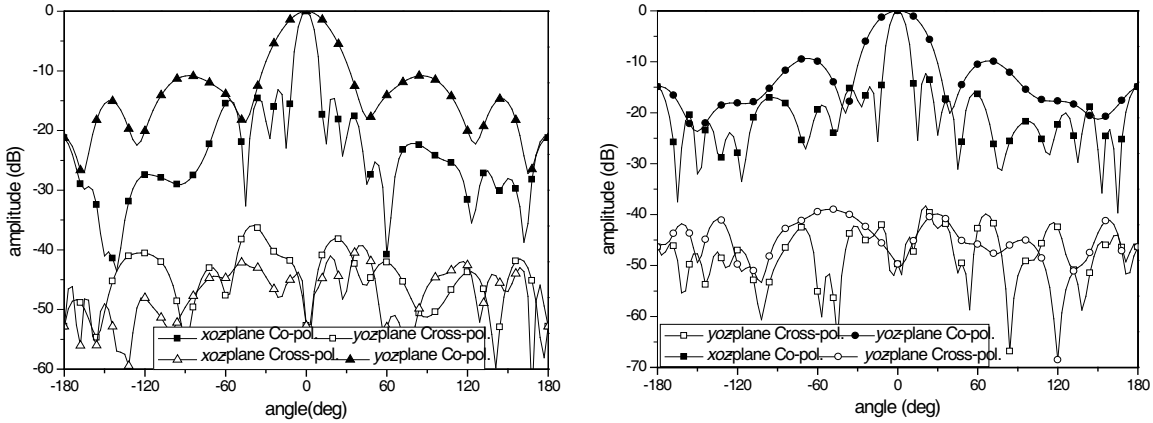

(a) Horizontal polarization (b) Vertical polarization

Figure 7: Simulated radiation patterns of X-band 2×6 array.

5. CONCLUSION

A novel dual-band dual-polarized hybrid antenna array has been introduced for SAR application by using the combination of the microstrip antenna and the dielectric resonator antenna elements. From the simulated results, it is noted that the antenna array achieves an impedance bandwidth of 6.6% (3.08–3.29 GHz) for S-band and 11.5% (8.92–10.01 GHz) for X-band. The cross-polarization levels at S-band and X band are -27 dB and -37 dB in both planes, respectively. The antenna array has advantages such as small size, high efficiency, and perfect polarization purity and easy to expand into a large array, which will be a promising candidate for the SAR application.

ACKNOWLEDGMENT

This work was supported by the National High-Technology Research and Development (863) Program of China, under Grant No. 2007AA12Z125.

REFERENCES

1. Pozar, D. M. and S. D. Targonski, "A shared-aperture dual-band dual-polarized microstrip array," *IEEE Trans. Antennas and Propag.*, Vol. 49, No. 2, 150–157, 2001.
2. Pokuls, R., J. Uher, and D. M. Pozar, "Dual-frequency and dual-polarized microstrip antenna for SAR application," *IEEE Trans. Antennas and Propag.*, Vol. 46, No. 9, 1289–1296, 1998.
3. Vetharatnam, G., C. Kuan, and C. H. Teik, "Combined feed network for a shared-aperture dual-band dual-polarized array," *IEEE Antennas and Wireless Propag. Lett.*, Vol. 4, 297–299, 2005.
4. Shafai, L. L., W. A. Chamma, M. Barakat, P. C. Strickland, and G. Seguin, "Dual-band dual-polarized perforated microstrip antennas for SAR application," *IEEE Trans. Antennas and Propag.*, Vol. 48, No. 1, 58–66, 2000.

5. Lai, Q., G. Almpanis, C. Fumeaux, H. Benedickter, and R. Vahldieck, "Comparison of the radiation efficiency for the dielectric resonator antenna and the microstrip antenna at Ka band," *IEEE Trans. Antennas and Propag.*, Vol. 56, No. 11, 3589–3592, 2008.
6. Qu, X., S. S. Zhong, Y. M. Zhang, and W. Wang, "Design of an S/X dual-band dual-polarised microstrip antenna array for SAR applications," *IET Microw. Antennas Propag.*, Vol. 1, No. 2, 513–517, 2007.
7. Tang, X.-R., S.-S. Zhong, L.-B. Kuang, and Z. Sun, "Dual-polarised dielectric resonator antenna with high isolation and low cross-polarisation," *Elect. Lett.,* Vol. 45 No. 14, 719–720, 2009.
8. Woelders, K. and J. Granholm, "Cross-polarization and sidelobe suppression in dual linear polarization antenna arrays," *IEEE Trans. Antennas and Propag.*, Vol. 45, No. 12, 1727–1740, 1997.

An Outdoor Bistatic Scattering Assessment Using Array Antennas

Chih-Yao Hsieh, **Wen-Jiao Liao**, **and Long-Kun Li**
Department of Electrical Engineering, National Taiwan University of Science and Technology
43, Sec. 4, Keelung Rd., Taipei 106, Taiwan

Abstract— Passive coherent location (PCL), which is also known as passive radar, is of increasing interest lately. In a passive radar system, the transmitting and receiving antennas are placed at different locations. Therefore, it detects targets' bistatic scattering instead of monostatic scattering in conventional radars. In this work, we conducted experiments that evaluate the bistatic radar cross section (RCS) from targets in the UHF band. The variation in the amount of bistatic scattering was examined and analyzed by changing the parameters which include the target's shape, orientation, distance to antenna, and antenna polarization.

1. INTRODUCTION

In 1936, German deployed radio frequency radar at warship Graf Spee for the first time. Since then, the radar technology has dramatically evolved and played an important role on the battlefield. Among the many different types of radar, the air surveillance radar is of crucial importance. However, the conventional air surveillance radar, which continuously emits strong radiation in the order of hundreds of kilowatts or even megawatts, is likely to expose its location. Therefore, the concept of passive radar has been brought up and implemented. Unlike tradition active radars, passive radars do not require high power transmitters and come with receivers only. Passive radar receivers continuously monitor the background radio signals, such as commercial TV broadcasting, mobile telecommunication or satellite signals. The presence of air targets may perturb the magnitudes, phases and even frequencies of background signals. A passive radar may therefore be able to detect the perturbation and determine if an air target is present.

In the passive radar operation scenario, the transmitting and receiving antennas are not placed at the same position. Unlike traditional radars, which detect the monostatic back scattering from the target, passive radars exploit the bistatic RCS property of targets [1–4]. In this paper, we designed a series of experiments that measures the bistatic RCS values of elevated targets in the UHF band. The experiment set-up includes two antennas, one is for transmission, and the other is for reception. Because the signal magnitude may be very weak due to propagation, an RF transmitter of 10 watts at the UHF band was assembled to conduct measurements. The components used in the transmitter include two stages of amplifier, attenuators, a power supply, a circulator and a termination. The mock-up targets that scatter impinging radio frequency waves are placed in front of directive antennas. A network analyzer was employed to provide radio source and measure the properties of scattered signals. In order to minimize scatterings from background clutters experiments were conducted on a roof top.

The design and performance improving measures of the antennas used in experiments are presented in Section 2. The measurement range set up as well as measurement results and analysis are provided in Section 3. A conclusion and future work topics are drawn in the end.

2. DIPOLE ARRAY ANTENNA FOR BISTATIC RCS MEASUREMENTS

A dipole antenna is used as the building block for the development of the array antenna used in bistatic RCS measurements. Four dipole antennas are assembled to form a directive array antenna. The operation frequency band of the antenna expands from 530 to 600 MHz. In order to make the array antenna more directive, a metal board is put behind the dipoles with a quarter wavelength separation. So that the radiation travels backward is reflected and adds up constructively with forward going waves. The four dipole antennas are connected via an one-to-four Wilkinson power divider. The array structure is supported by a chrome finish wire frame storage shelf of 120 cm by 60 cm. The antenna's reflection coefficient spectrum is measured to validate its bandwidth performance. The radiation pattern is measured in 3D near field anechoic chamber.

The dipole antenna in principle is omni-directional on the azimuth plane. However, a high gain directive antenna is needed for scattering measurements. A 300 mm × 200 mm FR4 board is placed behind the dipole as a reflector to increase the antenna directivity. The measurement results show

an approximately 3 dB gain improvement is achieved by adding the reflector. Fig. 1 provides a comparison of gain spectra with and without the reflector.

In order to further increase the antenna gain, we used four dipole antennas to formulate a 4 by 1 dipole array. Therefore, a one-to-four power divider that provides multiple feeds is needed. The Wilkinson power divider configuration is used to take advantage of its good isolation performance.

A 120 cm by 60 cm chrome-finish metal wire frame storage shelf is used to provide a sturdy support for dipole antenna elements. The fabricated dipole array antenna is shown in Fig. 2. The wire frame of the shelf also helps to increase the reflective ground plane size. This is because the frame wires are running in parallel with the antenna polarization and can be regarded as a solid ground plane. The separation distance among dipole antennas is 26 cm, which is about half of a wavelength at 550 MHz. The radiation pattern is measured in a 3D nearfield chamber. The gain is about 10 to 11 dBi, which meets our expectation if taking line and connector losses into consideration. Figs. 3(a) and (b) provides the E-plane and H-plane patterns respectively. The front-to-back ratio is approximately 14 dB. The 3 dB beamwidth is 75 degree on the E-plane and 30 degree on the H-plane.

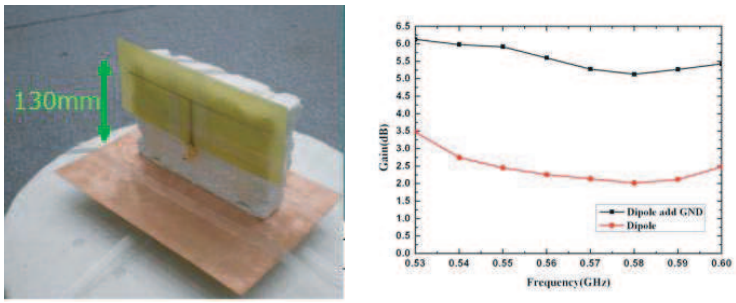

Figure 1: Fabricated dipole antenna and measured gain spectra.

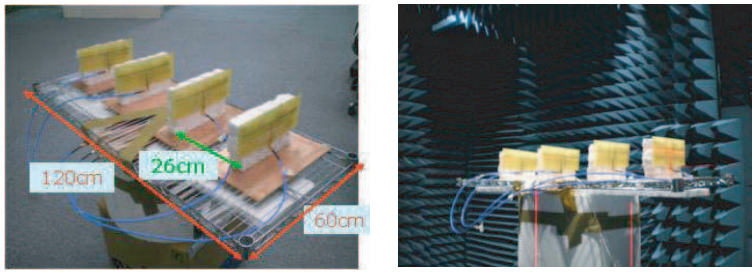

Figure 2: Fabricated dipole array antenna.

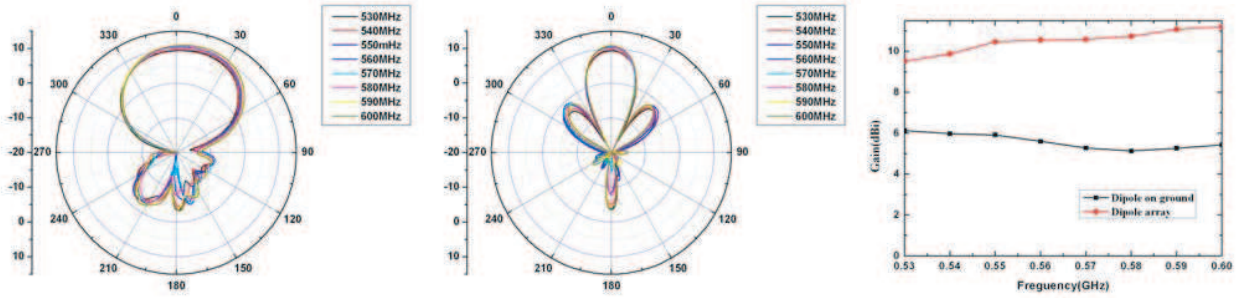

(a) E-plane (b) H-plane (c) The antenna of gain

Figure 3: Measured radiation patterns and gain spectra of the fabricated dipole array antenna.

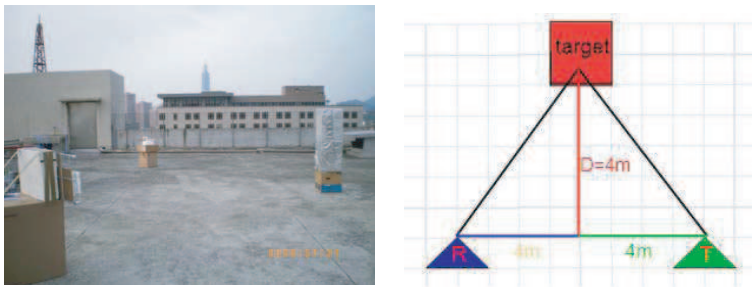

Figure 4: Test range setup.

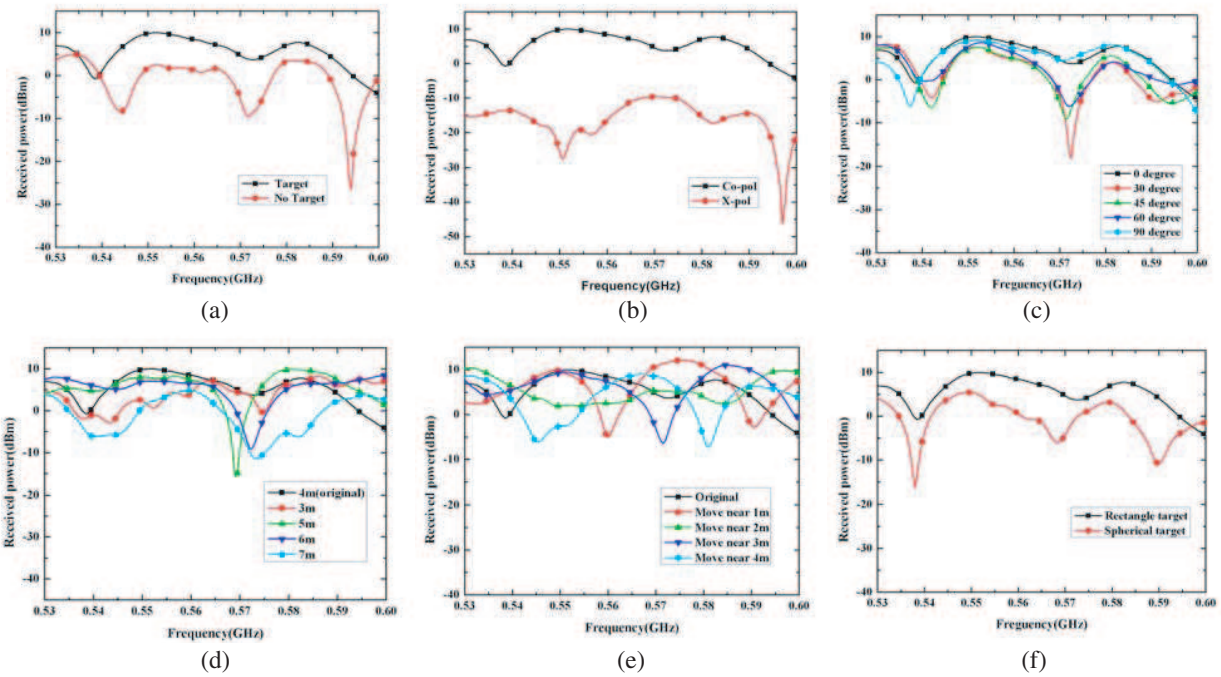

Figure 5: Received power spectra of various measurement setups. (a) With and without the rectangular target. (b) Collinear and perpendicular antenna displacement. (c) Various target orientations. (d) Various distances between target and antennas. (e) Various distances between antennas. (f) Rectangular and special targets.

3. BISTATIC SCATTERING MEASUREMENTS

The purpose of this experiment is to evaluate the validness of our testing range and assess the bistatic RCS of mock-up under various operation scenarios. Parametric studies such as the target orientations and target shapes are conducted. Fig. 4 shows the testing range setup. The fabricated dipole array antenna is used for transmission while a Yagi antenna is used for reception.

Following figures present the measured transmission spectra under various setups. Fig. 5(a) compares the received power spectra with and without a cubical target, which is made with a cardboard box wrapped in aluminum foils. The presence of target increases the amount of return by approximately 10 dB. However, note that there is a substantial return power level in the case of no target. This is because the test range, which is located at the roof top, has fences and some elevated structure that may introduce additional scattering.

Figure 5(b) shows scattering spectra of co-pol and cross-pol arrangements among transmitting and receiving antennas. According to the plot, the return level of collinear antenna arrangement exceeds the one of perpendicular arrangement by nearly 20 dB. This is because the target surfaces, which are flat in general, provide little cross-pol reflection. Note that the target dimensions are close to the wavelength, the scattering spectra therefore exhibit some interference patterns

Next, the box target is rotated by various angles to examine the changes in return level. The results are shown in Fig. 5(c). When the target is set to zero degree, one side of the box is facing

toward the transmitting and receiving antennas. The antennas and the box exhibit a specular return relationship and therefore yield the strongest return. Similar return level is observed when the box is rotated by 90 degrees.

Figure 5(d) shows the scattering spectra of different separation distances between the target and the antennas. The target is moved along the red line shown in Fig. 4. Intuitively, the return level should increases as the separation distance diminishes. However, the curve of 3 m separation is in general lower than the ones of 4 m and 5 m. This may be attributed to that the coupling among transmitting and receiving antennas gets larger so that the multipath interference affects the reception level.

Next, we change the distance between the transmitting and receiving antennas while the target is set 4 m in front of antennas. The two antenna positions are moved along the green line in Fig. 4 from 1 m to 4 m. The results are shown in Fig. 5(e). Because of multipath interference, the curves exhibit substantial ripples. Constructive and destructive additions appear in a periodic fashion on those curves.

In Fig. 5(f), the return spectrum of the rectangular target is compared with the one of a spherical target. The target radius is 0.3 m. As expected, the return level becomes smaller due to widely distributed scattering from a curved surface.

The measured return level presented above can be transformed into RCS values using the radar equation shown in (1). Note this equation is modified to cope with the bistatic scattering scenario. The measurement parameters are substituted into this equation as followings. The transmitting power, P_t, is equal to 39 dBm. The transmitting antenna gain, G_t, is set to 10 dBi. The receiving antenna gain, G_r, is set to 7 dBi. The wavelength is equal to 0.53 m. The distance between receiving antenna and the target is R_1, and the distance between transmitting antenna and the target is R_2. The target's bistatic RCS value can be calculated accordingly. In Tables 1 and 2, the maxima, average and minima RCS values are tabulated for different parametric studies. The actual target cross section area size is also listed for reference.

$$P_r = P_t G_t G_r \left[\frac{\lambda^2}{(4\pi)^3 R_1^2 R_2^2}\right] \sigma_{bistatic} \tag{1}$$

According to Table 1, the RCS values of collinear antenna displacement are larger than the ones of perpendicular displacement. This result indicates that flat surfaces produce little cross polarization scattering. Note that under the collinear displacement, the RCS value of the rectangular target indicates the electrical size of the target is much bigger than its physical size.

Table 2 provides the comparison of RCS values of rectangular and spherical targets. The spherical target generates no specular reflection and therefore yields smaller RCS values. Nevertheless, the electrical size of the spherical target is still larger than its physical size.

Table 1: Calculated biststic RCS of collinear and perpendicular antenna displacements (Unit m^2).

Pr Value / Polarization	Peak	Average	Minimum	Target Area
Co-pol	5.85	1.21	0.21	0.72
X-pol	0.065	0.018	0.000014	0.72

Table 2: Calculated bistatic RCS of rectangular and spherical targets (Unit m^2).

Pr Value / Target	Peak	Average	Minimum	Target Area
Rectangular box	5.85	1.21	0.21	0.72
Sphere	2.03	0.43	0.03	0.28

4. CONCLUSION

Using the dipole array antenna and the high power transmitter developed in this work, a bistatic scattering measurement range was deployed to evaluate bistatic RCS of various targets and antenna displacement. The RCS values are calculated from received power levels based on the bistatic radar equation. Parametric studies were conducted for target's shape, orientation and the antenna displacement. The experimental results show the RCS variation in different measurement setups

comply with physical expectations. However, the measurement results also reveal that the testing range is not ideal, substantial scattering are generated from nearby building structures such as walls and iron railings. Furthermore, the significant coupling among antennas perturbs the measurement results in certain degree. As to future measurement work, a wild open testing site should be chosen with elevated targets to minimize background scattering.

REFERENCES

1. Howland, P. E., "Target tracking using television-based bistatic radar," *IEE Proc. — Radar. Sonar Navig.*, Vol. 146, No. 3, 166–174, Jun. 1999.
2. Cherniakov, M., D. Nezlin, and K. Kubik, "Air target detection via bistatic radar based on LEOS communication signals," *IEE Proc. — Radar. Sonar Navig.*, Vol. 149, No. 1, 33–38, Feb. 2002.
3. Howland, P. E., D. Maksimiuk, and G. Reitsma, "FM radio based bistatic," *IEE Proc. — Radar Sonar Navig.*, Vol. 152, No. 3, 107–115, Jun. 2005.
4. Gould, D. M., R. S. Orton, and R. J. E. Pollard, "Forward scatter radar detection," *Radar 2002*, 36–40, Oct. 2002.

Design of a Printed Antenna Array for Cost-effective ATE to Reduce the Radiated EMI Yield Loss

Cheng-Nan Hu[1], **Hsuang-Chung Ko**[2], **and Deng-Yao Chang**[2]

[1]CRC, Oriental Institute of Technology
No. 58, Sec. 2, Sihchuan Rd, Ban-Ciao City, Taipei County, Taiwan, R.O.C.
[2]King Yuan Electronics Co. Ltd.
No. 58, Sec. 2, Sihchuan Rd, Ban-Ciao City, Taipei County, Taiwan, R.O.C.

Abstract— This work proposes a printed antenna array for cost-effective ATE test approach to decrease RF testing yield loss. Background noise of the system-under-test is surveyed based on a prototype load-board equipped with the proposed printed antenna system to analyze the correlation between the test data and background noise in order to identify the root causes of yield loss. Theoretical analysis based on the Monte-Carlo procedure validates the proposed cost-effective ATE design approach. Experimental results of RF testing in the EMI environment correlate well with a low yield mass production scenario that is estimated to address the EMI issue.

1. INTRODUCTION

RF semiconductor devices are changing to match the needs of increasingly innovative wireless standards with the result that device functionality and integration drive core parametric, configuration, and usage trends for RF ATE (auto-test-equipment), along with signal bandwidths and carrier frequencies supporting greater data throughput rates are steadily increasing [1–3]. Generally, RFIC manufacturers conduct the go no-go test procedure (Fig. 1(a)) to perform the qualification test. However, this approach has to suffer yield loss caused by radiated EMI noise existing in the testing environment. To improve the radiated EMI yield loss, a printed antenna array performed as an EMI senor of the RF ATE test bench is present to monitor the existing interference signals. When the radiated EMI is detected at production line, a re-testing procedure is trigged by ATE test program (Fig. 1(b)) to reduce the radiated EMI yield loss.

In this study, a system model based on the Monte-Carlo procedure (Fig. 2) is used to numerically validate the proposed method and an experimental study using a printed array with four multi-band, dual-polarization antennae is built onto the load-board of an ATE tester. Finally the system validation at production line is conducted to prove the yield loss improvement by 21% and thus validates this design approach.

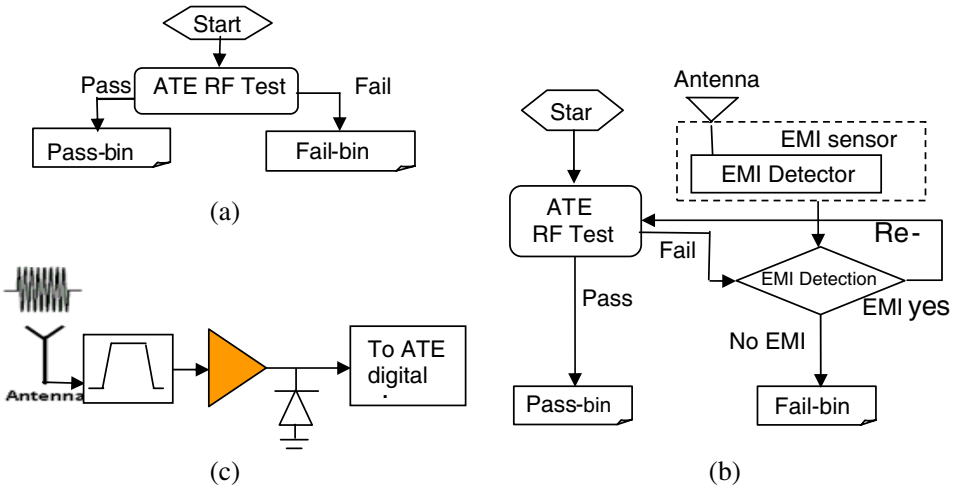

Figure 1: (a) Typically used ATE Go-No-GO test concept; (b) Proposed ATE test concept; (c) Functional block diagram of EMI sensor.

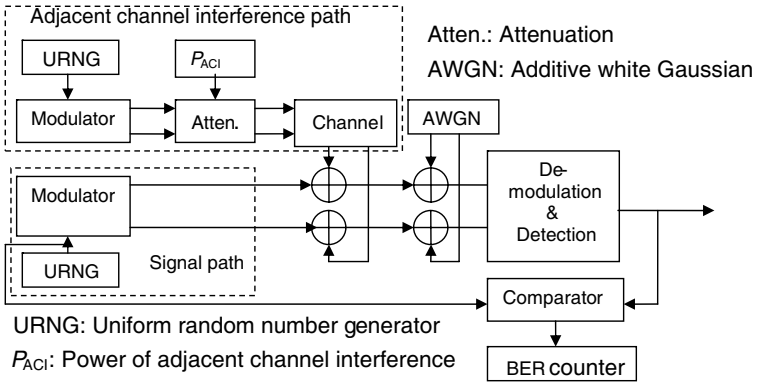

Figure 2: System model to simulate the ATE functionality using Monte-Carlo procedure.

2. SYSTEM MODEL FOR THEORETICAL VALIDATION

To assess BER performance, a Matlab program based on the Monte-Carlo procedure is developed to simulate the functionalities of ATE to perform yield loss analysis using go no_go procedure (Fig. 1(a)) and the proposed approach (Fig. 1(b)) for comparison. In this simulation, the PHS signaling specification for base-mobile transmission was assumed. Each PHS TDMA frame is 5 ms long, with 2.5 ms for each of the uplink and the downlink. In transmission, pulsed radio signals modulated by the $\pi/4$ DQPSK scheme are transmitted at 32 kbps per channel. The channel bandwidth is 300 kHz. For simplicity, a super-het receiver is currently under study. Fig. 3 plots the signal levels at various stages of interest. For a specified P_{ACI} (presenting the detected power of the radiated EMI), a Mont-Carlo simulation can be conducted to assess the degradation of BER performance caused by ACI in the AWGN channel. Simulated results show that the adjacent channel suppression (ACS) of 50 dBc, specified by the RCR STD-28 PHS standard, can be achieved provided that ACR exceeds 18.75 dB, which condition can be reasonably and easily met using a poly-phase filter [4]. The value of detected power of radiated EMI with zero mean uniform distribution is examined. In the go no_go test procedure (Fig. 1(a)), the theoretical yield loss shall be 50% because the distribution is uniform. Fig. 4 plots the simulation results corresponding to three independent runs, showing the numerical yield losses obtained using the go no_go procedure (Fig. 1(a)) are 53%, 50%, and 46%, respectively, which are values very close to the theoretical value of 50%. However, the yield loss simulated using the proposed scheme (Fig. 1(b)) can be reduced to 28%, 30%, and 27%, indicating an improvement of 25%, 20%, and 19%, respectively, and a mean value of 21.3%. The simulation results numerically validate that the proposed ATE testing concept (Fig. 1(b)) instead of Fig. 1(a)) can be used to reduce the radiated EMI yield loss. Similarly, the proposed approach can be applied to other communication systems.

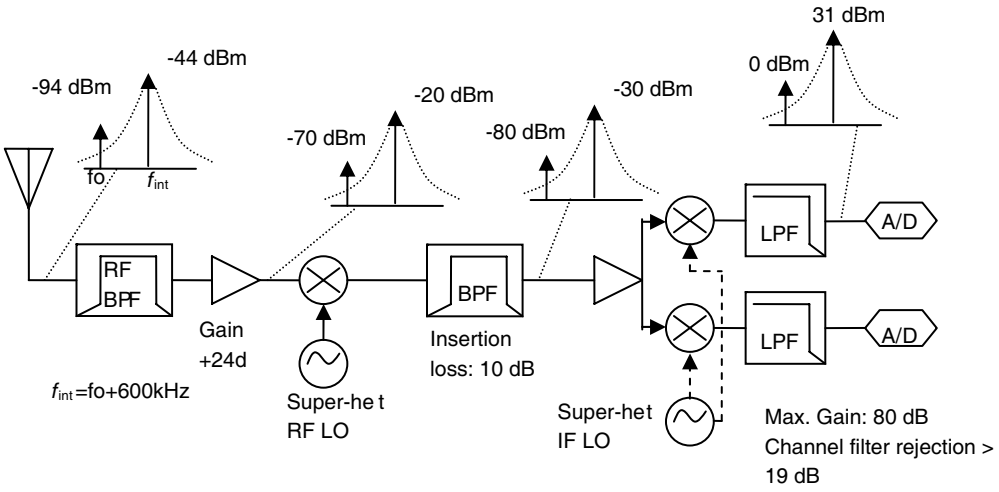

Figure 3: Typical Super-het receiver Architecture in which the approximately signal levels at each stage of interest is labeled.

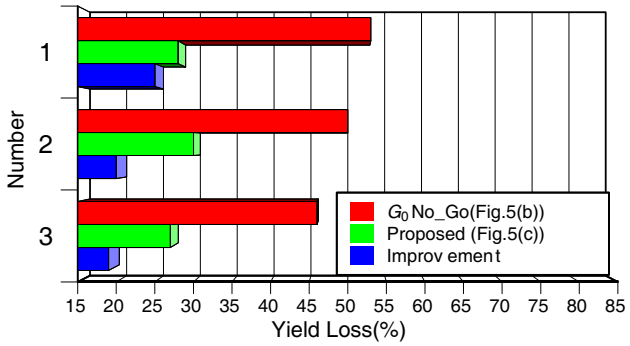

Figure 4: Monte-Carlo simulated results of yield loss at three independent runs, showing the.

3. EXPERIMENTAL STUDY

Wireless standards, including PHS, DECT, GSM/DCS, Bluetooth, WLAN 802.11b(g), and GPS, generate electromagnetic signals. This work categorizes electromagnetic signals as either a) PHS, DECT and GSM/DCS bands (880–960/1710–1910 MHz) or b) GPS/WLAN 802.11b(g) (1570-/2450 MHz) systems. To obtain signals from each group, two meander-line folded monopole antenna designs [5] are utilized to cover the frequencies of interest.

Figure 5(a) illustrates the prototype design, including a front housing and an embedded PCB antenna array above the back housing, which is mounted onto the load-board. Fig. 5(b) and Table 1 display the detailed antenna design. The radiating structure of the antenna consists of the first end and an opposing second end. The second radiating structure, which has a meander-line shape, is electrically connected with the end of the first radiating unit. The second radiating unit has at least one meander-line section. The meander-line reduces the physical length desired by the fundamental resonant frequency and, then, introduces a weak coupling mechanism for a broad high-band resonance. A power combination network with three broadband combiners (Part No: Mini-circuits TCP-2-25) and four coaxial cables, can detect surrounding EMI noise of interest via four antennae. The antenna input impedance is measured using an Agilent network analyzer E5071A (see Fig. 6(a)). Fig. 6(b) plots the measured return loss of the embedded antenna array, showing acceptable results at desired frequencies. Finally, radiation patterns of the antenna array are measured by a 3D far-field measurement system in an anechoic chamber supported by Sportan Lab, i.e., a certified laboratory in Taiwan. Table 2 summarizes the measured radiated characteristics, showing the measured antenna gain of −2.7/3.3/2.69/6.3 dBi at frequencies of 900/1570/1800/2450 MHz, respectively.

To validate proposed design concept, the prototype antenna array has been implemented onto the load-broad as an EMI sensor of an ATE to test a DECT transceiver. Pilot-run measured results [6] show that no low yield alarm occurred during the night time on the first day, the second day and the third day. The major yield loss came from the failed test of Bit-Error-Rate (BER) during the day time of the first and third days. The root cause of this occasionally yield loss identified by the EMI senor is the adjacent channel interference due to the nearby PHS station

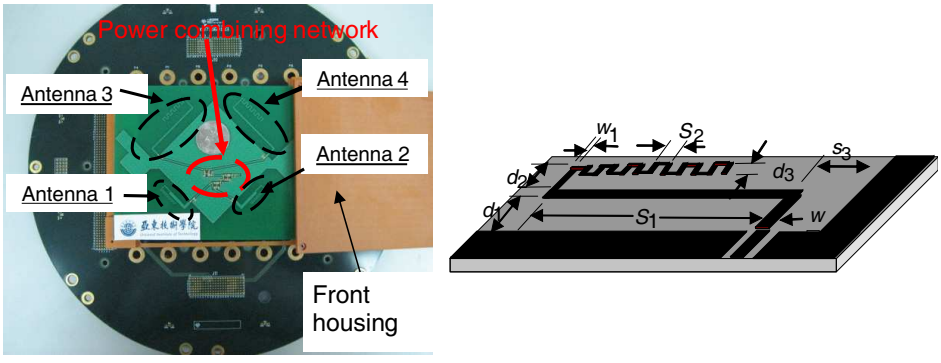

(a) (b)

Figure 5: (a) Proposed embedded antenna array for experimental study; (b) Circuit configuration of the meander-line folded monopole design.

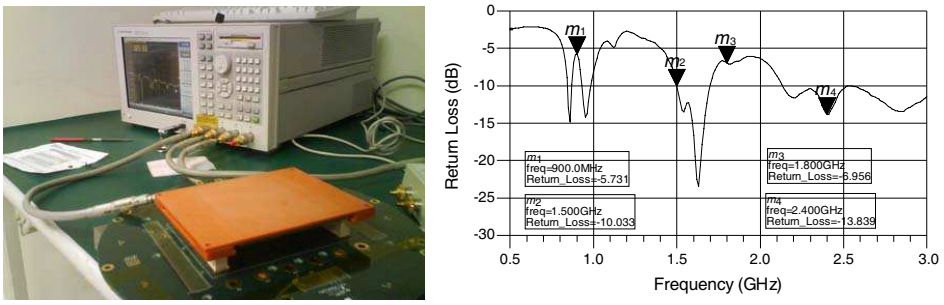

(a) (b)

Figure 6: (a) Return loss measurement setup; (b) Measured return loss of the embedded antenna array (after power combination).

Table 1: Antenna dimension.

Category / Dimensions	Antennae 1&2	Antennae 3&4
d_1 (mm)	5.5	7
d_2 (mm)	4.25	10
d_3 (mm)	1.6	3
S_1 (mm)	21	44
S_2 (mm)	1.5	3
S_3 (mm)	NA	5

Table 2: The measured gain performance.

Frequency (MHz)	900	1570	1800	2450
Directivity (dBi)	6.20	8.52	8.74	10.50
Efficiency (dB)	−8.88	−5.22	−6.05	−4.22
Efficiency (%)	12.94	30.08	24.86	37.88
Gain (dBi)	−2.68	3.30	2.69	6.28

since the frequency band of PHS cordless phone overlaps the DECT system. Thus, a retest is then triggered in time when EMI signals are detected; otherwise, the continuous failed test is classified as EMI failure that indicates the worst EMI environment. This experiment [6] shows an improved yield of about 21% from 34% to 13% with the implementation of retest.

4. CONCLUSSIONS

This work presents a printed antenna array for cost-effective ATE approach as an EMI sensor to identify the root cause of yield loss due to the radiated EMI issue in order to improve testing yield. A system model based on Monte-Carlo procedure is first proposed to validate this novel ATE design concept numerically. Experimental results of the EMI sensor design confirm the performance of EMI sensor. System validation of the specified device that occurred with a suspected EMI low yield in the production line indicates that the proposed approach can reduce yield loss from 34% to 13%, or by 21%.

ACKNOWLEDGMENT

The authors would like to thank the King Yuan Electronics Co. Ltd. for financially supporting.

REFERENCES

1. Brown, D., J. Ferrario, R. Wolf, J. Li, and J. Bhagat, "RF testing on a mixed signal tester," *2004 IEEE ITC International Test Conference*, 793–800, 2004.
2. Bhagat, J., J. Ferrario, R. Wolf, and M. Slamani, "Challenges of incorporating an RF test system on a broad," *3rd Workshop on Test of Wireless Circuits and Systems*, 2004.
3. Demmerle, F., "Integrated RF-CMOS transceivers challenge RF test," *2006 IEEE International Test Conference*, 1–8, 2006.
4. Chen, G.-J., H.-H. Chiu, and T.-V. Lee, "A 4-channel poly-phase filter for cognitive radio systems," *International Symp. on VLSI Design, Automation and Test, VLSI-DAT-2007*, 1–4, April 25–27, 2007.
5. Hu, C.-N., H.-C. Ko, and D.-Y. Chang, "Employing a compact PCB antenna array to detect the EMI noise for transceiver performance-based test," *Asia Pacific Microwave Conference APMC2008*, 3–45, Hong Kong, December 16–22, 2008.
6. Ko, H.-C., D.-Y. Chang, and C.-N. Hu, "Cost-effective approach to improve yield loss," *2009 IEEE ITC International Test Conference*, Vol. 14.2, Autin, Texas USA, 2009, to be appeared.

Wang-shaped Patch Antenna with a Simple Feed Network

Chi H. Wong and Kwok L. Chung
Department of Electronic and Information Engineering, The Hong Kong Polytechnic University
Hung Hom, Hong Kong, China

Abstract— A Wang-shaped suspended patch antenna has been designed for wireless communication systems covering the 1.66 GHz–2.43 GHz frequency range. This frequency range covers the major standards in mobile communications such as PCS1900 (1.88 GHz–1.9 GHz), UMTS (1.92 GHz–2.17 GHz), and WiBro (2.3 GHz–2.39 GHz). The Wang-shaped patch is proposed in this paper for bandwidth broadening whilst maintaining symmetrical radiation patterns in both the E and H-plane. By using a simple low-cost feed network, Wang-shaped patch fed by dual L-probe yields a return loss bandwidth (10-dB) of 37.7% and max gain of 6.5 dBi at the mid-band frequencies. The radiation patterns and the cross-polarization of the antenna are also examined.

1. INTRODUCTION

Microstrip patch antennas have attracted much attention of antenna engineers due to its low production cost and low profile. Its narrow bandwidth is a major disadvantage that limits its applications. Bandwidth broadening techniques such as the inclusion of U-slot [1] on a rectangular patch, the E-shaped patch [2], or the patch added with a pair of wide-slits [3] have been reported for the purposes of enhancing impedance bandwidth. These techniques are all about to generate the additional nearby resonances by creating the extra current paths on the patch so that a wide impedance/return-loss bandwidth can be obtained by merging the resonant frequencies whilst pushing the return losses above 10-dB (reflection coefficient below -10 dB). The U-slotted the E-shaped patch and/or the patch included a pair of wide-slits designs are capable of achieving more than 10-dB return-loss of 25% at the centre frequency but suffering from the asymmetrical radiation pattern in E-plane and/or high cross-polar levels in H-plane [1–3]. By nature, the geometries of the U-slotted patch and the E-shaped patch are asymmetrical in one plane. It is well-known that the impedance bandwidth can be significantly enhanced by using a suspended patch technique [4]. This technique is equivalent to a metallic patch printed on an electrically thick dielectric slab with a lowest dielectric-constant, according to microstrip patch antenna theory. However, as the substrate height goes beyond $0.1\lambda_o$, the radiation performances of the suspended plate antennas will be degraded due to the generation of the undesired higher order modes at the higher frequencies of bandwidth. Consequently, the co-polarization patterns in E-plane distort severely whereas the cross-polarization levels in H-plane increase significantly.

Recently, a Wang-shaped patch fed by a dual L-probe using an external power divider has been reported [5]. The enhanced return-loss bandwidth and the excellent cross-polarization levels were obtained. In this paper, an advanced version of the Wang-shaped patch antenna is present. As a further step, the external power divider is replaced by a simple low-cost feed network, which is integrated with the dual L-probe to excite the copper patch, as a completed singly-fed antenna. A substantial antenna height of 32 mm ($0.22\lambda_o$ at 2.0 GHz) is used in the current design. In addition to the wide return-loss bandwidth, symmetrical radiation patterns and low cross-polarization levels are obtained.

2. ANTENNA GEOMETRY

The U-slotted patch and the E-shaped patch antennas have the capability of enhancement in return-loss bandwidth because additional resonance is created due the insertion of slots. The prices paid for that are the possible asymmetrical radiation pattern and the high cross-polarization levels. These are mainly owing to the irregular surface currents induced on the asymmetrical patch at some frequencies. Wang-shaped patch is designed by combining two E-shaped patches, one mirrored to the other, which in turn leads to a symmetrical geometry in both the principle planes. The antenna geometry in top (xy-plane) and side (xz-plane) views is shown in Fig. 1 whereas a low-cost simple microstrip-line feed network is shown in Fig. 2. The Wang-shaped copper plate has a thickness of 0.5 mm and is suspended over the ground plane by means of foam supports (not shown in the figure). Rogers RO3003 dielectric substrate ($\varepsilon_r = 3.0$, $\tan\delta = 0.0013$) is used for fabricating the feed network. Based on the former version of Wang-shaped patch reported in [5], the parameters

of the current design are optimized after wavelength-scaling. Dual L-probe in anti-phase is applied instead of a single one because the two probes are set 180-degree out of phase by means of differential microstrip-line length. Hence, the leakage radiation from the vertical portion of the L-probes and the higher order modes currents excited on the copper patch are expected to be cancelled out [6]. As a result, stable symmetrical radiation patterns as well as the suppression of cross-polarizations can be achieved in a wide range of frequency. Throughout the study, the EM simulator HFSS was used in the design and optimization phases. An aluminum plate having a size of 300 mm × 300 mm is used as the ground plane in the present design.

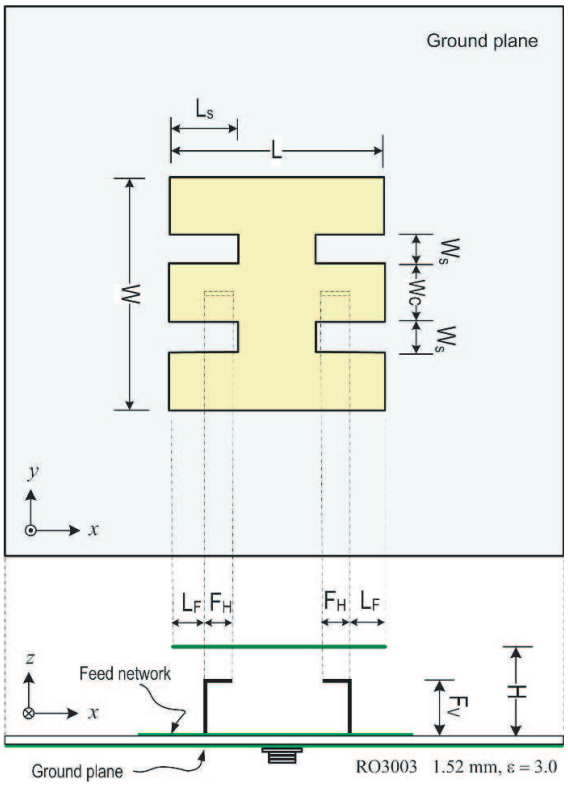

Figure 1: Top view and side view of the Wang-shaped patch antenna ($W = 50$, $L = 37.5$, $L_S = 12.5$, $L_F = 7.5$, $F_H = 7.5$, $W_S = 2.5$, $W_C = 5$, $H = 32$, $F_V = 27.5$. Unit: mm).

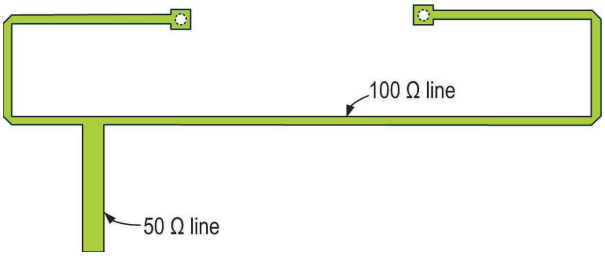

Figure 2: The simple feed network.

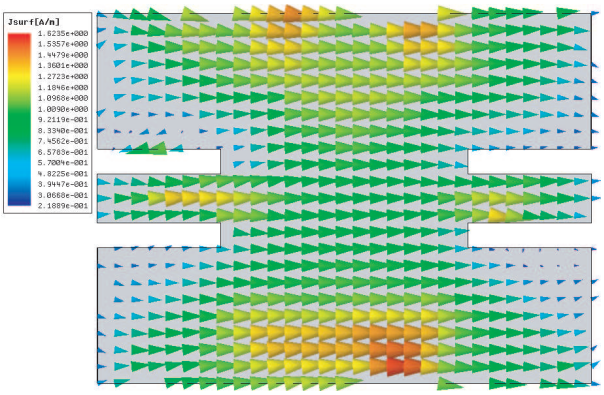

Figure 3: Surface current distributions on the Wang-shaped patch at the mean frequency of 2.05 GHz.

3. RESULTS AND DISCUSSIONS

Unlike the U-slotted patch and the E-shaped patch antennas, which have large amount of surface currents in the orthogonal directions against the main flow, the proposed Wang-shaped patch

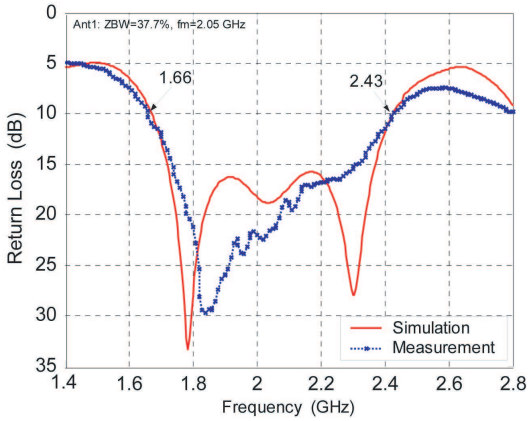

Figure 4: Simulated and measured return losses of the Wang-shaped patch antenna.

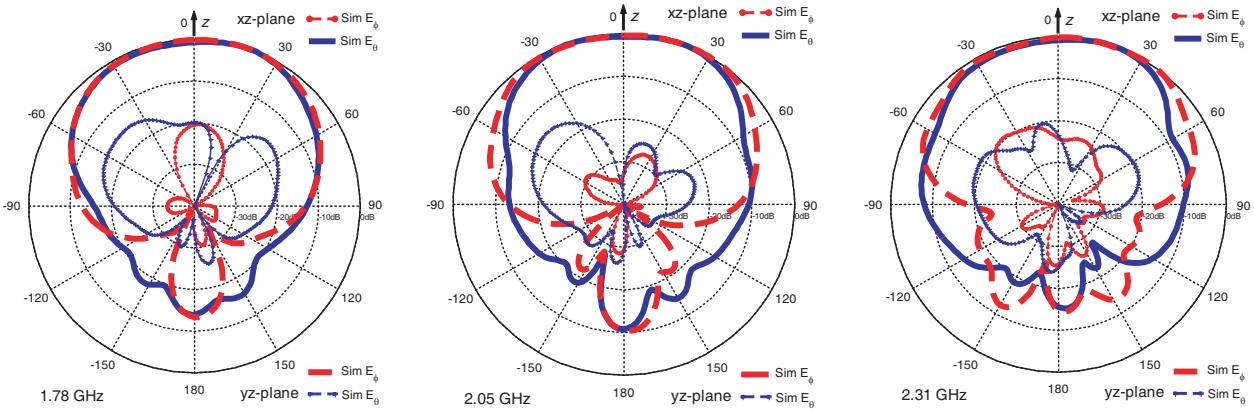

Figure 5: Simulated radiation patterns of the Wang-shaped patch antenna at (a) 1.78 GHz, (b) 2.05 GHz and (c) 2.31 GHz.

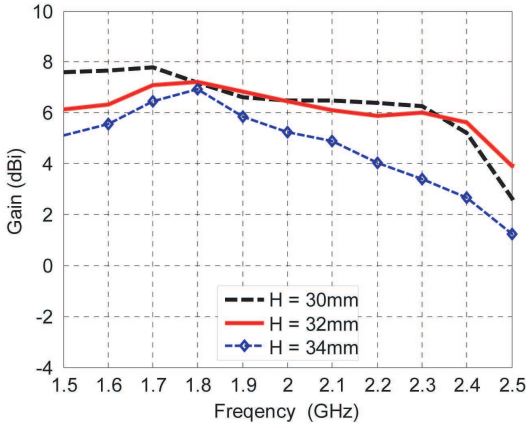

Figure 6: The realized gain versus frequency with the variation of patch heights.

has a minimum of such problems. Wang-shaped patch diminishes surface currents in orthogonal directions but in parallel with the *E*-field as shown in Fig. 3. Current path is lengthened at certain frequencies because the equivalent area of the Wang-shaped patch is larger than that of the U-slotted and E-shaped counterparts. Nevertheless, the additional resonances can still be obtained due to the extra inductance and capacitance introduced by the slots. The measured return-loss together with the simulated one shown in Fig. 4 has verified this. The 10-dB return-loss bandwidth is obtained as 37.7% at a mean frequency of 2.05 GHz. The measured return loss shifts slightly

toward higher frequencies whereas the second resonance becomes less obvious due to the fabrication tolerances. The simulated radiation patterns, shown in Figs. 5(a) to 5(c), within the bandwidth are remained symmetrical. The cross-polarization ($< -20\,\mathrm{dB}$) bandwidth decides the operating bandwidth that is about 26%, with the lower and the higher ends at 1.78 GHz and 2.31 GHz, respectively. The realized gain versus frequency for a variation of patch heights (H) from 30 to 34 mm is shown in Fig. 6. At $H = 32\,\mathrm{mm}$, the realized gain of $> 6\,\mathrm{dBi}$ is obtained from 1.5 GHz to 2.3 GHz. In general, the results of dual L-probe fed Wang-shaped patch antenna using a simple feed network presented in this paper are interior to that when using an external power divider. The phase and amplitude errors incurred from the narrow-band feed network give the answers for the degraded results. Nevertheless, the large return-loss bandwidth is achieved in reduction of Q-factor at the cost of a higher antenna height of 32 mm ($0.22\lambda_o$ at 2.0 GHz) whereas the effects due to the excitation of higher-order can be suppressed to a minimum.

4. CONCLUSIONS

A dual L-probe fed Wang-shaped suspended patch antenna using a simple feed network is presented in this paper. The antenna exhibits a wide return-loss bandwidth of 37.7% and has fulfilled the usages of several popular communication standards such as PCS1900 (1.88 GHz–1.9 GHz), UMTS (1.92 GHz–2.17 GHz), and WiBro (2.3 GHz–2.39 GHz). Owing to the phase and amplitude errors in the microstrip-line feed network, which is a narrow band device, the performance of Wang-shaped patch antenna is degraded when compared to an external power divider case. However, the simple feed network can retain the advantages of simplicity and low production cost.

ACKNOWLEDGMENT

This work was supported in part by the Hong Kong Polytechnic University under Grant A-PJ23.

REFERENCES

1. Luk, K. M., Y. X. Guo, K. F. Lee, and Y. L. Chow "L-probe proximity fed U-slot patch antenna" *Electronic Letters*, Vol. 34, 1806–1807, Sep. 1998.
2. Yang, F., X. X. Zhang, X. Ye, and Y. Rahmat-Samii, "Wide-band E-shaped patch antennas for wireless communications," *IEEE Trans. Antennas Propagat.*, Vol. 49, 1094–1100, Jul. 2001.
3. Wong, K. L. and W. H. Hsu, "A board-band rectangular patch antenna with a pair of wide slits," *IEEE Trans. Antennas Propagat.*, Vol. 49, 1345–1347, Sep. 2001.
4. Chen, Z. N. and M. Y. W. Chia, "Broad-band suspended probe-fed plate antenna with low cross-polarization levels," *IEEE Trans. Antennas Propagat.*, Vol. 51, 345–346, Feb. 2003.
5. Fung, H. Y. and K. L. Chung, "A Wang-shape suspended patch antenna," *Proceedings of the 11th Australian Symposium on Antennas*, 18, Sydney, Australia, Feb. 18–19, 2009.
6. Levis, K., A. Ittipiboon, and A. Petosa, "Probe radiation cancellation in wideband probe-fed microstrip arrays," *Electronic Letters*, Vol. 36, No. 7, 606–607, Mar. 2000.

Biological Model in Electromagnetic Exposure Safety

Sergey Perov[1], **Quirino Balzano**[2], **and Niels Kuster**[3]

[1]RAMS Research Institute of Occupational Health, Moscow, Russia
[2]Department of Electrical and Computer Engineering, University of Maryland, Maryland, USA
[3]Foundation for Research on Information Technologies in Society, Zurich, Switzerland

Abstract— At present time, there are two very different criteria for setting electromagnetic field (EMF) exposure safety (hygienic) standards. These regulations are based on different science-based approaches using different metrics, such as specific absorption rate (SAR-ICNIRP) and power exposure (PE-Russia) [1, 2].

The exposure metrics of the International Commission on Non-Ionizing Radiation Protection (ICNIRP) require the measurement of electric, magnetic field strength and power density (PD). In the frequency band 100 kHz–10 GHz, the ICNIRP basic restrictions hinge on the concept of specific absorption rate (SAR) which is defined as

$$\mathrm{SAR} = \frac{\sigma E^2}{\rho} = c_i \frac{dT}{dt} \tag{1}$$

where E is the RMS value of the electric field in tissue, σ and ρ are the tissue conductivity and mass density. In (1) also, c_i and $\frac{dT}{dt}$ are the specific heat of tissue and the time derivative of the temperature at the onset of the RF exposure. SAR measures the rate of EMF energy absorption in the unit of weight of an exposed object. SAR is used to quantify tissue exposure from EMF in the far and the near field of RF sources, where PD might not be defined or even definable. The SAR basic restrictions of ICNIRP are time independent because the rate of energy absorption is limited, not its total amount.

The Russian approach to exposure assessment and dosimetry has two main differences from those of ICNIRP. First, the concept of SAR was never adopted, because near field measurements were not required until recently. The near field evaluation is performed by computations extrapolating the far field measurement values using theoretical equations. Second, the dosimetry is based on the parameter "power exposition" (PE) which is a dynamic estimate of the EMF biological effects from the exposure. This parameter differentiates the exposure dose during a given time interval. In other words, the Russian exposure limitations consider cumulative the biological effects of RF EMF. PE values depend on time, field level and frequency range.

The Russian exposure limitation approach and its dosimetry define a dose-dependent biological action of RF EMF and, so, a dependence of time and intensity of the safe RF exposure.

Unfortunately, both approaches have not fully developed a common consistent assessment of EMF exposure and biological effects. That's why there is a need to establish accurate criteria for the definition of biological effects that are of import for the safety of humans exposed to EMF.

At present time there are no universally recognized biological models. In lethal action electromagnetic field levels have been researched and are well known. Diagrams of "dose-effect" relations are well-defined in 100 and 50% fatal outcome cases (ld_{100} and ld_{50}) [3, 4]. These relations can extrapolate PD and SAR to lower intensity levels for safety standardization. However, for other EMF exposures, clear correlation between biological effects and dose exposure remains undefined. Some generally acknowledged results are: specific corticosterone levels in plasma rat blood (Figure 1) and cataract of the rabbit eye (Figure 2) [5, 6]. All of these results were concomitant with a temperature increase in subjects under EMF exposure. Attempts to define "dose-effect" relationships in other biological systems have been undertaken, but definitive results have been elusive. Also there are no reliable data about "dose-effect" relations in non thermal EMF exposures of biological objects.

In this connection there is a necessity of the standardized biological model allowing to define biological effects as a "dose-effect" relationship.

Influence on an organism from external factors can cause nonspecific response-stress. Stress influences at organism level are perceived through system of specialized organs and tissues. Recognition of stress action and response realization at cellular level is connected with the protein synthesis of

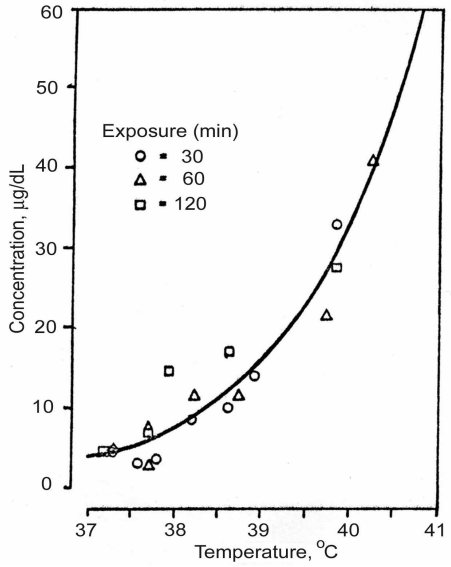

Figure 1: Correlation between plasma corticosterone and colonic temperature in rats exposed to 2.45 GHz fields [5].

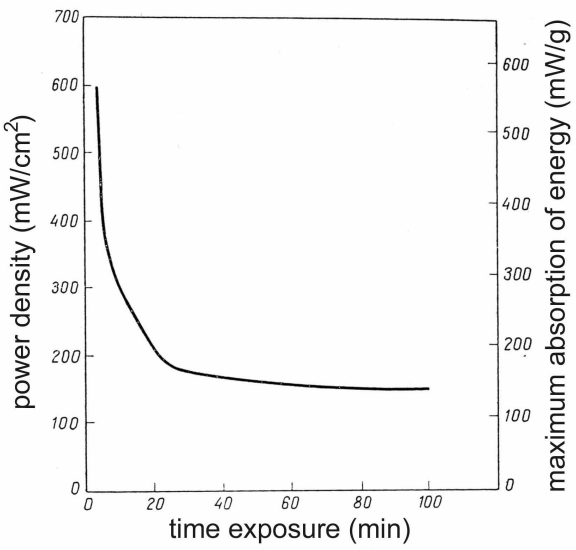

Figure 2: Threshold time values and PD for cataract formation in an eye of a rabbit as a result of a unitary exposure in a near field [6].

the cell. It is playing one of the main roles in detection of cell stability to stress of factors. Actions of environmental factors activate protection and reparative processes in cells. In particular, display of that is synthesis of new proteins-stress proteins. The stress protein induction, discovered in 1962, has proved subsequently an universal response of biological systems, at various levels of organization, to the action of external physical and chemical factors.

In cells, in response to stress or damage, protein factors are induced, called *heat shock proteins* (HSP). The synthesis of these proteins induces different factors.

For the first time the induction of the synthesis of these proteins, for a temperature rise from 20 to 37°C has been described F. Pulocca in 1962 as a result of research on the drosophila. Subsequently, the universality of the response of biological systems for different levels of the stress action, in which syntheses of HSP were shown, has been proved. It appears that HSP synthesis is specific not only on thermal exposure. It can be induced by various other factors, such as UV-radiation, hypoxia, action of some chemical agents (heavy metals, hydrogen peroxide, arsenic, etc.). Now the heat shock proteins (HSP) are accepted more widely, as reflecting an essence of process — "stress proteins". These proteins are induced not only in reply to rise in temperature, but also on its decrease, both under other normal conditions. These facts about HSP synthesis has been found out in those biological objects (plant cells, the fresh-water amoebas, some kinds of fish) in which the life cycle is connected with seasonal periodic changes in temperature [7, 8]. Its evolution caused a type of adaptive reactions allowing biological objects to better acclimate to the constantly changing temperature modes of the environment conditions, as both an increase and fall of temperature below physiological values is a stress stimulus. Regulatory mechanisms which are started in the exposed cells causing HSP induction are not clear, at present time. It is obvious that HSP induction is an universal mechanism of nonspecific adaptive updating.

However historically developed first, the name of this protein family remains unchanged until now, but the generality of the HSP synthesis process in biological objects in response to thermal and cold influence is of great importance.

All thermal shock proteins share on two basic groups: constitutive proteins of a thermal shock (HSC) and induced proteins of a thermal shock (HSP) [9]. The synthesis of HSC occurs constantly and in physiological conditions. They are endocellular components at molecular level. Fast synthesis of HSP (stress proteins) occurs in reply to various physical, chemical and environmental exposures as a mechanism of cell of protection.

HSP are found in practically all live organisms — from bacterial to human. Name HSP is connected with their molecular weights and the most studied proteins of thermal shock are the Hsp60, Hsp70 and Hsp90, families of proteins with molecular weights 60, 70 and 90 kDa, accordingly. HSP have a limited presence in various organisms, and the proteins of the family Hsp70 are

Table 1: Published studies of the EMF biological effects with stress proteins.

Studied Hsp	Biological model	Exposure conditions	Reference
Hsp70, Hsp27	Human amnion cells	960 MHz; 2.1 mW/kg	[11]
Hsp27	EA.hy926 cells	900 MHz (GSM); 2–2.4 W/kg	[12]
Hsp70	Human glioma cells	2.45 GHz (CW); 20 W/kg	[13]
Hsp16	C. elegans	750 MHz; 1 mW/kg	[10, 14]
Hsp70	Rat brain	2.06 GHz; 2.2 W/cm^2	[15]
Hsp70	Chick embryo	915 MHz; 1.57–2.5 W/kg	[16,17]
Hsp70, Hsp27	Human glioma cells	1950 MHz; 1–10 W/kg	[18]

most extended. One of the most remarkable properties of Hsp70 is the protective function which the protein shows during the reaction of a cell or an organism to the action of various adverse environmental factors, providing survival in stressful and normal conditions.

These HSP participate in the repair of non-lethal damages, including increase temperature in biological objects. Upon collecting research data de Pomerai et al. [10] suggested a possible use of HSP70 as an indicator in biological model. The HSP70 can be used in thermal and non thermal EMF exposure.

Today HSP are used as biomarkers to check the bioeffects of the components of magnetic resonance imaging (MRI) [19].

We suggest that in proper conditions it is possible to get "dose-effect" relation as SAR-effect and PD-effect, which can develop a novel safety standard approach to EMF biological effect assessment.

The simplest and most direct approach to finding correlation between SAR and PE is based on common and clear biological models. Using this approach we can establish adequate and reliable assessments of EMF exposure levels and the related biological effects. This is a necessary foundation step to find the safe EMF levels for safety standard harmonization. Biomarkers such as the HSP can be used as a first biological model to initiate the confluence of the regulations based on SAR(ICNIRP) and power exposure (Russia).

REFERENCES

1. ICNIRP Guidelines, "Guidelines for limiting exposure to time-varying electric, magnetic and electromagnetic fields (up to 300 GHz)," *Health Physics*, Vol. 74, No. 4, 494–522, 1998.
2. "SanPiN 2.2.4.1191-03 Sanitary norms and rules," *Electromagnetic Fields in Occupational Conditions*, Moscow, 2003 (in Russian).
3. Lobanova, E. A., "Survival rate and development of animals at different intensity and duration of UHF exposure, about biological action of ultra high frequency," *NII Occupational Health and Occupational Diseases AMN USSR*, 61–64, 1960 (in Russian).
4. Schrot, J. and T. D. Hawkins, "Lethal effects of 3000 MHz radiation on the rat," *Radiat. Res.,* Vol. 59, No. 2., 504–512, 1974.
5. Lotz, W. G. and S. M. Michaelson, "Temperature and corticosterone relationships in microwave-exposed rats," *J. Appl. Physiol.*, Vol. 44, No. 3, 438–445, 1978.
6. Guy, A. W., G.-S. Lin, P. O. Kramer, and A. F. Emery, "Effects of 2450 MHz radiation on the rabbit eye," *IEEE Trans. Microwave. Theory Tech.*, Vol. 23, No. 6, 492–498, 1975.
7. Tsutsaeva, A. A., Y. E. Mikulinskiy, A. O. Kotlyarov, and I. P. Visekantsev, "Metabolism cell activity after stress action," *Cold Stress and Biological Systems*, 48–66, Naukova Dumka, Kiev, 1991.
8. Evgenev, M. B., D. G. Garbuz, and O. G. Zatsepina, "Heat shock proteins: Function and role in adaptation for hyperthermia," *Ontogeny*, Vol. 36, No. 4, 265–273, 2005.
9. Schlesinger, M. J., "Heat shock proteins," *J. Biol. Chem.*, Vol. 265, No. 21, 12111–1211, 1990.
10. Daniells, C., I. Duce, D. Thomas, P. Sewell, J. Tattersall, and D. De Pomerai, "Transgenic nematodes as biomonitors of microwave-induced stress," *Mutat. Res.*, Vol. 399, No. 1, 55–64, 1998.
11. Kwee, S., P. Raskmark, and S. Velizarov, "Changes in cellular proteins due to environmental non-ionizing radiation, I. heat-shock proteins," *Electro.-Magnetobiol.*, Vol. 20, 141–152, 2001.

12. Leszczynski, D., S. Joenväärä, J. Reivinen, and R. Kuokka, "Non-thermal activation of the hsp27/p38MAPK stress pathway by mobile phone radiation in human endothelial cells: Molecular mechanism for cancer- and blood-brain barrier-related effects," *Differentiation*, Vol. 70, No. 3–4, 120–129, 2002.
13. Tian, F., T. Nakahara, K. Wake, M. Taki, and J. Miyakoshi, "Exposure to 2.45 GHz electromagnetic fields induces hsp70 at a high SAR of more than 20 W/kg but not at 5 W/kg in human glioma MO54 cells," *Int. J. Radiation Biology.*, Vol. 78, No. 5, 433–440, 2002.
14. De Pomerai1, D., C. Daniells, H. David, and J. Allan, "Cell biology: Non-thermal heat-shock response to microwaves," *Nature*, Vol. 405, 417–418, 2001.
15. Walters, T. and K. Ryan, "Mason Regional distribution of Hsp70 in the CNS of young and old food-restricted rats following hyperthermia," *Brain Research Bulletin*, Vol. 55, 367–374, 2001.
16. Rishikof, D., D. Ricupero, P.-P. Kuang, H. Liu, and R. Goldstein, "Interleukin-4 regulates connective tissue growth factor expression in human lung fibroblasts," *Journal of Cellular Biochemistry*, Vol. 85, No. 3, 490–496, 2002.
17. Di Carlo, A., N. White, F. Guo, P. Garrett, and T. Litovitz, "Chronic electromagnetic field exposure decreases HSP70 levels and lowers cytoprotection," *Journal of Cellular Biochemistry*, Vol. 84, No. 3, 447–454.
18. Miyakoshi, J., K. Takemasa, Y. Takashima, G.-R. Ding, H. Hirose, and S. Koyama, "Effects of exposure to a 1950 MHz radio frequency field on expression of Hsp70 and Hsp27 in human glioma cells," *Bioelectromagnetics*, Vol. 26, No. 4, 251–257, 2005.
19. Guisasola, C., M. Desco, O. Millán, F. J. Villanueva, and P. García-Barreno, "Biological dosimetry of magnetic resonance imaging," *J. Magn. Reson. Imaging.*, Vol. 15, No. 5, 584–590, 2002.

Human Exposure Assessment for Wireless Power Transmission System

J. H. Oh[1], **T. H. Kim**[1], **J. H. Yoo**[1], **J. K. Pack**[1], **Y. M. Yoon**[2], **M. Y. Choi**[2], **and S. Y. Lee**[2]

[1]Chungnam National University, South Korea
[2]Korea Radio Promotion Agency, South Korea

Abstract— In this paper, we investigated the possible health effects of the human exposure due to WPT (Wireless Power Transmission) system for MICS (Medical Implanted Communication Service) devices, by numerical simulation for the Korean phantom model. The input power of the WPT system was estimated from the power loss calculation in human body, and then magnetic field strengths or SAR values were calculated. We found that human exposure due to WPT systems can exceed the exposure guidelines.

1. INTRODUCTION

Most of the medical devices generally use batteries as a power source due to its limited space. However the primary cells have several limitations such as high cost, limited power and no reuse. To solve these problems, new wireless power transmission technologies are considered as the alternative methods. There are three methods using inductive coupling, magnetic resonance and RF transmission. Currently, these technologies are being studied for applying to medical devices such as CE (Capsular Endoscope), pacemaker and so on. However, it can cause the excessive EMF absorption exceeding human protection guidelines. So, in this paper, we calculated the exposure levels due to WPT systems and compared the results with the representative exposure guidelines.

2. PHANTOM MODEL AND SIMULATION RESULTS

We investigated many MICS systems to which WPT technology can be applied. The MICS systems considered in this study is shown in Fig. 1.

One of such systems is CE. To send enough information, a large battery with enough power is required, but it is almost impossible to enlarge the battery because of the limited volume of CE. For this reason, the inductive coupling technology has been studied as one of the alternative methods delivering the power continuously to CE. It was found that a magnetic field has very low loss inside human body in the frequency below 1 MHz [1, 2]. CE needs at least 30 mW to be driven regardless of position and direction. To solve this problem, many transmitting and receiving coil structures have been proposed and analyzed [3].

Figure 2 shows the configuration of coils used in the simulation for WPT system for CE proposed in [4]. The detailed specifications are given in Table 1. The source generates 770 kHz sinusoidal waveform and the current through the coil generates a high magnetic field (~ 100 A/m) inside the coil.

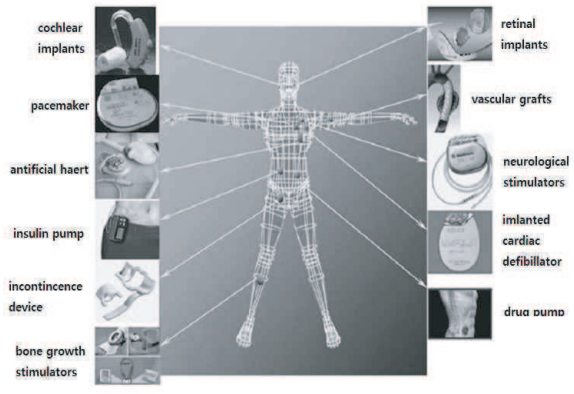

Figure 1: Locations of the MICS system investigated.

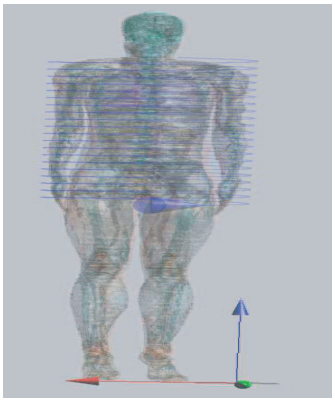

Figure 2: Configuration of coils in the simulation for the WPT system for CE.

We analyzed the health effects of the inductive coupling system using these parameters. The simulation was performed using the SEMCAD tool, and the Korean phantom model was used, which was developed by ETRI (Electronics and Telecommunications Research Institute in South Korea). The electrical parameters of tissues at 770 kHz were used [5]. We analyzed the distribution of power density along the depth of the body, and then we estimated the required input power of the WPT system. After that, the rms magnetic fields were calculated for the estimated input power. Fig. 3 shows the relative levels of the transmitted power density, and Table 2 shows the magnitude of the magnetic field for the representative positions of CE. The values in the esophagus were calculated at the deepest point which is located at the height of the heart. For estimation of the input power, we assumed the conversion efficiency (from AC to DC) of 50%. Table 2 shows that the exposure level due to the WPT system is higher than both Korean guideline (2.0 A/m at 800 kHz) and FCC guideline (20.4 A/m at 800 kHz).

Table 1: Specifications of transmitting and receiving coil structure.

Resonant frequency	770 kHz
External coil size	400 mm (width) * 400 mm (depth) * 300 mm (height) Wire diameter = 0.15 mm
Winding number of times	38 turns
Coil current	2.6 A

Table 2: Magnitude of rms magnetic field for three representative positions of CE.

Input power	1.66 A (Small-intestines)	1.54 A (Stomach)	1.75 A (Esophagus)
Mean rms H [A/m]	25.95	25.98	26
Max. rms H [A/m]	36.7	36.75	36.8

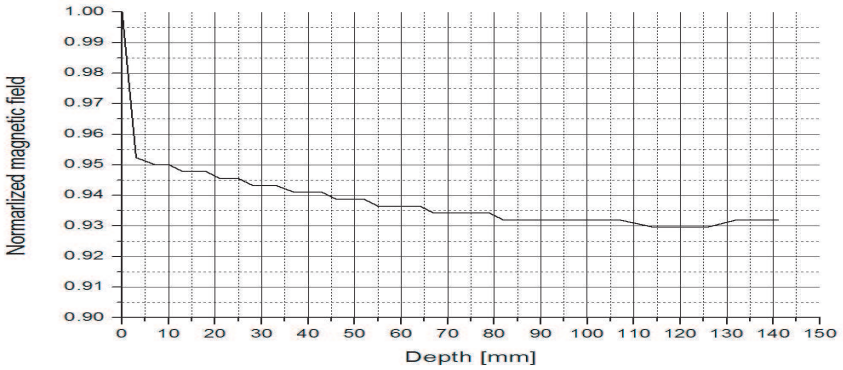

Figure 3: Distribution of power density (770 kHz).

Table 3: Power requirement of IMD devices.

IMD	Typical power requirement
Pacemaker	1 mW $\sim$ 10 μW
Cardiac Defibrillator	30 $\sim$ 100 μW
Neurological Stimulator	30 μW to several mW
Drug Pump	100 μW to 2 mW
Cochlear Implants	1 mW
Capsule Endoscope	37 mW

We also investigated the exposure levels due to the WPT systems using RF transmission method. In recent years, the power consumption of the Implantable Medical Devices (IMD) has been increased dramatically. Table 3 shows the typical power requirement of these devices [6].

In the RF transmission method, the rectenna is usually used. It can transmit power up to the distance greater than several meters with high efficiency. In simulation, Remcom's XFDTD 6.6 version was used. We put a point source located at 22 mm from the sternum. The distribution of the power density along the depth of the body was calculated at 403 MHz (MICS band) and 900 MHz (ISM band) using the Korean phantom model, and then required input power of the WPT system was estimated as before. The SAR values for the estimated input power were then calculated for each frequency.

Figures 4 and 5 show the relative levels of the transmitted power density, and Table 2 shows the SAR values for each frequency. For 1 W input power, average SAR, maximum 1 g SAR and maximum 10 g SAR in the human body at the 403 MHz are 0.016, 3.34, and 1.7 [W/kg], respectively. The corresponding SAR values at the 900 MHz are 9.53×10^{-3}, 7.84, and 4.37 [W/kg], respectively.

The estimated required input power as well as 1 g and 10 g SAR values for the input power are summarized in Table 5. For estimation of the input power, we assumed the conversion efficiency of 50%, in which the effective aperture of rectenna and RF to DC conversion efficiency were taken into account. The values in the parenthesis are 1 g SAR and 10 g SAR in W/kg. We can see that the SAR values for Cochlear Implant and Capsule Endoscope are pretty much higher than human protection guideline.

Table 4: SAR values for 1 W input power at 403 MHz and 900 MHz.

403 MHz	Average SAR in exposed Object [W/kg]	0.016
	Maximum 1 g SAR [W/kg]	3.34
	Maximum 10 g SAR [W/kg]	1.7
900 MHz	Average SAR in exposed Object [W/kg]	9.53×10^{-3}
	Maximum 1 g SAR [W/kg]	6.9
	Maximum 10 g SAR [W/kg]	3.74

Table 5: Required input power and 1 g, 10 g SAR.

	Pacemaker	Neurological Stimulator	Drug Pump	Cochlear Implants	Capsule Endoscope
403 MHz	0.02 W (0.07, 0.03)	0.28 W (0.93, 0.48)	0.11 W (0.37, 0.19)	0.54 W (1.8, 0.92)	56.1 W (187, 95.5)
900 MHz	0.05 W (0.34, 0.18)	0.3 W (2.06, 1.12)	0.13 W (0.89, 0.49)	0.7 W (4.82, 2.62)	96.4 W (663, 360.6)

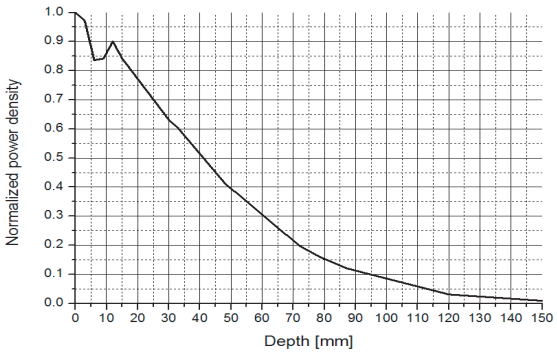

Figure 4: Distribution of power density at 403 MHz.

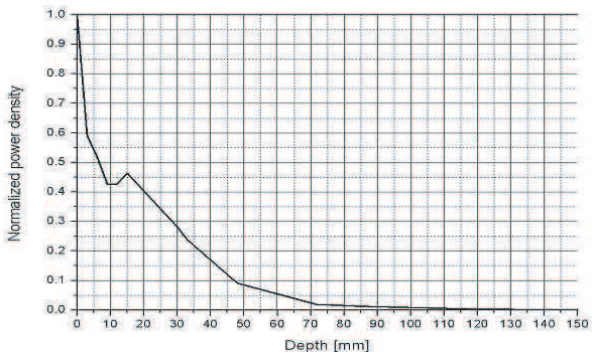

Figure 5: Distribution of power density at 900 MHz.

3. CONCLUSION

WPT technology is useful for MICS devices. However, it can cause possible health effects. We investigated such effects using numerical simulation. The results show that for some MICS devices,

which are located deep position inside human body, exposure levels of WPT systems can exceed the exposure limits of the protection guidelines. Thus, more intensive studies as well as some kind of standardization for WPT systems seem to be necessary.

ACKNOWLEDGMENT

"This research was supported by the MKE (Ministry of Knowledge Economy), Korea, under the ITRC (Information Technology Research Center) support program supervised by the NIPA (National IT Promotion Agency)" (NIPA-2009-(C1090-0902-0034)).

REFERENCES

1. Gimm, Y.-M., et al., "125 kHz magnetic field attenuation characteristics in some of the homogeneous human organs," *Electronic Proceedings of the 2007 International Symposium on Antennas and Propagation*, 430–433, Niigata, Japan, April 2007.
2. Gimm, Y.-M., et al., "Frequency dependence of magnetic field attenuation in some stimulant homogeneous human tissue," *Electronic Proceedings of the Bioelectromagnetics Society (BEMS) 30th Annual Meeting*, San Diego, USA, July 2008.
3. Seo, M.-S., Y. S. Ko, and S. Park, "A wireless energy transmission for capsule endoscopes," *KEES*, May 2008.
4. Gimm, Y.-M., "Receiving coil analysis of wireless power transmission with inductive coupling," *Korea-Japan Microwave Conference*, 2007.
5. http://niremf.ifac.cnr.it/tissprop.
6. Poon, A. da S. Y., S. O'Driscoll, and T. H. Meng, "Optimal operating frequency in wireless power transmission for implantable devices, *Proceeding of the 29th Annual International Conference of the IEEE EMBS Cite International*, Lyon, France, August 23–26, 2007.

A Comparison of Ansoft HFSS and CST Microwave Studio Simulation Software for Multi-channel Coil Design and SAR Estimation at 7 T MRI

M. Kozlov and R. Turner
Max Planck Institute for Human Cognitive and Brain Sciences
Stephanstrasse 1A, D-04103, Leipzig, Germany

Abstract— We present a comparison of RF simulations with Ansoft HFSS and CST Microwave studio software, for a commercially available 7 T multi-channel coil. We investigated the conditions influencing precision and simulation time. When simulation parameters (such as mesh size) are appropriately selected and full coverage of the results is ensured, there is agreement between simulated and experimentally determined S parameters, between simulated and actual capacitor values, and between simulated and measured RF field. At this point, both simulation methods then provide comparable results, to within 15%. In their current implementations, the Ansoft HFSS frequency domain solver converges much faster than the CST time domain solver. HFSS based RF circuit and 3-D EM fields co-simulation significantly speeds up MRI coil design, because the simulation time no longer depends strongly on simulated port numbers and the length of the smallest mesh cell.

1. INTRODUCTION

Human magnetic resonance imaging (MRI) studies conducted at high magnetic fields (7 T and above) operate in the regime where the wavelength of radio frequency (RF) fields inside an object is less than the object dimensions. In this regime electrical ($\mathbf{E}$) and magnetic ($\mathbf{B}_1$) components of RF fields, as well as the specific absorption ratio (SAR) profiles in the object imaged (e.g., human head or body) are highly complex and spatially non-uniform.

Reliable estimation of SAR values has become a very important concern since lack of full knowledge is the reason for the typically conservative vendor-provided RF power limits. It is impossible to measure SAR in-vivo, but reliable SAR values can be easily obtained from $\mathbf{E}$ field data. Therefore numerical simulation is a very important component of MRI coil design/analysis and SAR estimation.

Despite the current rapid development of novel 3-D EM tools, as well as the significant improvement of those already available, there is limited information regarding the suitability of the commercially-available simulation tools for high-field MRI coil design and validation, and which setup parameters are important for reliable simulation. Selection of the tools can be made on the basis of simulation data uncertainties, simulation time, model design limitation, and hardware requirements. Our goal was to compare simulation results obtained for a commercially-available Rapid BioMed 7 T multi-channel coil using Ansoft HFSS frequency-domain and CST Microwave Studio time-domain solvers with the results from actual measurement, and to investigate the conditions that influence the simulation time and the precision of simulated results.

2. METHOD

The realistic coil 3-D EM model includes all construction details for 8 resonance elements, modelled with precise dimensions (inner $\varnothing = 235$ mm, outer $\varnothing = 310$ mm) and material electrical properties. The scanner gradient shield was defined as a copper cylinder with $\varnothing = 683$ mm and 0.045 mm thickness. A perfect absorbing boundary (PAB) was offset to 40 mm from gradient shield in X/Y directions, the axial distance from coil to the PAB was more than 500 mm ($\lambda/2$ in air for 300 MHz). We employed co-simulation of the RF circuit and 3-D EM fields [1]. For each coil element, the RF feed network and trim capacitor, which is on the opposite side to the element's feed point, were substituted with 50 Ohm ports. This gave a total number of ports as high as 16. For tuning the coil for each simulation setup, the vendor-provided procedure was used — a Siemens 7 liter water-based phantom was placed inside the coil. As a result one 3-D EM simulation of the given setup was enough to tune/match the coil. The simulation values obtained for tune/match capacitors were compared with the actual values.

Because this coil cannot be re-tuned once installed in the MRI scanner, we kept variable capacitor values and mesh definition fixed for each simulation setup when conducting an investigation of

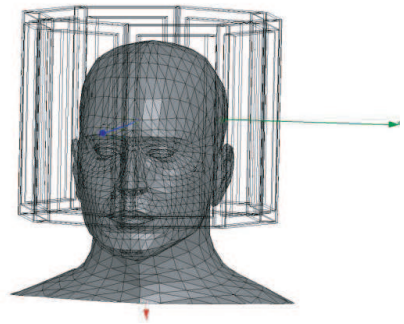

Figure 1: Simulation setup.

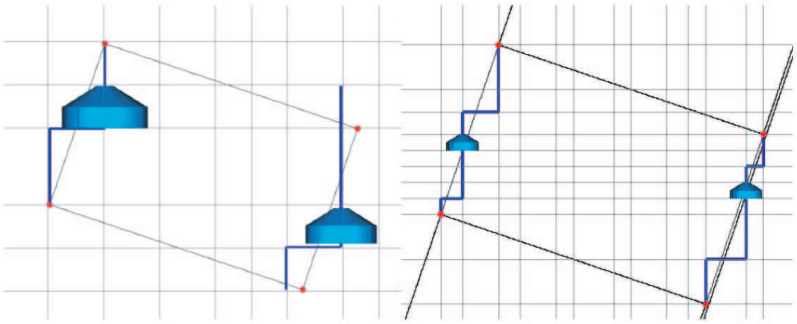

Figure 2: Lumped element mesh. Left: wrong mesh, right: correct mesh.

SAR. In this case, changing the simulation object from the phantom to a head model corresponds to experimental substitution of the phantom by an in-vivo subject inside the tuned and matched MRI coil. SAR was evaluated using an in-vivo load consisting of the head and part of the shoulders of the Ansoft surface-based human body model (Fig. 1), with different spatial scaling factors.

Since the SAR calculation procedure incorporated within CST is very slow (up to 10 hours for 50 million mesh cells) and HFSS does not include IEC-recommended SAR evaluation, we generally used a home-built fast and reliable SAR calculation procedure, versatile with regard to both 3-D EM solver strategies, and adapted to multi-core processing [2]. We found negligible difference in the SAR data evaluated by CST procedure and this in-house method.

3. RESULTS AND DISCUSSION

HFSS offers a reliable mesh adaptation algorithm and several simulation coverage criteria, sufficient to obtain reliable data in one simulation run. Correct trim capacitor estimation was obtained in an HFSS simulation, in which initial manual mesh seeding was provided to get at least 3 tetrahedra within each current-conducting element cross section. The S-parameter coverage criteria were defined to be better than 0.0025. The project mesh reached ∼2.4 million tetrahedra after 5 mesh adaptation steps.

CST also includes several coverage criteria but its suitable for multi-channel MRI coil simulation mesh adaptation procedure is based on increasing the "*Lines per wavelength*" and "*Lower mesh limit*" settings. This refinement over the entire model volume is a less robust approach, compared with HFSS mesh refinement, which is performed mostly in the volumes containing maximum field values. For complex MRI coil simulations, CST coverage criteria are used rather seldom, due to the extremely long computational times. In addition, mesh refinement for a given wavelength makes it impossible to keep the same mesh of coil elements for phantom and human model simulations. As it will be shown below the latter is important for reliable SAR prediction.

For CST simulations, mesh definition has a significant influence on representation of areas that include ports and lumped elements. In the simulated coil, ports and lumped elements are not aligned parallel to a coordinate axis. In these areas the mesh step was decreased until the relevant mesh vertexes were accurately positioned as start and end points for integration across ports or lumped elements (Fig. 2). If too coarse a mesh is used, integration defining a significant dependence of port impedance and lumped element properties may erroneously include conductor material. This may result in overestimation or underestimation of SAR by up to 30%.

Keeping correct port and lumped element mesh definition (mesh step size as small as 0.25 mm) the coil element mesh size was manually decreased, step by step, until the difference between experimental and simulated trim capacitor values vanished (Table 1). Because the current distribution is maximal on the conductor edges, a relatively small hexahedral mesh step must be used for the reliable representation of radiative coil elements when these are not aligned parallel to a coordinate axis. This result underlines the importance of keeping the same coil element mesh definition between phantom and human model simulations.

For CST simulation, increasing the number of mesh cells resulted in nearly the same shape of B_1+ profile within a phantom (Fig. 3), but approximately a 75% variation of peak SAR value for some head models (Table 1). SAR was found to be coupled to two different **E** field sources (conservative and non-conservative). The first is the penetration of the **E** field from the distributed

capacitors commonly used in high field MRI coils, the second is the **E** field that accompanies the propagating magnetic field. When the conservative **E** field has significant influence, care must be taken to ensure that the mesh definition is smaller than 1.25 mm, whenever a part of the human body model is close to a capacitor (Fig. 4).

For the mainly non-conservative **E** field within the body, changes of the SAR value for the coil investigated are less than $+/-10\%$, once the mesh cell size is less than 2 mm isotropic for coil elements.

There is less than 15% difference between field and SAR (point to point data comparison) for HFSS and CST simulations, once simulation setup and parameters are correctly chosen. For CST this means that the steady state monitor must be set below -60 dB, in addition to the precautions discussed above that ensure full coverage and agreement between simulated and actual capacitor values. This monitor guides CST solver accuracy during time domain simulation by comparing

Table 1: CST and HFSS simulation data.

	CST						HFSS
Coil element mesh, isotropic [mm]	2.25	2	1.5	1.25	1	0.8	variable
Tune capacitor value [pF]	29.8	24.9	17.1	16.1	12.8	11.3	11.2
SAR for Head model	2.00	1.87	1.43	1.38	1.30	1.28	1.21
SAR for Head 0.8 scaled model	1.73	1.64	1.68	1.71	1.74	1.70	1.76

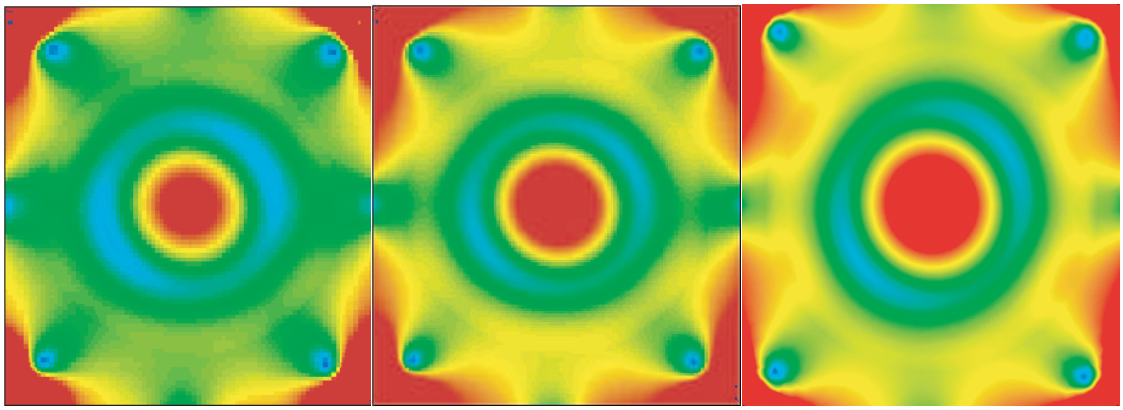

Figure 3: Transversal $\mathbf{B}_1+$ maps for Siemens phantom. Left: CST coil mesh 2.25 mm, center: CST coil mesh 1 mm, right: HFSS.

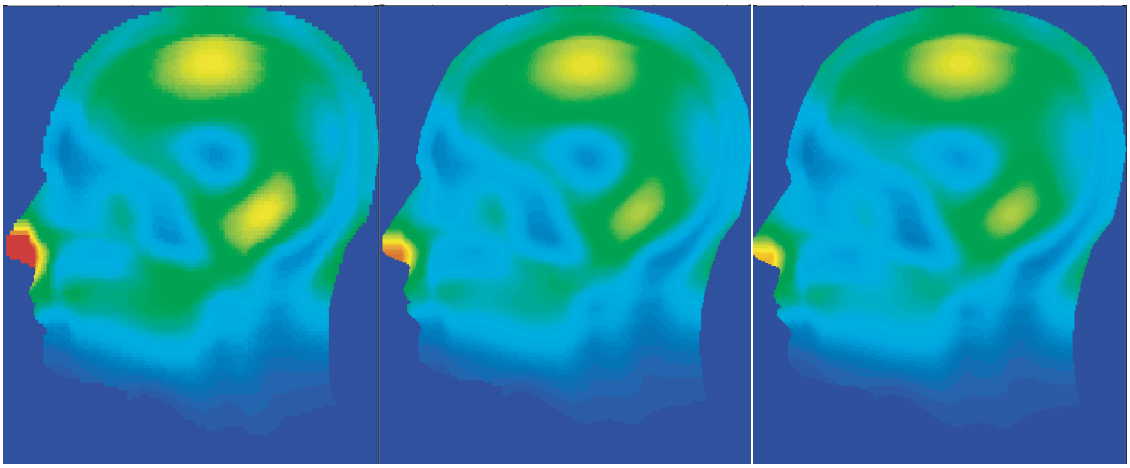

Figure 4: Head with scaling 1. Left: CST SAR for coil mesh 2.25 mm, center: CST SAR for coil mesh 0.8 mm, right: HFSS SAR data.

the total energy at each time point within the volume of interest relative to the peak value of this total energy. The simulation terminates when the defined level is reached. The lower this level, the more accurate are both the S parameters and the field simulation data obtained by the Fourier transformation of the time domain values. The simulations of the coil investigated required several months and about 16 GB RAM memory for CST, and two days and 62 GB RAM memory for HFSS projects running on the same computer, without simulation parallelization and hardware acceleration. The memory size disadvantage for HFSS is not severely problematic today, with commercially available 64 GB memory workstations. The computational time disadvantage for CST is a consequence of the inverse proportionality of the simulation time to the length of the smallest mesh cell, which has to be quite small for reliable simulation of a complex MRI coil. In addition, if the computation is performed in CST, each port is simulated independently. This means that the simulation time for the entire project is linearly proportional to the number of ports, and simulation of 8-channel coil with 16 ports, could take several weeks, despite use of several computers for port simulation parallelization.

Usage of the RF circuit and 3-D EM co-simulation approach is not a reason for the extremely long CST simulation time (Table 2). In opposite, if the approach is used simulation time is the shortest for coils, which effective coil-loss resistance ($\mathbf{R}_\Sigma$) is less than 6.25 Ohm. $\mathbf{R}_\Sigma$ is calculated from the power absorbed by coil and the sum of each element's feed current. $\mathbf{R}_\Sigma = 0.52$ Ohm for the coil investigated.

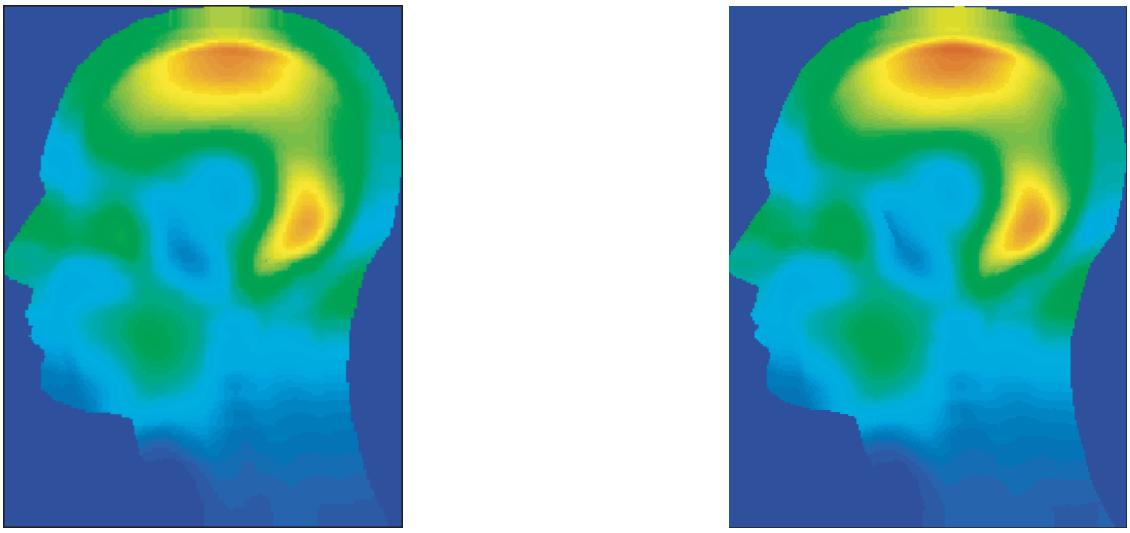

Figure 5: Head with scaling 0.8. Left: CST SAR for coil mesh 1 mm, right: HFSS SAR data.

Table 2: Comparison of CST FDTD simulation time for an 8 channel coil with given coil quality factor $\mathbf{Q}$.

	Simultaneous port excitation of tuned/matched coil	Individual ports excitation of tuned/matched coil	RF circuit 3-D EM co-simulation
Number of excitations	1	8	16
Simulation time of single excitation in proportion to	$\mathbf{Q}$	$\mathbf{Q}$	$\mathbf{Q} \times \frac{\mathbf{R}_\Sigma}{2 \times \mathbf{R}_{port}}$
Total simulation time in proportion to	$\mathbf{Q}$	$8 \times \mathbf{Q}$	$\mathbf{Q} \times \frac{16 \times \mathbf{R}_\Sigma}{2 \times \mathbf{R}_{port}}$

4. CONCLUSION

When simulation parameters (such as mesh size and coverage criteria) are appropriately selected, there is agreement between simulated and experimentally determined S parameters, and also between simulated and actual capacitor values. At this point, RF field simulations and measurements also agree and both simulation methods then provide comparable results. In their current implementations, the Ansoft HFSS frequency domain solver converges much faster than the CST time domain solver. HFSS based RF circuit and 3-D EM fields co-simulation significantly speeds up MRI coil design, because the simulation time no longer depends strongly on simulated port numbers and the length of the smallest mesh cell. To obtain reliable CST data, the CST solver accuracy requires a steady state monitor setting that is better than $-60\,\mathrm{dB}$, and the mesh size must be manually decreased step-by-step to ensure full coverage of the results. Furthermore, simulation must be performed using a realistic head model, together with the same mesh definition and tune/match network as used for simulation with a phantom corresponding to the standard product tuning procedure. For the reliable simulation of distributed capacitance, the CST mesh has to be smaller than the thinnest dielectric elements of the coil. This is more important for coil tuning (e.g., trim capacitor) estimation than for SAR.

REFERENCES

1. Kozlov, M. and R. Turner, "Fast MRI coil analysis based on 3-D electromagnetic and RF circuit co-simulation," *Journal of Magnetic Resonance*, Vol. 200 147–152, 2009.
2. Kozlov, M. and R. Turner, "Optimization of SAR calculation for 3-D EM time and frequency domain data," *Proceedings of International Society for Magnetic Resonance in Medicine*, 4779, Honolulu, USA, April 2009.

Development of Wave Absorbing Coating Optimization Software

Jianzhou Li, **Changying Wu**, **Gao Wei**, **and Jiadong Xu**
School of Electronics and Information, Northwestern Polytechnical University
Xi'an 710072, China

Abstract— Design and optimization of wave absorbing coating are of great interest in engineering practice to decrease the scattering intensity of typical targets, such as missiles and aircrafts. Aimed to automatically select particular materials from the material database and design the thickness of each layer to form the optimized multi-layer wave absorbing coating, a universal software based on the genetic algorithm is developed using C++. Many important features and functions, such as optimization in multiple bands with multiple incident angles and different incident wave polarizations, partial assignment and partial optimization of wave absorbing layer parameters, build-in radar absorbing material database management, reflection coefficients calculation and display of arbitrary wave absorbing coating are achieved in the developed software. The software development flow chart and basic modules are discussed. The functions and corresponding friendly user interface are given. Sufficient numerical examples are shown at last, which demonstrate reasonable optimization results, high efficiency and stability of the developed software.

1. INTRODUCTION

Radar absorbing material coating is one of the most effective and successive techniques widely used in the design and modification of stealth targets to reduce the back scattering. Wave absorbing layers are often coated on the area of strong back scattering to reduce the radar cross section (RCS) and the possibility of being detected. Currently, too many kinds of wave absorbing materials are using in engineering practice. Optimization is necessary to choose the specific material from the wave absorbing material database and design the thickness of each layer to form the optimized wave absorbing layer. By coating the optimized wave absorbing layer, significant RCS reduction thereof stealth performance enhancement can be achieved. Recently, many researches on wave absorbing coating optimization have been reported [1–4], but all were limited to theoretical research and did not form any universal optimization software. Based on genetic algorithm [5] to minimize the reflection coefficients or the RCS of multi-layer wave absorbing layer coated on a certain kind of material, say a PEC structure, a universal easy-using software is developed using C++ for engineering practice to design optimized wave absorbing layer. Important functions implemented in the developed software are as follows:

- Multi-band optimization
- Multi-incident angle optimization
- Optimization for both the TE and TM polarization
- Partial assignment and partial optimization of wave absorbing layer parameters
- Build-in wave absorbing material database management
- Reflection coefficients calculation and display of arbitrary wave absorbing coating

The following features are achieved:

- Reliable optimization results due to mature and stable genetic algorithm used in the developed software.
- High optimization efficiency.
- Full function for coatings optimization and easy use with user friendly interfaces.

The basic flow chart, the modules and the user interface will be discussed firstly. Some optimization results are followed to validate the developed software. The genetic algorithm is not the focus of this paper and could be consulted from reference [1] and [2] if interested.

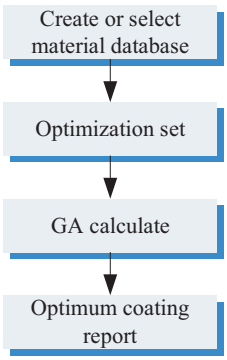

Figure 1: The basic flow chart of the optimization software.

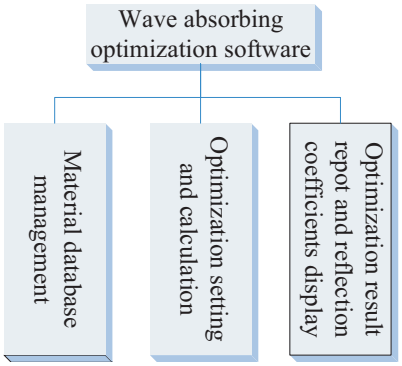

Figure 2: The modules of the optimization software.

2. THE OPTIMIZATION SOFTWARE DEVELOPMENT

The optimization software is developed with C++. The basic flow chart and the modules are shown in Figures 1 and 2. The wave absorbing material database is built in to create and maintain the candidate material database. A material database is a combination of some wave absorbing materials. All the material parameters, such as permittivity and permeability at different frequency are stored in certain data sets in the database. The proper wave absorbing material can be chosen automatically by the optimization algorithm from the selected database to form the optimized wave absorbing layer.

In the developed software, optimization setting is the main user interaction module which consists of optimization object setting, optimization variables setting, optimization condition setting and optimization control setting. Either reflection coefficients or RCS can be set to be the optimization object in optimization object setting module. The material of the underlay structure is also assigned here. In optimization variable setting module (shown in Figure 3), all the variables of the coating can be set, which includes the number of the layer, the total thickness, the material and the thickness of each layer. Because the material and the thickness of each layer can be set separately, it is possible to partially assign and partially optimize wave absorbing layer parameters. Take a two-layered wave absorbing structure as an example, one can assign the material of the first layer and the thickness of the second layer, and then let the software optimize the thickness of the first layer and the material of the second layer. So, great flexibility of optimization is achieved in the developed software. In optimization condition setting module (shown in Figure 4), the polarization, frequency and incident angle of the incident wave are assigned. For incident wave frequency, single frequency, multiple frequencies or multiple frequency bands are allowed. So does incident angle. All the basic parameters of the genetic algorithm, such as the crossover possibility, mutation possibility, population, generation and so on, are set in the optimization control module. The optimization calculation module consists of two sub modules, i.e., reflection coefficients calculation and the genetic evolution. As the basic algorithm of the objective function in the genetic algorithm, calculation of the reflection coefficients for the multilayered structure is done using a recursive procedure listed in [6]. Full functional genetic algorithm is developed to perform the optimization according to all the control parameters set in the optimization setting module. The optimal scenario report and display module (shown in Figure 5) is called at last to report the optimal wave absorbing structure and then calculate and display the reflection coefficients. Another function of this module is to export the optimal wave absorbing coating into the RCS calculating software for further simulation.

Because all the codes of the software including the genetic algorithm are developed with C++, high optimization efficiency has been achieved. With the developed friendly user interface, the universal and easy using software can be used a powerful optimization tool for wave absorbing coating design.

3. THE OPTIMIZATION EXAMPLES

To validate the developed software, five optimization examples are given. An additional result is also given to show the optimization stability of the software. In all the optimization examples, PEC is used as the underlay structure and the crossover possibility, the mutation possibility, the population and the generation of the genetic algorithm are set to be 0.7, 0.01, 50, and 400 respectively.

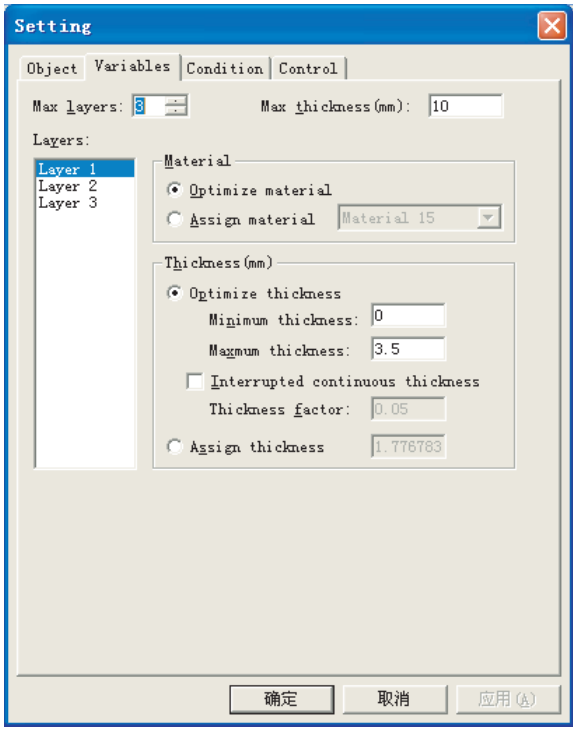

Figure 3: Optimization variable setting.

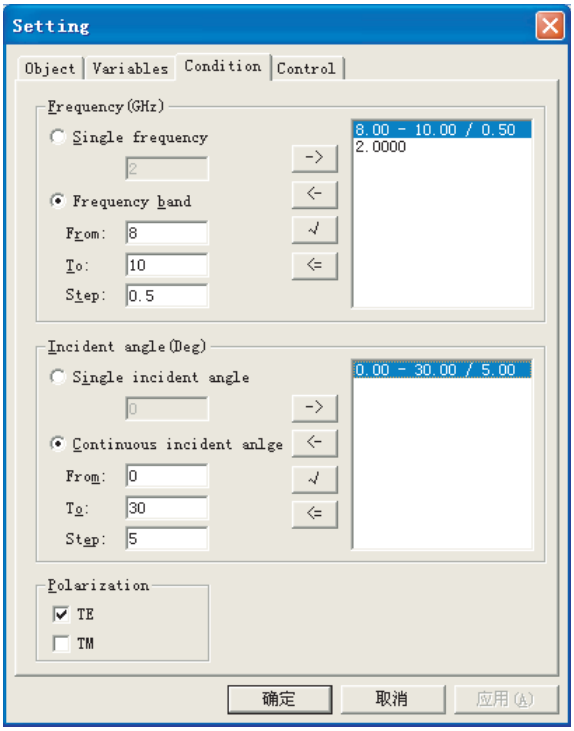

Figure 4: Optimization condition setting.

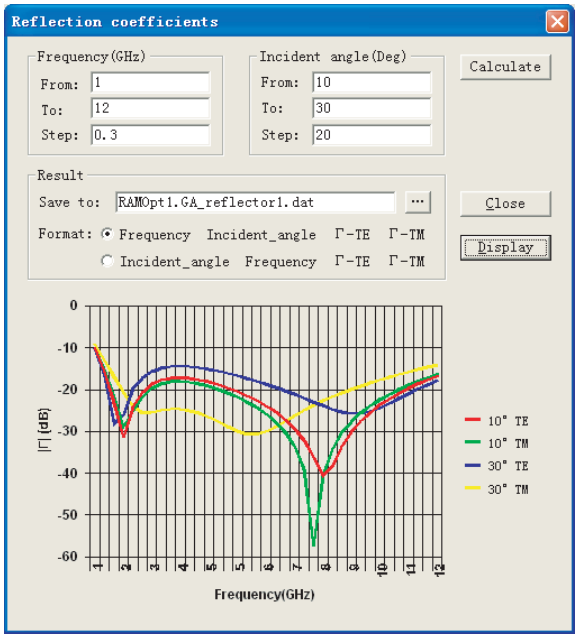

Figure 5: Optimal scenario report and display.

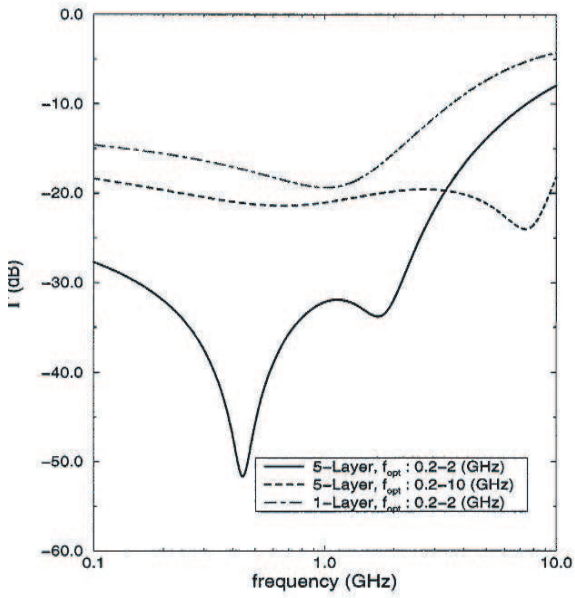

Figure 6: Reflection coefficients of optimum coatings in reference [1].

3.1. Example 1. 5-layered RAM Structure Optimized in the Frequency Band 0.2–2 GHz

In this example, the maximum thickness of the coating is set to be 10 mm, and the thickness of each layer is less than 2 mm. To compare with reference [1], only normal incidence is considered. The optimum coatings are listed in Table 1. Although the configurations of the optimum coatings from this software and reference [1] are different, the reflection coefficients versus frequency agree very well (shown in Figures 6 and 7 with solid lines), which means almost the same effect of wave absorbing can be achieved with different coatings. Actually, random seeds are used in the genetic algorithm to generate the initial population. That is why the result coatings of this software are different for two simulations even with the same optimization settings.

3.2. Example 2. 5-layered RAM Structure Optimized in the Frequency Band 0.2–10 GHz

All the optimization settings in this example are the same as example 1 except in the frequency band 0.2–10 GHz. The optimum coatings are also listed in Table 1 and the corresponding reflection coefficients of the coated structure are shown with dash lines in Figures 6 and 7. The result from the developed software agrees again with that of reference [1]. It can be seen that the reflection coefficients reduce less as compared with example 1 because wider frequency band is considered here.

3.3. Example 3. 1-layered RAM Structure Optimized in the Frequency Band 0.2–2 GHz

In this example, the maximum thickness of the coating is 10 mm and normal incidence is considered. The optimum coatings of reference [1] and this software are listed in Table 1 and the reflection coefficients of the coated structure are shown with dash dot lines in Figures 6 and 7. A good agreement of the optimum coatings and the corresponding reflection coefficients is revealed again.

3.4. Example 4. 5-layered RAM Structure Optimized in the Frequency Band 0.2–2 GHz with Material of Each Layer Assigned

In this example, the material of each layer is assigned according to the designed coating in [1] and the thickness of each layer is optimized with all the other optimization settings keeping the same with example 1. The reference coating [1] and the result coating are listed in Table 1. Because the materials of the last three layers in the coatings are the same, the total thickness of the last three layers is 3.745 mm, which is only 0.014 mm less than that of the reference coating. Besides, the thicknesses of the first and the second layer are also quite close to those of the reference coating. So the partially optimized coating is almost the same as the reference one. This can be corroborated by the reflection coefficients shown with dot lines in Figures 6 and 7.

3.5. Example 5. 5-layered RAM Structure Optimized in the Frequency Band 0.2–2 GHz with Thickness of Each Layer Assigned

In this example, the thickness of each layer is assigned according to the designed coating in [1] and the material of each layer is optimized with all the other optimization settings keeping the same with example 1. Now exactly the same coating with reference [1] is gotten, which is listed in Table 1. This validates the developed software again.

3.6. Example 6. Verification of Optimization Stability

Optimization stability is an important performance. The reflection coefficients of the optimized coatings from different simulation with the same optimization settings should converge to certain values, which means once the optimization settings are fitted, the resulted coatings should keep almost the same wave absorbing performance. To validate the stability of the developed software, five simulations with the same optimization settings according to example 1 are performed. The reflection coefficients of the five coatings are shown in Figure 8. A good convergence is revealed which means although the different coatings are gotten, they have almost the same wave absorbing performance.

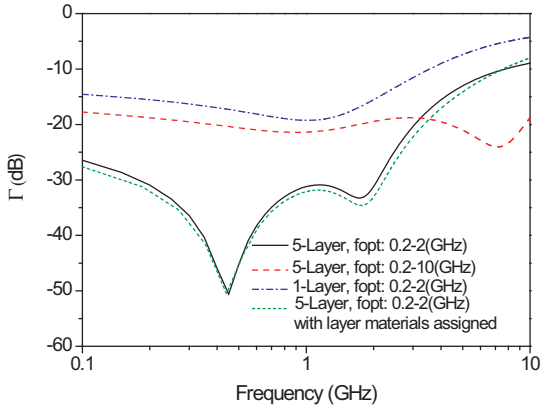

Figure 7: Reflection coefficients of optimum coatings by the developed software.

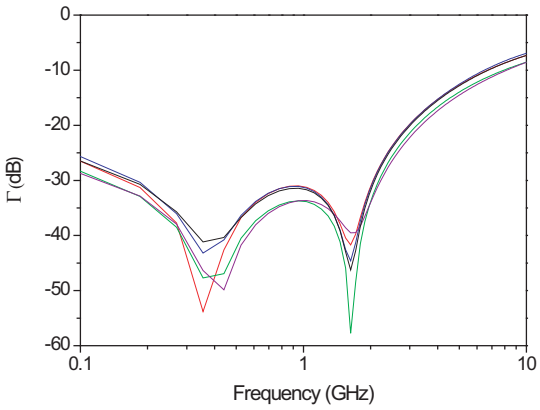

Figure 8: Optimization stability verification.

Table 1: Optimum coatings of example 1–5 and the corresponding results in reference [1].

	Layer	Reference [1]		This software	
		Material No.	Thickness (mm)	Material No.	Thickness (mm)
Example 1	1	14	0.888	16	1.0562
	2	6	1.43	4	1.0794
	3	4	0.559	8	1.744
	4	4	1.66	4	1.6024
	5	4	1.54	4	0.903
Example 2	1	14	0.434	16	0.4378
	2	6	1.77	6	1.4783
	3	5	1.4	1	0.0914
	4	4	1.93	4	1.9399
	5	2	0.649	5	1.1302
Example 3	1	4	2.49	4	2.479
Example 4	1	14	0.888	14	0.8744
	2	6	1.43	6	1.4178
	3	4	0.559	4	0.9792
	4	4	1.66	4	0.7834
	5	4	1.54	4	1.9819
Example 5	1	14	0.888	14	0.888
	2	6	1.43	6	1.43
	3	4	0.559	4	0.559
	4	4	1.66	4	1.66
	5	4	1.54	4	1.54

4. CONCLUSIONS

A universal software based on the genetic algorithm is developed to design multi-layer wave absorbing coatings. Many important features and functions, such as optimization in multiple bands with multiple incident angles and different incident wave polarizations, partial assignment and partial optimization of wave absorbing layer parameters, build-in radar absorbing material database management, reflection coefficients calculation and display of arbitrary wave absorbing coating are revealed in the discussion of the basic modules and the numerical examples of the developed software. Sufficient optimization examples demonstrate that the reflection coefficients calculation and the genetic algorithm for wave absorbing coating optimization in the developed software are accurate, efficient, stable and reliable. Wave absorbing coatings with good performance can be designed with the developed software to meet the application in engineering practice.

REFERENCES

1. Mosallaei, H. and Y. Rahmat-Samii, "RCS reduction of canonical targets using genetic algorithm synthesized RAM," *IEEE Trans. on AP*, Vol. 48, No. 10, 1594–1606, 2000.
2. Michielssen, E., J. M. Sajer, et al., "Design of lightweight, broad-band microwave absorbers using genetic algorithms," *IEEE Trans. Microwave Thoery Tech.*, Vol. 41, No. 6/7, 1024–1031, 1993.
3. Pesque, J., D. Bouche, and R. Mittra, "Optimization of multilayered antireflection coatings using an optimal control method," *IEEE Trans. Microwave Thoery Tech.*, Vol. 40, No. 11, 1789–1796, 1992.
4. Park, H. S., I. S. Choi, et al., "Optimized design of radar absorbing materials for complex targets," *Journal of Electromagnetic Waves and Applications*, Vol. 18, No. 8, 1105–1117, 2004.
5. Haupt, R. L., "An introduction to genetic algorithm for electromagnetics," *IEEE Antennas Propagat. Mag.*, Vol. 37, No. 2, 7–15, 1995.
6. Chew, W. C., *Waves and Fields in Inhomogeneous Media*, Van Nostrand Reinhold, New York, 1990.

Rotational Vector Addition Theorem and Its Effect on T-matrix

M. S. Khajeahsani and F. Mohajeri
Shiraz University, Iran

Abstract— In this paper we prove the vector addition theorem for rotation of vector spherical wave with zero divergence by the use of vector rotation operator. In this theorem a rotated vector spherical wave function is extended by fixed vector spherical wave functions. Then by the use of this theorem the relation between T-matrices for one object in two different concentric coordinate systems is formulated. Also, the relation between two coordinate systems is considered by Euler angles.

1. INTRODUCTION

Waterman's T-matrix formalism is widely used in acoustic and electromagnetic scattering problems [1–4]. This method, based on the linearity of Maxwell's equations, is a widely used technique for the determination of light-scattering properties by nonspherical particles. While it is applicable to any kind of shape, most practical applications are centered on revolution (axisymmetric) particles, for it is then that the T-matrix divides itself into independent submatrices [5]. Further simplifications, like particles with a plane of symmetry, allow for a faster and more efficient calculation of light-scattering properties [6].

Vector spherical wave functions, i.e., canonical solutions of the Helmholtz equation in spherical coordinates, form complete sets that can be used as bases to expand more general solutions of the Helmholtz equation. The translation formulas are examples of such expansions since they express translated spherical waves as superposition of untranslated spherical waves. Friedman and Russek [7] were among the first to give explicit statements of translation formulas for scalar spherical waves. In this paper we prove rotational formulas and express rotated spherical waves as superposition of unrotated spherical waves. Using this method, it is more convenient to calculate T-matrix in new bases.

2. ROTATION OPERATOR

2.1. Euler Angles

The general displacement of a rigid body due to a rotation about a fixed point may be obtained by performing three rotations about two of three mutually perpendicular axes fixed in the body. We shall assume a right-handed frame of axes. The rotations (see Figure 1) are to be performed successively in the order:

1. A rotation α about the z-axis, bringing the frame of axes from the initial position S into the position S'.

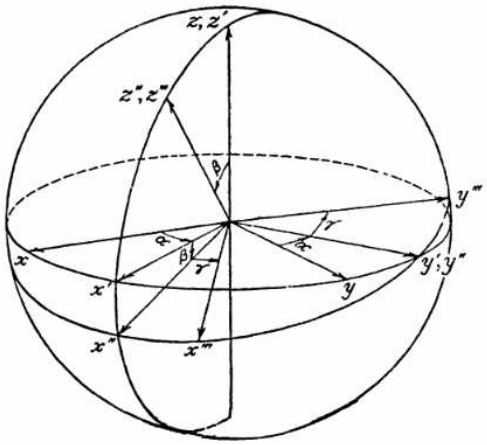

Figure 1: Euler rotation angles.

2. A rotation β about the y-axis of the frame S'. The resulting position of the frame of axes is symbolized by S''.
3. A rotation γ about the z-axis of the frame of axes S. The final position of the frame is symbolized by S'''.

It should be noted that the polar coordinates φ, θ with respect to the original frame S of the z-axis in its final position are identical with the Euler angles α, β respectively.

Therefore any rotation denoted by $\mathcal{R}$ can be mathematically expressed as:

$$\mathcal{R}(\alpha,\beta,\gamma) = \mathcal{R}_{z''}(\gamma)\mathcal{R}_{y'}(\beta)\mathcal{R}_z(\alpha) \tag{1}$$

In addition, we can show that the rotation operator can be written as [8, 9]:

$$\mathcal{R}(\alpha,\beta,\gamma) = \mathcal{R}_z(\alpha)\mathcal{R}_y(\beta)\mathcal{R}_z(\gamma) \tag{2}$$

In the next section we use Eq. (2) instead of Eq. (1).

2.2. Mathematical Form of Rotation Operator

To calculate the mathematical form of rotation operator we consider an infinitesimal rotation α about the z axis (represented by $\mathcal{R}(\alpha,0,0)$). For convenience the Cartesian components of the vector field and the Cartesian coordinates of the field points are employed. The field is described in the original frame S by $V_x(x,y,z)$, $V_y(x,y,z)$, $V_z(x,y,z)$. In the new frame S' obtained from S. By the rotation $(\alpha,0,0)$ the components are

$$V_{x'}(x',y',z') = V_x(x'-\alpha y', y'+\alpha x', z') + \alpha V_y(x'-\alpha y', y'+\alpha x', z') \tag{3}$$
$$V_{y'}(x',y',z') = -\alpha V_x(x'-\alpha y', y'+\alpha x', z') + V_y(x'-\alpha y', y'+\alpha x', z') \tag{4}$$
$$V_{z'}(x',y',z') = V_z(x'-\alpha y', y'+\alpha x', z') \tag{5}$$

And by use of Taylor series we can conclude that

$$\vec{V}' = \vec{V} + i\alpha\left[\frac{1}{i}\left(x'\frac{\partial}{\partial y'} - y'\frac{\partial}{\partial x'}\right) + i\hat{a}_z\times\right]\vec{V} \tag{6}$$

The two term appearing in brackets are called L (Orbital angular momentum operator) and S (Spin angular momentum operator) respectively. So

$$L_z = \frac{1}{i}\left(x\frac{\partial}{\partial y} - y\frac{\partial}{\partial x}\right) \tag{7}$$
$$S_z = i\hat{\alpha}_z\times \tag{8}$$

Similarly for infinitesimal rotation about x and y axis we can define rotation operator as follows:

$$L_x = \frac{1}{i}\left(y\frac{\partial}{\partial z} - z\frac{\partial}{\partial y}\right), \quad S_x = i\hat{\alpha}_x\times \tag{9}$$
$$L_y = \frac{1}{i}\left(z\frac{\partial}{\partial x} - x\frac{\partial}{\partial z}\right), \quad S_y = i\hat{\alpha}_y\times \tag{10}$$

it is better to show these operators in matrix form as follows:

$$S_x = i\begin{pmatrix}0&0&0\\0&0&-1\\0&1&0\end{pmatrix},\ S_y = i\begin{pmatrix}0&0&1\\0&0&0\\-1&0&0\end{pmatrix},\ S_z = i\begin{pmatrix}0&-1&0\\1&0&0\\0&0&0\end{pmatrix} \tag{11}$$

It is clear that a finite rotation around z-axis is given by multiplying a large number of these operators:

$$\mathcal{R}_z(\alpha) = \lim_{N\to\infty}\left[1 + i\frac{\alpha}{N}(L_z+S_z)\right]^N = \exp(i\alpha(L_z+S_z)) \tag{12}$$

2.3. Properties of Orbital Angular Momentum Operator

The square of the total angular momentum is defined as:

$$L^2 = L_x^2 + L_y^2 + L_z^2 = -\left[\frac{1}{\sin^2\theta}\frac{\partial^2}{\partial\phi^2} + \frac{1}{\sin\theta}\frac{\partial}{\partial\theta}\left(\sin\theta\frac{\partial}{\partial\theta}\right)\right] \tag{13}$$

Then it can be shown that [8]:

$$L_z Y_n^m(\theta,\phi) = mY_n^m(\theta,\phi) \tag{14}$$

$$L^2 Y_n^m(\theta,\phi) = n(n+1)Y_n^m(\theta,\phi) \tag{15}$$

where $Y_n^m(\theta,\phi)$ is a spherical harmonic function. Also we have:

$$L_x Y_n^m(\theta,\phi) = \frac{1}{2}\left[\sqrt{(n-m)(n+m+1)}Y_n^{m+1}(\theta,\phi) + \sqrt{(n+m)(n-m+1)}Y_n^{m-1}(\theta,\phi)\right] \tag{16}$$

$$L_y Y_n^m(\theta,\phi) = \frac{1}{2i}\left[\sqrt{(n-m)(n+m+1)}Y_n^{m+1}(\theta,\phi) - \sqrt{(n+m)(n-m+1)}Y_n^{m-1}(\theta,\phi)\right] \tag{17}$$

If we define commutator bracket of A, B as:

$$[A,B] = AB - BA \tag{18}$$

Then it can be shown that

$$\left[L^2, L_i\right] = 0 \qquad i = x,y,z \tag{19}$$

So it is expected that

$$\left[L^2, \exp(iL_j\alpha)\right] = 0 \qquad j = x,y,z \tag{20}$$

Now by the use of Eq. (20) and Eq. (15)

$$L^2[\exp(iL_j\alpha)Y_n^m(\theta,\phi)] = n(n+1)[\exp(iL_j\alpha)Y_n^m(\theta,\phi)] \tag{21}$$

2.4. Properties of Spin Angular Momentum Operator

The commutation relations for spin angular momentum operator are:

$$[S_x,S_y] = iS_z,\ [S_y,S_z] = iS_x,\ [S_z,S_x] = iS_y \tag{22}$$

Also by use of Eq. (11) it can be shown that

$$S_i = S_i^3 = S_i^5 = \ldots = S_i^{2n+1} \quad i = x,y,z; \quad n = 1,2,3,\ldots \tag{23}$$

$$S_i^2 = S_i^4 = S_i^6 = \ldots = S_i^{2n} \quad i = x,y,z; \quad n = 1,2,3,\ldots \tag{24}$$

2.5. Calculation of Finite Rotation Operator $\boldsymbol{L}$

In this section we want to calculate the matrix form of $\exp(iL_z\alpha)$ and $\exp(iL_y\alpha)$ operators. With respect to Eq. (14) and Eq. (21) it can be concluded that

$$\exp(i\alpha L_z) = \mathrm{diag}\left(\mathcal{R}_z^1(\alpha), \mathcal{R}_z^2(\alpha)), \ldots, \mathcal{R}_z^n(\alpha)\right) \tag{25}$$

where

$$\mathcal{R}_z^n(\alpha) = \exp(i\alpha \times \mathrm{diag}(-n, -n+1, \ldots, n-1, n)) \tag{26}$$

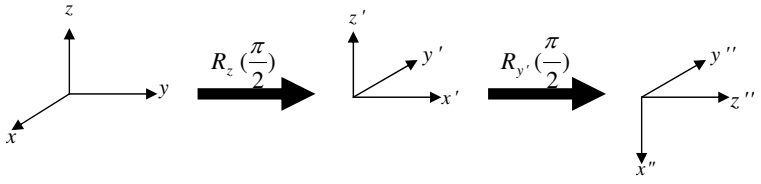

Figure 2: Changing of rotation about y-axis to rotation about z-axis.

To calculate matrix form of $\exp(iL_y\alpha)$, at first we change rotation about y-axis to rotation about z-axis. With respect to Figure 2 we can write

$$\exp(i\alpha L_y) = \exp\left(iL_z\frac{\pi}{2}\right)\exp\left(iL_y\frac{\pi}{2}\right)\exp\left(iL_z\alpha\right)\exp\left(iL_y\frac{\pi}{2}\right)\exp\left(iL_z\frac{\pi}{2}\right) \tag{27}$$

By use of Eq. (27) we must only calculate $\exp(iL_y\frac{\pi}{2})$. For $n=1$ by use of Eq. (17)

$$L_y^{(n=1)} = \frac{\sqrt{2}}{2i}\begin{bmatrix} 0 & -1 & 0 \\ 1 & 0 & -1 \\ 0 & 1 & 0 \end{bmatrix} \tag{28}$$

By use of the peroperty

$$\left(L_y^{(n=1)}\right)^3 = L_y^{(n=1)} \tag{29}$$

And Taylor series can be shown that

$$\mathcal{R}_y^{(n=1)} = \exp(iL_y\alpha) = \begin{bmatrix} \frac{1}{2}(1+\cos\alpha) & \frac{1}{\sqrt{2}}\sin\alpha & \frac{1}{2}(1-\cos\alpha) \\ -\frac{1}{\sqrt{2}}\sin\alpha & \cos\alpha & \frac{1}{\sqrt{2}}\sin\alpha \\ \frac{1}{2}(1-\cos\alpha) & -\frac{1}{\sqrt{2}}\sin\alpha & \frac{1}{2}(1+\cos\alpha) \end{bmatrix} \tag{30}$$

For other n by the use of recursive relation [9]

$$(\mathcal{R}_y^n(\alpha))_{m'm} = \sqrt{\frac{n-m'}{n-m}}\left(\mathcal{R}_y^{n-\frac{1}{2}}(\alpha)\right)_{m'+\frac{1}{2},m+\frac{1}{2}}\cos\left(\frac{\alpha}{2}\right) - \sqrt{\frac{n+m'}{n-m}}\left(\mathcal{R}_y^{n-\frac{1}{2}}(\alpha)\right)_{m'-\frac{1}{2},m+\frac{1}{2}}\sin\left(\frac{\alpha}{2}\right) \tag{31}$$

We can calculate $\mathcal{R}_y^n(\alpha)$. Also for the calculation of $\exp(-iL_y\frac{\pi}{2})$ we can use

$$\mathcal{R}_y^n(-\alpha) = \mathcal{R}_y^n(\alpha)^T \tag{32}$$

where A^T denotes the transpose of A matrix. Therefore we can calculate $\mathcal{R}_y(\alpha)$ easily.

2.6. Calculation of Finite Rotation Operator S

In the same manner we must calculate only the matrix form of $\exp(i\alpha S_z)$ and $\exp(i\alpha S_y)$ operators. In this case by Eq. (11) and the use of Taylor series, we can conclude that:

$$\exp(i\alpha S_z) = \begin{bmatrix} \cos\alpha & \sin\alpha & 0 \\ -\sin\alpha & \cos\alpha & 0 \\ 0 & 0 & 1 \end{bmatrix},\ \exp(i\alpha S_y) = \begin{bmatrix} \cos\alpha & 0 & -\sin\alpha \\ 0 & 1 & 0 \\ \sin\alpha & 0 & \cos\alpha \end{bmatrix} \tag{33}$$

3. T-MATRIX FORMULATION

The formulation of the T-matrix algorithm is based upon the spherical wave expansion of electromagnetic field. These functions composed of the field vectors $\vec{M}$ and $\vec{N}$ are arranged into a vector $\vec{\vec{\Psi}}$ of varying spherical waveform expansions. In the first case, the vectors are three-dimensional, one dimension for each direction in space. For $\vec{\vec{\Psi}}$ however, the vectors have a dimension of $2n_{\max}(n_{\max}+2)$, where the parameter, $n_{\max}$, is the maximum order of spherical Bessel function. A vector of spherical wave functions can be written as

$$\vec{\vec{\Psi}} = \left[\vec{M}_{(-1)(1)}\vec{M}_{01}\ldots\vec{M}_{mn}\vec{N}_{(-1)(1)}\vec{N}_{01}\ldots\vec{N}_{mn}\right] \tag{34}$$

where

$$\vec{M}_{mn}(kr,\theta,\phi) = \frac{1}{\sqrt{n(n+1)}}\nabla\times[\vec{r}\psi] \quad \text{and} \quad \vec{N}_{mn}(kr,\theta,\phi) = \frac{1}{k}\nabla\times\vec{M}_{mn}(kr,\theta,\phi) \tag{35}$$

$$\psi_{mn} = h_n^{(1)}(kr)Y_{mn}(\theta,\phi) \qquad \text{and} \qquad Rg\psi_{mn} = j_n(kr)Y_{mn}(\theta,\phi) \tag{36}$$

In the above equations, j_n and $h_n^{(1)}$ are the spherical Bessel and Henkel functions of order, n, and Y_{mn} is the associated Legendre polynomial [10].

A generalized incident field, $\vec{E}_{\text{inc}}$ may be decomposed into spherical wave functions as in

$$\vec{E}_{\text{inc}} = Rg\vec{\bar{\Psi}}\overline{\mathbf{a}_l} \tag{37}$$

Similarly, the scattered electric field can be expressed in terms of the scattered field coefficients, $\overline{a_s}$, such that

$$\vec{E}_s = \vec{\bar{\Psi}}\overline{\mathbf{a}_s} \tag{38}$$

The T-matrix (or transition matrix) is then defined by the relation

$$\overline{\mathbf{a}_s} = \overline{\overline{\mathbf{T}}}\overline{\mathbf{a}_l} \tag{39}$$

4. ADDITION THEOREM FOR SPHERICAL VECTOR WAVE FUNCTIONS

Now we can use the rotation operator Eq. (2) to rotate the spherical vector wave functions Eq. (35). Note that in this case the vector field is rotated rather than coordinate system. Hence, Eq. (2) is written as follows

$$\mathcal{R}(\alpha,\beta,\gamma) = \mathcal{R}_z(-\alpha)\mathcal{R}_y(-\beta)\mathcal{R}_z(-\gamma) \tag{40}$$

If we define total angular momentum operator as

$$\vec{L} = L_x\hat{a}_x + L_y\hat{a}_y + L_z\hat{a}_z \tag{41}$$

In spherical coordinate we will have

$$\vec{L} = i\left[\hat{\theta}\frac{1}{\sin\theta}\frac{\partial}{\partial\phi} - \hat{\phi}\frac{\partial}{\partial\theta}\right] \tag{42}$$

So we can rewrite Eq. (35) as

$$\vec{M}_{mn}(kr,\theta,\phi) = -i\frac{j_n(kr)}{\sqrt{n(n+1)}}\vec{L}Y_{mn}(\theta,\phi) \tag{43}$$

To expand the rotated spherical wave function by fixed spherical wave functions, we must solve the below equation:

$$\exp(-iJ_z\alpha)\exp(-iJ_y\beta)\exp(-iJ_z\gamma)\vec{M}_{\mu n} = \Sigma_{m=-n}^{n} c_{mn}\vec{M}_{mn} \quad \mu = -n,\ldots,n \tag{44}$$

where

$$J_i = L_i + S_i \quad i = x,y,z \tag{45}$$

Also we can assert that

$$\exp(-iJ_z\alpha)\exp(-iJ_y\beta)\exp(-iJ_z\gamma)\vec{N}_{\mu n} = \Sigma_{m=-n}^{n} c_{mn}\vec{N}_{mn} \quad \mu = -n,\ldots,n \tag{46}$$

Also we can assert that

$$\exp(-iJ_z\alpha)\exp(-iJ_y\beta)\exp(-iJ_z\gamma)\vec{N}_{\mu n} = \Sigma_{m=-n}^{n} c_{mn}\vec{N}_{mn} \quad \mu = -n,\ldots,n \tag{47}$$

An important point to the proof of this assertion is the following relation

$$J_i\nabla\times = \nabla\times J_i, \qquad i = x,y,z \tag{48}$$

So the following relation can be concluded:

$$\exp(-iJ_i\alpha)\nabla\times = \nabla\times\exp(-iJ_i\alpha), \quad i = x,y,z \tag{49}$$

Employing curl operation for Eq. (46), Eq. (44) can and using Eq. (49), we have

$$\exp(-iJ_z\alpha)\exp(-iJ_y\beta)\exp(-iJ_z\gamma)\nabla\times\vec{M}_{\mu n} = \Sigma_{m=-n}^{n} c_{mn}\nabla\times\vec{M}_{mn} \quad \mu = -n,\ldots,n \tag{50}$$

With respect to Eq. (35), the assertion is proved.

By solving Eq. (44) for different values of n, $\overline{\overline{\mathbf{c}}}^{n}$ whose dimension is $(2n+1)\times(2n+1)$, is calculated, then

$$\overline{\overline{\mathbf{c}}} = \mathrm{diag}\left(\overline{\overline{\mathbf{c}}}^{(n=1)}, \overline{\overline{\mathbf{c}}}^{(n=2)}, \overline{\overline{\mathbf{c}}}^{(n=3)}, \ldots, \overline{\overline{\mathbf{c}}}^{(n=n_{\max})}\right) \tag{51}$$

where $\overline{\overline{\mathbf{c}}}$ is the coefficient matrix used in Eq. (44).

Thus relationship between the rotated spherical wave functions and fixed spherical wave functions can be shown as below

$$\left[\vec{M}_{-1,1},\ldots,\vec{M}_{mn},\vec{N}_{-1,1},\ldots,\vec{M}_{mn}\right]_{\text{rotated}} = \left[\vec{M}_{-1,1},\ldots,\vec{M}_{mn},\vec{N}_{-1,1},\ldots,\vec{M}_{mn}\right]_{\text{unrotated}} \begin{bmatrix} \overline{\overline{\mathbf{c}}} & 0 \\ 0 & \overline{\overline{\mathbf{c}}} \end{bmatrix} \tag{52}$$

By taking into cosideraition Eq. (39) and Eq. (52), T-matrix in the new coordinate system can be written as follows:

$$\overline{\overline{\mathbf{T}}}_{\text{new}} = \begin{bmatrix} \overline{\overline{\mathbf{c}}} & 0 \\ 0 & \overline{\overline{\mathbf{c}}} \end{bmatrix}^{-1} \overline{\overline{\mathbf{T}}} = \begin{bmatrix} \overline{\overline{\mathbf{c}}} & 0 \\ 0 & \overline{\overline{\mathbf{c}}} \end{bmatrix} \tag{53}$$

5. CONCLUSION

In this paper we derived the rotational addition theorems for the vector spherical wave by applaying rotation operator on vector spherical wave. By use of this theorem, the relation between two different coordinate system is formulated. The advantage of this method is that the cofficient of expansion can be calculated recursively.

REFERENCES

1. Waterman, P. C., "Symmetry, unitarity, and geometry in electromagnetic scattering," *Phys. Rev. D*, Vol. 3, 825–839, 1971.
2. Mishchenko, M. I., L. D. Travis, and A. A. Lacis, *Scattering, Absorption, and Emission of Light by Small Particles*, Cambridge University Press, Cambridge, 2002.
3. Tsang, L., J. A. Kong, and K. H. Ding, *Scattering of Electromagnetic Waves*, Advanced Topics, Wiley, New York, 2001.
4. Mackowski, D. W. and M. I. Mishchenko, "Calculation of the T matrix and the scattering matrix for ensembles of spheres," *J. Opt. Soc. Am*, Vol. 13, 2266–2278, 1996.
5. Tsang, L. T., J. A. Kong, and R. T Shin, "Radiative transfer theory for active remote sensing of a layer of nonspherical particles," *Radio Science*, Vol. 19, No. 2, 629–642, 1984.
6. Barber, P. W. and S. C. Hill, *Light Scattering by Particles: Computational Methods*, World Scientific, Singapore, 1990.
7. Friedman, B. and J. Russek, "Addition theorems for spherical waves," *Quart. Appl. Math.*, Vol. 12, 130–23, 1954.
8. Sakurai, J. J., *Modern Quantum Mechanics*, Addison-Wesley, New York, 1994.
9. Edmonds, A. R., *Angular Momentum in Quantum Mechanics*, Princeton University Press, Princeton, 1957.
10. Abramowitz, M. and I. A. Stegun (Eds.), *Handbook of Mathematical Functions*, Dover Publications, New York, 1970.

The Nonlinear Absorption of a Strong Electromagnetic Wave by Confined Electrons in Rectangular Quantum Wires

N. Q. Bau and H. D. Trien
Faculty of Physics, Hanoi University of Science, Vietnam National University, Vietnam

Abstract— Analytic expressions for the nonlinear absorption coefficient of a strong electromagnetic wave by confined electrons in rectangular quantum wires with infinite potential are calculated by using the quantum kinetic equation for electrons in two cases: electron-optical phonon scattering and electron-acoustic phonon scattering. The dependence of the nonlinear absorption coefficient on the intensity E_0 and frequency Ω of the external strong electromagnetic wave, the temperature T of the system and size L of wires are obtained. The analytic expressions are numerically calculated and discussed for GaAs/GaAsAl rectangular quantum wires. The results are compared with those for the normal bulk semiconductors and quantum well to show the difference.

1. INTRODUCTION

It is well known that in one dimensional systems, the motion of electrons is restricted in two dimensions, so that they can flow freely in one dimension. The confinement of electron in these systems has changed the electron mobility remarkably. This has resulted in a number of new phenomena, which concern a reduction of sample dimensions. These effects differ from those in bulk semiconductors, for example, electron-phonon interaction and scattering rates [1, 2] and dc electrical conductivity [3, 4]. The problem of optical properties in bulk semiconductors, as well as low dimensional systems has also been investigated [5–10]. However, in those articles, the linear absorption of a weak electromagnetic wave has been considered in normal bulk semiconductors [5], in two dimensional systems [6, 7] and in quantum wire [8]; the nonlinear absorption of a strong electromagnetic wave (EMW) has been considered in the normal bulk semiconductors [9] and quantum wells [10], but in cylindrical quantum wires, the nonlinear absorption of a strong electromagnetic wave (EMW) still opens for studying. In this paper, we use the quantum kinetic equation for electrons to theoretically study the nonlinear absorption coefficient of a strong EMW by confined electrons in rectangular quantum wires (RQW). The problem is considered in two cases: electron-optical phonon scattering and electron-acoustic phonon scattering. Numerical calculations are carried out with a specific GaAs/GaAsAl quantum wires.

2. THE NONLINEAR ABSORPTION COEFFICIENT OF A STRONG EMW IN A RQW

In our model, we consider a wire of GaAs with rectangular cross section ($Lx \times Ly$) and length Lz, embedded in GaAlAs. The carriers (electron gas) are assumed to be confined by an infinite potential in the (x, y) plane and are free in the z direction in Cartesian coordinates (x, y, z). The laser field propagates along the x direction. In this case, the state and the electron energy spectra have the form [11]

$$|n, \ell, \vec{p}\rangle = \frac{2e^{ip_z z}}{\sqrt{L_z L_x L_y}} \sin\left(\frac{\pi n x}{L_x}\right) \sin\left(\frac{\pi \ell y}{L_y}\right);\ \varepsilon_{n,\ell}(\vec{p}) = \frac{p_z^2}{2m} + \frac{\pi^2}{2m}\left(\frac{n^2}{L_x^2} + \frac{\ell^2}{L_y^2}\right) \tag{1}$$

where n and ℓ (n, $\ell = 1, 2, 3, \ldots$) denote the quantization of the energy spectrum in the x and y direction, $\vec{p} = (0, 0, p_z)$ is the electron wave vector (along the wire's z axis), m is the effective mass of electron (in this paper, we select $\hbar = 1$).

Hamiltonian of the electron-phonon system in a rectangular quantum wire in the presence of a laser field $\vec{E}(t) = \vec{E}_0 \sin(\Omega t)$ can be written as

$$\begin{aligned} H(t) \ &= \ \sum_{n,l,\vec{p}} \varepsilon_{n,l}\left(\vec{p} - \frac{e}{c}\vec{A}(t)\right) a^+_{n,l,\vec{p}}\, a_{n,l,\vec{p}} + \sum_{\vec{q}} \omega_{\vec{q}}\, b^+_{\vec{q}} b_{\vec{q}} \\ &+ \sum_{n,l,\acute{n},\acute{l},\vec{p},\vec{q}} C_{\vec{q}} I_{n,l,\acute{n},\acute{l}}(\vec{q}) a^+_{n,l,\vec{p}+\vec{q}}\, a_{\acute{n},\acute{l},\vec{p}}\, (b_{\vec{q}} + b^+_{-\vec{q}}) \end{aligned} \tag{2}$$

where e is the electron charge, c is the light velocity, $\vec{A}(t) = \frac{c}{\Omega}\vec{E}_0\cos(\Omega t)$ is the vector potential, $\vec{E}_0$ and Ω is the intensity and frequency of EMW, $a^+_{n,\ell,\vec{p}}$ ($a_{n,\ell,\vec{p}}$) is the creation (annihilation) operator of an electron, $b^+_{\vec{q}}$ ($b_{\vec{q}}$) is the creation (annihilation) operator of an phonon for state have wave vector $\vec{q}$, $C_{\vec{q}}$ is the electron-phonon interaction constants. $I_{n,l,\acute{n},\acute{l}}(\vec{q})$ is the electron form factor, it is written as [12]

$$\begin{aligned} I_{n,l,\acute{n},\acute{l}}(\vec{q}) &= \frac{32\pi^4(q_xL_xn\acute{n})^2(1-(-1)^{n+\acute{n}}\cos(q_xL_x))}{[(q_xL_x)^4-2\pi^2(q_xL_x)^2(n^2+\acute{n}^2)+\pi^4(n^2-\acute{n}^2)^2]^2} \\ &\times\frac{32\pi^4(q_yL_y\ell\acute{\ell})^2(1-(-1)^{\ell+\acute{\ell}}\cos(q_yL_y))}{[(q_yL_y)^4-2\pi^2(q_yL_y)^2(\ell^2+\acute{\ell}^2)+\pi^4(\ell^2-\acute{\ell}^2)^2]^2} \end{aligned} \tag{3}$$

The carrier current density $\vec{j}(t)$ and the nonlinear absorption coefficient of a strong electromagnetic wave α take the form [9, 10, 13]

$$\vec{j}(t) = \frac{e}{m}\sum_{n,\ell,\vec{p}}\left(\vec{p}-\frac{e}{c}\vec{A}(t)\right)n_{n,\ell,\vec{p}}(t);\ \alpha = \frac{8\pi}{c\sqrt{\chi_\infty}E_0^2}\left\langle\vec{j}(t)\vec{E}_0\sin\Omega t\right\rangle_t \tag{4}$$

where $n_{n,\ell,\vec{p}}(t)$ is electron distribution function, $\langle X\rangle_t$ means the usual thermodynamic average of X at moment t, χ_∞ is the high-frequency dielectric constants.

In order to establish analytical expressions for the nonlinear absorption coefficient of a strong EMW by confined electrons in RQW, we use the quantum kinetic equation for particle number operator of electron $n_{n,\ell,\vec{p}}(t) = \langle a^+_{n,\ell,\vec{p}}a_{n,\ell,\vec{p}}\rangle_t$

$$i\frac{\partial n_{n,\ell,\vec{p}}(t)}{\partial t} = \langle[a^+_{n,\ell,\vec{p}}a_{n,\ell,\vec{p}},H]\rangle_t \tag{5}$$

From Eq. (5), using Hamiltonian in Eq. (2) and realizing calculations, we obtain quantum kinetic equation for confined electrons in RQW. Using the first order tautology approximation method (The approximation is applied for a similar exercise in bulk semiconductors [9, 13] and quantum wells [10]) to solve this equation, we obtain the expression of electron distribution function $n_{n,\ell,\vec{p}}(t)$.

$$\begin{aligned} n_{n,\ell,\vec{p}}(t) &= -\sum_{\vec{q},n',\ell'}|C_{\vec{q}}|^2|I_{n,\ell,n',\ell'}|^2\sum_{k,l=-\infty}^{\infty}J_k\left(\frac{e\vec{E}_0,\vec{q}}{m\Omega^2}\right)J_{k+l}\left(\frac{e\vec{E}_0,\vec{q}}{m\Omega^2}\right)\frac{1}{l\Omega}e^{-il\Omega t} \\ &\times\left\{-\frac{\bar{n}_{n,\ell,\vec{p}}(N_{\vec{q}}+1)-\bar{n}_{n',\ell',\vec{p}+\vec{q}}N_{\vec{q}}}{\varepsilon_{n',\ell',\vec{p}+\vec{q}}-\varepsilon_{n,\ell,\vec{p}}+\omega_{\vec{q}}-k\Omega+i\delta}-\frac{\bar{n}_{n,\ell,\vec{p}}N_{\vec{q}}-\bar{n}_{n',\ell',\vec{p}+\vec{q}}(N_{\vec{q}}+1)}{\varepsilon_{n',\ell',\vec{p}+\vec{q}}-\varepsilon_{n,\ell,\vec{p}}-\omega_{\vec{q}}-k\Omega+i\delta}\right. \\ &\left.+\frac{\bar{n}_{n',\ell',\vec{p}-\vec{q}}(N_{\vec{q}}+1)-\bar{n}_{n,\ell,\vec{p}}N_{\vec{q}}}{\varepsilon_{n,\ell,\vec{p}}-\varepsilon_{n',\ell',\vec{p}-\vec{q}}+\omega_{\vec{q}}-k\Omega+i\delta}+\frac{\bar{n}_{n',\ell',\vec{p}-\vec{q}}N_{\vec{q}}-\bar{n}_{n,\ell,\vec{p}}(N_{\vec{q}}+1)}{\varepsilon_{n,\ell,\vec{p}}-\varepsilon_{n',\ell',\vec{p}-\vec{q}}-\omega_{\vec{q}}-k\Omega+i\delta}\right\} \end{aligned} \tag{6}$$

where $N_{\vec{q}}$ ($\bar{n}_{n,\vec{p}}$) is the time independent component of the phonon (electron) distribution function, $J_k(x)$ is Bessel function, the quantity δ is infinitesimal and appears due to the assumption of an adiabatic interaction of the electromagnetic wave. We insert the expression of $n_{n,\ell,\vec{p}}(t)$ into the expression of $\vec{j}(t)$ and then insert the expression of $\vec{j}(t)$ into the expression of α in Eq. (4). Using properties of Bessel function and realizing calculations, we obtain the nonlinear absorption coefficient of a strong EMW by confined electrons in RQW

$$\begin{aligned} \alpha &= \frac{8\pi^2\Omega}{c\sqrt{\chi_\infty}E_0^2}\sum_{n,\ell,n',\ell'}|I_{n,\ell,n',\ell'}|^2\sum_{\vec{q},\vec{p}}|C_{\vec{q}}|^2N_{\vec{q}}\sum_{k=-\infty}^{\infty}\left[\bar{n}_{n,\ell,\vec{p}}-\bar{n}_{n',\ell',\vec{p}+\vec{q}}\right] \\ &\times kJ_k^2\left(\frac{eE_0\vec{q}}{m\Omega^2}\right)\delta(\varepsilon_{n',\ell',\vec{p}+\vec{q}}-\varepsilon_{n,\ell,\vec{p}}+\omega_{\vec{q}}-k\Omega) \end{aligned} \tag{7}$$

where $\delta(x)$ is Dirac delta function.

In the following, we study the problem with different electron-phonon scattering mechanisms. We only consider the absorption close to its threshold because in the rest case (the absorption

far away from its threshold) α is very smaller. In the case, the condition $|k\Omega - \omega_0| \ll \bar{\varepsilon}$ must be satisfied [9]. We restrict the problem to the case of one photon absorption and consider the electron gas to be non-degenerate:

$$\bar{n}_{n,\ell,\vec{p}} = n_0^* \exp\left(-\frac{\varepsilon_{n,\ell,\vec{p}}}{k_b T}\right), \text{ with } n_0^* = \frac{n_0 (e\pi)^{\frac{3}{2}}}{V(m_0 k_b T)^{\frac{3}{2}}} \tag{8}$$

where, V is the normalization volume, n_0 is the electron density in RQW, m_0 is the mass of free electron, k_b is Boltzmann constant.

2.1. Electron-optical Phonon Scattering

In this case, $\omega_{\vec{q}} \equiv \omega_0$ is the frequency of the optical phonon in the equilibrium state. The electron-optical phonon interaction constants can be taken as [6–8] $|C_{\vec{q}}|^2 \equiv |C_{\vec{q}}^{op}|^2 = e^2\omega_0(1/\chi_\infty - 1/\chi_0)/2\epsilon_0 q^2 V$, here V is the volume, ϵ_0 is the permittivity of free space, χ_∞ and χ_0 are the high and low-frequency dielectric constants, respectively. Inserting $C_{\vec{q}}$ into Eq. (7) and using Bessel function, Fermi-Dirac distribution function for electron and energy spectrum of electron in RQW, we obtain the explicit expression of α in RQW for the case electron-optical phonon scattering

$$\begin{aligned}\alpha \;=\; & \frac{\sqrt{2\pi}e^4 n_0^* (k_b T)^{3/2}}{4c\epsilon_0\sqrt{m\chi_\infty}\Omega^3 V}\left(\frac{1}{\chi_\infty} - \frac{1}{\chi_0}\right)\sum_{n\ell,\acute{n},\acute{\ell}} |I_{n\ell,\acute{n},\acute{\ell}}|^2 \left[\exp\left\{\frac{1}{k_b T}(\omega_0 - \Omega)\right\} - 1\right] \\ & \times \exp\left\{\frac{1}{k_b T}\frac{\pi^2}{2m}\left(\frac{\acute{n}^2}{L_x^2} + \frac{\acute{\ell}^2}{L_y^2}\right)\right\}\left[1 + \frac{3e^2 E_0^2 k_b T}{8m\Omega^4}\left(1 + \frac{B}{2k_b T}\right)\right]\end{aligned} \tag{9}$$

where $B = \pi^2[(\acute{n}^2 - n^2)/L_x^2 + (\acute{\ell}^2 - \ell^2)/L_y^2]/2m + \omega_0 - \Omega$.

2.2. Electron-acoustic Phonon Scattering

In the case, $\omega_{\vec{q}} \ll \Omega$ ($\omega_{\vec{q}}$ is the frequency of acoustic phonons), so we let it pass. The electron-acoustic phonon interaction constants can be taken as [6–8, 10] $|C_{\vec{q}}|^2 \equiv |C_{\vec{q}}^{ac}|^2 = \xi^2 q/2\rho\upsilon_s V$, here V, ρ, υ_s, and ξ are the volume, the density, the acoustic velocity and the deformation potential constant, respectively. In this case, we obtain the explicit expression of α in RQW for the case electron-acoustic phonon scattering

$$\begin{aligned}\alpha \;=\; & \frac{\sqrt{2m\pi}e^2 n_0^* \xi^2 (k_b T)^{5/2}}{4c\sqrt{\chi_\infty}\rho\upsilon_s^2\Omega^3 V}\sum_{n,\ell,n',\ell'} |I_{n,\ell,n',\ell'}|^2 \exp\left\{\frac{1}{k_b T}\frac{\pi^2}{2m}\left(\frac{\acute{n}^2}{L_x^2} + \frac{\acute{\ell}^2}{L_y^2}\right)\right\} \\ & \times \left[\exp\left\{\frac{\Omega}{k_b T}\right\} - 1\right]\left[1 + \frac{D}{2k_b T}\left[1 + \frac{3e^2 E_0^2 (k_b T)^2}{4m\Omega^4 D}\left(\frac{D^2}{4(k_b T)^2} + \frac{3D}{4k_b T} + 3\right)\right]\right]\end{aligned} \tag{10}$$

where $D = \pi^2[(\acute{n}^2 - n^2)/L_x^2 + (\acute{\ell}^2 - \ell^2)/L_y^2] - \Omega$.

From analytic expressions of the nonlinear absorption coefficient of a strong EMW by confined electrons in RQWs with infinite potential (Eq. (9) and Eq. (10)), we see that when the term in proportion to quadratic intensity of EMW (E_0^2) (in the expressions of the nonlinear absorption coefficient of a strong EMW) tend toward zero, the nonlinear result will turn back to the linear result.

3. NUMERICAL RESULTS AND DISCUSSIONS

In order to clarify the results that have been obtained, in this section, we numerically calculate the nonlinear absorption coefficient of a strong EMW for a GaAs/GaAsAl RQW. The nonlinear absorption coefficient is considered as a function of the intensity E_0 and energy of strong EMW, the temperature T of the system , and the parameters of RQW. The parameters used in the numerical calculations [5, 11] are $\xi = 13.5\,\text{eV}$, $\rho = 5.32\,\text{gcm}^{-3}$, $\upsilon_s = 5378\,\text{ms}^{-1}$, $\epsilon_0 = 12.5$, $\chi_\infty = 10.9$, $\chi_0 = 13.1$, $m = 0.066m_0$, m_0 being the mass of free electron, $\hbar\omega_0 = 36.25\,\text{meV}$, $k_b = 1.3807 \times 10^{-23}\,\text{J/K}$, $n_0 = 10^{23}\,\text{m}^{-3}$, $e = 1.60219 \times 10^{-19}\,\text{C}$, $\hbar = 1.05459 \times 10^{-34}\,\text{J·s}$, $q_x = q_y = 2 \times 10^5\,\text{m}^{-1}$.

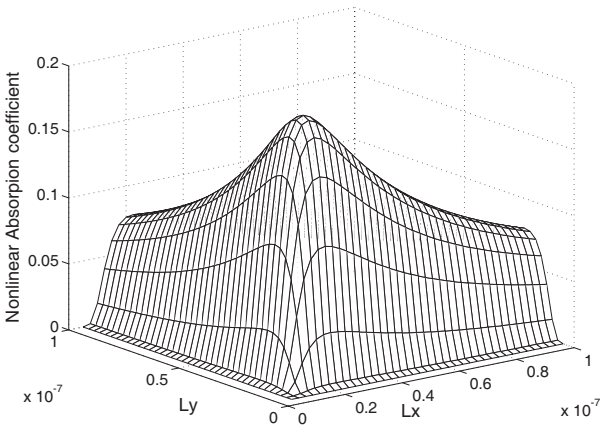

Figure 1: Dependence of α on L_y and L_x (electron-acoustic phonon scattering).

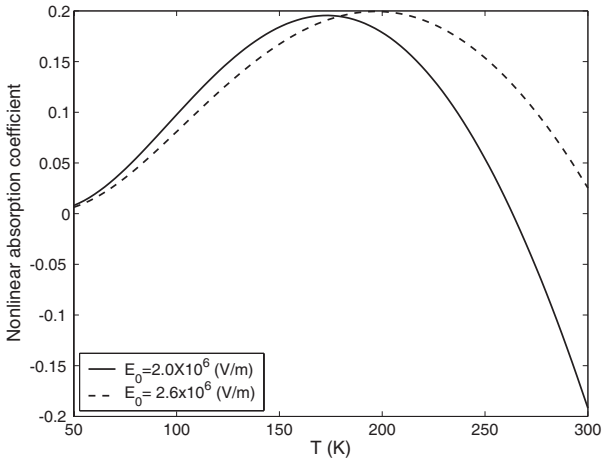

Figure 2: Dependence of α on T (electron-acoustic phonon scattering).

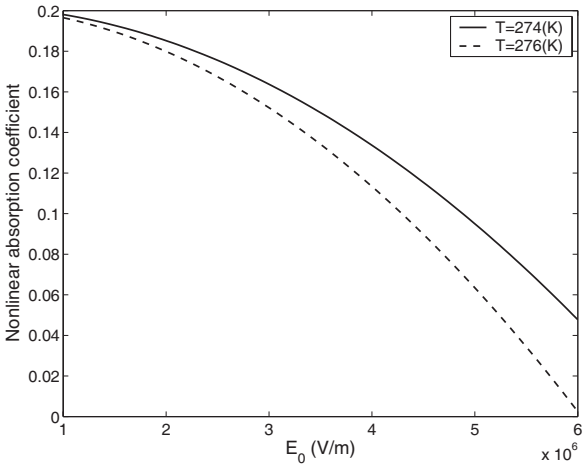

Figure 3: Dependence of α on E_0 (electron-acoustic phonon scattering).

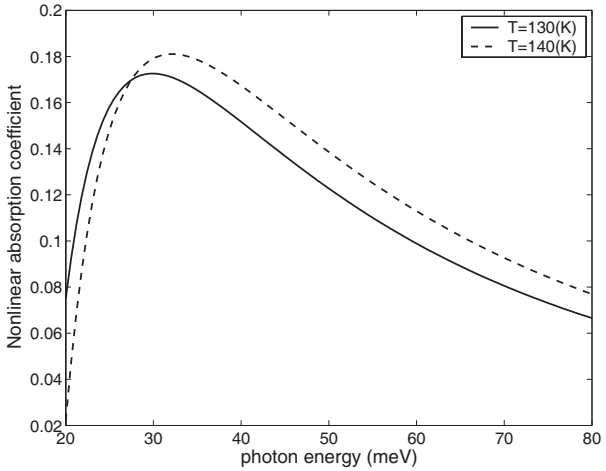

Figure 4: Dependence of α on $\hbar\Omega$ (electron-acoustic phonon scattering).

3.1. Electron-acoustic Phonon Scattering

Figure 1 shows the dependence of α of a strong EMW on the size L (L_y and L_x) of wire. It can be seen from this figure that α depends strongly and nonlinear on size L of wire. When L decreases, the nonlinear absorption coefficient will increases until its maximum at L_x and $L_y \sim 24\,\text{nm}$ then started to decrease.

Figure 2 presents the dependence of the nonlinear absorption coefficient α on the temperature T of the system at different values of the intensity E_0 of the external strong electromagnetic wave. It can be seen from this figure that the nonlinear absorption coefficient α has depends strongly and nonlinearly on the temperature T and it has the same maximum value but with different values of T. For example, at $E_0 = 2.6 \times 10^6\,\text{V/m}$ and $E_0 = 2 \times 10^6\,\text{V/m}$, the peaks correspond to $T \sim 170\,\text{K}$ and $190\,\text{K}$, respectively, this fact was not seen in bulk semiconductors [9] as well as quantum wells [10], but it fit the case of linear absorption [8].

Figure 3 shows the dependence of α on intensity E_0 of EMW. It can be seen from this figure that α depends strongly and nonlinearly on T and E_0. Like in quantum well, the nonlinear absorption coefficient in quantum wire α increases when the intensity E_0 decreases. But different from normal bulk semiconductors [9] and quantum well [10], values α in RQW is bigger.

Figure 4 presents the dependence of the nonlinear absorption coefficient α on the EMW energy at different values of the temperature T. It is seen that different from the bulk semiconductors [9] and the quantum well [10], the nonlinear absorption coefficient α in quantum wire has the maximum values (peaks). It is demonstrated that α has changed strongly by the confinement. of electron in RQW. The EMW energy at which α has a maximum are changed as the radius R of wire is varied.

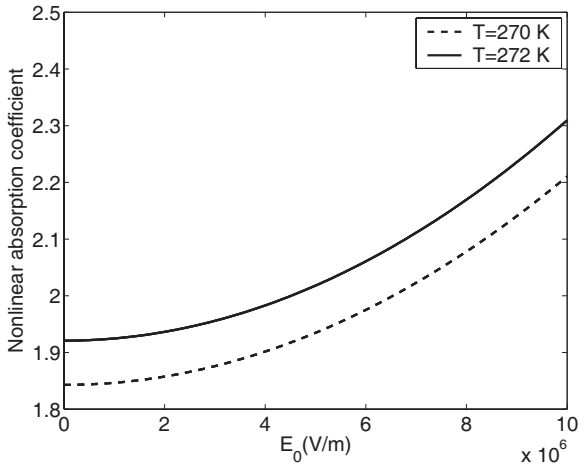

Figure 5: Dependence of α on E_0 (electron-optical phonon scattering).

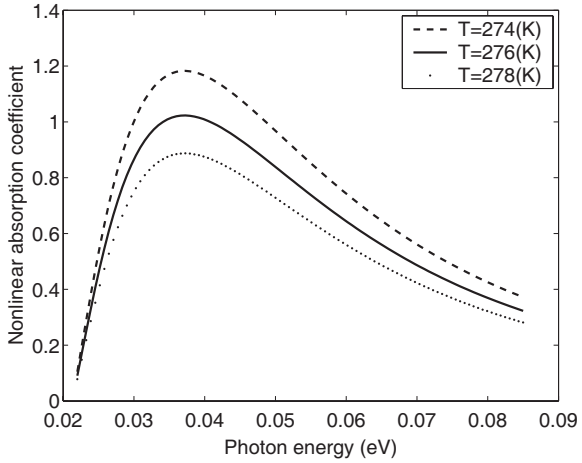

Figure 6: Dependence of α on $\hbar\Omega$ (electron-optical phonon scattering).

3.2. Electron-optical Phonon Scattering

Figure 5 presents the dependence of α on the intensity E_0 of EMW in the case electron-optical phonon scattering. Different from the case electron-acoustic phonon scattering, in this case, α increases when the intensity E_0 of EMW increases.

Figure 6 presents the dependence of α on the EMW energy at different values of the radius of wire. It is seen that α has the same maximum values (peaks) at $\Omega \equiv \omega$. The EMW energy at which α has a maximum are not changed as the radius of wire is varied. This means that α depends strongly on the frequency Ω of the EMW and resonance conditions are determined by the EMW energy.

4. CONCLUSION

In the present paper, we have obtained analytical expressions for the nonlinear absorption of a strong EMW by confined electrons in RQWs for both mechanisms of electron-phonon scattering. The dependence of α on the intensity E_0 and frequency Ω of the external strong EMW, the temperature T of the system and size L of wires is complex and different compared to those obtained in normal bulk semiconductors [9] and quantum well [10]. From the analytic results, we see that when the term in proportion to quadratic intensity of EMW (E_0^2) (in the expressions of the nonlinear absorption coefficient of a strong EMW) tend toward zero, the nonlinear result will turn back to the linear result.

The numerical results obtained for a GaAs/GaAsAl RQW show that α depends strongly and nonlinearly on the intensity E_0 and frequency Ω of the external strong EMW, the temperature T of the system and size L_y of wires. This dependence has differences in comparison with that in normal bulk semiconductors [9] and two dimensional systems [10]. The nonlinear absorption coefficient in RQW also is bigger. The results show a geometrical dependence of the nonlinear absorption coefficient due to the confinement of electrons in one dimensional systems.

ACKNOWLEDGMENT

This work is completed with financial support from the NAFOSTED (103.01.18.09) and QG.09.02.

REFERENCES

1. Mori, N. and T. Ando, *Phys. Rev. B*, Vol. 40, 6175, 1989.
2. Pozela, J. and V. Juciene, *Sov. Phys. Tech. Semicond.*, Vol. 29 459, 1995.
3. Vasilopoulos, P., M. Charbonneau, and C. N. Van Vlier, *Phys. Rev. B*, Vol. 35, 1334, 1987.
4. Suzuki, A., *Phys. Rev. B*, Vol. 45, 6731, 1992.
5. Shmelev, G. M., L. A. Chaikovskii, and N. Q. Bau, *Soc. Phys. Tech. Semicond.*, Vol. 12, 1932, 1978.
6. Bau, N. Q. and T. C. Phong, *J. Phys. Soc. Japan*, Vol. 67, 3875, 1998.
7. Bau, N. Q., N. V. Nhan, and T. C. Phong, *J. Korean. Phys. Soc.*, Vol. 41, 149, 2002.
8. Bau, N. Q., L. Dinh, and T. C. Phong, *J. Korean. Phys. Soc.*, Vol. 51, 1325, 2007.

9. Pavlovich, V. V. and E. M. Epshtein, *Sov. Phys. Solid State*, Vol. 19, 1760, 1977.
10. Quang, B. N., H. M. Do, and N. B. Nguyen, *J. Korean. Phys. Soc.*, Vol. 54, 765, 2009.
11. Phong, T. C., L. Dinh, N. Q. Bau, and D. Q. Vuong, *J. Korean. Phys. Soc.*, Vol. 49, 2367, 2006.
12. Mickevicius, R. and V. Mitin, *Phys. Rev. B*, Vol. 48, 17194, 1993.
13. Malevich, V. L. and E. M. Epstein, *Soc. Quantum Electronic*, Vol. 1, 1468, 1974.

Theory of the Acoustomagnetoelectric Effect in a Superlattice

N. Q. Bau and N. V. Hieu
Faculty of Physics, Hanoi University of Science, Vietnam National University, Hanoi, Vietnam

Abstract— The acoustomagnetoelectric (AME) effect in a superlattice (SL) induced by the interaction of acoustic phonons with the conducting electrons is calculated for an acoustic wave whose wavelength $\lambda = 2\pi/q$ is smaller than the mean free path l of the electrons and hypersound in the region $ql \gg 1$ (where q is the acoustic wave number). The analytical expression for the AME current j^{AME} is obtained by using the classical Bonltzmann kinetic equation in the case of relaxation time of momentum τ constant approximation. The result indicates that the existense of j^{AME} in a SL is attributed to the finite gap band, and the periodicity of the electron spectrum along the SL axis. Numerical calculations have been done and the result is analysed for the GaAs/AlAs SL. In the limit case at $\omega_q = 10^{13}\,\mathrm{s}^{-1}$, $H = 2.10^3\,\mathrm{A\ m}^{-1}$ we have $j^{\mathrm{AME}} = 10^{-4}\,\mathrm{mA\ cm}^{-2}$, which agrees with the experimental result, and this result is also compared with the result of the experiment in normal bulk semiconductors in the weak magnetic field region to show the difference.

1. INTRODUCTION

It is well known that, when an acoustic wave propagates through a conductor, it is accompanied by a transfer of energy and momentum to the conducting electrons. This gives rise to what is called the acoustoelectric effect. The study of acoustoelecric effect in the bulk semiconductor has received a lot of attention [1, 4]. Recently, Mensah has investigated this effect in a superlattice [5] and there has been a growing interest in observing this effect in mesoscopic structures [6–8]. However, in the presence of the magnetic field the acoustic wave propagating in the conductor can produce another effect called the acoustomagnetoelectric (AME) effect. The AME effect is creating an AME current (if the sample is short circuited in the Hall direction), or an AME field (if the sample is open) when a sample placed in a magnetic field $\vec{H}$ carries an acoustic wave propagating in a direction perpendicular to $\vec{H}$.

The AME effect was first foreseed theoretically by Grinberg and Kramer [9] for bipolar semiconductors and was observed experimentally in bismuth by Yamada [10]. In past times, there are more and more interests in studying and discovering this effect, such as in a monopolar semiconductor [11], and in a Kane semiconductor [12] in this specimen they observed that the AME effect occurs mainly because of the dependence of the electron relaxation time τ on the energy and when τ = constant, the effect vanishes. Like the classical magnetic field, the effect also exists in the case of a quantized magnetic field. Recently, D. Margulis and A. Margulis [13, 14] have studied the quantum acoustomagnetoelectric (QAME) effect due to Rayleigh sound waves.

The AME effect is similar to the Hall effect in the bulk semiconductor, where, the sound flux $\vec{\Phi}$ plays the electric current $\vec{j}$ role. The essence of the AME effect is due to the existence of partial current generated by the different energy groups of electrons, when the total acoustoelectric (longitudinal) current in specimen is equal to zero. When this happens, the energy dependence of the electron momentum relaxation time will cause average mobilities of the electrons in the partial current, in general, to differ, if an external magnetic field is perpendicular to the direction of the sound flux, the Hall currents generated by these groups will not, in general, compensate one another, and a non-zero AME effect will result. The AME effect problem in bulk semiconductors for the case $ql \gg 1$ (where q is the acoustic wave number, l is the mean fee path) has been investigated [11, 12, 15]. The AME effect in a superlattice still, however, opens for studying, in this paper, we examine this effect in a superlattice for the case of electron relaxation time is not dependent on the energy. Furthermore, we think that the research of this effect may help us to understand the properties of SL material. It will be seen that, due to the anisotropic nature of the dispersion law, the AME effect is obtained at τ = constant. It is also nonlinear dependent on the SL parameters. Numerical calculations are carried out a specific GaAs/AlAs SL to clarify our results.

The paper is organized as follows. In Section 2, we outline the theory and conditions necessary to solve the problem. In Section 3, we discuss the results and in Section 4, we have some conclusion.

2. ACOUSTOMAGNETOELECTRIC CURRENT

Following the method developed in [6] we calculate the AME current in a SL. The acoustic wave will be considered as a hypersound in the region $ql \gg 1$ and then treated as monochromatic phonons (frequency ω_q). The problem will be solved in the quasi-classcal case, i.e., $2\Delta \gg \tau^{-1}$ (2Δ is the width of the miniband, τ is the electron relaxation time). The magnetic field will also be considered classically, i.e., $\Omega < \nu$, $\hbar\Omega \ll k_BT$ (ν is the frequency of electron collisions, Ω is the cyclotron frequency), and weak, thus limiting ourselves to the linear approximation of $\vec{H}$.

The density of the acoustoelectric current in the presence of magnetic field can be written in the form [15]

$$j^{\mathrm{AE}} = \frac{2e}{(2\pi)^3}\int U^{\mathrm{AE}}\psi_i d^3\vec{p}, \tag{1}$$

where

$$\begin{aligned} U^{\mathrm{AE}} &= \frac{2\pi\Phi}{\omega_{\vec{q}} v_s}\Big\{ \mid G_{\vec{p}-\vec{q},\vec{p}} \mid^2 [f(\epsilon_{n,\vec{p}-\vec{q}}) - f(\epsilon_{n,\vec{p}})]\delta(\epsilon_{n,\vec{p}-\vec{q}} - \epsilon_{n,\vec{p}} + \omega_{\vec{q}}) \\ &\quad + \mid G_{\vec{p}+\vec{q},\vec{p}} \mid^2 [f(\epsilon_{n,\vec{p}+\vec{q}}) - f(\epsilon_{n,\vec{p}})]\delta(\epsilon_{n,\vec{p}+\vec{q}} - \epsilon_{n,\vec{p}} - \omega_{\vec{q}})\Big\}. \end{aligned} \tag{2}$$

Here Φ is the sound flux, v_s is the velocity sound, $f(\epsilon_{n,\vec{p}})$, $\epsilon_{n,\vec{p}}$ are the distribution function and the energy of the electron, respectively, n denotes quantization of the energy spectrum, $G_{\vec{p}\pm\vec{q},\vec{p}}$ is the matrix element of the electron-phonon interaction and ψ_i is the root of the kinetic equation given by [8]

$$\frac{e}{c}\left(\vec{V}\times\vec{H}\right)\frac{\partial\psi_i}{\partial p} + \widehat{W}_{\vec{p}}\{\psi_i\} = \vec{V}_i. \tag{3}$$

Here $\vec{V}_i$ is the electron velocity and $\widehat{W}_{\vec{p}}\{\ldots\} = (\partial f/\partial\epsilon)^{-1}\widehat{W}_{\vec{p}}(\partial f/\partial\epsilon\ldots)$. The operator $\widehat{W}_{\vec{p}}$ is the collision operator describing relexation of the non-equilibrium distribution of electron, and $\widehat{W}_{\vec{p}}$ is assumed to be Hermitian [16]. In the 'τ-approximation constant', the collision operator has form $\widehat{W}_{\vec{p}} = 1/\tau$. We shall seek the solution of Eq. (3) as

$$\psi_i = \psi_i^{(0)} + \psi_i^{(1)} + \ldots \tag{4}$$

substituting Eq. (4) into Eq. (3) and solving by the method of iteration, we get for the zero and the first approximation. Inserting into Eq. (1) and taking into account the fact that $\mid G_{\vec{p},\vec{p}'} \mid^2 = \mid G_{\vec{p}',\vec{p}} \mid^2$, we obtain for the acoustoelectric current the expression

$$\begin{aligned} j_i^{\mathrm{AE}} &= -\frac{e\Phi}{2\pi^2 v_s\omega_{\vec{q}}}\int \mid G_{\vec{p}+\vec{q},\vec{p}}\mid^2 [f(\epsilon_{n,\vec{p}+\vec{q}}) - f(\epsilon_{n,\vec{p}})]\times[V_i(\vec{p}+\vec{q})\tau - V_i(\vec{p})\tau]\,\delta(\epsilon_{n,\vec{p}+\vec{q}} - \epsilon_{n,\vec{p}} - \omega_{\vec{q}})d^3\vec{p} \\ &\quad -\frac{e^2\Phi\tau^2}{2\pi^2 mc\omega_{\vec{q}} v_s}\int \mid G_{\vec{p}+\vec{q},\vec{p}} \mid^2 [f(\epsilon_{n,\vec{p}+\vec{q}}) - f(\epsilon_{n,\vec{p}})] \\ &\quad \times\left[\left(\vec{V}(\vec{p}+\vec{q})\times\vec{H}\right)_i - \left(\vec{V}(\vec{p})\times\vec{H}\right)_i\right]\delta(\epsilon_{n,\vec{p}+\vec{q}} - \epsilon_{n,\vec{p}} - \omega_{\vec{q}})d^3\vec{p}. \end{aligned} \tag{5}$$

The matrix element of the electron-phonon interaction for $qd \ll 1$ (d is the period of the SL) is given as $\mid G_{\vec{p}+\vec{q},\vec{p}} \mid^2 = \frac{\wedge^2\vec{q}^2}{2\sigma\omega_{\vec{q}}}$, where $\wedge$ is the deformation potential constant and σ is the density of the SL.

In solving Eq. (5), we shall consider a situation whereby the sound is propagating along the SL axis (oz), the magnetic field $\vec{H}$ is parallel to the (ox) axis and the AME current appears parallel to the (oy) axis. Under such orientation the first term in Eq. (5) is responsible for the acoustoelectric current and solution is found in [6]. The second term is the AME current and is expressed as

$$j_y^{\mathrm{AME}} = -\frac{e\Phi\vec{q}^2\tau^2\wedge^2\Omega}{4\pi v_s\omega_{\vec{q}}^2\sigma}\int\left[f(\epsilon_{n,\vec{p}+\vec{q}}) - f(\epsilon_{n,\vec{p}})\right]\times[V_z(\vec{p}+\vec{q}) - V_z(\vec{p})]\,\delta(\epsilon_{n,\vec{p}+\vec{q}} - \epsilon_{n,\vec{p}} - \omega_{\vec{q}})d^3\vec{p}, \tag{6}$$

where $\Omega = eH/mc$.

The distribution function $f(\epsilon_{n,\vec{p}})$ of degenerate electrons gas is given by

$$f(\vec{p}) = \Theta(\epsilon_F - \epsilon_{n,\vec{p}}) = \begin{cases} 0 & \epsilon_{n,\vec{p}} > \epsilon_F \\ 1 & \epsilon_{n,\vec{p}} < \epsilon_F \end{cases} \tag{7}$$

where ϵ_F is Fecmi energy. The energy spectrum $\epsilon_{n,\vec{p}}$ of electron in the SL is given using the usual notation by [17]

$$\epsilon_{n,\vec{p}} = \frac{\vec{p}_\perp^2}{2m} + \Delta_n(1 - \cos(p_z d)). \tag{8}$$

Here, $\vec{p}_\perp$ and p_z are the transverse and longitudinal (relative to the SL axis) components of the quasi-momentum, respectively; Δ_n is the half width of the nth allowed miniband, m is the effective mass of electron.

We assume that electrons are confined to the lowest conduction miniband ($n = 1$) and omit the miniband indicates. This is to say that the field does not induce transitions between the filled and empty minibands, thus the Δ_n can be written the Δ.

Substituting Eqs. (7) and (8) into Eq. (6) we obtain for the AME current satisfying the condition

$$\epsilon_F > \Delta \left[1 - \frac{\omega_{\vec{q}}}{2\Delta} + \left(\cos\frac{qd}{2} \left(1 - \frac{\omega_{\vec{q}}}{2\Delta \sin\left(\frac{qd}{2}\right)} \right)^2 \right)^{1/2} \right] + \omega_{\vec{q}} + \frac{\vec{p}_\perp^2}{2m}. \tag{9}$$

The inequality (9) is condition for acoustic wave $\vec{q}$ to the AME effect exists. Therefore, we have obtained the expression of the AME curent

$$j_y^{\mathrm{AME}} = \frac{e\Phi \wedge^2 \vec{q}^2\tau^2 m\Omega}{2\pi v_s \omega_{\vec{q}} \sigma} \left[1 - \left(\frac{\omega_{\vec{q}}}{2\Delta \sin\left(\frac{qd}{2}\right)} \right)^2 \right]^{1/2}, \tag{10}$$

the Eq. (10) is the AME current in SL for the case degenerate electron gas, that is only obtained if the condition of inequality (9) is satisfied. We can see that the dependence of the AME current on the frequency $\omega_{\vec{q}}$ is nonlinear.

3. NUMERICAL AND DISCUSSION

The parameters used in the calculations are as follow [12, 13, 16]: $\Delta = 0.1\,\mathrm{eV}$, $d = 100\,\mathrm{A}^\circ$, $\tau = 10^{-12}\,\mathrm{s}$, $m = 0.067m_0$, m_0 being the mass of free electron, $H = 2.10^3\,\mathrm{A\ m^{-1}}$, $\Phi = 10^4\,\mathrm{W\ m^{-2}}$, $v_s = 5370\,\mathrm{m\ s^{-1}}$.

The result in Eq. (10) can be written in terms of the acoustoelectric current

$$j_y^{\mathrm{AME}} = j_z^{\mathrm{AE}} \Omega\tau, \tag{11}$$

the AME current depends on the magnetic field $\vec{H}$, the quantity $\Omega\tau$ serving as a measure of the magnetic strength. The ratio of $j^{\mathrm{AME}}/j^{\mathrm{AE}}$ is equal to $\Omega\tau$. This result is quite interesting as a similar ratio calculated for the case of the QAME due to the Rayleigh sound wave was of that order [15]. In their case, $\Omega\tau \gg 1$ (quantized magnetic field) and the sample was a bulk material, bulk semiconductor [12, 13].

It is plausible that mechanism responsible for the existence of the AME effect in a SL may be due to the finite band gap and the periodicity of the electron spectrum along the z axis and not the dependence of τ on $\epsilon_{\vec{p}}$ [12, 15]. The calculation was done on the basis of τ = constant and according to [11] the AME effect should be zero. However, for $\omega_{\vec{q}} > \Delta$ when the SL behaves as a bulk monopolar semiconductor with the parabolic law of dispersion, $j^{\mathrm{AME}} \to 0$ as expected for τ = constant [11]. This is readily deduced from the conservation laws. The non-linear dependence of j^{AME} on the SL parameters Δ and d and the frequency $\omega_{\vec{q}}$ and particularly the strong spatial dispersion of j^{AME} once again can only be attributed to the finite band gap and periodicity of the energy spectrum of electron along the z axis.

Figure 1 shows the dependence of the AME current on the acoustic wave number in the case of the bulk semiconductor n-InSb [14]. It can be see from Figure 1, when the $\vec{q}$ rises up, the AME

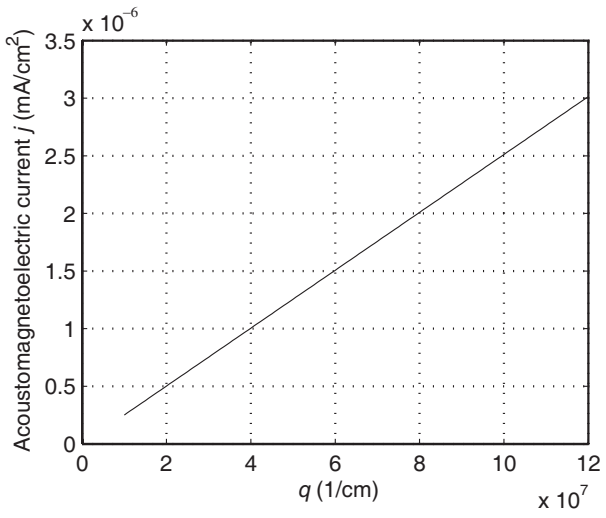

Figure 1: The dependence of AME current on the q for the case of the bulk semiconductor.

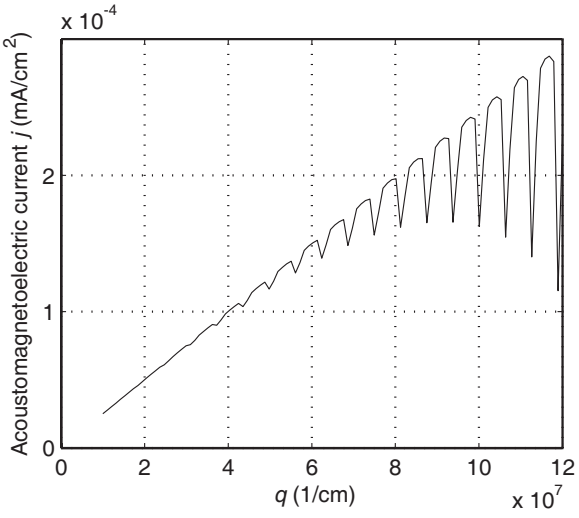

Figure 2: The dependence of AME current on the q for the case of the superlattice.

current increases linear and value of AME current is very small, approximation 10^{-6} mA cm^{-2}. However, in Figure 2 when we have investigated for the case of superlattice, there appear distinct maxima and the value of the AME current is larger than that of the AME current in the case of bulk semiconductor n-InSb. The cause of the difference between the bulk semiconductor and the superlattice, because of the low-dimensional systems characteristic, meanly, in the low-dimensional systems the energy spectrum of electron is quantized, like this, the AME effect have been appeared in SL for the case degenerates electrons gas, and note that it exists even if the relaxation time τ of the carrier independs on the carrier energy and has a strong spatial dispersion. In the limit case at $\omega_q = 10^{13}\,\mathrm{s}^{-1}$, and $H = 2.10^3\,\mathrm{Am}^{-1}$ the AME current is obtained the value about 10^{-4} mA cm^{-2}, this value fits with the experimental result in [13].

4. CONCLUSION

In this paper, we have obtained analytical expressions for the AME current in a SL for the case of the degenerate electron gas. The strong dependences of j_y^{AME} on the frequency Ω of the magnetic field, $\omega_{\vec{q}}$ of the acoustic wave, the SL parameters Δ and d are the miniband half width and the period of the SL, respectively. The result shows that it exists even if the relaxation time τ of the carrier does not depend on the carrier energy and has a strong spatial dispersion, which result is different compared to those obtained in bulk semiconductor [11, 12], according to [11] in the case τ = constant the effect only exists if the electron gas is non-degenerate, if the electron gas is degenarate, the effect does not appear. However, our result indicates that in (SL) the AME effect exists both the non-degenerate and the degenerate electron gas when the relaxation time τ of the carrier does not depend on the carrier energy. In addition, our analysis shows that the result has value, which is smaller than its in [5, 12, 15, 17] and increases linearly Ω of the magnetic field. This result is similar to the semiconductor and the superlattice for the case of the non-degenerate electron gas in the weak magnetic field region [12, 14, 15]. Unlike the semiconductor, in the SL the AME current is non-linear with the acoustic wave $\vec{q}$. Especially, in the limit case at $\omega_q = 10^{13}\,\mathrm{s}^{-1}$, and $H = 2.10^3\,\mathrm{Am}^{-1}$ the AME current is obtained the value about 10^{-4} mA cm^{-2}, this value fits with the experimental result in [13].

The numerical result obtained for a GaAs/AlAs SL shows that the AME effect exists when the $\vec{q}$ of the acoustic wave complies with specific conditions (9) which condition depends on the frequency of the acoustic wave $\omega_{\vec{q}}$, Fermi energy, the mass of electrons, the miniband half width Δ and the period of the SL d. Namely, to have AME current, the acoustic phonons energy are high enough and satisfied in the some interval to impact much momentum to the conduction electrons.

ACKNOWLEDGMENT

This work is completed with financial support from the NAFOSTED (103.01.18.09) and QG-09.02.

REFERENCES

1. Parmenter, R. H., *Phys. Rev.*, Vol. 89, 990, 1973.
2. Rotter, M., A. V. Kalameit, and A. O. Grovorov, *Phys. Rev. Lett.*, Vol. 82, 2171, 1999.
3. Lippens P. E., P. Lannoo, and J. F. Pouliquen, *J. Appl. Phys.,* Vol. 66, 1209, 1989.
4. Afonin, V. V. and Y. Gal'prin, *Semiconductor,* Vol. 27, 61, 1993.
5. Mensah, S. Y., F. K. A. Allotey, and S. K. Adjepong, *J. Phys.*, Vol. 6, 6783, 1994.
6. Shilton, J. M., V. I. Talyanskii, M. Pepper, and D. Ritchie, *Condens. Matter*, Vol. 531, 8, 1996.
7. Maa, F. A. and F. Galperin, *Phys. Rev. B*, Vol. 56, 4028, 1997.
8. Hoskins, M. J., J. Morko, and B. J. Hunsinger, *Appl. Phys. Lett.,* Vol. 41, 332, 1982.
9. Kramer, N. I., *Sov. Phys. Dokl.*, Vol. 9, 552, 1965.
10. Yamada, T., *J. Phys. Soc. Japan*, Vol. 20, 1424, 1965.
11. Epshtein, E. M. and Y. V. Gulyaev, *Sov. Phys. Solids State*, Vol. 9, 28, 1967.
12. Anh, N. Q., N. Q. Bau, and N. V. Huong, *J. Phys.*, Vol. 2, 12, 1990.
13. Margulis, A. D., *J. Phys.,* Vol. 6, 6139, 1994.
14. Mineichi, K. and D. Shoji, *J. Phys. Soc. Japan,* Vol. 30, 3, 1970.
15. Mensah, S. Y., F. K. A. Allotey, and S. Adjepong, *J. Phys.,* Vol. 8, 1235, 1996.
16. Kaganov, M. I., *Sov. Phys. — JETP,* Vol. 51, 189, 1967.
17. Shmelev, G. M., E. M. Epshtien, and N. Q. Anh, *Soviet Phys. Sol. St.,* Vol. 11, 3472, 1981.

Influence of the Output Electrical Parameters on Multistage Depressed Collector Characteristics in a Coupled Cavity TWT

Yinghui Zhang, Jirun Luo, Wei Guo, and Min Zhu
Institute of Electronics, Chinese Academy of Sciences, Beijing 100190, China

Abstract— Using a depressed collector to collect the residual energy of the electron beam is an important way to improve the total efficiency of traveling wave tube (TWT). In this article, the influence of the output electrical parameters on the characteristics of a three-stage depressed collector in a Coupled Cavity TWT is discussed by analyzing the deviation angle $\sigma(\alpha)$, which shows that a relatively high electronic efficiency can be reached with relatively uniform electron beam distribution.

1. INTRODUCTION

TWT is a kind of vacuum microwave device with very wide bandwidth, large output power, and high gain, and it has wide applications in radar, communication, electron counteraction, and so on. However, the electron efficiency is relatively low because the electron beam interacts with traveling wave [1]. There are two methods to enhance the efficiency: one is improving its interaction system, the other is the electron beam energy is used again. The former is limited by the interaction mechanism of the TWTs, the latter includes the recycle of the electron beam (only for some large-scale installations) and the depressed collector, which has been widely used in many TWTs [2].

In all the TWTs, Coupled Cavity TWT (CCTWT) can generate the higher output power with the higher efficiency and higher gain, especially when it possesses a depressed collector. However, the heat dissipation in the depressed collector is a key technical problem. In this article, considering the electron beam after the beam-wave interaction process (calculated with a TWT simulation code, Orprogr) as the initial situation of the depressed collector design, the influence of the frequency of output electrical parameters on a three stage depressed collector in the CCTWT was discussed for improving the design and heat dissipation ability of the depressed collector.

2. INLET CONDITION

Utilizing the TWT simulation code, Orprogr, we had designed a CCTWT, which showed 127 $\sim$ 152 kW output power could be reached with over 39 dB saturated gain, over 18% electronic efficiency, about 19.2% of -1 dB band width (8.108 $\sim$ 9.836 GHz) at the beam voltage of 48 kV and the beam current of 14.34 A. The output beam is directly sent to the depressed collector design module as the initial condition.

Supposing that the electrons initially spread on the cathode emission surface homogeneously, the position of different electron in the radial direction is almost a straight line. At the inlet of the depressed collector, every electron from center to edge is affected because of the action of the focusing magnet field (without the beam-wave interaction). However, these electrons are still laminar flow in the static state. In the dynamic state (after the beam-wave interaction), the radial coordinate of the inner and outer layer electrons fluctuates and the fluctuation intensity of the outer layer electrons is more serious. Figure 1 shows the distribution in the radial direction of all electrons (N) for the above-mentioned three situations.

The corresponding ratio of the electron beam radial velocity with its axial velocity after beam-wave interaction is illustrated in Figure 2 for each electron. It can be found from Figure 2 that the ratio is disordered, but, in general, the ratio in the outer layer is higher than that in the inner layer, which means that the beam-wave interaction in the outer layer is stronger. This phenomenon may lead to disorder of electron trajectory and cause the greater deflection of the electron away from the axial direction.

3. INFLUENCE OF THE OUTPUT ELECTRICAL PARAMETERS ON THE DEPRESSED COLLECTOR CHARACTERISTICS

Based on above-mentioned inlet condition, a three stage depressed collector had been designed (Figure 3). Table 1 lists the designed results and the electron beam can evenly spread on the surface of each sub-area of the depressed collector by choosing appropriate electrode shape and

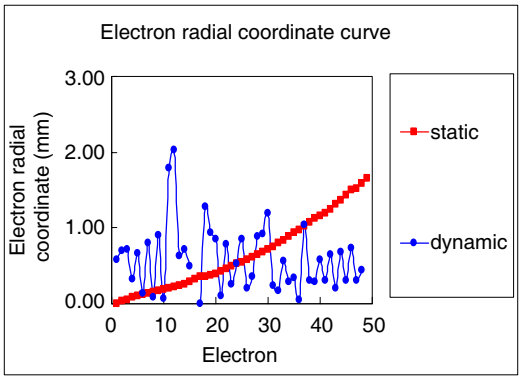

Figure 1: Electron distribution in radial direction.

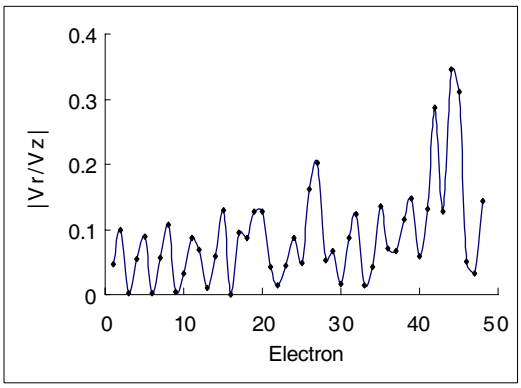

Figure 2: The ratio of the radial velocity with the axial velocity.

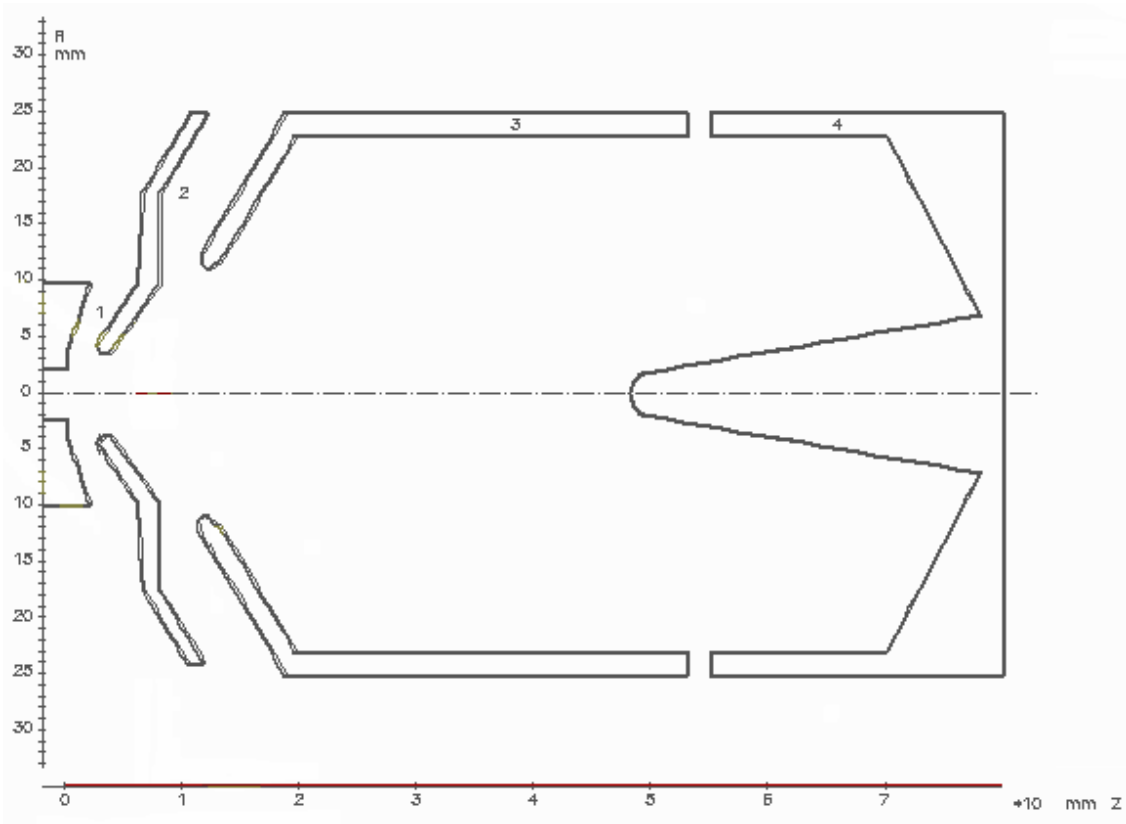

Figure 3: Model of a three-stage depressed collector.

voltage drop, which shows that the collector efficiency is larger than 71.5% and the total efficiency of the CCTWT is larger than 36% in the operational frequency range. These data show that the depressed collector effectively increases the total RF output efficiency by decreasing the power dissipation on the collector surface. Although the electron beam energy can be decreased by the depressed collector, the distribution of the beam on the depressed collector is a key problem for its heat dissipation, which needs to carefully design the structure of the depressed collector to avoid that the electrons excessively focus on its local area.

In order to improve the CCTWT's stability, it is necessary analyzing the effect of the output electrical parameters on the beam distribution on the collector surface. The deviation angle [3] $\sigma(\alpha)$ is defined as a kind of describing mode to distinguish the moving status of the electron beam in the depressed collector.

$$\sigma(\alpha) = \sqrt{\frac{1}{N}\sum_{k=1}^{N}\left(\alpha_k - \frac{1}{N}\sum_{k=1}^{N}\alpha_k\right)} \tag{1}$$

where $\alpha_k = \tan^{-1}({}^{v_r}/_{v_z})_k$, $({}^{v_r}/_{v_z})_k$ is the ratio of the radial velocity of kth electron with its axial

velocity. $\sigma(\alpha)$ versus the electronic efficiency for the situation discussed here has been given in Figure 4 after the beam-wave interaction for different frequencies, which shows that the larger the electronic efficiency, the larger the $\sigma(\alpha)$, that is to say, the larger the deviation angle in this frequency, the more difficultly the electron beam to be collected.

The simulation results show that when the electron efficiency increases with electrical parameter variation, the longitudinal velocity of the electron beam decreasesits laminar flow may become worse and the trajectories of the electron beam are more disordered in the collector. The landing point of electron beam on the collector surface moves backward and distribute unevenly, and the $\sigma(\alpha)$ increases, which may effectively suppress the production of secondary electrons. When the electron efficiency decreases, the longitudinal velocity of the electron beam increases and its laminar flow may become better. However, the electron beam landing on the collector surface becomes dense, the electron energy intercepted by the depressed collector increases and the heat dissipation may become more difficult, and the $\sigma(\alpha)$ decreases, which may promote the production of secondary electrons.

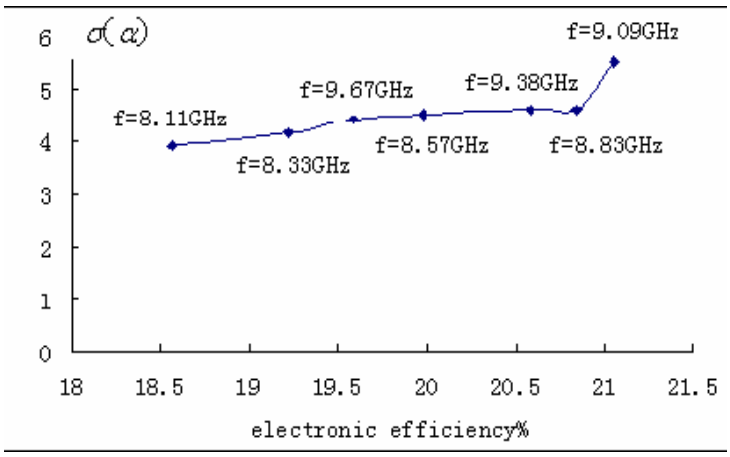

Figure 4: $\sigma(\alpha)$ versus the electronic efficiency.

Table 1: Simulation results of the CCTWT with the three-stage depressed collector for different frequencies.

Frequency (GHz)	Electron efficiency (%)	Total efficiency	RF output power (W)	Power sent to collector (W)	Power intercepted by Collector (W)	Collector efficiency
8.108	18.56	0.364	127657	468853.5	128052.4	0.7268
8.333	19.219	0.37	132417	467117.9	129181.1	0.7234
8.571	19.974	0.39	138240	464619.9	121639.8	0.7381
8.824	20.844	0.399	142828	460748.2	121623.9	0.736
9.091	21.057	0.409	144317	452483.6	115646.8	0.7444
9.231	21.034	0.407	143550	454974.4	116967.5	0.7429
9.667	19.581	0.369	133679	463684.4	132055.7	0.7152
9.836	22.201	0.401	152830	446646.3	126754.4	0.7162

4. CONCLUSION

In this paper, a three-stage depressed collector had been designed. The electronic efficiency of larger than 71.5% and the total efficiency of 36% can be reached at 127 $\sim$ 152 kW output power, over 39 dB saturated gain, about 19.2% of -1 dB band width (8.108 $\sim$ 9.836 GHz) at the beam voltage of 48 kV and the beam current of 14.34 A with relatively uniform electron beam distribution on the collector surface.

REFERENCES

1. Liao, P., Z.-H. Yang, B. Li, W.-Q. Lei, L. Liao, and X.-H. Gao, "Application of M AFIA in three-dimensional dynamic PIC simulation of TWT multistage depressed collector," *Journal of Electronics & Information Technology*, Vol. 27, No. 3, Mar. 2005.
2. Granastein, V. L., R. K. Parker, and C. M. Armstrong, "Vacuum electronics at the dawn of the twenty-first century," *Proc. IEEE*, Vol. 87, No. 5, 702–716, 1999.
3. Stankiewicz, N., "Analysis of spent beam refocusing to achieve optimum collector efficiency," *IEEE Transaction on Electron. Devices*, Vol. ED24, No. 1, 1977.
4. Liu, S., *Microwave Electronics*, 285, Beijing, 1985.

Numerical Study on Readout Characteristics of Near-field Optical Disk

S. Iwata and T. Kitamura
Faculty of Engineering Science, Kansai University, Osaka, Japan

Abstract— We investigated readout characteristics of a near-field optical disk with an acute-edged metallic nano-aperture. We analyzed electromagnetic field distributions of optical near-field around the aperture and calculated far-field scattering pattern from the phase change disk by means of FDTD method. We showed that field intensity of near-field light can be increased by adjusting edge angles of the aperture. We also investigated the influence of the edge angles on output through the recorded marks.

1. INTRODUCTION

The capacity of optical storage system has been improved by shortening wavelength or increasing the numerical aperture of an objective lens. However, the recording density has a limitation due to optical diffraction limit. Recording methods based on near-field optical principles are one of the candidates that can overcome the limitation. Many researchers have been interested nano-apertures for the method to obtain near-field light and many types of apertures have been proposed so far [1–4].

In this study, we focus on readout characteristics of recorded marks on an optical disk illuminated by near-field optical light through an acute-edged metallic nano-aperture. We deal with a two-dimensional structure in order to simplify the discussion and a phase change disk system is assumed. In the analysis, we use FDTD method into which motion equations of free electrons are installed to analyze a metallic material [5].

We show that field intensity of near-field light can be increased by adjusting edge angles of the aperture. We also investigate the influence of the edge angles on output through the recorded marks.

2. FIELD INTENSITY OF NEAR-FIELD LIGHT

The acute-edged metallic nano-aperture and the coordinate axes are shown in Fig. 1. Here, the thickness of a metallic film is t, the width of the aperture w_a, and the edge angles θ, respectively. Here, we assume silver as a metallic material and the complex refractive index $N = 0.07 - 4.2j$. A p-polarized plane wave with the wavelength of 650 nm is illuminated vertically to the aperture. The electric field is evaluated on a line at the distance of 10 nm along the x axis from the aperture. The field intensity of near-field light is shown in Fig. 2.

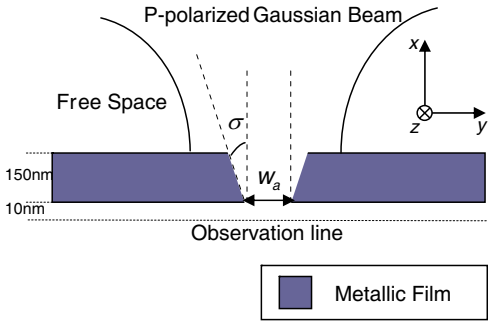

Figure 1: Two-dimensional metallic nano-aperture model.

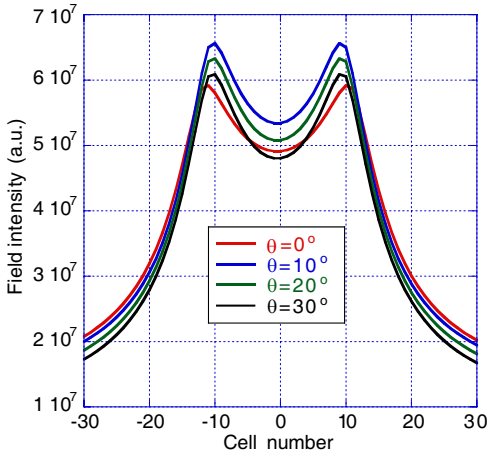

Figure 2: Field intensity of near-field light.

3. READOUT CHARACTERISTICS

We show a structure of a near-field optical disk that consists of a metallic nano-aperture, a phase change disk, two protect films and a substrate in Fig. 3. Here, we assume silver as a metallic material. The refractive indexes of the optical disk structure are shown in Table 1. The incident light is a p-polarized Gaussian beam with the wavelength of 650 nm and the numerical aperture of an object lens is assumed to be 0.6. We investigate the readout characteristics with the width of the aperture (w_a) and the angle of the metal edges (θ) as parameters.

The ratios of output through a recorded mark to one through a non-recorded mark as a function of the width of the recorded mark (w_r) are shown in Fig. 4. The output is calculated from the scattered far field of the transmitted wave.

As shown in this figure, the output ratios increase almost linearly as w_r increases and the slopes of the lines become larger as w_a is smaller. Therefore, the larger output ratios can be obtained by using the smaller aperture. However, it is thought to be difficult to maintain high output intensity when an aperture width is small.

We show the normalized output as a function of θ when $w_r = 50$ nm in Fig. 6. The output is calculated from the scattered far field of the transmitted waves and normalized by the output with $w_a = 100$ nm and $\theta = 0$ degrees. It can be seen that optimum angles (θ) that can obtain the highest output exist and the angles depend on the width of the recorded mark (w_r).

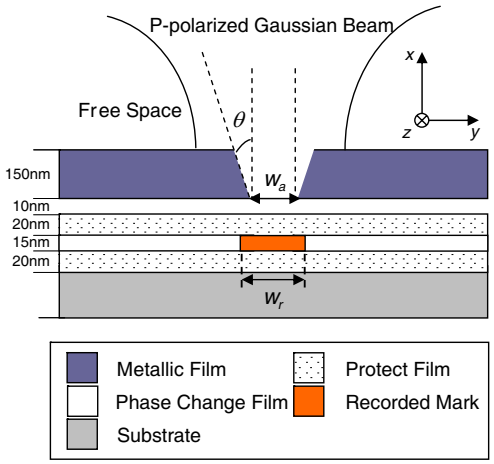

Figure 3: Two-dimensional near-field optical disk model.

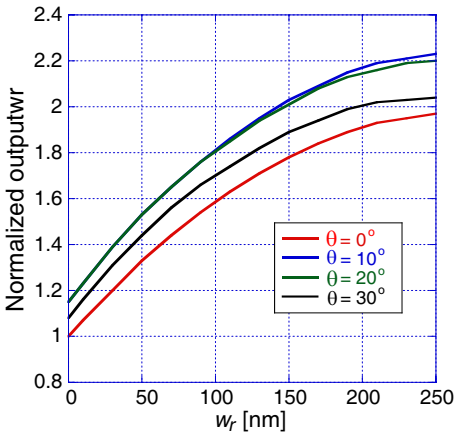

Figure 4: The change of signal as a function of the size of recorded mark.

Table 1: Refractive indexed of optical disk structure.

Metallic film (Ag)	0.070–4.20j
Phase change film	4.2–1.9j (amorphous) 4.6–4.2j (crystalline)
Protection film	2.2
Substrate	1.5

4. CONCLUSIONS

The readout characteristics of a near-field optical disk with an acute-edged metallic nano-aperture were studied. We analyzed electromagnetic field distributions of optical near-field around the aperture and calculated far-field scattering pattern from the phase change disk by means of FDTD method into which motion equations of free electrons are installed. It was shown that field intensity of near-field light can be increased by adjusting edge angles of the aperture. The influence of the edge angles on output through the recorded marks was also investigated.

REFERENCES

1. Chen, Y., J. Fang, C. Tien, and H. D. Shien, "Double-corrugated C-shaped aperture for near-field recording," *Jpn. J. Appl. Phys.*, Vol. 45, No. 2B, 1348–1350, 2006.

2. Eom, G. S., D. Yang, E. Lee, S. Park, Y. Lee, and J. W. Hahn, "Wave propagation characteristics of a figure-eight shaped nanoaperture," *J. Appl. Phys.*, Vol. 101, No. 103101, 1–4, 2007.
3. Park, D., H. J. Kim, B. H. O, S. G. Park, E. Lee, and S. G. Lee, "Effect of incident beam width on light transmission enhancement by bow-tie-shaped nano-aperture," *Jpn. J. Appl. Phys.*, Vol. 46, No. 12, 7991–7994 , 2007.
4. Omodani, S., T. Saiki, and M. Obara, "Metallic slit aperture as a near-field optical head for heat-assisted magnetic recording," *J. Appl. Phys.*, Vol. 105, No. 013101, 1–5, 2009.
5. Kagawa, S., Y. He, and T. Kojima, "Two-dimentional FDTD analysis of the readout characteristics of an optical near field disk," *IEICE Trans. Electron.*, Vol. E91-C, No. 1, 48–55, 2008.

Getting Excitation Characteristic Curves of PTs with Linear Interpolation Method

Zheng-Wang Du[1], **Heng-Xu Ha**[2], **Lei Zhai**[3], **Hai-Quan Zhou**[2], **Song-Bo Gou**[1], **and Chong-Shan Zhong**[1]

[1]ShengLi Oil Field Power Company, Dong Ying, China
[2]Dept. of Electric & Electronics Engineering, Shandong University of Technology, Zibo 255049, China
[3]School of Electrical Engineering Automation, Hebei University of Technology, Tianjin, China

Abstract— The flux-current characteristic of the voltage transformer plays an important role for non-linear Ferro-magnetic analysis. The disadvantage of traditional excitation curve fitting method using the model of polynomial terms lies in that the linear part fitting is not perfect, while, the non-linear part has the good fitting results, which is not accord with the PT excitation characteristic. With fitting order number increasing, insufficient samples will also lead to unfavorable fitting results. In this paper, line interpolation will be first carried out for the linear part of the measuring volt-ampere characteristics, then sample points will be increased by utilizing least squares fit, which will greatly improves the fitting precision of the linear part and the overall fitting accuracy of the non-linear part. The simulation results show that the error of the linear part does not exceed 0.3% and the error of the non-linear part drops from 2.5% to 1.5% when the linear part is given 11 order line interpolations.

1. INTRODUCTION

In distribution network, it is a very common phenomenon that nonlinear ferroresonance caused by the saturation of voltage transformer core. So, over-voltage and over-current caused by ferroresonance often lead to burning of the voltage transformer [1, 2]. According to statistics, in 2007, the transformer burning occurred 16 times in ShengLi Oilfield, which lead to 36 transformers are burned down, it involved 9 substations and more than 50 lines cut off, and caused huge economic losses.

Voltage transformer excitation characteristic curve is indispensable for the nonlinear ferroresonance both in theoretical analysis and in simulation. The traditional excitation characteristic curve is the volt-ampere characteristic curve composed by the RMS values required from the test, but, what the analysis of the ferroresonance required is the instantaneous flux-current characteristic curve. At present, there are two categories to obtain the excitation curve: one is the measurement which hardly used because it has high equipment requirements and complex measurement methods; the other is indirecttion fitted, which assume flux-current characteristic curve as some kinds of models [3], and turn them into RMS voltage-RMS current, then use the measured values of the votage-ampere characteristics to fit the parameters [4–8].

Transformer flux-current model is usually assumed to be four types: the first is assumed to be piecewise linear model; the second is the assumption of rational polynomial model; the third is to hyperbolic function model assumption; the fourth is comperhensive subsection model. Piecewise linear model [9–11] has not smoothly enough fitting curve, and it is hardly to calculate and to analyze when there are more segmentation. The defect of the rational polynomial model [12–14] is that the fitting precision of the linear part is not good, moreover, when the flux value is larger, the curve is not monotonous. For the hyperbolic function model [15], it is not easy to converge in the fitting process, in addition, the feature of the linear part is not ideal. In paper [16], it fits the curve by three-stage approach, namely, the first (linear part) one is the rational polynomial model, the second one is the hyperbolic function model, the third one is assumed as a stright line. The method greatly improved the fitting accuracy, however, the fitting result of the linear part is still not ideal because of the deficency of sample points, but also it makes quantitative analysis of nolinear ferroresonance relatively complicated for dividing the excitation curve into three complex functions.

In this paper, it employs flux-current model which is divided into two parts, that is , to use the rational polynomial model in the volt-ampere characteristic curve measurement scale, and to use stright line model in the depth saturated scope. In order to solve the defect that the linear part has poor results in the fitting process, in this paper, line interpolation will be first carried out for the linear part of the measuring volt-ampere characteristics, then sample points will be increased

by utilizing least squares fit, which will greatly improves the fitting precision of the linear part and the overall fitting accuracy of the non-linear part. The simulation results show that the error of the linear part does not exceed 0.3% and the error of the non-linear part drops from 2.5% to 1.5% when the linear part is given 11 order line interpolations.

2. BISIC PRINCIPLE

2.1. Flux-current Characteristic Curve Fitting

For iron coil, the flux φ and the current i are non-linear. According to the characteristic of the odd function between flux and the current, the paper uses the following polynomial to fit the excitation characteristic curve [3], the model that is:

$$i\left(t\right) = \sum_{n=0}^{\infty} a_{2n+1}\varphi\left(t\right)^{2n+1} \tag{1}$$

In the mearsuring of volt-ampre characteristics, voltage is an sine function:

$$u(t) = \sqrt{2}U\cos\omega_0 t$$

According to the ralationship between the flux and the voltage, the flux is:

$$\varphi\left(t\right) = -\sqrt{2}\left(\frac{U}{\omega_0}\right)\sin\omega_0 t \tag{2}$$

Put type (2) into type (1), we can get the instantaneous relation between the current and the voltage:

$$i\left(t\right) = g[a_1, a_3, \ldots, a_{2N+1}, U] \tag{3}$$

Then get the relationship between the RMS of current and the RMS of voltage:

$$I^2 = f[a_1, a_3 \ldots a_{2N+1}, U] \tag{4}$$

According to the measured volt-ampere value U_k and I_k, $k = 1, \ldots, M$, M is the measured volt-ampere characteristic data points. Then we utilize the least squares to estimate the parameters $(a_0, \ldots, a_n)$, here, the objective function of the least squares is the minimum variance, that is:

$$J = \min\left\{\sum_{k=1}^{N}[I_k^2 - f(a_0, \ldots a_n, U_k)]^2\right\} = \left[Y - F(A,U)\right]^T\left[Y - F(A,U)\right] \tag{5}$$

Here

$$Y = [I_1^2, \ldots, I_M^2]^T \quad U = [U_1, \ldots, U_M]^T \quad A = [a_0, \ldots, a_n]$$

I_k and U_k is number k volt-ampere characteristic value.

So, we put the problem of parameter fitting into the optimization problem of the minimum variance, the solution of the optimization that is the solution of the following algebraic equation:

$$\frac{\partial J}{\partial A} = \left(\frac{\partial F}{\partial A}\right)^T\left[Y - F(A,U)\right] = 0 \tag{6}$$

2.2. Solving the Nonlinear Algebraic Equation with the New-ton Method

As we know from above: Equation (6) is nonlinear, which solved by the New-ton method. We assume the parameter to solve of the k times as A_k, and the difference between the real value (revised value) as ΔA_k. So the first order Taylor series of $F(A_k, U)$ as:

$$F\left(A,U\right) = F\left(A_k,U\right) + \left.\frac{\partial F}{\partial A}\right|_{A_k}\cdot\Delta A_k \quad = F\left(A_k,U\right) + H_k\Delta A_k \tag{7}$$

Here

$$H_k = \begin{bmatrix} \frac{\partial f(A,U_1)}{\partial a_1} & \frac{\partial f(A,U_1)}{\partial a_3} & \cdots & \frac{\partial f(A,U_1)}{\partial a_{2N+1}} \\ \frac{\partial f(A,U_2)}{\partial a_1} & \frac{\partial f(A,U_2)}{\partial a_3} & \cdots & \frac{\partial f(A,U_2)}{\partial a_{2N+1}} \\ \cdots & \cdots & \cdots & \cdots \\ \frac{\partial f(A,U_M)}{\partial a_1} & \frac{\partial f(A,U_M)}{\partial a_3} & \cdots & \frac{\partial f(A,U_M)}{\partial a_{2N+1}} \end{bmatrix}$$

H_k is the Jacobin matrix.

Put type (7) into type (6) ,we can get the linear modifier equation:

$$\frac{\partial J}{\partial A} = H_k^T [Y - F(A_k, U) - H_k \Delta A_k] = 0 \tag{8}$$

Then, we get the modifier value $\Delta A_{(k)}$

$$\Delta A_{(k)} = (H_k^T H_k)^{-1} H_k^T [Y - F(A_k, U)] \tag{9}$$

Assuming the fitting order is $2N+1$, then, we know the numbers of the parameter is N, the vector A and ΔA are $N \times 1$ matrix, the measured volt-ampere samples are M $(M > N)$, then we can know that: matrix H is $N \times M$, matrix Y is $M \times 1$.

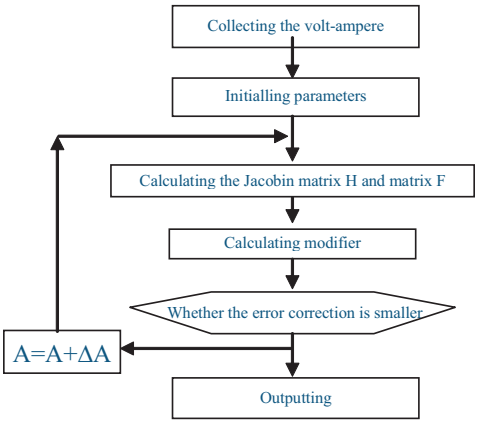

Figure 1: Excitation charcteristic curve fitting method.

number	voltage (per unit)	current (per unit)	number	voltage (per unit)	current (per unit)
1	0	0	10	1.501	3.067
2	0.289	0.367	11	1.559	3.533
3	0.577	0.600	12	1.631	4.387
4	0.866	0.867	13	1.674	5.087
5	1.000	1.000	14	1.732	6.000
6	1.097	1.207	15	1.790	7.330
7	1.212	1.540	16	1.847	8.667
8	1.328	1.733	17	1.905	10.20
9	1.443	2.533	18	1.963	11.93

Table 1: The Voltage-Current characteristic of VT.

2.3. The Calculation Method about the Fitting Parameter with the New-ton Methods

The method and the steps of the least-square fitting calculation with New-ton method are as follow:

The first: input the measured volt-ampere characteristic value (U_k, I_k)

The second: to assign A_0 to the parameter to estimate;

The third: calculate the vector Y, F, H_0 with the volt-ampere characteristic, then, get the modifier value by type (9);

The fourth: correction:

$$A_{k+1} = A_k + \Delta A_k$$

If the error correction is smaller than the setting value, modify and output the result, else, return to the third step and calculate repeatly, until the correction meets the setting value. The calculation procedure of the fitting parameter by the Newton is shown in Figure 1.

2.4. Improvement of the Fitting Excitation Characteristic

Though the above analysis, we can know that, the polynomial model has two defects in fitting flux-current characteristic: one is that sample points limit fitting order number; the other is that the linear parts have the poor pricision, which is not in accord with the PT excitation characteristic. We hope that the whole nonlinear part errors do not increase, while, the linear part errors decreasing.

Obviously, the polynomial orders higher, the fitting precision better, meanwhile, the ploynomial orders higher, the parameters to estimate will be more. Assuming for fitting orders is $2N+1$, and the number of unknown parameters is N, like this, the sample points measured in volt-ampere characteristic M must be much more than N, in order to effectively eliminate the error influence which brought by measuring. Therefore, the samples points is insuffient when the fitting orders increase.

Secondly, the estimated parameters is the minimum error when we fit the curve by the least square method, because the objective function is the variance sum. It is not in accord with the

actual PT excitation characteristic that the linear parts have obvious calculation error, so, we can control the error to adjust the error distribution in order to make the linear part error smaller. To meet this, the weighting coeffcients method can do this, but the effect is not good in controlling errors because of the insuffient sample points.

In this paper, we carry out the line interpolation for the linear part of the volt-ampere characteristics, then sample points will be increased, which will greatly improves the fitting precision of the linear part.

In the linear part (before number k as the linear part), we get the current values $[I_1, I_2, \ldots, I_K]$ from the volt-ampere characteristic, accordingly, the RMS voltage value also $[U_1, U_2, \ldots, U_K]$, then to carry out the line interpolation, and require a group new points:

$$\left[\frac{I_k + I_{k-1}}{2}, \frac{U_k + U_{k-1}}{2}\right], k = 1, \ldots, K$$

We carry out as before, so, when interpolation is done every time, the volt-ampere sample points of the linear part will increase $K - 1$, that is, the number of interploation more, the volt-ampere data more, while utilizing the least square makes the linear part errors smaller. At the same time, because the least square makes the overall variance minimum, correspondingly, the error of the non-linear parts will relatively increase (the simulation results in the follow show that the error of the nonlinear parts have the little increase and the overall error down), so we can reach the results that the precision of the linear parts has been improved.

3. SIMULATION RESULTS

In this paper, with the volt-ampere characteritic of the 6 kV voltage transformer in the literature [15] for example, the data presented in Table 1, here, all the values are P.U. values, the benchmark of the voltage and the current are:

$$U_B = 6000/\sqrt{3}\,\mathrm{V} \qquad I_B = 1.5\,\mathrm{mA}$$

It is the first step to identify the order of the rational polynomial model, to fit the curve precisely, in the paper, we adopt 7 times polynomial, that is, $N = 3$, the flux-current model just as follow:

$$i(t) = a_1\varphi(t) + a_3\varphi^3(t) + a_5\varphi^5(t) + a_7\varphi^7(t)$$

Based on the model, comparing the improved fitting curve with the actual curve firstly, then comparing the error on the line interpolation with the curve and without it. Finally, to analyze the relationship between the interpolation time and the error.

Here, the volt-ampere characteristic curve is derived from the fitting parameters, that is, the fitting volt-ampere characteristic curve is derived from the RMS current which is calculated according to the RMS flux (the per unit values of the flux's RMS and the voltage's RMS are equal).

3.1. Improved Fitting Results and the Errors

Figure 2(a) shows that the convergence of the parameter A after 11th interpolation, Figure 2(b) presents that the fitting flux-current curve and the actual flux-current curve (under per unit values, the actual flux-current curve is the volt-ampere curve), Figure 2(c) is the error curve.

Figure 2 indicates that the fitting results is very ideal after 11th interpolation, especially in the linear part (in the example, the current's per unit value is lesser or equal than 1), while the overall error in the non-linear part also become smaller.

3.2. Comparison on the Fitting Results and the Errors Before and After Improvement

Figure 3 shows that the constract between the improvement fitting excitation curve and the traditional fitting curve.

Figure 3 shows that the error of the linear part not only greatly reduced, but also the overall error decreases. Before the improvement, the maximum error is about 2.5%, after that, the biggest error decreases about to 1.8%. It is the important reason that we utilize the polynomial model which leads to that the error mainly concentrated in the linear region. Then a lot of the linear interpolation are carried out and the data will increase greatly, which descrease the error of the linear part. After 11 times interpolation, the fitting of the linear part which based on polynomial model is very ideal.

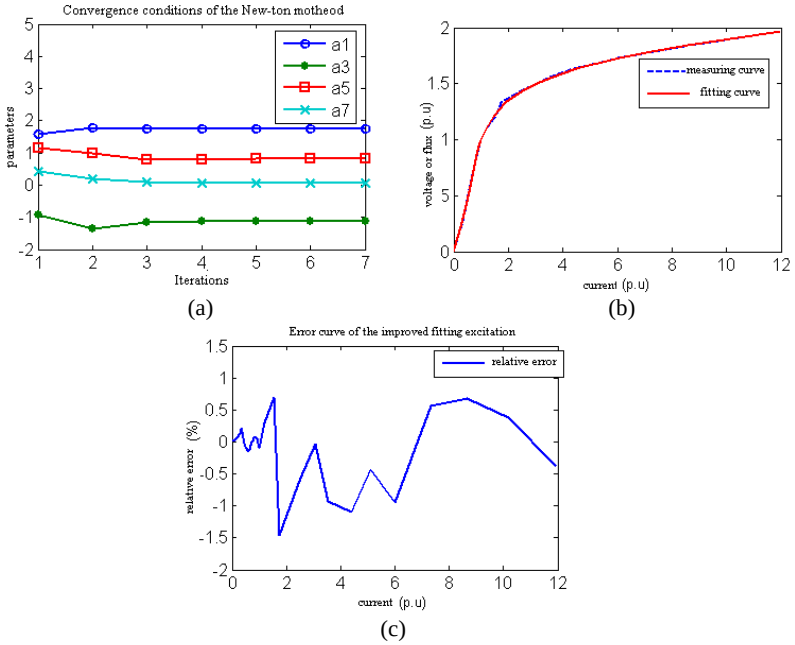

Figure 2: The improved fitting excitation curve and its error.

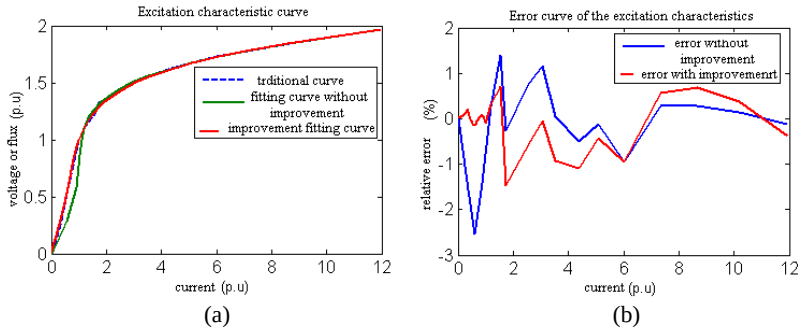

Figure 3: The comparison of improved fitting excitation curve with the traditional fitting curve.

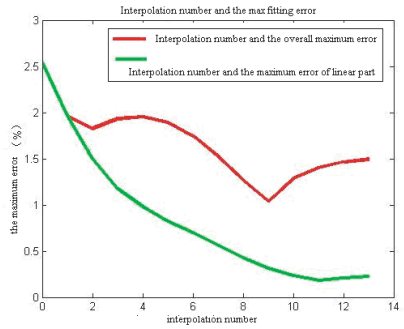

Figure 4: Interpolation number and the max fitting error.

3.3. Interpolation Orders and the Fitting Results

After the analysis above, we maybe have such question: whether the interpolation orders more, the fitting results better. Through using MATLAB to simulate repeatly, the results show that: the interpolation number is not proportional to the fitting results, and the maximum overall relative error is minimax when number is 9, and the maximum relative error of the linear region is the smallest after 11th interpolation, and the particularcase as shown in Figure 4.

Figure 4 also shows that the error of the linear part drastically reduces and the overall error also has a marked decrease after interpolation, but due to the interpolation error exists during the interpolation, the interpolation's number more, the error bigger. For the linear part, which is the

reason that the error of the interpolation is minimum at number 11, that is, the reason why the lowest point exists in the green curve, which is also the reason why the lowest points in the red curve at number 9. Then the error become bigger when the interpolation's number increases, so two curves are both rising after reaching the lowest point.

4. CONCLUSION

In this paper, it employs flux-current model which is divided into two parts, the rational polynomial mode is used in the measurement scale of volt-ampere characteristic curve, and the stright line model is used out reach to depth saturated scope.

Then, in the paper, the linear interpolation which belong to the mathematical scope is brought in the fitting process, which make up for the insufficent defects of measuring sample points of volt-ampere characteristic, and the simulations show that the interpolation's number is not proporational to the fitting result.

Finally, in the paper, with the help of MATLAB, it is verified and contrasted by simulations that the error of the flux-current characteristics before and after linear interpolation, moreover concluded that the error of the linear part does not exceed 0.3% and the error of the non-linear part drops from 2.5% to 1.5% when the linear part is given line interpolatons,which provides the important prerequisite to analyze the ferroresonance precisely in the future.

REFERENCES

1. Jin, X.-F. and Z.-K. Li, "Research review on ferroresonance in power systerm," *Sichuan Electric Power Technology*, No. 1, 2004.
2. Zhang, X.-D., H.-L. Zhang, and Y. Li, "Danger distinction and prevention and cure treatment on ferro-resonance in electricity system," *Journal of Electric Power*, Vol. 17, No. 4, 283–286, 2002.
3. Xie, G.-R., *Over-voltage in Power System*, Water Conservancy and Electric Power Press, Bei Jing, 1985.
4. Gu, D.-X., "Over-voltage designproblems and improvement measures in 500 kV power transmission project," *Electric Power Construction*, Vol. 23, No. 7, 26–30, 2002.
5. Luan, Q.-R., W. Shi, and Z.-Q. Sang, "The issue of 750 kVGIL application considered in Laxiwa hydropower station," *High Voltage Apparatus*, Vol. 39, No. 4, 66–71, 2003.
6. Al-Tai, M. A. and H. S. B. Elayyan, "The simulation of surge corona on transmission lines," *IEEE Trans. on PWRD*, Vol. 4, No. 2, 1360–1368, 1989.
7. Li, X. R., O. P. Malik, and Z. D. Zhao, "A practical mathematical model of coronafor calculation of transients on transmission lines," *IEEE Trans. on PWRD*, Vol. 4, No. 2, 1145–1152, 1989.
8. Carneiro, S., "Evaluation of corona and line models in electromagnetic transients simulations," *IEEE Trans. on PWRD*, Vol. 6, No. 1, 334–342, 1991.
9. Chen, L.-J., B. Du, and W. Shi, "Study on 750 kV switching transient overvoltage when taking into account the corona struck by lightning," *High Voltage Apparatus*, Vol. 40, No. 3, 167–169, 2004.
10. Dong, H.-B. and L.-P. Shi, "Analysis and application of the conversion method of the excitation character curve of the electric-magnetic type TV and the transformer," *Electro-technical Journal*, No. 2, 36–38, 1992.
11. Shi, L.-P. and H.-B. Dong, "Analysis and applic ation of the conversion method of the nonlinearexcitation character curve," *Journal of China Mining University*, Vol. 28, No. 2, 1999.
12. Li, Y.-G. and W. Shi, "Novel analytical solution to fundamental ferroresonance in grounded neutral system — Solution to the power frequency excitation characteristic of non-linear inductors," *Proceeding of the CSEE*, Vol. 23, No. 10, 94–98, 2003.
13. Zhao, X.-M. and Z.-H. Yu, "Instances and numerical simulation of ferroresonance in 35 kV side of 500 kV main transformer," *Zhe Jiang Electric Power*, No. 3, 2008.
14. Yan, J., Z.-Y. Ma, and A. Tang, "Calculation method for excitation characteristic of coil with iron core," *High Voltage Engineering*, Vol. 32, No. 8, 11–14, 2006.
15. Li, Q. and X.-Y. Wang, "Reaearch on fittingg method of core excitation characteristics of transformer," *High Voltage Engineering*, Vol. 23, No. 1, 19–21, 1997.
16. Li, Q., "An improved method for the fitting of excitation curve of electromagnetic voltage transformer," *Transformer*, Vol. 35, No. 3, 1998.

A New Approach to Periodical Structure Analysis

R. Kadlec, P. Drexler, and P. Fiala
Department of Theoretical and Experimental Electrical Engineering, Brno University of Technology
Kolejni 2906/4, Brno 612 00, Czech Republic

Abstract— Paper presents usage numerical modeling of propagation electromagnetic waves. For this method a numerical model was prepared. The numerical model was created in the MatLab program environment. For layered heterogeneous medium is deduced algorithm for reflection on several layers. Several layers are in form of periodical structures which are composite of homogenous material. The reflection and refraction are analyzing accordance with Snell's law for electromagnetic waves. Deduced algorithm was project for the visible spectrum. Reflection and refraction on heterogonous material is solving by numerical method. This method is suitable for design application of the metamaterial. This method is suitable for specific purposes of detail analysis for design nanomaterial. Analysis propagation of wide THz band signal for $\lambda \in \langle 400;\ 700\ \mathrm{nm} \rangle$ as propagation of electromagnetic waves is very time demanding.

1. INTRODUCTION

In this respect, it is important to mention the fact that illumination designs will be further facilitated by improvements introduced into program design methods. The present study deals with the numerical modeling of lighting systems applying a concrete numerical modeling technique.

Ray-tracing is a realistic imaging technique of monitoring a ray. This method is based on a global illumination model, where we imagine the scene as a set of objects and sources of light. Rays, which propagate between the sources of light and the scene, are determined by the direction, color, and intensity. Some rays hit the objects, and this is where they refract, reflect, and disperse according to their optical properties. The image of the scene is formed by the rays that fall onto the projection surface. The principle of the technique is indicated in Figure 1.

2. ILLUMINATION CALCULATION USING THE RAY-TRACING

The main objective consisted in the three steps that follow, namely the aim was to find an applicable method for the calculation of illumination, to use the method in order to create the numerical model of the selected lighting system, and to verify experimentally the calculation results. Eventually, the method accepted as the most suitable of the described options was the ray-tracing technique, which was used in making the model of a room with two sources of light. The projection of the room is shown in Figure 2.

The numerical model was created in the MatLab program environment. The laws of geometrical optics and computational relations of photometry were applied in performing the calculation. Primarily, the program generates a matrix of points P; through the points there pass the rays. Each ray is assigned a luminance value according to the luminance characteristics of the given lighting unit. After each instance of ray incidence upon the surface, the trajectory magnitude is calculated. The program is capable of recording the maximum of three instances of reflection of each ray.

The results obtained in the numerical model were experimentally verified. With the help of an illuminometer, the measurement was performed of the stratification of illumination intensity **E**.

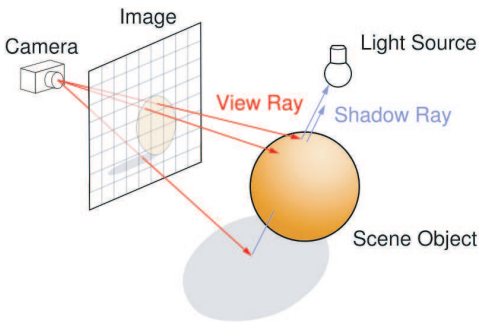

Figure 1: Ray-tracing [6].

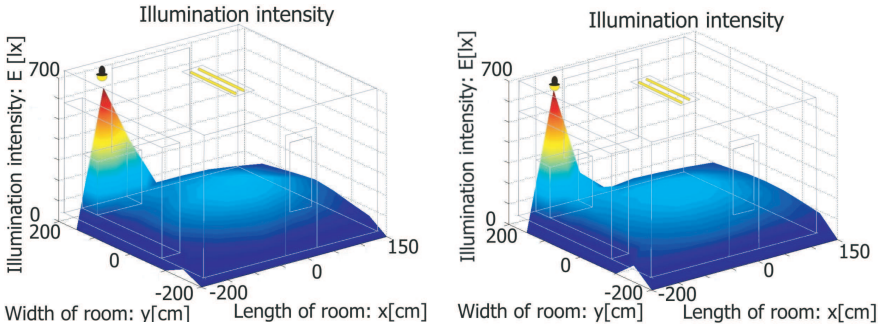

Figure 2: (a) Calculated values and (b) measured values of illumination intensities **E** [lx].

The measured values did not feature any essential differences, therefore it was not necessary to perform any additional measuring in view of the eight instances referred to. Figures 2(a) and (b) shows the comparison between the measured and the calculated values of illumination intensity.

3. UTILIZATION OF ELECTROMAGNETIC WAVES IN DESIGN OF LIGHTING

The numerical model was created in the MatLab program environment. The laws of geometrical optics and electromagnetic waves were applied in performing the calculation. The numerical model is capable of recording any amount of reflection of each ray. Generally, record of six reflections is sufficient amount of reflection for sufficient exact results. Reflection is possible on several layers. The reflection is calculated accordance with Snell's law for electromagnetic waves. The reflection and refraction are shown in Figure 3.

Form of Snell's law is

$$\frac{\sin\theta_0}{\sin\theta_2} = \frac{\mathbf{k}_2}{\mathbf{k}_1}, \tag{1}$$

where **k** is wave number

$$\mathbf{k} = \sqrt{j\omega\mu\cdot(\gamma + j\omega\varepsilon)}, \tag{2}$$

where γ is conductivity, ε permittivity and μ permeability. Relation (1) is defining for boundary line between dielectrics medium. Generally $\mathbf{k}_1$ and $\mathbf{k}_2$ is complex, then angle θ_2 is complex. Propagation of light as electromagnetic wave is understanding as propagation electric field strength and magnetic field strength. Electric component incident wave according to Figure 3 is according to formula:

$$\mathbf{E}_i = \mathbf{E}_0 e^{-jk_1\,\mathbf{u}_{n0}\cdot\mathbf{r}}, \tag{3}$$

where $\mathbf{E}_0$ is amplitude electric field strength on boundary line, **r** is positional vector and $\mathbf{un}_0$ is unit vector of direction of propagation.

Intensity of reflection rays and intensity of refraction rays are declared according to formula

$$\mathbf{E}_r = \mathbf{E}_1 e^{-j\mathbf{k}_1\vec{u}_{n1}\cdot\vec{r}}, \quad \mathbf{E}_t = \mathbf{E}_2 e^{-j\mathbf{k}_2\vec{u}_{n2}\cdot\vec{r}}, \tag{4}$$

where $\mathbf{E}_1$ is calculated from intensity on boundary line $\mathbf{E}_0$ and reflection coefficient $\rho_\mathbf{E}$ and $\mathbf{E}_2$ is calculated from intensity on boundary line $\mathbf{E}_0$ and transmission factor $\tau_\mathbf{E}$:

$$\mathbf{E}_1 = \rho_\mathbf{E}\cdot\mathbf{E}_0, \quad \mathbf{E}_2 = \tau_\mathbf{E}\cdot\mathbf{E}_0. \tag{5}$$

Calculation of reflection coefficient $\rho_\mathbf{E}$ and transmission factor $\tau_\mathbf{E}$ is according to these relations:

$$\rho_\mathbf{E} = \frac{\mathbf{E}_1}{\mathbf{E}_0} = \frac{\mathbf{Z}_{v2}\cos\theta_1 - \mathbf{Z}_{v1}\cos\theta_2}{\mathbf{Z}_{v2}\cos\theta_1 + \mathbf{Z}_{v1}\cos\theta_2}, \tag{6}$$

$$\tau_\mathbf{E} = \frac{\mathbf{E}_2}{\mathbf{E}_0} = \frac{2\mathbf{Z}_{v2}\cos\theta_1}{\mathbf{Z}_{v2}\cos\theta_1 + \mathbf{Z}_{v1}\cos\theta_2}. \tag{7}$$

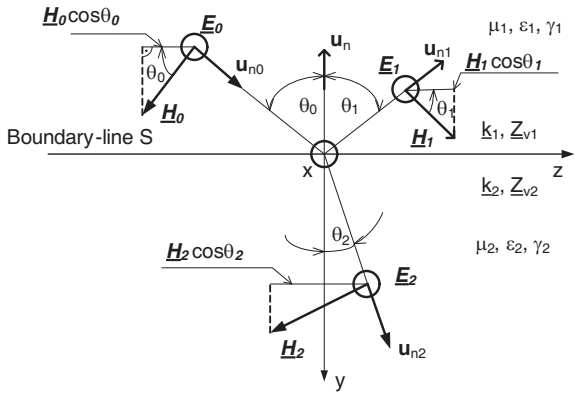

Figure 3: The reflection and refraction of light [1].

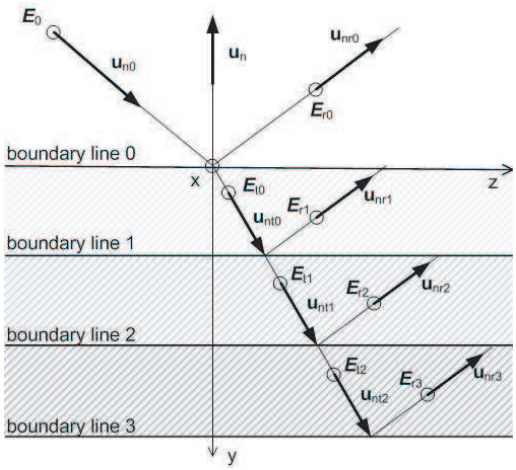

Figure 4: Layered heterogenous material.

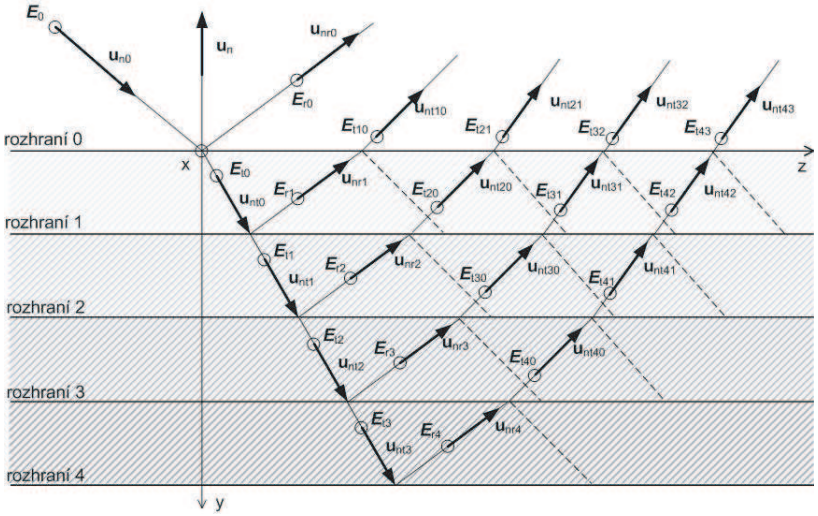

Figure 5: Reflection of wave on surface layered heterogenous material.

For numerical modeling is suitable relation in form

$$\mathbf{E}_r = \frac{\mu_2\mathbf{k}_1\cos\theta_0 - \mu_1\sqrt{\mathbf{k}_2^2 - \mathbf{k}_1^2\sin^2\theta_0}}{\mu_2\mathbf{k}_1\cos\theta_0 + \mu_1\sqrt{\mathbf{k}_2^2 - \mathbf{k}_1^2\sin^2\theta_0}}\mathbf{E}_0\cdot e^{-j\mathbf{k}_1\,\mathbf{u}_{n1}\cdot\mathbf{r}}, \tag{8}$$

$$\mathbf{E}_t = \frac{2\mu_2\mathbf{k}_1\cos\theta_0}{\mu_2\mathbf{k}_1\cos\theta_0 + \mu_1\sqrt{\mathbf{k}_2^2 - \mathbf{k}_1^2\sin^2\theta_0}}\mathbf{E}_0\cdot e^{-j\mathbf{k}_2\,\mathbf{u}_{n2}\cdot\mathbf{r}}. \tag{9}$$

These relations are calculation from basic variable and then speed up the calculation.

Interpretation of Fresnel relations and Snell laws is simple in case of refraction on boundary line between dielectrics medium. In case of refraction in losing medium is angle θ_2 complex. According to relation (1) angle θ_2 depends on wave numbers $\mathbf{k}_1$ a $\mathbf{k}_2$, which are generally complex, then in medium 2 is propagated inhomogeneous wave.

For layered heterogeneous medium is deduced algorithm for reflection on several layers. Reflection and refraction on heterogonous material is solving by numerical method. Layered material is shown in Figure 4. Reflection on n layers generates n primary electromagnetic waves (in Figure 5. wave reflected on 5 layers generates 5 wave on surface). Interpretation of propagation o electromagnetic waves on layered heterogeneous medium is according to relation:

$$\mathbf{E}_{rl} = \mathbf{E}_{il}\rho_{El}\cdot e^{-j\mathbf{k}_{(l+1)}\,\mathbf{u}_{nrl}\cdot\mathbf{r}_l}, \tag{10}$$

$$\mathbf{E}_{tl} = \mathbf{E}_{il}\tau_{El}\cdot e^{-j\mathbf{k}_{(l+2)}\,\mathbf{u}_{ntl}\cdot\mathbf{r}_l}, \tag{11}$$

where $\mathbf{E}_{rl}$ a $\mathbf{E}_{tl}$ are reflection and refraction electromagnetic waves on boundary line ($l = 0, \ldots,$ max) according to Figure 4, $\mathbf{E}_{il}$ is amplitude electric field strength on boundary line l, ρ_{El} a τ_{El} are reflection coefficient and transmission factor on boundary line l, $\mathbf{k}_l$ is wave number of layer, $\mathbf{r}_l$ is positional vector of electromagnetic wave on boundary line l a $\mathbf{u}_{ntl}$ a $\mathbf{u}_{nrl}$ are unit vectors of direction of propagation.

4. CONCLUSIONS

The results obtained by numerical modeling applying the ray-tracing method were verified by means of an experimental measurement. As indicated in Figure 2, shape conformity was reached between the results obtained by calculation (Figure 2(a)) and the measurement results (Figure 2(b)). The ray-tracing method was proved to be a method applicable in practice for the verification of illumination designs. The method renders a very precise representation of illumination intensity distribution on the floor of a room.

Calculation of improving model, which calculate propagation of light as propagation of electromagnetic waves is very time demanding. This method is suitable for specific purposes of detail analysis.

ACKNOWLEDGMENT

The research described in the paper was financially supported by the research programs MSM 0021630516 and research plan MSM 0021630513.

REFERENCES

1. Dedek, L. and J. Dedková, *Elektromagnetismus*, Vol. 2, 232, Brno, VITIUM, 2000.
2. Moss, C., *Numerical Metods for Electromagnetic Wave Propagation and Scattering in Comlex Media*, 240, 2004. Available from http://portal.acm.org/citation.cfm?id=1023429.
3. Stratton, J. A., *Teorie Elektromagnetického Pole*, STNL, Praha, 1961.
4. Zhang, J. J., J. T. Huangfu, Y. Luo, H. S. Chen, J. A. Kong, and B.-I. Wu, "Cloak changing with background," *PIERS Online*, Vol. 4, No. 5, 596–600, 2008.
5. Fiala, P., "Finite element method analysis of a magnetic field inside a microwave pulsed generator," *2nd European Symposium on Non-Lethal Weapons*, Ettlingen, SRN, May 13–15, 2003.
6. Wikiknihy: *Raytracing* [online]. 15. 12. 2008 [cit. 2009-03-03]. Available from http://cs.wikibooks.org/wiki/Raytracing.

A Numerical Simulation Study of the Effect of Array Shape on the Performance of Antennas

Danoosh Davoodi and Shahin Sharifzad
Sadjad Instate of Higher Education, Mashhad, Iran

Abstract— A single-element antenna is usually not enough to achieve technical needs. That happens because its performance is limited. A set of discrete elements, which constitute an antenna array, offers the solution to the transmission and/or reception of electromagnetic energy. The geometry and the type of elements characterize an antenna array. This paper presents a comprehensive study on the performance of a half- wave length dipole antenna standalone and in various types of arrays. The dipole antenna length is 150 mm. All the simulations are done for three deferent distances between the antennas ($d = \lambda/10, \lambda/4, \lambda/2$). All antennas are excited with a 50 Ω microstrip feed line. Number of antenna elements in each array is 10. Radiation patterns and VSWR of this antenna are computed for standalone antenna as well as each array. In addition, radiation efficiencies, gain, directivity of the antennas are discussed. All numerical simulations are performed using the Ansoft HFSS software.

1. INTRODUCTION

Antennas have become ubiquitous devices and occupy a salient position in wireless systems. Radio and TV as well as satellite and new generation mobile communications have experienced the largest growth among industry systems. Every wireless communication network requires its specific sets of antenna characters such as: directivity, gain etc. Single element antennas commonly fail to fulfill network requirement in terms of transmitted and received power at station terminals. Combining several single antenna elements in an array can be a possible solution. An antenna array is a group of isotropic radiators such that the currents running through them might be of different amplitudes and phases in order to produce certain radiation pattern. This is due to the so called array factor. This factor quantifies the effect of combining radiating elements in an array without the element specific radiation pattern taken into account. The overall radiation pattern of an array is determined by this array factor combined with the radiation pattern of the antenna element. The array radiation pattern depends on series of factors, number of elements, the element spacing, amplitude and phase of the applied signal to each element [1].

In this paper the objective is, to study the effect of element spacing on the above mentioned characteristics. There are a few different general types of antenna arrays. When the array is arranged in a straight line this is called a linear array (1D). Antennas arranged in parallel lines on one plane are called planner arrays (2D). Arrays consisting of many planes of antennas results in a conformal array (3D) [2].

Three antenna arrays are investigated in this paper. Each consists of 10 half-wavelength dipole elements. VSWR of elements are further discussed. In addition radiation patterns, radiation efficiencies, directivity and gain of arrays are presented. All numerical simulations are performed using the Ansoft HFSS v10.

2. HALF-WAVELENGTH DIPOLE ANTENNA

The simulated antenna is a half-wavelength dipole radiating at 1 GHz. The radiating elements are 75 mm in length consisting of two parts. Material used for simulating the radiating element is copper ($\varepsilon_r = 1$, $\sigma = 58000000$). Fig. 1 illustrates the geometry of the antenna and its associating microstrip feed line.

3. SIMULATED ARRAYS

All simulations were performed at 1 GHz ($\lambda = 300$ mm). In order to demonstrate element spacing influence on the array's radiation pattern, directivity, gain etc, each array type were examined with three configuration of the distance between elements ($d = \lambda/10, \lambda/4, \lambda/2$).

Three different array types were investigated in this paper: 1. Linear (1D), tripod (2D) and circular (2D). Fig. 2 depicts three array types.

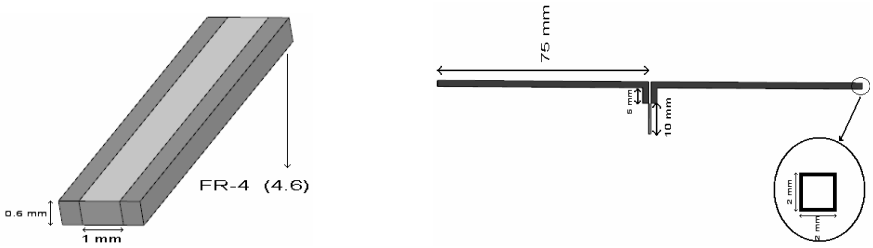

Figure 1: Antenna and the microstrip feed line.

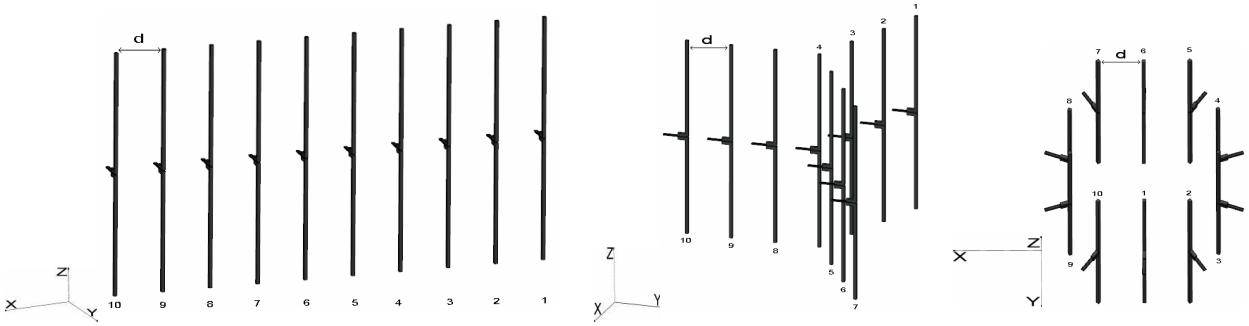

Figure 2: Simulated arrays and element numbers. (a) Linear. (b) Tripod. (c) Circular.

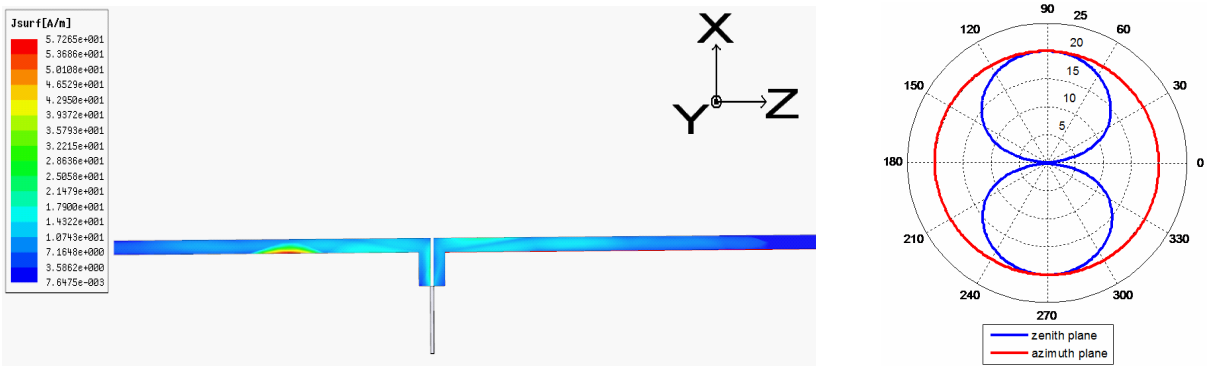

Figure 3: (a) Distribution of current on the radiating element. (b) Radiation patterns.

4. VALIDATION OF THE HALF-WAVELENGTH DIPOLE ANTENNA

In order to achieve the best performance for the dingle element antenna, as well as an acceptable tuning condition of the radiating element and feed line, the antenna was examined and the following results were obtained: (1 GHz).

VSWR = 1.41 : 1, Radiation Efficiency = 98.79%, Peak Directivity = 1.7759, Peak Gain = 1.8077.

Figure 3 presents distribution of current on the antenna and radiation patterns in azimuth and zenith planes.

5. SIMULATION RESULTS

In this paper, all the simulations performed using Finite Element Method based on Ansoft HFSS v10. In this section, antenna properties mentioned earlier are discussed under various situations.

All the elements were excited with 1W in the input of the microstrip feed line.

5.1. VSWR

The amount of power delivered to the antenna strongly depends on the voltage standing ratio (VSWR) between the feed line and antenna input. Values of VSWR for each element obtained from simulation in frequency range between 0.95–1.05 GHz is gathered in Table 1.

Table 1: Maximum and Minimum of VSWR (0.95–1.05 GHz). (a) Linear. (b) Tripod. (c) Circular.

(a)

D \ N		1	2	3	4	5	6	7	8	9	10
$\lambda/2$	Min	1.462	1.529	1.542	1.537	1.544	1.558	1.557	1.543	1.519	1.423
	Max	1.963	1.983	1.999	2.008	1.980	2.011	2.0.24	2.006	1.978	1.955
$\lambda/4$	Min	1.145	1.230	1.174	1.175	1.185	1.191	1.164	1.190	1.208	1.147
	Max	2.249	3.191	3.125	3.122	3.124	3.124	3.066	3.101	3.129	2.242
$\lambda/10$	Min	1.292	2.115	2.058	1.944	1.974	1.983	1.960	2.071	2.098	1.310
	Max	2.442	3.746	3.596	3.300	3.449	3.467	3.265	3.595	3.736	2.412

(b)

D \ N		1	2	3	4	5	6	7	8	9	10
$\lambda/2$	Min	1.588	1.589	1.675	1.470	1.649	1.617	1.614	1.664	1.591	1.581
	Max	2.003	2.020	1.994	2.489	1.944	2.071	2.021	1.988	2.020	2.107
$\lambda/4$	Min	1.158	1.162	1.051	1.333	1.070	1.163	1.164	1.094	1.142	1.157
	Max	2.121	2.781	2.650	3.585	2.676	2.793	2.120	2.697	2.765	2.103
$\lambda/10$	Min	1.277	1.904	2.323	2.385	2.323	1.936	1.275	2.363	1.906	1.285
	Max	2.632	3.398	3.963	3.981	3.886	3.419	2.608	3.940	3.355	2.664

(c)

D \ N		1	2	3	4	5	6	7	8	9	10
$\lambda/2$	Min	1.644	1.652	1.639	1.660	1.685	1.650	1.684	1.652	1.638	1.620
	Max	1.983	1.971	1.958	1.976	2.001	1.954	2.003	1.970	1.963	1.955
$\lambda/4$	Min	1.183	1.177	1.173	1.114	1.106	1.095	1.162	1.075	1.092	1.111
	Max	2.747	2.797	2.790	2.785	2.826	2.788	2.817	2.756	2.766	2.799
$\lambda/10$	Min	2.268	1.803	1.963	1.994	1.818	2.230	1.814	1.905	1.930	1.803
	Max	3.910	3.298	3.262	3.282	3.243	3.974	3.289	3.264	3.354	3.276

The above numbers indicate quality of matching between the feed line and antenna input. Greater values of VSWR results in a decrement of delivered power to the antenna. Furthermore these numbers can be interpreted as Z-parameter of the antenna as long as the impedance of the feed line, excitation port and the incident wave are known. For instance a VSWR of $1.462:1$ shows that the Z-parameter of the antenna is closer to the feed line than that of a $1.963:1$.

5.2. Radiation Patterns

Figure 4 shows the total-power radiation patterns of the arrays. Radiation patterns are plotted in zenith ($\varphi = 90°$) and azimuth ($\theta = 90°$) planes at 1 GHz.

Table 2: HPBW in the azimuth plane ($\theta = 90°$).

D \ Array	Linear	Tripod	Circular
$\lambda/2$	10.5°	-	-
$\lambda/4$	19.8°	29.2°	-
$\lambda/10$	46.1°	107°	-

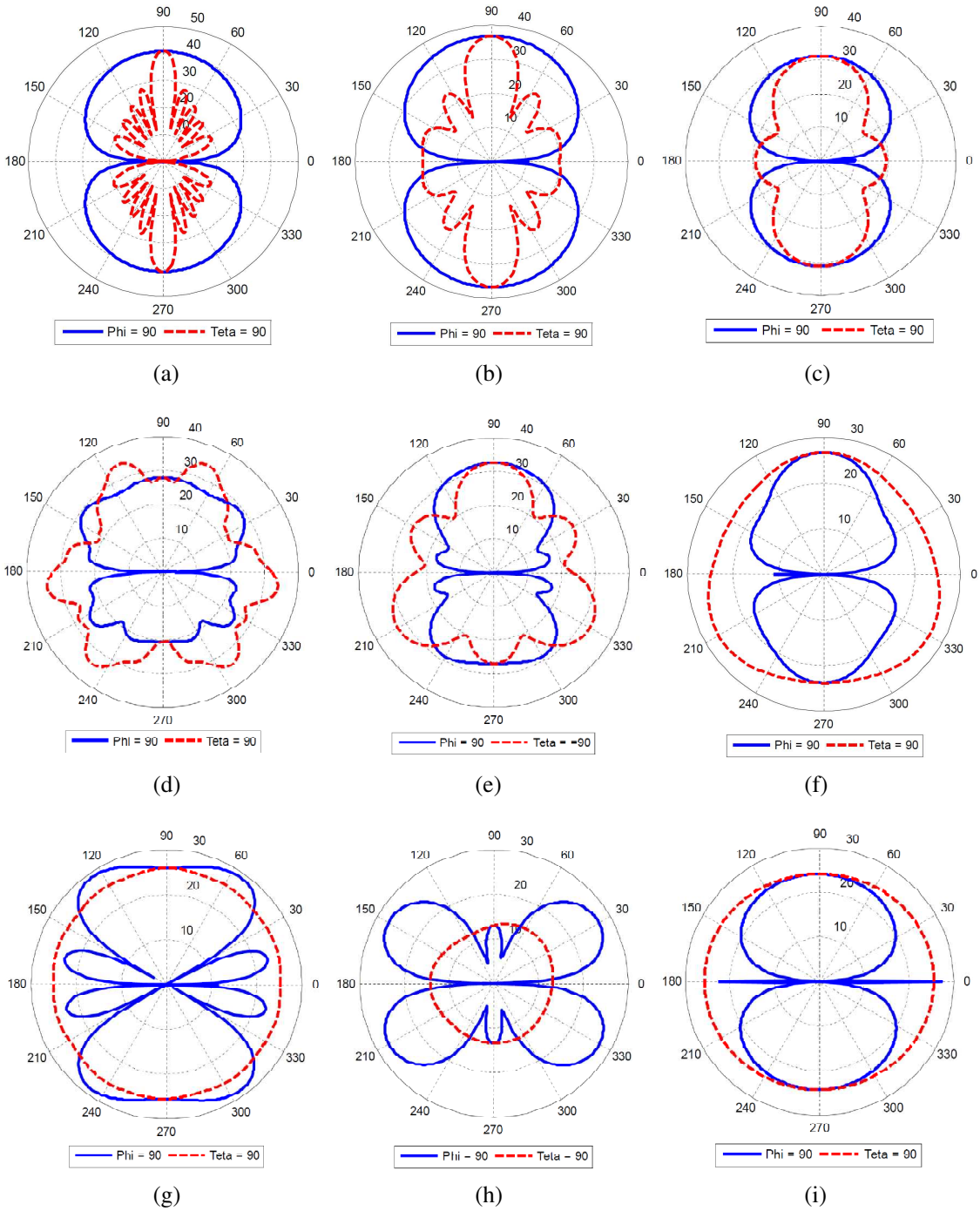

Figure 4: Radiation patterns. (a), (b) and (c) linear array. (d) , (e) and (f) tripod array. (g), (h) and (i) circular array. (a), (d) and (g) for $d = \lambda/2$. (b), (e) and (h) for $d = \lambda/4$. (c), (f) and (i) for $d = \lambda/10$.

Half power bandwidths (HPBW) of arrays are presented in Table 2. These values are computed in the azimuth plane. Decrement of radiated power in circular array did not reach the margin of 3 dB.

5.3. Radiation Efficiency and Directivity

Directivity and radiation efficiency, as mentioned before, are major aspects of antenna's radiation characteristics that could be improved by implementation of array instead of a single element antenna. Fig. 5 illustrates directivity of simulated arrays obtained in 0.95–1.05 GHz frequency range.

Figure 6 presents the calculated radiation efficiencies for each array.

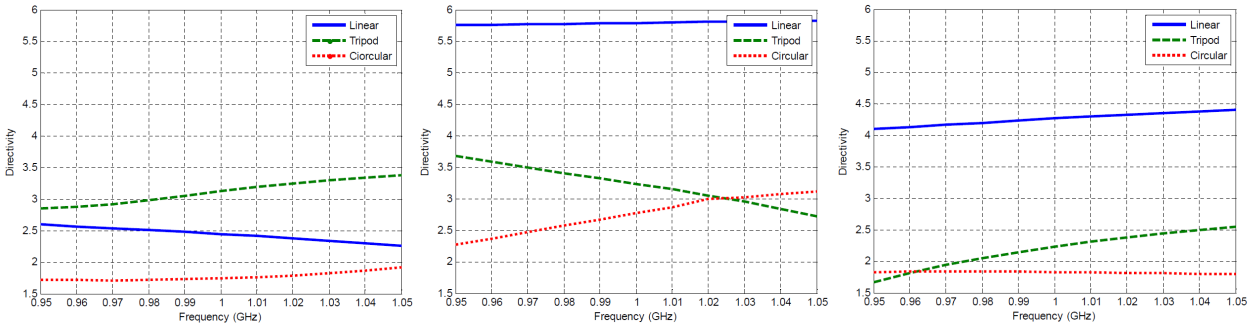

Figure 5: Directivity. (a) $d = \lambda/2$, (b) $d = \lambda/4$, (c) $d = \lambda/10$.

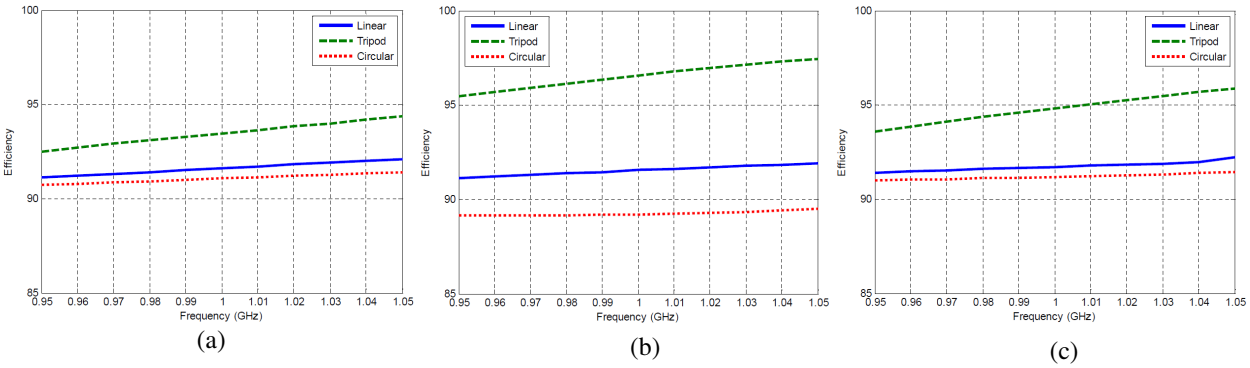

Figure 6: Radiation efficiency. (a) $d = \lambda/2$, (b) $d = \lambda/4$, (c) $d = \lambda/10$.

6. CONCLUSION

From what have been presented in this paper in can be concluded that, implementation of antenna arrays in wireless communication networks is truly an adequate technique to meet the required characteristics, especially in the field of EM radiated power. Results produced in this paper indicate that, overall array configuration regardless of the spacing factor, is the most influential parameter in shaping the radiation pattern. The spacing factor between the elements results in significant changes in radiation pattern main and side lobes associated with variations of array pattern directivity and gain. However, it seemed to be a much more ineffective factor in array's pattern shape than that of the array configuration.

REFERENCES

1. Balanis, C. A., *Antenna Theory*, 2nd Edition, Wiley, 1997.
2. Josefsson, L. and P. Persson, "Mutual coupling investigations on cylindrical array antennas," *AP2000*, Davos, Switzerland, April 2000.

Analysis of Electromagnetic Field Affected by Liquid in Water Area Magnetotelluric Exploration

Ling-Hua Xu[1], **Jian-Xin Liu**[1], **Jian-Rong Xu**[2], **Zhen-Wei Guo**[1], **Ya Sun**[1], **and Xiao-Zhong Tong**[1]

[1]School of Info-physics Geomatics Engineering, Central South University, Changsha 410083, China
[2]Team 814, East China Bureau of Noneferometal Geological Exploration, Zhenjiang 212005, China

Abstract— By studying the relation of electromagnetic fields and impedance of sill like medium between water surface and water floor, we have gained the attenuated coefficient and the attenuation law of electromagnetic fields in water area. It is obvious that the signals are attenuated worse when the frequency increases, but the liquid attenuation characters upon electric field and magnetic field are different. First, the attenuation amplitude of magnetic field is far greater than electric field in same condition, and the frequency range is wider. Second, the attenuation of electric field not only lies on mostly the character of liquid self (the depth and resistivity of liquid), but also on the media property below the water, that is, the higher the resistivity is the more severe the attenuation of the magnetic field, the attenuation of magnetic field relates to the characters of liquid medium. The condition in which the water effect can be neglected in water magnetotelluric sounding (MT) exploration of electromagnetic signal sampling is as follows: The water depth is less than 3 m in MT and 2 m in CSAMT.

1. INTRODUCTION

The waters of magnetotelluric sounding (MT) referred to the exploration of MT in the ocean and inland waters (lakes, ponds, rivers and even the northern ice field in winter). MT in marine exploration, electric and magnetic signal acquisition device were lay in the seabed, and the exploration results were only the electricity characteristics of following seabed medium, the water did not affect the result, which was its principle [1, 2]. However, because of ocean water attenuated the electromagnetic signals, which made the weak natural electromagnetic field signal become very weak, therefore, the apparatus should not only consider the water-proof, resistance problem, also consider the sensitivity of signal acquisition apparatus, and therefore it was great significance for studying the water attenuation of electromagnetic signals [3, 4]. When the MT explored in the inland waters or a part of the measuring point of exploration projects in the waters, the electrode was laid on at the bottom of seabed and the magnetic field was laid on the land, and we collected their signal separately. That was the electromagnetic signal separation Acquisition method [5]. Because of the Collected electromagnetic signal was not on the same interface, the measured results would be affected by the liquid, therefore, the impact of the law as well as correction method were studied.

2. ELECTROMAGNETIC FIELD

As shown in Figure 1, the electromagnetic field of a layer (i) in the level of layered media is [6, 7]:

$$\begin{cases} E_x = A_i e^{jk_i z} + B_i e^{-jk_i z} \\ H_y = \dfrac{1}{z_i}\left(A_i e^{jk_i z} - B_i e^{-jk_i z}\right) \end{cases} \tag{1}$$

where $k_i = \sqrt{j\omega\mu\sigma}$; $j = \sqrt{-1}$; ω is angular frequency, and $\mu = 4\pi \times 10^{-7}$ H/m; σ is conductivity of the ith layer; $z_i = \frac{\mu\omega}{k_i}$; $z_{i-1} \le z \le z_i$; A_i and B_i were undetermined coefficient.

By the formula (1), we could give the solution of A_i and B_i as follows:

$$\begin{cases} A_i = \dfrac{1}{Z_i}\left(E_x + Z_i H_y\right) e^{-jk_i z} \\ B_i = \dfrac{1}{Z_i}\left(E_x - Z_i H_y\right) e^{jk_i z} \end{cases} \tag{2}$$

E_x^i and H_y^i were the electromagnetic field of the ith layers at the end of interface, E_x^{i0} and H_y^{i0} were the electromagnetic field of the ith layers on the top of interface. We could obtain from the

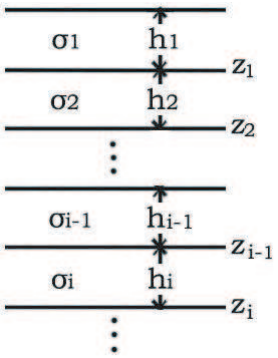

Figure 1: Horizontal layer model.

formula (2):

$$\begin{cases} E_x^{(i)} + Z_i H_y^{(i)} = \left(E_x^{(i0)} + Z_i H_y^{(i0)}\right) e^{jk_i h_i} \\ E_x^{(i)} - Z_i H_y^{(i)} = \left(E_x^{(i0)} - Z_i H_y^{(i0)}\right) e^{-jk_i h_i} \end{cases} \tag{3}$$

For the electromagnetic field on the tangential border was continuity, so the following boundary conditions were:

$$\begin{cases} E_x^{(i0)} = E_x^{(i-1)} \\ H_y^{(i0)} = H_y^{(i-1)} \end{cases} \tag{4}$$

The water media was the first layer ($i = 1$) in water area MT exploration, then the formula (3) and (4) would be:

$$\begin{cases} E_x^{(i)} + Z_i H_y^{(i)} = \left(E_x^{(i-1)} + Z_i H_y^{(i-1)}\right) e^{jk_i h_i} \\ E_x^{(i)} - Z_i H_y^{(i)} = \left(E_x^{(i-1)} - Z_i H_y^{(i-1)}\right) e^{-jk_i h_i} \end{cases} \tag{5}$$

In here: h_1 was water depth E_x^i and H_y^i were the electromagnetic field at the end of interface, E_x^{i0} and H_y^{i0} were the electromagnetic field on the top of interface. The relationship of electromagnetic fields between interface and the bottom was given by formula (5).

3. ELECTROMAGNETIC FIELD IN WATER

Due to the medium absorption in the spread from the surface to the bottom, the electromagnetic fields would be attenuated. The attenuation coefficient for C_E and C_H of electric and magnetic fields were defined as:

$$\begin{cases} E_x^{(1)} + Z_1 H_y^{(1)} = \left(E_x^{(0)} + Z_1 H_y^{(0)}\right) e^{jk_1 h_1} \\ E_x^{(1)} - Z_1 H_y^{(1)} = \left(E_x^{(0)} - Z_1 H_y^{(0)}\right) e^{-jk_1 h_1} \end{cases} \tag{6}$$

or

$$\begin{cases} E_x^{(0)} + Z_1 H_y^{(0)} = \left(E_x^{(1)} + Z_1 H_y^{(1)}\right) e^{-jk_1 h_1} \\ E_x^{(0)} - Z_1 H_y^{(0)} = \left(E_x^{(1)} - Z_1 H_y^{(1)}\right) e^{jk_1 h_1} \end{cases} \tag{7}$$

To divide E_x^0 on both sides of Equation (6), then the two formulas (6) and (7) were added, we would obtain:

$$C_E = ch(jk_1 h_1) + \frac{Z_1}{Z^{(0)}} sh(jk_1 h_1) \tag{8}$$

At the same, we would obtain:

$$C_H = ch(jk_1h_1) + \frac{z^{(0)}}{z_1} sh(jk_1h_1) \tag{9}$$

Now the characteristics of their decay would be studied by the test of theoretical model in following. M_1 model was designed for the 4 layers media, the parameters of every layer as follows: $\rho_1 = 0.25\,\Omega{\cdot}$m, $h_1 = 30\,$m; $\rho_2 = 100\,\Omega{\cdot}$m, $h_2 = 500\,$m; $\rho_3 = 10\,\Omega{\cdot}$m, $h_3 = 1000\,$m; $\rho_4 = 100\,\Omega{\cdot}$m. The first layer was the simulation of the liquid (water), $\rho_1 = 0.25\,\Omega{\cdot}$ m, $h = 30\,$m.

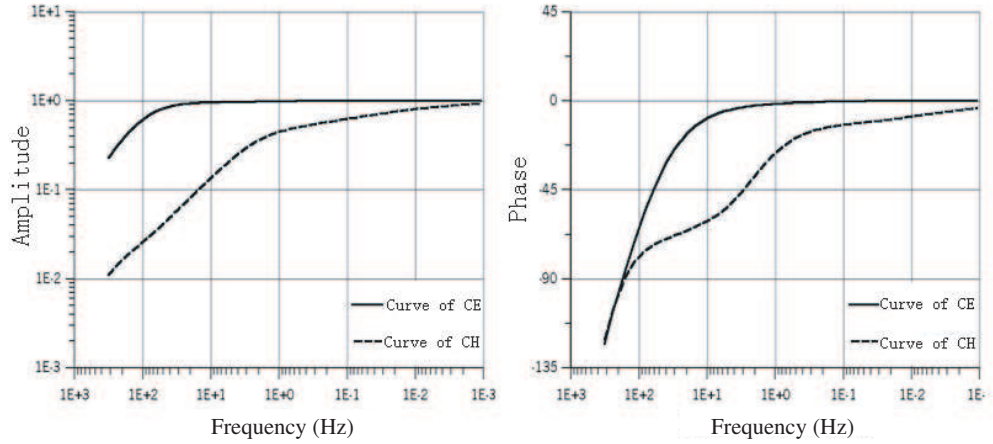

Figure 2: Attenuated coefficient curve of electromagnetic fields.

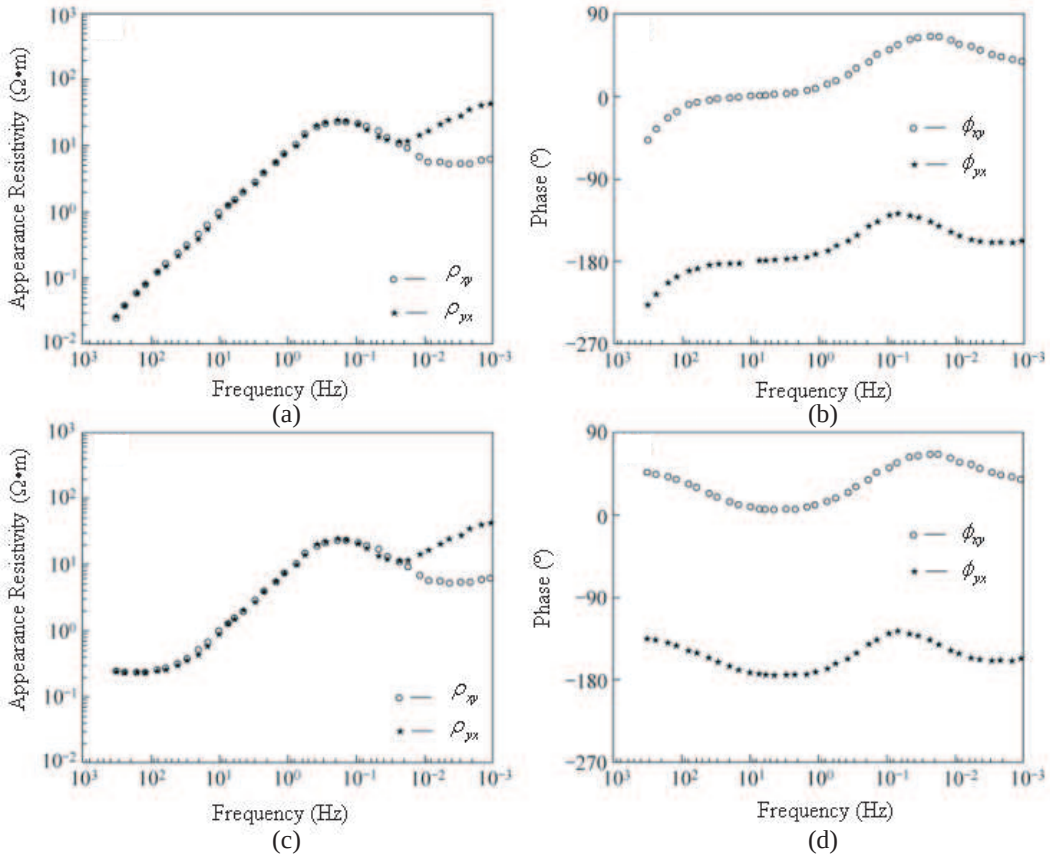

Figure 3: The correcting results of the field data. (a) xy-mode apparent resistivity, (b) xy-mode phase, (c) yx-mode apparent resistivity, (d) yx-mode phase.

Firstly, the impedance function $z^{(0)}$ of this model was calculated [8], the frequency characteristics of the attenuation coefficient of electromagnetic field, including amplitude and phase, can be obtained under the model conditions, which were shown in Figure 2.

4. THE FIELD DATA CORRETION

In Figure 3, there is an example of turning raw data into water surface data. The sites, 30 km off the bank, locate in South Sea, LeiQiong District of GuanDong province, China. The depth and resistivity of water is 23 m, 0.25, separately. After Remote Reference and Removing Noise of data, we estimate impedance tensor with ROBUST, and calculate apparent resistivity and phase. The raw apparent resistivity of high frequency is near 0.02 and the impedance phase is lagging almost 90 due to the attenuation of seawater to electric field. After correcting, the main change is happened in high frequency: The first apparent resistivity is recovered to 0.25 in accordance with seawater's apparent resistivity; the impedance phase is changed to 45 or -135, which is normal to MT curve.

It is inaccessible to achieve underwater apparent resistivity and phase with correcting for the precision of raw data is low. The waters refers not only oceans, and lakes, rivers and pools. The latter is shallow with high resistivity. The attenuation of electric field is weak comparing to ocean. The error of high frequency data in MT is 5%, which means if the inaccuracy of apparent resistivity caused by water is less than 5%, we should not consider that. From the relation between apparent resistivity and impedance, the attenuation coefficient of electric field must not less than 0.975 to let the inaccuracy of apparent resistivity less than 5%.

5. CONCLUSION

We deduce the equation of attenuation coefficient of electromagnetic field in the sea bed through studying the relation of electromagnetic field's function of upper and nether interface of water. Water is more influential to magnetic field than to electric field. The decrease of electric field is mainly depended on water's resistivity and depth, while the magnetic field's reduction not only has something to do with water's resistivity and depth, and the characteristics of underwater medium. Moreover, the high resistivity of underwater medium, the worse magnetic field we'll get.

ACKNOWLEDGMENT

This work is supported by the National Natural Science Foundation of China (No. 60672032) and the Ministry of Education Doctoral Foundation in China (No. 20070533102).

REFERENCES

1. Cagniard, L., "Basic theory of the magnetotelluric method of geophysical prospecting," *Geophysics*, Vol. 63, No. 4, 605–636, 1953.
2. Chave, A. D., "Electromagnetic induction field in the deep ocean off California: oceanic and ionospheric sources," *Geophys. J. R. Astr. Soc.*, Vol. 77, No. 1, 143–171, 1984.
3. Liu, J.-X. and S.-Y. Zhang, *Magnetotelluric Sounding Progressing in Sea*, Central South University Press, Changsha, 2004.
4. Wei, W.-B., "New advance and prospect of magnetotelluric sounding in China," *Progress in Geophysics*, Vol. 17, No. 1, 245–254, 2002.
5. Li, T.-L., J. Lin, and D.-P. Wang, *The Oceanic and Terrestrial Noise and Shallow Marine Magnetotelluric Study*, Geophysics Press, Beijing, 2001.
6. Kavfman, A. A. and G. V. Keller, "The magnetotelluric sounding method," *Elesiver*, Vol. 18, No. 2, 595–603, 1981.
7. Hermance, J. F. and R. E. Thayer, "The telluric-magnetotelluric method," *Geophysics*, Vol. 40, No. 1, 664–675, 1975.

The Study of Field Source Static Shift in Frequency Domain Controlled-source Electromagnetic Sounding with Long Wire Source

Ya Sun[1], **Zhan-Xiang He**[2], **and Jian-Xin Liu**[1]

[1]The Institute of Info-physics and Geometrics Engineering, Central South University
Changsha, Hunan 410083, China
[2]Graduate Workstation of Geophysical and Geochemical, BGP, Zhuozhou 0727511, China

Abstract— In frequency domain controlled-source electromagnetic sounding with long wire source, the static shift is generated by shallow abnormalities which is placed in the measurement points has been extensively studied and taken good correction. According to reciprocal principle, when the abnormalities is placed in the long wire source, like-static shift will also be existed, and this is called field source static shift. So the law of field source static shift is studied, in this paper, The results, which based on the discipline of the target's size and depth and the simulation of horizontal electric field and it's all time apparent resistivity, states that source effect would change due to the position, size and varying resistivity of abnormality, which is a little different with the static shift of surveying site. Only when the whole source is above the abnormal body, the effect of source is the same as the effect of site.

1. INTRODUCTION

The controlled-source electromagnetic sounding with long wire source in frequency domain have been an important method in geophysical survey since 1970. With it, we had achieved a great many of successful applications in finding deep mine, oil, coal under volcanic or decked, geothermic and engineering surveying [1, 2].

However, many scholars have studied broadly about it since it was proposed and applied, and knew it not only had other electromagnetic methods' shortcomings (e.g., the static shift in MT), which had been researched by many people and they got some ideas about how to suppress them; and it had the specific problems, such as the source effect and additional effect learnt by experts some years ago [3, 4]. But there is a sort of questions which is still unknown. That is when source is above the inhomogeneous body, how can we call it? The source effect or the static shift? According to theory of exchange, we know that there is the same effect as static shift when source is near to abnormalities. So we call it field source static shift.

In this paper, the field source static shift of different situations was studied with 3D integral equation code. The factor and characteristic response of it was discussed by calculating the horizontal electric field and all field apparent resistivity in the position of abnormalities and source, the size and depth of abnormalities and other aspects. Hy, one of the magnetic field components and parallel to the source AB, is suggested for the length of the paper. And other results will be given out in another paper.

2. THE BASIC OF SIMULATED RESEARCH

The team of electromagnetic simulation and inversion, led by Zhdanov of Utah University, deduced some simulation and inversion ways and fulfilled fast simulation of 3D integral equation with different type of sources and under the inhomogeneous background [5–8]. We carried out the research based on former discussion.

Generally speaking, when there are conductive abnormalities near the surface earth, electric current running through it can lead to the accumulation of electric charge in the surface of abnormalities, which produces an additional electric field directly related to the electric current. Furthermore, the result is apparent resistivity of each frequency will get a constant change, compared to the situation without the abnormalities. And the curve of apparent resistivity move upwards or downwards along the axis of apparent resistivity. (The curve move downwards when there is low resistivity abnormality, while the curve moves upwards when there is high resistivity abnormality.) This was called normal static shift. However, there will be an additional electric field when the source is above the inhomogeneous body. The curve of apparent resistivity will have a static displacement, according to theory of exchange. Though the cause of displacement varies, we can call it field source static shift.

For finite-long line resource, the magnetic field Hy in the remote zone is entirely different from it in the near zone. The electric field in the remote zone is mainly radiation, and can be expressed in a simple equation of resistivity and frequency of earth. But the field in the near zone is mainly conduction current, while the transition zone is relatively difficult to obtain all field apparent resistivity defined by electric field. We calculate the all field apparent resistivity by iterative method with double dipole source [14]. The equation of horizontal electric field of all field apparent resistivity with horizontal electric dipole is:

$$H_y = \frac{Idl\rho}{4\pi r^3\sqrt{\mu\omega\sigma}}[\sin^2\varphi(6I_1K_0 + ikr(I_1K_0 - I_0K_1)) - 2\cos^2\varphi I_1K_1]kr \cdot e^{i\frac{\pi}{4}}$$

$$C_H = \frac{Idl}{4\pi r^3\sqrt{\mu\omega\sigma}} \cdot [\sin^2\varphi(6I_1K_0 + ikr(I_1K_0 - I_0K_1)) - 2\cos^2\varphi I_1K_1]kr$$

I is the current intensity, dl is the dipole length.

The long wire source is divided into several electric dipoles to get the all field apparent resistivity with integral equation method, which is:

$$H_y = \sum_{i=1,N}^{N} H_{yi} = \sum_{i=1,N}^{N} C_{Hi} \cdot \rho \quad \text{and we know: } \rho_\omega^{H_y} = \left| \frac{H_y}{\sum\limits_{i=1,N}^{N} C_{Hi}} \right|.$$

3. FIELD SOURCE SIMULATION AND ANALYSIS OF THE STATIC EFFECT

For comprehensive studying of field source static shift effect, the relationship between the field source and the abnormalities is divided into three kinds (for example the Figure 1): Model (1): Field source at one end is located above the abnormalities; Model (2): Sources at both ends across the heterogeneity; Model (3): Source at both ends completely is located above the abnormalities. The resistivity of the half space homogenous is 100 ohm-meter, AB as the line source is laid along the x direction with a length of 2 km, the dance between the sender and receiver is 6 km, the electric current is 1 A, the length of measuring line along the source direction is from -2000 km to 2000 km, Hy amplitude and its all time apparent resistivity are only studied in this paper.

For model 1, Abnormalities can be designed the following several situations, single0 is the half homogenous.

Single1, $200 \times 100 \times 100\,\mathrm{m}^3$, the top of abnormalities' depth is 0 m, and the resistivity is 10 ohm-meter.

Single2, $500 \times 200 \times 100\,\mathrm{m}^3$, the top of abnormalities' depth is 0 m, and the resistivity is 10 ohm-meter.

Single3, $200 \times 100 \times 100\,\mathrm{m}^3$, the top of abnormalities' depth is 0 m, and the resistivity is 1 ohm-meter.

Single-1, $200 \times 100 \times 100\,\mathrm{m}^3$, the top of abnormalities' depth is 300 m, and the resistivity is 10 ohm-meter.

For model 2, Abnormalities can be designed the following several situations, middle0 is the half homogenous.

Middle1, $1000 \times 200 \times 100\,\mathrm{m}^3$, , the top of abnormalities' depth is 0 m, and the resistivity is 10 ohm-meter.

Middle2, $500 \times 200 \times 100\,\mathrm{m}^3$, the top of abnormalities' depth is 0 m, and the resistivity is 10 ohm-meter.

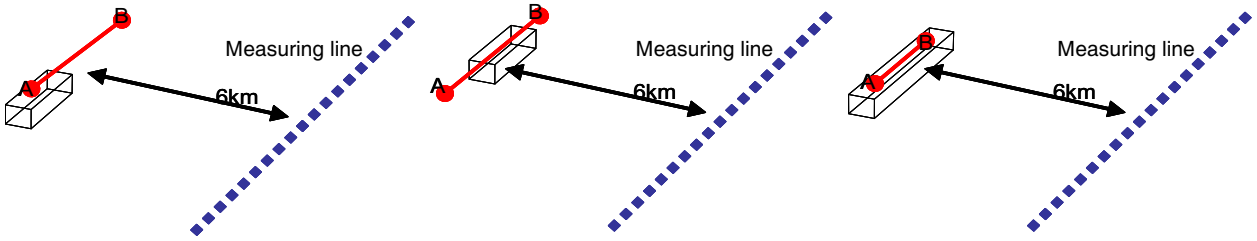

Figure 1: Simulation the basic model of the field source static shift (from the light to right be model1, model2, model3.)

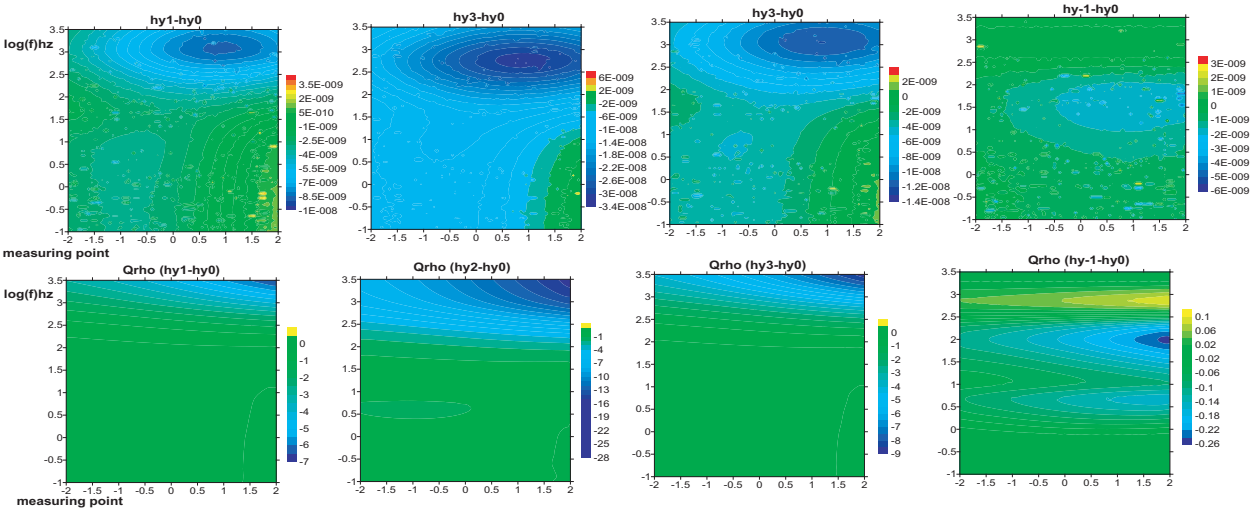

Figure 2: The differential profile between single model and the half homogenous with Hy's amplitude and all time apparent resistivity.

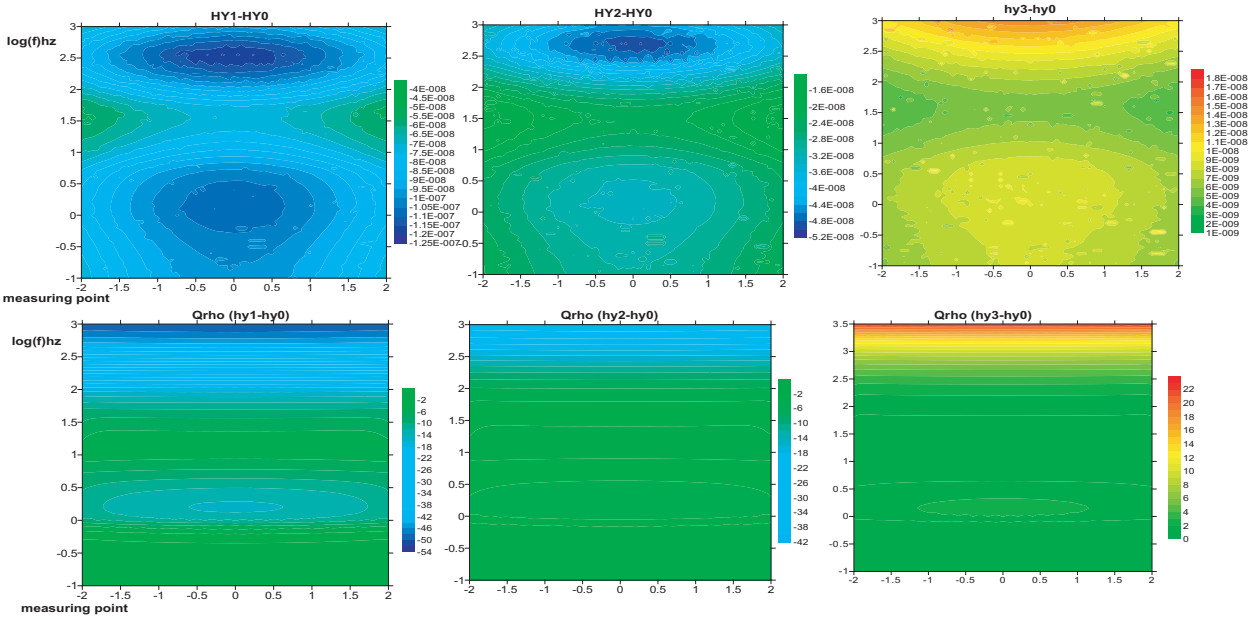

Figure 3: The differential profile between middle model and the half homogenous with Hy's amplitude and all time apparent resistivity.

Middle3, $500 \times 200 \times 100\,\mathrm{m}^3$, the top of abnormalities' depth is 0 m, and the resistivity is 1000 ohm-meter.

For model 3, Abnormalities can be designed the following several situations, cover0 is the half homogenous.

Cover1, $500 \times 200 \times 40\,\mathrm{m}^3$, the top of abnormalities' depth is 0 m, and the resistivity is 10 ohm-meter.

Cover2, $1000 \times 200 \times 40\,\mathrm{m}^3$, the top of abnormalities' depth is 0 m, and the resistivity is 10 ohm-meter.

Cover3, $200 \times 200 \times 40\,\mathrm{m}^3$, the top of abnormalities' depth is 0 m, and the resistivity is 10 ohm-meter.

From the Figure 5, we can obtain the Following:

1) When the abnormalities (low resistivity body) is laid under the field at one end (Figure 5, model 1), the all-time apparent resistivity with the model is the coincided with the homogeneous half-space completely in the low frequency region, only the all-time apparent resistivity decreased by the low resistivity effect in the high-frequency. But obviously, there are differ-

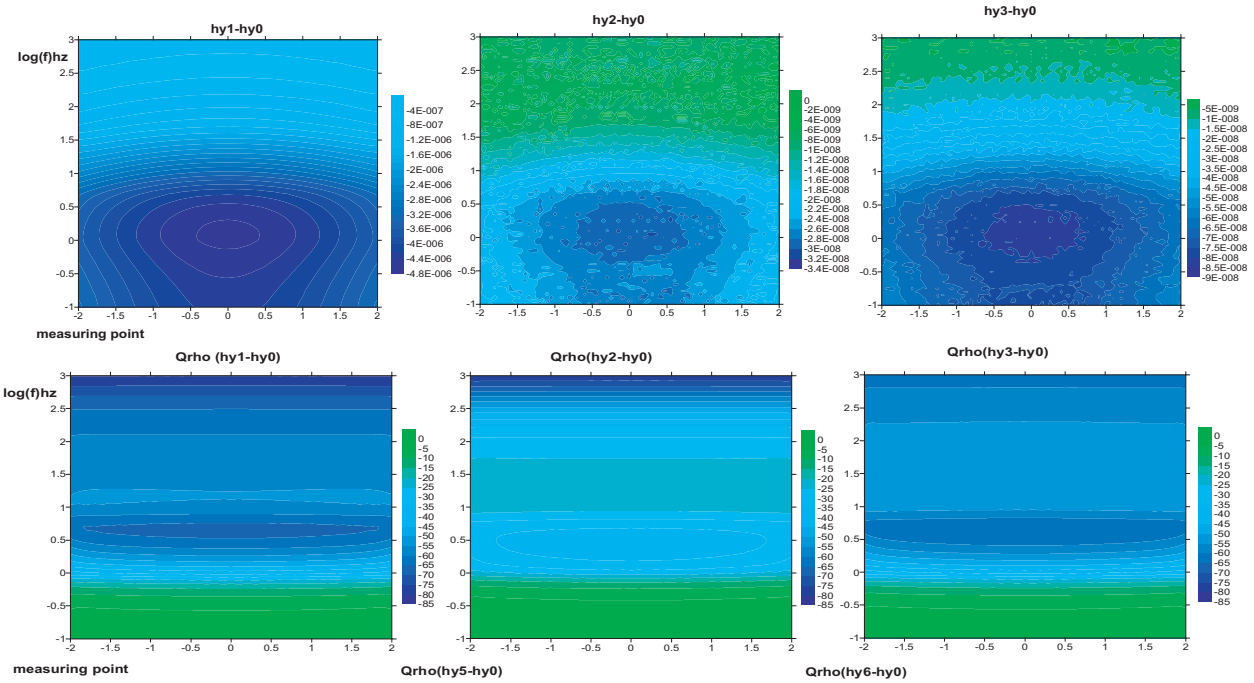

Figure 4: The differential profile between cover model and the half homogenous with Hy's amplitude and all time apparent resistivity.

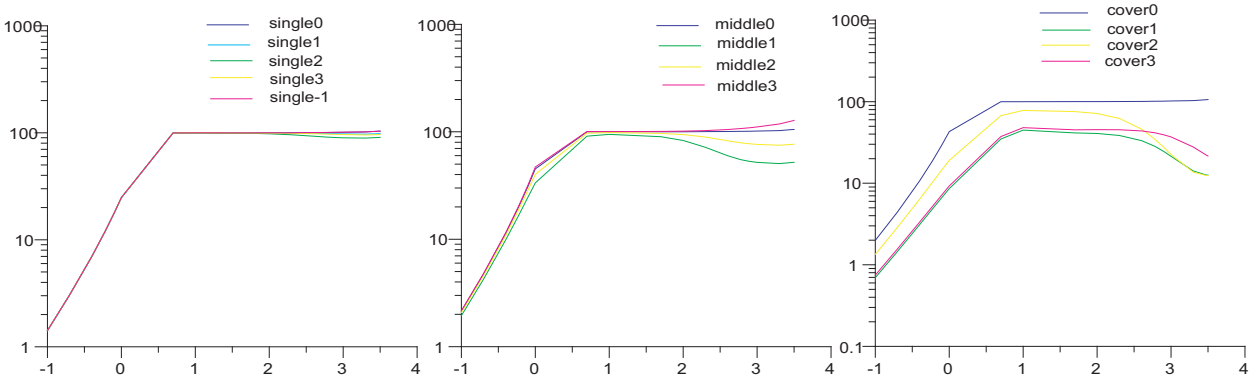

Figure 5: One measuring point map of several models (from the light to right be model1, model2, model3).

ences with the static shift effect, not the entire shift. In the differential cross-section (see Figure 2), the nearest measurement point to abnormalities is affected largest and the effect become smaller with the offset greater, and the a low magnetic anomaly zone is formed corresponds to the low resistivity body in cross-section; and these features can also shown by the magnetic all-time apparent resistivity profiles, but the largest effect in the endpoint of profile, which may be caused by fitting in the calculation of apparent resistivity.

2) When the source crosses the abnormalities (Figure 5, the model2), the magnetic apparent resistivity curve shape of the Middle is same with the homogeneous half-space model, but the value of the middle is lower than the homogenous half-space, which is similar to the static shift effect. Only the effect of abnormalities in the high-frequency is larger than the low frequency, and the calculated apparent resistivity is also having this feature. In the differential profiles (see Figure 3), the nearest measurement point to abnormalities is affected largest and the effect become smaller with the offset greater. The entire low-frequency values of the magnetic apparent resistivity are negative in differential profiles, which indicate there is a static shift. However, this static shift is still different with the tradition static shift.
3) The source is laid under above the abnormalities completely (Figure 5, model3), the magnetic apparent resistivity curve shape of the Middle is same with the homogeneous half-space model,

but the value of the middle is lower than the homogenous half-space, which is similar to the static shift effect. Only the effect of abnormalities in the high-frequency is larger than the low frequency, and the calculated apparent resistivity is also having this feature. This source effect is consistent with the static shift basically. That is to say that only the source is laid above the abnormalities completely, the field source static shift can be.

4. CONCLUSION

The so-called static shift only focused on the influence of abnormalities to electric field, which led to the parallel movement of Cagniard apparent resistivity in loglog coordinate of resistivity and frequency. But the effect of magnetic field was not considered. So the difference of source static shift and traditional static shift is analyzed based on the amplitude of horizontal magnetic field and all field resistivity. We concluded some thoughts as follows:

1) when the abnormalities are comparatively low resistivity with fixed size, the high frequency moves downward. And the lower resistivity of abnormalities we assume the more influential curves we get. However, when the abnormalities are comparatively high resistivity, the high frequency moves upward;
2) when the thickness of abnormalities is constant and the abnormalities enlarge from one side of finite length in the direction of source; the source static effect is wax. When the length of abnormalities is five times about the sources, the effect is largest. But after that, the source static effect is getting smaller in low frequency and bigger in high frequency.
3) when the abnormalities have the fixed size, we will get a smaller influence with enlarging depth of abnormalities. And the effect varies from different position of abnormalities, which suggest the effect is the largest when depth is shallow.

The curves of apparent resistivity differ largely with each other, even the receiver is in the same position. Because the stratum structure and its characteristic below the source is varying. So we should avoid distract the sources in surveying or we should put different sources in places with high-depth floor, simple geology structure and small difference.

REFERENCES

1. Wang, J.-Y., "Review of China's oil exploration and electrical," *Progress in Explore Geophysics*, Vol. 29, No. 2, 77–81.
2. He, Z.-X., "The role of non2seismic techniques in exploration and development of oil and gas," *Petroleum Exploration and Development*, Vol. 28, No. 4, 70–72, 2001.
3. Shi, K.-F., *Controlled Source Audio Frequency Magnetotelluric Theory and Applications*, Science Publish in Beijing, 1999.
4. Ueda, T. and M. S. Zhdanov, "Fast numerical modeling of marine controlled-source electromagnetic data using quasi-liner approximation," *75th Annual International Meeting, SEG, Expanded Abstracts*, 506–509, 2005.
5. Zhdanov, M. S. and S. K. Lee, "Integral equation method for 3D modeling of EM field in complex structures with inhomogeneous background conductivity in marine CSEM applications," *75th Annual Internat SEG Houston. Expanded Abstracts*, 510–513, 2005.
6. Zhdanov, M. S. and W. Le, "Rapid seabed imaging by frequentcy domain EM migrateon," *75th Annual Internat SEG Houston. Expanded Abstracts*, 518–521, 2005.
7. Zhdanov, M. S. and K. Yoshioka, "3D iterative inverseon of the marine CSEM data," *75th Annual Internat SEG Houston. Expanded Abstracts*, 518–521, 2005.
8. Liu, Y., Z.-X. He, and J.-X. Liu, "The calculation of the all time apparent resistivity with horizontal electric field component in the bipolar source," *The 9th International Conference on Electromagnetic*, 1994.

The Physical Modeling Experiments Analysis of the Exploration Depth of Conventional Electric Survey

Jie Li, **Jian-Xin Liu**, **Xiao-Zhong Tong**, **and Zhen-Wei Guo**
School of Info-physics and Geometrics Engineering, Central South University, Changsha, China

Abstract— Conventional electric survey is one of the most important geophysical methods. The chief issue which affects the level and the foreground of application area of the conventional electric survey is the depth of exploration and its resolving power.

Direct current electrical method and dual frequency induced polarization method was used in this text. At first we analyze their exploration ability of these two methods in the theory, and then we analyze the depth of exploration and the resolving power of the conventional electric survey by the experiment which takes place in a tank laboratory with a graphite nodule act as a unconventional object. The experiment is carried on in the tank with 5.0 m in length, 4.0 m in breadth and 2.0 m in depth. The model we used a graphite nodule whose semidiameter is 10 cm and a graphite columniation whose diameter is 10 cm. The equipment we adopted is symmetry quadrupole setting of the electrical sounding method. In the direct current electrical method, we use the DDC-5 to find out the infection to the depth of exploration by changing the AB's polar distance. In the induced polarization method, we use the SQ-3C to find out the infection to the depth of exploration by changing the AB's polar distance, supply current and frequency.

The experimental results indicate that the exploration depth and the resolving power of the direct current electrical method and dual frequency induced polarization method are related with the distance between AB-polar and its shape. In the dual frequency induced polarization method, the supply current and frequency do not influence the exploration ability very much.

1. INTRODUCTION

Conventional electric surveys are used as a common method for hidden defects detection of dams and dikes. With the rapid development of geophysical exploration work, the major problem we face is how to improve the maximum vertical resolution capacity of hidden defects of dams and dikes. In this paper, we analyze the exploration ability of the direct current electrical method and dual frequency induced polarization method [1] which contains in the conventional electric survey in the theory, and then we analyze the depth of exploration and the resolving power of the conventional electric survey by the experiment which takes place in a tank laboratory where a graphite nodule and graphite cylinder act as unconventional objects.

2. THEORETICAL STUDY ON THE DEPTH OF EXPLORATION

We can give a definition of the depth of electrical exploration as following: When the subjective and objective conditions are given, we can identify the maximum depth of exploration targets by collecting the information of the electrical or electromagnetic fields, processing and analyzing the data. Or simplified as follows: The maximum depth of exploration targets we can identify under certain conditions. The percentage of depth to diameter is usually used to represent the depth of exploration when we analyze the sphere and cylinder.

2.1. Theoretical Study on the Dual Frequency Induced Polarization Method

In order to simplify the calculation of depth of exploration, we set the target as a spherical ore with surface polarization, and when $\rho_2 = 0$ is its resistivity, r_0 is its radius, $\lambda = 1$ m is its electrochemical coefficient of surface polarization, ρ_1 is the rock's resistivity, h_0 is the depth from the ground.

In this paper, the secondary polarization electric potential is what we mainly observe. Along the main profile, the secondary polarization electric potential is derived from:

$$U_2 = \frac{3I\rho_1^3\lambda}{\pi\left(2\rho_2+\rho_1\right)\left(2\rho_2+\rho_1+2\dfrac{\lambda}{r_0}\rho_1\right)} \cdot \frac{r_0^2}{\left(h_0^2+x^2-r_0^2\right)\left(h_0^2+x^2\right)}$$

x is the projection distance of measuring point and the centre of sphere from the ground. When $\frac{x}{h_0} = 0$, U_2 gets the maximum value:

$$U_{2\max} = \frac{3I\rho_1^3\lambda}{\pi(2\rho_2+\rho_1)\left(2\rho_2+\rho_1+2\frac{\lambda}{r_0}\rho_1\right)} \cdot \frac{r_0^2}{h_0^2\left(h_0^2-r_0^2\right)}$$

When r_0 is much smaller than h_0 (the formula has a high degree of approximation), $U_{2\max}$ is basically proportional to r_0^2.

We know that r_0 is much smaller than h_0, so we can similarly take $h_0^2 - r_0^2 = h_0^2$, then D can be expressed as:

$$D = \sqrt[4]{\frac{3I\rho_1^3\lambda}{\pi(2\rho_2+\rho_1)\left(2\rho_2+\rho_1+\frac{2\lambda}{r_0}\rho_1\right)\cdot\frac{1}{U_{2\max}}}}$$

When $U_{2\max} = 0.5\,\text{mV}$, $I = 100\,\text{mA}$, $\lambda = 1\,\text{m}$, $\rho_1 = 100\,\Omega\cdot\text{m}$, the largest depth of exploration will be shown in Table 1 with several different numerical values of r_0:

Table 1: The relationship between the radius and depth of exploration.

r_0 (m)	0.025	0.05	0.1	1	5	10	20	30	50	100
D (m)	0.62	1.04	1.74	8.94	25.1	35.5	51.4	63.4	82.7	117

When $r_0 = 10\,\text{m}$, the relationship between D and I will be shown in Table 2 if we change the value of I:

Table 2: The relationship between the current and depth of exploration.

I (mA)	1	10	100	200	300	500	700	1000
D (m)	11.2	20	35.5	42.3	46.8	53.2	57.8	63.2

Thus, comparing the supply current with the size of ore or the numerical value of r_0 is more apparent to impact the depth of exploration.

2.2. Theoretical Study on the Direct Current Electrical Method [2–5]

The apparent resistivity expression is $\rho_s = E_{MN}/j_0\,\rho_s = E_{MN}/j_0$. $E_{MN} = -\partial U/\partial X$ is the electric field strength between the MN, and j_0 is the current density. Then we get the following formula:

$$\begin{aligned}
\rho_s &= \rho_0\left[1+2\frac{(\rho_1-\rho_0)}{(2\rho_1+\rho_0)}\frac{a^3\left(H^2-2X^2\right)}{\left(H^2+X^2\right)^{2/5}}\right] \\
\rho_{\max s} &= \rho_0\left[1+2\frac{(\rho_1-\rho_0)}{(2\rho_1+\rho_0)}\left(\frac{1}{1+2\frac{h}{D}}\right)^3\right] \\
a_{\max l} &= \frac{\rho_s-\rho_0}{\rho_0}\times 100\%
\end{aligned}$$

In the above formulas, $a = D/2$ (D is the diameter of the ball), $H = h + D/2$ (h is the depth of the ball from the ground). The maximum anomaly is just above the centre of the sphere. Set $X = 0$, and we can get:

$$\rho_{\max s} = \rho_0\left[1+2\frac{(\rho_1-\rho_0)}{(2\rho_1+\rho_0)}\left(\frac{1}{1+2\frac{h}{D}}\right)^3\right]$$

The definition of the relative anomaly range can be expressed as : $a_{\max l} = \frac{\rho_s-\rho_0}{\rho_0}\times 100\%$.

So the relationship between the relative anomaly range and depth of the sphere from the ground can be calculated ($AB/2 = 23\,\text{cm}$, $MN = 6\,\text{cm}$).

Table 3: The relationship between the relative anomaly range and the maximum depth of detection.

h (m)	D (m)	Percentage of depth to diameter	Apparent resistivity (ohm)	the relative anomaly range
0.02	0.2	0.10	18.12	57.07%
0.03	0.2	0.15	23.43	44.48%
0.04	0.2	0.20	27.33	35.24%
0.05	0.2	0.25	30.26	28.30%
0.06	0.2	0.30	32.50	22.98%
0.07	0.2	0.35	34.25	18.84%
0.08	0.2	0.40	35.63	15.58%
0.09	0.2	0.45	36.73	12.96%
0.10	0.2	0.50	37.63	10.84%
0.11	0.2	0.55	38.36	9.11%
0.12	0.2	0.60	38.96	7.67%
0.13	0.2	0.65	39.47	6.48%
0.14	0.2	0.70	39.89	5.48%
0.16	0.2	0.80	40.55	3.90%

3. PHYSICAL SIMULATION

The general principle of the simulation is called the "similarity" principle. In the conventional electrical method, it has a very simple "similarity" relationship. The relationship between the model and the actual geometric parameters (shape, size, depth) is independent from the relationship between the model and the electrical parameters, and each of them is linear.

Symmetric four-pole sounding is mainly used in the experiment, and the equipment which we use in the experiment is DDC-5 and SQ-3C. First we measure the background resistivity (water), next we put the graphite specimen in the water (to simulate the objects with low resistance surrounded by high impedance), then we can measure the variation of apparent resistivity and apparent polarizability, and at last the trends of apparent resistivity and apparent polarization are analyzed when the low-resistance objects are presented in the water.

In the experiment, the model we used is a graphite sphere whose semidiameter is 10 cm and a graphite cylinder whose diameter is 10 cm. The results of the experiment will be shown in the following tables (We will use Kh representative Percentage of depth to diameter and $a_{\max l}$ representative the relative anomaly range):

Table 4: Date of the dual frequency induced polarization method (graphite sphere).

No.	$MN/2$ (cm)	$AB/2$ (cm)	VL (mV)	VH (mV)	FS (%)	K	Depth (cm)
1	6	82	10.40	9.82	6.00	17.50	0
2	6	82	14.43	13.96	3.30	17.50	1
3	6	82	17.42	17.03	2.20	17.50	2
4	6	82	19.10	18.79	1.60	17.50	3
5	6	82	20.83	19.76	1.30	17.50	4
6	6	82	21.98	21.84	0.60	17.50	5
7	6	82	22.35	22.25	0.40	17.50	6
8	6	82	22.68	22.60	0.30	17.50	7
9	6	82	23.12	23.06	0.20	17.50	8
10	6	82	23.56	23.54	0.00	17.50	9
11	6	82	23.95	23.93	0.00	17.50	10

From Table 4, we can see that when the depth is 9 cm, the trend of FS (%) is 0. So the depth of exploration of the sphere is about 9 cm when $AB/2$ is 82 cm.

From Table 5, we can know that when the depth is 11 cm, the trend of FS (%) is 0. So the depth of exploration of the cylinder is about 11 cm when $AB/2$ is 83 cm.

Table 5: Date of the dual frequency induced polarization method (graphite cylinder).

NO.	$MN/2$ (cm)	$AB/2$ (cm)	VL (mV)	VH (mV)	FS (%)	K	Depth (cm)
1	6	83	10.39	10.13	2.52	17.93	1
2	6	83	11.01	10.78	2.18	17.93	2
3	6	83	12.17	11.97	1.63	17.93	3
4	6	83	13.42	13.26	1.18	17.93	4
5	6	83	14.62	14.49	0.91	17.93	5
6	6	83	15.37	15.27	0.62	17.93	6
7	6	83	16.23	16.17	0.35	17.93	7
8	6	83	16.96	16.92	0.21	17.93	8
9	6	83	17.32	17.31	0.12	17.93	9
10	6	83	17.77	17.77	0.02	17.93	10
11	6	83	18.24	18.26	0	17.93	11
12	6	83	18.49	18.51	−0.11	17.93	12

Table 6: Date comparison of the direct current electrical method.

(graphite sphere)

Kh	$a_{\max l}$ ($AB/2 = 23$ cm)	$a_{\max l}$ ($AB/2 = 33$ cm)	$a_{\max l}$ ($AB/2 = 43$ cm)
0	70.31%	67.59%	62.07%
0.05	57.89%	58.69%	55.58%
0.1	49.38%	50.73%	47.59%
0.15	39.81%	41.47%	40.87%
0.2	31.69%	33.87%	33.88%
0.25	24.60%	24.98%	28.76%
0.3	19.73%	20.87%	22.45%
0.35	16.04%	17.06%	19.41%
0.4	12.96%	14.47%	15.93%
0.45	10.11%	12.17%	12.64%
0.5	8.19%	9.81%	10.15%
0.55	6.99%	8.55%	9.46%
0.6	5.63%	7.56%	7.92%
0.65	4.77%	6.26%	6.48%
0.7	3.70%	4.85%	5.76%
0.75	3.28%	3.76%	4.91%

(graphite cylinder)

Kh	$a_{\max l}$ ($AB/2 = 24$ cm)	$a_{\max l}$ ($AB/2 = 34$ cm)	$a_{\max l}$ ($AB/2 = 43$ cm)
0.1	44.67%	46.76%	41.95%
0.2	39.43%	41.87%	37.97%
0.3	29.12%	34.04%	33.43%
0.4	25.25%	27.48%	27.96%
0.5	21.27%	24.36%	23.54%
0.6	17.29%	20.99%	19.28%
0.7	14.07%	17.71%	17.32%
0.8	11.26%	16.09%	14.32%
0.9	8.73%	12.78%	12.51%
1	7.60%	10.60%	10.38%

Kh	$a_{\max l}$ ($AB/2 = 24$ cm)	$a_{\max l}$ ($AB/2 = 34$ cm)	$a_{\max l}$ ($AB/2 = 43$ cm)
1.1	6.25%	9.45%	9.72%
1.2	4.57%	7.55%	7.38%
1.3	2.54%	6.25%	6.76%
1.4	1.74%	5.01%	6.11%
1.5	1.12%	4.20%	5.05%
1.6	1.12%	3.15%	4.78%

From Table 6, we can find that the depth of exploration increases when we increase the distance of electrode. Compare the smaller $AB/2$ to the larger $AB/2$, the power supply has greater impact on the smaller one. So when Kh and $AB/2$ is relatively small, $a_{\max l}$ will be relatively large. The shape of target we want to detect also has a certain impact on the depth of exploration.

Table 7: Date comparison of different frequencies (graphite sphere).

No.	$MN/2$ (cm)	$AB/2$ (cm)	VL (mV)	VH (mV)	Fs (%)	I (mA)	F (Hz)
1	6	80.00	16.39	16.07	1.90	7.56	(2/13)
	6	80.00	16.37	16.04	2.00	7.57	(4/13)
	6	80.00	16.37	16.04	2.00	7.57	(8/13)
2	6	80.00	16.89	16.30	3.00	7.64	(2/13)
	6	80.00	16.60	16.10	3.10	7.66	(4/13)
	6	80.00	16.56	16.07	3.00	7.64	(8/13)
3	6	80.00	16.62	15.93	4.30	7.75	(2/13)
	6	80.00	16.62	15.95	4.20	7.74	(4/13)
	6	80.00	16.62	15.95	4.20	7.74	(8/13)

From Table 7, we find that there is little effect on the frequency of measurement.

4. CONCLUSION

The results show that the depth of exploration will increase when we increase the distance of electrodes. However, this situation only occurs in the case of a small distance of electrodes. The anomaly will tend to a saturation value when the distance of electrodes is increased further. The distance of electrodes we choose should be done with a premise of achieving the greatest anomaly. In the dual frequency induced polarization method, the supply current and frequency do not influence the exploration ability very much.

ACKNOWLEDGMENT

I would like to show my deepest gratitude to my supervisor, Dr. Jian-Xin Liu, a respectable, responsible and resourceful scholar, who has provided me with valuable guidance at every stage of the writing. I extend my thanks to Xiao-Zhong Tong and Zhen-Wei Guo for their support. Special thanks to Man-Qiu Wang for correcting the English.

REFERENCES

1. He, J. S., *Dual Frequency Induced Polarization Method*, Higher Education Press, Beijing, 2005.
2. Ruan, B.-Y., Y.-Z. Lu, J.-K. Qiang, and J.-G. Huang, "The sensitivity of D.C. Resistivity sounding exploration and its application," *Geophysical & Geochemical Exploration*, Vol. 26, No. 5, 392–394, 2002.
3. Zhong, S.-H., "The depth sensitivity of D.C. resistivity sounding on shallow investigation," *Geophysical & Geochemical Exploration*, Vol. 28, No. 1, 46–52, 2004.
4. Frohlich, R. K., "The depth penetration of dipole arrays compared with schlumberger arrangement," *Geoexploration*, Vol. 5, No. 3, 273–281, 1967.
5. Schlumberger, C. and M. Schlumberger, "Depth of investigation attainable by potential methods of electrical exploration," *AIME Trans.*, Prospect, 127–133, 1932.

Cole-Cole Model Based on the Frequency-domain IP Method of Forward Modeling

Wei Zhang[1, 2], **Jian-Xin Liu**[1, 2], **Zhen-Wei Guo**[1, 2], **and Xiao-Zhong Tong**[1, 2]

[1]The Institute of Info-physics and Geometrics Engineering, Central South University
Changsha, Hunan 410083, China
[2]Key Laboratory of Non-ferrous Resources and Geological Hazard Detection
Changsha, Hunan 410083, China

Abstract— Induced polarization method (IP) is based on rock, ore, metal induced polarization effects to find and solve hydro-geological, engineering geological issues such as a group of electrical prospecting methods. It consists of DC-induced polarization method (time domain method) and the exchange of induced polarization method (frequency-domain method). At present, Frequency-domain induced polarization method (frequency method) because of its advantages is widely used in actual production. However, as rock, ore, induced polarization effects are very complex and affected by many factors, the current induced polarization effects very difficult to achieve an accurate description. Therefore, interpretation of induced polarization method in data analysis problems. In the application subject to certain restrictions.

Cole-Cole model is used to describe the formula-mediated electric polarization in the form of complex resistivity and induced polarization equation in the form of the same frequency characteristics. The use of Cole-Cole model to be more a description of the image of rock, ore, induced polarization phenomenon, as the basis of the frequency-domain IP for effective forward modeling, can accurately describe the rock, ore characteristics of the induced polarization effects, developed a suitable IP method forward simulation software.

1. INTRODUCTION

Induced polarization method with the material based on the ip effect difference of different rocks, ore in the earth crust is a branch methods of electrical prospecting for prospecting and solving geological problems by observing and studying the distribution regularity of artificial established induced electrical field of DC or AC. It can be divided into DC-induced polarization method (time-domain method) and AC-induced polarization method (frequency-domain method). Its conventional array are central gradient array, dipole-dipole array, symmetrical quadrupole array and so on.

Practice shows that Induced polarization method is the main methods for the exploration of various metal mineral, especially the infection type metal deposits which resistivity has little difference with surrounding rock, compare to the resistivity and electromagnetic method, it is more effective. But the method in numerical simulation and field data processing, there are still a lot of deficiencies, forward modeling and inversion algorithm developed from basis of forward and inversion algorithm of dc resistivity method are numerical simulation method of time domaininduced polarization. For the frequency-domain IP method, besides some of regular body, we can calculate their amplitude-frequency anomalies, most of them can not understand and its inverse problem is more complex. The data processing is limited to some qualitative interpretation and empirical method, making the interpretation results are more difference with the actual situation. A thorough understanding of studing IP forward problem is beneficial to develop the development of IP method in theory and the improvement of interpretation level of IP field data.

The author based on the Cole-Cole dispersion theory, choose the sphere model as a research object and research forward modeling problem of IP method.

2. COLE-COLE MODEL

Cole-Cole model is a formula spectrum to describe the complex resistivity induced by IP effect. is also the basic formula of IP forward modeling. Its expressed as:

$$\rho(i\omega) = \rho_0 \left\{ 1 - m \left[1 - \frac{1}{1 + (i\omega\tau)^c} \right] \right\} \tag{1}$$

where, ρ_0 is resistivity (when frequency is 0); m is charging rate, corresponding to the limit polarizability in time-domain; c is frequency dependent factor (dimensionless); τ is time-constant (time dimension).

In formula (1):

$$\begin{aligned}(i\omega\tau)^c &= (\omega\tau)^c e^{i(4n+1)\frac{\pi}{2}c} \\ &= (\omega\tau)^c \left[\cos(4n+1)\frac{\pi}{2}c + i\cdot\sin(4n+1)\frac{\pi}{2}c\right] \\ &= R - 1 + iI \end{aligned} \tag{2}$$

where:

$$R = 1 + (\omega\tau)^c \cos(4n+1)\frac{\pi}{2}c \qquad I = (\omega\tau)^c \sin(4n+1)\frac{\pi}{2}c \tag{3}$$

taking principal value ($n = 0$), when, R and I can be expressed as the following forms:

$$R = 1 + (\omega\tau)^c \cos\frac{\pi c}{2} \qquad I = (\omega\tau)^c \sin\frac{\pi c}{2} \tag{4}$$

To take Equation (2) into Equation (1), can be:

$$\begin{aligned}\rho(i\omega) &= \rho_0\left[1 - m\left(1 - \frac{1}{R+iI}\right)\right] \\ &= \rho_0\left[1 - m\left(1 - \frac{R-iI}{R^2+I^2}\right)\right] \\ &= \rho_0\left[1 - m + \frac{mR}{R^2+I^2} - i\frac{mI}{R^2+I^2}\right] \end{aligned} \tag{5}$$

3. INDUCED POLARIZATION FIELD IN THE POINT SOURCE CURRENT FIELD DOMAIN

By the corresponding conditions of un-polarization and the formula of DC apparent resistivity ρ_s transformation, we get the expression of apparent complex resistivity $\rho_s(i\omega)$ in inhomogeneous underground of bulk-polarizability. In the inhomogeneous underground of conductivity, without considering ip effect, DC apparent resistivity of some devices ρ_s can be expressed as a function of each part of media resistivity ρ_j, when the medium being induce polarization, each part of medium has complex resistivity of cole-cole dispersion form in frequency-domain:

$$\rho_j(i\omega) = \rho_{j0}\left\{1 - m_j\left[1 - \frac{1}{1+(i\omega\tau_j)^{c_j}}\right]\right\} \quad (j = 1, 2, \ldots, N) \tag{6}$$

where, ρ_{j0} is medium resistivity with the frequency is 0, that is limit equivalent resistivity; m_j is media charge rate in vacuum, that is limit polarizability η_j; c_j is frequency dependent factor of medium in vacuum; τ_j is media time constant in vacuum.

The following, we take a complex resistivity expression of sphere in the central gradient array as an example, as follows graph:

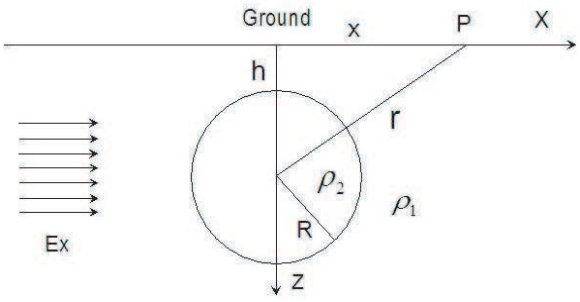

Figure 1: A sphere model in horizontal homogeneous underground.

Suppose there is a polarized sphere in homogeneous half-space with the resistivity is ρ_1, the radius is R and resistivity is ρ_2, without considering IP effect, the approximate expression of DC apparent resistivity ρ_s of central gradient array on the main cross-section can be expressed as follow:

$$\rho_s = \rho_1\left(1 + \frac{\rho_2 - \rho_1}{2\rho_2 + \rho_1}\cdot f\right) \tag{7}$$

where $f = 2R^3 \frac{r^2-3x^2}{r^5}$.

When the sphere produce bulk-polarization with the rock, their resistivity has complex resistivity of cole-cole dispersion form in frequency-domain:

$$\rho_j = \rho_{j0}\left\{1 - m_j\left[1 - \frac{1}{1+(i\omega\tau_j)^{c_j}}\right]\right\} = P_j - iQ_j \tag{8}$$

Take Equation (8) into Equation (7), we can get the apparent complex resistivity approximate expression of sphere under IP effect:

$$\rho_s(i\omega) = P_1(1+M\cdot f) - Q_1\cdot N\cdot f - i\left[Q_1(1+M\cdot f) + P_1\cdot N\cdot f\right] \tag{9}$$

where: $\begin{cases} M = \frac{(P_2-P_1)(2P_2+P_1)+(Q_2-Q_1)(2Q_2+Q_1)}{(2P_2+P_1)^2+(2Q_2+Q_1)^2} \\ N = \frac{(Q_2-Q_1)(2P_2+P_1)-(P_2-P_1)(2Q_2+Q_1)}{(2P_2+P_1)^2+(2Q_2+Q_1)^2} \end{cases}$.

Each component of apparent complex resistivity is:

Imaginary component: $\mathrm{Im}\rho_s = -\left[Q_1(1+M\cdot f) + P_1\cdot N\cdot f\right]$

Real component: $\mathrm{Re}\rho_s = P_1(1+M\cdot f) - Q_1\cdot N\cdot f$

Amplitude: $A_s = \sqrt{(\mathrm{Im}\rho_s)^2 + (\mathrm{Re}\rho_s)^2}$

Phase: $\varphi_s = \mathrm{arctg}\frac{\mathrm{Im}\rho_s}{\mathrm{Re}\rho_s}$

4. FORWARD RESULTS

To take sphere model as an example, using central gradient array of IP method forward modeling, mesh generation can be self-designed according to requirement.

Here, we take $AB = 100$, $MN = 2$, the radius of sphere $R = 18$, the parameters are $\rho_2 = 10\,\Omega\cdot$m, $\rho_1 = 45\,\Omega\cdot$m; $\eta_2 = 15\%$, $\eta_1 = 1\%$. The most depth of mesh generation is 50, subdivision mesh is 2×2. Through the forward modeling, we can get the apparent resistivity curve and apparent chargeability curve with different depth as follows:

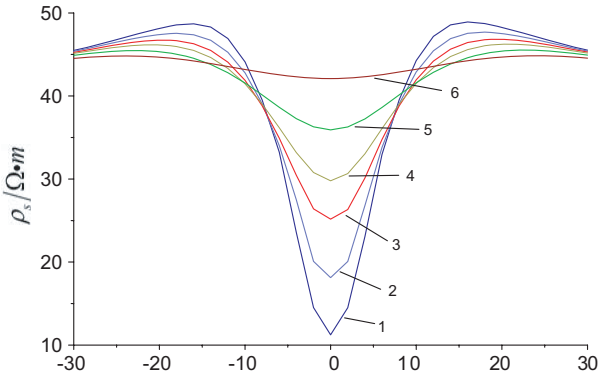

Figure 2: Apparent resistivity curve with different depth (1 — $h = 2$, 2 — $h = 4$, 3 — $h = 6$, 4 — $h = 8$, 5 — $h = 12$, 6 — $h = 24$, h is the buried depth of globe-roof).

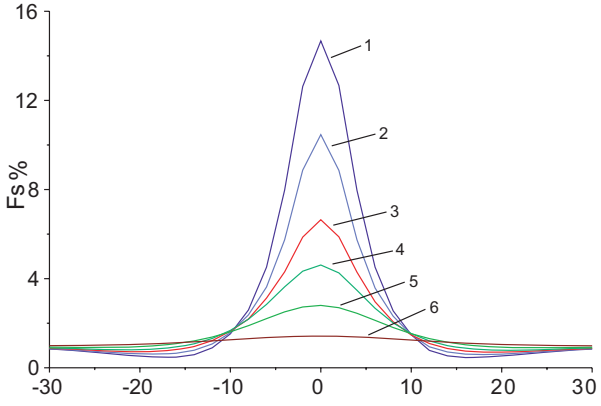

Figure 3: Apparent chargeability curve with different depth (1 — $h = 2$, 2 — $h = 4$, 3 — $h = 6$, 4 — $h = 8$, 5 — $h = 12$, 6 — $h = 24$, h is the buried depth of globe-roof).

Reference to the other theoretical curve of central gradient array, it is easy to see out the result of forward simulation has a good effect and achieve expected purpose through. it can veritably reflect the IP characteristics of rock, ore body with different geometry size and polarization.

5. CONCLUSION

With the forward formula of Cole-Cole model, can be approximately simulated the IP anomaly of rock, ore body with different geometry size and polarization underground; by a change of the electrical parameter of rock and polarization body, can understand the anomaly characteristics in different polarized conditions. To provide reliable basis for further studying the IP phenomenon

of rock and ore and provide reference for the IP method in practical application; improve the IP data interpretation accuracy, that is beneficial to improve application value of IP. In addition, the method has some needing improvements places, what need us to further study to improve validity of the method.

REFERENCES

1. Fu, L.-K., *Induced Polarization Method*, Geological Press, Beijing, 1982.
2. Li, J.-M., *Geoelectric Field and Electrical Exploration*, Geological Press, Beijing, 2005.
3. Luo, Y.-Z. and G.-Q. Zhang, *Principle of Frequency-domain IP*, Geological Press, Beijing, 1988.
4. Qiang, J.-K. and J.-S. He, "Algorithm of forward and inversion of dual-frequency induced polarization method on elliptical sphere," *Journal of Central South University* (*Science and Technology*), Vol. 38, No. 6, Dec. 2007.
5. Ken, Y. and S. Z. Michael, "Three-dimensional nonlinear regularized inversion of the induced polarization data based on the Cole-Cole model," *Physics of the Earth and Planetary Interiors*, Vol. 150, 29–43, 2005.
6. Yang, X.-H. and J.-S. He, "Numerical simulation of frequency — Domain IP with FEM," *Journal of Central South University* (*Science and Technology*), Vol. 38, No. 4, Jul. 2008.

Electric Field around a Metal Disk within a Microwave Resonator: Electrostatic Approximation

Gholamreza Shayeganrad[1] and Leila Mashhadi[2]

[1]Islamic Azad University, Karaj Branch, Karaj, Iran
[2]Physics Department, Amirkabir University of Technology, Tehran, Iran

Abstract— In this work, a rectangular resonator cavity with non-ionization electromagnetic radiation at frequency of 2.45 GHz or wavelength of 12.24 cm involving a metal disk has been considered. We have shown electrostatic field is a suitable approximation to study a metal disk within a cavity with alternative field at frequency of 2.45 GHz and it leads to solve Laplace's equation. We have solved this equation in elliptical coordinates in detail considering boundary conditions and determined electric field around the disk. Solving Laplace's equation in elliptical coordinates is the appropriate method for determining electric and magnetic fields in the vicinity of the metals with striped or circular types.

1. INTRODUCTION

A cavity can be considered as a volume enclosed by a conducting surface and within which an electromagnetic field can be excited. The electric and magnetic energies are stored in the volume of the cavity. The power loss effects of the finite conducting walls have been accurately investigated in the previous work [1].

Here, we have briefly shown that the electrostatic approximation is the appropriate method for determining electric field and electrostatic potential function around the conductors subjected at microwave frequency. Laplace's equation is derived for static electric field within free-source rectangular and cylindrical cavities considering this approximation and therefore the potential everywhere in the region can be found by solving it for specified Dirichlet, Neumann or mixed boundary conditions. The method of separation of variables is straightforward. This method yields solutions involving circular cosine and sine functions, Bessel and Legendre polynomials to Laplace's equation in cartesian, cylindrical and elliptical coordinates, respectively. However, the analytical expressions are obtained only in rather idealized cases that certain symmetries must exist and the boundaries must not be irregular which their mathematical analysis is not very difficult.

In other cases, field calculations often become very complicated and the ultimate objective, however, is obtaining a numerical result. Some numerical methods that have used to solve Laplace's equation in a given region are the finite-element method, finite-difference method, or the method of moments [2–4]. Among them, the Finite Difference Time Domain (FD-TD) method is a numerical technique widely used in electromagnetics for solution of the Maxwell's Curl equations in those cases where exact analytical methods cannot be applied and approximated solutions are not satisfactory [5].

An advantage of having analytical expressions is that the general behavior of the solution for different values of the problem parameter may be observed. The curvilinear coordinates to solve the Laplace's equation offers many advantages in solving practical engineering problems, which satisfies some special boundary conditions. We have proposed in this work a simple and exact theoretical method for determining the explicit electric field and electrostatic potential function in the vicinity of the metal disk subjected within a rectangular microwave cavity, considering electrostatic approximation. We have generally derived an analytical expression for electric field around the metal disk by solving Laplace's equation in elliptical coordinate system. Substituting numerical values for the problem parameters into these expressions yields the solution to a particular problem.

2. THEORY

According to the Drude's model, the electrical conductivity of a metal is given by [6]:

$$\sigma = \frac{f_0 \mathrm{N e}^2}{m(\gamma_0 - i\omega)} \tag{1}$$

in which f_0N is number of free electrons per unit volume in the metal and γ_0/f_0 damping constant that can be determined empirically from experimental, typically of the order of $10^{17}\,\mathrm{sec}^{-1}$. This means that, for frequencies beyond the microwave region ($\omega \leq 10^{11}\,\mathrm{s}^{-1}$), ω in the dominator of the Eq. (1) is negligible and σ is approximated by:

$$\sigma = \frac{f_0 \mathrm{Ne}^2}{m\gamma_0} \tag{2}$$

It indicates that conductivity of metals in microwave region is essentially real and independent to frequency. Therefore, electrostatic approximation is sufficient to investigate conductors located in the microwave resonator. Figure 1 shows a thin metal disk lies in the xy-plane, with its center at the origin and radius, a, introduced into a uniform electric field with magnitude E_0 directed along the x-axis, $\vec{E} = E_0\hat{x}$. The resonant modes inside the microwave cavity has the magnitude of $E_0 \approx 10^5\,\mathrm{V/m}$ [1].

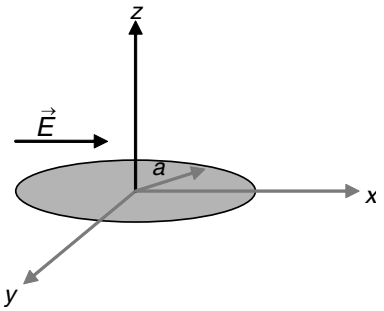

Figure 1: A metal disk with radius, a, to a uniform electric field $\vec{E} = E_0\hat{x}$.

Of particular interest is the determination of the distribution of electric field around the disk. First, we obtain the electrostatic potential function, ϕ, by solving Laplace's equation in elliptical coordinate. Knowing the potential function, we can find the electric field, $\vec{E}$, from $\vec{E} = -\nabla\phi$. At this point, two assumptions have made: i) at points far away from the disk compared to its radius, the field becomes to $E_0\hat{x}$, and ii) the electric field becomes zero on the surface of disk.

We specify the location of a point in this coordinate system by giving its coordinates in the form (u, φ, v). The conversion between the cylindrical coordinate (ρ, φ, z) and elliptical (u, φ, v) coordinate systems are given by:

$$\rho = a\cosh u\cos v \quad -\pi/2 < v < \pi/2 \tag{3a}$$
$$z = a\sinh u\sin v \quad 0 < u < \infty \tag{3b}$$
$$\varphi = \varphi \quad 0 < \varphi < 2\pi \tag{3c}$$

The boundary conditions in elliptical coordinate for this problem are:

$$\phi = 0 \quad \text{at} \quad v = 0 \tag{4a}$$
$$\phi = -aE_0\cosh u\cos v\cos\varphi \quad \text{at} \quad u \to \infty \tag{4b}$$

Expanding $\nabla^2\phi$ in elliptical coordinate, we find that Laplace's equation given by:

$$\nabla^2\phi = \frac{1}{D^2(u,v)}\left(\frac{1}{\cosh u}\frac{\partial}{\partial u}\cosh u\frac{\partial}{\partial u} + \frac{1}{\cos v}\frac{\partial}{\partial v}\cos v\frac{\partial}{\partial v}\right)\phi + \frac{1}{a^2\cosh^2 u\cos^2 v}\frac{\partial^2\phi}{\partial^2\varphi} = 0 \tag{5}$$

where $D^2(u,v) = a^2(\cosh^2 u - \cos^2 v)$.

Equation (5) can be solved by the method of separation of variables. The result would have been:

$$\phi = \psi_m(u,v)(A_m\cos m\varphi + B_m\sin m\varphi) \tag{6}$$

where m is an integer. Finally, we obtain for most general form:

$$\phi = \sum_{m=0}^{\infty}\psi_m(u,v)(A_m\cos m\varphi + B_m\sin m\varphi) \tag{7}$$

From the boundary conditions (4a) and (4b) for all values of $(0 < \varphi < 2\pi)$ we can obtain:

$$\phi = \psi(u, v) \cos \varphi \tag{8}$$

Considering $\psi(u, v) = \sum_{\mu} X_{\mu}(u) Y_{\mu}(v)$ combination with (8) and substituting in (5), we obtain

$$\left[\frac{1}{\cosh u}\frac{\partial}{\partial u}\cosh u\frac{\partial}{\partial u} + \frac{1}{\cosh^2 u}\right] X = \mu X \tag{9a}$$

$$\left[\frac{1}{\cos v}\frac{\partial}{\partial v}\cos v\frac{\partial}{\partial v} - \frac{1}{\cos^2 v}\right] Y = -\mu Y \tag{9b}$$

The Eq. (9b) can be rewritten as Legendre's equation:

$$\left[\left(1-\xi^2\right)\frac{\partial^2}{\partial^2 \xi} - 2\xi\frac{\partial}{\partial \xi} - \frac{1}{1-\xi^2}\right] Y = -\mu Y \tag{10}$$

in which $\xi = \sin v$. Considering $\mu = l(l+1)$, the solution is the first order of Legendre's polynomial. Therefore:

$$\psi = \sum_{l=1}^{\infty} X_l(u) P_l^1(\sin v) \tag{11}$$

Substituting (11) in (8) and comparing by (4b), we keep only first term, and consequently it becomes

$$\psi(u, v) = X_1(u) \cos v. \tag{12}$$

As a result, the (9a) becomes:

$$\left[\frac{1}{\cosh u}\frac{\partial}{\partial u}\cosh u\frac{\partial}{\partial u} + \frac{1}{\cosh^2 u}\right] X_1 = 2X_1 \tag{13}$$

The solutions of this differential equation are:

$$X_1 = \cosh u \tag{14a}$$

and

$$X_1 = \tanh u + \cosh u \tan^{-1}(\sinh u) \tag{14b}$$

According to the boundary conditions of (4a) and (4b), (14b) is the acceptable solution and then we obtain:

$$\psi(u, v) = \left[\tanh u + \cosh u \tan^{-1}(\sinh u)\right] \cos v \tag{15}$$

Substituting (15) in (8) gives the final solution as:

$$\phi = -\frac{2aE_0}{\pi}\left[\tanh u + \cosh u \tan^{-1}(\sinh u)\right] \cos v \cos \varphi \tag{16}$$

It is perhaps most common to find the components of electric field in cylindrical coordinates. The electric field in the cylindrical coordinate system can be expressed as

$$\vec{E} = -\vec{\nabla}\phi = \hat{\rho}\left(\frac{\partial u}{\partial \rho}\frac{\partial}{\partial u} + \frac{\partial v}{\partial \rho}\frac{\partial}{\partial v}\right)\phi + \hat{z}\left(\frac{\partial u}{\partial z}\frac{\partial}{\partial u} + \frac{\partial v}{\partial z}\frac{\partial}{\partial v}\right)\phi + \hat{\varphi}\frac{\partial \phi}{\partial \varphi} \tag{17}$$

Assuming the Jacobian $J(\rho, z)$ defined by

$$J(\rho, z) \equiv \begin{pmatrix} \dfrac{\partial u}{\partial \rho} & \dfrac{\partial v}{\partial \rho} \\ \dfrac{\partial u}{\partial z} & \dfrac{\partial v}{\partial z} \end{pmatrix} = \frac{1}{a^2\left(\cosh^2(u) - \cos(v)\right)} \begin{pmatrix} a\sinh(u)\cos(v) & -a\cosh(u)\sin(v) \\ a\cosh(u)\sin(v) & a\sinh(u)\sin(v) \end{pmatrix} \tag{18}$$

and Eqs. (16) and (17), the electric components in cylindrical coordinate system are given by:

$$E_\rho = \frac{2E_0}{\pi}\left[\frac{(\cosh^2(u)+\cos^2(v))\sinh(u)}{(\cosh^2(u)-\cos^2(v))\cosh^2(u)} + \tan^{-1}(\sinh(u))\right]\cos\varphi \tag{19a}$$

$$E_\varphi = \frac{-2E_0}{\pi}\left[\frac{\sinh(u)}{\cosh^2(u)} + \tan^{-1}(\sinh(u))\right]\sin\varphi \tag{19b}$$

$$E_z = \frac{2E_0}{\pi}\left[\frac{\sin(2v)\cos\varphi}{\cosh(u)(\cosh^2(u)-\cos^2(v))}\right] \tag{19c}$$

where

$$\cos^2 v = \frac{a^2+\rho^2+z^2-\sqrt{(a^2+\rho^2+z^2)^2-a\rho^2a^2}}{2a^2}$$

$$\cos^2 hu = \frac{a^2+\rho^2+z^2+\sqrt{(a^2+\rho^2+z^2)^2-a\rho^2a^2}}{2a^2}$$

Notice that at $\varphi = 0$ and $\varphi = \pi$ the φ-component of electric field is zero, $E_\varphi = 0$. The other components are $E_\rho \approx \frac{2E_0}{\pi}\left(\frac{a}{z}\right)^{1/2}$ and $E_z \approx \frac{2E_0}{\pi}\left(\frac{a}{z}\right)^{1/2}$ at $\rho = a$ and for points that are sufficiently close to the edge of the disk by allowing $z \to 0$ and $\rho = a + 10^{-x}a$, they simplified to $E_\rho = \frac{2E_0}{\pi}10^x$ and $E_z = 0$.

3. CONCLUSIONS

The curvilinear coordinates to solve the Laplace's equation analytically offers many advantages in solving practical engineering problems, which satisfies some special boundary conditions. We have shown the electrostatic approximation is suitable for determining electric field and electrostatic potential functions around the conductors subjected at microwave frequency. Solving Laplace's equation in curvilinear elliptical coordinate is a simple method for determining the electric field analytically around a metal disk subjected within a source-free rectangular microwave cavity. Finally, we have derived the electric field components in the cylindrical coordinates that are most convenient.

REFERENCES

1. Shayeganrad, G. and L. Mashhadi, "Theoretically and experimentally investigation of sparking of metal objects inside a microwave oven," *PIERS Proceedings*, 632–641, Beijing, China, March 2009.
2. De Vries, P. L., *A First Course in Computational Physics*, 4th Edition, John Wiley & Sons, Inc., New York, 1994.
3. Chapra, S. C. and R. P. Canale, *Numerical Method for Engineers: With Software and Programming Applications*, Tata McGrow-Hill, 2002.
4. Harrington, R. F., *Field Computation by Moment Methods*, Wiley-IEEE Press, 1994.
5. Bellanca, G., P. Bassi, and G. Erbacci, "Optimized microwave oven design via fd-td simulation on parallel computer," *Science and Supercomputing at CINECA*, 2001.
6. Jackson, J. D., *Classical Electrodynamics*, 3rd Edition, John Wiley & Sons, Inc., New York, 1999.

Study on Compact UWB Filter Composed of Defected Parallel Plates and Meander Line

H. Takeuchi[1], **T. Kitamura**[1], **and Y. Horii**[2]

[1]Faculty of Engineering Science, Kansai University, Osaka, Japan
[2]Faculty of Informatics, Kansai University, Osaka, Japan

Abstract— In this study, we propose a compact ultra-wideband bandpass filter that is composed of a pair of defected parallel plates and a meander line. We analyzed the filtering characteristics by using a full-wave EM-simulator Ansoft HFSS Ver. 11 based on the finite element method. The results show that the wide passband from about 2.0 GHz to 11.0 GHz is obtained and attenuation poles are created at both sides of the passband. It is also shown that the flat group delay characteristics are achieved in the wide frequency range.

1. INTRODUCTION

Since the unlicensed use of ultra-wideband (UWB) frequency spectrum (3.1–10.6 GHz) for indoor and hand-held wireless communications is released in 2002, great attention has been paid to applications of UWB technology on wireless communication system. According to this, various kinds of bandpass filters with specified ultra-wide passbands have been proposed [1–5]. Miniaturization of the filter is an important issue in order to reduce a total circuit size. In this study, we propose a compact ultra-wideband bandpass filter that is composed of a pair of defected parallel plates and a meander line. We analyze the filtering characteristics by using a full-wave EM-simulator Ansoft HFSS Ver. 11 based on the finite element method.

2. FILTER STRUCTURE

We show an overview of the proposed filter in Fig. 1. It is composed of I/O striplines, a pair of parallel plates (size 2.0 mm × 2.0 mm, distance between the plates 0.31 mm), a meander line (line width 0.1 mm, slit width 0.1 mm, total length 6.1 mm), and a thin conductor column (diameter 0.2 mm, length 0.31 mm). The metallization patterns of the I/O ports, parallel plates and meander line are shown in Fig. 2. The column is located between the parallel plates and links them in the center of each one. One side of the meander line is connected to the center of the column and the other is terminated to the ground. They construct a kind of quarter-wavelength resonator. The center of each parallel plate is defected in a square shape (0.6 mm × 0.6 mm) and thin lines (width 0.1 mm, length 0.3 mm) are added between the column and parallel plates. The I/O striplines are located on either side of the parallel plates. The whole structure is fabricated in a ground enclosure filled with a dielectric material with a relative permittivity of 2.59.

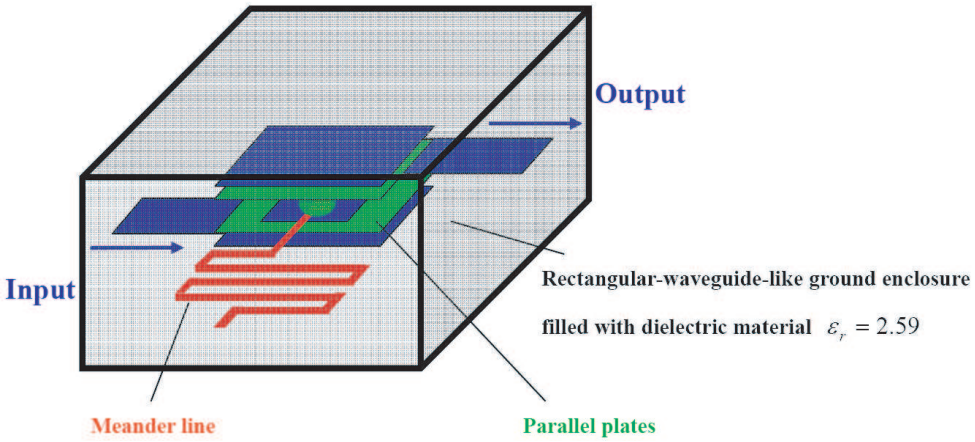

Figure 1: Whole structure of filter.

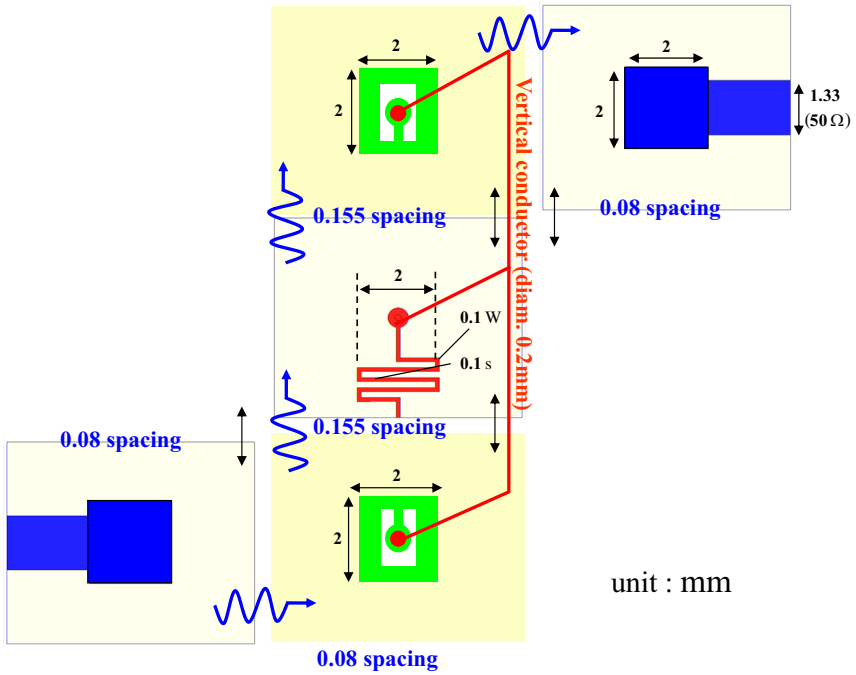

Figure 2: Metallization patterns.

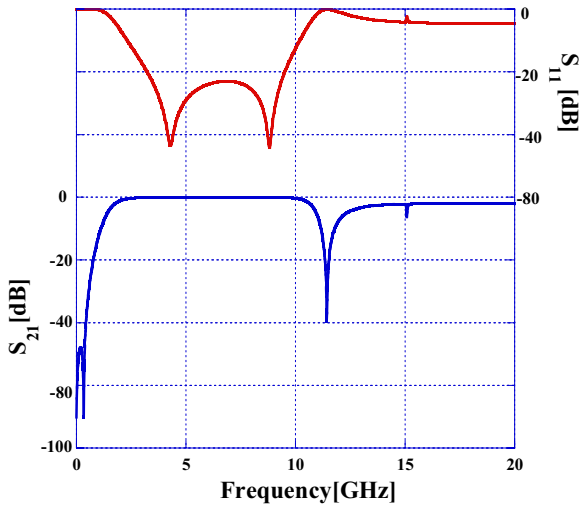

Figure 3: Scattering parameters.

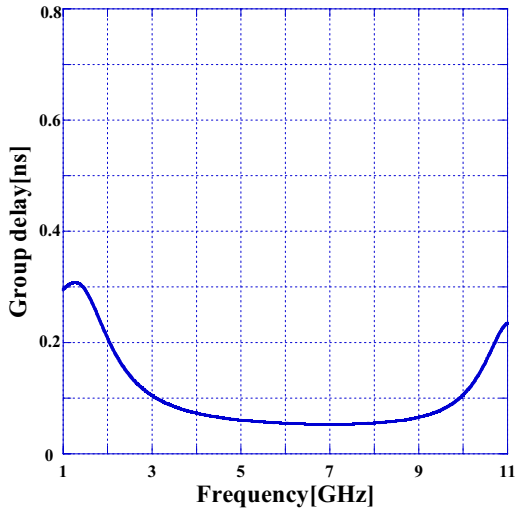

Figure 4: Group delay.

3. NUMERICAL RESULTS

The frequency characteristics of the scattering parameters are shown in Fig. 3. It is shown that the wide passband from about 2.0 GHz to 11.0 GHz is obtained and attenuation poles are created at both sides of the passband. We show the frequency characteristics of the group delay in Fig. 4. It is understood that the flat group delay characteristics are achieved in the wide frequency range.

4. CONCLUSIONS

We proposed a compact ultra-wideband bandpass filter that is composed of a pair of defected parallel plates and a meander line. It was shown that the wide passband from about 2.0 GHz to 11.0 GHz is obtained and attenuation poles are created at both sides of the passband. It was also shown that the flat group delay characteristics are achieved in the wide frequency range.

REFERENCES

1. Yao, B., Y. Zhuo, Q. Cao, and Y. Chen, "Compact UWB bandpass filter with improved upper-stopband performance," *IEEE Microw. Wireless Compon. Lett.*, Vol. 19, No. 1, 27–29, 2009.
2. Song, K. and Y. Fan, "Compact ultra-widebband bandpass filter using dual-line coupling structure," *IEEE Microw.Wireless Compon. Lett.*, Vol. 19, No. 1, 30–32, 2009.
3. Wong, S. W. and L. Zhu, "Quadruple-mode UWB bandpass filter with improved out-of-band rejection," *IEEE Microw. Wireless Compon. Lett.*, Vol. 19, No. 3, 152–154, 2009.
4. Li, R., S. Sun, and L. Zhu, "Synthesis design of ultra-wideband bandpass filters with designable transmission poles," *IEEE Microw. Wireless Compon. Lett.*, Vol. 19, No. 5, 284–286, 2009.
5. Hao, Z. C. and J. S. Hong, "Compact wide stopband ultra wideband bandpass filter using multilayer liquid crystal polymer technology," *IEEE Microw. Wireless Compon. Lett.*, Vol. 19, No. 5, 290–292, 2009.

FDTD Analysis of Light-beam Scattering from DWDD Disk with Control Layer

Yuya Matsunami and Toshiaki Kitamura
Faculty of Engineering Science, Kansai University, Osaka, Japan

Abstract— In this study, we investigated readout characteristics of a domain wall displacement detection (DWDD) disk with a control layer by means of FDTD method. DWDD is one of the high-density storage technologies of magneto-optical (MO) disks and the control layer is used to suppress ghost signal due to rear process. We studied the effects of the control layer on the readout characteristics.

1. INTRODUCTION

Magneto-optical (MO) disks are used as rewritable type of storage media. Domain wall displacement detection (DWDD) is one of the high-density storage technologies of MO disk system that exceed optical resolution and have been put to practical use. It utilizes a magnetic domain wall displacement due to a temperature gradient [1].

In this study, we analyze the scattering of blue-laser light from a DWDD disk with a control layer by means of FDTD method [2]. The control layer is used to suppress ghost signal due to rear process. We study the effects of the control layer on the readout characteristics.

2. DWDD DISK STRUCTURE

Figure 1 shows a three-dimensional DWDD disk structure used in the analysis. Here, x and y directions are parallel and normal to the track, respectively, and z direction is normal to the disk surface. And we assume that upward and downward magnetizations correspond to recorded and non-recorded states, respectively. The incident laser beam is assumed to be an x-polarized Gaussian beam of 405 nm wavelength in free space. The bit length of perpendicular magnetization is assumed to be 80 nm, and the grooves and lands have the same width of 540 nm.

The structural parameters are shown in Table 1. The values of the non-diagonal permittivity are chosen so that the p-polarized angle of detected light from the MO medium becomes about 0.3 degrees [3]. In Table 1, ε_0 indicates the permittivity of free space.

3. NUMERICAL RESULTS

Figures 2 and 3 show the main-polarized (x-directed) and cross-polarized (y-directed) components, respectively, of far-zone scattered electric fields in y-z plane. Here, the length of the displacement layer (d) is chosen as a parameter. In these figures, the results of (a) three-layer (without a control

Table 1: Structural parameters.

		Permitivity[F/m]		Layer Thickness [nm]
		ε	ε_{xy}	
PC Substrate		$2.5\varepsilon_0$	0.0	Semi-infinite
Protect Layer 1		$4.0\varepsilon_0$	0.0	35
Displacement Layer	(Non-rec.)	$2.0\varepsilon_0$	$-0.05\varepsilon_0$	d
	(Rec.)	$2.0\varepsilon_0$	$0.05\varepsilon_0$	
Control Layer	(Non-rec.)	$2.0\varepsilon_0$	$-0.1\varepsilon_0$	5
	(Rec.)	$2.0\varepsilon_0$	$0.1\varepsilon_0$	
	(Non-mag)	$2.0\varepsilon_0$	0.0	
Switching Layer	(Non-rec.)	$2.0\varepsilon_0$	$-0.05\varepsilon_0$	15
	(Rec.)	$2.0\varepsilon_0$	$0.05\varepsilon_0$	
	(Non-mag)	$2.0\varepsilon_0$	0.0	
Memory Layer	(Non-rec.)	$2.0\varepsilon_0$	$-0.1\varepsilon_0$	60
	(Rec.)	$2.0\varepsilon_0$	$0.1\varepsilon_0$	
Protect Layer 2		$4.0\varepsilon_0$	0.0	55

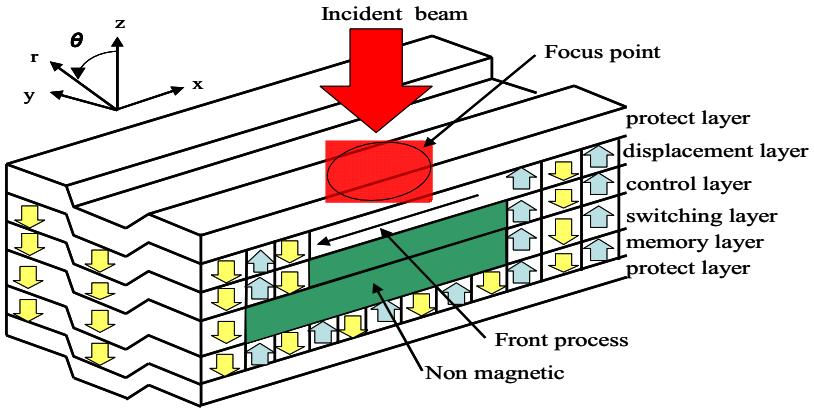

Figure 1: DWDD disk structure.

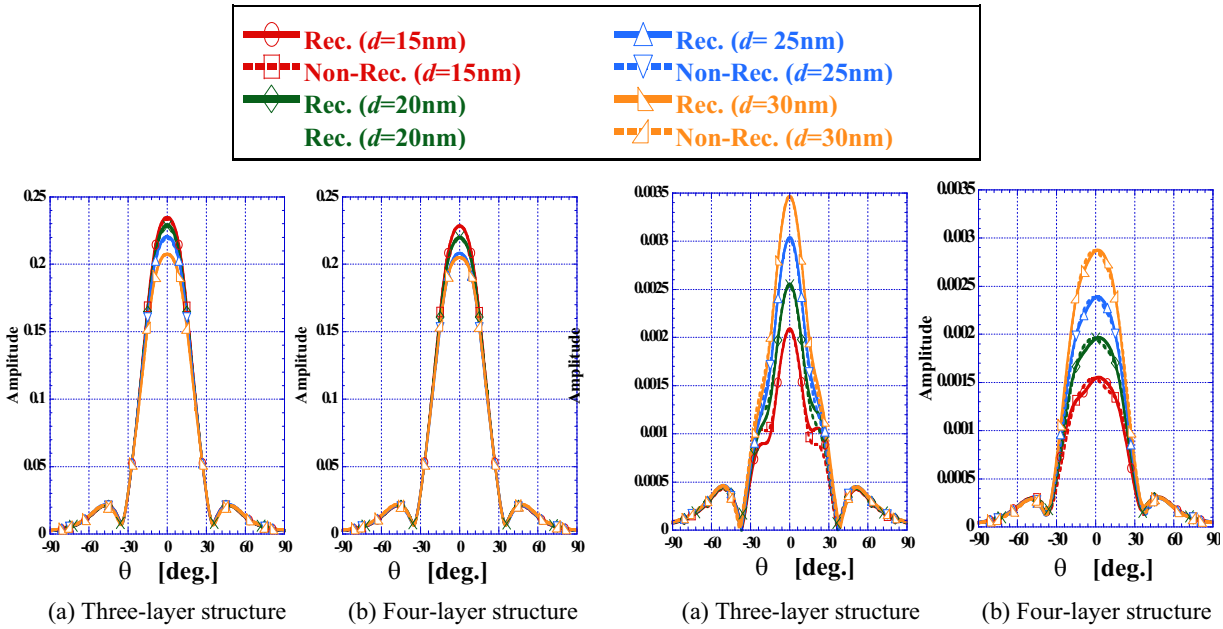

(a) Three-layer structure (b) Four-layer structure

Figure 2: Main-polarized components.

(a) Three-layer structure (b) Four-layer structure

Figure 3: Cross-polarized components.

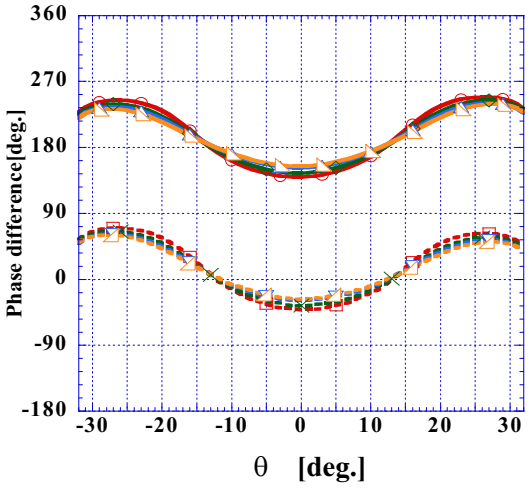

Figure 4: Phase differences (three-layer structure).

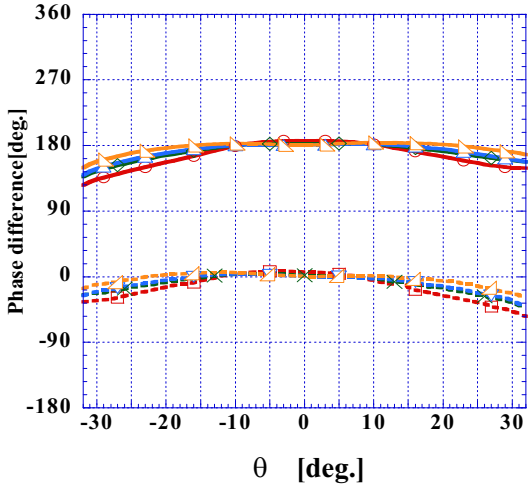

Figure 5: Phase differences (four-layer structure).

layer) and (b) four-layer (with a control layer) structures are shown. Here, the scattering patterns are normalized by the maximum field amplitude that is scattered from a perfectly conducting plane. As shown in these figures, the diffraction patterns of the main-polarized and cross-polarized components depend on d. However, they hardly depend on whether the state is recorded or non-recorded. It is also understood that the cross-polarized components of the three-layer structure are stronger than those of the four-layer one.

The phase differences between the main-polarized and cross-polarized components collected by object lens are shown in Figs. 4 and 5. As shown in Fig. 4, the phase differences of the three-layer structures vary almost sinusoidally with respect to θ for both of recorded and non-recorded states. On the other hand, from Fig. 5, the phase differences of four-layer structures take almost constant values (0 degrees for non-recorded states and 180 degrees for recorded ones) when $|\theta|$ is less than about 15 degrees. Therefore, it is understood that when the control layer is added better readout properties can be achieved as far as the phase differences are concerned.

4. CONCLUSIONS

In this study, we investigated readout characteristics of a DWDD disk with a control layer by means of FDTD method. We studied the effects of the control layer on the readout characteristics. It was shown that when the control layer is added better readout properties can be achieved as far as the phase differences are concerned.

REFERENCES

1. Kai, S., A. Fukumoto, K. Aratani, S. Yoshimura, K. Tsutsumi, and M. Arai, "Over 15-GB capacity domain wall displacement detection magneto optical recording using a digital versatile disc dimensional optical head," *Jpn. Appl. Phys.*, Vol. 39, No. 4A, 1757–1761, 2000.
2. Kobayashi, I., T. Kojima, S. Fukai, and Y. He, "Numerical analysis of light-beam diffraction from magneto-optical disk medium by FDTD method," *IEICE Trans. Electron.*, Vol. E84-C, No. 9, 1189–1195, 2001.
3. Irifune, Y., M. Miyake, and T. Kojima, "Three-dimensional numerical analysis of light-beam scattering from DWDD disk model," *Progress In Electromagnetics Reserch Symposium*, 219, 2006.

Study on Stepped Impedance Comb-line Filter with Defected Ground Structure

N. Tatsumi[1], **T. Kitamura**[1], **and Y. Horii**[2]

[1]Faculty of Engineering Science, Kansai University, Osaka, Japan
[2]Faculty of Informatics, Kansai University, Osaka, Japan

Abstract— A stepped impedance comb-line filter with defected ground structure (DGS) is proposed. The filter consists of two stepped impedance microstrip resonators. By using DGS, a coupling capacitor is inserted into the ground plane in order to build strong coupling locally along the resonators. The filtering characteristics were investigated through numerical simulations by means of FDTD method. Filtering characteristics that have attenuation poles at both sides of the passband were obtained. We discussed the input susceptances of even and odd modes.

1. INTRODUCTION

Ceramic laminated filters [1–4] have been widely used for mobile phones especially, and in particular, comb-line filters have extensively made practical use. In this study, we consider stepped impedance comb-line filters with DGS. Comb-line filters consist of two quarter-wavelength resonators, and attenuation poles can be created in the frequency characteristics of the transmission parameter by changing the coupling locally along the resonators. The stopband characteristics can be improved by arranging the attenuation poles around the passband.

We discuss the method of installing a coupling capacitor by using DGS [5–7]. In this method, a coupling capacitor can be realized without using a multilayered structure. We investigate the filtering characteristics through numerical simulations by means of FDTD method. We also discuss the input susceptances of even and odd modes.

2. FILTER STRUCTURE

We show an overview of a stepped impedance comb-line filter with a DGS structure in Fig. 1. Two microstrip stepped impedance resonators (SIRs) are arranged on the substrate, and each resonator is terminated through the ground plane at one end using a through hole. As an I/O port, a microstrip line with a characteristic impedance of $50\,\Omega$ is directly connected to each resonator. A square-shaped coupling capacitor is fabricated by inserting slots into the ground plane. The coupling capacitor is a patch conductor that is not terminated through the ground plane and produces a strong coupling locally along the resonators. The thickness and relative permittivity of the substrate are assumed to be 1.27 mm and 10.2, respectively, and the diameter of the through hole is 0.3 mm.

The metallization patterns and dimensions of the filter are shown in Fig. 2. The dimensions and position of the coupling capacitor are also shown. The size of the coupling capacitor is $d \times 5.2\,\mathrm{mm}^2$. The other structural parameters are also shown in Fig. 2.

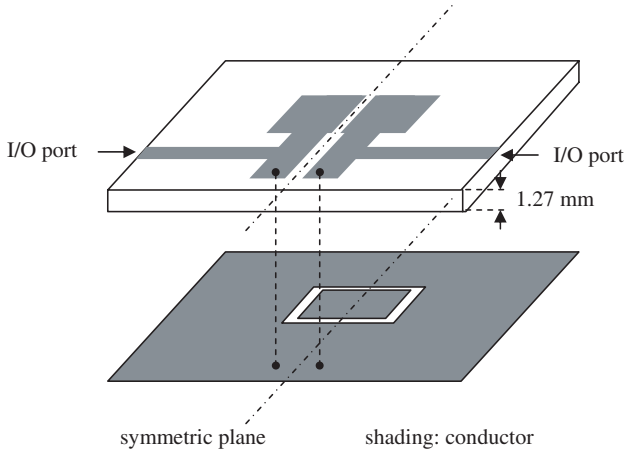

Figure 1: Whole structure of filter.

3. NUMERICAL RESULTS

We investigate the filtering characteristics through numerical simulations by means of FDTD method. We show the frequency characteristics of the scattering parameters with L and d as parameters in Figs. 3(a) and (b). As shown in Fig. 3(a), the higher attenuation-pole frequency becomes lower and the bandwidth of the passband narrower as L increases. It is also understood from Fig. 3(b) that as d increases the higher attenuation-pole frequency gets lower while the bandwidth of the passband is almost maintained. We illustrate the equivalent circuit of the comb-line filter in Fig. 4. Attenuation poles appear at the frequencies where the input susceptances of the even and odd modes are equal to each other. The frequency characteristics of the input susceptances of the even and odd modes when $d = 5.2\,\text{mm}$ and $L = 3.6\,\text{mm}$ are shown in Figs. 5(a) (lower frequency) and (b) (higher frequency). The input susceptances of the even and odd modes were calculated by setting the magnetic and electric wall, respectively, on the symmetric plane shown in Fig. 1.

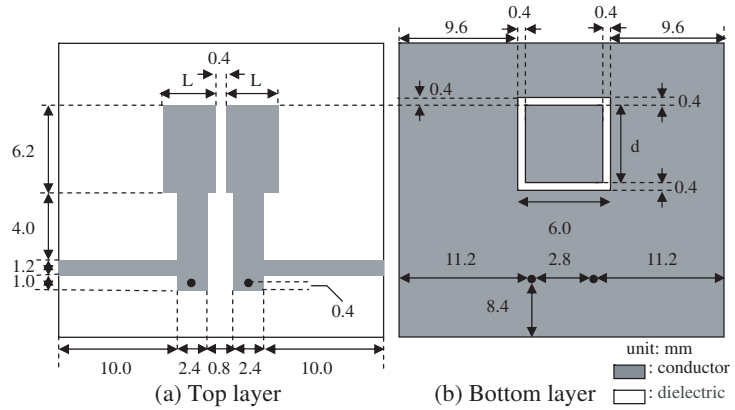

(a) Top layer (b) Bottom layer

Figure 2: Metallization patterns.

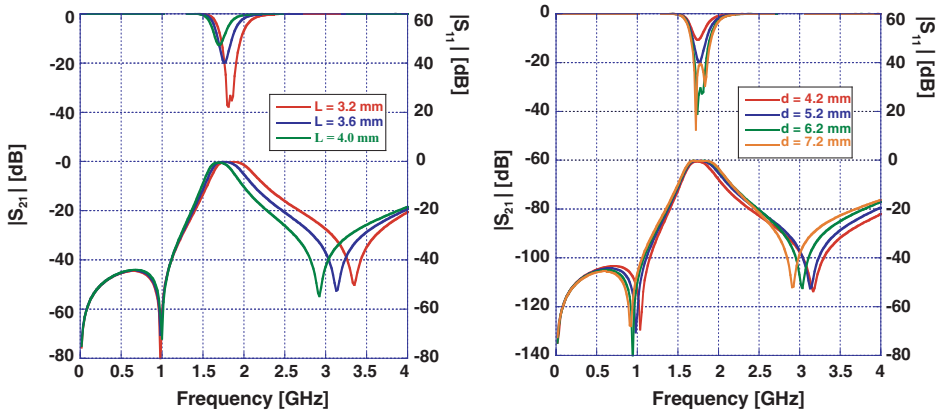

(a) $d = 5.2$ mm (b) $L = 3.6$ mm

Figure 3: Frequency characteristics of the scattering parameters.

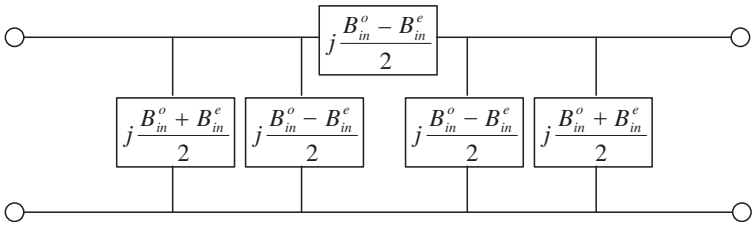

Figure 4: Equivalent circuit.

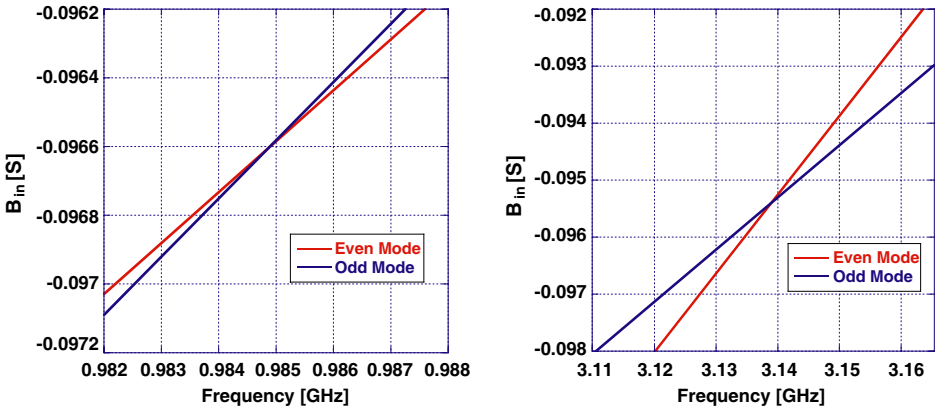

(a) Lower frequency (b) Higher frequency

Figure 5: Input susceptances ($L = 3.6\,\text{mm}$, $d = 5.2\,\text{mm}$).

4. CONCLUSION

We proposed a stepped impedance comb-line filter with DGS. By using DGS, a coupling capacitor is inserted into the ground plane in order to build strong coupling locally along the microstrip resonators. We investigated the filtering characteristics through numerical simulations by means of FDTD method and obtained filtering characteristics having attenuation poles at both sides of the passband. We discussed the input susceptances of even and odd modes.

REFERENCES

1. Ishizaki, T., M. Fujita, H. Kagata, T. Uwano, and H. Miyake, "A very small dielectric planar filter for portable telephones," *IEEE Trans. Microw. Theory Tech.*, Vol. 42, 2017–2022, 1994.
2. Ishizaki, T., T. Uwano, and H. Miyake, "An extended configuration of a stepped impedance comb-line filter," *IEICE Trans. Electron.*, Vol. E79-C, No. 5, 671–678, 1996.
3. Ishizaki, T., T. Kitamura, M. Geshiro, and S. Sawa, "Study of the influence of grounding for microstrip resonators," *IEEE Trans. Microw. Theory Tech.*, Vol. 45, 2089–2093, 1997.
4. Kitamura, T., M. Geshiro, T. Ishizaki, T. Maekawa, and S. Sawa, "Characterization of triplate strip resonators with a loading capacitor," *IEICE Trans. Electron.*, Vol. E81-C, No. 12, 1793–1799, 1998.
5. Safwat, A. M. E., F. Podevin, P. Ferrari, and A. Vilcot, "Tunable bandstop defected ground structure resonator using reconfigurable dumbbell-shaped coplanar waveguide," *IEEE Trans. Microw. Theory Tech.*, Vol. 54, No. 9, 3559–3564, 2006.
6. Wang, M., Y. Chang, H. Wu, C. Huang, and Y. Su, "An inverse S-shaped slotted ground structure applied to miniature wide stopband lowpass filters," *IEICE Trans. Electron.*, Vol. E90-C, No. 12, 2285–2288, 2007.
7. Yang, J., C. Gu, and W. Wu, "Design of novel compact coupled microstrip power divider with harmonic suppression," *IEEE Microw. Wireless Compon. Lett.*, Vol. 18, No. 9, 572–574, 2008.

Generalized Coherent States for Quantized Electromagnetic Fields in Time-varying Linear Media

Jeong Ryeol Choi[1] and Mustapha Maamache[2]

[1]School of Electrical Engineering and Computer Science, Kyungpook National University
Daegu 702-701, Republic of Korea
[2]Laboratoire de Physique Quantique et Systèmes Dynamiques, Faculté des Sciences
Université Ferhat Abbas de Sétif, Sdtif 19000, Algeria

Abstract— If the parameters of the materials, such as electric permittivity, magnetic permeability, and conductivity, vary explicitly with time, the corresponding Hamiltonian is a time-dependent form and such materials are classified as the time-varying media of light. The quantization of electromagnetic fields in time-varying linear media is well described by means of the invariant operator theory of Lewis-Riesenfeld. The Coulomb gauge is chosen in the development of theory, which allows us to evaluate quantized electric and magnetic fields by expanding only the vector potential in charge free space, since the scalar potential in this situation vanishes. The generalized coherent state, i.e., Gaussian-Klauder state, of electromagnetic fields confined inside a cavity filled with a nontrivial conductive medium is investigated. The Gaussian-Klauder state provides a general means of construction for Husimi-Wigner distributions and can be used to show the quantum and classical correspondence. We confirmed that the uncertainty product in Gaussian-Klauder state is the same as the minimum uncertainty product in number state. This property of the generalized coherent state is well agree with that of the well known Glauber coherent state.

1. INTRODUCTION

Coherent states are important concept in quantum physics, since they are fruitfully being utilized in many areas of dynamical systems. In recent years much interest was aroused in generalizing the coherent states, together the concern in their applications to particular systems. Various schemes to prepare generalized coherent states are proposed through different definitions of coherent states. Soon after the suggestion of the standard coherent states for harmonic oscillator by Glauber [1], a generalization of Glauber's coherent states is suggested by Titulaer and Glauber [2]. Afterwards, many attempts to build different families of coherent states have been followed. For such a large class of generalized coherent states and their properties, one may refer to Refs. [3–6].

About a decade ago, a significant progress has been made in constructing generalized coherent states for the problem of Coulomb potential system by Klauder [3] and by Majumdar et al. [4]. Fox [5] established and studied the genuine Gaussian generalized coherent states for hydrogen atom, so called the Gaussian-Klauder states, along a construction procedure proposed by Klauder [3]. Gaussian-Klauder states provide a general means for constructing Husimi-Wigner distributions [6] and can be used to show the quantum and classical correspondence. Recently the Gaussian-Klauder states are applied to diverse quantum systems beyond simple harmonic oscillator and standard Coulomb potential system [7, 8].

The purpose of this paper is to apply Gaussian-Klauder states into quantized electromagnetic fields in time-varying linear media. When the parameters of media such as the conductivity, electric permittivity, and magnetic permeability are explicitly dependent on time, the medium is classified as time-varying media. Recently, the quantization problem of light in time-varying linear media is interested in the community of quantum optics. A quantum model associated to producing excitation of the radiation modes in a time-dependent dielectric inside a double cavity is studied by Cirone et al. [9]. Several years ago, a simple scalar model is proposed by Crocce et al. in order to explain resonant photon creation from vacuum state in a thin semiconductor film, induced by the time-dependent conductivity in the presence of periodically irradiating short laser pulses [10].

It was shown on the basis of the Maxwell's equations that the light in time-varying media is described by a time-dependent Hamiltonian [11–13]. The quantization on a fundamental level for the time-dependent Hamiltonian systems like this can be fulfilled via the invariant operator formulation [11–17] of quantum electrodynamics. In the previous papers [11, 12], we used Lewis-Riesenfeld (LR) invariant operator method [14, 15] with the choice of Coulomb gauge in order to study the quantum properties of light in time-varying linear media. Further, the time behavior of

electric and magnetic field operators have been analyzed for the light confined in a cavity filled with time-varying media and the light propagating under periodic boundary condition in time-varying media [11].

This paper is organized as follows. In Sec. 2, we present the quantization problem of electromagnetic fields in time-varying linear media on the basis of LR invariant operator method. The generalized coherent states of the system, that are Gaussian-Klauder types, will be investigated in Sec. 3 by taking advantage of the results obtained in Sec. 2. Finally, the concluding remarks are addressed in the last section.

2. QUANTIZATION OF ELECTROMAGNETIC FIELDS IN TIME-VARYING MEDIA

The quantization of electromagnetic fields in vacuum cavities or in infinite free space, that is treated in most text books of quantum optics, gives the same results as the case of standard harmonic oscillator. Such traditional quantization procedure may also be extended to that of electromagnetic fields described by time-dependent Hamiltonians by means of LR invariant operator method introduced by Lewis and Riesenfeld. The LR invariant operator method is very useful in investigating the quantum properties of various types of time-dependent Hamiltonian systems.

We start from fundamental Maxwell's equations in charge free space, that are given by

$$\begin{aligned} \nabla \cdot \mathbf{D} = 0, \quad \nabla \times \mathbf{E} = -\frac{\partial \mathbf{B}}{\partial t}, \\ \nabla \cdot \mathbf{B} = 0, \quad \nabla \times \mathbf{H} = \mathbf{J} + \frac{\partial \mathbf{D}}{\partial t}. \end{aligned} \tag{1}$$

If electric permitivity ϵ, magnetic permiability μ, and conductivity σ do not depend on field strength, it is recognized that the medium is linear. The fields and current in time-varying linear media follow the relations

$$\mathbf{D} = \epsilon(t)\mathbf{E}, \quad \mathbf{H} = \frac{\mathbf{B}}{\mu(t)}, \quad \mathbf{J} = \sigma(t)\mathbf{E}. \tag{2}$$

We use Coulomb gauge that provides a convenient way to quantize the electromagnetic fields. The velocity of light in time-varying media is given by $c(t) = 1/[\epsilon(t)\mu(t)]^{1/2}$. We can expand the electric and magnetic fields only in terms of vector potential since the scalar potential vanishes in charge free space under the choice of Coulomb gauge. Thus we have

$$\nabla^2 \mathbf{A} - \mu\left(\sigma + \dot{\epsilon}\right)\frac{\partial \mathbf{A}}{\partial t} - \epsilon\mu\frac{\partial^2 \mathbf{A}}{\partial t^2} = 0. \tag{3}$$

According to well known method of separation of variables, we can represent the vector potential in terms of mode functions $\mathbf{u}_l(\mathbf{r})$ and time functions $q_l(t)$ of each cavity mode such that

$$\mathbf{A}(\mathbf{r}, t) = \sum_l \mathbf{u}_l(\mathbf{r}) q_l(t), \tag{4}$$

where l denotes different cavity modes of the field.

Once the vector potential is identified, we can easily derive the electric and the magnetic fields from

$$\mathbf{E}(\mathbf{r}, t) = -\frac{\partial \mathbf{A}(\mathbf{r}, t)}{\partial t}, \quad \mathbf{B}(\mathbf{r}, t) = \nabla \times \mathbf{A}(\mathbf{r}, t). \tag{5}$$

The scalar potential does not regarded in the first equation of the above, since it is zero in charge free space.

Some algebra after substituting Eq. (4) into Eq. (3) yields

$$\nabla^2 \mathbf{u}_l(\mathbf{r}) + \frac{\omega_l^2(0)}{c^2(0)}\mathbf{u}_l(\mathbf{r}) = 0, \tag{6}$$

$$\frac{\partial^2 q_l(t)}{\partial t^2} + \frac{\sigma(t) + \dot{\epsilon}(t)}{\epsilon(t)}\frac{\partial q_l(t)}{\partial t} + \omega_l^2(t) q_l(t) = 0, \tag{7}$$

where $\omega_l(t)$ is the time-dependent natural frequency of mode l, that is given by

$$\omega_l(t) = \left(\frac{\epsilon_0\mu(0)}{\epsilon(t)\mu(t)}\right)^{1/2}\omega_l(0) \qquad \epsilon_0 = \epsilon(0). \tag{8}$$

The mode function is determined by the geometric of the medium. For instance, it is given by

$$\mathbf{u}_{l,(l')}(\mathbf{r}) = \frac{2}{\sqrt{V}}\hat{\varepsilon}_x \sin\frac{l\pi y}{L}\sin\frac{l'\pi z}{L}, \tag{9}$$

for the light confined in cubic cavity of side L, where $V = L^3$ is the volume of the cube and $\hat{\varepsilon}_x$ is the unit vector to the direction of x.

The quantum Hamiltonian which gives the classical equation of motion, Eq. (7), is

$$\hat{H}_l\left(\hat{q}_l, \hat{p}_l, t\right) = e^{-\Lambda(t)}\frac{\hat{p}_l^2}{2\epsilon_0} + \frac{1}{2}e^{\Lambda(t)}\epsilon_0\omega_l^2(t)\hat{q}_l^2, \tag{10}$$

where operator $\hat{p}_l$ is defined by $\hat{p}_l = -i\hbar\partial/(\partial q)$ and

$$\Lambda(t) = \int_0^t \frac{\sigma(s) + \dot{\epsilon}(s)}{\epsilon(s)}ds. \tag{11}$$

We can readily see that the commutation relation between the two conjugate canonical variables is $[\hat{q}_l, \hat{p}_{l'}] = i\hbar\delta_{ll'}$. If we use the Maxwell's equations $\nabla\cdot\mathbf{E} = 0$ and $\nabla\times\mathbf{B} = \mu\mathbf{J} + \mu\epsilon\partial\mathbf{E}/\partial t$ instead of the first and the forth of Eq. (1), the term involving $\dot{\epsilon}$ does not appears in Eq. (11) [11, 12].

Let us suppose that the classical solution of Eq. (7) takes the form

$$q_l(t) = M_l(t)\left[C_+e^{i\gamma_l(t)} + C_-e^{-i\gamma_l(t)}\right], \tag{12}$$

where C_+ and C_- are constants and $M_l(t)$ and $\gamma_l(t)$ are some time functions that are real. By substituting the above equation into Eq. (7), we have the two equations from the real and the imaginary parts:

$$\ddot{M}_l(t) = \left[\dot{\gamma}_l^2(t) - \omega_l^2(t)\right]M_l(t) - \frac{\sigma(t) + \dot{\epsilon}(t)}{\epsilon(t)}\dot{M}_l(t), \tag{13}$$

$$\ddot{\gamma}_l(t) = -\left(2\frac{\dot{M}_l(t)}{M_l(t)} + \frac{\sigma(t) + \dot{\epsilon}(t)}{\epsilon(t)}\right)\dot{\gamma}_l(t). \tag{14}$$

Since the time-dependent function in the Hamiltonian Eq. (10) does not separated out from the function of canonical variables, the quantization procedure using conventional method may be quite difficult. In this case the employ of invariant operator is very helpful in quantizing the system. It is fully recognized in the community of theoretical physics researchers that the invariant operator method of LR [14, 15] provides a convenient way to quantize the time-dependent Hamiltonian system. By solving $d\hat{I}_l/dt = \partial\hat{I}_l/\partial t + [\hat{I}_l, \hat{H}_l]/(i\hbar) = 0$, we have the invariant operator in the form [11]

$$\hat{I}_l = \hbar\Omega_l\left(\hat{a}_l^\dagger\hat{a}_l + \frac{1}{2}\right), \tag{15}$$

where Ω_l is a time-constant given by

$$\Omega_l = \frac{M_l^2(t)}{M_l^2(0)}e^{\Lambda(t)}\dot{\gamma}_l(t), \tag{16}$$

and $\hat{a}_l$ and $\hat{a}_l^\dagger$ are the annihilation and creation operators which take the form

$$\hat{a}_l = \sqrt{\frac{1}{2\hbar\epsilon_0\dot{\gamma}_l}}e^{-\Lambda(t)/2}\left[\epsilon_0e^{\Lambda(t)}\left(\dot{\gamma}_l - i\frac{\dot{M}_l}{M_l}\right)\hat{q}_l + i\hat{p}_l\right], \tag{17}$$

$$\hat{a}_l^\dagger = \sqrt{\frac{1}{2\hbar\epsilon_0\dot{\gamma}_l}}e^{-\Lambda(t)/2}\left[\epsilon_0e^{\Lambda(t)}\left(\dot{\gamma}_l + i\frac{\dot{M}_l}{M_l}\right)\hat{q}_l - i\hat{p}_l\right]. \tag{18}$$

The ladder operators, Eqs. (17) and (18), are somewhat different from those of the simple harmonic oscillator and one can easily verify that they satisfy boson commutation relation, $[\hat{a}_l, \hat{a}_{l'}^\dagger] = \delta_{ll'}$.

From now on, we consider only the monochromatic plane wave so that we can omit under subscript l from all notations for the shake of convenience. Let us write the eigenvalue equation of the invariant operator as $\hat{I}|n(t)\rangle = \lambda_n|n(t)\rangle$. Then, the eigenstates of the invariant operator in configuration space are given by [11]

$$\langle q|n(t)\rangle = \frac{1}{\sqrt{2^n n!}}\left(\frac{\epsilon_0\dot{\gamma}}{\pi\hbar}\right)^{1/4} e^{\Lambda(t)/4} H_n\left(\sqrt{\frac{\epsilon_0\dot{\gamma}}{\hbar}}e^{\Lambda(t)/2}q\right)\exp\left[-\frac{\epsilon_0}{2\hbar}e^{\Lambda(t)}\left(\dot{\gamma}-i\frac{\dot{M}}{M}\right)q^2\right]. \tag{19}$$

According to the invariant operator theory, the wave functions that satisfy Schrödinger equation can be expressed in terms of $\langle q|n(t)\rangle$:

$$\langle q|\psi_n(t)\rangle = \langle q|n(t)\rangle\exp\left[-i\gamma(t)\left(n+\frac{1}{2}\right)\right]. \tag{20}$$

Hence the difference of the wave functions from the eigenstates of the invariant operator is as much as the time-dependent phases $-\gamma(t)\,(n+1/2)$.

From inverse representations of Eqs. (17) and (18) together, we see that the canonical variables are written as

$$\hat{q} = \sqrt{\frac{\hbar}{2\epsilon_0\dot{\gamma}}}e^{-\Lambda(t)/2}\left(\hat{a}^\dagger+\hat{a}\right), \tag{21}$$

$$\hat{p} = i\sqrt{\frac{\hbar\epsilon_0}{2\dot{\gamma}}}e^{\Lambda(t)/2}\left[\left(\dot{\gamma}-i\frac{\dot{M}}{M}\right)\hat{a}^\dagger-\left(\dot{\gamma}+i\frac{\dot{M}}{M}\right)\hat{a}\right]. \tag{22}$$

With the help of Eq. (20), it is possible to derive the fluctuations of canonical variables, $\Delta\hat{q}$ and $\Delta\hat{p}$. By multiplying them, we have the corresponding uncertainty relation in number state

$$\Delta\hat{q}\Delta\hat{p} = \left(n+\frac{1}{2}\right)\hbar\left[1+\frac{1}{\dot{\gamma}^2}\left(\frac{\dot{M}}{M}\right)^2\right]^{1/2}. \tag{23}$$

Thus, the time variation of $M(t)$ and $\gamma(t)$ directly affects to the magnitude of the uncertainty relation. The uncertainty relation is always larger than or equal to $\hbar/2$ which is the physically allowed minimum uncertainty value for harmonic oscillator, since it is assumed that $M(t)$ and $\gamma(t)$ are real. When $M(t)$ is constant with time, $\Delta\hat{q}\Delta\hat{p}$ reduces to $(n+1/2)\hbar$ which is the same as the uncertainty relation for the simple harmonic oscillator in number states.

3. GENERALIZED COHERENT STATES

In this section, we apply Klauder's construction of generalized coherent states for Hamiltonians which have discrete eigenvalue spectra to the system of electromagnetic fields in time-varying linear media The Gaussian-Klauder state for harmonic oscillator are defined as [6]

$$|n_0,\phi_0\rangle = \frac{1}{\sqrt{N(n_0)}}\sum_{n=0}^{\infty}\exp\left[-\frac{(n-n_0)^2}{4\varsigma^2}\right]e^{in\phi_0}|n(t)\rangle, \tag{24}$$

where n_0 is the center of the Gaussian distribution, ϕ_0 initial phase factor of the superposition of states, ς the standard deviation of the Gaussian, and $N(n_0)$ is a normalization factor. From the normalization condition $\langle n_0,\phi_0|n_0,\phi_0\rangle = 1$, we can see that $N(n_0) = \sum_{n=0}^{\infty}\exp\left[-\frac{(n-n_0)^2}{2\varsigma^2}\right]$. Using Eqs. (21) and (22) and the state Eq. (24), the expectation value of canonical variables and their

squares are evaluated to be

$$\langle n_0,\phi_0|\hat{q}|n_0,\phi_0\rangle = \sqrt{\frac{\hbar}{2\epsilon_0\dot{\gamma}}}\frac{2e^{-\Lambda(t)/2}}{N(n_0)}\cos\phi_0\sum_{n=0}^{\infty}\sqrt{n+1}G(n)G(n+1), \tag{25}$$

$$\langle n_0,\phi_0|\hat{p}|n_0,\phi_0\rangle = \sqrt{\frac{2\hbar\epsilon_0}{\dot{\gamma}}}\frac{e^{\Lambda(t)/2}}{N(n_0)}(\dot{\gamma}\sin\phi_0+\frac{\dot{M}}{M}\cos\phi_0)\sum_{n=0}^{\infty}\sqrt{n+1}G(n)G(n+1), \tag{26}$$

$$\left\langle n_0,\phi_0\left|\hat{q}^2\right|n_0,\phi_0\right\rangle = \frac{\hbar e^{-\Lambda(t)}}{2\epsilon_0\dot{\gamma}N(n_0)}\left[2\cos(2\phi_0)\sum_{n=0}^{\infty}\sqrt{(n+1)(n+2)}G(n)G(n+2)+\sum_{n=0}^{\infty}(2n+1)G^2(n)\right], \tag{27}$$

$$\begin{aligned}\left\langle n_0,\phi_0\left|\hat{p}^2\right|n_0,\phi_0\right\rangle = &-\frac{\hbar\epsilon_0 e^{\Lambda(t)}}{2\dot{\gamma}N(n_0)}\left\{2\left[\left(\dot{\gamma}^2-\frac{\dot{M}^2}{M^2}\right)\cos(2\phi_0)-2\dot{\gamma}\frac{\dot{M}}{M}\sin(2\phi_0)\right]\right.\\ &\left.\times\sum_{n=0}^{\infty}\sqrt{(n+1)(n+2)}G(n)G(n+2)-\left(\dot{\gamma}^2+\frac{\dot{M}^2}{M^2}\right)\sum_{n=0}^{\infty}(n+1)G^2(n)\right\},\end{aligned} \tag{28}$$

where we abbreviated the Gaussian factor as $G(n)\equiv\exp\left[-\frac{(n-n_0)^2}{4\varsigma^2}\right]$. If we consider Eqs. (4) and (5), the expectation values of particular mode electric and magnetic fields in this state are

$$\langle n_0,\phi_0|\mathbf{E}(\mathbf{r},t)|n_0,\phi_0\rangle = -\mathbf{u}(\mathbf{r})\frac{1}{\epsilon_0}e^{-\Lambda(t)}\langle n_0,\phi_0|\hat{p}|n_0,\phi_0\rangle, \tag{29}$$

$$\langle n_0,\phi_0|\mathbf{B}(\mathbf{r},t)|n_0,\phi_0\rangle = \nabla\times\mathbf{u}(\mathbf{r})\langle n_0,\phi_0|\hat{q}|n_0,\phi_0\rangle. \tag{30}$$

We expand all factors around $n=n_0$ since $G(n)$ is largest at $n=n_0$. This leads to [6]

$$\sqrt{n+1}\simeq\sqrt{n_0+1}\exp\left[\frac{n-n_0}{2(n_0+1)}-\frac{1}{4}\left(\frac{n-n_0}{n_0+1}\right)^2\right], \tag{31}$$

$$2n+1\simeq(2n_0+1)\exp\left[\frac{2(n-n_0)}{2n_0+1}-2\left(\frac{n-n_0}{2n_0+1}\right)^2\right], \tag{32}$$

$$\sqrt{(n+1)(n+2)}\simeq\left(n_0+\frac{3}{2}\right)\exp\left[\frac{n-n_0}{2(n_0+1)}-\frac{1}{4}\left(\frac{n-n_0}{n_0+1}\right)^2-\frac{1}{4}\left(\frac{n-n_0}{n_0+2}\right)^2+\frac{n-n_0}{2(n_0+2)}\right]. \tag{33}$$

Now replacing sums by Gaussian integrals under the assumption that n_0 is sufficiently large, Eqs. (25)–(28) become

$$\langle n_0,\phi_0|\hat{q}|n_0,\phi_0\rangle = \sqrt{\frac{2\hbar}{\epsilon_0\dot{\gamma}}}e^{-\Lambda(t)/2}\cos\phi_0\ f_1, \tag{34}$$

$$\langle n_0,\phi_0|\hat{p}|n_0,\phi_0\rangle = \sqrt{\frac{2\hbar\epsilon_0}{\dot{\gamma}}}e^{\Lambda(t)/2}\left(\dot{\gamma}\sin\phi_0+\frac{\dot{M}}{M}\cos\phi_0\right)f_1, \tag{35}$$

$$\left\langle n_0,\phi_0\left|\hat{q}^2\right|n_0,\phi_0\right\rangle = \frac{\hbar}{2\epsilon_0\dot{\gamma}}e^{-\Lambda(t)}[2\cos(2\phi_0)f_2+f_3], \tag{36}$$

$$\left\langle n_0,\phi_0\left|\hat{p}^2\right|n_0,\phi_0\right\rangle = -\frac{\hbar\epsilon_0}{2\dot{\gamma}}e^{\Lambda(t)}\left\{2\left[\left(\dot{\gamma}^2-\frac{\dot{M}^2}{M^2}\right)\cos(2\phi_0)-2\dot{\gamma}\frac{\dot{M}}{M}\sin(2\phi_0)\right]f_2-\left(\dot{\gamma}^2+\frac{\dot{M}^2}{M^2}\right)f_3\right\}, \tag{37}$$

where

$$f_1=\sqrt{n_0+1}\left(1-\frac{\varsigma^2}{4n_0^2}\right)\exp\left[\frac{\varsigma^2\left(1-\frac{\varsigma^2}{2n_0^2}\right)}{2}\left(\frac{1}{4n_0^2}+\frac{1}{4\varsigma^4}-\frac{1}{2n_0\varsigma^2}-\frac{1}{2n_0^3}+\frac{1}{2n_0^2\varsigma^2}\right)-\frac{1}{4\varsigma^2}\right], \tag{38}$$

$$f_2=\left(n_0+\frac{3}{2}\right)\left(1-\frac{\varsigma^2}{2n_0^2}\right)\exp\left[\frac{\varsigma^2}{2n_0^2}-\frac{\varsigma^2}{2n_0^3}-\frac{1}{2\varsigma^2}-\frac{1}{n_0}+\frac{1}{n_0^2}-\frac{\varsigma^4}{2n_0^4}+\frac{3\varsigma^4}{2n_0^5}-\frac{3\varsigma^2}{2n_0^4}\right], \tag{39}$$

$$f_3=(2n_0+1)\left(1-\frac{\varsigma^2}{2n_0^2}\right)\exp\left[\frac{\varsigma^2}{2n_0^2}\left(1-\frac{\varsigma^2}{n_0^2}-\frac{1}{n_0}\right)\right]. \tag{40}$$

The leading orders for $\varsigma^2 = n_0$ reduce to

$$\langle n_0, \phi_0|\hat{q}|n_0, \phi_0\rangle = \sqrt{\frac{2\hbar n_0}{\epsilon_0\dot{\gamma}}} e^{-\Lambda(t)/2}\cos\phi_0, \tag{41}$$

$$\langle n_0, \phi_0|\hat{p}|n_0, \phi_0\rangle = \sqrt{\frac{2\hbar\epsilon_0 n_0}{\dot{\gamma}}} e^{\Lambda(t)/2}\left(\dot{\gamma}\sin\phi_0 + \frac{\dot{M}}{M}\cos\phi_0\right), \tag{42}$$

$$\langle n_0, \phi_0|\hat{q}^2|n_0, \phi_0\rangle = \frac{\hbar}{2\epsilon_0\dot{\gamma}} e^{-\Lambda(t)}[2\cos(2\phi_0)n_0 + 2n_0 + 1], \tag{43}$$

$$\langle n_0, \phi_0|\hat{p}^2|n_0, \phi_0\rangle = -\frac{\hbar\epsilon_0}{2\dot{\gamma}} e^{\Lambda(t)}\left\{2\left[\left(\dot{\gamma}^2 - \frac{\dot{M}^2}{M^2}\right)\cos(2\phi_0) - 2\dot{\gamma}\frac{\dot{M}}{M}\sin(2\phi_0)\right]n_0 - \left(\dot{\gamma}^2 + \frac{\dot{M}^2}{M^2}\right)(2n_0+1)\right\}. \tag{44}$$

Among various properties for generalized coherent states, we are interested in fluctuations of the fields and the uncertainty relation for canonical variables. Theoretical and experimental studies on quantum fluctuations for quantized electromagnetic fields may give great promise for understanding their quantum behaviors. The fluctuation of any observable $\hat{\mathcal{O}}$ in the generalized coherent states is defined as

$$(\Delta\hat{\mathcal{O}})_{\mathrm{GCS}} = [\langle n_0, \phi_0|\hat{\mathcal{O}}^2|n_0, \phi_0\rangle - (\langle n_0, \phi_0|\hat{\mathcal{O}}|n_0, \phi_0\rangle)^2]^{1/2}. \tag{45}$$

Hence form Eqs. (41)–(44), the fluctuations of the canonical variables are

$$(\Delta\hat{q})_{\mathrm{GCS}} = \sqrt{\frac{\hbar}{2\epsilon_0\dot{\gamma}}} e^{-\Lambda(t)/2}, \quad (\Delta\hat{p})_{\mathrm{GCS}} = \sqrt{\frac{\hbar\epsilon_0}{2\dot{\gamma}}}\left(\dot{\gamma}^2 + \frac{\dot{M}^2}{M^2}\right)^{1/2} e^{\Lambda(t)/2}. \tag{46}$$

By multiplying the above two equations, we can readily identify the uncertainty relation as

$$(\Delta\hat{q})_{\mathrm{GCS}}\,(\Delta\hat{p})_{\mathrm{GCS}} = \frac{\hbar}{2}\left[1 + \frac{1}{\dot{\gamma}^2}\left(\frac{\dot{M}}{M}\right)^2\right]^{1/2}. \tag{47}$$

This exactly coincides with the zero-point uncertainty relation in the number state, that is identified from Eq. (23) with $n = 0$. For ordinary damped harmonic oscillator the parameters ϵ, μ and σ become constant, i.e., $\dot{\epsilon}(t) = 0$, $\dot{\mu}(t) = 0$, $\dot{\sigma}(t) = 0$. Then, the time functions in Eq. (12) reduces to $\gamma(t) = \Omega t$, $M(t) = \exp(-\frac{\sigma}{2\epsilon}t)$, where the time-constant Ω becomes a modified frequency which is the form $\Omega = [\omega^2 - \sigma^2/(4\epsilon^2)]^{1/2}$. The natural frequency ω is also constant in this case. Further, the uncertainty relation becomes

$$(\Delta\hat{q})_{\mathrm{GCS}}\,(\Delta\hat{p})_{\mathrm{GCS}} = \frac{\hbar\omega}{2\Omega}. \tag{48}$$

This precisely coincides with that of the Glauber coherent states [18]. Though the magnitude of this uncertainty relation does not affected by the value of μ, it increases as σ/ϵ grows. If σ vanishes, Eq. (48) reduces to $\hbar/2$ which is the uncertainty relation for the simple harmonic oscillator in coherent states.

From the substitution of Eqs. (41) and (42) into Eqs. (29) and (30), we have the expectation value of electric and magnetic fields

$$\langle n_0, \phi_0|\mathbf{E}(\mathbf{r}, t)|n_0, \phi_0\rangle = -\mathbf{u}(\mathbf{r})\sqrt{\frac{2\hbar n_0}{\epsilon_0\dot{\gamma}}} e^{-\Lambda(t)/2}\left(\dot{\gamma}\sin\phi_0 + \frac{\dot{M}}{M}\cos\phi_0\right), \tag{49}$$

$$\langle n_0, \phi_0|\mathbf{B}(\mathbf{r}, t)|n_0, \phi_0\rangle = \nabla\times\mathbf{u}(\mathbf{r})\sqrt{\frac{2\hbar n_0}{\epsilon_0\dot{\gamma}}} e^{-\Lambda(t)/2}\cos\phi_0. \tag{50}$$

It is not difficult to find the expectation value of the square of the fields, with the aid of Eqs. (43) and (44). Hence, from Eq. (45), the corresponding fluctuations of the electric and magnetic fields

are

$$[\Delta\mathbf{E}(\mathbf{r},t)]_{\mathrm{GCS}} = \mathbf{u}(\mathbf{r})\sqrt{\frac{\hbar}{2\epsilon_0\dot{\gamma}}}\left(\dot{\gamma}^2+\frac{\dot{M}^2}{M^2}\right)^{1/2}e^{-\Lambda(t)/2}, \tag{51}$$

$$[\Delta\mathbf{B}(\mathbf{r},t)]_{\mathrm{GCS}} = \nabla\times\mathbf{u}(\mathbf{r})\sqrt{\frac{\hbar}{2\epsilon_0\dot{\gamma}}}e^{-\Lambda(t)/2}. \tag{52}$$

Thus, not only the fields but also their fluctuations decrease exponentially with time when $\Lambda(t)$ is positive. If we consider Eq. (11), the dissipation of electromagnetic fields occurs when the conductivity σ is present in the medium and when the permitivity ϵ increases monotonically as time goes by. On the other hand, the fields are amplified exponentially when $\Lambda(t)$ is negative.

4. CONCLUSION

The generalized coherent state, i.e., Gaussian-Klauder state is investigated for the electromagnetic fields in time-varying linear media using invariant operator method of LR. Two differential equations, each are related to two separated functions, i.e., mode function $\mathbf{u}_l(\mathbf{r})$ and time function $q_l(t)$, are obtained under the choice of Coulomb gauge. Since the Hamiltonian given in Eq. (10) is explicitly dependent on time, we used invariant operator method in order to derive quantum solutions of the system. In terms of the creation and the annihilation operators that are different from those of the simple harmonic oscillator, the invariant operator is represented as a simple form [see Eq. (15)]. From the eigenvalue equation of $\hat{I}_l$, we derived its eigenstates $\langle q|n(t)\rangle$ in configuration space. The wave functions that satisfy Schrödinger equation are represented in terms of $\langle q|n(t)\rangle$ as shown in Eq. (20).

Gaussian-Klauder state defined in Eq. (24) in terms of eigenstates $|n(t)\rangle$ provides the basic understanding for the classical limit of quantum electrodynamics and yields some insight into control of quantized electromagnetic fields. This state is characterized by the three parameters, n_0, ϕ_0, and ς: n_0 determines the motion of the quantum wave packet along the classical orbit; ϕ_0 determines the initial phase distribution of the states forming the wave packet; ς determines the standard deviation of quantum states that effectively form the coherent state [8]. If ς is large, the wave packet is initially well localized. Whereas the packet is initially less localized for small ς.

Using Eqs. (21) and (22), the fluctuations of canonical variables and the uncertainty relation are derived. By comparing Eq. (47) with Eq. (23), we see that the uncertainty relation in generalized coherent states is the same as that of the minimum value in number states. For ordinary damped harmonic oscillator, the uncertainty relation in generalized coherent states is reduced to that of the Glauber coherent states. The fluctuations of the electric and the magnetic fields are also derived. You can see from Eqs. (51) and (52) that both $[\Delta\mathbf{E}(\mathbf{r},t)]_{\mathrm{GCS}}$ and $[\Delta\mathbf{B}(\mathbf{r},t)]_{\mathrm{GCS}}$ decrease exponentially with time provided that $\Lambda(t)$ is positive. Whereas they increase when $\Lambda(t)$ is negative: this situation corresponds to the case of, for example, the electromagnetic field confined in dielectric media whose permitivity decreases monotonically with time.

Thus, the Gaussian-Klauder state enabled us to understand the fluctuation information that is of critical importance in quantum physics, leading the increment of our ability to understand the properties of the generalized coherent states and their valuable distributions. In general, the study of the coherent states (and squeezed states) provide a fundamental information of quantum fluctuations and open the way for new schemes of quantum communication that permits long-distance transmission of quantum cryptographic keys over ordinary fiber [19].

ACKNOWLEDGMENT

This work was supported by National Research Foundation of Korea Grant funded by the Korean Government (No. 2009-0077951).

REFERENCES

1. Glauber, R. J., "The quantum theory of optical coherence," *Phys. Rev.*, Vol. 130, No. 6, 2529–2539, 1963.
2. Titulaer, U. M. and R. J. Glauber, "Density operators for coherent fields," *Phys. Rev.*, Vol. 145, No. 4, 1041–1050, 1966.

3. Klauder, J. R., "Coherent states for the hydrogen atom," *J. Phys. A: Math. Gen.*, Vol. 29, No. 12, L293–L298, 1996.
4. Majumdar, P. and H. S. Sharatchandra, "Coherent states for the hydrogen atom," *Phys. Rev. A*, Vol. 56, No. 5, R3322–R3325, 1997.
5. Fox, R. F., "Generalized coherent states," *Phys. Rev. A*, Vol. 59, No. 5, 3241–3255, 1999.
6. Fox, R. F. and M. H. Choi, "Generalized coherent states and quantum-classical correspondence," *Phys. Rev. A*, Vol. 61, No. 3, 032107, 1–11, 2000.
7. Choi, J. R., "Gaussian Klauder coherent states of general time-dependent harmonic oscillator," *Phys. Lett. A*, Vol. 325, No. 1, 1–8, 2004.
8. Vela-Arevalo, L. V. and R. F. Fox, "Coherent states of the driven Rydberg atom: Quantum-classical correspondence of periodically driven systems," *Phys. Rev. A*, Vol. 71, No. 6, 063403, 1–12, 2005.
9. Cirone, M., K. Rzążewski, and J. Mostowski, "Photon generation by time-dependent dielectric: A soluble model," *Phys. Rev. A*, Vol. 55, No. 1, 62–66, 1997.
10. Crocce, M., D. A. R. Dalvit, F. C. Lombardo, and F. D. Mazzitelli, "Model for resonant photon creation in a cavity with time-dependent conductivity," *Phys. Rev. A*, Vol. 70, No. 3, 033811, 1–6, 2004.
11. Choi, J. R. and K. H. Yeon, "Quantum properties of light in linear media with time-dependent parameters by Lewis-Riesenfeld invariant operator method," *Int. J. Mod. Phys. B*, Vol. 19, No. 14, 2213–2224, 2005.
12. Choi, J. R., "Coherent and squeezed states of light in linear media with time-dependent parameters by Lewis-Riesenfeld invariant operator method," *J. Phys. B: At. Mol. Opt. Phys.*, Vol. 39, No. 3, 669–684, 2006.
13. Pedrosa, I. A. and A. Rosas, "Electromagnetic field quantization in time-dependent linear media," *Phys. Rev. Lett.*, Vol. 103, No. 1, 010402, 1–4, 2009.
14. Lewis, Jr., H. R., "Classical and quantum systems with time-dependent harmonic-oscillator-type Hamiltonians," *Phys. Rev. Lett.*, Vol. 18, No. 13, 510–512, 1967.
15. Lewis, Jr., H. R. and W. B. R. Riesenfeld, "An exact quantum theory of the time-dependent harmonic oscillator and of a charged particle in a time-dependent electromagnetic field," *J. Math. Phys.*, Vol. 10, No. 8, 1458–1473, 1969.
16. Choi, J. R., "The decay properties of a single-photon in linear media," *Chinese J. Phys.*, Vol. 41, No. 3, 257–266, 2003.
17. Maamache, M., "Unitary transformation approach to the exact solution for the singular oscillator," *J. Phys. A: Math. Gen.*, Vol. 29, No. 11, 2833–2837, 1996.
18. Choi, J. R., "Coherent and squeezed states for light in homogeneous conducting linear media by an invariant operator method," *Int. J. Theor. Phys.*, Vol. 43, No. 10, 2113–2136, 2004.
19. Rao, Q. and R.-H. Xie, "Generation of dipole squeezing in a two-mode system with entangled coherent states of a quantized electromagnetic field," *Physica A*, Vol. 326, Nos. 3–4, 441–455, 2003.

An Alternative Explanation for the Fraunhofer Sun Lines

S. L. Vesely[1] and A. A. Vesely[2]

[1]I.T.B., C.N.R., via Fratelli Cervi 93, Segrate (MI) I-20090, Italy
[2]via L. Anelli 13, Milano 20122, Italy

Abstract— Since their observation by J. Fraunhofer, the dark lines in the Sun spectrum have been exploited as markers to calibrate the dispersion spectra produced by glass prisms. G. Kirchhoff stressed their fundamental meaning by interpreting them as absorption lines typical of each chemical element in the gas state. He based on a thermodynamic principle established by himself, according to which cooler gases above both the Sun's and the Earth's surfaces strip many lines from the continuous Sun emission spectrum, as they can absorb the same wavelengths they can emit. In this paper we argue that, although Fraunhofer lines allow wavelength scale calibration, they can actually be interpreted as an interference pattern produced by collimated Sun light beams.

1. INTRODUCTION

In this paper we put forth an alternative explanation for the origin of the Sun lines J. Fraunhofer observed around 1814. He came about their discovery as he was trying to improve the resolution of optical systems by correcting the lenses' chromatic aberrations. The lens chromatism can actually be minimized by combining together different kinds of glasses, and by taking into account the eye sensitivity to colors. To this end, he started scrutinizing the total dispersive power of high quality homogeneous glass prisms, and ascertained that, besides affecting the extent of the whole angular dispersion range, the refractive index shows an additional dependence on each color, which disrupts the proportionality to one another of the abscissa scales. Hence, Fraunhofer began to look for markers independent of the glass composition, so as to draw all of the spectra to the same scale [1]. Eventually, he found that the lines named after him allow such a scale calibration. However, his successors argued that his claim lacked whatever theoretical basis; in addition, they took a stance that the use of the grating diffraction spectrum as *the universal* linear wavelength scale reference could not be taken for granted either. Around 1860, G. Kirchhoff succeeded in explaining Foucault's observations on the disappearance of the sodium D line against the solar spectrum, and Fraunhofer's Sun lines, both in exactly the same manner, in the theoretical framework of equilibrium thermodynamics. That way, he opened the way to the energetic interpretation of spectra, where logical necessity can be derived from [2]. He gave an account of two circumstances: Both phenomena allow an optical insight into chemical composition, and band-pass distortions can be independent of the radiation sources. For the relation between emission and absorption lines in particular, his celebrated law of thermal radiation, which states that at thermal equilibrium the emissivity of a body equals its absorptivity, seems to justify the assumption that each phenomenon is the photographic negative of the other.

By the close of that century, a few thousand Fraunhofer lines had been mapped. However, the task of matching each observed line with one from a known gas absorption spectrum had to be abandoned. Rather, it was put forward for consideration that, much like thick glass slabs get greenish, a great depth of diluted gases may become colored. Hence, it was alleged that many absorption lines belonging to transparent gases could become visible just because of the huge size of the photosphere. It also became clear that reproducing in a laboratory the conditions prevailing near the solar surface was a major challenge. Accordingly, to try and reproduce the effects of hot temperatures, several different salt assays were heated or put to the flame until they passed off in vapor, and their absorption line spectra could be recorded. The ever-changing total amount of monitored lines evidenced, however, that the experimental conditions were not easily reproducible. The sublimation temperatures change with pressure and differ for different elements. Attention was also drawn to the fact that the volatility sometimes may as well depend on each chemical compound containing a given element. Many alternative methods, such as electric arch or discharge, or even electromagnetic induction, were tried out, to "raise the atomic energy levels over the ground state", although it was pretty unclear what equilibrium temperatures could have been attained, if any. Finally, we remark that as burning vapors do indeed radiate [3], emission spectra could have been taken in lieu of the absorption ones more often than not, as we shall discuss presently.

At any rate, as the difficulties were deemed on the whole of experimental origin, and there were no doubts about the effectiveness of the absorption mechanism to explain the origin of the dark lines within thermodynamics, a tremendous effort was undertaken at the theoretical level. Our proposal is to show that there is at least one explanation for the Fraunhofer dark lines, which is alternative to the absorption mechanism, and may likely be plausible and possibly more akin to current telecommunications' practices.

2. ABSORPTION AND DISPERSION IN TRANSPARENT MEDIA IN THE OPTICAL RANGE

The pursuit of image formation by optical systems has always been of foremost interest to optics. However, due to the image aberrations, the *light properties*, i.e., the luminous patterns in the focal planes of centered systems, have been studied too. The chromatic aberration deserves attention in this respect, for it consists of the fact that glass lenses bring radiations in the optical range to focus on different planes, blurring both the commonly observed images and their pattern in each focal plane. As such, it is reported to affect partly the imaging capabilities of the system, and partly the properties of white light. If, as usual, it is imagined that a collimated white-light beam is composed of several different colors, then the observed aberration in the image plane is linked to their "dispersion", and is associated with the dependence of the refraction index of glass materials on them. The major achievements in the theory of optical dispersion are reported in many review articles, for instance by Korff and Breit [4].

Today, glass dispersion is associated with the simultaneous occurrence of an absorption band, similarly characterized by a color-dependent extinction coefficient, whose low-wavelength edge starts near the middle UV range for the common glass kinds [5]. By "absorption" we mean the attenuation of each beam of monochromatic radiation perpendicularly transmitted across a glass slab of known depth, and measured by a detector aligned with the beam on the opposite side of the slab with respect to the light source. Compared with it, the so called *normal* glass dispersion consists, as already mentioned, of the *angular deflection* of radiation through a prism, that is minimum at the red end of the spectrum and grows toward the blue end (at minimum dispersion conditions). The *anomalous* glass dispersion region, which follows the UV absorption band, does not belong to optics. Nevertheless, it is known that, when the absorption band of a substance occurs entirely within the visible range, the color order accustomed to by the glass prism spectra is not preserved [6, 7]. In the case of glasses, the Sun spectrum is considered to be normally dispersed by definition. In addition, the far UV radiation is invisible. However, far UV beams may fold onto the normally dispersed spectrum exactly as the anomalous dispersion ranges in the visible part do, resulting in the normal order not being preserved even for glasses, as shown by the emergence of Talbot's interference bands upon insertion of a phase filter on the side not covering the apex of the prism [8] or not covering its basis [9].

Telecommunications use the complex plane to represent the response of simple linear inductive and capacitive filters, inserted between input and output terminals of series or shunt circuits. They use either the rectangular, i.e., $Z = R \pm jX$, or the polar form, i.e., $Z = \sqrt{(Z)}\angle \arg(Z) = Ze^{j \arg Z}$ of complex numbers. The meanings attributed to the right members' variables are not perfectly equivalent. In the rectangular form the attenuation or gain amplitude is drawn in phase with the (real) input signal, whereas the pure reactance component is phased in quadrature. In polar coordinates usually a dephasing from pure resistance conditions is described instead. For lossless systems, the phase is ascribed to the pure reactance, which therefore becomes liable for the dispersion. As there are no perfectly linear filters, in practice there is no sharp criterion based on baseline adjustments for separating in a broad-band spectrum the absorptive part of the response from the dispersive one.

Reverting to our topic, in Foucault's and Kirchhoff's times the so called *line absorption spectra* [10] of diluted vapors were obtained momentarily in the laboratory by superimposing the gas emissions on a nearly uniform very broad banded signal. There was no good reason whatsoever to refrain from adjusting the phase so as to obtain maximum contrast between the lines and the background, particularly with regard to the aimed comparison with the Fraunhofer dark lines. This is why we presume that in those experiments the observed dark spots arose from offhand baseline adjustments of the burning vapors' emissions, and that one therefore could dispense with the absorption concept in those cases.

Another kind of dark lines, the so called *inversion lines*, are observed to occur at steady selective irradiation conditions along with other saturation effects, that cannot be removed by simply adjust-

ing the baseline. It is not customary to identify those lines with absorption ones [11]. Rather, they are somehow perceived as pertaining to a resonance phenomenon. They may come about naturally when the Earth's atmosphere is illuminated in the daytime, and produce some fluctuating lines. Yet, we don't think that they would naturally provide the permanent thin marks Fraunhofer was looking for, as we surmise that the Sun doesn't behave as a frequency stabilized generator. We would rather be inclined to ascribe the blue of the sky to the Sun's transmitted power, and to consider it a fluorescence radiation corresponding to a saturation effect in the UV. It is a matter of convenience. If the blue is attributed to Rayleigh scattering, the sky is taken to be equivalent to a thick glass slab. If the blue is attributed to the saturation of the electromagnetic response of the air, then the Fraunhofer lines don't feature as an intrinsic characteristic of the solar light, and they possibly show up because of the intervening distance. Our explanation will be given on account of the assumption that the Sun lines are an effect of collimation.

3. A LINK BETWEEN FRAUNHOFER'S LINES AND SCHLIEREN CONTOUR FRINGES

Foucault came across schlieren effects around 1858, when he shared with Fraunhofer the aim to ameliorate the performance of lenses. Those effects provide a technique permitting to discover small inhomogeneities in optical glasses, whose presence cause the images to be distorted. To connect the Fraunhofer Sun lines with the interference fringes shown in later experiments on schlieren, one needs to consider both the planes of the geometrical images of the slit, and those of its diffraction patterns. Though schlieren are considered a typical wave-phenomenon, the geometric picture due to Huygens and Kirchhoff falls short of correctly displaying the fronts' propagation through those particular planes. It neither allows to distinguish them among the whole of the propagating wavefronts, nor provides a fair account of the energy flow across them. Therefore, for describing the simplest method of obtaining schlieren, we shall avoid referring to the diffraction theory, and avail ourselves of the integral transforms conceptual scheme.

The schlieren method we consider [12] allows to obtain a kind of "radiograph" of transparent media by using visible light. Small inhomogeneities originating in an otherwise homogeneous body, from density or temperature gradients, from tensions or stresses, et cetera, are mapped on the resulting picture. This task is accomplished by letting a collimated beam of white or monochromatic light illuminate a transparent sample through its whole volume, and by revealing its tiny refractive index variations. For detection purposes, half of the diffraction pattern of the sample is screened off in the focal plane of the lens, or mirror, where the beam impinges, like a single sideband with suppressed carrier.

A flat picture of the whole of its volume is obtained by further projecting the halved pattern onto an image plane at infinity. The dephasings in the light path become visible there as intensity (or color) variations. An alternative method for visualizing phase distortions consists in a double exposure on the same negative of two images of the same transparent sample, the first of whom is taken before conditioning and acts by subtraction on the image, like a reinserted carrier. To relate the former schlieren method to the dark lines appearing in the solar spectrum, we mention that it is possible to generate a system of interference fringes contouring the schlieren, which was proposed for calibrating stress or density levels. In the above experimental setup, fringes are obtained by inserting a narrow slit aperture into the collimated beam to reduce its size, before it enters the sample volume so as to preserve homogeneous illuminating conditions of the field of view. With this complement, the diffraction pattern in the filter plane is "multiplied" by the slit aperture, while in the image plane interference lines finely subdivide the schlieren.

Now we are going to analyze Fraunhofer's concern with the operation of the lenses in accordance with the same conceptual scheme. Because his problem was still that of bringing the images of multicolored subjects into focus (which was to be solved using achromatic lenses' systems), his experiments were designed to observe the light dispersion characteristics of prisms rather than their homogeneity. Thus, differently from the above schlieren experimental setup, it was the light, not the glass, that he inspected with his keplerian refracting telescope. Of course, thinking of the schlieren methods, clear air is expected to affect the sunlight passing through it, even if it is transparent in the optical range. However, the solar emission band is so broad and so powerful that it may cause chemical actions as well as strong thermal gradients. The spectrum of the visible light formed by a glass prism is itself so broad, that it goes out of focus because of its varying inclination with respect to the telescope axis. Chromatic aberration itself originates this way, and, in our opinion, it is apt to generate some sort of phase filter. To wit, consider a lens constituted

in a first approximation by two prisms that are joined together base to base, and form an image of the slit: The image will not be sharp because different colors focalize on different planes, and it would rather shape an inclined grating composed of very many differently colored images of the slit. To try and obtain a sharp *image* of the spectrum, Fraunhofer restricted the beam by means of a narrow slit: This procedure is similar to the one encountered when subdividing the schlieren. With Fraunhofer's experimental setup, looking into the eyepiece, the first maximum of the slit's diffraction pattern appears multiplied by the whole of the prism dispersion spectrum. Now, while the magnified images of the Sun unveil intriguing features, on the Earth, the solar disc's angular aperture amounts to about $\frac{1}{2}^{\circ}$. Hence, the sunlight belonging to the first diffraction maximum is quite well collimated. Turning our attention to the focal plane of the objective, the "slit's grating" forms there, and projects its light toward the eyepiece. Looking directly into it, i.e., looking at the nearly closed slit through the eyepiece, as soon as a spot in the spectrum is put in focus, fine interference fringes superimpose on it. Fraunhofer himself listed 576 lines, which seemed to him remarkably definite.

As far as the glass distortion is concerned, we consider a lens analogous to a zone plate, and likewise a prism analogous to a linear filter. Despite this simplification, prism dispersion is correlated to the absorption band, as already mentioned. However, Fraunhofer's lines form independently. They form for the same reasons in diffraction spectra, where the colors too are assumed to be generated by pure interference. This fact allows to calibrate glass dispersion spectra basing on a diffraction grating scale.

4. CONCLUSION

We have tried to distinguish between two major occurrences of dark lines in spectra: Those arising in emission spectra of chemicals against a bright background, and those observed in the spectra of celestial bodies. The currently accepted theory assumes that both kinds of lines identify chemical elements according to the same rules. In our opinion, it goes too far in taking for granted that the narrow emission/absorption bands pertaining to gases and vapors on Earth have the same origin as the dark lines from Stars' sources. We have conjectured an alternative explanation whereby the latter can be considered raw signals that characterize their sources in a broader sense. In particular, we would explain Fraunhofer's lines basing on diffraction. To this end, we have compared Fraunhofer's setup with the methods of obtaining schlieren. According to our alternative explanation, the dark lines received with Fraunhofer's experimental settings exhibit distinctive traits of the activity of the Sun or other Stars, which may be broadly called "of chemical origin". However, the line pattern pertains rather to the received signal than to the local processes per se. It is acquired with spatial collimation and therefore it would not be visible on the Stars' surface. Finally, as long as the dark lines are considered to be superimposed on the dispersion spectrum of the glass prism being used, both explanations can justify the calibration procedure propounded by Fraunhofer for correcting chromatic lens aberrations.

ACKNOWLEDGMENT

We wish to thank C. A. Dolci for her kind help.

REFERENCES

1. Fraunhofer, J., *Bestimmung des Brechungs-und Farbenzerstreuungsvermögens Verschiedener Glasarten in Bezug auf die Vervollkommnung Achromatischer Fernröhre*, Verlag von Wilhelm Engelmann, Leipzig, 1905.
2. Schirrmacher, A., "Experimenting theory: The proofs of Kirchhoff's radiation law before and after Planck," *HSPS*, Vol. 33, No. 2, 299–335, 2003.
3. King, A. S., "An attempt to detect the mutual influence of neighboring lines in electric furnace spectra showing anomalous dispersion," *PNAS*, Vol. 2, No. 8, 461–464, 1916.
4. Korff, S. A. and G. Breit, "Optical dispersion," *Rev. Mod. Phys.*, Vol. 4, No. 3, 471–503, 1932.
5. Osada, K., "Ultraviolet absorption spectra of glasses containing Ti, and heavy metals," *J. Phys. Soc. Japan,* Vol. 8, No. 2, 226–228, 1953.
6. Hurion, A., "Recherches sur la dispersion anomale," *Annales Scientifiques de l'É.N.S.*, Série 2, Vol. 6, 367–412, 1877.
7. Wood, R. W., "On cyanine prisms and a new method of exhibiting anomalous dispersion," *Proc. Phys. Soc. London,* Vol. 17, 671–674, 1899.

8. Beach, A. C. G., "An experiment bearing on Talbot's bands," *Proc. Roy. Soc.,* Vol. 45, 474–481, 1933.
9. Doubt, T. E., "Talbot's bands and the resolving power of spectroscopes," *Phys. Rev.,* Vol. 10, 322–334, 1917.
10. Laubenthal, G., "Über messungen im absorptionsspektrum," Ph.D. Thesis, Görres-Druckerei, Koblenz, 1901.
11. Shimoda, K., "Precise frequency of the 3.3 inversion line of ammonia," *J. Phys. Soc.,* Vol. 12, 558, Japan, 1957.
12. Gayhart, E. L. and R. Prescott, "Interference phenomenon in the schlieren system," *J.O.S.A.,* Vol. 39, No. 7, 546–550, 1949.

Simulations of an Electromagnetic Microsystem Used in Biomedical Applications

T. Creutzburg and H. H. Gatzen
Institute for Microtechnology, Leibniz Universität Hannover, Garbsen, Germany

Abstract— Simulations of an electromagnetic microsystem intended to be used in a microactuator which serves as an ear implant to overcome amblyacousia were conducted. Using the ANSYS^{TM} simulation software, the design and optimization of the electromagnetic microsystem were accomplished by Finite Element Method (FEM) analyses. The design process contained 2-D and 3-D simulations. 2-D simulations served as parametric studies of the system. Afterwards, a 3-D simulation was carried out to fine-tune the results of the 2-D simulation. Comparing the 3-D with the 2-D simulation, the resulting force-air gap data were very close. With respect to the simulations, the designed electromagnetic system fulfils the requirements to drive the microactuator.

1. INTRODUCTION

In the year 2001, the World Health Organization (WHO) reported that there were about 250 million people worldwide suffering from a disabling hearing impairment. About 70 million of those people lived in Europe and 28 million in the USA [1]. The therapy for hearing impaired patients reaches from simple-plug in to implantable active hearing aids as well as Total or Partial Ossicular Replacement Prostheses (TORP/PORP), depending basically on the type and severity of the hearing loss [2]. For implantable active hearing aids, there are alternatives: middle and inner ear implants as well as Bone Anchored Hearing Aids (BAHA's). On the market of middle ear implants, several conventionally fabricated hearing implants are available [3]. The goal of this work was to design an electromagnetic device for a hearing implant fabricated by Micro Electromechanical Systems (MEMS) technology. A main advantage of such an approach is the batch fabrication, reducing the costs for the system [4]. The desired hearing implant located at the round window is intended to stimulate the perilymph using a plunger. A schematic view of the ear implant is shown in Fig. 1(a).

By applying the electromagnetic principle, different microactuators like a bi-stable optical microswitch [5] or an integrated second stage microactuator for a hard disk recording head [6] were designed and fabricated at the Institute for Microtechnology (imt). A proven approach for the design of such microsystems is to create a Finite Element Method (FEM) model for these systems and simulate their behavior when excited [7]. Applying this approach, the electromagnetic device used in the hearing implant was designed by 2-D and 3-D electromagnetic simulations. Design limitations were given by the microtechnological fabrication and the maximum dimensions of the hearing implant resulting from the physiological restrictions in the middle ear and the cochlea.

The electromagnetic device consists of a microcoil system and soft-magnetic flux guides. Basically, the structure corresponds to a pot magnet. The circular-shaped soft-magnetic lower core and inner pole, the flux closure (fixed to a membrane) as well as the ring-shaped outer pole consist of NiFe45/55. The Cu coil system is located above the lower core between inner and outer pole

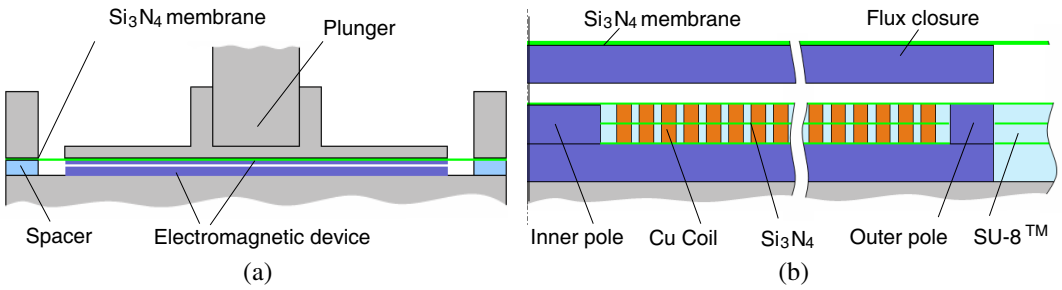

Figure 1: Schematic representation of the electromagnetic inner ear implant: (a) Cross section of the ear implant; (b) Cross section of the electromagnetic device.

underneath the flux closure. The system is embedded in the photosensitive epoxy SU-8^{TM}. Si_3N_4 is used as an insulator between the coil layers. The system is shown in Fig. 1(b).

2. REQUIREMENTS OF THE MICROACTUATOR

The requirement the electromagnetic device has to fulfill is to supply the force necessary to stimulate the perilymph through the round window. This force was determined by simulating the ear implant under the load of the cochlea. For carrying out the simulations, the cochlea was modeled as a damper and the system's behavior in a frequency range of 100 Hz to 10 kHz was simulated. The minimum force the electromagnetic device has to provide at an air gap of 10 µm is about 11 mN.

Due to the maximal dimensions of the implant and the desired resonant frequency the system has to reach, a diameter of 1,750 µm was chosen for the electromagnetic device. This diameter was determined by simulating the mechanical parts of the implant using different diameters of the flux closure until the desired resonant frequency was reached. These simulations are discussed in [8].

3. 2-D SIMULATIONS

Based on the selected system diameter of 1,750 µm, four different electromagnetic systems were modelled using the ANSYS^{TM} Parametric Design Language (APDL). By combing ANSYS^{TM} rectangle primitives, the structures of the systems, i.e., the flux guides and the coil system, were created considering the rotational symmetry of the systems. Overlapping the structures with a half circle representing the surrounding air resulted in the final axially symmetric model. The SU8^{TM} embedding and the Si_3N_4 insulations were neglected because both materials behave like air in an electromagnetic simulation. Using the elements Infin110 and Plane53, the models were meshed applying the appropriate material properties. These material properties were the relative permeability for air, the relative permeability and resistivity for Cu as well as a non-linear *BH*-loop and the respective coercive force for NiFe45/55. Infin110 elements were used to mesh the outer element layer of the surrounding air, modelling the effect of far-field decay. Additionally, the outer nodes were selected and flagged as infinite surface. Plane53 elements were applied to mesh the rest of the model. In the following, a component was created containing the elements of the flux closure. Using the macro FMAGBC, Maxwell and virtual work force boundary conditions were applied to this component. The excitation was carried out by providing current density loads to the areas of the coil system. A meshed model of one system is shown in Fig. 2.

The steps described were carried out for each of the four systems considered. The four systems were modeled step by step, changing the properties of the initial system 1 until a configuration matched the requirements of the ear implant. By varying the air gap between 2.5 µm and 10 µm and simulating the systems, the force depending on the respective air gap was analyzed. The main properties of the systems are given in Table 1.

The first system investigated consisted of a 10 µm thick lower core and flux closure, an inner pole with a diameter of 50 µm, an outer pole with a width of 20 µm, and a single-layer coil. The

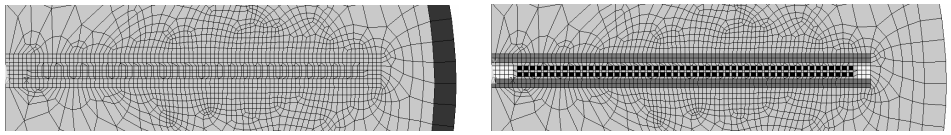

(a) (b)

Figure 2: 2-D FEM simulation: (a) Mesh showing element types; (b) Mesh showing material types.

Table 1: Main properties of the simulated systems.

System	Number of the coil layers	Number of the coil windings	Height of the flux guides	Diameter of the inner pole	Width of the outer pole	Force at 10 µm air gap
1	1	54	10 µm	50 µm	20 µm	2.4 mN
2	2	108	10 µm	50 µm	20 µm	4.0 mN
3	2	108	20 µm	50 µm	20 µm	9.6 mN
4	2	104	20 µm	100 µm	30 µm	11.2 mN

system did not match the requirements, reaching a maximum force of only 2.4 mN for an air gap of 10 µm. The second system analyzed was a double-layer coil version of the first system. The intention for the doubling was to increase the flux density and the corresponding attractive force. Nevertheless, with a maximum of 4.0 mN, the system did not supply the desired force either. In a third attempt, the height of the lower core and the flux closure was changed to 20 µm. Increasing the height of these flux guides, the used *BH*-loop for NiFe45/55 had to be changed. In case of a thicker layer, the relative permeability μ_r reduces, but the cross sectional area of the flux guide increases, thus decreasing the reluctance. As a result, an increase in the flux density and the corresponding attractive force could be assumed. The simulation provided a force of 9.6 mN at an air gap of 10 µm. Nevertheless, parts of the flux guides were magnetically saturated. For that reason, the number of coil windings was reduced and the diameter of the inner pole and the width of the outer pole were increased to 100 µm and 30 µm, respectively. This approach increased the area featuring the height of the attractive force. The system provided a force of 11.2 mN matching the requirements. The results of the simulations of each electromagnetic device modeled are shown in Fig. 3.

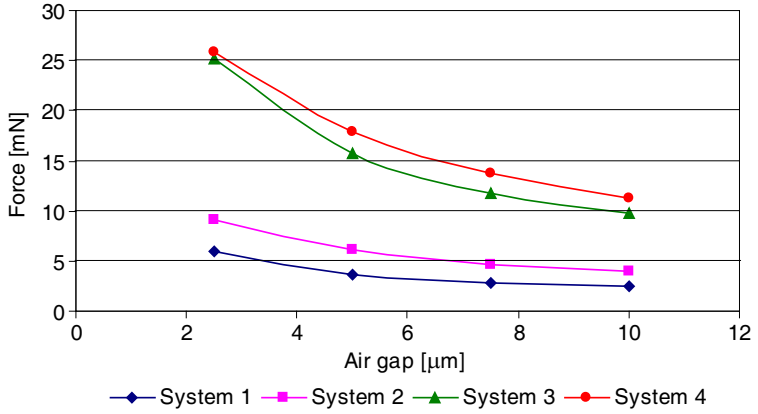

Figure 3: 2-D FEM simulation results for the forces of systems 1 through 4 as a function of the air gap.

4. 3-D SIMULATION

System 4 was modeled in 3-D to confirm the results of the 2-D simulation. The modeling procedure was carried out like in the 2-D simulation. The geometry model was generated using ANSYS^{TM} primitives. The coil system was chosen as a stranded coil, defining the properties with a real constant. The surrounding air was represented by an overlapping sphere. The meshing of the model was carried out using Solid97, Infin111, and Circu124 elements. Infin111 elements were used for the outer layer of the modeled air acting like Infin110 elements in the 2-D simulation. The creation of the Infin111 elements was realized by selecting the outer area of the already meshed surrounding air and extruding the existing elements by one element. After that, all outer nodes were selected and flagged as infinite surface. Since Solid97 elements were used, a *BH*-loop could not be used to define the magnetic properties of the NiFe45/55. Instead, the *BH*-loop applied in the 2-D simulations was linearized in three sections and the respective relative permeability was used for the 3-D simulation. The excitation of the stranded coil was done by coupling the coil to a Circu124 element. Initially, the elements of the meshed stranded coil were selected and coupled in relation to current and electromotive force. In the next step, two single nodes were created outside the model. Afterwards, a Circu124 coupling element was generated by the use of the two nodes and a third node of the stranded coil. After applying the boundary conditions voltage (0 V) and current (0.1 A) to the nodes of the coupling element, the 3-D model was simulated. Changing the air gap, the force depending on the respective air gap was analyzed.

5. COMPARISON OF 2-D AND 3-D SIMULATIONS

In Fig. 4, the flux density distribution in the flux closure of the 2-D and 3-D models is shown. The result of the 2-D simulation is shown as an axially symmetric expansion to get a 3-D view for a better comparison. Fig. 5 presents the forces depending on the respective air gap for the 2-D and 3-D simulations. Comparing the 3-D with the 2-D simulation, the flux density distributions

are quite similar. This is due to the fact that there is a good agreement between 2-D and 3-D simulations for axially symmetrical structures.

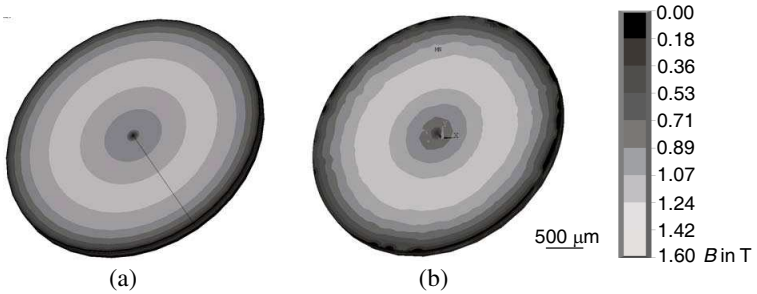

Figure 4: Flux density distribution of system 4: (a) 2-D simulation results; (b) 3-D simulation results.

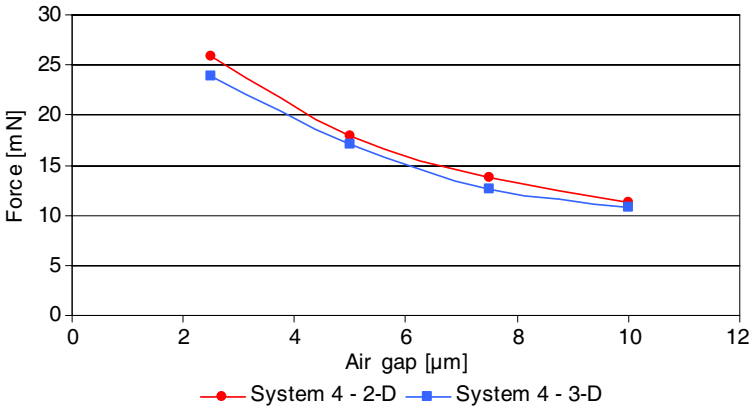

Figure 5: Simulated forces of system 4 — comparison between the 2-D and 3-D models.

6. CONCLUSIONS

Using 2-D FEM-simulations, an electromagnetic device could be designed which fulfills the requirements to drive the ear implant. By comparing the 2-D simulation with a 3-D simulation, the results of the 2-D simulation could be fine-tuned. Thus, performing 2-D simulations are a suitable way to design such an electromagnetic device due to the fact that less modelling and simulation time is needed in the 2-D simulation.

ACKNOWLEDGMENT

This research is sponsored by the DFG (German Research Foundation) within the program "Inner Ear Microtransducer for the Stimulation of the Perilymph in case of Amblyacousia".

REFERENCES

1. Shield, B., "Evaluation of the social and economic costs of hearing impairment," A Report for Hear-It, 2006
2. Wintermantel, E. and S.-W. Ha, *Medizintechnik*, Berlin Heidelberg, Springer, 2009.
3. Haynes, D. S., J. A. Young, G. B. Wanna, and M. E. Glasscock, "Middle ear implantable hearing devices: An overview," *Trends in Amplification*, Vol. 13, No. 3, 206–214, 2009.
4. Schomburg, W. K., R. Ahrens, W. Bacher, C. Goll, S. Meinzer, and A. Quinte, "Amanda-low-cost production of microfluidic devices," *Sensors and Actuators A: Physical*, Vol. 70, No. 1–2, 153–158, 1998.
5. Gatzen, H. H., E. Obermeier, T. Kohlmeier, T. Budde, H. D. Ngo, B. Mukhopadhyay, and M. Farr, "An electromagnetically actuated bi-stable MEMS optical Microswitch," *12th International Conference on Transducers, Solid-state Sensors, Actuators and Microsystems*, 1514–1517, Boston, USA, June 2003.

6. Dinulovic, D., H. Saalfeld, Z. Celinski, S. B. Field, and H. H. Gatzen, "Integrated electromagnetic second stage microactuator for a hard disk recording head," *IEEE Transactions on Magnetics*, Vol. 44, No. 11, Part 2, 3730–3733, 2008.
7. Dinulovic, D. and H. H. Gatzen, "An approach for simulating magnetic microactuators," *International Conference on Thermal, Mechanical and Multi-physics Simulation and Experiments*, 1–4, Freiburg, Germany, April 2008.
8. Creutzburg, T. and H. H. Gatzen, "Design of a microactuator for the stimulation of the perilymph," *International Conference on Thermal, Mechanical and Multi-physics Simulation and Experiments*, Bordeaux, France, April 2010, (submitted).

Using Fictitious Currents for Calculating Electric Fields Produced by Capacitor Dielectrics

R. Ravaud and G. Lemarquand
Universite du Maine, France

Abstract— This paper introduces the concept of fictitious currents for calculating the electric field produced by capacitors with dielectrics. We use the Maxwell dual equations and introduce the concept of equivalent potential vector for calculating analytically the radial electric field created by capacitors with cylindrical topologies. The interest of such an approach lies in the fact that it allows us to obtain analytical expressions without using any numerical integrals. Our approach is compared to the coulombian model. Our simulations show that our analytical approach has a lower computational cost than the colombian model.

1. INTRODUCTION

Electric fields created by capacitors with dielectrics are generally determined by using the classical Maxwell's equations. These equations lead us to use the coulombian model which is a well known approach for calculating the electric or magnetic fields produced by charge distributions. Indeed, according to this model in electrostatics, some fictitous electric charge densities appear on the faces of the dieletric as well as in its volume. This model is useful in many cases because it leads to analytical expressions of the electric field. Dielectrics with parallelepiped topologies generate electric fields that can be expressed in terms of fully analytical expressions based on the arctan and ln functions [1]. For arc-shaped topologies, the coulombian model is not suitable for calculating the three electric field components produced by dielectrics [2]. Indeed, in this approach, the contributions of the volume charge densities are difficult to express in terms of fully analytical expressions and are often omitted [3]. This is the case of the arc-shaped dielectrics with radial polarizations. Consequently, it is more interesting to introduce the concept of equivalent vector potential whose curl gives the same electric field as the one obtained with the coulombian model.

We present an academic example in which the Maxwell dual equations are more suitable than the classical Maxwell equations for calculating the electric field produced by arc-shaped capacitors with dielectrics. Our approach can be used for the design of devices using dieletrics with arc-shaped topologies.

2. BASIC EQUATIONS

The Maxwell's Equations are widely used for solving magnetostatics or electrostatics problems. These local equations characterize the magnetic or electric fields produced by charge or current distributions. For magnetostatics or electrostatics problems, the Maxwell's Equations can be divided in two equation groups (Eqs. (1) and (2)). This separation is interesting for calculations involving dielectrics or magnetized materials.

$$\begin{aligned} \nabla\vec{D} &= \rho_f \\ \nabla\times\vec{E} &= \vec{0} \end{aligned} \tag{1}$$

$$\begin{aligned} \nabla\vec{B} &= 0 \\ \nabla\times\vec{H} &= \vec{j} \end{aligned} \tag{2}$$

where $\vec{D}$ is the electric displacement vector, ρ_f is the free electric charge volume density, $\vec{E}$ is the electric field vector, $\vec{B}$ is the magnetic induction field vector, $\vec{H}$ is the magnetic field vector and $\vec{j}$ is the current density.

The previous equations involve that the magnetic field derives from a vector potential though the electric field derives from a scalar potential [1]. Consequently, the magnetic field created by currents are often modeled by using the Biot-Savart Law [2, 3] or by using the amperian current model [4–6]. In the other hand, the electric field is rather determined by using the coulombian model [7, 8]. For arc-shaped permanent magnets, the coulombian model is suitable for obtaining analytical expressions based on special functions [9–11]. Consequently, it seems to be more judicious

to introduce in some cases equivalent models for calculating the magnetic field created by arc-shaped permanent magnets. In short, the dual Maxwell's Equations involving the coulombian model of a magnet are the following:

$$\begin{aligned} \nabla\vec{B} &= \rho^* \\ \nabla\times\vec{H} &= \vec{0} \\ \nabla\vec{D} &= 0 \\ \nabla\times\vec{E} &= \vec{j}^* \end{aligned} \tag{3}$$

where ρ^* is a magnetic charge volume density and $\vec{j}^*$ is a fictitious current density. The coulombian model of a magnet corresponds to the case when $\nabla\vec{B} = \rho^*$. Furthermore, for linear media, the two following equations are useful to define the main properties of the magnetized media.

$$\begin{aligned} \vec{B} &= \mu_0\vec{H} + \vec{J} \\ \vec{D} &= \epsilon_0\vec{E} + \vec{P} \end{aligned} \tag{4}$$

2.1. Introducting the Vector Potential from the Fictious Currents

The previous section introduces the basic equations for calculating the electric field created by capacitors with dielectrics by using the analogy between the classical Maxwell's equations and the dual Maxwell's equations. As we have introduced equivalent the dual Maxwell's equations, we can define a vector potential $\vec{A}$ that verifies the following properties:

$$\begin{aligned} \vec{E} &= \nabla\times\vec{A} \\ \nabla\vec{E} &= 0 \end{aligned} \tag{5}$$

This vector potential is determined by using the following equation

$$\vec{A} = \frac{1}{4\pi}\int_V \vec{P}\times\nabla\left(\frac{1}{\left|\vec{r}-\vec{r'}\right|}\right)d\tilde{V} \tag{6}$$

By using the Stokes theorem, we obtain the final expression:

$$\vec{A} = \frac{\epsilon_0}{4\pi}\left[\int_S \frac{\dfrac{\vec{P}}{\epsilon_0}\times\vec{n}}{\left|\vec{r}-\vec{r'}\right|}d\tilde{S} + \int_V \frac{\nabla\times\left(\dfrac{\vec{P}}{\epsilon_0}\right)}{\left|\vec{r}-\vec{r'}\right|}d\tilde{V}\right]$$

We find the two equivalent surface and volume currents distributions giving the same electric field as the one obtained in the coulombian approach.

For the rest of this paper, we use the notation X_{magn} when we consider a charged distribution related to magnetostatics and X_{elec} for electrostatics. According to the coulombian model, a permanent magnet can be represented by fictious magnetic pole surface and volume densities that are expressed as follows:

$$\begin{aligned} \sigma^*_{magn} &= \vec{J}\cdot\vec{n} \\ \rho^*_{magn} &= -\nabla\cdot\vec{J} \end{aligned} \tag{7}$$

Applying the coulombian model in the case of dielectric capacitors, we obtain:

$$\begin{aligned} \sigma^*_{elec} &= \vec{P}\cdot\vec{n} \\ \rho^*_{elec} &= -\nabla\cdot\vec{P} \end{aligned} \tag{8}$$

The amperian current model used for calculating the magnetic field created by permanent magnets implies the determination of fictitous currents of surface and volume densities:

$$\begin{aligned} \vec{K}^*_{magn} &= \frac{\vec{J} \times \vec{n}}{\mu_0} \\ \vec{j}^*_{magn} &= \frac{\nabla \times \vec{J}}{\mu_0} \end{aligned} \tag{9}$$

It is emphasized here that the previous relations are commonly used in the literature. In this paper, we choose to introduce fictious currents in electrostatics for calculating the electric field produced in cylindrical capacitors with dielectrics.

$$\begin{aligned} \vec{K}^*_{elec} &= \frac{\vec{P} \times \vec{n}}{\epsilon_0} \\ \vec{j}^*_{elec} &= \frac{\nabla \times \vec{P}}{\epsilon_0} \end{aligned} \tag{10}$$

3. APPLICATION OF THE CASE OF A CYLINDRICAL CAPACITOR WITH DIELECTRIC MATERIAL

3.1. Notation and Geometry

We present in this section the 3D analytical expression of the electric field created by a cylindrical capacitor with dielectric material. This is typically an academic example for showing the properties of the Maxwell's equations and the interest of using equivalent models. To do so, let us first consider the representation shown in Figure 1. According to the coulombian model, the outer face is charged with the surface density $+\sigma = \frac{q}{S_2}$ and the inner face is charged with the surface density $\sigma = \frac{-q}{S_1}$. The dielectric has also a charge volume density σ_v that is given by

$$\sigma_v = -\nabla \vec{P} \tag{11}$$

According to the amperian current model, this cylindrical capacitor with dielectric has two current layers flowing in the upper and lower faces. Consequently, there is not any volume integrals to determine for calculating the two electric components created by this capacitor.

3.2. Radial component determined with the amperian current model

The radial component $E_r(r, z)$ can be determined by calculating the projection of $\vec{H}(\vec{r})$ along $\vec{u}_r$:

$$E_r(r, z) = \vec{E}(\vec{r}) \cdot \vec{u}_r = \left(\frac{1}{\epsilon_0} \nabla \times \vec{A}(\vec{r}) \right) \cdot \vec{u}_r \tag{12}$$

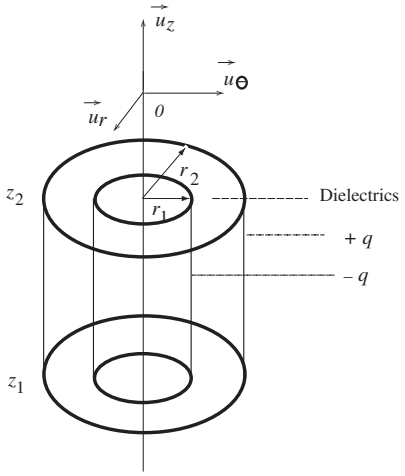

Figure 1: Representation of a cylindrical capacitor charged with two arc-shaped planes.

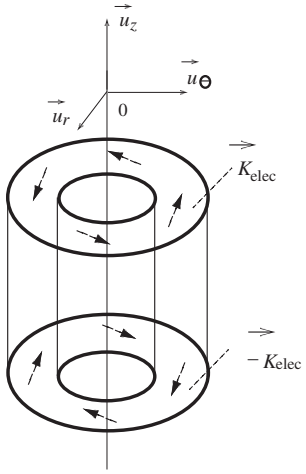

Figure 2: Representation of a cylindrical capacitor modeled by fictious currents flowing on the upper and lower faces.

The interest of using the amperian current model for this configuration lies in the fact that only two integrals must be calculated. Consequently, we obtain an analytical expression of the radial field component based on elliptic integrals. By using Mathematica, the arguments of the elliptic integrals used are defined as follows:

$$\begin{aligned}\phi_{\mathbf{1}}^{+,-} &= \frac{(b+2e)x}{bx \pm \sqrt{2}\sqrt{xe^2(x-c)}} \\ \phi_{\mathbf{2}} &= i\sinh^{-1}\left(\sqrt{\frac{-1}{b+2e}}\sqrt{b-2e\cos(\tilde{\theta})}\right) \\ \phi_{\mathbf{3}} &= \frac{b+2e}{b-2e}\end{aligned} \tag{13}$$

It is noted that we mainly use the elliptic integrals of the second and third kind for the calculation of the radial component. These special functions have been used in [9, 12]. However, no further numerical integrations are required here. In short, the radial component $E_r(r,z)$ can be expressed as follows:

$$E_r(r,z) = \frac{P}{4\pi\epsilon_0}\sum_{i=1}^{2}\sum_{k=1}^{2}(-1)^{i+k}\left(g(i,k,2\pi) - g(i,k,0)\right) \tag{14}$$

with

$$g\left(i,k,\tilde{\theta}\right) = 2(z-z_k)f\left(r^2+(z-z_k)^2,\ r^2+r_i^2+(z-z_k)^2,\ rr_i,\ -r^2-2(z-z_k)^2,\ \tilde{\theta}\right)$$

where

$$\begin{aligned}f\left(a,b,e,c,x,\tilde{\theta}\right) \ =\ & \eta\left(2\xi_1\left(2ce^2+\xi_2\right)\right)\mathbf{F}^*[\phi_{\mathbf{2}},\phi_{\mathbf{3}}]+\eta\left(-e^2(c-x)(bx\sqrt{2}+2\xi_1)\right)\mathbf{\Pi}^*\left[\phi_1^+,\phi_2,\phi_3\right] \\ & +\eta\left(e^2(c-x)(bx\sqrt{2}-2\xi_1)\right)\mathbf{\Pi}^*\left[\phi_1^-,\phi_2,\phi_3\right]-2\eta ax\left(xe^2-ce^2\sqrt{2}+b\xi_1\right)\mathbf{\Pi}^*\left[\phi_{\mathbf{1}}^+,\phi_{\mathbf{2}},\phi_{\mathbf{3}}\right] \\ & -2\eta ax\left(-xe^2+ce^2\sqrt{2}+b\xi_1\right)\mathbf{\Pi}^*\left[\phi_{\mathbf{1}}^-,\phi_{\mathbf{2}},\phi_{\mathbf{3}}\right]\end{aligned} \tag{15}$$

where $\mathbf{F}^*[\mathbf{x},\mathbf{y}]$ and $\mathbf{\Pi}^*[\mathbf{x},\mathbf{y},\mathbf{z}]$ are the incomplete elliptic integrals of the second and third kind that have been used in previous papers [9, 12]. In addition, the parameters ξ_1, ξ_2, η are defined as follows:

$$\begin{aligned}\xi_1 &= \sqrt{e^2x(x-c)} \\ \xi_2 &= x\left(b^2-2e^2\right) \\ \eta &= \frac{i\sqrt{\frac{-e^2\sin\left(\tilde{\theta}\right)^2}{(b-2e)^2}}csc\left(\tilde{\theta}\right)}{2\sqrt{\frac{-1}{b+2e}}x\xi_1\left(2ce^2+\xi_2\right)}\end{aligned} \tag{16}$$

3.3. Axial Component $E_z(r,z)$

The axial component $E_z(r,z)$ can be determined by calculating the projection of $\vec{E}(\vec{r})$ along $\vec{u}_z$:

$$E_z(r,z) = \vec{E}\left(\vec{r}\right)\cdot\vec{u}_z = \left(\frac{1}{\epsilon_0}\nabla\times\vec{A}\left(\vec{r}\right)\right)\cdot\vec{u}_z \tag{17}$$

By using the relation $a_{ik} = (r-r_i)^2+(z-z_k)^2$, this axial component $H_z(r,z)$ is thus given by:

$$E_z(r,z) = \frac{P}{4\pi\epsilon_0}\sum_{i=1}^{2}\sum_{k=1}^{2}(-1)^{i+k}\left(\frac{-4r_i}{\sqrt{a_{ik}}}\mathbf{K}^*\left[\frac{-4rr_i}{a_{ik}}\right]+I_2(r,z)\right) \tag{18}$$

where $\mathbf{K}^*[x]$ is the complete elliptic integral of the first kind [9].

$$I_2(r,z) = \int_0^{2\pi}\ln\left[r_i - r\cos\left(\tilde{\theta}\right)+\sqrt{r^2+r_i^2+(z-z_k)^2-2rr_i\cos\left(\tilde{\theta}\right)}\right]d\tilde{\theta} \tag{19}$$

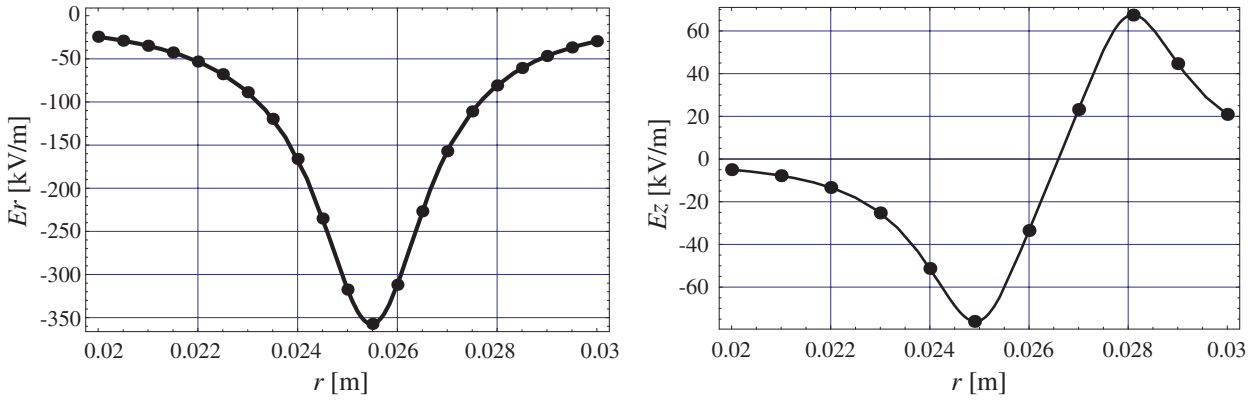

Figure 3: Representation of the radial electric field versus the radial observation point for the following dimensions: Radial component: $r_{in} = 0.025\,\mathrm{m}$, $r_{out} = 0.026\,\mathrm{m}$, $z = 0.003\,\mathrm{m}$, $P = 1.1 \times 10^{-4}\,\mathrm{C/m^2}$, $z = 0.02\,\mathrm{m}$, axial component: $r_{in} = 0.025\,\mathrm{m}$, $r_{out} = 0.028\,\mathrm{m}$, $z = 0.003\,\mathrm{m}$, $P = 1.1 \times 10^{-4}\,\mathrm{C/m^2}$, $z = 0.001\,\mathrm{m}$ (Line = amperian current model, Points = coulombian model).

3.4. Comparison between the Classical Coulombian Model and the Fictitious Current Model

We illustrate in Figure 3 the equivalence between the two approaches (Amperian current model and coulombian model) in the case of the electric field created by the capacitor with dielectric material.

4. CONCLUSION

This paper has presented an analytical method based on the dual Maxwell's equations for calculating the electric field in cylindrical capacitors using dielectrics. The interest of such an approach lies in the fact that no volume integrals are required for the determination of the two electric field components though such a volume integral is required with the classical coulombian model. The comparison between two approaches shows the accuracy of the amperian current model used in electrostatics.

REFERENCES

1. Durand, E., *Magnetostatique*, Masson Editeur, Paris, France, 1968.
2. Akyel, C., S. I. Babic, and M. M. Mahmoudi, "Mutual inductance calculation for non-coaxial circular air coils with parallel axes," *Progress In Electromagnetics Research*, PIER 91, 287–301, 2009.
3. Babic, S. I., F. Sirois, and C. Akyel, "Validity check of mutual inductance formulas for circular filaments with lateral and angular misalignments," *Progress In Electromagnetics Research M*, Vol. 8, 15–26, 2009.
4. Furlani, E. P., S. Reznik, and A. Kroll, "A three-dimensonal field solution for radially polarized cylinders," *IEEE Trans. Magn.*, Vol. 31, No. 1, 844–851, 1995.
5. Ravaud, R. and G. Lemarquand, "Comparison of the coulombian and amperian current models for calculating the magnetic field produced by radially magnetized arc-shaped permanent magnets," *Progress In Electromagnetics Research*, PIER 95, 309–327, 2009.
6. Ravaud, R., G. Lemarquand, V. Lemarquand, and C. Depollier, "Discussion about the analytical calculation of the magnetic field created by permanent magnets," *Progress In Electromagnetics Research B*, Vol. 11, 281–297, 2009.
7. Emets, Y. P., N. V. Barabanova, Y. P. Onofrichuk, and L. Suboch, "Force on insulated wire at the interface of 2 dielectric media," *IEEE Trans. Dielectrics and Electrical Insulation*, Vol. 1, No. 6, 1201–1204, 1994.
8. Ye, Q. Z., J. Li, and J. C. Zhang, "A displaced dipole model for a two-cylinder system," *IEEE Trans. Dielectrics and Electrical Insulation*, Vol. 11, No. 3, 542–550, 2004.
9. Ravaud, R., G. Lemarquand, V. Lemarquand, and C. Depollier, "Analytical calculation of the magnetic field created by permanent-magnet rings," *IEEE Trans. Magn.*, Vol. 44, No. 8, 1982–1989, 2008.
10. Ravaud, R., G. Lemarquand, and V. Lemarquand, "Magnetic field created by tile permanent magnets," *IEEE Trans. Magn.*, Vol. 45, No. 7, 2920–2926, 2009.

11. Azzerboni, B., G. A. Saraceno, and E. Cardelli, "Three-dimensional calculation of the magnetic field created by current-carrying massive disks," *IEEE Trans. Magn.*, Vol. 34, No. 5, 2601–2604, 1998.
12. Ravaud, R., G. Lemarquand, V. Lemarquand, and C. Depollier, "The three exact components of the magnetic field created by a radially magnetized tile permanent magnet," *Progress In Electromagnetics Research*, PIER 88, 307–319, 2008.

Numerical Modeling of Light Sources with R-FEM Method in CFX Environment

J. Mikulka, T. Kříž, E. Kroutilova, and P. Fiala
Department of Theoretical and Experimental Electrical Engineering, Brno University of Technology
Kolejní 2906/4, Brno 612 00, Czech Republic

Abstract— Paper presents usage of the R-FEM method in the CFX environment. The R-FEM method was used for modeling of special light sources and to compute lighting of surfaces from these sources with very good results. Basic description of the R-FEM method is described below. For modeling of the light sources in the CFX environment was used combination of the Finite Volume Method and the radiation method which are included with the CFX (The Discrete Transfer Model and The Monte Carlo Model). Numerical results are presented by models with basic optical geometry (parabolic surface with light source placed in focus point and reflecting surfaces with different angular displacement). There are presented numerical results for mirrored reflecting surfaces and diffusion reflecting surfaces with different degrees of diffusion.

1. INTRODUCTION

Various software tools for lighting systems design are available presently. These tools are focused to specific part of lighting systems problematic unfortunately. These programs are suitable for lamps calculation for interiors calculation or exterior calculation solely. Different numerical methods are used for the calculations in these programs.

There are used these methods for numerical modeling of lighting systems: Ray-Tracing, Radiosity, Flow method, Point method and Elementary transformation method. Ray-Tracing and Radiosity methods are most widely used methods in lighting systems. We can get realistic projection with this method. This methods are often used for project the 3D scenes and lighting calculation. It enables modeling of indirect lighting, shadows and color transition, by this we can manage realistic projection of the scene. Elementary transformation method is used for lighting calculation from lamp shield or calculation of light source with shield based on requirement on surface light. Flow and Point methods are intended to lighting calculation of room interior based on initial conditions (number of light sources and their shapes). The Point method is the simplified Flow method. There are used point light sources in Point method.

The disadvantage of the described methods is limited usability for close area in lighting system computation or their high computational time-consuming for good results resolution.

We are trying to find numerical method which enables the solving of the light from all areas of lighting systems. One possibility is usage of sophisticated numerical method together with finite volume method, for example the ANSYS CFX program. The ANSYS CFX program uses standard program tools such as modeling, discretization into a net of elements, solvers, evaluation, and interpretation of the results. The basic idea of problem is in the transformation of thermal field quantities into optical quantities. This can be done using the general rules described in [4]. In the following text the basics of modeling the primitive light problem are described.

2. THE R-FEM METHOD

The R-FEM method is a new way in the modeling of lighting systems. It utilizes the similarity between physical models. This paragraph demonstrates the usage of analogy between different physical models for the modeling of light problems. The R-FEM method is able to solve tasks that fulfill the condition $\lambda_S \ll \max(D) \wedge \lambda_S < 10 \cdot \max(D)$, where λ_S is the source of light wavelength and D is one of the geometrical dimensions of the modeling task. It can be used for models with more complicated physical structures than the methods mentioned up to now. An example of a more complicated physical problem, which we can solve by the R-FEM method, is the modeling of light intensity distribution in interior or exterior spaces with non-homogeneous environment, where the light has passed through some impure air (e.g., filled with smoke, fog, mist, vapour, dust, etc.) [3, 4].

3. THE USE OF THE R-FEM METHOD IN ANSYS CFX ENVIRONMENT

ANSYS CFX environment can be exploited for lighting system computation when we use analogy between thermal field quantities and optical quantities [3]. There are three basic principles for heat propagation by conduction, convection or radiation. Main principle of heat propagation for lighting system computation is heat transfer by radiation. There are four methods for calculation of heat propagation by radiation (Rosseland Model, P1 Model, Discrete Transfer Model and Monte Carlo Model) in ANSYS CFX, but only Discrete Transfer method and Monte Carlo method can be used for calculation of lighting systems with mirror surfaces.

3.1. Monte Carlo Model Principle

Monte Carlo model principle is based on interaction between photons and environment. The photons are emitted from a source through the model until their mass decreases to minimum. When the photons drop on surface they are reflected or absorbed. The photons sources are chosen by the emitted energy. In gas environment the part of photon energy is absorbed. Each volume element affects the absorption and scattering. Heat transfer is described by Equation (1). This method allows calculation of heat transfer independently of spectrum or performs calculation in the range of chosen frequencies. It is described in [6].

3.2. Discrete Transfer Model Principle

This method is based on tracing of the beam of rays which are emitted from the surface. The beam of rays is discretized on the particular volume elements. The beam of rays is tracked in the whole path during the passing by the domain. This Discrete Transfer model uses the same advance as the Monte Carlo model. It is described in [6].

$$\frac{dI_v\left(\mathbf{r},\mathbf{s}\right)}{ds} = \left[-\left(K_{av}+K_{sv}\right) I_v\left(\mathbf{r},\mathbf{s}\right) + K_{av} I_b\left(\nu,T\right) + \frac{K_{sv}}{4\pi} \int\limits_{4\pi} dI_v\left(\mathbf{r},\mathbf{s}'\right) \Phi\left(\mathbf{s}\cdot\mathbf{s}'\right) d\Omega' + S, \right] \quad (1)$$

where v is frequency, $\mathbf{r}$ is position vector, $\mathbf{s}$ is direction vector, s is path length, K_a is absorption coefficient, K_s is scattering coefficient, I_b is Blackbody emission intensity, I_v is Spectral radiation intensity which depends on position (r) and direction (s), T = local absolute temperature, Ω is solid angle, Φ is in-scattering phase function and S = radiation intensity source term [6].

The described methods we can use for the numerical modeling of lighting systems. The radiation approach can be used for modeling of heat transfer between surfaces only with or without reflecting the environment properties. It is possible to simulate various impurities in air (e.g., filled with smoke, fog, mist, vapour, dust, etc.). ANSYS CFX environment is useful to create the numerical model independent on radiation spectrum or numerical model for specific spectrum. With numerical model which depends on frequency we can obtain the results for various colors.

4. ILLUSTRATIVE EXAMPLES

There are results from two illustrative models created in ANSYS CFX environment in this part. First example is reflecting parabolic surface with light source placed in focus point. Model dimensions are shown in left side of Fig. 1. Numerical model is composed of 165 875 nodes and of 945 186 elements. There is an air surround around solid parts in the model. The mesh cross-section is shown in the right side of Fig. 1. There were created three versions of model by the Monte Carlo method. In all model versions were set the emissivity of parabolic surface to value 0.1. In the first version is the reflecting surface set up as mirror surface (without scattering). The results for this version are shown in Fig. 2. There is the Wall Irradiation Flux (incoming radiative flux) distribution on parabolic surface shown in Fig. 2 (left) and the Wall Irradiation Flux distribution on observed surface is shown in Fig. 2 (right). For the second model version was the surface diffusion on parabolic surface set to value 1. The Wall Irradiation Flux distribution on observed surface is shown in Fig. 3 (left). For the third model version was set the surface diffusion on parabolic surface to value 0.3. The Wall Irradiation Flux distribution on observed surface is shown in Fig. 3 (right).

The second model was created with plane source, two mirrors and observed surface by Discrete Transfer method. Model dimensions are shown in Fig. 4 (left). The numerical model is composed of 578 655 nodes and of 555 080 elements. There is an air surround around solid parts in the model. There was set the emissivity to value 0.1 and surfaces diffusion to zero on reflecting surfaces. The Wall Irradiation Flux distribution on observed surface is shown in Fig. 4 (right).

The both models were computed independent on surrounding environment. The conversion to light units was described in [3].

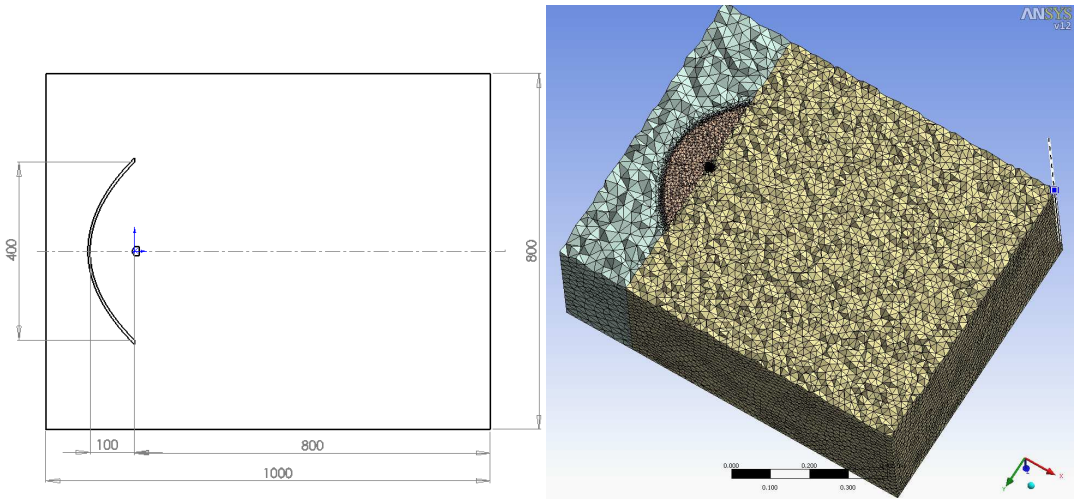

Figure 1: Model dimensions (left), mesh (right).

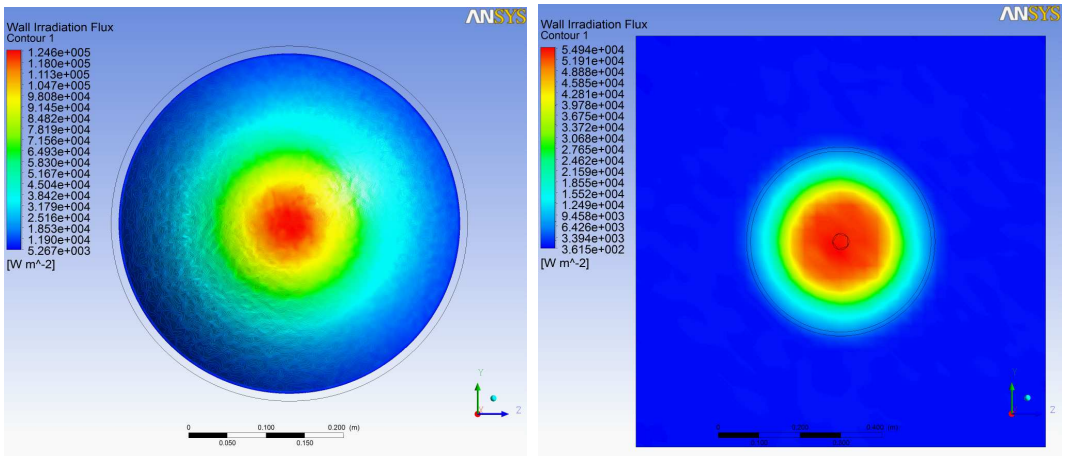

Figure 2: The Wall Irradiation flux distribution on parabolic mirror surface and on observed surface.

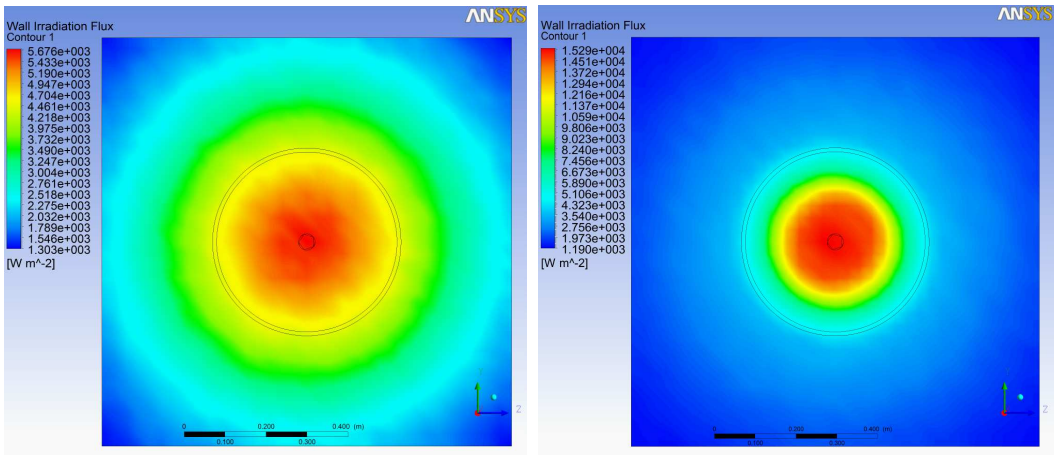

Figure 3: The irradiation flux distribution on observed surface for diffusion = 1 and diffusion = 0.3.

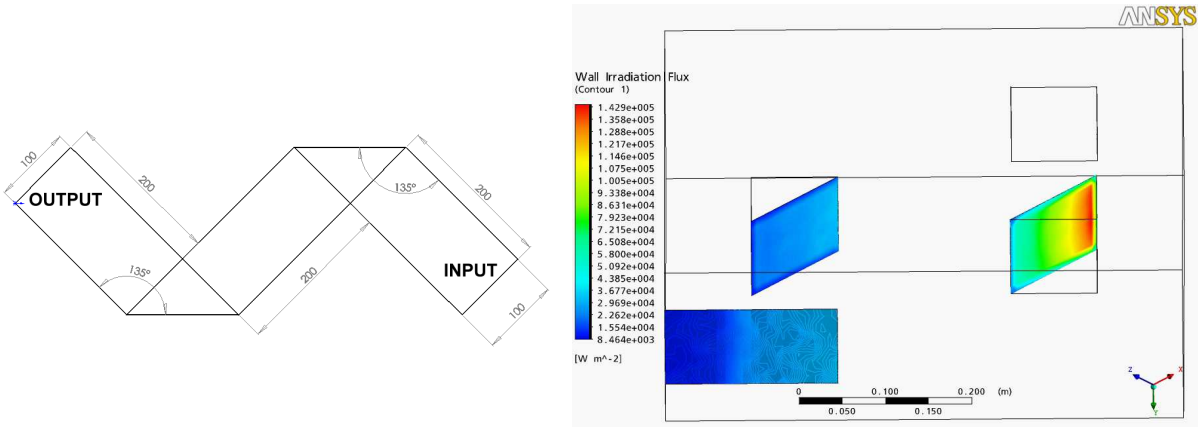

Figure 4: Model dimensions and results.

5. ADVANTAGES OF THE R-FEM METHOD

One of the biggest advantages of this method is the wide spectrum of its usage. We can design the interior and also exterior scenes with its specifications in the materials quality, climatic dissimilarities and geometrical dimension varieties. We can use all types of sources of light with their diversity of the color distribution in the light spectrum. The designers are not limited by the geometrical dimension varieties, color distribution in the light spectrum, material qualities or climatic dissimilarities. The other advantage is that the method is very accurate. The degree of accuracy depends on the choosing of the method of generating nets of elements and the solution algorithm because all this is provided by the ANSYS CFX standard program tools.

6. CONCLUSION

In this paper was shown the usage of R-FEM method in the ANSYS CFX environment. There were presented the results for two different models with several settings created in the ANSYS CFX environment. There was shown a possibility of the lighting systems modeling with different optical properties by various settings of the model parameters. It is possible to compute the lighting systems with mirror surfaces and diffusion surfaces or combination of them.

ACKNOWLEDGMENT

The researches described in the paper were financially supported by research plan No. MSM 0021630516 and research plan No. MSM 0021630513 and MPO FR-TI1/368.

REFERENCES

1. Kroutilová, E., M. Bernard, and P. Fiala, "Illumination of interiors by the hollow light guides," *14th International Conference Light*, ISBN 80-233-0488-7, Bratislava, 2003.
2. Kroutilová, E. and P. Fiala, "Light guide modeling," *Energy Forum 2004*, 338–341, ISBN 80-986-1619-1, Technical University, Sofia, Bulgaria, 2004.
3. Kadlecova, E., "Automated system of calculation of reflecting surface of light sources," Ph.D. thesis VUT v Brně, FEKT, Brno srpen, 2004.
4. Fiala, P., E. Kroutilova, and T. Kriz, "Numerical modelling of the special light source with novel R-FEM method," *PIERS Proceeding*, 822–826, Cambridge, USA, July 2–6, 2008.
5. Tsang, K.-F., W.-S. Chan, D. Jing, K. Kang, S.-Y. Yuen, and W.-X. Zhang, "Radiosity method: A New propagation model for microcellular communication," *IEEE Antennas and Propagation Society International Symposium*, Vol. 4, 2228–2231, June 21–26, 1998.
6. Ansys User's Manual, Svanson Analysys Systém, Inc., Huston, USA registered ISO 9001:2000, 2008.
7. Kroutilova, E., *Způsob návrhu odrazných ploch reflexních zařízení pomocí analogie teplotního pole-radiace a vlnové rovnice a zařízení v podobě světelné soustavy určené pro numerickou optimalizaci požadovaných světelných parametrů odrazných ploch*, Patent No. PV 2008-65, Leden, Czech Republic, 2008.

Two-dimensional Magnetotelluric Regularization Inversion Jointed with TE- and TM-mode Data

Jian-Xin Liu, **Ling-Hua Xu**, **Xiao-Zhong Tong**, **Ya Sun**, **and Zhen-Wei Guo**
School of Info-physics Geomatics Engineering, Central South University
Changsha 410083, China

Abstract— The magnetotelluric inverse problem is ill-posed and the inverse results are unstable and non-unique. It means that different geo-electrical model could fit the observed data with the same accuracy. A stable solution of the ill-posed inverse problem can be obtained by utilizing the regularization methods in the objective function. Solving large scale linear equation of inverse problem, the damped Gauss-Newton algorithm was adopted, which can improve local convergence of Gauss-Newton method. On the one hand, inversion of TE-mode data is more sensitive for the low abnormal body and has poor resolution for the high abnormal body. On the other hand, inversion of TM-mode data has better resolution for the high abnormal body. Jointed two-mode data inversion is able to achieve better model and stack quality in considerably fewer iterations. In order to better inversion results, TE- and TM-mode magnetotelluric data are jointed. Through the synthetic model simulation, the inversion results truly reflected the geo-electrical parameters of the model and accurately showed the depth and size of the abnormal body.

1. INTRODUCTION

The purpose of magnetotelluric inversion is to find a reasonable geo-electrical model for matching the observed magnetotelluric data. Inversion of the core must be attributed to the optimization process, inversion methods can be divided into two categories: linear and nonlinear inverse method. The magnetotelluric inverse problem can be formulated into an optimization problem with a cost function which depends on the geological property parameters to be determined [1]. At present, there are some solutions for two-magnetotelluric: OCCAM method [2], RRI method [3], NLCG method [4] and ABIC method [5]. The two-dimensional magnetotelluric inverse problem still poses difficult in spite of efforts to develop efficient methods for its solution.

The two-dimensional magnetotelluric inverse problem is ill-posed and the inverse results are unstable and non-unique. It means that different geo-electrical model could fit the observed data with the same accuracy. A stable solution of the ill-posed inverse problem can be obtained by utilizing the regularization methods in the objective functional subjected to minimum. In this paper, we suggest the generalized cross validation (GCV) as method to estimate the global regularization parameter and the damped Gauss-Newton method to impose the two-dimensional magnetotelluric ill-posed inverse problem.

2. FORWARD PROBLEM

For the two-dimensional magnetotelluric forward problem, Maxwell's equation can be combined to yield two decoupled equations:

$$\nabla \cdot (\tau \nabla u) + \lambda u = 0 \tag{1}$$

TE-mode:

$$u = E_x, \quad \tau = \frac{1}{i\omega\mu}, \quad \lambda = \sigma; \tag{2}$$

TM-mode:

$$u = H_x, \quad \tau = \frac{1}{\sigma}, \quad \lambda = i\omega\mu. \tag{3}$$

$\mu = \mu_0 = 4\pi \cdot 10^{-7}\,\mathrm{Vs}\cdot(\mathrm{Am})^{-1}$ is the free space magnetic permeability, ω is the angular frequency of the observed time-harmonic fields and σ the isotropic conductivity.

According to finite element method, equations can be expressed in matrix-vector form as

$$Kv = p \tag{4}$$

where v is either a column vector of the electric field E_y or the magnetic field H_y at each node in TE and TM mode respectively. K is referred to as stiffness matrix.

The remaining field components H_x for TE-mode and E_x for TM-mode can be determined at each grid node by

$$H_x = \frac{1}{i\omega\mu}\frac{\partial E_y}{\partial z}, \quad H_z = -\frac{1}{i\omega\mu}\frac{\partial E_y}{\partial x}, \quad E_x = -\frac{1}{\sigma}\frac{\partial H_y}{\partial z}. \tag{5}$$

The apparent resistivity ρ_a and the phase ϕ for TE- and TM-mode can be computed as

$$\rho_a = \frac{1}{\omega\mu}\left|\frac{E_{y|x}}{H_{x|y}}\right|^2, \quad \phi = \arctan\left(\frac{\mathrm{Im}\left(E_{y|x}/H_{x|y}\right)}{\mathrm{Re}\left(E_{y|x}/H_{x|y}\right)}\right) \tag{6}$$

3. INVERSE PROBLEM

The two-dimensional magnetotelluric inverse problem can be formulated as a numerical solution of the operator equation:

$$d = F(m) \tag{7}$$

where d is the data vector, m is the model vector, and F is the forward modeling function.

The magnetotelluric inverse problem is ill-posed and the inverse results are unstable and non-unique. It means that different geo-electrical model could fit the observed data with the same accuracy. A stable solution of the ill-posed inverse problem can be obtained by utilizing the regularization methods in the objective function. The conventional method of solving ill-posed problems is based on minimization of the Tikhonov parametric functional [6, 7]:

$$P^\alpha(m) = \phi(m) + \alpha s(m) \tag{8}$$

where $\phi(m)$ is the misfit functional determined as the square norm of difference between the observed and predicted (theoretical) data; α is the regularization parameter; $s(m)$ is the stabilizing functional, called the stabilizer. The stabilizer can be treated as a tool for including some priori information about the geological structures in the inverse problem solution.

Therefore, the parametric functional for solving two-dimensional magnetotelluric inverse problem can be written

$$P^\alpha(m) = \left\|W_d\left[d^{obs} - F(m)\right]\right\|^2 + \alpha\left\|W_m\left(m - m^{ref}\right)\right\|^2 \tag{9}$$

W_d is the data weighting matrix, W_m is the model weighting matrix, and m^{ref} is the priori model.

Using Taylor series approximation, $F(m)$ can be written as

$$F\left(m^k + \Delta m\right) = F\left(m^k\right) + J^k\Delta m + O\left\|(\Delta m)^2\right\| \tag{10}$$

The Eq. (10) is also can be written as

$$d^{k+1} \approx d^k + J^k\Delta m \tag{11}$$

where $d^k = F\left(m^k\right)$, $\Delta m = m^{k+1} - m^k$, J^k is the Jacobian matrix of sensitivities:

$$J_{ij}^k = \frac{\partial d_i}{\partial m_j}\Big|_{m^k} \tag{12}$$

Substituting Eq. (11) into the objective function in Eq. (10) gives:

$$P^\alpha\left(m^{k+1}\right) = \left\|W_d\left(d^{obs} - d^k - J^k\Delta m\right)\right\|^2 + \alpha\left\|W_m\left(m^k - m^{ref}\right)\right\|^2 \tag{13}$$

Differentiating this expression with respect to the elements of Δm and the resulting derivatives to zero yields the following linear system of equation to solve:

$$\left(J^{k^T}W_d^TW_dJ^k + \alpha W_m^TW_m\right)\Delta m = J^{k^T}W_d^TW_d\left(d^{obs} - d^k\right) + \alpha W_m^TW_m\left(m^{ref} - m^k\right) \tag{14}$$

In this paper, we adopted the damped Gauss-Newton method for this linear equation.

4. REGULARIZATION PARAMETER

The key point for the regularized inverse problem is to choose regularization parameter. There are three choosing method: discrepancy principle [8], generalized cross validation (GCV) method [9] and L-Curve method [10]. In this paper, the GCV method is adopted.

For the magnetotelluric inverse problem, the GCV function for the kth iteration is given by

$$GCV\left(\alpha\right) = \frac{\left\|W_d\hat{d} - W_d J^{k-1} M^{-1}\left(J^{k-1} W_d^T W_d \hat{d} + r\right)\right\|^2}{\left[trace\left(I - W_d J^{k-1} M^{-1} J^{k-1^T} W_d^T\right)\right]^2} \tag{15}$$

where

$$M\left(\alpha\right) = \left(J^{k-1^T} W_d^T W_d J^{k-1} + \alpha W_m^T W_m\right) \tag{16}$$

$$r = \alpha W_m^T W_m \left(m^{ref} - m^{k-1}\right) \tag{17}$$

and $\hat{d} = d^{obs} - d^{k-1}$, $trace$ is the trace of the square matrix.

Although the GCV estimates of the regularization parameter at the early iterations can be close to what its final value will be, it has been shown that using these estimates can cause too much structure to appear too early in the model. The GCV criterion is therefore combined with a cooling-schedule-type behavior, just as for the discrepancy principle, choosing the value of α at the kth iteration to be:

$$\alpha^k = \max\left(c\alpha^{k-1}, \alpha^*\right) \tag{18}$$

where $0.01 \leq c \leq 0.5$, and α^* is the minimized of the GCV function given in Eq. (15).

5. SYNTHETIC EXAMPLE

The model consists of two rectangular bodies with resistivities of 250 and 10 ohm-m embedded in a 50 ohm-m homogeneous half-space. The locations of these bodies are shown in Figure 1. Two sets of synthetic apparent resistivities and phase ware generated for TE and TM mode at 49 stations using fourteen frequencies (0.01, 0.03, 0.1, 0.3, 1, 5, 10, 15, 30, 50, 100, 300, 1000 Hz). The mesh used for the inversion consists of 78 columns and 40 rows, giving rise to 3120 blocks to inverse.

Inversion was performed combined with TE- and TM-mode data. The starting model for each was a $50\,\Omega \cdot$ m half-space, and the priori mode was set to zero. After 20 iterations with damped Gauss-Newton method, the misfit of TE and TM mode was reached 0.031. Inversion results were shown Figure 2, it truly reflected the geo-electrical parameters of the model and accurately showed the depth and size of the abnormal body.

Figure 3 shows pseudosections for original data(including apparent resistivity and phase) and the obtained from jointed inversion for TE- and TM-mode. Figure 4 shows the same response for the TM-mode. We generated these pseudosections in order to compare the original synthetic data to that obtained from the inversion. These pseudosections show that the inversion of synthetic data yields acceptable results.

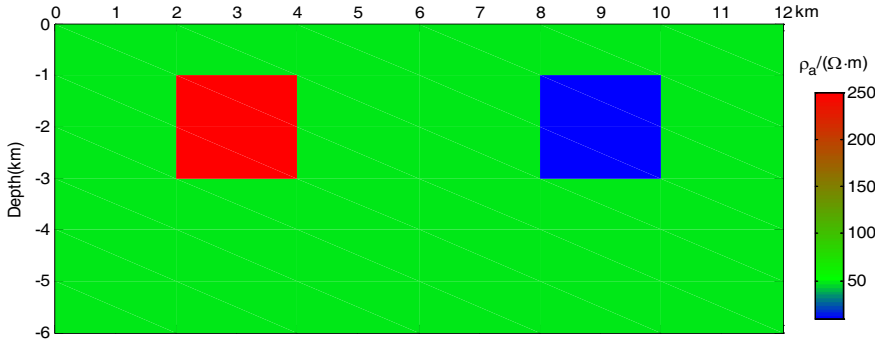

Figure 1: The two-dimensional geo-electrical model.

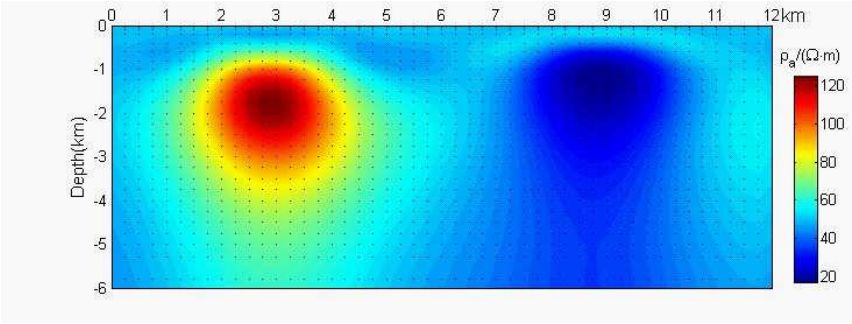

Figure 2: Inversion result of the two-dimensional geo-electrical model.

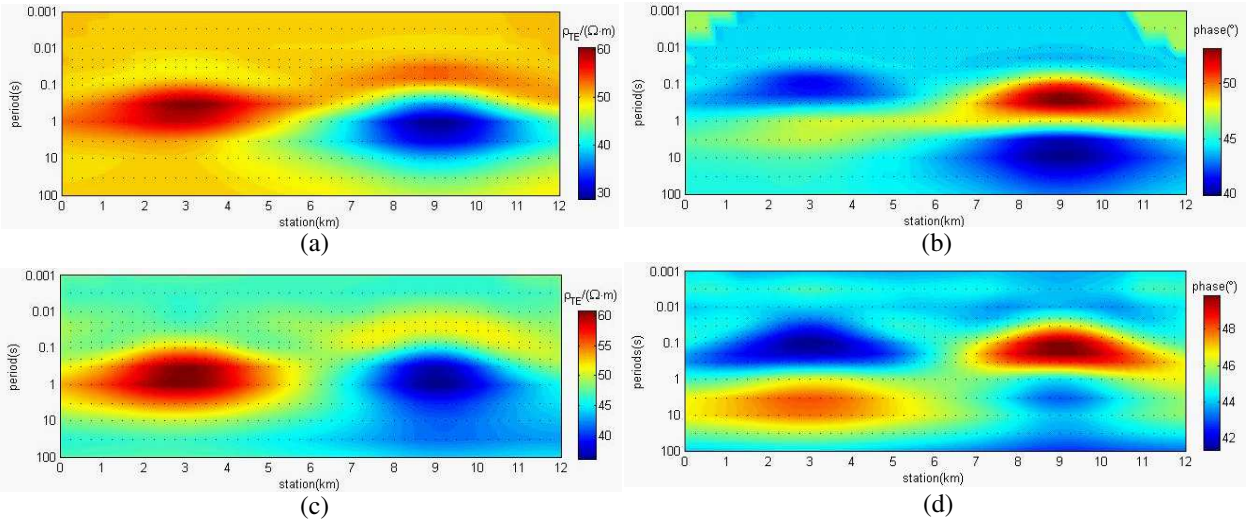

Figure 3: Comparisons between the observed and predicted TE-mode data, (a) observed apparent resistivity; (b) observed phase; (c) predicted apparent resistivity; (d) predicted phase.

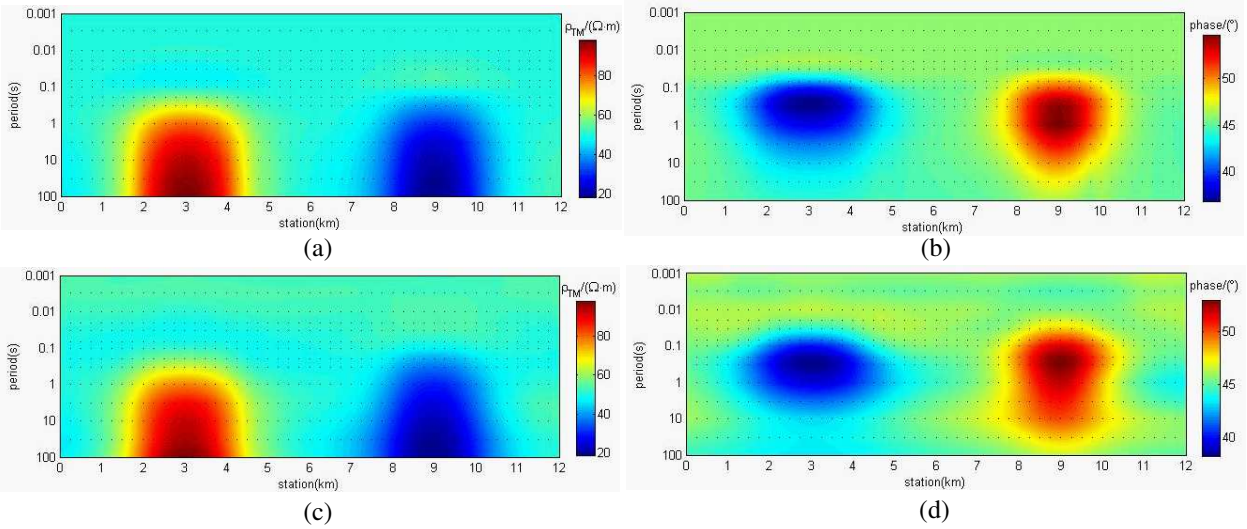

Figure 4: Comparisons between the observed and predicted TM-mode data, (a) observed apparent resistivity; (b) observed phase; (c) predicted apparent resistivity; (d) predicted phase.

6. CONCLUSION

The magnetotelluric inverse problem is ill-posed and the inverse results are unstable and non-unique. It means that different geo-electrical model could fit the observed data with the same accuracy. A stable solution of the ill-posed inverse problem can be obtained by utilizing the

regularization methods in the objective function. Solving large scale linear equation of inverse problem, the damped Gauss-Newton algorithm was adopted, which can improve local convergence of Gauss-Newton method. On the one hand, inversion of TE-mode data is more sensitive for the low abnormal body and has poor resolution for the high abnormal body. On the other hand, inversion of TM-mode data has better resolution for the high abnormal body. Jointed two-mode data inversion is able to achieve better model and stack quality in considerably fewer iterations. Through the synthetic model simulation, the inversion results truly reflected the geo-electrical parameters of the model and accurately showed the depth and size of the abnormal body.

ACKNOWLEDGMENT

This paper is supported by National Natural Science Foundation Project (60672042) and the Ministry of Education Doctorate Foundation Project (20070533102).

REFERENCES

1. Chen, L.-S., R. Liu, and T.-S. Wang, *The Magnetotelluric Sounding Data Processing and Interpretation Methods*, Petroleum Industry Press, Beijing, 1989.
2. DeGroot-Hedlin, C. and S. Constable, "Occam's inversion to generate smooth, two-dimensional models from magnetotelluric data," *Geophysics*, Vol. 55, 1613–1624, 1990.
3. Smith, J. and J. Booker, "Rapid inversion of two- and three-dimensional magnetotelluric data," *Journal of Geophysical Research*, Vol. 96, 3905–3922, 1991.
4. Rodi, W. and R. Mackie, "Nonlinear conjugate gradients algorithm for 2-D magnetotelluric inversion," *Geophysics*, Vol. 66, 174–187, 2001.
5. Uchida, T., "Smooth 2-D inversion for magnetotelluric for magnetotelluric data based on statistical criterion ABIC," *Journal of Geomagnetism and Geoelectricity*, Vol. 45, 841–858, 1993.
6. Tikhonov, A. N. and V. Y. Arsenin, *Solution of Ill-posed Problems*, Wiley, New York, 1977.
7. Farquharson, C. G. and D. W. Oldenburg, "A comparison of automatic technique for estimating the regularization parameter in non-linear inverse problems," *Geophysical Journal International*, Vol. 156, 411–425, 2004.
8. Pereverzev, S., "Morozov's discrepancy principle for Tikhonov regularization of severely ill-posed problem in finite-dimensional subspaces," *Numerical Functional Analysis and Optimization*, Vol. 21, 901–916, 2000.
9. Haber, E. and D. Oldenburg, "A GCV based method for nonlinear ill-posed problems," *Computational Geosciences*, Vol. 4, 41–63, 2000.
10. Hansen, P. C. and D. P. Leary, "The use of the L-curve in the regularization of discrete ill-posed problems," *Society for Induction and Applied Mathematics*, Vol. 14, 1487–1503, 1993.

Three-dimensional Magnetotelluric Forward Modeling for Static-shifted Model

Xiao-Zhong Tong, **Jian-Xin Liu**, **Ya Sun**, **and Zhen-Wei Guo**
School of Info-physics Geomatics Engineering, Central South University
Changsha 410083, China

Abstract— Magnetotelluric static shift is a non-inductive change of the magnetotelluric apparent resistivity response that severely impairs the interpretation of data. For two-dimensional models, static shift is manifested in the data as vertical, parallel shifts of log-log apparent resistivity sounding curves, the impedance phase being unaffected. In order to get the static shift features of three-dimensional model, we use the finite element method for three-dimensional magnetotelluric forward modeling. The finite element algorithm is very efficient, ant it has a lot of advantages: the high precision, the canonical process of solving problem, meeting the internal boundary condition automatically and adapting to all kinds of distribution of multi-substances. Through the simulation of the three-dimensional magnetotelluric static-shifted model, the results show that the apparent resistivity at every site is affected and the impedance phase is normal.

1. INTRODUCTION

Surficial bodies can severely distort magnetotelluric apparent resistivity data to arbitrarily low frequency. This distortion, known as the magnetotelluric static shift, is due to an electric field generated from boundary charges on surficial in homogeneities, and persists throughout the entire magnetotelluric recording range. Static shift is manifested in the data as vertical, parallel shifts of log-log apparent resistivity sounding curves, the impedance phase being unaffected [1, 2]. In order to get the static shift features of three-dimensional model, we use the finite element method for three-dimensional magnetotelluric forward modeling.

Calculation of magnetotelluric responses for there-dimensional model of the earth must rely on numerical methods. These numerical solutions are obtained by approximating the relevant differential or integral equations and solving a matrix equation. For magnetotelluric forward modeling, three methods have been used most for this approximation, namely, integral equation (IE) method [3, 4], finite difference (FD) method [5, 6] and finite element (FE) method [7–9].

2. FORWARD MODELING

To obtain magnetotelluric (MT) responses at the surface, one must solve for the electric ($\mathbf{E}$) and magnetic ($\mathbf{H}$) fields simultaneously via the first order Maxwell's equations [10],

$$\nabla \times \mathbf{E} = i\omega\mu\mathbf{H} \tag{1}$$

$$\nabla \times \mathbf{H} = \sigma\mathbf{E} \tag{2}$$

subjected to appropriate boundary conditions at the top, bottom and sides of the domain. Here μ is the magnetic permeability of the free space ($4\pi \times 10^{-7}\,\mathrm{Hm}^{-1}$), ω is the angular frequency, and σ is the spatially variable electrical conductivity (the inverse of resistivity, ρ). The same equations, with addition of source terms (and different boundary conditions), must be solved for more general EM modeling problems.

The couple system (1) and (2) can be solved the second order Maxwell's equations, in $\mathbf{E}$ form,

$$\nabla \times \nabla \times \mathbf{E} = i\omega\mu\sigma\mathbf{E} \tag{3}$$

or, in $\mathbf{H}$ form,

$$\nabla \times \rho\nabla \times \mathbf{H} = i\omega\mu\sigma\mathbf{H} \tag{4}$$

For solving Eq. (3), through general variation method, the functional can be generated as follow

$$F(\mathbf{E}) = \frac{1}{2}\int_V \left((\nabla \times \mathbf{E}) \cdot (\nabla \times \mathbf{E}) - k^2\mathbf{E} \cdot \mathbf{E}\right) \mathrm{d}V \tag{5}$$

Utilizing the finite element method, we can derived the linear system as follows

$$\mathbf{KE} = 0 \tag{6}$$

Considering surface boundary conditions, we can obtain the linear equation

$$\mathbf{KE} = \mathbf{p} \tag{7}$$

The system of equation of our finite element algorithm is a large sparse, banded, symmetric, ill-conditioned, non-Hermitian complex matrix equation. Its condition number is far larger than 1, and it is a seriously ill-conditioned matrix. Solving this large scale ill-conditioned linear equation is very difficult, which can be solved using the Bi-CGSTAB method [11, 12]. Once the electric fields have been determined on the mesh, the magnetic fields, **H** can be determined from Faraday's law,

$$\mathbf{H} = \nabla \times \mathbf{E}/-i\omega\mu \tag{8}$$

The apparent resistivity ρ_a and the phase ϕ for xy- and yx-mode can be computed as

$$\rho_a = \frac{1}{\omega\mu}\left|\frac{E_{y|x}}{H_{x|y}}\right|^2, \quad \phi = \arctan\left(\frac{\mathrm{Im}\left(E_{y|x}/H_{x|y}\right)}{\mathrm{Re}\left(E_{y|x}/H_{x|y}\right)}\right) \tag{9}$$

3. SOLUTION STRATEGIES

For three-dimensional magnetotelluric forward problem, in order to improve computing efficiency of finite element method, we chose non-uniform gird. The study area was classified as the target area and the extension area. The target area is the occurrence of regional geology, which is the area of data acquisition, and uniform grid is adopted. The grid step of the extension area by more than 1 is increasing, which was ensuring the accuracy of the circumstance, reducing post-score gird and saving computing time. Three-dimensional forward modeling non-uniform grid is shown in Figure 1.

To solve the large scale ill-conditioned linear equation, we chose the Bi-CGSTAB algorithm with incomplete LU decomposition for preconditioning. The Bi-CGSTAB method uses two residual vectors, $\{\mathbf{s}\}$ and $\{\mathbf{r}\}$, at each iteration, it was defined by $\{\mathbf{s}\} = \{\mathbf{r}\} = \{\mathbf{p}\} - [\mathbf{K}]\{\mathbf{E}\}$. When either of the convergence criteria, $\|\{\mathbf{s}\}\|^2/\|\{\mathbf{p}\}\|^2 \leq \varepsilon$ or $\|\{\mathbf{r}\}\|^2/\|\{\mathbf{p}\}\|^2 \leq \varepsilon$, is satisfied given a specified tolerance ε, the iterative process ends. In the simulation show below, $\varepsilon = 10^{-10}$.

4. NUMERICAL EXPERIMENT

The three-dimensional model has a relatively low resistivity contrast with a $4 \times 4 \times 0.03$ km conductive block ($1\,\Omega \cdot$ m) embedding a homogeneous background earth ($100\,\Omega \cdot$ m). It is shown in Figure 2.

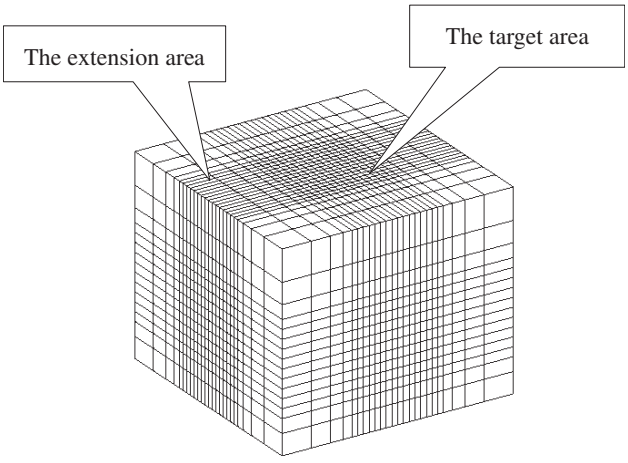

Figure 1: The non-uniform grid.

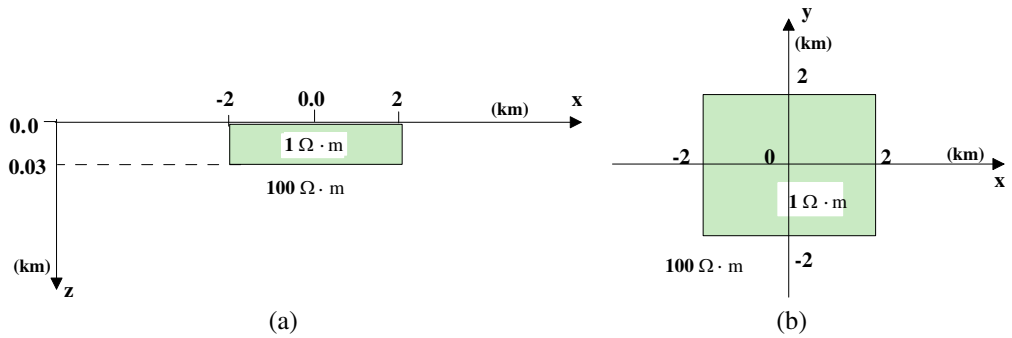

Figure 2: The three-dimensional static-shifted model. (a) Section view; (b) plan view.

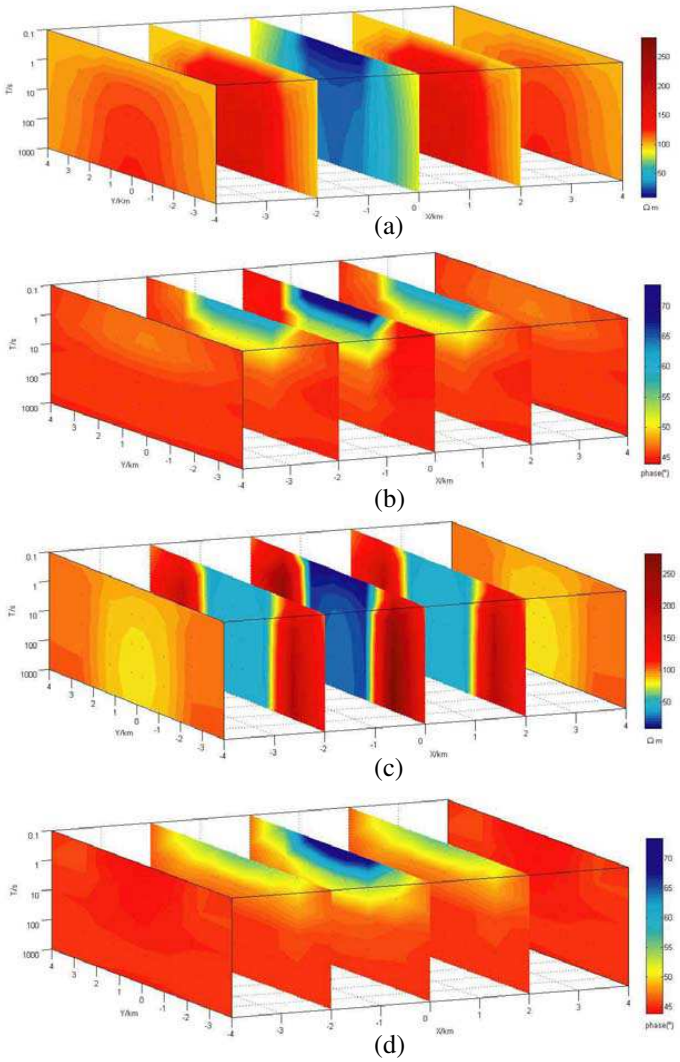

Figure 3: The magnetotelluric responses for three-dimensional static-shifted model. (a) Apparent resistivity of xy-mode; (b) impedance phase of xy-mode; (c) apparent resistivity of yx-mode; (d) impedance phase of yx-mode.

In forward simulation, using $28 \times 28 \times 26$ elements (including five air layers) for the subdivision, the extension of the air layer is 90.75 km. The grid unit along the x direction of the interval (unit: km):

20	20	15	10	10	8	5	3	2	1	0.5	0.5	0.5	0.5
0.5	0.5	0.5	0.5	1	2	3	5	8	10	10	15	20	20

The grid unit along the y direction of the interval (unit: km):

20	20	15	10	10	8	5	3	2	1	0.5	0.5	0.5	0.5
0.5	0.5	0.5	0.5	1	2	3	5	8	10	10	15	20	20

The grid unit along the z direction down of the interval (unit: km):

0.03	0.03	0.04	0.1	0.2	0.2	0.4	0.5	0.5	0.5	0.5	1	1	2	2	3	5	8	10	15	20

Extension of the air unit interval (unit: km): 0.75 2.25 6.75 20.25 60.75.

We compute the three-dimensional magnetotelluric responses of the static-shifted model using fourteen periods (0.001, 0.003, 0.01, 0.03, 0.1, 0.3, 1, 5, 10, 15, 30, 50, 100 s). Figure 3 is the contour map of the apparent resistivity and impedance phase by three-dimensional FE method, which basically reflects the geo-electrical parameters of the model. The apparent resistivity of xy-mode and yx-mode is affected and the impedance phase is normal.

For two-dimensional models, static shift is manifested in the data as vertical, parallel shifts of log-log apparent resistivity sounding curves, the impedance phase being unaffected. Also, the static shift mainly exists in the TM-mode magnetotelluric response. So, it can be show that two-mode apparent resistivity of three-dimensional static-shifted model is affected.

5. CONCLUSION

Surficial bodies can severely distort magnetotelluric apparent resistivity data to arbitrarily low frequency. This distortion, known as the magnetotelluric static shift, is due to an electric field generated from boundary charges on surficial in homogeneities, and persists throughout the entire magnetotelluric recording range. Through the simulation of the three-dimensional magnetotelluric static-shifted model, the results show that the apparent resistivity at every site is affected and the impedance phase is normal.

ACKNOWLEDGMENT

This paper is supported by National Natural Science Foundation Project (60672042.) and the Ministry of Education Doctorate Foundation Project (20070533102).

REFERENCES

1. Pellerin, L. and G. W. Hohmann, "Transient electromagnetic inversion: A remedy for magnetotelluric static shifts," *Geophysics*, Vol. 55, No. 9, 1242–1250, 1990.
2. Ledo, J. and A. Marcuello, "Static shift leveling using geomagnetic transfer functions," *Earth Planets Space*, Vol. 54, 493–498, 2002.
3. Wannmaker, P. E., "Advances in three-dimensional magnetotelluric modeling using integral equations," *Geophysics*, Vol. 56, No. 6, 1716–1728, 1991.
4. Xiong, Z., "EM modeling of three-dimensional structures by the method of system iteration using integral equations," *Geophysics*, Vol. 57, No. 1, 1556–1561, 1992.
5. Mackie, R. L., T. R. Madden, and P. E. Wannamaker, "Three-dimensional magnetotelluric modeling using difference equations — Theory and comparisons to integral equation solutions," *Geophysics*, Vol. 58, No. 9, 215–226, 1994.
6. Fomenko, E. Y. and T. Mogi, "A new computation method for a staggered grid of 3D EM field conservative modeling," *Earth Planets Space*, Vol. 54, No. 7, 499–509, 2002.
7. Mogi, T., "Three-dimensional modeling of magnetotelluric data using finite-element method," *Journal of Applied Geophysics*, Vol. 35, No. 6, 185–189, 1996.
8. Huang, L.-P. and S.-K. Dai, "Finite element calculation method of 3D electromagnetic field under complex condition," *Earth Science — Journal of China University of Geosciences*, Vol. 27, No. 6, 775–779, 2002 (in Chinese).
9. Tong, X.-Z. and J.-X. Liu, "Three-dimensional forward modeling for magnetotelluric sounding by finite element method," *Journal of Central South University*, Vol. 16, No. 1, 135–142, 2008.
10. Chen, L.-S., R. Liu, and T.-S. Wang, *The Magnetotelluric Sounding Data Processing and Interpretation Methods*, Petroleum Industry Press, Beijing, 1989.
11. Smith, J. T., "Conservative modeling of 3D electromagnetic fields; Part II: Biconjugate gradient solution and an accelerator," *Geophysics*, Vol. 61, No. 3, 1319–1324, 1996.
12. Haber, E., U. M. Ascher, and D. W. Oldenburg, "Fast simulation of 3D electromagnetic problems using potentials," *Journal of Computational Physics*, Vol. 163, No. 2, 150–171, 2000.

A Practical Scheme for 3D Geoelectrical Forward Modeling with Finite-infinite Element Coupling Method

Jing-Tian Tang and Jin-Zhe Gong
School of Info-physics and Geomatics Engineering, Central South University, Changsha 410083, China

Abstract— In this study, fast and visualized pre and post processing for finite element method was achieved by customized development based on the universal 3D modeling software named GiD, while infinite elements were introduced to form the finite-infinite element coupling method, which could substitute the conventional mixed boundary conditions and solve the problems cased by artificial boundary conditions. For the customized development on GiD, we only need to program the so-called *problem types* with simple script language, then models could be build in the graphic interface and output in the format fitting our calculation program. As to our finite-infinite element method, Astley mapped wave envelope infinite elements were employed to continue the electrical potential to infinity. Then, a new type of shape functions was created and it was proved to be the optimal one in both accuracy and time consumption by comparing with several other shape functions. Finally, the availability and superiority of this coupling algorithm were confirmed by several numerical tests with various electrode arrays.

1. INTRODUCTION

Currently, there are two problems that baffle the 3D DC resistivity finite element method forward modeling. The first is how to build complex 3D geoelectrical model efficiently and effectively. A lot of scholars are still build 3D models within a .txt file and by manual input, which is time consuming, error prone and not applicable for complex ones. The second is, though by enforcing mixed boundary conditions we can get relatively high accuracy in an acceptable discretization domain, because the global system matrix is affected by the locations of sources, once the locations have been changed the matrix has to be formed over again, which would make the forward modeling for some survey configurations, such as dipole-dipole array, very time consuming and worthless for inversions [1]. The solutions commonly used for solving the problems mentioned above include taking replacement of the mixed boundary conditions by Dirichlet [2] or Neumann [3] boundary conditions or assuming the distance between the source and boundary in the mixed boundary conditions to be a constant [1]. All the schemes need the domain of discretization to be set so large that the effect of the truncated boundaries can be eliminated to some extent, while what is inevitable is that the number of grid nodes must be increasing and so is the computational complexity.

In order to address these issues, we firstly employed a software named GiD, which is a universal, adaptive and user-friendly graphical user interface for geometrical modeling, data input and visualisation of results [4]. Then infinite elements were attached outward the conventional finite elements to replace all the artificial boundary conditions. By applying appropriate coordinates mapping and infinite element interpolation shape functions, the electrical potential can distribute continuously in half space and decay to zero at infinity, meaning the artificial boundary conditions are never needed and the mesh domain for finite elements can be reduced.

2. PRE AND POST PROCESSING WITH GID

To create a 3D model we just need to draw it in the graphic interface of GiD but to enforce boundary conditions or other information on the model we should firstly design our problem type with the script language. For the 3D direct current (DC) forward modeling problems, among the four controlling files required by GiD, the two with suffix of .bas and .cnd are critical. The former one controls the format of the output model files and the latter one defines the conditions or attributes. In our case, the .bas file describe a format of the .poly files [5], while the .cnd file should be defined as following. Note that the remarks following "//" are not obligatory.

```
CONDITION: Survey-Station      //Name of the condition
CONDTYPE: over points          //Where should it be applied on (points, faces or bodies)
CONDMESHTYPE: over nodes       //Where should it be spread on when meshing
QUESTION: Marker               //Marker for this condition
VALUE: 99                      //Default values for this condition
```

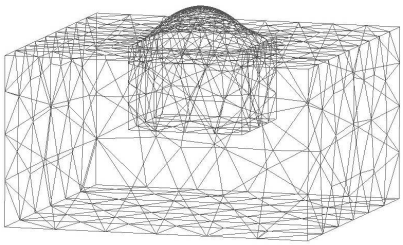

Figure 1: Mesh result of the ridge model.

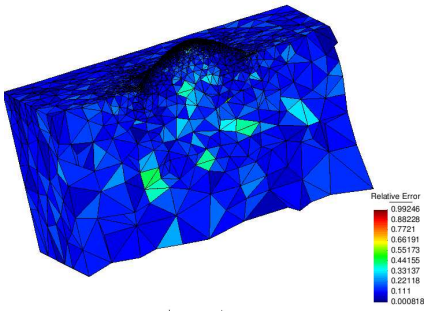

Figure 2: Relative error distributions on elements.

HELP: Survey Station/Point //Help or notes
END CONDITION //End a condition

Figure 1 illustrates the mesh of a ridge model. We performed unstructured surface mesh and divide the domain into an inner region with dense grids and an outer region with the mesh density decreases towards the boundaries. The source points, survey stations, boundary identities and regional resistivity values are all included in the model and can be read by our calculation program. The unstructured volume tetrahedralization will be implemented by our calculation program because some times we need adaptive meshes [6].

Regarding to the post processing, results files with given format should be output by the calculation program. Fortunately, a GiDpost library is available on the official web site, so we just need to use the functions to output our results without caring about the inner procedures. Figure 2 shows the relative error distributions on elements obtained by our program and visualized by GiD.

3. FINITE-INFINITE ELEMENT COUPLING METHOD

3.1. Finite Element Equations

When a point source is placed on the ground surface of a 3D semi-infinite space Ω, the electrical potentials are governed by the a differential equation and boundary conditions. By employing the variational principle, we can get the variational problem equivalent to the boundary value problem [7]. Finally, after the discretization with finite elements, a linear system of equations can be obtained and the system matix $\mathbf{A}$ is combined with

$$\mathbf{A}_{ij} = \int_{\Omega} \sigma \nabla N_i \nabla N_j d\Omega + \int_{\Gamma_\infty} N_i \sigma \frac{\cos(r,n)}{r} N_j d\Gamma \tag{1}$$

where σ is the arbitrary conductivities, $N_{i,j}$ are shape functions, Γ_∞ represents the subsurface boundaries and r is the distance from source to the boundaries. The second part in the right hand of the above equation represents the mixed boundary conditions and only exists at the subsurface boundary points. When the mixed boundary conditions are replaced by infinite elements, this part will be eliminated.

3.2. Coordinates Mapping for Infinite Elements

In 3D case and using unstructured tetrahedral finite elements to couple with the six-node infinite elements [8, 9], the mapping geometry can be presented in Figure 3. The distances from point P to points 4, 5 and 6 are double of those from P to points 1, 2 and 3, respectively. The outmost three points lying at infinity, which make the potential fields distribute to infinity, are not displayed in the figure.

The mapping functions for 3D infinite elements are given by

$$N_i = L_i M_1, \ N_{i+3} = L_i M_2 \qquad i = 1, 2, 3 \tag{2}$$

where

$$L_1 = \xi, \ L_2 = \eta, \ L_3 = 1 - \xi - \eta \tag{3}$$

$$M_1(\zeta) = -2\zeta/(1-\zeta), \ M_2(\zeta) = (1+\zeta)/(1-\zeta) \tag{4}$$

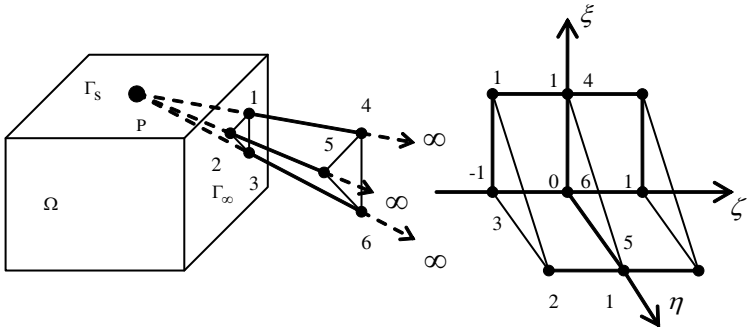

Figure 3: 3D infinite element mapping.

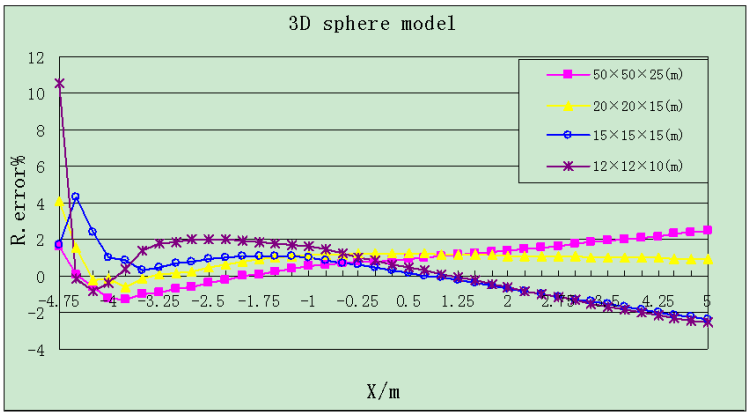

Figure 4: Relative errors obtained with different domain size.

3.3. Infinite Elements Shape Functions

The new shape functions for 3D infinite elements proposed by us are

$$M_i = L_i \frac{1-\zeta}{2} \frac{-(1-\zeta)}{2} \zeta, \quad M_{i+3} = L_i \frac{1-\zeta}{2}(1-\zeta^2) \qquad i = 1, 2, 3 \tag{5}$$

The coefficient $(1-\zeta)/2$ is introduced to modify the quadratic Lagrange polynomials. It can be easily proved that the electric potential is damping with the law of $\frac{C_1}{r} + \frac{C_2}{r^2} + \frac{C_3}{r^3}$, which is compatible with the physical law of the distribution of a point source in semi-infinite space. This type of shape function will lead to symmetric system matrices when applying the variational approach other than asymmetric ones derived from classical Astley infinite method [10]. We also compared it with some other types of infinite element shape functions, including the one employed in reference [8], and found it performed best both in accuracy and efficiency.

4. NUMERICAL RESULTS

4.1. 3D Sphere Model

The 3D sphere with a radius of 2.25 m and the central point being 5 m beneath the central of the horizontal ground surface had a resistivity of $10\,\Omega\cdot$m, while the resistivity for the half space was $1\,\Omega\cdot$m. AM configuration was employed. The source point A was set at (0, −5, 0) and the 40 survey stations were placed from (0, −4.75, 0) to (0, 5, 0) with the space of 0.25 m.

There were four models with different extensions (length × width × height) and the curves for relative errors are showed in Figure 4.

Due to the singularity of the source points, large errors occurred near the source, while most errors were lower than 3%. These numerical tests suggest that our finite-infinite coupling method was effective and could lead to accurate results for AM configuration within a relatively small mesh domain.

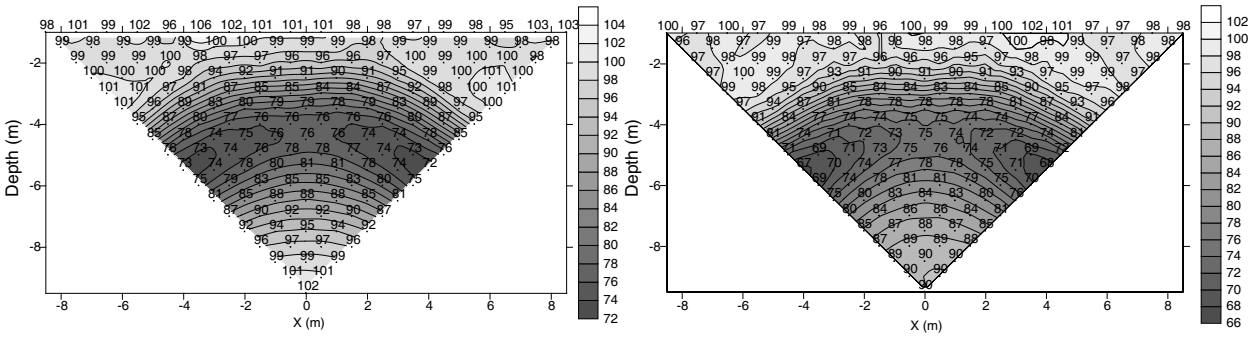

(a) $50 \times 50 \times 50$ (m) (b) $24 \times 24 \times 20$ (m)

Figure 5: Profiles of apparent resistivity for the 3D cube models.

4.2. A Cube in Half Space

This model was introduced from reference [1]. A cube with resistivity of $1\,\Omega \cdot$m was buried in the center of a half space with resistivity of $100\,\Omega \cdot$m. The side length of this cube was 4 m and the depth of its top surface was 3 m. Dipole-dipole configuration was employed and the space between electrodes was 1 m. Two models with different sizes of the discretization domain were employed. One was $50 \times 50 \times 50$ (m) and the other was $24 \times 24 \times 20$ (m). The profiles of apparent resistivity were depicted in Figure 5.

The two profiles both reflected the low-resistant anomalous body clearly and the curves were compatible with those in reference [1], which indicated the validity of our algorithm. In the first profile with model size of $50 \times 50 \times 50$ (m), the values of apparent resistivity above and beneath the low-resistant cube were tending to $100\,\Omega \cdot$m gradually, which was compatible with the resistiviy of the half space. While for the second one, though the values below the cube were lower than the true resistivity of the half space, the morphology of the curves could still disclose the low-resistant anomalous body. In general, the finite-infinite element coupling method is applicable with dipole-dipole configuration and can obtain reasonable results within such a small size of domain.

5. CONCLUSIONS

From model creation to calculation with finite-infinite element coupling method and then to results visualization, a practical scheme for 3D geoelectrical forward modeling was proposed. The models were built efficiently and applicable to any calculation program, while the finite-infinite element method could derive solutions with high accuracy in a comparatively small descretization domain and without any artificial boundary condition, thereby helping to reduce the number of nodes and speed up inversion process.

ACKNOWLEDGMENT

This project was financially supported by the National Natural Science Fund (No. 40874072).

REFERENCES

1. Qiang, J. K., "The research on 3-D resistivity forward and inversion algorithm on undulate topography," Ph.D. Thesis, Geodetection and Information Technology, China University of Geosciences, Wuhan, 2006.
2. Huang, J. G., B. Y. Ruan, and G. S. Bao, "Fem under quantic-boundary condition for modeling resistivity on 3D geoelectric section," *Journal of Guilin Institute of Technology*, Vol. 22, No. 1, 11–14, 2002.
3. Zhao, S. K. and M. J. Yedlin, "Some refinements on the finite-difference method for 3D DC resistivity modeling," *Geophysics*, Vol. 61, No. 5, 1301–1307, 1996.
4. GiD manual. http://gid.cimne.upc.es/.
5. Si, H., Tetgen manual. http://tetgen.berlios.de/fformats.poly.html.
6. Ren, Z. Y., "Direct current resistivity modeling by adaptive finite element method with unstructured mesh," Master's Thesis, Applied Geophysics, Central South University, Changsha, 2007.
7. Xu, S. Z., *Finite Element Method for Geophysics*, Science Press, Peking, 1994.

8. Blome, M., H. R. Maurer, and K. Schmidt, "Advances in three-dimensional geoelectric forward solver techniques," *Geophys. J. Int.*, Vol. 176, 740–752, 2009.
9. Shi, G. C., "Research on post-failure mechanical properties of brittle — plastic rocks by OOFEM coupled with IEM," Ph.D. Thesis, Wuhan Institute of Rock and Soil Mechanics, The Chinese Academy of Sciences, Wuhan, 2005.
10. Astley, R. J. and J. P. Coyette, "Conditioning of infinite element schemes for wave problems," *Communications in Numerical Methods in Engineering*, Vol. 17, 31–41, 2001.

MPI-based Parallel FDTD for EM Scattering from Coated Complex Targets

Xiao-Fei Qi, **Li-Xin Guo**, **and Hao Tsang**
School of Science, Xidian University, Xi'an 710071, China

Abstract— This paper discusses the Parallel Finite Difference Time Domain Method (FDTD) using Message Passing Interface (MPI) protocol for the electromagnetic (EM) scattering by coated complex targets. The parallel programs have run on the Cluster of Workstation (COW) parallel computing system including several PC nodes, by which the correctness of the algorithm is verified, the accelerating ratio and computational efficiency of the parallel programs are also researched.

1. INTRODUCTION

The study of EM scattering by radar scattering section [1] has been playing an important role in areas such as radar detection, target identification, and remote sensing. Many high-frequency algorithm [2, 3] and numerical algorithm [4, 5] have been proposed to solve this problem. Among these methods the FDTD algorithm attracts more and more attention since its first used by A. K. Fung [6]. FDTD has the unique advantages in dealing with the surface scattering of coated complex targets: It could be either dielectric or conductor, and it is convenient to obtain the composite scattering of rough surface with targets placed anywhere [7].

However, it needs more storage capacity and more computing time to solve the problems of scattering from rough surface with electrically large size, which restricts the realization of FDTD resulting from PC's capacity and computing power. Until recently, the computing power of a stand-alone PC still cannot meet the agreement with the electrically large size problems, although it has been rising that the local PC performance in the rapid development of computing speed and storage capacity. The parallel FDTD method [8] is an effective way to solve such problems. The FDTD algorithm has the natural ability for parallel computing, because of its special feature of involving only the neighbor interactions when the electric (magnetic) filed components are updated at each time step.

2. MPI-BASED PARALLEL FDTD COMPUTATION

2.1. The Following is the Formula for Parallel Computing to the Process

Here shows the process, the whole FDTD region is divided into several subregions, and each subregion is attributed to one processor. There are several options for the region to be divided as 2D problem, and it can be divided into 1D and 2D structures, shown in Fig. 1.

It is convenient to establish the Cartesian topology with the procedure "**MPI_CART_CREAT**" in MPI library. As is shown in Fig. 2, the 2D FDTD domain is divided into 6 subregions, and each represents a processor which could be located by its serial number or Cartesian coordinates.

2.2. Data Exchange of Parallel FDTD

The FDTD method is based on a time-stepping algorithm in which the electric and magnetic field values in a cell are computed from the field values in neighboring cell at earlier times. In the serial program the electric and magnetic field values for updating are always available. As

Figure 1: Domain decomposition of parallel FDTD. (a) 1D structure, (b) 2D structure.

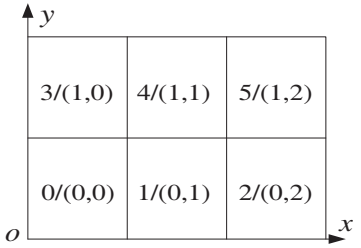

Figure 2: 2D Cartesian 2×3 topological diagram.

for the parallel platform, however, these field values need to be acquired by communication with neighboring processors after each time step. Take as an example the regional division of parallel FDTD calculation along x-axis, similar to the other directions.

The use of overlapping area, containing one cell, is to achieve information exchange between 2 subregions, as is shown in Fig. 4. With this method, only the magnetic field components on the interface need to be exchanged, and the tangential electric field on subregion interface and material information are included in the current subregion.

2.3. Synchronization Technology

In parallel FDTD any processor can only continue its computation when all data transmission has been finished to achieve synchronization. While the out-of-synchronization may result from communication and waiting for the delay between processors, the process of different speed, the data transmission order, as well as many other factors, which will causes the processors to wait for inefficiency, even may arise a step-by-step data exchange at different time steps. In order to ensure the synchronization for all the processors the procedure "**MPI_BARRIER**" in MPI library is invoked to set blocks in the point needing to wait for other process, mandatory for all processes to achieve the synchronization point before moving ahead, so all this process should be able to exchange data at the same time step for the accuracy of the calculation.

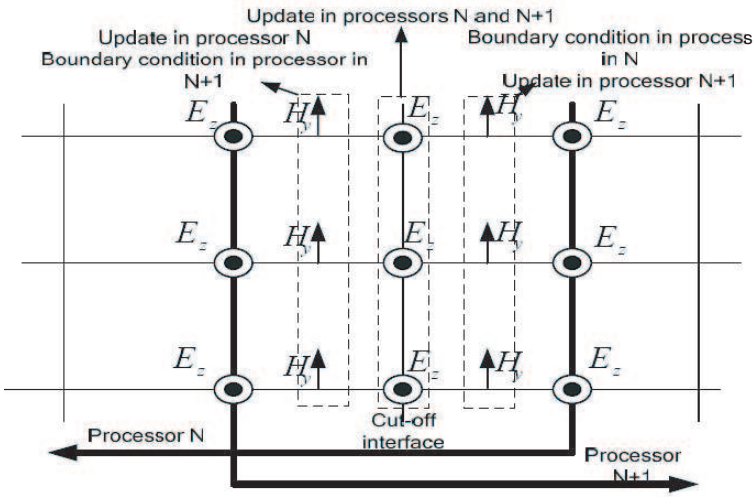

Figure 3: Exchange of magnetic field with overlapping area.

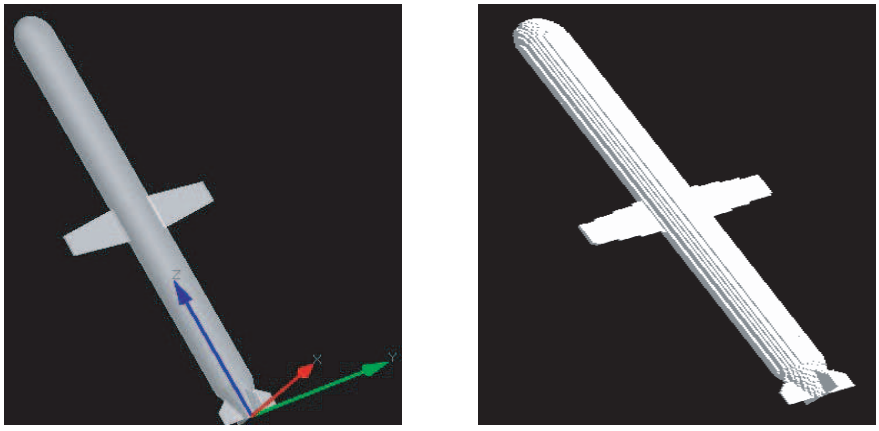

(a) (b)

Figure 4: Tomahawk missile. (a) Tomahawk missiles before subdivision, (b) tomahawk missiles before subdivision.

3. NUMERICAL RESULTS

3.1.

The following pictures show two Tomahawk missiles, both before and after subdivision by and HFSS XFDTD and coated layer of the dielectric constant of 3.6.

3.2.

The following pictures are based on FDTD parallel algorithm for computing the radar scattering section. The left picture without coated and right picture wih coated, the direction of the incident electromagnetic wave Ying-warhead plane wave incident, Tomahawk missile, the length of 6.0 meters, 0.52 meters diameter, has a wingspan 3.65 meters. $\sigma = \Delta x = \Delta y = \Delta z = 15\,\text{mm}$ in FDTD unit and timestep is $\sigma/(2c)$, both of the pictures, $-180^\circ \leq \theta \leq 180^\circ$ and $0 \leq \Phi \leq 360^\circ$ in the polar coordinate system.

The result, in Fig. 5, shows that RCS with coated missile has a good sidelobe compared with missile in PEC, it is also consistent with the theory at 1 GHz, the reason is that when the frequency is fixed, when the electromagnetic waves of objects encountered in metallic reflection coefficient when it is almost one, but when the waves encounter an object class, dielectric or metal objects coated with dielectric material class, according to electromagnetic wave theory, the knowledge of this electromagnetic wave will be when the dielectric in the rapid decay, known as ingratiate oneself depth. Therefore, in this case, the radar scattering section is very small.

The result, in Fig. 6, shows that RCS, both the different coatings at 1 GHz,is contrasted. As picture indicates that when ε becomes big, RCS have a good result. By the electromagnetic wave theory we can see, at the same frequency, $\sigma = \sqrt{\frac{2}{\omega\mu\varepsilon}}$, $\varepsilon = \varepsilon_0\varepsilon_r$, the depth of the formula by ingratiate oneself available. When accompanied by the relative dielectric constant is increasing, and ingratiate oneself depth getting smaller and smaller, it is because the relative dielectric constant in the growing case of dielectric materials electromagnetic wave absorption rates were high. The results as shown in the figure is also very easy to see.

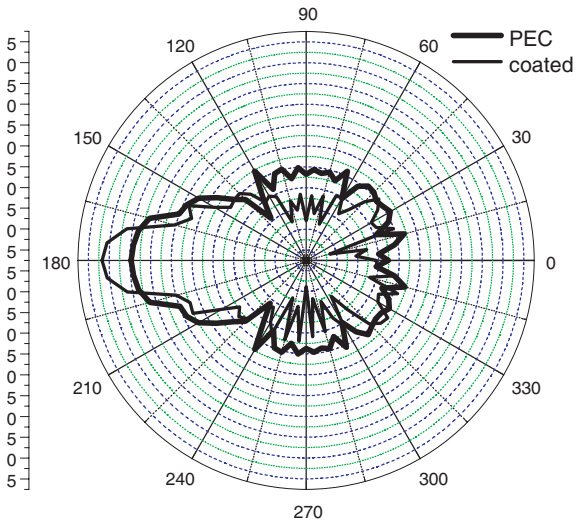

Figure 5: Tomahawk missile radar scattering section.

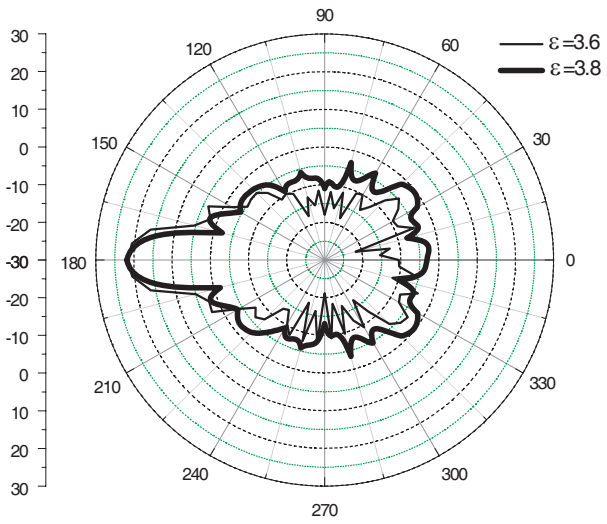

Figure 6: Tomahawk missile radar scattering section.

4. CONCLUSION

In this paper, the EM scattering from coated target located below the one-layered dielectric is investigated through the FDTD, as can be seen from the figure, the radar cross-section diagram of the theoretical value and the actual missiles, radar cross-section diagram from a very good match. After the software and the corresponding comparison, FDTD grid parallel to the missile scattering cross-section calculation results can be acceptable, on the bistatic scattering are exhibited. The properties of EM scattering of this composite models under the horizontal incidence will be studied in the next step.

ACKNOWLEDGMENT

By the Aviation Science Foundation of China (Grant No. 20080181001). This work was supported by the National Natural Science Foundation of China (Grant No. 60971067).

REFERENCES

1. Tsang, L., et al., *Scattering of Electromagnetic Waves: Numerical Simulations*, John Wiley & Sons, 2001.
2. Thorsos, E. and D. R. Jackson, "The validity of the perturbation approximation for rough surface scattering using a Gaussian roughness spectrum," *J. Acoust. Soc. Am.*, Vol. 86, No. 1, 261–277, 1989.
3. Guo, L. and Z. Wu, "Application of the extended boundary condition method to electromagnetic scattering from rough dielectric fractal sea surface," *Journal of Electromagnetic Waves and Applications*, Vol. 18, No. 9, 1219–1234, 2004.
4. Wang, R. and L. Guo, "Numerical simulations wave scattering from two-layered rough interface," *Progress In Electromagnetics Research B*, Vol. 10, 163–175, 2008.
5. BInan, K. and V. B. Ertrk, "Application of iterative techniques for electromagnetic scattering from dielectric random and reentrant rough surfaces," *IEEE Trans. Geosci. Remote Sensing*, Vol. 44, No. 11, 3320–3329, 2006.
6. Fung, A. K., M. R. Shah, and S. Tjuatja, "Numerical simulation of scattering from three-dimensional randomly rough surfaces," *IEEE Trans. Geosci. Remote Sensing*, Vol. 32, No. 5, 986–994, 1994.
7. Kuang, L. and Y. Q. Jin, "Bistatic scattering from a three-dimensional object over a randomly rough surface using the FDTD algorithm," *IEEE Trans. Antennas Propag.*, Vol. 55, No. 8, 2302–2312, 2007.

Galerkin's Method Using the Annular Patch Segments to Solve a Round Disk Capacitor

Kyung-Soo Kim and Che-Young Kim
School of Electrical Engineering and Computer Science, Kyungpook National University
Sankyuk-dong Puk-gu, Daegu 702-701, South Korea

Abstract— In this paper, a numerical method is presented to calculate the charge density distribution and capacitance of a round disk capacitor by using the annular patch segments to gain more benefits over the conventional triangular patches. The proposed annular patches successfully eliminate the discretizing errors often encountered in the triangular patches, thereby it leads us to get more accurate solutions. Furthermore, the Galerkin's method is utilized to accelerate the solution convergence and also to obtain more accuracy at the matrix formulation stage. By specializing the method of moments to an integral equation, the charge distribution and capacitance can be obtained. To examine the accuracy of the proposed method, numerically computed charge density and capacitance are compared to the corresponding exact solutions for a single circular disk. Based on these error comparisons, the Galerkin's method equipped with annular patches ensures the superiority to the triangular patches and to the point matching method. The proposed Galerkin's method is applied to the round disk capacitor to calculate the equipotential lines.

1. INTRODUCTION

To find a solution of the three dimensional capacitor has been a problem of interest in academic or practical aspect. Special interest goes to the round disk capacitor because it is often encountered in the microstrip structure. In particular, since the analytic solution is known for the single circular disk, the exact solution can play the role of umpire on the numerically obtained results to estimate the numerical errors involved.

One way of solving the round disk capacitor is using the integral equation, which will be transformed into the algebraic linear equations by using Galerkin's method in the method of moments technique [1]. Traditionally, the surfaces of a round disk capacitor are generally divided into triangular or rectangular patches [2, 3]. However, this type of patch shapes yields somewhat big numerical errors due to the geometrically unmatched shape to the actual geometry, called discretizing error. To mitigate this error, we introduced the annular patch shapes providing the perfect shape match for the round disk capacitor. Once the same technique has been applied to the round disk capacitor [5], but the different point between the previous approach and present is the use of Galerkin's method at present rather than the point matching as before.

2. FORMATION OF THE INTEGRAL EQUATION

Figure 1(a) shows a round disk capacitor with a homogeneous dielectric constant ε_r, radius a, and height h. One may replace the PEC and the dielectric by the equivalent surface charges lying in a free space based on the equivalent principle. Those equivalent charges lying on each boundary interfaces are represented in Figure 1(b).

Then, the potential and the electric flux density of a round disk capacitor can be described by;

$$V(\underline{r}) = \frac{1}{4\pi\varepsilon_0} \iint_S \frac{\sigma_T(\underline{r}')}{|\underline{r} - \underline{r}'|}\, dS' \tag{1}$$

$$\underline{D}(\underline{r}) = -\varepsilon \nabla V(\underline{r}) \tag{2}$$

In (1) and (2), S is the surface of a round disk capacitor, $\sigma_T(\underline{r}')$ is total charge density mixed up with the equivalent free charge density and bound charge densities. Note that two Equations (1) and (2) are the free space Green's function because the dielectric is equivalently substituted into the free space charges. In order to calculate the total charge density numerically, the surfaces of a round disk capacitor are divided into the concentric annular patches. Now, the total charge density is expanded by the expansion functions $f_{n1}(\underline{r})$ and $f_{n2}(\underline{r})$ as usually done in the method of moments.

$$\sigma_T \cong \sum_{n=1}^{M} [\sigma_{Tn} f_{n1}(\underline{r}) + \sigma_{Tn} f_{n2}(\underline{r})] \tag{3}$$

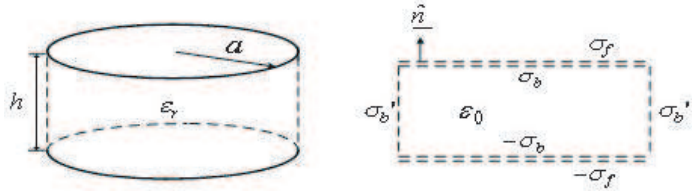

(a) (b)

Figure 1: The structure of a round disk capacitor. (a) Original geometry. (b) Equivalent model.

According to the Galerkin's method, substituting the above expansion function (3) into (1) and (2) shows

$$V_i = \sum_{m=1}^{N_c}\sum_{n=1}^{M}\frac{1}{4\pi\varepsilon_0}\sigma_{Tn}\left[\iint_{\Delta S_{n1}}\frac{dS}{|\underline{r}_{m1}-\underline{r}_{n1}|}+\iint_{\Delta S_{n2}}\frac{dS}{|\underline{r}_{m1}-\underline{r}_{n2}|}+\iint_{\Delta S_{n1}}\frac{dS}{|\underline{r}_{m2}-\underline{r}_{n1}|}+\iint_{\Delta S_{n2}}\frac{dS}{|\underline{r}_{m2}-\underline{r}_{n2}|}\right] \tag{4}$$

$$\Delta D_n = \sum_{m=N_c+1}^{M}\sum_{n=1}^{M}\frac{\varepsilon^+-\varepsilon^-}{4\pi\varepsilon_0}\sigma_{Tn}\left[\iint_{\Delta S_{n1}}\frac{(\underline{r}_{m1}-\underline{r}_{n1})\cdot\hat{\underline{n}}_{m1}}{|\underline{r}_{m1}-\underline{r}_{n1}|^3}dS+\iint_{\Delta S_{n2}}\frac{(\underline{r}_{m1}-\underline{r}_{n2})\cdot\hat{\underline{n}}_{m1}}{|\underline{r}_{m1}-\underline{r}_{n2}|^3}dS+\iint_{\Delta S_{n1}}\frac{(\underline{r}_{m2}-\underline{r}_{n1})\cdot\hat{\underline{n}}_{m2}}{|\underline{r}_{m2}-\underline{r}_{n1}|^3}dS+\iint_{\Delta S_{n2}}\frac{(\underline{r}_{m2}-\underline{r}_{n2})\cdot\hat{\underline{n}}_{m2}}{|\underline{r}_{m2}-\underline{r}_{n2}|^3}dS\right]+\sum_{m=N_c+1}^{M}\frac{\varepsilon^++\varepsilon^-}{2\varepsilon_0}\sigma_{Tm} \tag{5}$$

where $i = 1, 2$, and $M = N_c + N_d$. In here, N_c and N_d are the number of segment on the conductors and on the dielectric boundary. ΔD_n represents the difference between normal electric flux density at the inside and outside of dielectric. ε^- and ε^+ denotes the dielectric constant of inside and outside, and $\hat{\underline{n}}$ is the normal unit vector pointing from inside to outside in dielectric. Testing (4) and (5) with each testing function $f_{n1}(\underline{r})$ and $f_{n2}(\underline{r})$ onto the patch surfaces and casting the resultant equation into matrix form yields;

$$\begin{bmatrix}\Phi_m(f_n)\\ \vdots\\ \Delta D_m(f_n)\end{bmatrix}[\sigma_{Tn}]=\begin{bmatrix}V_i\\ \vdots\\ 0\end{bmatrix} \tag{6}$$

By the matrix inversion on (6), the total charge density σ_{Tn} can be determined, and many informative parameters on the round capacitor may be deduced from the determined σ_{Tn} without extra numerical burden.

3. CALCULATION OF MATRIX ELEMENTS

By using the annular patches shown in Figure 2 together with a pertinent distance vector, the matrix elements in (6) can be calculated. Based on the shown coordinates, the self term and the mutual term of the voltage matrix elements are found to be

$$\Phi_{mi}(f_{nj}) = \frac{\rho_{nj}\Delta W_n}{4\pi\varepsilon_0 A_{minj}}K(k_{minj}) \tag{7a}$$

$$A^2_{minj} = (\rho_{mi}+\rho_{nj})^2+(h_m-h_n)^2, \quad k^2_{mi}nj=\frac{4\rho_{mi}\rho_{nj}}{A^2_{minj}}<1 \tag{7b}$$

$$K(x) = \int_0^{\frac{\pi}{2}}\frac{d\phi}{\sqrt{1-x^2\sin^2\phi}} \tag{7c}$$

$$\Phi_{mi}(f_{nj}) = \frac{\Delta W_n}{2\pi\varepsilon_0}\ln\left(1+\sqrt{2}\right)+\frac{\Delta W_n}{4\pi\varepsilon_0}\ln\left(\cot\frac{\theta_{n1}}{8}\cdot\cot\frac{\theta_{n2}}{8}\right)+\frac{\Delta W_n}{4\pi\varepsilon_0}\left[\frac{\rho_{n2}}{A_{m1n2}}K(k_{m1n2})+\frac{\rho_{n1}}{A_{m2n1}}K(k_{m2n1})\right] \tag{8}$$

where $i = 1, 2$, $j = 1, 2$, ΔW_n represents the width of annular patch on ΔS_n, θ_{n1} is $\Delta W_n/\rho_{n1}$, and θ_{n2} is $\Delta W_n/\rho_{n2}$. Equations (7) and (8) are the mutual term and the self term for the voltage matrix element, respectively.

Next, $\Delta D_m(f_n)$ should be calculated both on the plates and on dielectric interfaces. The former is denoted by $\Delta D_m(f_n)_z$ and the latter by $\Delta D_m(f_n)_x$. They are given by

$$\Delta D_{mi}(f_{nj})_z = \frac{(1-\varepsilon_r)(h_m - h_n)\Delta W_n}{4\pi}\left[\frac{\rho_{nj}E(k_{minj})}{A^3_{minj}\left(1-k^2_{minj}\right)}\right] \tag{9a}$$

$$E(x) = \int_0^{\frac{\pi}{2}} \sqrt{1-x^2\sin^2\phi}\,d\phi \tag{9b}$$

$$\Delta D_{ni}(f_{nj})_z = \frac{1+\varepsilon_r}{2} \tag{10}$$

$$\Delta D_{mi}(f_{nj})_x = \frac{(1-\varepsilon_r)\rho^2_{nj}\Delta W_n}{4\pi A^3_{minj}}\left[\left(1+\frac{\rho_{mi}}{\rho_{nj}}-\frac{2}{k^2_{minj}}\right)\frac{E(k_{minj})}{1-k^2_{minj}}+\frac{2}{k^2_{minj}}K(k_{minj})\right] \tag{11}$$

$$\begin{aligned}\Delta D_{mi}(f_{nj})_x = {} & \frac{(1-\varepsilon_r)\Delta W_n}{8\pi}\left[\rho_{n1}\ln\left(\cot\frac{\theta_{n1}}{8}\right)+\rho_{n2}\ln\left(\cot\frac{\theta_{n2}}{8}\right)\right] \\ & +\frac{1+\varepsilon_r}{2}+\frac{(1-\varepsilon_r)\rho^2_{n2}\Delta W_n}{4\pi A^3_{m1n2}}\left[\left(1+\frac{\rho_{m1}}{\rho_{n2}}-\frac{2}{k^2_{m1n2}}\right)\frac{E(k_{m1n2})}{1-k^2_{m1n2}}+\frac{2}{k^2_{mn21}}K(k_{m1n2})\right] \\ & +\frac{(1-\varepsilon_r)\rho^2_{n1}\Delta W_n}{4\pi A^3_{m2n1}}\left[\left(1+\frac{\rho_{m2}}{\rho_{n1}}-\frac{2}{k^2_{m2n1}}\right)\frac{E(k_{m2n1})}{1-k^2_{m2n1}}+\frac{2}{k^2_{m2n1}}K(k_{m2n1})\right]\end{aligned} \tag{12}$$

Equations (9) and (10) are the mutual and self term for $\Delta D_m(f_n)_z$, and Equations (11) and (12) are the mutual and self term for $\Delta D_m(f_n)_x$, respectively. Thus all matrix elements needed in (6) have been obtained.

4. NUMERICAL RESULTS

In order to confirm the validity of this method, the charge density of a single circular disk was calculated. The exact charge density of a single circular disk is written by

$$\sigma(\rho) = \frac{4V_0\varepsilon_0}{\pi\sqrt{a^2-\rho^2}} \tag{13}$$

where V_0 is a constant potential applied to the disk, a is a radius of the disk, and ρ is the distance from the center of the disk. Exact capacitance is $8\varepsilon_0 a$ [4]. A numerical solution and an exact solution of the disk are shown in Figure 3 when $a = 1$ and $V_0 = 1\,[V]$. This graph ensures that two results are well matched together.

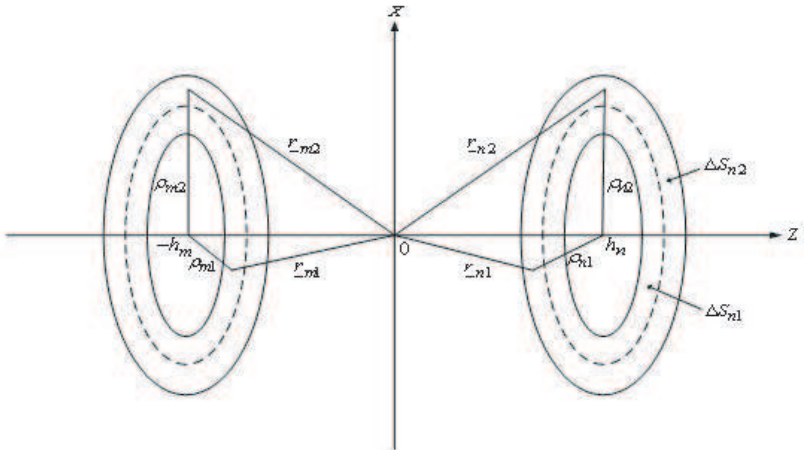

Figure 2: Coordinated to calculate the matrix elements.

The compared results between the proposed and the other methods are tabulated in Table 1. As presented in this table, Galerkin's result is the most accurate than the other two methods.

Once the surface charges are known for each boundary layers, then the equipotential lines can be found around the capacitor by substituting these charges into Equation (1). The determined lines are illustrated in Figure 4 for $\varepsilon_r = 1.0$ and $\varepsilon_r = 3.0$, respectively. A small shaded area marked with slant lines are magnified on the first quadrant plane. It is noted that lines for $\varepsilon_r = 3.0$ are bent at the corner due to the fringing field effects.

Table 1: Comparison of normalized capacitance for a single circular disk.

Annular patch					Triangular patch [6]		
Galerkin's method			Point matching method [5]				
M	C/a	% error	C/a	% error	M	C/a	% error
10	69.91	1.31	69.57	1.76	18	59.80	15.57
15	70.22	0.86	70.01	1.16	30	61.10	13.74
20	70.38	0.63	70.22	0.86	42	61.80	12.75
25	70.47	0.51	70.35	0.68	54	62.24	12.13
30	70.53	0.42	70.43	0.56	60	66.03	6.78
40	70.61	0.31	70.55	0.41	84	66.72	5.80
Exact	70.83 [pF/m]						

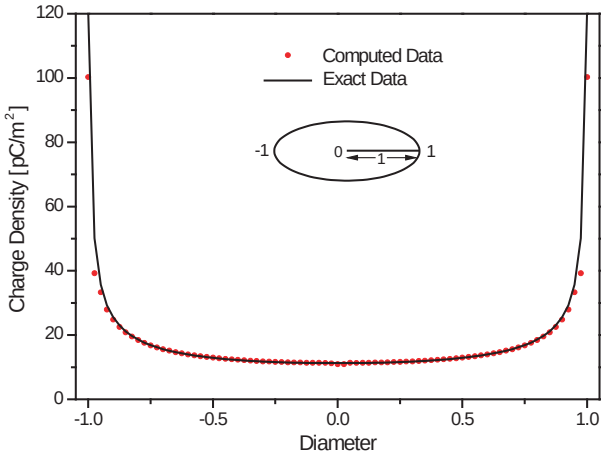

Figure 3: The charge density distributions of a single circular disk.

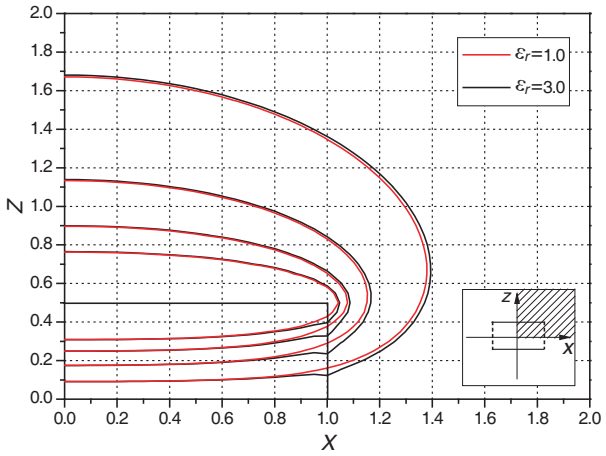

Figure 4: Equipotential lines around the round disk capacitor.

5. CONCLUSION

The numerical method for a round disk capacitor was presented by using the annular patch segments. The charge density distribution and the capacitance of a single circular disk were calculated and compared to the exact solution and to the other methods. Based on these results, the charge density and capacitance calculated by the proposed Galerkin's method are more accurate than those of the other ones, especially, Galerkin's solution shows fast convergence for the single disk.

REFERENCES

1. Bancroft, R., *Understanding Electromagnetic Scattering Using the Moment Method*, 20–31, A Practical Approach, Artech House, Inc., 1996.
2. Harrington, R. F., *Field Computation by Moment Methods*, 24–28, N. Y. Macmillan Co., 1968.
3. Reitan, D. R., "Accurate determination of the capacitance of rectangular parallel-plate capacitor," *Journ. Appl. Phys.*, Vol. 30, No. 2, 172–176, Feb. 1959.
4. Smythe, W. R., *Static and Dynamic Electricity*, 144, McGraw-Hill, New York, 1950.
5. Kim, C. Y., "A numerical solution for the round disk capacitor by using annular patch subdomains," *Progress In Electromagnetics Research B*, Vol. 8, 179–194, Jun. 2008.
6. Rao, S. M., A. W. Glisson, D. R. Wilton, and B. S. Vidula, "A simple numerical solution procedure for static problems involving arbitrary-shaped surfaces," *IEEE Trans. Antennas Propagat.*, Vol. 27, No. 5, 604–608, Sep. 1979.

Determination of Eigenvalues of Closed Lossless Waveguides Using the Least Squares Optimization Technique

O. Demiryurek[1] and N. Yener[2]

[1]Gungoren Endustri Meslek Lisesi, Tozkoparan Mah., Esitler Sok. No. 3, Gungoren, Istanbul, Turkey
[2]Technical Education Faculty, Kocaeli University, Umuttepe Campus, Izmit 41380, Kocaeli, Turkey

Abstract— It is known that in lossless and closed guides filled with gyroelectric or gyromagnetic media, Maxwell's equations are transformed into an infinite linear algebraic equation system by application of the Galerkin version of Moment method. Propagation constant of the problem whose exact solution is not known is found as the square root of the eigenvalue of the coefficient matrix of this infinite linear algebraic equation system. However the quantities determined from the Moment method do not have much physical meaning by themselves. This is why it is desired to express the propagation constant as a function of frequency. Therefore with the help of algebraic function theory we attempt to express eigenvalues of the coefficient matrix, i.e., the squares of the propagation constants, as a series expansion. By this technique Laurent and Puiseux series expansions in the neighborhood of singular points are obtained for these functions. The series expansions which are obtained by the algebraic function approximation in the eigenvalue problems of closed, lossless, uniform waveguides, bring about a function theoretic insight in order to investigate the properties of the propagation constant functions. In previous work reported in the literature there exists a derivation of these expansions accomplished by using differentiation of the characteristic equation of above coefficient matrix, considering it as an implicit function of the propagation constant function and the frequency. In this work computation of the necessary expansion coefficients of the Laurent and Puiseux series, is achieved by the least squares technique (LST) which is a curve fitting method. In this way we attempt to find a simple solution to the problem of computation of these coefficients, which dates back to Sir Isaac Newton and in general which is rather tedious.

1. INTRODUCTION

Maxwell's partial differential equations and boundary conditions for closed waveguides loaded with heterogeneous and/or anisotropic medium, are transformed into a coupled system of an infinite number of ordinary differential equations (ODE) called transmission line equations [1]. In uniform waveguides these equations are transformed into a linear algebraic equation system because then z dependence has the form $e^{-\gamma z}$, where γ is the propagation constant. When the filling medium is gyrotropic this equation system takes the particular form:

$$\gamma(p)\begin{bmatrix} v(p) \\ i(p) \end{bmatrix} = \begin{bmatrix} 0 & Z(p) \\ Y(p) & 0 \end{bmatrix}\begin{bmatrix} v(p) \\ i(p) \end{bmatrix} \tag{1}$$

In (1), $Z(p)$ and $Y(p)$ square matrices with infinite dimensions are truncated to be $n \times n$ as an approximation [2–4]. Linear algebraic equation system in (1) is in particular an eigenvalue problem. When $Z(p)$ and $Y(p)$ are truncated, call the eigenvalue of the matrix product $Z(p)Y(p)$ or $Y(p)Z(p)$, which two matrices share the same eigenvalues, as $\gamma_1^2(p)$. $v(p)$ and $i(p)$ are then eigenvectors of these matrix products $Z(p)Y(p)$ and $Y(p)Z(p)$, respectively. When the polynomial consisting of the characteristic equation of these matrices is set equal to zero and is multiplied by the common denominator of its terms, the characteristic equation of $Z(p)Y(p)$ (or $Y(p)Z(p)$) becomes as in (2).

$$G\left(\gamma_1^2, p\right) = a_0(p)\gamma_1^{2n}(p) + a_1(p)\gamma_1^{2(n-1)}(p) + \ldots + a_{n-1}(p)\gamma_1^2(p) + a_n(p) = 0 \tag{2}$$

In fact, the method implemented to obtain (1) is the Galerkin version of Moment method. This is because expansion functions have been taken equal to test functions in the Moment method. However the quantities determined from the Moment method do not have much physical meaning by themselves. Because they are merely data points for propagation constants versus frequency. That is why we expand the function (the roots) into Puiseux and Laurent series. Puiseux series is a power series with fractional powers. The information obtained from these series gives us a physical insight and this is why it is desired to expand the roots of the algebraic equation into series [2].

The aim of this work is to compute by the method of optimization the expansion coefficients in Laurent and Puiseux series of squares of propagation constants obtained by the Moment method through use of elementary algebraic function theory. These coefficients were determined using approximate expressions based on differentiations of (2) considering it as an implicit function in [2]. In [2] only two expansion coefficients were found by the described technique. If additional coefficients are required, operational load will increase sharply. The difficulty in determining the coefficients by Newton's solution with polygons exists for our problem. Because the explicit analytic coefficients of the characteristic equation are impossible to obtain at least in our case, determining the coefficients by Newton polygons is impossible.

The impossibility of analytic determination of these coefficients explicitly necessarily leads us to resort to use of optimization methods as an alternative. To compute the expansion coefficients we shall use the least squares method which is an optimization method. Although Newton's solution with polygons is suitable for programming, the least squares technique is introduced in this paper for our problem as a simple alternative due to above reasons.

2. MODELING OF DISPERSION EQUATION USING THE LST

In (2), $G(\gamma_1^2, p) = 0$ equality has n different roots for each p. An exception occurs only when a) $a_0(p_0) = 0$, b) $G(\gamma_1^2, p)$ has multiple roots. The exception under a) and b) are only for a finite number of special values of p which are the critical points. These critical points constitute only algebraic singularities for $\gamma_1^2(p)$ (please see [3]). Thus let solution of approximate propagation constant of our problem in the neighborhood of a singularity $p_0 = j\omega_0$ be $\gamma_1^2(p)$ in (3).

$$\gamma_1^2\left(p_i\right) = \sum_{n=n_2}^{\infty} C_n \rho_i^n \tag{3}$$

Here, if $n_2 < 0$ and $\rho_i = (p_i - p_0)$, Equation (3) is a Laurent series, if $n_2 = 0$ and $\rho_i = (p_i - p_0)^{1/q}$, Equation (3) is a Puiseux series. It has been established that pole branch points are ruled out for structures represented by (1) [3]. Then for both Laurent and Puiseux series expansions the below method explained will be valid. However when we apply the method, we use only finite truncations of (3) as in (4).

$$\gamma'^2_1\left(p_i\right) = \sum_{n=n_2}^{N} \tilde{C}_n \rho_i^n \tag{4}$$

Here $\tilde{C}_n$ are the approximate coefficients to take places of C_n in (3) and our problem is to determine the $\tilde{C}_n$ optimally to best approximate (3) by (4). At point p_i when the error between approximate function $\gamma_1^{'2}$ and exact dispersion equation solution $\gamma^2(p_i)$ is shown by s_i, it can be defined as follows.

$$s_i = \gamma^2\left(p_i\right) - \gamma'^2_1\left(p_i\right) = \gamma^2\left(p_i\right) - \sum_{n=n_2}^{N} \tilde{C}_n \rho_i^n \tag{5}$$

The square of propagation constant is a function of a complex variable. If the error is required to be a real and positive value, the error for M frequency points can be defined as S in (6).

$$S = \sum_{i=1}^{M} \left|\gamma^2\left(p_i\right) - \gamma'^2_1\left(p_i\right)\right|^2 = \sum_{i=1}^{M} \left[\gamma^2\left(p_i\right) - \gamma'^2_1\left(p_i\right)\right] \times \left[\gamma^2\left(p_i\right) - \gamma'^2_1\left(p_i\right)\right]^* \tag{6}$$

According to the LST, derivative of the error function with respect to expansion coefficients of approximate function of (4) must be zero, in order for the full error to be minimum.

Approximate function $\gamma'^2_1(p)$ is a complex function, so the expansion coefficient $\tilde{C}_n$ is a function of real variables $\overline{C}_n$ and $\overline{\overline{C}}_n$ where $\tilde{C}_n = \overline{C}_n + j\overline{\overline{C}}_n$. When coefficients of (4) are defined as $\tilde{C}_n = \overline{C}_n + j\overline{\overline{C}}_n$ and substituted for $\gamma_1^{'2}$ in (6) rearranged, Equation (7) is obtained.

$$S = \sum_{i=1}^{M} \left[\gamma^2\left(p_i\right) - \sum_{n=n_2}^{N} \left\{\overline{C}_n + j\overline{\overline{C}}_n\right\} \rho_i^n\right] \times \left[\gamma^2\left(p_i\right) - \sum_{n=n_2}^{N} \left\{\overline{C}_n + j\overline{\overline{C}}_n\right\} \rho_i^n\right]^* = 0 \tag{7}$$

In order to devise a minimization algorithm for determination of the optimum coefficients based on the LST, it is necessary to evaluate the partial derivatives of S with respect to $\overline{C}_n$ and $\overline{\overline{C}}_n$ [6] and equate them to zero. Then denoting the complex conjugate by $(*)$, we obtain the following equations for mth coefficient where $n_2 < m < N$:

$$\frac{\partial S}{\partial \overline{C}_m} = \sum_{i=1}^{M} \rho_i^m \left[\gamma^2(p_i) - \sum_{n=n_2}^{N} \left\{\overline{C}_n + j\overline{\overline{C}}_n\right\}\rho_i^n\right]^* + \sum_{i=1}^{M} \rho_i^{m*} \left[\gamma^2(p_i) - \sum_{n=n_2}^{N} \left\{\overline{C}_n + j\overline{\overline{C}}_n\right\}\rho_i^n\right] = 0 \quad (8)$$

$$\frac{\partial S}{\partial \overline{\overline{C}}_m} = \sum_{i=1}^{M} j\rho_i^m \left[\gamma^2(p_i) - \sum_{n=n_2}^{N} \left\{\overline{C}_n + j\overline{\overline{C}}_n\right\}\rho_i^n\right]^* + \sum_{i=1}^{M} j\rho_i^{m*} \left[\gamma^2(p_i) - \sum_{n=n_2}^{N} \left\{\overline{C}_n + j\overline{\overline{C}}_n\right\}\rho_i^n\right] = 0 \quad (9)$$

In the following two examples, we have the complex frequency $p_i = j\omega_i$ in all of our formulas.

3. EXAMPLE 1: DIELECTRIC ROD LOADED CYLINDRICAL GUIDE

First we consider a dielectric rod loaded cylindrical guide (inset of Figure 1). Radius of the guide is 0.25" whereas ratio of radii of rod and guide is 0.67. Relative dielectric permittivity of rod is 15. The normalized frequency $j\omega_0$ is a zero of the discriminant of (2) and this singularity is an algebraic branch point where the eigenvalue is finite and multiple. Then in Equation (3), $q = 2$ is the degree of cycle of functions with an algebraic branch point at $j\omega_0$ [2], in other words there are two multiple roots at this point.

We obtain the Puiseux series expansion in the neighborhood of the algebraic branch point for one root of Equation (2) using properties of algebraic Equation (2) [7].

$$\gamma_1'^2(j\omega) = \gamma_1^2(j\omega_0) + A_1\sqrt{j\omega - j\omega_0} + A_2(j\omega - j\omega_0) + \ldots + A_n\left(\sqrt{j\omega - j\omega_0}\right)^n + \ldots \quad (10)$$

The propagation constant versus frequency has been recomputed with the help of the series expansion which is obtained by taking the first four optimum coefficients and is shown together with the exact solution in Figure 1. Optimization is built in the interval $0.94297 < V < 0.97298$ and the coefficients of (10) are computed by the LST in this interval. The approximate propagation constant has been recalculated in the interval $0.5094 < V < 1.19798$ using these optimum first four coefficients. Results obtained by exact dispersion equation and proposed method are illustrated in the normalized frequency range $0.5094 < V < 1.19798$ in Figure 1, where $V = \omega\sqrt{\varepsilon_0\mu_0}r_1$ is the normalized frequency.

As it is seen, between the solution of exact dispersion relation and the LST a very close agreement has been achieved on a very wide frequency band. The coefficients found by help of this optimization method are as in Table 1(a).

The close agreement between the solution of optimization method and [2] for the coefficients A_1 and A_2 confirms the validity of optimization method used (see Table 1(a)). Because of the

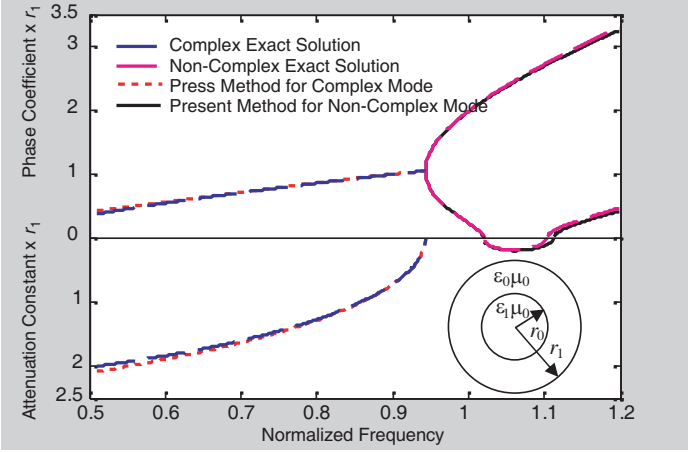

Figure 1: Comparison of exact solution and present method for propagation constant. Inset: Guide cross-section for Example 1.

Table 1: (a) Expansion coefficients of Puiseux series for Example 1 by the LST and method in [2], (b) expansion coefficients of Laurent series for Example 2 by the LST and method in [2].

Coefficients of Puiseux series	Computed by the LST	Computed in [2]
A_1	$5.2687(1-j)$	$5.259648(1-j)$
A_2	$0.4775\times10^{-8}+j14.9630$	$j19.3257$
A_3	$-7.7460-j7.7460$	-
A_4	$6.4291-j0.1141\times10^{-6}$	-

(a)

Coefficients of Laurent series	Computed by the LST	Computed in [2]
C_{-1}	$0.4597\times10^{-7}+j1.7258\times10^{5}$	$j1.7809\times10^{5}$
C_0	$1.4580\times10^{8}-j0.7217\times10^{-2}$	1.7234×10^{8}
C_1	$0.3004\times10^{-2}+j7.8581\times10^{4}$	-
C_2	$-53.9799+j0.1880\times10^{-5}$	-

(b)

flexibility of algorithm used, in the LST the number of coefficients can be increased at will, in order to better approximate the exact dispersion equation. The coefficients can be found very efficiently using the derived algorithm.

4. EXAMPLE 2: FERRITE TUBE LOADED CYLINDRICAL GUIDE

Next, we consider a structure consisting of a ferrite tube filled cylindrical waveguide (inset of Figure 2(a)). The permeability tensor for the ferrite medium magnetized axially is given in (11) [8].

$$\hat{\mu}=\mu_0\begin{bmatrix}\mu_r & -j\kappa & 0\\ j\kappa & \mu_r & 0\\ 0 & 0 & 1\end{bmatrix}\quad\text{where}\quad \mu_r=1-\frac{\omega_0\omega_m}{\omega^2-\omega_0^2}\quad\text{and}\quad \kappa=\frac{\omega\omega_m}{\omega^2-\omega_0^2} \tag{11}$$

The parameter values of the structure are as follows [8]. $r_1=8\,\text{mm}$, $r_0/r_1=5/8$, $\varepsilon_1=12.9\varepsilon_0$, resonance frequency $f_0=\omega_0/(2\pi)=6.998206\,\text{GHz}$, $f_m=\omega_m/(2\pi)=0.6683\,\text{GHz}$. For this structure $a_0(j\omega_0)$ in (2), vanishes at resonance frequency ω_0 and at least one root of (2) attains

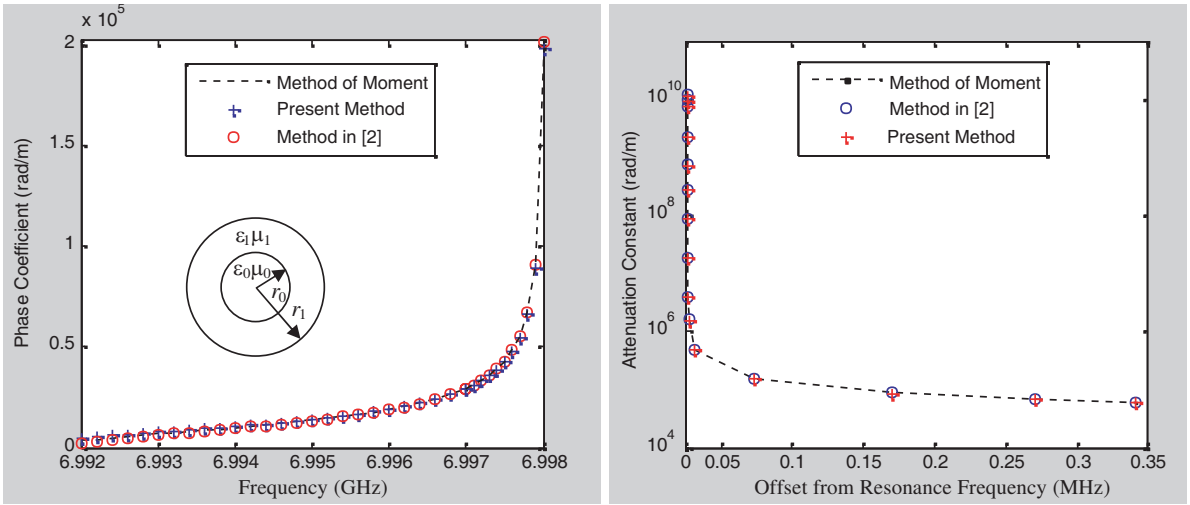

(a) (b)

Figure 2: (a) Phase coefficient computed by Moment method, by the LST method and the method in [2] Inset: Guide cross-section for Example 2, (b) attenuation constant of the evanescent mode obtained by Moment, the LST method and the method in [2].

an infinite value at this point. This means that ω_0 is a singularity point. Actually $Z(p)$ and $Y(p)$ matrices constructed for Moment method have a pole at $j\omega_0$. On the other hand a pole branch point is not possible in the structures of this type [2]. Therefore Laurent expansion is obtained as (12) in the neighborhood of pole point $j\omega_0$ at which $a_0(j\omega_0) = 0$.

$$\gamma_1^2(p) = \frac{C_{-m}}{(p - j\omega_0)^m} + \ldots + \frac{C_{-1}}{(p - j\omega_0)} + C_0 + C_1(p - j\omega_0) + \ldots \tag{12}$$

Number of negative power terms or the order of pole in (12) has been found as $m = 1$ [9]. For the proposed method result closest to the exact dispersion relation has been found when the first four coefficients of Laurent series expansions are taken into consideration. These coefficients are given in Table 1(b). The results obtained for the phase coefficient by the help of Moment method, proposed method and method in [2] are indicated in Figure 2 for the first mode of right hand circularly polarized wave. The close agreement between the solution of the LST and [2] (see Table 1(b)) for the first two coefficients confirms the validity of used method. The values found for the coefficients are also used to compute the propagation constant above the ferrite resonance frequency as illustrated in Figure 2(b).

REFERENCES

1. Schelkunoff, S. A., "Generalized telegraphist's equations for waveguide," *BSTJ*, Vol. 31, 784–801, 1952.
2. Yener, N., "Algebraic function approximation in eigenvalue problems of lossless metallic waveguides: Examples," *Journal of Electromagnetic Waves and Applications*, Vol. 20, No. 6, 731–745, 2006.
3. Yener, N., "Algebraic function approximation to eigenvalue problems of lossless metallic waveguides (revisited)," *Progress In Electromagnetics Research*, PIER 55, 147–174, 2005.
4. Noble, D. F., "Circuit properties of dispersive coupled transmission lines and waveguides," Ph.D. Dissertation, School of Electrical Engineering, Cornell University, Ithaca, New York, 1971.
5. Bliss, G. A., *Algebraic Functions*, Dover Publications, 1966.
6. Oraizi, H., "Application of the method of least squares to electromagnetic engineering problems," *IEEE Antennas and Propagation Magazine*, Vol. 48, No. 1, 2006.
7. Knopp, K., *Theory of Functions*, Part II, Dover Publications, New York, 1996.
8. Jerby, E., A. Kesar, A. Ahorony, and G. Breitmeier, "Ferrite-guided cyclotron-resonance maser," *Physical Review E*, Vol. 65, 066502, 2002.
9. Demiryurek, O., "Determining of the eigenvalues of closed waveguide by the transmission line equivalences and optimization methods," MSc. Thesis, Kocaeli University, 2009.

The Study of Numerical Simulation on Dual-frequency IP Method with FEM

Jiayong Lin[1, 2], **Maobin Ding**[1], **Jing-Tian Tang**[1], **and Hong Yan**[1, 3]

[1]School of Info-physics and Geomatics Engineering, Central South University
Changsha 410083, China
[2]Geophysical and Geochemical Exploration Team
Yunnan Geology and Mineral Resources Bureau, Yunnan 652100, China
[3]The Third Institute of Geology and Mineral Exploration of Qinghai Province
Qinghai 810008, China

Abstract— Based on the finite element method and Cole-Cole model, the paper studied the numerical simulation on dual-frequency IP method. First of all, the paper introduced the primary theory of the dual-frequency IP method and gave the boundary value problem and variational equations, then replaced the complex resistivity of the model with the Cole-Cole model's parameters under ignoring the EM effect. Through solving the last linear equations, electric potentials of all the model's points were obtained. With changing model's parameters, we got different curves of the F_s and phases. Finally, according to the results of the simulations, the algorithm was proved to be correct and adaptable.

1. FOREWORD

Dual-channel Induced Polarization method was based on "variation-frequency method" and invented by He Jishan in the early 70s of 20th century. The core technique of it is to combine the two square-wave currents of different frequency as a synthesized source and receiving the response from the ground, which contains the IP response of two frequencies [1]. Compared with the variation-frequency method, it does not need to change the frequency and has advantages of portability, efficiency, high accuracy and strong anti-interference ability; with the odd harmonics method, the amplitudes of the currents in two frequencies are same and the frequencies can be changed artificially, so that it could overcome the disadvantage of lower amplitude with higher harmonic. Due to all the merits mentioned above, the Dual-channel Induced Polarization method was widely used in mineral prospecting [2].

For any method of geophysical prospecting, the interpretations of the data always have multiple solutions. Because physical simulations are very expensive and analytical computing is not suitable for complex geological conditions, numerical simulation became a powerful tool for the majority of geophysicists [3]. As a result, this article attempts to study the characteristics and attributes of frequency-domain IP responses through implementing forward numerical modeling in dual-frequency IP method.

2. THE BASIC PRINCIPLES OF DUAL-FREQUENCY IP METHOD

In dual-frequency IP method, two components of current with the same amplitude but different frequency are synthesized according to a certain phase relationship (Figure 1). Then we set the combined current as the source to inject into the earth and observe the induced electric response on the surface [1].

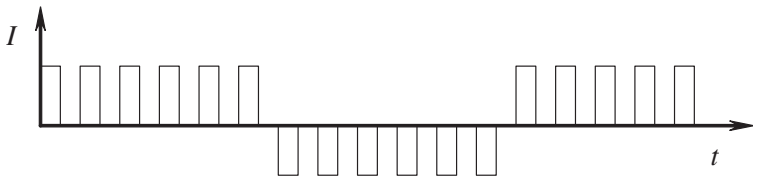

Figure 1: Map of dual-frequency synthetic current.

Been observed on the surface are potential differences of high frequency and low frequency, according to which we can calculate the apparent frequency, apparent resistivity and other parameters, thereby obtaining the information about the buried polarizable body.

The measurement parameters of dual-frequency IP method are usually apparent frequency F_s and absolute phrase $\varphi(\omega)$. According to the definition of apparent frequency

$$F_s = \frac{\Delta V_L - \Delta V_H}{\Delta V_L} \times 100\% \tag{1}$$

where ΔV_L and ΔV_H are potential differences of low frequency and high frequency, respectively.

The absolute phrase is defined as

$$\varphi(\omega) = \text{arctg}\frac{\text{Im}\Delta V(i\omega)}{\text{Re}\Delta V(i\omega)} \tag{2}$$

where $\text{Im}\Delta V(i\omega)$ and $\text{Re}\Delta V(i\omega)$ are imaginary part and real part of complex electric potential surveyed on the earth surface under a certain frequency.

3. BOUNDARY VALUE PROBLEMS AND VARIATIONAL EQUATIONS FOR ELECTRIC POTENTIAL

The dual-frequency IP method is typically frequency domain IP method, where the frequency is usually range from 10^{-2} to 10^2 Hz. so that the effects of displacement current can be eliminated [3]. To simplify the calculation, we ignore the electromagnetic effect (vector potential A is invariant with the changing of time). In the condition of volume polarization, the resistivities of the earth and anomalous body in 3-D model are replaced with the complex resistivity in Cole-Cole model, then through numerical simulation the complex potentials of different frequencies are obtained. The boundary value problem for potentials in 3-D and dipole sources model is [4]

$$\begin{cases} \nabla \cdot (\sigma \nabla u) = -2I\delta(A) + 2I\delta(B) & \in \Omega \\ \partial u/\partial n = 0 & \in \Gamma_s \\ \partial u/\partial n + 1/(r_B - r_A) \cdot [r_B/r_A \cos(r_A, n) - r_A/r_B \cos(r_B, n)]\, u = 0 & \in \Gamma_\infty \end{cases} \tag{3}$$

where u is electric potential, σ is conductivity in 3-D ground, I is amplitude of current, Ω is domain of the model, n is the unit vector of exterior normal direction of the boundary, Γ_s is the ground surface boundary, r_A, r_B are distances between survey point to source points A and B, respectively, Γ_∞ is infinite boundary.

The variational equation being equivalent to the boundary value problem (3) is

$$\begin{cases} F(u) = \displaystyle\int_\Omega \left[\frac{1}{2}\sigma(\nabla u)^2 d\Omega - 2I\delta(A)u + 2I\delta(B)u\right] d\Omega \\ \qquad\quad + \dfrac{1}{2}\displaystyle\int_{\Gamma_\infty} \sigma/(r_B - r_A)[r_B/r_A \cos(r_A, n) - r_A/r_B \cos(r_B, n)]u^2 d\Gamma \\ \delta F(u) = 0 \end{cases} \tag{4}$$

Through seeking the variation of Equation (4), a set of linear equations formatted as $Ax = b$ are derived, where A is a large coefficient matrix and x is a matrix of complex potentials on each point of the model. Because the intermediate gradient method is one of the most widely used prospecting methods in induced polarization method and it is suitable for detecting vertical ore vein with high resistivity and horizontal ore vein with low resistivity, so this method was adopted in our numerical simulations.

4. NUMERICAL TESTS

The model is showed in Figure 2. The size of the half space is 500 m × 100 m × 100 m and the parameters in Cole-Cole model are as following: Resistivity in zero frequency $\rho_1 = 10\,\Omega\cdot$m, charging rate $M_1 = 0.04$, time constant $\tau_1 = 1$, frequency dependent factor $c_1 = 0.25$. In the center of the half space is a polarized anomalous body with size of 10 m × 10 m × 10 m. The corresponding parameters in Cole-Cole model are $\rho_2 = 10\,\Omega \cdot$ m, $M_2 = 0.8$, $\tau_2 = 50$ and $c_2 = 0.25$. Distance between sources is $AB = 1000$ m and electrode spacing is $MN = 10$. The intermediate gradient method is employed.

When the depth of the polarized anomalous body is becoming deeper from 30 m by a spacing of 10 m, adopting two frequencies as $f_1 = 1$ Hz and $f_2 = 13$ Hz, the electric differences on each points

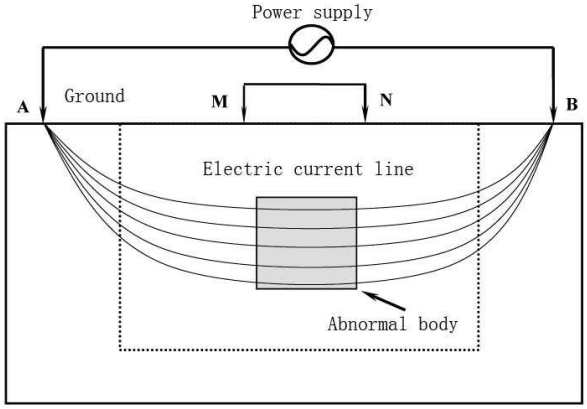

Figure 2: Map of dual-frequency IP model.

along the central line are obtained by numerical simulation, from which the curves of apparent frequency can be drawn. Figure 3 are curves of apparent frequency varying with depth. When charging rate is set as 0.1, 0.3, 0.5, 0.7 and 0.9, curves of apparent frequency varying with charging rate can be derived.

As showed in Figure 3, the curves have varied characteristics with different buried depth. With increasing of the buried depth of anomalous body, the maximum value of apparent frequency curve is decreasing, which is accordant with field cases. At the same time, the secondary potential is declining, which brings difficulty for detecting deep orebody. Then it could be concluded from Figure 4 that with the increase of charging rate, the peak of apparent frequency curve is raising, which proves that the charging rate is a critical factor for apparent frequency.

When the frequencies were set to be invariant (1, 13 Hz) and $\tau_2 = 50$ s, $c_2 = 0.25$, $m_2 = 0.3$, the curves for absolute phrase of low and high frequency along the central line could be derived by numerical simulation (Figure 5). When the time constant was set as 1000 s and all other parameters were keeping invariant, we got the values of absolute phrase along the central line (Figure 6).

It could be concluded from Figures 5 and 6 that when the charging rate of the polarized anomalous body is higher than that of the back ground, the curves of absolute phrase along the central line are mostly minus and the minimum value is reached on the central point of the polarized anomalous body. The same conclusion can be drawn when the time constant is 1000 s and the minimum value of the high frequency is always higher than that of the lower frequency.

Figure 7 shows a sounding profile of dual-frequency IP method with frequencies of 1 Hz and 13 Hz. We can easily ascertain the location of the anomalous body through the characteristic of the curves obtained on horizontal earth surface. Through numerical simulation by finite element

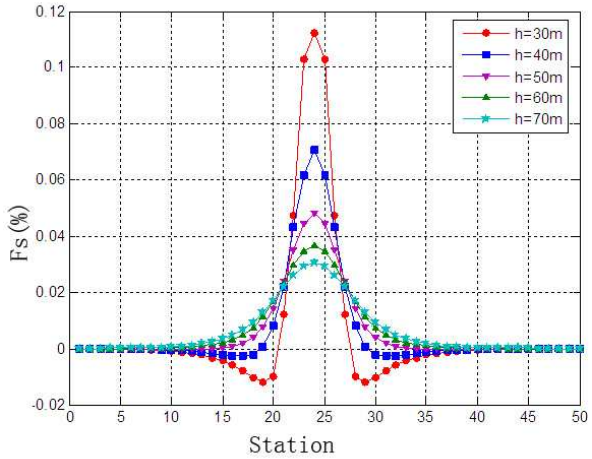

Figure 3: Map of the F_s at different deepth.

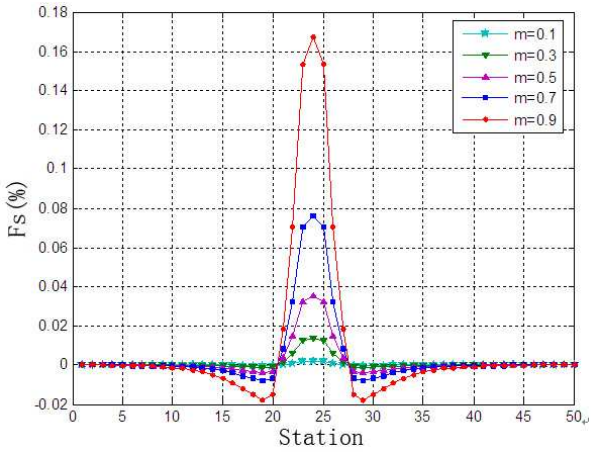

Figure 4: Map of the F_s at different m.

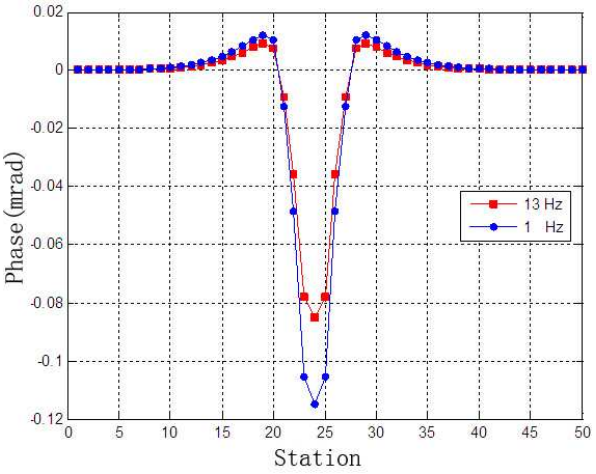

Figure 5: Map of the φ at $m_2 = 0.3$.

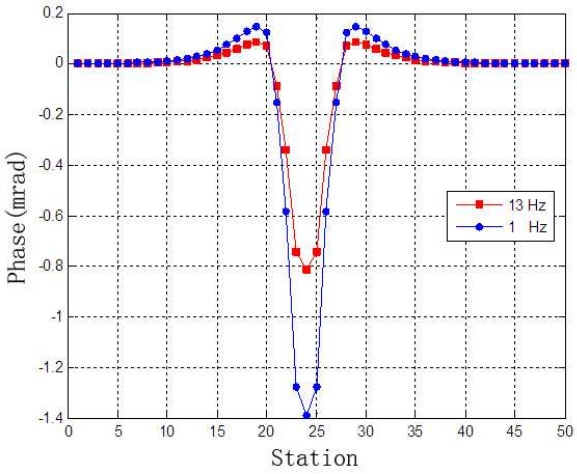

Figure 6: Map of the φ at $\tau = 1000$.

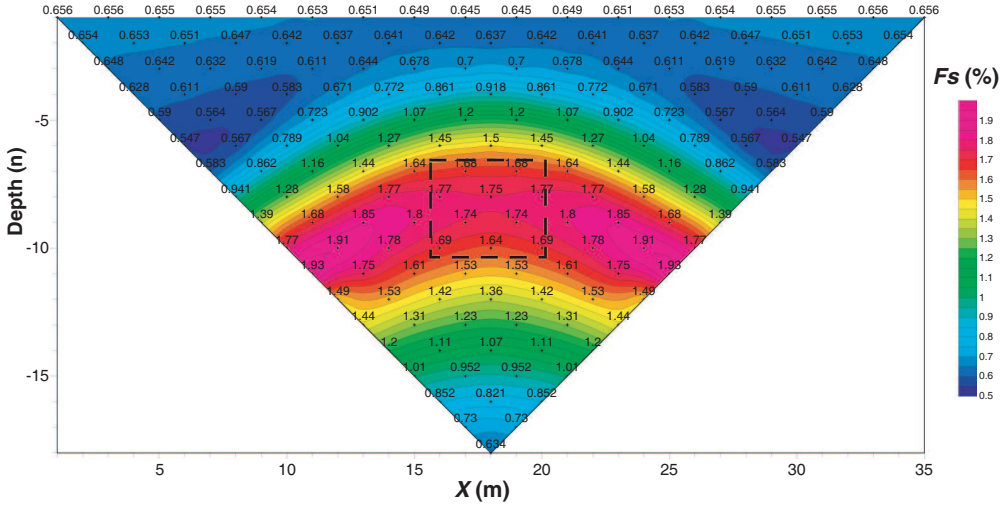

Figure 7: The sketch map of modeling.

method it could be derived that just like the apparent frequency, the anomalous body can also be detected by means of absolute phrase.

5. CONCLUSION

1. The successful numerical tests show that the finite element method can be used for dual-frequency IP method forward modeling. The merits of dual-frequency IP method, such as portability, efficiency, high accuracy and strong anti-interference ability, can be combined with the advantage of finite element method that it is suitable for complex geophysical conditions, which could possibly deduce the multiple solutions in geophysical prospecting.
2. Based on the results showed by numerical simulations, we can see that by finite element method the characteristics of apparent frequency and absolute phrase could be obtained from all kinds of geoelectrical models, which also proves that the method is correct and applicable.

REFERENCES

1. He, J.-H., *Dual-frequency IP Method*, Higher Education Press, Beijing, 2006.
2. Li, J.-M., "About the development of electrical prospecting methods," *Geophysical and Geochemical Exploration*, Vol. 20, No. 4, 93–95, 1996.
3. Huang, J.-G., "3D resistivity/IP modeling and inversion based on FEM," Central South University, Changsha, 2003.
4. Huang, J.-G., B.-Y. Ruan, and J.-L. Wang, "The fast inversion for advanced detection using DC resistivity in tunnel," *Chinese J. Geophys.*, Vol. 50, No. 2, 618–624, 2007 (in Chinese).

5. Wu, W.-L., Z.-N. Guan, Y.-F. Gao, and G.-W. Gu, "Interactiv man/computer moding 3D body of gravity and magnetic anomaly data," *Computing Techniques for Geophysical and Geochemical Exploration*, Vol. 27, No. 3, 2005.
6. Xu, S.-Z., "The integral-iteration method for continuation of potential fields," *Chinese J. Geophys.*, Vol. 49, No. 4, 1176–1182, 2006.
7. Xu, S.-Z., *The Finite Element Method in Geophysics*, Science Press, Beijing, 1994 (in Chinese).
8. Wang, R., M.-Y. Wang, and Q.-Y. Di, "Electromagnetic modeling due to line source in frequency domain using finite element method," *Chinese J. Geophys.*, Vol. 49, No. 6, 1858–1866, 2006 (in Chinese).
9. Song, Z.-P., Z.-W. Li, W.-Z. Li, and Y. Li, "Reserch on seismic modeling with high accuracy for a complicated model," *Computing Techniques for Geophysical and Geochemical Exploration*, Vol. 29, No. 6, 2007.
10. Zheng, S.-T., Z.-F. Zeng, and F.-S. Wu, "High frequency electromagnetic modeling in time domain," *Computing Techniques for Geophysical and Geochemical Exploration*, Vol. 29, No. 6, 2007.
11. Yang, X. H., J. S. He, and X. Z. Tong, "Numerical simulation of frequency-domain IP with FEM," *Progress in Geophysics*, Vol. 23, No. 4, 1186–1189, 2008 (in Chinese).
12. Fu, L.-K., *Induced Polarization Method*, Geological Publishing House, Beijing, 1982.
13. Li, Q., *Introduction to Geophysical Numerical Methods*, Geological Publishing House, Beijing, 1991.
14. Tang, J.-T., Z.-Y. Ren, and X.-R. Hua, "The forward modeling and inversion in geophysical electromagnetic field," *Progress in Geophysics*, Vol. 22, No. 4, 1181–1194, 2007 (in Chinese).
15. Yang, W.-C., *Geophysical Inversion Theory and Method*, Geological Publishing House, 1996.
16. Tang, J.-T., Z.-Y. Ren, and X.-R. Hua, "Theoretical analysis of geo-electromagnetic modeling on Coulomb gauged potentials by adaptive finite element method," *Chinese J. Geophys.*, Vol. 50, No. 5, 1584–1594, 2007.